สัญญาเลขที่ DPG5880003

รายงานฉบับสมบูรณ์

การศึกษาเครื่องปฏิกรณ์แบบหลายหน้าที่และการรวมกระบวนการสำหรับอุตสาหกรรมเคมี ปิโตรเคมีและไบโอรีไฟเนอรี

โดย ศาสตราจารย์ ดร. สุทธิชัย อัสสะบำรุงรัตน์
จุฬาลงกรณ์มหาวิทยาลัย

สนับสนุนโดยสำนักงานกองทุนสนับสนุนการวิจัย
(ความเห็นในรายงานนี้เป็นของผู้วิจัย สกว. ไม่จำเป็นต้องเห็นด้วยเสมอไป)

บทคัดย่อ

รายงานฉบับนี้สรุปผลผลิตจากโครงการ “การศึกษาเครื่องปฏิกรณ์แบบหลายหน้าที่และการรวมกระบวนการสำหรับอุตสาหกรรมเคมี ปิโตรเคมีและไบโอรีไฟเนอรี” ซึ่งได้รับการสนับสนุนโดยสำนักงานกองทุนสนับสนุนการวิจัย โครงการนี้มุ่งพัฒนาความรู้พื้นฐานเกี่ยวกับเครื่องปฏิกรณ์แบบหลายหน้าที่และการรวมกระบวนการสำหรับอุตสาหกรรมเคมีและปิโตรเคมี กระจายความรู้ผ่านบทความวิชาการระดับนานาชาติ ผลิตมหาบัณฑิตและดุษฎีบัณฑิต และสร้างความร่วมมือในการวิจัยที่เข้มแข็งทั้งในและนอกประเทศ

ผลผลิตจากโครงการนี้ได้แก่ บทความระดับนานาชาติในฐานข้อมูล ISI 35 บทความ บทความที่ไม่ได้อยู่ในฐานข้อมูล ISI 4 บทความ บทความที่อยู่ระหว่างการแก้ไข 2 บทความ บทความที่อยู่ระหว่างการพิจารณา 3 บทความ หนังสือ 4 เล่ม ดุษฎีบัณฑิต 8 คน มหาบัณฑิต 18 คน และสิทธิบัตร 1 ผลงาน ผู้ร่วมโครงการหลายท่านได้รับการเลื่อนตำแหน่งทางวิชาการและได้รับรางวัลต่าง ๆ ความร่วมมือในการวิจัยระหว่างผู้ร่วมโครงการ ระดับประเทศ และระดับนานาชาติได้ถูกสร้างขึ้น ความสำเร็จของโครงการนี้ได้ร่วมเป็นส่วนหนึ่งของการพัฒนาประเทศไทย

คำสำคัญ: เครื่องปฏิกรณ์แบบหลายหน้าที่ การรวมกระบวนการ ตัวเร่งปฏิกิริยาเคมี คาตาไลซิส ปิโตรเคมี

Abstract

This report summarizes the outputs from the project entitled "Study on Multifunctional Reactors and Process Intensification for Chemical and Petrochemical Industries and Biorefinery" which was supported by the Thailand Research Fund. The project was aimed to develop new basic knowledge related to multifunctional reactors and process intensification for chemical and petrochemical industries, to disseminate the knowledge via international publications, to graduate master and Ph.D. students, and to establish strong research collaboration in both national and international levels.

From this project, the overall outputs can be summarized as follows: 35 accepted international papers in ISI database, 4 accepted papers outside ISI database, 2 papers under revision, 3 international papers under consideration, 4 reviews/book chapters, 8 Ph.D., 18 MEng. and 1 Patent. The research team members have been academically promoted and received a number of important awards. Strong research collaborations have been established among the research team members and collaborators both in national and international levels. The success of this project is certainly beneficial to the growth of Thailand economy.

Keywords: multifunctional reactor; process intensification; catalyst; catalysis; petrochemical

สัญญาเลขที่ DPG5880003

โครงการวิจัย: การศึกษาเครื่องปฏิกรณ์แบบหลายหน้าที่และการรวมกระบวนการสำหรับอุตสาหกรรมเคมี ปิโตรเคมีและไบโอรีไฟเนอรี

รายงานฉบับสมบูรณ์

ชื่อหัวหน้าโครงการ ศ.ดร. สุทธิชัย อัสสะบำรุงรัตน์

รายงานในช่วงเวลาตั้งแต่วันที่ 1 พฤษภาคม พ.ศ. 2558 **ถึง** 31 กรกฎาคม พ.ศ. 2561

1. กิจกรรมที่ได้ดำเนินการ

1.1 ด้านการประสานงานระหว่างผู้ดำเนินการ

เนื่องจากคณะผู้วิจัยประกอบด้วยนักวิจัยที่ทำงานประจำอยู่ที่ จุฬาลงกรณ์มหาวิทยาลัย จำนวน 7 ท่านแล้วยังประกอบด้วยนักวิจัยอีก 9 ท่านที่ทำงานประจำต่างสถาบัน ได้แก่ มหาวิทยาลัยเทคโนโลยีพระจอมเกล้าธนบุรี (1 ท่าน) สถาบันเทคโนโลยีพระจอมเกล้าเจ้าคุณทหารลาดกระบัง (2 ท่าน) มหาวิทยาลัยเทคโนโลยีพระจอมเกล้าพระนครเหนือ (1 ท่าน) มหาวิทยาลัยศิลปากร (1 ท่าน) มหาวิทยาลัยศรีนครินทร์วิโรฒ (1 ท่าน) มหาวิทยาลัยบูรพา (2 ท่าน) และมหาวิทยาลัยเทคโนโลยีราชมงคลกรุงเทพ (1 ท่าน) จึงได้มีการประชุมกลุ่มย่อยในโครงการย่อยต่างๆ ตามระยะเวลาที่เหมาะสม

2. ผลงาน

2.1 บทความวิจัยในวารสารระดับนานาชาติ

2.1.1 ผลงานที่ได้รับการตอบรับให้ตีพิมพ์แล้ว (ฐาน ISI) จำนวน 35 ผลงาน

1) Pajareeya Songserm, Sitanan Thitiprasert, Vasana Tolieng, Jiraporn Piluk, Somboon Tanasupawat, Sutthichai Assabumrungrat, Shang-Tian Yang, Aphichart Karnchanatat, **Nuttha Thongchul**, "Regulating Pyruvate Carboxylase in the Living Culture of *Aspergillus Terreus* Nrrl 1960 by l-Aspartate for Enhanced Itaconic Acid Production", Applied Biochemistry and Biotechnology, 177 (2015) 595-609. (IF-2016 = 1.751) (ภาคผนวก 1) **Q2**
2) Janewit Phromprasit, Jonathan Powell, **Suttichai Assabumrungrat**, "Metals (Mg, Sr and Al) modified CaO based sorbent for CO_2 sorption/desorption stability in fixed bed reactor for high temperature application", Chem. Eng. J., 284 (2016) 1212–1223. (IF-2016 = 6.216) (ภาคผนวก 2) **Q1**

3) Pichayapan Kongpanna, Deenesh K. Babi, Varong Pavarajarn, **Suttichai Assabumrungrat**, Rafiqul Gani, "Systematic methods and tools for design of sustainable chemical processes for CO_2 utilization", Comp. Chem. Eng., 87 (2016) 125–144. (IF-2016 = 3.024) (ภาคผนวก 3) **Q1**

4) T. Jiwanuruk, S. Putivisutisak, P. Bumroongsakulsawat, T. Tagawa, H. Yamada, **S. Assabumrungrat**, "Effect of flow arrangement of micro membrane reformer for H_2 production from methane", Chem. Eng. J., 293 (2016) 319-326. (IF-2016 = 6.216) (ภาคผนวก 4) **Q1**

5) Sitanan Thitiprasert, Varunee Pimtong, Kentaro Kodama, Sarintip Sooksai, Somboon Tanasupawat, Sutthichai Assabumrungrat, Vasana Tolieng, **Nuttha Thongchul**, "Correlative effect of dissolved oxygen and key enzyme inhibitors responsible for l-lactate production by immobilized *Rhizopus oryzae* NRRL395 cultivated in a static bed bioreactor", Process Biochemistry, 51 (2016) 204-212. (IF-2016 = 2.497) (ภาคผนวก 5) **Q2**

6) Janewit Phromprasit, Jonathan Powell, Suwimol Wongsakulphasatch, Worapon Kiatkittipong, Palang Bumroongsakulsawat, **Suttichai Assabumrungrat**, "Activity and stability performance of multifunctional catalyst (Ni/CaO and Ni/$Ca_{12}Al_{14}O_{33}$-CaO) for bio-hydrogen production from sorption enhanced biogas steam reforming", International Journal of Hydrogen Energy, 41 (2016) 7318-7331. (IF-2016 = 3.582) (ภาคผนวก 6) **Q1**

7) Jutipong Poosumas, Kanokwan Ngaosuwan, Armando T. Quitain, **Suttichai Assabumrungrat**, "Role of ultrasonic irradiation on transesterification of palm oil using calcium oxide as a solid base catalyst", Energy Conversion and Management, 120 (2016) 62-70. (IF-2016 = 5.589) (ภาคผนวก 7) **Q1**

8) Anamol Tripathi, Kajornsak Faungnawakij, Apirat Laobuthee, Suttichai Assabumrungrat, **Navadol Laosiripojna**, Catalytic activity of bimetallic Cu-Ag/MgO-SiO_2 toward the conversion of ethanol to 1,3-butadiene, International Journal of Chemical Reactor Engineering, 14 (2016) 945-954. (IF-2016 = 0.623) (ภาคผนวก 8) **Q3**

9) F. Alzahrani, M. Aldehani, H. Rusi, M. McMaster, D.L.A. Fernandes, Suttichai Assabumrungrat , M. N. tSaoir and **F. Aiouache**, "Gas flow visualisation in low aspect ratio packed beds by three-dimensional modelling and near-infrared tomography", Industrial & Engineering Chemistry Research, 54 (2016) 12714-12729. (IF-2016 = 2.843) (ภาคผนวก 9) **Q1**

10) Mohammed Aldehani, Faris Alzahrani, Meabh Nic An tSaoir, Suttichai Assabumrungrat and **Farid Aiouache**, "Kinetics and reactive stripping modelling of hydrogen isotopic exchange of deuterated waters", Chem. Eng. Proc., 108 (2016) 58-73. (IF-2016 = 2.234) (ภาคผนวก 10) **Q1**

11) Chayanit Choomwattana, Aksornchan Chaianong, Worapon Kiatkittipong, Pichayapan Kongpanna, Armando T. Quitain, **Suttichai Assabumrungrat**, "Process Integration of Dimethyl Carbonate and Ethylene Glycol Production from Biomass", Chem. Eng. Proc., 107 (2016) 80-93. (IF-20156 = 2.234) (ภาคผนวก 11) **Q1**

12) Janewit Phromprasit, Jonathan Powell, Suwimol Wongsakulphasatch, Worapon Kiatkittipong, Palang Bumroongsakulsawat, **Suttichai Assabumrungrat**, "H_2 production from sorption enhanced steam reforming of biogas using multifunctional catalysts of Ni over Zr-, Ce- and La-modified CaO sorbents", Chemical Engineering Journal, 313 (2017) 1415-1425. (IF-2016 = 6.218) (ภาคผนวก 12) **Q1**

13) Varunee Pimtong, Siriporn Ounaeb, Sitanan Thitiprasert, Vasana Tolieng,Sarintip Sooksai, Ruethairat Boonsombat, Somboon Tanasupawat, Suttichai Assabumrungrat, **Nuttha Thongchul**, "Enhanced effectiveness of Rhizopus oryzae by immobilization in a static bed fermentor for l-lactic acid production", Process Biochemistry, 52 (2017) 44-52. (IF-2016 = 2.497) (ภาคผนวก 13) **Q2**

14) **Authayanun, S.**, Saebea, D., Patcharavorachot, Y., Assabumrungrat, S. and Arpornwichanop, A., "Optimal design of different reforming processes of the actual composition of bio-oil for high-temperature PEMFC system", International Journal of Hydrogen Energy 42 (2017) 1977-1988. (IF-2016 = 3.582) (ภาคผนวก 14) **Q1**

15) Visitdumrongkul, N., Tippawan, P., Authayanun, S., Assabumrungrat, S. and **Arpornwichanop, A.**, "Enhanced performance of solid oxide electrolysis cells by integration with a partial oxidation reactor: Energy and exergy analyses", Energy Conversion and Management, 129 (2016) 189-199. (IF-2016 = 5.589) (ภาคผนวก 15) **Q1**

16) Simasatitkul, L., Kaewwisetkul, P., Wiyaratn, W., Assabumrungrat, S. and **Arpornwichanop, A.**, "Optimal design and performance analyses of the glycerol ether production process using a reactive distillation column", Journal of Industrial and Engineering Chemistry, 43 (2016) 93-105. (IF-2016 = 4.421) (ภาคผนวก 16) **Q1**

17) Tippawan, P., Thammasit, T., Assabumrungrat, S. and **Arpornwichanop, A.,** "Using glycerol for hydrogen production via sorption-enhanced chemical looping reforming: Thermodynamic analysis", Energy Conversion and Management, 124 (2016) 325-332. (IF-2016 = 5.589) (ภาคผนวก 17) **Q1**

18) Nakyai, T., Authayanun, S., Patcharavorachot, Y., Arpornwichanop, A., Assabumrungrat, S. and **Saebea, D.,** "Exergoeconomics of hydrogen production from biomass air-steam gasification with methane co-feeding", Energy Conversion and Management, 140 (2017) 228-239. (IF-2016 = 5.589) (ภาคผนวก 18) **Q1**

19) Wiranarongkorn, K., Authayanun, S., Assabumrungrat, S. and **Arpornwichanop, A.** (2016). Analysis of thermally coupling steam and tri-reforming processes for the production of hydrogen from bio-oil. International Journal of Hydrogen Energy, 41, 18370-18379. (IF-2016 = 3.582) (ภาคผนวก 19) **Q1**

20) Phunpee, S., Ruktanonchai, U.R., Yoshii, H., Assabumrungrat, S., **Soottitantawat, A.**, "Encapsulation of lemongrass oil with cyclodextrins by spray drying and its controlled release characteristics", Bioscience, Biotechnology and Biochemistry, 81 (2017) 718-723. (IF-2015 = 1.176) (ภาคผนวก 20) **Q2**

21) Tara Jiwanuruk, Sompong Putivisutisak, Paravee Vas-Umnuay, Palang Bumroongsakulsawat, Chin Kui Cheng, **Suttichai Assabumrungrat**, "Modeling of thermally-coupled monolithic membrane reformer for vehicular hydrogen production", International Journal of Hydrogen Energy, 42 (2017) 26308-26319. (IF-2016 = 3.582) (ภาคผนวก 21) **Q1**

22) Nattawat Petchsoongsakul, Kanokwan Ngaosuwan, Worapon Kiatkittipong, Farid Aiouache, **Suttichai Assabumrungrat**, "Process design of biodiesel production: Hybridization of ester- and transesterification in a single reactive distillation", Energy Conversion and Management, 153 (2017) 493–503. (IF-2016 = 5.589) (ภาคผนวก 22) **Q1**

23) Budsabathip Prasirtsak, Sitanan Thitiprasert, Vasana Tolieng, Suttichai Assabumrungrat, Somboon Tanasupawat, **Nuttha Thongchul**, “Characterization of D-lactic acid, spore-forming bacteria and *Terrilactibacillus laevilacticus* SK5-6 as potential industrial strains”, Annals of Microbiology, 67 (2017) 763-778. (IF-2016 = 1.122) (ภาคผนวก 23) **Q3**

24) Sitanan Thitiprasert, Kentaro Kodama, Somboon Tanasupawat, Phatthanon Prasitchoke, Tanapawarin Rampai, Budsabathip Prasirtsak, Vasana Tolieng, Jiraporn Piluk, Suttichai

Assabumrungrat, **Nuttha Thongchul**, “A homofermentative *Bacillus* sp. BC-001 and its performance as a potential L-lactate industrial strain” Bioprocess and Biosystems Engineering, 40 (2017) 1787-1799. (IF-2016 = 1.870) (ภาคผนวก 24) **Q2**

25) Natnirin Phanthumchinda, Tanapawarin Rampai, Budsabathip Prasirtsak, Sitanan Thitiprasert, Somboon Tanasupawat, Suttichai Assabumrungrat, **Nuttha Thongchul**, “Alternative reverse osmosis to purify lactic acid from a fermentation broth” Chemical Industry & Chemical Engineering Quarterly, 24 (2018) 179-190. (IF-2016 = 0.664). (ภาคผนวก 25) **Q3**

26) Wilasinee Wisaijorn, Yingyot Poo-arporn, Pablo Marin, Salvador Ordonez, Suttichai Assabumrungrat, Piyasan Praserthdam, Dang Saebea, **Soipatta Soisuwan**, "Reduction of carbon dioxide via catalytic hydrogenation over copper based catalysts modified by oyster shell derived calcium oxide", Journal of Environmental Chemical Engineering, 5 (2017) 3115-3121. (CiteScore: 3.83; Source Normalized Impact per Paper (SNIP): 1.385) (ภาคผนวก 26) **Q1**

27) Natnirin Phanthumchinda, Sitanan Thitiprasert, Somboon Tanasupawat, Suttichai Assabumrungrat, **Nuttha Thongchul**, “Process and cost modeling of lactic acid recovery from fermentation broths by membrane-based process”, Process Biochemistry, 68 (2018) 205-213. (IF-2016 = 2.497) (ภาคผนวก 27) **Q2**

28) Pajareeya Songserm, Aphichart Karnchanatat, Sitanan Thitiprasert, Somboon Tanasupawat, Suttichai Assabumrungrat, Shang-Tian Yang, **Nuttha Thongchul**, “Metabolic responses of *Aspergillus terreus* under low dissolved oxygen and pH levels”, Annals of Microbiology 68 (2018) 195-205. (IF-2016 = 1.122) (ภาคผนวก 28) **Q3**

29) Osarieme Uyi Osazuwa, Maksudur R. Khan, Su Shiung Lam, Suttichai Assabumrungrat, **Chin Kui Cheng**, An Assessment of the Longevity of Samarium Cobalt Trioxide Perovskite Catalyst during the Conversion of Greenhouse Gases into Syngas, Journal of Cleaner Production, 185 (2018) 576-587. (IF-2016 = 5.715) (ภาคผนวก 29) **Q1**

30) Unchalee Suwanmanee, Dang Saebea, Viktor Hacker, Suttichai Assabumrungrat, Amornchai Arpornwichanop and **Suthida Authayanun**, “Conceptual design and life cycle assessment of decentralized power generation by HT-PEMFC system with sorption enhanced water gas shift loop”, Energy Conversion and Management, 171 (2018) 20-30. (IF-2016 = 5.589) (ภาคผนวก 30) **Q1**

31) Nattanan Wongtanyawat, Possawat Lusanandana, Nawaporn Khwanjaisakun, Pichayapan Kongpanna, Janewit Phromprasit, Lida Simasatitkul, Suksun Amornraksa, **Suttichai Assabumrungrat**, "Comparison of different Kraft lignin-based vanillin production processes", Computers & Chem. Eng., 117 (2018) 159-170. (IF-2016 = 3.024) (ภาคผนวก 31) **Q1**

32) Kraisornkachit, P., **Vivanpatarakij, S.**, Powell, J., Assabumrungrat, S., "Experimental study of dual fixed bed biochar-catalytic gasification with simultaneous feed of O_2-steam-CO_2 for synthesis gas or hydrogen production", International Journal of Hydrogen Energy, in press. (IF-2016 = 3.582) (ภาคผนวก 32) **Q1**

33) Piya Pecharaumporn, **Suwimol Wongsakulphasatch**, Thongchai Glinrun, Atthaphon Maneedaeng, Zulkafli Hassan, Suttichai Assabumrungrat, "Synthetic CaO-based sorbent for high-temperature CO_2 capture in sorption-enhanced hydrogen production", International Journal of Hydrogen Energy, in press (IF-2016 = 3.74) (ภาคผนวก 33) **Q1**

34) **Patcharavorachot**, **Y.**, Chatrattanawet, N., Arpornwichanop, A. and Assabumrungrat, S. "Optimization of hydrogen production from three reforming approaches of glycerol via using supercritical water with *in situ* CO_2 separation", International Journal of Hydrogen Energy, accepted (IF-2016 = 3.582) (ภาคผนวก 34) **Q1**

35) Ghochapon Mongkhonsiri, Rafiqul Gani, Pomthong Malakul, **Suttichai Assabumrungrat**, "Integration of the Biorefinery Concept for the Development of Sustainable Processes for Pulp and Paper Industry", Comp. Chem. Eng., accepted (IF-2016 = 3.024) (ภาคผนวก 35) **Q1**

2.1.2 ผลงานที่ได้รับการตอบรับให้ตีพิมพ์แล้ว (ไม่อยู่ในฐาน ISI) จำนวน 4 ผลงาน

1) **Wiyaratn W**, Manundawee S, Arpornwichanop A, Assabumrungrat S, Watanapa S and Worawimut C, "Two-dimensional Mathematical Modeling of the Oxidative Coupling of Methane in a Membrane Reactor", Engineering Journal, 20 (2016) 17-33 (IF-2014 = -). (ภาคผนวก 36)

2) Saebea, D., Patcharavorachot, Y., Hacker, V., Assabumrungrat, S., Arpornwichanop, A. and **Authayanun, S.** (2017). Analysis of unbalanced pressure PEM electrolyzer for high pressure hydrogen production. Chemical Engineering Transactions, 57, 1615-1620. (Scopus) (SJR-2016 = 0.346) (ภาคผนวก 37)

3) **Saebea, D.**, Authayanun, S., Patcharavorachot, Y., Soisuwan, S., Assabumrungrat, S. and Arpornwichanop, A. (2017). Performance analysis of solid-oxide electrolysis cells for syngas production by H_2O/CO_2 co-electrolysis. Chemical Engineering Transactions, 57, 1672-1632. (Scopus) (SJR-2016 = 0.346) (ภาคผนวก 38)

4) Worawimut, C., **Vivanpatarakij, S.**, Watanapa, A., Wiyaratn, W., Assabumrungrat, S., (2018). Purification and Upgrading from Biogas to Biomethane. Journal of Japan Institute of Energy, accepted (Scopus) (SJR-2016 = 0.202) (ภาคผนวก 39)

2.1.3 จำนวนผลงานที่อยู่ในขั้นตอนการแก้ไข จำนวน 2 ผลงาน

1) Pichamon Mongkolsiri, Salinee Jitkeaw, Yaneeporn Patcharavorachot, Amornchai Arpornwichanop, Suttichai Assabumrungrat and **Suthida Authayanun**, "Comparative analysis of biomass and coal based co-gasification processes with and without CO_2 capture for HT-PEMFCs", International Journal of Hydrogen Energy (IF-2016 = 3.582) **Q1**

2) Tanutporn Laosuttiwong, **Kanokwan Ngaosuwan,** Worapon Kiatkittipong, Doonyapong Wongsawaeng, Suttichai Assabumrungrat, "Performance comparison of different cavitational reactors for biodiesel production via transesterification of palm oil", Journal of Cleaner Production, (IF-2016 = 5.715) **Q1**

2.1.4 ผลงานที่อยู่ระหว่างการพิจารณา จำนวน 3 ผลงาน

1) **Wiyaratn W**, Manundawee S, Arpornwichanop A, and Assabumrungrat S, Two-dimensional modeling of the oxidative coupling of methane in a fixed bed reactor: a comparison among different catalysts", Songklanakarin Journal of Science and Technology (SJST) (Q2 index:14)

2) Winatda Prachumsai, Suwat Pangtaisong, Suttichai Assabumrungrat, Piyasan Praserthdam, Dang Saebae, **Soipatta Soisuwan**, "Thermodynamic analysis and intrinsic characteristics of Tosoh zirconia supported copper-based catalysts for CO_2 hydrogenation", submitted to Chemical Engineering & Technology (IF-2016 = 2.051). **Q1**

3) Hattachai Aeowjaroenlap, **Supawat Vivanpatarakij**, Amornchai Arpornwichanop, Suttichai Assabumrungrat and Wisitsree Wiyaratn, "Design and development of Ethylene Carbonate production process from biogas", submitted to Chemical Engineering & Technology (IF-2017 = 1.588). **Q2**

2.2 Book/reviews

1) หนังสือเรื่อง เคมีฟิสิกัลสำหรับวิศวกรรมเคมีและวิทยาศาสตร์ประยุกต์ เรียบเรียง โดย สร้อยพัทธา สร้อยสุวรรณ (ตีพิมพ์ ISBN: 978-616-468-232-0)
2) หนังสือเรื่อง ระบบเซลล์เชื้อเพลิงชนิดออกไซด์แข็ง: การจำลอง การออกแบบ และการวิเคราะห์ แต่งโดย อมรชัย อาภรณ์วิชานพ (ต้นฉบับอยู่ที่สำนักพิมพ์จุฬาลงกรณ์มหาวิทยาลัย)
3) หนังสือเรื่อง วัสดุของแข็งรูพรุนสำหรับดูดซับก๊าซคาร์บอนไดออกไซด์ แต่งโดย สุวิมล วงศ์สกุลเภสัช (ระหว่างการจัดเตรียม)
4) หนังสือเรื่อง เชื้อเพลิงชนิดกรีนดีเซล แต่งโดย วรพล เกียรติกิตติพงษ์ (ระหว่างการจัดเตรียม)

2.3 จำนวนนิสิตที่จบ

2.3.1 ดุษฎีบัณฑิต สำเร็จการศึกษา 8 คน

1) นายพิชญพันธ์ คงปันนา	จุฬาลงกรณ์มหาวิทยาลัย
2) นายธารา จิวานุรักษ์	จุฬาลงกรณ์มหาวิทยาลัย
3) นายเจนวิทย์ พรหมประสิทธิ์	จุฬาลงกรณ์มหาวิทยาลัย
4) นายทรงพล พิมเสน	มหาวิทยาลัยศิลปากร
5) นางสาวปาจรีรยา ส่งเสริม	จุฬาลงกรณ์มหาวิทยาลัย
6) นางสาวบุษบาทิพย์ ประเสริฐศักดิ์	จุฬาลงกรณ์มหาวิทยาลัย
7) นางสาวณัฏฐ์นิรินทน์ พันธุมจินดา	จุฬาลงกรณ์มหาวิทยาลัย
8) นายเกียรติคุณ เผือกพ่วง	จุฬาลงกรณ์มหาวิทยาลัย

2.3.2 มหาบัณฑิต สำเร็จการศึกษา 18 คน

1) นางสาวบงกช วกุลชัย	จุฬาลงกรณ์มหาวิทยาลัย
2) นายเอกชน ผู้เลื่องลือ	จุฬาลงกรณ์มหาวิทยาลัย
3) นางสาวปิยา ชักชวน	จุฬาลงกรณ์มหาวิทยาลัย
4) นางสาววรรัตน์ รัตนชัย	สถาบันเทคโนโลยีพระจอมเกล้าเจ้าคุณทหารลาดกระบัง
5) นางสาวธนาภรณ์ หาเคน	จุฬาลงกรณ์มหาวิทยาลัย
6) นางสาวศิราภา ทองดี	จุฬาลงกรณ์มหาวิทยาลัย
7) นายณัฐวัตร เพชรสูงสกุล	จุฬาลงกรณ์มหาวิทยาลัย
8) นางสาววิลาสินี วัสัยจร	มหาวิทยาลัยบูรพา
9) นางสาววิณัฐดา ประชุมสาย	มหาวิทยาลัยบูรพา
10) นางสาวกฤตยา ศรัณยโชติ	มหาวิทยาลัยบูรพา

11) นางสาวชนิตา วัฒนสมบูรณ์ จุฬาลงกรณ์มหาวิทยาลัย
12) นางสาวศิริพร เอี่ยมสุขใส จุฬาลงกรณ์มหาวิทยาลัย
13) นางสาวนวพร ขวัญใจสกุล จุฬาลงกรณ์มหาวิทยาลั
14) นางสาวศิริกานต์ สัตถวิชยพิชญ์ จุฬาลงกรณ์มหาวิทยาลัย
15) นางสาวกันต์กนิษฐ์ กิจสหวงศ์ จุฬาลงกรณ์มหาวิทยาลัย
16) นายพิสิษฐ์ วิริกุลเจริญ จุฬาลงกรณ์มหาวิทยาลัย
17) นายธนัชพร เหล่าสุทธิวงศ์ จุฬาลงกรณ์มหาวิทยาลัย
18) นายคุณวัฒน์ อุนทักษิณกุล จุฬาลงกรณ์มหาวิทยาลัย

2.4 สิทธิบัตร

ชื่อหัวข้อ: เครื่องปฏิกรณ์แบบเยื่อแผ่นประเภทโมโนลิทควบคู่ความร้อนสำหรับผลิตไฮโดรเจน
Thermally Coupled Monolithic Membrane Reformer for Hydrogen Production
ชื่อผู้ประดิษฐ์: นายสุทธิชัย อัสสะบำรุงรัตน์ นายสมพงษ์ พุทธิวิสุทธิศักดิ์ นายธารา จิวานุรักษ์
เลขที่คำขอ: 1401004679 วันที่ยื่น 15 พฤศจิกายน 2559 (ภาคผนวก 40)

2.5 สัมมนา

ครั้งที่ 1

เมื่อวันศุกร์ที่ 27 พฤษภาคม พ.ศ. 2559 คณะผู้วิจัยได้จัดการสัมมนาเชิงวิชาการหัวข้อ “การศึกษาเครื่องปฏิกรณ์แบบหลายหน้าที่และการรวมกระบวนการสำหรับอุตสาหกรรมเคมี ปิโตรเคมี และไบโอรีไฟเนอรี” ณ ห้องประชุม 209 อาคารสาม คณะวิศวกรรมศาสตร์ จุฬาลงกรณ์มหาวิทยาลัย การสัมมนาครั้งนี้มีผู้เข้าร่วมประมาณ 60 คน

ครั้งที่ 2

เมื่อวันศุกร์ที่ 14 กรกฎาคม พ.ศ. 2560 คณะผู้วิจัยได้จัดการสัมมนาเชิงวิชาการหัวข้อ “การศึกษาเครื่องปฏิกรณ์แบบหลายหน้าที่และการรวมกระบวนการสำหรับอุตสาหกรรมเคมี ปิโตรเคมี และไบโอรีไฟเนอรี” ณ ห้องประชุม 209 อาคารสาม คณะวิศวกรรมศาสตร์ จุฬาลงกรณ์มหาวิทยาลัย การสัมมนาครั้งนี้มีผู้เข้าร่วมประมาณ 70 คน

ครั้งที่ 3

เมื่อวันศุกร์ที่ 1 มิถุนายน พ.ศ. 2561 ได้ร่วมกับ Kumamoto University จัด Joint International Symposium ในหัวข้อ “Multifunctional Reactors and Process Intensification for Chemical, Petrochemical and Biorefinery Industries” ณ ห้อง 105 อาคารมหาจุฬาลงกรณ์ คณะอักษรศาสตร์ จุฬาลงกรณ์มหาวิทยาลัย มีทีมวิจัยจาก Kumamoto จำนวน 11 คน ประเทศฟิลิปปินส์

1 คน ประเทศมาเลเซีย 3 คน ประเทศอินโดนีเซีย 1 คน สิงคโปร์ 1 คน และจากประเทศไทยอีก ประมาณ 80 คน

3. อื่น ๆ

3.1 การประชุมวิชาการ

1) Malithong, S., Assabumrungrat, S. and **Arpornwichanop, A.** (2016). Investigating the Performance of Circulating Fluidized Bed-Oxyfuel Combustion in a Coal Fired Power Plant. Pure and Applied Chemistry International Conference 2016 (PACCON 2016), Feb. 9-11, 2016, Bangkok, Thailand.
2) Rattanachai, W., Saebea, D., Authayanun, S., Arpornwichanop, A. and **Patcharavorachot, Y.** Performance of an Integrated Adsorption-Enhanced Glycerol Supercritical Water Reforming and Pressurized SOFC System. The 2nd International Conference on Chemical, Metallurgy and Environmental Engineering (CMAEE-16). 12-13 April, 2016, Kyoto, Japan.
3) **Authayanun, S.** and Arpornwichanop, A. Theoretical study of hydrogen production from high pressure PEM electrolyzer stack. The ECS Conference on Electrochemical Energy Conversion & Storage with SOFC-XIV. 26 – 31 July, 2015, Glasgow, Scotland.
4) **Authayanun, S.**, Saebea, D., Patcharavorachot, Y., Arpornwichanop, A. Theoretical analysis of different bio-oil reforming processes integrated with PEMFC system. The 5th International Conference on Green and Sustainable Innovation (ICGSI). 8-10 November, 2015, Pattaya, Thailand.
5) W. Rattanachai, A. Arpornwichanop and **Y. Patcharavorachot**. Performance Analysis of an Integrated System of Pressurized SOFC and Glycerol Reformer with Different CO_2 Removal Process. The 5th International Conference on Green and Sustainable Innovation (ICGSI). 8-10 November, 2015, Pattaya, Thailand.
6) **Saebea, D.** and Nakyai, T. Energy and exergy analysis of high temperature air-steam gasification of biomass with methane co-feeding. The 5th TIChE International Conference 2015. November 8-10, 2015, Pattaya, Thailand.
7) Chayanit Choomwattana, Aksornchan Chaianong, Worapon Kiatkittipong, Pichayapan Kongpanna, **Suttichai Assabumrungrat**. Evaluation of Dimethyl Carbonate and Ethylene Glycol Production from Biomass. 12th International Symposium on Process Systems Engineering and 25th European Symposium on Computer Aided Process Engineering. 31 May – 4 June 2015, Copenhagen, Denmark.

8) **Suttichai Assabumrungrat**. Overviews of Biorefinery Activities in Thailand. 2nd Workshop on ProBioRefine, December 7-8, 2015, UTM Johor Bahru, Johor, Malaysia (Invited speaker).

9) **Worapon Kiatkittipong**, S. Phimsen, K. Kiatkittipong, S. Wongsakulphasatch, N. Laosiripojana, S. Assabumrungrat Bio-hydrogenated diesel production from refining palm oil, 2nd Workshop on ProBioRefine, December 7-8, 2015, UTM Johor Bahru, Johor, Malaysia.

10) A. Phuluanglue, W. Khaodee, S. Wongsakulphasatch, W. Kiatkittipong, A. Arpornwichanop, and **S. Assabumrungrat**. Simulation of Modified Sorption Enhanced Chemical Looping Reforming for Hydrogen Production from Biogas, International Journal of Chemical, Environmental & Biological Sciences (IJCEBS) (ISSN 2320–4087) Vol 3, Iss 4 (2015) 339-343.

11) Kunlanan Kiatkittipong and **Suttichai Assabumrungrat**, "Understanding Phase Transformation of Titanate Nanoribbons by Heat Treatment", 23rd International Symposium on Chemical Reaction Engineering (ISCRE 23) and 7th Asia-Pasific Chemical Reaction Engineering Symposium (APCRE 7), Bangkok, Thailand, 7th – 10th September 2014, pp 688 – 692.

12) Thanyarutt Teerachaiyapat, **Kunlanan Kiatkittipong**, Worapon Kiatkittipong and Suttichai Assabumrungrat, "Ti-O Nanoribbon Photocatalyst: The Ion Exchange Process of Co^{2+} Intercalated in Layered Nanoribbons", 23rd International Symposium on Chemical Reaction Engineering (ISCRE 23) and 7th Asia-Pasific Chemical Reaction Engineering Symposium (APCRE 7), Bangkok, Thailand, 7th – 10th September 2014, pp 666 – 669.

13) Winatda Prachumsai, Kawin Simawattana, Nattaphone Yuchomya , Suwat Paetaisong, Wuttipatr Ruangsri, Dang Saebea, Suttichai Assabumrungrat, **Soipatta Soisuwan**, Products from Carbon Dioxide Hydrogenation by Gibb Minimization, SECAT 17, Oviedo, Spain, 26-28 June, 2017.

14) Tanutporn Laosuttiwong**, Kanokwan Ngaosuwan**, Worapon Kiatkittipong, Suttichai Assabumrungrat, Effect of mixer types on biodiesel production**,** Green Convergence on Chemical Frontier (PACCON 2017), Centra Government Complex Hotel and Conventional Center, Bangkok, Thailand, 2-3 February, 2017.

15) Winatda Prachumsai, Suwat Pangthaisong, Patipan Bunruam, Chantra Nakvachiratrakul, Dang Saebae, Suttichai Assabumrungrat and **Soipatta Soisuwan**, Carbon dioxide hydrogenation over Cu-Zn based catalysts supported on different materials and thermodynamics analysis , publication in MRS-Thailand 2017 E-proceeding, 1st MRS Thailand International Conference, Conventional Center, The Empress Hotel, Chiang Mai, Thailand, October 31st - November 3rd, 2017

16) S. Boonsuk, **W. Kiatkittipong**, K. Ngaosuwan, D. Wongsawaeng, S. Assabumrungrat, "Design and performance evaluation of sustainable process combining hydrotreating and hydrogen generation for biojet fuel production from palm oil" Pure and Applied Chemistry International Conference (PACCON2018), February 7-9, 2018

17) Phisit Wirikulcharoen, **Worapon Kiatkittipong**, Kanokwan Ngaosuwan, Suttichai Assabumrungrat, Bimetallic NiCu/HZSM-5 Catalyst in hydroprocessing of palm fatty acid distillate for green fuel production, Pure and Applied Chemistry International Conference (PACCON2017), February 2-3, 2017

18) Siriporn Aeamsuksai, Thirawat Mueansichai, Weerinda Appamana, Kanokwan Ngaosuwan, Worapon Kiatkittipong, Palang Bumroongsakulsawat and **Suttichai Assabumrungrat**, Process simulation of sodium methoxide production from methanol and sodium hydroxide using reactive distillation, Pure and Applied Chemistry International Conference (PACCON2017), February 2-3, 2017

19) B. Akassupha, **W. Kiatkittipong**, K. Kiatkittipong, N. Laosiripojana, S. Assabumrungrat Aviation fuel production from palm fatty acid distillate by a single-step hydrotreating process, 6th International Conference on Advances in Engineering Sciences and Applied Mathematics (ICAESAM'2016) Dec. 21-22, 2016 Kuala Lumpur (Malaysia)

20) Songphon Phimsen, **Worapon Kiatkittipong**, Hiroshi Yamada, Tomohiko Tagawa, Kunlanan Kiatkittipong, Navadol Laosiripojana, Suttichai Assabumrungrat, Green Diesel Production from Oil Extracted from Spent Coffee Grounds, 3rd ProBioRefine Workshop hosted by Auburn University, Alabama, 7-8 December 2016

3.2 รางวัล/การรับเชิญ

1) นายเจนวิทย์ พรหมประสิทธิ์ รางวัลนำเสนอผลงานแบบโปสเตอร์ดีเด่น RGJ-Ph.D. Congress XVII"ASEAN: Emerging Research Opportunities" วันพฤหัสบดีที่ 11 – วันเสาร์ที่ 13 มิถุนายน 2558 ณ โรงแรมจอมเทียน ปาล์ม บีช รีสอร์ท เมืองพัทยา จังหวัดชลบุรี
2) Scientific committee of XXII International conference on Chemical Reactors (CHEMREACTOR-22), University College London, UK, September 19-23, 2016. (Prof. Suttichai Assabumrungrat)
3) นายธารา จิวานุรักษ์ รางวัลนำเสนอผลงานแบบโปสเตอร์ดีเด่น RGJ-Ph.D. Congress XVII"ASEAN: Emerging Research Opportunities" วันพฤหัสบดีที่ 11 – วันเสาร์ที่ 13 มิถุนายน 2558 ณ โรงแรมจอมเทียน ปาล์ม บีช รีสอร์ท เมืองพัทยา จังหวัดชลบุรี
4) Janewit Phromprasit, Best Poster Presentation Award, CHEMREACTOR-22, University College London, 19-23 September 2016
5) Tara Jiwanuruk, Award of ACS Publications, Industrial & Engineering Chemistry Research Journal (American Chemical Society) in CHEMREACTOR-22, University College London, 19-23 September 2016
6) Scientific committee of The 8th Asia-Pacific Symposium on Chemical Reaction Engineering (APCRE 2017) North American Symposium on Chemical Reaction Engineering and European Symposium on Chemical Reaction Engineering, in Shanghai, China, November 11-13, 2017. (Prof. Suttichai Assabumrungrat)
7) Invited speaker in The 8th Asia-Pacific Symposium on Chemical Reaction Engineering (APCRE 2017) North American Symposium on Chemical Reaction Engineering and European Symposium on Chemical Reaction Engineering, in Shanghai, China, November 11-13, 2017. (Prof. Suttichai Assabumrungrat)
8) International Program Committee of Process Systems Engineering, PSE 2018, Manchester Grand Hyatt San Diego, July 1-5, 2018. (Prof. Suttichai Assabumrungrat)
9) SCIENTIFIC COMMITTEE IN THE 4th INTERNATIONAL CONFERENCE OF CHEMICAL ENGINEERING AND INDUSTRIAL BIOTECHNOLOGY 2018, 1 - 2 August 2018 in Kuala Lumpur, Malaysia. The theme for this conference is “Sustainable Technological Solutions for Industry and Society”. ICCEIB 2018 (Prof. Suttichai Assabumrungrat)
10) Invited speaker, "Sorption Enhanced Steam Reforming and Sorption Enhanced Chemical-Looping Reforming Technologies for Hydrogen Production", the Pure and Applied

Chemistry International Conference 2018 (PACCON 2018), in conjunction with the Chemical Society of Thailand (CST) under the patronage of Professor Dr. Her Royal Highness Princess Chulabhorn Mahidol. PACCON 2018, Hat Yai, Songkhla, Thailand, February 7-9, 2018.

11) Invited speaker, "Process synthesis and design of integrated biorefinery in pulp and paper industry", The 8th IUPAC International Conference on Green Chemistry (Session: Green Manufacturing / Engineering Processes), 9-14 September 2018, Bangkok.
12) ผศ.ดร.อมรชัย อาภรณ์วิชานพ ได้รับรางวัล PTIT Scholar Awards จากสถาบันปิโตรเลียมแห่งประเทศไทย ประจำปี พ.ศ. 2560-2561
13) ผศ.ดร.อมรชัย อาภรณ์วิชานพ ได้รับรางวัล นักวิจัยดีเด่น จากจุฬาลงกรณ์มหาวิทยาลัย ประจำปี 2559
14) ผศ.ดร.อมรชัย อาภรณ์วิชานพ ได้รับรางวัล ศักดิ์อินทาเนีย ประเภทผลงานได้รับการอ้างอิงสูงสุด จากคณะวิศวกรรมศาสตร์ จุฬาลงกรณ์มหาวิทยาลัย ประจำปี พ.ศ. 2559
15) ผศ.ดร.อมรชัย อาภรณ์วิชานพ ได้รับรางวัล TRF-OHEC-Scopus Researcher Award จากสำนักงานกองทุนสนับสนุนการวิจัย สำนักงานคณะกรรมการการอุดมศึกษา และ Scopus (6 ม.ค. 2559)
16) ผศ.ดร.กนกวรรณ ง้าวสุวรรณ ได้รับรางวัล ***Renewable Energy*** **Reviewer Award 2016** จากวารสาร Renewable Energy Journal สำนักพิมพ์ Elsevier
17) ผศ.ดร.แดง แซ่เบ๊ ได้รับรางวัล ผู้ที่ได้รับการตีพิมพ์เผยแพร่บทความวิจัย ระดับนานาชาติ สูงสุดอันดับที่ 1 จาก มหาวิทยาลัยบูรพา ประจำปี พ.ศ. 2560
18) ผศ.ดร.แดง แซ่เบ๊ ได้รับรางวัล ผู้ที่ที่ได้รับการตีพิมพ์เผยแพร่บทความวิจัย ระดับนานาชาติ ที่มี impact factor สูงสุดอันดับที่ 3 จาก มหาวิทยาลัยบูรพา ประจำปี พ.ศ. 2560
19) ผศ.ดร.สุธิดา อรรถยานันทน์ ได้รับรางวัล 2017-Bernd Rode Award (Junior Researcher) from the Austrian-South-East-Asian Academic University Network (ASEA-UNINET)
20) ผศ.ดร.ญาณีพร พัชรวรโชติ ได้รับรางวัล อาจารย์ที่มีผลงานตีพิมพ์ในวารสารนานาชาติ ISI ที่มี Impact factor สูงที่สุด จาก คณะวิศวกรรมศาสตร์ สถาบันเทคโนโลยีพระจอมเกล้าเจ้าคุณทหารลาดกระบัง ประจำปี พ.ศ. 2560
21) ผศ.ดร.วรพล เกียรติกิตติพงษ์ บทสัมภาษณ์เรื่อง Green diesel สถานีวิทยุจุฬา FM101.5 MHz ออกอากาศเมื่อ 4 มกราคม 2560
22) Dr. Worapon Kiatkittipong, International Program Committee for Process Systems Engineering (PSE) 2018, San Diego, California, USA , July 1-5, 2018

23) ผศ.ดร. กุลนันทน์ เกียรติกิตติพงษ์ ได้รับรางวัลอาจารย์ที่มีผลงานการถูกอ้างอิง (Citations) ในฐานข้อมูล Scopus มากที่สุด จากคณะวิศวกรรมศาสตร์ สถาบันเทคโนโลยีพระจอมเกล้าเจ้าคุณทหารลาดกระบัง

24) นายทรงพล พิมเสน ผลงานเรื่อง การผลิตเชื้อเพลิงดีเซลชนิดไฮโดรทรีตจากน้ำมันกากกาแฟ ได้รับรางวัลเป็น 1 ใน 9 ผลงานวิจัยเด่นของ คปก. ประจำปี 2560

25) นายทรงพล พิมเสน รางวัลการนำเสนอแบบปากเปล่าดีเด่นในสาขา Engineering and Technology ในการประชุมวิชาการ โครงการปริญญาเอกกาญจนาภิเษกครั้งที่ 18 ในปี 2560

26) นายพิสิษฐ์ วิริกุลเจริญ รางวัลนำเสนอผลงานแบบโปสเตอร์ดีเด่น Pure and Applied Chemistry International Conference (PACCON2017), February 2-3, 2017

4. กิจกรรมอื่นๆ

4.1 การสนับสนุนการสร้างกลุ่มวิจัย

การทำวิจัยเป็นทีมเป็นกลไกที่สำคัญอย่างมากในการสร้างสรรค์ผลงานวิจัยที่มี Impact ให้กับประเทศไทย ดังนั้นภารกิจที่สำคัญส่วนหนึ่งของหัวหน้าโครงการฯ คือการสนับสนุนให้เกิดทีมวิจัยที่ทำงานเป็นเครือข่ายและมีความเข้มแข็ง ซึ่งจะเป็นกลุ่มวิจัยที่สามารถสร้างฐานเทคโนโลยีที่จำเป็นเป็นการแก้ปัญหาต่างๆ และชี้นำทิศทางของประเทศไทย

- กลุ่มวิจัยด้าน CO_2 capture and utilization

ร่วมมือกับ ผศ.ดร.เกรียงไกร มณีอินทร์ (ภาควิชาวิศวกรรมเหมืองแร่และปิโตรเลียม จุฬาลงกรณ์มหาวิทยาลัย) รวมทีมวิจัยทางด้าน CO_2 capture and utilization technology ซึ่งเป็นการรวมทีมคณาจารย์ที่หน่วยงานต่างๆ ได้แก่ รศ.ดร.วุฒิชัย พาราสุข (ภาควิชาเคมี คณะวิทยาศาสตร์ จุฬาลงกรณ์มหาวิทยาลัย) รศ.ดร.ธิติ บวรรัตนารักษ์ (ภาควิชาฟิสิกส์ คณะวิทยาศาสตร์ จุฬาลงกรณ์มหาวิทยาลัย) รศ.ดร.เบญจพล เฉลิมสินสุวรรณ (ภาควิชาเคมีเทคนิค คณะวิทยาศาสตร์ จุฬาลงกรณ์มหาวิทยาลัย) ผศ.ดร. กิติพัฒน์ สีมานนท์ (วิทยาลัยปิโตรเลียมและปิโตรเคมี จุฬาลงกรณ์มหาวิทยาลัย) ผศ.ดร.สมพงษ์ พุทธิวิสุทธิศักดิ์ (ภาควิชาวิศวกรรมเครื่องกล คณะวิศวกรรมศาสตร์ จุฬาลงกรณ์มหาวิทยาลัย) ผศ.ดร. สุวิมล วงศ์สกุลเภสัช (ภาควิชาวิศวกรรมเคมี คณะวิศวกรรมศาสตร์ มหาวิทยาลัยเทคโนโลยีพระจอมเกล้า พระนครเหนือ) ดร.สุภวัฒน์ วิวรรธ์ภัทรกิจ (สถาบันวิจัยพลังงาน จุฬาลงกรณ์มหาวิทยาลัย) และ ดร.ตติยา โชคบุญเปี่ยม (ภาควิชาเคมี คณะวิทยาศาสตร์ มหาวิทยาลัยรามคำแหง) เพื่อรับทุนวิจัยสนับสนุนจากกองทุนรัชดาภิเษกสมโภช จุฬาลงกรณ์มหาวิทยาลัย (ทุน Inter Cluster) งบประมาณ 8 ล้านบาท (ศ.ดร.สุทธิชัย อัสสะบำรุงรัตน์ เป็นหัวหน้าโครงการ) ซึ่งต่อมากลุ่มวิจัยได้รับการสนับสนุนจากจุฬาลงกรณ์มหาวิทยาลัย

จัดตั้งเป็น STAR โดยมี ผศ.ดร.เกรียงไกร มณีอินทร์ เป็นหัวหน้ากลุ่ม และขณะนี้อยู่ในขั้นตอนเตรียมข้อเสนอโครงการเพื่อขอทุนสนับสนุนจากต่างประเทศ

- กลุ่มวิจัยด้าน CFD Simulation

ร่วมมือกับ ผศ.ดร.สมพงษ์ พุทธิวิสุทธิศักดิ์ (ภาควิชาวิศวกรรมเครื่องกล จุฬาลงกรณ์มหาวิทยาลัย) ได้จัดตั้ง Research Unit ทางด้านพลศาสตร์ของไหลเชิงคำนวณขั้นสูง มีสมาชิกกลุ่มคือ ดร.พิมพ์พร พลเพชร ดร.ปารวี วาศน์อำนวย (ภาควิชาวิศวกรรมเคมี จุฬาลงกรณ์มหาวิทยาลัย) รศ.ดร.เบญจพล เฉลิมสินสุวรรณ (ภาควิชาเคมีเทคนิค จุฬาลงกรณ์มหาวิทยาลัย) ศ.ดร.พรพจน์ เปี่ยมสมบูรณ์ (ภาควิชาเคมีเทคนิค จุฬาลงกรณ์มหาวิทยาลัย) โดยรับการสนับสนุนจากจุฬาลงกรณ์มหาวิทยาลัย

- กลุ่มวิจัยด้าน Biorefinery

ร่วมมือกับ รศ.ดร.ณัฏฐา ทองจุล (สถาบันวิจัยเทคโนโลยีชีวภาพและวิศวกรรมพันธุศาสตร์ จุฬาลงกรณ์มหาวิทยาลัย) ในการรวมทีมวิจัยในจุฬาลงกรณ์มหาวิทยาลัยเพื่อจัดตั้ง Research Unit ทางด้านเทคโนโลยีชีวภาพเพื่ออุตสาหกรรม โดยมีความร่วมมือกับทีมคณาจารย์ต่างๆ ได้แก่ รศ.ดร. อลิสา วังใน (ภาควิชาชีวเคมี คณะวิทยาศาสตร์) ศ.ดร.สมบูรณ์ ธนาศุภวัฒน์ (ภาควิชาชีวเคมีและจุลชีววิทยา คณะเภสัชศาสตร์) ศ.ดร.อัญชริดา สวารชร (ภาควิชาจุลชีววิทยา คณะวิทยาศาสตร์) ผศ. ดร.อภินันท์ สุทธิธารธวัช (ภาควิชาวิศวกรรมเคมี คณะวิศวกรรมศาสตร์) ดร.สิตานัน ธิติประเสริฐ อาจารย์วาสนา โตเลี้ยง น.ส.จิราภรณ์ พิลึก (สถาบันวิจัยเทคโนโลยีชีวภาพและวิศวกรรมพันธุศาสตร์) - ขณะนี้ได้รับการอนุมัติจากทางจุฬาลงกรณ์มหาวิทยาลัยแล้ว

- งานวิจัยด้าน Biodiesel production

ร่วมมือกับคณาจารย์ประจำภาควิชาวิศวกรรมเคมีและวัสดุ มหาวิทยาลัยเทคโนโลยีราชมงคลธัญบุรี เพื่อทำวิจัยในหัวข้อต่างๆ ได้แก่ การพัฒนาการผลิตไบโอดีเซลในเครื่องปฏิกรณ์แบบจานหมุน (spinning disc reactor) (ดร.วีรินทร์ดา อัปมานะ) การผลิตโซเดียมเมทอกไซด์โดยใช้เทคนิคการเกิดปฏิกิริยาพร้อมการตกผลึก (ดร.ธีระวัฒน์ เหมือนศรีชัย) และการจำลองกระบวนการผลิตโซเดียมเมทอกไซด์ในหอกลั่นแบบมีปฏิกิริยา (ดร. ชัยภพ ศิระวรกุล)

ร่วมมือกับ รศ.ดร.ดุลยพงศ์ วงศ์แสวง ภาควิชาวิศวกรรมนิวเคลียร์ คณะวิศวกรรมศาสตร์ จุฬาลงกรณ์มหาวิทยาลัย เพื่อทำวิจัยในหัวการพัฒนาเครื่องปฏิกรณ์แบบพลาสมาสำหรับการผลิตไบโอดีเซล

- งานวิจัยด้าน Electrochemistry

ร่วมมือกับ รศ.ดร.เกรียงศักดิ์ ไกรวัฒนวงศ์ (ภาควิชาวิศวกรรมเคมี สถาบันเทคโนโลยีพระจอมเกล้าเจ้าคุณทหารลาดกระบัง) ให้เกิดความร่วมมือทางด้านงานวิจัยในหัวข้อ Electric double layer capacitors (EDLC) by using porous carbon materials โดยร่วมมือกับ ดร.พลัง บำรุงสกุลสวัสดิ์ (ภาควิชาวิศวกรรมเคมี จุฬาลงกรณ์มหาวิทยาลัย)

- งานวิจัยด้าน Biorefinery

ร่วมมือกับ ผศ.ดร.สุขสันต์ อมรรักษา (บัณฑิตวิทยาลัยวิศวกรรมศาสตร์นานาชาติสิรินธร ไทย-เยอรมัน) ดร.ลิดา สิมะสาธิตกุล (ภาควิชาเคมีอุตสาหกรรม มหาวิทยาลัยเทคโนโลยีพระจอมเกล้า พระนครเหนือ) ทำวิจัยในหัวข้อการสังเคราะห์กระบวนการผลิตวานิลลินจากลิกนิน (เป็นงานวิจัยด้าน Biorefinery) และหัวข้อการผลิตพลังงานทดแทนจากน้ำทิ้งสู่ทะเล

4.2 กิจกรรมการส่งเสริมการสร้างนวัตกรรมจากงานวิจัย

ศ.ดร.สุทธิชัย อัสสะบำรุงรัตน์ ได้ร่วมกับทีมบรรณาธิการจากบวท. (ศ.ดร.อภิชาต สุขสำราญ ศ.ดร.สักกมล เทพหัสดิน ณ อยุธยา และศ.ดร.นวดล เหล่าศิริพจน์) ในการจัดทำหนังสือ "วิจัยไม่ขึ้นหิ้ง - ความสำเร็จบนเส้นทางการพัฒนางานวิจัยไปสู่การสร้างนวัตกรรม) โดยรับการสนับสนุนจาก สกว.

5. สรุปผลงาน

ตารางที่ 1 สรุปผลงานตามข้อเสนอโครงการและผลงานทั้งหมด

ผลงาน	ผลงานตามข้อเสนอโครงการ				ผลงานที่ได้จนถึงปัจจุบัน
	ปีที่ 1	ปีที่ 2	ปีที่ 3	รวม	
1. บทความในวารสารนานาชาติ (อยู่ในฐาน ISI)	8	8	9	25	35 + (2)[1] + (3)[2]
2. บทความในวารสารนานาชาติ (ไม่อยู่ในฐาน ISI)	-	-	-	-	4
3. ดุษฎีบัณฑิต	1	1	2	4	8
4. มหาบัณฑิต	6	6	6	18	18
5. Book chapter/review	-	-	2	2	2 + (2)[3]
6. สิทธิบัตร	-	-	1	1	1
7. สัมมนา	1	1	1	3	3
8. International conference	-	-	-	-	20

หมายเหตุ [1] อยู่ระหว่างการแก้ไขตามคำแนะนำของ Reviewers

[2] อยู่ระหว่างการพิจารณา

[3] อยู่ระหว่างการจัดเตรียม

ลงนาม .....

(ศ.ดร. สุทธิชัย อัสสะบำรุงรัตน์)

หัวหน้าโครงการ

Appl Biochem Biotechnol (2015) 177:595–609
DOI 10.1007/s12010-015-1763-3

Regulating Pyruvate Carboxylase in the Living Culture of *Aspergillus Terreus* Nrrl 1960 by L-Aspartate for Enhanced Itaconic Acid Production

Pajareeya Songserm[1] · Sitanan Thitiprasert[2] · Vasana Tolieng[2] · Jiraporn Piluk[2] · Somboon Tanasupawat[3] · Sutthichai Assabumrungrat[4] · Shang-Tian Yang[5] · Aphichart Karnchanatat[2] · Nuttha Thongchul[2]

Received: 14 April 2015 / Accepted: 14 July 2015 /
Published online: 25 July 2015
© Springer Science+Business Media New York 2015

Abstract *Aspergillus terreus* was reported as the promising fungal strain for itaconic acid; however, the commercial production suffers from the low yield. Low production yield was claimed as the result of completing the tricarboxylic acid (TCA) cycle towards biomass synthesis while under limiting phosphate and nitrogen; TCA cycle was somewhat shunted and consequently, the metabolite fluxes move towards itaconic acid production route. By regulating enzymes in TCA cycle, it is believed that itaconic acid production can be improved. One of the key responsible enzymes involved in itaconic acid production was triggered in this study. Pyruvate carboxylase was allosterically inhibited by L-aspartate. The presence of 10 mML-aspartate in the production medium directly repressed PC expression in the living *A. terreus* while the limited malate flux regulated the malate/citrate antiporters resulting in the increasing cis-aconitate decarboxylase activity to simultaneously convert cis-aconitate, citrate isomer, into itaconic acid. The transport of cis-aconitate via the antiporters induced citrate

Submitted to Applied Biochemistry and Biotechnology

✉ Nuttha Thongchul
Nuttha.T@chula.ac.th

[1] Biotechnology Program, Faculty of Science, Chulalongkorn University, Bangkok 10330, Thailand

[2] Institute of Biotechnology and Genetic Engineering, Chulalongkorn University, Bangkok 10330, Thailand

[3] Department of Microbiology, Faculty of Pharmaceutical Sciences, Chulalongkorn University, Bangkok 10330, Thailand

[4] Department of Chemical Engineering, Faculty of Engineering, Chulalongkorn University, Bangkok 10330, Thailand

[5] William G. Lowrie Department of Chemical and Biomolecular Engineering, The Ohio State University, Columbus, OH 43210, USA

synthase and 6-phosphofructo-1-kinase activities in response to balance the fluxes of TCA intermediates. Successively, itaconic acid production yield and final concentration could be improved by 8.33 and 60.32 %, respectively, compared to those obtained from the control fermentation with the shortened lag time to produce itaconic acid during the production phase.

Keywords Itaconic acid · L-aspartate · Pyruvate carboxylase · Cis-aconitate decarboxylase · 6-phosphofructo-1-kinase · *Aspergillus terreus* · Allosteric inhibition · Fermentation

Introduction

Itaconic acid, or methylene succinic acid ($C_5H_6O_4$), is an unsaturated 5-carbon dicarboxylic acid. It is a naturally occurring nontoxic compound which is readily compostable. Itaconic acid plays a crucial role as a monomer or an additive in many industrial applications including synthetic resins, synthetic fibers, artificial glass, detergents, and paints [1]. Most importantly, from the US Department of Energy (DOE) report, itaconic acid has been classified as one of the top 12 chemical building blocks derived from biomass that can be used as a precursor in the production of various high-value bio-based chemicals or materials [2].

To date, itaconic acid is commercially produced via *Aspergillus terreus* fermentation, which occurred towards the glycolytic pathway and the early step of the oxidative route in tricarboxylic acid (TCA) cycle [3]. Fungal fermentation process to produce itaconic acid usually suffers from low product yield and long production time. As a result, the production capacity cannot guarantee the increasing market demand to substitute the petroleum-based feedstock in the near future. Several optimization techniques to develop the conditions that favor itaconic acid have been applied during fermentation but to date, none of them was well-accomplished. Though the patents from the 1960s showed very good itaconic acid production processes, the results varied a lot by the slight change in trace elements present in the medium to the bioreactor geometries. Even the results obtained from the same strains were fluctuated between the shaking flasks and different fermentor geometries (stirred tank vs. air lift) [4]. In 2012, Kuenz et al. reported itaconic acid production using different bioreactors by *A. terreus* strains [1]. From the previous literatures, reproducibility seems to be a major problem in the production process. Recent progress argued that overproduction of itaconic acid required an interaction of several factors including a nutrient limitation for uncoupled glycolysis and oxidative phosphorylation, a possibility to decrease the high energy level, a specific transporter system to transport TCA intermediates into the cytosol and cis-aconitate decarboxylase (CAD) to decarboxylate cis-aconitate to itaconic acid. However, the exact regulation of itaconic synthesis is not yet fully understood [5].

It was claimed that ATP plays a key role in controlling the metabolic fluxes in the glycolytic pathway and TCA cycle. ATP is the major energy molecule required in many metabolic reactions to produce the value-added industrial products. It can serve as the substrate, product, activator, and inhibitor in the metabolic network [6]. Also, in itaconic acid production, ATP helps maintain the intracellular pH near the physiological pH at 7.0 and facilitates acid transport into the surrounding environment (pH 2.0). Therefore, conserving ATP with the regulated metabolic fluxes in TCA cycle towards itaconic acid production route is the challenging way to improve its production.

To increase the availability of ATP during itaconic acid fermentation, it was hypothesized that by inhibiting pyruvate carboxylase (PC), more ATP would be available for itaconic acid

production and transport. PC, a biotin-dependent carboxylase, converts 1 mol of pyruvate into 1 mol of oxaloacetate (OAA) with supplemented 1 mol of CO_2 and 1 mol of ATP input. By inhibiting PC conversion to OAA, 2 mol of ATP would be conserved for itaconic acid production and transport that eventually resulted in the improved yield and productivity. The in vitro study on fungal PC inhibition claimed that L-aspartate was an allosteric inhibitor that competitively bound to PC [7]. The activity of purified PC from the fungal cultures such as *Rhizopus arrhizus* and *Aspergillus nidulans* was inhibited when L-aspartate was added into the reaction assay [8, 9]. From the previous findings, adding L-aspartate into the living culture of *A. terreus* would help decrease the activity of PC; thus, conserving ATP for itaconic acid production and TCA products transport. In this work, we reported the response of the living *A. terreus* on L-aspartate present in the fermentation medium during the cultivation for itaconic acid production. The optimized concentration of this well-reported in vitro PC inhibitor was elucidated for its role as the direct PC regulator in the living fungal culture. Also, the change in metabolic flux when L-aspartate was added into the culture broth was reported in term of the fermentation kinetics and the activities of the key enzymes in the pathway.

Materials and Methods

Itaconic acid production with the presence of pyruvate carboxylase regulator was investigated in the living culture of *A. terreus* NRRL1960 grown in the glucose-based medium in a shake flask. The effects of pyruvate carboxylase regulator on fungal growth, expression of key enzymes in the metabolic pathway, and end metabolite production were determined and compared with those obtained from the culture without the inhibitor (control).

Microorganism and Inoculum Preparation

Aspergillus terreus NRRL1960, a filamentous fungus producing itaconic acid kindly provided by the Agricultural Research Service Culture Collection, US Department of Agriculture, Peoria, IL, USA, was used in this study. The stock culture was maintained on Czapek's agar plates and subcultured every month to maintain fungal activity. The conidiospores were collected from the 7-day culture on Czapek's agar plates incubated at 30 °C by shaving and extracting the spores with sterile water. The spore suspension was adjusted to 10^6 spores/mL by dilution with sterile deionized (DI) water for inoculation.

Growing *A. terreus* in the Fermentation Medium Containing L-aspartate

Itaconic acid fermentation by *A. terreus* consists of two phases. During the growth phase, the growth medium consisting of 30 g/L glucose and 5 g/L yeast extract was used to promote spore germination and initial cell growth. Then, 0.5-mL spore suspension (10^6 spores/mL) was inoculated into a 250-mL Erlenmeyer flask containing 50-mL sterile growth medium. The initial pH during growth phase was 3.0. The culture was incubated at 30 °C in a rotary shaker at 150 rpm for 48 h. At the end of the growth phase, the growth medium was replaced by the production medium containing 100 g/L glucose, 2.36 g/L $(NH_4)_2SO_4$, 0.11 g/L KH_2PO_4, 2.08 g/L $MgSO_4{\cdot}7H_2O$, 0.13 g/L $CaCl_2.2H_2O$, 0.074 g/L NaCl, 0.2 mg/L $CuSO_4.5H_2O$, 5.5 mg/L $FeSO_4.7H_2O$, 0.7 mg/L $MnCl_2.4H_2O$, and 0.088 g/L $ZnSO_4{\cdot}7H_2O$. The pH of the production medium was initially adjusted to 2.0. The culture was incubated at the same

conditions as those during the growth phase for another 192 h. During the fermentation, samples were taken every 12 h for analyses of glucose, itaconic acid, and other byproducts as well as for enzyme assays.

L-aspartate was added into the fermentation medium at different concentrations. The effects of L-aspartate on growth and metabolite production were investigated during the growth and production phases.

Product Yields and Volumetric Productivities

Cell growth and product formation during fermentation were determined. The product yield was calculated from the ratio of product formed to glucose consumed. The volumetric productivity was defined as the total amount of product formed per volume per time.

Cell biomass

The concentration of cell biomass was determined from the cell dry weight. Cell biomass present in the fermentation broth was harvested by filtration using Whatman filter paper (No. 4). The filtered cell biomass was thoroughly rinsed with DI water before drying at 80 °C until constant weight was obtained. Cell biomass concentration present in the fermentation broth was calculated by the following equation.

$$\text{Cell concentration}\left(\frac{\text{g}}{\text{L}}\right)=\frac{\text{Cell dry weight on filter paper (g)}-\text{dry weight of filter paper (g)}}{\text{Fermentation broth volume (L)}}$$

Analysis of glucose and end products

Fermentation broth sample was centrifuged at 10,000*g* for 7 min. The supernatant was kept for analyses of remaining glucose, itaconic acid, and byproducts using high-performance liquid chromatography (HPLC; Shimadzu model 10Ai). Before injecting the sample into the HPLC system, the sample was diluted with double distilled water and filtered through the hydrophilic PTFE membrane. The particle-free sample (15 μL) was automatically injected into an organic acid column (Bio-Rad, Aminex HPX-87H ion exclusion organic acid column; 300 mm × 7.8 mm) maintained at 45 °C in a column oven. H_2SO_4 (0.4 mM) was used as an eluent at the flow rate of 0.4 mL/min. A refractive index detector was used to detect the organic compounds including glucose, itaconic acid, citric acid, cis-aconitic acid, succinic acid, oxaloacetic acid, L-malic acid, and pyruvic acid. The standard containing 0–2 g/L of each component indicated prior was injected as the reference to determine the concentrations of each compounds present in the sample. The peak area was used for the comparison basis.

Cell Extraction, Partial Enzyme Purification, and Protein Determination

Following the method described in Thitiprasert et al., fresh fungal mycelia from the fermentation were washed thoroughly with sterile DI water three times before drying between filter paper [10]. Filter-dry mycelia were weighed into 1 g and frozen at −20 °C for 1 h before grinding in an ice-cold mortar for 5 min. TrisHCl buffer (1.5 mL, 0.2 M, pH 8.0) was added into the ground mycelia. The suspension of the fungal mycelia with the glass beads was then

homogenized in the cell disrupter for 16.75 min (30-s interval with 45-s break). Later, the glass beads were removed by filtration and the suspension was then centrifuged at 12,000*g* for 30 min at 4 °C. The supernatant to be called later the cell extract was used for protein determination and enzyme assays. The protein content was determined by Lowry's method using a bovine serum albumin (BSA) as a standard [11].

Enzyme Assays

6-phosphofructo-1-kinase (PFK) activity was determined by phosphofructokinase colorimetric assay kit (Sigma). The enzyme activity was determined from a couple enzyme reaction, in which PFK catalyzed the conversion of fructose-6-phosphate and ATP to fructose-1,6-diphosphate and ADP. ADP was later converted by the enzyme in the mixture into AMP and NADH. The reaction mixture containing 42 μL PFK assay buffer, 2 μL PFK enzyme mix, 2 μL PFK developer, 2 μL ATP, and 2 μL PFK substrate was added into a 96-well plate. Then, 10 μL crude enzyme extract was added into each well. The resulting NADH reduced the colorless indicator resulting in a colorimetric product at 450 nm proportionally to the PFK activity present in the enzyme mixture. The absorbency at 450 nm of the reaction mixture was recorded every 57 s for 5 min. The average rate of the increasing absorbency at 450 nm per min was calculated. The activity of PFK was subsequently determined using the calibration plot of absorbency at 450 nm versus NADH concentration in micromoles. One unit of PFK was determined by the amount of enzyme that generated 1.0 μmol NADH in 1 min at 37 °C, pH 7.4.

Pyruvate carboxylase (PC) was determined from a couple enzyme reaction. PC catalyzed the carboxylation of pyruvate into oxaloacetate (OAA) (Eq. 1). OAA was then reacted with acetyl CoA to form citryl CoA by citrate synthase, which was subsequently hydrolyzed to citrate and CoA (Eq. 2). In the spectrophotometer, the rate-limiting reaction catalyzed by PC (Eq. 1) is coupled to the effectively irreversible chemical reaction (Eq. 3). The reaction product thionitrobenzoic acid (TNB) was the absorbing substance with intense absorption at 412 nm.

$$\mathrm{ATP} + \mathrm{pyruvate} + \mathrm{HCO_3^-} = \mathrm{ADP} + \mathrm{phosphate} + \mathrm{oxaloacetate} \quad (1)$$

$$\mathrm{Acetyl{-}CoA} + \mathrm{oxalacetate} + \mathrm{H_2O} = \mathrm{citrate} + \mathrm{CoA{-}SH} \quad (2)$$

$$\mathrm{CoA{-}SH} + \mathrm{DTNB} = \mathrm{TNB} + \mathrm{CoA{-}S{-}S{-}TNB} \quad (3)$$

PC activity was determined in the reaction mixture containing 0.050 M $NaHCO_3$, 0.005 M $MgCl_2$, 0.050 mM acetyl CoA, 0.005 M pyruvate, 0.005 M ATP, 0.200 mM 5,5′-dithio-bis(2-nitrobenzoic acid), and 5 U/mL citrate synthase in 0.1 M Tris HCl buffer (pH 8.0) in a total volume of 1.0 mL. The reaction was initiated by adding 50-μL crude enzyme extract into the reaction mixture with a run time of 60 s at 30 °C. The increase in absorbency at 412 nm of 5-dithio-2-nitrobenzoate (DTNB) was measured. The PC activity was determined by using the standard curve of absorbency at 412 nm versus oxaloacetate concentration in micromoles. One unit of PC activity was corresponded to the formation of 1 μmol oxaloacetate in 1 min at 30 °C.

Pyruvate dehydrogenase complex (PDC) activity was assayed by following the depletion of NADH at 340 nm [12]. The reaction mixture contained 25 mM sodium pyruvate, 5 mM MgCl2, 0.2 mM thiamine pyrophosphate (TPP), 11 U/mL alcohol dehydrogenase, and 0.15 mM NADH in 100 mM MES buffer (pH 6.5) in a total volume of 1.2 mL. The reaction

was started by adding diluted enzyme sample in crude extract and the absorbency at 340 nm was recorded every 57 s for 5 min at 30 °C. The average rate of the increase in absorbency at 340 nm per min was determined. PDC activity was monitored at 340 nm corresponding to the amount of NADH (in micromoles) oxidized per minute using the calibration plot of absorbency at 340 nm versus NADH concentration (micromoles).

Cis-aconitate decarboxylase (CAD) activity was assayed by Bently method [13]. Crude enzyme extract (0.1 mL) was incubated with 0.4 mL cis-aconitic acid solution (to the final concentration of 8.0 mM) and 2.5 mL sodium phosphate (0.2 M, pH 6.2) for 10 min at 37 °C. The reaction was terminated by adding 0.1 mL HCl (12.0 M). The released itaconic acid was analyzed by HPLC using the similar method described earlier.

Citrate synthase (CS) was assayed by DTNB method [14]. The reaction mixture contained 0.1 M Tris HCl buffer (pH 8.0), 0.2 mM 5,5′-dithio-bis(2-nitrobenzoic acid), 0.05 mM oxaloacetate, and 0.05 mM acetyl CoA in a total volume of 1.0 mL. The reaction was started by adding 50 μL crude enzyme extract into the reaction mixture. The absorbance at 340 nm was measured every 57 s for 5 min at 30 °C; then, the average rate of the increase in absorbency at 450 nm per min was calculated. One unit of CS was defined as 1 μmol oxaloacetate converted per minute. The amount of oxaloacetate present in the reaction mixture determines from the calibration the curve of absorbency at 412 nm versus amount of oxaloacetate (in micromoles) (see in Eqs. 2 and 3).

Aconitase activity was determined by aconitase activity assay kit (Sigma). The enzyme catalyzed the stereospecific and reversible isomerization of citrate to isocitrate. This resulted in a colorimetric (450 nm) product proportional to the enzymatic activity present. Before assay, crude enzyme extract was activated by adding 10 mL aconitase activation solution to 100 mL sample on ice for 1 h. Then, 10-μL activated sample was added into the reaction mixture containing 46 μL aconitase assay buffer, 2 μL aconitase substrate, and 2 μL enzyme in 96 well plate at 25 °C for 60 min. After incubation, 10 μL developer was added into each well, mixed and further incubated at 25 °C for 10 min. The absorbency was measured at 450 nm. One unit of aconitase was defined as the amount of enzyme that isomerized 1.0 μmol citrate from isocitrate per minute at 25 °C, pH 7.4. The calibration plot of absorbency at 450 nm versus isocitrate concentration (micromoles) was used to determine the isocitrate.

Results and discussions

Glucose-Based Fermentation of *A. terreus* NRRL1960

Figure 1 shows the fermentation kinetics of *A. terreus* NRRL 1960 grown in two phases for itaconic acid production. Unlike other itaconic acid fermentation processes reported elsewhere in the literatures, 2-phase fermentation was aimed to achieve high cell density during the growth phase by growing *A. terreus* in the rich medium containing organic nitrogen source with the subsequent itaconic acid production by the high cell density using other medium compositions that promoted itaconic acid synthesis. During the growth phase, cell biomass was built up rapidly (8.96 g/L with 1.34 g cell per gram glucose consumed and 0.19 g cell/L/h) while there was no itaconic acid produced. After 48 h, the growth medium was discarded and the culture was filled up with the production medium containing $(NH_4)_2SO_4$ as the sole nitrogen source at the high C/N weight ratio of 42:1. Increasing cell biomass production was continuously observed at the slightly lower rate compared to that during the growth phase

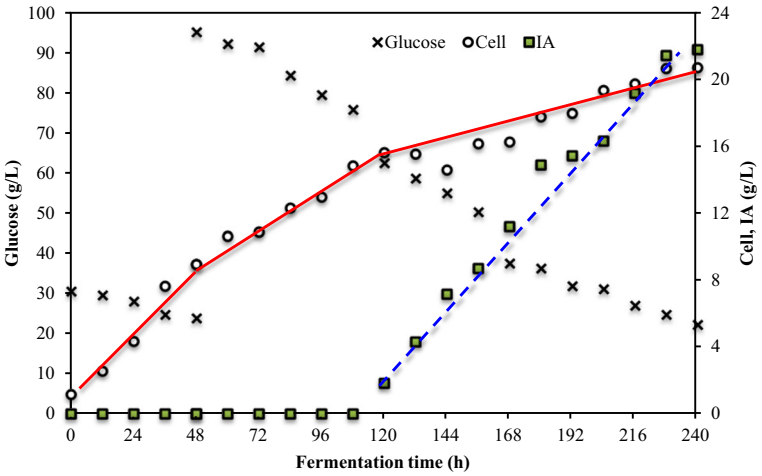

Fig. 1 Fermentation kinetics of *A. terreus* NRRL1960 grown in glucose-based medium in the shake flask culture. Fermentation consisted of two phases. The growth phase took 48 h where yeast extract was used as a sole nitrogen source. The growth medium was replaced by the production medium containing the inorganic nitrogen source after 48 h. The fermentation was prolonged until 240 h. The *red trend lines* indicate two growth rates of *A. terreus* during cultivation. The corresponding *blue trend line* indicates itaconic acid production during the slow growth

until 120 h (red line). When changing the medium, inorganic nitrogen ($(NH_4)_2SO_4$) with the supplemented phosphate in KH_2PO_4 in the production medium maintained the growth of *A. terreus*; however, at a lower rate compared to that cultivated in the growth medium with yeast extract. The lower growth rate confirmed the evidence of the lower ATP regeneration due to limited phosphate pool; thus, the regeneration process occurred by substrate level phosphorylation rather than oxidative phosphorylation. At 120 h, itaconic acid was firstly observed in the fermentation broth. Later, the growth rate was dropped while glucose consumption rate remained constant and itaconic acid was produced at the constant rate (0.16 g/L/h). This finding indicated growth-limiting condition was necessary for itaconic acid synthesis by *A. terreus*. Similar growth pattern of *A. terreus* NRRL 1960 was observed by Riscaldati et al. (2000) [15]. The evidence of phosphate and nitrogen limitation led to the accumulation of itaconic acid [16]. Nonetheless, from the kinetics model, non growth condition did not give the better itaconic acid production. The results show in Fig. 1 and those in Riscaldati et al. (2000) reveal that the fermentation exhibited mixed growth associate product formation kinetics [15]. With the proper N/P ratio in the production medium, it is believed that itaconic acid production can be further improved in 2-phase fermentation.

Key Enzymes Responsible for Itaconic Acid Synthesis

To better understand the synthesis of itaconic acid by *A. terreus* during 2-phase fermentation cultivation, the activity of the key enzymes related in itaconic acid production was assayed (Fig. 2). During the growth phase, the specific activity of PFK was approximately 2 U/mg protein while later in the production phase, the PFK-specific activity dramatically dropped. This was presumably due to the change in medium compositions from organic to inorganic nitrogen for slight cell growth and maintenance during the production phase. It was claimed

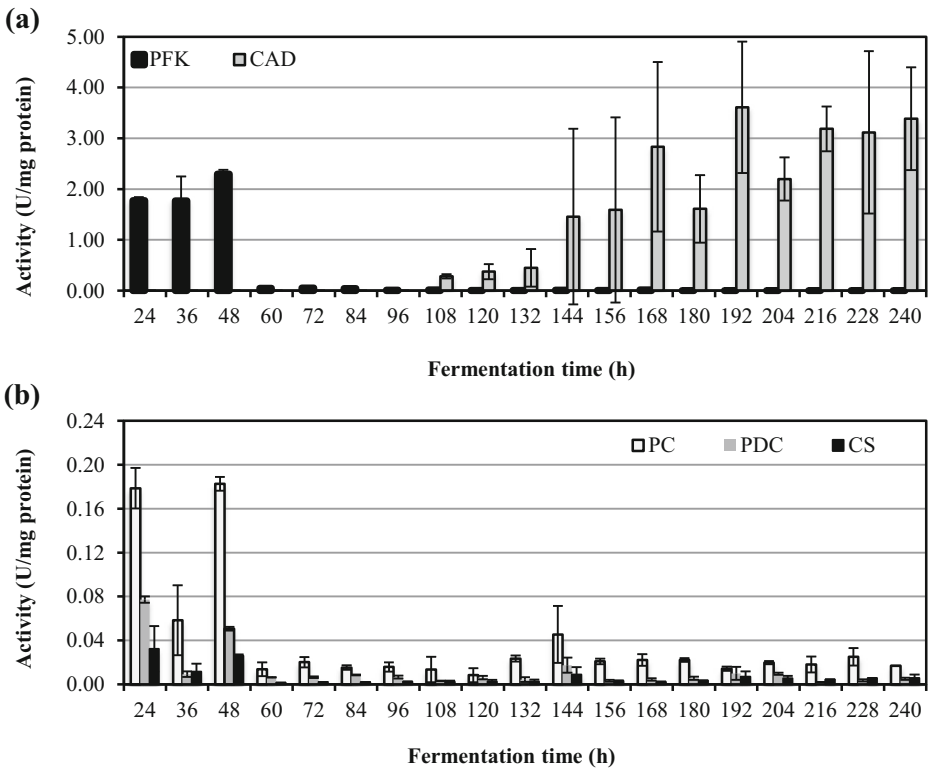

Fig. 2 Key responsible enzymes in itaconic acid production by *A. terreus*. The specific activity of these enzymes was assayed from the collected fermentation samples during cultivation of *A. terreus* in the glucose-based medium in 2-phase fermentation. Enzyme assay was carried out after 24-h cultivation when sufficient cell biomass was produced. The high expression levels of PFK and CAD were observed (more than ×20 larger) (**a**) compared to those of PC, PDC, and CS, the key intermediate enzymes in TCA cycle (**b**)

that a univalent cations such as NH_4^+ had a role in PFK regulation as it might provoke inhibition by citrate in vivo [16, 17]. Subsequently, the increasing activity of CAD (Fig. 2a) and the accumulation of itaconic acid (Fig. 1) were observed with the lowered PFK activity during the production phase. When growing *A. terreus* using yeast extract under sufficient oxygen supply, glucose was rapidly metabolized into pyruvate through the Embden-Meyerhof-Parnas (EMP) pathway. Pyruvate was then either transported to the mitochondria and later converted into acetyl CoA or carboxylated into oxaloacetate (OAA) in the cytosol [5]. Completed TCA cycle coupling with an electron transport chain (ETC) resulted in cell biomass and a large amount of ATP generation [6, 18]. Changing the medium to the production medium containing a small amount of $(NH_4)_2SO_4$ as well as decreasing the initial pH to 2.0 caused the lowered PFK activity due to lower oxygen solubility at low pH and the stimulated citrate inhibition of PFK by NH_4^+. In order to balance citrate flux in the mitochondria compartment under nitrogen limitation so that glucose flux towards the glycolysis could proceed, OAA in the cytosol was converted to malate, which was transported into the mitochondria by malate/citrate antiporters. In the mitochondria, acetyl CoA and OAA were irreversibly condensed into citric acid by CS. Citric acid was then reversibly converted to isocitrate and cis-aconitate by aconitase (ACO). Cis-aconitate was transported back to the

cytosol using mitochondrial tricarboxylic transporter (MTT) and then decarboxylated into itaconic acid by CAD (Fig. 3) [19]. The increasing CAD activity during the production phase was the evidence of MTT function in order to lower citrate isomer in the mitochondria thus glycolytic flux could be still driven towards pyruvate (Fig. 2a). Similarly, the specific activities of PC, PDC, and CS were high during the growth phase. This confirmed the high level of the oxidative phosphorylation in *A. terreus* with sufficient oxygen supply and rich nitrogen source (Fig. 2b). When nitrogen was limited in the production phase, the enzyme activities dropped dramatically. This finding suggested that 2-phase fermentation of itaconic acid was successfully used to stimulate cell growth under sufficient oxygen supply and rich nitrogen source which later being used to synthesize itaconic acid under limited nitrogen.

L-Aspartate as an Allosteric Inhibitor of PC and Its Role on metabolism of *A. terreus*

In this study, further growth was observed after changing the medium to the production medium (Fig. 1) while the activity of PFK, PC, PDC, and CS dramatically dropped (Fig. 2). This rather implied ATP conservation process instantaneously occurred at the beginning of the production phase when phosphate became limited. Nonetheless, as observed from the expression level of CAD, itaconic acid production started later at 120 h under both phosphate and nitrogen limitation condition [15]. To immediately initiate itaconic acid synthesis in 2-phase fermentation process after changing to the production medium, not only balancing the ratio of C/N/P in the medium is necessary, in term of the biosynthesis flux, the rate of OAA/acetyl CoA formation, citrate isomerization, and malate/cis-aconitate transport must be balanced while ATP regeneration must be also regulated (Fig. 3).

To investigate the metabolic response of *A. terreus* on medium change during 2-phase fermentation, acetyl CoA allosteric inhibitor and L-aspartate, was added into the fermentation medium. Figure 4 shows the morphology of *A. terreus* grown in the glucose-based medium

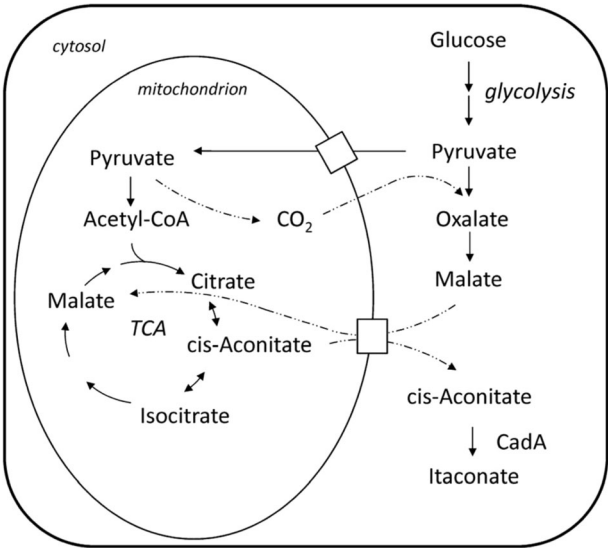

Fig. 3 Biosynthesis pathway of itaconic acid in *A. terreus*. Malate/citrate transport during nitrogen limitation played role controlling itaconic acid synthesis. (Reprinted from Steiger et al. [19])

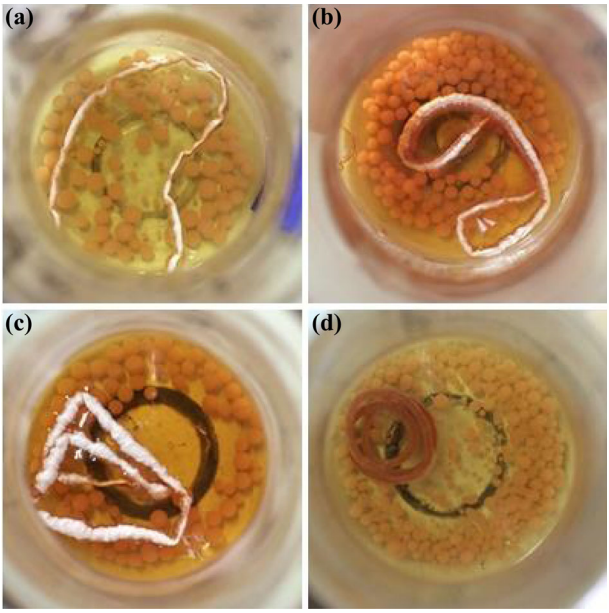

Fig. 4 Morphology of *A. terreus* cultivated in the growth medium containing L-aspartate. **a** control (no L-aspartate). **b** 0.1 mM L-aspartate. **c** 1.0 mM L-aspartate. **d** 10.0 mM L-aspartate

containing L-aspartate. It is clear that the morphology changed with the presence of L-aspartate. Smaller pellets were obtained when the concentration of L-aspartate was increased in the growth medium. Cell biomass production was also lower with the increasing L-aspartate concentration (Table 1). The specific activity of the key enzymes involving in biosynthesis confirmed the evidence of PC feedback inhibition by L-aspartate (Fig. 5). Lower PFK activity (Fig. 5a) was found with the increasing L-aspartate concentration in the growth medium. This was apparently due to the fact that L-aspartate triggered PC by binding at its allosteric site; thus, limiting PC action (Fig. 5b) and consequently reducing pyruvate flux towards OAA and malate. This eventually led to the reduction in biomass synthesis [7, 20].

Table 1 Cell biomass production during the growth phase of 2-phase fermentation of *A. terreus* for itaconic acid synthesis

L-aspartate conc. (mM)	Cell biomass production during the growth phase		
	Final conc. at 48 h (g/L)	Yield (g/g glucose consumed)	Productivity (g/L/h)
0 (control)	8.96±3.02	1.12	0.17
0.1	5.32±0.34	1.39	0.09
1.0	6.96±0.45	1.13	0.13
10.0	2.31±0.11	0.21	0.03

L-aspartate at different concentration was added into the glucose-based growth medium. The fermentation was carried out at 30 °C and 200 rpm in a shaken flask. The initial pH was 3.0

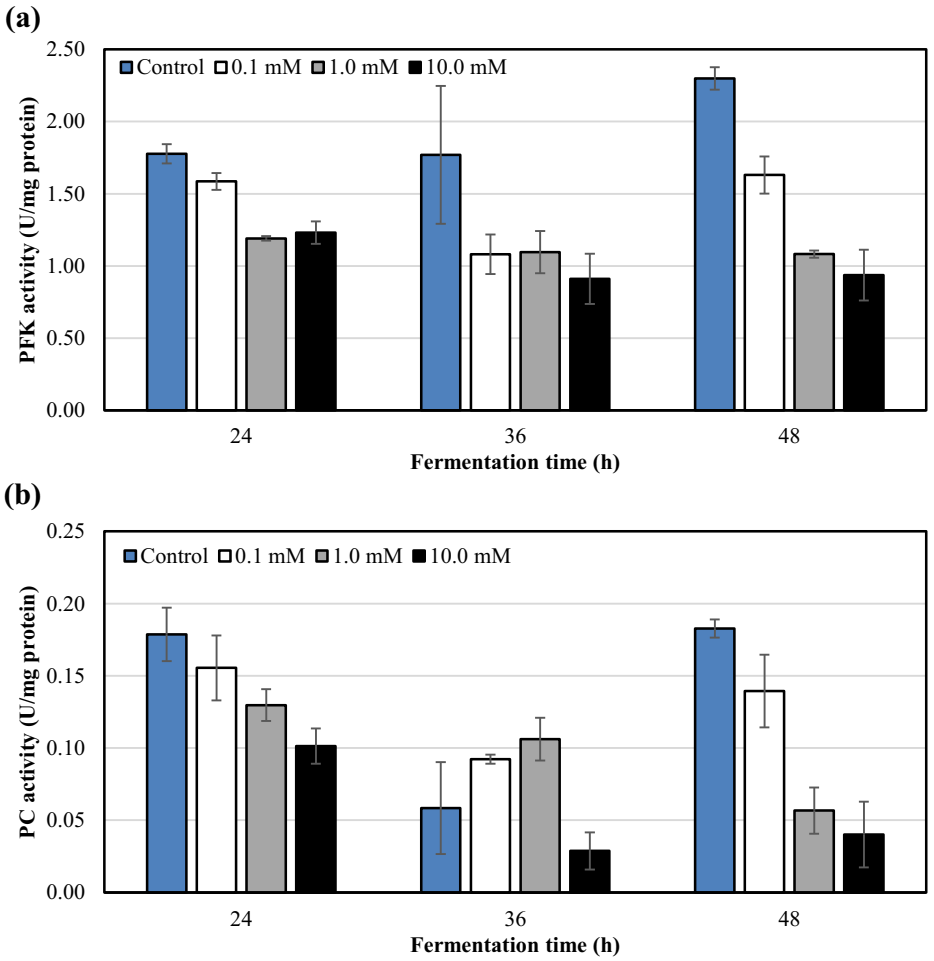

Fig. 5 The metabolic response of *A. terreus* when L-aspartate, the allosteric PC inhibitor was present during the growth phase. Key enzymes responsible for growth and ATP regeneration including PFK (**a**) and PC (**b**) were observed for their changes of activities when PC inhibitor was present

Using L-aspartate to Control Metabolic Flux in *A. terreus* for Improved Itaconic Acid Production

Most PCs have an α_4 quaternary structure with the four identical subunits containing a biotin carboxylase (BC) domain, a carboxyl transferase (CT) domain, and a biotin carboxyl carrier protein (BCCP) domain. The α_4 PCs are commonly activated by acetyl CoA [21]. From the above-mentioned claim and the metabolic response of *A. terreus* to L-aspartate during the growth phase, L-aspartate was introduced into the pregrown culture of *A. terreus* during the production phase. Increasing the concentration of L-aspartate up to 10.0 mM improved itaconic acid production (Fig. 6). Not only the higher titer could be achieved, but also sufficient amount of L-aspartate shortened the lag time before itaconic acid production after changing the medium. Nonetheless, excess L-aspartate

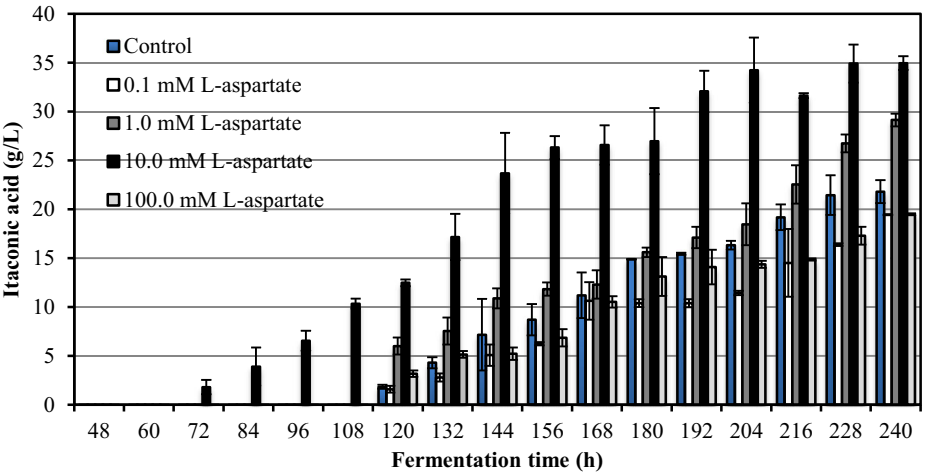

Fig. 6 Itaconic acid accumulation during the production phase of 2-phase fermentation of *A. terreus* in the glucose-based media containing an allosteric acetyl CoA inhibitor (L-aspartate) at different concentrations. *A. terreus* was pregrown in the growth medium and later, it was added into the culture during the production phase. Control represented the fermentation without L-aspartate

somewhat caused the adverse effect on itaconic acid production when 100.0 mM was added into the production medium (Table 2). PC was strongly inhibited at 100.0 mM L-aspartate as it competitively bound at the active site preventing the conversion of pyruvate to OAA and subsequently to malate. The lowered malate pool reduced the transport fluxes between malate and cis-aconitate, the CAD substrate for itaconic acid via

Table 2 Fermentation performance of *A. terreus* during the production phase with the presence of PC allosteric inhibitor, L-aspartate

Itaconic acid production	L-aspartate conc.				
	Control[c]	0.1 mM	1.0 mM	10.0 mM	100.0 mM
Final conc. (g/L)	21.80±1.17	19.45±0.04	29.14±0.65	34.95±0.70	19.49±0.10
Yield (g/g)	0.43±0.00	0.34±0.01	0.36±0.01	0.47±0.05	0.25±0.02
Productivity (g/L·h)	0.17±0.00	0.14±0.01	0.19±0.01	0.19±0.01	0.14±0.01
Time started to produced (h)[a]	120	120	120	72	120
Time reached highest concentration (h)[b]	240	240	240	240	240
Remaining glucose concentration at time[b] (g/L)	22.34±10.89	21.92±0.07	5.64±0.87	0.00±0.00	0.99±1.40

A. terreus was initially pregrown in the glucose-based medium for 48 h at 30 °C, 200 rpm with the initial pH of 3.0. After 48 h, the growth medium was discarded and the culture was filled up with the production medium containing L-aspartate at different concentrations and further cultivated at the same operating conditions with the initial pH of 2.0

[a] Total time (started from growth phase of 48 h and prolonged production phase) until itaconic acid was produced

[b] Total time (started from growth phase of 48 h and prolonged production phase) until the highest itaconic acid concentration was achieved

[c] Fermentation without L-aspartate (control fermentation)

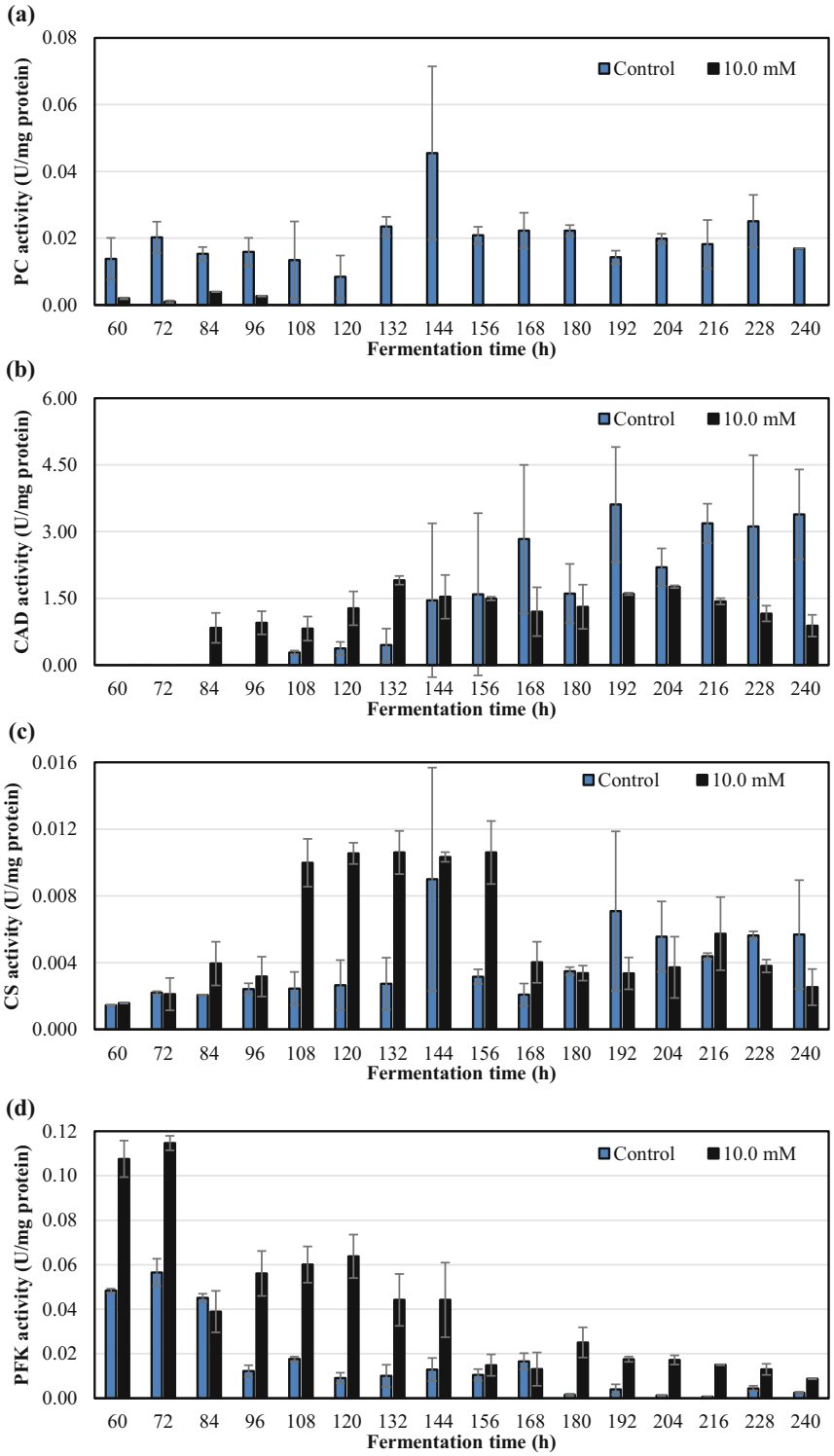
(a)
PC activity (U/mg protein)
0.08
0.06
0.04
0.02
0.00
Control
10.0 mM
60 72 84 96 108 120 132 144 156 168 180 192 204 216 228 240
Fermentation time (h)
(b)
CAD activity (U/mg protein)
6.00
4.50
3.00
1.50
0.00
Control
10.0 mM
60 72 84 96 108 120 132 144 156 168 180 192 204 216 228 240
Fermentation time (h)
(c)
CS activity (U/mg protein)
0.016
0.012
0.008
0.004
0.000
Control
10.0 mM
60 72 84 96 108 120 132 144 156 168 180 192 204 216 228 240
Fermentation time (h)
(d)
PFK activity (U/mg protein)
0.12
0.10
0.08
0.06
0.04
0.02
0.00
Control
10.0 mM
60 72 84 96 108 120 132 144 156 168 180 192 204 216 228 240
Fermentation time (h)

◀ **Fig. 7** Specific activities of the key responsible enzymes in itaconic acid production by *A. terreus* when L-aspartate, the allosteric PC inhibitor was present at 10.0 mM during the production phase in 2-phase fermentation

the malate/cis-aconitate antiporter (Fig. 3). At the same time, the large pool of acetyl CoA induced citrate formation. When high citrate concentration was present, it eventually inhibited PFK in glycolysis. This consequently slowed down the metabolism of *A. terreus* as observed from the prolonged turnover time of 120 h for itaconic acid production. As a result, itaconic acid production dropped when 100.0 mM L-aspartate was present in the production medium. From the concentration of L-aspartate studied, 10.0 mM gave the well-optimized condition that promoted itaconic acid synthesis. Approximately one third shorter lag time was achieved at this concentration of L-aspartate present in the fermentation. While the production yield reached up to 65 % of the theoretical yield compared with that obtained from the control fermentation (60 %).

The expression of PC confirmed the evidence of improved itaconic acid fermentation (Fig. 7a). Dramatically decreasing PC activity was observed resulting in lowered OAA in the cytosol. Subsequently, malic acid concentration was decrease in the cytosol. Malate/citrate antiporters subsequently drove the transport of cis-aconitate to the cytosol so that the malate could be transported into the mitochondria in response to the living *A. terreus* to complete TCA cycle. The presence of cis-aconitate in the cytosol-induced CAD as observed from the increasing activity of this enzyme (Fig. 7b) and itaconic acid formation; after 24 h, the production phase started (Fig. 6) while the control fermentation required up to 72 h for itaconic acid production firstly observed (Fig. 6). The flux of citrate towards cis-aconitate and the transport of malate/citrate antiporters induced the activities of CS and PFK as the results of lowering citrate flux (Fig. 7c, d). As aforementioned, L-aspartate played a role in allosteric inhibition of PC in the living culture of *A. terreus*. This resulted in metabolic flux shift towards itaconic acid production. The incomplete TCA cycle with the enhanced PFK activity revealed that TCA intermediates were bypassed towards itaconic acid as the result of PC inhibition and ATP conservation by the well-optimized concentration of allosteric PC inhibitor, L-aspartate, during the production phase with the limited growth of *A. terreus* [22, 23].

Conclusion

In this work, we attempted to regulate *A. terreus* metabolism for enhanced itaconic acid production. PC was allosterically inhibited by L-aspartate. The results show that 10 mM L-aspartate present in the production medium of *A. terreus* repressed PC expression while improving CAD activity. This could be explained by the decrease in oxaloacetate (OAA) and subsequently malate fluxes induced the transport of malate and cis-aconitate, citrate isomer, towards the antiporters as the metabolic response of the living culture of *A. terreus* to completely balance the metabolites fluxes in TCA and itaconic acid production routes. Malate transported into the mitochondria was then further converted to OAA and subsequently reacted with acetyl CoA to form citrate isomer that being transported via the antiporters to the cytosol. CAD further converted cis-aconitate, citrate isomer, into itaconic acid to balance the metabolic fluxes. This eventually resulted in the improved itaconic acid yield (0.47 g/g) of 8.33 % and final concentration (34.95 g/L) of 60.32 % compared to those obtained from the control fermentation (0.43 g/g and 21.80 g/L, respectively).

Acknowledgments This work was supported by the Ratchadapisek Somphot Endowment Fund (2014), Chulalongkorn University (CU-57-041-AM) and the National Research Council of Thailand via the annual statement of expenditure (GRB_APS_45_57_61_03). Partial financial support from Grant for International Research Integration: Chula Research Scholar, Ratchadaphiseksomphot Endowment Fund and Thailand Research Fund via the Distinguished Research Professor Grant (DPG5880003) was also highly acknowledged. Pajareeya Songserm is the recipient of the Royal Jubilee Scholarship Program, Thailand Research Fund. The supported expenditure via this program throughout her Ph.D. study is highly acknowledged.

References

1. Kuenz, A., Gallenmuller, Y., Willke, T., & Vorlop, K.-D. (2012). Microbial production of itaconic acid: developing a stable platform for high product concentrations. *Applied Microbiology and Biotechnology., 96*, 1209–1216.
2. US Department of Energy. (2004) Top value added chemicals from biomass, volume I: results of screening for potential candidates from sugars and synthesis gas. In: T. Werpy and G. Petersen (eds), pp. 42–44.
3. Bonnarme, P., Gillet, B., Sepulchre, A. M., Role, C., Beloeil, J. C., & Ducrocq, C. (1995). Itaconate biosynthesis in *Aspergillus terreus*. *Journal of Bacteriology, 177*, 3573–3578.
4. Okabe, M., Lies, D., Kanamasa, S., & Park, E. Y. (2009). Biotechnological production of itaconic acid and its biosynthesis in *Aspergillus terreus*. *Applied Microbiology and Biotechnology., 84*, 597–606.
5. Klement, T., & Buchs, J. (2013). Itaconic acid—a biotechnological process in change. *Bioresource Technology, 135*(17), 422–431.
6. Zhou, J., Liu, L., Shi, Z., Du, G., & Chen, J. (2009). ATP in current biotechnology: regulation, applications and perspectives. *Biotechnology Advances., 27*(5), 94–101.
7. Zeczycki, T. N., Maurice, M., & Attwood, P. V. (2010). Inhibitors of pyruvate carboxylase. *Open Enzyme Inhibition Journal, 3*(6), 8–26.
8. Osmani, S. A., Marston, F. A., Selmes, I. P., Chapman, A. G., & Scrutton, M. C. (1981). Pyruvate carboxylase from *Aspergillus nidulans*, regulatory properties. *European Journal of Biochemistry, 118*(7), 271–278.
9. Stephen, A. O., & Michael, C. S. (1984). The sub-cellular localization and regulatory properties of pyruvate carboxylase from *Rhizopus arrhizus*. *European Journal of Biochemistry, 147*(8), 119–128.
10. Thitiprasert, S., Songserm, P., Boonkong, W., Sooksai, S., Kodama, K., & Thongchul, N. (2014). Manipulating pyruvate decarboxylase by addition of enzyme regulators during fermentation of *Rhizopus oryzae*. *Applied Biochemistry and Biotechology, 174*(9), 1795–1809.
11. Lowry, O. H., Rosebrough, N. J., Farr, A. L., & Randall, R. J. (1951). Protein measurement with the folin phenol reagent. *Journal of Biological Chemistry, 193*(10), 265–275.
12. Acar, S., Yucel, M., & Hamamci, H. (2007). Purification and characterization of two isozymes of pyruvate decarboxylase from *Rhizopus oryzae*. *Enzyme and Microbial Technology, 40*(11), 675–682.
13. Kanamasa, S., Dwiarti, L., Okabe, M., & Park, E. Y. (2008). Cloning and functional characterization of the cis-aconitic acid decarboxylase (CAD) gene from *Aspergillus terreus*. *Applied Microbiology and Biotechnology, 80*(12), 223–229.
14. Srere, P. A. (1969). Citrate synthase. *Methods in Enzymology, 13*(13), 3–11.
15. Riscaldati, E., Moresi, M., Federici, F., & Petruccioli, M. (2000). Effect of pH and stirring rate on itaconate production by *Aspergillus terreus*. *Journal of Biotechnology, 83*(14), 219–230.
16. Tevz, G., Bencina, M., & Legisa, M. (2010). Enhancing itaconic acid production by *Aspergillus terreus*. *Applied Microbiology and Biotechnology, 87*(15), 1657–1664.
17. Mosojednik, S., & Legisa, M. (2005). Posttranslational modification of 6-phosphofructo-1-kinase in *Aspergillus niger*. *Applied and Environmental Microbiology, 71*(16), 1425–1432.
18. Huang, X., Lu, X., Li, Y., Li, X., & Li, J.-J. (2014). Improving itaconic acid production through genetic engineering of an industrial *Aspergillus terreus* strain. *Microbial Cell Factories, 13*, 1–9.
19. Steiger, M. G., Blumhoff, M. L., Mattanovich, D., & Sauer, M. (2013). Biochemistry of microbial itaconic acid production. *Frontiers in Microbiology, 4*, 1–5.
20. Myers, D. E., Tolbert, B., & Utter, M. F. (1983). Activation of yeast pyruvate carboxylase: interactions between acyl coenzyme A compounds, aspartate, and substrates of the reaction. *Biochemistry, 22*, 5090–5096.
21. Adina-Zada, A., Zeczycki, T. N., & Attwood, P. V. (2012). Regulation of the structure and activity of pyruvate carboxylase by acetyl CoA. *Archives of Biochemistry and Biophysics, 519*, 118–130.
22. Li, A., Lujik, N. V., ter Beek, M., Caspers, M., Punt, P., & van der Werf, M. (2011). A clone-based transcriptomics approach for the identification of genes relevant for itaconic acid production in *Aspergillus*. *Fungal genetics and Biology, 48*, 602–611.
23. Li, A., Pfelzer, N., Zuijderwijk, R., & Punt, P. (2012). Enhanced itaconic acid production in *Aspergillus niger* using genetic modification and medium optimization. *BMC Biotechnology, 12*, 1–9.

Chemical Engineering Journal 284 (2016) 1212–1223

Contents lists available at ScienceDirect

Chemical Engineering Journal

journal homepage: www.elsevier.com/locate/cej

Metals (Mg, Sr and Al) modified CaO based sorbent for CO_2 sorption/desorption stability in fixed bed reactor for high temperature application

Janewit Phromprasit [a], Jonathan Powell [b], Suttichai Assabumrungrat [a,*]

[a] Center of Excellence in Catalysis and Catalytic Reaction Engineering, Department of Chemical Engineering, Faculty of Engineering, Chulalongkorn University, Bangkok 10330, Thailand
[b] International School of Engineering, Faculty of Engineering, Chulalongkorn University, Bangkok 10330, Thailand

HIGHLIGHTS

- CaO was modified by inserting compounds of Mg^{2+}, Sr^{2+} and Al^{3+} into its structure.
- Sorbents were prepared by dry powder mixing and wet mixing methods.
- CaO hydration followed by wet mixing could improve sorption stability of sorbents.
- Fixed bed reactor was employed for CO_2 sorption/desorption testing.

GRAPHICAL ABSTRACT

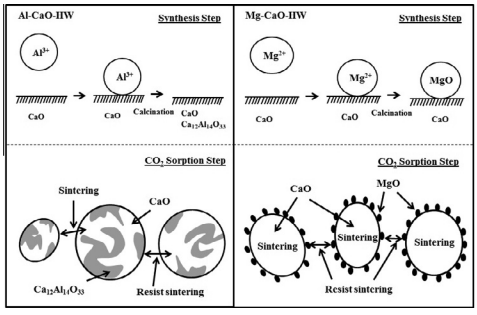

ARTICLE INFO

Article history:
Received 23 May 2015
Received in revised form 8 September 2015
Accepted 11 September 2015
Available online 21 September 2015

Keywords:
CO_2 sorption/desorption
Mg, Sr and Al modified CaO
Dry powder mixing
Wet mixing
CaO hydration
Fixed bed reactor

ABSTRACT

Modified sorbents – produced by adding compounds of Mg^{2+}, Sr^{2+} and Al^{3+} to calcium oxide – have been tested in terms of their CO_2 sorption/desorption performance in a fixed bed reactor at high temperatures. In particular this study focuses on the stability of the sorbents as well as the sorption capacity, both of which are important factors when selecting sorbents. X-ray diffraction (XRD) and scanning electron microscope (SEM), coupled with energy dispersive X-ray spectroscopy (EDX), were used for characterization of the modified sorbents. XRD results indicated that samples produced using the wet mixing process and those produced using the hydration with wet mixing process, contained MgO–CaO, $Ca_{0.2}Sr_{0.8}O$–CaO and $Ca_{12}Al_{14}O_{33}$–CaO phases, respectively.

The operating conditions have been investigated and results showed that the CaO showed the highest sorption capacity ($0.571 g_{CO_2}/g_{sorbent}$) when compared with MgO, SrO and Al_2O_3 at temperature of 600 °C. In terms of sorption capacity performance for sorbents produced by the CaO hydration and wet mixing method, Mg-CaO-HW showed the best sorption/desorption stability for more than 10 cycles (CO_2 sorption capacity of 0.259 for 1st cycle to $0.252 g_{CO_2}/g_{sorbent}$ for the 10th cycle). Al-CaO-HW and Sr-CaO-HW exhibited a decrease in sorption capacity due to the sintering as confirmed by SEM images (0.257 and $0.286 g_{CO_2}/g_{sorbent}$ for 1st cycle dropping to 0.243 and $0.251 g_{CO_2}/g_{sorbent}$ for 10th cycle resulting in decreasing approximately of 5.45% and 12.24%, respectively).

© 2015 Elsevier B.V. All rights reserved.

1. Introduction

The most abundantly used energy sources are fossil fuels such as petroleum, natural gas and coal, the combustion of which results in the emission of carbon dioxide contributing to global warming and a decrease in local air quality. CO_2 emissions originate from both delocalized sources such as automobiles, but also from large centralized sources such as power plants [1–4], and in the production of chemicals such as hydrogen [5–8], ethylene, ammonia and various petrochemicals [9], all of which have a high environmental impact. CO_2 capture techniques are concerned with

* Corresponding author. Tel.: +66 2 2186868; fax: +66 2 2186877.
E-mail address: suttichai.a@chula.ac.th (S. Assabumrungrat).

http://dx.doi.org/10.1016/j.cej.2015.09.038
1385-8947/© 2015 Elsevier B.V. All rights reserved.

large centralized CO_2 emission sources, where implementation of the CO_2 capture technologies can have the largest impact at minimal cost and infrastructure changes.

Typically CO_2 is absorbed using liquid sorbents such as amine [10–12] and solid sorbents such as CaO (Eq. (1)) [13–20], Li based sorbents (Eqs. (2) and (3)) [21–26] and hydrotalcite [27–38]. Amine is normally limited to small scales use, low temperatures (40–150 °C) and incurs high costs [39] due to thermal degradation of the amine. For CO_2 sorption at high temperature application, the solid sorbents are a good alternative because they have higher thermal stability than liquid sorbents. Ochoa-Fernández et al., [40] have investigated solid sorbents such as CaO, Li_2ZrO_3, K-Li_2ZrO_3, Na_2ZrO_3 and Li_4SiO_4 in term of CO_2 sorption capacity and the results indicated CaO has the highest CO_2 sorption capacity ($0.495 g_{CO_2}/g_{sorbent}$) at a temperature of 575 °C. Moreover, the CO_2 sorption capacity of CaO was compared to that of hydrotalcite and results also demonstrated a higher CO_2 sorption capacity than hydrotalcite (MG61-K_2CO_3: $0.070 g_{CO_2}/g_{sorbent}$) at a temperature of 300 °C and P_{CO_2} of 0.6 [29], however CaO has the disadvantage of relatively low CO_2 sorption/desorption stability.

$$\text{Calcium oxide}: \quad CaO + CO_2 \leftrightarrow CaCO_3 \quad \Delta H_{289\ K} = -178\ \text{kJ/mol} \tag{1}$$

$$\text{Lithium based sorbent}: \quad Li_2ZrO_3 + CO_2 \leftrightarrow Li_2CO_3 + ZrO_2 \quad \Delta H_{289\ K} = -160\ \text{kJ/mol} \tag{2}$$

$$Li_4SiO_4 + CO_2 \leftrightarrow Li_2SiO_3 + Li_2CO_3 \quad \Delta H_{289\ K} = -142\ \text{kJ/mol} \tag{3}$$

To improve the stability of CaO, metal oxides were added to the structure of CaO. Metal oxides were selected with Tammann temperatures higher than the carbonation/calcination temperature. The Tammann temperature is the minimum temperature at which the ions, atoms or molecules of a solid acquire sufficient energy for bulk mobility and thus take part in solid state reactions and sintering [41,42]. Several researchers have investigated the use of various dopants on CaO, such as compounds of Si^{4+}, Co^{2+}, Cr^{3+}, Ce^{4+}, Zr^{4+} [43], Ti^{4+} [43,44], Y^{3+} [45], La^{3+} [46], Mg^{2+} [47] and Al^{3+} [48–51] having high Tammann temperatures as shown in Table 1. Lu et al. [43] studied CaO sorbent doped with metal ions (Si^{4+}, Co^{2+}, Ti^{4+}, Cr^{3+}, Ce^{4+} and Zr^{4+}) produced by flame spray pyrolysis. The carbonation was carried out at a temperature of 700 °C, with a 30% CO_2 feed stream, whilst regeneration took place under helium. The results indicated that the Zr/Ca sorbent showed the best sorption stability due to the reaction of ZrO_2 with CaO forming to $CaZrO_3$. They proposed that calcium zirconate resisted the growth of CaO grains resulting from sintering-agglomeration. Martavaltzi et al. [48] investigated the use of $Ca_{12}Al_{14}O_{33}$ inert material synthesized from calcium acetate and aluminum nitrate. The synthesis procedure consisted of: calcination of the calcium acetate (step 1); the precipitation of the CaO with aluminum nitrates (step 2); calcination at a temperature of 500 °C for nitrates removal (step 3); addition of water and drying at a temperature of 120 °C (Step 4); calcination at 900 °C for the synthesis of $Ca_{12}Al_{14}O_{33}$ (step 4). The sorbent showed an initial 35% weight increase for the first cycle which was maintained for the subsequent 45 cycles. Moreover, $Ca_{12}Al_{14}O_{33}$ was transformed to $Ca_9Al_6O_{33}$ by diffusion of Ca^{2+} into the structure. Zhou et al. [52] has proposed a mechanism of $Ca_{12}Al_{14}O_{33}$ and $Ca_9Al_6O_{18}$ formation and investigated their sorption stability performance. The CaO–$Ca_9Al_6O_{18}$ sorbent with a CaO content of 80 wt% (weight fraction) synthesized from calcium citrate and aluminum nitrate exhibited the best performance for CO_2 capture. The CO_2 capture capacity decreased from 0.59 ($g_{CO_2}/g_{sorbent}$) for the first cycle to 0.51 ($g_{CO_2}/g_{sorbent}$) for the 28th cycle representing a 13.6% decrease. Furthermore, several sorbents have been studied for CO_2 sorption at high temperature by using multiple cycles operation as shown in Table 2.

Table 1
Tammann temperature of material.

Material	Tammann temperature (°C)
SiO_2	725
CoO	779
TiO_2	785
Cr_2O_3	1028
CeO_2	1064
ZrO_2	1218
Al_2O_3	900
MgO	1290
SrO	1129
CaO	1313
$CaCO_3$	533

In addition, the parameters which affect results obtained on CO_2 sorbent performance are (i) synthesis methods, (ii) metal precursors and (iii) instruments for CO_2 sorption/desorption testing. For production of CO_2 sorbents on an industrial scale, simple and easy synthesis methods are considered such as the physical mixing method (dry powder mixing), the wet mixing method, the impregnation method or the hydration with wet mixing method. In contrast, the sol–gel or co-precipitation methods use metal precursors such as $Ca(NO_3)_2{\cdot}4H_2O$ for CaO [45,46] and $Al(NO_3)_3{\cdot}9H_2O$ for Al_2O_3 [46] which increase the operation cost due complex and energy intensive synthesis steps.

The operating conditions for CO_2 sorption are also important for CO_2 capture in several industry applications such as power plants and petrochemical and chemical production. This study investigates the effect of various factors pertinent to these applications, namely the effect of supports, the effect of sorption temperatures and the effect of CO_2 concentration. Furthermore, the synthesis methods – physical mixing (dry powder mixing); wet mixing; CaO hydration followed by wet mixing – have been investigated, comparing samples produced using compounds of Mg^{2+}, Sr^{2+} and Al^{3+} with CaO. Samples were tested in terms of their CO_2 sorption/desorption performance over multiple cycles in a fixed bed reactor, measured in terms of sorption capacity and sorption stability.

2. Experiment

2.1. Preparation of modified sorbents

Three synthesis methods have been investigated including methods referred to as the physical mixing method (dry powder mixing), the wet mixing method and the CaO hydration with mixing method. Firstly, the dry powder mixing method involved mixing dry metal oxide powders – namely magnesium oxide (MgO, Sigma–Aldrich), strontium oxide (SrO, Aldrich) and aluminum oxide (Al_2O_3, Sigma–Aldrich) – with calcium oxide powder (CaO, Sigma–Aldrich). Compositions of 80% w/w CaO and 20% w/w of each metal oxide (MgO, SrO and Al_2O_3) were dry mixed by shaking by hand for 10 min until are uniform mixture was obtained, which was then calcined at 900 °C for 3 h in air. In this report samples produced using the dry powder mixing method are denoted with a D i.e. Mg-CaO-D, Sr-CaO-D and Al-CaO-D for samples containing MgO, SrO and Al_2O_3 as precursors, respectively.

The metal precursors used for synthesis of the modified sorbents by wet mixing and CaO hydration followed by wet mixing, were calcium oxide (CaO, Sigma–Aldrich), magnesium nitrate hexahydrate ($Mg(NO_3)_2{\cdot}6H_2O$, Merck), strontium nitrate anhydrous ($Sr(NO_3)_2$, Fluka) and aluminum nitrate nanohydrate ($Al(NO_3)_3{\cdot}9H_2O$, Sigma–Aldrich).

Table 2
Comparison of CO_2 sorption capacity at 1st–10th cycle.

Sorbent	Method	Temp.	CO_2 concentration	1st ($g_{CO_2}/g_{sorbent}$)	10th ($g_{CO_2}/g_{sorbent}$)	% Decrease	Ref.
$CaO–Ca_{12}Al_{14}O_{33}$	Wet mixing	690 °C	15% CO_2	0.37[a]	0.34[a]	8.11	[48]
$CaO–CaZrO_3$	FSP	700 °C	30% CO_2	0.50[b]	0.50[b]	0.00	[43]
	FSP	700 °C	30% CO_2	0.38[b]	0.38[b]	0.00	[43]
$CaO–Ca_9Al_6O_{18}$	Wet mixing	650 °C	15% CO_2	0.58	0.54	6.90	[50]
$CaO–CaTiO_3$	Coprecipitate	750 °C	100% CO_2	0.40[a]	0.37[a]	7.50	[44]
$CaO–Y_2O_3$	Sol–gel combustion synthesis	650 °C	20% CO_2	0.60	0.58	3.33	[45]
$NanoCaO–Al_2O_3$	–	600 °C	33% CO_2	0.22[c]	0.14[c]	37.50	[51]
$CaO–La_2O_3$	Sol–gel combustion synthesis	850 °C	100% CO_2	0.60	0.59	1.67	[46]
CaO–MgO	Co-precipitate and hydration	700 °C	90% CO_2	0.48[a]	0.45[a]	6.25	[47]

[a] Sorption capacity which calculated from weight increasing.
[b] Sorption capacity which calculated from molar conversion.
[c] Sorption capacity which calculated from sorption ratio.

The wet mixing process involved dissolving CaO in deionized water and then adding the metal precursors (magnesium nitrate, strontium nitrate and aluminum nitrate) into the CaO solution at a temperature of 75 °C for 3 h. After that they were dried in an oven at a temperature of 110 °C overnight and calcined at 900 °C for 3 h in air. In this report samples produced using the wet mixing method are denoted with a W i.e. Mg-CaO-W, Sr-CaO-W and Al-CaO-W for samples produced using magnesium nitrate, strontium nitrate and aluminum nitrate precursors, respectively.

The final sample preparation method used was the CaO hydration followed by wet mixing method. This involved dissolving CaO in deionized water at a temperature of 75 °C for 2 h then adding the metal precursors, mixing and maintaining a temperature of 75 °C for 2 h. They were then dried at a temperature of 110 °C overnight and calcined at a temperature of 900 °C for 3 h in air. In this report, the sorbents produced using this method are denoted with a HW i.e. Mg-CaO-HW, Sr-CaO-HW and Al-CaO-HW for samples produced using magnesium nitrate, strontium nitrate and aluminum nitrate precursors, respectively.

2.2. Characterization

X-ray diffraction (XRD) was used to characterize the samples. XRD patterns were obtained using a D8 Advance, Bruker, equipped with a long fine focus Cu K_α X ray source. The pattern was recorded at room temperature, range of $10° < 2\theta < 80°$ with an increasing step of 0.04°, wavelength of 1.54056 nm and scan speed of 0.5.

The morphologies of modified sorbents before and after CO_2 sorption/desorption were observed using a scanning electron microscope, SEM, (Hitachi S-3400 N) coupled with X-ray energy dispersive spectroscopy, X-ray EDS, (AMETEK EDAX, APOLLO X) for analyzing the local dispersion of elements.

2.3. CO_2 sorption testing

One gram of fresh sample was placed into a fixed bed quartz reactor (inner diameter of 15 mm and outer diameter of 18 mm) and pretreated at a temperature of 850 °C with a heating rate of 10 °C/min under pure N_2 flow and total flow rate of 60 mL/min, for desorption of moisture and CO_2. After that CO_2 was fed into the reactor at a temperature of 600 °C, a pressure of 1 atm and a concentration of 8% or 15%. The outlet gases were analyzed by gas chromatography (GC) equipped with two columns – a Molecular Sieve 5A and a Poraplot Q and mass spectrometer (MS). The equipment for CO_2 sorption/desorption testing is depicted in Fig. 1. The CO_2 sorption capacity was calculated using Eq. (4).

$$\text{Sorption capacity} = \frac{F_{CO_2,in} \times \int_0^t \left(1 - A \cdot \frac{C_{CO_2,out}}{C_{CO_2,in}}\right) dt}{W} \quad (4)$$

where F_{CO_2} is the feed rate (g/min), C is the CO_2 concentration at the outlet of reactor (%), C_0 is the CO_2 concentration at inlet of reactor (%), W is the sorbent weight (g), t is sorption time (min), A is $\frac{\upsilon_{N_2}}{\upsilon_{Total,in}} \cdot \left(1 + \frac{y_{CO_2}}{(1-y_{CO_2})}\right)$, υ_{N_2} is volumetric flow rate of N_2 (mL/min), $\upsilon_{Total,in}$ is total volumetric flow rate of feed stream (mL/min) and y_{CO_2} is molar fraction of CO_2 at outlet stream.

3. Results and discussion

3.1. CO_2 sorption performance

3.1.1. Effect of support

Alkali earth metal oxides including MgO, CaO and SrO, and Al_2O_3 are commonly used as catalyst supports and were selected due to their ability to absorb CO_2 gas. All samples were tested in terms of CO_2 sorption by added 1 g of the solid powder into a fixed bed quartz reactor. The results (Fig. 2) show the CaO exhibited the best sorption capacity (0.571 $g_{CO_2}/g_{sorbent}$) when compared with MgO (0.038 $g_{CO_2}/g_{sorbent}$), SrO (0.065 $g_{CO_2}/g_{sorbent}$) and Al_2O_3 (0.037 $g_{CO_2}/g_{sorbent}$) at a temperature of 600 °C, pressure of 1 atm and with an 8% CO_2 feed stream.

3.1.2. Effect of temperature

For the test on the CaO sorbent, temperatures were varied from 500 to 700 °C, at a pressure of 1 atm and with an 8% CO_2 feed stream. The sorption capacity increased with increasing temperature from 500 to 600 °C (sorption capacity at 500 °C of 0.211 $g_{CO_2}/g_{sorbent}$ and at 600 °C of 0.571 $g_{CO_2}/g_{sorbent}$). For temperatures of 700 °C and above CO_2 sorption capacity decreased with increasing temperature. The optimum temperature for CO_2 sorption capacity in the fixed bed reactor was found to be approximately 600 °C. However, with increasing sorption temperature, the breakthrough time consistently decreased (11.67, 9.66, 3.41 min for 500, 600 and 700 °C, respectively), meaning that the time required for CO_2 gas to reach the outlet of the reactor decreased with increasing temperature. The breakthrough curves for CaO (Fig. 3) indicated a two-step sorption process was taking place. It is proposed that for the first step the sorption occurred at the surface only (step 1: $CaO + CO_2 \rightarrow CaCO_3$). It is proposed that the second step is related to the diffusion of CO_2 into the CaO particles, as indicated in Fig. 4(a). At a temperature of 500 °C, the sorption capacity is limited by step 2 the diffusion of CO_2 into the CaO particles, meaning the slow diffusion of CO_2 below the surface but relatively fast adsorption of CO_2 onto the CaO surface because $CaCO_3$ generated at the surface layers were not sintered by thermal activity because sorption temperature (500 °C) was lower than the Tammann temperature (533 °C) therefore CO_2 sorption at surface continued. In contrast, at temper-

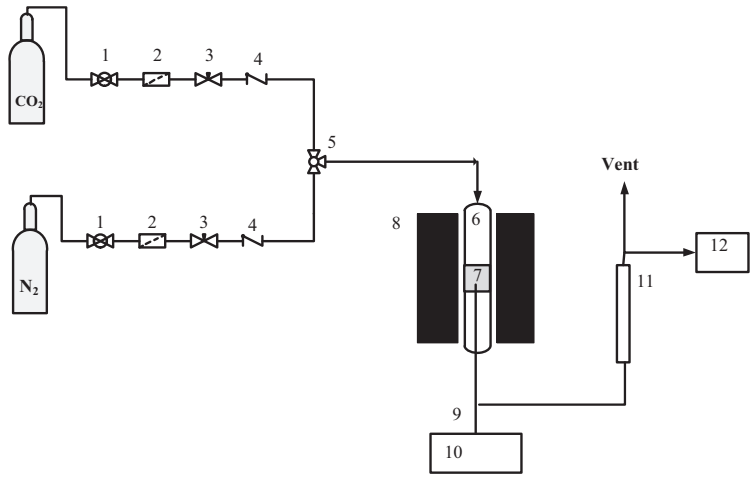

1. Ball valve 2. Filter 3. Needle valve 4. Check valve 5. Mixing valve 6. Quartz reactor
7. Bed 8. Furnace 9. Thermocouple 10. Temperature controller 11. Bubble flow meter
12. Mass spectrometer

Fig. 1. Equipment for CO_2 sorption/desorption testing.

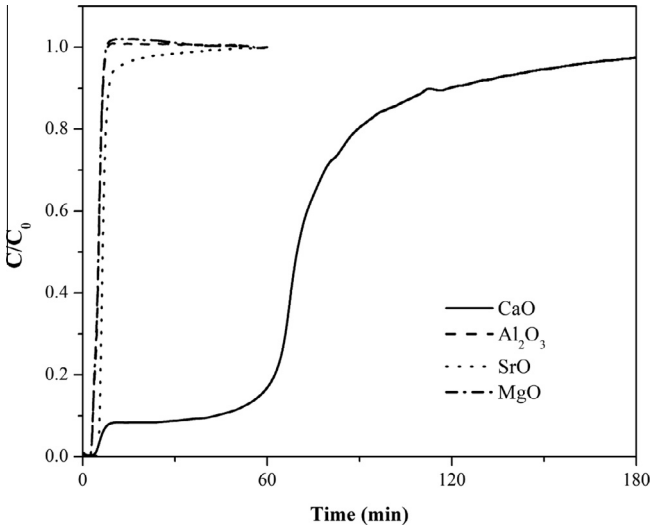

Fig. 2. Breakthrough curves of various supports (MgO, SrO, CaO and Al_2O_3) at temperature of 600 °C, pressure of 1 atm and 8% CO_2 feed stream.

atures of 600 and 700 °C an increase in CO_2 concentration at the outlet indicates less adsorption of CO_2 taking place at the CaO surface (step 1) due to sintering of the $CaCO_3$ at surface (propose mechanism in Fig. 4(b)) which reduces the surface area and reduces the open porosity. However, the sorption capacity at a temperature of 700 °C (0.363 $g_{CO_2}/g_{sorbent}$) was observed to be lower than at 600 °C. This is due to two reasons: (i) carbonation (Eq. (1)) is an exothermic reaction and so desorption of CO_2 is favored by higher temperature; (ii) the CO_2 diffusion rate into sub surface CaO layers (step 2) is low due to reduced surface area as a result of surface sintering.

3.1.3. Effect of synthesis method

3.1.3.1. Dry powder mixing method. Experimental results obtained for the sorbents produced by the dry powder mixing method (Mg-CaO-D, Sr-CaO-D and Al-CaO-D), as shown in Fig. 5, indicate that the CO_2 sorption capacities are similar to each other (0.256, 0.219, 0.248 $g_{CO_2}/g_{sorbent}$ for Mg-CaO-D, Sr-CaO-D and Al-CaO-D, respectively). This is partly because the same mass of each metal oxide (MgO, SrO and Al_2O_3) was loaded on to the CaO (20% by weight) reducing the mass of CaO in the sorbent mixture by the same mass each time; moreover, the metal oxides and CaO remained as separate phases as confirmed by XRD patterns as shown in Fig. 6, for example XRD pattern of the Al-CaO-D sample showed Al_2O_3 phase, CaO showed CaO and $Ca(OH)_2$ phases. The fact that none of the samples contained complex materials or materials resulting from chemical interactions between each other, is due to the Tammann temperature (>900 °C) of the metal oxides being higher than the temperature of the calcination process (900 °C), and so migration of the respective ions and hence solid state reactions and sintering would not be expected.

3.1.3.2. Wet mixing method. Fig. 7 shows the breakthrough curves of the modified sorbents (Mg-CaO-W, Sr-CaO-W, Al-CaO-W) and the results show that the highest CO_2 sorption capacity was obtained for Mg-CaO-W (0.319 $g_{CO_2}/g_{sorbent}$). It is proposed that this

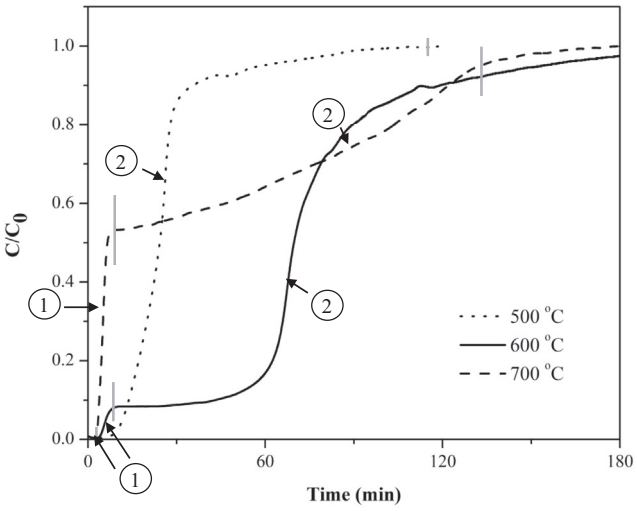

Fig. 3. Breakthrough curves of CaO at temperature of 500–700 °C, pressure of 1 atm and 8% CO_2 feed stream: ① refers to step 1 – surface reaction and ② refers to step 2 – CO_2 diffusion.

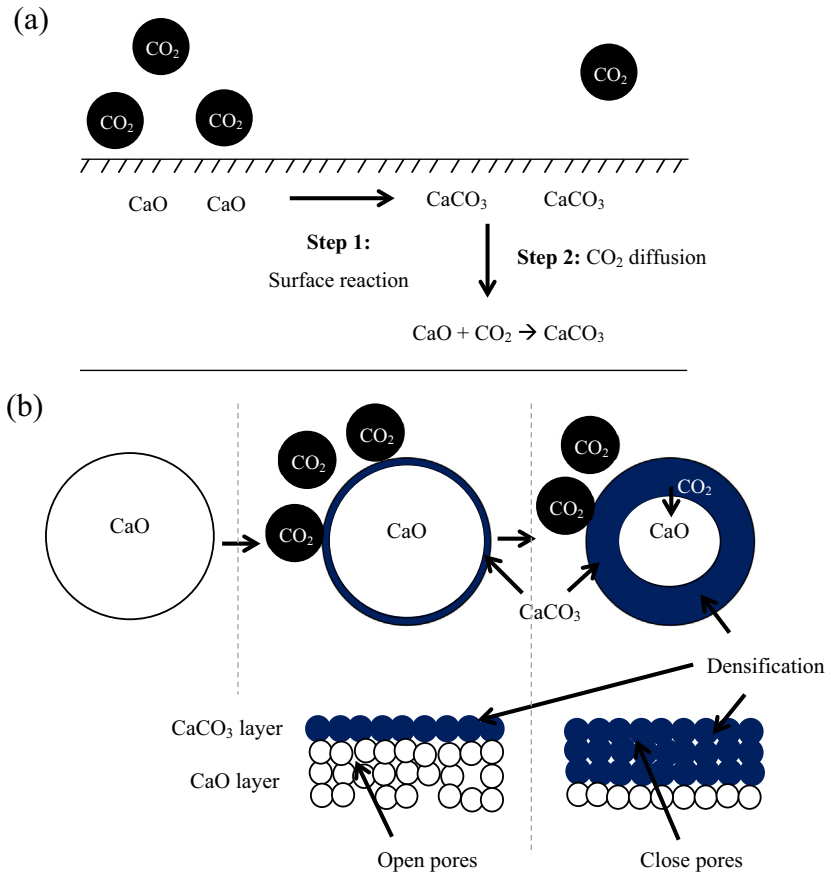

Fig. 4. Propose mechanisms: (a) CO_2 sorption step and (b) densification phenomena at sorption temperature of 600 and 700 °C.

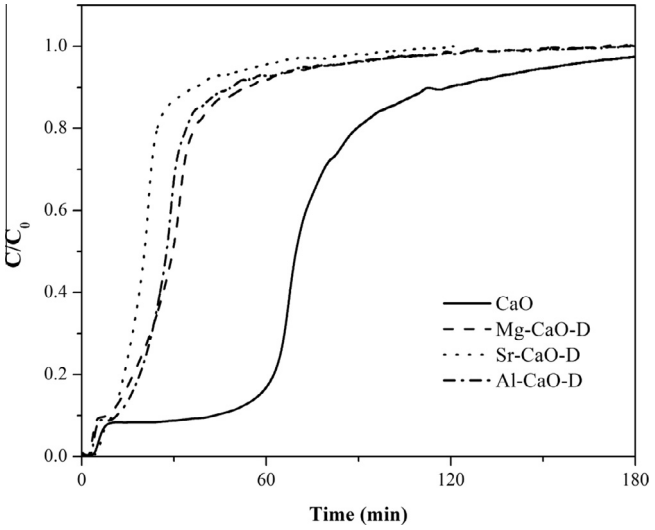

Fig. 5. Breakthrough curves of modified sorbents by dry powder mixing method (Mg-CaO-D, Sr-CaO-D, Al-CaO-D and CaO) at temperature of 600 °C, pressure of 1 atm and 8% CO_2 feed stream.

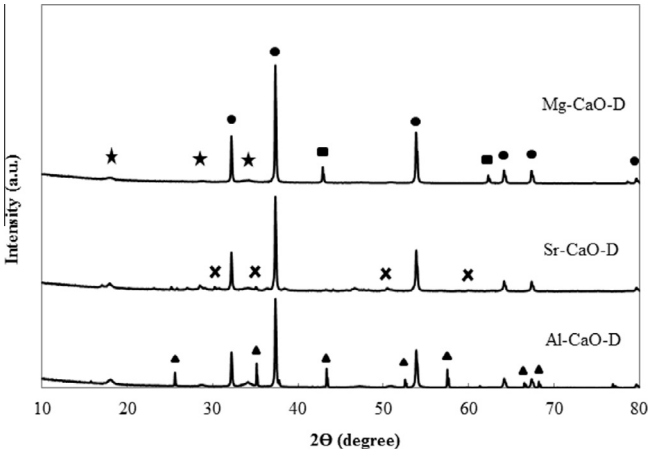

Fig. 6. XRD patterns of modified sorbents by dry powder mixing method: ● CaO, ■ MgO, ✖ SrO, ▲ Al_2O_3 and ★ $Ca(OH)_2$.

is due to the MgO and CaO remaining as separate phases. This is confirmed by the XRD patterns shown in Fig. 8. However, the breakthrough time for Mg-CaO-W is shown to be shorter than those of Al-CaO-W and Sr-CaO-W, implying less CO_2 sorption on the CaO surface (CO_2 concentration at outlet rapidly increased) due to a surface coating of MgO, thus reducing the availability of the CaO surface but also reducing the open porosity.

The results of Al-CaO-W and Sr-CaO-W showed these materials to have a lower sorption capacity than Mg-CaO-W. This is explained by a lower content of CaO in the sorbent as a result of chemical reactions of CaO with the dopant, forming $Ca_{12}Al_{14}O_{33}$ and $Ca_{0.2}Sr_{0.8}O$, as confirmed by XRD patterns which shown in Fig. 8. However, Al-CaO-W was shown to have the longest breakthrough time (18.42 min) as compared to Mg-CaO-W (4.90 min), Sr-CaO-W (6.00 min) and CaO (9.66 min). $Ca_{12}Al_{14}O_{33}$ that formed in the Al-CaO-W sample, possesses an oxygen vacancy or oxygen defect in the structure which promotes CO_2 sorption at the surface

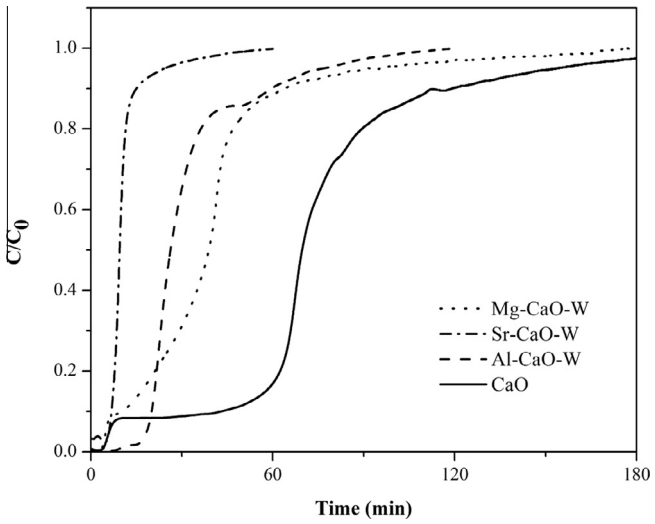

Fig. 7. Breakthrough curves of modified sorbents by wet mixing method (Mg-CaO-W, Sr-CaO-W, Al-CaO-W and CaO) at temperature of 600 °C, pressure of 1 atm and 8% CO_2 feed stream.

and CO_2 diffusion into core of CaO particles resulting in improved sorption performance.

Sr-CaO-W sorbent exhibited the lowest sorption capacity (0.088 $g_{CO_2}/g_{sorbent}$) due to the formation of $Ca_{0.2}Sr_{0.8}O$ as confirmed by XRD patterns (Fig. 8). These patterns show a reduced amount of CaO sorbent as indicated by the intensity of the main peak of CaO ($2\theta = 37.35°$) which is smaller than other the modified sorbents (Mg-CaO-W and Al-CaO-W) produced by the wet mixing method.

3.2. Stability of modified sorbents by wet mixing method

Modified sorbents produced by wet mixing (Mg-CaO-W, Sr-CaO-W and Al-CaO-W) were tested by CO_2 sorption/desorption over multiple cycles as shown in Fig. 9. The CaO showed decreasing CO_2 sorption capacity with an increasing number of cycles (0.390 $g_{CO_2}/g_{sorbent}$ at 1st cycle to 0.168 $g_{CO_2}/g_{sorbent}$ at 25th cycle which decreasing of 56.92%). This is due to the sintering of particles resulting in pores decreasing in size or even closing as shown in Fig. 10(d). To reduce this effect some metal oxides with Tammann temperatures greater than 900 °C were selected and added to CaO structure. The modified sorbents (Mg-CaO-W, Sr-CaO-W and Al-CaO-W) showed the same trend with decreasing sorption capacity with increasing number of cycles, however the degree to which it took place was much lower. This decrease in sorption capacity is attributed to the agglomeration of particles due to sintering as shown in Fig. 10(a)–(c).

All modified sorbents produced by the wet mixing method (Mg-CaO-W, Sr-CaO-W and Al-CaO-W) exhibited low stability performance. This is possibly due to incomplete formation of CaO and poor dispersion of metal dopants (Mg^{2+}, Sr^{2+} and Al^{3+}) within the CaO. Furthermore, due to a low surface area of the CaO, metal dopants (Mg^{2+}, Sr^{2+} and Al^{3+}) were deposited on CaO surface meaning that dopant phases (MgO, $Ca_{0.2}Sr_{0.8}O$ and $Ca_{12}Al_{14}O_{33}$) were occurred only at the surface resulting in occurred the densification of particles when CO_2 sorption/desorption were tested as shown propose mechanism in Fig. 11. In order to increase the CaO surface area, the CaO hydration step was implemented before adding the dopant (Mg^{2+}, Sr^{2+} and Al^{3+}). The results indicated the Al-CaO-HW to be stable for more than 10 cycles (0.130 $g_{CO_2}/g_{sorbent}$ at 1st cycle and 0.127 $g_{CO_2}/g_{sorbent}$at 10th cycle). This is attributed to the hydration of CaO to form $Ca(OH)_2$, increasing the pore volume [47] therefore allowing the Al^{3+} precursor to diffuse into the $Ca(OH)_2$ structure, resulting in it being more highly dispersed on the CaO and subsequently more highly dispersed $Ca_{12}Al_{14}O_{33}$ after calcination. In addition, the inert phase ($Ca_{12}Al_{14}O_{33}$) – which has defect of oxygen vacancies [53] – can promote absorption of adsorbed CO_2 to below the CaO surface and also during CO_2 regeneration subsurface CaO can be released to the surface [54]. Furthermore, $Ca_{12}Al_{14}O_{33}$ also resisted the agglomeration between CaO particles therefore the sintering was not observed as shown in Fig. 10(e) used.

3.2.1. Effect of CO_2 concentration

The Al-CaO-HW samples synthesized by hydration of the CaO followed by wet mixing, were tested with an 8% CO_2 feed gas and a 15% CO_2 feed gas, both with a N_2 balance. These concentrations were tested as they represent a typical range in CO_2 concentrations in emissions from various industrial sources such as flue gas from power plants, fired heaters from oil refineries and petrochemical plants as shown in Table 3. Furthermore, several researchers have investigated the modified sorbent for CO_2 sorption in a 15% CO_2 atmosphere and at high temperatures

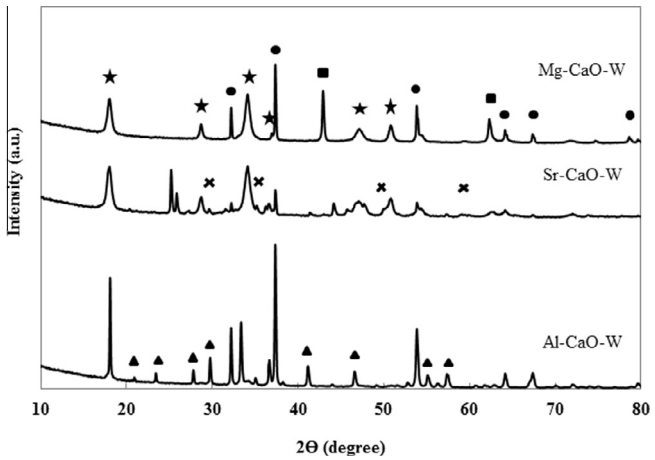

Fig. 8. XRD patterns of modified sorbents by wet mixing method: ● CaO, ■ MgO, ✘ $Ca_{0.2}Sr_{0.8}O$, ▲ $Ca_{12}Al_{14}O_{33}$ and ★ $Ca(OH)_2$.

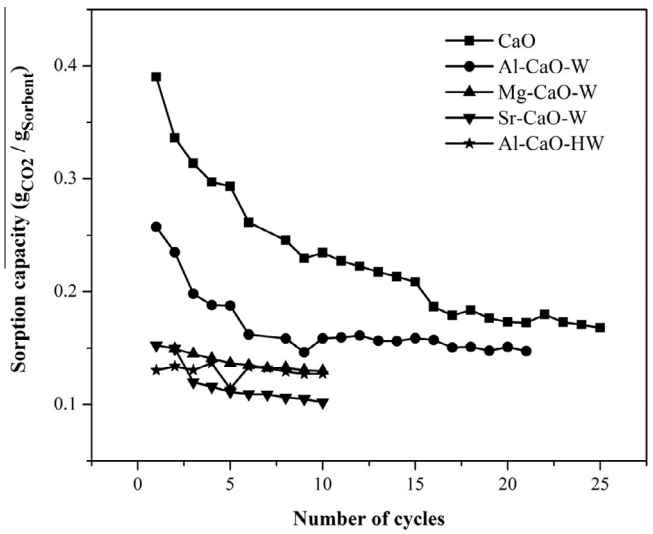

Fig. 9. CO_2 sorption/desorption cycles of modified sorbents by wet mixing method at temperature of 600 °C, pressure of 1 atm and 8% CO_2 in feed stream.

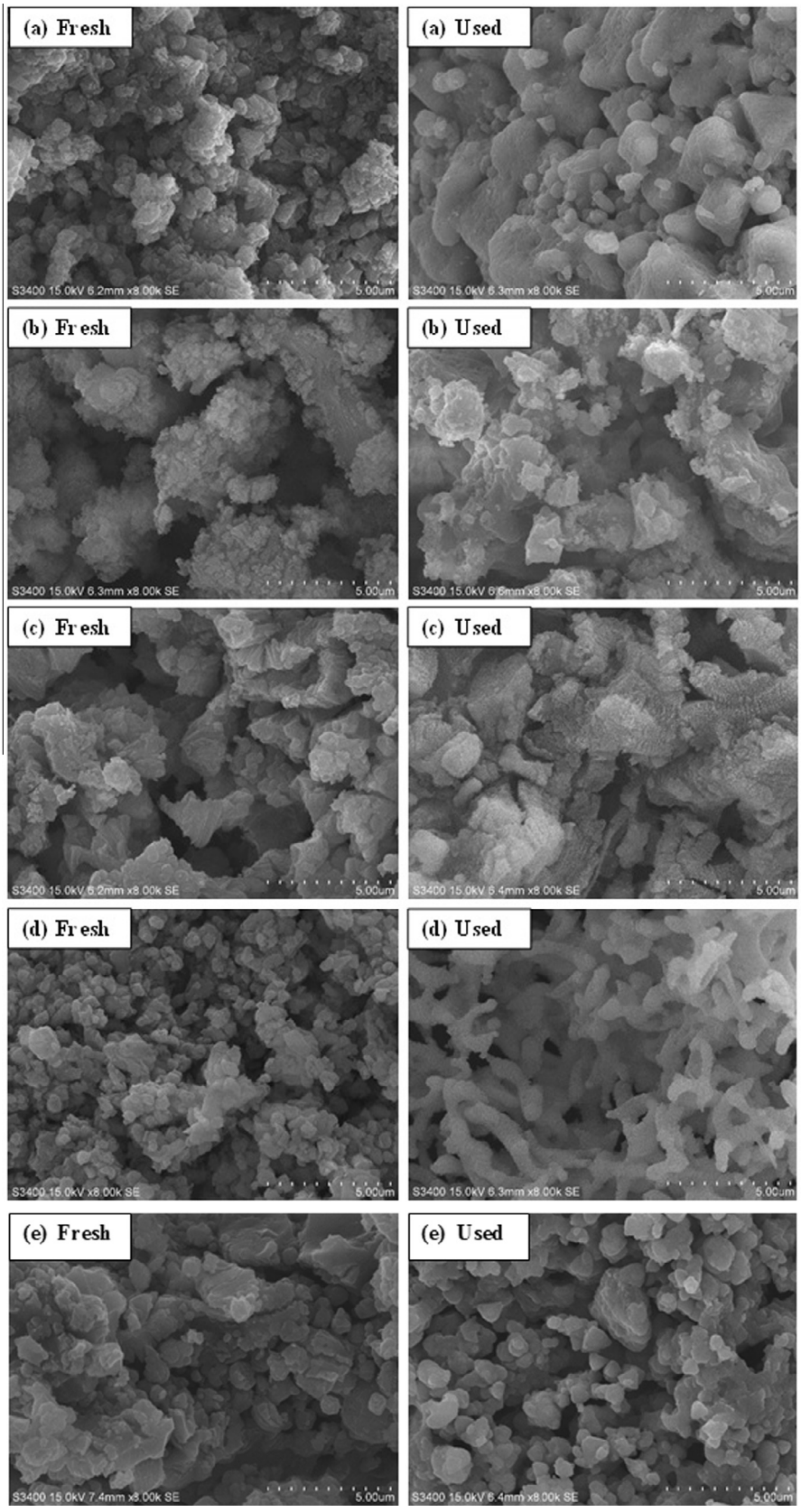

Fig. 10. SEM images of fresh and used modified sorbents by wet mixing method: (a) Al-CaO-W, (b) Mg-CaO-W, (c) Sr-CaO-W, (d) CaO commercial and (e) Al-CaO-HW.

[52,55–57]. This was done to enable the comparison of our modified sorbents with the sorption capacity results from other studies. As would be expected the results indicate that when the feed CO_2 concentration is increased, the CO_2 sorption capacity also increases (1st cycle: 0.130 $g_{CO_2}/g_{sorbent}$ at 8% CO_2 in feed to 0.257 $g_{CO_2}/g_{sorbent}$ at 15% CO_2 in feed which increasing of 97.7%) as shown in Fig. 12.

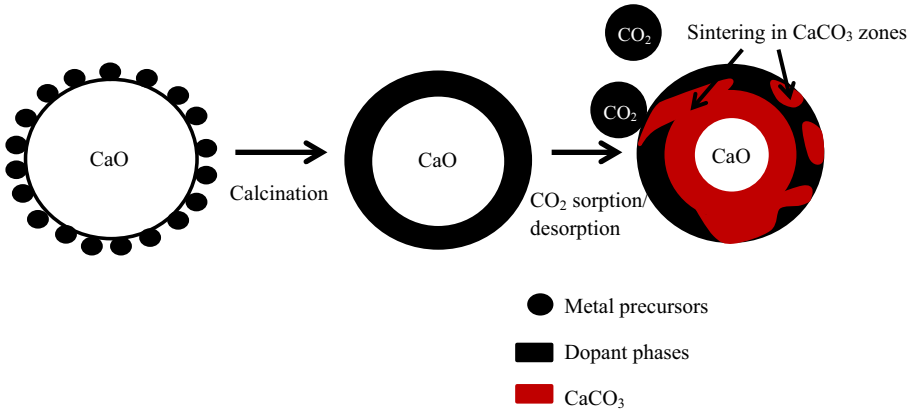

Fig. 11. Propose mechanism of occurring the dopant phases (MgO, $Ca_{0.2}Sr_{0.8}O$ and $Ca_{12}Al_{14}O_{33}$) on CaO by wet mixing method and their densification phenomena.

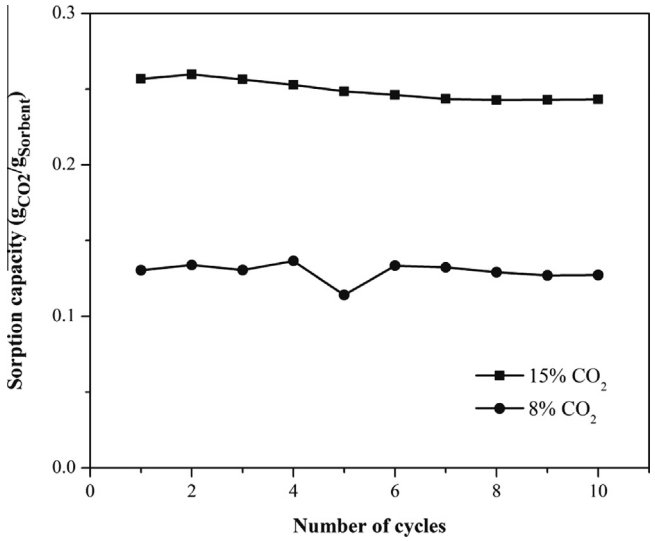

Fig. 12. CO_2 sorption/desorption cycles of Al-CaO-HW at temperature of 600 °C, pressure of 1 atm and CO_2 concentration of 8% and 15%.

This increase in partial pressure of the CO_2 leads to a greater driving force for sorption and hence an increase in capacity [13]. Furthermore, this phenomena was supported by equilibrium partial pressure of CO_2 resulting from the decomposition of $CaCO_3$ [44,58] which indicated that the increasing of partial pressure of CO_2 at constant temperature will promote further capture of CO_2 by CaO. This in itself is not of particular interest, but we will see further on in this section that the increase in concentration of the CO_2 has a greater positive impact upon the sorption capacity of the modified sorbents.

Table 3
Sources of CO_2 [9].

Source	CO_2 concentration % vol (dry)
Power station flue gas:	
Natural gas fired boilers	7–10
Gas turbines	3–4
Oil fired boilers	11–13
Coal fired boilers	12–14
Oil refinery and petrochemical plant fired heaters	8
Chemical reaction (s)	
Ethylene oxide	8
Hydrogen production	15
Methanol production	10

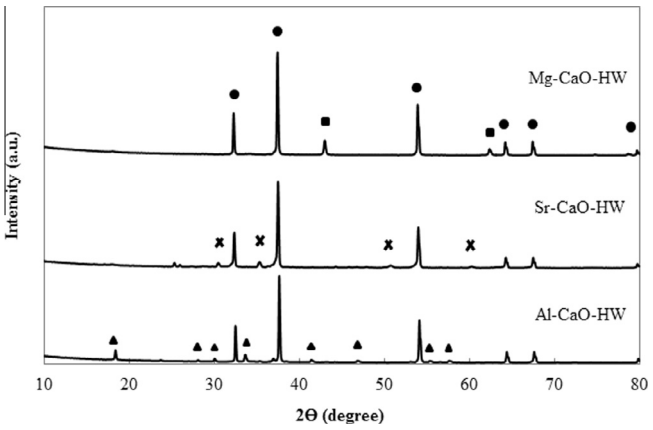

Fig. 13. XRD patterns of modified sorbents by CaO hydration followed by wet mixing method (Mg-CaO-HW, Sr-CaO-HW and Al-CaO-HW): ● CaO, ■ MgO, ✖ $Ca_{0.2}Sr_{0.8}O$ and ▲ $Ca_{12}Al_{14}O_{33}$.

3.2.2. Stability of modified sorbents by CaO hydration followed with wet mixing method

Comparing Fig. 14 to Fig. 9 we see that the increase in CO_2 concentration had relatively little effect on the CO_2 capacity of the CaO

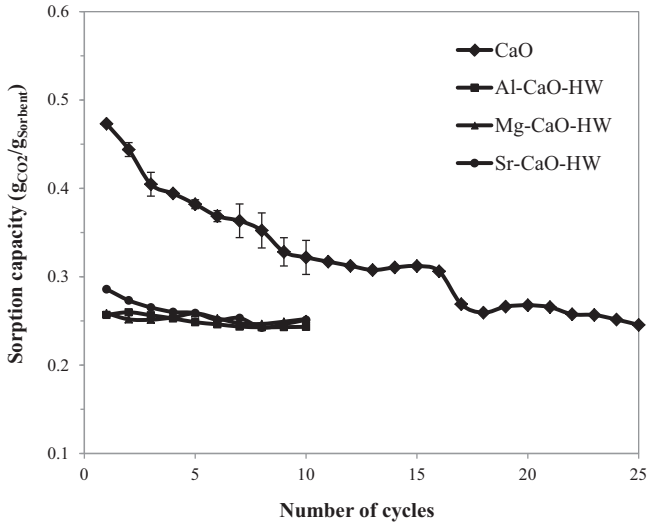

Fig. 14. CO_2 sorption/desorption cycles of modified sorbents by CaO hydration followed with wet mixing method (Mg-CaO-HW, Sr-CaO-HW and Al-CaO-HW) at temperature of 600 °C, pressure of 1 atm and 15% CO_2 feed stream.

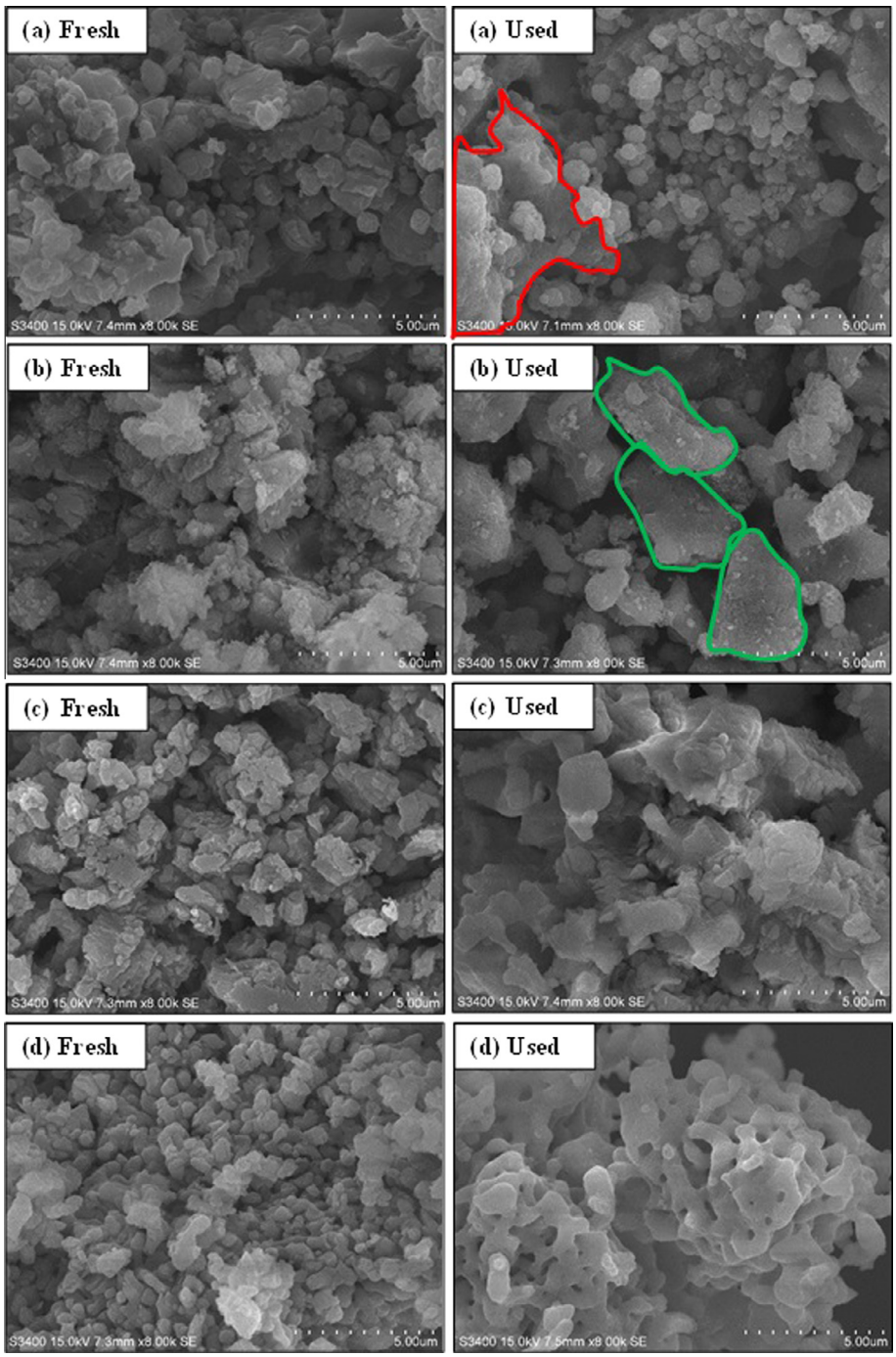

Fig. 15. SEM images of fresh and used of modified sorbents synthesized by CaO hydration followed by wet mixing method: (a) Al-CaO-HW, (b) Mg-CaO-HW, (c) Sr-CaO-HW and (d) CaO commercial. (For interpretation of the references to colour in this figure caption, the reader is referred to the web version of this article.)

sorbent but had a relatively significant positive impact upon the sorption capacity of the modified sorbents. The results in Fig. 14 imply that after 17 cycles the modified sorbents would start to out-perform the CaO at a CO_2 concentration of 15%. This, however, is conjecture based upon a possibly unreliable extrapolation of experimental data, but it does indicate a need for further investigation. Furthermore, 10 cycle CO_2 sorption capacity tests of CaO were repeated (Fig. 14) with results having 4% variation between these two sets of data.

The modified sorbents synthesized by CaO hydration followed by wet mixing (Mg-CaO-HW, Sr-CaO-HW and Al-CaO-HW) were characterized by XRD and results (Fig. 13) indicate the following: the MgO and CaO exist as separate phases in the Mg-CaO-HW samples; Sr-CaO-HW is composed of $Ca_{0.2}Sr_{0.8}O$ and CaO phases; Al-CaO-HW is composed of $Ca_{12}Al_{14}O_{33}$ and CaO. The modified sorbents were tested over multiple CO_2 sorption/desorption cycles with the results shown in Fig. 14. The results indicate that Mg-CaO-HW is the most stable with sorption capacities of 0.259 $g_{CO_2}/g_{sorbent}$ for 1st cycle and 0.252 $g_{CO_2}/g_{sorbent}$ for the 10th cycle.

SEM images (Fig. 15(b) used) also support the suggestion that Mg-CaO-HW has relatively small grains and less evidence of sintering than Al-CaO-HW, Sr-CaO-HW and CaO. However, the used Mg-CaO-HW sorbent (Blue circle line in Fig. 15(b) used) is shown to have larger particles than the Mg-CaO-HW fresh sorbent

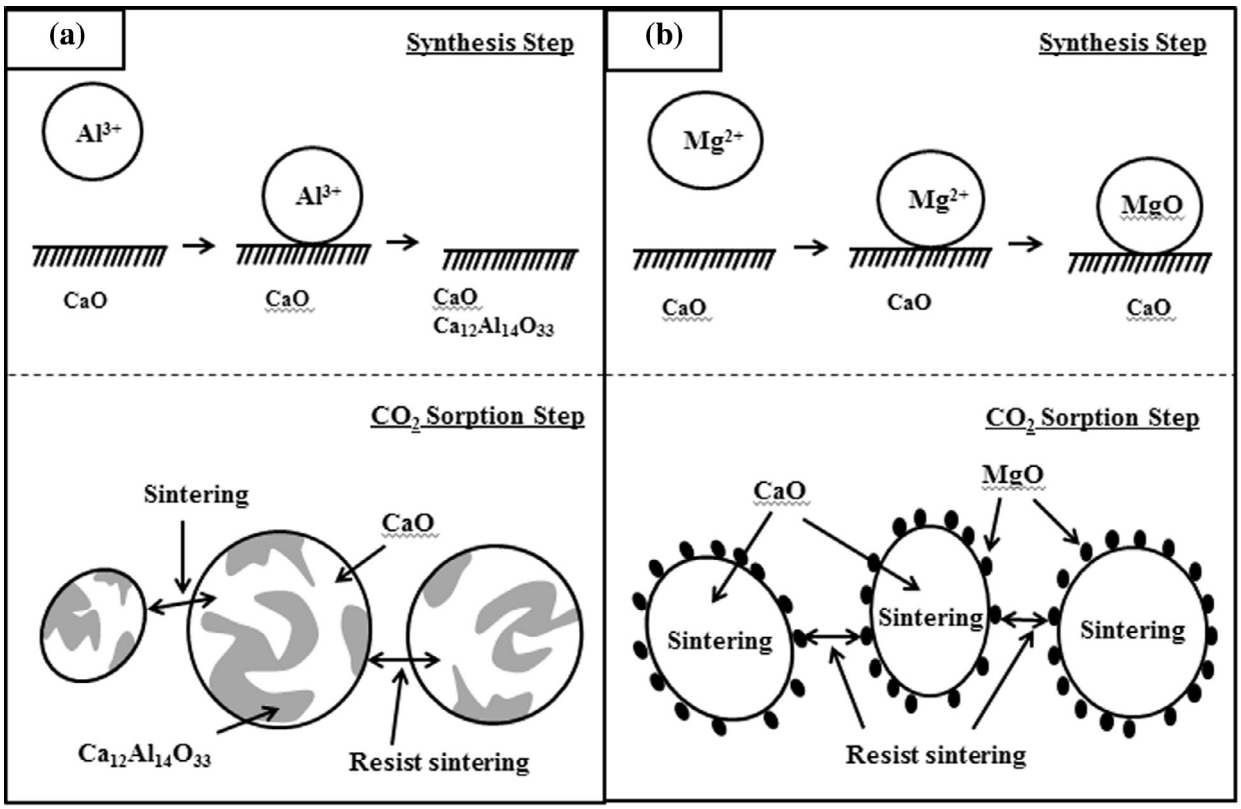

Fig. 16. Propose mechanism of metal precursors doped on CaO and their resisting sintering phenomena: (a) Al^{3+} doped on CaO and (b) Mg^{2+} doped on CaO.

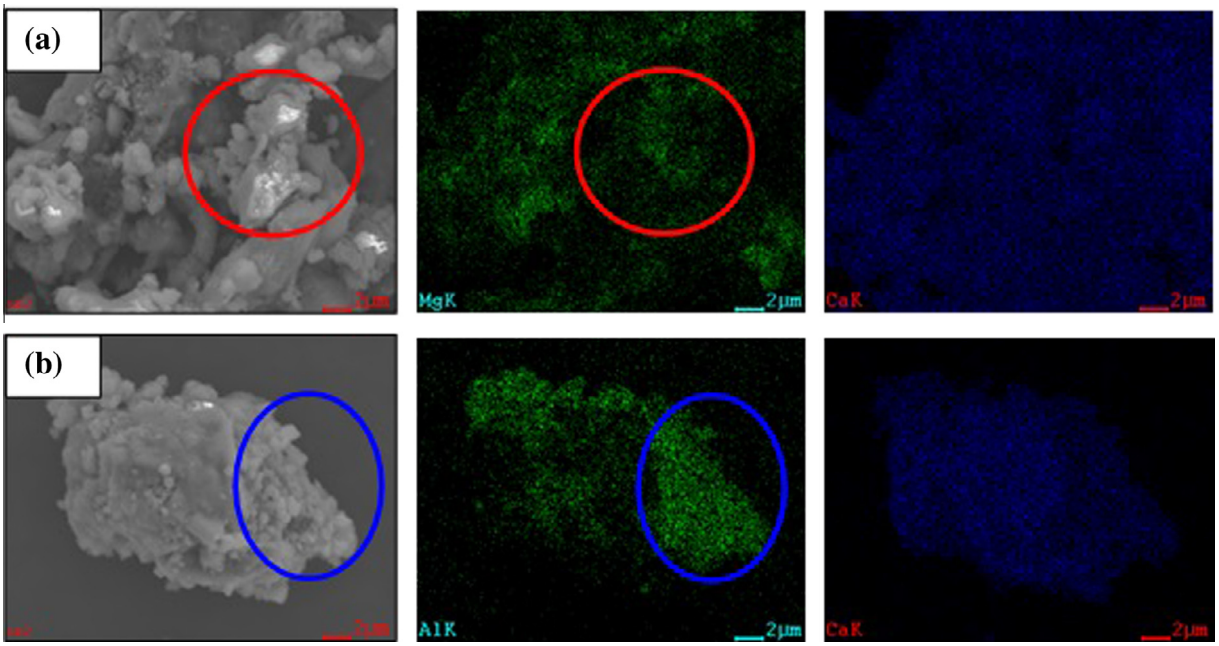

Fig. 17. SEM-EDX images of modified sorbents by CaO hydration followed by wet mixing method (a) Mg-CaO-HW and (b) Al-CaO-HW.

(Fig. 15(b) fresh) due to sintering of the exposed CaO particles and surfaces but on CaO particle surfaces covered by MgO as proposed in Fig. 16(b) and supported by the SEM-EDX images showed the MgO prevented sintering, but in areas where CaO surfaces are exposed, sintering took place, as shown in Fig. 17(a).

Al-CaO-HW was shown to have a sorption capacity of 0.257 $g_{CO_2}/g_{sorbent}$ for the 1st cycle dropping to only 0.243 $g_{CO_2}/g_{sorbent}$ for the 10th cycle representing a 5.45% decrease. This is attributed to the sorbent particulates being largely covered by the inert phase thus limiting the degree to which sintering could take place as

shown in Fig. 15. Fig. 16(a) schematically represents the mechanism by which the inert phase prevented sintering. However, even with this partial coverage of the inert phase, sintering can still take place, but is nevertheless limited. The SEM-EDX images (Fig. 17(b)) confirm the presence of this coating, shown by the elemental mapping (Al and Ca), which indicates a dispersion of Al on CaO, where there is only CaO but no Al (complex phase), there is sintering. On the other hand, Al (complex phase) prevents sintering where it is present at the surface. At the Sr-CaO-HW interface, $Ca_{0.2}Sr_{0.8}O$ complex was formed; however, the sorption capacity was still slightly decreased from 0.286 $g_{CO_2}/g_{sorbent}$ at 1st cycle to 0.251 $g_{CO_2}/g_{sorbent}$ at 10th cycle which decreasing of 12.24%. This is supported by evidence of sintering from the SEM images shown in Fig. 15(c) used. In addition, Sr-CaO-HW complex prevents sintering as observed for Al-CaO-HW.

4. Conclusion

The material with the highest CO_2 sorption capacity was found to be CaO (0.571 $g_{CO_2}/g_{sorbent}$), in comparison with MgO (0.038 $g_{CO_2}/g_{sorbent}$), SrO (0.065 $g_{CO_2}/g_{sorbent}$) and Al_2O_3 (0.037 $g_{CO_2}/g_{sorbent}$) at temperature of 600 °C. Modified sorbents produced using the dry powder mixing method (Mg-CaO-D, Sr-CaO-D and Al-CaO-D) were shown to have only separate phases of CaO and the respective additive i.e. MgO, SrO and Al_2O_3 due MgO, SrO, Al_2O_3 and CaO having higher Tammann temperatures than the calcination temperature (900 °C), therefore resulting in the materials having similar CO_2 sorption capacities (0.256, 0.219, 0.248 $g_{CO_2}/g_{sorbent}$ for Mg-CaO-D, Sr-CaO-D and Al-CaO-D, respectively), as a result of them all containing the same amount of CaO.

Modified sorbents produced by the wet mixing method (Mg-CaO-W, Sr-CaO-W and Al-CaO-W) and by the CaO hydration and wet mixing method (Mg-CaO-HW, Sr-CaO-HW and Al-CaO-HW) produced XRD patterns indicating the presence of; MgO and CaO in Mg-CaO samples; $Ca_{0.2}Sr_{0.8}O$ and CaO in Sr-CaO samples; $Ca_{12}Al_{14}O_{33}$ and CaO in Al-CaO samples. Samples produced by wet mixing exhibited decreasing CO_2 sorption capacity with an increasing number of cycles due to decreasing surface area and pore volume; both of which result in a decrease in the capacity for surface adsorption but also decrease the rate at which absorption into the bulk can take place.

The CaO hydration step was implemented to increase the pore volume and surface area of CaO and thus improved diffusion of CO_2 into the bulk material. The experimental results from samples produced by CaO hydration and wet mixing indicate that over 10 cycles the Mg-CaO-HW performed the best in terms of CO_2 sorption/desorption (CO_2 sorption capacity of 0.259 for 1st cycle to 0.252 $g_{CO_2}/g_{sorbent}$ for the 10th cycle). Whereas Al-CaO-HW and Sr-CaO-HW exhibited a decrease in CO_2 sorption capacity corresponding to a 5.45 and 12.24% decrease over 10 cycles (0.257 and 0.286 $g_{CO_2}/g_{sorbent}$ for 1st cycle dropping to 0.243 and 0.251 $g_{CO_2}/g_{sorbent}$ for 10th cycle, respectively). Extrapolating the results from the modified CaO to 17 cycles and comparing to that of the CaO results, we can see a potential for the modified sorbents to surpass the performance of the CaO over this number of cycles. This is a subject for possible further investigation.

Acknowledgements

This work was supported by the Royal Golden Jubilee Ph.D. Program from the Thailand Research Fund and Chulalongkorn University, and The Thailand Research Fund. The authors would like to thank Dr. Worapon Kiatkittipong and Dr. Suwimon Wongsakulphasatch for useful suggestions.

References

[1] G. Xu, Y.-P. Yang, J. Ding, S. Li, W. Liu, K. Zhang, Analysis and optimization of CO_2 capture in an existing coal-fired power plant in China, Energy 58 (2013) 117–127.
[2] M.G. Rasul, S. Moazzem, M.M.K. Khan, Performance assessment of carbonation process integrated with coal fired power plant to reduce CO_2 (carbon dioxide) emissions, Energy 64 (2014) 330–341.
[3] G. Xu, Y. Hu, B. Tang, Y. Yang, K. Zhang, W. Liu, Integration of the steam cycle and CO_2 capture process in a decarbonization power plant, Appl. Therm. Eng. 73 (2014) 277–286.
[4] D.P. Hanak, C. Biliyok, V. Manovic, Rate-based model development, validation and analysis of chilled ammonia process as an alternative CO_2 capture technology for coal-fired power plants, Int. J. Greenhouse Gas Control 34 (2015) 52–62.
[5] H.J. Alves, C. Bley Jr., R.R. Niklevicz, E.P. Frigo, M.S. Frigo, C.H. Coimbra-Araújo, Overview of hydrogen production technologies from biogas and the applications in fuel cells, Int. J. Hydrogen Energy 38 (2013) 5215–5225.
[6] S.M. Lee, S.C. Hong, Effect of palladium addition on catalytic activity in steam methane reforming over Ni-YSZ porous membrane, Int. J. Hydrogen Energy 39 (2014) 21037–21043.
[7] S.Y. Lee, H. Lim, H.C. Woo, Catalytic activity and characterizations of Ni/$K_2Ti_xO_y$–Al_2O_3 catalyst for steam methane reforming, Int. J. Hydrogen Energy 39 (2014) 17645–17655.
[8] T. Mondal, K.K. Pant, A.K. Dalai, Catalytic oxidative steam reforming of bio-ethanol for hydrogen production over Rh promoted Ni/CeO_2–ZrO_2 catalyst, Int. J. Hydrogen Energy 40 (2015) 2529–2544.
[9] B. Metz, O. Davidson, H. de Coninck, M. Loos, L. Meyer, Carbon Dioxide Capture and Storage, Cambridge University Press, 2005. pp. 77–100.
[10] W. Conway, S. Bruggink, Y. Beyad, W. Luo, I. Melián-Cabrera, G. Puxty, P. Feron, CO_2 absorption into aqueous amine blended solutions containing monoethanolamine (MEA), N, N-dimethylethanolamine (DMEA), N, N-diethylethanolamine (DEEA) and 2-amino-2-methyl-1-propanol (AMP) for post-combustion capture processes, Chem. Eng. Sci. 126 (2015) 446–454.
[11] Y.G. Ko, S.S. Shin, U.S. Choi, Primary, secondary, and tertiary amines for CO_2 capture: designing for mesoporous CO_2 adsorbents, J. Colloid Interface Sci. 361 (2011) 594–602.
[12] D. Thimsen, A. Maxson, V. Smith, T. Cents, O. Falk-Pedersen, O. Gorset, E.S. Hamborg, Results from MEA testing at the CO_2 technology centre mongstad. Part I: Post-combustion CO_2 capture testing methodology, Energy Proc. 63 (2014) 5938–5958.
[13] B. Dou, Y. Song, Y. Liu, C. Feng, High temperature CO_2 capture using calcium oxide sorbent in a fixed-bed reactor, J. Hazard. Mater. 183 (2010) 759–765.
[14] T. Witoon, Characterization of calcium oxide derived from waste eggshell and its application as CO_2 sorbent, Ceram. Int. 37 (2011) 3291–3298.
[15] S.D. Kenarsari, Y. Zheng, CO_2 capture using calcium oxide under biomass gasification conditions, J. CO_2 Util. 9 (2015) 1–7.
[16] S. Castilho, A. Kiennemann, M.F. Costa Pereira, A.P. Soares Dias, Sorbents for CO_2 capture from biogenesis calcium wastes, Chem. Eng. J. 226 (2013) 146–153.
[17] M. Olivares-Marín, E.M. Cuerda-Correa, A. Nieto-Sánchez, S. García, C. Pevida, S. Román, Influence of morphology, porosity and crystal structure of $CaCO_3$ precursors on the CO_2 capture performance of CaO-derived sorbents, Chem. Eng. J. 217 (2013) 71–81.
[18] H.R. Radfarnia, M.C. Iliuta, Metal oxide-stabilized calcium oxide CO_2 sorbent for multicycle operation, Chem. Eng. J. 232 (2013) 280–289.
[19] M. Mohammadi, P. Lahijani, A.R. Mohamed, Refractory dopant-incorporated CaO from waste eggshell as sustainable sorbent for CO_2 capture: experimental and kinetic studies, Chem. Eng. J. 243 (2014) 455–464.
[20] M. Mohammadi, P. Lahijani, Z.A. Zainal, A.R. Mohamed, Capture of carbon dioxide from flue/fuel gas using dolomite under microwave irradiation, Chem. Eng. J. 240 (2014) 169–178.
[21] J. Ortiz-Landeros, C. Gómez-Yáñez, H. Pfeiffer, Surfactant-assisted hydrothermal crystallization of nanostructured lithium metasilicate (Li_2SiO_3) hollow spheres: II—textural analysis and CO_2–H_2O sorption evaluation, J. Solid State Chem. 184 (2011) 2257–2262.
[22] M. Mizunuma, M. Tsuda, Y. Maruo, T. Nakagaki, CO_2 capture system using lithium silicate for distributed power supply, Energy Proc. 37 (2013) 1194–1201.
[23] M. Seggiani, M. Puccini, S. Vitolo, Alkali promoted lithium orthosilicate for CO_2 capture at high temperature and low concentration, Int. J. Greenhouse Gas Control 17 (2013) 25–31.
[24] P.R. Díaz-Herrera, M.J. Ramírez-Moreno, H. Pfeiffer, The effects of high-pressure on the chemisorption process of CO_2 on lithium oxosilicate (Li_8SiO_6), Chem. Eng. J. 264 (2015) 10–15.
[25] A. Iwan, H. Stephenson, W.C. Ketchie, A.A. Lapkin, High temperature sequestration of CO_2 using lithium zirconates, Chem. Eng. J. 146 (2009) 249–258.
[26] S.M. Amorim, M.D. Domenico, T.L.P. Dantas, H.J. José, R.F.P.M. Moreira, Lithium orthosilicate for CO_2 capture with high regeneration capacity: kinetic study and modeling of carbonation and decarbonation reactions, Chem. Eng. J. 283 (2016) 388–396.
[27] Y. Ding, E. Alpay, High temperature recovery of CO_2 from flue gases using hydrotalcite adsorbent, Process Saf. Environ. Protect. 79 (2001) 45–51.

[28] M.H. Halabi, M.H.J.M. de Croon, J. van der Schaaf, P.D. Cobden, J.C. Schouten, High capacity potassium-promoted hydrotalcite for CO_2 capture in H_2 production, Int. J. Hydrogen Energy 37 (2012) 4516–4525.
[29] M. Maroño, Y. Torreiro, L. Gutierrez, Influence of steam partial pressures in the CO_2 capture capacity of K-doped hydrotalcite-based sorbents for their application to SEWGS processes, Int. J. Greenhouse Gas Control 14 (2013) 183–192.
[30] A. Hanif, S. Dasgupta, S. Divekar, A. Arya, M.O. Garg, A. Nanoti, A study on high temperature CO_2 capture by improved hydrotalcite sorbents, Chem. Eng. J. 236 (2014) 91–99.
[31] Z. Yong, V. Mata, A.E. Rodrigues, Adsorption of carbon dioxide on basic alumina at high temperature, J. Chem. Eng. Data 45 (2000) 1093–1095.
[32] Z. Yong, V.G. Mata, A.E. Rodrigues, Adsorption of carbon dioxide on chemically modified high surface area carbon-based adsorbents at high temperatures, Adsorption 7 (2001) 41–50.
[33] Z. Yong, V. Mata, A.E. Rodrigues, Adsorption of carbon dioxide onto hydrotalcite-like compounds (HTlcs) at high temperatures, Ind. Eng. Chem. Res. 40 (2001) 204–209.
[34] Z. Yong, V. Mata, A.E. Rodrigues, Adsorption of carbon dioxide at high temperature – a review, Sep. Purif. Technol. 26 (2002) 195–205.
[35] Z. Yong, A.E. Rodrigues, Hydrotalcite-like compounds as adsorbents for carbon dioxide, Energy Conv. Manag. (2002) 1865–1876.
[36] E.L.G. Oliveira, C.A. Grande, A.E. Rodrigues, CO_2 sorption on hydrotalcite and alkali-modified (K and Cs) hydrotalcites at high temperatures, Sep. Purif. Technol. 62 (2008) 137–147.
[37] C.V. Miguel, R. Trujillano, V. Rives, M.A. Vicente, A.F.P. Ferreira, A.E. Rodrigues, A. Mendes, L.M. Madeira, High temperature CO_2 sorption with gallium-substituted and promoted hydrotalcites, Sep. Purif. Technol. 127 (2014) 202–211.
[38] Z. Yong, A.E. Rodrigues, Adsorbent materials for carbon dioxide, Adsorpt. Sci. Technol. 19 (2001) 255–266.
[39] D.W. Bailey, P.H.M. Feron, Post-combustion decarbonisation processes, Oil Gas Sci. Technol. 60 (2005) 461–474.
[40] E. Ochoa-Fernández, G. Haugen, T. Zhao, M. Rønning, I. Aartun, B. Børresen, E. Rytter, M. Rønnekleiv, De. Chen, Process design simulation of H_2 production by sorption enhanced steam methane reforming: evaluation of potential CO_2 acceptors, Green Chem. 9 (2007) 654–662.
[41] A. Davidson, B. Morin, M. Che, ESR determination of TiO_2 and SnO_2 Tammann temperatures, Colloids Surf. A-Physicochem. Eng. Aspects 72 (1993) 245–255.
[42] R.T.K. Baker, The relationship between particle motion on a graphite surface and Tammann temperature, J. Catal. 78 (1982) 473–476.
[43] H. Lu, A. Khan, S.E. Pratsinis, P.G. Smirniotis, Flame-made durable doped-CaO nanosorbents for CO_2 capture, Energy Fuels 23 (2009) 1093–1100.
[44] C.T. Yu, W.C. Chen, Preparation, characterization of Ca/Al carbonate pellets with TiO_2 binder and CO_2 sorption at elevated-temperature conditions, Powder Technol. 239 (2013) 492–498.
[45] X. Zhang, Z. Li, Y. Peng, W. Su, X. Sun, J. Li, Investigation on a novel CaO–Y_2O_3 sorbent for efficient CO_2 mitigation, Chem. Eng. J. 243 (2014) 297–304.
[46] C. Luo, Y. Zheng, N. Ding, C. Zheng, Enhanced cyclic stability of CO_2 adsorption capacity of CaO-based sorbents using La_2O_3 or $Ca_{12}Al_{14}O_{33}$ as additives, Korean J. Chem. Eng. 28 (2011) 1042–1046.
[47] J. Park, K.B. Yi, Effects of preparation method on cyclic stability and CO_2 absorption capacity of synthetic CaO–MgO absorbent for sorption-enhanced hydrogen production, Int. J. Hydrogen Energy 37 (2012) 95–102.
[48] C.S. Martavaltzi, A.A. Lemonidou, Parametric study of the CaO–$Ca_{12}Al_{14}O_{33}$ synthesis with respect to high CO_2 sorption capacity and stability on multicycle operation, Ind. Eng. Chem. Res. 47 (2008) 9537–9543.
[49] K. Wang, X. Guo, P. Zhao, C. Zheng, Cyclic CO_2 capture of CaO-based sorbent in the presence of metakaolin and aluminum (hydr)oxides, Appl. Clay Sci. 50 (2010) 41–46.
[50] M. Xie, Z. Zhou, Y. Qi, Z. Cheng, W. Yuan, Sorption-enhanced steam methane reforming by in situ CO_2 capture on a CaO–$Ca_9Al_6O_{18}$ sorbent, Chem. Eng. J. 207–208 (2012) 142–150.
[51] S.F. Wu, Q.H. Li, J.N. Kim, K.B. Yi, Properties of a Nano CaO/Al_2O_3 CO_2 Sorbent, Ind. Eng. Chem. Res. 47 (2008) 180–184.
[52] Z. Zhou, Y. Qi, M. Xie, Z. Cheng, W. Yuan, Synthesis of CaO-based sorbents through incorporation of alumina/aluminate and their CO_2 capture performance, Chem. Eng. Sci. 74 (2012) 172–180.
[53] J. Janek, D.K. Lee, Defect chemistry of the mixed conducting cage compound $Ca_{12}Al_{14}O_{33}$, J. Korean Ceram. Soc. 47 (2010) 99–105.
[54] K.B. Yi, C.H. Ko, J.H. Park, J.N. Kim, Improvement of the cyclic stability of high temperature CO_2 absorbent by the addition of oxygen vacancy possessing material, Catal. Today 146 (2009) 241–247.
[55] N. Florin, P. Fennell, Synthetic CaO-based sorbent for CO_2 capture, Energy Proc. 4 (2011) 830–838.
[56] C.S. Martavaltzi, A.A. Lemonidou, Parametric study of the CaO–$Ca_{12}Al_{14}O_{33}$ synthesis with respect to high CO_2, Ind. Eng. Chem. Res. 47 (2008) 9537–9543.
[57] C.S. Martavaltzi, A.A. Lemonidou, Hydrogen production via sorption enhanced reforming of methane: development of a novel hybrid material—reforming catalyst and CO_2 sorbent, Chem. Eng. Sci. 65 (2010) 4134–4140.
[58] N.H. Florin, A.T. Harris, Enhanced hydrogen production from biomass with in situ carbon dioxide capture using calcium oxide sorbents, Chem. Eng. Sci. 63 (2008) 287–316.

Computers and Chemical Engineering 87 (2016) 125–144

Contents lists available at ScienceDirect

Computers and Chemical Engineering

journal homepage: www.elsevier.com/locate/compchemeng

Systematic methods and tools for design of sustainable chemical processes for CO_2 utilization

Pichayapan Kongpanna[a], Deenesh K. Babi[c], Varong Pavarajarn[b], Suttichai Assabumrungrat[a,*], Rafiqul Gani[c]

[a] Center of Excellence in Catalysis and Catalytic Reaction Engineering, Department of Chemical Engineering, Faculty of Engineering, Chulalongkorn University, Bangkok 10330, Thailand
[b] Center of Excellence in Particle Technology, Department of Chemical Engineering, Faculty of Engineering, Chulalongkorn University, Bangkok 10330, Thailand
[c] SPEED, Department of Chemical and Biochemical Engineering, Technical University of Denmark, Soltofts Plads 1, Building 229, DK-2800 Lyngby, Denmark

ARTICLE INFO

Article history:
Received 16 August 2015
Received in revised form
29 December 2015
Accepted 6 January 2016
Available online 16 January 2016

Keywords:
CO_2 utilization
Dimethyl carbonate
Process intensification
Superstructure generation
Mixed-integer non-linear program (MINLP)

ABSTRACT

A systematic computer-aided framework for sustainable process design is presented together with its application to the synthesis and generation of processing networks for dimethyl carbonate (DMC) production with CO_2 utilization. The framework integrated with various methods, tools, algorithms and databases is based on a combined process synthesis–design–intensification method. The method consists of three stages. The synthesis-stage involves superstructure based optimization to identify promising networks that convert a given set of raw materials to a desired set of products. The design-stage involves selection and analysis of the identified networks as a base case design in terms of operational feasibility, economics, life cycle assessment factors and sustainability measures, which are employed to establish targets for improvement in the next-stage. The innovation-stage involves generation and screening of the more sustainable alternatives through a phenomena-based process intensification method. Applications of the framework are highlighted for the DMC production process.

© 2016 Elsevier Ltd. All rights reserved.

1. Introduction

The mathematical programming problem representing the combined process synthesis, design and intensification to obtain more sustainable process designs is potentially very large and complex, involving a large collection of models and associated data. A decomposition based solution approach, where the problem is decomposed into three hierarchical stages is considered in this paper. Obviously, this approach may not find a global optimal solution, but the objective in sustainable process design is to find more sustainable solutions and not necessarily a unique optimal solution. According to the three stages decomposition approach, an optimal processing route is obtained first (synthesis stage) through network superstructure optimization (Quaglia et al., 2013) based on known data on all possible available technologies related to the conversion of the raw materials to a desired set of products. Next, the optimal processing route is converted into a base case process design (design stage) with the help of rigorous process simulation and analysed in terms of sustainability, including economics and LCA factors (Mansouri et al., 2013; Kongpanna et al., 2015). Based on the analysis, targets for further improvements are defined. In the final stage (innovation stage) a targeted design problem is solved by generating alternatives that match the specified targets (Babi et al., 2014). All identified alternatives are therefore potentially more sustainable than the base case design and are ordered according to a set of predefined performance criteria to determine the most sustainable process design.

The objective of this paper is to first, highlight the main features and architecture of the framework for process synthesis–design–intensification where the three-stage decomposition approach has been implemented together with the associated work-flow and data-flow; and second, to highlight the application of the three-stages framework to the synthesis–design of a more sustainable CO_2 utilization based process. In this work, in addition to environmental and economic measures, the performance criteria also considers measures for more sustainable alternatives, such as, energy consumption, net CO_2 emission, raw material depletion and life cycle assessment factors at their targeted levels or better.

In the past decades, there have been increasing concerns and therefore, more attention on global warming and emission of gases

* Corresponding author. Tel.: +66 2 2186868; fax: +66 2 2186877.
E-mail address: Suttichai.A@chula.ac.th (S. Assabumrungrat).

http://dx.doi.org/10.1016/j.compchemeng.2016.01.006
0098-1354/© 2016 Elsevier Ltd. All rights reserved.

Nomenclature

Indexes

i	component
j	index for piece-wise linear capital cost model
k	process interval (origin)
kk	process interval (destination)
$react$	key reactant
rr	reaction
st	process step
t	time (years)

Parameters

MW_i	molecular weight (g/mol)
$P1_{i,kk}$	raw materials prices (USD/kg)
$P2_i$	utilities prices (USD)
$P3_{i,kk}$	products prices (USD/kg)
$SW_{i,kk}$	wastes fraction
$S_{k,kk}$	superstructure (binary)
$\alpha_{j,kk}$	coefficient for capital cost estimation
$\beta_{j,kk}$	coefficient for capital cost estimation
$\alpha_{i,kk}$	specific utility consumption (USD/MT)
$\gamma_{i,kk,rr}$	stoichiometric coefficient of component i in reaction rr (based on flow F^M)
$\xi^P_{k,kk}$	equal to 1 if a primary connection may exist between interval k and interval kk, zero otherwise
$\xi^S_{k,kk}$	equal to 1 if a secondary connection may exist between interval k and interval kk, zero otherwise
$\upsilon_{st,k}$	allocation of interval k to step st
$\theta_{react,kk,tt}$	conversion of key reactant react in reaction rr (based on flow F^M)
$\mu_{j,i,kk}$	amount of utility j consumed per kilogram of component i (based on flow F^M)
$\varepsilon i,kk$	separation split factor

Variables

$F_{i,k,kk}$	component i flow from process intervals k to process intervals kk
$ff_{i,kk}$	component flow after mixing (kg)
$R_{i,kk}$	utility flow (MT)
$F^M_{i,kk}$	component flow after mixing (kg)
$F_{i,kk}$	component flow after waste separation (kg)
$F^{out1}_{i,kk}$	component flow leaving process intervals kk through primary outlet (kg)
$F^{out2}_{i,kk}$	component flow leaving process intervals kk through secondary outlet (kg)
$F^R_{i,kk}$	component flow after reaction (kg)
$dist_{k,kk}$	transportation distance (km)
$C_{Trk,kk}$	cost for transportation from interval k to kk (USD/km)
$F^{WASTE}_{i,kk}$	component flow as waste leaving process intervals kk
y_{kk}	selection of process intervals (binary)
$w_{j,kk}$	binary variable for piece-wise linear approximation of capital cost constraints
$Q_{j,kk}$	partition variable for flow in piece-wise linear approximation of capital cost constraints

Abbreviations

NRAW	number of raw materials
NPROC	number of processing unit
CAPEX	capital expenditure (USD)
PBS	phenomena-based synthesis
SPB	simultaneous phenomena building block
PB	phenomena building block
PI	process intensification

such as methane (CH_4), nitrogen dioxide (N_2O), chlorofluorocarbon (CFC) and carbon dioxide (CO_2), which are considered to be greenhouse gases (GHGs) because of their contribution to global warming. Since the beginning of the industrial revolution around 1850, the average atmospheric concentration of CO_2 has increased from 280 ppm in 1850 to 400 ppm currently and as a result, the average global temperature has increased by between 0.6 and 1 °C during this period (NOAA, 2015; WMO, 2015; Stewart and Hessami, 2005). The use of fossil fuel systems such as coal-fired power plants are regarded as one of the major sources of CO_2 emissions, which accounts for about 33–40% of the total anthropogenic emissions of carbon worldwide (Yang et al., 2008). The need for the reduction of the GHGs emissions on a global scale is urgent. The awareness that fossil fuel consumption has perturbed the carbon cycle, with feedbacks to global climate, has motivated researchers and funding agencies worldwide to invest in carbon cycle research (Bolstad et al., 2004; Luyssaert et al., 2007). Several options may be considered to reduce the effect of GHG, for example, lowering energy consumption by increasing the efficiency of energy utilization, using clean combustion fuels or, using renewable energies, in addition to developing technologies of CO_2 capture, storage, and utilization. The report from "The Intergovernmental Panel on Climate Change" (IPCC)'s fifth assessment on climate change stated that climate change is acerbating with rapidly increasing greenhouse gases (IPCC, 2014). Technology and innovation in clean energy division might arguably play an important role in solving this climate change problem. Carbon dioxide Capture, Utilization, and Storage (CCUS) technology has been established aiming at reducing emissions from power plants, petrochemicals and other industrial process worldwide. Nevertheless, due to high costs, high energy penalty, uncertain technological feasibility, and uncertain risks of CO_2 storage, the development of CCUS has not yet followed the speed of rising CO_2 emissions (IPCC, 2014). Carbon Dioxide Utilization Technology (CUT) has grown attention over the recent years with an expectation that it can offset the extra costs caused by carbon capture facility. As a result, CUTs may motivate private sector to demonstrate CCUS large-scale project, which is in essential of the sustainable development. In recent years, the transformation of CO_2 to valuable chemicals has attracted much attention (Dai et al., 2009). Many researchers have investigated CO_2 utilization in various reactions such as CO_2 based hydrogenation to methanol, CO_2 based cycloaddition to epoxides, CO_2 based carbonylation of amines or alcohols to carbonate compounds, and, CO_2 based reduction under photo-irradiation or electrolytic conditions. The current research and process design of CO_2 utilization are spread through many areas. For examples, large-scale microalgae cultivation for CO_2 bio-sequestration from power plants has been proposed by Rezvani et al. (2016). It could be an alternative process to conventional technologies if the capital investments associated with carbon capture, transport and storage can be reduced or avoided. Sahebdelfar and Ravanchi (2015) performed thermodynamic simulation for CO_2 conversion to methane. Dindi et al. (2015) studied the integration of a modified Solvay process with conventional amine based post-combustion carbon dioxide capture for the simultaneous capture and conversion of CO_2 into solid bicarbonates. For the CO_2 utilization to liquid fuels, conceptual design of two options of carbon dioxide utilized gas-to-liquids process (CUGP), which mainly produces light olefins and Fischer–Tropsch (F–T) synthetic oils were studied in term of techno-economic evaluation (Zhang

et al., 2015). An interesting option is the production of organic carbonates, which can be roughly categorized into cyclic and linear carbonates, such as ethylene carbonate (EC), propylene carbonate (PC) and dimethyl carbonate (DMC). With rising demand for organic carbonates, the feasibility of CO_2 based reaction to produce them becomes an interesting and more sustainable choice. Obviously, CO_2 utilization also cannot solve the global warming problem. However, it can contribute to a more global and sustainable solutions approach where all means to reduce the CO_2 emission or are encouraged. Therefore, in this paper, the issue of CO_2 utilization is addressed and in particular, the sustainable production of DMC is considered.

The paper presents first the framework for synthesis–design–intensification in terms of the work-flow where the work-steps are explained together with the associated methods and tools that are needed for the step. Next, the application of the implemented framework is highlighted through a case study involving the sustainable production of DMC. All the necessary details are provided in the main text and as Supplementary material so that the interested reader can reproduce the reported results and/or solve similar problems using the same set of methods and tools.

2. Framework for synthesis–design–intensification

As shown in Fig. 1, the overview of the framework proposed by Babi et al. (2015) consists of three-stages involving a synthesis-stage, a design-stage and an innovation-stage that are briefly discussed below.

Stage-I: synthesis-stage

The objective here is to quickly find an optimal processing network or a small set of most promising networks for converting a given set of raw materials to a desired set of products. Data on known technologies are used to generate a superstructure of alternatives, based on an integrated business and engineering framework for synthesis and design of processing networks (Zondervan et al., 2011; Quaglia et al., 2013). Different mathematical programming problems are formulated and solved, employing factors such as product yield, minimization of waste, operating-material costs, etc., as performance criteria. The result from this stage is an optimal processing route or a set of promising processing routes for converting the given raw materials to the desired products using known technologies for each processing step.

Stage-II: design-stage

The objective here is to establish a base case design by selecting one or more promising process routes from stage-1 in terms of a selected set of performance criteria (energy consumption, net CO_2 emission, raw material depletion and life cycle assessment factors); to perform economic analysis, life cycle assessment analysis and sustainability analysis on the base case design to identify process "hot-spots" (process limitations or bottlenecks); to define targets for process improvements through the minimization and/or elimination of the process "hot-spots". A rigorous simulation is performed in this stage to generate the necessary data.

Stage-III: innovation-stage

The objective here is to generate and evaluate process alternatives that match the established targets for process improvements. The phenomena-based process intensification method (Lutze et al., 2013; Babi et al., 2015) is employed here. Process alternatives that match the targets are better, by definition, than the base case design and are also more sustainable. In the final step, a rigorous simulation is performed to verify all aspects of the selected more sustainable process alternative.

The work-flow of the combined synthesis–design-intensification framework is highlighted in Fig. 2. A step-by-step description of the work-flow is given below.

The superstructure optimization in Stage I determines all feasible process alternatives and identifies those that correspond to the best for different objective function (or design scenario). The result from Stage I is in the form of a processing route described in terms of a sequence of processing steps and processing intervals (unit operations) used in them and satisfying the constraints of mass-energy balances and specified process constraints (purity of products, conversions in reactors, etc.). The optimal processing route from Stage I is therefore used as a base case, which if further investigated to determine a detailed design suitable for simulation with rigorous steady state models. The simulation results are analysed in terms of costs, sustainability and LCA to determine process hot-spots (bottlenecks), which are then used to define targets for improvements. In Stage III, process intensification by the phenomena based synthesis is subsequently applied to match the defined targets for improvement. Here new unit operations and/or configurations may results, including new processing routes.

Step 1. Problem definition

The objective of this step is to define the problem that needs to be investigated and solved. The products to be produced, the raw materials (feed-stocks) to be converted, the performance criteria to be used, etc., are defined here. Based on these, the appropriate data need to be collected. The problem definition step is broken-down into the following two sub-steps:

Step 1.1. Data requirement: the main products and by products, the feed-stock to be used and the list of known technologies to connect the raw material to the desired products are specified here.

Step 1.2. Selection of the objective function, the performance criteria and process constraints are made here.

Step 2. Data collection and superstructure definition

The objective of this step is to collect the data needed to define and solve the more sustainable process synthesis–design problem. The network superstructure consists of processing steps and under each processing step, known process technologies are arranged as intervals. In a process interval, operations such as reaction, separation, mixing, etc., can take place. The concept of a network (superstructure) of processing routes in term of processing steps and intervals is illustrated in Fig. 3.

Based on the known technologies for the conversion of the selected feed-stocks to the desired products, a superstructure of processing networks is developed. Fig. 4 shows the process interval model where operational-processing tasks, such as mixing, reaction, separation, transportation, or their combination may take place. The important data for each of the process intervals are collected and organized in a predefined knowledge structure (Quaglia et al., 2013) in this step.

Step 3. Mathematical programming problem

This step is divided into two sub-steps:

Step 3.1. Model generation – The objective of this step is to select the mathematical models for each interval so that a total mathematical model of the superstructure can be developed and validated. The model equations corresponding to the generic model of a process interval are listed in by Quaglia et al. (2013). For each processing step and the corresponding interval description, the appropriate models are retrieved and the consistency of the model-data is checked (that is, the collected data should include all the model parameter values). A check of consistency of available data and the generated model is also performed in this step. At the end of

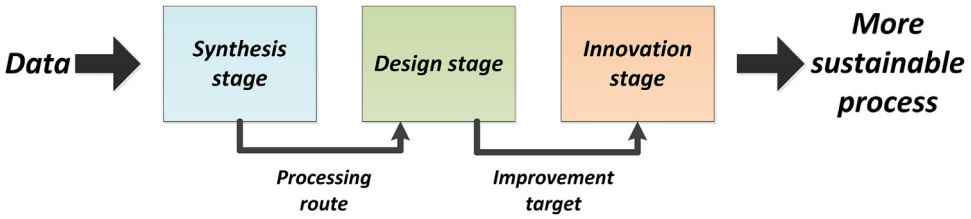

Fig. 1. The overall framework for synthesis–design–innovation of more sustainable process designs as inspiration from the paper by Babi et al. (2015).

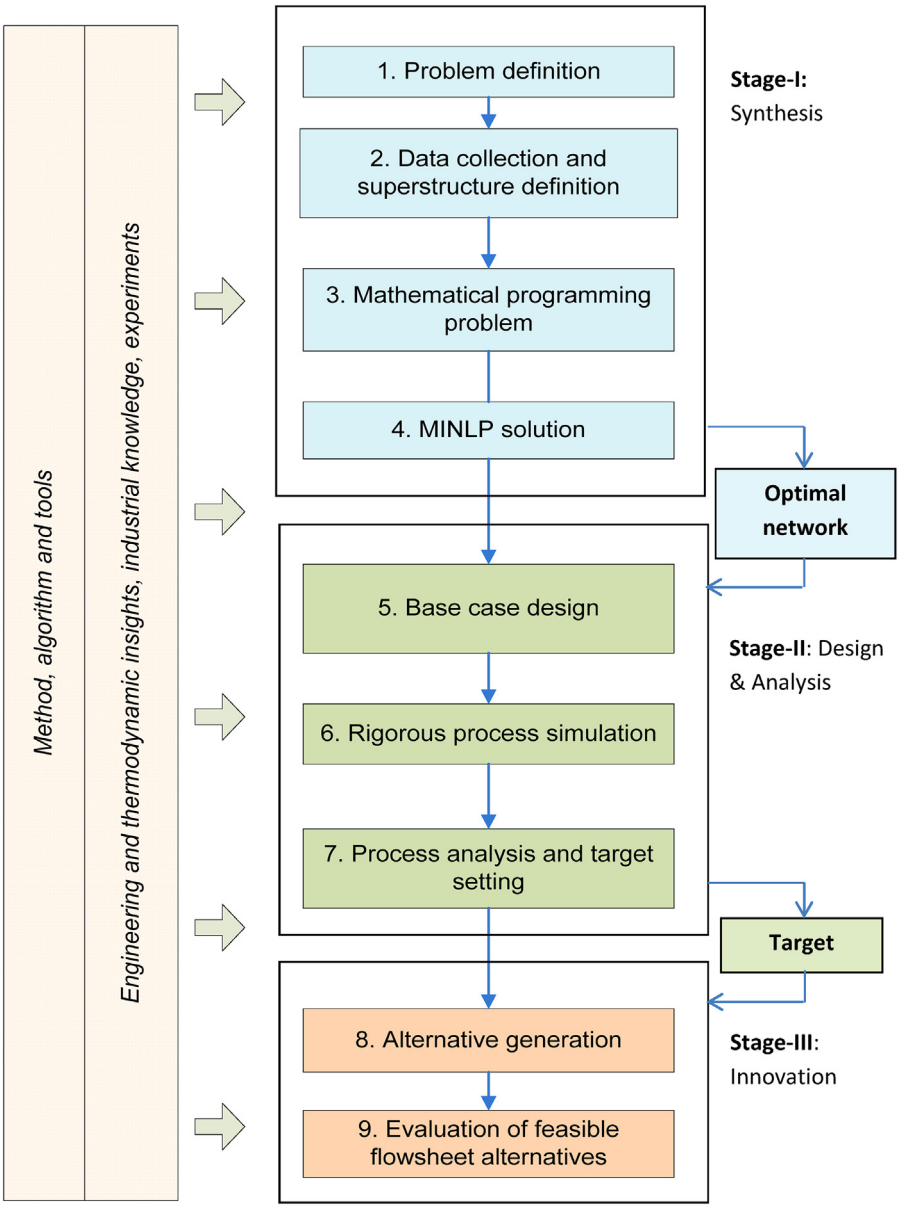

Fig. 2. Framework for more sustainable process synthesis and design.

this step, all the model equations representing the superstructure are obtained.

Step 3.2. Here, the mathematical programming problem is formulated, based on the problem definition of step 1, the collected data of step 2 and the mathematical model from step 3.1. The objective function maybe given as indicated in Eq. (1). The superstructure, the interval models, the logical constraints and the variable bounds defined in step 2 constitute an MILP or MINLP model (Eqs. (1)–(6)) (Zondervan et al., 2011; Quaglia et al., 2012, 2013).

$$\max f(x, y) \tag{1}$$

s.t.

$$g(x, y) \geq 0 \tag{2}$$

$$h(x, y) = 0 \tag{3}$$

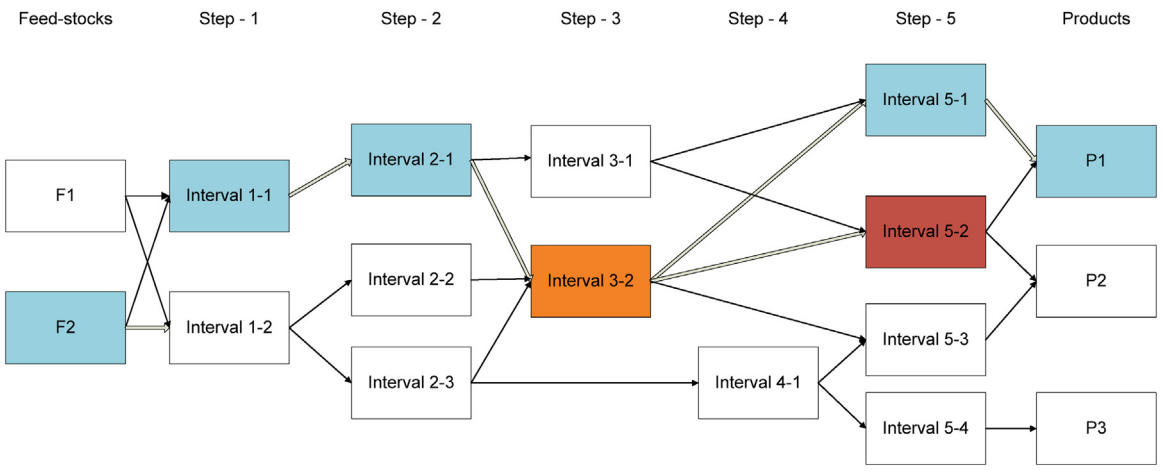

Fig. 3. The generic form of superstructure and GAMS user interface for superstructure generation. (The blue boxes indicate a likely processing route the optimal network is indicated, interval 4-1 is for bypass. Red box indicates the interval from where recycle is sent back and orange box indicates the interval that receives the recycle. In the mathematical formulation potentially all intervals can send back or receive streams.). (For interpretation of the references to colour in this figure legend, the reader is referred to the web version of the article.)

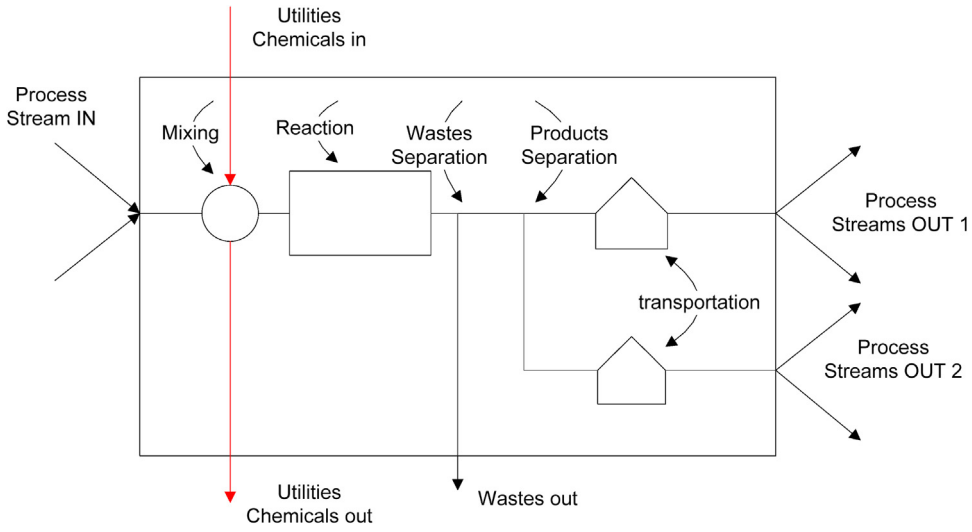

Fig. 4. Generic model of a process interval.

Adapted from Quaglia et al. (2013).

$$x \in X \tag{4}$$

$$x^{LO} \leq x \leq x^{UP} \tag{5}$$

$$y \in \{0;1\}^n \tag{6}$$

where f is the objective function, x represents the vector of continuous variables defined by their upper and lower bounds x^{UP} and x^{LO} in a continuous feasible region X; y is the vector of binary variables where intervals may or may not be connected at a processing step, g and h represent inequality and equality constraints, respectively. The process model consisting of component mass balance and energy balance equations are represented by Eq. (7).

$$F(\gamma_{i,kk,rr}, \theta_{react,kk,rr}, \alpha_{i,kk}, MW, SW_{i,kk}, S_{i,kk}, \xi^{P}_{k,kk}) = 0 \tag{7}$$

An example of Eq. (1) is given by Eq. (8).

$$\text{max Profit} = \sum_{i,kk}(P3_{i,kk} \cdot F^{out}_{i,kk}) - \sum_{i,kk}(P2_{i,kk} \cdot R_{i,kk}) - \sum_{i,kk}(P1_{i,kk} \cdot F^{out}_{i,kk}) - W^{Price} \cdot \sum_{i,kk}(F^{R}_{i,kk} \cdot SW_{i,kk}) - \frac{CAPEX}{\#year} \tag{8}$$

where γ represents the stoichiometric, θ is the fraction of converted reactant, α is the quantity of chemical consumed, MW_i contains the molecular weight of the components, SW contains the produced quantities of waste, S_i are the split factors of the components entering and interval and ξ is a matrix to match interval k and kk. Based on the information collected, the superstructure is created together with the list of decision variables that will need to be determined. The process model equations (Eq. (7)) are obtained from the generic interval model (Quaglia et al., 2013). Special software (Quaglia et al., 2013) is employed to create the superstructure network and the corresponding mathematical programming problem to be solved by GAMS (IBM Corp, 2009).

Step 4. MILP/MINLP solution

Here, the MILP/MINLP problem formulated in step 3 is solved with GAMS (IBM Corp, 2009). Different objective functions may be defined to obtain different processing paths. The selection of the interval model equation options decides if the problem is MILP or MINLP.

Step 5. Base case design

The objective here is to add details to the optimal processing route from step 4 to obtain a base case design in terms of

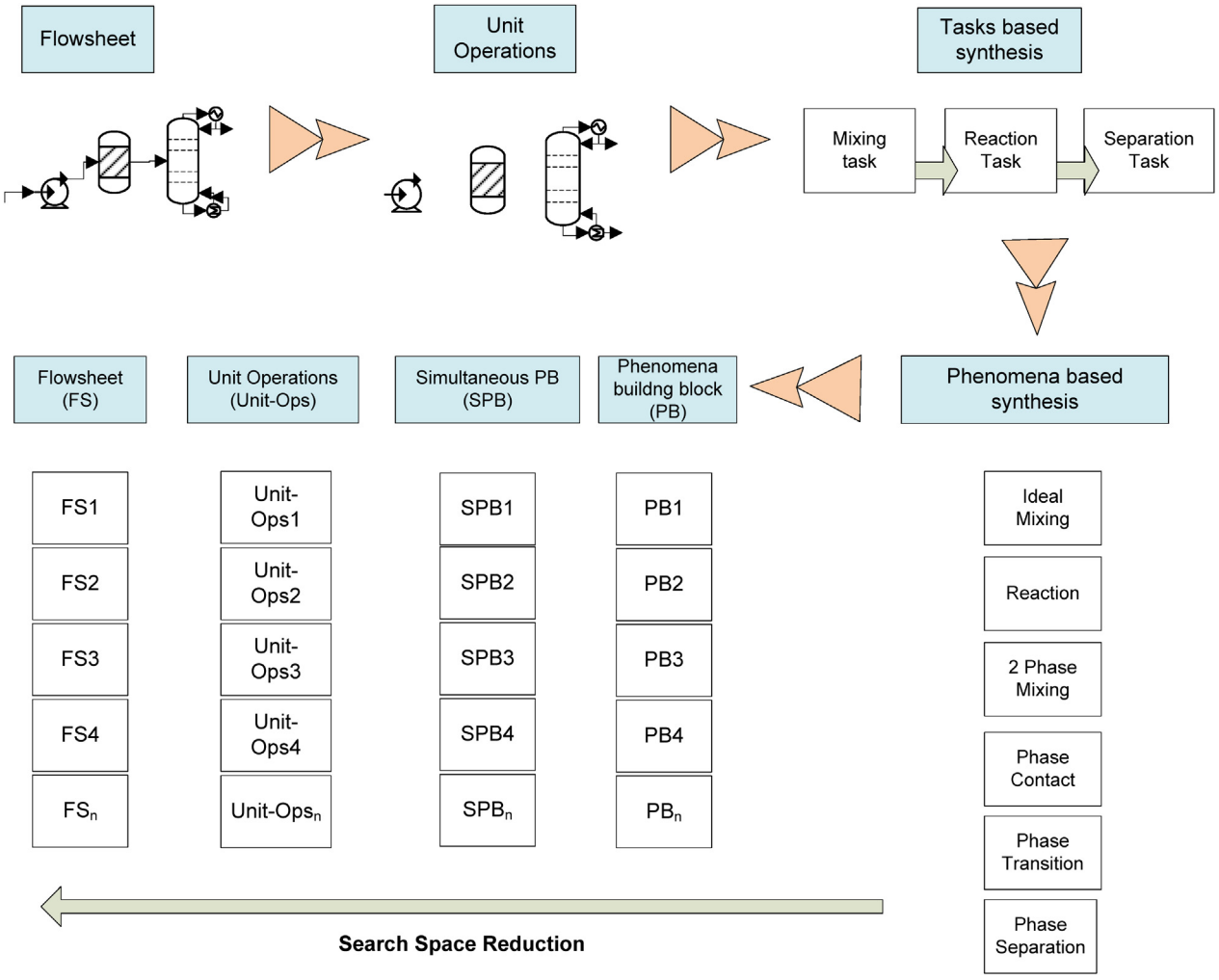

Fig. 5. Illustration of phenomena based synthesis of process alternatives.
Adapted from Babi et al. (2014).

Table 1
List of potential catalysts for DMC production by CO_2-utilization based processes.

Raw material	Alcohol	Catalyst	Molar ratio	Temperature (°C)	Pressure (bar)	Yield (%)	Reference
For CO_2 utilization							
$CO_2 + NH_3$	–	–	1:3.9	195	171.6	70	Ono et al. (1982)
			1:2	185	175	90	Kojima and Fujii (1999)
			1:4	186	145	79.2	Zhang et al. (2005)
CO_2 + EO	–	SalenCo(II)-MCM-41	–	110	125	85.6	Dai et al. (2009)
		SalenAlCl/*n*-Bu_4NBr	–	10	250	30	Lu et al. (2002)
		SalenAlCl/*n*-Bu_4NBr	–	30	250	96	Lu et al. (2002)
CO_2 + PO	–	(TCPPCo(III)X/PTAT, X = CF_3COO, OAc, Br, Cl)	–	25	12	80	Li et al. (2012)
		[Zn(BHBPDI)] and (TBAB)	–	110	40	97.8	Wang et al. (2012b)
		Fe/porphyrin	–	80	7	73.5	Dai et al. (2009)
$N_2 + H_2$	–	$K_2[Ru(CO)_4]$ + K		300	1	71	Yunusov et al. (2004)
For DMC production							
CO_2	Methanol	Cu–Ni/graphite	–	105	12	0.91	Bian et al. (2009)
		Ni–Cu/MoSiO	–	140	1	14.16	Zhong et al. (2002)
		Potassium methoxide (CH_3OK)		80	20	14.1	Cai et al. (2009)
Urea	Methanol	Dibutyltindimethyloxide	1:10	180	20	37.5	Lin et al. (2004)
		Polyphosphoric acid	1:14	140	8	67.4	Sun et al. (2005)
		$Et_3NHCl–ZnCl_2$	1:36.6	160	1	26.4	Wang et al. (2009a)
EC	Methanol	–	1:8	250	90	81.2	Feng et al. (2005)
		Poly-4-vinyl pyridine	1:4	140	10	82	Jagtap et al. (2008)
		1,4-Diazobicyclo[2.2.2]octane	1:15	70	1	84	Yang et al. (2010)
PC	Methanol	Verkade superbase catalysed	1:20	45	1	70	Williams et al. (2009)
		K_2CO_3–KI/ZnO		150	165	43.4	Chang et al. (2004)
		KI/ZnO		150	165	36.8	Chang et al. (2004)
CO_2 + EC	Methanol	MgO	–	150	80	66.1	Bhanage et al. (2001)
CO_2 + PC	Methanol	K_2CO_3–KI/ZnO	–	150	165	57.9	Chang et al. (2004)

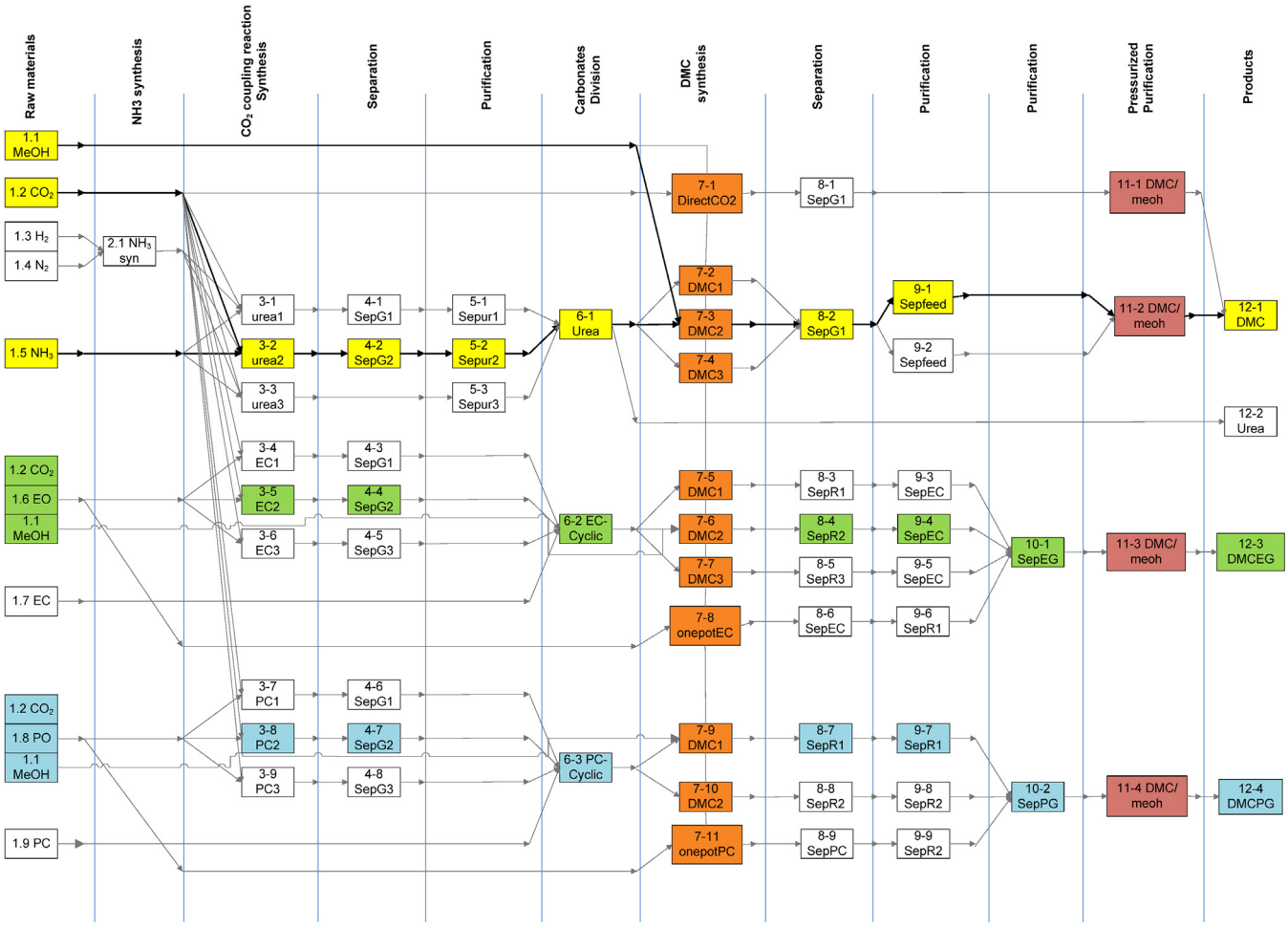

Fig. 6. Superstructure for DMC production network highlighting the optimal processing steps. Yellow indicates the optimal process configuration (urea route), light green indicates the second best (EC route) and light blue indicates the third best processing route (PC route). Red box indicates the interval from where recycle is sent back and orange box indicates the interval that receives the recycle. In the mathematical formulation potentially all intervals can send back or receive streams. (For interpretation of the references to colour in this figure legend, the reader is referred to the web version of the article.)

equipment (design) parameters. For example, for a distillation column, the number of stages, the feed location, product recovery rates, etc., are fixed at this stage so that a rigorous simulation of the base case can be performed.

Step 6. Rigorous process simulation

The objective here is to perform a rigorous process simulation of the base case design. In principle, any process simulator could be used. However, before a rigorous simulation can be performed, it is important to check if all the necessary data are available. The appropriate unit operation models together with the consistent thermodynamic models will need to be employed from the selected simulator.

Step 7. Process analysis and target setting

The objective of this step is to perform analyses of the base case design in terms of sustainability, including LCA factors and economics so that process deficiencies (regarded as process "hot-spots") can be identified and targets for overcoming these "hot-spots" are defined. Here, the sustainable design method of Carvalho et al. (2013) is employed.

Step 8. Alternative generation

The objective of this step is to find alternatives that match the design targets and thereby lead to a more sustainable design. The design targets are specified in terms of process efficiency, productivity and sustainability as well as reduced energy consumption, waste generation, and environmental impact. More details of the process intensification based method employed here can be found in Babi et al. (2014). The method operates at the phenomena level and the concept is similar to that of computer-aided molecular design (CAMD) where groups of atoms are used as building blocks to generate new as well as known molecules with desired (target) properties. Like computer-aided molecular design (CAMD), the phenomena based synthesis (PBS) method also operates at different levels of aggregation where the flowsheet is decomposed in terms of unit operations, which are represented by a set of tasks (Siirola et al., 1971; Siirola, 1996) for which, all selected phenomena that satisfy these tasks are identified. By combining the phenomena in different ways (using connectivity rules), the same and new

Table 2
Summary of the mathematical programming (MINLP) problem for DMC production by CO_2-utilization based processing steps.

Number of processing steps	12
Number of process intervals	59
Number of total processing routes represented by the superstructure	7128
Block of equations	37
Block of variables	24
Non-zero elements	144,825
Single equations	50,752
Single variables	53,737
Discrete variables	5430

Table 3
Summary of the results from the MINLP solution.

Issues	CO_2 direct synthesis	DMC from urea (1st rank)	DMC from PC	DMC from EC (2nd rank)
Objective function (max profit, USD/yr)	−76,044,817	24,243,436	13,900,692	19,356,971
Total sale price (USD/yr)	50,827,500	54,646,380 (DMC + NH_3)	106,615,860 (DMC + PG)	84,412,800 (DMC + EG)
Raw material cost (USD/yr)	123,033,600 (CO_2 + MeOH)	21,450,240 (CO_2 + MeOH)	20,653,056 (CO_2 + MeOH)	19,210,880 (CO_2 + MeOH)
		25,269,120 (CO_2 + NH_3 + MeOH)	83,803,572 (CO_2 + PO + MeOH)	57,341,370 (CO_2 + EO + MeOH)
Utilities cost (USD/yr)	153,379	632,053	542,496	517,023
Capital investment cost (USD/yr) Project life 10 years	2,727,270	7,163,341	6,315,100	5,437,436
Transportation cost (neglected)	–	–	–	–
Waste penalty cost and use of hazardous materials (USD/yr)	958,068	1,157,310	2,054,000	1,760,000
CO_2 utilization in overall process (kmol/h)	445	104	91.61	77.81

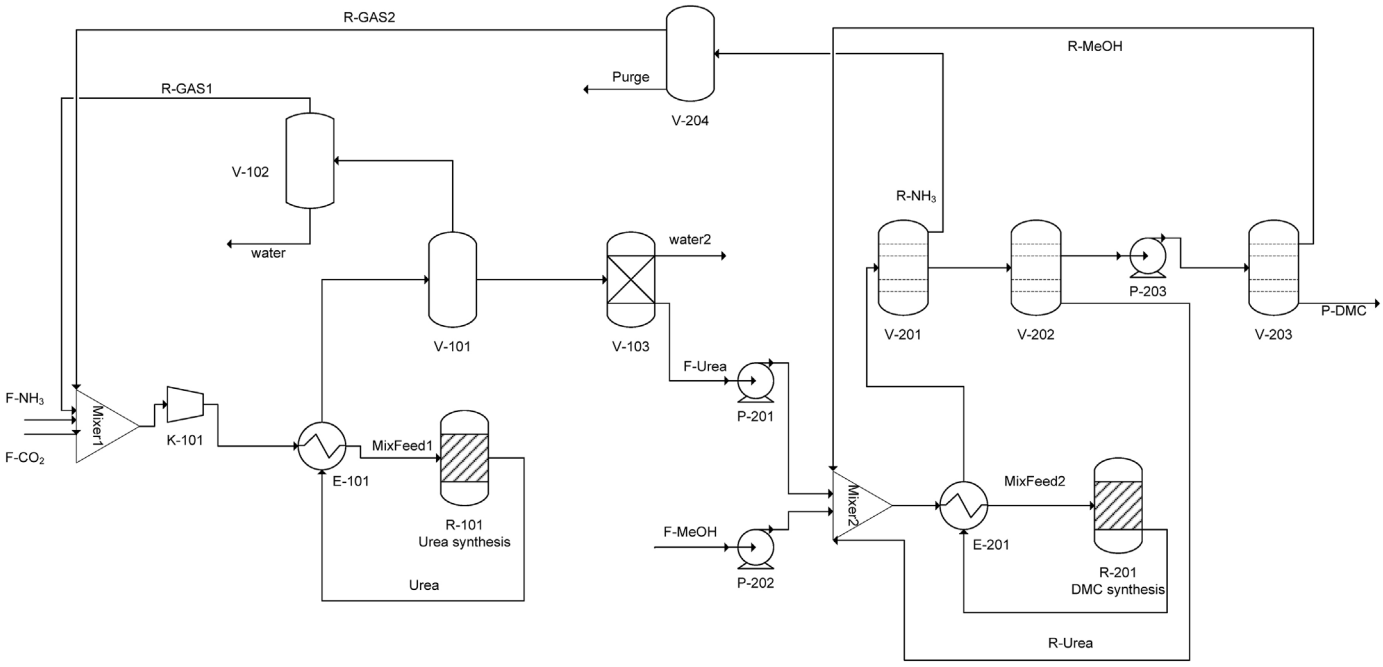

Fig. 7. The optimal DMC production process by urea route (base case design).

Table 4
List of identified "hot-spots" in the open-paths and closed-paths in the DMC processes of Fig. 7.

Path (No.)	Component	Flowrate (kg/h)	MVA (10^3 USD/yr)	EWC (10^3 USD/yr)	TVA (10^3 USD/yr)	Design sensitivity analysis (%improvement)
OP12	MeOH	1309.95	−565.01	215.68	−780.69	High
OP13	MeOH	648.380	−281.00	195.09	−476.09	High
OP7	Urea	2677.82	−1.928	184.10	−186.02	High
OP15	DMC	6072.00	28,298.16	156.45	28,141.71	Low
CP17	MeOH	2089.10	0	1004.32	−1004.32	High
CP15	Urea	1957.80	0	33.63	−33.63	Low
CP18	DMC	974.53	0	25.06	−25.06	Low

(combined) tasks can be performed, thereby leading to new and more sustainable alternatives that match the design targets. The concept of phenomena based synthesis is illustrated through Fig. 5, where it can be noted that starting with a base case flowsheet, a set of phenomena are identified, which are then combined to form multiple flowsheets that are likely better than the base case. Where it can be noted that starting with a base case flowsheet, a set of phenomena found in it are identified, which are then combined to form multiple flowsheets that are likely better than the base case.

The phenomena currently considered are classified as: (1) mixing-M (mass flow within one or several phases), (2) phase contact-PC (the contact and resistances at phase boundaries of phases), (3) phase transition-PT (mass transfer of compounds between two phases), (4) phase change-2phM (state change of a complete stream at no phase transition), (5) phase separation-PS (the degree of separation of two phases), (6) reaction-R (change in mass of a compound or compounds generated or consumed between inlet and outlet), (7) energy transfer-H/C (energy transfer between sources and sinks of energy) and (8) stream dividing-D (division of a stream into two or more streams).

Step 9. Process evaluation

After the process alternatives are generated in step 8, they are further analysed in terms of economic and LCA evaluations. The objective of this step is to evaluate the alternatives to identify the

best (or a sub-set) process. The performance evaluation of process alternatives are established in terms of carbon footprint (CF), which is the overall amount of carbon dioxide and other greenhouse gas emissions associated with 1 kg of product. The carbon footprint is related to other indicators such as the global warming potential (GWP) in terms of kg of CO_2 equivalent (Piyarak, 2012; Kalakul et al., 2014). For the health issues, an indicator such as the human toxicity-carcinogenic (HTC) is used in terms of kg of benzene equivalent. Economic evaluation is calculated using ECON (Saengwirun, 2011) which provides the needed cost and economic potential data.

3. Results and discussion

The CO_2 based DMC production process is considered here to illustrate the application of implemented framework for more sustainable process synthesis and design of CO_2-utilization based chemical process. DMC is considered as an oxygenate compound for gasoline additives (octane enhancer) and as a means of converting natural gas to a liquid transportation fuel. Evaluation of DMC production technologies and fuel properties has become important to the oil industry, because recent economic studies have shown that it is more economical to use DMC in reformulated gasoline than MTBE produced from butane. Although DMC is not a cost effective octane enhancer, it is one of the most cost-effective oxygenates to meet with an oxygen specification in gasoline, added 10% volume of DMC increases the blending octane value (B.O.V) from 85 to 106 (Pacheco and Marshall, 1997). DMC can be produced from various types of reactions. A conventional route is the production of DMC from phosgene, where phosgene initially reacts with methanol to form methyl chloroformate (CH_3OCOCl) that further reacts with an additional mole of methanol to form DMC. However, phosgene is an extremely hazardous chemical and is classified as a class-A poison. Consequently, the use of phosgene is being phased out (Matsuzaki and Nakamura, 1997). The uses of carbon monoxide (CO) in a partial carbonylation process and a methyl nitrile process for DMC production have been reported in commercial scale (Tundo and Selva, 2002).

3.1. Problem formulation

Step 1. Problem definition

The product is DMC, and to produce it, CO_2 must be used as a feedstock. Therefore, information on all known technologies where CO_2 may be used to produce DMC is necessary. The CO_2 to be used is assumed to be available from CO_2 capture processes. The available data of DMC production such as price of raw materials, capital cost, utilities cost, waste treatment cost, etc., are needed for step 2. The obtained DMC specification is set at a purity higher than 99 wt%. The best process alternative will be established in terms of *Max profit* which considered sale price, raw material cost, capital investment cost, utilities cost and waste penalty cost.

Step 2. Data collection and superstructure definition

This work investigates DMC production from CO_2 via transesterification with methanol. This can be achieved via direct reaction between CO_2 and methanol to form DMC. Also via indirect routes, in which CO_2 is first utilized by the reaction with compounds such as ammonia (NH_3), ethylene oxide (EO), or propylene oxide (PO) to form chemical intermediates, i.e., urea, ethylene carbonate (EC), or propylene carbonate (PC), respectively. Then, DMC is produced by the transesterification of the intermediate with methanol. Available data for several DMC processing routes ranging from CO_2 direct synthesis, urea route, EC route and PC route are collected from reported technologies in the literature. For the direct use of CO_2 to produce DMC, it has been reported that CO_2 could react with methanol at critical temperature and critical pressure of CO_2 (Gu et al., 2008). This direct transformation of CO_2 and methanol could avoid the use of toxic chemicals such as phosgene. Nevertheless, the direct utilization of CO_2 in commercial scale is challenging because CO_2 lies in a deep potential energy well of about −400 kJ/mol that requires huge amount of energy for activation (Sheppard and Yakobsin, 2003). On the other hand, other processes, such as urea-, EC-, or PC-routes are considered as new alternatives for integrating CO_2 utilization with the production of DMC.

Table 5
The indicator sensitivity analysis results for the open-paths.

OP12	Improvement (%)		
Variable variation (%)	F-MeOH	V-202	R-201 DMC synthesis reactor
5	3.47	0.00	5
10	7.05	0.00	10
15	10.75	0.00	15

Table 6
The indicator sensitivity analysis results for the closed-paths.

CP17	Improvement (%)	
Variable variation (%)	R-201 DMC synthesis reactor	Flow CP-17
5	5	4.27
10	10	8.60
15	15	13.00

The different catalysts applied for CO_2 utilization and DMC production can be classified as: alkali catalyst, acid catalyst, solid base catalyst and ionic liquids, which have been considered in the generation of multiple processing routes as shown in Table 1. (For more information, see Table 1S in the Supplementary material where the data collected for setting up the superstructure (network of processing steps) is given.)

Based on the information collected, the superstructure of processing steps is generated (see Fig. 6), where 10 processing steps with multiple intervals for each step have been used. There are 23 parameters and 21 variables which are represented in Table 2S.

Step 3. Mathematical programming problem

For each interval in Fig. 6, the appropriate model equations are retrieved from Quaglia et al. (2013) to obtain the full network model.

The MINLP problem is formulated with the simplified process model of Table 1 and solved in GAMS. The objective function for finding the optimal processing route is *Max profit* as given by Eq. (8). The summary of DMC production by CO_2 based processing problem formulation statistics is reported in Table 2.

In this case study, the objective function (see Eq. (8)) is described by products sale price (DMC and by-products such as EG and PG), raw material cost (CO_2, nitrogen, hydrogen, ammonia, ethylene oxide, propylene oxide, ethylene carbonate, propylene carbonate and methanol), utilities cost (HP and LP steam, hot oil, cooling water and electricity), waste penalty (water treatment and gas emission) and capital investment. The results of MINLP problem indicate that the DMC production by urea route gives the maximum objective function value, and the second optimal processing route is the DMC production by EC route and the third is DMC production by PC route. These three processing routes are shown through the shaded intervals in Fig. 6, and the determined values of the objective function for each processing route are given in Table 3. Note that the superstructure allows recycle as well as bypass options. Also, the superstructure highlighted in Fig. 6 has 10 processing steps and a total of 59 processing intervals, not counting the raw materials and the products. Obviously, many more flowsheets can be generated from this superstructure than the original known technologies used to create it.

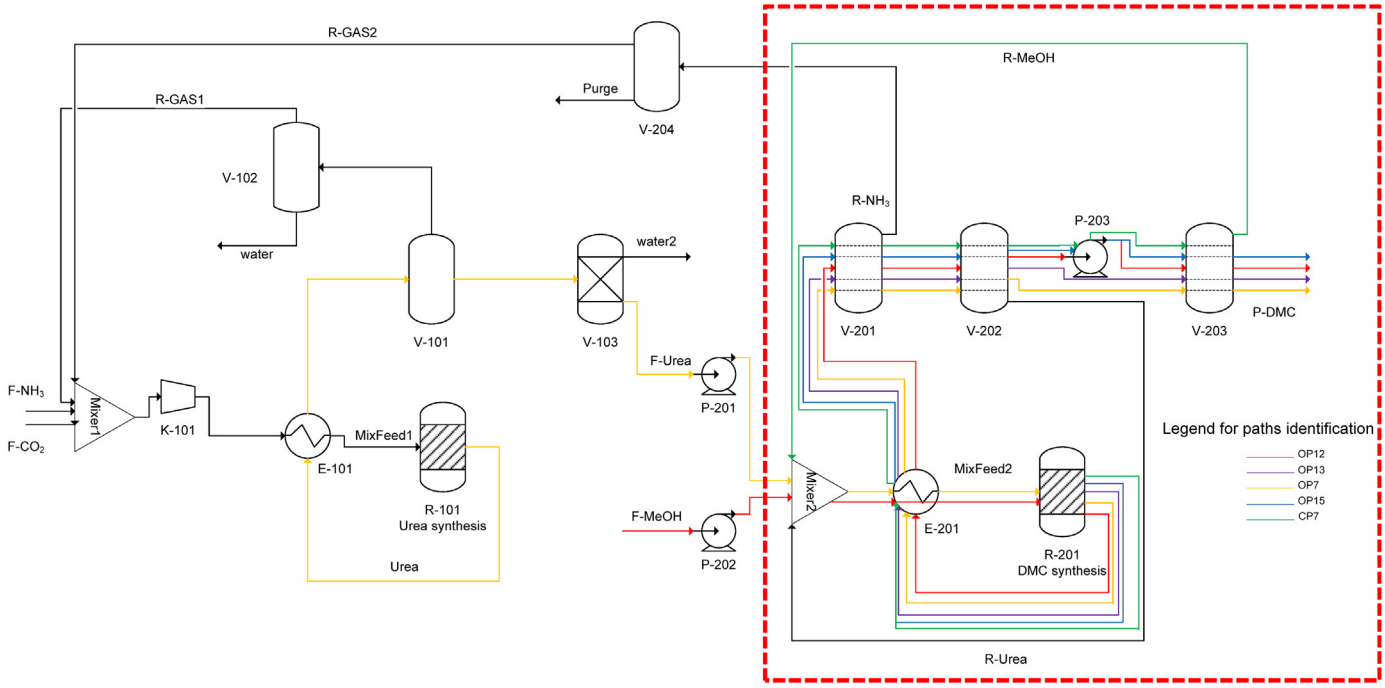

Fig. 8. Identification of open-path and closed-path having major bottlenecks in the process flowsheet. (For interpretation of the references to colour in this sentence, the reader is referred to the web version of the article.

Table 7
Results from preliminary evaluation of the base case design.

Sustainability metrics	
Total energy consumption (MJ/h)	86,710.92
Energy consumption in CO_2 utilization section (MJ/h)	23,841.80
Energy consumption in DMC synthesis section (MJ/h)	62,869.12
DMC production (kg/h)	6071.96
Energy consumption/kg of product DMC (MJ/kg)	10.35
Economic indicators	
Total sale prices (USD/yr)	52,461,734.4
Total cost (USD/yr)	33,064,514.0
Net profit margin (USD/yr)	19,397,220.4
Fixed-capital investment (USD/yr)	7,163,341.0
Operating cost (USD/yr)	632,053.0
Raw material cost (USD/yr)	25,269,120.0
Cooling water usage (GJ/yr)	194,954.4
Fuel usage (GJ/yr)	295,783.2
Life cycle assessment indicators	
CO_2 emission/kg of product DMC	1.281
HTC/kg of product DMC	0.0003
GWP/kg of product DMC	2.256

As supplementary data, the simple process flowsheet for using in process interval in the DMC production through the urea route is shown in Fig. 1S.

Step 4. MINLP solution

The MINLP problem described above has been solved with GAMS (IBM Corp, 2009). On average, a typical MINLP needed 363 iterations and 3167 ms computing time on an Intel® Core™ i5-3230 CPU 2.60 GHz, RAM 8 GB, 64-bit operating system, Window 7 computer.

The MINLP solution results are given in Table 3 and are based on a DMC production rate of 62.75 kmol/h or 5647.5 kg/h (40,662 MMT/year). The best process candidate in the "synthesis" stage is DMC production via urea route, which offers the maximum profit of 24,243,436 USD/yr. The competitiveness of the EO and PO routes depends significantly on the price of petroleum. The equivalent profit can be achieved when the price of EO decreases from 1.55 to 1.415 USD/kg (9.7% reduction) and the price of PO decreases from 1.65 to 1.381 USD/kg (16.3% reduction), respectively. These routes earn more benefit from the sale of valuable by-products ethylene glycol (EG) and propylene glycol (PG). It should be noted that the best process candidate reported in our previous work (Kongpanna et al., 2015) was the EC route. The different results are mainly due to the use of a different objective function. In the previous work, only energy consumption, CO_2 emission and life cycle assessment were considered; however, in this study the main objective function is '*Max profit*' that includes raw material costs, product sell prices, fixed capital investment costs, waste penalty cost and utilities cost.

So, as base case design, the two best process flowsheets are used as process candidates: the DMC production by urea route and the EC route. Only the detailed results for the urea route are given for the next steps while the results of the EC route are included only in the analysis and assessment in step 9.

Step 5. Base case design

The DMC production route via urea highlighted in Fig. 7, is the base case design. The process design is divided into two sections, the CO_2 utilization section which uses CO_2 and NH_3 as raw materials for producing urea and then urea is sent to the next section, the DMC synthesis section. Here, urea and MeOH react in the DMC synthesis reactor followed by a series of separation and purification steps to obtain the specified DMC product. The mass balance and design specification of all unit operations are given in the Supplementary material (see Tables 3S and 4S).

Step 6. Rigorous simulation

The detailed process data for the urea route are obtained through process simulation and forms the basis for design decisions. The simulation of this base case involves 16 unit operations, 30 streams and seven compounds (see Fig. 7). The extended electrolytic UNIQUAC equation is used to describe nonideality of liquid phase, which is NH_3–CO_2–H_2O–urea mixture under high pressure and high temperature, while the perturbed-hard-sphere (PHS) equation of state is used to predict the fugacity coefficients of the vapour in the VLE calculation of the CO_2–NH_3–urea system (Zhang et al., 2005). Missing binary interaction parameters for the UNIQUAC model in ASPEN simulator of the DMC/MeOH system were collected from the literature reported by Holtbruegge et al. (2013).

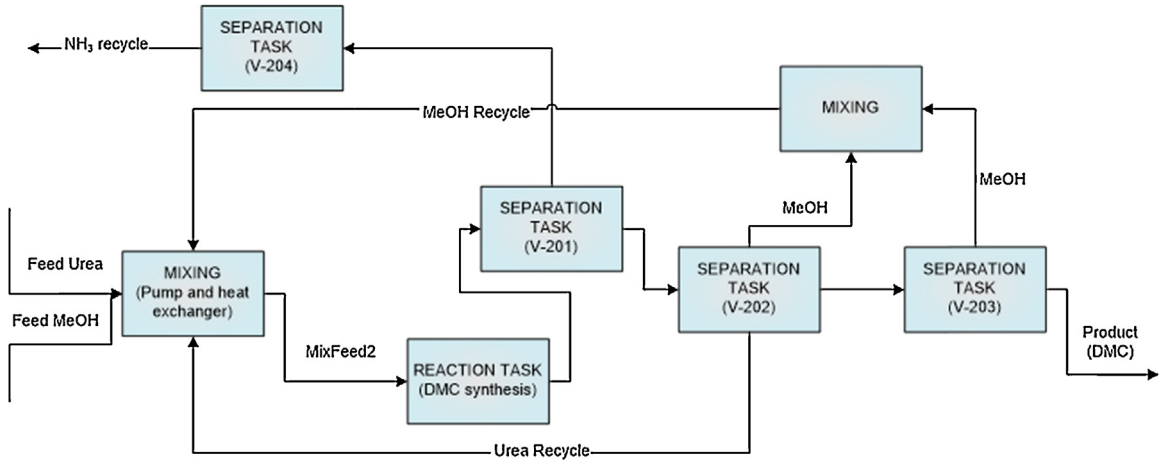

Fig. 9. Task-based representation of the base case flowsheet for DMC production by urea route (Siirola, 1996).

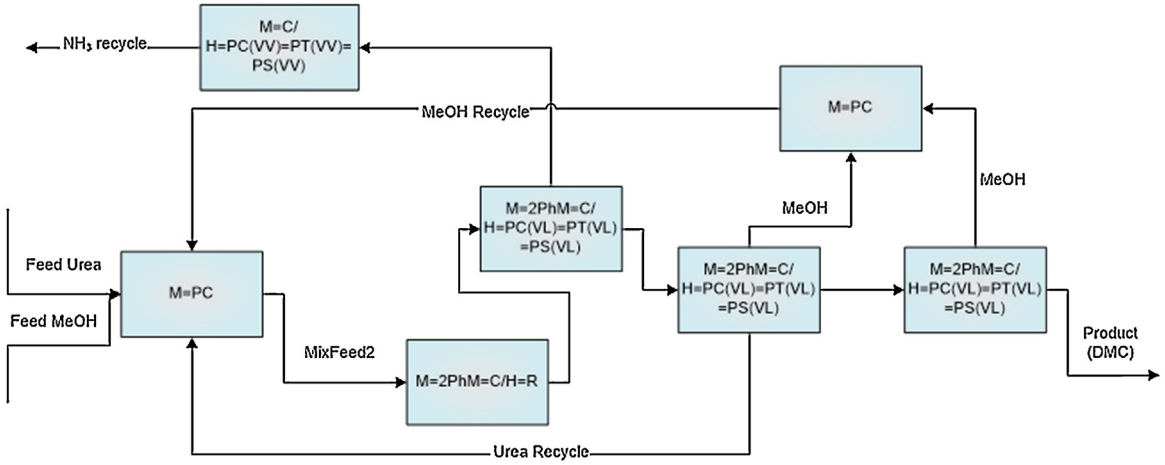

Fig. 10. Phenomena-based representation of the base case flowsheet for DMC production by the urea route.

Table 8
Operating window for the considered phenomena in this study.

No	Phenomena	Operating window
PBB. 1	*R*	T_{low} = 120 °C (lowest melter or insufficient for activation energy) T_{high} = 170 °C (catalyst degrade or inhibit reaction equilibrium)
PBB. 2	M_{ID} *(mixing)*	
PBB. 3	$M_{FL,tube}$ *(mixing)*	T_{low} = −98.68 °C (lowest melter)
PBB. 4	$M_{FL,rec}$ *(mixing)*	T_{high} = 132.70 °C (highest boiler)
PBB. 5	M_V *(mixing)*	
PBB. 6	*2phM (mixing)*	T_{low} = 64.70 °C (lowest boiling azeotrope) T_{high} = 177.0 °C (highest boiler)
PBB. 7	*PC(VL)* Conventional separation vapour–liquid	V–L present
PBB. 8	*PT(VV)* Conventional separation vapour–vapour	Component affinity
PBB. 9	*PT(VL)*	T_{low} = 64.70 °C (lowest boiling azeotrope)
PBB. 10	*PT(PVL)* Non-conventional separation vapour–liquid	$T_{operate}$ = 70.0 °C (membrane stability in pervapouration unit)
PBB. 11	*PS(VL)*	V–L present
PBB. 12	*PS(VV)* Non-conventional separation vapour–vapour	V–V present
PBB.13	*H*	Heating
PBB. 14	*C*	Cooling
PBB. 15	*D*	Dividing

Adapted from Babi et al. (2015).

Table 9
Computed binary ratio matrix for a selected set of compounds for the DMC production process.

Ratio of properties of binary pairs	*Mw* (g/mol)	*Tm* (K)	*Tb* (K)	*RG* (Å)	*Solubility parameter* ($MPa^{0.5}$)	V_{VDW} (m^3/mol)	V_M (m^3/mol)	Vapour pressure (atm)	Dipole moment (debye)
DMC/MC	1.2868	0.8514	0.8072	–	–	–	–	–	–
DMC/NH_3	5.2891	1.4080	1.5159	3.8065	0.2990	3.3478	2.8700	7.38E-03	0.6120
DMC/MeOH	2.8112	1.5680	1.0756	2.0921	1.63E+04	2.1290	1.9664	2.3278	0.5289
MeOH/urea	0.5335	0.4323	0.7265	0.5969	1.20E−03	0.6718	0.7720	6.26E+03	0.3730
MeOH/MC	0.4577	0.5429	0.7505	–	–	–	–	–	–
MeOH/NH_3	1.8813	0.8979	1.4093	1.8194	1.82E−05	1.5724	1.4600	3.17E−03	1.1571
Urea/MC	0.8579	1.2559	1.0329	–	–	–	–	–	–
Urea/DMC	0.6667	1.4750	1.2795	0.8007	5.10E−02	0.6991	0.6590	6.87E−05	5.0682
Urea/NH_3	3.5262	2.0769	1.9397	3.0480	1.52E−02	2.3405	1.8900	5.07E−07	3.1021

Mw – molecular weight (g), *Tb* – normal boiling point (K), *RG* – radius of gyration (Å), *Tm* – normal melting point (K), V_M – molar volume (m^3/mol), SolPar (Hansen) solubility parameter, V_{VDW} (m^3/mol) – Van der Waals volume, V_P (atm) – vapour pressure.

Table 10
List of selected (desirable) PBBs linked to the identified tasks *V* – vapour, *L* – liquid, LL – liquid–liquid, MSA – mass separating agent (Babi et al., 2015).

Hot-spot	Main task	Property/binary ratio	Alternative task	MSA	PBB (desirable)
Azeotrope	Separation	Vapour pressure, solubility parameter	Separation	Yes	PC(LL), PT(LL), PS(LL)
Azeotrope Difficult separation due to low driving force	Separation	Radius of gyration, van der Waals volume, solubility parameter	Separation	No	PT(PVL), PT(VV), PS(VV)

Table 11
The partial list of identified feasible *SPBs* together with corresponding interconnection phenomena and inlet and outlet conditions.

SPB	Interconnection phenomena	In	Out
SPB.1	*M*	1. . .*n*(L,VL,V)	1(L,VL,V)
SPB.2	*M* = *R*	1. . .*n*(L,VL,V)	1(L,VL,V)
SPB.3	*M* = *H*	1. . .*n*(L,VL,V)	1(L,VL,V)
SPB.4	*M* = *C*	1. . .*n*(L,VL,V)	1(L,VL,V)
SPB.5	*M* = *R* = *H*	1. . .*n*(L,VL,V)	1(L,VL,V)
SPB.6	*M* = *R* = *C*	1. . .*n*(L,VL,V)	1(L,VL,V)
SPB.7	*M* = *2phM*	1. . .*n*(L,VL)	1(V/L)
SPB.8	*M* = *R* = *2phM* = *PC(VL)* = *PT(VL)*	1. . .*n*(L,VL)	1(V/L)
SPB.9	*M* = *2phM* = *PC(VL)* = *PT(VL)* = *PS(VL)*	1. . .*n*(L,VL)	2(V;L)
SPB.10	*M* = *R* = *2phM* = *PC(VL)* = *PT(VL)* = *PS(VV)*	1. . .*n*(L,VL)	2(V;L)
SPB.11	*M* = *R* = *2phM* = *PC(VL)* = *PT(VL)* = *PS(VL)*	1. . .*n*(L,VL)	2(V;L)
SPB.12	*M* = *R* = *2phM* = *PC(VL)* = *PT(VV)* = *PS(VV)*	1. . .*n*(L,VL)	2(V;V)
SPB.13	*M* = *C* = *2phM* = *PC(VL)* = *PT(VL)*	1. . .*n*(L,VL)	1(V/L)
SPB.14	*M* = *H* = *2phM* = *PC(VL)* = *PT(VL)*	1. . .*n*(L,VL)	1(V/L)
SPB.15	*M* = *H* = *R* = *2phM* = *PC(VL)* = *PT(PVL)*	1. . .*n*(L,VL)	1(V/L)
SPB.16	*M* = *C* = *R* = *2phM* = *PC(VL)* = *PT(PVL)*	1. . .*n*(L,VL)	1(V/L)
SPB.17	*M* = *H* = *R* = *2phM* = *PC(VL)* = *PT(VL)* = *PS(PVL)*	1. . .*n*(L,VL)	2(V;L)
SPB.18	*M* = *H* = *R* = *2phM* = *PC(VL)* = *PT(VL)* = *PS(VL)*	1. . .*n*(L,VL)	2(V;L)
SPB.19	*M* = *H* = *R* = *2phM* = *PC(VV)* = *PT(VV)* = *PS(VV)*	1. . .*n*(L,VL)	2(V;V)
SPB.20	*M* = *2phM* = *PC(VL)* = *PT(PVL)* = *PS(VL)*	1. . .*n*(L,VL)	2(V;L)
SPB.21	*M* = *2phM* = *PC(VL)* = *PT(VL)* = *PS(VV)*	1. . .*n*(L,VL)	2(V;L)
SPB . . .	. . .	. . .	. . .
SPB.72	*D*	1. . .*n*(L,VL,V)	1. . .*n*(L;VL;V)

Note: *V* = vapour; *L* = liquid; "/" means "or"; ";" means "and"; "In" provides number of inlet streams (1 to *n*) and phase, "Out" provides number of outlet streams (1 or 2) and phase.

Section 1 description (see Fig. 7): Urea is synthesized from ammonia and carbon dioxide in the first reactor modelled by using equilibrium reactor module (REQUI) in Aspen simulation. The details of the validation and simulations were reported in our previous work (Kongpanna et al., 2015). The simulation results agree well with the experimental data. This process can utilize 3435 kg/h of CO_2 coupling reaction with NH_3 3069 kg/h for producing 4612 kg/h of urea. The feed stream to reactor (with additional recycled stream) molar ratio of NH_3:CO_2 was 2:1. The simulation revealed a high urea yield of 76.8% when the reactor is operated at 180 bar and 200 °C. The value agrees well with the experimental data (70%) reported by Zhang et al. (2005). The reaction product stream flows into separators V-101 and V-102 for recovery and recycle of the unreacted raw materials. The removal of water to obtain purified urea is done in a separator V-103.

Section 2 description (see Fig. 7): In this section, urea and methanol reacted to produce DMC. The feed streams contain 4565 kg/h of urea and 4361 kg/h of MeOH and some of urea and MeOH which remain in the recycle stream. The reactor is operated at 140 °C and 8 bar, assuming equilibrium reaction. Yield of DMC achieved is 67.4%, which is relatively close to the reported experimental data (Sun et al., 2005). The product stream flows to the separation and purification section having azeotropic distillation for DMC/MeOH separation. The first column is a flash separator (V-201) employed to separate NH_3 gas for recycle to the urea synthesis section, the bottom stream contains the

unconverted urea 1957 kg/h, MeOH 2087 kg/h and DMC 7046 kg/h. Then, the product stream is sent to the series of pressurized distillation columns (V-202 and V-203) to separate the azeotropic mixture of DMC/MeOH. The production rate of this base case design is 6071 kg/h (67.4 kmol/h) with the 99.11 wt% purity.

Step 7. Process analysis and target setting

The base case process design is further evaluated by SustainPro (Carvalho et al., 2008) to identify the process "hot-spots", that is, the locations in the process that have the highest potential for improvement. The hot-spots that are found in the DMC production section are listed in Table 4.

It can be seen in Table 4 that there is high material loss (−TVA values) of methanol accompanied by energy consumption (+EWC values) in the open-paths (OP). Furthermore, high energy consumption is also observed in the given closed-path (CP) associated with methanol. It can be seen that the energy waste cost of OP12 and CP17 is large, comparing with other paths. The "indicator sensitivity analysis" algorithm in SustainPro, which is capable of identifying the design targets as well as determining their desired target values, is used to identify the potential for significant improvements in the process. These identified indicators are designated as design targets for new process alternatives (Carvalho et al., 2008). The results given in Tables 5 and 6 indicate that there is high potential for improvement in OP12, the energy usage for methanol flow in open-path and CP17, the energy usage for methanol recirculating in the DMC synthesis section. So, the hot-spots of this process are the DMC synthesis reactor and the downstream separation of DMC/MeOH azeotropic mixture, which require high energy consumption for the separation task.

It should be noted that the closed-path (CP17) having the highest values of EWC is also considered as a bottleneck (see Fig. 8).

The economic and life cycle assessment analyses are also updated for the base case after rigorous simulations. The results are given in Table 7, which are used in step 9.

The paths OP12 and CP17 are identified as process bottlenecks with respect to TVA, MVA and EWC are located in the path of the DMC synthesis reactor (R-201), and series of separators (V-201, V-202 and V-203). The process bottlenecks occur due to the reaction equilibrium (with low conversion) and separation of azeotropic mixtures, requiring thereby a large amount of energy to separate

Table 12
Generation of hybrid/intensified unit operations from combination of PBBs.

SPB no.	Combined SPBs (basic structure)	Task performed	Unit operations
SPB. 5	*M = R = H*	Urea + MeOH → R-Task → DMC, NH_3 Urea, MeOH	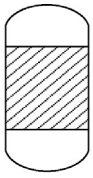 Conventional Reactor
SPB. 7 SPB. 9 SPB. 4 SPB. 12	*M = 2phM* *M = 2phM = PC(VL) = PT(VL) = PS(VL)* *M = C* *M = R = 2phM = PC(VL) = PT(VV) = PS(VV)*	DMC + MeOH → S-Task → DMC; MeOH	Conventional distillation column
SPB. 20	*M = 2phM = PC(VL) = PT(PVL) = PS(VL)*	DMC + MeOH → S-Task → DMC; MeOH	Pervaporation membrane unit 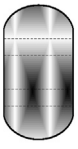 Vapor permation membrane unit

Table 12 (*Continued*)

SPB no.	Combined SPBs (basic structure)	Task performed	Unit operations
SPB. 13	*M = C = 2phM = PC(VL) = PT(VL)*	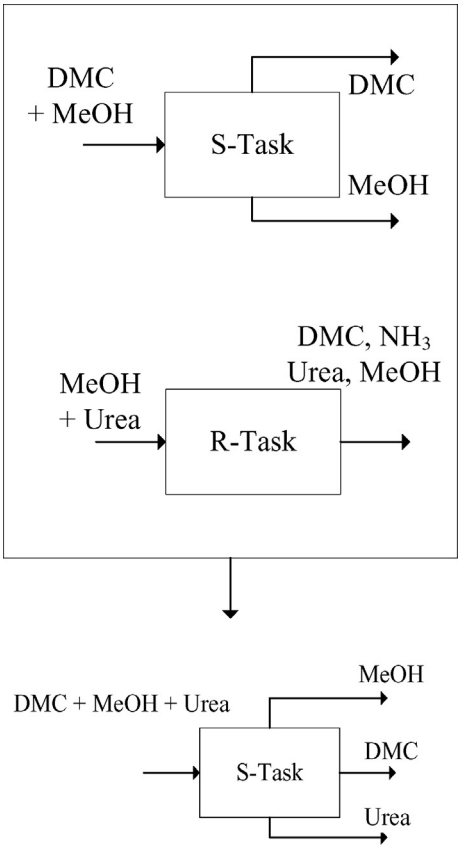	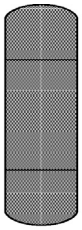
SPB. 8	*M = R = 2phM = PC(VL) = PT(VL)*		
SPB. 9	*M = 2phM = PC(VL) = PT(VL) = PS(VL)*		
SPB. 14	*M = H = 2phM = PC(VL) = PT(VL)*		

Task are merged

the ternary mixture of urea/DMC/MeOH and the binary azeotrope mixture of DMC/MeOH. Therefore, the DMC synthesis reactor and the downstream separation of DMC/MeOH azeotropic mixture in the DMC synthesis section are taken as the target of the process debottlenecking. Based on economic and sustainability analysis, the process performance improvement must be made and matched with the target indicator for achieving more sustainable process. Therefore, the new process alternatives need to match the following target indicators:

- Reduction in process separation energy consumption.
- Improvement in process sustainability factors.
- Improvement in process economic and life cycle assessment indicators.
- Reduction in waste generation (by-product formation).
- Reduction utilities consumption and waste generation in the overall process.

Step 8. Alternative generation

The objective of this step is to generate process alternatives that match the design targets: higher yield of DMC in the DMC synthesis reactor and reduced energy consumption in downstream separation of DMC/MeOH to obtain more sustainable designs.

3.2. Problem and objective function definition

Problem definition: The identification of more sustainable (innovative) process designs for the production of DMC through the improvement in economic and sustainability.

The objective function: The objective here is to identify the best process alternatives with respect to sustainability metrics, economic and life cycle assessment indicators. The LCSoft and ECON software are used as performance evaluation tools that point to more sustainable process alternatives compared to the base case design. The equation for the objective function in process alternative evaluation is the "*Net profit margin*" which is shown in Eq. (9). Note that the project lifetime is set at 10 years for capital cost calculation.

$$(Max\, F_{Obj})Net\ \ Profit\ \ Margin = Total\ \ Sale\ \ Prices - Total\ \ Cost \quad (9)$$

- Total sale prices – calculated from products prices (USD/kg) × production rate (kg/yr).
- Total cost – calculated from fixed capital cost (USD/yr) + operating cost (utilities) (USD/yr) + raw material cost (USD/yr).

3.3. Analysis of the process

Data from steady-state mass and energy balances are collected from rigorous simulation results of the base case design. The DMC

synthesis reactor and the downstream separation of DMC/MeOH azeotropic mixture in the DMC synthesis section are taken as the target of the process debottlenecking (see steps 6 and 7). Thus the generation of (more sustainable) intensified flowsheet alternatives is performed on the DMC synthesis section (red dotted box) as shown in Fig. 8.

The base case design flowsheet is first transformed into a task-based flowsheet (Fig. 9) using the means-ends method (Siirola, 1996) and then into a phenomena-based flowsheet (Fig. 10) where the tasks (representative of the unit operations) are decomposed into phenomena building blocks (Lutze et al., 2013; Babi et al., 2015) that verify the application of a task. These phenomena building blocks (PBBs) are derived from the analysis of chemical/biochemical processes where it has been found that most processes can be represented by nine individual PBBs. These are mixing (*M*), heating (*H*), cooling (*C*), reaction (*R*), 2 phase mixing (*2phM*), phase contact (*PC*), phase transition (*PT*), phase separation (*PS*) and dividing (*D*).

The PBBs identified for the base case design (initial set of PBBs) are: M, 2phM, H, C, R, PC(VL), PT(VL), PS(VL) and D, where VL represents vapour–liquid.

3.4. Identification of desirable task and phenomena

According to Babi et al. (2014), the process hot-spots can be reduced/eliminated through the use of additional, desirable PBBs using thermodynamic insights (Jaksland et al., 1995). Each process hot-spot is linked to a binary ratio property (Jaksland et al., 1995) that translates into a (desirable) PBB (see examples in Table 11). For example, if the molar volume binary ratio of an azeotrope pair is greater than 1.5 (Jaksland et al., 1995) then the PBB PT(PVL) is selected and added to the initial set of PBBs. This PBB is the building block of a pervapouration membrane or unit operation that incorporates pervapouration at the unit operations scale. An excerpt of the binary ratio matrix for the compounds is given in Table 9. It can be seen that for the DMC/MeOH binary pair, the radius of gyration is 2.09 and van deer Waals volume is 2.13. Therefore, the following desirable PBBs are selected: PT(PVL), PT(VV) and PS(VV). The final set of PBBs are: M (considering four types), 2phM, H, C, R, PC(VL), PT(VL), PT(PVL), PT(VV), PS(VL), PS(VV) and D and their operating window is defined in Table 8.

3.5. Generation of feasible operation/flowsheet option

A simultaneous phenomena building block (SPB) is defined as the combination of one or more phenomena building blocks using predefined combination rules (Babi et al., 2015) for example, SPBs containing the combination of H and C PBBs to form =H=C= are rejected because of thermodynamic infeasibility, SPBs containing the combination of R and C PBBs to form =R=C represent a liquid phase reaction coupled with cooling (Babi et al., 2014). The 15 identified PBBs are combined to form SPBs and the possible number of combinations based on the formula proposed by Lutze et al. (2013) is calculated to be 16,728. Using the connectivity rules proposed by Lutze et al. (2013) and Babi et al. (2015), identification of desirable tasks to *PBBs*, given in Table 10, the number of (feasible) SPBs is reduced to 72 (see Table 11). Note that when combining PBBs into SPBs, the combination of simultaneous reaction and separation is feasible (see SPB 11) which verifies the merging of reaction and separation tasks into one single task.

Process alternatives are generated from the *SPBs* listed in Table 11. The criteria for generating new process alternatives are given in Table 6S as Supplementary material. The new process alternatives are based on the reaction and raw materials defined in the base case design. MeOH (raw material) forms an azeotrope with DMC (desired product) (see Fig. 2S). From the constraints defined in Table 6S, the separation involving mass separating agents (solvents) are not considered in order to minimize waste generation. From the mixture property analysis (Kongpanna et al., 2015), MeOH/DMC has azeotrope that is also pressure dependent. For the separation of the MeOH/DMC azeotrope (and based on the desirable PBBs selected in step 8.3) SPBs consisting of PT(PVL) and PT(VV) are selected.

The following flowsheet alternatives are considered for the DMC synthesis section (red dotted box in Fig. 8):

- Flowsheet alternatives 1–2 – Pervapouration or vapour-permeation membrane unit for the separation of DMC/MeOH.
- Flowsheet alternative 3 – Membrane reactor and in situ product removal for shifting the reaction equilibrium.
- Flowsheet alternative 4 – Reactive distillation and membrane reactor where simultaneous reaction and product separation is performed.

These flowsheet alternatives (flowsheet alternatives 1–4) are generated using the following SPBs and further explained in Table 12:

- The pervapouration and vapour permeation membrane for separation of the DMC/MeOH azeotrope: SPB. 20 *(M = 2phM = PC(VL) = PT(PVL) = PS(VL))* and SPB. 21 *M = 2phM = PC(VL) = PT(VL) = PS(VV)*.
- Membrane reactor and reactive distillation for simultaneous reaction and separation: SPB. 17 *(M = H = R = 2phM = PC(VL) = PT(VL) = PS(PVL))* and SPB. 18 *(M = H = R = 2phM = PC(VL) = PT(VL) = PS(VL))*.

The generated flowsheet alternatives are shown in Figs. 11–13. Fig. 11 shows flowsheet alternatives 1 and 2 where a pervapouration and vapour permeation membrane are used for the separation of the DMC/MeOH (azeotrope forming) mixture. Figs. 12 and 13 show flowsheet alternatives 3 and 4 where a membrane reactor and reactive distillation are used for in situ reaction and separation.

3.6. Screening of flowsheet alternatives

From the generation of feasible operation/flowsheet option, the four process alternatives are generated. From the four generated alternatives only one is screened out, the vapour-permeation membrane for downstream separation of DMC/MeOH azeotrope (process alternative 2) which have SPB. 21 M = 2phM = PC(VL) = PT(VL) = PS(VV) as a phenomena building blocks. This process alternative was screened out due to insufficient data.

In order to check feasibility of the proposed three intensified process alternatives for the production of DMC they are first simulated with Aspen Plus®. The steady state process simulation has been performed. The liquid activity calculation, the UNIQUAC model has been reported by Holtbruegge et al. (2013). For the reactor, the equilibrium model and RADFRAC model for reactive distillation column have been employed for obtain mass flow rate and energy consumption. For distillation columns, the RADFRAC model has been used. The details of the all process alternatives used are given in the corresponding simulation results.

The first process intensification concept for use as the process alternatives shown in Fig. 11, is pervapouration system taken from literatures using crosslinked poly(vinyl alcohol) (PVA) membranes and poly(acrylic acid)/poly(vinyl alcohol) blended membranes (Wang et al., 2007, 2009b). The results reveal that the use of crosslinked PVA membrane could achieve high concentration of MeOH of 98.6 wt% in the permeate side from the feed mixture containing 40–70 wt% MeOH at 50–70 °C. Therefore,

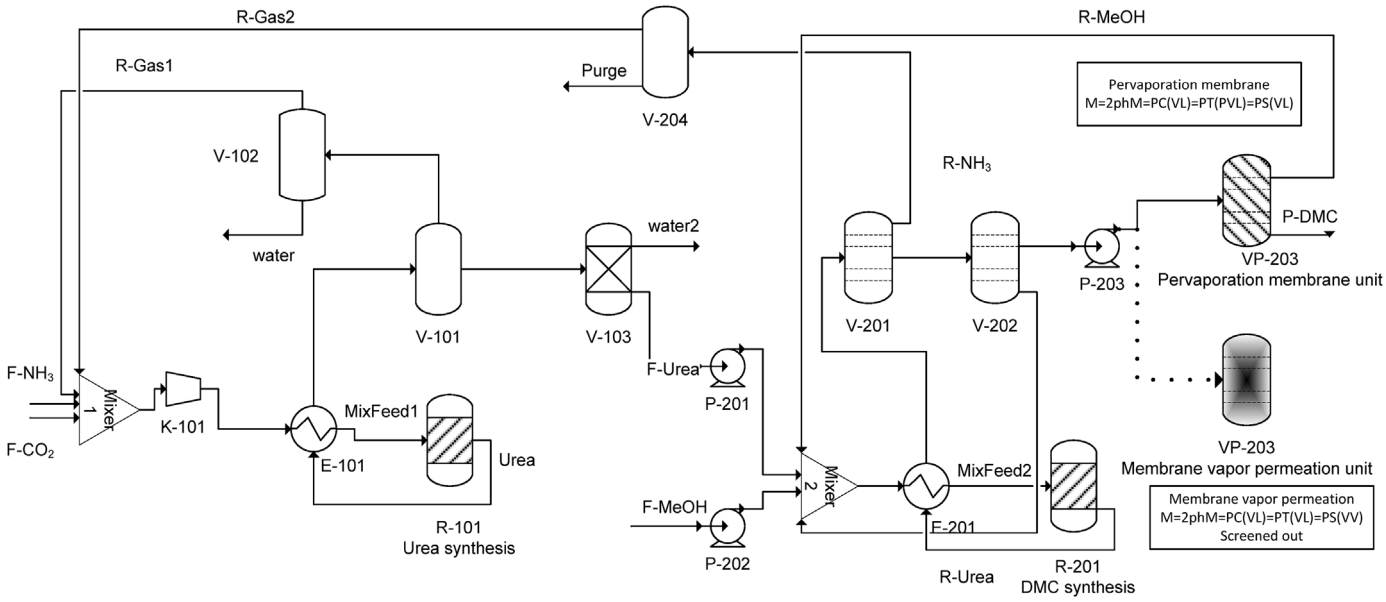

Fig. 11. DMC production process by urea route – process alternative 1 using pervapouration unit (VP-203) in downstream separation.

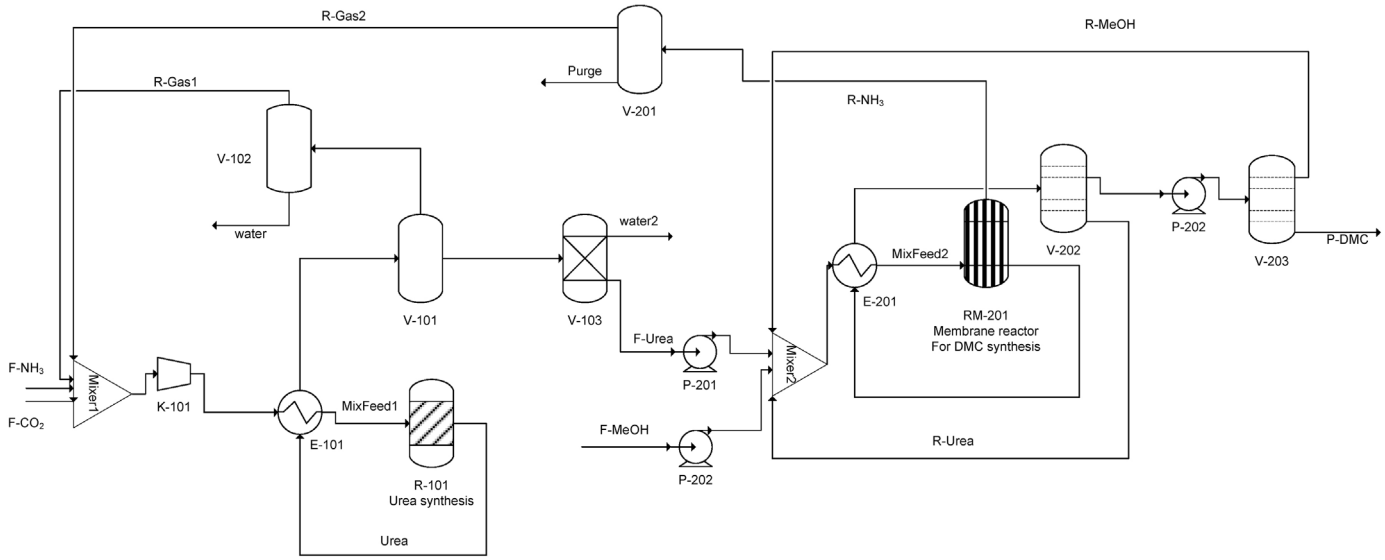

Fig. 12. DMC production process by urea route – process alternative 2 using membrane reactor (RM-201) for NH_3 removal.

the pervapouration (VP-203) (as shown in Fig. 4S) is set for the separation of DMC/MeOH azeotrope mixture instead of using the conventional pressurized distillation column (V-203) in the base case for reducing energy consumption which can refer to the less amount of methanol flowrate. The azeotropic mixture is moved from the distillate stream of V-202 to the pervapouration unit with a flowrate of 8434 kg/h. The pressure at the upstream side and the downstream side in the pervapouration unit was maintained at about 2 bar and 0.2 bar, respectively. According to the simulation, the flow of methanol on the permeate side is 2057 kg/h which is recycled to the separation section. The remaining of methanol is 29.21 kg/h in the product stream and DMC achieved as the product is 6072 kg/h (67.41 kmol/h) with 99.50 wt% purity of DMC.

The next alternative for process intensification shown in Fig. 12, focuses on DMC synthesis reactor (as shown in Fig. 5S). A combination of a reactor model and a separator model is used as a membrane reactor (RM-201) that can draw by-product (i.e., NH_3) out of the reactor to shift the reaction equilibrium (Wang et al., 2007) and thereby increasing the yield of DMC. The reaction occurs at 12 bar and 185 °C with a MeOH:urea feed molar ratio of 2.6:1 and a reflux ratio of 2. The simulation results show that this membrane reactor offers DMC yield of 80%. The product stream is sent to the separation and purification section to obtain a flowrate of 5924 kg/h (65.76 kmol/h) with 99.78 wt% purity of DMC.

The third alternative process shown in Fig. 13, focuses on integration of reaction and separation together (as represented in Fig. 6S) reduces the number of unit operations, while the yield of DMC and energy efficiency are increased has been given in Fig. 14. Reactive distillation is used in this alternative (Wang et al., 2012a). The feed streams contain 4565 kg/h of urea and 5126 kg/h of MeOH plus with the recycled MeOH from downstream separation at the molar ratio of urea:MeOH of 2:1. The reactive distillation (RD-201) has 40 stages, whereas the reaction zone is stage 17–36. Urea is fed at stage 16 and MeOH is fed at stage 26. The distillate stream, which contains NH_3, urea, MeOH and DMC is sent to the flash separator to separate and recycle NH_3 to the urea synthesis section, the

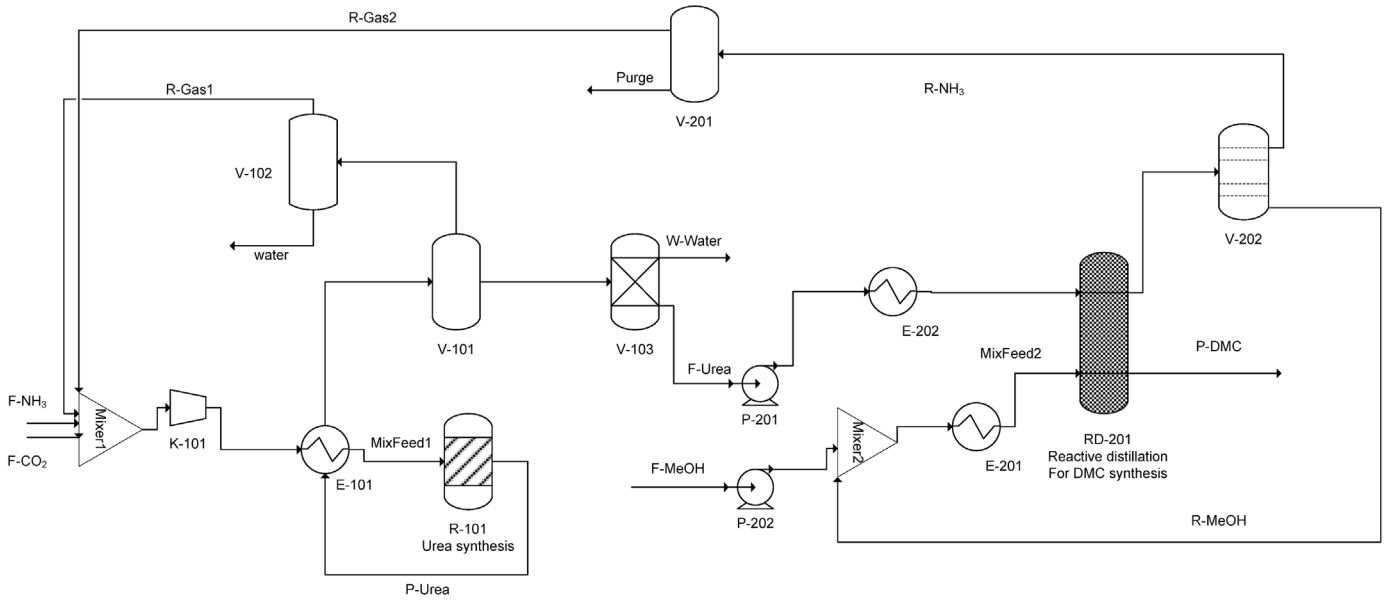

Fig. 13. DMC production process by urea route – process alternative 3 using reactive distillation (RD-201) for integrating reaction and separation system.

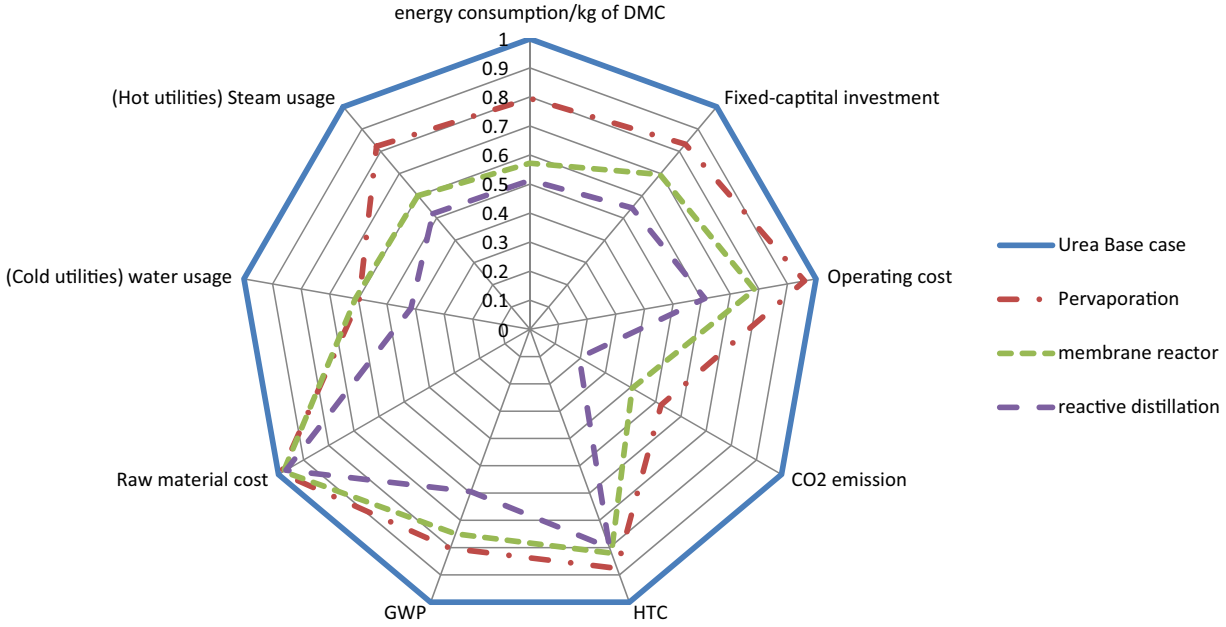

Fig. 14. Process performance evaluation of the process alternatives compared to the base case design.

unreacted urea, MeOH and some DMC product would be recycled and sent to the reaction section. For the DMC product which is the bottom stream of DMC synthesis reactor has the production rate of 6190 kg/h (69.10 kmol/h). This process resulted in very high yield of DMC (97.5%) and high purity of DMC in the product 99.88 wt%.

3.7. Evaluation of feasible flowsheet alternatives

Here, the performances of the generated alternatives are compared in terms of sustainability selected metrics, economic factors and life cycle assessment factors as summarized in Table 13. The product purity is 99% weight or higher for DMC. Energy consumption which are obtained from the process simulator are considered in term of energy usage per one unit of product as sustainability selected metrics, fixed capital investment cost and operating cost, HTC and GWP, CO_2 emission considered in term of CO_2 emission per one unit of product, are considered. The three process alternatives obviously offer superior performance in terms of all indicators to the base case process. The best process alternative is the reactive distillation option (Process 3). The energy consumption per one unit of DMC is significantly reduced (51.28%) as well as the fixed-capital cost (54.61%) and the operating cost (61.14%). The cold utilities (cooling water) and hot utilities (steam) usage were reduced to 41.63% and 52%, respectively. In addition, the CO_2 footprint, HTC and GWP were reduced to 19.59%, 80.00% and 59.49%, respectively.

More studies have been carried out to compare the DMC production by the urea route with the other process candidates, including: (1) the EC process and (2) the intensified EC process by using reactive distillation (Hsu et al., 2010) as the DMC synthesis reactor and (3) conventional BAYER process by partial carbonylation reaction of carbon monoxide (CO) process (Kricsfalussy et al., 1996), the process flowsheets are given in Supplementary data Figs. 7S, 8S and 9S,

Table 13
Comparison of the base case design of urea route with generated alternative process flowsheets, ethylene carbonate route, BAYER as conventional processing route and the alternatives with process intensification concept.

Sustainability metrics	Base case: urea route	Prc 1 (Pervap)	Prc 2 (MBR)	Prc 3 (RD)	Base case: EC route	Intensified EC route	BAYER process
Total energy consumption (GJ/yr)	624,318	531,692	491,166	407,444	488,099	444,133	294,393
Energy consumption in CO_2 utilization section (GJ/yr)	171,836	171,661	171,661	171,661	169,634	169,634	–
Energy consumption in DMC synthesis section (GJ/yr)	452,482	360,031	319,505	235,783	318,464	274,527	294,393
DMC production (MT/yr)	43,718	43,721	42,653	44,328	41,309	46,609	27,888
Energy consumption/kg of product DMC (MJ/kg)	10.35	8.23	7.49	5.31	7.70	5.89	10.55
EG production (MT/yr)	–	–	–	–	26,701	32,241	–
Energy consumption/kg of product EG (MJ/kg)	–	–	–	–	11.92	8.51	–
Economic indicators (analysis in CO2 utilization section and DMC production section)							
Production cost/kg of product (USD/kg)							
DMC	0.7563	0.7216	0.6823	0.6499	0.9307	0.7834	0.5908
EG	–	–	–	–	0.9352	0.8017	–
Total sale prices: calculated from products prices × production rate (USD/yr)	52,461,734.4	52,466,227.2	51,184,742.4	53,194,320.0	84,283,538.4	97,845,451.2	33,466,089.6
Total cost: calculated from fixed capital cost + operating cost (utilities) + raw material cost (USD/yr)	33,064,514.0	31,552,815.0	30,244,488.0	28,809,448.0	63,295,829.0	61,742,620.0	16,481,700.0
Net profit margin: calculated from total sale price – total cost (USD/yr)	19,397,220.4	20,913,412.2	20,940,254.4	24,384,872.0	20,987,709.4	36,102,831.2	16,984,389.6
Profit (USD/kg)							
Product DMC	0.4437	0.4784	0.5177	0.5501	0.2693	0.4166	0.6092
Product EG	–	–	–	–	0.3648	0.4983	–
Fixed-capital investment (USD/yr)	7,163,341	5,929,793	4,984,436	3,911,958	5,437,436	3,955,566	2,708,148
Operating cost (USD/yr)	632,053	606,592	496,314	386,444	517,023	445,684	298,061
Raw material cost (USD/yr)	25,269,120	25,016,430	24,763,738	24,511,046	57,341,370	57,341,370	13,475,491
Cooling water usage (GJ/yr)	194,954.4	116,424.0	118,958.4	81,172.8	132,602.4	121,910.4	98,496
Fuel usage (GJ/yr)	295,783.2	243,187.2	177,696.0	153,813.6	285,235.2	284,104.8	175,824
CO_2 usage in process as raw material (MT/yr)	24,732.0	24,732.0	24,732.0	24,732.0	24,411.6	24,411.6	–
Life cycle assessment indicator							
CO_2 emission from process (MT/yr)	80,769.87	53,942.57	46,933.38	35,867.34	41,484.72	41,936.82	14,557.74
CO_2 reduction by utilization (MT/yr)	24,732.0	24,732.0	24,732.0	24,732.0	24,411.6	24,411.6	–
Net CO_2 reduction; calculated from CO_2 emission from process – CO_2 reduction by utilization (MT/yr)	56,037.87	29,210.57	22,201.38	11,135.34	17,073.12	17,525.22	14,557.74
CO_2 emission kg/kg of product DMC	1.2818	0.6681	0.5205	0.2512	0.4133	0.3760	0.5220
HTC/kg of product DMC	0.000306	0.000268	0.000251	0.000245	0.000454	0.000362	0.000493
GWP/kg of product DMC	3.5528	2.8504	2.6626	2.1138	4.2048	2.4448	1.808

respectively. The results indicate that among the CO_2-based processes, the intensified-urea route for DMC production still shows the best performance in terms of sustainability, economic, life cycle assessment factors due to the lower raw material cost, less CO_2 emission per unit of product and avoidance of hazardous materials usage such as ethylene oxide from EC route and carbon monoxide from BAYER process. Moreover, the DMC production by the intensified option of urea route and the EC route indicate the competitive prices when compared to the BAYER process. Because for the urea route, the cost of production is quite small (0.6499 USD/kg) when compared to the BAYER process (0.5908 USD/kg) and for the EC route, EG is also produced as a valuable by-product but has the higher cost of raw materials (0.9307 USD/kg for EC route base case and 0.7834 USD/kg for intensified EC route). It should be noted that process alternatives cannot be guaranteed unless all the possible alternatives are generated at the phenomena level and then screened to find the optimal solution. In this work only the DMC production by urea route and urea process alternatives are represented in Fig. 14. The energy consumption was reduced 48.71%, fixed capital investment cost was reduced 45.38%, operating cost was reduced 38.85%, CO_2 emission was reduced 80.40%, human toxicity by carcinogenic was reduced 19.93%, global warming potential was reduced 40.50%, raw material cost was reduced 3%, cold utilities was reduced 58.36% and hot utilities was reduced 47.99%. In this work, although only the reaction for DMC synthesis and the adjacent separations have been targeted for intensification, it can be claimed that a more sustainable alternative has been achieved.

4. Conclusion

The decomposition based approach of process synthesis–design and process intensification has been implemented into a systematic framework, which has been applied to a CO_2-based utilization process. The application of all three stages: network synthesis, base

case design and the determination of innovative more sustainable process alternatives have been highlighted through the production of dimethyl carbonate process as a case study. A superstructure of processing routes has been generated and superstructure-based optimization performed to determine the most promising processing route together with user-added "known" processing routes. The selected processing routes have been further designed and analysed in terms of economics, sustainability and LCA factors to identify process hot-spots and design targets for improvement. Through a phenomena-based method, new and more sustainable process alternatives matching the design improvement targets have been identified. For the evaluation of alternatives, the measures used in this paper, include sustainability metrics, economic potential indicators as well as LCA factors. It has been found that the alternative options that have been generated through the phenomena based synthesis method, are better than the base case design. It should be noted, however, that for the case study (DMC production), other options also producing methanol from CO_2 have not been considered, but it is a topic of further research as continuation of this work. As developed, the framework is generic and can be applied to any chemical or biochemical processes and current work involves the application of it to determination of sustainable biorefinery solutions as well as sustainable wastewater treatment networks and a more comprehensive CO_2-utilization based processes covering more than one product. Also, the question of operability and control of the more sustainable intensified alternatives are being studied through the appropriate process models. The objective here is to show that the phenomena based synthesis together with driving force based design leads also to an optimally operable intensified process.

Acknowledgments

The financial support from The Thailand Research Fund is gratefully acknowledged. In addition, Pichayapan Kongpanna and Suttichai Assabumrungrat would like to acknowledge the Ph.D. scholarship from Dussadeepipat Scholarship, Chulalongkorn University and the stay as a visiting researcher at the SPEED project at DTU Chemical Engineering. Department of Chemical Engineering, Faculty of Engineering, Chulalongkorn University also would like to acknowledge the support from the Thailand Research Fund under the Institutional Research Grant IRG 5780014 and Chulalongkorn University Contract No. RES_57_411_21_076.

Appendix A. Supplementary data

Supplementary data associated with this article can be found, in the online version, at doi:10.1016/j.compchemeng.2016.01.006.

References

Babi DK, Holtbruegge J, Lutze P, Gorak A, Woodley JM, Gani R. Sustainable process synthesis–intensification. Comput Chem Eng 2015., http://dx.doi.org/10.1016/j.compchemeng.2015.04.030.

Babi DK, Lutze P, Woodley JM, Gani R. A process synthesis–intensification framework for the development of sustainable membrane-based operations. Chem Eng Process: Process Intensif 2014;86:173–95.

Bhanage BM, Fujita S, Ikushima Y, Arai M. Synthesis of dimethyl carbonate and glycols from carbon dioxide, epoxides, and methanol using heterogeneous basic metal oxide catalysts with high activity and selectivity. Appl Catal A: Gen 2001;219:259–66.

Bian J, Xiao M, Wang S, Wang X, Lu Y, Meng Y. Highly effective synthesis of dimethyl carbonate from methanol and carbon dioxide using a novel copper–nickel/graphite bimetallic nanocomposite catalyst. Chem Eng J 2009;147:287–96.

Bolstad PV, Davis KJ, Martin J, Cook BD, Wang W. Component and whole-system respiration fluxes in northern deciduous forests. Tree Physiol 2004;24:493–504.

Cai Q, Lu B, Guo L, Shan Y. Studies on synthesis of dimethyl carbonate from methanol and carbon dioxide. Catal Commun 2009;10:605–9.

Carvalho A, Gani R, Matos HA. Design of sustainable chemical processes: systematic retrofit analysis generation and evaluation of alternatives. Process Saf Environ Prot 2008;86:328–46.

Carvalho A, Matos HA, Gani R. SustainPro: a tool for systematic process analysis, generation and evaluation of sustainable design alternatives. Comput Chem Eng 2013;50:8–27.

Chang Y, Jiang T, Han B, Liu Z, Wu W, Gao L. One-pot synthesis of dimethyl carbonate and glycols from supercritical CO_2, ethylene oxide or propylene oxide, and methanol. Appl Catal A: Gen 2004;263:179–86.

Dai WL, Luo SL, Yin SF, Au CT. The direct transformation of carbon dioxide to organic carbonates over heterogeneous catalysts. Appl Catal A: Gen 2009;366:2–12.

Dindi A, Quang DV, Abu-Zahra MRM. Simultaneous carbon dioxide capture and utilization using thermal desalination reject brine. Appl Energy 2015;154:298–308.

Feng XJ, Li XG, He R, Zhou H. A new process for synthesis of dimethyl carbonate from ethylene carbonate and methanol without any catalyst under supercritical conditions. Chin Chem Lett 2005;16:767–70.

Gu XC, Qin ZF, Wang GF, Wang JG. Critical temperatures and pressures of reacting mixture in synthesis of dimethyl carbonate with methanol and carbon dioxide. Chin Chem Lett 2008;19:249–52.

Holtbruegge J, Heile S, Lutze P, Gorak A. Synthesis of dimethyl carbonate and propylene glycol in a pilot-scale reactive distillation column: experimental investigation, modeling and process analysis. Chem Eng J 2013;234:448–63.

IBM Corp. IBM ILOG CPLEX V 12.1. IBM Corp; 2009.

Intergovernmental Panel on Climate Change (IPCC), https://www.ipcc.ch/pdf/assessment-report/ar5/syr/AR5_SYR_FINAL_SPM.pdf; 2014 [accessed 22.12.15].

Jagtap SR, Bhor MD, Bhanage BM. Synthesis of dimethyl carbonate via transesterification of ethylene carbonate with methanol using poly-4-vinyl pyridine as a novel base catalyst. Catal Commun 2008;9:1928–31.

Jaksland CA, Gani R, Lien KM. Separation process design and synthesis based on thermodynamic insights. Chem Eng Sci 1995;50:511–30.

Hsu KY, Hsiao YC, Chien IL. Design and control of dimethyl carbonate-methanol separation via extractive distillation in the dimethyl carbonate reactive-distillation process. Ind Eng Chem Res 2010;49:735–49.

Kalakul S, Malakul P, Siemanond K, Gani R. Integrated of life cycle assessment software with tools for economic and sustainability analyses and process simulation for sustainable process design. J Clean Prod 2014;71:98–109.

Kongpanna P, Pavarajarn V, Gani R, Assabumrungrat S. Techno-economic evaluation of different CO_2-based processes for dimethyl carbonate production. Chem Eng Res Des 2015;93:496–510.

Kojima, Y., Fujii, H. Urea synthesis process and apparatus therefore, United States Patent, Patent Number: 5,936,122; 1999.

Kricsfalussy, Z., Steude, H., Waldmann, H., Hallenberger, K., Wagner, W., Traenckner, H.J. Process for preparing dimethyl carbonate, United States Patent, Patent Number: 5,523,452; 1996.

Li B, Zhang L, Song Y, Bai D, Jing H. Bronsted acid improved cycloaddition of carbon dioxide to propylene oxide. J Mol Catal A: Chem 2012;364:26–30.

Lin H, Yang B, Sun J, Wang X, Wang D. Kinetics studies for the synthesis of dimethyl carbonate from urea and methanol. Chem Eng J 2004;103:21–7.

Lu XB, He R, Bai CX. Synthesis of ethylene carbonate from supercritical carbon dioxide/ethylene oxide mixture in the presence of bifunctional catalyst. J Mol Catal A: Chem 2002;186:1–11.

Lutze P, Babi DK, Woodley JM, Gani R. A phenomena based methodology for process synthesis incorporating process intensification. Ind Eng Chem Res 2013;52:7127–44.

Luyssaert S, Inglima I, Jung M, Richardson AD, Reichstein M, Papale D, et al. CO_2 balance of boreal, temperate, and tropical forests derived from a global database. Global Change Biol 2007;13:2509–37.

The National Oceanic and Atmospheric Administration (NOAA), http://www.noaa.gov; 2015 [accessed 22.12.15].

Mansouri S, Ismail M, Babi D, Simasatitkul L, Huusom J, Gani R. Systematic sustainable process design and analysis of biodiesel processes. Processes 2013;1:167–202.

Matsuzaki T, Nakamura A. Dimethyl carbonate synthesis and other oxidative reactions using alkyl nitrites. Catal Surv Jpn 1997;1:77–88.

Ono, H., Fujii, H., Morikawa, H., Fukui, A. Method of stripping unreacted materials in urea synthesis process, United States Patent, Patent Number: 4,321,410; 1982.

Pacheco MA, Marshall CL. Review of dimethyl carbonate (DMC) manufacture and its characteristics as a fuel additive. Energy Fuels 1997;11:2–29.

Piyarak S. [Master of Science Thesis] Development of software for life cycle assessment [Master of Science Thesis]. Thailand: The Petroleum and Petrochemical College, Chulalongkorn University; 2012.

Quaglia A, Sarup B, Sin G, Gani R. Integrated business and engineering framework for synthesis and design of enterprise-wide processing networks. Comput Chem Eng 2012;38:213–23.

Quaglia A, Sarup B, Sin G, Gani R. A systematic framework for enterprise-wide optimization: synthesis and design of processing networks under uncertainty. Comput Chem Eng 2013;59:47–62.

Rezvani S, Moheimani NR, Bahri PA. Techno-economic assessment of CO_2 biofixation using microalgae in connection with three different state-of-the-art power plants. Comput Chem Eng 2016;84:290–301.

Saengwirun P. [Master of Science Thesis] ECON: a software for cost calculation and economic analysis [Master of Science Thesis]. Thailand: The Petroleum and Petrochemical College, Chulalongkorn University; 2011.

Sahebdelfar S, Ravanchi MK. Carbon dioxide utilization for methane production: a thermodynamic analysis. J Pet Sci Eng 2015;134:14–22.

Sheppard, R.O., Yakobsin, D.L. Integrated urea manufacturing plants and processes, United States Patent, Patent Number: 6,632,846 B2; 2003.
Siirola JJ, Powers GJ, Rudd DF. Synthesis of system designs: III. Toward a process concept generator. AIChE J 1971;17:677–82.
Siirola JJ. Strategic process synthesis: advances in the hierarchical approach. Comput Chem Eng 1996;20:1637–43.
Stewart C, Hessami M. A study of methods of carbon dioxide capture and sequestration: the sustainability of a photosynthetic bioreactor approach. Energy Convers Manag 2005;46:403–20.
Sun J, Yang B, Wang X, Wang D, Lin H. Synthesis of dimethyl carbonate from urea and methanol using polyphosphoric acid as catalyst. J Mol Catal A: Chem 2005;239:82–6.
Tundo P, Selva M. The chemistry of dimethyl carbonate. Acc Chem Res 2002;35:706–16.
Wang F, Zhao N, Xiao F, Wei W, Sun Y. The design and simulation of the synthesis of dimethyl carbonate and the product separation process plant. Distill Adv Model Appl 2012a, ISBN 978-953-51-0428-5.
Wang H, Lu B, Wang X, Zhang J, Cai Q. Highly selective synthesis of dimethyl carbonate from urea and methanol catalyzed by ionic liquids. Fuel Process Technol 2009a;90:1198–201.
Wang L, Li J, Lin Y, Chen C. Crosslinked poly(vinyl alcohol) membranes for separation of dimethyl carbonate/methanol mixtures by pervaporation. Chem Eng J 2009b;146:71–8.
Wang M, Wang H, Zhao N, Wei W, Sun Y. High-yield synthesis of dimethyl carbonate from urea and methanol using a catalytic distillation process. Ind Eng Chem Res 2007;46:2683–7.
Wang Z, Bu Z, Cao T, Ren T, Yang L, Li W. A novel and recyclable catalytic system for propylene carbonate synthesis from propylene oxide and CO_2. Polyhedron 2012b;32:86–9.
Williams DBG, Sibiya MS, Van Heerden PS, Kirk M, Harris R. Verkade super base-catalysed transesterification of propylene carbonate with methanol to co-produce dimethyl carbonate and propylene glycol. J Mol Catal A: Chem 2009;304(1–2):147–52, http://dx.doi.org/10.1016/j.molcata.2009.02.005.
World Meteorological Organization (WMO). Record Greenhouse Gas Levels Impact Atmosphere and Oceans, Press Release No. 1002; 2015, https://www.wmo.int [accessed 22.12.15].
Yang HQ, Xu ZH, Fan MH, Gupta R, Slimane RB, Bland AE. Progress in carbon dioxide separation and capture: a review. J Environ Sci 2008;20:14–27.
Yang ZZ, He LN, Dou XY, Chanfreau S. Dimethyl carbonate synthesis catalyzed by DABCO-derived basic ionic liquids via transesterification of ethylene carbonate with methanol. Tetrahedron Lett 2010;51:2931–4.
Yunusov SM, Kalyuzhnaya ES, Moroz BL, Ivanova AS, Reshetenko TV, Avdeeva LB, et al. New ammonia synthesis catalysts based on supported potassium carbonyl ruthenates as precursors of catalytically active ruthenium particles and potassium promoter. J Mol Catal A: Chem 2004;219:149–53.
Zhang C, Jun KW, Gao R, Lee YJ, Kang SC. Efficient utilization of carbon dioxide in gas-to-liquids process: process simulation and techno-economic analysis. Fuel 2015;157:285–91.
Zhang X, Zhang S, Yao P, Yuan Y. Modelling and simulation of high-pressure urea synthesis loop. Comput Chem Eng 2005;29:983–92.
Zhong SH, Wang JW, Xiao XF, Li HS. Dimethyl carbonate synthesis from carbon dioxide and methanol over Ni–Cu/MoSiO(VSiO) catalysts. Stud Surf Sci Catal 2000;130:1565–70.
Zondervan E, Nawaz M, Haan AB, Woodley JM, Gani R. Optimal design of a multiproduct biorefinery system. Comput Chem Eng 2011;35:1752–66.

Chemical Engineering Journal 293 (2016) 319–326

Contents lists available at ScienceDirect

Chemical Engineering Journal

journal homepage: www.elsevier.com/locate/cej

Effect of flow arrangement on micro membrane reforming for H_2 production from methane

T. Jiwanuruk [a], S. Putivisutisak [b], P. Ponpesh [c], P. Bumroongsakulsawat [a], T. Tagawa [d], H. Yamada [d], S. Assabumrungrat [a,e,*]

[a] Center of Excellence in Catalysis and Catalytic Reaction Engineering, Department of Chemical Engineering, Faculty of Engineering, Chulalongkorn University, Bangkok 10330, Thailand
[b] Department of Mechanical Engineering, Faculty of Engineering, Chulalongkorn University, Bangkok 10330, Thailand
[c] Department of Chemical Engineering, Faculty of Engineering, Chulalongkorn University, Bangkok 10330, Thailand
[d] Department of Chemical Engineering, Faculty of Engineering, Nagoya University, Chikusa-ku, Nagoya-shi, Aichi 464-8603, Japan
[e] PTT Group Frontier Research Center, PTT Public Company Limited, Bangkok 10900, Thailand

HIGHLIGHTS

- 3D CFD simulation for H_2 production in micro membrane reformer.
- Performance comparison between parallel and checked arrangements.
- H_2 accumulation inside reformer wall was pronounced for the parallel arrangement.
- The checked arrangement provided higher performance due to larger surface area.

GRAPHICAL ABSTRACT

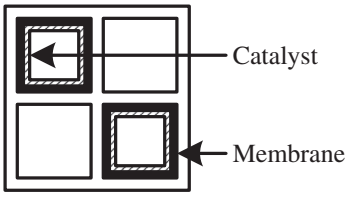

Checked arrangement

ARTICLE INFO

Article history:
Received 14 October 2015
Received in revised form 14 February 2016
Accepted 19 February 2016
Available online 27 February 2016

Keywords:
Micro-reactor
Flow pattern
Membrane reactor
CFD modeling

ABSTRACT

Three-dimensional computational fluid dynamics (CFD) simulation of methane reforming reaction in micro membrane reformer was performed to compare the effects of the parallel arrangement and the checked arrangement on reformer efficiency. At the predetermined base condition, methane conversions of 54.93% and 59.28% were obtained from the parallel arrangement and the checked arrangement, respectively. In terms of hydrogen separation factor, the checked arrangement provided 77.75% separation which was higher than the parallel arrangement by 4.92%. Furthermore, only half of the membrane area was effectively utilized in parallel arrangement, and hydrogen accumulation occurred. Similar results were obtained when operating and design parameters were changed. Methane conversion and hydrogen separation were significantly higher when the checked arrangement was used. The effects of the arrangement were increased with the increase of temperature, GHSV of SC and channel width, but the increase of GHSV of RC and reactor length weakened the effects. In this type of flow pattern, the entire membrane area was utilized and hydrogen flux is enhanced. Efficient separation of hydrogen in turn promoted methane conversion by equilibrium shift. Therefore, the checked arrangement significantly improved reactor performance and is recommended to be employed in micro membrane reactors.

© 2016 Published by Elsevier B.V.

1. Introduction

Hydrogen is one of the cleanest energy source which can be used to produce electricity by the proton exchange membrane (PEM) fuel cell. However, the performance of a PEM fuel cell is often limited by carbon monoxide (CO) poisoning on the hydrogen

* Corresponding author at: Center of Excellence in Catalysis and Catalytic Reaction Engineering, Department of Chemical Engineering, Faculty of Engineering, Chulalongkorn University, Bangkok 10330, Thailand. Tel.: +66 2 2186868; fax: +66 2 2186877.
E-mail address: suttichai.a@chula.ac.th (S. Assabumrungrat).

http://dx.doi.org/10.1016/j.cej.2016.02.075
1385-8947/© 2016 Published by Elsevier B.V.

Nomenclature

p	pressure (Pa)
T	temperature (K)
Q_i	source term of species i (mol s^{-1} m^{-2})
r_j	rate of reaction j (mol s^{-1} m^{-2})
A_i	pre-exponential factor
E_a	activation energy (kJ/mol)
$D_{i,eff}$	effective mass diffusion coefficient of species i in mixture (m^2 s^{-1})
$D_{i,mix}$	mass diffusivity of species i in mixture (m^2 s^{-1})
$D_{i,KA}$	Knudsen diffusion of species i (cm^2 s^{-1})
MW_i	molar mass of species i (kg $kmol^{-1}$)
F_i	mole flow of species i (mol s^{-1})
$\vec{v}$	velocity (m s^{-1})
d_p	pore diameter of solid phase (cm)

Greek symbols

ρ	density (kg m^{-3})
μ	dynamic viscosity (Pa s)
ω_i	mass fraction of species i
ε	porosity
τ	tortuosity

Abbreviations

GHSV	gas hourly space velocity (h^{-1})
RC	reforming channel
SC	sweep gas channel

side at the anode. In a conventional process, steam reforming reaction is employed to produce high hydrogen selectivity stream with lower CO. The CO in hydrogen stream is treated by water gas shift reactor. However, more than 3000 ppm of CO still persists [1–4]. CO in hydrogen stream should be limited at 10 ppm to prevent the poisoning of the platinum in the PEM fuel cell [2,3,5–9]. Therefore, a purification unit is required in the hydrogen production process. Metal membrane separation is used to purify hydrogen produced from steam reforming [7]. Membrane separation provides several advantages such as reduced energy consumption, lower operating costs and fewer number of clean-up units [10]. Palladium membrane is usually employed because of its high hydrogen permeability [10–12].

Micro channel reactors for hydrogen production are studied to reduce size and enhance the performance of the reactors. They provide several advantages such as low pressure drop, low heat and mass transfer resistance, and high surface to volume ratio [13–18]. Monolith with multi micro channel structure can be employed as a multi-system reactor for hydrogen production by integrating with evaporator, heat exchanger or membrane separation, etc. This combined reactor can reduce the weight, the size and the number of units, all of which are important factors in portable systems. When the reactor is integrated with membrane, reactor performance is improved by the shift in reaction equilibrium [5]. As mentioned earlier about the limitation of the PEM fuel cell, the reforming reactor with membrane has been studied in both the conventional scale and the micro scale [11,19–23]. Kim et al. fabricated a palladium membrane within cordierite honeycomb monoliths by electroless plating [21]. The highest H_2 flux was 5.5×10^{-3} mol m^{-2} s^{-1}, and the best H_2 per He selectivity was 360. This fabrication of palladium membrane in monoliths seems feasible and could be integrated with reformers to produce hydrogen. Simulation of a microchannel reformer integrated with H_2 selective membrane was also studied by Xuan et al. [22]. A Pd–Ag layer was coated with a Ni catalyst in an autothermal reformer. The reactants and the sweep gas were fed separately into the reformer. In this study, relevant physicochemical phenomena during the fuel processing were discussed, and optimized gaseous hourly space velocity (GHSV) was suggested. Karnik et al. [23] investigated a micro-membrane for the water gas shift reaction. A palladium membrane-supported copper catalyst was fabricated. The hydrogen flux of the 200 nm thick Pd film at 100 °C was 5.2 mol m^{-2} s^{-1}.

The reactants and the sweep gas are fed separately into the micro channel of the membrane reactor. The two streams can be arranged as parallel or checked as shown in Fig. 1. The parallel arrangement (Fig. 1a) is the conventional flow configuration because of the simple feed flow distributor which is easily constructed. On the other hand, the checked arrangement required a more complicated structure of the flow distributor. This arrangement however provides higher contact area between the two flows. In the previous study, the flow arrangement in a thermally coupled reactor was studied [24]. The checked arrangement eliminated the cold and hot spots which was significantly present in the parallel arrangement. Thus, the heat distribution was better in the checked arrangement. This study showed that the stream arrangement affected the performance of the combined micro reactor.

In this work, the two types of flow arrangement, parallel and checked, were studied using three dimensional computational fluid dynamics (CFD) model to compare their effects on the performance of the micro membrane reactor. The base case study was conducted to explain the phenomena of different arrangements in the micro membrane reactor. The effects of stream arrangement according to varied operating and design parameters were also studied. The operating parameters included the inlet temperature and the gas hourly space velocity (GHSV) of both channels. The design parameters were the channel width and the reformer length. The influence of the parameters and the flow arrangement which provided high reactor performance were suggested to be a suitable design of the micro membrane reactors.

2. Micro structure configuration

In this study, square channel monoliths were employed (Fig. 1). The channels were divided into a reforming channel (RC) and a sweep gas channel (SC). Reactions and separation occurred only in RC, thus only the inside of RC was coated with a catalyst and a membrane. The palladium film was deposited on the inner wall as a hydrogen selective membrane, and Ni-$MgAl_2O_4$ was applied over the membrane layer as the catalyst. The arrangement of both channels is shown in Fig. 1a and b in both the parallel arrangement and the checked arrangement, respectively. The dimensions of a monolith reactor used for the base case study are presented in Table 1.

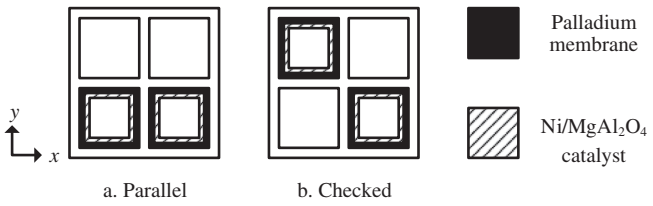

Fig. 1. Reactor configuration.

Table 1
Monolith reactor dimensions for base case study.

Parameter	Value (unit)
Channel width	1 (mm)
Reformer length	10 (mm)
Catalyst loading in RC	0.04 (kg m^{-2})
Wall thickness	0.3 (mm)
Gas hourly space velocity in RC	6,000 (h^{-1})
Gas hourly space velocity in SC	16,000 (h^{-1})
Outlet pressure	1 (atm)
Inlet temperature	773 (K)
Steam to carbon ratio in RC	1.5

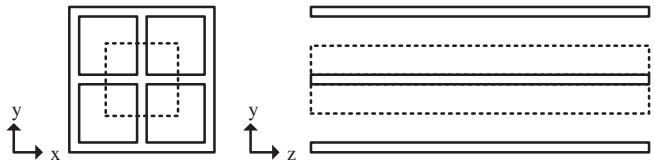

Fig. 2. Simulation configuration.

The center volume of the 2 × 2 unit channel was chosen as the study domain due to the symmetry condition as indicated by the dashed lines in Fig. 2. The thickness of the membrane adopted from Kim et al. [21] was extremely thin at 8 μm, so the thickness was neglected in the calculations. In the case of the catalyst, Irani et al. [25] suggested that simulation that excluded the thickness of the catalyst provided results which were close to the experimental data. Therefore, the catalyst and membrane thickness were neglected in the calculation with the configurations shown in Fig. 2 and the reaction was considered as a surface reaction.

3. Modeling description

3.1. Governing equations

Three dimensional CFD simulation of the system was conducted with the steady state governing equations, i.e., mass, momentum and chemical species conservation equations, which can be written as Eqs. (1)–(3), respectively. As an isothermal study, the temperature was assumed to be constant along the length of the reactor so the energy conservation equation was not included in this study.

$$\rho(\nabla \cdot \vec{v}) = 0 \tag{1}$$

$$\rho(\vec{v} \cdot \nabla \vec{v}) = -\nabla p + \nabla \cdot [\mu(\nabla \vec{v} + \nabla \vec{v}^T)] + \rho \vec{g} \tag{2}$$

$$\rho \nabla \cdot (\vec{v} \omega_i) = \rho \nabla \cdot (D_{i,eff} \nabla \omega_i) + Q_i \tag{3}$$

The gravity term in Eq. (2) was neglected. The last term in Eq. (3) which is a source term appeared specifically on the inner surface in RC. The source term of this equation was calculated from the hydrogen flux and the surface reaction rate. The hydrogen flux shown in Eq. (4) was adopted from Gallucci et al. [26].

$$H_2 flux = \frac{1.12e^{-5}(\mathrm{mol/m \cdot s \cdot Pa^{0.5}})}{\text{Membrane thickness}} \cdot e^{\frac{-29.16(\mathrm{kJ/mol})}{Rg \cdot T}} \cdot (P^{0.5}_{H_2,retentate} - P^{0.5}_{H_2,permeate}) \tag{4}$$

The mechanisms and kinetic models of methane steam reforming reaction (MS) were reported by Xu and Froment [27]. The mechanisms including methane steam reforming (R1), (R3) and water gas shift (R2) were used:

$$CH_4 + H_2O \leftrightarrow CO + 3H_2 \tag{R1}$$

$$CO + H_2O \leftrightarrow CO_2 + H_2 \tag{R2}$$

$$CH_4 + 2H_2O \leftrightarrow CO_2 + 4H_2 \tag{R3}$$

The kinetic models of MS reactions (R1)–(R3) are expressed as Eqs. (5)–(7):

$$r_1 = \frac{\frac{k_1}{p^{2.5}_{H_2}}\left(p_{CH_4}p_{H_2O} - \frac{p^3_{H_2}p_{CO}}{K_{eq1}}\right)}{\left(1 + K_{CO}p_{CO} + K_{H_2}p_{H_2} + K_{CH_4}p_{CH_4} + \frac{K_{H_2O}p_{H_2O}}{p_{H_2}}\right)^2} \tag{5}$$

$$r_2 = \frac{\frac{k_2}{p_{H_2}}\left(p_{CO}p_{H_2O} - \frac{p_{H_2}p_{CO_2}}{K_{eq2}}\right)}{\left(1 + K_{CO}p_{CO} + K_{H_2}p_{H_2} + K_{CH_4}p_{CH_4} + \frac{K_{H_2O}p_{H_2O}}{p_{H_2}}\right)^2} \tag{6}$$

$$r_3 = \frac{\frac{k_3}{p^{3.5}_{H_2}}\left(p_{CH_4}p^2_{H_2O} - \frac{p^4_{H_2}p_{CO_2}}{K_{eq3}}\right)}{\left(1 + K_{CO}p_{CO} + K_{H_2}p_{H_2} + K_{CH_4}p_{CH_4} + \frac{K_{H_2O}p_{H_2O}}{p_{H_2}}\right)^2} \tag{7}$$

where K_{eq} are the equilibrium constants of reactions (R1)–(R3) according to their numbers.

The reaction rate constants are expressed in Eqs. (8) and (9) and the kinetic parameters are reported in Table 2.

$$k_i = A_i \exp\left(\frac{-E_a}{RT}\right) \tag{8}$$

$$K_i = A_i \exp\left(\frac{-\Delta H}{RT}\right) \tag{9}$$

The gas mixture density is a function of gas composition, temperature and pressure at each point along the reformer according to the ideal gas law. Data of Perry's Chemical Engineers' Handbook [28] was employed to compute the gas viscosity. Diffusivity in the gas phase was calculated by Fuller correlation and the diffusivity of gas mixtures ($D_{i,mix}$) was computed using Stefan and Maxwell theory. In the solid phase, the effective diffusion was calculated by:

$$D_{i,eff} = \frac{\varepsilon}{\tau}\left(\frac{1}{D_{i,mix}} + \frac{1}{D_{i,KA}}\right)^{-1} \tag{10}$$

where ε and τ are the porosity and the tortuosity, respectively, of the solid phase. The porosity was fixed at 0.4, and the tortuosity was specified at 4.0. The Knudsen diffusion coefficient, $D_{i,KA}$, was computed by:

$$D_{i,KA} = 4850 d_p \sqrt{\frac{T}{MW_i}} \tag{11}$$

where d_p, the pore diameter of the solid phase, was fixed at 1×10^{-3} cm (10 μm) [29].

Methane conversions and hydrogen separation factors were used as the indicators of the reactor performance. The methane conversions were computed using Eq. (12), and the hydrogen separation factors were calculated by Eq. (13):

$$\text{Conversion}_{CH_4} = \left(\frac{F_{CH_4,inlet} - F_{CH_4,outlet}}{F_{CH_4,inlet}}\right) \times 100 \tag{12}$$

Table 2
Kinetic parameters of methane steam reforming reactions in Eqs. (5)–(7) [27].

Parameters	Pre-exponential factors (A)	E_a (kJ/mol)	ΔH (kJ/mol)
k_1	4.225×10^{15}	240.10	
k_2	1.955×10^{6}	67.13	
k_3	1.020×10^{15}	243.90	
K_{CO}	8.23×10^{-5}		−70.65
K_{H_2}	6.12×10^{-9}		−82.90
K_{CH_4}	6.65×10^{-4}		−38.28
K_{H_2O}	1.77×10^{5}		88.68

Table 3
Boundary conditions.

Boundary	Conditions
Inlet	Composition: $\omega_i = \omega_{i,0}$ Velocity: $\vec{v} = \vec{v}_0$
Outlet	Zero flux: $\frac{\partial \omega_i}{\partial z} = \frac{\partial \vec{v}}{\partial z} = 0$ Pressure: $P = P_{atm}$
Lateral	Symmetry: $\frac{\partial \omega_i}{\partial x} = \frac{\partial \vec{v}}{\partial x} = 0$ $\frac{\partial \omega_i}{\partial y} = \frac{\partial \vec{v}}{\partial y} = 0$
Inner surface wall of RC	No-slip wall condition: $\vec{v} = 0$ Source term: $Q_i = \sum_j (r_j MW)_i$ $Q_{H_2} = \sum_j (r_j MW)_{H_2} - H_2 flux$
Inner surface wall of SC	No-slip wall condition: $\vec{v} = 0$

$$\text{Hydrogen separation factor} = \left(\frac{F_{H_2,\text{SC outlet}}}{F_{H_2,\text{SC outlet}} + F_{H_2,\text{RC outlet}}}\right) \times 100 \quad (13)$$

3.2. Boundary conditions

As shown in Fig. 2, the symmetry condition was applied for all lateral boundaries inside the area within the dashed lines. The velocities and the mass fractions were specified at the inlet, while atmospheric pressure was specified at the outlet. The no-slip condition is assumed at the walls of the insides of both RC and SC. In RC, the surface reactions and the hydrogen flux was applied at the inner surfaces of the walls of the reformer, which were coated with the membrane and the catalyst. The boundary conditions were described in Table 3.

3.3. Simulation method

COMSOL Multiphysics® version 4.4 [30] was employed to solve numerical simulation by the finite element method. Tetrahedral mesh was fixed at 2.56×10^6 elements, which were specifically finer at the inner wall surfaces to accommodate the surface reactions and the hydrogen flux. The validation of the methane steam reforming simulation was reported in our previous study [24]. The computed conversions were acceptably close to the experimental data of Shu et al. [31]; thus the model accuracy was ensured.

4. Results and discussion

4.1. Base case study

In this section, the parallel arrangement and the checked arrangement were studied by using the base case parameters tabulated in Table 1. The methane conversions and hydrogen mole fractions obtained from this simulation are shown in Fig. 3. In Fig. 3a, the gray and black lines are the methane conversions for the parallel arrangement and the checked arrangement, respectively. The methane conversions of both arrangements increased along the reactor length. At the outlet, the methane conversions were 54.93% and 59.28% for the parallel arrangement and the checked arrangement, respectively. The methane conversion in the checked arrangement was about 4% higher than that of the parallel arrangement under this condition. The hydrogen mole fractions for both arrangements in SC and RC are shown in Fig. 3b. The hydrogen mole fractions of the checked arrangement was higher in SC but lower in RC when compared with those from the parallel arrangement. Therefore, hydrogen transfer was better in the checked arrangement. Moreover, the hydrogen separation factor of the checked arrangement was 77.75%. This was higher than that of the parallel arrangement (72.83%). It can be seen that the larger contact area of the checked arrangement resulted in the increase in hydrogen separation, which consequently enhanced methane conversion by equilibrium shift given in the step-wise mechanism (R1–R3).

In Fig. 4, the hydrogen mole fractions for both arrangements were reported as slice profiles in three dimensions. In the case of the parallel arrangement (Fig. 4a), the accumulation of hydrogen appeared inside the reformer walls between RC. On the other hand, hydrogen was transferred smoothly in the checked arrangement (Fig. 4b) and accumulation was not present. As shown in Fig. 5, hydrogen flux appeared only at the surface between RC and SC in the parallel arrangement (Fig. 5a). Thus, the effective area for hydrogen transferred to SC was only a half of the membrane area; hence hydrogen accumulation occurred. In the case of checked arrangement (Fig. 5b), the hydrogen flux was present in the entire contact area so the entire membrane area was used for separating hydrogen. Simulation results showed average hydrogen flux of 3.69 and 4.65 mmol m^{-2} s^{-1} along the reactor for the parallel arrangement and the checked arrangement, respectively. As a result, the hydrogen production rate and the hydrogen permeation rate in the checked arrangement were 6.49×10^{-4} and 5.05×10^{-4} mol h^{-1}. On the other hand, lower hydrogen production rate and the hydrogen permeation rate were reported at 5.76×10^{-4} and 4.20×10^{-4} mol h^{-1} in the parallel arrangement.

Based on these results, the checked arrangement in the base case study provided a higher methane conversion and hydrogen separation factor in a monolithic membrane reformer. All areas in contact with the membrane was effectively used for separating hydrogen, and the hydrogen accumulation in the reformer wall, which causes cracking by hydrogen embrittlement, was not present in the checked arrangement.

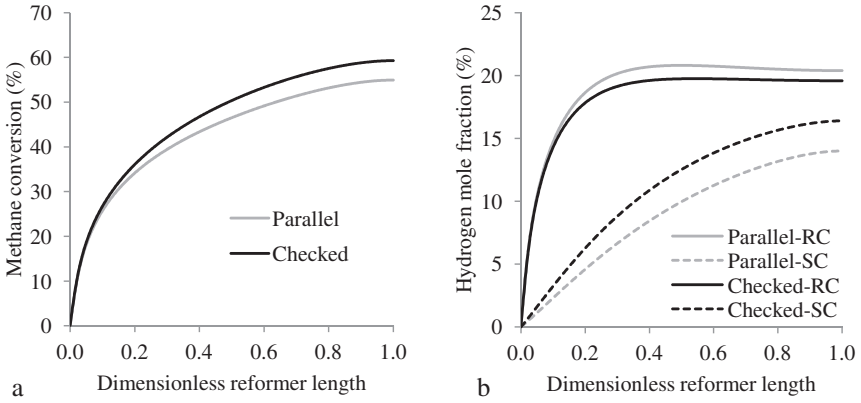

Fig. 3. Methane conversion (a) and hydrogen mole fraction (b) of parallel and checked arrangements (in percentage).

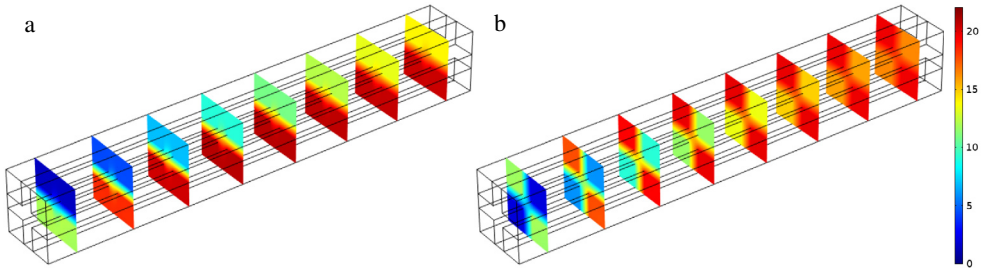

Fig. 4. Hydrogen mole fraction profile (in percentage) in base case study for the (a) parallel and (b) checked arrangements.

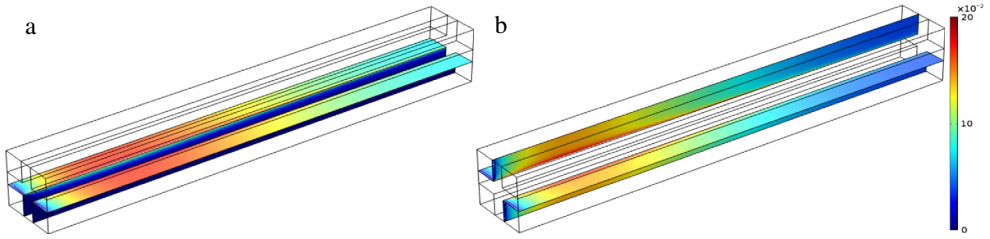

Fig. 5. Hydrogen flux (in mol m^{-2} s^{-1}) in base case study for the (a) parallel and (b) checked arrangements.

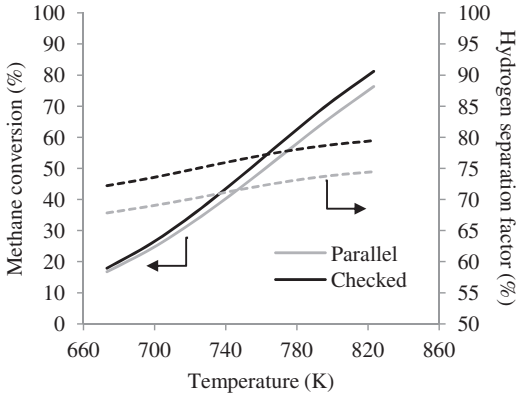

Fig. 6. Effect of temperature on methane conversion and hydrogen separation factor (in percentage).

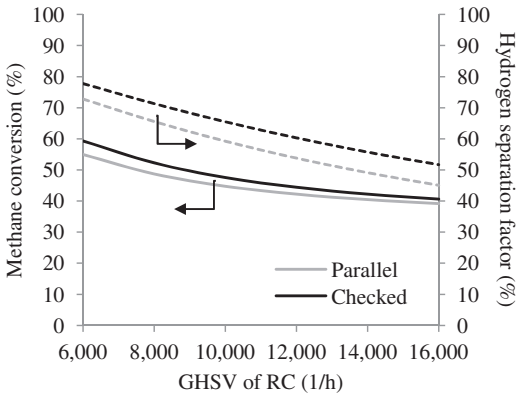

Fig. 7. Effect of GHSV in RC on methane conversion and hydrogen separation factor (in percentage).

4.2. Operating parameter study

In this section, the temperature and the GHSV of both channels were studied to find the influence of the parallel arrangement and the checked arrangement on the performance of the monolithic membrane reactor. As an isothermal study, temperature was set at a constant value between 673 and 823 K. GHSV in both channels were fixed within the same range of 6,000–16,000 h^{-1}.

4.2.1. Effects of reaction temperature

In Fig. 6, the effect of varying the temperature on the methane conversion and hydrogen separation factor at the predetermined range are presented as straight and dashed lines, respectively. Increasing the temperature increases the rate of reactions and hydrogen flux were promoted. Thus, the methane conversions and hydrogen separation factors were enhanced for both arrangements. The methane conversions from the checked arrangement were higher than those from the parallel arrangement at all temperatures and the differences were over 4% beyond 773 K. With increased hydrogen flux and reaction rates, hydrogen separation factors of both arrangements increased as the temperature increases. The checked arrangement provided higher hydrogen separation factors due to the larger separation area. The effects of the arrangement were more apparent at high temperature because the separation was significantly promoted.

4.2.2. Effects of reactant gas feed rate in RC

Increasing GHSV increased the gas flow rate and the gas velocity, all of which affected the performance of the reactor. Fig. 7 shows the effects of GHSV on the performance of the reactor. Increasing the flow rate of the reactants in RC led to decreases in the methane conversions and hydrogen separation factors in both arrangements. The reactant flow rate, which was raised by increasing GHSV, diluted hydrogen in RC. Thus, the driving force for the separation (Eq. (4)) was weakened and resulted in a lower hydrogen flux. The methane conversions and hydrogen separation factors were higher in the checked arrangement because of its better hydrogen transfer. Hydrogen separation of both arrangements was decreased significantly at high GHSV in RC. Therefore, the effect of the arrangement became less significant when GHSV in RC was increased.

4.2.3. Effects of reactant gas feed rate in SC

The effects of GHSV in SC on the performance of the reactor are shown in Fig. 8. The methane conversions and hydrogen separation

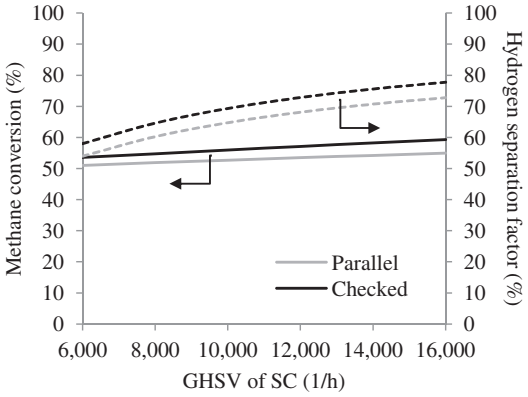

Fig. 8. Effect of GHSV in SC on methane conversion and hydrogen separation factor (in percentage).

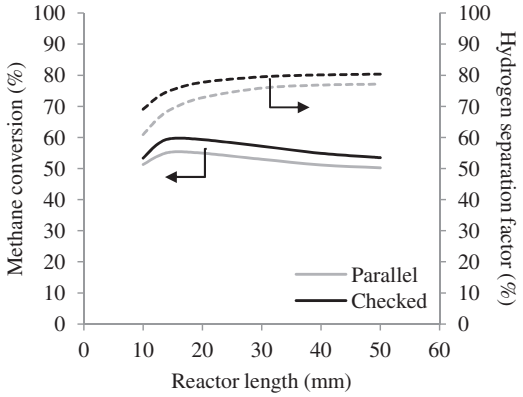

Fig. 9. Effects of reactor length on methane conversion and hydrogen separation factor (in percentage).

factors decreased with decreased GHSV in SC. A lower sweep gas flow rate led to an increased hydrogen concentration in SC. The hydrogen flux dropped with a decrease in the driving force (Eq. (4)). Thus, the reactor performance of both arrangements was lower. The checked arrangement with a higher exchange ability provided higher methane conversions and hydrogen separation factors. The effects of the checked arrangement and the parallel arrangement were weakened by a lower hydrogen flux when GHSV in SC was decreased.

In Section 4.2, the effects of the operating parameters, i.e., temperature and GHSV, were also compared. The checked arrangement provided higher methane conversions and hydrogen separation factors in a monolithic membrane reactor at various operating parameters. The hydrogen separation was obtained 4% larger from the checked arrangement within the studied operating parameters. Thus, the larger contact area in the checked arrangement is important since it significantly improves the performance of the membrane reactor. Moreover, the effects of the arrangement were enhanced with an increase in the temperature and GHSV of SC or a decrease in GHSV of RC.

4.3. Design parameter study

The design parameters including the reactor length and the channel width for both arrangements were investigated. Reactor lengths between 10 to 50 mm and channel widths between 0.5 and 1.25 mm were used in this study.

4.3.1. Effects of reactor length

In determining the effect of the reactor length, all other parameters were fixed as in the base case study. Increasing the length resulted in an increase in the flow rate of the reactants and the sweep gas in both channels. The methane conversions and hydrogen separation factors at different reactor lengths are shown in Fig. 9. Increasing the reactor length led to enhanced hydrogen separation factors by increasing the surface area of the membrane. Furthermore, the hydrogen separation factors rose sharply with the increased reactor length up to 15 mm. A further increase in the reactor length resulted in only a slight increase in the hydrogen separation factors. This phenomenon was attributed to the changes in the hydrogen concentrations of both channels, which was the driving force for the separation. The hydrogen concentrations were largely constant at reactor lengths of 15 mm and beyond. Therefore, increases in the hydrogen separation factors and methane conversions only occurred in a relatively short length. However, increasing the velocity in both channels resulted in decreases in the methane conversions after a length of 15 mm.

The checked arrangement provided higher reactor performance in terms of methane conversions and hydrogen separation factors as shown in Fig. 9. The increased contact areas between RC and SC promoted the reactor performance. The effects of arrangement reported in terms of the differences in hydrogen separation factor between both arrangements are shown in Fig. 10. The hydrogen separation factor differences decreased sharply at shorter lengths, i.e. 10–30 mm, and were almost constant at around 3% beyond 30 mm. At a longer length, the hydrogen separation factor increased slightly and reached a constant value in both arrangements. Thus, the effects of arrangement was suppressed as the reactor length was increased.

4.3.2. Effects of channel width

The effects of channel widths on the reactor performance of both arrangements are reported in Fig. 11. The methane conversions and hydrogen separation factors were both decreased with the increasing channel width for both arrangements. Increasing the channel width led to an increase in the reactant flow rate at a fixed GHSV and increased the mass transfer resistance inside both channels. When the methane conversions dropped, the hydrogen concentrations were also decreased and diluted by the reactants. Consequently, the hydrogen separation factors were reduced by dilution. The parallel and checked arrangements provided nearly identical methane conversions and hydrogen

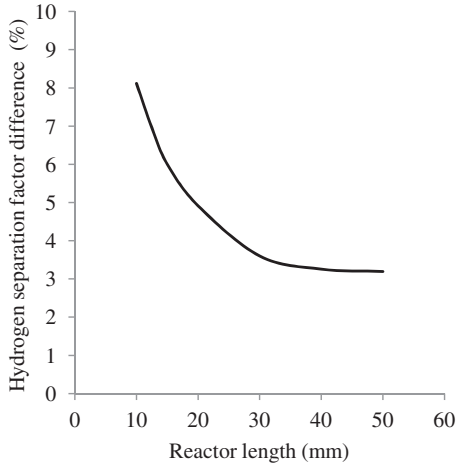

Fig. 10. Differences in hydrogen separation factor between the parallel and checked arrangements.

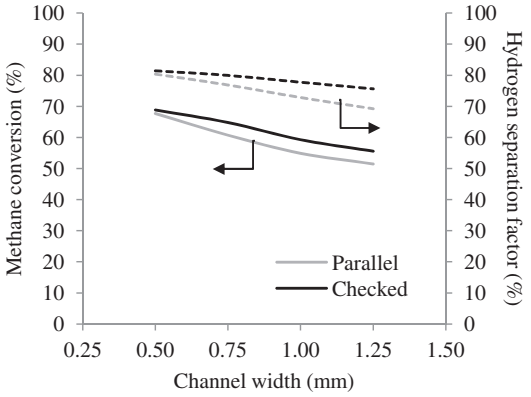

Fig. 11. Effects of channel width on methane conversion and hydrogen separation factor (in percentage).

separation factors at a small channel width (0.5 mm), but the checked arrangement offered slightly higher reactor performance. As the channel width was further increased, the methane conversions and hydrogen separation factors became significantly higher in the checked arrangement because of the larger surface area. The arrangement effects were strong when the channel width was larger than 0.5 mm. As the channel width was increased, the hydrogen separation factor dropped sharply in the parallel arrangement. Thus, the checked arrangement increased hydrogen separation and suppressed the effects from increasing the channel width.

The performance of the reactor was affected by the length and width of the channels. The hydrogen separation was promoted at short channel lengths and reached a nearly constant value after 15 mm. On the other hand, increasing the channel width resulted in a sharp decrease in the reactor performance. The checked arrangement provided higher methane conversions and hydrogen separation factors in this micro membrane reactor. In conclusion, increased contact areas of the checked arrangement significantly promoted hydrogen transfer, which was affected by the reactor length and the channel width.

5. Conclusion

The flow arrangements: parallel and checked were studied with three dimensional computational fluid dynamics (CFD) models in order to compare their effects on the performance of the micro membrane reactor. Both arrangements used a base case condition for computation. The results clearly showed that checked arrangement provided higher methane conversions and hydrogen separation. Moreover, hydrogen accumulation in the checked arrangement was significantly lower, and the total membrane area in this arrangement was fully utilized, resulting in higher hydrogen flux. The effects of the operating and design parameters for both arrangements on the reactor performance were also investigated. The operating parameters were the temperature and GHSV and the design parameters were the reactor length and the channel width. Varying design parameters increases the methane conversions and the hydrogen separation in the checked arrangement. Therefore, the checked arrangement provided higher reactor performance of the micro membrane reactors. The effects of the arrangement became more significant with the increased temperature, GHSV of SC and channel width, while increasing GHSV of RC and reactor length suppressed the effects. The influence of parameters can be utilized as a guidance to optimize the condition when using the checked arrangement in the micro membrane reactors.

Acknowledgments

The authors acknowledge the supports from the Royal Golden PhD Program from the Thailand Research Fund and Chulalongkorn University, the Thailand Research Fund and PTT Group Research Scholar from PTT Group Frontier Research Center. The JSPS Kaken-hi #015H04178 (Japan) is gratefully acknowledged.

References

[1] O. Korotkikh, R. Farrauto, Selective catalytic oxidation of CO in H_2: fuel cell applications, Catal. Today 62 (2000) 249–254.
[2] D. Montané, E. Bolshak, S. Abelló, Thermodynamic analysis of fuel processors based on catalytic-wall reactors and membrane systems for ethanol steam reforming, Chem. Eng. J. 175 (2011) 519–533.
[3] N. Katiyar, S. Kumar, S. Kumar, Polymer electrolyte membrane fuel cell grade hydrogen production by methanol steam reforming: a comparative multiple reactor modeling study, J. Power Sources 243 (2013) 381–391.
[4] K. Babita, S. Sridhar, K.V. Raghavan, Membrane reactors for fuel cell quality hydrogen through WGSR – review of their status, challenges and opportunities, Int. J. Hydrogen Energy 36 (2011) 6671–6688.
[5] B.N. Lukyanov, D.V. Andreev, V.N. Parmon, Catalytic reactors with hydrogen membrane separation, Chem. Eng. J. 154 (2009) 258–266.
[6] D. Hotza, J.C. Diniz da Costa, Fuel cells development and hydrogen production from renewable resources in Brazil, Int. J. Hydrogen Energy 33 (2008) 4915–4935.
[7] A. Qi, B. Peppley, K. Karan, Integrated fuel processors for fuel cell application: a review, Fuel Process. Technol. 88 (2007) 3–22.
[8] A. Ersoz, H. Olgun, S. Ozdogan, Reforming options for hydrogen production from fossil fuels for PEM fuel cells, J. Power Sources 154 (2006) 67–73.
[9] J.M. Ogden, Review of small stationary reformers for hydrogen production, report to the international energy agency, 2001.
[10] S. Yun, S. Ted Oyama, Correlations in palladium membranes for hydrogen separation: a review, J. Membr. Sci. 375 (2011) 28–45.
[11] F. Gallucci, A. Comite, G. Capannelli, A. Basile, Steam reforming of methane in a membrane reactor: an industrial case study, Ind. Eng. Chem. Res. 45 (2006) 2994–3000.
[12] A. Knapton, Palladium alloys for hydrogen diffusion membranes, Platinum Met. Rev. 21 (1977) 44–50.
[13] O. Sanz, F. Echave, F. Romero-Sarria, Advances in structured and microstructured catalytic reactors for hydrogen production, Renewable Hydrogen Technol. Prod. Purif. Storage Appl. Saf. (2013) 201.
[14] J.D. Holladay, Y. Wang, E. Jones, Review of developments in portable hydrogen production using microreactor technology, Chem. Rev. 104 (2004) 4767–4790.
[15] G. Kolb, Review: microstructured reactors for distributed and renewable production of fuels and electrical energy, Chem. Eng. Process. 65 (2013) 1–44.
[16] Y.L.A. Leung, K.L. Yeung, Microfabricated ZSM-5 zeolite micromembranes, Chem. Eng. Sci. 59 (2004) 4809–4817.
[17] J. Bravo, A. Karim, T. Conant, G.P. Lopez, A. Datye, Wall coating of a CuO/ZnO/Al_2O_3 methanol steam reforming catalyst for micro-channel reformers, Chem. Eng. J. 101 (2004) 113–121.
[18] T. Zhang, X. Zhang, X. Yan, L. Kong, G. Zhang, H. Liu, J. Qiu, K.L. Yeung, Synthesis of Fe_3O_4@ZIF-8 magnetic core–shell microspheres and their potential application in a capillary microreactor, Chem. Eng. J. 228 (2013) 398–404.
[19] F. Gallucci, Ethanol steam reforming in a dense Pd–Ag membrane reactor: a modelling work. Comparison with the traditional system, Int. J. Hydrogen Energy 33 (2008) 644–651.
[20] J. Tong, Y. Matsumura, H. Suda, K. Haraya, Experimental study of steam reforming of methane in a thin (6 μm) Pd-based membrane reactor, Ind. Eng. Chem. Res. 44 (2005) 1454–1465.
[21] D. Kim, A. Kellogg, E. Livaich, B.A. Wilhite, Towards an integrated ceramic micro-membrane network: electroless-plated palladium membranes in cordierite supports, J. Membr. Sci. 340 (2009) 109–116.
[22] J. Xuan, D.Y.C. Leung, M.K.H. Leung, M. Ni, H. Wang, Chemical and transport behaviors in a microfluidic reformer with catalytic-support membrane for efficient hydrogen production and purification, Int. J. Hydrogen Energy 37 (2012) 2614–2622.
[23] S.V. Karnik, M.K. Hatalis, M.V. Kothare, Towards a palladium micro-membrane for the water gas shift reaction: microfabrication approach and hydrogen purification results, J. Microelectromech. Syst. 12 (2003) 93–100.
[24] T. Jiwanuruk, S. Putivisutisak, P. Ponpesh, C. Kositanont, T. Tagawa, H. Yamada, C. Fukuhara, S. Assabumrungrat, Comparison between parallel and checked arrangements of micro reformer for H_2 production from methane, Chem. Eng. J. (2015).
[25] M. Irani, A. Alizadehdakhel, A.N. Pour, N. Hoseini, M. Adinehnia, CFD modeling of hydrogen production using steam reforming of methane in monolith reactors: surface or volume-base reaction model?, Int J. Hydrogen Energy 36 (2011) 15602–15610.
[26] F. Gallucci, L. Paturzo, A. Basile, Hydrogen recovery from methanol steam reforming in a dense membrane reactor: simulation study, Ind. Eng. Chem. Res. 43 (2004) 2420–2432.
[27] J. Xu, G.F. Froment, Methane steam reforming, methanation and water–gas shift: I. Intrinsic kinetics, AlChE J. 35 (1989) 88–96.

[28] D.W. Green, R.H. Perry, Perry's Chemical Engineers' Handbook, eighth ed., McGraw-Hill, 2008.
[29] J.R. Welty, C.E. Wicks, R.E. Wilson, G.L. Rorrer, Fundamentals of Momentum, Heat, and Mass Transfer, fifth ed., Wiley, 2007.
[30] COMSOL multiphysics®, COMSOL Inc., 2013.
[31] J. Shu, B.P. Grandjean, S. Kaliaguine, Methane steam reforming in asymmetric Pd- and Pd–Ag/porous SS membrane reactors, Appl. Catal. A 119 (1994) 305–325.

Process Biochemistry 51 (2016) 204–212

Contents lists available at ScienceDirect

Process Biochemistry

journal homepage: www.elsevier.com/locate/procbio

Correlative effect of dissolved oxygen and key enzyme inhibitors responsible for L-lactate production by immobilized *Rhizopus oryzae* NRRL395 cultivated in a static bed bioreactor

Sitanan Thitiprasert[a], Varunee Pimtong[b], Kentaro Kodama[a], Sarintip Sooksai[a], Somboon Tanasupawat[c], Suttichai Assabumrungrat[d], Vasana Tolieng[a], Nuttha Thongchul[a,*]

[a] *Institute of Biotechnology and Genetic Engineering, Chulalongkorn University, Bangkok, Thailand*
[b] *Program in Biotechnology, Faculty of Science, Chulalongkorn University, Bangkok, Thailand*
[c] *Department of Biochemistry and Microbiology, Faculty of Pharmaceutical Sciences, Chulalongkorn University, Bangkok, Thailand*
[d] *Department of Chemical Engineering, Faculty of Engineering, Chulalongkorn University, Bangkok, Thailand*

ARTICLE INFO

Article history:
Received 30 August 2015
Received in revised form 4 November 2015
Accepted 23 November 2015
Available online 9 December 2015

Keywords:
Rhizopus oryzae
L-Lactic acid
Ethanol
Enzyme inhibitor
Dissolved oxygen
Alcohol dehydrogenase
Pyruvate decarboxylate
Static bed bioreactor

ABSTRACT

In typical fermentation by *Rhizopus oryzae*, ethanol was found as the major byproduct. The simplest way to limit ethanol was to supply high dissolved oxygen (DO) during fermentation. Our previous work showed metabolic fluxes shifted toward lactate production with lower ethanol formation in the fermentation containing enzyme inhibitors including 1,2-diazole, 2,2,2-trifluoroethanol, 4-methylpyrazole, and 3-hydroxypyruvate. In this study, we further investigated the dynamic responses of the living *R. oryzae* cultivated in the static bed bioreactor to the effects of enzyme inhibitors and DO levels together. Either increasing DO level or adding inhibitor alone limited ethanol and promoted lactate production while cell biomass remained unchanged. Lactate yield was increased by 24% with the increasing DO from 40% to 80% during the fermentation. Among 4 inhibitors studied, 2,2,2-trifluoroethanol gave the maximum improvement in fermentation efficiency. Approximately, 32% increasing lactate yield was obtained in the fermentation at 40% DO with 0.1 mM 2,2,2-trifluoroethanol. Together, inhibitor and high DO level better controlled metabolic flux toward lactate production. Dramatic increasing lactate yield of 54% was obtained in the fermentation containing 2,2,2-trifluoroethanol at 80% DO control with 100% improved productivity. Findings from this work exhibited the simple yet effective way to improve lactate fermentation by *R. oryzae*.

© 2015 Elsevier Ltd. All rights reserved.

1. Introduction

Lactic acid has long been widely used in food, pharmaceutical, cosmetic, and chemical industries. Lactic acid production is currently attracting a great deal of research and development. Nowadays, lactic acid consumption is increased as the consequence of an emerging market of polylactic acid, a renewable, compostable, and biocompatible polymer, which provides an environmental friendly alternative to biodegradable plastics derived from petrochemicals [1–3]. Naturally, lactic acid can be found in 2 optical isomers, i.e., D(−) and L(+)-lactic acids. However, the existing commercial applications in food and health cares are mostly limited to L-lactic acid due to the toxicity of D-lactate to living cells [4].

The optically pure L-lactate can be obtained via microbial fermentation process. *Rhizopus oryzae* only possesses L-lactate dehydrogenase and lacks racemase; thus, being considered as one promising strain for L-lactate fermentation with low nutrient requirements [5–14]. Nonetheless, lactate fermentation by *R. oryzae* yields lower production comparable to typical bacterial fermentation process. While the theoretical lactate yield from glucose by bacterial fermentation was about 0.85 g/g, lactate yield from glucose fermentation by *R. oryzae* was only 0.6–0.8 g/g [15]. Recently, L-lactate fermentation by *R. oryzae* was extensively studied for improved yield and productivity. Submerged fermentation in several bioreactor designs was conducted. Stirred fermentor, a typical bioreactor widely used in submerged microbial fermentation, provided high oxygen supply so that limiting ethanol byproduct;

* Corresponding author. Fax: +66 2 2533543.
E-mail address: Nuttha.T@chula.ac.th (N. Thongchul).

http://dx.doi.org/10.1016/j.procbio.2015.11.034
1359-5113/© 2015 Elsevier Ltd. All rights reserved.

however, generating high shear stress that caused damage to fungi and reduced lactate production [16,17]. In addition, morphological changes were commonly observed during fungal fermentation. This led to changes of nutrient supply including oxygen along the cultivation and subsequently difficulty in operational control to achieve stable run and high production rate [16,18–20].

Cell immobilization was introduced in lactate fermentation by *R. oryzae*. Via immobilization using several techniques, lactate production was successfully improved as the results of better mass transport especially oxygen and high cell density fermentation [7–10,12,16]. Not only improving lactate production, immobilization could also provide ease of operation and possibility of long-term operation [21–24]. A static bed bioreactor is one of the immobilized cell bioreactors developed for lactate fermentation by *R. oryzae*. Remarkably improved lactate yield approaching the theoretical value was obtained in this bioreactor; nonetheless, trace amount of ethanol still existed in this immobilized culture system [24].

The results obtained from our previous study in a shaken flask culture of *R. oryzae* proved that ethanol production could be controlled by adding the inhibitors that regulated the alcohol fermentative pathway [25–27]. This subsequently gave the increasing lactate yield and productivity. It was observed that introducing substrate/cofactor analogs of alcohol dehydrogenase (ADH) such as 1,2-diazole and 2,2,2-trifluoroethanol as well as those analogs of pyruvate decarboxylase (PDC) including 4-methylpyrazole and 3-hydroxypyruvate into the production medium during cultivation of *R. oryzae* led to changes of metabolic fluxes and eventually showed the positive impact on lactate production [25–27].

In this study, further improved lactate yield and productivity by using both enzyme inhibitors and high DO level in lactate fermentation was attempted. The static bed bioreactor was applied for cell immobilization to enhance oxygen transfer under varied DO levels while ADH and PDC inhibitors were added during the production phase in order to inhibit ethanol formation. By these combinatorial effects, glucose flux would be driven toward lactate resulting in the increase in yield and productivity. The fermentation kinetics and the specific activities of key enzymes responsible for lactate and ethanol production were described. The fermentation efficiency was investigated.

2. Materials and methods

ADH and PDC inhibitors were tested for their effects on metabolic responses of immobilized *R. oryzae* cultivated in the static bed bioreactor under different dissolved oxygen (DO) levels. Changes of end product yield and productivity were investigated. The dynamic responses of the living culture to both changes in DO level and inhibitor were described and compared.

2.1. Microorganism, inoculum preparation, and medium compositions

R. oryzae NRRL395 was obtained from Agricultural Research Service Culture Collection, US Department of Agriculture, Peoria, IL, USA. Spore suspension was prepared from the 7-day sporagiospores harvested from potato dextrose agar plate suspended in sterile DI water. The spore concentration was adjusted to 10^6 spores/mL before inoculation.

Lactic acid fermentation by *R. oryzae* consisted of 2 phases. Growth medium was used for spore germination and initial growth during the growth phase. Growth medium contained (per liter) 50 g glucose and 5 g yeast extract. After growth was successively initiated, the production medium was used during lactate production phase. The production medium consisted of (per liter) 70 g glucose, 0.6 g KH_2PO_4, 0.25 g $MgSO_4{\cdot}7H_2O$, 0.088 g $ZnSO_4{\cdot}7H_2O$, and 0.3 g urea [21,24].

2.2. Bioreactor construction

As shown in Fig. 1, a static bed bioreactor was modified from a 5-L stirred fermentor by mounting a perforated stainless steel covered by a cotton towel at the top plate of the bioreactor [24]. The bioreactor was equipped with the automatic control of temperature, pH, agitation, and aeration. The air fed into the bioreactor was sterilized by passing through a membrane filter (0.2 μm).

2.3. Bioreactor start up and fermentation operation

The fermentor containing 3 L growth medium was autoclaved at 121 °C, 15 psig for 30 min. After the fermentor was cool down, the temperature was set at 30 °C and DO probe was calibrated with nitrogen and air. The fermentor was then inoculated with 10 mL spore suspension (10^6 spores/mL). The agitation and aeration rates were set at 700 rpm and 1.0 vvm air, respectively. Spores were allowed to germinate and immobilize onto the cotton cloth for 48 h. The growth medium was withdrawn at the end of the growth phase. The fermentor was filled up with 3 L sterile production medium. The bioreactor was controlled at the same temperature (30 °C) and aeration rate (1.0 vvm). The pH was controlled at 6.0 by 5 M NaOH. To control the DO levels at 40%, 60%, and 80%, cascade control was applied by varying the agitation speed between 100 rpm and 300 rpm and volumetric flow ratio of oxygen to air. During the production phase, enzyme inhibitors regulating alcohol fermentative pathway including 1 mM 1,2-diazole, 1 mM 2,2,2-trifluoroethanol, 0.1 mM 4-methylpyrazole, and 1 μM 3-hydroxypyruvate were added into the medium. It should be noted that the concentrations of the selected inhibitors were previously optimized elsewhere [25,26]. Both DO level and enzyme inhibitor were observed for their effects on fungal metabolism. Growth reported as cell dry weight, glucose consumption, end product formation as well as enzyme activity were investigated. During the production phase, sample was collected every 6 h for analyzing remaining glucose and end products. After 72 h, cell biomass was harvested from the fibrous bed for cell biomass determination and enzyme assays.

2.4. Analysis of remaining glucose and end products

High performance liquid chromatography was used to analyze the fermentation broth sample for the remaining glucose, lactate, and ethanol. Before analyzing, the broth sample was filtered through cellulose acetate membrane and diluted with double distilled water. Diluted particle-free sample (15 μL) was injected into an organic acid analysis column (Biorad, Aminex HPX-87H ion exclusion organic acid column; 300 mm × 7.8 mm) maintained at 45 °C in a column oven. 0.005 M H_2SO_4 was used as an eluant at the flowrate of 0.6 mL/min. A refractive index detector was used to detect the organic compounds. Standards containing glucose, lactate, and ethanol at different concentrations in between 0 and 2 g/L were injected as the references. The peak area was used for the comparison basis.

2.5. Cell biomass

At the end of fermentation, cell biomass immobilized on the cotton towel was collected from the perforated stainless steel. The

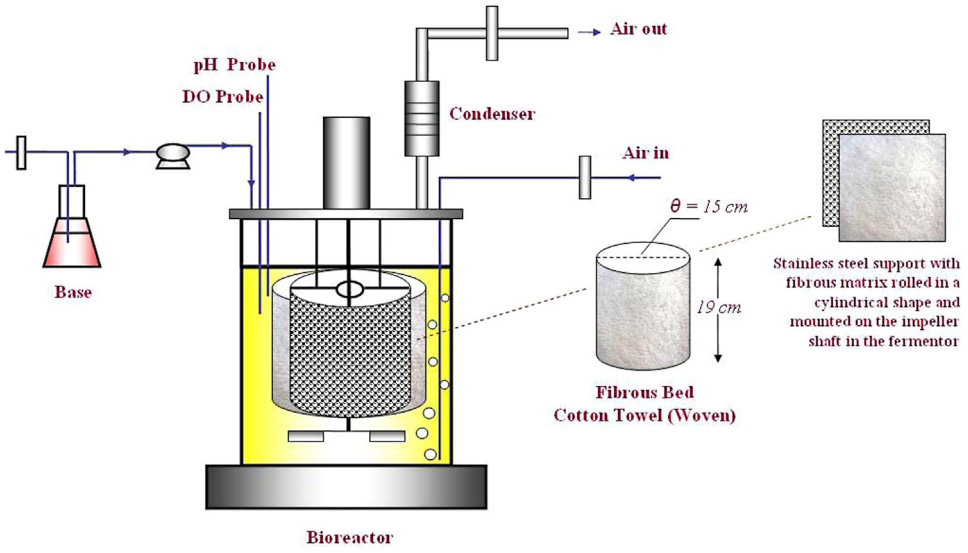

Fig. 1. A static bed bioreactor used in this study [24].

sample was thoroughly rinsed with DI water and dried at 80 °C until constant weight. Cell concentration was measured by Eq. (1).

$$\text{Cell conc.}\left(\frac{g}{L}\right) = \frac{\text{DW of immobilized on cotton cloth} - \text{DW of pre weighed cotton cloth}}{\text{Fermentation broth volume}} \quad (1)$$

2.6. Cell extraction, partial enzyme purification, and protein determination

Fresh mycelia immobilized on the cotton cloth were harvested at the end of fermentation. The mycelia were thoroughly rinsed with DI water before drying between filter paper to remove surface water. One gram of mycelia (wet basis) was frozen at −20 °C for 1 h before grinding in an ice-cold mortar with 1.5 mL 50 mM Tris HCl containing 10 mM β-mercaptoethanol at pH 7.8 for 5 min. The frozen grinded mycelia with 0.5 g glass beads (425–600 μm) were subjected to an ultrasonic disruptor for 10 min with the working time of every 30 s and breaking interval of 45 s. After that the suspension was centrifuged at 12,000 g for 30 min. The obtained supernatant, later called cell extract, was used for protein determination and enzyme assays. Lowry method was used to determine the protein content in the cell extract using a standard bovine serum albumin as the reference [28].

2.7. Enzyme assays

Cell extract previously obtained was used to assay for the activities of lactate dehydrogenase (LDH), PDC, and reversible ADH (ADH(F) and ADH(B)).

NAD^+-dependent LDH was assayed by following the oxidation of NADH at 340 nm in the reaction mixture containing 250 μmol phosphate buffer (pH 6.5), 1 μmol NADH, 25 μmol sodium pyruvate, and 0.2 mL cell extract in the total volume of 3.15 mL. The detailed procedure was described elsewhere in [25–27].

PDC activity was assayed by following the consumption of NADH at 340 nm. The reaction mixture contained 25 mM sodium pyruvate, 5 mM $MgCl_2$, 0.2 mM thiamine pyrophosphate (TPP), 11 U/mL ADH from baker yeast, and 0.15 mM NADH in 100 mM MES buffer in the total volume of 1.2 mL [29]. Detailed procedure can be found elsewhere [26].

Reversible activities of ADH were also determined. In forward reaction, ADH(F) activity was determined by following the oxidation of NADH at 340 nm in the reaction mixture containing 250 μmol Tris HCl buffer (pH 7.7), 250 μmol acetaldehyde, 4 μmol NADH, and 0.2 mL cell extract in the total volume of 3.15 mL [30]. More details can be found elsewhere [25,27]. Whilst ADH(B) was measured by following the reduction of NAD^+ at 340 nm in the reaction mixture containing 250 μmol Tris HCl buffer (pH 7.7), 250 μmol ethanol, 4 μmol NAD^+, and 0.2 mL cell extract in the total volume of 3.15 mL [30]. The protocol was described elsewhere [25–27].

3. Results and discussions

3.1. Preparing the immobilized cells for lactate production in the static bed bioreactor

As previously mentioned, lactate production by *R. oryzae* consisted of 2 phases. The growth phase was for germinating spores and developing sufficient growth to obtain high cell density that could be used as the machinery for lactate formation later in the production phase. Fig. 2 shows that the suitable cotton towel surface inside the static bed bioreactor could yield complete self immobilization resulting in good morphological control, cell-free broth, improved mass transport especially oxygen, and eventually increased lactate production by *R. oryzae*. The thin layer of mycelia immobilized on the cotton matrix in general provided the beneficial outcomes because the shear force exerted by mean of agitation and aeration helped maintain the thin and loose mycelia on the cotton matrix over the period of time; thus, facilitated the oxygen transport into the immobilized structure. A relatively large surface area of the immobilized layer also promoted mass transport [21,24]. The results obtained in this work was consistent to those reported in Chotisubha-anandha et al. [24]. After inoculation, spores started to germinate and subsequently immobilized onto the cotton towel surface within the first 6 h during the growth phase (data not shown). Later cells continued to grow and immobilized on the cotton towel resulting in high cell density ready for lactate production during the production phase. Lactate production phase was started by replacing the growth medium with the production medium containing Zn^{2+} in order to limit growth [31]. The production medium also contained urea as the nitrogen source for reviving cell activity throughout the fermentation.

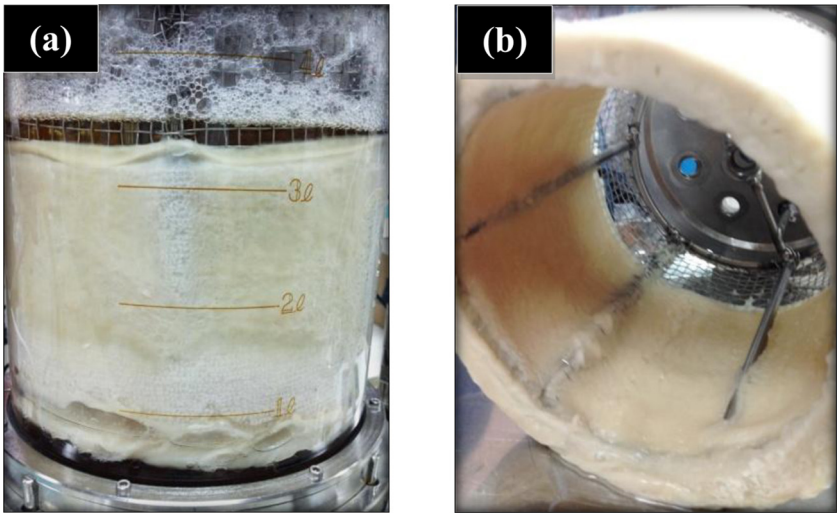

Fig. 2. Immobilized *R. oryzae* on a sheet of cotton cloth affixed on the non-moving bed inside the fermentor during cultivation (a) and its appearance as the thin layer tightly attached on the cotton cloth at the end of fermentation (b).

3.2. Roles of DO during production phase of lactate fermentation by R. oryzae

Several studies claimed that DO significantly affected lactate production by *R. oryzae* [20,22]. It was reported that high DO concentration gave improved lactate production because of the limitation of glucose substrate to ethanol production route [21,24]. However, excess oxygen could lead to cell biomass production that subsequently lowered lactate yield. Several techniques have been applied to sufficiently provide oxygen so that both ethanol and cell biomass production were limited while glucose flux was mainly driven for lactate [24]. Those included optimization of agitation and aeration rates towards novel bioreactor design. Chotisubha-anandha et al. compared fermentation kinetics of *R. oryzae* cultivated in the stirred tank bioreactor to those in the static bed bioreactor operated under the same agitation and aeration rates [24]. They found that at the same operating conditions, oxygen transfer coefficient in the static bed bioreactor was much higher than that in the stirred tank. This successively provided improved lactate production. They also reported that increasing both agitation and aeration rates in the static bed bioreactor could reduce ethanol production [24]. It was found that DO concentration changed during the fermentation when operating the static bed bioreactor at the constant rates of agitation and aeration. Low DO concentration at the certain time somewhat led to the chance of low oxygen transport rate which might result in limited local oxygen concentration in the immobilized structure and eventually ethanol production. On the other hand, in this study, aeration rate was maintained at 1.0 vvm. The oxygen enriched air was used to feed the bioreactor instead of air in order to maintain the constant DO level during the production phase and the fermentation kinetics of *R. oryzae* under different controlled DO levels was investigated.

Fig. 3 shows the fermentation kinetics of *R. oryzae* during the production phase. Obviously, at high DO level (80%), glucose was rapidly consumed by *R. oryzae* resulting in glucose depletion within 48 h while at 40% and 60% DO, glucose was completely consumed 6 h later (54 h). Higher final lactate concentration was obtained when increasing the DO level. Approximately 18% increase in final lactate concentration was obtained when changing the controlled DO level at 40% (30.40 g/L lactate) to 80% (35.82 g/L lactate) (Fig. 3). From Table 1, increasing DO level from 40% to 80% in control fermentations resulted in lower ethanol yield by 45% and productivity by 43% while cell biomass yield and productivity remained unchanged. Although fermentation was carried out under high oxygen level, cell biomass production did not increase (Table 1 and Fig. 3). This confirmed that limited nitrogen source and $ZnSO_4$ present in the production medium successfully controlled cell biomass production and maintained fungal activity [31]. Together with the sufficiently high DO level maintained throughout the fermentation, glucose was rapidly metabolized via glycolysis providing a large pool of pyruvate flux that mainly shifted to lactate production route resulting in increasing lactate yield and productivity by 24% and 43%, respectively [32–35].

Although high DO concentration yielded high lactate production, ethanol was still observed during the production phase. This somewhat indicated pyruvate flux was still driven to ethanol production route in regardless of high DO concentration. Our previous studies reported the activities of key enzymes responsible for lactate and ethanol production during fermentation of *R. oryzae* in the shaken flask culture [25–27]. It was found that the specific activity of ADH(F) was about 5 times higher than that of LDH [27]. This revealed that ADH had the stronger binding affinity to substrate compared with LDH. As a consequence, ethanol still existed although high oxygen concentration was maintained during lactate fermentation.

3.3. Limiting ethanol production during the production phase of lactate fermentation by R. oryzae

From our previous studies, adding either ADH or PDC inhibitors into the fermentation medium caused dynamic changes of specific enzyme activities and metabolic fluxes. This resulted in increasing lactate production [25–27]. Our previous studies reported that when 1,2-diazole and 2,2,2-trifluoroethanol which competitively bound at the active sites of ADH present in the production medium, they did not only strongly limited ethanol but they also indirectly regulated lactate fermentation. Therefore, with the proper concentration of these inhibitors during fermentation, increased lactate production was obtained. Approximately 12% lactate yield was increased in the fermentation with 1,2-diazole or 2,2,2-trifluoroethanol at 1 mM [25,26]. When PDC inhibitors were present during fermentation, increasing lactate yield was also observed. With 0.1 mM 4-methylpyrazole, 12% increasing lactate yield was obtained while only 1 μM 3-hydroxypyruvate helped improve lactate yield by 32% [27].

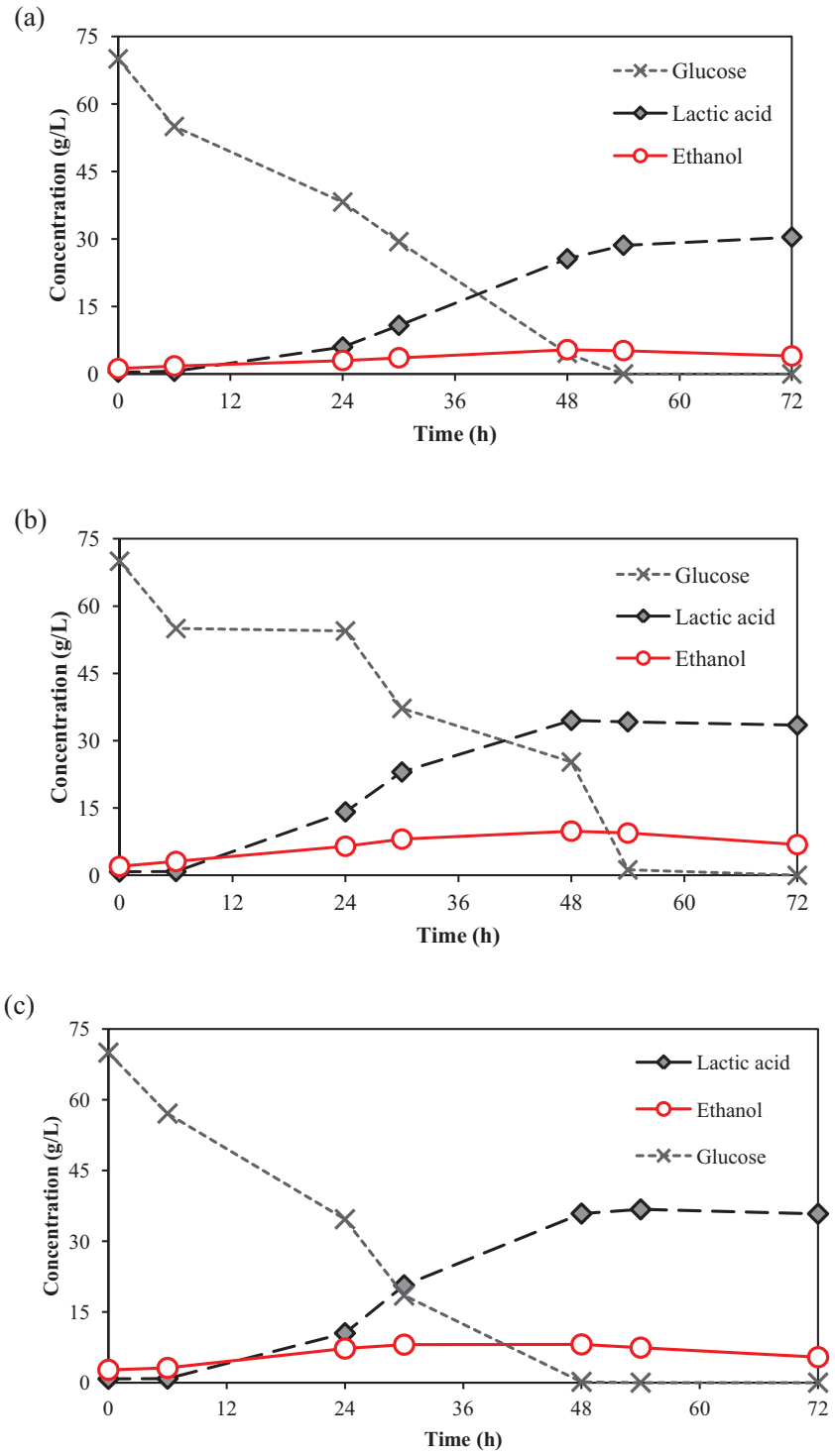

Fig. 3. Kinetics profiles of immobilized *R. oryzae* on a cotton cloth during the production phase in the static bed bioreactor operated at 30 °C, pH 6.0 (5 M NaOH), and 1.0 vvm air. The agitation speed and the volumetric flow ratio of oxygen to air were varied in order to obtain the constant DO profiles at 40% (a), 60% (b), and 80% (c), respectively.

In this work, further investigation on 4 inhibitors mentioned above during lactate fermentation was conducted under controlled DO level. It was hypothesized that with the inhibitors and sufficiently high DO level, more pyruvate could be driven to lactate production route rather than when each of them exploited alone. It was found that cell biomass production was not affected by the increasing DO level as well as the inhibitors present in the production medium. Slightly similar yield and productivity of biomass were obtained in all fermentation runs (Table 1). Decrease in ethanol yield was observed in the fermentation with 2,2,2-trifluoroethanol while other inhibitors did not show strong effect on ethanol yield during fermentation and so did the productivity obtained in all runs (Table 1). In contrast, lactate yield and productivity were increased with the presence of the inhibitors. It was found that 2,2,2-trifluorothanol showed the strongest effect on lactate production resulting in the largest improved yield and productivity. While 1,2-diazole, 4-methylpyrazole, and 3-hydroxypyruvate rather influenced on lactate yield and

Table 1
Product yields and productivities obtained from fermentations by immobilized *R. oryzae* on a cotton cloth during the production phase with the presence of ADH an PDC inhibitors. The static bed bioreactor was operated at 30 °C, pH 6.0 (5 M NaOH), and 1.0 vvm air. The agitation speed and the volumetric flow ratio of oxygen to air were varied in order to obtain the constant DO profiles at 40%, 60%, and 80%.

Inhibitors	Control			1 mM PZ			1 mM TFE			0.1 mM MPZ			1 μM 3HP		
DO level (%)	40	60	80	40	60	80	40	60	80	40	60	80	40	60	80
Yield (g/g glucose)															
Cell biomass	0.07	0.07	0.06	0.08	0.06	0.07	0.06	0.07	0.07	0.06	0.07	0.09	0.05	0.06	0.06
Lactic acid	0.41	0.48	0.51	0.44	0.50	0.58	0.54	0.55	0.63	0.50	0.54	0.54	0.42	0.51	0.53
Ethanol	0.11	0.12	0.06	0.11	0.09	0.05	0.08	0.08	0.04	0.10	0.07	0.05	0.10	0.07	0.05
Productivity (g/L h)															
Cell biomass	0.08	0.07	0.06	0.08	0.07	0.07	0.06	0.08	0.08	0.06	0.08	0.09	0.05	0.07	0.06
Lactic acid	0.49	0.66	0.70	0.51	0.67	0.75	0.71	0.75	0.98	0.60	0.77	0.79	0.56	0.70	0.77
Ethanol	0.14	0.17	0.08	0.16	0.12	0.08	0.10	0.10	0.09	0.13	0.09	0.10	0.13	0.09	0.08

PZ: 1,2-diazole; TFE: 2,2,2-trifluoroethanol; MPZ: 4-methylpyrazole; 3HP: 3-hydroxypyruvate.

productivity at the similar level when presenting in the fermentation medium (Table 1).

In addition, improved lactate yield and productivity were more profound at high DO level. Maximum lactate concentration (43.14 g/L), yield (0.63 g/g glucose) approaching the theoretical value, and productivity (0.98 g/L h) along with the minimum ethanol yield of 0.04 g/g glucose were obtained from fermentation containing 1 mM 2,2,2-trifluoroethanol at 80% DO. The maximum lactate concentration obtained under this condition was increased by 42% with the increasing yield and productivity of 54% and 100%, respectively, compared with the control fermentation without the inhibitor operated at 40% DO (Table 1). Whereas increasing the DO level alone from 40% to 80% during fermentation resulted in increasing final lactate concentration by 18% with the increase in yield and productivity by 24% and 43%. Likewise, adding 2,2,2-trifluoroethanol in the fermentation under 40% DO gave the increase in final concentration, yield, and productivity by only 26%, 32%, and 45%, respectively. Therefore, it could be summarized that when controlling dissolved oxygen at high level, the inhibitors successfully controlled glucose flux to lactate production route. Improved lactate yield was resulted from the inhibitors limiting pyruvate entering ethanol production route while profound effect on productivity under high DO level could be explained by rapid regeneration of ATP and NAD^+/NADH [32].

3.4. How ADH and PDC inhibitors worked during lactate fermentation by R. oryzae

The results shown in Table 1 suggested that the inhibitors were responsible for the change of metabolic fluxes during fermentation. At the proper concentration, this led to lowered ethanol but increased lactate production. Fig. 4 shows the specific activities of the key enzymes. It can be seen that at sufficiently high DO levels (60% and 80%), the specific activity of LDH to the substrate (pyruvate) was higher than that of PDC in all fermentation runs including the control fermentation. The similar phenomena were observed in the fermentation with the inhibitors at 40% DO but not the control fermentation. When controlling DO at 40% in the control fermentation, PDC activity seemed to be a bit higher than that of LDH. This was presumably due to at low DO level, *R. oryzae* recognized insufficient local oxygen concentration. As a result of metabolic response to such a condition, the activity of PDC was enhanced in order to be ready for converting pyruvate to ethanol in addition to some that entering aerobic route for ATP and regeneration of NAD^+/NADH. When comparing the activity of ADH(F) with ADH(B), it was clear that ADH(B) activity was dramatically higher than that of ADH(F). This somewhat revealed the strong feedback inhibition that might easily occur when ethanol or it analog was present.

Considering the specific activity of LDH at 72 h (Fig. 4(a)), it is clear that the highest LDH activity was achieved when 2,2,2-trifluoroethanol was present during the production phase. At the same high DO level of 80%, about 2.9 times higher LDH activity was obtained compared with the control experiment while at the low DO level of 40%, about 2 times higher activity was acquired. DO level also considerably influenced LDH activity in the fermentation with 3-hydroxypyruvate. Approximately, the enzyme activity reached 2.4 times higher at 80% DO compared with the control experiment at the same DO level while 1.5 times higher activity was acquired at 40% DO. This could be explained by the similarity in structure of 2,2,2-trifluoroethanol to ethanol and that of 3-hydroxypyruvate to pyruvate. At high DO level with 2,2,2-trifluoroethanol during fermentation, while 2,2,2-trifluoroethanol competitively bound at the catalytic site of ADH, *R. oryzae* rapidly metabolized glucose via glycolysis resulting in a large pyruvate pool. With the limited nitrogen and the presence of Zn^{2+}, the specific activity of LDH was increased in order to balance the metabolic flux by converting pyruvate to lactate as the end product [31,32]. Likewise, when 3-hydroxypyruvate was present at high DO level, glucose was rapidly metabolized resulting a large pool of pyruvate. Though oxygen concentration was high, *R. oryzae* recognized a large pool of pyruvate along with the presence of 3-hydroxypyruvate and Zn^{2+} with limited nitrogen. This resulted in the increase in LDH activity as the metabolic response.

On the other hand, DO seemed not to be responsible for the change of LDH specific activity in the fermentation with 1,2-diazole or 4-methylpyrazole in the same way as that observed in fermentation with 2,2,2-trifluoroethanol or 3-hydroxypyruvate, though the activity obtained at 3 DO levels studied were higher (Fig. 4(a)). The structure of 1,2-diazole was close to that of NAD^+/NADH, the cofactor of both LDH and ADH. When present in the fermentation, it led to the dynamic change of metabolic fluxes at the pyruvate node [26]. Thitiprasert et al. [27] reported the lower affinity of 1,2-diazole to LDH than that to ADH. When it was present during fermentation, it rather bound at the catalytic site of ADH resulting in the increasing availability of NADH to be bound at LDH . With a large available pyruvate pool and sufficient regeneration of NAD^+/NADH, the specific activity of LDH was increased. In case of 4-methylpyrazole, it competed with thiamine pyrophosphate to bind at the cofactor site of PDC [26,32]. Its effect on LDH during fermentation was not directly observed though the activity of the enzyme was increased.

In control fermentation and fermentation with 1,2-diazole, the specific activity of PDC was decreased with the increasing DO level whereas the increasing activity was observed in the fermentation with 2,2,2-trifluoroethanol (Fig. 4(b)). The specific activity of PDC was similarly low when 3-hydroxypyruvate was present in the fermentation at all DO levels studied but fluctuated trends was observed in the fermentation with 4-methylpyrazole (Fig. 4(b)). The fluctuation in PDC activity observed in this study could be explained by under aerobic condition, PDC was the first enzyme of the pyruvate dehydrogenase complex which converted

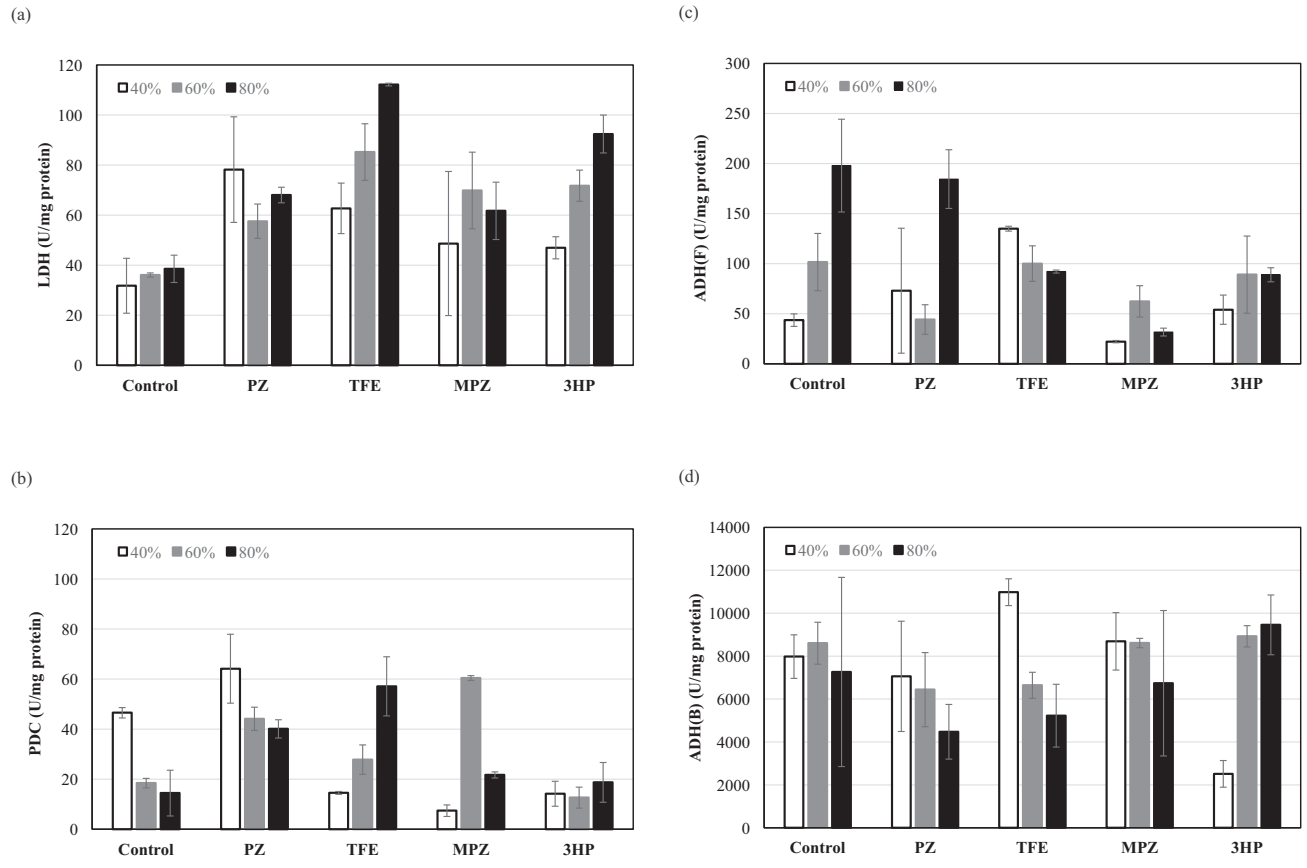

Fig. 4. Specific activities of LDH (a), PDC (b), ADH(F) (c), and ADH(B) (d) observed at the end of fermentation (72 h). Immobilized *R. oryzae* was cultivated in the static bed bioreactor for lactate production with the presence of enzyme inhibitors including 1 mM 1,2 diazole (PZ), 1 mM 2,2,2-trifluoroethanol (TFE), 0.1 mM 4-methylpyrazole (MPZ), and 1 μM 3-hydroxypyruvate (3HP). The fermentor was operated at 30 °C, pH 6.0 (5 M NaOH), and 1.0 vvm. The agitation speed and the volumetric flow ratio of oxygen to air were varied in order to obtain the constant DO profiles at 40%, 60%, and 80%.

pyruvate into acetyl CoA. Whereas under anaerobic condition, PDC was responsible for converting pyruvate into acetaldehyde and CO_2. Two thiamine pyrophosphate and 2 Mg^{2+} ions were required as the cofactors. Therefore, it could be concluded that DO level was relevant to the inhibitors' effect on PDC [28]. Nonetheless, the effect was dependent on the binding affinity. When comparing among 4 inhibitors, 3-hydroxypyruvate successfully lowered PDC activity due to its similar structure to pyruvate, the PDC substrate (Fig. 4(b)).

In contrary to LDH and PDC, the strong affinity of ADH to substrate was observed in the reversible reaction by this enzyme (Fig. 4(c and d)). It was found that increasing the activity of both ADH(F) and ADH(B) were observed with the increasing DO level in the control fermentation. The increasing activity of both enzymes responsible for the reversible conversion of acetaldehyde to ethanol was due to the response mechanism of *R. oryzae* to the presence of a large pool of pyruvate at high DO. This subsequently resulted in the increase in activities of both ADH(F) and ADH(B) to be ready for converting pyruvate to the end product. This dynamic change in the living *R. oryzae* was clearly explained in previous studies done by Thitiprasert et al. [27]. Similarly, increasing activities of both ADH(F) and ADH(B) was observed in the fermentation with 3-hydroxypyruvate; however, the resulting activity was not so high as that obtained in the control fermentation (particularly when comparing the activity at 60% and 80% DO with that at 40% DO). This was probably due to the lower existing acetaldehyde in the fermentation with 3-hydroxypyruvate than that should have been at high DO level (60% and 80%). In contrary to those found in the control fermentation and the fermentation with 3-hydroxypyruvate, the decreasing activities of both ADH(F) and ADH(B) were observed in the fermentation with 2,2,2-trifluoroethanol when the DO level was increasing. At high DO level, pyruvate was likely to enter the aerobic route. With the presence of 2,2,2-trifluroethanol, ethanol analog, the feedback inhibition in ethanol fermentation route also initiated; therefore, this successively reduced the activity of ADH. The results shown in Fig. 4(c and d) strongly showed the combinatorial effect of 2,2,2-trifluroethanol and oxygen on directly controlling ethanol production.

In the fermentation containing 1,2-diazole, the specific activity of ADH(B) was decreased with the increasing DO level while the change in ADH(F) activity seemed to be fluctuated with a large standard error at 40% DO (Fig. 4(c and d)). At high DO level, pyruvate was rather driven towards the aerobic route; therefore, *R. oryzae* apparently recognized low level of acetaldehyde; thus, resulting in the increasing ADH(B) activity while lowering ADH(F). The activity of ADH(B) in the fermentation with 4-methylpyrazole was slightly lower than that observed from the control fermentation while dramatic decrease in ADH(F) activity was observed. The effect of 4-methylpyrazole on the activities of both ADH(F) and ADH(B) seemed not to be evident.

3.5. Substrate analogs exhibited greater effect than cofactor analogs on improved lactate production

It seemed that the substrate analogs including 2,2,2-trifluoroethanol and 3-hydroxypyruvate strongly manipulated the target enzyme. When the DO level was increased from 40% to 80%, 3-hydroxypyruvate lowered the activities of PDC and ADH; thus, reshuffling pyruvate flux towards lactate formation resulted in

increasing LDH activity. This was presumably owing to at high DO level, glucose was rapidly converted to pyruvate. The presence of 3-hydroxypyruvate, on the other hand, bound at PDC catalytic site, resulted in a large remaining pyruvate pool that eventually had to be converted to end product lactate for metabolic flux balance. When 2,2,2-trifluoroethanol was present during the production phase, it competitively bound at the catalytic site of ADH; thus, limited ethanol conversion from pyruvate pool. High glycolysis rate obtained at high DO level resulted in a large pyruvate pool. This induced both LDH and PDC expression in order to balance pyruvate flux toward the end products as can be seen from the increasing activities of these 2 enzymes when DO level was increased. Nonetheless, due to inhibition occurring at ADH catalytic site, pyruvate conversion toward ethanol was limited causing the lowered activity of PDC compared with LDH.

In contrary to substrate analogs, cofactor analogs did not show significant impact on enzyme activity with the increasing DO level. NAD^+/NADH analog, 1,2-diazole, competitively bound at the cofactor site of ADH causing incorrect conformation; thus, preventing the reversible reaction of acetaldehyde to ethanol. Generally, regeneration rate of NAD^+/NADH was increased with the increasing DO level [32]. As a result, the activities of both ADH and LDH in control fermentation were enhanced (Fig. 4(a, c–d)). It was found that when increasing the DO level, 1,2-diazole somewhat lowered the activities of ADH and PDC while LDH activity remained rather unchanged. Moreover, 4-methylpyrazole, the analog of thiamine pyrophosphate binding to PDC substrate binding site during the catalytic cycle, strongly affected ADH instead of its target enzyme PDC as observed from lower activity. This was presumably due to the signaling response of *R. oryzae* to the binding of 4-methylpyrazole at PDC. By this, it was presumably confirmed the lower acetaldehyde pool, ADH substrate. But change in DO level did not lead to decreasing PDC and ADH activities as expected. Nevertheless, the presence of 4-methylpyrazole gave the increased LDH activity.

4. Conclusion

Generally, oxygen played key role controlling lactate production by *R. oryzae*. High DO level usually yields high lactate production along with cell biomass generation while ethanol was still observed as the major byproduct. In this study, PDC and ADH inhibitors were introduced to lactate fermentation by *R. oryzae*. The results revealed that ethanol limitation could be acquired in the fermentation under high DO level with the presence of both PDC and ADH inhibitors while cell biomass production did not increase along with high oxygen supply. As a result, lactate production was significantly improved. The findings in this study confirmed an effective but simple way to improve lactate production by *R. oryzae*.

Acknowledgments

This work was financially supported by Ratchadapiseksomphot Endowment Fund (2014), Chulalongkorn University (CU-57-041-AM). Partial supports from Grant for International Research Integration: Research Pyramid, Ratchadapiseksomphot Endowment Fund (GCURP_58_01_33_01), Thailand Research Fund via the Distinguished Research Professor Grant (DPG5880003), and National Research Council of Thailand via the annual government statement of expenditure (GRB_APS_45_57_61_03) are also acknowledged. Research facility support by Chulalongkorn Academic Advancement into its 2nd Century Project (CUAASC) is highly appreciated.

References

[1] R. Datta, S.P. Tsai, P. Bonsignor, S. Moon, J. Frank, Technological and economic potential of poly(lactic acid) and lactic acid derivatives, FEMS Microbiol. Rev. 16 (1995) 221–231.
[2] J. Lunt, Large-scale production, properties and commercial applications of polylactic acid polymers, Polym. Degrad. Stab. 59 (1998) 145–152.
[3] A. Sodergard, M. Stolt, Properties of lactic acid based polymers and their correlation with composition, Prog. Polym. Sci. 27 (2002) 1123–1163.
[4] F.A.C. Martinez, E.M. Balciunas, J.M. Salgado, J.M. Dominguez, G.A. Converti, R.P.D.S. Oliveira, Lactic acid properties, applications and production: a review, Trends Food Sci. Technol. 30 (2013) 70–83.
[5] Y.D. Hang, W. Suntornsuk, Strain improvement of *Rhizopus oryzae* for production of L(+)-lactic acid and glucoamylase, Lett. Appl. Microbiol. 19 (1994) 249–252.
[6] C.R. Soccol, V.I. Sonoga, M. Raimbault, Production of L-lactic acid by *Rhizopus* species, World J. Microbiol. Biotechnol. 10 (1994) 433–435.
[7] Y. Kosakai, Y.S. Park, M. Okabe, Enhancement of L(+)-lactic acid production using mycelial flocs of *Rhizopus oryzae*, Biotechnol. Bioeng. 55 (1997) 461–470.
[8] X.Y. Dong, S. Bai, Y. Sun, Production of L(+)-lactic acid with *Rhizopus oryzae* immobilized in polyurethane foam cubes, Biotechnol. Lett. 18 (1996) 225–228.
[9] E.Y. Park, Y. Kosakai, M. Okabe, Efficient production of L(+)-lactic acid using mycelial cotton-like flocs of *Rhizopus oryzae* in an air-lift bioreactor, Biotechnol. Prog. 14 (1998) 699–704.
[10] Y. Sun, Y.L. Li, S. Bai, Modeling of continuous L(+)-lactic acid production with immobilized *R. oryzae* in an airlift bioreactor, Biochem. Eng. J. 3 (1999) 87–90.
[11] Y. Liu, W. Liao, C. Liu, S. Chen, Optimization of L-(+)-lactic acid production using pelletized filamentous *Rhizopus oryzae* NRRL395, Appl. Biochem. Biotechnol. 129–132 (2006) 844–853.
[12] P.M. Yin, N. Nishina, Y. Kosakai, K. Yahiro, Y. Park, M. Okabe, Enhanced production of L(−)-lactic acid from corn starch in a culture of *Rhizopus oryzae* using an air-lift bioreactor, J. Ferment. Bioeng. 84 (1997) 249–253.
[13] Y. Zhou, J.M. Dominguez, N. Cao, J. Du, G.T. Tsao, Optimization of L-lactic acid production from glucose by *Rhizopus oryzae* ATCC 52311, Appl. Biochem. Biotechnol. 77-79 (1999) 401–407.
[14] J.P. Lin, S.D. Ruan, P.L. Cen, Mathematical model of L(+)-lactic acid fermentation in RDC coupled with product separation by ion exchange, Chem. Eng. Commun. 168 (1998) 59–79.
[15] N. Thongchul, Production of lactic acid and polylactic acid for industrial applications, in: S.-T. Yang, H.A. El Enshasy, N. Thongchul (Eds.), Bioprocessing Technologies in Biorefinery for Sustainable Production of Fuels, Chemicals, and Polymers, John Wiley & Sons, New Jersey, 2013, pp. 293–316.
[16] D.M. Bai, M.Z. Jia, X.M. Zhao, R. Ban, F. Shen, X.G. Li, S.M. Xu, L(+)-Lactic acid production by pellet-form *Rhizopus oryzae* R1021 in a stirred tank fermentor, Chem. Eng. Sci. 58 (2003) 785–791.
[17] Z.Y. Zhang, B. Jin, J.M. Kelly, Production of lactic acid from renewable materials by *Rhizopus* fungi, Biochem. Eng. J. 35 (2007) 251–263.
[18] X.F. Wu, S.T. Jiang, M. Liu, L.J. Pan, Z. Zheng, S.Z. Luo, Production of L-lactic acid by *Rhizopus oryzae* using semicontinuous fermentation in bioreactor, J. Ind. Microbiol. Biotechnol. 38 (2011) 565–571.
[19] M. Papagianni, Fungal morphology and metabolite production in submerged mycelial processes, Biotechnol. Adv. 22 (2004) 189–259.
[20] R. Krull, T. Wucherpfennig, M.E. Esfandabadia, R. Walisko, G. Melzer, D.C. Hempel, I. Kampen, A. Kwade, C. Wittmann, Characterization and control of fungal morphology for improved production performance in biotechnology, J. Biotechnol. 163 (2013) 112–123.
[21] A. Tay, S.-T. Yang, Production of L(+)-lactic acid from glucose and starch by immobilized cells of *Rhizopus oryzae* in a rotating fibrous bed bioreactor, Biotechnol. Bioeng. 80 (2002) 1–12.
[22] Z. Wang, Y. Wang, S.-T. Yang, R. Wang, H. Ren, A novel honeycomb matrix for cell immobilization to enhance lactic acid production by *Rhizopus oryzae*, Bioresour. Technol. 101 (2010) 5557–5564.
[23] T. Yamane, R. Tanaka, Highly accumulative production of L(+)-lactate from glucose by crystallization fermentation with immobilized *Rhizopus oryzae*, J. Biosci. Bioeng. 115 (2012) 90–95.
[24] N. Chotisubha-anandha, S. Thitiprasert, V. Tolieng, N. Thongchul, Improved oxygen transfer and increased L-lactic acid production by morphology control of *Rhizopus oryzae* in a static bed bioreactor, Bioproc. Biosyst Eng. 34 (2011) 163–172.
[25] S. Thitiprasert, S. Sooksai, N. Thongchul, The in vivo regulation of alcohol dehydrogenase and lactate dehydrogenase in *Rhizopus oryzae* to improve L-lactic acid fermentation, Appl. Biochem. Biotechnol. 164 (2011) 1305–1322.
[26] T. Thitiprasert, P. Songserm, W. Boonkong, S. Sooksai, K. Kodama, N. Thongchul, Manipulating pyruvate decarboxylase by addition of enzyme inhibitors during fermentation of *Rhizopus oryzae* to enhance lactic acid production, Appl. Biochem. Biotechnol. 174 (2014) 1795–1809.
[27] S. Thitiprasert, S. Sooksai, N. Thongchul, 1,2-Diazole and 2,2,2-trifluoroethanol and their inhibitory effects on ethanol and lactic acid formation in the living culture of *Rhizopus oryzae*, Appl. Biochem. Biotechnol. 172 (2014) 1673–1686.
[28] O.H. Lowry, N.J. Rosebrough, A.L. Farr, A.J. Rardall, Protein determination with the folin phenol reagent, J. Biol. Chem. 193 (1951) 265–275.

[29] S. Acar, M. Yucel, H. Hamamci, Purification and characterization of two isozymes of pyruvate decarboxylase from *Rhizopus oryzae*, Enzyme Microb. Technol. 40 (2007) 675–682.
[30] G.G. Pritchard, An NAD^+-independent L-lactate dehydrogenase from *Rhizopus oryzae*, Biochim. Biophys. Acta 250 (1971) 25–34.
[31] B. Preetha, T. Viruthagiri, Biosorption of zinc(II) by *Rhizopus arrhizus*: equilibrium and kinetic modelling, Afr. J. Biotechnol. 4 (2005) 506–508.
[32] P. Songserm, S. Thitiprasert, V. Tolieng, J. Piluk, S. Tanasupawat, S. Assabumrungrat, S.-T. Yang, A. Karnchanatat, N. Thongchul, Regulating pyruvate carboxylase in the living culture of *Aspergillus terreus* NRRL1960 by L-aspartate for enhanced itaconic acid production, Appl. Biochem. Biotechnol. 177 (2015) 595–609.
[33] C.D. Skory, Induction of *Rhizopus oryzae* pyruvate decarboxylase genes, Curr. Microbiol. 47 (2003) 59–64.
[34] Y.Q. Fu, Q. Xu, S. Li, Y. Chen, H. Huang, Strain improvement of *Rhizopus oryzae* for over-production of fumaric acid by reducing ethanol synthesis pathway, Korean J. Chem. Eng. 27 (2010) 183–186.
[35] B. Zhang, C.D. Skory, S.-T. Yang, Metabolic engineeringof *Rhizopus oryzae*: effects of overexpressing pyc and pepc genes on fumaric acid biosynthesis from glucose, Metab. Eng. 14 (2012) 512–520.

INTERNATIONAL JOURNAL OF HYDROGEN ENERGY XXX (2016) 1–14

Available online at www.sciencedirect.com

ScienceDirect

journal homepage: www.elsevier.com/locate/he

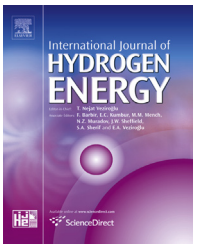

Activity and stability performance of multifunctional catalyst (Ni/CaO and Ni/$Ca_{12}Al_{14}O_{33}$–CaO) for bio-hydrogen production from sorption enhanced biogas steam reforming

Janewit Phromprasit [a], *Jonathan Powell* [b], *Suwimol Wongsakulphasatch* [c], *Worapon Kiatkittipong* [c], *Palang Bumroongsakulsawat* [a], *Suttichai Assabumrungrat* [a,*]

[a] *Center of Excellence in Catalysis and Catalytic Reaction Engineering, Department of Chemical Engineering, Faculty of Engineering, Chulalongkorn University, Bangkok 10330, Thailand*

[b] *International School of Engineering, Faculty of Engineering, Chulalongkorn University, Bangkok 10330, Thailand*

[c] *Department of Chemical Engineering, Faculty of Engineering and Industrial Technology, Silpakorn University, Nakhon Pathom 73000, Thailand*

ARTICLE INFO

Article history:
Received 27 October 2015
Accepted 20 March 2016
Available online xxx

Keywords:
CO_2 capture
CaO
Multifunctional catalyst
H_2 production
Sorption enhanced biogas steam reforming

ABSTRACT

Modified sorbents (NiO–CaO and $Ca_{12}Al_{14}O_{33}$–CaO) were synthesized by hydration followed by wet mixing (HW) and tested in terms of their CO_2 sorption/desorption performance over multiple cycles. The results indicated the sorption capacities for Ni–CaO-HW and Al–CaO-HW decreased by only 3.8% and 6.4%, respectively, over 10 cycles. Various sequences of Ni^{2+} loading onto modified CaO were investigated. The results indicated Ni–Al–CaO-HW to be the best performing exhibiting a pre-breakthrough time 30 min longer than the other samples. However, the H_2 purity and CH_4 conversion did not differ significantly amongst the various sorbents (approx. 94% purity H_2 and approx. 90% CH_4 conversion pre-breakthrough). The stability of the Ni–Al–CaO-HW was also investigated and the results indicated that the pre-breakthrough CH_4 conversion could be maintained at steady values for five cycles. However, the post-breakthrough CH_4 conversion decreases slightly over five cycles. A plausible explanation is that the formation of $CaCO_3$ results in the blockage of pores and active sites, which is supported by XPS results.

Copyright © 2016, Hydrogen Energy Publications, LLC. Published by Elsevier Ltd. All rights reserved.

Introduction

With an increase in global populations and industrial activity, global energy demand is having an ever increasing impact upon the environment. As a way of mitigating these environmental problems, clean energy technologies such as energy from solar cells [1–3], wind turbines [4,5] and hydrogen fuel cells [6–8] are continuing to play a greater role in a modern day power generation and energy mix.

* *Corresponding author*. Tel.: +66 2 2186868; fax: +66 2 2186877.
E-mail address: suttichai.a@chula.ac.th (S. Assabumrungrat).

http://dx.doi.org/10.1016/j.ijhydene.2016.03.125

0360-3199/Copyright © 2016, Hydrogen Energy Publications, LLC. Published by Elsevier Ltd. All rights reserved.

Please cite this article in press as: Phromprasit J, et al., Activity and stability performance of multifunctional catalyst (Ni/CaO and Ni/$Ca_{12}Al_{14}O_{33}$–CaO) for bio-hydrogen production from sorption enhanced biogas steam reforming, International Journal of Hydrogen Energy (2016), http://dx.doi.org/10.1016/j.ijhydene.2016.03.125

Normally, conventional hydrogen production involves the steam methane reforming process (SMR, Eqs. (1)–(3)) which is performed at high temperatures (700–1000 °C). To reduce the reaction temperature whilst continuing to achieve high H_2 purities, sorption enhanced techniques offer promising alternatives for the future. Sorption enhanced steam methane reforming (SESMR) is a process that combines a steam reforming reactor and a gas separator into a single unit operation. The process involves the simultaneous sorption of CO_2 in the reactor allowing hydrogen to be purified and promoting the production of hydrogen according to Le Chatelier's principle. The advantages of sorption enhanced steam reforming process are: (i) the reaction unit and separation unit are combined in one unit operation leading to a reduction of overall size of the process; (ii) the overall reforming reaction is enhanced yielding high methane conversion and hydrogen purity [9]; (iii) operating costs are reduced as the reaction can be operated under milder conditions when compared with conventional steam reforming processes; (iv) capital cost and operating costs are reduced due to lower reaction temperatures and cost of reactor wall materials [10].

$$\text{Stream methane reforming (SMR)}: \ CH_4 + H_2O \leftrightarrow CO + 3H_2 \quad (1)$$

$$\text{Water gas shift (WGS)}: \ CO + H_2O \leftrightarrow CO_2 + H_2 \quad (2)$$

$$\text{Overall}: \ CH_4 + 2H_2O \leftrightarrow CO_2 + 4H_2 \quad (3)$$

Several sorbents such as lithium based sorbents (Eqs. (4) and (5)) [11–18], hydrotalcites [19–22], and CaO (Eq. (6)) [23–28], etc., have been shown to have characteristics making them suitable for use in CO_2 sorption at high temperatures as summarized in Table 1 [29]. Advantages of CaO are its high sorption capacity and fast sorption kinetics. Ochoa-Fernández et al. [30] showed that the sorption capacity of CaO is greater than that of lithium based sorbents with a maximum measured sorption capacity of 0.495 $g_{CO_2}/g_{sorbent}$ compared to that of Li_2ZrO_3 (0.271 $g_{CO_2}/g_{sorbent}$), K-doped Li_2ZrO_3 (0.207 $g_{CO_2}/g_{sorbent}$), Na_2ZrO_3 (0.163 $g_{CO_2}/g_{sorbent}$) and Li_4SiO_4 (0.229). However, the main limitation of CaO is its stability after multiple operating cycles. To improve the stability of CaO, several researchers have investigated the addition of metal ions into CaO structure. Metals added to the CaO were selected to increase the Tammann temperatures above the carbonation/calcination temperature [31].

$$\text{Lithium based sorbent}: \ Li_2ZrO_3 + CO_2 \leftrightarrow Li_2CO_3 + ZrO_2 \quad (4)$$

$$Li_4SiO_4 + CO_2 \leftrightarrow Li_2SiO_3 + Li_2CO_3 \quad (5)$$

$$\text{Calcium based sorbent}: \ CaO + CO_2 \leftrightarrow CaCO_3 \quad (6)$$

Lu et al. [31] investigated the use of various metal dopants including Si^{4+}, Ti^{4+}, Cr^{3+}, Co^{2+} and Zr^{4+} on CaO. The modified sorbents were synthesized by flame spray pyrolysis (FSP). The results showed the best CO_2 sorbent to be Zr-doped CaO with a Zr/Ca ratio of 3:10 atomic ratio. The XRD results indicated the presence of a $CaZrO_3$ phase with the authors proposing that $CaZrO_3$ formation inhibits the growth of CaO particulates, thus inhibiting the sintering-agglomeration phenomenon. Park and Yi [32] investigated the use of Mg^{2+} doped on CaO. MgO–CaO was prepared by the co-precipitation method. The results showed that the addition of Mg^{2+} led to improved sorption stability but low sorption capacity (0.08–0.14). As a consequence, the authors added a hydration step during the synthesis and the results exhibited a significant increase in the sorption capacity (0.174–0.478 $g_{CO_2}/g_{sorbent}$) with excellent sorption/desorption performance. This behavior is believed to be a result of sintering inhibition, leading to the maintaining of high porosity and pore connectivity within CaO particles. Radfarnia and Iliuta [33] studied the use of Al^{3+}, Zr^{4+}, Mg^{2+} and Y^{3+} to stabilize CaO. The optimum composition of Zr- and Al-stabilized CaO in terms of the metal/Ca molar ratio was found to be 0.1, providing maximum activities of 0.29 $g_{CO_2}/g_{sorbent}$ and 0.33 $g_{CO_2}/g_{sorbent}$, respectively at the end of operation. The optimum composition of Mg-stabilized CaO in terms of metal/Ca molar ratio was 0.4 which gave an absorptivity of 0.28 $g_{CO_2}/g_{sorbent}$.

More recently, modified CO_2 sorbents used in various high temperature cycles have been applied to sorption enhanced steam methane reforming (SESMR) process by various researchers such as Martavaltzi and Lemonidou [34], Kim et al. [35], Feng et al. [36], Xie et al. [37], etc. Martavaltzi and Lemonidou [34] investigated the use of hybrid CO_2 sorbent and reforming catalyst for sorption enhanced steam methane reforming process. The catalyst NiO–CaO–$Ca_{12}Al_{14}O_{33}$ was synthesized by the liquid chemistry route. The sorption testing results showed that the material was able to capture a quantity of CO_2 equivalent to more than 31% of its own weight and remained stable, continuing to capture this quantity for up to 45 sorption/desorption cycles. The authors suggest that NiO acts synergistically with the $Ca_{12}Al_{14}O_{33}$ to improve the stability of the CaO. In addition, the hybrid material containing 16 wt.% Ni led to CH_4 conversions of 80%, a high H_2 purity of 90% along with low CO_2 (2.8%) and CO (2%) contents, when operating with a steam to methane ratio of 3.4 and a temperature of 650 °C for almost 100 min.

Kim et al. [35] investigated the incorporation of Ni into CaO and $Ca_{12}Al_{14}O_{33}$ for sorption enhanced steam methane reforming, prepared by the precipitation and hydration method. The sorbent showed excellent cyclic stability due to the formation of $Ca_{12}Al_{14}O_{33}$ providing commodious pathways for CO_2 diffusion as well as an agglomeration resisting

Table 1 – Characteristics of CO_2 sorbent materials [29].

Group	Representative member	Sorption capacity	Stability	Kinetics
Metal oxides	CaO	Good	Poor	Good
Hydrotalcites	$Mg_6Al_2(OH)_{16}[CO_3]\cdot 4H_2O/K_2CO_3$	Poor	Good	Poor
Li metal oxide	Li_4SiO_4	Fair	Fair	Good

Please cite this article in press as: Phromprasit J, et al., Activity and stability performance of multifunctional catalyst (Ni/CaO and Ni/$Ca_{12}Al_{14}O_{33}$–CaO) for bio-hydrogen production from sorption enhanced biogas steam reforming, International Journal of Hydrogen Energy (2016), http://dx.doi.org/10.1016/j.ijhydene.2016.03.125

skeleton. The catalytic sorbent containing 7 wt.% Ni was found to exhibit an excellent performance in terms of hydrogen production and methane conversion. The Ni doped sorbent catalyst provided a product gas with a 94–95% H_2 concentration during the pre-breakthrough period (70–80 min) at a temperature of 630 °C and with a steam to carbon ratio of 3. NiO–CaO/Al_2O_3 was also modified using La_2O_3 [36]. The complex catalyst was synthesized using the impregnation method. The results showed the formation of a complex catalyst with La_2O_3 modification, stable for up to 30 cycles of reactive sorption enhanced reforming (ReSER) with 92% + H_2 purity at a temperature of 600 °C, a steam to carbon ratio of 4 and a regeneration temperature of 800 °C. In comparison, the complex catalyst without La_2O_3 modification was stable for only seven cycles. The improved performance is attributed to La_2O_3 enhancing the interaction between NiO and the support, resulting in an increase in catalyst stability as the nickel dispersed evenly on the support preventing the growth and agglomeration of particles. In addition, Xie et al. [37] investigated the use of CaO–$Ca_9Al_6O_{18}$ sorbent for sorption enhanced steam methane reforming. The operating conditions were varied in terms of temperature, steam to carbon ratio, space velocity and the sorbent to catalyst ratio, showing that low temperatures favor H_2 purity but decrease H_2 yield, high steam to carbon ratios or low space velocities increase the H_2 purity, the sorbent to catalyst ratio has little or no effect on H_2 purity but can reduce or extend the breakthrough time. Other metal ions loaded on CaO were also investigated for application to sorption enhanced steam methane reforming such as Zr^{4+} [38,39] and Ce^{4+} [39]. For example, bifunctional Ni/CaO–Zr was prepared by using wet mixing and sonication techniques [38]. A 20.5 wt.% NiO loading on sorbent-catalyst exhibited suitable activity producing a 91% H_2 purity at the end of the 10th SESMR cycle.

Production of hydrogen via steam reforming has been performed with the use of different raw materials such as methane [40–45], methanol [46–49], ethanol [50–54], biomass [55–59], or biogas [60–64]. Among these, biogas is an interesting renewable resource for hydrogen production as it can be produced by anaerobic digestion of residual biomass such as animal waste, industrial waste water, and agricultural waste inside a landfill [65]. Typically biogas is composed of 55–70% CH_4, 27–44% CO_2, <1% H_2 and <3% H_2S as well as traces of NH_3 [66]. It is noted that the biogas is not commonly used as an energy source due to its high CO_2 content which decreases the heating value and flame stability of the gas mixture [67]. Therefore to extract the latent energy from biogas, the decomposition of biogas to hydrogen by sorption enhanced steam reforming is a good alternative for investigation.

The work reported in this paper is composed of two parts: (i) studies into CO_2 sorption stability and (ii) hydrogen production performance using a multifunctional catalyst (nickel catalyst over calcium aluminate sorbent). Performances of modified sorbents produced by adding compounds of Ni^{2+} or Al^{3+} into CaO have been investigated in terms of CO_2 sorption capacity, sorption/desorption stability over 10 cycles in a fixed bed reactor. The hydrogen production and stability of the multifunctional catalyst over 5 reaction cycles are tested using the sorption enhanced biogas steam reforming reaction.

Experiment

Sorbents and catalysts preparation

The modified sorbents are synthesized by CaO hydration followed by wet mixing. Firstly, CaO was added in DI water at a temperature of 75 °C for 2 h and then an equal weight of 20 wt.% of Al_2O_3 and NiO were added into the CaO suspension, then kept at 75 °C for 2 h. Aluminum nitrate nanohydrate ($Al(NO_3)_3 \cdot 9H_2O$, Sigma–Aldrich) and nickel nitrate hexahydrate ($Ni(NO_3)_2 \cdot 6H_2O$, Sigma–Aldrich) were used as precursors for Al_2O_3 and NiO, respectively. The mixture suspensions were dried at 100 °C overnight to produce a powder, after that the powder was dried at a temperature of 500 °C for 3 h and calcined at 900 °C for 3 h in air atmosphere. In this report the samples produced by CaO hydration followed by wet mixing are denoted with a HW i.e. Ni–CaO-HW and Al–CaO-HW.

Multifunctional catalysts containing Ni and a modified sorbent (CaO/$Ca_{12}Al_{14}O_{33}$) were also synthesized by hydration followed by wet mixing. Ni deposited on a commercial support (Al_2O_3, Fluka) or a commercial sorbent (CaO, Sigma–Aldrich) were synthesized by hydration followed by wet mixing and used for comparison to the multifunctional catalysts in terms of H_2 production performance. First, CaO or Al_2O_3 were added in DI water and stirred at 75 °C for 2 h. After that $Ni(NO_3)_2 \cdot 6H_2O$ was dissolved in DI water (equal to 12.5 wt.% Ni) which was added to a CaO or Al_2O_3 suspension then stirred at a temperature of 75 °C for 2 h. After that the solution was dried at 100 °C overnight and heated up to 500 °C for 3 h. The powder was then calcined at 900 °C for 3 h. In this report these samples are denoted as Ni–Al_2O_3-HW and Ni–CaO-HW.

The sequence of Ni loading on modified sorbent is important and has a significant impact upon the hydrogen production performance. This study has investigated three different sequences of Ni loading. First, a Ni^{2+} solution and an Al^{3+} solution were added into the CaO suspension at the same time then stirred at a temperature of 75 °C for 2 h. The suspension was dried at 100 °C overnight and followed by 500 °C for 3 h. The powder was then calcined at 900 °C for 3 h. In this report these samples are denoted as Ni–Al–CaO-HW. For the second and third sequences, Ni solution was loaded onto the Al–CaO powder after drying of an Al–CaO suspension at 500 °C and the after calcination of the powder at 900 °C. The sample produced by adding Ni solution after drying is named as Ni–Al–CaO-HWO and samples produced adding Ni solution after calcination is denoted as Ni–Al–CaO-HWC. The samples were sieved through a 105 μm sieve.

Material characterization

Phases and crystallite sizes of the modified sorbents and multifunctional catalysts were determined by X-ray diffraction technique (XRD) using a D8 Advance, Bruker equipped with a long fine focus Cu K_α X ray source. The XRD

Please cite this article in press as: Phromprasit J, et al., Activity and stability performance of multifunctional catalyst (Ni/CaO and Ni/$Ca_{12}Al_{14}O_{33}$–CaO) for bio-hydrogen production from sorption enhanced biogas steam reforming, International Journal of Hydrogen Energy (2016), http://dx.doi.org/10.1016/j.ijhydene.2016.03.125

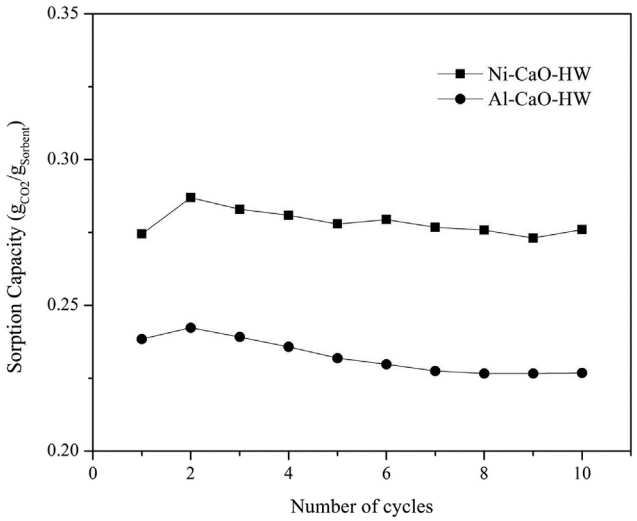

Fig. 1 – Sorption capacity of Ni–CaO-HW and Al–CaO-HW at 600 °C, 1 atm and CO_2 concentration of 15% v/v for different sorption/desorption cycles.

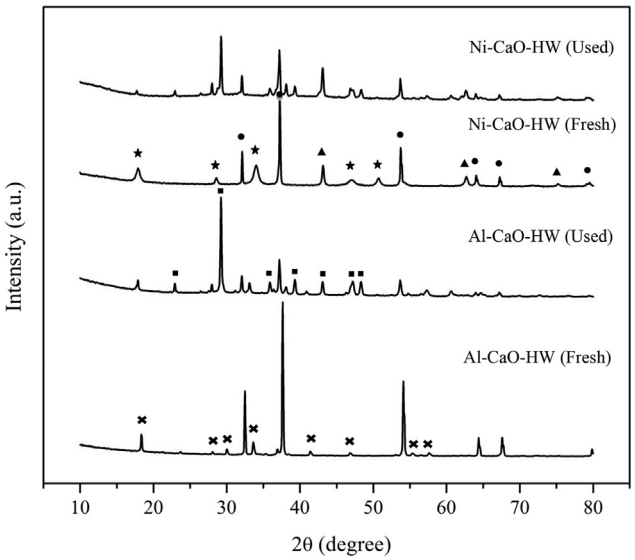

Fig. 3 – XRD pattern of modified sorbents Al–CaO-HW and Ni–CaO-HW: ● CaO, ★ $Ca(OH)_2$, ▲ NiO, × $Ca_{12}Al_{14}O_{33}$ and ■ $CaCO_3$.

patterns were recorded at $10° < 2\theta < 80°$ with a step of 0.04°, wavelength of 1.54056 nm and scan speed of 0.5 s/step. The surface areas of the samples were determined by the Brunauer–Emmett–Teller (BET) method by nitrogen adsorption (Micromeritics Chemisorp 2750). Pore sizes and pore volumes of the samples were determined from desorption isotherms using the Barret–Joyner–Halender (BJH) method. The morphology of the modified sorbents and multifunctional catalysts (both fresh and used) was analyzed by

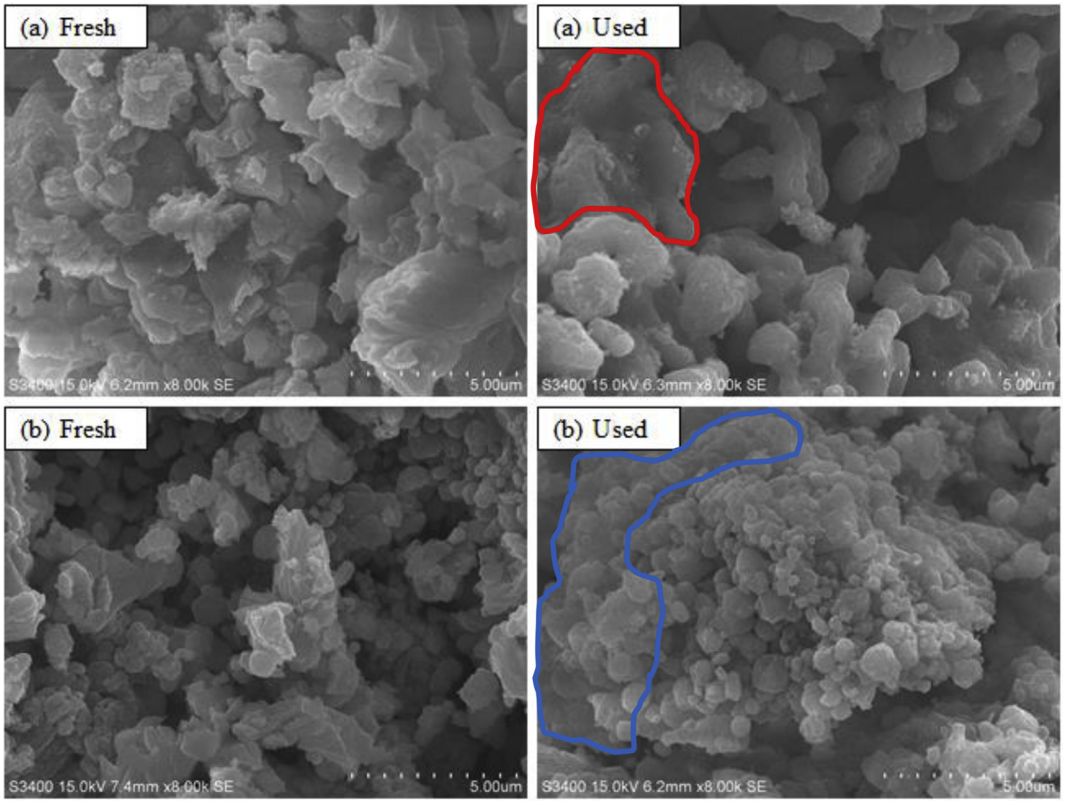

Fig. 2 – SEM images of (a) Ni–CaO-HW and (b) Al–CaO-HW freshly prepared and after 10 CO_2 sorption/desorption cycles.

Please cite this article in press as: Phromprasit J, et al., Activity and stability performance of multifunctional catalyst (Ni/CaO and Ni/$Ca_{12}Al_{14}O_{33}$–CaO) for bio-hydrogen production from sorption enhanced biogas steam reforming, International Journal of Hydrogen Energy (2016), http://dx.doi.org/10.1016/j.ijhydene.2016.03.125

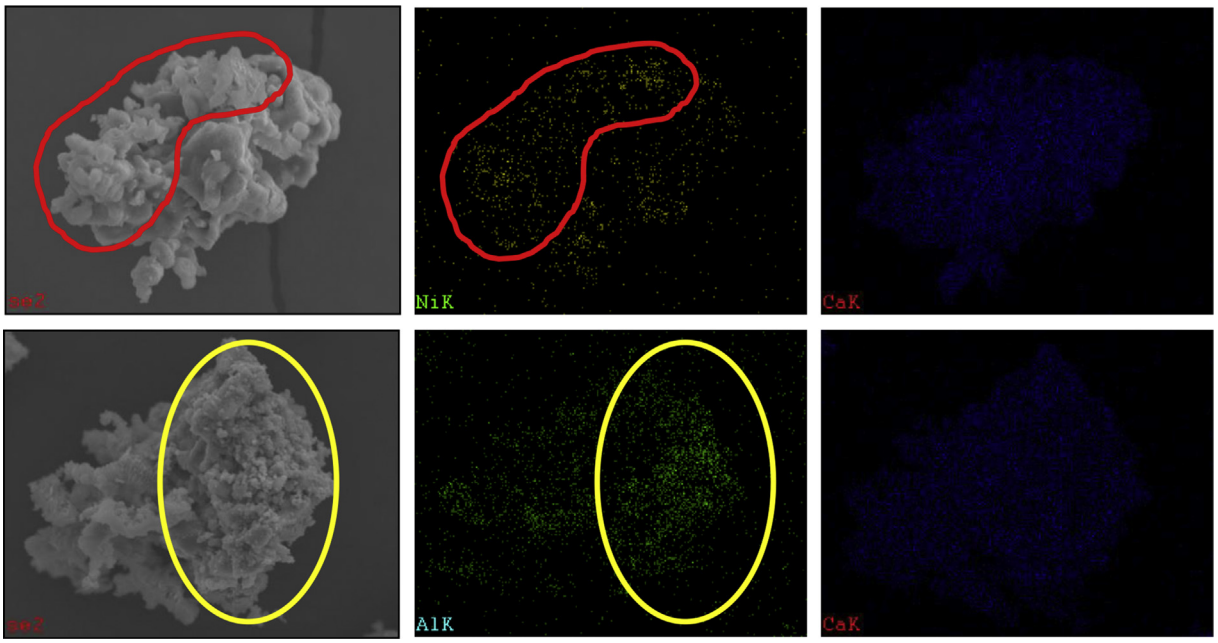

Fig. 4 – SEM–EDS images of (a) Ni–CaO-HW and (b) Al–CaO-HW after 10 CO_2 sorption/desorption cycles.

scanning electron microscope, SEM, (Hitachi S-3400N) coupled with X-ray energy dispersive spectroscopy, X-ray EDS, (AMETEK EDAX, APOLLO X) for analyzing the local dispersion of elements. Atomic concentrations at the surface were characterized by X-ray photoelectron spectroscopy (XPS) using a Kratos Amicus X-ray photoelectron spectrometer. The analyses were carried out with a Mg K_α X-ray source under a working pressure of 1×10^{-6} Pa at a current of 20 mA and 12 kV. Temperature programmed reduction (TPR) was used to determine reducibility of

Table 2 – BET surface areas and crystallite sizes of different catalytic sorbents.

Sample	BET surface area (m^2/g)	Pore size (nm)	Pore volume (cm^3/g)	Crystallite size of CaO (nm)
Ni–CaO-HW	35.9	5.0	0.08	50.7
Ni–Al–CaO-HW	14.1	7.9	0.04	51.7
Ni–Al–CaO-HWO	18.3	7.9	0.06	46.3
Ni–Al–CaO-HWC	8.9	20.4	0.05	47.4

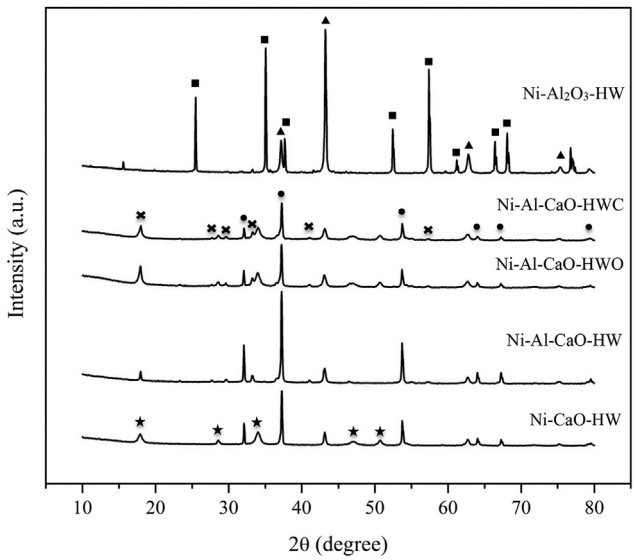

Fig. 5 – XRD pattern of different catalytic sorbents: ● CaO, ★ $Ca(OH)_2$, ▲ NiO, × $Ca_{12}Al_{14}O_{33}$ and ■ Al_2O_3.

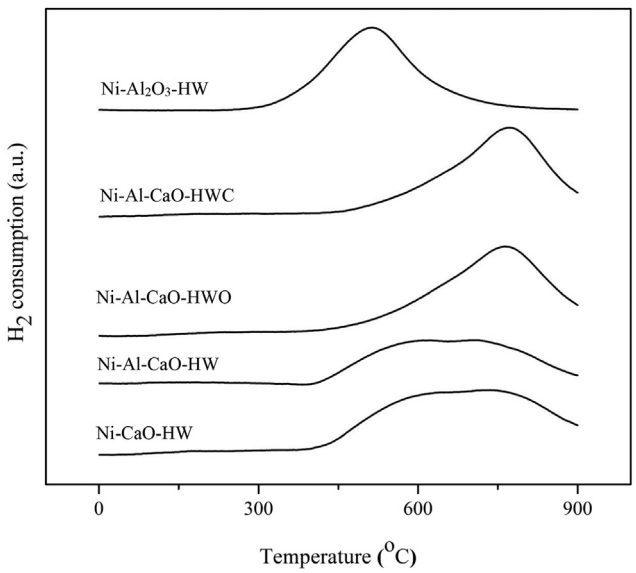

Fig. 6 – Temperature programmed reduction (TPR) profiles of Ni over multifunctional catalytic sorbents.

Please cite this article in press as: Phromprasit J, et al., Activity and stability performance of multifunctional catalyst (Ni/CaO and Ni/$Ca_{12}Al_{14}O_{33}$–CaO) for bio-hydrogen production from sorption enhanced biogas steam reforming, International Journal of Hydrogen Energy (2016), http://dx.doi.org/10.1016/j.ijhydene.2016.03.125

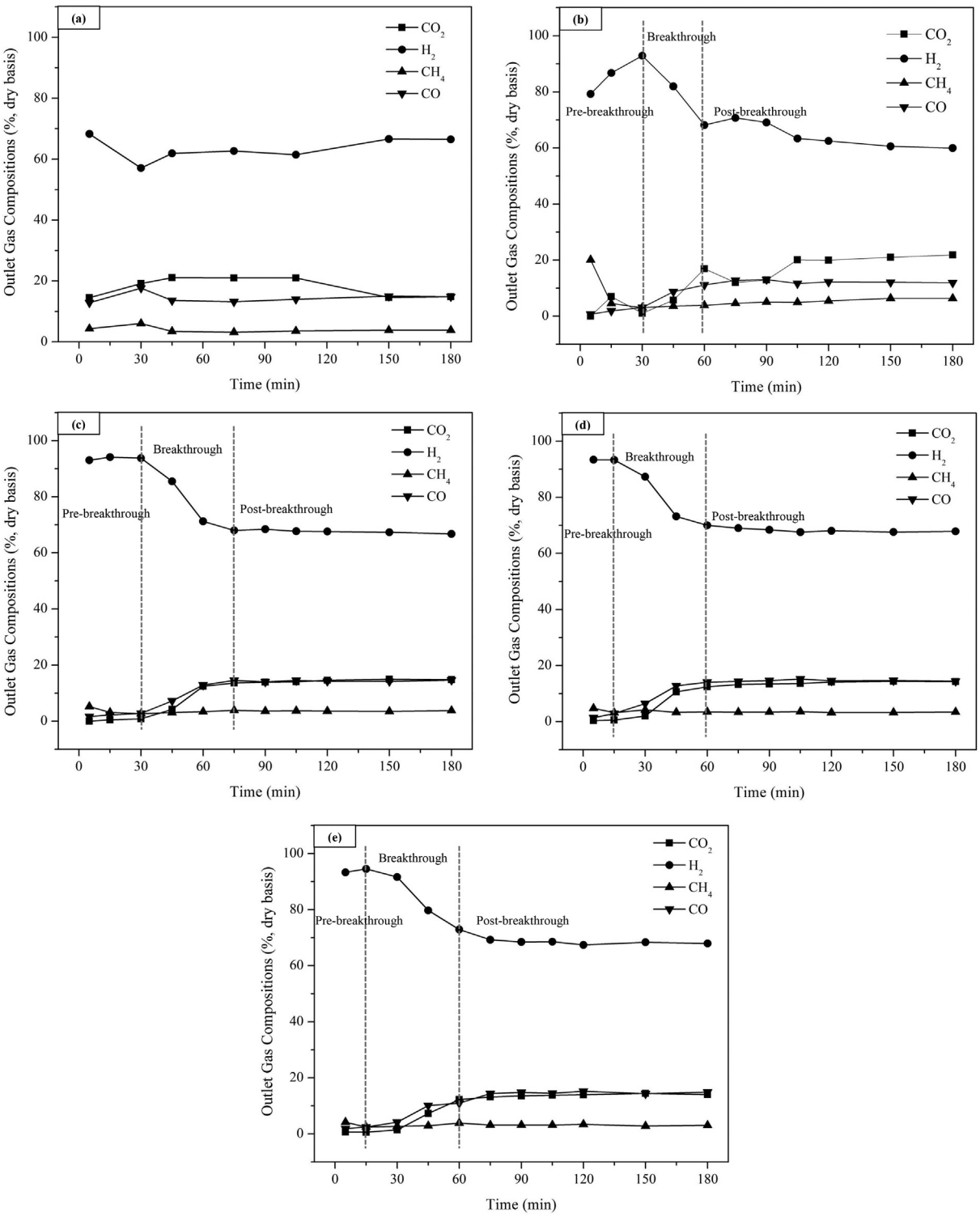

Fig. 7 – Outlet gas compositions of: (a) Ni–Al_2O_3-HW, (b) Ni–CaO-HW, (c) Ni–Al–CaO-HW, (d) Ni–Al–CaO-HWO and (e) Ni–Al–CaO-HWC.

Please cite this article in press as: Phromprasit J, et al., Activity and stability performance of multifunctional catalyst (Ni/CaO and Ni/$Ca_{12}Al_{14}O_{33}$–CaO) for bio-hydrogen production from sorption enhanced biogas steam reforming, International Journal of Hydrogen Energy (2016), http://dx.doi.org/10.1016/j.ijhydene.2016.03.125

multifunctional catalyst. The samples were tested in a fixed bed quartz reactor connected to a mass spectrometer to analyze gaseous products (H_2 and N_2) at the outlet stream. For each experiment, 0.5 g sample was packed in the reactor supported by quartz wool. The sample was pretreated at 850 °C for 30 min under N_2 flow to remove water and other contaminants before performing the experiment. TPR profile was recorded by heating the samples from 30 to 900 °C at a heating rate of 10 °C/min under 10% v/v H_2/N_2 flowing at 50 mL/min.

CO_2 sorption/desorption test

Sorption/desorption tests were performed in a fixed bed quartz reactor (15 mm inner diameter, 18 mm outer diameter and 500 mm length). One gram of modified sorbent (Ni–CaO-HW or Al–CaO-HW) was sandwiched between quartz wool in the fixed bed quartz reactor. The sorbents were pretreated at 850 °C for 30 min under flowing N_2 before running an experiment. To test the ability of CO_2 sorption, 15% v/v CO_2 concentration (balanced N_2) was fed to the reactor with a total flow rate of 60 mL/min at 600 °C and 1 atm. Outlet gas products were collected and analyzed by the mass spectrometer.

H_2 production

For each experiment, two grams of catalyst (Ni–CaO-HW, Ni–Al_2O_3-HW, Ni–Al–CaO-HW, Ni–Al–CaO-HWO and Ni–Al–CaO-HWC) was filled in the fixed bed reactor, which was supported by quartz wool. The catalyst was pretreated at 850 °C for 30 min under 100% N_2 flow and then reduced by 10% H_2 (balanced N_2) at 850 °C for 1 h. The temperature was thereafter decreased to the reaction temperature of 600 °C. The simulated biogas composition used in this work had a CH_4:CO_2 molar ratio of 3:2 [68]. The operating conditions were: steam to methane molar ratio (S/C) of 3:1 (18 mL/min of steam and 6 mL/min of methane balanced with 22 mL/min of N_2); a total flow rate of 50 mL/min; a temperature of 600 °C and a pressure of 1 atm. The product gas compositions were measured by gas chromatography (GC-8A, SHIMADZU) equipped with two columns – Molecular Sieve 5A and PoraPLOT Q.

Results and discussion

CO_2 sorption/desorption testing

The performance of CaO as a sorbent in H_2 production was improved by incorporation of metal ions to enhance stability of the sorbent. In this section, the modified sorbents, Ni–CaO-HW and Al–CaO-HW, were tested for CO_2 sorption/desorption for 10 cycles. The results shown in Fig. 1 indicate that the CO_2 sorption capacity increases from 0.275 $g_{CO_2}/g_{sorbent}$ and 0.238 $g_{CO_2}/g_{sorbent}$ in the 1st cycle to 0.287 $g_{CO_2}/g_{sorbent}$ and 0.242 $g_{CO_2}/g_{sorbent}$ in the 2nd cycle for Ni–CaO-HW and Al–CaO-HW, respectively. After the 2nd cycle, the CO_2 sorption capacities slightly decreases to 0.276 $g_{CO_2}/g_{sorbent}$ and 0.227 $g_{CO_2}/g_{sorbent}$ in the 10th cycle for Ni–CaO-HW and Al–CaO-HW, respectively.

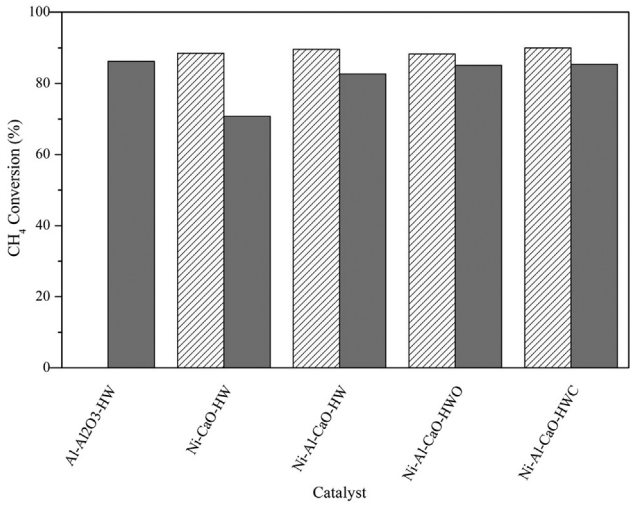

Fig. 8 – CH_4 conversions of Ni–Al_2O_3-HW, Ni–CaO-HW, Ni–Al–CaO-HW, Ni–Al–CaO-HWO and Ni–Al–CaO-HWC (▨ refers the pre-breakthrough period and ▬ refers the post-breakthrough period).

The reason for the increase in CO_2 sorption capacity observed for the 2nd cycle is not yet clear; however, this behavior is in agreement with other literature data reported [34,69,70]. After 10 cycle tests, the CO_2 sorption capacity decreases slightly by about 3.8% for Ni–CaO-HW and 6.4% for Al–CaO-HW, which is significantly less than that of CaO of which the sorption capacity decreases by 37% as reported by Phromprasit et al. [71]. However, the slight decrease of CO_2 sorption capacity observed with Ni–CaO-HW and Al–CaO-HW is likely caused by partial densification of $CaCO_3$ as evidenced in Fig. 2, resulting in pore closure [32], surface area reduction [31] and an increase of intraparticle diffusion resistance [34].

As supported by the SEM images, the BET surface area analysis results show a decrease in surface area between the 1st and the 10th cycles (30.7 and 15.1 m^2/g (fresh sorbent) to 17.1 and 12.43 m^2/g (used sorbent) for Ni–CaO-HW and Al–CaO-HW, respectively). CO_2 sorption capacity of Ni–CaO-HW is higher than that of Al–CaO-HW and this is due to a higher content of CaO as Ni–CaO-HW consists of separate phases of NiO and CaO while Al–CaO-HW shows complex phases of $Ca_{12}Al_{14}O_{33}$ and CaO as evidenced by XRD results depicted in Fig. 3. There was not significant difference in crystallite sizes for the fresh and used CaO 46.6 nm and

Table 3 – XPS analysis results of the multifunctional catalysts.

Sample	Binding energy of Ni (eV)	Atomic concentration of elements on surface (%)			
		Ni 2p	O 1s	Ca 2p	Al 2p
Ni–CaO-HW	854.8	1.99	84.67	13.34	–
Ni–CaO-HW (Used)	853.1	0.49	89.56	9.39	–
	854.7	0.56			
Ni–Al–CaO-HW	854.6	2.56	82.54	11.55	3.35
Ni–Al–CaO-HWO	856.4	2.04	80.87	11.70	5.39
Ni–Al–CaO-HWC	857.2	2.89	80.83	10.10	6.18

Please cite this article in press as: Phromprasit J, et al., Activity and stability performance of multifunctional catalyst (Ni/CaO and Ni/$Ca_{12}Al_{14}O_{33}$–CaO) for bio-hydrogen production from sorption enhanced biogas steam reforming, International Journal of Hydrogen Energy (2016), http://dx.doi.org/10.1016/j.ijhydene.2016.03.125

50.9 nm for fresh Ni–CaO-HW and used Ni–CaO-HW, respectively, and 54.0 nm and 50.5 nm for fresh and used Al–CaO-HW. It is believed that the decrease in the sorption capacities was caused by partial densification of particles as confirmed by SEM–EDS images (Fig. 4).

H_2 production

As shown in Section Introduction, both NiO and $Ca_{12}Al_{14}O_{33}$ can enhance the stability of CaO sorbent for high-temperature CO_2 sorption. As a consequence, the incorporation of metal ions into CaO was further tested for the sorption enhanced steam reforming process in this section.

XRD patterns of different catalytic sorbents shown in Fig. 5 reveal that the addition of Ni^{2+} results in Ni–CaO-HW and Ni–Al_2O_3-HW possessing separate phases of NiO, CaO and $Ca(OH)_2$ in the case of Ni–CaO-HW, and NiO and Al_2O_3 in the case of Ni–Al_2O_3-HW. On the other hand, a complex phase of $Ca_{12}Al_{14}O_{33}$ was formed in the presence of CaO and NiO when Al^{3+} ions were added into CaO as observed with Ni–Al–CaO-HW, Ni–Al–CaO-HWO and Ni–Al–CaO-HWC. Note that the observed $Ca(OH)_2$ phase was plausibly formed when CaO is exposed to atmospheric moisture. The crystallite size of CaO for all samples did not differ significantly (46–51 nm) as shown in Table 2. Ni–Al–CaO-HW, Ni–Al–CaO-HWO and Ni–Al–CaO-HWC possess lower BET surface areas than Ni–CaO-HW, which could be explained by the presence of Al^{3+} in the CaO leading to the blockage of pores, resulting in reduced surface area and pore volume. Furthermore, Ni–Al–CaO-HWC exhibits a lower surface area than that of Ni–Al–CaO-HW and Ni–Al–CaO-HWO. This result is plausibly caused by the sequence of Ni^{2+} loading after formation of the modified sorbent ($Ca_{12}Al_{14}O_{33}$).

The reducibility of the multifunctional catalysts, which were synthesized by hydration followed by wet mixing, was tested by temperature program reduction (TPR) as shown in Fig. 6. Ni–CaO-HW and Ni–Al–CaO-HW, which were fabricated in only a single synthesis step, show two peaks including (i) small peak at 560 °C, which could be a result of free NiO reduction [72], and (ii) larger peak at 720 °C, which could be attributed to Ni–Ca oxide interactions. Ni–Al–CaO-HWO and Ni–Al–CaO-HWC – fabricated in two synthesis steps – show only a single peak at 760 °C, which is probably due to the spinel phase of $NiAl_2O_4$ [72]. According to the results, Ni–Al–CaO-HWO and Ni–Al–CaO-HWC are more difficult to be reduced than Ni–CaO-HW and Ni–Al–CaO-HW, which implies that NiO–$Ca_{12}Al_{14}O_{33}$ interactions formed by the two-step synthesis are stronger than that of NiO–⊕ $Ca_{12}Al_{14}O_{33}$ or NiO–CaO interactions synthesized in a single step. A reduction temperature of 850 °C, which is higher than the highest peak temperature, was therefore chosen to ensure the complete reduction of Ni with 10% v/v H_2 in N_2.

Commercial catalyst Ni–Al_2O_3-HW was tested for use in hydrogen production via biogas steam reforming as a base case as shown in Fig. 7(a). The results show that approximately 67% hydrogen purity (Fig. 7(a)) and 88% CH_4 conversion (Fig. 8) were achieved. Fig. 7(b) shows the performance of Ni–CaO-HW for sorption enhanced biogas steam reforming. The results show that during the pre-breakthrough period the hydrogen purity increases from 79% to 93%, and after a further

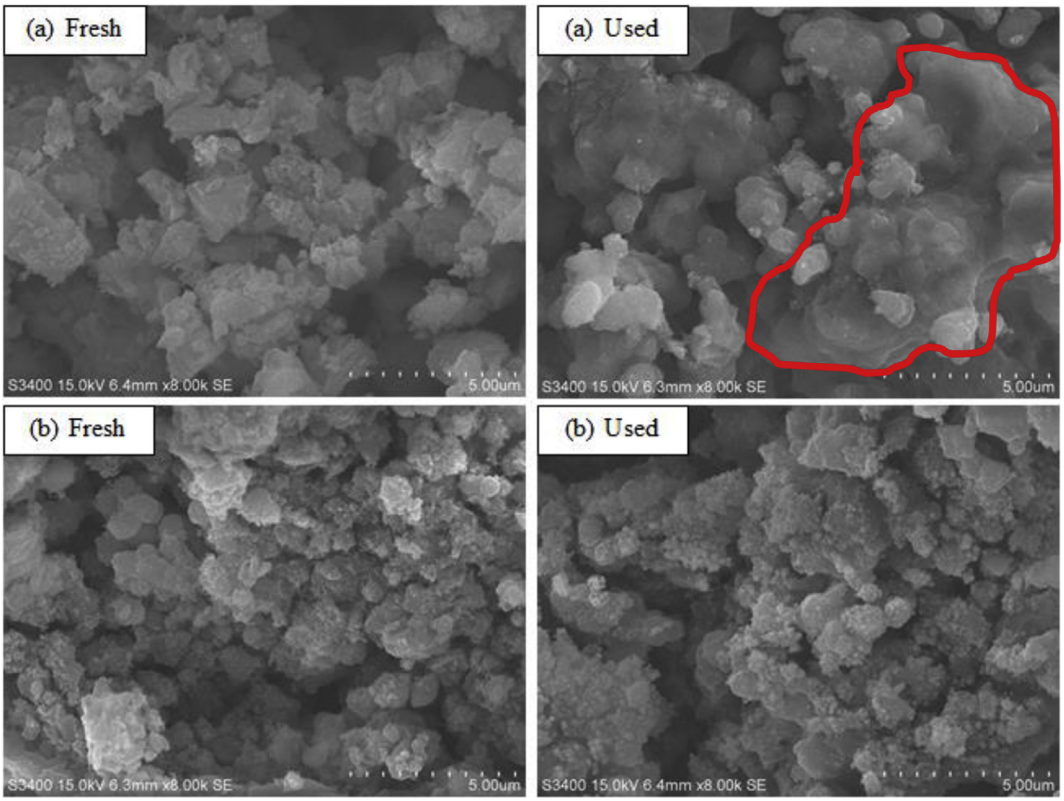

Fig. 9 – SEM images of multifunctional catalysts: (a) Ni–CaO-HW and (b) Ni–Al–CaO-HW.

Please cite this article in press as: Phromprasit J, et al., Activity and stability performance of multifunctional catalyst (Ni/CaO and Ni/$Ca_{12}Al_{14}O_{33}$–CaO) for bio-hydrogen production from sorption enhanced biogas steam reforming, International Journal of Hydrogen Energy (2016), http://dx.doi.org/10.1016/j.ijhydene.2016.03.125

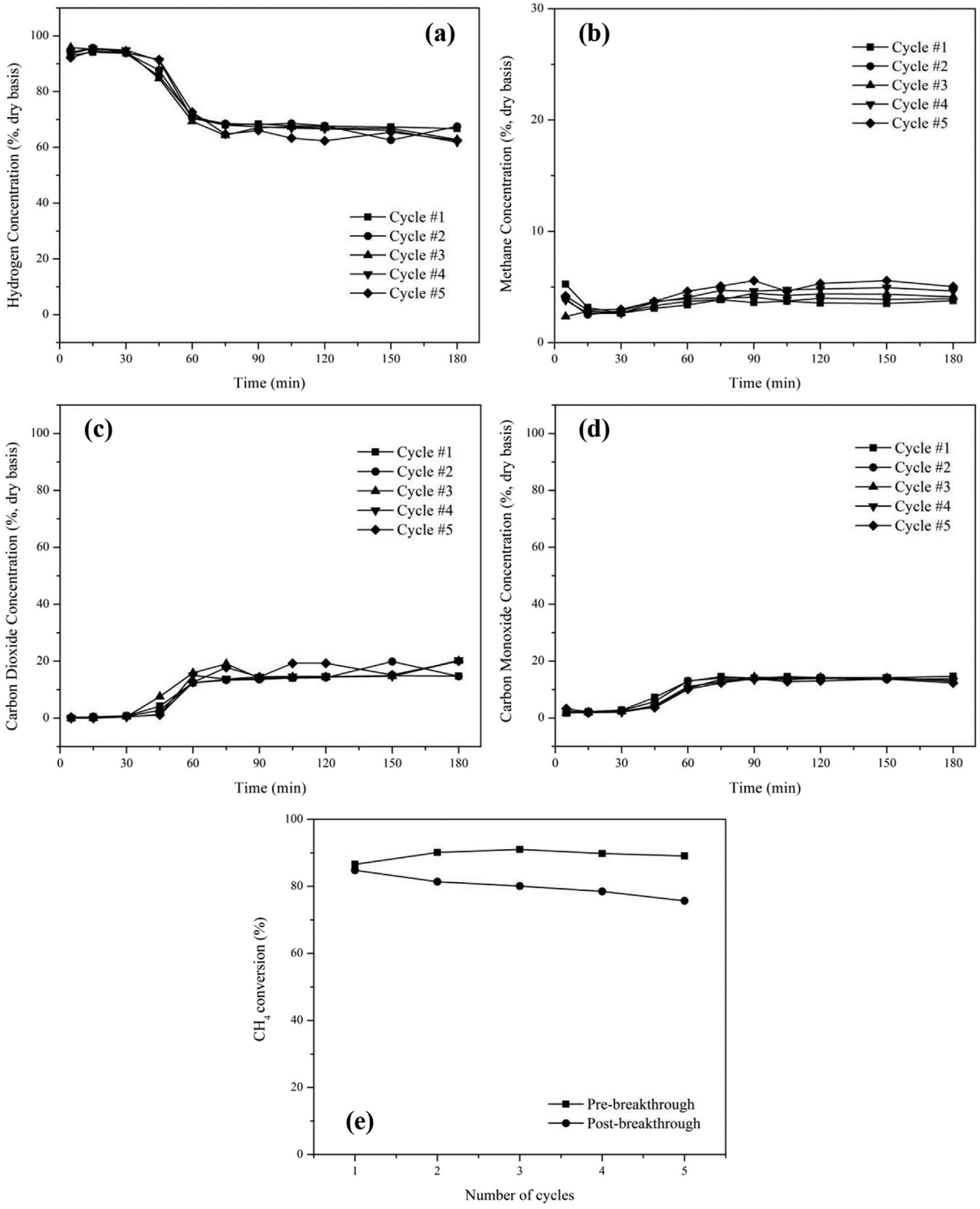

Fig. 10 – Gas product compositions and CH_4 conversion of Ni–Al–CaO-HW sample: (a) hydrogen concentration, (b) methane concentration, (c) carbon dioxide concentration, (d) carbon monoxide concentration and (e) CH_4 conversion.

30 min the CH_4 conversion was 91% as shown in Fig. 8. As the reaction time progressed, CaO sorbent was gradually converted into $CaCO_3$ due to the reaction with CO_2, leading to an increase of CO_2 concentration and hence a decrease of H_2 concentration in the product stream. After that, the H_2 purity dropped to equilibrium in the breakthrough period (approx. 68% H_2 purity and 87% CH_4 conversion at 60 min). The Ni–CaO-HW performance decreased with (i) H_2 purity dropping to 60% at 180 min and (ii) CH_4 conversion decreasing to 78% at 180 min. This is plausible because the catalyst lost its active sites as confirmed by XPS results shown in Table 3. The concentration of Ni at the surface decreased from 1.99% on the

Please cite this article in press as: Phromprasit J, et al., Activity and stability performance of multifunctional catalyst (Ni/CaO and Ni/$Ca_{12}Al_{14}O_{33}$–CaO) for bio-hydrogen production from sorption enhanced biogas steam reforming, International Journal of Hydrogen Energy (2016), http://dx.doi.org/10.1016/j.ijhydene.2016.03.125

Table 4 – XPS analysis results of Ni-Al-CaO-HW catalyst.

Sample	Binding energy of Ni (eV)	Atomic concentration of elements on surface (%)			
		Ni 2p	O 1s	Ca 2p	Al 2p
Fresh	854.6	2.56	82.54	11.55	3.35
Used (1st cycle)	852.8	0.44	83.64	9.16	4.84
	856.4	1.92			
Used (5th cycle)	853.1	0.43	83.69	10.22	4.64
	855.7	1.02			

fresh catalyst (the binding energy of 854.8 eV indicated the formation of NiO) to 1.05% on the used catalyst (0.46% Ni and 0.56% NiO). The decrease in the number of active sites is plausible because a result of pore closure due to the formation of $CaCO_3$, confirmed by SEM images (Fig. 9). Fig. 9(a) suggests that $CaCO_3$ expansion is caused by densification resulting in the loss of active sites (Ni).

Al^{3+} ion is used to dope CaO in order to improve the thermal stability by the formation of an inert phase ($Ca_{12}Al_{14}O_{33}$). The sequence of Ni loading on to CaO to produce the modified sorbent ($Ca_{12}Al_{14}O_{33}$–CaO) was tested in order to investigate the effect on sorbent and hydrogen production performances. Fig. 7(c) and Fig. 8 show the performance of Ni–Al–CaO-HW on H_2 purity and CH_4 conversion. The results show that 94% H_2 purity and 90% CH_4 conversion could be obtained during the pre-breakthrough period. The pre-breakthrough time was 30 min, indicating that Ni–Al–CaO-HW can absorb CO_2 for 30 min. After that, CO_2 concentrations increases and remains constant in the post-breakthrough period. Meanwhile, H_2 purity decreased after 30 min (breakthrough) and remained constant at 68% after the breakthrough period. The steady H_2 and CO_2 concentrations in the post-breakthrough period suggested that the sorbent can retain its original morphology as shown in Fig. 9(b). Furthermore, the Ni–Al–CaO-HW result shows an increase in H_2 purity of 26% and an increase in CH_4 conversion of 5% between the pre-breakthrough and the post-breakthrough period.

In the case of Ni–Al–CaO-HWO, 93% H_2 purity can be obtained (Fig. 7(d)) and the CH_4 conversion of 88% (Fig. 8) was achieved in the pre-breakthrough period. The pre-breakthrough time of Ni–Al–CaO-HWO (15 min) was lower than that of Ni–Al–CaO-HW (30 min). Hence Ni–Al–CaO-HWO has a poorer CO_2 sorption performance than Ni–Al–CaO-HW. Previously, the XRD results indicated the formation of $Ca_{12}Al_{14}O_{33}$ phase in the presence of Al^{3+}. The higher atomic concentration of Al at the surface of Ni–Al–CaO-HWO (Table 3) therefore suggests the presence of the inert phase ($Ca_{12}Al_{14}O_{33}$) is higher than that of Ni–Al–CaO-HW, resulting in reduced CO_2 sorption performance.

The performances of Ni–Al–CaO-HWC are shown in Fig. 7(e) and Fig. 8. The H_2 purity of 92% and CH_4 conversion of 90% were achieved in the pre-breakthrough period. The pre-breakthrough time of Ni–Al–CaO-HWC (15 min) is lower than that of Ni–Al–CaO-HW for the same reasons discussed in the case of Ni–Al–CaO-HWO.

It is suggested that the best sequence for loading Ni^{2+} on a modified sorbent ($Ca_{12}Al_{14}O_{33}$) is the single-step synthesis method, used to produce Ni–Al–CaO-HW. Low concentration of Al atomic at the surface, which indicates that Al can well disperse in the bulk of CaO, leads to the best CO_2 sorption performance. This performance is also confirmed by the longer pre-breakthrough period of Ni–Al–CaO-HW when compared with other samples. From these results, we therefore extended the investigation of the catalytic sorbent performance of Ni–Al–CaO-HW for the production of hydrogen under multiple cycles.

Stability of multifunctional catalyst

The stability of the multifunctional catalyst Ni–Al–CaO-HW over 5 cycles of bio-hydrogen production produced by sorption enhanced biogas steam reforming is shown in Fig. 10. The results show that H_2 purity and CH_4 conversion can be maintained at about 94% and 90% in the pre-breakthrough

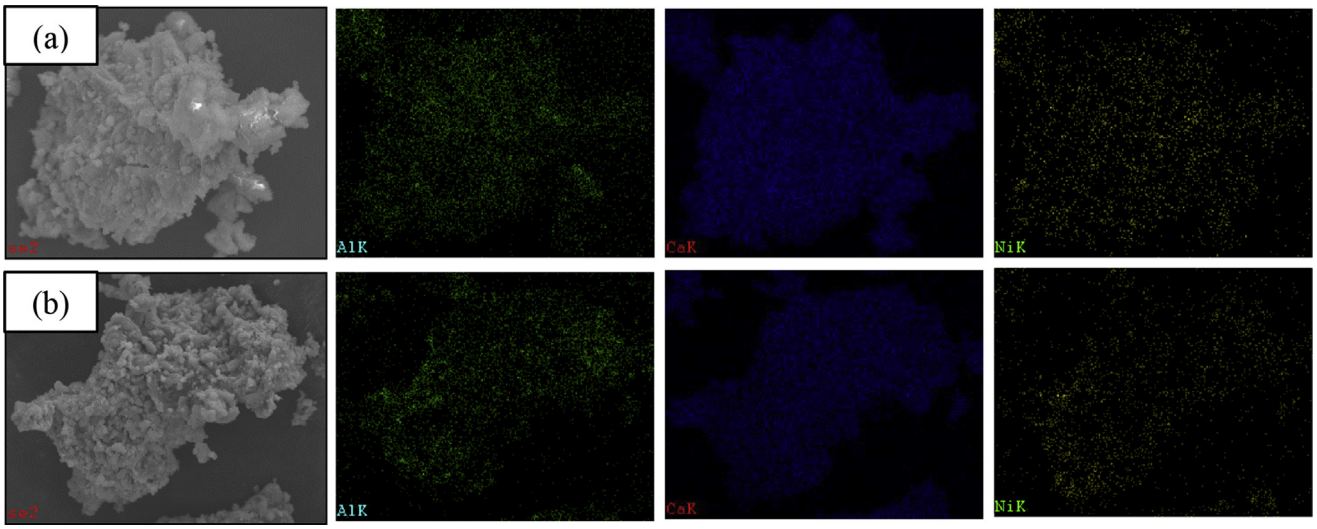

Fig. 11 – SEM–EDS images of Ni–Al–CaO-HW: (a) fresh and (b) used catalyst.

Please cite this article in press as: Phromprasit J, et al., Activity and stability performance of multifunctional catalyst (Ni/CaO and Ni/$Ca_{12}Al_{14}O_{33}$–CaO) for bio-hydrogen production from sorption enhanced biogas steam reforming, International Journal of Hydrogen Energy (2016), http://dx.doi.org/10.1016/j.ijhydene.2016.03.125

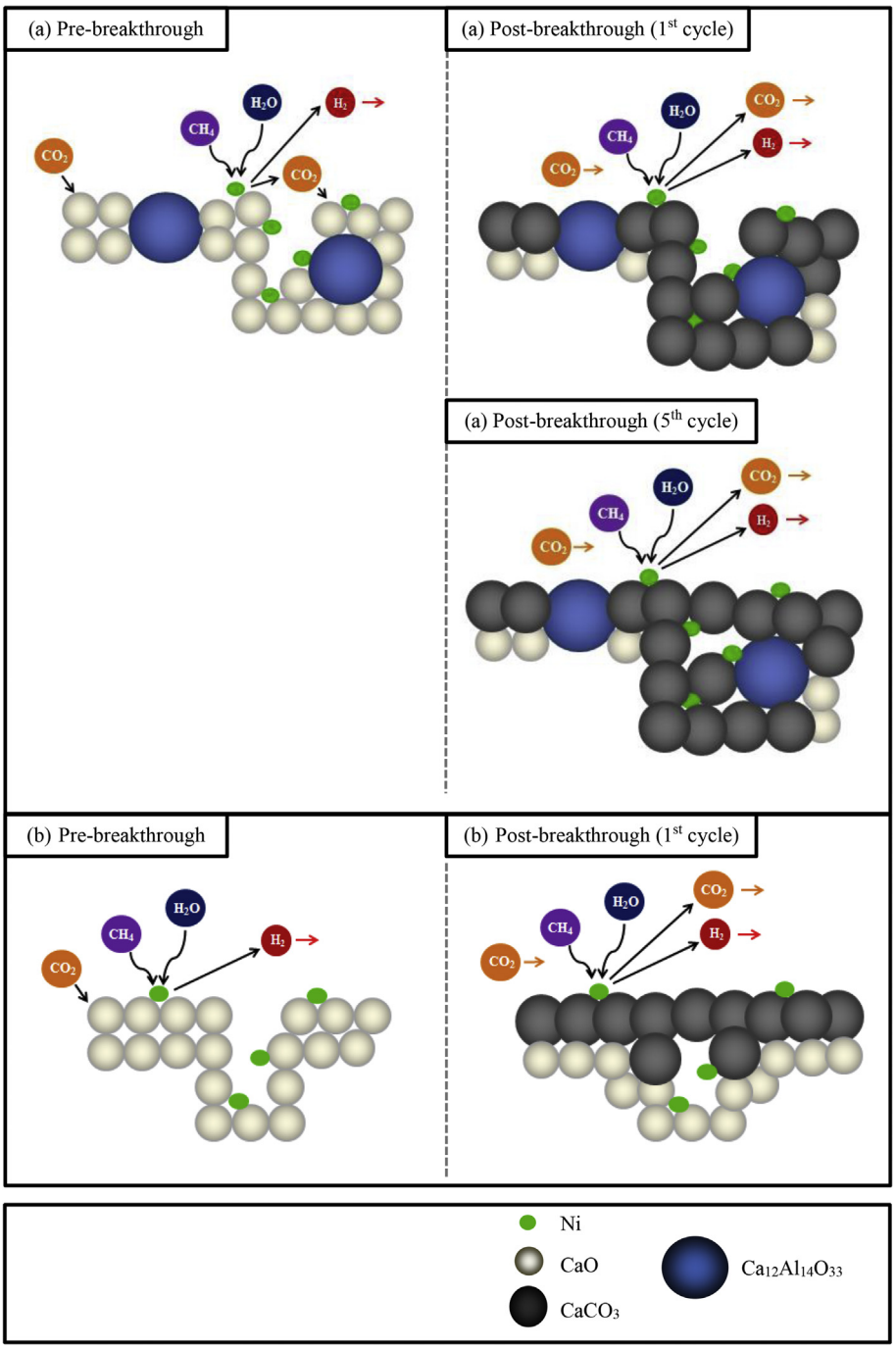

Fig. 12 – Schematic diagram of our proposes sorption enhanced H_2 production mechanism of (a) Ni–Al–CaO-HW and (b) Ni–CaO-HW at pre-breakthrough and post-breakthrough periods.

period, respectively. However, during the post-breakthrough period, H_2 purity and CH_4 conversion decreases from 68% (1st cycle) to 64% (5th cycle) and from 85% (1st cycle) to 75% (5th cycle), respectively. A plausible explanation for the reduction of H_2 purity and CH_4 conversion in the post-breakthrough period is the formation of $CaCO_3$, which leads to pore blockage, reducing the number of active sites as indicated by the XPS results shown in Table 4. The binding energy of 854.6 eV for the fresh catalyst indicated that 2.56% of the atomic concentration of Ni at the surface is in the form of NiO. According to XPS results, after the 1st and the 5th cycles, the used catalysts contained two Ni species, one at (i) 852–853 eV attributed to metallic Ni and another at (ii) 855–856 eV attributed to $NiAl_2O_4$. These results suggested that the total concentration of Ni was reduced as the number of sorption/desorption cycles increases (2.56% Ni from the fresh catalyst decreased to 2.36 and 1.45% after the 1st cycle and the 5th cycle, respectively).

Please cite this article in press as: Phromprasit J, et al., Activity and stability performance of multifunctional catalyst (Ni/CaO and Ni/$Ca_{12}Al_{14}O_{33}$–CaO) for bio-hydrogen production from sorption enhanced biogas steam reforming, International Journal of Hydrogen Energy (2016), http://dx.doi.org/10.1016/j.ijhydene.2016.03.125

As shown above from our results that Ni–Al–CaO-HW provides a good performance for sorption enhanced hydrogen production from biogas both in terms of catalytic/sorption performance and stability. This might be due to well dispersed Al in the multifunctional catalyst as shown in Fig. 11, which results in high CO_2 sorption capacity and stability. We proposed here the mechanism of H_2 production with the use of Ni–Al–CaO-HW with the comparison to the case of Ni–CaO-HW as shown in Fig. 12. For Ni–Al–CaO-HW (Fig. 12(a) pre-breakthrough), CH_4 and H_2O feed are adsorbed at the surface of Ni site and produced H_2 and CO_2 while CaO absorbs CO_2 both from the feed stream and from the steam reforming reaction enhancing hydrogen production yield and also high purity of H_2 in the product stream. Hydrogen production was found to decrease in the post-breakthrough period due to part of the sorbent CaO has interacted with CO_2 and formed inactive phase of $CaCO_3$ as shown in Fig. 12(a) post-breakthrough (1st cycle). At this stage, the concentration of H_2 in the product stream can be maintained for a long period of time because the densification and pore closure are inhibited by inert phase ($Ca_{12}Al_{14}O_{33}$). However, slight reduction of H_2 production over 5-cycle reused is attributed to partial densification of sorbents leading to the hindrance of Ni active site as shown in Fig. 12(a) post-breakthrough (5th cycle). The good impact of adding metal into catalytic sorbent Ni–Al–CaO-HW is compared with that without metal Ni–CaO-HW as pictured in Fig. 12(b), where lower H_2 production performance was obtained due to densification effect of $CaCO_3$.

Conclusion

This work studied the effect of the metal ion loading sequence on the H_2 production performance. Firstly, modified sorbents (NiO–CaO and $Ca_{12}Al_{14}O_{33}$–CaO) were synthesized by hydration of CaO followed by an incorporation of metal ion using wet mixing method and the sorbents were tested for CO_2 sorption performances up to 10 cycles at 600 °C. Our results reveal that the sorption capacity reduces by only 3.8% and 6.4% for Ni–CaO-HW and Al–CaO-HW, respectively. The SEM–EDS images indicated a smaller decrease in the CO_2 sorption capacity for multiple cycle testing is due to partial densification of both modified sorbents. Secondly, sequences of Ni^{2+} loading on modified CaO were studied for bio-hydrogen production from sorption enhanced biogas steam reforming. Three sequences of Ni^{2+} loading on modified CaO were investigated: (i) simultaneous adding Ni^{2+} and Al^{3+} into CaO solution (Ni–Al–CaO-HW), (ii) adding Ni^{2+} after drying the modified sorbent (Ni–Al–CaO-HWO) and (iii) adding Ni^{2+} after calcination the modified sorbent (Ni–Al–CaO-HWC). The results show that the sorbent synthesized by loading Ni^{2+} and Al^{3+} simultaneously (Ni–Al–CaO-HW) is the best catalytic sorbent for H_2 production as the longest pre-breakthrough time (30 min) could be obtained. Nevertheless, H_2 purity and CH_4 conversion are not significantly different when compared to other samples (94% H_2 purity and 90% CH_4 conversion in the pre-breakthrough period). The stability of Ni–Al–CaO-HW in the production of H_2 was tested over 5 cycles. The results show that CH_4 conversion is still higher than 90% during the pre-breakthrough period for 5 cycle operations. However, during the post-breakthrough period the CH_4 conversion decreases slightly from 85% to 75% at 1st to 5th cycle, respectively. The plausible explanation is due to the reduction of Ni concentration at the surface of the catalyst (Ni concentration at surface of 1.93% after 1st cycle and of 1.02% after 5th cycle) caused from pore blockage by $CaCO_3$.

Acknowledgment

This work is financially supported by Ratchadaphiseksomphot Endowment Fund of Chulalongkorn University (RES560530168-EN) and the Thailand Research Fund. The authors also would like to acknowledge the Royal Golden Jubilee PhD Program from the Thailand Research Fund and Chulalongkorn University. Department of Chemical Engineering, Faculty of Engineering, Chulalongkorn University also would like to acknowledge the support from the Thailand Research Fund under the Institutional Research Grant IRG 5780014 and Chulalongkorn University Contract No. RES_57_411_21_076.

REFERENCES

[1] Brabec CJ, Sariciftci NS, Hummelen JC. Plastic solar cells. Adv Funct Mater 2001;11:15–26.
[2] Huynh WU, Dittmer JJ, Alivisatos AP. Hybrid nanorod-polymer solar cells. Science 2002;295:2425–7.
[3] Hagfeldt A, Boschloo G, Sun L, Kloo L, Pettersson H. Dye-sensitized solar cells. Chem Rev 2010;110:6595–663.
[4] Müller S, Deicke M, De Doncker RW. Doubly fed induction generator systems for wind turbines. IEEE Ind Appl Mag 2002;8:26–33.
[5] Chen Z, Guerrero JM, Blaabjerg F. A review of the state of the art of power electronics for wind turbines. IEEE Trans Power Electron 2009;24:1859–75.
[6] Kreuer KD. On the development of proton conducting polymer membranes for hydrogen and methanol fuel cells. J Membr Sci 2001;185:29–39.
[7] Wang C-Y. Fundamental models for fuel cell engineering. Chem Rev 2004;104:4727–65.
[8] Zhang J, Xie Z, Zhang J, Tang Y, Song C, Navessin T, et al. High temperature PEM fuel cells. J Power Sources 2006;160:872–91.
[9] Jang HM, Lee KB, Caram HS, Sircar S. High-purity hydrogen production through sorption enhanced water gas shift reaction using K_2CO_3-promoted hydrotalcite. Chem Eng Sci 2012;73:431–8.
[10] Johnsen K, Ryu HJ, Grace JR, Lim CJ. Sorption-enhanced steam reforming of methane in a fluidized bed reactor with dolomite as CO_2-acceptor. Chem Eng Sci 2006;61:1195–202.
[11] Bretado ME, Velderrain VG, Gutiérrez DL, Collins-Martínez V, Ortiz AL. A new synthesis route to Li_4SiO_4 as CO_2 catalytic/sorbent. Catal Today 2005;107–108:863–7.
[12] Ochoa-Fernández E, Rusten HK, Jakobsen HA, Rønning M, Holmen A, Chen D. Sorption enhanced hydrogen production by steam methane reforming using Li_2ZrO_3 as sorbent: sorption kinetics and reactor simulation. Catal Today 2005;106:41–6.
[13] Olivares-Marín M, Drage TC, Maroto-Valer MM. Novel lithium-based sorbents from fly ashes for CO_2 capture at high temperatures. Int J Greenh Gas Control 2010;4:623–9.

Please cite this article in press as: Phromprasit J, et al., Activity and stability performance of multifunctional catalyst (Ni/CaO and Ni/$Ca_{12}Al_{14}O_{33}$–CaO) for bio-hydrogen production from sorption enhanced biogas steam reforming, International Journal of Hydrogen Energy (2016), http://dx.doi.org/10.1016/j.ijhydene.2016.03.125

[14] Guo L, Wang X, Zhong C, Li L. Synthesis and CO_2 capture property of high aspect-ratio Li_2ZrO_3 nanotubes arrays. Appl Surf Sci 2011;257:8106–9.
[15] Xiao Q, Tang X, Liu Y, Zhong Y, Zhu W. Citrate route to prepare K-doped Li_2ZrO_3 sorbents with excellent CO_2 capture properties. Chem Eng J 2011;174:231–5.
[16] Shan S, Jia Q, Jiang L, Li Q, Wang Y, Peng J. Novel Li_4SiO_4-based sorbents from diatomite for high temperature CO_2 capture. Ceram Int 2013;39:5437–41.
[17] López Ortiz A, Escobedo Bretado MA, Guzmán Velderrain V, Meléndez Zaragoza M, Salinas Gutiérrez J, Lardizábal Gutiérrez D, et al. Experimental and modeling kinetic study of the CO_2 absorption by Li_4SiO_4. Int J Hydrogen Energy 2014;39:16656–66.
[18] Wang K, Zhao P, Guo X, Li Y, Han D, Chao Y. Enhancement of reactivity in Li_4SiO_4-based sorbents from the nano-sized rice husk ash for high-temperature CO_2 capture. Energy Convers Manage 2014;81:447–54.
[19] Oliveira ELG, Grande CA, Rodrigues AE. CO_2 sorption on hydrotalcite and alkali-modified (K and Cs) hydrotalcites at high temperatures. Sep Purif Technol 2008;62:137–47.
[20] Hanif A, Dasgupta S, Divekar S, Arya A, Garg MO, Nanoti A. A study on high temperature CO_2 capture by improved hydrotalcite sorbents. Chem Eng J 2014;236:91–9.
[21] Bhatta LKG, Subramanyam S, Chengala MD, Olivera S, Venkatesh K. Progress in hydrotalcite like compounds and metal-based oxides for CO_2 capture: a review. J Clean Prod 2015;103:171–96.
[22] Pramod CV, Upendar K, Mohan V, Sarma DS, Dhar GM, Prasad PSS, et al. Hydrotalcite-SBA-15 composite material for efficient carbon dioxide capture. J CO_2 Util 2015;12:109–15.
[23] Chen S, Xiang W, Wang D, Xue Z. Incorporating IGCC and CaO sorption-enhanced process for power generation with CO_2 capture. Appl Energy 2012;95:285–94.
[24] Nieto-Sanchez AJ, Olivares-Marin M, Garcia S, Pevida C, Cuerda-Correa EM. Influence of the operation conditions on CO_2 capture by CaO-derived sorbents prepared from synthetic $CaCO_3$. Chemosphere 2013;93:2148–58.
[25] Ridha FN, Manovic V, Wu Y, Macchi A, Anthony EJ. Post-combustion CO_2 capture by formic acid-modified CaO-based sorbents. Int J Greenh Gas Control 2013;16:21–8.
[26] Kazi SS, Aranda A, Meyer J, Mastin J. High performance CaO-based sorbents for pre- and post- combustion CO_2 capture at high temperature. Energy Procedia 2014;63:2207–15.
[27] Radfarnia HR, Sayari A. A highly efficient CaO-based CO_2 sorbent prepared by a citrate-assisted sol–gel technique. Chem Eng J 2015;262:913–20.
[28] Ridha FN, Wu Y, Manovic V, Macchi A, Anthony EJ. Enhanced CO_2 capture by biomass-templated $Ca(OH)_2$-based pellets. Chem Eng J 2015;274:69–75.
[29] Reijers HTJ, Valster-Schiermeier SEA, Cobden PD, van den Brink RW. Hydrotalcite as CO_2 sorbent for sorption-enhanced steam reforming of methane. Ind Eng Chem Res 2006;45:2522–30.
[30] Ochoa-Fernández E, Haugen G, Zhao T, Rønning M, Aartun I, Børresen B, et al. Process design simulation of H_2 production by sorption enhanced steam methane reforming: evaluation of potential CO_2 acceptors. Green Chem 2007;9:654.
[31] Lu H, Khan A, Pratsinis SE, Smirniotis PG. Flame-made durable doped-CaO nanosorbents for CO_2 capture. Energy Fuels 2009;23:1093–100.
[32] Park J, Yi KB. Effects of preparation method on cyclic stability and CO_2 absorption capacity of synthetic CaO–MgO absorbent for sorption-enhanced hydrogen production. Int J Hydrogen Energy 2012;37:95–102.
[33] Radfarnia HR, Iliuta MC. Metal oxide-stabilized calcium oxide CO_2 sorbent for multicycle operation. Chem Eng J 2013;232:280–9.
[34] Martavaltzi CS, Lemonidou AA. Hydrogen production via sorption enhanced reforming of methane: development of a novel hybrid material—reforming catalyst and CO_2 sorbent. Chem Eng Sci 2010;65:4134–40.
[35] Kim J-N, Ko CH, Yi KB. Sorption enhanced hydrogen production using one-body CaO–$Ca_{12}Al_{14}O_{33}$–Ni composite as catalytic absorbent. Int J Hydrogen Energy 2013;38:6072–8.
[36] Feng HZ, Lan PQ, Wu SF. A study on the stability of a NiO–CaO/Al_2O_3 complex catalyst by La_2O_3 modification for hydrogen production. Int J Hydrogen Energy 2012;37:14161–6.
[37] Xie M, Zhou Z, Qi Y, Cheng Z, Yuan W. Sorption-enhanced steam methane reforming by in situ CO_2 capture on a CaO–$Ca_9Al_6O_{18}$ sorbent. Chem Eng J 2012;207–208:142–50.
[38] Radfarnia HR, Iliuta MC. Hydrogen production by sorption-enhanced steam methane reforming process using CaO-Zr/Ni bifunctional sorbent–catalyst. Chem Eng Process Process Intensif 2014;86:96–103.
[39] Sultana KS, Chen D. Enhanced hydrogen production by in situ CO_2 removal on $CaCeZrO_x$ nanocrystals. Catal Today 2011;171:43–51.
[40] Laosiripojana N, Chadwick D, Assabumrungrat S. Effect of high surface area CeO_2 and Ce-ZrO_2 supports over Ni catalyst on CH_4 reforming with H_2O in the presence of O_2, H_2, and CO_2. Chem Eng J 2008;138:264–73.
[41] Oliveira ELG, Grande CA, Rodrigues AE. Methane steam reforming in large pore catalyst. Chem Eng Sci 2010;65:1539–50.
[42] Lee SM, Hong SC. Effect of palladium addition on catalytic activity in steam methane reforming over Ni-YSZ porous membrane. Int J Hydrogen Energy 2014;39:21037–43.
[43] Lee SY, Lim H, Woo HC. Catalytic activity and characterizations of Ni/$K_2Ti_xO_y$–Al_2O_3 catalyst for steam methane reforming. Int J Hydrogen Energy 2014;39:17645–55.
[44] Kim NY, Yang E-H, Lim S-S, Jung JS, Lee J-S, Hong GH, et al. Hydrogen production by steam reforming of methane over mixed Ni/MgAl + $CrFe_3O_4$ catalysts. Int J Hydrogen Energy 2015;40:11848–54.
[45] Nawfal M, Gennequin C, Labaki M, Nsouli B, Aboukaïs A, Abi-Aad E. Hydrogen production by methane steam reforming over Ru supported on Ni–Mg–Al mixed oxides prepared via hydrotalcite route. Int J Hydrogen Energy 2015;40:1269–77.
[46] Yang R-X, Chuang K-H, Wey M-Y. Hydrogen production through methanol steam reforming: effect of synthesis parameters on Ni–Cu/CaO–SiO_2 catalysts activity. Int J Hydrogen Energy 2014;39:19494–501.
[47] Das D, Llorca J, Dominguez M, Colussi S, Trovarelli A, Gayen A. Methanol steam reforming behavior of copper impregnated over CeO_2–ZrO_2 derived from a surfactant assisted coprecipitation route. Int J Hydrogen Energy 2015;40:10463–79.
[48] Deshmane VG, Abrokwah RY, Kuila D. Synthesis of stable Cu-MCM-41 nanocatalysts for H_2 production with high selectivity via steam reforming of methanol. Int J Hydrogen Energy 2015;40:10439–52.
[49] Lytkina AA, Zhilyaeva NA, Ermilova MM, Orekhova NV, Yaroslavtsev AB. Influence of the support structure and composition of Ni–Cu-based catalysts on hydrogen production by methanol steam reforming. Int J Hydrogen Energy 2015;40:9677–84.
[50] Wu YJ, Li P, Yu JG, Cunha AF, Rodrigues AE. Sorption-enhanced steam reforming of ethanol on NiMgAl multifunctional materials: experimental and numerical investigation. Chem Eng J 2013;231:36–48.
[51] Chiou JYZ, Lai CL, Yu S-W, Huang H-H, Chuang C-L, Wang C-B. Effect of Co, Fe and Rh addition on coke deposition over Ni/$Ce_{0.5}Zr_{0.5}O_2$ catalysts for steam reforming of ethanol. Int J Hydrogen Energy 2014;39:20689–99.

Please cite this article in press as: Phromprasit J, et al., Activity and stability performance of multifunctional catalyst (Ni/CaO and Ni/$Ca_{12}Al_{14}O_{33}$–CaO) for bio-hydrogen production from sorption enhanced biogas steam reforming, International Journal of Hydrogen Energy (2016), http://dx.doi.org/10.1016/j.ijhydene.2016.03.125

[52] Wu Y-J, Li P, Yu J-G, Cunha AF, Rodrigues AE. Sorption-enhanced steam reforming of ethanol for continuous high-purity hydrogen production: 2D adsorptive reactor dynamics and process design. Chem Eng Sci 2014;118:83–93.
[53] Bednarczuk L, de la Piscina PR, Homs N. H_2-production from CO_2-assisted ethanol steam reforming: the regeneration of Ni-based catalysts. Int J Hydrogen Energy 2015;40:5256–63.
[54] Ma H, Zeng L, Tian H, Li D, Wang X, Li X, et al. Efficient hydrogen production from ethanol steam reforming over La-modified ordered mesoporous Ni-based catalysts. Appl Catal B 2016;181:321–31.
[55] Ashok J, Kawi S. Steam reforming of toluene as a biomass tar model compound over CeO_2 promoted Ni/CaO–Al_2O_3 catalytic systems. Int J Hydrogen Energy 2013;38:13938–49.
[56] Ashok J, Kathiraser Y, Ang ML, Kawi S. Bi-functional hydrotalcite-derived NiO–CaO–Al_2O_3 catalysts for steam reforming of biomass and/or tar model compound at low steam-to-carbon conditions. Appl Catal B 2015;172–173:116–28.
[57] Gao N, Liu S, Han Y, Xing C, Li A. Steam reforming of biomass tar for hydrogen production over NiO/ceramic foam catalyst. Int J Hydrogen Energy 2015;40:7983–90.
[58] Zamboni I, Zimmermann Y, Kiennemann A, Courson C. Improvement of steam reforming of toluene by CO_2 capture using Fe/CaO–$Ca_{12}Al_{14}O_{33}$ bi-functional materials. Int J Hydrogen Energy 2015;40:5297–304.
[59] Oh G, Park SY, Seo MW, Kim YK, Ra HW, Lee J-G, et al. Ni/Ru–Mn/Al_2O_3 catalysts for steam reforming of toluene as model biomass tar. Renew Energy 2016;86:841–7.
[60] Phromprasit J, Powell J, Arpornwichanop A, Rodrigues A, Assabumrungrat S. Hydrogen production from sorption enhanced biogas steam reforming using nickel-based catalysts. Eng J 2013;17:19–34.
[61] Assabumrungrat S, Sonthisanga P, Kiatkittipong W, Laosiripojana N, Arpornwichanop A, Soottitantawat A, et al. Thermodynamic analysis of calcium oxide assisted hydrogen production from biogas. J Ind Eng Chem 2010;16:785–9.
[62] Ahmed S, Lee SHD, Ferrandon MS. Catalytic steam reforming of biogas – effects of feed composition and operating conditions. Int J Hydrogen Energy 2015;40:1005–15.
[63] Appari S, Janardhanan VM, Bauri R, Jayanti S. Deactivation and regeneration of Ni catalyst during steam reforming of model biogas: an experimental investigation. Int J Hydrogen Energy 2014;39:297–304.
[64] Italiano C, Vita A, Fabiano C, Laganà M, Pino L. Bio-hydrogen production by oxidative steam reforming of biogas over nanocrystalline Ni/CeO_2 catalysts. Int J Hydrogen Energy 2015;40:11823–30.
[65] Alves HJ, Bley Junior C, Niklevicz RR, Frigo EP, Frigo MS, Coimbra-Araújo CH. Overview of hydrogen production technologies from biogas and the applications in fuel cells. Int J Hydrogen Energy 2013;38:5215–25.
[66] Kolbitsch P, Pfeifer C, Hofbauer H. Catalytic steam reforming of model biogas. Fuel 2008;87:701–6.
[67] Kohn MP, Castaldi MJ, Farrauto RJ. Biogas reforming for syngas production: the effect of methyl chloride. Appl Catal B 2014;144:353–61.
[68] Izquierdo U, Barrio VL, Requies J, Cambra JF, Güemez MB, Arias PL. Tri-reforming: a new biogas process for synthesis gas and hydrogen production. Int J Hydrogen Energy 2013;38:7623–31.
[69] Li Z-S, Cai N-S, Huang Y-Y, Han H-J. Synthesis, experimental studies, and analysis of a new calcium-based carbon dioxide absorbent. Energy Fuels 2005;19:1447–52.
[70] Martavaltzi CS, Lemonidou AA. Parametric study of the CaO-$Ca_{12}Al_{14}O_{33}$ synthesis with respect to high CO_2 sorption capacity and stability on multicycle operation. Ind Eng Chem Res 2008;47:9537–43.
[71] Phromprasit J, Powell J, Assabumrungrat S. Metals (Mg, Sr and Al) modified CaO based sorbent for CO_2 sorption/desorption stability in fixed bed reactor for high temperature application. Chem Eng J 2016;284:1212–23.
[72] Cesário MR, Barros BS, Courson C, Melo DMA, Kiennemann A. Catalytic performances of Ni–CaO–mayenite in CO_2 sorption enhanced steam methane reforming. Fuel Process Technol 2015;131:247–53.

Please cite this article in press as: Phromprasit J, et al., Activity and stability performance of multifunctional catalyst (Ni/CaO and Ni/$Ca_{12}Al_{14}O_{33}$–CaO) for bio-hydrogen production from sorption enhanced biogas steam reforming, International Journal of Hydrogen Energy (2016), http://dx.doi.org/10.1016/j.ijhydene.2016.03.125

Energy Conversion and Management 120 (2016) 62–70

Contents lists available at ScienceDirect

Energy Conversion and Management

journal homepage: www.elsevier.com/locate/enconman

Role of ultrasonic irradiation on transesterification of palm oil using calcium oxide as a solid base catalyst

Jutipong Poosumas [a], Kanokwan Ngaosuwan [b], Armando T. Quitain [c], Suttichai Assabumrungrat [a,*]

[a] Centre of Excellence in Catalysis and Catalytic Reaction Engineering, Department of Chemical Engineering, Faculty of Engineering, Chulalongkorn University, Bangkok 10330, Thailand
[b] Division of Chemical Engineering, Faculty of Engineering, Rajamangala University of Technology Krungthep, Bangkok 10120, Thailand
[c] Department of Applied Chemistry and Biochemistry, Faculty of Engineering, Kumamoto University, Kumamoto 860-8555, Japan

ARTICLE INFO

Article history:
Received 12 January 2016
Received in revised form 20 March 2016
Accepted 18 April 2016
Available online 28 April 2016

Keywords:
Biodiesel
Ultrasonic reactor
Calcium oxide
Transesterification
Catalyst stability

ABSTRACT

Biodiesel production from transesterification of palm oil using a circulated continuous flow ultrasonic reactor was investigated. Transesterification was carried out at 60 °C, 1 atm and a methanol-to-oil molar ratio of 9:1. The highest reaction rate was achieved at the catalyst loading of 2 wt%, and biodiesel yield constantly increased until transesterification equilibrium (about 80%) was reached. A higher ultrasonic frequency (50 kHz) promoted the heterogeneously catalyzed transesterification of refined palm oil, because the three-phase system (packed solid catalyst, methanol and oil) required more spatial distribution by ultrasonic irradiation. Moreover, the highest ultrasonic power also provided highest transesterification rate and biodiesel yield due to cavitation activity enhancement. Reusability of calcium oxide catalysts was also investigated, and results showed that this can be reused to provide high biodiesel yield for at least three operations with slight decrease in the rate of reaction due to counter balance effect of organic compounds deposition on the catalyst surface. The results from this study can be a basis for scaling up of the process to industrial scale.

© 2016 Elsevier Ltd. All rights reserved.

1. Introduction

Energy is an essential part of human daily activities, and has long been associated with civilization for many centuries. It is expected that the demand for energy will continuously increase along with increasing human population. The conventional energy source such as petroleum, natural gas and coal will not be able to cope up with the increasing global demand for energy in the next 40 years [1]. Search for alternative and renewable energies such as solar, wind, hydro or geothermal has been a big issue.

Biodiesel is a promising alternative energy that has been studied and explored in recent years. This is not only an environmentally friendly fuel, but is also considered sustainable and renewable form of energy. It consists of compounds of fatty acid alkyl ester (FAAE) produced from vegetable oils, animal fats and waste cooking oils [2,3] from several methods such as dilution (blending), micro-emulsification, pyrolysis (thermal cracking), esterification or transesterification using catalysts [4,5].

Transesterification, also called alcoholysis, has been mainly used for biodiesel production (Fig. 1). This is a chemical reaction of oils or fats to form esters and glycerol with or without the presence of any catalysts. However, there are two obstacles for the transesterification of oil and low molecular weight alcohol. Firstly, the biodiesel yield is limited by reaction equilibrium which involves a sequence of three consecutive reversible reactions. Secondly, the mass transfer between two immiscible reactants and also catalyst are hindered by the solubility of oil and alcohol, resulting in a low process efficiency [6].

A catalyst is a substance that accelerates chemical reaction because it decreases activation energy of reaction. The catalysts used in the transesterification are broadly divided into two types: homogeneous catalysts and heterogeneous catalysts. Common homogenous catalysts for transesterification are sodium hydroxide [7], potassium hydroxide [8], sodium methoxide [9], potassium methoxide [10], etc. Although the activities of homogeneous catalysts are higher than that of heterogeneous ones, their use has some drawbacks including the difficulty of separating from the products [11]. It also requires a tremendous amount of water for separation, thus having a large impact to the environment [12]. In contrast, heterogeneous catalysts form different phase from reaction mixture leading to easy separation, and it can also be recycled. Common heterogeneous catalysts for biodiesel production are calcium oxide [13], magnesium oxide [14], strontium oxide [15], zinc oxide, titanium oxide [16] or even natural-based such as eggshell [17,18], mollusk shell [19], sea sand [20] and bones [21].

* Corresponding author.
E-mail address: Suttichai.A@chula.ac.th (S. Assabumrungrat).

http://dx.doi.org/10.1016/j.enconman.2016.04.063
0196-8904/© 2016 Elsevier Ltd. All rights reserved.

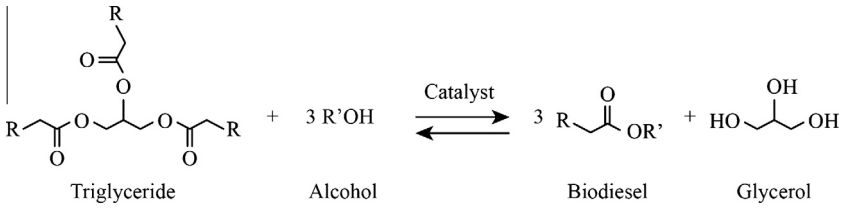

Fig. 1. Transesterification reaction of triglyceride to form biodiesel.

Ultrasonic assisted biodiesel reactor is a practical solution to increase the level of mixing and shift the reaction equilibrium by cavitation phenomena in fluid. This reactor can improve the hydrodynamics of reaction mixture by increasing the interfacial area of reactant bubbles to active site of catalyst with cavitation jet. The cavitation phenomena also produces a locally extreme reaction condition around 5000 °C and 1000 atm. Ultrasonic irradiation induces more mixing efficiency for reducing the activation energy of transesterification and increases the rate of reactions and biodiesel yield using less energy consumption and lower alcohol-to-oil molar ratio as compared to the conventional mechanical stirring reactor [22].

For the homogeneous catalyst, the effect of ultrasonic parameters on biodiesel yield depends on amplitude, pulse of vibration, diameter of the ultrasonic probe, irradiation distance and reactant flowrate [23]. Our previous work found that the dual ultrasonic frequency (20 and 50 kHz) has slightly effect on biodiesel yield [24]. This is likely due to the homogeneously catalyzed transesterification where specific active sites do not exist. Moreover, the presence of solid particles in the reaction medium might affect the scattering of cavitation phenomena. Using heterogeneous catalyst, only a few studies had been carried out on the effect of ultrasonic parameters on biodiesel yield and these remain unclear. Choudhury et al. [25] proposed the kinetics and mechanism of calcium oxide catalyzed transesterification. Several parameters such as catalyst loading, methanol-to-oil molar ratio, and reaction temperature were also investigated using Box–Behnken statistic design. However, all experiments were performed in a batch reactor which could not provide a closer basis for the use of ultrasonic assisted reactor in an industrial scale.

Therefore, this research focuses on the effect of ultrasonic and operating parameters (ultrasonic frequency including single and dual frequency, and ultrasonic power) on the catalytic activity of heterogeneous catalyzed transesterification of refined palm oil under circulated flow process with catalysts packed in a basket. A simple ultrasonic sign wave was used to elucidate the effect of ultrasonic frequency and ultrasonic power on biodiesel yield. The reusability of calcium oxide catalysts was also investigated to provide significant information for the use of flow ultrasonic reactor for biodiesel production in an industrial scale. Moreover, this research revealed the importance of ultrasonic operating parameter for flow heterogeneous system (using calcium oxide as a catalyst) compared with flow homogeneous system to gain more understanding about highly efficient biodiesel production in ultrasonic assisted reactor.

2. Experimental

2.1. Reactants

Commercial refined palm oil was purchased from a local store in Thailand. Analytical grade (99.8% purity) methanol, the reactant of transesterification reaction, were provided by QRëC. Analytical standard ($\geqslant$99% purity) methyl heptadecanoate and heptane were used as internal standard and solvent respectively for GC analysis are provided by Sigma–Aldrich. Refined palm oil consists of triglycerides such as tripalmitin, triolein, trilinolein and tristearin which are sorted here in order of their composition, from most to least abundant.

2.2. Catalysts and characterization techniques

There are two types of catalyst used the transesterification reaction including of;

(1) Homogeneous catalyst: High purity sodium hydroxide (NaOH) was provided by Loba Chemie and grinded to powder. Sodium hydroxide powder is easier to dissolve in alcohol, and reacted faster with alcohol to produce alkoxide ion.
(2) Heterogeneous catalyst: 96% purity calcium oxide (CaO) fine powder catalyst was provided by Sigma–Aldrich, and then was calcined in a muffle furnace with a heating rate of 10 °C/min to 550, 700 and 900 °C with a holding time of 5 h. This prepared catalyst was kept in a desiccator cabinet before use.

Characterization techniques include nitrogen adsorption, particle size, X-ray diffraction and thermogravimetric analysis (TGA). The details were described in our previous work [32].

2.3. Ultrasonic irradiation experiment

A schematic diagram of the ultrasonic irradiation experimental apparatus used in this study is shown in Fig. 2. A 500 mL Erlenmeyer flask was used to preheat and maintain the temperature of oil and methanol at 60 °C. A magnetic stirrer was used in the early-stage of mixing (pretreatment) before the reactants were fed to the reactor using a peristaltic pump with a feed flow rate of 55 mL/min through a 6 mm diameter silicone tube with a residence time of 4 min. This feed flow rate was found to obtain the highest biodiesel yield in this flow ultrasonic reactor as observed in the previous study [24]. The heterogeneous catalysts were packed into screened mesh baskets inside the rectangular shape reactor ($2.5 \times 2.5 \times 30\ cm^3$). The three catalyst baskets were held by a horizontal axial and allow to spin by axial screw along the reactor length with a speed of 25 rpm. The wall outside of the reactor was attached by 16 transducers (4 per each side, two different frequency 20 and 50 kHz) with total power of 800 W. The substances were introduced from the bottom to the top of the reactor before circulating through the flask. Sample was taken out through a sampling valve. Then, it was centrifuged at 3000 rpm for 10 min to separate solid catalyst, glycerol and biodiesel before analyzing with a gas chromatography (GC).

2.4. Biodiesel analysis

Biodiesel yield was analyzed following the EN14103 standard using Shimadzu GC-2010 Plus, with DB-WAX (0.25 mm $\times$ 30 m) capillary column. Helium and nitrogen were used as carrier gas and makeup gas. Oven temperature ramp program was started at

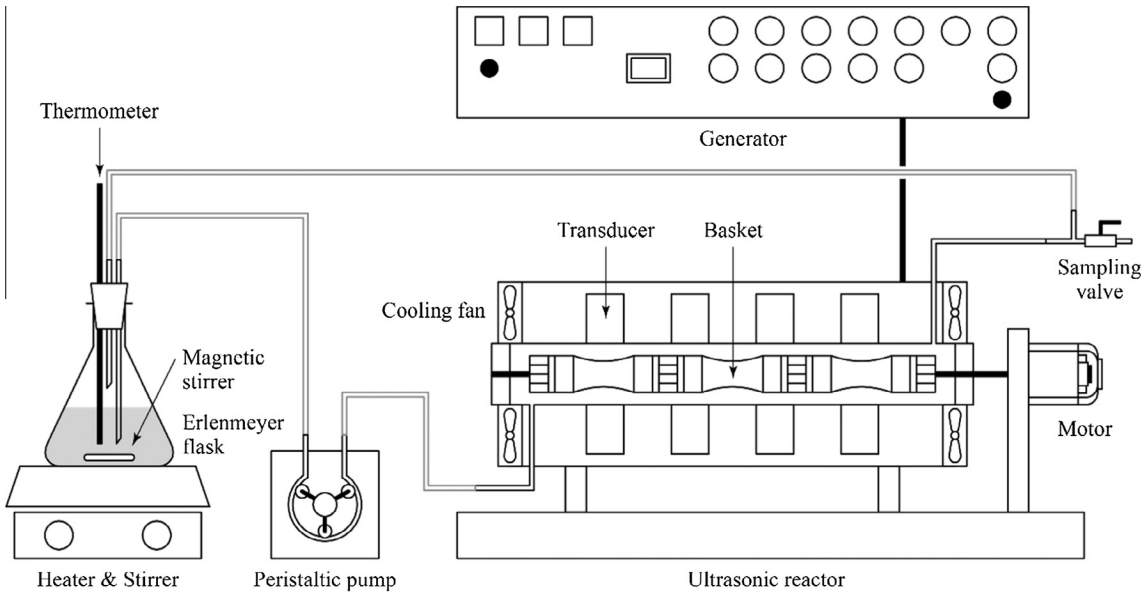

Fig. 2. Schematic diagram of the ultrasonic process.

150 °C and held for 5 min, heated up to 190 °C with a rate of 3 °C/min and held for 5 min, then heated up to 220 °C with a rate of 3 °C/min and held for 5 min. The injector and flame ionization detector (FID) temperatures were 250 °C. Biodiesel yield was calculated by Eq. (1)

$$\text{Biodiesel yield } (\%) = \frac{(\sum A) - A_{IS}}{A_{IS}} \times \frac{C_{IS} \times V_{IS}}{m_S} \times 100\% \quad (1)$$

where

$\sum A$ Total area of peak,
A_{IS} Area of methyl heptadecanoate (internal standard),
C_{IS} Concentration of methyl heptadecanoate (mg/mL),
V_{IS} Volume of methyl heptadecanoate (mL),
m_S Mass of biodiesel sample (mg).

3. Results and discussion

3.1. Preliminary test for transesterification in the flow ultrasonic reactor

Base catalyst used in the transesterification reaction is mainly divided into two types; i.e., homogeneous and heterogeneous catalysts. In this work, sodium hydroxide was used as homogeneous catalyst. Sodium hydroxide was grinded and dissolved in methanol before use. Calcium oxide was used as heterogeneous catalyst. Calcium oxide was calcined at the desired temperature in a muffle furnace before use. Transesterification was operated at 60 °C, 1 atm, a methanol-to-oil molar ratio of 9:1 and a catalyst loading of 2 wt% with different catalyst types. Fig. 3 shows that the rate of biodiesel yield changed with the reaction time. Homogeneous sodium hydroxide provided better yield compared with that of heterogeneous calcium oxide catalyst because homogeneous catalyst such as sodium hydroxide has no hindrance between active site of catalyst and the substrates. Choudhury et al. [25] also found that the activation energy of calcium oxide catalyzed transesterification of soy bean oil was about 3 times higher than that of homogeneous catalyzed transesterification under ultrasonic irradiation. This is because of the presence of three phase (solid–oil–methanol) in the system leading to higher mass transfer limitation.

As seen in Fig. 3, longer reaction time leads to higher biodiesel yield for all catalysts. In order to confirm the advantages of using ultrasonic irradiation, calcium oxide catalyzed transesterification of palm oil using mechanically stirred reactor (MS) was also performed. It can be noted that an induction period was observed for calcium oxide catalyst which is a significant difference in the biodiesel yield due to the effect of mixing type for each reactor. Using the mechanically stirred reactor, the induction period was much longer than that of the ultrasonic reactor (US) (180 min and 40 min, respectively for calcined calcium oxide at 550 °C). However, the induction period was not observed for homogeneously catalyzed transesterification.

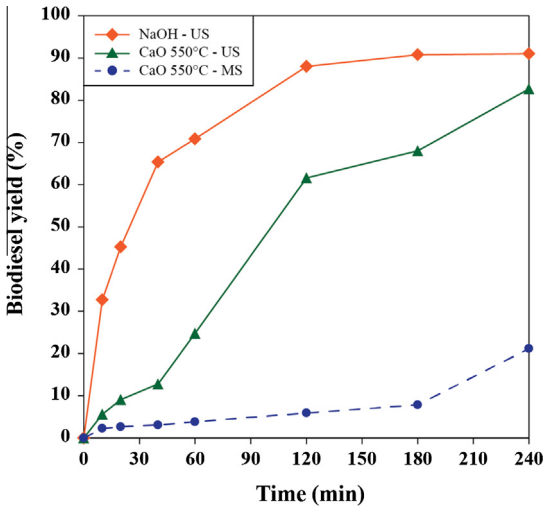

Fig. 3. Homogeneous and heterogeneous catalyzed transesterification of palm oil using ultrasonic reactor (US) and mechanically stirred reactor (MS).

Ultrasonic reactor can accelerate the reaction rate and reduce induction period by an increase in the level of mixing due to cavitation phenomena in fluid (external convection of the reactants from the bulk fluid to the external surface of the catalyst pellet) and carrying reactants to active sites of catalyst (internal convection of the reactant from the pore entry through the catalyst pores, and into the immediate vicinity of the internal catalytic surface) before adsorption of reactants onto the catalyst surface. This is different from the mechanically stirred reactor where it only affects

external convection [26]. It has also been observed that the ultrasonic reactor for biodiesel production from waste cooking oil provided more energy efficiency (9.23 kJ/g) as compared with the conventional mechanical stirring method (20.45 kJ/g) [27]. In addition, the use of ultrasonic irradiation can also significantly reduce the settling time of suspended glycerol in biodiesel product [11,28].

Under ultrasonic irradiation, glycerol has more chances to be adsorbed on the surface of calcium oxide catalyst and generate the calcium-glyceroxide specie. This specie can be one of the active sites that promote the rate of reaction. Kouzu et al. [29,30] and Granados et al. [31] reported that the glyceroxide specie was more active for transesterification than that of calcium oxide active specie. Our previous research also found that the glyceroxide species present in the used calcium oxide catalyst can enhance the biodiesel yield for the consecutive cycles [32].

Generally, the excessive reaction time of reversible reaction may cause reverse reaction. Thus, biodiesel yield may decrease after reaching the reaction equilibrium. In this case, biodiesel yield obtained from sodium hydroxide catalyzed transesterification reached a plateau after 3 h while biodiesel yield using calcium oxide catalyzed transesterification continued to increase along with the reaction time. Sheng-Ho et al. [22] reported that biodiesel produced from refined palm oil and crude palm oil using heterogeneous palm oil mill fly ash supported calcium oxide catalyst under ultrasonic irradiation reached the maximum yield of 84.72% and 73.23%, respectively in 30 min, and decreased to 75.93% and 64.49%, respectively at 60 min.

3.2. Effect of calcination temperature of calcium oxide catalyst

In this study, calcium oxide was calcined at 550, 700 and 900 °C for 5 h. This catalyst was loaded to the reactor at 2 wt% based on the amount of oil. Biodiesel yield is shown in Fig. 4. Uncalcined calcium oxide catalyst in this study was not active for transesterification. This could be due to impurities present in calcium hydroxide ($Ca(OH)_2$). Other components present in the catalyst were also confirmed by XRD [9,10] (data not shown). Calcium hydroxide was one of the impurities as also reported in the study of Esipovich et al. [33]. It was also noted that there was no peak of calcium carbonate ($CaCO_3$) contamination for all catalysts. The calcination temperature has a dramatic effect on impure calcium oxide, especially the calcium oxide which was naturally derived [18], but too high calcination temperature could lead to sintering of fine particles, promote cluster agglomeration and result in a reduction of surface area of this catalyst [34,35]. It can be noted that the high purities of calcium oxide obtained from the highest calcination temperature could result in a better transesterification rate. Thus, calcination temperature at 900 °C was selected in the subsequent experiments. Moreover, the particles size and surface area of calcium oxide at this calcination temperature were 143 mm and 15.68 m^2/g, respectively, which are in agreement with our previous work [32].

3.3. Effect of catalyst loading

The higher catalyst loading provides faster rate of reactions due to greater chances of contact between substrates and active sites of catalyst. However, excessive catalyst loading may hinder mass transfer in the reaction system. It was found that the biodiesel yield using catalyst loading of 1, 2 and 3 wt% reached the same equilibrium with different reaction rates (Fig. 5). The equilibrium reaction time for catalyst loading of 1 wt% was 240 min, while for the other catalyst loadings (2 and 3 wt%) the equilibrium was reached in 180 min. An increase in catalyst loading (2 and 3 wt%) significantly improved biodiesel yield due to more active sites available to catalyze transesterification. Moreover, the increase in catalyst loading also enhanced the cavitation activity of ultrasonic irradiation. However, when the catalyst loading was increased to 3 wt%, the biodiesel yield did not improve further. Excessive catalyst loading might have reduced mass transfer from bulk reaction to the catalyst surface, and produced scattering of ultrasonic irradiation resulting in a weaker cavitation effect [36]. The reactants could not have easy access to the active site of the catalyst, thus leading to lower biodiesel yield.

3.4. Effect of ultrasonic operating parameters

3.4.1. Effect of ultrasonic frequency

In order to investigate the effect of ultrasonic frequency on biodiesel yield, the reaction temperature for transesterification was kept constant at 60 °C, 1 atm, a methanol-to-oil molar ratio of 9:1 and a catalyst loading of 2 wt%. The maximum ultrasonic power was 800 W produced by a total of 16 transducers (50 W per each transducer). The position of operating frequency can be divided to 4 patterns: none (all deactivated transducers), 20 kHz (8 each), 50 kHz (8 each) and 20 kHz (4 each) combined with

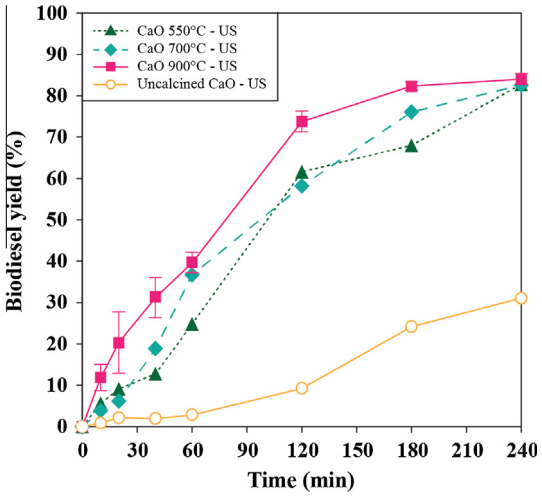

Fig. 4. Effect of calcination temperature of catalyst on biodiesel yield.

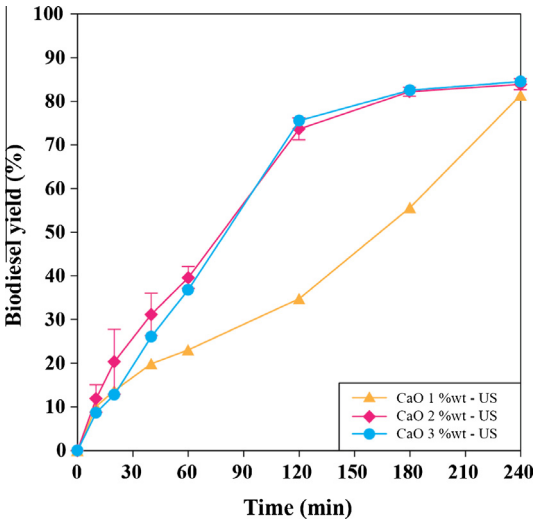

Fig. 5. Effect of calcium oxide heterogeneous catalyst loading on biodiesel yield.

Table 1
Operating frequency patterns and FAME yield at 240 min in the ultrasonic reactor.

Pattern	Position of 20 kHz transducer				Position of 50 kHz transducer				FAME yield (%)
	1	2	3	4	1	2	3	4	
1	–	–	–	–	–	–	–	–	10.16
2	✓	✓	✓	✓	–	–	–	–	43.50
3	–	–	–	–	✓	✓	✓	✓	59.49
4	–	✓	–	✓	✓	–	✓	–	55.61

50 kHz (4 each) as summarized in Table 1 where employed in 4 positions along the reactor. The results are shown in Fig. 6.

The significantly higher biodiesel yield was found in the second to fourth patterns because ultrasonic irradiation offers more mixing rate by cavitation phenomena. The cavitation phenomena generates an emulsification of methanol in oil to increase the contact area between methanol oil and surface of calcium oxide catalyst resulting in a higher biodiesel yield. In contrast to the first pattern (without ultrasonic irradiation), biodiesel yield was very low with a longer induction period due to mass transfer limitation of three phase system (solid phase of packed catalyst, methanol and oil phase) was dominated. It can be concluded that mass transfer limitation was more pronounced for this reactor configuration with packed catalyst.

The difference in operating frequency was illustrated in the second and third patterns. It was found that a single transducer frequency of 50 kHz provided higher biodiesel yield than that of a single transducer frequency of 20 kHz for 1.4 times along the reaction period. Based on the same ultrasonic power of 400 W, using frequency of 50 kHz provides a smaller bubbles for generating the cavitation activity in the reaction mixture. Thus, the smaller bubble has a higher surface area per volume ratio, and the contact area between the substances and active sites of calcium oxide was higher than using the frequency of 20 kHz.

Based on the same ultrasonic power, the amplitude of lower frequency (20 kHz) is greater compared to the higher frequency. However, they do not provide higher biodiesel yield because the available ultrasonic power was in the localized regions for this reactor configuration with catalyst packing. The higher frequency (50 kHz) contributed more distribution of available ultrasonic power throughout the reactor volume [37]. The effect of dual transducer frequencies (20 kHz combined with 50 kHz) was also studied in the fourth pattern. It was found that the dual frequencies provided a biodiesel yield between both two single frequencies (20 and 50 kHz). Furthermore, this ultrasonic frequency did not affect biodiesel yield when using homogenous catalyst (NaOH), as found in our previous studies [24]. This could be due to different catalyst packing configurations in the reactor (homogeneous versus heterogeneous system). For this system, calcium oxide catalyst was packed in the meshed basket. The presence of solid catalysts in the sonication medium (reaction medium) can act like a nucleation site for cavitation bubbles [38]. Therefore, the low ultrasonic frequency (20 kHz) is more likely to provide the less distribution of cavitation per unit volume as compared to the high ultrasonic frequency (50 kHz) in the reactor resulting to lower biodiesel yield.

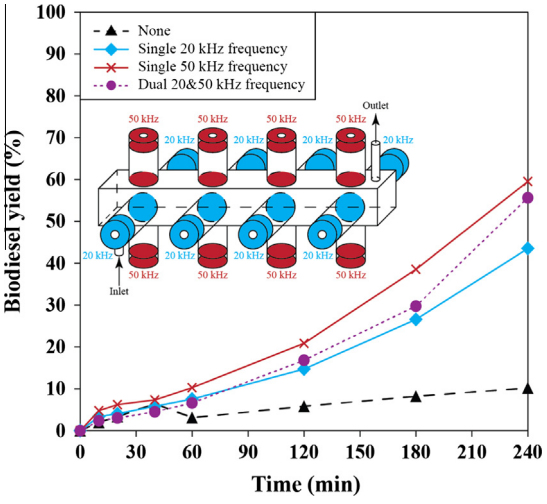

Fig. 6. Effect of ultrasonic frequency on biodiesel yield.

The simple ultrasonic wave in the liquid-phase reaction was proposed to provide more understanding in the effect of ultrasonic frequency on biodiesel yield in this system. This can be expressed by general wave equations (Eqs. (2) and (3)) [39]. The wave equations of second (20 kHz, 400 W), third (50 kHz, 400 W) and fourth (20 kHz, 200 W combined with 50 kHz, 200 W) patterns within 1 s period can be expressed by Eqs. (4)–(6), respectively. The calculated amplitude value was presented in Appendix A.

$$y = A\sin(kx - \omega t) \tag{2}$$

$$y = A\sin\left(\frac{2\pi}{\lambda}x - 2\pi ft\right) \tag{3}$$

$$y_{20\text{kHz}} = 0.442\sin\left(\frac{2\pi}{66.712}x - 2\pi \times 20{,}000 \times 1\right) \tag{4}$$

$$y_{50\text{kHz}} = 0.177\sin\left(\frac{2\pi}{26.685}x - 2\pi \times 50{,}000 \times 1\right) \tag{5}$$

$$y_{20+50\text{kHz}} = 0.312\sin\left(\frac{2\pi}{66.712}x - 2\pi \times 20{,}000 \times 1\right) + 0.125\sin\left(\frac{2\pi}{26.685}x - 2\pi \times 50{,}000 \times 1\right) \tag{6}$$

where

A Amplitude of the wave (m or mm),
k Angular wavenumber of the wave, which $k = \frac{2\pi}{\lambda}$,
ω Angular frequency of the wave, which $\omega = 2\pi f$,
t Time period (s),
λ Wave length (m or mm),
f Wave frequency (Hz).

Fig. 7 shows the relation between distance from ultrasonic source and amplitude of the ultrasonic wave derived from the above equations. The magnitude of amplitude (A) presented in Eqs. (3)–(6) showed that the higher ultrasonic frequency resulted to the lower ultrasonic amplitude. The ultrasonic wave obtained from ultrasonic frequency of 50 kHz was more spatially distributed based on the same distance from the ultrasonic source, while the lower ultrasonic frequency of 20 kHz provides more ultrasonic power in terms of amplitude. The obtained cavitation phenomena corresponded to this ultrasonic wave pattern. Based on the same operation parameter, the ultrasonic frequency of 50 kHz has more spatial distribution resulting to higher chance of cavitation on the catalyst surface. Choudhury et al. [25] concluded that the ultrasonic irradiation can enhance the rate of methoxide species by adsorption of methanol on the calcium oxide catalyst surface. Therefore, the highest biodiesel yield was obtained from ultrasonic frequency of 50 kHz under the same operating condition. Dual frequency (20 and 50 kHz) could not promote biodiesel yield because this also provided the lower spatial distribution of ultrasonic irradiation as compared to ultrasonic frequency of 50 kHz. It can be noted that multi-frequency ultrasonic irradiation which is less likely to enhance biodiesel yield in the flow reactor with catalyst packing disagreed with the results of previous researches [24,40].

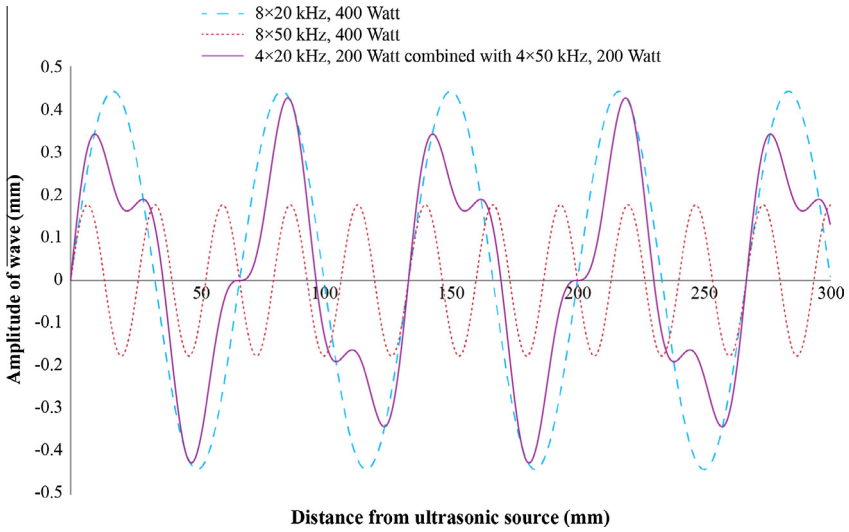

Fig. 7. Ultrasonic sign wave with different frequency.

3.4.2. Effect of ultrasonic power

Ultrasonic power is one of the main factor affecting biodiesel yield. The expression of ultrasonic power input to the process must be evaluated in terms of intensity (ultrasonic power per liquid volume in the reactor) as shown in Eq. (7). To investigate the effect of ultrasonic power on the biodiesel yield, transesterification was performed at 60 °C, 1 atm, a methanol-to-oil molar ratio of 9:1 and a catalyst loading of 2 wt%. The dual ultrasonic frequencies of 20 combined with 50 kHz were used to investigate this effect. The operating power was divided into three levels: 0%, 50% and 100% of maximum power. The liquid volume in the reactor was 300 mL, and the maximum ultrasonic power was 800 W. Thus, the ultrasonic irradiation for each case were calculated as 0, 1.33 and 2.66 W/mL, respectively. The effect of ultrasonic power on biodiesel yield are also shown in Fig. 8.

$$\textit{Ultrasonic intensity}\ (\mathrm{W/mL}) = \frac{\textit{Ultrasonic power}\ (\mathrm{W})}{\textit{Reaction mixture volume in the reactor}\ (\mathrm{mL})} \quad (7)$$

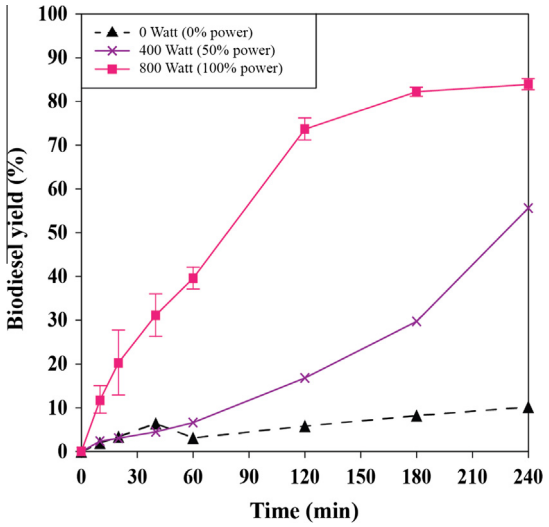

Fig. 8. Effect of ultrasonic power on biodiesel yield.

There was no ultrasonic irradiation for 0% power. Therefore, the mixing was only provided in the pre-heater tank (Erlenmeyer flask), inline mixing (in the silicone tube and peristaltic pump) and horizontal stirrer in the reactor. It was found that the biodiesel yield was only 10% at 240 min of reaction period.

For a maximum power of 50% (400 W or 1.33 W/mL), the biodiesel yield increased due the acoustic movement and cavitation phenomena promoted by ultrasonic irradiation. The acoustic movement provides a mixing in the medium but cavitation of low ultrasonic power tends to form a stable cavitation that does not collapse [41]. However, the induction period was also observed when a maximum power of 50% was applied. This indicated that the ultrasonic irradiation of 1.33 W/mL was not enough for reducing the mass transfer limitation. Gupta et al. [27] found that the ultrasonic intensity above 1.58 W/mL provided significantly higher biodiesel yield.

For the maximum power of 100% (800 W or 2.66 W/mL), the rate of biodiesel yield was significantly faster compared to that obtained from maximum power of 50%, because ultrasonic irradiation promotes acoustic movement and cavitation phenomena. In this case, the cavitation formed with the high power was not stable, and collapsed with the release of energy (called transient cavitation). Moreover, the collapse of the cavitation bubble leads to the higher micro-mixing and jet velocity at the phase boundary between the oil and methanol phases. This leads to the formation of finer emulsion which provided a higher mass-transfer coefficient, and thus higher biodiesel yield was achieved [42]. Biodiesel yield via transesterification tends to reach the equilibrium after 180 min. The minimum amount of energy required to produce ultrasonic cavities must be above the cavitation threshold. In other words, the ultrasonic waves must have enough pressure amplitude to overcome the natural molecular bonding forces and the natural elasticity of the liquid medium in order to grow the cavities [37].

The correlation between ultrasonic power input and amplitude of the wave was also proposed to look into the effect of ultrasonic power on the biodiesel yield in this study. This can be expressed by kinetic energy equation (Appendix A) [43]. The correlation between power and amplitude for single 20 kHz and 50 kHz transducer was expressed in Eqs. (8) and (9), respectively.

$$A_{20\mathrm{kHz}} = 2.209 \times 10^{-5} P^{0.5} \quad (8)$$

$$A_{50\mathrm{kHz}} = 8.834 \times 10^{-6} P^{0.5} \quad (9)$$

The higher ultrasonic power provides higher amplitude of wave resulting to the higher biodiesel yield. This corresponds to the transesterification using barium oxide (BaO) and strontium oxide (SrO) heterogeneous catalysts reported by Salamatinia et al. [44].

Gupta et al. [27] also found that high ultrasonic power resulted into higher energy efficiency. It should be noted that the power or energy input could not be completely transferred to the medium because part of it was absorbed by the material of reactor in the form of heat or vibration. The reactor is made of 316 stainless steel which absorbed ultrasonic energy of 10.6%, reflected the energy back to medium of around 88% and loss to the environment of 1.4% [45]. Therefore, the liquid medium in the reactor only absorbed ultrasonic energy of about 352 W (1.17 W/mL) and 704 W (2.35 W/mL) for 50% and 100% of maximum power, respectively. This calculated ultrasonic intensities were used to clarify the obtained biodiesel yield.

Hence, for flow ultrasonic reactor with solid catalyst packing, consideration for biodiesel production requires a single high ultrasonic frequency to provide more spatial cavitation distribution that would assist the reactant to be easily adsorbed onto the active site of catalysts. Furthermore, a high ultrasonic intensity is also required to enhance the strength of ultrasonic cavitation activity.

3.5. Catalyst stability

Stability is one of the important key points that make heterogeneous calcium oxide catalysts more promising than homogeneous sodium hydroxide catalyst. Sodium hydroxide cannot be easily reused by the general technique, and requires a lot of water for washing from biodiesel product. Calcium oxide, however, can be easily separated by mechanical techniques such as sedimentation or filtration.

This stability test could not be performed using ultrasonic frequency of 50 kHz with maximum power (800 W) due to the limitation of reaction configuration. Therefore, transesterification was operated at 60 °C, 1 atm and a methanol-to-oil molar ratio of 9:1 using a catalyst loading of 2 wt% based on oil under ultrasonic irradiation at maximum power with dual frequency of 20 and 50 kHz. Biodiesel yield for three consecutive cycles are shown in Fig. 9.

Calcium oxide catalyst can be reused to produce biodiesel and provide high biodiesel yield (more than 80% yield) for three cycles with slightly decreasing rate of reaction. It was found that calcium oxide catalyst recovered by sedimentation changed color from white to gray, and was more darkened with the reuse due to deposition of reaction mixture. The catalyst layer in reaction mixture was also observed to widen because catalyst was suspended more in the mixture.

The reused catalyst was characterized by thermogravimetric analysis (TGA) to investigate the catalyst deactivation caused by surface coverage from organic compounds in the reaction mixture [46–48].

The weight of calcium oxide catalyst after 1st, 2nd and 3rd cycles also showed significant losses in mass along the temperature compared to the fresh calcium oxide catalyst (Fig. 10). It was found that the main weight losses of samples were divided into 3 periods. The first period referred to the decomposition of saturated fatty acid methyl esters (100–230 °C) and water as a by-product of the formation of calcium methoxide. Weight loss in the second period was due to the decomposition of unsaturated fatty acid methyl esters, glycerol and triglycerides (230–500 °C). Lastly, the decomposition of carbon residuals occurring at high temperatures (500–850 °C) resulted into weight loss in the third period [32]. It indicated that there were some organic compounds deposited on the catalyst surface that might have caused reduction of reaction rate for each cycle. However, the biodiesel yields obtained from the used calcium oxide catalysts (2nd and 3rd cycles) were also similar to that of fresh calcium oxide catalyst in 4 h of reaction period. Therefore, it can be considered to be another positive effect in making biodiesel yield reach the same equilibrium as seen in Fig. 9. There are two possible explanations to the decreasing reaction rate for catalyst reusability in each cycle: (1) the reaction mixture was bonded on the catalyst surface to form new active species such as glycerol adsorbed on the calcium oxide to form calcium glycerol compound and (2) ultrasonic irradiation probably aided desorption of reaction mixture to obtain the same final biodiesel yield. Choedkiatsakul et al. [32] also reported that the new active site species of used calcium oxide catalyst as calcium glyceroxide was present under ultrasonic irradiation.

Moreover, using ultrasonic irradiation for heterogeneous catalytic system can enhance the desorption of the products from catalyst surface and provide the higher turnover rate on the surface reaction to achieve its original biodiesel yield at 4 h [32]. Since both calcium glycerol complex and products desorption under ultrasonic irradiation have positive effects on the reaction, the final biodiesel yield was still high even with the reuse of catalysts.

Catalyst washing is one of the parameters that affect final biodiesel yield (at 240 min). In this study, methanol was used to wash

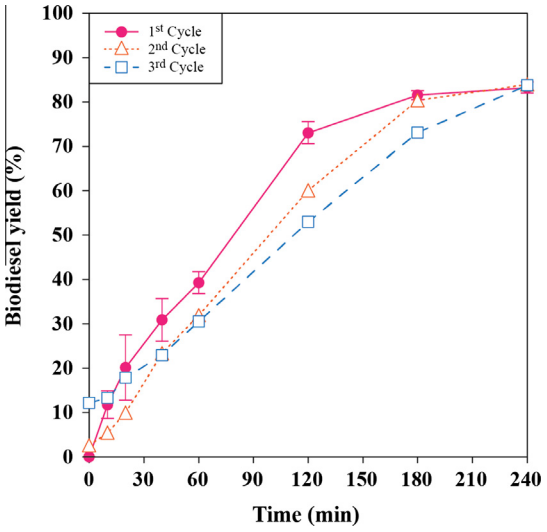

Fig. 9. Reusability of calcium oxide for transesterification of palm oil.

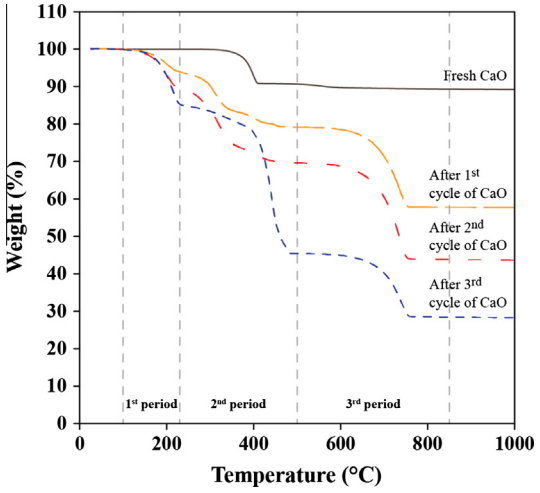

Fig. 10. TGA profiles of fresh and reused calcium oxide catalyst (after each cycle).

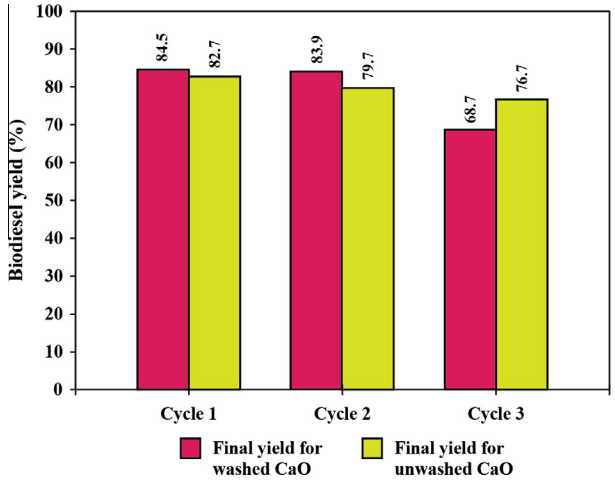

Fig. 11. Biodiesel yield for washed and unwashed calcium oxide catalyst at 4 h.

the calcium oxide using a magnetic stirrer at ambient temperature and pressure for three times before reloading to the reactor. Biodiesel yield at 4 h using washed catalyst was comparable to unwashed catalyst as shown in Fig. 11.

However, the biodiesel yield at 4 h for unwashed catalyst was still high. Thus, the unwashed calcium oxide catalyst is more practical in the industrial scale. These results also agreed with our previous work on calcium oxide-catalyzed transesterification of palm oil in a sonication bath (batch reactor). The sonication reactor provided significantly higher biodiesel yield than that of the conventional mechanical stirred reactor [32]. This should be noted that ultrasonic irradiation for calcium oxide catalyzed transesterification is more promising for industrial scale due to their advantages of minimizing mass transfer limitation of two immiscible reactants and catalyst, provide high turnover rate on the catalyst surface and generate more active species as calcium glyceroxide.

4. Conclusions

In this work, biodiesel production from palm oil by using flow ultrasonic reactor was investigated and compared to a mechanically stirred reactor. Transesterification was carried out at 60 °C, 1 atm, and a methanol-to-oil molar ratio of 9:1. It was found that the highest rate of reaction was achieved in the ultrasonic reactor with the highest catalyst loading of 2 wt%, and biodiesel yield increased constantly until reaching transesterification equilibrium of about 80%. The single high ultrasonic frequency (50 kHz) promoted heterogeneously catalyzed transesterification of refined palm oil because it produced fine emulsion of methanol in oil phase and provided more distribution of ultrasonic irradiation as indicated by ultrasonic sign wave. High biodiesel yield was also obtained from high ultrasonic power because ultrasonic power affected the cavitation activity in term of ultrasonic amplitude. Reusability of calcium oxide catalyzed transesterification in the circulated flow ultrasonic reactor was also studied. It was found that calcium oxide catalyst can be reused to produce biodiesel, and provided high biodiesel yield for three cycles with slightly decreasing rate of reaction. It can be concluded that it is favorable to use a single high frequency and high intensity irradiation in an ultrasonic reactor for heterogeneous catalyzed synthesis of biodiesel. All information provided in this present work can be used in the design of an industrial scale biodiesel production plant. In addition, calcium oxide is a promising catalyst for biodiesel production in a flow ultrasonic reactor.

Acknowledgements

This work was financially supported by The Thailand Research Fund (DPG5880003). Department of Chemical Engineering, Faculty of Engineering, Chulalongkorn University would like to acknowledge The Institutional Research Grant (The Thailand Research Fund), IRG 5780014, and Chulalongkorn University, Contract No. RES_57_411_21_076.

Appendix A. Supplementary material

Supplementary data associated with this article can be found, in the online version, at http://dx.doi.org/10.1016/j.enconman.2016.04.063.

References

[1] EIA. Energy consumption and energy sources for the year 2014; 2014. Available from: <http://www.eia.gov/petroleum> [cited 2014].
[2] Zhang H et al. Biodiesel produced by waste cooking oil: review of recycling modes in China, the US and Japan. Renew Sustain Energy Rev 2014;38:677–85.
[3] Talebian-Kiakalaieh A, Amin NAS, Mazaheri H. A review on novel processes of biodiesel production from waste cooking oil. Appl Energy 2013;104:683–710.
[4] Aransiola EF et al. A review of current technology for biodiesel production: state of the art. Biomass Bioenergy 2014;61:276–97.
[5] Shuit SH et al. Membrane technology as a promising alternative in biodiesel production: a review. Biotechnol Adv 2012;30(6):1364–80.
[6] Choedkiatsakul I et al. Patent review on biodiesel production process. Recent Patents Chem Eng 2011;4:265–79.
[7] Sinha S, Agarwal AK, Garg S. Biodiesel development from rice bran oil: transesterification process optimization and fuel characterization. Energy Convers Manage 2008;49(5):1248–57.
[8] Tomasevic AV, Siler-Marinkovic SS. Methanolysis of used frying oil. Fuel Process Technol 2003;81(1):1–6.
[9] Rashid U, Anwar F. Production of biodiesel through optimized alkaline-catalyzed transesterification of rapeseed oil. Fuel 2008;87(3):265–73.
[10] Casas A et al. Optimization of the reaction parameters for fast pseudo single-phase transesterification of sunflower oil. Fuel 2010;89(3):650–8.
[11] Amit S. Biodiesel production & properties. The Royal Society of Chemistry; 2012.
[12] Tasić MB, Stamenković OS, Veljković VB. Cost analysis of simulated base-catalyzed biodiesel production processes. Energy Convers Manage 2014;84:405–13.
[13] Veljković VB et al. Kinetics of sunflower oil methanolysis catalyzed by calcium oxide. Fuel 2009;88(9):1554–62.
[14] Suppes G. Transesterification of soybean oil with zeolite and metal catalysts. Appl Catal A 2004;257(2):213–23.
[15] Zabeti M, Wan Daud WMA, Aroua MK. Activity of solid catalysts for biodiesel production: a review. Fuel Process Technol 2009;90(6):770–7.
[16] Jitputti J et al. Transesterification of crude palm kernel oil and crude coconut oil by different solid catalysts. Chem Eng J 2006;116(1):61–6.
[17] Chen G et al. Ultrasonic-assisted production of biodiesel from transesterification of palm oil over ostrich eggshell-derived CaO catalysts. Bioresour Technol 2014;171:428–32.
[18] Wei Z, Xu C, Li B. Application of waste eggshell as low-cost solid catalyst for biodiesel production. Bioresour Technol 2009;100(11):2883–5.
[19] Viriya-Empikul N et al. Waste shells of mollusk and egg as biodiesel production catalysts. Bioresour Technol 2010;101(10):3765–7.
[20] Muciño GG et al. Biodiesel production from used cooking oil and sea sand as heterogeneous catalyst. Fuel 2014;138:143–8.
[21] Obadiah A et al. Biodiesel production from palm oil using calcined waste animal bone as catalyst. Bioresour Technol 2012;116:512–6.
[22] Ho WWS et al. Ultrasound-assisted transesterification of refined and crude palm oils using heterogeneous palm oil mill fly ash supported calcium oxide catalyst. Energy Sci Eng 2015;3(3):257–69.
[23] Mostafaei M et al. Optimization of ultrasonic assisted continuous production of biodiesel using response surface methodology. Ultrason Sonochem 2015;27:54–61.
[24] Choedkiatsakul I et al. Biodiesel production from palm oil using combined mechanical stirred and ultrasonic reactor. Ultrason Sonochem 2014;21(4):1585–91.
[25] Choudhury HA, Chakma S, Moholkar VS. Mechanistic insight into sonochemical biodiesel synthesis using heterogeneous base catalyst. Ultrason Sonochem 2014;21(1):169–81.
[26] Cárcell JA et al. Ultrasound effects on the mass transfer processes during drying kinetic of olive leaves. Defect Diffus For 2010:1083–90.
[27] Gupta AR, Yadav SV, Rathod VK. Enhancement in biodiesel production using waste cooking oil and calcium diglyceroxide as a heterogeneous catalyst in presence of ultrasound. Fuel 2015.
[28] Somnuk K, Smithmaitrie P, Prateepchaikul G. Optimization of continuous acid-catalyzed esterification for free fatty acids reduction in mixed crude palm oil

using static mixer coupled with high-intensity ultrasonic irradiation. Energy Convers Manage 2013;68(1):193–9.
[29] Kouzu M et al. Heterogeneous catalysis of calcium oxide used for transesterification of soybean oil with refluxing methanol. Appl Catal A 2009;355(1–2):94–9.
[30] Kouzu M et al. Solid base catalysis of calcium oxide for a reaction to convert vegetable oil into biodiesel. Adv Powder Technol 2010;21(4):488–94.
[31] López Granados M et al. Surface chemical promotion of Ca oxide catalysts in biodiesel production reaction by the addition of monoglycerides, diglycerides and glycerol. J Catal 2010;276(2):229–36.
[32] Choedkiatsakul I, Ngaosuwan K, Assabumrungrat S. Application of heterogeneous catalysts for transesterification of refined palm oil in ultrasound-assisted reactor. Fuel Process Technol 2013;111:22–8.
[33] Esipovich A et al. Improving methods of CaO transesterification activity. J Mol Catal A: Chem 2014;395:225–33.
[34] Meng YL et al. Effect of calcination temperature on the activity of solid Ca/Al composite oxide-based alkaline catalyst for biodiesel production. Bioresour Technol 2013;128:305–9.
[35] Zeng D et al. Preparation and characterization of a strong solid base from waste eggshell for biodiesel production. J Environ Chem Eng 2015;3(1):560–4.
[36] Zhao H et al. MnO_2/CeO_2 for catalytic ultrasonic decolorization of methyl orange: process parameters and mechanisms. Ultrason Sonochem 2015;27:474–9.
[37] Awad SB, Nagarajan R. Developments in surface contamination and cleaning. Ultrasonic cleaning. Elsevier Inc.; 2010.
[38] Yusof NS et al. Physical and chemical effects of acoustic cavitation in selected ultrasonic cleaning applications. Ultrason Sonochem 2016;29:568–76.
[39] Walker J. Principles of physics. 9th ed. Wiley; 2011.
[40] Manickam S, Arigela VND, Gogate PR. Intensification of synthesis of biodiesel from palm oil using multiple frequency ultrasonic flow cell. Fuel Process Technol 2014;128:388–93.
[41] Santos HM, Lodeiro C, Capelo-Martinez J. Ultrasound in chemistry: analytical applications. The power of ultrasound. Weinheim: WILEY-VCH Verlag GmbH & Co. KGaA; 2009.
[42] Shahraki H, Entezari MH, Goharshadi EK. Sono-synthesis of biodiesel from soybean oil by KF/gamma-Al_2O_3 as a nano-solid-base catalyst. Ultrason Sonochem 2015;23:266–74.
[43] Eyland P. Waves, wave equation and intensity; 2015. Available from: <http://www.insula.com.au/physics/1279/L14.html> [cited 2015].
[44] Salamatinia B et al. Optimization of ultrasonic-assisted heterogeneous biodiesel production from palm oil: a response surface methodology approach. Fuel Process Technol 2010;91(5):441–8.
[45] NDT-Research-Center. Reflection and transmission coefficients (pressure). Available from: <https://www.nde-ed.org/EducationResources/CommunityCollege/Ultrasonics/Physics/reflectiontransmission.htm> [cited 2015].
[46] Jain S, Sharma MP. Thermal stability of biodiesel and its blends: a review. Renew Sustain Energy Rev 2011;15(1):438–48.
[47] Araújo BQ et al. Synthesis and characterization of beef tallow biodiesel. Energy Fuels 2010;24:4476–80.
[48] Dou B et al. Thermogravimetric kinetics of crude glycerol. Bioresour Technol 2009;100(9):2613–20.

Anamol Tripathi, Kajornsak Faungnawakij, Apirat Laobuthee, Suttichai Assabumrungrat and Navadol Laosiripojna*

Catalytic Activity of Bimetallic Cu-Ag/MgO-SiO_2 Toward the Conversion of Ethanol to 1,3-Butadiene

DOI 10.1515/ijcre-2015-0164

Abstract: In the present work, the catalytic conversion of ethanol to 1,3-butadiene (1,3-BD) was studied over monometallic of Cu and Ag, and bimetallic Cu-Ag supported on MgO-SiO_2 (with MgO/SiO_2 ratio of 2.0) under the temperature range from 250 to 325 °C. All catalysts were prepared by 4 different techniques including (i) conventional impregnation, (ii) microwave-assisted method, (iii) polyvinyl alcohol/sodium borohydride (PVA/$NaBH_4$) assisted method, and (iv) benzoxaxine-assisted method to elucidate the effect of catalyst preparation method on their catalytic performance. All fresh and spent catalysts were also characterized by X-ray diffraction (XRD), N_2 adsorption and Temperature-programmed reduction (TPR) techniques to understand the relation between their physical/chemical properties and catalytic performance. From the reaction test, it was found that 5 %Ag/MgO-SiO_2 showed greater activity towards 1,3-BD production than 5 %Cu/MgO-SiO_2; nevertheless, higher deactivation after 6 h of operation was observed from 5 %Ag/MgO-SiO_2. Importantly, this study revealed that bimetallic 2.5 %Cu-2.5 %Ag/MgO-SiO_2 enhanced significantly higher activity and stability towards the reaction than monometallic catalysts. In addition, 2.5 %Cu-2.5 %Ag/MgO-SiO_2 prepared by benzoxaxine-assisted method enhanced significantly higher reaction activity and stability than other preparation techniques, from which 1,3-BD yield of 46.40 % after 6 h of operation can be achieved. From the characterization, the good activity of this catalyst is mainly due to the dispersion improvement of metal over MgO-SiO_2 support.

Keywords: ethanol, 1,3-butadiene, bimetallic Ag-Cu, dehydrogenation

1 Introduction

Currently, 1,3-butadiene (1,3-BD) is one of the most important building block chemicals for several chemical industries because the polymerization of 1,3-BD with itself and with other olefin monomers represents its largest commercial use. Typically, 1,3-BD can be isolated from the fractions resulting from the steam cracking of naphtha, with the 1,3-BD being separated after distillation and extractive distillation processes but 1,3-BD was a by-product for this process and the desired product is ethylene. Due to the future projection of crude oil shortage, several alternative approaches for 1,3-BD production have been widely investigating.

One of the current most sustainable processes for producing 1,3-BD is from the catalytic conversion of ethanol, which can be renewably produced from the fermentation of sugars (Jones 2014; Rass-Hansen et al. 2007). With the increasing of availability and decreased in cost, ethanol is potentially a promising compound for the production of various value-added chemicals such as hydrogen and hydrocarbons ranging from light olefins to longer chain alkenes, alkanes and aromatics, and other oxygenates including 1-butanol, acetaldehyde, acetone, diethyl ether, and ethyl acetate, 1,3-BD (Sun and Wang 2014). Currently, it is known that the mechanism of ethanol transformation to 1,3-BD is very complicated and is still subject of debate (Rass-Hansen et al. 2007; Bhattacharyya and Ganguly 1962; Corson et al. 1950; Gruver, Sun, and Fripiat 1995; Janssens et al. 2015; Sun and Wang 2014 Kovarik, Benisek, and Zavrel 1960). However, it is commonly accepted that the process involves with these following steps (i) dehydrogenation

***Corresponding author: Navadol Laosiripojna,** The Joint Graduate School of Energy and Environment, CHE Center for Energy Technology and Environment, King Mongkut's University of Technology Thonburi, Thailand, E-mail: navadol@jgsee.kmutt.ac.th
Anamol Tripathi, The Joint Graduate School of Energy and Environment, CHE Center for Energy Technology and Environment, King Mongkut's University of Technology Thonburi, Thailand
Kajornsak Faungnawakij, Nanomaterials for Energy and Catalysis Laboratory, National Nanotechnology Center (NANOTEC), NSTDA, Thailand Science Park, Khlong Luang, Pathum Thani 12120, Thailand
Apirat Laobuthee, Department of Materials Engineering, Faculty of Engineering, Kasetsart University, Ladyao, Chatuchak, Bangkok 10900, Thailand
Suttichai Assabumrungrat, Department of Chemical Engineering, Faculty of Engineering, Chulalongkorn University, Bangkok, Thailand

Unauthenticated
Download Date | 4/25/16 9:52 AM

of ethanol to acetaldehyde which continuously undergoes an aldol condensation with ethanol to form acetaldol; (ii) dehydration of acetaldol to produce cis/trans crotonaldehyde, in which both aldehydes undergoes a Meerwein–Ponndorf–Verley (MPV) reduction (Janssens et al. 2015) to either 3-hydroxybutanol or crotyl alcohol also generated acetaldehyde; (iii) both alcohols i. e. 3-hydroxybutanol and crotyl alcohol generated are rapidly dehydrated to form 1,3-BD. It is noted that acid sites of the catalyst can convert ethanol into ethylene and diethyl ether as a by-products for this processes (Bhattacharyya and Avasthi 1963). Recently, various materials have been proposed as catalysts to perform this reaction (Bhattacharyya and Ganguly 1962; Corson et al. 1950; Gruver, Sun, and Fripiat 1995; Silva, Frety, and Lam 1984; Berak, Guczalski, and Wojcik 1966; Bhattacharyya and Ganguly 1962; Chang et al. 2006; Gole and White 2001; Jones, Stahly, and Corson 1949; Kitayama, Satoh, and Kodama 1996; Suzuki, Idemura, and Ono 1988; Tsuchida et al. 2008 Hao, Tao, and Zheng 1994). Basic materials based on mixtures of MgO and SiO_2 were most widely studied. Several researchers noticed that a Mg/Si ratio equal or higher than unity was essential to achieve high 1,3-BD activity. The yields of 1,3-BD on this type of catalyst were in the range of 9–42 % with a selectivity between 30 and 84 % (Corson et al. 1950; Kovarik, Benisek, and Zavrel 1960; Bhattacharyya and Avasthi 1963; Berak, Guczalski, and Wojcik 1966; Bhattacharyya and Ganguly 1962; Chang et al. 2006; Gole and White 2001; Jones, Stahly, and Corson 1949; Kitayama, Satoh, and Kodama 1996; Silva, Frety, and Lam 1984; Suzuki, Idemura, and Ono 1988; Tsuchida et al. 2008 Hao, Tao, and Zheng 1994). It has also been reported that acid-base properties also play an important role on the catalytic activity toward this reaction. Baylon, Sun, and Wang (2016) have studied the type of acidity needed for this reaction over Zn/Zr mixed oxide catalysts, and Na have been doped to control the surface acid–base properties. They reported that small amount of Na doping over ZnO-ZrO_2 can balance base and weak Brønsted acid sites and provides high selectivity toward 1,3-BD production (Baylon, Sun, and Wang 2016). Several researchers have also reported that impregnation of transition metals oxides to the magnesia–silica (MgO-SiO_2) support affects the acid-base properties of the catalyst and significantly improve the catalyst performance toward 1,3-BD production. A series of transition metals which have been studied for this process includes manganese (Mn), iron (Fe), cobalt (Co), nickel (Ni), copper (Cu), silver (Ag) and zinc (Zn) oxides and metallic (Janssens et al. 2015; Baylon, Sun, and Wang 2016; Makshina et al. 2012; Larina, Kyriienko and Soloviev 2015; Larina, Kyriienko, and Soloviev 2015; Sushkevich et al. 2014; Zhang et al. 2015). Among all metal doping, Ag supported over SiO_2-based materials (e. g. SiO_2-MgO, SiO_2-ZrO_2) has been reported to generate the highest yield of 1,3-BD (Sun and Wang 2014; Sushkevich et al. 2014). The optimal Ag loading is 1–2 wt % on a SiO_2-MgO support with a molar Mg/Si ratio of 2, from which the Ag species and basic sites (Mg-O pairs and basic OH groups) are of prime importance in the 1,3-butadiene production, catalyzing mainly the ethanol dehydrogenation and the aldol condensation, respectively (Sun and Wang 2014).

In the present work, the catalytic conversion of ethanol to 1,3-butadiene (1,3-BD) over monometallic of Cu and Ag, and bimetallic Cu-Ag supported by MgO-SiO_2 was studied under the temperature range from 250 °C to 325 °C. The co-doping of Ag with Cu was interested in the present work since the benefit of bimetallic Cu-Ag over some specific chemical reactions due to the synergistic electronic effect between Cu and Ag metals has been recently reported (Zhang et al. 2015). It is noted that the support was prepared by wet-kneading of MgO and SiO_2 in ethanol with MgO/SiO_2 ratio of 2.0. The effect of catalyst preparation method on the catalyst characteristics and activity was also tested since several works have reported the strong influence of catalyst preparation technique on the catalyst physical and chemical properties. In detail, catalysts were prepared by ((i) conventional impregnation, (ii) microwave-assisted method, (iii) polyvinyl alcohol/sodium borohydride (PVA/$NaBH_4$) assisted method, and (iv) benzoxaxine-assisted method. The additional of PVA/$NaBH_4$ and benzoxaxine as reducing agent during metal impregnation, particularly for Ag doping, has been reported to enhance good catalyst properties in term of small metal size and high metal dispersion (Kaewvilai et al. 2015). The benzoxazine method is a novel and simple method, which can be done in mild condition (no heat and catalysts required and any solvents could be used), providing a good dispersion of the silver nano-particles on the surface of powder supports in short time (15–30 min) (Kaewvilai et al. 2015). Before reaction testing, the catalysts were characterized by X-ray diffraction (XRD), N_2 adsorption and Temperature-programmed reduction (TPR) to elucidate the effect of active metal types and catalysts preparation methods on their catalytic activity.

Unauthenticated
Download Date | 4/25/16 9:52 AM

2 Materials and methods

2.1 Materials

Magnesium oxide (MgO) nanopowder was purchased from Sigma-Aldrich. Copper (II) nitrate trihydrate was purchased from Qrec. Silver nitrate was purchased from VWR, Prolabo. Polyvinyl alcohol was purchased from Ajax Finechem Pty Ltd. Sodium borohydride was purchased from Himedia. Fumed silica was purchased from Sigma-Aldrich.

2.2 Preparation of catalysts

The magnesia-silica ($MgO–SiO_2$) support (Mg/Si ratio of 2.0) was prepared by wet-kneading of magnesium oxide and fumed silica in ethanol for 8 h at room temperature using rotary evaporator. Sample was dried at 80 ◦C and calcined at 400 ◦C for 4 h. Fumed silica was used as the silica source. The prepared support containing MOx promoter where M is a monometallic (Cu and Ag) and bimetallic of copper and silver (Cu-Ag) were prepared by four different techniques. Catalysts prepared by incipient wetness impregnation method were dried at 80 ◦C in an oven and calcined at 400 ◦C for 4 h, while catalysts prepared by incipient wetness impregnation method were dried at 80 ◦C in a microwave instead of using an oven and calcined at 400 ◦C for 4 h. For the catalysts prepared with PVA protection method, copper (Cu) and silver (Ag) precursors were reduced by using $NaBH_4$ as a reducing agent. The details of catalysts preparation are as following:

(i) Weighed out the calculated amount of Cu precursor ($Cu(NO_3)_2.3H_2O$) and Ag precursor ($AgNO_3$) and dissolve Cu and Ag precursor in DI water,
(ii) Polyvinyl alcohol (PVA) 2%wt. was added into the solution from step 1 and then $NaBH_4$ was added under vigorous stirring,
(iii) $MgO\text{-}SiO_2$ support was added under vigorous stirring and kept it for 3 h, and finally the mixture was filtrated and washed the filtrate with ethanol and DI water, and dried the filtrate in an oven.

Lastly, catalysts prepared by using benzoxazine as a reducing agent can be achieved by addition of 2.5%wt. of Cu and 2.5%wt. of Ag which already has impregnated on the support, dissolved with dichloromethane (CH_2Cl_2) and addition of excess benzoxazine to reduce metal species and stirred all the samples for 3–6 h to evaporate the solvent, filtered the catalysts and kept the filtrate to dry in an oven and calcined at 400 ◦C for 4 h.

2.3 Catalyst characterizations

2.3.1 Surface area and pore analysis

The specific surface area, pore diameter, and pore volume of all catalysts were measured by Brunauer-Emmett-Teller (BET) technique in a NOVA 2000e apparatus. This method used N_2 adsorption-desorption isotherm. Before measurement, all catalysts were degassed under vacuum conditions at 150 °C for 3 h.

2.3.2 Phase identification

X-ray diffraction (XRD) pattern was obtained by an X-ray diffraction instrument with Cu Kα radiation of a wavelength of 1.54006 Å, from 10 to 90◦ of 2θ at a rate of 0.05 ◦/s. X-ray diffraction is one of a technique that can be used to identify the metal species and obtain information about the crystalline phase of catalysts. The samples prepared by conventional method have been pretreated with hydrogen gas (H_2) for 3 h at 400 °C before the XRD measurement because metallic Cu was detected.

2.3.3 Reduction temperature of catalysts

Temperature-programmed reduction (TPR) was used to characterize the reducibility and the strength of metal support. Prior to the test, a sample of 50 mg of catalyst precursor was placed in a quartz tube and purged with N_2 for 30 min. Then, the temperature was ramped from 25 °C to 850 °C at a rate of 10 °C/min in 5%v/v H_2/Ar with a flow rate of 30 ml/min. The leaving gas from the reactor was cooled down in a cold trap to remove water from the gas stream prior to being analyzed by a thermal conductivity reactor (TCD) of which the signal was analyzed by a computer-aided integrator. The rate of H_2 consumed was measured as the temperature increased.

2.4 Catalyst activity testing

To undergo the catalytic testing, the system with fixed bed quartz reactor was applied. For all testing, the feed gases i. e. nitrogen (as carrier gas) was controlled by mass

Unauthenticated
Download Date | 4/25/16 9:52 AM

flow controllers. Ethanol was introduced by the heated syringe pumps and vaporized by our designed quartz vaporizer-mixer system. All feeds were introduced to a quartz reactor, which is mounted vertically inside tubular furnace. It is noted that a Type-K thermocouple covered with small closed-end quartz rod was inserted in the middle of the quartz tube to measure the actual temperature gradient during the reaction. In each experiment, 20 mg of catalyst was used. The catalysts were firstly reduced with 10 % H_2 and 90 % N_2 at 300 °C for 4 h before testing. Range of temperature from 250 °C to 400 °C has been used for this study. The total flow rate was kept at 20 ml/min (with ethanol flow rate of EtOH flow rate in liquid form of 0.1 ml/min). The products were sampled through a six-port valve and were analyzed by on-line gas chromatography (GC) with thermal conductivity detector (TCD) and flame ionization detector (FID) by using CP-Lowox column. The yield of 1,3-BD production was calculated by carbon balance, defined as molar fraction of 1,3-BD produced to total molar fractions of carbon compounds in the products.

3 Results and discussion

3.1 Catalyst characterization

Values of specific surface area, average pore diameter and pore volume of the supports and the synthesized catalysts after being reduced in 10 % v/v H_2 in N_2 for 3 h at 150 °C were determined by the BET method. The results are summarized in Table 1. The specific surface area of catalysts were determined by multi-point technique while the total pore volume and average pore size diameter were analyzed by the Barrett, Joyner and Halenda (BJH) technique. It can be seen that the BET surface area of magnesia-silica (MgO-SiO_2) support is 138 m^2/g. After impregnation with monometallic (Cu and Ag) and bimetallic of Cu-Ag, the specific surface area of all prepared catalysts were decreased significantly as well as the pore volume. This was due to the particles of metals species blocked the MgO-SiO_2 pores. Among all preparation techniques, the catalysts prepared by microwave-assisted and benzoxaxine-assisted methods show relatively higher surface area and pore volume than conventional impregnation and PVA/$NaBH_4$-assisted method.

Table 1: Results of BET analysis.

Catalysts	Surface area (m^2/g)	Pore volume (cc/g)	Pore diameter (nm)
MgO-SiO_2-oven	138.2	0.674	3.678
5 % Cu/MgO-SiO_2-oven	109.1	0.213	4.512
5 % Cu/MgO-SiO_2-microwave	122.4	0.627	3.784
5 % Cu/MgO-SiO_2-PVA/$NaBH_4$	87.3	0.119	6.391
5 % Ag/MgO-SiO_2-oven	91.5	0.185	4.874
5 % Ag/MgO-SiO_2- microwave	114.2	0.576	3.914
5 % Ag/MgO-SiO_2- PVA/$NaBH_4$	71.6	0.101	6.781
5 % CuAg/MgO-SiO_2- oven	101.4	0.202	4.611
5 % CuAg/MgO-SiO_2- microwave	119.7	0.597	3.872
5 % CuAg/MgO-SiO_2- PVA/$NaBH_4$	76.2	0.114	6.552
5 % CuAg/MgO-SiO_2-benzoxaxine	124.7	0.603	3.714

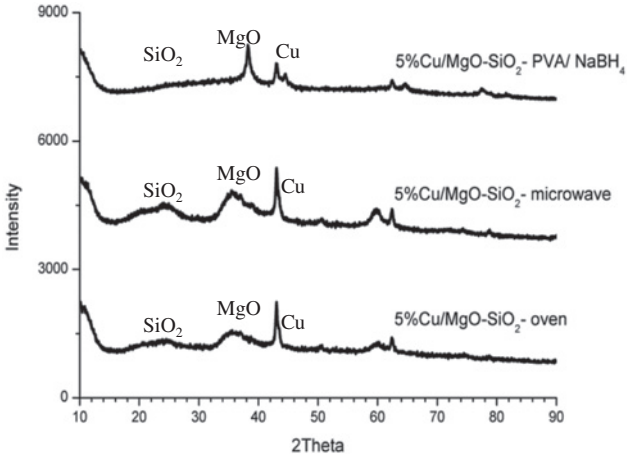

Figure 1: XRD pattern of 5 %wt. Cu/MgO-SiO_2.

From the XRD analysis, the nitrate hydrate under the thermal treatment was converted to an oxide in the form of CuO, as indicated in Figure 1. The component of Cu_2O seems to be absent or its content is below the detection limit. The occurrence of the broad peaks around $2\theta = 20^\circ$ and 30° can undoubtedly be attributed to the amorphous SiO_2, used as one of the support. XRD patterns of binary Mg–Si materials showed the presence of crystalline MgO oxide phase with peak positions at $2\theta = 36.6^\circ$ and 42.8°, which are attributed to (1 1 1) and (2 0 0) planes of periclase. The full-width at half-maximum (FWHM) of MgO reflections were slightly different for the samples prepared by different synthetic procedures due to the different particle size and crystallinity. The X-ray diffraction pattern of the copper nanoparticles synthesized by different methods is also presented in Figure 1. A number of strong Bragg reflections can be corresponding to the (111), (200), (220), (311) and (222) reflections of FCC copper.

Unauthenticated
Download Date | 4/25/16 9:52 AM

The high intense peak for FCC materials is generally (111) reflection, which is observed in the samples. The intensity of peaks reflected the high degree of crystallinity of the copper nanoparticles. Three peaks at 2θ values of 43.0370, 50.6570 and 74.4697 degree corresponding to (111), (200) and (220) planes of Copper is observed. The XRD study confirms and indicates that the resultant particles are (FCC) copper nanoparticles. There are few less intense peaks at 35.5673°, 37.0713° and 62.3879° in the XRD patterns of samples. This could be corresponding to the presence of CuO in the samples. The appearance of peaks related to CuO may be due to the oxidation of copper after the synthesis process.

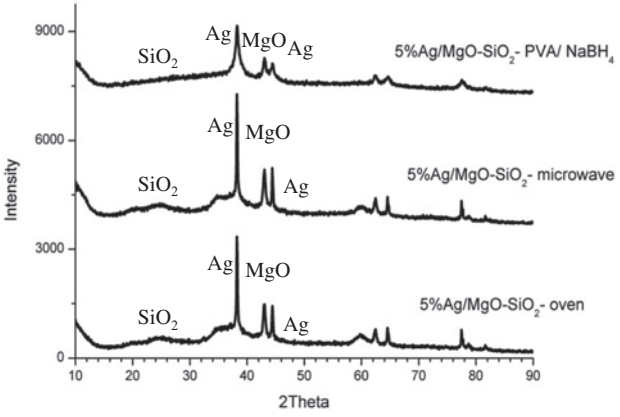

Figure 2: XRD pattern of 5 %wt. Ag/MgO-SiO_2.

The X-ray diffraction pattern of the silver nanoparticles synthesized by different methods is given in Figure 2. Indexing process of powder diffraction pattern was done and Miller Indices (h k l) to each peak was assigned in first step. A number of strong Bragg reflections can be seen which corresponding to the (111), (200), (220) (311) and (222) reflections of FCC silver. All the reflections correspond to pure silver metal with face centered cubic symmetry. The high intense peak for FCC materials was generally (111) reflection, which can be observed in the samples. The intensity of peaks reflected the high degree of crystallinity of the silver nanoparticles. However, the diffraction peaks were broad which indicating that the crystallite size was very small. The XRD showed that silver nanoparticles formed are crystalline. Five peaks at 2θ values of 38.3246, 44.4407, 64.5436, 77.4776 and 81.6386 degree corresponding to (111), (200), (220), (311) and (222) planes of silver was observed. The XRD study confirmed and indicated that the resultant particles were (FCC) silver nanoparticles.

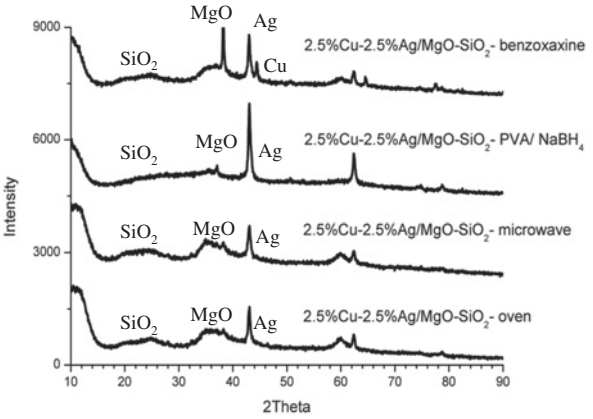

Figure 3: XRD patterns of 2.5 %wt. Ag – 2.5 %wt. Cu/MgO-SiO_2.

In order to see the crystalline behavior of the Ag-Cu nanoparticles, XRD measurements of the catalysts containing Ag-Cu particles were carried out, as presented in Figure 3.

The dispersion of metal species and the interactions between the metal ions and support was studied in detail by a temperature-programmed reduction (TPR) technique. A reducing gas composed of 5 % H_2 plus 95 % Ar was employed at a flow rate of 30 ml/min, with a heating ramp of 10 °C/min. The H_2 consumption was detected with a thermal conductivity detector (TCD), of which the signal was analyzed by a computer-aided integrator. For the precursor with 5 %wt copper metal loading, two hydrogen consumption peaks adjacent to each other and with a fraction lumped together exhibit the reduction temperatures centered at about 420–440 °C and 510–573 °C, respectively, as revealed by Figure 4. The peak centered at 420–440 °C may be ascribed to the highly dispersed CuO with smaller size, whereas the peak at 510–573 °C

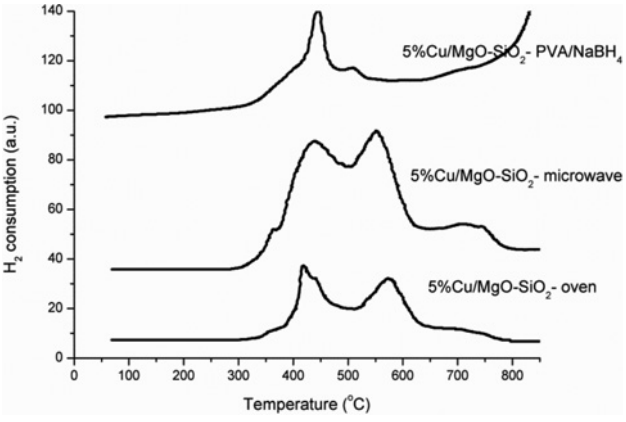

Figure 4: TPR profiles of 5 %wt. Cu/MgO-SiO_2.

Unauthenticated
Download Date | 4/25/16 9:52 AM

may be due to the bulk CuO with larger size since it was known that the maximum temperature at the climax of a peak depends on three factors, i. e. the heating rate, the amount of H_2 in the reducing gas, and the operating parameters of the reactor/flow system. The minor peak indicated a copper species other than CuO. It may be resulting from Cu^{2+} ions chemically interacting with the surface of the $MgO\text{-}SiO_2$ support. The formation for these types of ions was occasionally found in the precursors prepared impregnation technique. Therefore, the TPR profiles in this research implied the existence of both CuO and Cu^{2+} ions in the calcined catalysts. Therefore, copper metal loading with 5 % by weight given an asymmetric peak, which marks the superimposition of at least two isolated peaks indicating the discrimination in reduction behavior due to the difference in CuO crystallite size.

For the precursor with 5 %wt silver metal loading, one hydrogen consumption peak exhibited the reduction temperatures centered at about 300 °C to 350 °C as shown in Figure 5. The specific reaction was $AgO + H_2 \rightarrow Ag + H_2O$. For the precursor with 2.5 %wt. of silver metal loading plus 2.5 %wt. of copper metal loading, only one hydrogen consumption peak exhibited the reduction temperatures centered at 400–450 °C as shown in Figure 6.

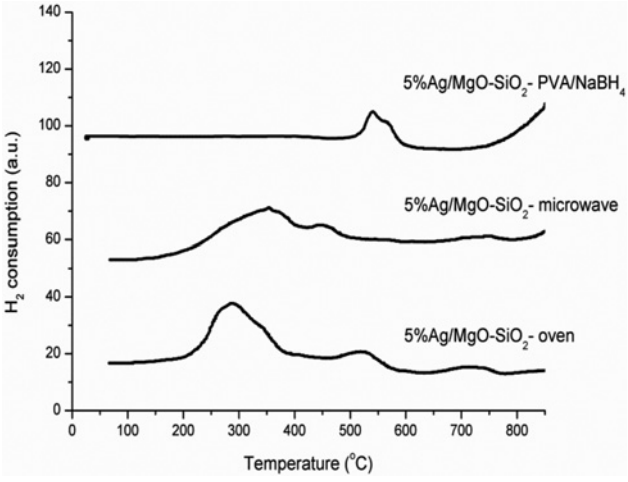

Figure 5: TPR profiles of 5 %wt. $Ag/MgO\text{-}SiO_2$.

3.2 Catalytic activity towards ethanol conversion to 1,3-butadiene

Firstly, all monometallic catalysts were tested toward the ethanol dehydrogenation for butadiene production at four different temperatures, range from 250 °C to 375 °C.

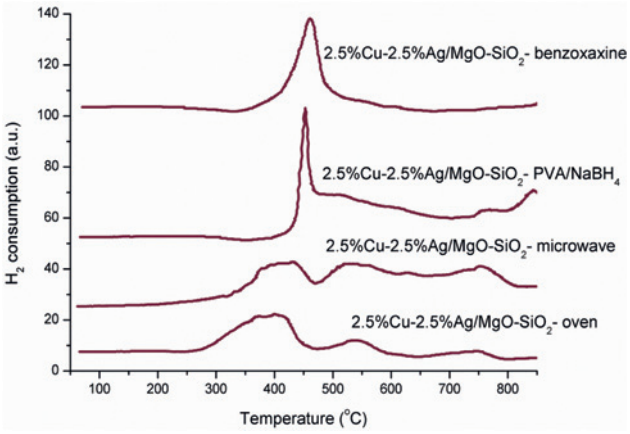

Figure 6: TPR profiles of 2.5 %wt. Cu-2.5 %wt. $Ag/MgO\text{-}SiO_2$.

From the test, three major products were observed in this study i. e. hydrogen, acetaldehyde, and 1,3-BD. Figures 7 and 8 show the ethanol conversion and products yield of 1,3-BD from dehydrogenation reaction of ethanol implemented in a temperature range from 250 °C to 375 °C in the presence of 5 %wt. $Cu/MgO\text{-}SiO_2$ and 5 %wt. $Ag/MgO\text{-}SiO_2$ prepared by conventional method, microwave-assisted technique, and $PVA/NaBH_4$ method, respectively. It can be seen from Figure 7 that, among all preparation technique, ethanol conversion and the yield of 1,3-BD from 5 %wt. $Cu/MgO\text{-}SiO_2$ prepared from microwave-assisted technique are the highest. When the temperature increased, ethanol conversion increased; nevertheless, the yield of 1,3-BD oppositely decreased, which is probably due to the thermal decomposition of butadiene or deactivation of the catalyst from the sintering of copper metal at high temperature. In case of 5 %wt. $Ag/MgO\text{-}SiO_2$, as shown in Figure 8, similar trend as 5 %wt. $Cu/MgO\text{-}SiO_2$ was observed, from which the highest performance for 5 %wt. $Ag/MgO\text{-}SiO_2$ catalysts was also prepared by microwave-assisted technique. When compared between 5 %wt. $Cu/MgO\text{-}SiO_2$ and 5 %wt. $Ag/MgO\text{-}SiO_2$, it is clear that at the same operating conditions 5 %wt. $Ag/MgO\text{-}SiO_2$ showed higher ethanol conversion and yield of 1,3-BD particularly at initial period of testing. Nevertheless, after long-term testing (6 h), significant higher deactivation was observed over 5 %wt. $Ag/MgO\text{-}SiO_2$ compared to the 5 %wt. $Cu/MgO\text{-}SiO_2$ (45.50 % and 20.40 % for conventional impregnation technique, 40.90 % and 13.90 % for microwave assisted technique, 47.80 % and 24.90 % for $PVA/NaBH_4$ method). This higher deactivation could be due to the high carbon formation on the surface of Ag catalyst

Unauthenticated
Download Date | 4/25/16 9:52 AM

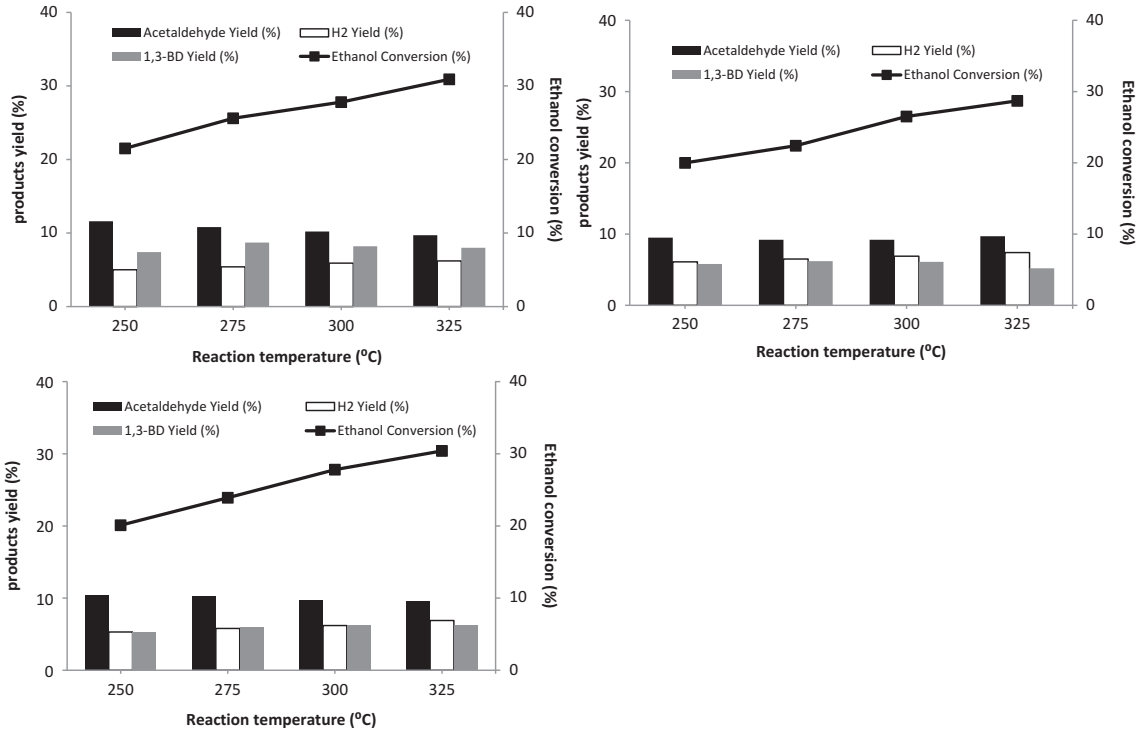

Figure 7: Ethanol conversion, acetaldehyde, hydrogen (H_2), and 1,3-BD yield as a function of reaction temperature for ethanol dehydrogenation reaction over 5 %wt. $Cu/MgO\text{-}SiO_2$ catalysts with different preparation techniques; (I) conventional method, (II) microwave-assisted technique, (III) $PVA/NaBH_4$ method.

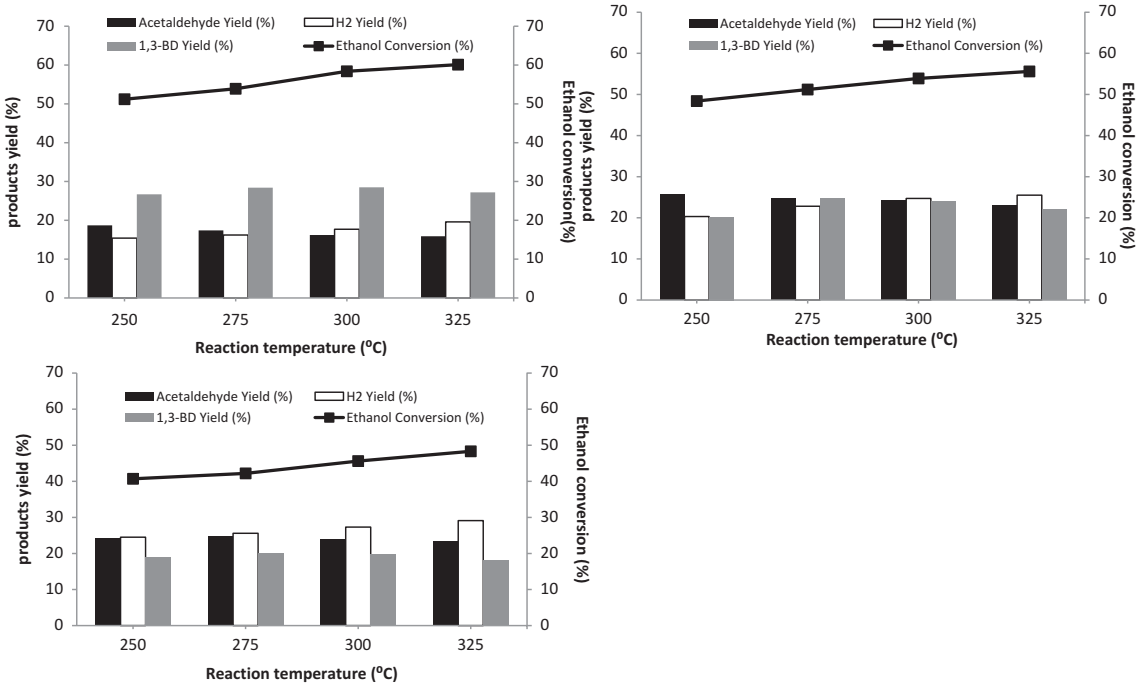

Figure 8: Ethanol conversion, acetaldehyde, hydrogen (H_2), and 1,3-BD yield as a function of reaction temperature for ethanol dehydrogenation reaction over 5 %wt. $Ag/MgO\text{-}SiO_2$ catalysts with different preparation techniques; (I) conventional method, (II) microwave-assisted technique, (III) $PVA/NaBH_4$ method.

Unauthenticated
Download Date | 4/25/16 9:52 AM

which has been widely reported in the literature. For comparison, the catalytic activity of MgO-SiO_2 without metal doping was also tested. Under the same operating condition (300 °C), relatively lower yield of 1,3-BD (4.8 %) was generated; this result therefore indicated the beneficial of Ag and Cu doping on the catalytic activity.

Bimetallic 5 %wt. CuAg/MgO-SiO_2 catalysts were then tested for comparison. It was noted that bimetallic catalysts have been widely used for industrial processes for many years because of their unique catalytic properties and high resistance toward carbon formation. In this research, it was found that bimetallic 5 %wt. CuAg/MgO-SiO_2 catalysts offer improvement in catalyst activity towards the ethanol dehydrogenation compared to 5 %wt. Ag/MgO-SiO_2 and 5 %wt. Cu/MgO-SiO_2 as shown in Figure 9. After long-term testing, it was found that bimetallic catalysts 5 %wt. CuAg/MgO-SiO_2 showed relatively higher deactivation than monometallic catalysts 5 %wt. Cu/MgO-SiO_2 but significantly less than 5 %wt. Ag/MgO-SiO_2 (30.40 %, 20.40 % and 45.50 % for conventional impregnation technique, 25.70 %, 13.90 % and 40.90 % for microwave-assisted technique, 35.50 %, 24.90 % and 47.80 % for PVA/$NaBH_4$ method). It was also observed that preparation technique for the catalysts strongly affects the yield of products. As shown in Figure 10, bimetallic Cu-Ag catalysts prepared by using benzoxaxine as a reducing agent technique gains the highest reaction activity and stability, from which 1,3-BD yield of 46.40 % after 6 h of operation can be achieved. This good activity could be due to the dispersion improvement of metal over the support by this preparation technique as well as the synergistic electronic effect between Cu and Ag metals, as previously reported in the literature (Zhang et al. 2015; Kaewvilai et al. 2015; Zheng et al. 2012). According to the literature, the benzoxazine method can provide considerably high dispersion of Ag over the surface of supports (Kaewvilai et al. 2015), while the additional of Cu can effectively regulate the size of Ag crystallites to restrain their agglomeration and withdraw electrons from nearby Ag and make Ag electropositive, which is beneficial to produce more active sites where electrophilic oxygen species can be absorbed (Zheng et al. 2012). Furthermore, Cu atom was reported to have a lower electron density in the bimetallic form than that in monometallic compound (Zhang et al. 2015).

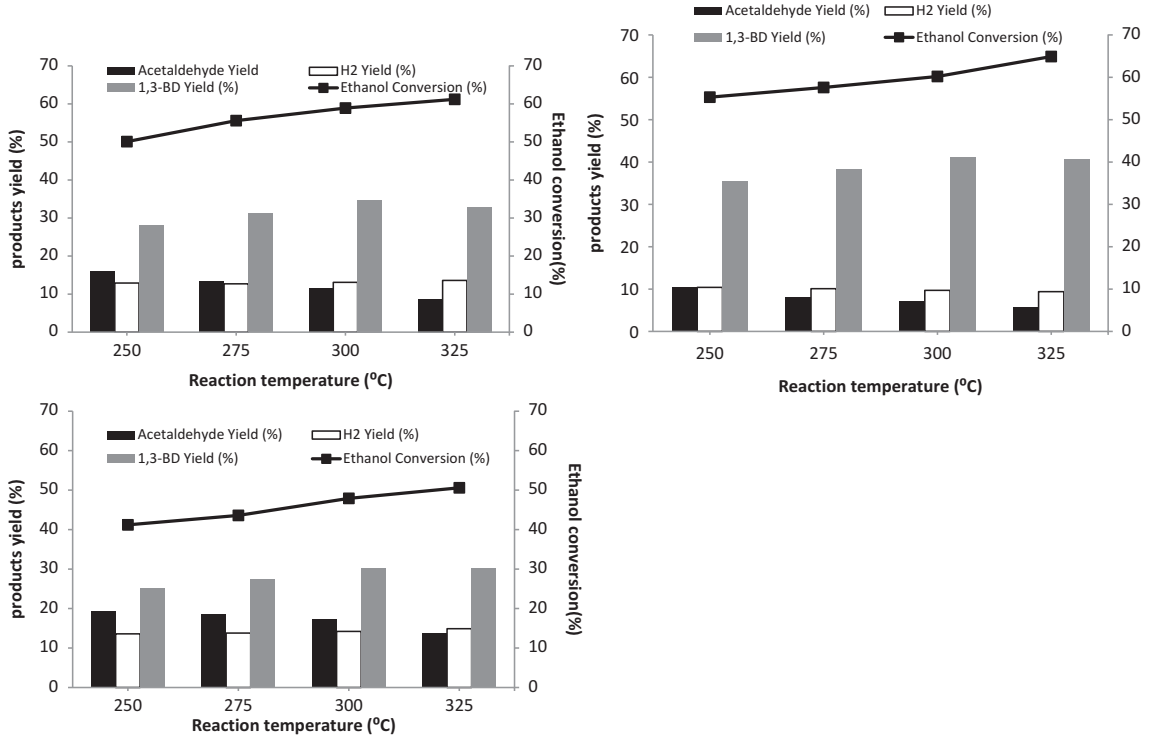

Figure 9: Ethanol conversion, acetaldehyde, hydrogen (H_2), and 1,3-BD yield as a function of reaction temperature for ethanol dehydrogenation reaction over 2.5 %wt Cu-2.5 %wt Ag/MgO-SiO_2 catalysts with different preparation techniques; (I) conventional method, (II) microwave-assisted technique, (III) PVA/$NaBH_4$ method.

Unauthenticated
Download Date | 4/25/16 9:52 AM

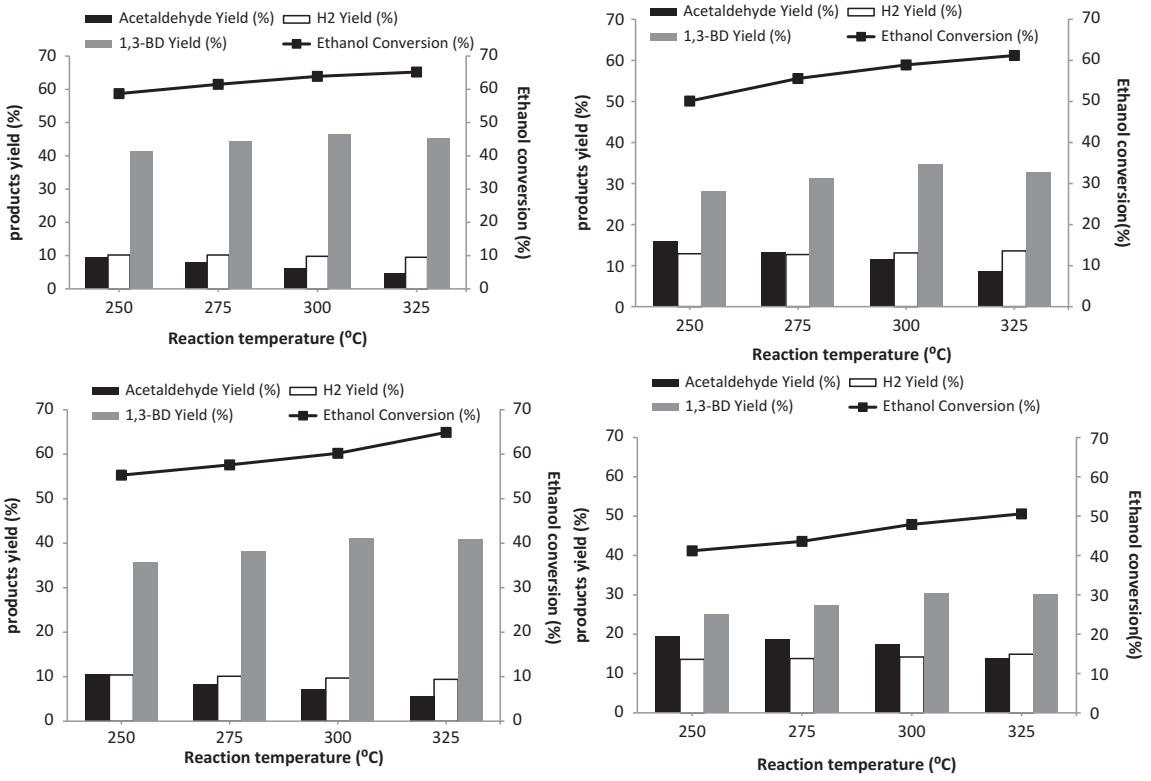

Figure 10: Ethanol conversion, acetaldehyde, hydrogen (H_2), and 1,3-BD yield as a function of reaction temperature for ethanol dehydrogenation reaction over 2.5 %wt Cu-2.5 %wt Ag/MgO-SiO_2 catalysts with different preparation techniques; (I) using benzoxaxine as a reducing agent technique, (II) conventional method, (III) microwave-assisted technique, (IV) PVA/$NaBH_4$ method.

4 Conclusions

This research revealed that types of active metals and catalysts preparation methods show significant influence on the catalyst activity toward the conversion of ethanol to 1,3-butadiene. In terms of active metals between Cu and Ag, Ag metal provided higher productivity of 1,3-BD compared to the Cu metal; nevertheless, higher deactivation was also observed. Bimetallic Cu-Ag offered relatively higher productivity of 1,3-BD with greater stability as compared with the monometallic ones. According to the effect of catalyst preparation techniques, it was found that the catalysts prepared using benzoxaxine as a reducing agent tended to produced more 1,3-BD along with the lower deactivation values, which are mainly due to the improvement of dispersion of metal species over the support by this preparation technique.

Acknowledgements: The financial support from The Thailand Research Fund (Contact no. DPG5880003) throughout this project is gratefully acknowledged.

References

1. Angelici, C., Velthoen, M.E.Z., Weckhuysen, B.M., Bruijnincx, P.C.A., 2014. Effect of Preparation Method and CuO Promotion in the Conversion of Ethanol into 1, 3-Butadiene over SiO_2–MgO Catalysts. Chemsuschem 7, 2505–2515.
2. Baylon, R.A.L., Sun, J., Wang, Y,, 2016. Conversion of ethanol to 1, 3-butadiene over Na doped $Zn_xZr_yO_z$ mixed metal oxides. Catalytic Science and Technology in Sustainable Energy 259, 446–452.
3. Berak, J.M., Guczalski, R., Wojcik, J., 1966. The influence of ZnO promotor on the activity and selectivity of the catalyst in butadine synthesis from ethyl alcohol. Acta Chimica Academiae Scientarium Hungaricae 50, 163.
4. Bhattacharyya, S.K., Avasthi, B.N., 1963. One-Step Catalytic Conversion of Ethanol to Butadiene in a Fluidized Bed. Ind. Eng. Chem. Process Des. Dev 2, 45–51.
5. Bhattacharyya, S.K., Ganguly, N.D., 1962. One-step catalytic conversion of ethanol to butadiene in the fixed bed. II Binary- And Ternary-Oxide Catalysts. Journal of Applied Chemistry 12, 105.
6. Bhattacharyya, S.K., Ganguly, N.D., 1962. One-step catalytic conversion of ethanol to butadiene in the fixed bed. I. Single-oxide catalysts. Journal of Applied Chemistry 12, 97.

Unauthenticated
Download Date | 4/25/16 9:52 AM

7. Chang, F.W., Yang, H.C., Roselin, L.S., Kuo, W.Y., 2006. Ethanol dehydrogenation over copper catalysts on rice husk ash prepared by ion exchange. Appl. Catal., A 304, 30–39.
8. Corson, B.B., Jones, H.E., Welling, C.E., Hinckley, J.A., Stahly, E.E., 1950. Butadiene from Ethyl Alcohol. Catalysis in the One- and Two-Stop Processes. Industrial and Engineering Chemistry 42, 359.
9. Gole, J.L., White, M.G., 2001. Nanocatalysis: Selective Conversion of Ethanol to Acetaldehyde Using Mono-atomically Dispersed Copper on Silica Nanospheres. J. Catal 204, 249–252.
10. Gruver, V., Sun, A., Fripiat, J.J., 1995. Catalytic properties of aluminated sepiolite in ethanol conversion. Catalysis Letters 34, 359.
11. Hao, Y.Z., Tao, L.X., Zheng, L.B., 1994. Ethanol dehydrogenation on silica pillared rectorite. Appl. Catal., A 115, 219–228.
12. Janssens, W., Makshina, E.V., Vanelderen, P., De Clippel, F., Houthoofd, K., Kerkhofs, S., Martens, J.A., Jacobs, P.A., Sels, B.F., 2015. Ternary Ag/MgO-SiO_2 Catalysts for the Conversion of Ethanol into Butadiene. ChemSusChem 8(6), 994–1008.
13. Jones, M.D., 2014. Catalytic transformation of ethanol into 1, 3-butadiene. Chemistry Central Journal 8, 53.
14. Jones, H.E., Stahly, E.E., Corson, B.B., 1949. Butadiene from Ethanol. Reaction Mechanism. J Am Chem Soc 71, 1822.
15. Kaewvilai, A., Wattanathana, W., Jongrungruangchok, S., Veranitisagul, C., Koonsaen, N., Laobuthee, A., 2015. 3, 4-Dihydro-1, 3–2H-benzoxazines: Novel reducing agents through one electron donation mechanism and their application as the formation of nano-metallic silver coating. Materials Chemistry and Physics 167, 9–13.
16. Kitayama, Y., Satoh, M., Kodama, T., 1996. Preparation of large surface area nickel magnesium silicate and its catalytic activity for conversion of ethanol into buta-1, 3-diene. Catalysis Letters 36, 95.
17. Larina OV, Kyriienko PI, Soloviev SO, 2015. Ethanol Conversion to 1, 3-Butadiene on ZnO/MgO–SiO_2 Catalysts: Effect of ZnO Content and MgO:SiO_2 Ratio. Catalysis Letters 145, 1162–1168.
18. Makshina, E.V., Janssens, W., Sels, B.F., Jacobs, P.A., 2012. Catalytic study of the conversion of ethanol into 1,3-butadiene. Catal Today. 198, 338–344.
19. Rass-Hansen, J., Falsig, H., Jorgensen, B., Christensen, C.H., 2007. Bioethanol: fuel or feedstock? J. Chem. Technol. Biotechnol 82, 329–333.
20. Sun, J., Wang, Y., 2014. Recent Advances in Catalytic Conversion of Ethanol to Chemicals. ACS Catalysis 4(4), 1078–1090.
21. Sushkevich, V.L., Ivanova, I.I., Ordomsky, V.V., Taarning, E., 2014. Design of a Metal-Promoted Oxide Catalyst for the Selective Synthesis of Butadiene from Ethanol. Chemsuschem 7, 2527–2536.
22. Tsuchida, T., Kubo, J., Yoshioka, T., Sakuma, S., Takeguchi, T., Ueda, W., 2008. Reaction of ethanol over hydroxyapatite affected by Ca/P ratio of catalyst. Journal of Catalysis 259, 183.
23. Zhang, M., Gao, M., Chen, J., Yu, Y., 2015. Study on key step of 1, 3-butadiene formation from ethanol on MgO/SiO_2. RSC Adv 5, 25959–25966.
24. Zhang, Z., Ji, Y., Li, J., Zhong, Z., Su, F., 2015. Synergistic effect in bimetallic copper–silver (CuxAg) nanoparticles enhances silicon conversion in Rochow reaction. RSC Adv 5, 54364–54371.
25. Zheng, X., Zhang, Q., Guo, Y., Zhan, W., Guo, Y., Wang, Y., Lu, G., 2012. Epoxidation of propylene by molecular oxygen over supported Ag–Cu bimetallic catalysts with low Ag loading. Journal of Molecular Catalysis A: Chemical 357, 106–111.

Unauthenticated
Download Date | 4/25/16 9:52 AM

I&EC research
Industrial & Engineering Chemistry Research

Article

pubs.acs.org/IECR

Gas Flow Visualization in Low Aspect Ratio Packed Beds by Three-Dimensional Modeling and Near-Infrared Tomography

Faris Alzahrani,[†] Mohammed Aldehani,[†] Hao Rusi,[‡] Michael McMaster,[‡] Daniel Luis Abreu Fernandes,[§] Suttichai Assabumrungrat,[∥] Meabh Nic An tSaoir,[‡] and Farid Aiouache*[,†]

[†]Department of Engineering, Lancaster University, Lancaster LA1 4YW, U.K.

[‡]School of Chemistry and Chemical Engineering, Queen's University Belfast, Belfast BT7 1NN, Northern Ireland, U.K.

[§]Department of Chemistry - Ångström Laboratory, Uppsala University, Uppsala 751 05, Sweden

[∥]Centre of Excellence in Catalysis and Catalytic Reaction Engineering, Department of Chemical Engineering, Chulalongkorn University, Pathumwan, Bangkok 10330, Thailand

Supporting Information

ABSTRACT: Nonuniform local flow inside randomly porous media of gas−solid packed beds of low aspect ratios ranging from 1.5 to 5 was investigated by three-dimensional modeling and near-infrared tomography. These beds are known to demonstrate heterogeneous mixing and uneven distributions of mass and heat. The effects of the confining wall on flow dynamics were found nonlinear, particularly for aspect ratios lower than 3. High velocities were mainly observed in regions near the wall of aspect ratio value of 1.5 and those of values higher than 3, owing to high local porosities in these zones. Mass dispersion characterized both by experimental near-infrared imaging and by particle tracking showed discrepancies with literature models, particularly for aspect ratios lower than 3. Uncertainties were more significant with the radial dispersion due to bed size limits. Beyond this value, the wall affected more the axial dispersion, confirming the nonlinear impact of the wall on global hydrodynamics.

1. INTRODUCTION

Packed beds of low aspect ratios (ARs) of tube to particle diameters are commonly used in various industrial applications, owing to their simple arrangement and high surface-area-to-volume ratios, leading to integrated heat and mass exchanges. Driven by reduced pressure drops and improved heat exchange, innovative designs of these low AR packed beds have been demonstrated for applications including catalytic reactors (i.e., steam reforming, composite structured packing, nuclear reactors, meso- and microchemical reactors),[1−5] separators (i.e., dehumidification adsorbers for energy storage,[6] chromatographic columns, filters, and CO_2 sequestration), and thermal exchangers (compact heat exchangers). These growing applications have attracted interest into understanding local phenomena taking place using both advanced experimental tools and advanced modeling. Unfortunately, these tools were not sufficiently dedicated toward very low AR packed beds (i.e., AR less than 5), owing to disperse phenomena taking place, requiring spatially resolved observations. This applies even more to gas flow dynamics where phenomena of mixing and dispersions are strongly affected by density and temperature changes.

Although limited by the confining walls, models of fluid flow in these packed beds have been historically based on simplified one-dimensional (1D) pseudohomogenous models or heterogeneous two-phase models. Improvements of these models contained introduction of the two-dimensional (2D) models with inclusion of concepts of axial or longitudinal dispersion and radial or transversal dispersion, relying on the average structure of porosity. The 2D models of heat and mass configurations rely on lumping the local structure and the local flow velocity inside the packing and between the packing and the containing wall, and their key parameters (i.e., porosity, permeability, viscosity, and dispersion constants) are estimated by experimental data and regression analysis of appropriate models.[7] These 1D and 2D models are as well driven by empirical solutions, yielding disagreements between the data of various literature works obtained inside the packing as well as those in regions in the vicinity of the confining walls, and thus rational understanding of crucial underlying phenomena is still challenging.[1−4] Furthermore, these models raise issues of arbitrary combinations of the non-Darcy (grain) and the nonporous Darcy scales and provide challenging representations of the nonslip/slip assumptions or actual viscosity at the surface of the grain.[8] This is particularly the case for low AR packing, where the tube wall effects and the local phenomena strongly dominate.[2−4,9] Owing to the limitation in space resolution of the detailed flow picture inside these beds, these models give few insights into the local mechanisms and possible methods of controlling the rates of chemical or transport events.[10] In reality, thermal energy is transported by radial convective flows as fluid is displaced around the packing elements, while features of the flow in regions of stagnant and reverse exits have been identified by a number of spatially resolved experiments.[11−13] Local insights are known to be linked to performances of flow dynamics as well as heat and mass transfers, leading to requirements of more realistic levels

Received: July 20, 2015
Revised: November 3, 2015
Accepted: December 10, 2015
Published: December 10, 2015

ACS Publications © 2015 American Chemical Society

DOI: 10.1021/acs.iecr.5b02635
Ind. Eng. Chem. Res. 2015, 54, 12714−12729

of knowledge of transport processes by three-dimensional (3D) modeling.

The 3D modeling of the flow field and transport using actual or computer-generated bed shapes has been growing through the past few years, as it offers comparable spatiotemporal resolution with 3D experimental methods, such as tomographic techniques (i.e., X-ray computer tomography, magnetic resonance imaging (MRI), laser Doppler anemometry, etc.).[2,3] From the 3D simulation results, profiles of radial porosity, velocity, temperature, and dispersion are becoming accessible from a sufficient amount of data, while a limited number of experiments are used. Laboratory experiments on local velocity profiles were visualized for liquid flow by Giese et al.,[10] using the refractive index matching technique, and by Gladden et al.,[14] using MRI, ascertaining many simulation works on fluid flow in porous media of different structures (spheres, cylinders, ordered, disordered, monodisperse and polydisperse, and so on).

The approaches using 3D modeling are still, however, limited by requirements of large memories and computational power.[3] Current simulations, consisting of hundreds to over a thousand packed particles, still require large computation time, leading to simulations being carried out for small or laboratory scales.[1,15] An alternative option to take into account actual or local structures of packed beds is to couple the fluid flow with the radial variation of porosity.[9] Radial distribution of porosity is a structural characteristic of packed beds and presents a significant importance for beds with low ARs of tube-to-particle diameters owing to the influence of the confining wall. The spheres near these walls form more ordered structures than spheres in the internal regions, leading to oscillatory trends of porosity and to damping behaviors in the near-wall regions. This damping profile has been demonstrated by Roblee et al.,[16] who used cork spheres within molten wax, as well as by Sederman et al.,[17] who used the MRI technique to observe the flow of water through a packing of ballotini spheres. The damping profile could be computed by combining the angularly averaged data from a limited number of cross-sectional projections of porosity and then expressed in terms of empirical, semiempirical, or analytical models.[18−22] The accuracies of these models were good in regions either near the wall or near the center of the packed bed, but they were rarely good for both regions. For instance, Mueller et al.,[23,24] who described the oscillations with a Bessel function of the first kind of order zero and the radial damping with an exponential function, developed a model that overpredicts the radial porosity near the wall but describes the radial porosity accurately when the radial distance increases from the wall. Govindarao et al.[4] developed analytical expressions using concentric cylindrical channels of good accuracies in the near wall regions, particularly for packed beds of large AR. Dixon et al.[25] improved the semiempirical models by computing the effect of the shape of beads (i.e., spheres, cylinders, or hollow cylinders). Theuerkauf et al.[15] used the discrete element method (DEM), which accounts for particle−particle and particle−wall mechanical interactions to measure particle-scale structure and porosity in a series of beds with AR in the range 3−20.

The confining wall of low AR packed beds affects not only the porosity distribution but also the fluid flow in terms of velocity and pressure drops as well. Early investigations by Kozeny[26] and Carman and Ergun[27,28] essentially used Darcy and Forchheimer approaches for randomly distributed particles. However, Happel,[29] Bertil Anderson,[30] Molerus,[31] and Eisfeld and Schnitzlein[32] used knowledge of the local flow behavior near the solid surface inside the packing. The distribution of the local velocity in the intergranular space, the pressure drop, and the permeability were found to be affected by the flow regime, the internal structure of the packed bed, and the dimensions and the shapes of both the particles and the packed bed.[33] The flow behavior was a function of interactions between the fluid, the particles, and the column wall.[34] In addition to the flow, the confining walls have effects on the dispersion of species and heat in packed beds of low AR. Influenced by the structural porosity of the packing, the interaction of convective and diffusive transport presents trends of residence time distribution and dispersions of different trends than those observed in large AR packed beds.[2] The mass dispersion of species inside 3D-packed beds is recurrently validated by means of the averaged radial component (D_{rad}) and the averaged axial component (D_{ax}) of dispersion. These components are computed by mass dispersion experiments which use either a continuous approach of chemical concentration tracing or a discontinuous approach of particle tracing to fit dispersion constants at dynamic operations. The later approach, which uses the DEM, is a Lagrangian method where movement of concentration equivalent particles is tracked instead of fluid species. The convective motion along streamlines and by a diffusive motion between different streamlines allows distribution of the particles to be reconstructed and the underlying models of axial and radial dispersions as a function of the dimensionless Peclet number (Pe) to be developed.[2]

These experimental works were mainly applied to liquid flow while those applied to local gas flow were rarely approached, owing to insufficient maturity of relevant methods, leading to uncertainty of existing simulation results, particularly under nonisothermal flow and changes in density, viscosity, etc. Optical tomography, such as laser-based near-infrared (NIR) tomography, was demonstrated as a promising technique to visualize fluid flow in packed beds of low scattering properties. Simultaneous measurements by absorption spectroscopy and two-line thermometry allowed 3D distributions of temperature and concentrations inside packed bed adsorbers and reactors to be visualized at spatial resolution of millimeters. Qualitative observations of NIR tomography results revealed uneven distributions of temperature and compositions caused by the flow maldistribution, channelling, and intraparticle rate limitations. The major advantage of laser-based tomography to fluid flow inside packed beds with low aspect ratio (AR) is driven by the low scattering of the source intensity. The values of the number of scattering or optical depth (OD), as expressed in Appendix A1, are lower than unity for packed beds of ARs less than 10, suggesting a ballistic light propagation through the packing and allowing the modified Beer−Lambert law to be applied to local concentration measurements.[35]

In this work, 3D modeling and spatially resolved NIR tomography are used to visualize the fluid flow and spatial distributions of species in gas−solid packed beds of randomly distributed particles, subject to wall effects. The approach is extended to packed beds of ARs ranging from 1.5 to 5 and to flow regime ranging from laminar to transitional flow limits ($Re \sim 400$). The results of experimental tests are used to validate 3D computer fluid dynamics (CFD) modeling. Knowledge of fluid flow in a low AR packed bed is still scarce, particularly for AR less than 3, where packed beds show more local heterogeneity, less fluid mixing, and uneven structural porosity,

DOI: 10.1021/acs.iecr.5b02635
Ind. Eng. Chem. Res. 2015, 54, 12714−12729

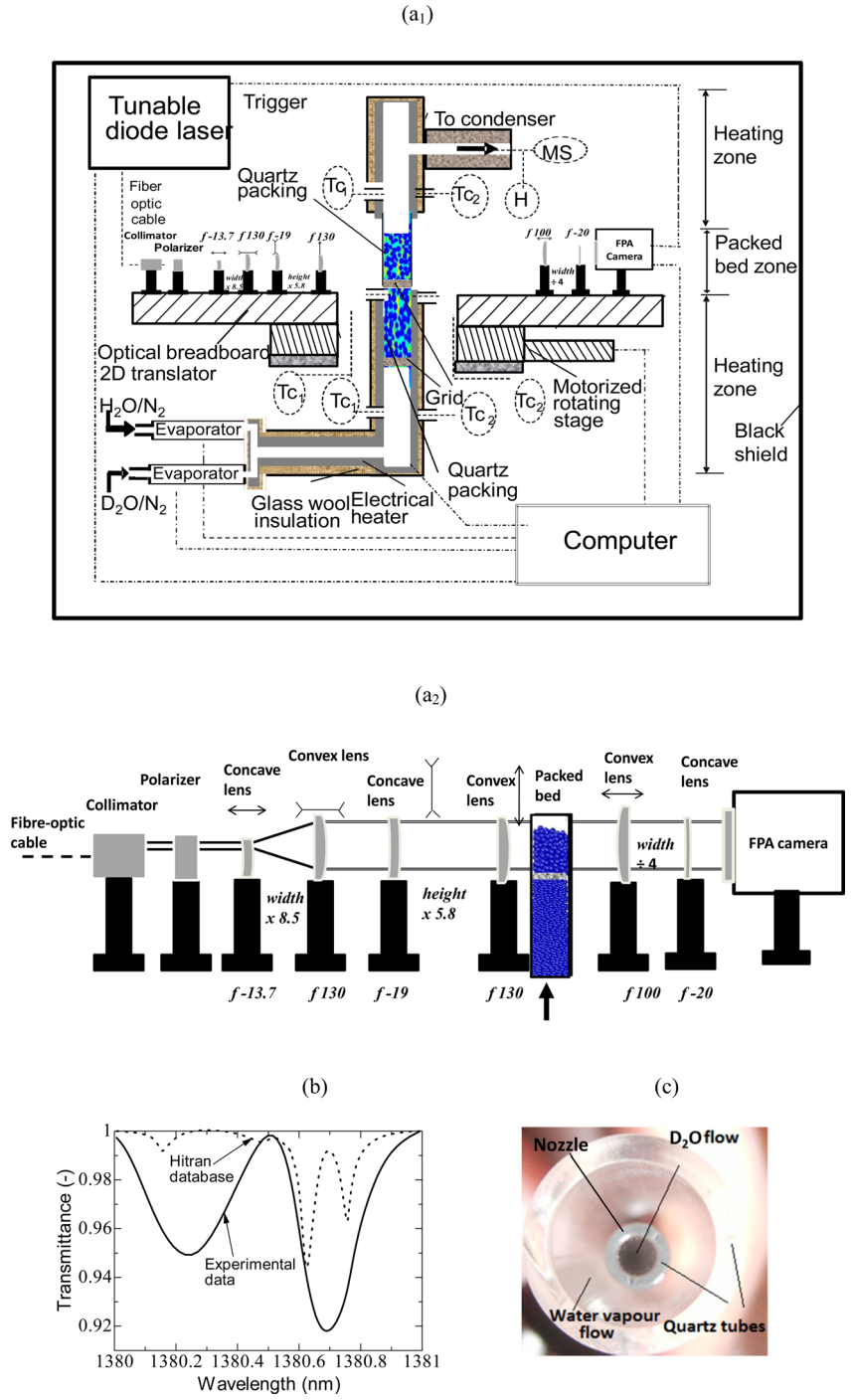

Figure 1. Scheme of the whole tomography apparatus (a_1), optical setup (a_2), spectra of water vapor (b), and Nozzle design top view (c). Nozzle diameter: 5 mm; packed bed tube diameter: 12 mm; thickness of both tubes: 1 mm; evaporator (Bronkhorst) = mass flow controller (N_2), air-actuated switching valve, distilled water bath; H: humidity sensor; TC_1 = thermocouples (monitoring); TC_2: thermocouples connected to programmable temperature controllers; MS: mass spectrometer; Optics = details of optics are shown in Figure 1b; Tunable diode laser: lock-in monomode connected to FPA camera; prepacked bed mixer; quartz bead packed bed = height: 39 cm; visible aperture by NIR camera: 1.20 × 5.4 cm^2. Monomode fiber-optic cable connected to a collimator with a top-hat beam shaper (size: 5 mm); polarizer, two couple of cylindrical lenses of focal points *f* (mm): *f*-13.7, *f*-130 and *f*-19, *f*-130, trans-illuminated backed bed and couple of lens (*f*-100, *f*-20) and intercepted beam size by FPA detector.

making fluid flow and dispersion profiles unexpected. We explore the effects of the confining wall under the knowledge of flow dynamics (i.e., local structure of the packed bed, pressure drop, and interstitial flow in the void space) by 3D CFD modeling, and the results are validated by those obtained by global pressure drops and spatially resolved NIR imaging and literature models. In order to ease the computation requirements of 3D modeling, the results are subsequently compared with those obtained by 2D modeling, where structural porosity maps were obtained from actual 3D porosity distributions. The work plan includes the following steps: (1) brief description of transient changes of water vapor H_2O_v in D_2O vapor by NIR

DOI: 10.1021/acs.iecr.5b02635
Ind. Eng. Chem. Res. 2015, 54, 12714−12729

tomography; (2) generation by DEM of representative bed geometries and comparison of the bed structure properties, such as average porosity and spatial distribution of porosity, with literature models; (3) observation of pressure drops and local velocity distributions and comparison with 3D modeling as well as relevant 2D literature models; and (4) observation of mass dispersion by NIR tomography and DEM modeling and comparison with those obtained by 2D modeling and literature models.

2. EXPERIMENTAL SECTION

2.1. Near-infrared imaging tomography tests. The experimental setup and procedure are detailed in our previous works.[12,35] Briefly, the packed bed tube was made of fused quartz (12 mm internal diameter (I.D.) and 39 mm length) and was filled with hydrophobic quartz glass beads as shown in Figure 1(a_1). the beads were made hydrophobic by surface cleaning in acid solution, methylization using a film solution of methyl-trichlorosilane in toluene, and washing with a solution of ethanol/water.[36] The tomography technique relied on 2D projected images from parallel scanning, where a NIR laser source (Santec TSL-510 with a modulating range from 1340 to 1440 nm) and a NIR detector (Mosir 950 detector, 1024 × 256 pixels, 26 × 26 μm^2/pixel) were rotated linearly by a servo-motor to acquire transmitted projections through the packing medium. The laser beam was tuned to the high-absorption frequencies of water vapor H_2O_v, polarized before being collimated by a series of mirrors and cylindrical lenses in order to shape a top-hat and rectangular sheet beam of 12.0 × 39.0 mm^2 size as shown in Figure 1(a_2). The tomographic reconstruction was performed by running a Matlab code based on the adaptive algebraic reconstruction technique, where the reconstructed 3D domain array of discrete voxels of absorbance or concentrations was solved by the Kaczmarz method.

Typically, water vapor was introduced to the system from a controlled evaporator mixer (Bronkhorst) at a flow rate of 0.1 to 0.5 $cm^3\ min^{-1}$ of N_2, a water composition of 6.0 mol % (relative humidity of 30.5%), and a temperature of 333 K, with all pre- and postpacked tube pipes being insulated and heated to the operating temperature. In addition, a humidity sensor (Exo Terra Digital Hygrometer, accuracy 2% at relative humidity >10%) was placed at the exit of the experimental setup. The water vapor was introduced to the system and was allowed to stabilize for a period of hours to reach packing saturated before the commencement of an experiment by switching to deuterated water vapor D_2O_v. The outlet products were validated by quadruple mass spectrometry. To prevent any inference from moisture in the surrounds of the experiment, the entire setup was enclosed in a black-shielded Perspex box. The extinction coefficients of H_2O_v across the packing section were obtained by using a squared quartz cell of 10 × 10 mm^2 cross section and 100 mm height, which was half-filled with the quartz beads. The laser source was modulated to absorption lines of H_2O_v at 1380.685 nm as shown in Figure 1(b), and the spectrum above the packing (free of scattering) was validated with deviation in the transmittance of 0.4 mol % for H_2O_v.

2.2. Pressure drop tests. Since literature data of fluid flow for low ARs are limited, experimental tests of pressure drops for ARs ranging from 1.5 to 5 were carried out by using a range of ARs. Air was used as a flowing gas, and the flow rate was controlled by a mass flow controller (ROD-4A, Advanced Energy). The pressure drops over the bed were measured free of pressure loss at the distributor with a differential pressure transducer (142PC02D, Sensortechnics GmbH), as shown in Figure 2(a).

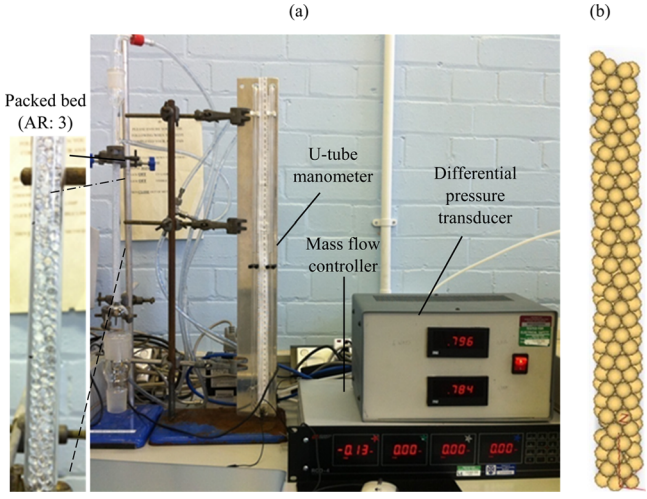

Figure 2. Pressure drops setup (a) and generated packing for AR of 3 by DEM (b).

2.3. 3D flow modeling. *2.3.1. Packing generation by DEM.* A granular packing of densely spherical particles was built by means of DEM in order to mimic experimental samples. The 3D DEM code was written in the built-in FISH programming language of particle flow code 3D (PFC^{3D}) and was used to generate realistic packing samples of random structures with ARs ranging from 1.5 to 5, as shown in Figure 2(b). The structure of the packing was the function of properties of both the container and the particles, including the stiffness, the density, and the friction coefficients between the particles or the particles and the confining wall. The compaction process was carried out until the maximum unbalanced contact force between particles reached a value of the order 10^{-7} N, resulting in a packing at static equilibrium. The stiffness coefficients of the wall and the particles were varied for maximum density of the packing. The overall setting parameters have been enlisted in Table 1. The packing geometry, which was defined by the 3D coordinates of particle centers, was then embedded into the commercial CFD package COMSOL Multiphysics 4.4 via 3D AutoCAD (Autodesk) processing, allowing a dedicated meshing to take place by using a computer with 128 GB RAM.

Table 1. Setting Parameters of DEM Based Modelling

	Wall parameters	Particle parameters
Normal stiffness coefficient	10^{13}	2.5×10^8
Tangential stiffness coefficient	10^{13}	2.5×10^8
Friction coefficient	0.2	0.2
Density		3900 kg/m^3

2.3.2. Fluid flow model. The model of a laminar gas flow in a 3D porous media is governed by both the mass conservation (eq 1) and the Navier−Stokes momentum (eq 2), where the inertial forces include both the pressure forces and viscous forces (the stress−strain tensor for a Newtonian fluid).

$$\rho \nabla \cdot u = 0 \quad (1)$$

DOI: 10.1021/acs.iecr.5b02635
Ind. Eng. Chem. Res. 2015, 54, 12714−12729

$$\rho(u\cdot\nabla u) = -\nabla pI + \nabla\cdot\left(\mu(\nabla u) + (\nabla u)^T - \frac{2}{3}\mu(\nabla\cdot u)I\right) \tag{2}$$

The inlet boundary was a fixed velocity inlet condition; this was spatially uniform over the inlet (eq 2.1). At the outlet, a constant atmospheric pressure (p_0) boundary condition (eq 2.2) was used. In addition, no slip conditions were assumed at wall−fluid and particle−fluid interphases.

$$u = -u_{in}\mathrm{n} = 0 \tag{2.1}$$

$$p = p_0, \quad \left(\mu(\nabla u) + (\nabla u)^T - \frac{2}{3}\mu(\nabla\cdot u)I\right)\mathrm{n} = 0 \tag{2.2}$$

In these equations, μ is the fluid molecular viscosity and ρ is the fluid mass density.

The stationary solver of the Comsol package with default settings was used. The governing equations (eqs 1 and 2) were solved using the finite volume approach. The domain of interest between the solid particles was divided into numerous cells where the governing equations were integrated across the volume of each cell. The integrals converted the governing equations into a set of difference equations which were solved numerically using the generalized minimal residual method (GMRES) with the Geometric Multigrid preconditioner. The GMRES algorithm is an iterative method for the numerical solution of a nonsymmetric system of linear equations. The method approximates the solution by the vector in a Krylov subspace with minimal residual. Trial studies with a variety of solvers (FGMRES, conjugate gradient, BiCgStab) indicated that, in these particular cases, the simulation result was fairly insensitive to the exact one. The convergence was evaluated based on relative tolerance, which was set to 0.0001.

The discretization was carried out by the built-in meshing module of Comsol using the Adaptative Mesh Refinement Method, which generated predominantly tetrahedral domain elements and triangular surfaces. The effects of the size of these elements on the viscous forces, particularly in areas where potential skewed meshes could be generated, such as particle contact points, were investigated. This was ensured by a mesh convergence check for each packed bed by increasing the number of mesh elements and monitoring the pressure values at three arbitrary locations from the CFD simulation. It was observed that the packed beds of high AR required more refined meshing than the low AR to reach approximately stable values of pressure. This result was subsequently confirmed by using the Grid Convergence Index (GCI) as described in Appendix A2.[37] The GCI reached values below 2%, validating the reasons to trust the accuracy of the present numerical simulations and to ensure that the solution is independent of the mesh size.

In addition, the quality of the mesh was analyzed by the minimum element quality statistics method, which expresses the contribution of the skewed elements. The spherical particles in the packed bed were expected to release skewed elements, which were extensively reported in the literature. These dealt with such elements by increase or decrease of particle sizes as well as using the range of features available in commercial CFD to smooth these skewed elements. Herein, the diameter size of particles was reduced by 1% in all our tests. Such shrinkage was found necessary to prevent highly skewed meshes at single-point contacts between particles while maintaining reasonable computation time.[2,23−25] A shrinkage higher than this value would yield no advantage in producing more accurate results and would be computationally more expensive.

2.3.3. Mass dispersion model. Dispersion of species in porous media is generally characterized by five regimes: pure molecular diffusion regime ($Pe < 0.3$), superposition regime ($0.3 < Pe < 5$), where the effects of molecular diffusion and dispersion are comparable; predominant mechanical dispersion regime ($5 < Pe < 300$); pure mechanical dispersion regime ($300 < Pe < 100000$), where the effect of molecular diffusion is negligible; and dispersion out of the Darcy domain regime ($Pe > 100000$), where the effects of inertia and turbulence cannot be neglected.[38] The dispersion in a packed bed is well described by the two-dimensional diffusive and convective model equation, assuming constant velocity u and constant dispersion coefficients.

$$\frac{\partial C}{\partial t} = D_{ax}\frac{\partial^2 C}{\partial z^2} + \frac{1}{r}\frac{\partial}{\partial r}\left(D_{rad} r\frac{\partial C}{\partial r}\right) - u\frac{\partial C}{\partial z} \tag{3}$$

The analytical solutions, by assuming a maximum concentration at the center of the packed bed, as expressed by eqs 4 and 5, require continuous species tracing under steady-state transversal and dynamic radial mass dispersion experiments.

$$\frac{C(r,z)}{C_o} = \frac{1}{2}\mathrm{erfc}\left(\frac{r}{2\sqrt{zD_{rad}/u}}\right) \tag{4}$$

$$\frac{C(t,z)}{C_o} = \frac{1}{2}\mathrm{erfc}\left(\frac{z-ut}{2\sqrt{D_{ax}t}}\right) + \frac{1}{2}\exp\left(\frac{uz}{D_{ax}}\right)\mathrm{erfc}\left(\frac{z+ut}{2\sqrt{D_{ax}t}}\right) \tag{5}$$

where C_0 is the inlet concentration. An alternative discontinuous approach relies on the Lagrangian method by following distinct particles along a trajectory in a steady-state velocity field. The method of moments, as shown in eq 3, is used to calculate axial and radial dispersion coefficients.[1]

$$D_{ax/rad} = \frac{1}{2}\frac{d\sigma^2_{ax/rad}}{dt} \tag{6}$$

Here, $\sigma_{ax/rad}$ is the second moment or mean square deviation, as defined by eqs 7 and 8:

$$\sigma^2_{ax}(t) = \frac{1}{NP}\sum_{n=1}^{NP}(x_n(t) - \bar{x}(t))^2 \tag{7}$$

$$\sigma^2_{rad}(t) = \frac{1}{NP}\sum_{n=1}^{NP}(r_n(t) - \bar{r}(t))^2 \tag{8}$$

Here, n is the particle index, NP is the total number of tracked particles, and x and r are displacements of particles along the axial and radial coordinates, respectively. $\bar{x}$ and $\bar{r}$ are the averaged displacements of all particles along the axial and radial coordinates, respectively.

3. RESULTS AND DISCUSSION

3.1. Fluid flow profiles by 3D modeling. *3.1.1. Structural porosity profiles.* It should be noted that the trends of packed bed porosity have been generally analyzed by two methods. The first, which was followed by early studies, relied on experimental data of packing structures and where much attention was paid to the wall effects and periodic variation of porosity away from the containing wall.[39,40] The second used

DOI: 10.1021/acs.iecr.5b02635
Ind. Eng. Chem. Res. 2015, 54, 12714−12729

computer-generated packing through a variety of computational algorithms.[40,41] Both computer-generated[42] or hand-built packing[43] relied on models which use a two-point correlation function of sphere centers and the tessellation of the void space distribution of the interparticle interstices using a number of schemes, such as tetrahedral,[44,45] Dirichlet,[46] or Voronoi types.[47,48] Although the tessellation permitted some statistical description of pores and interstices, it was unable to give a complete analysis which relies on the overall geometry of the individual pores. In contrast, direct analysis of the void space itself is possible via image analysis techniques, which take as input the 3D tomographic or 3D visualization data.[49] Compared with 2D images, the 3D visualization of the pore space allowed access to the 3D topology of the pore space (e.g., the connectivity of local elements) with similar resolution in each dimension. These structural characteristics determined the velocity, pressure drop, and mass transfer characteristics of the bed. Of course, the same information can be obtained by recording a succession of 2D slice sections for which the slice thickness is equal to or better than the in-slice resolution, and then reconstructing the 3D structure. It is the direct analysis via 3D visualization data that was followed in this work.

The procedure used available data in the 3D matrix that defines coordinates of particles inside the packed bed. For instance, Figure 2(b) illustrates generated packing arrangements for AR of 3 by experimental data and DEM. The porosity profiles of packed beds of different ARs were calculated by using the data of various spatial domains, which were denoted as "Domain Index (DI)" in COMSOL software. Domain index is a single integer number and was allocated to mesh boundaries of a single domain area (solid particle or between particles), allowing access to porosity distribution at any 3D coordinate with a spatial resolution at mesh size limits. Just like the distribution shown in Figure 3(a), the cylinder container of the packed bed of 100 mm length was cut into 100 slices, allowing a spatial resolution along the axial direction of 1 mm. A sample of DI data accessible for a single slice is shown in Figure 3(b). It is interesting to see that the distribution of accessible DI data is not uniform, as it follows mesh distribution (i.e., dense data at particle contact points). The exported data files were then processed for the porosity distribution of the packed bed by developing a Matlab code for the procedure illustrated in Figure 3(c). First, the domain index of the area between the particles was considered fully porous with an integer number of unity, and the remaining domain indexes that belong to solid particles were considered nonporous with an integer number of zero (step 1 in Figure 3(c)). The 3D DI data were angularly averaged into 2D data, where the angular weight of accessible DI data was taken into account (step 2 in Figure 3(c)). The released 2D data represent the surface fraction (ε_s) nonoccupied by the solid particles if the packed bed was represented by a 2D configuration. The surface fraction ε_s was subsequently reduced into the "1D" axially averaged porosity (step 3 in Figure 3(c)) and the global or averaged porosity of the full packed bed (step 4 in Figure 3(c)).

Table 2 illustrates the porosity data obtained in the present simulation for various aspect ratios. A comparison with a model from Zou et al.[49] shows a good agreement, particularly for low AR. With the exception of AR of 2, the loose structure of generated packing by shrinking the particles by 1% was well observed and it increased to a large AR. More insights into the loose structure have been shown in the 2D maps of the circumferentially averaged DI data in Figure 4. The loose

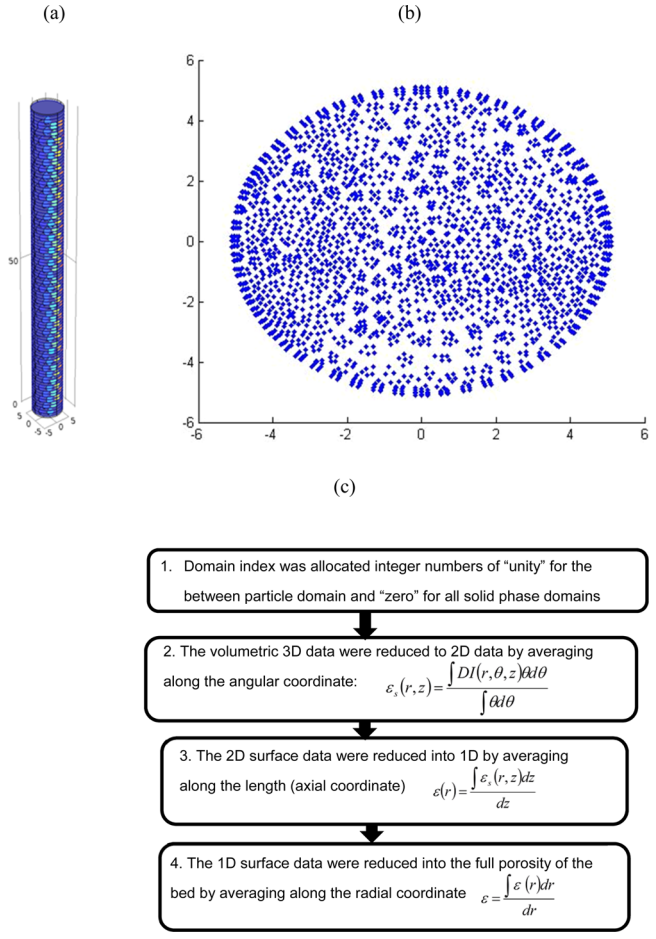

Figure 3. Reduction procedure of volumetric 3D domain index data. (a) Cross-sectional slicing of domain index, (b) irregular distribution of domain index data retrieved, and (c) averaging procedure from 3D domain index to 2D and to 1D data.

Table 2. Porosity Trends for AR from 1.5 to 5

Aspect Ratio D/dp	Porosity (ε)	Deviation (%)[a]
1.5	0.688	4.36
2.0	0.575	0.52
2.5	0.530	1.51
3.0	0.528	2.08
3.5	0.572	5.77
4.0	0.547	2.74
4.5	0.525	5.52
5.0	0.498	5.02

[a]Porosity data by Zou et al.[49]

structure along the axial coordinate is confirmed along the axial coordinate of the packed bed for various ARs. The surface fraction of empty space ε_s of a selected location of the packed bed could be larger or smaller than the entire corresponding bed, depending on where the location was selected and how many particles were included in the selected location.

Moreover, Figure 4 shows ε_s of the selected locations and how it deviated from the entire packed bed porosity in Table 2 when the numbers of particles in the segments varied. It is interesting to see the periodic variations of ε_s for all AR arrangements, corresponding to the layer changes in the packing. The deviations suffered from a jump every time additional particles constituted a new layer of packing and then

DOI: 10.1021/acs.iecr.5b02635
Ind. Eng. Chem. Res. 2015, 54, 12714−12729

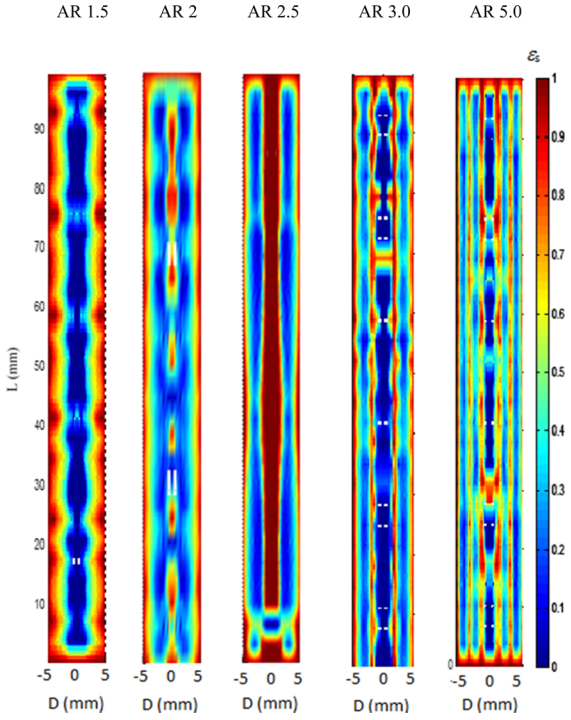

Figure 4. Spatial distribution of surface fraction ε_s of the solid particles for packed beds of ARs from 1.5 to 5.

decreased as more particles were added to the same layer. For high AR, the particle number further increased. The local porosity could be either larger or smaller than the entire bed, but the deviation was relatively small. The larger the AR was, the more particles were needed to reach this low-level deviation of packing porosity. This is because sufficient layers were required to represent the entire packed bed, and a packing with a larger AR contains more particles per layer. Such cyclic changes of the porosity of the height of the bed could be reflected by cyclic variations of interstitial flow velocity and mass dispersions.

Taking the axially averaged porosity for these figures, which represents the distribution of porosity along the radial coordinate within the packing system, was the next step to compare simulation results with the semianalytical model of the radial porosity distribution by Mueller et al.,[50] as shown in Figure 5. Similar oscillation trends with damping profiles toward the center of the packed beds were observed. The discrepancies in regions toward the center confirm the loose structure of the generated packing. On the other hand, the radial distribution of porosity obtained was in good agreement with the models of Mueller, especially close to the wall, while the porosity increased at low AR due to high porosity near the wall in packed beds. Such property distribution of porosity impacts the flow dynamics and mass transfer, as described in the following sections.

3.1.2. Pressure drop profiles. The pressure drops, in terms of dimensionless number *P*, in packed beds of ARs of 1.5 and 5 at flow regime of *Re* of 400 were compared with established models of Carman, Ergun, Zhavoronkov, and Reichelt as shown in Figure 6 (see Appendix A3 for more details about the four models). The results of pressure drops by CFD simulation fit the models predicted by Zhavoronkov, Reichelt, and Ergun well at high Reynolds numbers, but showed disagreements with the Carman model, which is suitable for packed beds of large AR.

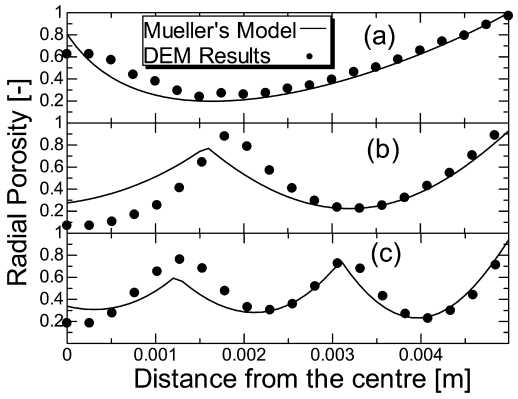

Figure 5. Averaged porosity variation along the radial coordinates at (a) AR: 2, (b) AR: 3, and (c) AR: 5. (Dots: simulation data; lines: Mueller's model.[50])

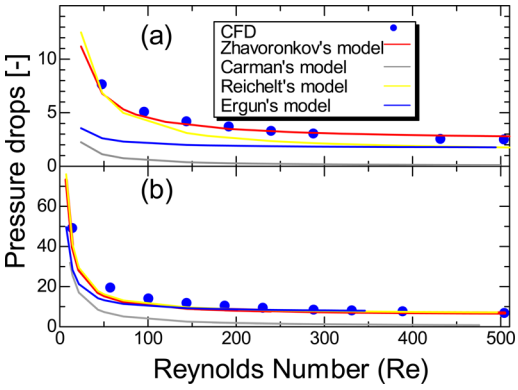

Figure 6. Pressure drop profiles for (a) AR: 1.5 and (b) AR: 5; dot: CFD simulation.

The pressure drops are as well represented in terms of pressure drops ratios, P/P_{inf}, in order to account for the effect of the wall for low AR values. P_{inf} is the dimensionless pressure drop for an infinite AR. The simulation results, as the effect of AR of packed beds on pressure drops at laminar and transitional flows, are shown in Figure 7(a) and were validated using experimental data and literature models, as shown in Figures 7(b_1–b_4), respectively. An increase of pressure drop ratios at low AR packed beds was observed at AR less than 3,

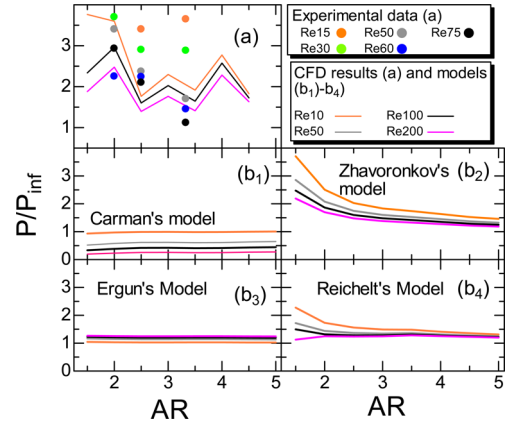

Figure 7. Ratio of pressure drop to pressure drop of infinite packing profiles, (a) simulation, and experimental data, and (b_1–b_4) Carman, Zhavoronkov, Ergun, and Reichelt models.

DOI: 10.1021/acs.iecr.5b02635
Ind. Eng. Chem. Res. 2015, 54, 12714–12729

while those obtained by the Ergun and Carman models were not sensitive to AR values. The simulation results fit the Reichelt model better, and the decrease in the pressure drops at AR lower than 3 was interpreted by Eisfeld and Schnitzlein by two counteracting effects of the wall: one to offer additional resistance due to wall friction (this effect will be less at Re > 200) and the other a positive effect, which represents reducing the pressure drop with Reynolds number due to increased porosity in the vicinity of the wall.[32]

In order to ascertain this important finding of the decrease of the wall effect at AR lower than 3, the fluid flow in a 2D porous medium of packed map of circumferentially averaged porosity in Figure 4 was carried out (see Appendix A4). The porosity distribution map for the 2D model was obtained by interpolation with a spline function, allowing access to data which were not visualized by the 3D nontransparent arrangement. As expected, the results clearly showed more porosity distribution in the center of the packed bed for even numbers of AR values (i.e., 2 and 4) and less porosity distribution for uneven numbers of AR (i.e., 3 and 5). Between consecutive even and odd numbers of AR, the trends were found, however, nonlinear for AR less than 3, shown by AR of 2.5. For this value of AR, the porosity distribution shifted toward the AR value of 2, allowing more flow in the center of the packed bed than AR values of 2, 3, or 5. The wall effect and subsequent porosity distribution along the radial direction thus took place progressively as the porosity increased in the vicinity of the wall toward AR of 3, offering more selective channelling and, by inference, velocity in these regions. The wall effect decreased again for AR higher than 4, owing to more mixing in the center of the packing. Thus, there is a nonlinear wall effect, which is the exclusive function of fluid flow rate as shown in Figure 7.

3.1.3. Velocity field profiles. Since no symmetry exists in the unstructured packing, the flow structure is expected to be highly dependent on the topology of the intergranular space at pore scale. Figure 8 shows the projections of local velocity on cross-sectional and vertical planes along the bed length at AR of 1.5. It is clear that interpreting a suitable visual output of velocity is a challenging task without a direct line of sight through the full packed bed. The disorder of the flow structure by 3D view, however, can reveal the presence of vortices and eddies in the pores, particularly at high velocity fields.

An alternative viewing option of the complex 3D domain is by a 2D angularly averaged domain, as it offers a more realistic full picture of flow behavior, as shown in Figure 9 for ARs of 1.5, 2, 2.5, and 3. Such detailed analysis of flow structure would be relevant provided that the 2D porous structures in Figure 4 are as close as possible to the real 3D structures. Figure 9(a) shows the velocity distribution for AR of 1.5 mainly in the near-wall regions, demonstrating the effect of the wall. This effect slightly decreases for AR value of 2, as shown in Figure 9(b), where some spots of velocity are displayed along with the continuous distributions near the wall regions. Increasing the value of AR to 2.5 promoted the spots of values into continuous values, which correspond to a more homogeneous velocity than those observed at an AR of 2, which in turn displays less homogeneous velocity than that at 3. This later packing, however, shows less homogeneous velocity distributions than at AR of 5, yielding to expected trends of the effect of the confining wall on fluid flows at low AR. Contrary to the magnitude of velocity inside the packed bed of AR of 2, the magnitudes of the spots along the tube wall for ARs of 3 and 5

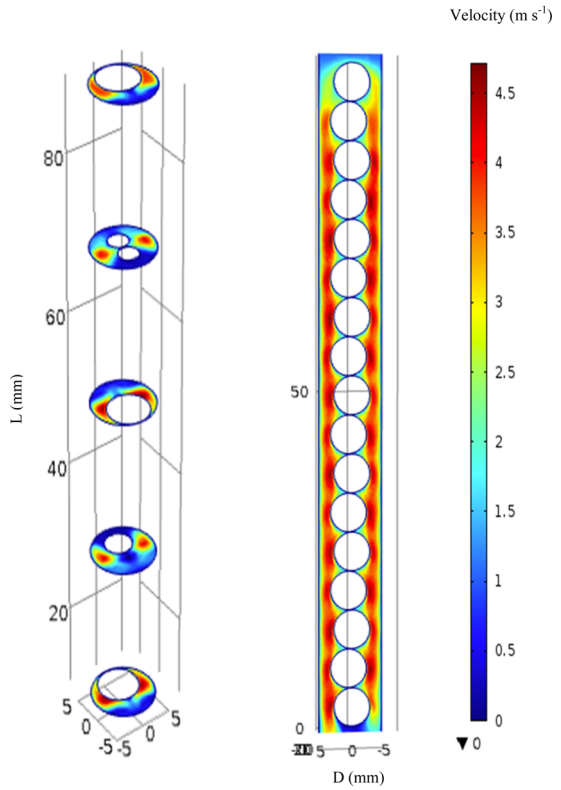

Figure 8. Cross-sectional and vertical cuts of the velocity (m/s) inside a packed bed reactor: AR 1.5 and Re = 375.

are not sufficiently high, confirming the looseness of the packing in these regions.

These results are in agreement with experimental data reported by Aiouache et al.,[12] where preferential channelling near the wall has been experimentally demonstrated. The fluid velocity was the greatest in the narrow spaces at ARs of 4 and 5 because it occurred in between particle-to-particle contacts and particle-to-wall contacts, where the flow was forced to accelerate through a relatively smaller space. Similar to porosity trends, cyclic variations of velocity along the bed height are again observed, confirming local variations of fluid flow in low AR, particularly those of less than 3. This caused several areas of local maximum velocity where the fluid sometimes found its way into the channels. The 2D modeling approach was ascertained by comparing the results of pressure drops with those obtained by 3D modeling, as shown in Figure 10. A deviation of 0.5% is observed for Re of 284, confirming the benefit of using the porosity distribution from 3D maps to access insights into industrial packed beds of large computation time and hardware power.

3.2. Mass dispersion profiles. *3.2.1. By spatially resolved NIR imaging.* The measurements of light extinction across the packing were performed by using a squared quartz cell. Owing to the combination of absorption and scattering occurring in the packing bed, the spectra retrieved were of a higher transmittance than those retrieved from the gas phase above the packing, as mentioned in section 2.1. The packing section, in the absence of H_2O_v, exhibited an optical depth of 0.25 for a packed bed of AR of 4, suggesting relevance of a straight light propagation, with little scattering, and validating the use of the modified Beer–Lambert law for concentration measurements.[35] Furthermore, the tests of validation of the NIR imaging were

DOI: 10.1021/acs.iecr.5b02635
Ind. Eng. Chem. Res. 2015, 54, 12714–12729

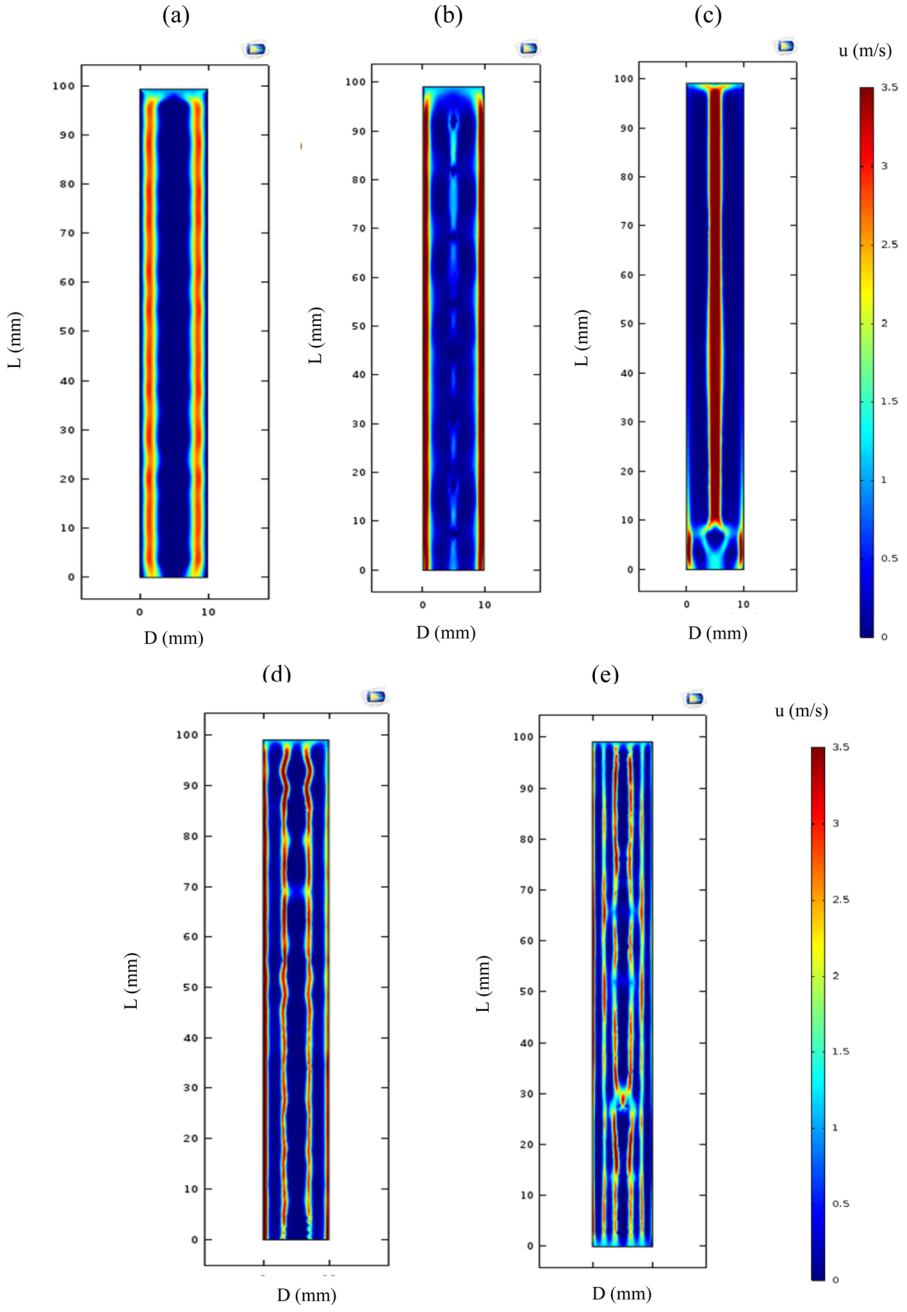

Figure 9. Velocity distribution in 2D profile in a packed bed reactor: (a) AR1.5, (b) AR2, (c) AR 2.5, (d) AR3, and (e) AR5.

carried out by using a similar procedure employed in previous works.[36] First saturating the packed column with H_2O_v and the inlet flow of the inner tube of 5 mm I.D., as shown in Figure 1(c), was then switched to D_2O_v to begin the experiment. Both inner and outer flows were at a similar velocity. 3D reconstructed images of H_2O_v composition were generated at steady-state conditions for the projections taken at fixed angle steps of 15° (13 projections/cycle) and lasted approximately 18 s. The maximum size of the pixel array of the NIR detector that could collect the trans-illuminated NIR beam (size of 12.0 × 39.0 mm^2) was 80 × 700 pixels, leading to a spatial resolution of 0.15 × 0.056 mm^2.

The reconstruction images of the H_2O_v composition, after the introduction of D_2O_v at 0.1 m s^{-1} (Figures 11(a) and (b)), show a vertical section and five cross sections of composition maps, respectively. A decrease in the composition of H_2O_v with time is well displayed in the center (inner flow), and a clear limit between the H_2O_v flow region (outer flow) and the D_2O_v flow region (inner flow) is well discernible in the bottom slice at a spatial resolution of submillimeter. Although a dispersion of the two flows was not expected owing to the high flow rates used, the inner (D_2O_v) and outer (H_2O_v) flows displayed some spots and increased mixing at sections of the packing at averaged deviations with those obtained from mass spectrometer of 8.1% for concentrations as low as 1.0 mol % of water vapor. The higher accuracy of a quartz bed compared to styrene divinylbenzene sulfonate resin packing used in previous work[35] is likely due to higher optical properties of the hydrophobic quartz beds.

These validation tests were then extended to tests for radial and axial dispersion measurements which were run through an isotopic exchange chemistry between H_2O_v and D_2O_v. A single

DOI: 10.1021/acs.iecr.5b02635
Ind. Eng. Chem. Res. 2015, 54, 12714−12729

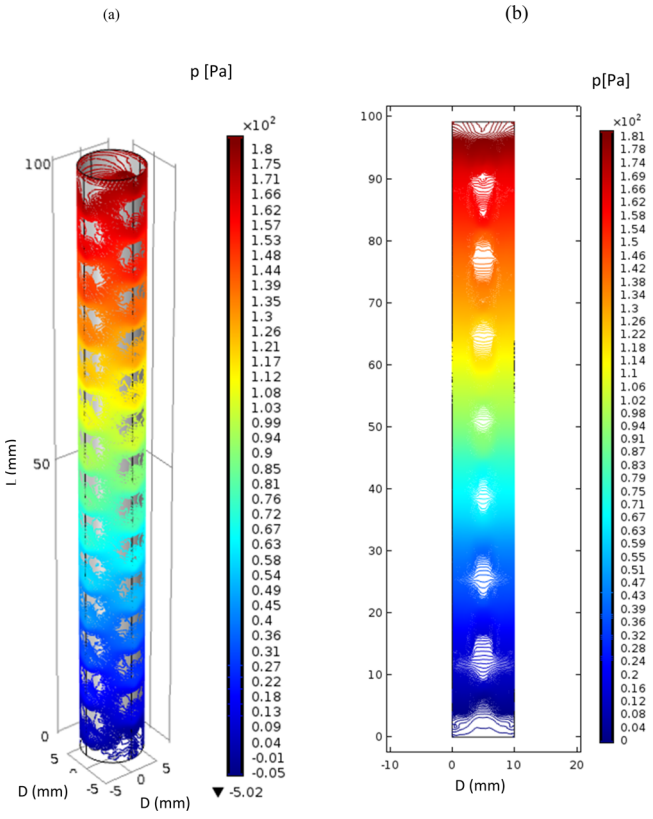

Figure 10. Pressure drop contours for AR = 2: (a) 3D modeling and (b) 2D modeling (*Re* = 284).

AR of 4 was used owing to design limits of the field of view (39 mm) of the NIR imaging while a minimum length of the packing to particle ratio of 12 was required to avoid length effects.[35]

3.2.1.1. Radial dispersion tests. The tests for radial dispersion were carried out using a similar procedure of phantom tests, but a much lower flow velocity was used (i.e., 0.00002 to 0.00011 ms^{-1}). The reconstruction images of the H_2O_v composition, after the introduction of D_2O_v m s^{-1} (Figures 12(a_1) and (a_2)) show composition maps of five cross sections and two vertical sections, respectively. A high composition of H_2O_v is well displayed in the vicinity of the wall (outer flow), but clear limits between the H_2O_v flow region and non-H_2O_v flow region are not easily discernible from the bottom slice (the exit of the inner tube) to the top slice (the end of the packed bed). Full 700 cross-sectional layers from the bottom to the top of the packed bed were gathered in a movie at a frame rate of 24 layers s^{-1}, as shown in the Supporting Information (S1).

In addition, the 3D data, once 2D angularly averaged as shown in Figure 12(c_1), show clear distinction between H_2O_v and non-H_2O_v regions, which extends radially from the bottom to the top of the packed bed. A comparison with the results from the mass spectrometer at the exit of the packing indicated relative deviations in H_2O_v composition of 9.1%. These results are satisfactory given inherent errors associated with the experimental design (acquisition time per tomography cycle, light diffusion through packing, diffraction by the packing tube, convenient signal-to-noise ratio, and both entrance and exit effects).[35]

3.2.1.2. Axial dispersion tests. The experimental procedures for axial dispersion tests were similar to those for the radial dispersion but were carried out under transient operations, and the full inlet flow was switched to D_2O_v to begin the experiments. Figures 12(a_2) and (b_2) show the composition profiles of five cross-sectional and two vertical layers along the packed bed, respectively, which are representative of the breakthrough of D_2O_v after a spent time of 30 min. Full 700 cross-sectional layers from the bottom to the top of the packed bed were gathered in a movie at a frame rate of 24 layers s^{-1}, as shown in the Supporting Information (S2). Axial dispersion might not be well observed through the composition changes of H_2O_v along the radial coordinates, which reached values of 4.5 mol %. A nonuniform distribution of composition is observed, however, in the packing, which indicates that the local flow

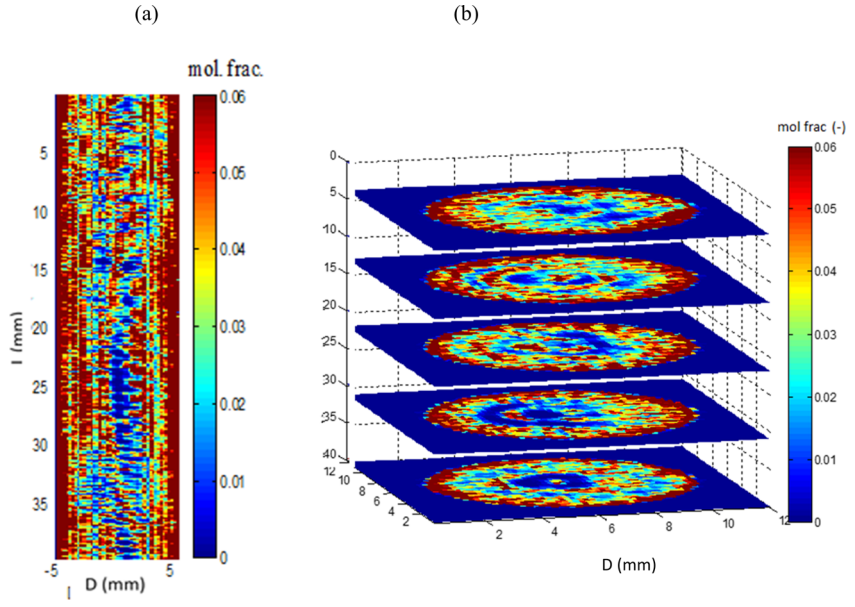

Figure 11. Phantom test by NIR tomography H_2O_v composition maps: (a) vertically sectional maps, (b) five equidistant cross-sectional maps. Inner nozzle diameter: 5 mm; outer tube diameter: 12 mm; thickness of both tubes: 0.5 mm; inlet velocity: 0.1 m s^{-1}.

DOI: 10.1021/acs.iecr.5b02635
Ind. Eng. Chem. Res. 2015, 54, 12714−12729

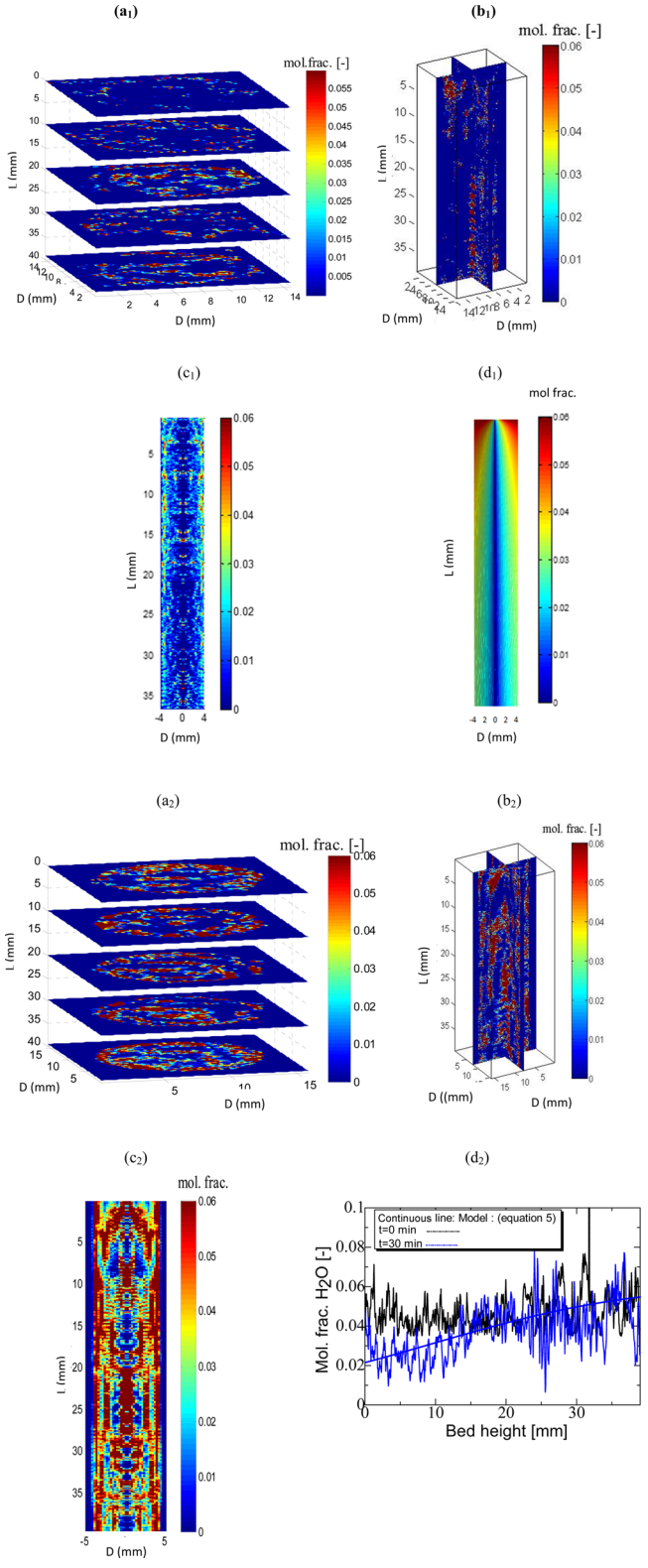

Figure 12. Visualization of H_2O_v composition by NIR imaging, (a_1–d_1) Radial dispersion experiments and (a_2–d_2) axial dispersion experiments. Inner nozzle diameter: 5 mm; quartz tube diameter: 12 mm; thickness of both tubes: 0.5 mm. a_1, a_2: equidistant cross-sectional maps of H_2O_v; b_1, b_2: vertically sectional maps; c_1, c_2: circumferentially averaged maps; and d_2: circumferentially and radially averaged maps (straight line model); inlet velocity: 0.00011 m s^{-1}.

could be channelling between the glass beads. There is less mixing, and thus dispersion, than in the bottom region, suggesting flow maps tend to be moving toward the center of the tube. These results of the 3D distribution of compositions agree with previous velocity maps in section 3.1.3: the flow maldistribution in the vicinity of the wall, where at the start the water vapor composition in the core remained smaller than the near-wall one. The 2D circumferentially (Figure 11(c_2)) shows the effect of the wall on the flow maldistribution associated with the high composition of water vapor near the wall and a damped one toward the core of the packed bed. Such profiles correlate well with general trends of porosity profiles in Figure 4.

3.2.1.3. Discussions. The spatially resolved NIR imaging confirmed the nonuniform distribution of species in both tests and demonstrated potential access to local variations of both D_{rad} and D_{ax} along the radial and axial coordinates, owing to the cyclic changes of porosity, and by inference interstitial velocity, as demonstrated in previous sections. Local D_{rad} and D_{ax} could have been determined if the maps of H_2O_v were of higher spatiotemporal resolutions. The overall trends of D_{rad} and D_{ax} for the full packed bed as a function of flow profiles were therefore investigated and were obtained by fitting experimental data of H_2O_v by NIR tomography in sections 3.2.1.1 and 3.2.1.2 to eqs 4 and 5, respectively, and minimizing the sum of squares of relevant residuals. A nonlinear least-squares algorithm based on the Marquardt method was then used to adjust the unknown dispersion constants.

As to axial dispersion study, the 2D experimental maps were first circumferentially and radially averaged into 1D composition profiles along the bed height as shown in Figure 12(d_2) and then fitted to the model of eq 5 to obtain unknown D_{ax} values. The model of eq 5 was also added to Figure 12(d_2), which shows a good fit of experimental data with the model. The slight deviation in the regions close to the inlet might be caused by the effect of the inlet on the flow, which is known to be significant in laminar regimes. Average relative overall deviations were less than 9.1% for all fluid flow values used. It is interesting then to see the advantages of spatial imaging to reduce the number of tests for axial dispersion studies.

On the other hand, the radial dispersion study used the full 2D maps of H_2O_v obtained at steady-state conditions. The result of 2D fitting, along axial and radial coordinates, along with eq 4 is shown in Figure 12(d_1). Average deviations between the experimental data of H_2O_v and those obtained from the model (eq 4) were much more important than the axial dispersion tests, ranging from 20 to 25% for all tests.

The results of both D_{rad} and D_{ax}, normalized to molecular diffusion D_m, were validated by comparing their profiles along with the flow dynamics *Pe* to popular literature models (i.e., Freund[1] and Delgado[51]) as shown in Figure 13. It should be noted that these two models are not straightforwardly applicable for the low *Pe* numbers used. The results are broadly consistent with the range of dispersion coefficients obtained for *Pe* number under diffusion control where the D_m/D_{ax} approaches the tortuosity of the bed (i.e., a theoretical value of 1.4). Again, the prediction of axial dispersion is in good agreement with literature models while the radial dispersion showed some discrepancies, confirming again the good fit of NIR imaging for axial dispersion studies.

3.2.2. By DEM modeling. The results of mass dispersion uncertainties achieved by NIR tomography were validated by DEM. This later is a valid tool which has been extensively used

DOI: 10.1021/acs.iecr.5b02635
Ind. Eng. Chem. Res. 2015, 54, 12714–12729

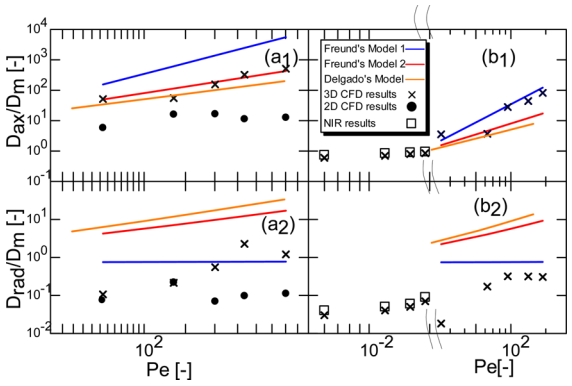

Figure 13. Axial and radial dispersion coefficients along with flow dynamics, respectively: (a_1, a_2) for AR of 2; (b_1, b_2) for AR of 4.

for mass dispersion studies.[1,52] It relied on a Lagrangian particle tracking procedure where the distinctive motions of individual particles were added to describe their trajectories: thus the macroscopic mixing of tracer particles along the axial and the radial directions of the packed beds. Herein, the particle tracking module of Comsol was coupled with the 3D fluid flow model (eqs 1 and (2)) to give trajectories to individual particles of similar trends to those developed by the carrying fluid. The particles were assumed to be of negligible mass and subject to bounce conditions at the fluid−solid interphase. The design of the packed bed required addition of an inlet for particle flow by using a small cylinder of 1 mm I.D. and 2 mm height at the top center of the packed bed. The size of the small cylinder was effective in terms of meshing requirements. About 500,000 particles were released for each test, and the displacement of these particles was followed with time.

Interaction of AR and mass transport was investigated by using two values of AR (i.e., 2 and 4) and two values of *Pe* (0.01 and 100). Although the particles were released at the center of the packed bed, their propagation at *Pe* of 100 along the axial direction was significant for both AR 2 and AR 4 and was dominant in comparison with the diffusive propagation along the radial direction, as shown in Figure 14. Significant holdups should be associated with zones where the fluid entered stagnant regions of reduced convective flow, leading to significant transport by diffusion. At *Pe* of 0.01, the particles, however, happened to collide at the solid/fluid interface, causing a significant diffusion along the radial direction. Compared with those observed in the vicinity of the wall at AR of 4, the particles were seen to circulate mainly along the center of the packing at AR of 2, which agrees with the results of porosity and fluid flow. Beyond this value of AR, particles again circulated more in the central region of the packed bed. It should be noted that no particle was seen as trapped in stagnation zones, except at the interface fluid/solid. This means that if there were vortices inside which the current lines loop on themselves, they would be too small in number to be observed. Owing to the no-slip assumption, particles that reached the wall were eliminated for the computation of mass transfer dispersions.

Quantitative values of dispersion coefficients were then computed by accessing first the trends of individual particle positions with time. These positions were used to compute trends of the second moment or mean square deviation of positions of these particles along axial and radial directions according to eqs 7 and 8, respectively. These values served to

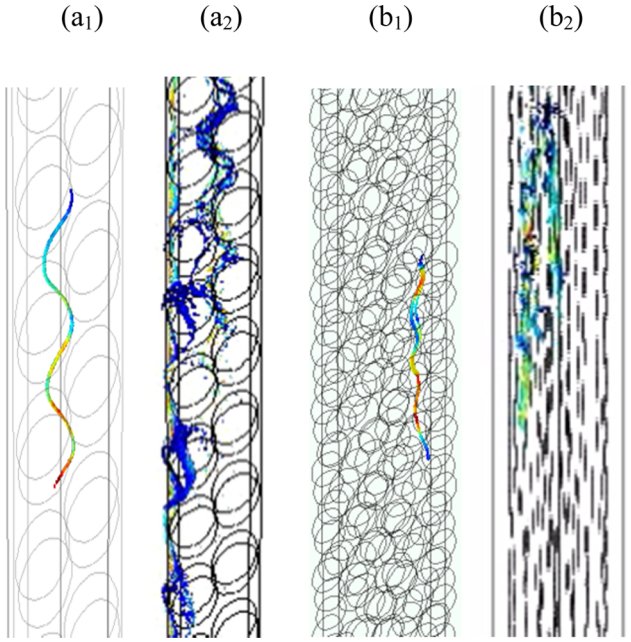

Figure 14. 2D vertical slices of particle tracers. AR 2 (a_1: Pe = 0.01 and a_2: Pe = 100) and AR 4 (b_1: Pe = 0.01 and b_2: Pe = 100).

calculate the asymptotic values of dispersion coefficients according to eq 6. The profiles of axial and radial dispersion coefficients normalized to molecular diffusion were added to Figure 13, along with those computed by the semianalytical models of Freund and Delgado.[2,51] The prediction of axial dispersion is in good agreement with those obtained by NIR tomography in section 3.2.1 and literature models. Similar to NIR tomography, the radial dispersion by DEM showed some discrepancies with literature models, although for an AR value of 1.5, there is some reasonable agreement with Freund's model. Similar trends were reported by Augier et al.,[52] and the explanation could be given by the size of the packed bed, which was not large enough to allow asymptotic profiles of velocity to be reached by the particles. Axial dispersion values for a larger aspect ratio of packed bed (AR of 4) were between the models of Freund and Delgado. Unlike the radial dispersion, the axial dispersion was more promoted by the wall, confirming the impact of the wall on global mixing within low-AR packed beds, and suggesting that the DEM approach is a helpful tool to characterize such a phenomenon. Finally, the validated results from the 3D DEM were compared with those obtained from the 2D DEM, which used 2D angularly averaged porosity, as shown in Figures 14(b_1) and (b_2). Unlike radial dispersion, axial dispersion by 2D modeling is in good agreement with that from 3D modeling, and thus validates the benefit of using 2D averaged maps of porosity for large-scale packed beds for mass dispersion studies.

4. CONCLUSIONS

In this work, gas/solid behavior in narrow packed beds was investigated by 3D modeling and near-infrared tomography. Bed configurations of low ARs were generated, and the structural porosity trends (3D, 2D, and 1D) of randomly distributed particles subject to wall effects were compared with semianalytical models. The results contributed to more understanding of fluid flow and mass transport in these low AR packed beds where knowledge is still scarce. The porosity

DOI: 10.1021/acs.iecr.5b02635
Ind. Eng. Chem. Res. 2015, 54, 12714−12729

profiles were in good agreement with the semianalytical models, such as Mueller's expression, especially in the zone near the wall. Similar oscillation trends with damping profiles toward the center of the packed beds were observed. The discrepancies in regions toward the center may have originated from the loose structure of the generated packing. In addition, the average porosity obtained by the CFD simulation was in reasonable agreement with Zou's model, where the porosity increased at low AR. The simulation results were validated by a pressure drop, and the results fitted well with Reichelt, Zhavoronkov, and Ergun's models at high Reynolds numbers. Distribution of velocity was investigated, and the results of high velocities were mainly observed in the regions near the confining wall of ARs of 3 and beyond, owing to high local porosities in these zones. Flow heterogeneity was also characterized by mass dispersion using both near-infrared imaging and DEM. Values of dispersions by near-infrared tomography were consistent with those expected under diffusion control, while some discrepancies for radial dispersion coefficients were observed due to the very short domain length, particularly for small values of AR. Unlike radial dispersion, axial dispersion showed agreements with DEM results and literature models. DEM has demonstrated that axial dispersion was promoted by the wall at AR of 3 and beyond, confirming the impact of the wall on global hydrodynamics inside low AR packed beds. Future works will extend use of NIR imaging to other applications, such as CO_2 storage in porous media, and to values of *Pe* of unity and beyond, where both diffusion and advection take place, requiring, however, even more reduced data collection time, and larger field of view and operating pressures.

APPENDIX A1

The number of scatterings or optical depth (OD) can be defined according to eq A.1.

$$\frac{I_{exit}}{I_{Inlet}} = e^{-OD} \tag{A.1}$$

where I_{exit} and I_{inlet} are the light intensities at the exit and the inlet of the packed bed.[34] The OD indicates the number of directional changes of the light through the packing. The imaging is, therefore, constructed by a combination of ballistic and snake photons (less than one scattering, OD < 1) and scattered photons (multiple scattering, OD > 1) that pass straight, roughly straight, scattered, or diffusively through the medium.

APPENDIX A2

The numerical errors of the simulation were assessed by guidelines provided by Celik et al.[37] to ensure if the results are independent of mesh size. First the representative grid size h procedure is defined as

$$h = \left(\frac{1}{N}\sum_{i=1}^{N}\Delta V_i\right)^{1/3} \tag{A.2.1}$$

where ΔV is the cell volume and N is the number of cells. A three grids grid refinement factor higher than 1.3 was used for the ultimate refinements. The apparent order m of the method is defined by eqs A.2.2 to A.2.4:

$$m = |\ln|\Theta_{32}/\Theta_{21}| + q(m)|/\ln(r_{21}) \tag{A.2.2}$$

$$q(m) = \ln\left(\frac{r_{21}^m - s}{r_{32}^m - s}\right) \tag{A.2.3}$$

$$s = 1\cdot\mathrm{sgn}(\Theta_{32}/\Theta_{21}) \tag{A.2.4}$$

where $h_1 < h_2 < h_3$, $r_{21} = h_2/h_1$, $r_{32} = h_3/h_2$, $\Theta_{32} = P_3 - P_2$, and $\Theta_{21} = P_2 - P_1$. $P_k(k = 1, 2, 3)$ expresses the pressure values taken at three arbitrary grid locations in the packed bed, and sgn is the function signum.

Equation A.2.3 should be solved numerically for m. This is then used to find the extrapolated value for the pressure (eq A.2.5), the relative error (eq A.2.6), and the fine grid convergence GCI (eq A.2.7)

$$P_{ext}^{21} = \frac{r_{21}^m P_1 - P_2}{r_{21}^m - 1} \tag{A.2.5}$$

$$e_a^{21} = \frac{P_1 - P_2}{P_1} \tag{A.2.6}$$

$$GCI = \frac{1.25e_a^{21}}{r_{21}^m - 1} \tag{A.2.7}$$

APPENDIX A3

Among well-established models, Carman,[27] Ergun,[28] Zhavoronkov et al.,[53] and Reichelt[54] are often cited in the literature to estimate pressure drops in low AR packed beds. Ergun proposed a semiempirical correlation (eq A.3.1) by linking the Kozeny–Carman equation for the creeping flow regime and the Burke–Plummer equation for the turbulent regime. Ergun's correlation accounts for viscous and inertial energy losses and relates them to the dynamic variable, the velocity of the fluid, as well as the structure of the bed, as characterized by the bed average porosity, ε. The dimensionless pressure drop, P, is expressed by eq A.3.1.

$$P = \frac{150(1-\varepsilon)^2}{\mathrm{Re}_{dp}\varepsilon^3} + 1.75\frac{1-\varepsilon}{\varepsilon^3} \tag{A.3.1}$$

where

$$P = \frac{\Delta p}{L}\frac{dp}{\rho u_s} \tag{A.3.2}$$

The above equation holds for the case of large AR (AR > 15), where the condition of near uniformity prevails in the porosity throughout the bed.

- The Carman model, as shown by eq A.3.3, predicts well pressure drop at large AR and therefore can be used as reference model to estimate pressure drop deviations at low AR.[53]

$$P = \frac{6^{3-n}k}{\mathrm{Re}_{dp}^{2-n'}}\frac{(1-\varepsilon)^{3-n}}{\varepsilon^3} \tag{A.3.3}$$

where $n' = 1$ and $k = 5$.

- The Zhavoronkov equation is illustrated by eq A.3.4[53]

$$P = \frac{165.35A_w}{\mathrm{Re}_{dp}}\frac{(1-\varepsilon)^2}{\varepsilon^3} + 1.2B_w\frac{1-\varepsilon}{\varepsilon^3} \tag{A.3.4}$$

where

DOI: 10.1021/acs.iecr.5b02635
Ind. Eng. Chem. Res. 2015, 54, 12714–12729

$$A_w = B_w = 1 + \frac{1}{2\left(\frac{D}{dp}\right)(1-\varepsilon)} \tag{A.3.5}$$

- The Reichelt model is illustrated by eq A.3.6

$$P = \frac{154A_w^2}{\mathrm{Re}_{d_p}}\frac{(1-\varepsilon)^2}{\varepsilon^3} + \frac{A_w}{B_w}\frac{1-\varepsilon}{\varepsilon^3} \tag{A.3.6}$$

with the wall correction terms

$$A_w = 1 + \frac{2}{3\left(\frac{D}{d_p}\right)(1-\varepsilon)} \tag{A.3.7}$$

$$B_w = \left[1.15\left(\frac{d_p}{D}\right)^2 + 0.87\right]^2 \tag{A.3.8}$$

where A_w and B_w are model constants, d_p is particle size, and D is the tube diameter.

The last two models of Zhavoronkov and Reichelt are based on extensive experimental data where Ergun's constants are corrected by considering wall effects.

APPENDIX A4

The fluid flow model was computed from a 2D Brinkman–Forchheimer model that accounts for porosity changes along the radial coordinate of the packing.[55,56]

$$\rho(u\cdot\nabla u) = -\nabla pI + \nabla\cdot\left(\mu(\nabla u) + (\nabla u)^T - \frac{2}{3}\mu(\nabla\cdot u)I\right) + F \tag{A.4.1}$$

$$\rho\nabla\cdot u = 0$$

The drag force per unit of volume F is expressed using Ergun's relation as

$$F = \frac{\mu u}{K} - \beta\rho u^2 \tag{A.4.2}$$

The permeability of the porous media K and the non-Darcy term β are calculated from Zhavoronkov's model.

ASSOCIATED CONTENT

Supporting Information

The Supporting Information is available free of charge on the ACS Publications website at DOI: 10.1021/acs.iecr.5b02635.

S1: *Radial dispersion:* Movie at 24 frame/s for the Full 700 cross-sectional layers from the bottom to the top of the packed bed (AVI)

S2: *Axial dispersion at 12 min:* Movie at 24 frame/s for the Full 700 cross-sectional layers from the bottom to the top of the packed bed (AVI)

AUTHOR INFORMATION

Corresponding Author

*E-mail: f.aiouache@lancaster.ac.uk.

Notes

The authors declare no competing financial interest.

ACKNOWLEDGMENTS

The authors would like to acknowledge the funding provided by the Department of Education and Learning (DEL), Saudi Arabia Government, a Lancaster University starting grant, and the Thailand Research Fund.

NOMENCLATURE

A_w = nondimensional pressure drops model constant (−)
B_w = nondimensional pressure drops model constant (−)
C = concentration (mol m^{-3})
D = tube diameter (m)
DI = domain index (−)
D_m = molecular diffusion coefficient (m^2 s^{-1})
d_p = particle diameter (m)
$D_{ax/rad}$ = axial or radial dispersion coefficient (m^2 s^{-1})
e_a^{21} = relative error (−)
F = drag force per unit of volume (N m^{-3})
K = permeability of the packed bed (m^2)
h = grid size (−)
k = Carman model constant (−)
m = apparent order (−)
n' = Carman model constant (−)
L = length of bed (m)
n = particle index
NP = number of Lagrangian tracer particles (−)
N = number of cells (−)
p = pressure drops (Pa)
P = dimensionless pressure drop (−)
Pe = Peclet number for mass dispersion (−)
r = radial coordinate (m)
$\overline{r}$ = averaged displacements of all particles along the radial coordinates (m)
r_{21} = refinement factor (−)
Re = Reynolds number (−)
t = time (s)
P_{inf} = dimensionless pressure drop of an infinite size packed bed (−)
u = fluid flow velocity (m s^{-1})
u_s = fluid flow superficial velocity (m s^{-1})
x = axial coordinate
$\overline{x}$ = averaged displacements of all particles along the axial coordinates
z = axial coordinate (m)

Greek letters

θ = angular coordinate (−)
Θ = pressure difference between two discretizations (−)
ρ = density (kg m^{-3})
ε = bed porosity (−)
μ = dynamic viscosity (m^2 s^{-1})
η = fluid kinematic viscosity (m^2 s^{-1})
σ = standard deviation (−)
β = non-Darcy coefficient (m^{-1})
Δ = V the cell volume
η = fluid kinematic viscosity (m^2 s^{-1})

Abbreviations

AR = aspect ratio
CFD = computer fluid dynamics
DEM = discrete element method
GCI = grid convergence index
GMRES = generalized minimal residual method
I.D. = internal diameter
MRI = magnetic resonance imaging
NIR = near-infrared
OD = optical depth
Pe = Peclet number

DOI: 10.1021/acs.iecr.5b02635
Ind. Eng. Chem. Res. 2015, 54, 12714−12729

v = vapor

REFERENCES

(1) Freund, H.; Bauer, J.; Zeiser, T.; Emig, G. Detailed simulation of transport processes in fixed-beds. *Ind. Eng. Chem. Res.* **2005**, *44*, 6423−6434.

(2) Dixon, A.; Taskin, M.; Nijemeisland, M.; Stitt, E. CFD method to couple three-dimensional transport and reaction inside catalyst particles to the fixed bed flow field. *Ind. Eng. Chem. Res.* **2010**, *49*, 9012−9025.

(3) Vortmeyer, D.; Schuster, J. Evaluation of steady flow profiles in rectangular and circular packed beds by a variational method. *Chem. Eng. Sci.* **1983**, *38*, 1691−1699.

(4) Govindarao, V. M. H.; Subbanna, M.; Rao, A. V. S.; Ramrao, K. V. S. Voidage profile in packed beds by multi-channel model:effects ofcurvature of the channels. *Chem. Eng. Sci.* **1990**, *45*, 362−364.

(5) Dautzenberg, F. M.; Mukherjee, M. Process intensification using multifunctional reactors. *Chem. Eng. Sci.* **2001**, *56*, 251−267.

(6) Pistocchini, L.; Silvia Garone, S.; Motta, M. Fluid Dynamics Optimization of a Novel Isothermal Adsorption Dehumidification System for Solar Driven Applications. *Energy Procedia* **2014**, *48*, 1689−1698.

(7) Durlofsky, L.; Brady, J. F. Analysis of the Brinkman equation as a model for flow in porous media. *Phys. Fluids* **1987**, *30*, 3329−3341.

(8) Jaree, A.; Hudgins, R.; Budman, H.; Silveston, P.; Yakhnin, V.; Menzinger, M. Hysteresis and extinction waves in catalytic CO oxidation caused by reactant concentration perturbations in a packed-bed reactor. *Ind. Eng. Chem. Res.* **2003**, *42*, 1662−1673.

(9) Zhang, W.; Thompson, K.; Reed, A.; Beenken, L. Relationship between packing structure and porosity in fixed beds of equilateral cylindrical particles. *Chem. Eng. Sci.* **2006**, *61*, 8060−8074.

(10) Giese, M.; Rottschafer, K.; Vortmeyer, D. Measured and modeled superficial flow profiles in packed beds with liquid flow. *AIChE J.* **1998**, *44*, 484−490.

(11) De Klerk, A. Voidage variation in packed beds at small column to particle diameter ratio. *AIChE J.* **2003**, *49*, 2022−2029.

(12) Aiouache, F.; TSaoir, M. N.; Kitagawa, K. Screening wall effects of a thin fluidized bed by near-infrared imaging. *Chem. Eng. J.* **2011**, *167*, 288−296.

(13) Winterberg, W.; Tsotsas, E.; Krischke, A.; Vortmeyer, D. A. Simple and coherent set of coefficients for modelling of heat and mass transport with and without chemical reaction in tubes filled with spheres. *Chem. Eng. Sci.* **2000**, *55*, 967−979.

(14) Gladden, L.; Akpa, B.; Anadon, L.; Heras, J.; Holland, D.; Mantle, M.; Matthews, S.; Mueller, C.; Sains, M.; Sederman, A. Dynamic MR Imaging of single- and two-phase flows. *Chem. Eng. Res. Des.* **2006**, *84*, 272−281.

(15) Theuerkauf, J.; Witt, P.; Schwesig, D. Analysis of particle porosity distribution in fixed beds using the discrete element method. *Powder Technol.* **2006**, *165*, 92−99.

(16) Roblee, L. H. S.; Baird, R. M.; Tierney, J. W. Radial porosity variation in packed beds. *AIChE J.* **1958**, *4*, 460−464.

(17) Sederman, A.; Alexander, P.; Gladden, L. Structure of packed beds probed by Magnetic Resonance Imaging. *Powder Technol.* **2001**, *117*, 255−269.

(18) Yang, R. T. *Gas separation by adsorption processes*; Imperial College Press: UK, 1997.

(19) Tobiś, J.; Vortmeyer, D. The near-wall channelling effect on isothermal constant-pattern adsorption. *Chem. Eng. Sci.* **1988**, *43*, 1363−1369.

(20) Kwapinski, W.; Winterberg, M.; Tsotsas, E.; Mewes, D. Modeling of the wall effect in packed bed adsorption. *Chem. Eng. Technol.* **2004**, *27*, 1179−1186.

(21) Romkes, S.; Dautzenberg, F.; Van de Bleek, C.; Calis, H. CFD modelling and experimental validation of particle-to-fluid mass and heat transfer in a packed bed at very low channel to particle diameter ratio. *Chem. Eng. J.* **2003**, *96*, 3−13.

(22) Ahmadi Motlagh, A. H.; Hashemabadi, S. H. CFD based evaluation of heat transfer coefficient from cylindrical particles. *Int. Commun. Heat Mass Transfer* **2008**, *35*, 674−680.

(23) Mueller, G. E. Radial void fraction distributions in randomly packed fixed beds of uniformly sized spheres in cylindrical containers. *Powder Technol.* **1992**, *72*, 269−275.

(24) Mueller, G. E. Prediction of radial porosity distributions in randomly packed fixed beds of uniformly sized spheres in cylindrical containers. *Chem. Eng. Sci.* **1991**, *46*, 706−708.

(25) Dixon, A. Correlations for wall and particle shape effects on fixed bed bulk voidage. *Can. J. Chem. Eng.* **1988**, *66*, 705−708.

(26) Kozeny, J. Uber kapillare leitung des Wassers im Boden. Sitzungsber. AKAD. Wiss. *Wien* **1927**, *136*, 271−306.

(27) Carman, P. Fluid flow through granular beds. *Trans. Inst. Chem. Eng.* **1997**, *75*, S32−S48.

(28) Ergun, S. Fluid flow through packed columns. *Chem. Eng. Prog.* **1953**, *48*, 89−94.

(29) Happel, J. Viscous flow in multiparticle systems: Slow motion of fluids relative to beds of spherical particles. *AIChE J.* **1958**, *4*, 197−201.

(30) Bertil Anderson, K. E. Pressure drop in ideal fluidization. *Chem. Eng. Sci.* **1961**, *15*, 276−297.

(31) Molerus, O. Druckverlustgleichung fur die Durchstromung von Kugelschuttungen im laminaren und im Ubergangsbereich. *Chem. Ing. Tech.* **1977**, *49*, 675.

(32) Eisfeld, B.; Schnitzlein, K. The influence of confining walls on the pressure drop in packed beds. *Chem. Eng. Sci.* **2001**, *56*, 4321−4329.

(33) Moise, A.; Tudose, R. Air isothermal flow through packed beds. *Exp. Therm. Fluid Sci.* **1998**, *18*, 134−141.

(34) Ding, Y.; Wang, Z.; Wen, D.; Ghadiri, M.; Fan, X.; Park, D. Solids behaviour in a gas-solid two-phase mixture flowing through a packed particle bed. *Chem. Eng. Sci.* **2005**, *60*, 5231−5239.

(35) Nic An tSaoir, M.; Fernandes, D. L. A.; Sa, J.; Kitagawa, K.; Hardacre, C.; Aiouache, F. Three dimensional water vapour visualization in porous packing by near-infrared diffuse transmittance tomography. *Ind. Eng. Chem. Res.* **2012**, *51*, 8875−8882.

(36) tSaoir, M. N.; Fernandes, D. L. A.; McMaster, M.; Kitagawa, K.; Hardacre, C.; Aiouache, F. Transient distributions of composition and temperature in a gas−solid packed bed reactor by near-infrared tomography. *Chem. Eng. J.* **2012**, *189*−*190*, 383−392.

(37) Celik, I. B.; Ghia, U.; Roache, P. J.; Freitas, C. J.; Coleman, H.; Raad, P. E. Procedure for estimation and reporting of uncertainty due to discretization in cfd applications. *J. Fluids Eng.* **2008**, *130*, 078001.

(38) Delgado, J. M. P. Q. Longitudinal and transverse dispersion in porous media. *Chem. Eng. Res. Des.* **2007**, *85*, 1245−1252.

(39) Spedding, P. L.; Spencer, R. M. Simulation of packing density and liquid flow in fixed beds. *Comput. Chem. Eng.* **1995**, *19*, 43−73.

(40) Reyes, S. C.; Iglesia, E. Monte Carlo simulations of structural properties of packed beds. *Chem. Eng. Sci.* **1991**, *46*, 1089−1099.

(41) Nolan, G. T.; Kavanagh, P. E. Computer simulation of random packing of hard spheres. *Powder Technol.* **1992**, *72*, 149−155.

(42) Crider, J. E.; Foss, A. S. Computational studies of transients in packed tubular chemical reactors. *AIChE J.* **1966**, *12*, 514−522.

(43) Nolan, G. T.; Kavanagh, P. E. Octahedral configurations in random close packing. *Powder Technol.* **1995**, *83*, 253−258.

(44) Benenati, R. F.; Brosilow, C. B. Void fraction distribution in beds of spheres. *AIChE J.* **1962**, *8*, 359−361.

(45) Chan, S. K.; Ng, K. M. Geometrical characteristics of the pore space in a random packing of equal spheres. *Powder Technol.* **1988**, *54*, 147−155.

(46) Spedding, P. L.; Spencer, R. M. Simulation of packing density and liquid flow fixed beds-II. Voronoi polyhedra studies. *Comput. Chem. Eng.* **1998**, *22*, 247−257.

(47) Parse, J.; Wert, J. A geometrical description of particle distributions in materials. *Modell. Simul. Mater. Sci. Eng.* **1993**, *1*, 275−296.

(48) Lindquist, W. B.; Lee, S. M.; Cork, D. A.; Jones, K. W.; Spanne, S. Medial axis analysis of void structure in three-dimensional

DOI: 10.1021/acs.iecr.5b02635
Ind. Eng. Chem. Res. 2015, 54, 12714−12729

tomographic images of porous media. *J. Geophys. Res.* **1996**, *101*, 8297−8310.
(49) Zou, R. P.; Yu, A. B. The packing of spheres in a cylindrical container: The thickness effect. *Chem. Eng. Sci.* **1995**, *50*, 1504−1507.
(50) Mueller, G. E. Radial porosity in packed beds of spheres. *Powder Technol.* **2010**, *203*, 626−633.
(51) Delgado, J. M. P. Q. A critical review of dispersion in packed beds. *Heat Mass Transfer* **2006**, *42*, 279−310.
(52) Augier, F.; Idoux, F.; Delenne, J. Y. Numerical simulations of transfer and transport properties inside packed beds of spherical particles. *Chem. Eng. Sci.* **2010**, *65*, 1055−1064.
(53) Zhavoronkov, N. M.; Aerov, M. E.; Umnik, N. N. Hydraulic reisistance and densityof packing of a granular bed. *J. Phys. Chem.* **1949**, *23*, 342−361.
(54) Reichelt, W. Zur Berechnung des Druckverlustes einphasig durchstromter Kugel-und Zylinderschuttungen. *Chem. Ing. Tech.* **1972**, *44*, 1068−1071.
(55) Atmakidis, T.; Kenig, E. Y. CFD-based analysis of the wall effect on the pressure drop in packed beds with moderate tube/particle diameter ratios in the laminar flow regime. *Chem. Eng. J.* **2009**, *155*, 404−410.
(56) Augier, F.; Laroche, C.; Brehon, E. Application of computational fluid dynamics to fixed bed adsorption calculations: Effect of hydrodynamics at laboratory and industrial scale. *Sep. Purif. Technol.* **2008**, *63*, 466−474.

DOI: 10.1021/acs.iecr.5b02635
Ind. Eng. Chem. Res. 2015, 54, 12714−12729

Chemical Engineering and Processing 108 (2016) 58–73

Contents lists available at ScienceDirect

Chemical Engineering and Processing: Process Intensification

journal homepage: www.elsevier.com/locate/cep

Kinetics and reactive stripping modelling of hydrogen isotopic exchange of deuterated waters

Mohammed Aldehani[a], Faris Alzahrani[a], Meabh Nic An tSaoir[b], Daniel Luis Abreu Fernandes[c], Suttichai Assabumrungrat[d], Farid Aiouache[a,*]

[a] Department of Engineering, Lancaster University, UK
[b] School of Chemistry and Chemical Engineering, Queen University Belfast, UK
[c] Department of Chemistry—Ångström Laboratory, Uppsala University, Sweden
[d] Centre of Excellence in Catalysis and Catalytic Reaction Engineering, Department of Chemical Engineering, Faculty of Engineering, Chulalongkorn University, Thailand

ARTICLE INFO

Article history:
Received 19 May 2016
Accepted 16 July 2016
Available online 21 July 2016

Keywords:
Isotopic exchange
Reactive stripping
Detritiation
Dedeuteriation
Rate-based modelling
Reactive separation

ABSTRACT

This work presents results of experimental kinetics and modelling of the isotopic exchange between hydrogen and water in a reactive stripping column for water dedeuteriation. The missing physical properties of deuterium and tritium isotopologues in hydrogen gas and water forms were predicted and validated using existing literature data. The kinetic model relevant to a styrene-divinyl-benzene co-polymer–supported platinum catalyst was used for modelling, by Aspen plus modular package, impact of design parameters including temperature, total pressure, gas to liquid flowrate ratio, pressure drop and flow mixing, on the separation of deuterium and further the separation of tritium. The modelling by the rate-based non-equilibrium, including design correlations of model of mass and heat transfers, chemical kinetic constants, mass transfer coefficients and overall exchange rate constants, allowed access to separation trends in a good agreement with published data. The synergy between the rates of chemical isotopic exchange and gas/liquid mass transfer, and by inference the performance of reactive stripping, was particularly sensitive to high temperatures, low hydrogen flow rates, pressure drops and internals properties. Extension to tritium confirmed a slightly slower mass transport compared with deuterium leading to potentially under-estimated design features for detritiation processing when deuterium is used instead.

© 2016 Elsevier B.V. All rights reserved.

1. Introduction

With energy demand growing at an alarming rate, nuclear energy has the potential to provide a long-term environmentally responsible solution for base-load electricity production. Next nuclear implementation strategy is envisioned as consisting of fusion power plants which include high temperature heat transfer loops for energy delivery [1]. These reactors contain passive safety features and are capable of withstanding postulated long-term, depressurized and loss–of–forced–convection accidents without damaging the fuel. However, radioactive effluents will be generated, mainly in the form of mixtures of tritiated and deuterated waters (i.e. HDO_L, HTO_L, DTO_L, T_2O_L and D_2O_L) and gases (i.e. DT, HT, HD, D_2 and T_2), at levels over ten thousand times higher than those produced by existing light water reactors [2]. There is evidence of adverse health effects on populations living near tritium facilities, owing to facile wall permeation by tritium even in low levels under the operated temperatures [1]. The simplest solution to preventing tritium contamination of down-stream facilities is to deploy detritiation systems on the heat transfer fluid loops between the facilities and the utility systems but the management of these detritiation systems remains one of

Abbreviations: CECE, combined electrolysis and catalytic exchange; CEPE, chemical equilibrium - bulk gas/liquid physical equilibrium; CKEP, chemical kinetics - bulk gas/liquid physical equilibrium; CKRN-E, chemical kinetics - rate-based gas/liquid non-equilibrium; DIPPR, Design Institute for Physical Properties Research; HETP, height equivalent to theoretical plate [m]; I.D., internal diameter [m]; LPCE, liquid phase catalytic exchange; MESH, material balance vapour–liquid equilibrium equations mole fraction summations and heat balance; NSD, normalized standard deviation (%); PTFE, polytetrafluoroethylene; RadFrac, rate-based equilibrium separation process model; RateFrac, rate-based non-equilibrium separation process model; SDBC, styrene-divinylbenzene copolymer; SRK, Soave-Redlich-Kwong equation-of-state.

* Corresponding author.
E-mail addresses: f.aiouache@lancaster.ac.uk, aiouache_farid@yahoo.com (F. Aiouache).

http://dx.doi.org/10.1016/j.cep.2016.07.008
0255-2701/© 2016 Elsevier B.V. All rights reserved.

Nomenclature

A	Sectional area of the column [m^2]
a	Interfacial area per unit bubbling area for trays [–]
a_l	Total interfacial area per unit volume of liquid, vapour [m^2/m^3]
a_F	Specific area of the packing [m^2/m^3]
a_w	Wetted surface area per unit volume of the column [m^2/m^3]
C_p	Specific molar heat capacity [J/kmol K]
D	Diffusivity [m^2/s]
d_F	Nominal packing size [m]
d_p	Bed particle diameter [m]
d_s	Sphere diameter [–]
Fr	Froude number [–]
g	Acceleration due to gravity [$m\,s^{-2}$]
G'	Gas flow rate [mol/s]
G'/L'	Gas to liquid flowrate ratio [–]
G	Matrix of thermodynamic factors [–]
H	Liquid enthalpy [J/mol]
h	Vapour enthalpy [J/mol]
h'	Heat transfer coefficient [W/m K]
h_F	Height of a packed section [m]
K	Equilibrium constant between phases [–]
$k_{r,i}$	Kinetic rate constant of reaction i [mol/kg s]
k_i	Film mass transfer coefficient of species i [mol/m^3 s]
K_{eq}	Equilibrium constant for isotope exchange [–]
$K_{g,overall}$	Gas/liquid rate constant
L'	Liquid flow rate [mol/s]
m_c	Mass of catalyst [kg]
N	Number of stages in the LPCE column [–]
n	Number of data points in the normalized standard deviation equation [–]
n_c	Number of components [–]
NM	Rate of mass transfer between phases [mol/s]
P	Total pressure [Pa]
P_c	Critical pressure [kPa]
q	Heat transfer rate between phases [J/s]
r_i	Rate of the isotopic exchange (mole/kg s)
Re	Reynolds number [–]
$Sep_{D,e}$	Separation factor [–]
Sc	Schmidt number
T	Temperature [K]
T_B	Boiling point temperature [K]
T_c	Critical temperature [K]
V_c	Critical molar volume [cm^3/mol]
V_b	Molar volume at the boiling point (cm^3/mol)
We	Weber number [–]
x	Mole fraction in the liquid phase [–]
x'_D	Atom fraction of deuterium in the liquid water
y	Mole fraction in the gaseous phase
y_{eq}	Equilibrium composition of deuterium in hydrogen phase
y'_D	Atom fraction of deuterium in hydrogen phase
Z_c	Critical compressibility factor [–]

Greek symbols

λ	Thermal conductivity [W/m.K]
φ	Fugacity coefficient [–]
ϕ	Fractional hole area per unit bubbling area [–]
μ	Dynamic viscosity [Pa.s]
ν	Kinematic viscosity [cP]
ρ	Density [$kg\,m^{-3}$]
σ	Liquid surface tension [N/m]
σ_c	Critical surface tension of packing [N/m]
δ	Kronecker delta: 1 if i = k, 0 otherwise
ε	Bed voidage [–]

Subscripts

D_2	Deuterium gas
D_2O	Heavy water or (deuterium oxide)
DT	Deuterated tritium gas
DTO	Tritiated heavy water
eq	Equilibrium state
G	Gas
HD	Deuterated hydrogen
HDO	Deuterated water
HT	Tritiated hydrogen gas
I	Interphase boundary between the gas and liquid HTO tritiated water
L	Liquid
T_2O	Tritium oxide or (super-heavy water)
T_2	Tritium gas
V	Vapour

the main technological challenges for future industrial development [3].

The recovery of tritium in the forms of DTO_L, HTO_L or T_2O_L is an important process, not only because it allows for the reduction of concentration of the radiation hazard of intermediate level wastes, but also because tritium is a precious element for fusion reactions, and tritium recovery can help offset the high costs of disposal and storage [4]. Various technologies have been developed for water detritiation, including combined electrolysis and chemical exchange (CECE), liquid hydrogen distillation, cryogenic adsorption, palladium membrane diffusion, thermal diffusion, laser separation and electrochemical isotope separation [5–7]. The CECE process combines a water electrolysis unit and a liquid phase exchange (LPCE) column in which the catalytic hydrogen exchange reaction and the vapour/liquid scrubbing process occur. In the CECE, the contaminated water is first fed into an electrolyser where it is split into gaseous oxygen and hydrogen gases (H_2, HD, T_2, D_2, HT and DT). The stream of hydrogen mixture is then directed up the LPCE column where it counter–currently interacts with water that is flowing down the catalytic packing column. As the liquid water trickles down the column, it becomes enriched in tritium while hydrogen gas becomes depleted, which causes an exchange of the HT/HD/T_2/D_2/DT gas with the scrubbing water to produce concentrated tritiated and deuterated waters (i.e. HDO_L, HTO_L, DTO_L, T_2O_L or D_2O_L) while H_2 is vented to the atmosphere. This catalytic exchange process is driven by two sets of isotopic exchange reactions: (1) a gaseous catalytic exchange between the hydrogen mixture and the stripped off water vapour (H_2O_V; Reaction (1)) and (2) the vapour–liquid concentration of the heavy water vapour isotopologues mixture $HDO_V/HTO_V/DTO_V$ in liquid water (H_2O_L; Reaction (2)).

$$HD/HT/DT + H_2O_V \Leftrightarrow HTO_V/HDO_V/DTO_V + H_2 \quad (1)$$

$$HTO_V/HDO_V/DTO_V + H_2O_L \Leftrightarrow HTO_L/HDO_L/DTO_L + H_2O_V \quad (2)$$

This leads to the overall reaction:

$$HT/HD/DT + H_2O_L \Leftrightarrow HTO_L/HDO_L/DTO_L + H_2 \quad (3)$$

The combined process, therefore, takes advantage of the wet scrubbing of $HTO_V/HDO_V/DTO_V$ (produced by Reaction (1)) by H_2O_L (as shown in Reaction (2)) and the reactive stripping of H_2O_V (produced by Reaction (2)) by hydrogen (as shown by Reaction (1)) to promote the rates and the equilibrium boundaries of both reactions. The catalytic Reaction (1) is known to be weakly exothermic (−15.9 J/mol) and preferentially operates at mild

temperatures [6]. It is also facilitated by hydrophobic or waterproof catalysts such as platinum, supported on carbons, polytetrafluoroethylene (PTFE) or resins (styrene-divinyl-benzene copolymer (SDBC)) [8–13]. Reaction (2) expresses the liquid/vapour distillation exchange of mixture including water and heavy water isotopologues. This reaction is also known to be promoted at mild temperatures, since the associated enthalpy of evaporation of heavy water is higher than that of water, and is known to be kinetically accelerated by packing structures of a hydrophilic nature [4,14,15].

The hazards associated with handling tritium have promoted the development of extensive works aimed at modelling the overall process of the isotopic exchange for tritium detritiation. Most of the studies used assumptions based on average physical and transport properties while neglecting the thermal properties of isotopologues such as (heat of vaporization, enthalpy, heat capacity and conductivity) and the underlying heat transfer phenomena. The liquid stream in the LPCE column is typically operated under a trickle flow and a partial wetting of the packing, causing both mass and heat dispersions and a boundary resistance to mass transfer between liquid water and gaseous hydrogen. The methods for solving the multi-component reactive stripping/scrubbing system were mainly taken from the binary component approaches which are more or less straightforward extensions of methods that have been developed for solving conventional scrubbing/stripping column problems. Until recently, the trends of mass transfer rates of Reaction (3)–, which lumps both the gaseous phase of Reaction (1) and gas/liquid mass evaporation/condensation (Reaction (2)) – in a wet scrubbing/stripping column, have been the general objectives of most modelling studies. In studies on packed columns, the effects of the flow dynamics, counter–current stream ratios, temperature, pressure and type of packing internal have been recurrently cited [16].

In addition, the presence of chemical reactions in multicomponent separation systems influenced the component mass transfer with variations in each component in a complex and unpredictable way[22]. In reality, equilibrium was rarely attained and both stripping and scrubbing of tritium and deuterium deviated towards rate controlled phenomena, leading to a separation efficiency less than unity. This means that mass and heat transfers were driven by gradients of the chemical potentials and temperature. Due to these facts, the equilibrium–based models are usually inadequate and resistances to mass and heat transfer can only be considered by rate–based models in which the gas and liquid phases are balanced separately taking into consideration the mass and heat fluxes across the interface. Rigorous predictive models must regard the accelerating or inhibiting effects of chemical reactions on mass transfer and vice–versa. The non-equilibrium gas/liquid model includes an interfacial mass transfer rate where the equilibrium between phases occurs exactly at the gas/liquid interphase only. The non-equilibrium model also takes into account the flow dynamics where the pressure drops across the packing is considered to be a function of the interstitial velocity, the physical properties and the hardware design. The column design information is then necessary, and must be specified, so that parameters such as mass transfer coefficients, interfacial areas and liquid hold-ups can be predicted. The model also requires thermodynamic and transport properties, not only for calculation of the phase equilibrium but also for calculation of the driving forces for mass and heat transfers in the reactive stripping/scrubbing column.

As conclusions, the models of previous mass transfer studies on the catalytic exchange process of hydrogen for water detritiation by reactive scrubbing relied on overall mass transfer coefficients that have been fitted to experimental data from dedicated columns [15–22]. Application of commercial software packages that carry advanced modelling methods and thermodynamic databases of prediction models for hydrogen isotopic exchange process has not been reported to our knowledge but dedicated simulation tools were developed in–house [19–23]. Herein, we present the applicability of the rigorous rate-based model of the commercial package Aspen plus Custom Modeler (AspenTech, 2013), as a promising tool to investigate the coupling of mass and heat transports, specific features of the reaction mixture and the synergic impact on isotope separation of the catalytic exchange process in a reactive stripping column. Taking advantage of extensive experimental results in literature on hydrogen isotopic exchange by stripping/scrubbing processing, this work presents the experimental results of chemical kinetics of the gaseous catalytic exchange, the results of modelling of reactive stripping process, including effects of significant design and operating parameters on the column performance. The methodology used is as follows: (1) the gaseous phase catalytic exchange is carried out independently and in the absence of the scrubbing process using a wet-proofed platinum/SDBC resin catalyst. A kinetic model for the overall rate of exchange process is developed, and relevant parameters are estimated based on data generated using deuterium. (2) The missing physical properties of deuterium and tritium isotopologues for hydrogen and water are predicted by using existing thermodynamic models, geometric mean interpolation and linear correlation of the critical properties. (3) The effects of transport and reaction kinetics on the transfer of deuterium between the liquid and gaseous phases is investigated by three types of models based on coupling as shown in Fig. 1: the chemical equilibrium and the bulk gas/liquid physical equilibrium (CEPE) controlled model (Fig. 1(a)), the chemical kinetics and the bulk gas/liquid physical equilibrium (CKPE) controlled model (Fig. 1(b)) and the chemical kinetics and the rate-based gas/liquid non-equilibrium (CKRN-E) controlled model (Fig. 1(c)). The results are discussed and validated by comparison with published data and a sensitivity analysis is extended to tritium separation.

2. Materials and methods

The kinetics tests were carried out by following the kinetics of transfer of deuterium from water vapour to hydrogen gas (i.e. the reverse Reaction of Eq. (1)) as it is more affordable to feed the CECE column with deuterated liquid water than deuterated hydrogen gas. Directed by experiments illustrated in previous studies on fluid flow in the isotopic exchange process, the resistance to external mass transport was reduced by setting the minimum flowrate of H_2O_V and H_2 to 300 cm^3/min and the internal mass transport inside catalyst was reduced by using particles as small as 0.08–0.10 mm [24]. The kinetic tests of the catalytic exchange were carried out in a packed bed reactor as shown in Fig. 2. The tube was made of fused quartz with a 12 mm internal diameter and filled with 0.75 g of hydrophobic Pt/SDBC resin (average pore size 110–175 Å, surface area 900 $m^2\,g^{-1}$ and 2% impregnated platinum) as reported by Nic An tSoir et al. [25]. The catalytic system was initially reduced under 25 mol% of H_2 and then purged with nitrogen. Typically, a D_2O_V composition of 12.0 mol% (relative humidity (RH) of 60.1%) was introduced at atmospheric pressure by bubbling a mixture of H_2 (20 mol% in N_2) at 338 cm^3/min and temperature of 333 K using a controlled evaporator mixer (Bronkhorst). All pre- and post-packed tube pipes were insulated and heated to the operating temperature. Thermocouples were placed in front and behind the packed bed. In addition, a humidity sensor (Exo Terra Digital Hygrometer, accuracy 2% at RH > 10%) was placed at the exit of the experimental setup. The output products were measured using a Pfeiffer Omistar GSD O mass spectrometer equipped with a quadrupole analyser.

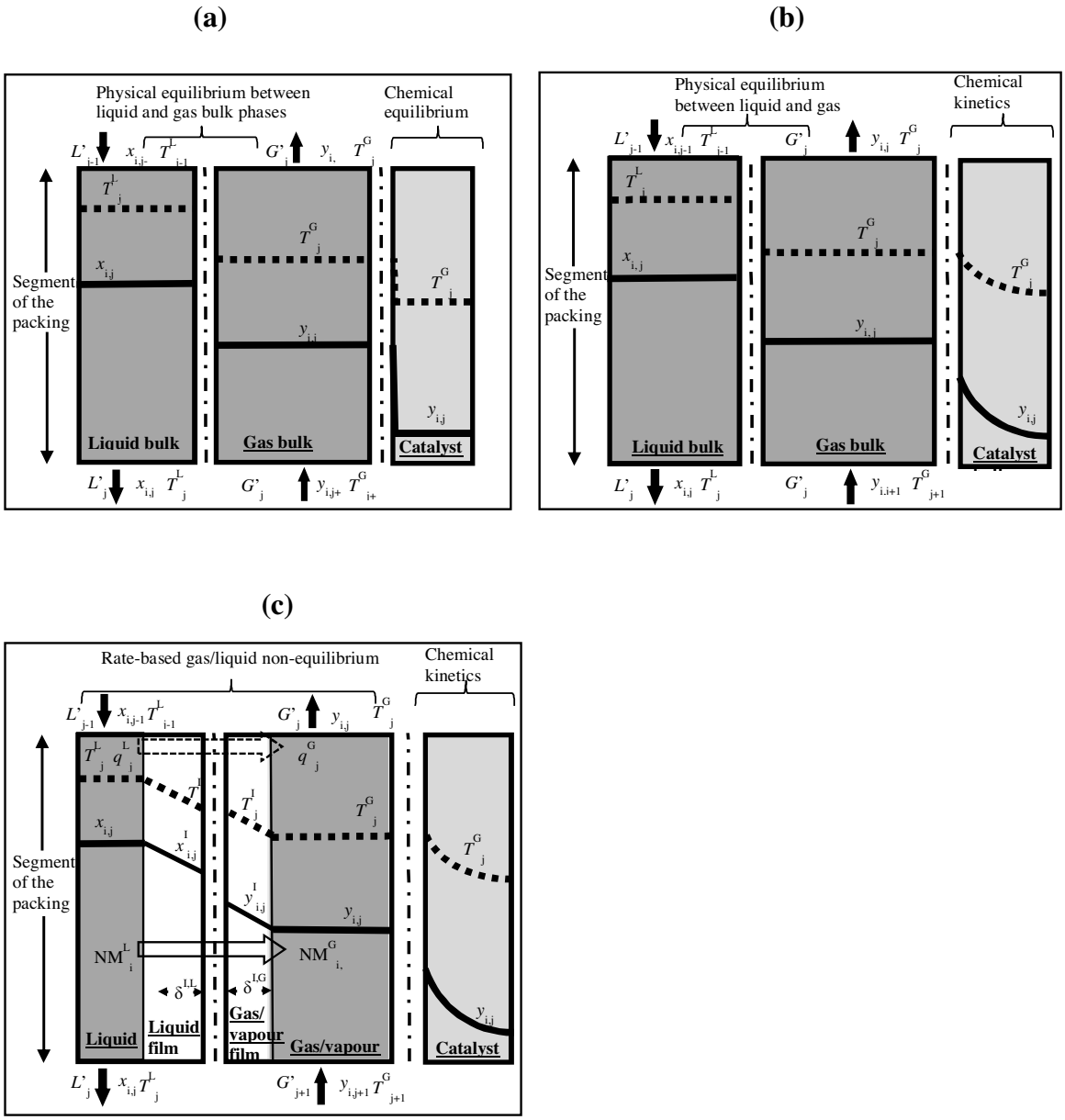

Fig. 1. Schematic representations of the three mass transfer models: (a) Chemical equilibrium and gas/liquid physical equilibrium (CEPE) model, (b) Chemical kinetics and gas/liquid physical equilibrium (CKPE) model, (c) Chemical kinetics and rate-based gas/liquid non-equilibrium (CKRN-E) model.

3. Results

3.1. Kinetic study and composition trends

The development of kinetic study of isotopic exchange was carried out because the rate of kinetic model impacts the driving forces of concentrations and temperature that are responsible of mass transfer rates in the reactive stripping process. Two approaches are available in literature on the kinetics of the isotopic exchange: the first uses a lumping model where trends of gathered atomic concentration of deuterium per phase (gas or vapour) is considered while the second proceeds with trends of concentration of each species in the gaseous phase mixture regardless the nature of the phase. Herein, the later approach was considered and investigated under gaseous/vapour operations only. Most of the studies in literature presented kinetic models that consider Reaction (1) only. Associated side reactions and intermediate isotopologues were however demonstrated in our previous works [10,11,24] and were validated by a recent study by Roland et al. [26]. Kawakami et al. [27] and Sagert and Pouteau [28] studied the kinetics of the gas-phase exchange reaction (Reaction (1)) with the deuterium isotopologue over the supported platinum catalysts and proposed a reaction mechanism based on the Langmuir–Hinshelwood approach. Kumar et al. [17] investigated the impact of external and internal mass transports on the intrinsic kinetics of catalytic exchange in absence of the gas/liquid scrubbing. Strong pore diffusion was observed, leading to internal effectiveness factors ranging from 13 to 20%, while the external mass transfer resistance was negligible at the operated conditions. Roland et al. [26] reported rate coefficients for the isotope exchange reactions between deuterium gas and water vapour taking place at the surface of a stainless steel vessel. Time transients of D_2O_V and HDO_V, produced via isotope exchange reactions in the mixture of D_2, H_2, and D_2O_V, H_2O_V, HD and HDO_V,

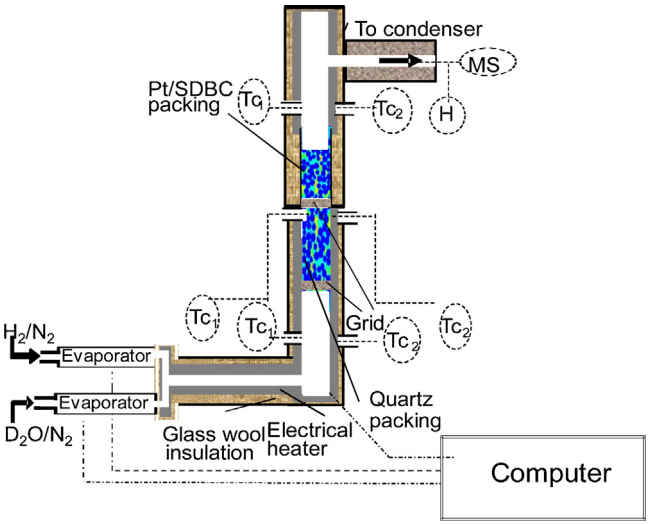

Fig. 2. Scheme of the whole tomography apparatus, packed bed tube diameter: 12 mm, thickness of both tubes: 1 mm, Evaporator (Bronkhorst) = Mass flow controller (N_2), air-actuated switching valve, distilled water bath; H: Humidity sensor; TC_1 = Thermocouples (monitoring), TC_2: Thermocouples connected to programmable temperature controllers; MS: Mass spectrometer.

were measured. The results were adequately represented by the kinetic model in the form of coupled rate equations and the validity of the model was reported to be limited to low pressure environments and large gas (D_2) to water ratios. In a previous work, we used the gas phase hydrogen catalytic exchange to visualize mass, heat and fluid flow distributions in a gas-solid packed bed reactor. The packed bed was filled with Pt/SDBC. The derived transient changes of H_2O_V, HDO_V and temperature of the vapour phase hydrogen isotopic exchange reaction, between heavy water vapour (D_2O_V) and hydrogen gas, were described by 3D distributions inside and at the exit of a packed bed reactor [24,25]. Herein, the kinetics of Reaction (1) were investigated by observing the evolution of the six molecular species of hydrogen gas (H_2, HD and D_2) and water vapour (H_2O_V, D_2O_V and HDO_V) involved in the overall catalytic process. Although a total of six reactions between the water vapour isotopes and hydrogen have been reported by Roland et al. [26], only three reactions were, in fact, independent as confirmed by Roland et al. [26]. Two of these reactions were determined to be under kinetic control.

Fig. 3(a) shows transient composition profiles of the water vapour (H_2O_V) isotopologues (D_2O_V and HDO_V) and hydrogen gas isotopologues (HD and D_2) by using inlet compositions of D_2O_V and H_2 of 12.0 and 25.0 mol% in N_2, respectively, and temperature of 333 K. The steady-state compositions were achieved after 50 min. It is

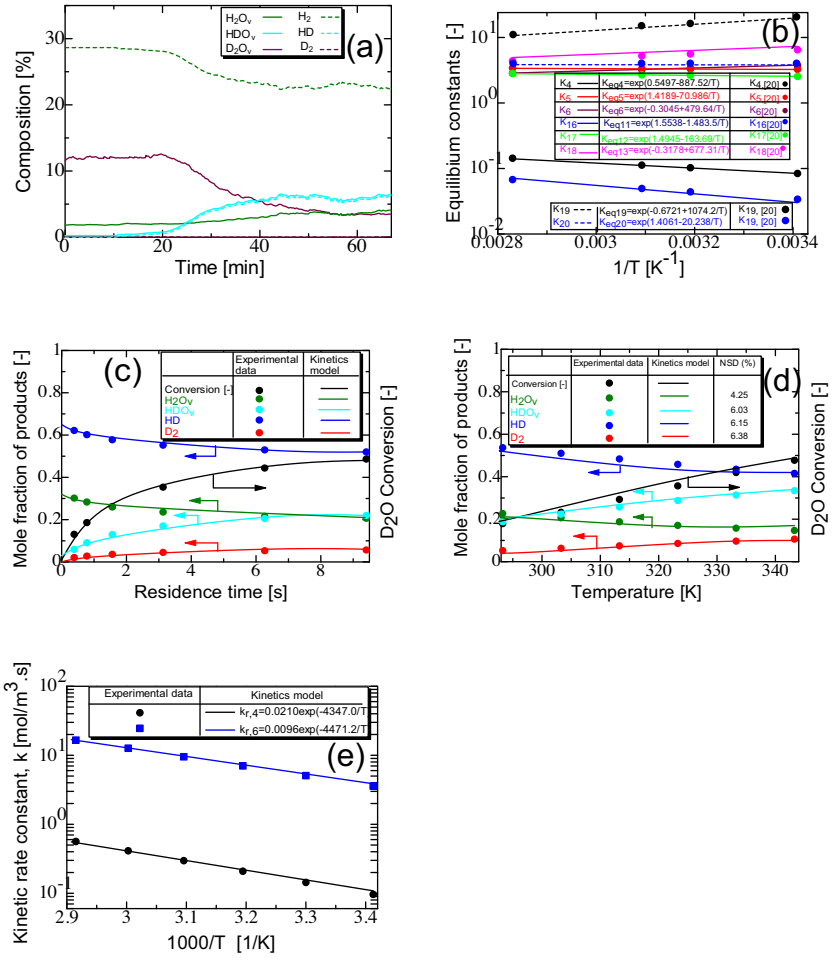

Fig. 3. Kinetic model for deuterium isotopic exchange. (a) Transient composition profiles of deuterium isotopologues in both hydrogen gas and water vapour, feed flow rate: 0.338 L/min, compositions of D_2O, H_2 and N_2: 12, 25 and 63%, respectively, temperature: 323 K, (b) chemical equilibrium constants with temperature, (c) Steady-state composition profiles of products of deuterium isotopologues with residence time in both hydrogen gas and water vapour, compositions of D_2O, H_2 and N_2: 12, 25 and 63%, respectively, temperature: 323 K, (d) Steady-state composition profiles of products of deuterium isotopologues with temperature in both hydrogen gas and water vapour, Feed flow rate: 0.338 L/min, compositions of D_2O, H_2 and N_2: 12, 25 and 63%, respectively, temperature: 323 K, (e) Arrhenius plots of chemical rate constants.

interesting to see that compositions of HD and HDO compounds followed similar trends, while amounts of D_2 were negligible, demonstrating a similar operating mechanism for the gaseous and vapour components. The production of water, even in small amounts (~2%), demonstrates that its production occurs via D_2 release. Deuterium was released from D_2O_V by single and double de-deuteriations: the first into HDO_V and HD, and the second into H_2O_V and D_2. D_2 compound was completely consumed while HD was partly consumed by H_2O_V into HDO_V. Therefore, the model of Roland et al. [26] is still valid but reduced to three reactions (i.e. Reactions (4)–(6)) where Reactions (4) and (6) were assumed to be under kinetic control and Reaction (5) under a quasi-equilibrium state [26].

$$H_2 + D_2O_V \Leftrightarrow D_2 + H_2O_V \quad (4)$$

$$H_2 + D_2 \Leftrightarrow 2HD \quad (5)$$

$$HD + H_2O_V \Leftrightarrow H_2 + HDO_V \quad (6)$$

The sum of these reactions (the reverse Reaction of Eq. (1)) leads to Eqs. (7.1) and (7.2)

$$H_2 + D_2O_V \Leftrightarrow HD + HDO_V \quad (7.1)$$

$$H_2 + D_2O_V \Leftrightarrow D_2 + H_2O_V \quad (7.2)$$

The kinetics of gas phase catalytic exchange have been generally modelled by the surface Langmuir–Hinshelwood (LH), Eley–Rideal (ER) or linear adsorption mechanisms where the hydrogen and water molecules are dissociatively adsorbed at common or separate active sites. The high dilution of deuterium in water and hydrogen gas, along with relevant high adsorption capacities, led the rate for each surface reaction to be assumed of the first-order in coverage for each species [17]. The reaction rates, r_j, for Reactions (4) and (6) are illustrated by Eqs. (8) and (9), respectively.

$$r_4 = k_{r,4}\left(\frac{y_{D_2O_V}}{y_{H_2O_V}} - \frac{1}{K_{eq_4}}\frac{y_{D_2}}{y_{H_2}}\right) \quad (8)$$

$$r_6 = k_{r,6}\left(\frac{y_{HD}}{y_{H_2}} - \frac{1}{K_{eq_6}}\frac{y_{HDO_V}}{y_{H_2O_V}}\right) \quad (9)$$

where y_i is the mole fraction of species i in the gaseous phase (i.e. hydrogen and vapours). The quasi-equilibrium state of Reaction (5) is taken into consideration by means of the mass action law:

$$K_{eq_5} = \frac{y_{HD}^2}{y_{D_2}y_{H_2}} \quad (10)$$

For the three Reactions (4)–(6), the equilibrium constants K_i were obtained from Gibbs free-energy which was predicted in Section 3.2.1 on property estimations and these equilibrium constants were compared with those reported by Yamanishi et al. [20], as shown in Fig. 3(b).

A plug flow packed bed gas–solid model was developed where dispersions inside the packing were assumed negligible. The minimization of the sum of squares of residuals was performed by the non-linear least squares method, using the Marquardt method to adjust the kinetic parameters. The validity of the kinetic model was verified by calculating the relative deviation between experimental data and predicted results from the kinetic model. Data fittings are illustrated by Fig. 3(e) for catalytic tests performed at various residence times and temperatures. The model clearly captures the trends in the data and fits the steady-state variations of the gas compositions well. The Arrhenius plots of the two kinetic constants $k_{r,4}$ and $k_{r,6}$ are given in Fig. 3(e) along with the activation energies and pre-exponential factors of each reaction. The activation energy for the hydrogen exchange from the D_2O_V reaction is slightly higher than that of HDO. This explains why the formation of HDO_V/HD is so prominent, accounting for the majority of products at the end of each reaction. The activation energy values are within the range of reported values [41,17], taking into account the weakening effect of platinum on hydrogen interactions due to the polarization by the SDBC resin. Figs. 3(c) and (d) confirm that HD and H_2O_V, as intermediate component in the reaction mechanism (Eqs. (4)–(6)), present the highest compositions of HD at low conversions of D_2O_V while HDO_V production increased constantly at high conversions. This result clearly anticipates the potential merit of using a gas/liquid counter-current flow of D_2O_L and H_2 in an LPCE column, in which D_2O_V is maximized along the column, and thus would maintain a high production of HD and low conversion to condensable components (H_2O_V and HDO_V) as illustrated in the following section on the reactive stripping process by the equilibrium and non-equilibrium controlled models.

3.2. Effect of mass transfer rate on the separation efficiency of reactive stripping process

The application of the kinetic model of Section 3.1 to the reactive stripping of deuterium from liquid water was validated by comparison with experimental data from literature. The reactive stripping extends the vapour/liquid phase exchange (Eq. (2)) of D_2O_L to the products HDO_V and H_2O_V of the gaseous catalytic exchange (Eqs. (7.1) and (7.2), respectively)

$$HDO_V + D_2O_L \Leftrightarrow HDO_L + D_2O_V \quad (11.1)$$

$$H_2O_V + D_2O_L \Leftrightarrow H_2O_L + D_2O_V \quad (11.2)$$

Summation of Eqs. (7.1), (7.2), (12.1) and (12.2) leads to the overall Eqs. (12.1) and (12.2).

$$H_2 + D_2O_L \Leftrightarrow HDO_L + HD \quad (12.1)$$

$$H_2 + D_2O_L \Leftrightarrow H_2O_L + D_2 \quad (12.2)$$

The overall exchange rate constant of isotopic exchange between hydrogen gas and liquid water (Eqs. (12.1) and (12.2)) was assessed by averaging the overall exchange rate of deuterium composition along the column height and illustrated by Eq. (14.1) and Eq. (14.2) [2].

At a given height of a column of height Z, the exchange rate is expressed by Eq. (13).

$$G'dy = K_{g,overall}\left(y_{D,eq} - y_D\right)dZ \quad (13)$$

Considering the dilution of deuterium in both phases, integration of Eq. (13) throughout the entire column leads to Eq. (14.1).

$$K_{g,overall} = \frac{G'}{h_F}\frac{(y_{D,out} - y_{D,in})}{\left(y_{D,eq} - y_D\right)_{out} - \left(y_{D,eq} - y_D\right)_{in}}\ln\frac{\left(y_{D,eq} - y_D\right)_{out}}{\left(y_{D,eq} - y_D\right)_{in}} \quad (14.1)$$

$$y_D' = \frac{y_{D_2} + \frac{1}{2}y_{HD}}{y_{H_2}} \quad (14.2)$$

where $y_D^{'}$ represent the atom fraction of deuterium in hydrogen gas, h_F is the height of the full packing, $K_{g,overall}$ is the overall exchange rate constant based on the gas phase and y_{eq} is the composition of deuterium that would be in equilibrium with the deuterium composition of the water at that same height in the column.

A universal equilibrium model for a maximum separation efficiency and a non-equilibrium model based on a description of a single stage section representing a packing segment of a column were developed. Unlike the universal equilibrium model, the non-equilibrium model required the gas and liquid phases to be balanced separately. Both the equilibrium–based model and the rate–based model, denoted RadFrac and RateFrac modules, respectively, in the Aspen Plus process software, were used to simulate the hydrogen exchange process. The equilibrium model, which assumes thermodynamic equilibrium between bulk gas and liquid phases of Reaction (2) in the column, did not require setting of the packing properties, while in the rate–based model, the separation process was treated as a heat and mass transfer process and was assumed that the equilibrium only exists at the gas/liquid interface. The mass– and heat–transfer resistances were considered according to the film theory, by directly accounting for interfacial fluxes, the film model equations and associated flow dynamics. Both models were combined with the relevant reactions and missing physical properties of single components as well as relevant mixtures. The equilibrium model was used to estimate the key operating parameters for maximum separation efficiency of deuterium and then the model was extended to the rate–based model.

3.2.1. Estimation of missing physical properties

Accurate values of thermo-physical properties are needed for the equilibrium and rate–based simulations. Despite their usefulness, measurements of the thermodynamic and transport properties of hydrogen isotopes in both hydrogen (HD, D_2, HT, DT and T_2) and hydrogen oxide (HDO, D_2O, HDO, DTO and T_2O) forms, and the effects of operating pressure and temperature on these parameters, are scarce in open literature, particularly for tritium isotopologues [29]. In the last 25 years, few thermodynamic property studies have been conducted on deuterium. An equation of state for tritium is not available in the literature and experimental measurements on tritium are rather rare. Souers [30] published a review on the properties of cryogenic hydrogen and the estimated physical and chemical properties of deuterium and tritium. Since this last analysis, there have been great advances in computer technologies and equation fitting techniques, implying a need for an updated property review [29]. In addition, available database on properties of aforementioned components is limited and conspicuously incomplete in commercial process simulation packages. This is important for modelling the hydrogen isotopic exchange since unlike the isotopes of other elements, the relatively large mass differences between H, D, and T cause appreciable differences in the properties of their compounds, and even sometimes in the properties of relevant allotropes such as the *ortho*- and *para*-forms of hydrogen gas [29].

Herein, it is not intended to investigate in detail the properties of deuterium and tritium, but instead we aimed to contribute to an open database for these isotopes (D, T), in both hydrogen gas and water forms, to be used for the isotopic exchange process. This database, as illustrated in the supporting document S1, was added to the property set package of Aspen Plus by using experimental data available in literature or predicted by using (1) existing thermodynamic models, (2) interpolation using the geometric mean of well-known data of analogous isotopologues [31] and (3) linear correlation of the critical properties (critical pressure, critical temperature and critical volume), Pitzer's acentric factor and the corresponding–states principle [32–37]. The results are illustrated in Tables S1.1 and S1.2 and Figs. S1 (a–e) of the supporting document S1. The property models for each component are defined in Tables S1.1 and S1.2. Figs. S1(a) and (b) which show trends with temperatures of vapour pressure and enthalpy predicted by the Soave-Redlich-Kwong (SRK) equation of state of both water and hydrogen forms of deuterium isotopologues (D_2, HD, D_2O_L and HDO_L) and tritium isotopologues (T_2, HT, T_2O_L and HDO_L). These results are in agreement with those given in the steam and hydrogen gas tables by Richardson et al. [29]. Other thermodynamic and transport properties of deuterium isotopologues, and their changes with temperature, were fitted to well-known literature models: dynamic viscosity using the Design Institute for Physical Properties (DIPPR) model and validated by data reported by Hill from Richardson et al. [29]; thermal conductivity using DIPPR model and validated by data from Richardson et al. [29] and Matsunaga [38]; surface tension using Crabtree and Siman-Tov's model; and binary diffusivity using Wilke-Chang's model for liquid isotopologues and Chapman-Enskog-Wilke-Lee's model for gas isotopologues and validated using Kumar's results [17]. The trends of these physical properties are presented in Fig. S1 (b–d).

As previously discussed, the thermodynamic and transport properties of tritium isotopologues are limited in open literature as they are experimentally difficult, expensive and tedious to evaluate. We proceeded therefore with Friedman's model which validates a linear trend of physical properties of analogous isotopologues along with the root of molecular weights [39]. The results achieved on deuterium isotopologues were therefore extended to each three isotopologues in hydrogen gas and water forms of tritium by using the plot of physical property versus the reciprocal of the square root of their molecular weights. Figs. S1 (e_1) and (e_2) shows profiles of critical properties, boiling point and molar volumes for both H_2O and H_2 isotopologues, respectively, and clearly demonstrate averaged standard deviations of 2.5 and 2.1%, respectively and a good fit with the Friedman model. Extension to tritium–based isotopologues for vapour pressure, molar volumes, enthalpy, Gibbs free energy, viscosity and surface tension were added to Fig. S1 (a–d). It is interesting to note the formation of non-ideal vapour isotopologue mixtures and negative deviation from Raoult's model, particularly at low concentrations of T_2O_V and D_2O_V and low temperatures (Fig. S1 (d)). The presence of the intermediates HTO_V and HDO_V tends to promote non-ideality. The impact of hydrogen bonds at low temperatures along with the vapour pressure of HDO and HTO_V of values which are different from the arithmetic mean of H_2O_V/D_2O_V and H_2O_V/T_2O_V pairs, respectively, might be responsible for such positive deviations [39].

3.2.2. Equilibrium model

The equilibrium model was first investigated as it does not require detailed information on properties of both hydrophobic catalytic packing and hydrophilic inert packing but requires information on thermodynamic properties of the physical and chemical equilibrium boundaries. The equilibrium model, which relies on assumption of ideal mixing between the liquid and the gaseous phases, would anticipate, according to Eqs. (12.1) and (12.2), the highest separation factor *Sep*D,eq of deuterium relevant to hydrogen isotopologues.

$$Sep_{D,eq} = \frac{x_{D,eq}^{'}\left(1 - y_{D,eq}^{'}\right)}{\left(1 - x_{D,eq}^{'}\right)y_{D,eq}^{'}} \tag{15.1}$$

$$x'_{D,eq} = \frac{x_{D_2O,eq} + \frac{1}{2}x_{HDO,eq}}{x_{H_2O,eq}} \text{ and } y'_{D,eq} = \frac{y_{D_2O,eq} + \frac{1}{2}y_{HDO,eq}}{y_{H_2O,eq}} \quad (15.2)$$

where $x'_{D,eq}$ and $y'_{D,eq}$ represent the atom fractions of deuterium in the liquid water and hydrogen phases, respectively, at equilibrium conditions.

3.2.2.1. Model development. The phase equilibrium model (CEPE), commonly known as MESH (Material balance, vapour–liquid equilibrium equations, mole fraction summations, and heat balance), along with the gas phase hydrogen catalytic exchange reaction (as expressed by Eqs. (4–6)) was used. Several assumptions have been made for formulating and solving the model equations: (1) equilibrium controlled Reactions, (2) equilibrium controlled mass transfer between bulk gas and liquid phases and (3) negligible flow dispersion and pressure drops in the column.

The MESH model for steady-state operations at the j^{th} theoretical stage is given by Eqs. (16.1)–(16.4), where the index j counts downwards.

- Mass balance

$$L'_{j-1}x_{i,j-1} - L'_j x_{i,j} + G'_{j+1}y_{i,j+1} - G'_j y_{i,j} + r_{i,j}m_{c,j} = 0 \quad (16.1)$$

- Energy balance

$$L'_{j-1}h_{j-1} - L'_j h_j + G'_{j+1}H_{j+1} - G'_j H_j = 0 \quad (16.2)$$

where, i = 1–6 (number of components), j = 1-N (number of stages) and $m_{c,j}$ is catalyst load at stage j. The heat associated with the process was assumed to be driven by liquid H and vapour/gas h enthalpies which were estimated in Section 3.2.1 and shown in Fig. S1 (b). L' and G' are the flow rates of liquid and gas phase, respectively and i is the reactive component. The reaction kinetic rates $r_{i,j}$ were set to zero for the CEPE model and to Eqs. (7)–(9) for CKPE model.

- Equilibrium between bulk phases

A good mixing between the phases is assumed between leaving streams at each stage, leading to equilibrium assumption between bulk phases as illustrated by Eq. (16.3).

$$y_{i,j} - K_{i,j}x_{i,j} = 0 \quad (16.3)$$

The gas/liquid equilibrium constant K values of H_2O, HDO, D_2O, HTO and T_2O were calculated from non-ideal gas/liquid fugacity equilibrium models where Antoine model and NRTL model were used for the saturated vapour pressures and fugacity coefficients, respectively.

- Summations

$$\sum_{i=1}^{N} x_{ij} = 1, \quad \sum_{i=1}^{N} y_{ij} = 1 \quad (16.4)$$

3.2.2.2. Model validation. The base case of the reactive stripping model was developed in accordance with the experimental run conditions and modelling provided by Ye et al. [21] who investigated the steady-state catalytic exchange of deuterium between HDO and water. As no data on kinetics were reported, we assume that the catalytic exchange (Reaction (1)) and gas/liquid scrubbing (Reaction (2)) under control of the chemical equilibrium and the bulk phase equilibrium, respectively, that is, the vapour leaving any stage was in physical equilibrium with the liquid at that stage, leading to maximum separation efficiency. The influence of the temperature, pressure, vapour to liquid flow ratios and catalyst loading on the distribution of deuterium at the top of the column was investigated. Thus, the stripping column was simulated by assuming chemical equilibrium controlled conditions of the reverse Reaction (1), which was expressed by reaction mechanism of Eqs. (4)–(6), and by assuming the wet scrubbing (Reaction (2)) takes place under gas/liquid bulk phase equilibrium or negligible mass/heat transfer control. A mixed deuterium–enriched water of 0.2 mol% and a high–purity natural hydrogen gas were counter-currently passed though the column. Typical operating conditions were run under a molar ratio of hydrogen gas to water flowrate of one, flow rate of H_2O_L of 3.5 mol/h, number of theoretical stages in the column of 5, and operated at atmospheric total pressure and temperature of 323 K. In order to maintain isothermal operations along the axial profile of the column and in absence of a heating jacket, a reboiler was added at the bottom of the column as a humidifier. The value of the reboiler heat duty for each run was not predicted but tuned until a constant profile of the desired temperature along the column height was achieved. The set of mass balance Eqs. (16.1)–(16.4) was computed by using the embedded Newton- Raphson's method based solver in Aspen plus. This method required setting of the initial values of temperatures and flowrates which were obtained from similar process and operations of stripping process without the catalytic exchange. The computation of this later allowed solutions with no convergence difficulty. The solutions by the Newton-Raphson method however, needed large computation efforts for the numerical evaluation of the element of the Jacobian matrix and calculation of its inverse matrix when the reactive stripping was added. This was caused by the small compositions of deuterium isotope, resulting in the minimization of the residuals to be more sensitive to such small amounts than the large compositions of water and hydrogen, and thus to inadequate stability in achieving convergence.

3.2.2.2.1. Effects of temperature and pressure. For deuterium removal from liquid water, the simulation was conducted at temperatures ranging between 293.3 and 353.3 K. The deuterium in D_2O_L was converted into HDO_V, D_2 and HD as shown by Eqs. (4)–(6). The top column released a non-condensable hydrogen gas mixture (i.e. H_2, HD and D_2) and a condensable water vapour mixture (i.e. H_2O_V, HDO_V and D_2O_V). Since the vapour phase is commonly condensed and recycled back to the column, the separation of deuterium from liquid water relies on its presence in the hydrogen gas mixture (D_2, HD in H_2) only. The composition of the condensable vapour phase (i.e. D_2O_V and HDO_V) and relevant atom fraction of deuterium in the vapour phase, x'_D as well as the composition of hydrogen phase (i.e. D_2 and HD) and relevant atom fraction of deuterium in hydrogen phase, y'_D, at the top exit are shown in Fig. 4(a). Similar to the results reported by Ye et al. [21]. At atmospheric pressure the concentration of deuterium in the hydrogen gas increased with temperature until about 348 K and then decreased owing to increased presence of H_2O_V at high temperatures, promoted by the higher relative volatility of H_2O_V compared with HDO_V, as illustrated in Fig. 2(a), leading to more condensation of HDO_V than H_2O_V, favouring a shift of the chemical equilibrium of Reaction (12.1) and (12.2) towards H_2O_V production. The trends of increase or decrease in HDO_V production was thus dominated by relevance of chemical equilibrium of Reactions (4)–(6) and Reaction (12). The CEPE model was first validated by the

separation factor $Sep_{D,e}$ of deuterium from water to hydrogen gas at as computed by Eq. (15.1). The values of separation factor at atmospheric pressure is within a reasonable agreement (i.e. deviation of 1.2%) with the model proposed by Rolston et al. [40].

The effect of total pressure was investigated by the CEPE model while a negligible deactivation by pore condensation of water was assumed. Increasing the total pressure, as suggested by Sugiyama et al. [4], would maintain high H_2O_L levels in the liquid phase at high temperatures. This is confirmed by Fig. 4(a), which validates that reducing the pressure leads to increased proportion of H_2O_V and a reduced concentration of deuterium in the hydrogen gas. Thus, operating at high pressures promoted the presence of deuterium, mainly in HD form, in the hydrogen gas at reduced H_2O_V and D_2O_V compositions but extending to temperatures beyond maximum HD compositions favoured relevance of Reaction (12) over Reactions (4)–(6) at reduced HD and HDO_V productions.

3.2.2.2.2. Effect of feed flow ratio of hydrogen to water (G′/L′). Since operations were carried out under chemical and physical equilibrium of Reactions (2) and (4)–(6), changing the feed flowrate ratio of H_2 to H_2O_L affected exclusively the equilibrium compositions of Reactions (2) and (4)–(6). Trends of HD again has shown maximum values with operating temperatures for each value of G′/L′ ratio. These temperature for maximum HD production were approximately 343, 323 and 293 K at G′/L′ values of 1, 2 and 4, respectively, as shown in Fig. 4(b). High G′/L′ ratios produced less pure deuterium in the hydrogen phase due to higher loads of hydrogen feed. Other potential advantages of increasing the feed rate of hydrogen, such as mass transfer rates and flow dynamics in the packing, were not accessible owing to assumption of bulk gas/liquid equilibrium operations.

3.2.2.2.3. Effect of number of stages. Alternatively, rather than reducing gas flowrates, increasing the number of stages or packing height would instead present similar trends of deuterium separation, as observed in Fig. 4 (c), which shows the effect of the number of stages (N = 2–8) on the concentration of deuterium at the top of the column. A set of simulations were run to determine the effect of packing height on deuterium capture at a constant value of unity for G′/L′ ratio. It is clear that the deuterium capture increased with increasing column height, up to a packing

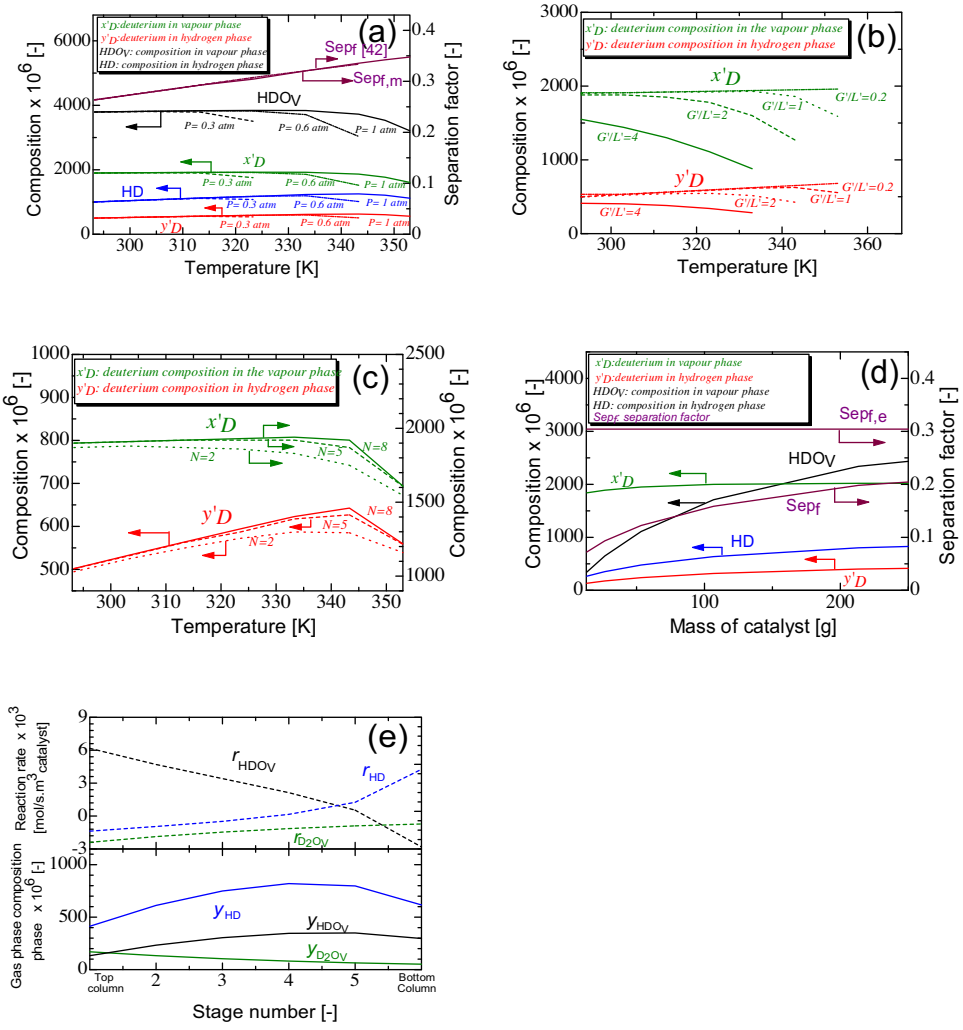

Fig. 4. Product distribution at the top (a–d) of the LPCE column and inside the LPCE column (e) by phase equilibrium modelling. Liquid feed composition: 0.2 mol% of D_2O, Pure hydrogen gas, liquid flow are L′: 3.5 mol/h, column ID: 0.025 m, height: 1.2 m, packing type: Dixon ring of 1.5 mm. (a) Effect of pressure and temperature, (b) Effect of gas to liquid flowrate ratio, (c) Effect of reactive stages, (d) Effect of mass of catalyst per stage, T = 333 K, G′/L′ = 1, P = 101.3 kPa and (e) product distribution inside the LPCE column, T = 333 K, G'/L' = 1, P = 101.3 kPa.

height of five theoretical stages and then remained reasonably unchanged thereafter. This may be due to attainment of maximum separation efficiency which was driven the chemical equilibrium compositions of both Reactions (12.1)–(12.2) and (4)–(6).

3.2.2.2.4. Effect of mass of catalyst. Under chemical kinetic operations, the reaction time of the catalytic exchange (Eqs. (4)–(6)) would affect the overall gas/liquid mass transfer boundaries. Thus, the chemical kinetic module in Aspen plus was then turned on and added to the phase equilibrium module. The chemical kinetic module included chemical kinetics of Reaction (4) and (6). The CKPE model is thus used instead of CEPE that has been used in Sections 3.2.2.1–3.2.2.3. Fig. 4(d) shows the benefit of using the reactive stripping when compared with gaseous phase catalytic exchange only in Section 3.1). Unlike the results in Fig. 3(c), which were obtained by operating the isotopic exchange under a gaseous phase only, the results of the reactive stripping process as illustrated in Fig. 4(d) shows an increase in conversion into HD gas when the mass of catalyst was increased. Increasing the mass of catalyst promoted the rate of conversion of D_2O_L into HD gas compared with HDO_V as shown in Fig. 4(d). Since the resistance to gas/liquid mass transfer was ignored in the phase equilibrium model, the amount of catalyst for HD conversion was over-predicted owing to rapid counter-current mass transfer of H_2O_L into the hydrogen gas phase and HDO_V into the liquid water phase compared with relevant chemical kinetics. At high values of catalyst mass, the conversion reached asymptotic values close to the equilibrium ones obtained in Fig. 4(a).

In addition, the composition profiles of isotopologues and corresponding reaction rates inside the column, as shown in Fig. 4(e), clearly indicates that most of the conversion into HD took place throughout the bottom part of the column (stages 4–6). Maximum values of HD composition were achieved over the packing height, justifying the role of HD as intermediate towards HDO_V production as shown in Eqs. (4)–(6) and the efficient condensation of this later (Eq. (11)) as assumed in the CEPE model, and thus demonstrating an excess use of reactive stages when the full column is packed with reactive packing.

3.2.3. Rate–based non-equilibrium model

Assuming well defined mass transfer inside the catalyst packing, the mass transfer rate of deuterium from the liquid water to hydrogen gas phase depends on the external mass transfer, which is a function of fluid dynamics. The fluid dynamics consist of an upflowing hydrogen gas, which gets saturated with water vapour at the operating temperature and offers a holdup equivalent to the open space of the reactor while the liquid water trickles down and covers the wettable surface of both the inert and reactive packings. Thus, the mass transfer is a function of the exposed surface area of the down-flowing H_2O_L and shaped by the packing material. The overall mechanism of mass transfer herein includes, according to the two–film theory, transport of D_2O_L reactant to the liquid film interface through the down-flowing H_2O_L, diffusion of D_2O_L through the film, evaporation at surface interphase into D_2O_V, diffusion of D_2O_V in the gas film and transport in the up-flowing gas, and opposite mass transfer pathway applies to condensation of produced HDO_V, transport of D_2O_V in core of the gas phase and surface reactions in the hydrophobic reactive packing. Thus, the mass transfer is a function of the chemical kinetics, packing properties and flow dynamics (accessible surface area, wettability, holdup and pressure and temperature).

The rate–based module of Aspen plus was used as a basis for simulating the reactive stripping process of hydrogen isotopic exchange. The module combines CKRN-E models and thus is a powerful tool for the design and scale-up analysis of the hydrogen exchange process, as it has the capability of employing real reactive stripping configurations of internals, multi-component mass and heat transfer methods, actual chemical kinetic and thermodynamic models. However, this model requires good underlying models for kinetics, thermodynamics and hydrodynamics.

3.2.3.1. Model development. The CKRN-E model uses separate mass balance models for each phase along with rate of mass and heat exchanges between the gas and liquid phases. The set of mass and heat balance equations for bulk phases and interphases is illustrated in Eqs. (17.1)–(17.10) while the set of mass transfer equations at interphase, mixing rules of properties, correlations for mass and heat transfer coefficients and pressure drops is illustrated in Appendix A.

- Mass balance:

-Material balance for bulk liquid

$$L'_{j-1}x_{i,j-1} + NM^L_{i,j} - L'_j x_{ij} = 0 \tag{17.1}$$

-Material balance for bulk gas

$$G'_{j+1}y_{i,j+1} - NM^G_{i,j} + r^G_{ij} - G'_j y_{ij} = 0 \tag{17.2}$$

-Material balance for liquid interphase film

$$NM^I_{ij} = NM^L_{ij} \tag{17.3}$$

-Material balance for gas interphase film

$$NM^I_{ij} = NM^G_{ij} \tag{17.4}$$

where NM is the rate of mass transfer between the liquid and gaseous phases

- Energy balance

-Energy balance for bulk liquid

$$L'_{j-1}H_{j-1} + q^L_j - L'_j H_j = 0 \tag{17.5}$$

- Energy balance for bulk gas

$$G'_{j+1}h_{j+1} - q^G_j - G'_j h_j = 0 \tag{17.6}$$

- Energy balance for liquid interphase film

$$q^I_j = q^L_j \tag{17.7}$$

- Energy balance for gas interphase film

$$q^I_j = q^G_j \tag{17.8}$$

where q is the heat transfer associated with the mass transfer between the phases

- Phases equilibrium at gas/liquid interphase

$$y^I_{ij} - K_{ij}x^I_{ij} = 0 \tag{17.9}$$

- Summations

$$\sum_{i=1}^{N} x_{ij} = 1,\ \sum_{i=1}^{N} y_{ij} = 1,\ \sum_{i=1}^{N} x^I_{ij} = 1\ ,\ \sum_{i=1}^{N} y^I_{ij} = 1 \tag{17.10}$$

3.2.3.2. Model validation. The thermodynamic model, physicochemical properties and chemical kinetic modules package were similar to those used in the equilibrium model,

whereas the mass and heat transfer models were switched to the mass and heat transfer rate–based model. This model included a transport rating module for the column used. The column rating allowed access to flow dynamic properties (i.e. liquid holdup, maximum liquid velocity before flooding and pressure drops) as well as to mass and heat transfer properties (i.e. interfacial area, heat and mass transfer coefficients, composition and temperature at gas/liquid interface and height equivalent to a theoretical plate (HETP). The rate-based model, which is based on the two film theory, included the mass and heat transfer rates between the contacting phases and was based on a detailed description of the combined diffusion and advection processes taking place in both the liquid and gaseous phases, while phase equilibrium existed at the gas and liquid interface and a relevant transfer model was used to calculate the gas/liquid phase resistances.

The "VPLUG" flow model (Eqs. A.1–A.10 in Appendix A) in which the bulk properties for each phase were assumed to be the same as the outlet conditions for that phase leaving that stage model, was used to calculate the bulk properties, including the reaction, energy and mass rates. Mass transfer coefficients and interfacial area were calculated using Onda's model [18] (Eqs. A.11–A.17 in Appendix A) as it is recommended for the Dixon packing used. In addition, the pressure drop model presented by Billet and Schultes [41] (Eqs. A.18–A.20 in Appendix A) was assumed applicable to the Dixon packing and the heat transfer coefficient was predicted by the Chilton and Colburn analogy [42]. The absorber heat loss was assumed negligible.

The results of Ye et al. [21] first validated this model as a means to investigate the actual separation efficiency of the mass transfer based non-equilibrium model. The reactive stripping column was set with a size of 0.025 m I.D. and 1.20 m length, resulting into five to six HETP depending on the operated flow rates used. This HETP corresponds approximately to a single section of packing inside Ye's column which was equally filled with inert hydrophilic packing and reactive hydrophobic packing. The model was validated as well with results from Kumar et al. [17] and a sensitivity analysis was then applied which utilized the packing configuration, kinetic models, gas and liquid mass transfer coefficients, and the effective interfacial area to determine the effects of different design parameters on performance of separation of deuterium into HD gas at the top of the reactive stripper.

Fig. 5(a_1) shows the trends of product profiles with temperature for the combined chemical kinetics and the rate-based gas/liquid non-equilibrium model (CKRN-E) along with the two previously discussed the chemical equilibrium and the bulk gas/liquid physical equilibrium (CEPE) model and the chemical kinetics and the bulk gas/liquid physical equilibrium (CKPE) model. The profiles of deuterium in hydrogen phase, by inference HD

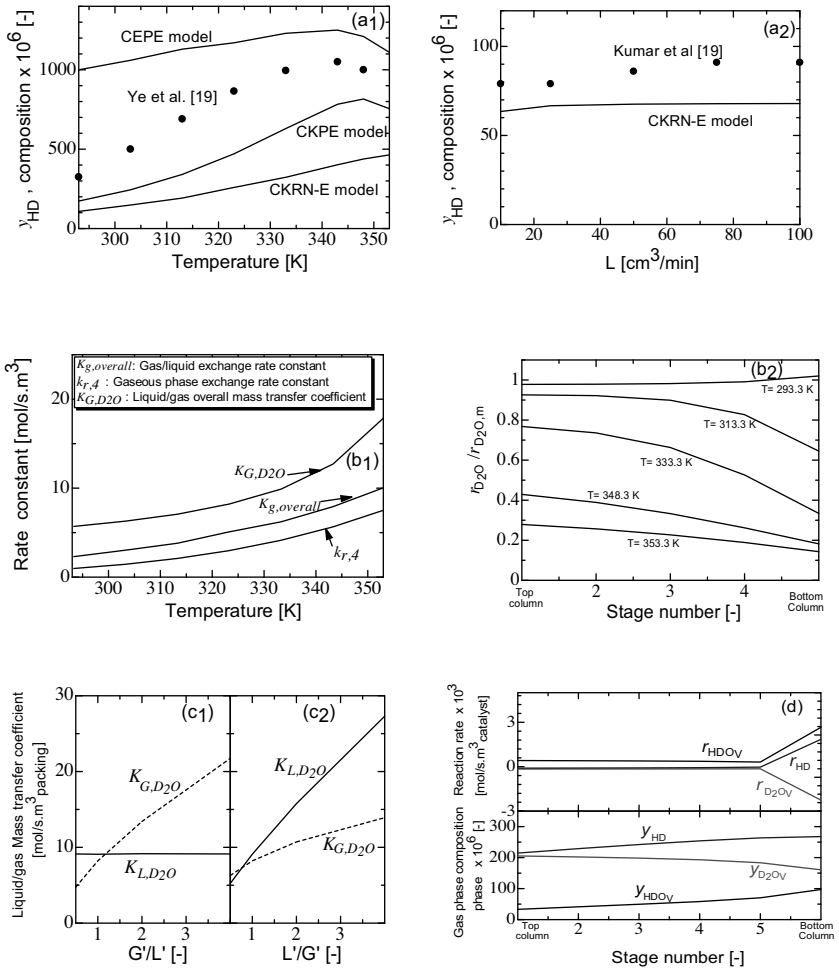

Fig. 5. Product distribution by rate-based non-equilibrium phase model: (a_1, a_2 and b) at the top of the LPCE column. (b_1) profiles of kinetic rate constants $k_{r,4}$, liquid/gas overall mass transfer coefficient based on the gaseous phase for D_2O species $K_{G,D2O}$, and gas/liquid exchange rate constant $K_{g,overall}$. (b_2) Ratio of kinetic rates of D_2O to mass transfer rate of D_2O. (c_1 and c_2) effect of gas to liquid flow rate at L': 3.5 mol/h and liquid to gas flow rate at G' = 3.5 mol/h, respectively. (d) Product distribution and relevant reaction rates inside the LPCE column.
Operating conditions: (a_1) and (b–d): Liquid feed composition: 0.2 mol% of D_2O, Pure hydrogen gas, liquid flow are L': 3.5 mol/h, column ID: 0.025 m, height: 1.2 m, packing type: Dixon ring of 1.5 mm. (a_2) Column diameter = 40 mm, diluted Raschig ring reactive packing into an inert packing at 50%, G' = 1.2 L (STP)/h, T = 323 K.

compositions, by the rate-based model were favoured at high temperatures owing to increase of both mass transfer rates and chemical kinetic rates. These trends are similar to those observed by Ye et al. [21] and the deviations from the chemical equilibrium model are more pronounced at low temperatures where conversion into HD was not significant. At high temperatures, these deviations were about one third those observed by Ye and about one half those observed in the CKPE equilibrium model, leading to conclude that the kinetic rate model would have fit the results of Ye well if the catalyst were more active.

The results were as well compared with those from Kumar et al. [17] who simplified the hydrogen exchange process into a single reaction involving the conversion of deuterated water into HD to facilitate the use of a two-phase model, and the sensible heat transfer between phases and back absorption of hydrogen gases by water were as well ignored. The trend of composition of deuterium at the top of column in hydrogen gas as shown in Fig. 5(a_2) shows negative deviation about 20%, which is reasonable, considering the catalytic activity of present packing along with the errors associated with the physical properties, fluid flow model, Onda's mass transfer correlations and experimental runs.

The trends observed using the equilibrium–based model (CEPE or CKPE) were also observed in the non-equilibrium model (CKRN-E), but with a significant deviation of HD composition at the top of the column, particularly at low temperatures. The contribution of gas/liquid mass transfer limitation at low temperature is also validated by the deviation of the rate constant of the gaseous catalytic exchange (Eq. (4)) from the overall gas/liquid rate constant as shown in Fig. 5(b_1) and ratio of gaseous reaction rate to gas/liquid mass transfer rate (Fig. 5(b_2)). This would demonstrate that the non-equilibrium model predicts mass transfer resistance between the gas phase and the liquid water phase, particularly the counter-current mass transfer of D_2O_L and H_2O_L mixture from the liquid to H_2 phase, and HDO_V from the gas phase to the liquid water phase.

The mass transfer at liquid/gas interphase boundary and the overall mass transfer from the H_2O_L to the catalytic packing were investigated and the model parameters, including mass transfer coefficients and relevant rates were validated by experimental tests of Kumar et al. [17]. Increasing the feed flow ratio (G′/L′) of hydrogen to water at constant liquid flowrate was effective on mass transfer coefficients in the gaseous phase only (Fig. 5(c_1)) while increasing the liquid flowrate (L′/G′) was relevant for both liquid and gas mass transfer coefficients (Fig. 5(c_2)), demonstrating the relevance of transport resistance inside the film on the gas phase side at present operating conditions. These values of mass transfer coefficients were in the range of those obtained by Kumar et al. [17], validating the use of Onda's model.

Unlike the equilibrium model (CKEP), where the temperature affected the chemical rate constants of reactions, saturation of hydrogen phase by water vapours (D_2O_V, HDO_V and H_2O_V) and flow enthalpies, the rate–based model (CKRN-E) was even more sensitive to temperature due to the dependency of additional physical property parameters on temperature, including the solubility of isotopologues in water, diffusivity in both gaseous and liquid phases, viscosity, surface tension, thermal conductivity and heat capacity.

Fig. 5(d) compares the profiles of compositions of HDO_V and HD components along the column height obtained using either the rigorous mass transfer CKRN-E model or the equilibrium CKEP model which were illustrated in Fig. 4(e). Literature on experimental data of compositions profiles of deuterium inside the column is limited and the following results were validated by those obtained by Kumar et al. [17] as well as by those derived from the top or bottom of the column. The equilibrium model significantly overestimates the stripping of D_2O as well as the scrubbing of HDO, and thus provides non-reliable results, leading to lower packing heights and hence to incorrect process designs. This is contrary to the rigorous rate–based model which produced less HD and HDO_V, particularly towards the top of the column, owing to lower chemical conversion of D_2O_L with the later model. The CKRN-E model exhibited steady trends of HD and HDO compared to the curvy trends observed in CEPE and CKEP models owing to inhibited counter-current mass transfer of D_2O_L and HDO_V to the H_2 and H_2O_L phases, respectively.

3.2.4. Sensitivity analysis of the rate-based model

The sensitivity of the rate-based model to column internals and to additional presence of tritium was investigated by observing the overall chemical exchange of the reactive stripping column. The column internals affect the trickling flow, pressure drops, liquid holdup and wetting efficiency of the reactive packing. The coexistence of deuterium along with tritium affects relevant separation boundaries of each as demonstrated by the thermodynamic properties in Section 3.2.1.

3.2.4.1. Effect of pressure drop. Pressure drop is an important design parameter which influences the size of the LPCE column. Significant energy savings can be achieved in the reactive stripper by using the appropriate size of the column, (i.e. the proper height–diameter ratio). A sensitivity analysis was performed to assess the pressure drops in the reactive stripper. The pressure drop profiles were evaluated using Billet's model [41] applied to Raschig like packing as models applied to Dixon packing are not available. As illustrated in Fig. 6(a), the predictions of the rate–based model are not in agreement with the pilot data reported by Ye et al. [21], as the value herein (i.e. 17.7 Pa/m for a Dixon packing of 1.5 mm particle size, G′/L′ ratio of unity, six theoretical stages and an inlet liquid flowrate of 3.5 mol/h) is about at least one fourth the values previously cited. However, a detailed knowledge of pressure drop measurement, in addition to column packing specifications including type of liquid distributors and liquid collector were missing in Ye's results, and matching our results to the measured pressure drop would not be possible. Changing the Dixon packing size from 1.5 to 6.0 mm led to a decrease in the pressure drop from 17.7 to 9.4 Pa/m. The composition profiles over the column height in Fig. 6 (a) clearly show s steady decrease of HD over the column height owing to HDO_V condensation (Eq. (11.1)). Even though the packing size of 1.5 produced a higher composition of HD at the bottom of the column, it exhibited a higher decrease over the column height compared with packing of 6.0 mm particle size. This result was expected since the pressure drops is known to be driven by the gaseous phase under trickling flow according to Billet and Schultes model, validating our previous finding of mass transfer control of D_2OL and HDO_V by hydrogen gas film only.

3.2.4.2. Effect of packing configuration. The configuration of the packing was insured by mixing both hydrophilic and hydrophobic packing in a single unit, allowing both chemical reactions (Reaction (1) or Reactions (4)–(6)) and gas/liquid mass transfer (Reaction (2)) to occur simultaneously throughout the packed bed. This configuration promoted the rate of mass transfer (Reaction (2)) but could deactivate, and thus inhibit, Reaction (1) after long-term use, owing to the partial wetting of catalyst surfaces. Layered packing, as suggested by Sugiyama et al. [8,43], represents another packing configuration where segregated modules that alternate catalytic packing layer and inert packing layer were designed, allowing both reactions to occur separately. This segregated arrangement allowed only the gaseous phase to flow through the catalyst packing surfaces, thus reducing potential deactivation. An arrangement of layered packing where stages 1, 3 and 5 included the catalytic packing and stages 2 and 4 included the

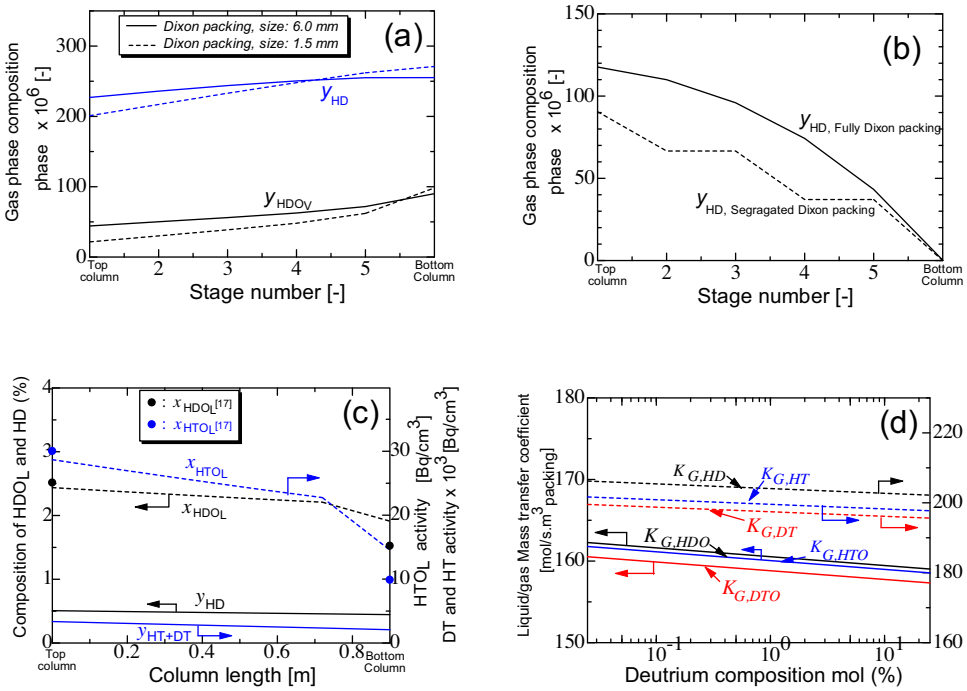

Fig. 6. (a) Product distributions inside the LPCE column by the size of Dixon packing, (b) Product distributions inside the LPCE column by type of packing arrangement (layered or mixed packing) and (c) Product distributions inside the LPCE column in presence of tritium and (d) effect of deuterium content on mass transfer coefficients based on the gaseous phase K_G.
Operating conditions: (a, b) Liquid feed composition: 0.2 mol% of D_2O, Pure hydrogen gas, liquid flow are L′: 3.5 mol/h, column ID: 0.025 m, height: 1.2 m, packing type: Dixon ring of 1.5 mm and 6 mm particle. (c, d) Liquid feed compositions: 30.3 Bq/cm^3 of HTO and 2.5 mol% of HDO, Hydrogen gas compositions: 0.4 mol% of HD, liquid flowrate: 120 cm^3/h, Hydrogen flow rate: 0.5 m^3/h, T = 338 K.

hydrophilic Dixon packing. This arrangement of layered and inert packing was compared herein with the homogeneous arrangement assuming similar packing properties (i.e. Dixon type, size of 1.5 mm and concentration of 50% inert packing and 50% of reactive packing). As evidenced in Fig. 6 (b), the homogeneous packing presented a higher HD production than the segregated packing under similar operating conditions. These results validate those obtained by Sugiyama et al. [8], where the production of HD gas was higher when homogeneous packing was employed. Thus, fresh catalysts beads would be suitable for homogeneous packing but for long-term operations of the isotopic exchange process, more investigation is needed on the rate-based model that would include the deactivation effect of catalyst.

3.2.4.3. Effect of presence of tritium. Existence of tritium along with deuterium in H_2O_L was investigated in terms of their conversions into HT and HD gases. Existing literature on kinetic studies on water detritiation processing deals however mainly with deuterium exchange while the kinetics of the gaseous catalytic exchange based on tritium are limited in open literature. Consideration of many tritium based technologies relies on prediction based on experimental data of species of close properties but operated cost–effectively and safely such as deuterium isotope [24]. However, care needs to be taken when converting data from deuterium to tritium. Fedorchenko et al. [44] investigated the gaseous phase kinetics of the catalytic exchange using tritium isotopologues and compared the rates of deuterium and tritium catalytic exchange. They reported that the effectiveness factor inside the catalyst was higher with deuterium than tritium, leading to higher resistance to diffusion with tritium. However, the intrinsic kinetic rate of tritium was about one third higher than that observed with deuterium, leading to potentially over-estimated design features based on deuterium only.

The combined model of kinetic isotopic exchange and the gas/liquid stripping process of deuterium (Eqs. (4)–(6)) were then extended to tritium as shown by Eqs. (16)–(20).

$$H_2 + T_2O_v \Leftrightarrow T_2 + H_2O_v \quad (16)$$

$$H_2 + T_2 \Leftrightarrow 2HT \quad (17)$$

$$HT + H_2O_v \Leftrightarrow H_2 + HTO_v \quad (18)$$

$$D_2 + T_2 \Leftrightarrow 2DT \quad (19)$$

$$DT + H_2O_v \Leftrightarrow H_2 + DTO_v \quad (20)$$

The sum of these reactions leads to the reverse reaction of Eq. (1). Perevezentsev et al. [6] observed that the mass transfer coefficient of tritium in presence of deuterium was function of concentration deuterium and gas to liquid ratio. Unlike deuterium, tritium presents extended equilibrium constant values for analogous Reactions (4)–(6) and Reactions (16)–(20) as well as higher enthalpy of evaporation of relevant isotopologues than those corresponding to deuterium. Herein, the equilibrium constants K_i for the five Reactions (16)–(20) were obtained from Gibbs free energy which was predicted in Section 3.2.1 on property estimations and these data were compared with those reported by Yamanishi al. [20], as shown in Fig. 3(b). In addition, Eqs. (19) and (20) clearly demonstrate impact of deuterium on overall

tritium separation owing to production of HD and HDO species containing both isotopes each.

In this sensitivity analysis, effect of deuterium presence along with tritium and gas/liquid ratio on mass transfer rates was investigated. Following the kinetic trends by Fedorchenko et al. [44], the kinetic model relevant deuterium based catalytic exchange was extended to tritium. The values of kinetic constants relevant to Eqs. ((16), (18) and (20)) were taken as one third higher than relevant constants used for deuterium (Eqs. (4) and (6)) while Eqs. (17) and (19) were again assumed under a quasi-equilibrium state [26]. The results were first validated using experimental data of Critescu et al. [16]. In this test, the H_2O_L feed at the top of the column contained composition of 2.5 mol% HDO and composition of HTO in terms of activity of 30.3 Bq/cm^3 (i.e. $\sim 5.1 \times 10^{-11}$ mol%) while the H_2 feed contained 0.4 mol% HD. Fig. 6(c) illustrates the results of composition profiles inside the column. The results of simulation show at the bottom of the column, lower HDO_L concentration (i.e. 1.9 mol%) and the tritium activity, (i.e. 14.5 Bq/cm^3) in the form of HTO_L and traces of DTO_L and T_2O_L) than those reached experimentally by Critescu et al. [16] (i.e. 1.5 mol% HDO and 9.3 Bq/cm^3 tritium activity). It should be noted that the operating temperature and a Dixon packing size of 3 mm allowed the column to be operated at 336 K and HETP of 0.18 m instead of 353 K and 0.65 m by Critescu et al. [16]. The higher values of HDO_L and HTO_L in the bottom of the column, although the overestimation of the mass transfer, demonstrated that the rate of kinetic model of Reaction set (16)–(20), and by inference activity of catalyst used by Critescu, was higher than the model used for our catalyst. The mass transfer coefficients of tritium in hydrogen and water isotopologues were smaller than those of deuterium. The HEPT of about 0.18 m was found to be smaller than the one reported by Critescu but packing details and column internals were missing, making rigorous matching our results uncertain. Furthermore, the coexistence of both isotopes may have a synergetic effect of relevant separations. Unlike tritium which exists at traces levels and thus can be ignored, deuterium may reach high levels in tritiated feeds, impacting therefore the separation efficiency of tritium. The effect of deuterium content ranging from natural water to 10 mol% contents was investigated in terms of mass transfer coefficients. Fig. 6(d) illustrates trends of mass transfer coefficients K_G of both vapours and gaseous species. Increasing deuterium to values of 10% content in the feed reduced mass coefficients by 4–5% of both deuterium and tritium based species, promoting mass transfer contribution and validating relevance of species contents on diffusivity coefficients, and by inference mass transfer coefficients according to Onda's model [18]. The applicability of the rate based model of Aspen plus package was therefore successful to assess complexity of separation of isotope mixtures by reactive stripping and demonstrated relevance of flow dynamics, process design and species loads on extend of separation efficiency from both thermodynamics and kinetic perspectives.

4. Conclusions

This work extends applicability of the equilibrium and rate–based models of commercial Aspen plus modular package to hydrogen catalytic exchange by using a reactive stripping column packed bed of Pt/SDBC resin catalyst. Compared with equilibrium model, the rate–based model, which governs the coupling of mass and heat transports and specific features of the reaction mixture of hydrogen isotope exchange, simulated more realistically the synergic effect of these on the de-deuteriation efficiency. The kinetic model confirmed a single into HD and HDO_V and double de-deuteriation into D_2 and H_2O_V when D_2O_L was used as the starting feed. The kinetic model fit the experimental data well and relevant parameters were estimated based on data generated using deuterium. The missing physical properties of deuterium and tritium isotopologues in hydrogen gas and water forms were predicted and validated within acceptable agreement with existing literature data. These physical data were needed for the bulk gas/liquid equilibrium model and even more for the rate-based non-equilibrium model. The equilibrium model (CEPE), which is independent of types of packing and catalysts but function of thermodynamic boundaries of underlying chemical reactions and gas/liquid physical exchange, allowed access to trends of maximum separation efficiency of deuterium isotope into HD that would ideally be reached under assumptions of efficient gas/liquid mixing and efficient reactive packing. The concentration of deuterium in the hydrogen gas increased with temperature and then decreased owing to increased presence of H_2O_V at high temperatures, leading to more condensation of HDO_V. Other operating parameters such as the operating pressure was effective to separation owing to reduced H_2O_V compositions, gas to liquid flow rate ratio reduced maximum separation efficiency and column height promoted local separation efficiency until a height where it remained unchanged. Under kinetic control, the phase equilibrium model (CEPE) indicated maximum values of deuterium in hydrogen over the packing height, demonstrating efficient condensation of HDO_V intermediate by the ideal mixing and limiting further de-deuteriation of this later into H_2O_V.

The rate-based model (CKRN-E) presented results close to real pilot scale data and relevant deviations of CKRN-E model from the equilibrium model allowed predictions of mass transfer rates, reactive mass transfer rates and separation efficiency of the reactive stripping column. Compared with equilibrium model, the rate–based model simulated the reactive stripping/scrubbing process more accurately, including the effects of temperature, type and properties of the packing, pressure drops and presence of tritium on the separation efficiency. The mass transfer control of D_2OL into the gaseous phase reduced overall production of HD compared with the equilibrium model. Maximum trends of HD over the packing height in the equilibrium model however were not observed in the rate-based model owing mass transfer control of HDO_V condensation, inhibiting further de-deuteriation into H_2OV and HD. The gas to liquid flow ratios demonstrated that the gas/liquid mass transfer was mainly driven by gas film side and this control was even more promoted at high temperatures, which was illustrated by overall mass transfer coefficients and isotopic exchange rate constants. The pressure drops which was mainly driven by the gaseous phase reduced the gas film resistance to mass transfer of D_2O_L into the gas phase and HDO_V into the liquid phase and thus promoted HD production for a given height of the packing only. In addition, the diluted reactive packing by an inert packing offered more separation efficiency than the layered hydrophobic/hydrophilic packing owing to liquid holdup distribution which was found more pronounced with the layered packing. Furthermore, the sensitivity of the rate-based model to the presence of tritium in a deuterated water validated over-estimated design features when deuterium is considered a reference compound for detritiation technologies owing to smaller mass transfer coefficients of tritium in hydrogen and slower kinetics leading to reduced overall isotopic exchange rates.

The originality in this work is the applicability of commercial packages such as Aspen plus modular software to catalytic isotopic exchange of hydrogen inside a reactive stripping column. Many features of the heat and mass transfer associated with reactive stripping inside the column, including local bulk properties (compositions, temperatures, enthalpies, fluid flow, holdup, pressure drops, etc.) as well as local gas/liquid interphases properties (mass and heat transfer coefficients, compositions,

temperature, mass and heat transfer rates of heat and mass transfer rates), could be computed or predicted for a rigorous design. The development of the module was demonstrated to be flexible and applicable to many similar processes including the water detritiation by reactive scrubbing processing.

Acknowledgments

The authors would like to acknowledge the support for funding provided by the Department of Education and Learning (DEL), Saudi Arabia Government, Lancaster University starting grant and the Thailand Research Fund.

Appendix A.

The equations below for flux demonstrate the so-called "mixed flow model" where outlet conditions are used for the bulk properties in each phase.

- Mass flux for liquid film

$$\left[\Gamma^{L}_{i,k,j}\right]\left(x^{I}_{j}-x_{j}\right)-\left[R^{L}_{j}\right]\left(N^{L}_{j}-N^{L}_{t}x_{j}\right)=0 \qquad (A.1)$$

$$\Gamma^{L}_{i,k,j}=\delta_{i,k}+x_{i,j}\frac{\partial \ln\varphi^{L}_{ij}}{\partial x_{i,j}}|_{T^{L}_{j},P_{j},\Sigma} \qquad (A.2)$$

where the symbol Σ means fixing the mole fractions of all components except the nth while evaluating the differentiation

$$R^{L}_{i,ij}=\frac{x_{ij}}{\rho^{L}_{j}a^{I}_{j}k^{L}_{i,m,j}}-\sum_{\substack{m=1\\ m\neq i}}^{N}\frac{x_{i,j}}{\rho^{L}_{j}a^{I}_{j}k^{L}_{i,m,j}}$$
$$for \quad i=1,2,....n_c-1,\ i\neq k \qquad (A.3)$$

$$R^{L}_{i,k,j}=-x_{i,j}\left(\frac{1}{\rho^{L}_{j}a^{I}_{j}k^{L}_{i,k,j}}-\frac{1}{\rho^{L}_{j}a^{I}_{j}k^{L}_{i,m,j}}\right)$$
$$for \quad i=1,2,\ldots.n_c-1,\ i\neq k \qquad (A.4)$$

- Mass flux for gas film

$$\left[\Gamma^{G}_{i,k,j}\right]\left(y^{I}_{j}-y_{j}\right)+\left[R^{G}_{j}\right]\left(N^{G}_{j}-N^{G}_{t}y_{j}\right)=0 \qquad (A.5)$$

$$\Gamma^{G}_{i,k,j}=\delta_{i,k}+x_{i,j}\frac{\partial \ln\phi^{G}_{ij}}{\partial y_{i,j}}|_{T^{L}_{j},P_{j},\Sigma} \qquad (A.6)$$

where the symbol Σ means fixing the mole fractions of all components except the nth while evaluating the differentiation

$$R^{G}_{i,ij}=\frac{G_{ij}}{\rho^{G}_{j}a^{I}_{j}k^{G}_{i,m,j}}-\sum_{\substack{m=1\\ m\neq i}}^{N}\frac{y_{i,j}}{\rho^{G}_{j}a^{I}_{j}k^{G}_{i,m,j}}$$
$$for \quad i=1,2,....n_c-1,\ i\neq k \qquad (A.7)$$

$$R^{G}_{i,k,j}=-y_{i,j}\left(\frac{1}{\rho^{G}_{j}a^{I}_{j}k^{G}_{i,k,j}}-\frac{1}{\rho^{G}_{j}a^{I}_{j}k^{G}_{i,m,j}}\right)$$
$$for \quad i=1,2,....n_c-1,\ i\neq k \qquad (A.8)$$

- Heat flux for the liquid film

$$a^{I}_{j}H_{j}\left(T^{I}_{j}-T^{L}_{j}\right)-q^{L}_{j}+\sum_{i=1}^{N}N^{L}_{i,j}\overline{H}_{i,j}=0 \qquad (A.9)$$

- Heat flux for gas film

$$a^{I}_{j}h^{'}_{j}\left(T^{G}_{j}-T^{I}_{j}\right)-q^{G}_{j}+\sum_{i=1}^{N}N^{G}_{i,j}\overline{h}^{L}_{i,j}=0 \qquad (A.10)$$

The rate-Based model uses well-known and accepted correlations to calculate binary mass transfer coefficients for the vapour and liquid phases, interfacial areas, heat transfer coefficients and liquid holdup. In general, these quantities depend on column diameter and operating parameters such as vapour and liquid flow rates, densities, viscosities, surface tension, and binary diffusion coefficients in both liquid and gaseous phases. Mass transfer coefficients, interfacial areas and liquid holdup also depend on the type, size, specific surface area, and construction material of packing and flow path length (packing tortuosity). Most parameters can vary by stage, but only depend on the properties for that stage. The subscript j on each variable is omitted in the equations for readability.

The Onda model [18] predicts mass transfer coefficients and interfacial area for random packing.

$$k^{L}_{i,k}=0.0051\ \mathrm{Re}^{0.667}Sc^{-0.5}_{L,i,k}(a_F d_F)^{0.4}\left(\frac{\mu^{L}g}{\rho^{L}_{t}}\right)^{0.333} \qquad (A.11)$$

$$k^{G}_{i,k}=\begin{cases}2.0\,\mathrm{Re}^{0.7}_{G}Sc^{0.333}_{G,i,k}a_F D^{G}_{i,k}(a_F d_F)^{-2} & \\ 5.23\,\mathrm{Re}^{0.7}_{G}Sc^{0.333}_{G,i,k}a_F D^{G}_{i,k}(a_F d_F)^{-2} & for\ d_F>0.015\end{cases} \qquad (A.12)$$

$$a^{I}=a_w A h_F \qquad (6-27)$$
$$a_w=a_F\left[1-\exp\left(-1.45\left(\frac{\sigma_c}{\sigma}\right)^{0.75}\mathrm{Re}^{0.1}_{L}Fr^{-0.05}_{L}We^{0.2}_{L}\right)\right] \qquad (A.14)$$

The heat transfer coefficient h was estimated by Chilton–Colburn method [42]

$$h_j=\overline{k}_j\overline{\rho}_j C_{pj}\left(\frac{\lambda_j}{\overline{D}_j\overline{\rho}_j C_{pj}}\right)^{2/3} \qquad (A.15)$$

$$where \quad \overline{D_j}=\frac{\sum_{i=1}^{nc-1}\sum_{k=i+1}^{nc}(x_{i,j}+\delta)(x_{k,j}+\delta)D_{i,k,j}}{\sum_{i=1}^{nc-1}\sum_{k=i+1}^{nc}(x_{i,j}+\delta)(x_{k,j}+\delta)D_{i,k,j}} \qquad (A.16)$$

$$and \quad \overline{k_j}=\frac{\sum_{i=1}^{nc-1}\sum_{k=i+1}^{nc}(x_{i,j}+\delta)(x_{k,j}+\delta)k_{i,k,j}}{\sum_{i=1}^{nc-1}\sum_{k=i+1}^{nc}(x_{i,j}+\delta)(x_{k,j}+\delta)D_{i,k,j}} \qquad (A.17)$$

where C_p is the specific molar heat capacity, $\overline{D}$ is the average diffusivity, $\overline{k}$ is the average mass transfer coefficient, $\overline{\rho}$ is the averaged density, M is the molecular weight, u is the average flow velocity, ρ is the molar density, λ is the thermal conductivity, n_c is the number of components and d is the Chilton-Colburn averaging parameter specified on the Rate-Based Setup Specifications sheet with a default recommended value of 0.0001. This parameter provides stability when compositions change, especially in reactive systems when some compositions may go to zero at the boundary.

The pressure drops through the Dixon packing were estimated using literature models applied to random Raschig packing as follows [41].

$$\Delta P/_{L} = C_{P,0}\left(\frac{64}{\mathrm{Re}_V}+\frac{1.8}{\mathrm{Re}_V^{0.08}}\right)\frac{a}{\varepsilon^3}\frac{u_V{}^2\rho}{2}\left(1+\frac{2}{31}\frac{1}{-\varepsilon}\frac{d_p}{d_s}\right) \quad (A.18)$$

$$\frac{1}{\mathrm{Re}_V}=\frac{(1-\varepsilon)\nu_V}{u_V d_p}\left(1+\frac{2}{31}\frac{1}{-\varepsilon}6\frac{1-\varepsilon}{a}\frac{1}{d_s}\right) \quad (A.19)$$

$$d_p = 6\frac{1-\varepsilon}{a} \quad (A.20)$$

Appendix A. Supplementary data

Supplementary data associated with this article can be found, in the online version, at http://dx.doi.org/10.1016/j.cep.2016.07.008.

References

[1] D. Greneche, W.J. Szymczak, The AREVA HTR Fuel Cycle: an analysis of technical issues and potential industrial solutions, Nucl. Eng. and Des. 336 (2006) 635–642.
[2] A. Bruggeman, J. Braet, S. Vanderbiesen, JET EFDA Contributors, Water detritiation: better catalysts for liquid phase catalytic exchange, 7th Tritium Science and Technology Conference, Baden, Germany, 12–17 September, 2004.
[3] S.R. Sherman, T.M. Adams, Tritium Barrier Materials and Separation Systems for the NGNP, Prepared for the NGNP Project Under MPO 00072051, Battelle Energy Alliance, Savannah River National Laboratory, 2008.
[4] T. Sugiyama, Y. Asakura, Y. Udaa, T. Shiozaki, Y. Enokida, I. Yamamoto, Present status of hydrogen isotope separation by CECE process at the NIFS, Fusion Eng. Des. 81 (2006) 833–838.
[5] A.N. Perevezentsev, A.C. Bell, Wet scrubber column for air detritiation, Fusion Sci. Technol. 56 (2009) 1455–1461.
[6] A.N. Perevezentsev, A.C. Bell, Development of water detritiation facility for JET, Fusion Sci. Technol. 53 (2008) 816–829.
[7] F. Huang, C. Meng, Method for the production of deuterium-depleted potable water, Ind. Eng. Chem. Res. 50 (2001) 378–381.
[8] M. Benedict, T.H. Pigford, H.W. Levi, Nuclear Chemical Engineering, McGraw-Hill Book Company, 1980.
[9] W. H. Stevens, Process and catalyst for enriching a fluid with hydrogen isotopes, Canadian Patent (1972) No.907292.
[10] M.N. tSaoir, J. Sa, D.L.A. Fernandez, M. McMaster, C. Hardacre, K. Kitagawa, F. Aiouache, Visualization of water vapour flow in a packed bed adsorber by near-infrared diffused transmittance tomography, Chem. Eng. Sci. 66 (2011) 6407–6419.
[11] M.N. tSaoir, D.L.A. Fernandez, M. McMaster, C. Hardacre, K. Kitagawa, F. Aiouache, Transient distributions of composition and temperature in a gas–solid packed bed reactor by near-infrared tomography, Chem. Eng. J. 189–190 (2012) 383–392.
[12] I. Cristescu, I.R. Cristescu, L. Dörr, M. Glugla, G. Hellriegel, R. Michling, D. Murdoch, P. Shaffer, S. Welte, W. Wurster, Commissioning of water detritiation and cryogenic distillation systems at TLK in view of ITER, Fusion Eng. Des. 82 (2007) 2126–2132.
[13] S. Paek, D.H. Ahn, H.J. Choi, K.R. Kim, M. Lee, S.P. Yim, The performance of a trickle-bed reactor packed with a Pt/SDBC catalyst mixture for the CECE process, Fusion Eng. Des. 82 (2007) 2252–2258.
[14] A.S. Sumchenko, A.N. Bukin, S.A. Marunich, Y.S. Pak, M.B. Rozenkevich, I.L. Selivanenko, Influence of packing columns starting modes on effectiveness of processes of water rectification and detritiation of gases by the method of phase isotopic exchange, Theor. Found. Chem. Eng. 49 (2015) 252–260.
[15] A. Perevezentsev, A.C. Bell, P.D. Brennan, J.L. Hemmerich, Measurement of pressure drop and HETP in columns packed with different hydrophobic catalysts for tritium isotopic exchange between water and hydrogen, Fusion Sci. Technol. 41 (2002) 1102–1106.
[16] I. Cristescu, U. Tammb, M. Glugla, C.J. Caldwell-Nichols, Investigation of simultaneous tritium and deuterium transfer in a catalytic isotope exchange column for water detritiation, Fusion Eng. Des. 61 (2002) 537–542.
[17] R. Kumar, S. Mohan, S.M. Mahajani, Reactive stripping for the catalytic exchange of hydrogen isotopes, Ind. Eng. Chem. Res. 52 (2013) 10935–10950.
[18] K. Onda, H. Takeuchi, Y. Okumoto, Mass transfer coefficients between gas and liquid phases in packed columns, J. Chem. Eng. Jpn. 1 (1968) 56–62.
[19] O. Fedorchenko, I. Alekseev, V. Uborsky, Water-hydrogen isotope exchange process analysis, Fusion Sci. Technol. 54 (2008) 450–453.
[20] T. Yamanishi, K. Okuno, Simulation Code Treating All Twelve Isotopic Species of Hydrogen Gas and Water for Multistage Chemical Exchange Column, Japan Atomic Energy Research Institute, 1994 (JAERI-Data Code, 94-019).
[21] L. Ye, L.D. Luo, T. Tang, W. Yang, P. Zhao, Process simulation for hydrogen/deuterium exchange in a packed column, Int. J. Hydrogen Energy 39 (2014) 6604–6609.
[22] R. Taylor, R. Krishna, Multicomponent Mass Transfer, Wiley, New York, 1993.
[23] M. Kinoshita, An efficient simulation procedure especially developed for hydrogen isotope distillation columns, Fusion Sci. Technol. 6 (1984) 574–583.
[24] M.N. tSaoir, D.L.A. Fernandes, J. Sa, K. Kitagawa, C. Hardacre, F. Aiouache, Three dimensional water vapour visualization in porous packing by near-infrared diffuse transmittance tomography, Ind. Eng. Chem. Res. 51 (2012) 8875–8882.
[25] F. Alzahrani, M. Aldehani, H. Rusi, M. McMaster, D.L.A. Fernandes, S. Assabumrungrat, M.N. tSaoir, F. Aiouache, Gas Flow visualization in low aspect ratio packed beds by three-dimensional modeling and near-infrared tomography, Ind. Eng. Chem. Res. 51 (2015) 12714–12729.
[26] T.F. Roland, J. Borysow, M. Fink, Surface mediated isotope exchange reactions between water and gaseous deuterium, J. Nucl. Mater. 353 (2006) 193–201.
[27] K. Kawakami, Y. Takao, K. Kusunoki, Kinetics of isotopic exchange reaction between hydrogen and water vapor over platinum supported on a hydrophobic carrier, Can. J. Chem. Eng. 64 (1986) 432–439.
[28] N.H. Sagert, M.L. Pouteau, The production of heavy water: hydrogen-water deuterium exchange over platinum metals on carbon supports, Platinum Met. Rev. 19 (1975) 16–21.
[29] A. Richardson, J.W. Leachman, Thermodynamic properties status of deuterium and tritium, advances in cryogenic engineering, AIP Conf. Proc. 1434 (2012) 1841–1848.
[30] P.C. Souers, Hydrogen Properties for Fusion Energy, University of California Press, Berkley, 1986.
[31] W.A. Van Hook, L.P.N. Rebelo, M. Wolfsberg, Isotope effects on VLE properties of fluids and corresponding states: critical point shifts on isotopic substitution, Fluid Phase Equilib. 257 (2007) 35–52.
[32] G. Vasaru, Tritium Isotope Separation, CRC Press, 1993.
[33] J. Cho, S. Cho, S. Yun, M.H. Chang, H. Kang, K.J. Jung, D.M. Kim, Estimation of physical properties for hydrogen isotopes using aspen plus simulator, Transactions of the Korean Nuclear Society Spring Meeting, Jeju, Korea, May 22, 2009, pp. 135–136.
[34] S. Noh, J. Rho, J. Cho, Cryogenic distillation simulation for hydrogen isotopes separation, J. Korea Acad. Ind. Coop. Soc. 14 (2013) 4643–4651.
[35] M. Sdomon, Thermodynamic Properties of Liquid H_2O and D_2O and Their Mixtures, Electronics Research Centre Cambridge, Mass, National Aeronautics and Space Administration, NASA TN D-5223, Washington, D. C, 1969.
[36] A. Durmayaz, Approximate functions for the fast computation of the thermodynamic properties of heavy water, Nucl. Eng. Des. 178 (1997) 309–329.
[37] H.W. Xianga, Vapor pressure and critical point of tritium oxide, J. Phys. Chem. Ref. Data 32 (2003) 1707–1711.
[38] N. Matsunaga, A. Nagashima, Saturation vapor pressure and critical constants of H_2O, D_2O, T_2O, and their isotopic mixtures, Int. J. Thermophys. 8 (1987) 681–694.
[39] A.S. Friedman, D. White, H.L. Hohnston, Critical constants, boiling points triple point constants, and vapor pressures of the six isotopic hydrogen molecules, based on a simple mass relationship, J. Chem. Phys. 19 (1951) 126–127.
[40] J.H. Rolston, J.D. Hartog, J.P. Butler, The deuterium isotope separation factor between hydrogen and liquid water, J. Phys. Chem. 80 (1976) 1064–1067.
[41] R. Billet, M. Schultes, Prediction of mass transfer columns with dumped and arranged packings: updated summary of the calculation method of billet and schultes, Chem. Eng. Res. Des. 77 (1999) 498–504.
[42] T. Chilton, A.P. Colburn, Mass transfer (absorption) coefficients prediction from data on heat transfer and fluid friction, Ind. Eng. Chem. 26 (1934) 1183–1187.
[43] T. Sugiyama, A. Ushida, I. Yamamoto, Effects of the gas-liquid ratio on the optimum catalyst quantity for the CECE process with a homogeneously packed LPCE column, Fusion Eng. Des. 83 (2008) 1447–1450.
[44] O.A. Fedorchenko, I.A. Alekseev, A.S. Tchijov, V.V. Uborsky, Modeling of the process of three-isotope (H, D, T) exchange between hydrogen gas and water vapour on Pt-SDBC catalyst over a wide range of deuterium concentration, Fusion Sci.Technol. 48 (2005) 120–123.

Chemical Engineering and Processing 107 (2016) 80–93

Contents lists available at ScienceDirect

Chemical Engineering and Processing: Process Intensification

journal homepage: www.elsevier.com/locate/cep

Process integration of dimethyl carbonate and ethylene glycol production from biomass and heat exchanger network design☆

Chayanit Choomwattana[a], Aksornchan Chaianong[a], Worapon Kiatkittipong[b], Pichayapan Kongpanna[a], Armando T. Quitain[c], Suttichai Assabumrungrat[a,d,*]

[a] Center of Excellence in Catalysis and Catalytic Reaction Engineering, Department of Chemical Engineering, Faculty of Engineering, Chulalongkorn University, Bangkok 10330, Thailand
[b] Department of Chemical Engineering, Faculty of Engineering and Industrial Technology, Silpakorn University, Nakhon Pathom 73000, Thailand
[c] Department of Applied Chemistry and Biochemistry, Faculty of Engineering, Kumamoto University, Kumamoto 860-8555, Japan
[d] PTT Group Frontier Research Center, PTT Public Company Limited, Bangkok 10900, Thailand

ARTICLE INFO

Article history:
Received 6 August 2015
Received in revised form 31 January 2016
Accepted 1 June 2016
Available online 3 June 2016

Keywords:
Biomass gasification
Process design
Process simulation
Dimethyl carbonate
Ethylene glycol

ABSTRACT

This work proposed an integrated production process of dimethyl carbonate (DMC) and ethylene glycol (EG) from biomass. The process started with biomass gasification, CO_2 separation and CO_2 conversion to ethylene carbonate. DMC and EG were produced via transesterification using reactive distillation and extractive distillation. Various key parameters were examined to optimize operating condition focusing on heat consumption. DMC and EG can achieve 99.5 mol% purity. The process can sustain itself without any external heat sources by using biomass combustion, and all performance indicators were considered under the energy self-sufficient conditions. The ratio of biomass fed to the gasifier and the combustor was found to be 0.38:0.62 where the C, H and O atom efficiencies of the process achieved were 35.83, 53.19 and 40.31%, respectively. When employing heat exchanger network, the atom efficiency of the process could be improved (C: 42.49, H: 61.83, O: 45.21), while the ratio of biomass fed to the gasifier and the combustor increased to 0.46:0.54. The energy consumptions were reported by mass allocation as 143 MJ/kg-DMC. Since all energy was supplied by biomass itself, the process was considered as carbon neutral with a fraction of carbon dioxide fixation from biomass into chemicals of 0.31.

© 2016 Elsevier B.V. All rights reserved.

1. Introduction

For over several decades, greenhouse gases such as carbon dioxide (CO_2) and methane (CH_4) have been considered as a crucial problem concerning global warming and climate change [1]. Some of many causes of greenhouse effect and climate change [2,3] include transportation [4], construction [5], industries [6], etc. Nowadays, many greenhouse gas reduction approaches have been considered to alleviate the effects of global warming, such as reducing energy consumption by increasing energy efficiency, using green fuels, clean combustion fuels and renewable energy resources. Also, novel approaches for the utilization or minimization of carbon dioxide emission in the system have been significantly investigated. CO_2 utilization processes have been continuously developed in research area. An interesting option is the production of organic carbonates, roughly categorized as cyclic (e.g. ethylene carbonate (EC), propylene carbonate (PC)) and linear (e.g. dimethyl carbonate (DMC)). With rising demand for organic carbonates, the feasibility of CO_2 based reaction for its production becomes an interesting and more sustainable approach. Recent researches have shown that utilization of CO_2 as a chemical feedstock can produce a variety of chemical products via chemical and electrochemical processes [7,8] such as dimethyl ether, formic acid, methane and dimethyl carbonate (DMC) [9,10].

CO_2 utilization to chemicals requires each synthetic route to be investigated for thermodynamic feasibility and selectivity for a

Abbreviations: AN, Aniline; DMC, Di-methyl carbonate; EC, Ethylene carbonate; EG, Ethylene glycol; ER, Equivalence ratio [kmol/kmol]; LHV, Lower heating value [MJ/kg]; HHV, Higher heating value [MJ/kg]; SBR, Steam to biomass ratio [kmol/kmol].

☆ Paper presented at 12th International Symposium on Process Systems Engineering and 25th European Symposium on Computer Aided Process Engineering, Copenhagen, Denmark, 31 May–4 June 2015.

* Corresponding author at: Center of Excellence in Catalysis and Catalytic Reaction Engineering, Department of Chemical Engineering, Faculty of Engineering, Chulalongkorn University, Bangkok 10330, Thailand.
E-mail address: suttichai.a@chula.ac.th (S. Assabumrungrat).

http://dx.doi.org/10.1016/j.cep.2016.06.001
0255-2701/© 2016 Elsevier B.V. All rights reserved.

Nomenclature

ΔH_r°	Heat of reaction at standard condition [kJ/mol]
M	Mass flow rate [kg/h]
H_2O/C	Mole of steam as gasifying agent per mole of carbon in biomass [−]
H_2/CO	Molar ratio of H_2 to CO in product syngas [−]
n_H	Molar flow rate of atomic hydrogen in biomass [kmol/h]
R_g	Gas constant [kJ/(kmol.K)]
X_C, X_H, X_O	Mass faction of carbon, hydrogen, and oxygen in biomass [−]
λ_{298}	Latent heat of vaporization of water at standard condition 298 K [MJ/kmol]

commodity chemical or higher value-added products based on available reaction data [11]. One interesting option is the production of dimethyl carbonate (DMC), a significant chemical product, and is used as methylating reagent, solvent, intermediate and fuel additive in many industries [12,13]. Moreover, DMC is considered a truly green chemical because it is a nontoxic substance for human health and environment [12]. The current proposed production of DMC, based on UBE Chemicals record in 2013, was approximately 94,000 ton/year, and the demand is expected to continuously increase [14,15]. Conventionally, phosgene has been used to produce DMC; nevertheless, phosgene has adverse effects to human health and environment [12]. The EniChem process has evolved the carbonylation of methanol in the presence of $CuCl_2$ as a catalyst but the major drawbacks of this process is low conversion of product due to catalyst deactivation at high temperature [14]. Thereafter, UBE Chemicals has developed a more efficient oxidative methyl nitrite carbonylation process using nitric oxide catalyst system. Nonetheless, catalyst deactivation and NO emission remain a problem [12,14]. Another interesting route for DMC production is the utilization of carbon dioxide as a raw material by coupling reaction with another chemical intermediate.

DMC production from carbon dioxide has been studied for several decades. DMC production based on a reaction between carbon dioxide and methanol has been reported [16]. However, in this manner, it has to be operated at critical temperature and pressure [16], leading to high energy consumption. DMC can also be produced by various reaction pathways which have potential for CO_2 utilization such as urea route, propylene carbonate route and ethylene carbonate route. DMC synthesized from urea and methanol is one of CO_2 utilization routes providing several advantages such as no formation of water in DMC synthesis section, thus the separation of DMC/MeOH/Urea/NH_3 can be easily done with only DMC/MeOH as azeotropic mixture. However, the DMC yield is very low at approximately 30% [17]. Another study reported is transesterification of methanol and alkylene carbonate groups- ethylene carbonate and propylene carbonate. The products from this reaction are DMC and ethylene glycol (EG) or propylene glycol (PG). Potential role of transesterification of alkylene carbonate is a highly safe process for DMC and EG production under mild conditions and with low corrosiveness [18,19]. In addition, to achieve the high conversion and yield of DMC and ethylene glycol production, the energy consumption in downstream separation of azeotropic mixtures of DMC/MeOH and EC/EG can be decreased by using reactive distillation [20,21]. Purification process of DMC and EG using reactive distillation would require the use of special techniques such as pressure-swing distillation and extractive distillation because of azeotropic composition of DMC and methanol. However, pressure-swing distillation was confirmed by [21] to be not effective for separating DMC and methanol, while extractive distillation is more preferable. Many entrainer types such as phenol, aniline and chlorobenzene were selected to use in this separation process in order to increase the relative volatility between methanol and DMC [20].

Ethylene carbonate, one of the intermediates used in this process, could be synthesized with high yield using the reaction between ethylene oxide and carbon dioxide [22]. Methanol, another reactant, can be synthesized via many routes; but mostly from syngas which is mainly produced by natural gas reforming. Alternatively, syngas and methanol could be produced from biomass gasification which increase renewability of the process [23]. The composition of synthesis gas from biomass gasification which is appropriate for methanol production is a $(H_2 - CO_2)/(CO + CO_2)$ ratio of 2, which is formed by adjusting certain gasification parameters and tailored in downstream process by water-gas shift reaction, by methane reforming, by CO_2 removal or by supplying hydrogen before entering into methanol synthesis [23–26].

The primary objective of this research was to develop a new integrated DMC and ethylene glycol production process from biomass via transesterification of ethylene carbonate and methanol. ASPEN Plus simulator was employed in order to optimize operating conditions in each main section i.e. biomass gasification, methanol synthesis, CO_2 separation, ethylene carbonate synthesis, and DMC and EG synthesis by focusing on heat consumption optimization. Validation of simulation models for different units was discussed. Heat exchanger network was adapted to minimize both cold and hot utilities of the overall system. Moreover, the atom efficiency and amount of CO_2 fixation into chemical is evaluated under energy self-sufficient condition where the process could sustain itself without any external heat source by partially utilizing biomass to generate heat.

2. Process description and system modeling

Fig. 1 shows a simplified process flow diagram of DMC and ethylene glycol production from biomass. Biomass was fed to gasifier where autothermal reforming takes place. The product stream was further processed for CO_2 separation to produce a mixture of H_2 and CO before entering to methanol production process. The separated CO_2 was utilized by reacting with ethylene oxide to produce ethylene carbonate. DMC and ethylene glycol was produced via transesterification of methanol and ethylene carbonate in reactive distillation. In the purification process of DMC, conventional distillation process was used; however, the high energy consumption of pressurized column and the large heat duty in the reboiler are required. The extractive separation of DMC/MeOH can be used to separate azeotropic mixture of DMC/MeOH. The extractive distillation and aniline recovery column were adapted to increase purity of DMC and methanol recovery. In order to operate under energy self-sufficient condition, biomass was split to a combustor for providing heat and electricity. A detailed simulation flowsheet is summarized in Fig. 2.

2.1. Biomass gasification for production of synthesis gas

The flowsheet of biomass gasification is shown in Fig. 2A. Biomass and other gasification agents (steam and oxygen) were supplied into a gasifier. Steam was produced from water at 25 °C and oxygen was supplied from air separation process [27] which has the energy consumption of 92.57 kW. The thermal decomposition of biomass takes place in the decomposition reactor and the volatiles are reacted with the gasifying agents producing synthesis gases. The main reactions of biomass gasification are as follows:

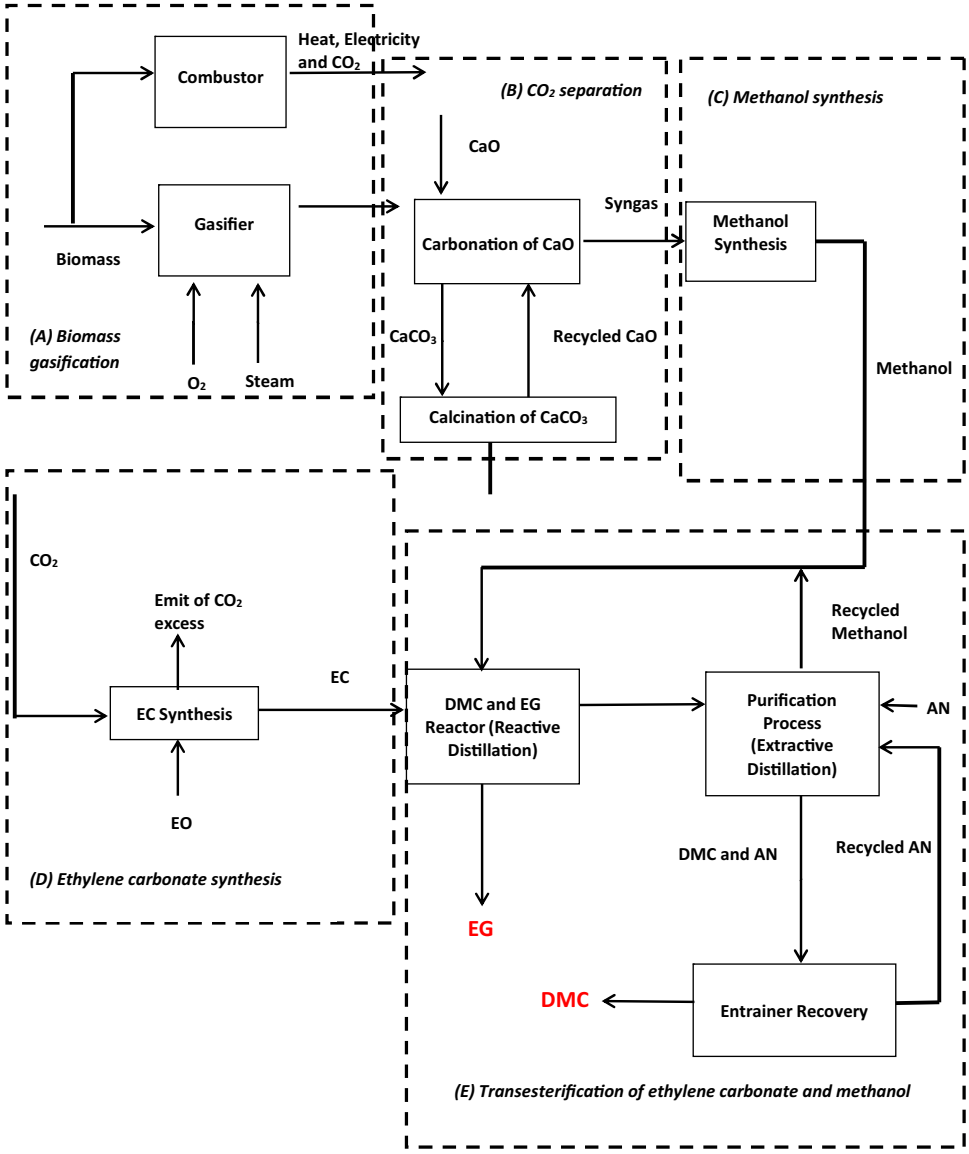

Fig. 1. Diagram of integrated process of DMC and ethylene glycol production from biomass.

Water gas shift:

$$CO + H_2O \rightleftharpoons CO_2 + H_2 \qquad \Delta H_r^\circ = -41\text{kJ/mol} \tag{1}$$

Steam reforming:

$$C + H_2O \rightleftharpoons CO + H_2 \qquad \Delta H_r^\circ = 131\text{kJ/mol} \tag{2}$$

Methanation:

$$C + 2H_2 \rightleftharpoons CH_4 \qquad \Delta H_r^\circ = -74\text{kJ/mol} \tag{3}$$

Reverse Boudouard reaction:

$$C + CO_2 \rightleftharpoons 2CO \qquad \Delta H_r^\circ = 172\text{kJ/mol} \tag{4}$$

Partial oxidation:

$$2C + O_2 \rightleftharpoons 2CO \qquad \Delta H_r^\circ = -221\text{kJ/mol}$$

Steam methane reforming:

$$CH_4 + H_2O \rightleftharpoons CO + 3H_2 \qquad \Delta H_r^\circ = 206\text{kJ/mol} \tag{6}$$

The products from gasification process mainly consisted of carbon monoxide, carbon dioxide and hydrogen.

The model of RYield in Aspen Plus was employed for calculating the yield distribution of products according to the biomass ultimate analysis. Afterwards, these elements were fed to RGibbs reactor together with gasifying agents. This reactor simulation was based on the method of Gibbs free energy minimization approach or nonstoichiometric approach. The compositions for the producer gas from biomass gasification predicted by the Gibbs free energy minimization approach show good accuracy with the experimental data [28]. Heat input in gasifier is the combination of heat duty in RYield and RGibbs reactors in order to maintain the gasifier at specified temperature. Oxygen, a highly energy intensive product, had to be preheated in the first utility section. The required energy for heating oxygen component to gasifier is 140 kW. The Peng-Robinson equation of state was selected to estimate all physical properties for the gasification process. The following assumptions were considered in the simulation of the biomass gasification process.

1. The whole process was at steady state and the reactions reached chemical equilibrium.
2. The gasifier was operated at isothermal condition

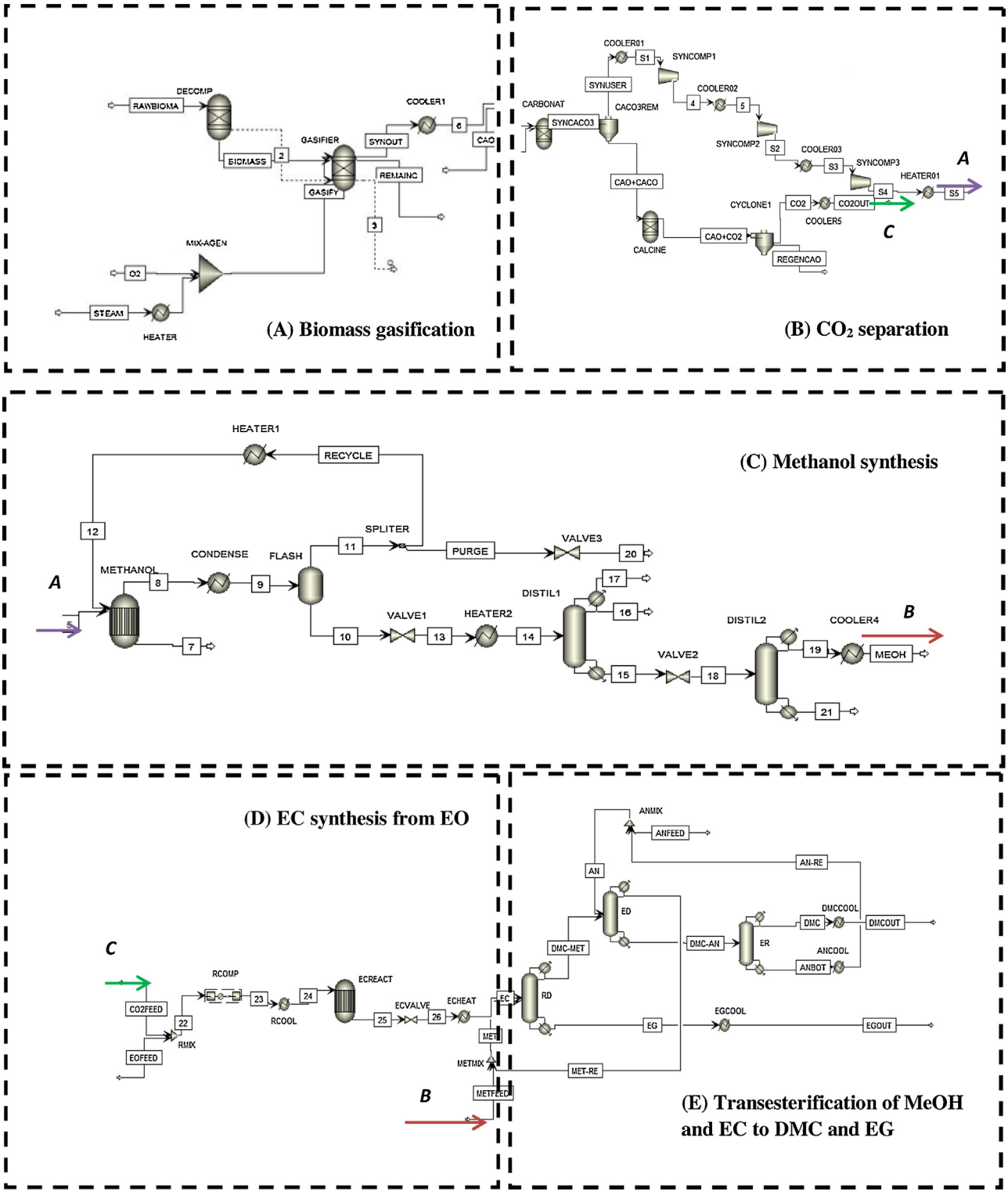

Fig. 2. Flowsheet of simulation of DMC and ethylene glycol production from biomass.

3. Energy consumption for oxygen production was not included in this study
4. The feedstock consisted of only carbon, hydrogen, and oxygen with no moisture content. The average formula of typical biomass used in this work can be represented by $CH_{1.4}O_{0.6}$ [29,30].
5. The biomass gasification product consisted of C, H_2, CH_4, H_2O, CO, CO_2; while tar was not taken into account in the simulation.
6. The high heating value (HHV) of biomass was calculated using the correlation [31] below [7].

$$\text{HHV (MJ/kg)} = 0.3491X_c + 1178.3X_H - 0.1034\,X_o \quad (7)$$

- The low heating value (LHV) of biomass is calculated using the Eq. (8)

$$\mathrm{LHV(MJ/kg)} = \frac{M_{\mathrm{biomass}}\mathrm{HHV}_{\mathrm{biomass}} - 0.5n_{\mathrm{H}}\lambda_{298}}{M_{\mathrm{biomass}}} \quad (8)$$

2.2. Carbon dioxide separation

The required ratio of carbon monoxide to hydrogen depends on the types of products in downstream process. As for methanol synthesis, the required ratio of $(H_2 - CO_2)/(CO + CO_2)$ should be 2 in order to achieve high yield in methanol synthesis. Therefore, the gas product from gasifier has to be removed of CO_2 from the gas stream before entering to the methanol synthesis reactor. In this study, the CaO was used as CO_2 sorbent because CaO provided excellent in high temperature operation, CO_2 capture capacity and high stability compared to other solid adsorbents [32]. Although, it is worth to note that although using CaO to remove CO_2 from syngas is not a recognized industrial alternative for large scale syngas conditioning. Using CaO sorbent is an interesting alternative since the sorption can be operated simultaneously with gasification, which is commonly referred to as "sorption enhanced gasification" which provides higher efficiency of the overall process. However, this is part of the scope of this present study. The $CaCO_3$ was subsequently regenerated in a calcination reactor. The reaction related to carbonation-regeneration cycles is as follow:

Carbonation-Calcination:

$$CaO + CO_2 \rightleftharpoons CaCO_3 \quad \Delta H_r^o = -178\,\mathrm{MJ/kmol} \quad (9)$$

Both carbonation and calcination reactors used RGibbs reactors for the calculation with the Peng-Robinson EOS property method [33]. The flowsheet of CO_2 separation is shown in Fig. 2B. The key parameters i.e. temperature, pressure, and CaO/CO_2 ratio were examined, and the amount of CO_2 removed from the product was determined.

2.3. Methanol synthesis

After that, synthesis gas having a H_2/CO ratio of 2 with negligible amount of CO_2 was introduced to methanol reactor which is typically operated within 50–150 bar and 230–270 °C, same as in industrial operation [23]. Methanol selectivity under this operation was higher than 99% [34]. There were small amounts of CO_2 and water as by products.

The main reactions considered in methanol synthesis are as follows:

Methanol synthesis reaction:

$$CO + 2H_2 \rightleftharpoons CH_3OH \qquad \Delta H_r^\circ = -90.6\,\mathrm{kJ/mol} \quad (10)$$

Secondary methanol synthesis reaction:

$$CO_2 + 3H_2 \rightleftharpoons CH_3OH + H_2O \qquad \Delta H_r^\circ = -49.5\,\mathrm{kJ/mol} \quad (11)$$

Water-gas shift:

$$CO + H_2O \rightleftharpoons CO_2 + H_2 \qquad \Delta H_r^\circ = -28.6\,\mathrm{kJ/mol} \quad (12)$$

The flowsheet of methanol synthesis is shown in Fig. 2C. An REquil reactor using the NRTL-RK property method was employed as for methanol synthesis reactor [35–37]. In this study, methanol synthesis was operated at 240 °C and 90 bar as the optimal operating condition [23,38,39].

2.4. Ethylene carbonate synthesis from ethylene oxide and carbon dioxide

Ethylene carbonate could be synthesized from the reaction of ethylene oxide and carbon dioxide.

Ethylene carbonate synthesis:

$$C_2H_4O + CO_2 \rightleftharpoons (CH_2O)_2C \quad \Delta H_r^o = -0.0837\,\mathrm{kJ/mol} \quad (13)$$

The flowsheet of ethylene carbonate production is shown in Fig. 2D. The reactor was heated and pressurized to the desired operating condition. A sensitivity analysis of operating parameters on reaction performance was presented.

2.5. DMC and ethylene glycol synthesis from transesterification of ethylene carbonate and methanol

2.5.1. Transesterification of ethylene carbonate and methanol in reactive distillation

In the conventional process, EC/MeOH as raw materials react in a conventional reactor and then the products containing DMC/MeOH/EC/EG were separated by a series of distillation columns [12,15–17]. However, the conventional process has some drawbacks including low EC conversion, high energy intensive and problems accompanying downstream separation. Thus, a new reaction and separation technique was proposed for DMC production via EC/MeOH based process [20].

After ethylene carbonate synthesis, the product stream was heated before entering to reactive distillation column in order to react with methanol synthesized from the biomass gasification.

DMC and ethylene glycol synthesis (transesterification of methanol and ethylene carbonate):

$$(CH_2O)_2C + 2CH_3OH \rightleftharpoons (CH_3O)_2CO + (CH_2OH)_2 \qquad \Delta H_r^o = -27.50\,\mathrm{kJ/mol} \quad (14)$$

The column was operated under atmospheric pressure and hold-up time was assumed to be 10 min [20]. Reactive distillation column was simulated using RadFrac model and the results were in good agreement with [20].

The kinetic equation for this reaction catalyzed by sodium methylate was taken from literature [40], and can be expressed as follows:

$$r_{EC} = k_+ C_{EC} C_{MeOH} - k_- \left(\frac{C_{EC} C_{DMC}}{C_{MeOH}}\right) \quad (15)$$

$$k_+ = 1.3246 \exp\left(-13060/R_g T\right) \quad (16)$$

$$k_- = 15022 \exp\left(-28600/R_g T\right) \quad (17)$$

The flowsheet of DMC and EG production is shown in Fig. 2E. The design variables of this system were methanol to ethylene carbonate molar ratio, total number of stages, number of reactive stages, methanol and ethylene carbonate feed location, distillate rate and reflux rate. Since low concentration of catalyst was employed, the catalyst component was neglected to simplify the simulations [20]. For each simulation run, two design specification parameters were identified to obtain ethylene glycol mole fraction in the bottom stream and ethylene glycol yield of 0.995 (Table 1).

2.5.2. Purification process of DMC and ethylene glycol production (extractive distillation and entrainer recovery column)

The purification process consisted of extractive distillation column and entrainer recovery distillation column to increase the relative volatility of DMC and methanol. Aniline was selected as a solvent due to their good performance [20]. Unreacted methanol was recycled from the overhead product of extractive distillation column to reactive distillation column while DMC and aniline were separated from each other using entrainer recovery column. Validation of the extractive distillation and entrainer recovery column models was performed. The simulation results show good agreement with those from [20].

Table 1
Design specification of reactive distillation, extractive distillation and entrainer recovery columns.

Unit operation	Design specification
Reactive distillation column	EG mole fraction in the bottom stream and EG yield of 0.995
Extractive distillation column	MeOH mole fraction in the distillate stream of 0.999 and MeOH mole fraction in the bottom stream of 0.0005
Entrainer recovery distillation column	Aniline mole fraction in the distillate stream of 0.001 and Aniline mole fraction in the bottom stream of 0.999

Table 2
UNIQUAC-RK model parameters of EC/MeOH/DMC/EG/AN system [20].

	i = DMC, *j* = EC	*i* = MeOH, *j* = EC	*i* = DMC, *j* = EG	*i* = EG, *j* = EC	*i* = MeOH, *j* = DMC	*i* = MeOH, *j* = EG	*i* = AN, *j* = MeOH	*i* = AN, *j* = DMC
a*ij*	2.5273	−0.54094	0	0	0	−32.587	0	0
a*ji*	−6.7598	15.892	0	0	0	2.2712	0	0
b*ij*(*K*)	167.34	4589.3	−236.13	−275.66	−18.065	10000	−288.28	−32.733
b*ji*(*K*)	442.34	−1278.9	−146.88	−27.961	−263.58	−599.11	85.941	101.44
c*ij*	−0.73211	−2.2771	0	0	0	0	0	0
c*ji*	1.0398	−2.0488	0	0	0	0	0	0

The design variables of this system were total number of stages of two columns, number of extractive stages, DMC-methanol feed location, aniline-DMC feed location, distillate rate of two columns and reflux rate of two columns. For each simulation run, four design specification parameters were set for the methanol mole fraction on top and bottom of the extractive distillation column at 0.999 and 0.0005, respectively, and aniline mole fraction on top and bottom of the entrainer recovery distillation column of 0.001 and 0.999, respectively (Table 1). The UNIQUAC-RK property method was selected to calculate liquid-phase and vapor-phase model, and the parameters are summarized in Table 2. The prediction of the *y-x* and *T-xy* plots of all six pairs by the thermodynamic model was performed and compared with the experimental data reported by [20]. It was found that UNIQUAC-RK model was excellent in predicting the VLE (results are not shown here).

2.6. Overall process of DMC and ethylene glycol production

In general, heat sources come from fossil fuels that lead to CO_2 emission problems. Thus, the effort to sustain the whole process system using renewable energy source like biomass by splitting biomass input to generate both heat/electricity was emphasized. Moreover, heat exchanger network was adapted to minimize both cold and hot utilities. Temperature approach was assumed to be 10 °C [41], and only heat exchangers were selected to be calculated in this network.

The energy consumptions were allocated to both DMC and EG products, and calculated by mass basis in this study. Typically, atom efficiency means the incorporation of materials (each elements and overall) used in the production of the desired product. However, the energy consume in the production process is not included in the typical atom efficiency consideration, since the material (biomass in this study) can be used as energy source. Considering the overall product (e.g. fuel and products) the energy self-sufficient which computes atom of raw materials as fuel in the process was proposed in this study. Therefore, the term "atom efficiency" would be more circumspect in this study. Moreover, similarly, since all energy was supplied by biomass itself, a fraction of carbon dioxide fixation from biomass into chemicals was considered under carbon neutral energy system.

3. Results and discussion

3.1. Biomass gasification

Sensitivity analysis was performed with the goal of analyzing and optimizing overall operating conditions in the gasifier. The aim of the gasifier in this study is to produce a mixture of H_2 and CO with H_2/CO of 2 for further methanol synthesis. The gasifier temperature, which is generally around 800–1000 °C, was one of the most important factors for syngas synthesis from biomass gasification in fixed bed [42,43]. The amounts of H_2O and external oxygen (which is represented by steam to biomass ratio (SBR) and equivalence ratio (ER), respectively) were adjusted to obtain H_2/CO ratio of 2, accompanying balance between endothermic and exothermic heat, in order to operate under energy self-sufficient gasification. Firstly, the investigation to find suitable SBR and ER was illustrated at the temperature of 900 °C (Fig. 3). As shown in the figure, SBR of 1.77 and ER of 0.718 could satisfy H_2/CO ratio of 2 and heat duty of 0 at the temperature of 900 °C. Fig. 4 shows a required SBR and ER along the gasifier temperature of 800–1200 °C, and corresponding equilibrium moles gas flow rate is shown in Fig. 5.

As shown in Fig. 4, under autothermal gasification with energy self-sufficient condition, the temperature of the gasifier is controlled by ER. This implies that the required oxygen for exothermic oxidation reaction should be higher with increasing temperature to promote oxidation of H_2 and CO to H_2O and CO_2 as illustrated in Fig. 5. In order to obtain H_2/CO of 2, the required SBR increased with increasing ER (as shown in Fig. 4). Within the ranges of temperatures from 800 °C to 1200 °C, it can be observed that the CH_4 content is low and not sensitive to the temperature. This is due to the steam methane reforming (6) along this range of temperature [43]. Although operating temperature of 800 °C would be suitable from thermodynamic consideration as higher

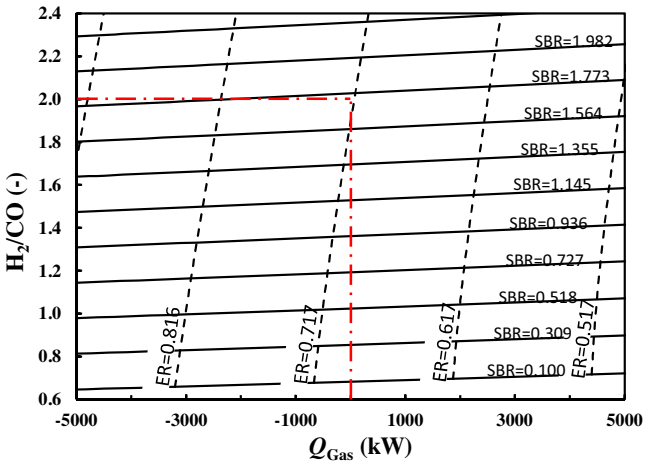

Fig. 3. Effect of oxygen equivalent ratio and steam biomass ratio on H_2/CO and heat duty at 900 °C.

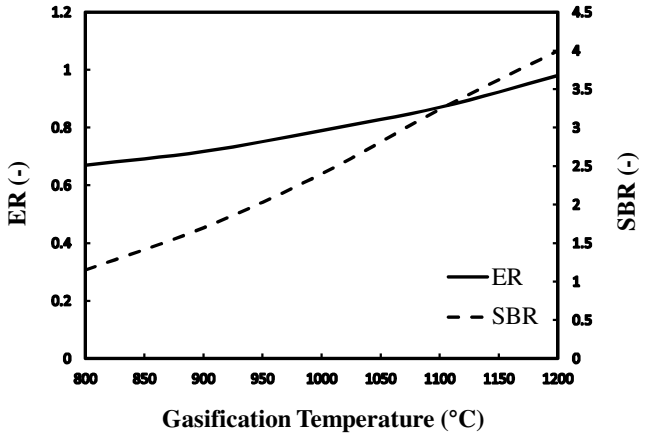

Fig. 4. Effect of gasifier temperature on oxygen equivalent ratio and steam biomass ratio (H_2/CO = 2, Heat duty = 0).

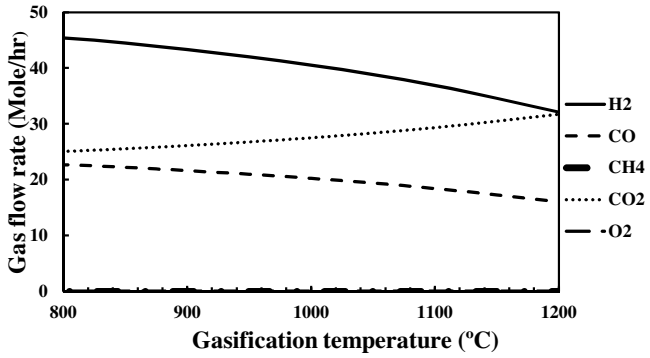

Fig. 5. Effect of gasification temperature on gas product flow rate (P = 1 bar).

amount of gas flow rate (Fig. 5). However, according to literatures, temperature of ca. 900 °C is practically being used, since most experimental studies have suggested that this temperature would also favor energy and carbon conversions, as well as gas yield [44,45]. The gasifier temperature of 900 °C at operating pressure of 1 bar was selected in this study. The suitable operating condition for biomass feed basis of 1100 kg/h are specified in Table 3.

3.2. Carbon dioxide separation

Based on CO_2 capture by carbonation and calcination reaction using CaO, the effect of CaO carbonation temperature on CO_2 capture at 1 bar was demonstrated as follows. CO_2 adsorption on CaO was less effective when temperatures was higher than 600 °C due to exothermic nature of carbonation reaction and the desorption of CO_2 from the product at the maximum temperature of 600 °C. The amount of CO_2 in the product gas was absorbed 97.8% by CaO, which was close or even higher to the values reported in literatures > 95% [46]. It was also observed that operating the carbonation reactor at high pressure has a slight effect on CO_2 separation. Moreover, the CO_2/CaO-equilibrium in Eq. (9) strongly depended on the process temperature at atmospheric conditions [47]. Thus, the carbonation reactor was operated at a pressure of 1 bar in this study. Adding excess CaO has no effect on CO_2 removal; hence, an optimum amount of CaO should be fed (i.e. CaO/CO_2 ratio is 1:1).

In the calcination reactor, $CaCO_3$ decomposes to CO_2 and CaO at adequately high temperature. At 1 bar complete calcination can be achieved at 860 °C [48,49]. Suitable operating conditions for carbonation and calcination reactor are summarized in Table 3. However, it is worth to note that the carbonation conversion of CaO sorbents decreases with the number of cycles due to agglomeration of CaO and diffusion related problems that cannot be taken into account in our calculation based on thermodynamic analysis. The determination of the recommend CaO/CO_2 ratio should be evaluated with a techno-economic study [33].

Table 3
Operating conditions for gasifier reactor and carbonation and calcination reactor.

Operating conditions for gasifier reactor	
Molecular formula of biomass feedstock	$CH_{1.4}$ $O_{0.6}$
Inlet temperature of biomass and O_2	25 °C
Inlet temperature of steam	25 °C
Biomass feed rate	1100 kg/h
Gasifier temperature	900 °C
Pressure	1 bar
Steam to biomass ratio	1.77
Equivalence ratio	0.718
Operating conditions for carbonation and calcination reactor	
CaO/CO_2	1:1
Inlet temperature CaO	25 °C
Inlet temperature of product gas	500 °C
Carbonation temperature	600 °C
Pressure	1 bar
Calcination temperature	860 °C

3.3. Design of ethylene carbonate synthesis

The temperature was varied from 30 to 130 °C along with the operating pressure of 1–40 bar, and the effects on carbonate yield is shown in Fig. 6. This sensitivity analysis was simulated with molar ratio of carbon dioxide to ethylene oxide as 1 or stoichiometric ratio since high ethylene carbonate yield could be achieved with this molar ratio.

According to Le Chatelier's principle, in an exothermic reaction, increasing the temperature decreases the equilibrium constant, thus operating at low temperature is preferable. Increasing the operating pressure favor the conversion of ethylene oxide, which can also be explained by Le Chatelier's principle.

If operating temperature is higher than 90 °C, ethylene carbonate yield drops significantly especially at low pressure where reaction cannot proceed well. Based on literature [22], the optimum operating condition should be 30 °C and 25 bar in order to achieve high yield of ethylene carbonate. At validation point (30 °C, 25 bar), the results of simulation for ethylene oxide conversion of 99.9% agree well with the experimental value (96%) from literature [22]. Therefore, in this study, the operating conditions of ethylene carbonate synthesis were selected at the same conditions as literature [22]. Multi-stage compressions with ratios of 3, 3 and 2.77 were employed due to technical limitations.

3.4. Transesterification of methanol and ethylene carbonate for DMC and ethylene glycol production

In this part, the design flowsheet consisted of reaction and separation sections, developed by minimizing energy consumption contributed mainly by reboilers from reactive distillation, extractive distillation and entrainer recovery distillation.

3.4.1. Design of reactive distillation column

By giving product specifications, the configuration of reactive distillation column from [20] was first adopted in the simulation. With respect to the reboiler of reactive distillation, recycled methanol flow rate was indicated the most important factor that affects its heat duty. Thus, the following steps were applied to obtain a near optimal design: 1) vary the recycled methanol to methanol inlet molar ratio 2) place the heavy reactant (N_{EC}) and light reactant feed location (N_{MeOH}) on the top and the lowest of

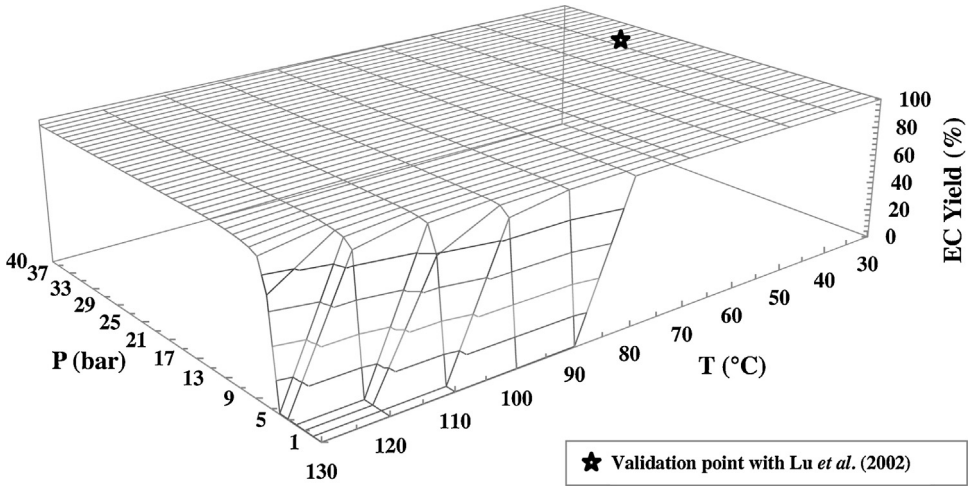

Fig. 6. Effect of pressure and temperature of ethylene carbonate synthesis from ethylene oxide and carbon dioxide (molar ratio of ethylene oxide and carbon dioxide as 1).

the reactive section, and 3) vary the numbers of stages in the rectifying, reaction and stripping section.

Based on Fig. 7, it was indicated that when the ratio of recycled methanol to methanol inlet is less than 2.5, ethylene carbonate conversion becomes much lower. The unreacted ethylene carbonate could contaminate ethylene glycol product in the bottom stream of reactive distillation, resulting in low yield and purity below the 99.5% target. The results were in good agreement with the experimental study from literature [50]. In this simulation, the molar ratio of recycled methanol to methanol fresh feed was selected to be 2.5, or the molar ratio of methanol to ethylene carbonate is approximated to be 7, to minimize the overall required heat of the process.

The optimal design flowsheet of this column is shown in Fig. 8. The output stream of ethylene glycol could achieve mole fraction purity of 0.995, and an overall ethylene glycol yield of 0.995 was able to reach. As the process was set up using optimal design specifications, a lower energy consumption comparing to the previous study [20] could be achieved in our proposed reactive distillation.

3.4.2. Design of extractive distillation and aniline recovery column

Considering the top stream of reactive distillation column (63 °C, 1 bar, methanol mole fraction of 0.833), azeotropic composition of DMC and methanol could be found. Thus, DMC and unreacted methanol could not be completely separated with the distillation column. Extractive distillation and entrainer recovery column were chosen to purify the primary products [20].

The design specification of the product stream of extractive distillation column and entrainer recovery distillation column is shown in Table 1. The azeotropic mixture of DMC-MeOH was designed for separation by extractive distillation column (ED) with flow rate of 60 kmol/hr (DMC purity 16.7%). Aniline was used as a solvent in extractive distillation column, followed by an entrainer recovery column (ER), which recovers aniline from DMC, to meet the specification of 99.95% purity. The optimum design flowsheet of this purification process is shown in Fig. 9. Methanol from extractive column was recycled back into the reactive distillation column, while the aniline-DMC stream was directed into the entrainer recovery column. The process was set up by using optimal design specifications of both columns, so a lower energy consumption in our proposed extractive and entrainer recovery system compared to the previous study [20] could be achieved.

3.5. Overall process of the optimal base case study

According to the suitable operating condition of each section including biomass gasification, CO_2 separation, methanol synthesis, ethylene carbonate synthesis, and DMC synthesis, the resulting mass balance of this overall process corresponding to the flowsheet of Fig. 2 are summarized in Table 4. The energy requirements of the different units calculated through mass and

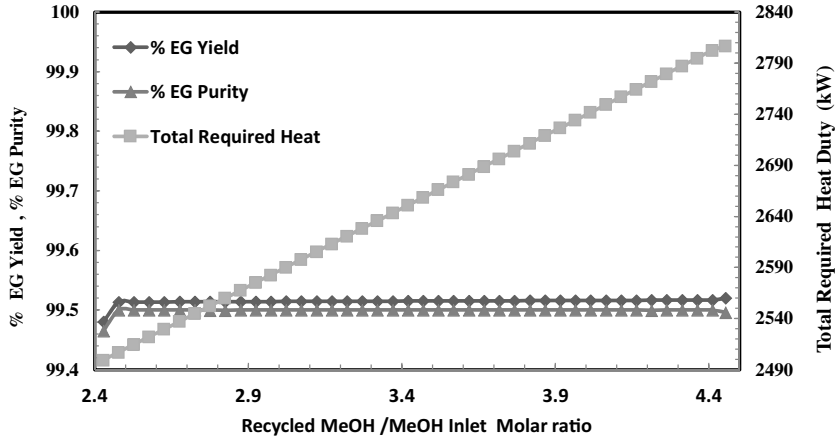

Fig. 7. Effect recycled methanol to methanol fresh feed molar ratio on ethylene glycol yield, ethylene glycol purity and total required heat duty (kW).

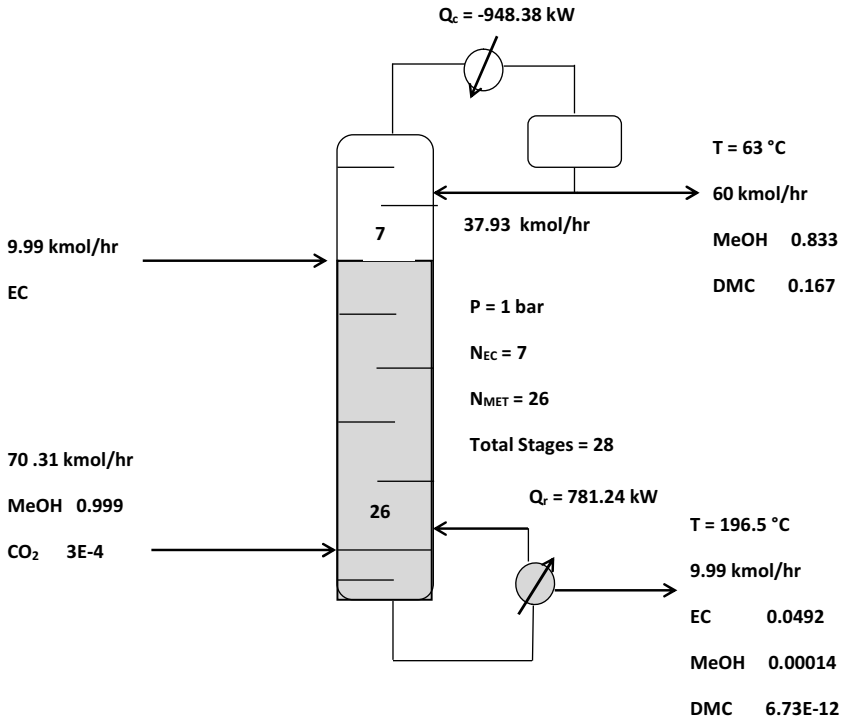

Fig. 8. Design flow sheet of reactive distillation column.

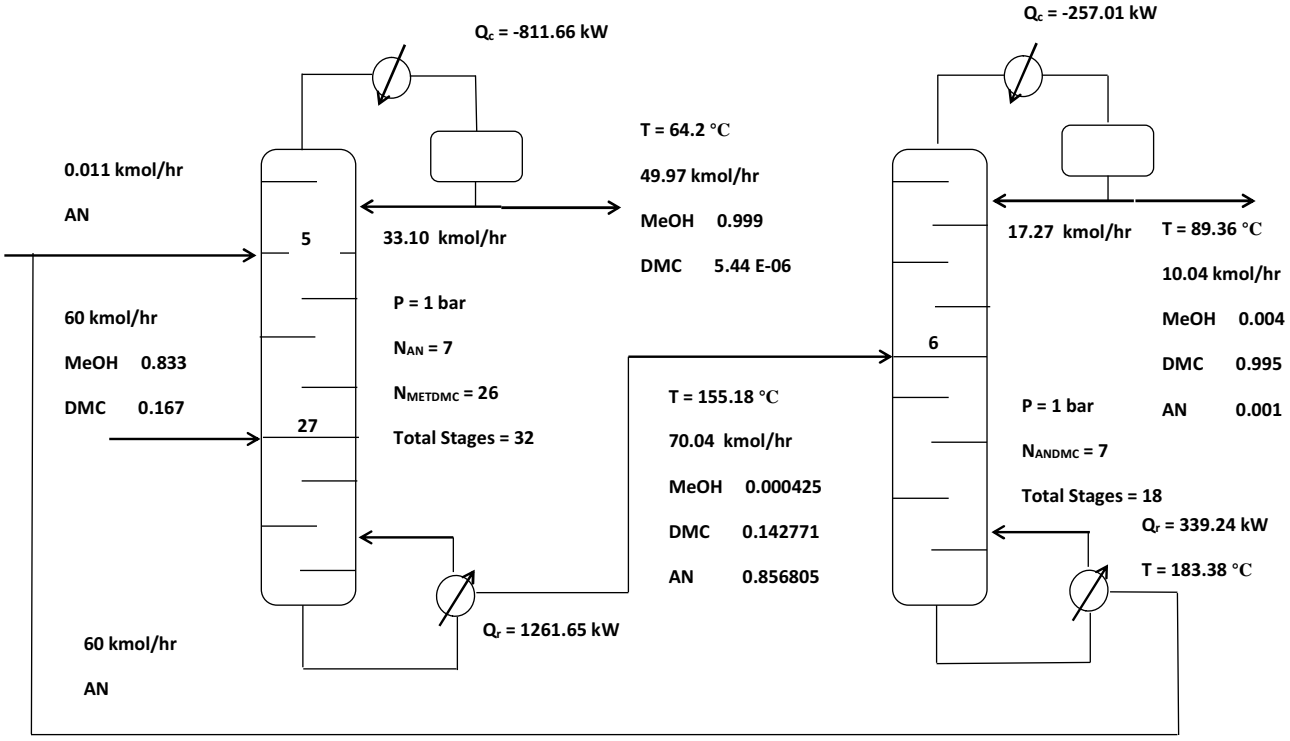

Fig. 9. Optimal design flow sheet of extractive distillation and entrainer recovery distillation column.

energy balances for each section are illustrated in Table 5. The energy requirements of each unit are reported as equivalent thermal energy requirements by assuming heat to electricity efficiency of 55%. It should be noted that based on current commercially available gas turbine combined-cycle power plants fueled by natural gas, distillate oil and low Btu gas, net plant efficiency typically achieves 55% LHV [51].

As shown in Table 5, the required heat energy (or equivalence heat energy) mainly came from the biomass-decomposer and heater in the reactant feed preparation section, calciner in CO_2 separation and reboilers of distillation column. In order to improve heat efficiency of the overall system, the manufacturer should optimize heat in the mentioned equipment or observe new catalytic conditions that can reduce pressure for methanol

Table 4
Mass balance simulation results of DMC and ethylene glycol production from biomass (base case study).

	1	STEAM	O2	GASIFY	RAWBIOMASS	BIOMASS	SYNOUT	REMAINC	S4	CAO	SYNCACO3
Temperature (°C)	600	25	25	507.80	25	900	900	–	124.1	25	600
Pressure (bar)	1	1	1	1	1	1	1	–	70	1	1
Total gas flow rate (kg/h)	1334.54	1334.54	561.97	1896.51	–	525.74	2996.51	–	1884.58	–	1884.58
Total solid flow rate (kg/h)	–	–	–	–	1100	574.26	–	0	–	1462.78	2574.71
Component flow rate (kg/h)											
O_2	0	0	561.97	561.97	0	458.75	5.64E-13	0	0	0	0
CO_2	0	0	0	0	0	0	1136.68	0	24.75	0	24.75
CO	0	0	0	0	0	0	615.73	0	615.73	0	615.73
H_2	0	0	0	0	0	67.00	86.83	0	86.83	0	86.83
H_2O	1334.54	1334.54	0	1334.54	0	0	1157.25	0	1157.25	0	1157.25
C	0	0	0	0	0	574.26	0	0	0	0	0
CH_4	0	0	0	0	0	0	0.012	0	0.012	0	0.012
CaO	0	0	0	0	0	0	0	0	0	1462.78	45.95
$CaCO_3$	0	0	0	0	0	0	0	0	0	0	2528.76
CH_3OH	0	0	0	0	0	0	0	0	0	0	0

	S1	S2	S3	4	5	CAO + CACO	SYNUSER	S5	6	REGENCAO	CO2OUT
Temperature (°C)	25	97.8	25	78.2	25	600	600	200	500	860	30
Pressure (bar)	1	17.5	17.5	4.375	4.375	0.93	0.93	70	1	0.093	1
Total gas flow rate (kg/h)	1884.58	1884.58	1884.58	1884.58	1884.58	–	1884.58	1884.58	2996.51	–	1111.93
Total solid flow rate (kg/h)	–	–	–	–	–	2574.71	–	–	–	1462.78	–
Component flow rate (kg/h)											
O_2	0	0	0	0	0	0	0	0	0	0	0
CO_2	24.75	24.75	24.75	24.75	24.75	0	24.75	24.75	1136.68	0	1111.93
CO	615.73	615.73	615.73	615.73	615.73	0	615.73	615.73	615.73	0	0
H_2	86.83	86.83	86.83	86.83	86.83	0	86.83	86.83	86.83	0	0
H_2O	1157.25	1157.25	1157.25	1157.25	1157.25	0	1157.25	1157.25	1157.25	0	0
C	0	0	0	0	0	0	0	0	0	0	0
CH4	0.012	0.012	0.012	0.012	0.012	0	0.012	0.012	0.012	0	0
CaO	0	0	0	0	0	45.95246	0	0	0	1462.78	0
$CaCO_3$	0	0	0	0	0	2528.758	0	0	0	0	0
CH_3OH	0	0	0	0	0	0	0	0	0	0	0

	7	8	9	10	11	RECYCLE	12	13	14	15	16
Temperature (°C)	–	240	45	45	45	45	220	46.50	164.48	165.79	−35.57
Pressure (bar)	–	90	90	78.13	78.13	78.13	78.15	12	12	12	12
Vapor fraction	–	1	1	1	1	1	1	0	0.1	0	0
Mass flow (kg/h)	–	4024.79	4024.79	1880.89	2143.90	2141.75	2140.21	1880.89	1880.89	1821.89	0.59
Component flow rate (kg/h)											
O_2	–	0	0	0	0	0	0	0	0	0	0
CO_2	–	432.06	432.06	59.39	372.66	372.29	372.230	59.39	59.39	0.96	0.59
CO	–	41.49	41.49	0.56	40.92	40.88	40.88	0.56	0.56	0	0.00084
H_2	–	1651.99	1651.99	0	1651.99	1650.33	1648.88	0	0	0	0
H_2O	–	1159.64	1159.64	1142.89	16.76	16.74	16.73	1142.88	1142.89	1142.89	0
C	–	0	0	0	0	0	0	0	0	0	0
CH4	–	0.13	0.13	0.012	0.11	0.11	0.11	0.012	0.012	0	0
CaO	–	0	0	0	0	0	0	0	0	0	0
$CaCO_3$	–	0	0	0	0	0	0	0	0	0	0
CH_3OH	–	739.49	739.49	678.04	61.45	61.39	61.31	678.04	678.04	678.04	0

	17	18	19	PURGE	20	21	MEOH
Temperature (°C)	−35.57	102.40	83.02	45	14.21	130.70	65
Pressure (bar)	12	2	2.07	78.13	12	2.78	2.07
Vapor fraction	1	0.18	0	1	1	0	0
Mass flow (kg/h)	58.41	1821.89	678.53	2.14	2.14	1143.36	678.53
Component flow rate (kg/h)							
O_2	0	0	0	0	0	0	0
CO_2	57.84	0.96	0.96	0.37	0.37	0	0.96
CO	0.56	0	0	0.041	0.041	0	0
H_2	0	0	0	1.65	1.65	0	0
H_2O	0	1142.88	0.044	0.017	0.017	1142.84	0.044
C	0	0	0	0	0	0	0
CH_4	0.012	0	0	0.00011	0.00011	0	0
CaO	0	0	0	0	0	0	0
$CaCO_3$	0	0	0	0	0	0	0
CH_3OH	0	678.04	677.53	0.061	0.061	0.51	677.53

	CO2FEED	EOFEED	22	23	24	25	26	EC	METFEED	MET-RE	MET
Temperature (°C)	30	30	29.88	60	30	30	31	65	65	64.20	64.17
Pressure (bar)	1	1	1	25	25	25	1	1	1	1	1
Vapor fraction	1	1	1	0.3	0	0	0	0	0.9	0	0.3
Mass flow (kg/h)	440.10	440.53	880.63	880.63	880.63	880.63	880.63	880.63	678.25	1601.20	2279.45

Table 4 (*Continued*)

	CO2FEED	EOFEED	22	23	24	25	26	EC	METFEED	MET-RE	MET
Component flow rate (kg/h)											
CO_2	440.10	0	440.10	440.10	440.10	0.26	0.26	0.26	0.88	0	0.88
EO	0	440.5	440.53	440.53	440.53	0.26	0.26	0.26	0	0	0
MEOH	0	0	0	0	0	0	0	0	677.37	1601.15	2278.53
DMC	0	0	0	0	0	0	0	0	0	0	0
AN	0	0	0	0	0	0	0	0	0	0	0
EG	0	0	0	0	0	0	0	0	0	0	0
EC	0	0	0	0	0	880.11	880.11	880.11	0	0	0

	DMC-MET	EG	EGOUT	ANFEED	AN-RE	AN	ANBOT	DMC-AN	DMC	DMCOUT
Temperature (°C)	63	196.50	30	10	54.50	54.49	183.38	155.18	89.36	30
Pressure (bar)	1	1	1	1	1	1	1	1	1	1
Vapor fraction	0	0	0	0	0	0	0	0	0	0
Mass flow (kg/h)	2502.90	621.64	621.64	1.05	5587.70	5588.75	5587.75	6490.45	902.70	902.70
Component flow rate (kg/h)										
CO_2	0	0	0	0	0	0	0	0	0	0
EO	0	0	0	0	0	0	0	0	0	0
MEOH	1602.11	0	0	0	0	0	0	0.95	0.95	0.95
DMC	900.79	0	0	0	0	0	0	900.76	900.58	900.58
AN	0	0	0	1.05	5587.70	5588.75	5587.56	5588.73	1.17	1.17
EG	0	617.36	617.36	0	0	0	0	0	0	0
EC	0	4.20	4.20	0	0	0	0	0	0	0

Table 5
Overall heat summary of cold and hot stream for DMC and ethylene glycol production (base case study).

Equipment name in each processing step	T_{in} (°C)	T_{out} (°C)	Exothermic Heat (kW)	Endothermic Heat (kW)	MC_P (kW/°C)
Biomass gasification					
Gasifier (BIOMASS-SYNOUT)	900	900	−2504.35		Large
Cooler1 (SYNOUT-6)	900	500	−671.10		1.677
Decomp (RAWBIOMASS-BIOMASS)	25	507.80		2504.35	2.845
Heater (STEAM-GASIFY)	500	600		1374.02	13.740
O_2 separation unit from ITM air separation unit (utility, required pressure 14.28 bar)	25	457.9		65.955	0.1523
O_2 heat supply (utility)	457.9	900		74.516	0.1685
CO_2 separation					
Carbonat (6-SYNCACO3)	500	600	−857.87		8.578
Cooler5 (CO2-CO2out)	860	30	−3250.89		3.916
Calcine (CAO + CACO − CAO + CAO2)	600	860		1,431.82	5.507
Compressor1 (S1-4) (Heat to Electricity efficiency = 55%) [52]	25	78.2		189.67	3.565
Compressor2 (5–S2)	25	97.80		177.71	2.441
Compressor3 (S3–S4)	25	124.10		182.31	1.839
Cooler01 (SYNUSER-S1)	600	25			0.814
Cooler02 (4–5)	78.20	25	−468.06		2.197
Cooler03 (S2–S3)	97.80	25	−116.92		1.337
Heater01 (S4–S5)	124.10	200	−97.35	125.775	1.657
Methanol synthesis					
Methanol (5,12–8)	200	240	−279.68		6.992
Condenser (Distil1) (14–16)	164.48	−35.57	−386.18		1.930
Condenser (Distil2) (18–19)	102.40	83.02	−737.27		38.042
Cooler4 (19-MEOH)	83.02	65	−11.94		0.662
Condense (8–9)	240	45	−2488.13		12.759
Reboiler(Distil1) (14–15)	164.48	165.79		318.27	281.65
Reboiler(Distil2) (18–21)	102.40	130.70		613.93	21.693
Heater1 (RECYCLE-12)	45	220		1,193.80	6.821
Heater2 (13–14)	46.50	164.48		343.05	2.907
Ethylene carbonate synthesis					
ECReactor (24–25)	30	30	−262.45		Large
RCool (23–24)	60	30	−14.33		0.477
ECHeat (26-EC)	31	65		12.71	0.373
Compressor (22–23) (Heat to Electricity efficiency = 55%) [67]	29.88	60		92.22	3.061
Transesterification of ethylene carbonate and methanol					
EGCool	196.50	30	−18.13		0.108
DMCCool	89.36	30	−26.50		0.446
ANCool	183.38	54.50	-462.01		7.846
Condenser (RD)	65	63	−948.38		474.190
Condenser (Extractive distillation)	65	64.20	−811.66		1014.575
Condenser (Entrainer recovery)	155.18	89.36	−257.01		3.904
Reboiler (RD)	65	196.50		781.10	5.939
Reboiler (Extractive distillation)	63	155.18		1261.65	13.595
Reboiler (Entrainer recovery)	155.18	183.38		339.24	12.029

production. Atom efficiency (or atom economy) is a criterion that considers efficiency of a chemical reaction in terms of atoms of reacting substances (for each element separately) that incorporate in the desired product. As for atom efficiency of the base case study, it is found that the atom efficiency is C: 73.20, H: 92.95, O: 58.69. However, with this criterion, atom efficiency does not refer to energy efficiency for the overall chemical process.

3.6. Overall process with an operation under energy self-sufficient condition

Since the feedstock in our study is biomass, it can be used as energy source effectively and can be considered as carbon neutral when consumed. Biomass was utilized as both heat sources and reactant of methanol synthesis. Overall biomass input was split into two lines. The first line was converted into syngas and then synthesized to methanol which is one of the reactants of DMC and ethylene glycol production. The other line of biomass input underwent combustion to generate heat to supply all endothermic equipment in the system. The low heating value (LHV) of biomass was chosen to determine heat generated (Eq. (7)). When the overall process was considered under energy self-sufficient conditions, the calculations of atom efficiency were more circumspect. We therefore propose key performance indicators of biomass to chemical i.e. 1) atom efficiency under energy self-sufficient condition and 2) carbon dioxide fixation from biomass into chemicals under energy self-sufficient condition. Note that atom efficiency of overall process is the percentage of each atom in desired product streams (DMC and EG) to atoms in all input substances (biomass, ethylene oxide, oxygen, steam) while carbon dioxide fixation from biomass into chemicals is a fraction of carbon from biomass that is present in desired chemical products.

The process performance indicators and design specification for DMC production from biomass under energy self-sufficient condition is summarized in Table 6. The appropriate fraction of biomass fed to combustor and gasifier should be 0.62 and 0.38, respectively, in order to sustain the energy of overall process. However, the amount of CO_2 from CO_2 separation unit is more than the required amount for chemical production, some excess of CO_2 was purged from the chemical production process such as purged CO_2 from cyclone in Section B, therefore, a fraction of total CO_2 emission (combustion and purge) from biomass input is 0.74, while carbon dioxide fixation into chemicals is 0.26. Considering atom efficiency (Table 6), it is found that the atom efficiency under energy self-sufficient conditions is C: 35.83, H: 53.19, O: 40.31. The equivalent thermal energy consumptions of the overall process were calculated and can be reported by mass-based allocation to EG co-product as 199 MJ/kg-DMC. Considering only the DMC production section (Section E of Fig. 1), the energy consumption is 5.95 MJ/kg-DMC. According to [11] for the DMC synthesis from ethylene carbonate, based on their calculations with an assumption of heat to electricity efficiency of 55% and mass-based allocation to EG by-product, equivalent thermal energy consumption could be calculated as 9.86 MJ/kg-DMC. The differences between these two processes come from the difference of separation process since our simulated process uses intensive design of reactive distillation along with extractive distillation and including its solvent recovery in the downstream separation, while the process considered by [11] used a conventional reactor and pressure-swing distillation. Our results agreed with [21], who proposed that DMC synthesis process via reactive distillation requires less energy than the pressure-swing distillation, thus lowering operating cost. For the issues of capital cost investment, the economic optimum steady-state designs of a conventional reactor/column/recycle process and a reactive distillation column have been quantitatively compared for a ternary system including two reactants and one product which is reported by [53]. With favorable chemistry and relative volatility, reactive distillation is more economic than a conventional process [54].

3.7. Overall process under energy self-sufficient condition with the design of heat exchanger network (HEN)

The operating condition and system performance of DMC production from biomass under energy self-sufficient condition with integration of heat exchanger network is summarized in Table 6. According to overall heat minimization with heat exchanger network, the energy consumptions could be reduced to 143 MJ/kg-DMC which decreased 28% energy consumption as compared to the process without heat exchanger network. Hot utility is not necessary to supply for heat exchangers because the heat exchanger network can exchange the heat supply completely (as shown in Fig. 10). Fig. 11 shows the relationship between temperature and enthalpy of hot and cold streams of the heat exchanger network, and explains the amount of utility supply, potential heat recovery, and temperature difference of overall system. The maximum energy recovery network for DMC production from biomass yielded the lowest minimum cold utility of 3728.58 kW. Additionally, the ellipse indicated that the hot utility is not required for this system since all cold streams are heated up by the potentially recovered heat.

The appropriate fraction of biomass fed to gasifier should be 0.46 to sustain overall process. A fraction of carbon dioxide fixation from biomass into chemicals of 0.31 could be achieved. Considering atom efficiency (Table 6) of overall process, it was found that the atom efficiency of the process with heat exchanger network indicated higher value (C: 42.29, H: 61.83, O: 45.21) than the process without heat exchanger network since biomass can be converted to methanol effectively, and less portion of biomass needed for combustion as heat sources.

It can be concluded that our DMC and EG production from biomass is a green process, considering that it is carbon neutral with a fraction of carbon dioxide fixation from biomass into chemicals of 0.31.

Table 6
Process performance indicators and design specification for DMC production from biomass under energy self-sufficient condition between with and without heat exchanger network.

Performance indicators	Without HEN	With HEN
Overall biomass mass flow rate (kg/h)	1100	1100
Biomass mass flow rate to the gasifier (kg/h)	415.88	507.37
Biomass mass flow rate to the combustor (kg/h)	684.12	592.63
Biomass fraction to the gasifier	0.38	0.46
Net equivalent thermal energy required for producing 1 kg of DMC production (MJ/kg)	200.67	144.20
Overall efficiency of atom from raw material to product yield (%)	43.11	49.84
Carbon atom efficiency (%)	35.83	42.49
Hydrogen atom efficiency (%)	53.19	61.83
Oxygen atom efficiency (%)	40.31	45.21
CO_2 fixation to chemicals	0.26	0.31

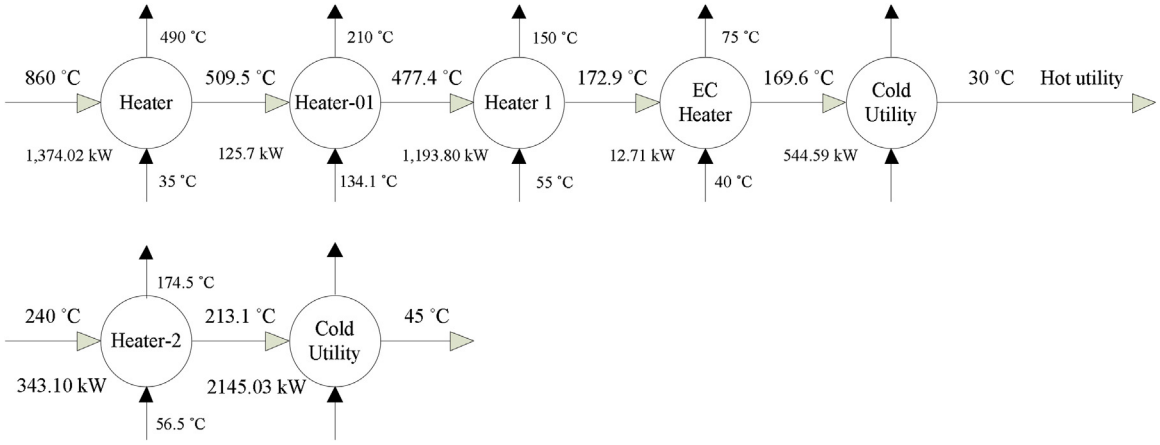

Fig. 10. Heat exchanger network diagram.

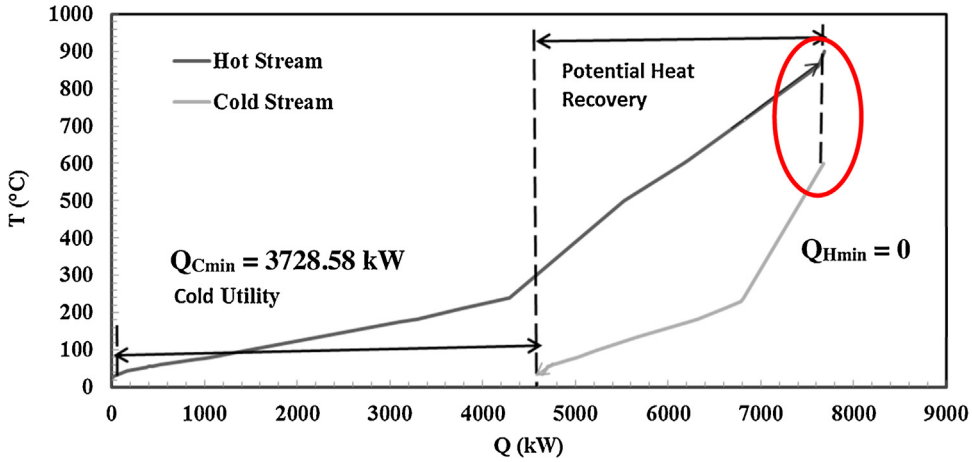

Fig. 11. Composite curve of heat exchanger network.

4. Conclusion

This paper, the overall process for DMC and ethylene glycol production from biomass was simulated using an ASPEN Plus® simulator. The process consisted of five main sections i.e. biomass gasification, CO_2 separation, methanol synthesis, ethylene carbonate synthesis and DMC synthesis. Autothermal gasification of biomass took place in the gasifier. The product stream was further processed for CO_2 separation to produce a mixture of H_2 and CO before entering to methanol production process. The separated CO_2 was reacted with ethylene oxide to produce ethylene carbonate. DMC and ethylene glycol was simultaneously synthesized via transesterification of methanol and ethylene carbonate in reactive distillation. The proposed process was capable of producing high-purity DMC and ethylene glycol (99.5% purity). Overall energy consumption of this system was optimized using design specification, and found the equivalent thermal energy consumption to be 199 MJ/kg-DMC. The atom efficiency of the optimal base case study was found to be C: 73.20, H: 92.95, O: 58.69.

In addition, the operation of overall process under energy self-sufficient conditions supplied by biomass itself only has been developed, and therefore the process could be considered as carbon neutral. Key performance indicators of biomass to chemical i.e. 1) atom efficiency under energy self-sufficient condition and 2) carbon dioxide fixation from biomass into chemicals under energy self-sufficient condition were considered. It was found that the atom efficiency of C: 35.83, H: 53.19, O: 40.31 with carbon dioxide fixation from biomass into chemicals value of 0.26 could be achieved under energy self-sufficient conditions.

Furthermore, when heat exchanger network was considered, heat utilization to produce DMC and EG could be effectively decreased to 143 MJ/kg-DMC. The atom efficiency of process with heat exchanger network indicated higher values (C: 42.29, H: 61.83, O: 45.21) than the process without heat exchanger network since less biomass was required for combustion to provide heat sources. With heat exchanger network, a fraction of carbon dioxide fixation from biomass into chemicals could be increased to 0.31.

Acknowledgment

Financial support from The Thailand Research Fund (Distinguished Research Professor Award, DPG5880003) and PTT Group Research Scholar from PTT Group Frontier Research Center is gratefully acknowledged. P. Kongpanna and S. Assabumrungrat would like to acknowledge the Ph.D. scholarship grants provided by Dussadeepipat Scholarship, Chulalongkorn University. Department of Chemical, Faculty of Engineering, Chulalongkorn University would like to acknowledge The Institutional Research Grant (The Thailand Research Fund), IRG 5780014, and Chulalongkorn University, Contract No. RES_57_411_21_076.

References

[1] E. Sorguven, M. Ozilgen, Energy utilization, carbon dioxide emission, and exergy loss in flavored yogurt production process, Energy 40 (2012) 214–225.
[2] J.Q. Wang, J. Sun, C.Y. Shi, W.G. Cheng, X.P. Zhang, S.J. Zhang, Synthesis of dimethyl carbonate from CO_2 and ethylene oxide catalyzed by K_2CO_3-based binary salts in the presence of H_2O, Green Chem. 13 (2011) 3213–3217.
[3] W. Wang, S. Wang, X. Ma, J. Gong, Recent advances in catalytic hydrogenation of carbon dioxide, Chem. Soc. Rev. 40 (2011) 3703–3727.
[4] L. Chapman, Transport and climate change: a review, J. Transp. Geogr. 15 (2007) 354–367.
[5] R.J. Stouffer, J. Yin, J.M. Gregory, K.W. Dixon, M.J. Spelman, W. Hurlin, A.J. Weaver, M. Eby, G.M. Flato, H. Hasumi, A. Hu, J.H. Jungclaus, I. Kamenkovich V, A. Levermann, M. Montoya, S. Murakami, S. Nawrath, A. Oka, W.R. Peltier, D.Y. Robitaille, A. Sokolov, G. Vettoretti, S.L. Weber, Investigating the causes of the response of the thermohaline circulation to past and future climate changes, J. Clim. 19 (2006) 1365–1387.
[6] J.E. Hansen, M. Sato, A. Lacis, R. Ruedy, I. Tegen, E. Matthews, Climate forcings in the Industrial era, Proc. Natl. Acad. Sci. 95 (1998) 12753–12758.
[7] M. Aresta. Carbon dioxide as chemical feedstock (2010) doi:10.1002/9783527629916.
[8] G.A. Olah, A. Goeppert, G.K.S. Prakash. Beyond oil and gas: the methanol economy: second edition (2009).
[9] T. Sakakura, J.C. Choi, H. Yasuda, Transformation of carbon dioxide, Chem. Rev. 107 (2007) 2365–2387.
[10] C.S. Song, Global challenges and strategies for control, conversion and utilization of CO_2 for sustainable development involving energy, catalysis, adsorption and chemical processing, Catal. Today 115 (2006) 2–32.
[11] P. Kongpanna, V. Pavarajarn, R. Gani, S. Assabumrungrat, Techno-economic evaluation of different CO_2-based processes for dimethyl carbonate production, Chem. Eng. Res. Des. 93 (2015) 496–510.
[12] D. Delledonne, F. Rivetti, U. Romano, Developments in the production and application of dimethylcarbonate, Appl. Catal. A 221 (2001) 241–251.
[13] P. Tundo, M. Selva, The chemistry of dimethyl carbonate, Acc. Chem. Res. 35 (2002) 706–716.
[14] M.A. Pacheco, C.L. Marshall, Review of dimethyl carbonate (DMC) manufacture and its characteristics as a fuel additive, Energy Fuels 11 (1997) 2–29.
[15] L. Ube Industries. Ube Industries to Establish Joint Venture for Dimethyl Carbonate in China (2012).
[16] X.C. Guo, Z.F. Qin, G.F. Wang, J.G. Wang, Critical temperatures and pressures of reacting mixture in synthesis of dimethyl carbonate with methanol and carbon dioxide, Chinese Chem. Lett. 19 (2008) 249–252.
[17] H. Wang, B. Lu, X. Wang, J. Zhang, Q. Cai, Highly selective synthesis of dimethyl carbonate from urea and methanol catalyzed by ionic liquids, Fuel Process. Technol. 90 (2009) 1198–1201.
[18] J.Q. Wang, J. Sun, C.Y. Shi, W.G. Cheng, X.P. Zhang, S.J. Zhang, Synthesis of dimethyl carbonate from CO_2 and ethylene oxide catalyzed by K_2CO_3-based binary salts in the presence of H_2O, Green Chem. 13 (2011) 3213–3217.
[19] W. Wang, S. Wang, X. Ma, J. Gong, Recent advances in catalytic hydrogenation of carbon dioxide, Chem. Soc. Rev. 40 (2011) 3703–3727.
[20] K.Y. Hsu, Y.C. Hsiao, I.L. Chien, Design and control of dimethyl carbonate-Methanol separation via extractive distillation in the dimethyl carbonate reactive-Distillation process, Ind. Eng. Chem. Res. 49 (2010) 735–749.
[21] S.J. Wang, C.C. Yu, H.-P. Huang, Plant-wide design and control of DMC synthesis process via reactive distillation and thermally coupled extractive distillation, Comput. Chem. Eng. 34 (2010) 361–373.
[22] X.B. Lu, R. He, C.X. Bai, Synthesis of ethylene carbonate from supercritical carbon dioxide/ethylene oxide mixture in the presence of bifunctional catalyst, J. Mol. Catal. A Chem. 186 (2002) 1–11.
[23] C.N. Hamelinck, A.P.C. Faaij, Future prospects for production of methanol and hydrogen from biomass, J. Power Sources 111 (2002) 1–22.
[24] Kaneko S., Sato S., Kobayashi Y., Kabata T., Kobayashi K., Takeuchi Y., Tokuda K., Hashimoto A., Shinoda K., Takeno K., 2006. Biomass gasifycation furnace and system for methanol synthesis using gas produced by gasifying biomass. Patent No: US 6,991, 769 B2.
[25] J.P. Lange, Methanol synthesis: a short review of technology improvements, Catal. Today 64 (2001) 3–8.
[26] X.L. Yin, D.Y.C. Leung, J. Chang, J.F. Wang, Y. Fu, C.Z. Wu, Characteristics of the synthesis of methanol using biomass-derived syngas, Energy Fuels 19 (2005) 305–310.
[27] Dyer, N. Paul, Robin E. Richards, Steven L. Russek, M. Dale, Troyer. Ion transport membrane technology for oxygen separation and syngas production, Solid State Ionics 134 (2000) 21–33.
[28] A. Melgar, J.F. Perez, H. Laget, A. Horillo, Thermochemical equilibrium modelling of a gasifying process, Energy Convers. Manag. 48 (2007) 59–67.
[29] A. Ravikiran, T. Renganathan, S. Pushpavanam, R.K. Voolapalli, Y.S. Cho, Generalized analysis of gasifier performance using equilibrium modeling, Ind. Eng. Chem. Res. 51 (2012) 1601–1611.
[30] T.B. Reed, A. Das, Handbook of Biomass Downdraft Gasifier Engine Systems, Biomass Energy Foundation Press, 1988.
[31] P. Chaiwatanodom, S. Vivanpatarakij, S. Assabumrungrat, Thermodynamic analysis of biomass gasification with CO_2 recycle for synthesis gas production, Appl. Energy 114 (2014) 10–17.
[32] K.M. Holmgren, T. Berntsson, E. Andersson, T. Rydberg, System aspects of biomass gasification with methanol synthesis – Process concepts and energy analysis, Energy 45 (2012) 817–828.
[33] C.S. Martavaltzi, E.P. Pampaka, E.S. Korkakaki, A.A. Lemonidou, Hydrogen production via steam reforming of methane with simultaneous CO_2 capture over CaO-$Ca_{12}Al_{14}O_{33}$, Energy Fuels 24 (2010) 2589–2595.
[34] J.T. Sun, I.S. Metcalfe, M. Sahibzada, Deactivation of Cu/ZnO/Al_2O_3 methanol synthesis catalyst by sintering, Ind. Eng. Chem. Res. 38 (1999) 3868–3872.
[35] N.O. Elbashir, Prospect of success in scaling-up fischer-tropsch synthesis reactor operates in near-critical and supercritical phase media, AIChE 100–2008 AIChE Annu. Meet. Conf. Proc (2008).
[36] F. Israel Gomez-Castro, V. Rico-Ramirez, J. Gabriel Segovia-Hernandez, S. Hernandez, Feasibility study of a thermally coupled reactive distillation process for biodiesel production, Chem. Eng. Process. 49 (2010) 262–269.
[37] F. Israel Gomez-Castro, V. Rico-Ramirez, J. Gabriel Segovia-Hernandez, S. Hernandez-Castro, Esterification of fatty acids in a thermally coupled reactive distillation column by the two-step supercritical methanol method, Chem. Eng. Res. Des. 89 (2011) 480–490.
[38] E. Johansson, Process Integration Study of Biomass-tomethanol (via Gasification) and Methanol-to Olefins (MTO) Processes in an Existing Steam Cracker Plant, Chalmers University of Technology, Göteborg, Sweden, 2013.
[39] K.S. Ng, J. Sadhukhan, Process integration and economic analysis of bio-oil platform for the production of methanol and combined heat and power, Biomass Bioenergy 35 (2011) 1153–1169.
[40] Y.J. Fang, W.D. Xiao, Experimental and modeling studies on a homogeneous reactive distillation system for dimethyl carbonate synthesis by transesterification, Sep. Purif. Technol. 34 (2004) 255–263.
[41] J.B. Jensen, S. Skogestad, Problems with specifying Delta T-min in the design of processes with heat exchangers, Ind. Eng. Chem. Res. 47 (2008) 3071–3075.
[42] A. Kumar, D.D. Jones, M.A. Hanna, Thermochemical biomass gasification: a review of the current status of the technology, Energies 2 (2009) 556–581.
[43] T. Song, J. Wu, L. Shen, J. Xiao, Experimental investigation on hydrogen production from biomass gasification in interconnected fluidized beds, Biomass Bioenergy 36 (2012) 258–267.
[44] C. Franco, F. Pinto, I. Gulyurtlu, I. Cabrita, The study of reactions influencing the biomass steam gasification process, Fuel 82 (2003) 835–842.
[45] P.M. Lv, Z.H. Xiong, J. Chang, C.Z. Wu, Y. Chen, J.X. Zhu, An experimental study on biomass air-steam gasification in a fluidized bed, Bioresour. Technol. 95 (2004) 95–101.
[46] M. Ryden, P. Ramos, H_2 production with CO_2 capture by sorption enhanced chemical-looping reforming using NiO as oxygen carrier and CaO as CO_2 sorbent, Fuel Process. Technol. 96 (2012) 27–36.
[47] N. Poboss, K. Swiecki, A. Charitos, C. Hawthorne, M. Zieba, G. Scheffknecht, Experimental investigation of the absorption enhanced reforming of biomass in a 20 kWth dual fluidized bed system, Int. J, Thermodyn. 15 (2012) 53.
[48] P. Phromprasit, J. Powell, S. Assabumrungrat, Metals (Mg, Sr and Al) modified CaO based sorbent for CO_2 sorption/ desorption stability in fixed bed reactor for high temperature application, Chem. Eng. J. 284 (2016) 1212–1223.
[49] B. Dou, C. Wang, Y. Song, H. Chen, B. Jiang, M. Yang, Y. Xu, 2016, Solid sorbents for in-situ CO_2 removal during sorption-enhanced steam reforming process: A review, Renewable Sustainable Energy Rev. 53 (2016) 536–546.
[50] X.J. Feng, X.G. Li, R. He, H. Zhou, A new process for synthesis of dimethyl carbonate from ethylene carbonate and methanol without any catalyst under supercritical conditions, Chin. Chem. Lett. 16 (2005) 767–770.
[51] D.L. Chase, Combined-cycle development evolution and future, GE Power Syst. GER 4206 (2001) 5–6.
[52] D.B.G. Williams, M.S. Sibiya, P.S. Van Heerden, M. Kirk, R. Harris, Verkade super base-catalysed transesterification of propylene carbonate with methanol to co-produce dimethyl carbonate and propylene glycol, J. Mol. Catal. A Chem. 304 (2009) 147–152.
[53] D.B. Kaymak, D. Yılmaz, S. Yılmaz, E. Hoşgör, Quantitative comparison of reactor/column/recycle process with reactive distillation column for ternary systems, in: S. Pierucci, G. Buzzi Ferraris (Eds.), 20th European Symposium on Computer Aided Process Engineering – ESCAPE20, 2010.
[54] W.L. Luyben, C.C, Yu. Reactive Distillation Design and Control. 574. ISBN: 978-0-470-22612-4.

Accepted Manuscript

H_2 production from sorption enhanced steam reforming of biogas using multi-functional catalysts of Ni over Zr-, Ce- and La-modified CaO sorbents

Janewit Phromprasit, Jon Powell, Suwimol Wongsakulphasatch, Worapon Kiatkittipong, Palang Bumroongsakulsawat, Suttichai Assabumrungrat

PII: S1385-8947(16)31613-8
DOI: http://dx.doi.org/10.1016/j.cej.2016.11.051
Reference: CEJ 16052

To appear in: *Chemical Engineering Journal*

Received Date: 13 August 2016
Revised Date: 21 October 2016
Accepted Date: 6 November 2016

Please cite this article as: J. Phromprasit, J. Powell, S. Wongsakulphasatch, W. Kiatkittipong, P. Bumroongsakulsawat, S. Assabumrungrat, H_2 production from sorption enhanced steam reforming of biogas using multifunctional catalysts of Ni over Zr-, Ce- and La-modified CaO sorbents, *Chemical Engineering Journal* (2016), doi: http://dx.doi.org/10.1016/j.cej.2016.11.051

This is a PDF file of an unedited manuscript that has been accepted for publication. As a service to our customers we are providing this early version of the manuscript. The manuscript will undergo copyediting, typesetting, and review of the resulting proof before it is published in its final form. Please note that during the production process errors may be discovered which could affect the content, and all legal disclaimers that apply to the journal pertain.

ACCEPTED MANUSCRIPT

Revised Manuscript No.: CEJ-D-16-05578R1

Type of contribution: Research paper

H_2 production from sorption enhanced steam reforming of biogas using multifunctional catalysts of Ni over Zr-, Ce- and La-modified CaO sorbents

Janewit Phromprasit[1], Jon Powell[2], Suwimol Wongsakulphasatch[3], Worapon Kiatkittipong[4], Palang Bumroongsakulsawat[1], Suttichai Assabumrungrat[1,*]

[1] Center of Excellence in Catalysis and Catalytic Reaction Engineering, Department of Chemical Engineering, Faculty of Engineering, Chulalongkorn University, Bangkok 10330, Thailand

[2] Department of Chemical & Environmental Engineering, The University of Nottingham Ningbo China, 199 Taikang East Road, Ningbo, 315100, China

[3] Department of Chemical Engineering, Faculty of Engineering, King Mongkut's University of Technology North Bangkok, Bangkok 10800, Thailand

[4] Department of Chemical Engineering, Faculty of Engineering and Industrial Technology, Silpakorn University, Nakhon Pathom 73000, Thailand

* Corresponding author (Suttichai.A@chula.ac.th)

ACCEPTED MANUSCRIPT

Abstract

Sorption enhanced steam reforming of biogas is a promising process for H_2 production by which biogas steam reforming is combined with simultaneous CO_2 capture in a single unit operation. In the first part, Zr^{4+}, Ce^{4+} and La^{3+} were doped on CaO and tested the performance for 10 CO_2 sorption/desorption cycles. Zr-CaO and Ce-CaO offered a stable CO_2 capture activity for at least 10 cycles (CO_2 sorption capacity of 0.30 and 0.22 $g_{CO_2}/ g_{sorbent}$ at the 1st cycle, and 0.29 and 0.23 $g_{CO_2}/ g_{sorbent}$ at the 10th cycle for Zr-CaO and Ce-CaO, respectively). On the other hand, La-CaO indicated decreasing of CO_2 sorption capacity about 16% over 10 cycle operations. This is due to the Zr-CaO and Ce-CaO presented oxygen storage at low temperature which is characterized by temperature program reduction oxidation (TPRO). This behavior promotes the CO_2 diffusion from the surface to the bulk (sorption) and the bulk to the surface (desorption) of the modified CaO. In the second part, Ni^{2+} was loaded on the modified sorbents for H_2 production. Ni-Zr-CaO and Ni-Ce-CaO can enable the production of H_2 with purities of approximately 90% and 85%, respectively, with repeating cycles; however, the CH_4 conversions decreased significantly over five cycles (the post-breakthrough period CH_4 conversion of Ni-Zr-CaO and Ni-Ce-CaO decreased from 65.6 and 56.3% during the 1st cycle to 33.0 and 28.9% during the 5th cycle). This is because the Ni active sites at the surface of multifunctional catalysts were lost (as confirmed by XPS results) by pore closure (as shown in SEM images) which was possibly due to the $CaCO_3$ formation.

Keywords:

H_2 production; sorption enhanced steam reforming; CO_2 capture; multifunctional catalyst; CaO; Biogas

ACCEPTED MANUSCRIPT

1. Introduction

The majority of the world's energy demands are currently met by energy production from fossil fuels such as oil, natural gas and coal [1, 2], which are known to produce moderate to severe environmental impacts and are non-renewable. Alternatively, hydrogen is a promising energy carrier which may be used for electrical power generation and transportation [3, 4] due to its high conversion efficiency, recyclability and low pollution at the point of use [2]. Hydrogen can be produced by but are not limited to the electrolysis of water [5, 6], steam reforming [7-11], partial oxidation reforming [7, 12, 13], autothermal reforming [14, 15] and photocatalysis of water [16-18].

The most prominent route for hydrogen production is steam methane reforming (SMR, Eqs. 1-3), which ultimately renders hydrogen non-renewable unless methane is derived from renewable sources such as biogas. Despite the maturity of the technology, there are still a number of issues; (i) the overall reaction is highly endothermic and hence highly energy-demanding; (ii) its product stream is often a mixture of H_2, CO and CO_2; (iii) the conversion of CH_4 is limited by equilibrium, with low pressures and high temperatures promoting the production of hydrogen.

All these three problems can be mitigated by sorption enhanced steam methane reforming (SESMR), which combines the highly endothermic SMR and exothermic CO_2 sorption in a single unit. This reduces the overall enthalpy change of the process and hence the energy demand. Furthermore, the product stream has a higher concentration of H_2 due to in situ CO_2 removal, which offers an additional benefit of shifting the SMR reaction forward.

Steam methane reforming (SMR): $CH_4 + H_2O \leftrightarrow CO + 3H_2$ (1)

Water gas shift (WGS): $CO + H_2O \leftrightarrow CO_2 + H_2$ (2)

Overall: $CH_4 + 2H_2O \leftrightarrow CO_2 + 4H_2$ (3)

ACCEPTED MANUSCRIPT

CO_2 sorbents for SESMR must be able to adsorb and/or absorb CO_2 at high temperatures (> 600 °C). Those that meet this criterion are hydrotalcite [19-21], lithium metal oxide [22, 23] and calcium oxide. The highest CO_2 sorption capacity of 0.49 $g_{CO_2}/g_{Sorbent}$ is achieved with CaO when compared with 0.27 $g_{CO_2}/g_{Sorbent}$ of lithium-based sorbents (Li_2ZrO_3) at 575 °C. However, the CO_2 sorption capacity of CaO decreases after multiple cycles of sorption/desorption [24, 25]. The reduction of CO_2 sorption capacity is associated with an increase in CaO grain sizes and the formation of a $CaCO_3$ layer on the sorbent surface, reducing the CO_2 adsorption rate and inhibiting CO_2 solid state diffusion, hence reducing the CO_2 capture capacity over multiple-cycles [26-28]. Therefore, to increase the stability of CaO, the effects of incorporating different metal ions into CaO have been investigated. Metal ions investigated include Al^{3+} [25, 29-33], Y^{3+} [34], Zr^{4+} [27, 29, 35, 36], La^{3+} [37], Mg^{2+} [25, 28], Ti^{4+} [27, 29] and Si^{4+} [27, 38]. These metal ions were selected based on their Tammann temperatures, the minimum temperature at which the ions, atoms or molecules of a solid acquire sufficient energy for bulk mobility and thus take part in solid state reactions and sintering. An approximate value of Tammann temperature is half of its melting temperature in Kelvin [39, 40]. The Tammann temperatures of the metal oxides are presented in Fig. 1.

Compounds of Al^{3+}, Ca^{2+} and O^{2-} can take several forms including $Ca_5Al_6O_{14}$, $Ca_9Al_6O_{18}$ and $Ca_{12}Al_{14}O_{33}$. All of these formations have been investigated and shown to act as inert phases enhancing the CO_2 sorption capacity of CaO. Xu *et al*. [41] studied the complex catalyst (Ni/CaO-$Ca_5Al_6O_{14}$) in sorption enhanced steam methane reforming involving CO_2 sorption and H_2 production. They found that Ni/CaO-$Ca_5Al_6O_{14}$ improved the durability of the sorbent for high temperature CO_2 sorption during 50 carbonation-calcination cycles. This is due to the presence of $Ca_5Al_6O_{14}$, which inhibits the sintering of CaO particles at high temperatures during calcination. The best catalytic performance of H_2 production was

ACCEPTED MANUSCRIPT

achieved with Ni/CaO-$Ca_5Al_6O_{14}$ containing 15 wt% Ni, 61.7 wt% CaO and 23.3 wt% $Ca_5Al_6O_{14}$ and remains consistent over 20 cycles.

CaO-$Ca_9Al_6O_{18}$ sorbent for CO_2 sorption was investigated by Xie *et al*. [42]. The material's high stability for CO_2 sorption/desorption was demonstrated by 50 carbonation/calcination cycles at 650 °C after which 83% of its initial sorption capacity was retained. Martavaltzi *et al*. [43] studied a mixture of nickel based catalyst and CaO-$Ca_{12}Al_{14}O_{33}$ sorbent at a ratio of 85:15 for sorption enhanced steam methane reforming. The results showed that more than 93% CH_4 conversion was obtained at 650 °C, 1 bar and a steam to methane ratio (S/M ratio) of 3.4. Moreover, a hydrogen purity greater than 92% was achieved in this SESMR, compared to the 77% hydrogen purity achieved with conventional steam reforming.

Lu *et al*. [27] investigated the addition of Si^{4+}, Ti^{4+}, Cr^{3+}, Co^{2+}, Zr^{4+} and Ce^{4+} to CaO for CO_2 sorption. The results indicated that Zr-CaO sorbent offers the best overall CO_2 sorption performance. At a Zr:Ca ratio of 3:10, the sorption capacity was stable for 100 cycles; 64% molar conversion of CaO was maintained. It was proposed that ZrO_2 reacted with CaO to form $CaZrO_3$, the presence of which inhibited the growth of CaO grains.

Wu and Wang [35] investigated the use of a ZrO_2 modified Ni-nano-Al-CaO complex catalyst in sorption enhanced steam methane reforming. The results showed no significant difference in the H_2 purities and CH_4 conversions obtained from the ZrO_2 modified Ni-Al-CaO and Ni-Al-CaO in the pre-breakthrough period (H_2 purity of 97.3% and 96.8%, and CH_4 conversion of 93.7% and 93.4%, respectively). However, the H_2 purity and CH_4 conversion from the Ni-Al-CaO decreased sharply within the first 10-minutes of operation to 48% and 22%, respectively. The authors argued that the observed difference between the two materials

ACCEPTED MANUSCRIPT

was due to ZrO_2 preventing the formation of $NiAl_2O_4$ in the sorption complex catalyst and thus improving its operating stability.

The role of Zr, Ce and La for catalytic behavior has also been investigated for CO_2 conversion [44-47]. Liu et al. [44] showed that the specific surface area of a Cu-Fe-Zr/HZSM-5 could be improved by adding Zr and hence H_2 and CO_2 adsorption capacity on metal active sites was enhanced. Ce and La were found to be able to promote metal dispersion and reduce the reduction temperature [46, 47]. As a consequence, in this work, doping of Zr, Ce and La on CaO is of interest in order to improve the stability of CaO sorbent and H_2 production especially when employing multiple cycle operations.

Steam reforming can be performed with various raw materials such as methane [48-50], methanol [51, 52], ethanol [53-56] and biogas [57, 58]. Biogas is an interesting feedstock for hydrogen production as it is renewable. However, the presence of high CO_2 contents in biogas (27-44% CO_2, 55-70% CH_4, <1% H_2 and <3% H_2S as well as traces of NH_3 [58]) decreases the heating value and flame stability of the gas mixture. To produce hydrogen from biogas, apart from the steam methane reforming (Eq. (1)), the dry methane reforming (Eq. (4)) also occurs. The application of sorption enhanced reforming to hydrogen production from biogas is challenging due to the high CO_2 content and so further investigation is required.

Dry methane reforming: $CH_4 + CO_2 \leftrightarrow 2CO + 2H_2$ (4)

The work reported in this paper is composed of two investigations: (i) CO_2 sorption/desorption and (ii) H_2 production by sorption enhanced steam reforming of synthetic biogas. In the first part, CaO was doped with various metal ions (Zr^{4+}, Ce^{4+} and La^{3+}), of which the corresponding metal oxides have Tammann temperatures greater than the calcination temperature (900 °C), by hydration followed by wet mixing and tested over

ACCEPTED MANUSCRIPT

multiple operation cycles. Hydrogen production was conducted with three modified sorbents (Ni-Zr-CaO, Ni-Ce-CaO and Ni-La-CaO).

2. Experimental

2.1 Preparation of modified sorbent and multifunctional catalyst

The metal modified sorbents (Zr-CaO, Ce-CaO and La-CaO) were synthesized by CaO hydration followed by wet mixing. Firstly, CaO was added to DI water and stirred at a 75 °C for 2 h. Metal precursors: zirconium (IV) oxynitrate hydrate (Aldrich), cerium (III) nitrate hexahydrate (Aldrich) or lanthanum (III) nitrate hexahydrate (Fluka) were dissolved in DI water and then added to the CaO suspensions. They were stirred further for 2 h at 75 °C, dried at 100 °C overnight and calcined at 900 °C for 3 h in flowing air. The multifunctional catalysts Ni-Zr-CaO, Ni-Ce-CaO and Ni-La-CaO were prepared by a similar method with nickel (II) nitrate hexahydrate (Sigma-Aldrich) as a Ni precursor in addition to the metal precursors which were dissolved in the DI water and added to the CaO suspension which was stirred at 75 °C for 2 h. After that the mixture was stirred at 75 °C for 2 h, followed by drying at 100 °C overnight and calcination at 900 °C for 3 h under air flow.

2.2 Characterization of modified sorbent and multifunctional catalyst

The surface area of the samples was determined by the Brunauer-Emmett-Teller (BET) adsorption of nitrogen. Pore sizes and pore volumes of the samples were analyzed from the desorption isotherms with Barret-Joyner-Halender (BJH). The phases and crystallite sizes of the modified sorbents and multifunctional catalysts were studied with X-ray diffraction (XRD, D8 Advance, Bruker, equipped with a long fine focus Cu K_α X ray source). The XRD patterns were recorded at $10° < 2\theta < 80°$ with a step of 0.04°, a wavelength of

ACCEPTED MANUSCRIPT

1.54056 nm and a scan speed of 0.5 s/step. The morphology of the modified sorbents and multifunctional catalysts were examined with a scanning electron microscope (SEM, Hitachi S-3400N). The atomic concentrations of metals at the surface of the multifunctional catalysts were determined by X-ray photoelectron spectroscopy (XPS, Kratos Amiccus). The analyses were carried out with a Mg K_α X-ray source under a working pressure of 1×10^{-6} Pa at a current of 20 mA and a voltage of 12 kV. The reducibility of the multifunctional catalysts was analyzed by temperature-programmed reduction (TPR).

The TPR samples were placed in a fixed bed quartz reactor connected to a mass spectrometer for analysis of gaseous products (H_2 and N_2) at the outlet stream. For each experiment, 0.5 g of a sample was packed in the reactor and pretreated at 850 °C for 30 min under N_2 flow to remove water and other contaminants. TPR profiles were recorded while the samples were heated from room temperature to 900 °C at a heating rate of 10 °C/min under 10% v/v H_2/N_2 flowing at 50 mL/min. The samples were then cooled to room temperature and after that 10% v/v O_2/N_2 was fed to the reactor to determine oxygen mobility and oxygen storage. Temperature-programmed reduction oxidation (TPRO) profiles were recorded by heating the samples from room temperature to 900 °C at a heating rate of 10 °C/min [59].

2.3 CO_2 sorption/desorption

Sorption/desorption experiments were performed in a fixed bed quartz reactor (15 mm inner diameter, 18 mm outer diameter and 500 mm length). One gram of the modified sorbent (Zr-CaO, Ce-CaO or La-CaO) was sandwiched between quartz wool in the fixed bed quartz reactor. The sorbents were pretreated at 850 °C for 30 min under flowing N_2. 15% v/v CO_2 balanced with N_2 was fed to the reactor at a total flow rate of 60 mL/min, 600 °C and 1 atm. Outlet gas products were collected and analyzed by the mass spectrometer. The modified

ACCEPTED MANUSCRIPT

sorbents were regenerated at 850 °C for 30 min under N_2 flow to desorb the CO_2 captured in the $CaCO_3$. The carbonation/calcination cycles were performed 10 times.

2.4 H_2 production

Two grams of the multifunctional catalysts (Ni-Zr-CaO, Ni-Ce-CaO or Ni-La-CaO) were placed in the fixed bed quartz reactor, supported by quartz wool. The multifunctional catalyst was pretreated at 850 °C for 30 min under 100% N_2 flow and then reduced by 10% v/v H_2 in N_2 at 850 °C for 1 h. The temperature was then reduced to the reaction temperature of 600 °C. The simulated biogas composition used in this work had a CH_4:CO_2 molar ratio of 3:2 [60]. The other operating conditions were: a steam to methane molar ratio (*S/C*) of 3:1 (18 mL/min of steam and 6 mL/min of methane balanced with 22 mL/min of N_2), a total flow rate of 50 mL/min, a temperature of 600 °C and a pressure of 1 atm. The product gas compositions were measured using a gas chromatogram (GC-8A, SHIMADZU) equipped with two columns - Molecular Sieve 5A and PoraPLOT Q. The methane conversion was determined by Eq. 5.

$$\mathrm{CH_4 conversion}\ (\%) = \frac{F_{\mathrm{CH_4,\ in}} - F_{\mathrm{CH_4,\ out}}}{F_{\mathrm{CH_4,\ in}}} \times 100\% \quad (5)$$

Where $F_{\mathrm{CH_4,\ in}}$ is the molar flow rate of methane at the inlet stream (mol/min) and $F_{\mathrm{CH_4,\ out}}$ is the molar flow rate of methane at the outlet stream (mol/min).

3. Results and discussion

3.1 CO_2 sorption stability

XRD patterns of the modified CaO sorbents are shown in Fig. 2. These results indicate that, for fresh materials, (i) the Zr-CaO sorbent contained CaO, as well as a complex

ACCEPTED MANUSCRIPT

phase ($CaZrO_3$) formed by a reaction between CaO and ZrO_2 as shown in Eq. 6; (ii) the Ce-CaO sorbent contained separate CaO and CeO_2 phases and (iii) the La-CaO sorbent also contained CaO and La_2O_3 phases. Then, the modified sorbents were tested in multiple CO_2 sorption/desorption cycles in the fixed bed quartz reactor.

$$CaO + ZrO_2 \rightarrow CaZrO_3 \quad (6)$$

The CO_2 sorption/desorption performances of Zr^{4+}, Ce^{4+} and La^{3+} modified CaO are shown in Fig. 3. The results indicate that the Zr-CaO and Ce-CaO sorbents possess the most stable sorption capacities, with CO_2 capacities of 0.306 and 0.224 $g_{CO_2}/g_{Sorbent}$ after the 1st cycle and 0.284 and 0.234 $g_{CO_2}/g_{Sorbent}$ after the 10th cycle, respectively. However, the La-CaO sorbent exhibited a significant decrease in its CO_2 sorption capacity from 0.293 $g_{CO_2}/g_{Sorbent}$ after the 1st cycle to 0.246 $g_{CO_2}/g_{Sorbent}$ after the 10th cycle, showing a 16% decrease. The decrease in the sorption capacity of La-CaO sorbent is possibly due to the partial densification due to volume expansion of $CaCO_3$, resulting in pore closures as evidenced by the SEM images (Fig.4) and the observed change in $CaCO_3$ content as shown by the XRD results (Fig. 2). Fig. 4(f) shows an SEM image of the used La-CaO sorbent, which indicates the partial densification (red outline) in comparison with the image of the fresh sample in Fig. 4(e). Noted that, the sintering of CaO was not observed as confirmed by the similar CaO crystallite sizes of both the fresh and used sorbents (Table 1).

Although, the Zr-CaO and Ce-CaO sorbents exhibited stable CO_2 sorption capacities over multiple cycles, the partial densification was observed nevertheless. The SEM images of the Zr-CaO (Figs. 4(a) and (b)) and Ce-CaO (Figs. 4(c) and (d)) show small partially densified regions. This phenomenon can be explained by the volume expansion due to the formation of $CaCO_3$ (confirmed by XRD results presented in Fig. 2), and the subsequent closure of void spaces between particles. However, the Zr-CaO and Ce-CaO sorbents possess

ACCEPTED MANUSCRIPT

a low-temperature oxygen storage capability, as characterized by temperature program reduction oxidation (TPRO) (Fig. 5 and Table 2). The low-temperature oxygen storage results in the availability of relatively mobile oxygen atoms compared to the oxygen stored at higher temperatures. This characteristic leads to the promotion of CO_2 diffusion between the surface and bulk of modified CaO. Furthermore, the sorption capacities of Ce-CaO sorbent were shown to be more stable than those of the Zr-CaO sorbent between the 1st and 10th cycle because Ce-CaO has oxygen storage at low temperature of 1.76 mmol/g which is higher than that of Zr-CaO sorbent of 0.04 mmol/g. However, the Zr-CaO sorbent has a higher sorption capacity, which the authors argue is probably due to its higher BET surface area of 17.7 m^2/g compared to that of Ce-CaO of 8.2 m^2/g. A higher surface area implies a greater number of active sites for CO_2 sorption. This has been reported in several investigations [27, 32, 36]. The formation of $CaCO_3$ observed for all sorbents after 10 CO_2 sorption/desorption operations is a result of the reaction of CaO with CO_2:

$$CaO + CO_2 \leftrightarrow CaCO_3 \quad (7)$$

3.2 H_2 production

The multifunctional catalysts Ni-Zr-CaO, Ni-Ce-CaO and Ni-La-CaO were synthesized by CaO hydration followed by wet mixing. The phases of the multifunctional catalysts were characterized by XRD. The XRD patterns (Fig. 6) indicates that (i) the Ni-Zr-CaO, Ni-Ce-CaO and Ni-La-CaO contained a NiO phase, which acts as the active sites for the catalyzed steam reforming; (ii) $CaZrO_3$ in the Ni-Zr-CaO samples and CeO_2 in the Ni-Ce-CaO samples are proposed to be inert materials inhibiting the agglomeration of CaO, while the CaO phase acts as a catalyst support and CO_2 sorption material and (iii) the Ni-La-CaO samples contained a complex phase $(La_{1.7}Ca_{0.3})(NiO_4)$ and a CaO phase acting as a support and CO_2 sorbent.

ACCEPTED MANUSCRIPT

In this work, the metallic Ni acts as the catalytic active site for H_2 production via the steam reforming of methane [48-50], therefore the reduction temperature and the reducibility of the multifunctional catalyst are important issues of concern. The reducibility of multifunctional catalysts Ni-Zr-CaO, Ni-Ce-CaO and Ni-La-CaO was tested by temperature-programmed reduction (TPR), the TPR profiles of which are presented in Fig. 7. It is found that free NiO is not observed in all the samples (500-550 °C) [26, 61]. The profiles from the Ni-Zr-CaO and the Ni-Ce-CaO multifunctional catalysts have a single common peak at 670 °C, which refers to the reduction of Ni^{2+} in low interaction with Zr-CaO or Ce-CaO. The TPR profile for the Ni-La-CaO multifunctional catalyst possesses two peaks (i) at a lower temperature of 640 °C, which is attributed to weak Ni-La-CaO interactions and (ii) at a higher temperature of 830 °C referring to the reduction of more stable Ni(II) interacting with the support. This result is probably an effect of progressive incorporation of Ni into the modified sorbent structure [62] supporting XRD evidence for the complex phase ($(La_{1.7}Ca_{0.3})(NiO_4)$). For all multifunctional catalysts the TPR results imply that the temperature for the reduction of the Ni(II) active sites is higher than 830 °C. However, the reduction temperatures of our multifunctional catalysts are not reduced when Zr, Ce and La promoters were added on the catalysts in contrast to the results reported by Qin and co-workers [44-47]. It is plausible the interaction within Ni-M-CaO are stronger than those within Cu-Fe-M-HZSM-5 (where M is Zr, Ce and La).

The multifunctional catalysts Ni-Zr-CaO, Ni-Ce-CaO and Ni-La-CaO were tested and compared with a commercial catalyst ($Ni-Al_2O_3$) used for SMR hydrogen production. Fig. 8 shows the $Ni-Al_2O_3$ catalyst to produce H_2 at a purity of 67% while all the multifunctional catalysts produced H_2 at purities greater than 81% during the pre-breakthrough period of 30 min in the 1^{st} cycle. However, the H_2 purities decreased towards the equilibrium concentration at approximately 64% in the post-breakthrough period of 180 min. During the

ACCEPTED MANUSCRIPT

pre-breakthrough period the purities of H_2 produced with the Ni-Zr-CaO and Ni-Ce-CaO multifunctional catalysts were similar (85% and 84%, respectively), but the purity of H_2 produced with Ni-La-CaO of 81% was significantly lower. This is possibly due to: (i) the lack of lower-temperature oxygen storage leading to relatively poor oxygen mobility as shown in Fig. 5 and Table 2 and (ii) the surface concentration of Ca of Ni-La-CaO samples being significantly lower (Table 3) and hence a lower concentration of active sites for CO_2 sorption resulting in lower CO_2 sorption rates. In the post-breakthrough period the H_2 purities from the multifunctional catalysts also exhibit the same trend as those during the pre-breakthrough period; The H_2 purities of Ni-Zr-CaO and Ni-Ce-CaO are 64% and 63%, respectively, compared to a significantly lower value of 61% from Ni-La-CaO.

To test the performance of the multifunctional catalysts over multiple cycles, the samples were regenerated at 850 °C under N_2 flow and reduced at the same temperature under 10% v/v H_2 balanced with N_2. Five cycles of operations were performed and the results are presented in the next section.

3.3 Stability of multifunctional catalysts

Fig. 9 indicates the performance of the multifunctional catalysts Ni-Zr-CaO, Ni-Ce-CaO and Ni-La-CaO tested by sorption enhanced steam reforming of biogas over five operation cycles. The Ni-Zr-CaO and Ni-Ce-CaO (Figs. 9(a) and (b)) offered the most stable H_2 purities over the five cycles, with pre-breakthrough H_2 purities of 85% and 84% during the 1st cycle and followed by 88% and 85% during the 5th cycle, respectively. This can be attributed to the most stable sorption capacities of Zr-CaO and Ce-CaO present in the Ni-Zr-CaO and Ni-Ce-CaO. Moreover, the low temperature oxygen storage in the supports (Zr-CaO and Ce-CaO) promoted the oxygen mobility and hence the sorption of CO_2 into the bulk CaO phase, ultimately enhancing the stability of H_2 purity. However, Ni-La-CaO (Fig. 9 (c))

ACCEPTED MANUSCRIPT

exhibited a low stability. The H_2 purity of the product gas from Ni-La-CaO decreased significantly from 81% during the 1st cycle to 57% during the 5th cycle. The associated deactivation of the Ni-La-CaO is explained by the same reasons discussed in the previous section.

The pre-breakthrough CH_4 conversions of Ni-Zr-CaO and Ni-Ce-CaO are shown to decrease slightly from 77% and 74% at 1st cycle to 70% and 61% at the 5th cycle, respectively, while in the post-breakthrough period the CH_4 conversions decreased rapidly with increasing number of cycles (the CH_4 conversion of the Ni-Zr-CaO and Ni-Ce-CaO samples decreased from 65.6 and 56.3% during the 1st cycle to 33.0 and 28.9% during the 5th cycle in the post-breakthrough period). This is attributed to the loss of Ni active sites as confirmed by XPS results shown in Table 3 due to pore closure as shown in Fig. 10 possibly caused by $CaCO_3$ formation [63] as shown in Fig. 6. It is clear that all the used multifunctional catalysts exhibit the $CaCO_3$ phase, metallic Ni, unreacted CaO and the respective inert phases. The $CaCO_3$ formed via a carbonation reaction (Eq. 7) and the metallic Ni phase is present due to the reduction of NiO by H_2 (Eq. 8). In addition, it should be noted that the Ni species at the surface of the multifunctional catalysts have different chemical states as indicated by the XPS data as shown in Fig. 11, which shows that nickel at the surface has binding energies (B.E.) of 852-853 eV for metallic Ni [64, 65] and 854-855 eV for NiO [64-66]. The concentration of these nickel active sites at the surface of the fresh multifunctional catalysts are 3.4% (B.E. of 855.4 eV indicates the chemical state of NiO), 2.5% (B.E. of 855.8 eV indicates the chemical state of NiO) and 2.8% (B.E. of 855.4 eV indicates the chemical state of NiO), for Ni-Zr-CaO, Ni-Ce-CaO and Ni-La-CaO, respectively. After the reaction the total nickel concentrations at the surface become significantly lower: (i) 1.2% of total nickel species consisting of 0.1% for metallic Ni (B.E. of 851.8 eV) and 1.1% for NiO (B.E. of 855.3 eV) on the Ni-Zr-CaO sample, (ii) 1.5% of

ACCEPTED MANUSCRIPT

metallic Ni (B.E. of 854.1 eV) on the Ni-Ce-CaO sample and (iii) 0.9% of total nickel species consisting of 0.6% for metallic Ni (B.E. of 852.4 eV) and 0.3% for NiO (B.E. of 855.4 eV) on the Ni-La-CaO sample. The presence of metallic nickel is due to the reduction of NiO in the fresh multifunctional catalysts by H_2, while the presence of NiO is caused by the oxidation of metallic nickel by steam according to Eq. 8.

$$NiO + H_2 \quad \leftrightarrow \quad Ni + H_2O \tag{8}$$

Note that observations from the SEM images (Fig. 10) and XPS results (Table 3) indicate the deactivation of the catalyst observed in this work could be due to the expansion of $CaCO_3$, resulting in pore closure and the loss of Ni active sites, rather than coke formation. It would be interesting to determine the amount of carbon deposition on the catalysts. However, the typical techniques such as thermogravimetric analysis (TGA) and temperature-programmed oxidation (TPO) are inapplicable for the measurement of the amount of carbon deposition on our used multifunctional catalysts (Ni on Zr-, Ce- and La-modified CaO) because $CaCO_3$ can release CO_2 during the measurements, therefore the weight loss from the TGA and the amount of CO_2 from the TPO cannot distinguish between those from $CaCO_3$ and those from carbon deposition. However, it is likely that the carbon deposition in this study is not pronounced owing to the following reasons; (i) Zr, Ce and La are the oxygen promoters that inhibit coke formation [67-70] – the oxygen storage in ZrO_2, CeO_2 and La_2O_3 can promote oxygen to react with carbon on the catalyst to form CO or CO_2; (ii) an (excess amount of steam is fed into the reactor – steam can readily react with carbon to form CO and H_2 as shown in Eq. 9 [11]; and (iii) CaO is a basic support which resists carbon formation [71]. Nevertheless, it is plausible that the deactivation was due to the densification of the multifunctional catalysts which is evidenced by the SEM images (Fig. 10). This indicates that all the multifunctional catalysts underwent densification due to the volume expansion accompanying the formation of $CaCO_3$, which resulted in pore closure and the loss of Ni

ACCEPTED MANUSCRIPT

active sites. The schematic illustration of the proposed mechanism of the densification of $CaCO_3$ is presented in Fig. 12.

$$C + H_2O \quad \leftrightarrow \quad CO + H_2 \qquad (9)$$

4. Conclusion

This report focuses on two parts: CO_2 sorption and H_2 production. In the first part, CaO was doped with Zr^{4+}, Ce^{4+} and La^{3+} and its performances as sorbents were tested over 10 CO_2 sorption/desorption cycles at 600 °C with a 15% v/v CO_2 in N_2 feed. Zr-, Ce- and La-modified CaO possess two roles: (i) acting as an inert phase in CaO inhibiting agglomeration when CO_2 sorption/desorption is performed and (ii) acting as an oxygen promoter to enhance the stability of CO_2 sorption/desorption and H_2 production over multiple cycles. The modified sorbents were synthesized by CaO hydration followed by wet mixing. Zr-CaO and Ce-CaO possessed stable CO_2 capacities over the 10 cycles (CO_2 sorption capacity of 0.30 and 0.22 $g_{CO_2}/ g_{sorbent}$ at the 1^{st} cycle, and 0.29 and 0.23 $g_{CO_2}/ g_{sorbent}$ at the 10^{th} cycle for Zr-CaO and Ce-CaO, respectively). On the other hand, La-CaO was shown to have a decrease in its CO_2 sorption capacity of 16% over the 10 cycles (CO_2 sorption capacity of La-CaO decreases from 0.29 $g_{CO_2}/ g_{sorbent}$ at 1^{st} cycle to 0.24 $g_{CO_2}/ g_{sorbent}$ at the 10^{th} cycle). This was due to the low-temperature oxygen storage properties of Zr-CaO and Ce-CaO, which enhanced the mobility of oxygen. This behavior promoted the CO_2 diffusion from the surface to the bulk and vice versa (sorption/desorption) of the modified CaO.

In the second part, Ni(II) was loaded on the modified sorbents Zr-CaO, Ce-CaO and La-CaO for H_2 production via sorption enhanced steam reforming of biogas. The reaction was carried out with a *S/C* ratio of 3 at 1 bar, a reaction temperature of 600 ºC, a regeneration temperature of 850 ºC and a CH_4/CO_2 ratio of 3/2. The results showed that Ni-Zr-CaO and Ni-Ce-CaO produced H_2 at stable purities (approximately of 90% and 85%, respectively) but

ACCEPTED MANUSCRIPT

with decreasing CH_4 conversions (CH_4 conversion of Ni-Zr-CaO and Ni-Ce-CaO samples decreased from 65.6 and 56.3% at the 1st cycle to 33.0 and 28.9% at the 5th cycle in the post-breakthrough period). This was attributed to the loss of nickel active sites at the surface of the multifunctional catalysts due to the formation of $CaCO_3$. The Ni-La-CaO was shown to produce H_2 at decreasing purity and decreasing CH_4 conversion in both the pre-breakthrough and the post-breakthrough periods. This was explained in terms of the unstable CO_2 sorption capacities of the support (La-CaO) and the subsequent loss of Ni active sites confirmed by the XPS results.

Acknowledgement

This work is financially supported by the Thailand Research Fund (DPG5880003) and the Royal Golden Jubilee PhD Program from the Thailand Research Fund and Chulalongkorn University.

References

[1] D. Das, T.N. Veziroglu, Hydrogen production by biological processes: a survey of literature, International Journal of Hydrogen Energy 26 (2001) 13-28.

[2] S.K. Gupta, S. Kumari, K. Reddy, F. Bux, Trends in biohydrogen production: major challenges and state-of-the-art developments, Environmental technology 34 (2013) 1653-1670.

[3] J. Meyer, J. Mastin, C.S. Pinilla, Sustainable Hydrogen Production from Biogas Using Sorption-Enhanced Reforming, Energy Procedia 63 (2014) 6800-6814.

ACCEPTED MANUSCRIPT

[4] D. Saebea, S. Authayanun, Y. Patcharavorachot, A. Arpornwichanop, Thermodynamic Analysis of Hydrogen Production from the Adsorption-enhanced Steam Reforming of Biogas, Energy Procedia 61 (2014) 2254-2257.

[5] B.S. Kwak, J. Chae, M. Kang, Design of a photochemical water electrolysis system based on a W-typed dye-sensitized serial solar module for high hydrogen production, Applied Energy 125 (2014) 189-196.

[6] S.M.M. Ehteshami, S. Vignesh, R.K.A. Rasheed, S.H. Chan, Numerical investigations on ethanol electrolysis for production of pure hydrogen from renewable sources, Applied Energy 170 (2016) 388-393.

[7] V.R. Choudhary, K.C. Mondal, CO_2 reforming of methane combined with steam reforming or partial oxidation of methane to syngas over $NdCoO_3$ perovskite-type mixed metal-oxide catalyst, Applied Energy 83 (2006) 1024-1032.

[8] M.-W. Lim, S.-T. Yong, S.-P. Chai, Combustion-synthesized Nickel-based Catalysts for the Production of Hydrogen from Steam Reforming of Methane, Energy Procedia 61 (2014) 910-913.

[9] M. Pan, Q. Wu, L. Jiang, D. Zeng, Effect of microchannel structure on the reaction performance of methanol steam reforming, Applied Energy 154 (2015) 416-427.

[10] Y. Jiao, J. Zhang, Y. Du, D. Sun, J. Wang, Y. Chen, J. Lu, Steam reforming of hydrocarbon fuels over M (Fe, Co, Ni, Cu, Zn)–Ce bimetal catalysts supported on Al_2O_3, International Journal of Hydrogen Energy 41 (2016) 10473-10482.

[11] W.-J. Jang, D.-W. Jeong, J.-O. Shim, H.-M. Kim, H.-S. Roh, I.H. Son, S.J. Lee, Combined steam and carbon dioxide reforming of methane and side reactions: Thermodynamic equilibrium analysis and experimental application, Applied Energy 173 (2016) 80-91.

ACCEPTED MANUSCRIPT

[12] H.-S. Wang, K.-Y. Huang, Y.-J. Huang, Y.-C. Su, F.-G. Tseng, A low-temperature partial-oxidation-methanol micro reformer with high fuel conversion rate and hydrogen production yield, Applied Energy 138 (2015) 21-30.

[13] C. Pirez, W. Fang, M. Capron, S. Paul, H. Jobic, F. Dumeignil, L. Jalowiecki-Duhamel, Steam reforming, partial oxidation and oxidative steam reforming for hydrogen production from ethanol over cerium nickel based oxyhydride catalyst, Applied Catalysis A: General 518 (2016) 78-86.

[14] S. Sepehri, M. Rezaei, G. Garbarino, G. Busca, Preparation and characterization of mesoporous nanocrystalline La-, Ce-, Zr-, Sr-containing $NiAl_2O_3$ methane autothermal reforming catalysts, International Journal of Hydrogen Energy 41 (2016) 8855-8862.

[15] J. Pasel, S. Wohlrab, S. Kreft, M. Rotov, K. Löhken, R. Peters, D. Stolten, Routes for deactivation of different autothermal reforming catalysts, Journal of Power Sources 325 (2016) 51-63.

[16] K. He, L. Guo, A-Novel-CdS-Nanorod with Stacking Fault Structures: Preparation and Properties of Visible-Light-Driven Photocatalytic Hydrogen Production from Water Splitting, Energy Procedia 61 (2014) 2450-2455.

[17] A.A. Ismail, D.W. Bahnemann, Photochemical splitting of water for hydrogen production by photocatalysis: A review, Solar Energy Materials and Solar Cells 128 (2014) 85-101.

[18] G. Colón, Towards the hydrogen production by photocatalysis, Applied Catalysis A: General 518 (2016) 48-59.

[19] E.L.G. Oliveira, C.A. Grande, A.E. Rodrigues, CO_2 sorption on hydrotalcite and alkali-modified (K and Cs) hydrotalcites at high temperatures, Separation and Purification Technology 62 (2008) 137-147.

ACCEPTED MANUSCRIPT

[20] C.V. Miguel, R. Trujillano, V. Rives, M.A. Vicente, A.F.P. Ferreira, A.E. Rodrigues, A. Mendes, L.M. Madeira, High temperature CO_2 sorption with gallium-substituted and promoted hydrotalcites, Separation and Purification Technology 127 (2014) 202-211.

[21] L.K.G. Bhatta, S. Subramanyam, M.D. Chengala, S. Olivera, K. Venkatesh, Progress in hydrotalcite like compounds and metal-based oxides for CO_2 capture: a review, Journal of Cleaner Production 103 (2015) 171-196.

[22] Q. Xiao, X. Tang, Y. Liu, Y. Zhong, W. Zhu, Citrate route to prepare K-doped Li_2ZrO_3 sorbents with excellent CO_2 capture properties, Chemical Engineering Journal 174 (2011) 231-235.

[23] M. Olivares-Marín, T.C. Drage, M.M. Maroto-Valer, Novel lithium-based sorbents from fly ashes for CO_2 capture at high temperatures, International Journal of Greenhouse Gas Control 4 (2010) 623-629.

[24] J. Wang, V. Manovic, Y. Wu, E.J. Anthony, A study on the activity of CaO-based sorbents for capturing CO_2 in clean energy processes, Applied Energy 87 (2010) 1453-1458.

[25] J. Phromprasit, J. Powell, S. Assabumrungrat, Metals (Mg, Sr and Al) modified CaO based sorbent for CO_2 sorption/desorption stability in fixed bed reactor for high temperature application, Chemical Engineering Journal 284 (2016) 1212-1223.

[26] J. Phromprasit, J. Powell, S. Wongsakulphasatch, W. Kiatkittipong, P. Bumroongsakulsawat, S. Assabumrungrat, Activity and stability performance of multifunctional catalyst (Ni/CaO and Ni/$Ca_{12}Al_{14}O_{33}$CaO) for bio-hydrogen production from sorption enhanced biogas steam reforming, International Journal of Hydrogen Energy 41 (2016) 7318-7331.

[27] H. Lu, A. Khan, S.E. Pratsinis, P.G. Smirniotis, Flame-Made Durable Doped-CaO Nanosorbents for CO_2 Capture, Energy & Fuels 23 (2009) 1093-1100.

ACCEPTED MANUSCRIPT

[28] J. Park, K.B. Yi, Effects of preparation method on cyclic stability and CO_2 absorption capacity of synthetic CaO–MgO absorbent for sorption-enhanced hydrogen production, International Journal of Hydrogen Energy 37 (2012) 95-102.

[29] M. Mohammadi, P. Lahijani, A.R. Mohamed, Refractory dopant-incorporated CaO from waste eggshell as sustainable sorbent for CO_2 capture: Experimental and kinetic studies, Chemical Engineering Journal 243 (2014) 455-464.

[30] J.-N. Kim, C.H. Ko, K.B. Yi, Sorption enhanced hydrogen production using one-body CaO–$Ca_{12}Al_{14}O_{33}$–Ni composite as catalytic absorbent, International Journal of Hydrogen Energy 38 (2013) 6072-6078.

[31] H.R. Radfarnia, M.C. Iliuta, Development of Al-stabilized CaO–nickel hybrid sorbent–catalyst for sorption-enhanced steam methane reforming, Chemical Engineering Science 109 (2014) 212-219.

[32] M.R. Cesário, B.S. Barros, C. Courson, D.M.A. Melo, A. Kiennemann, Catalytic performances of Ni–CaO–mayenite in CO_2 sorption enhanced steam methane reforming, Fuel Processing Technology 131 (2015) 247-253.

[33] C. Dang, H. Yu, H. Wang, F. Peng, Y. Yang, A bi-functional Co–CaO–$Ca_{12}Al_{14}O_{33}$ catalyst for sorption-enhanced steam reforming of glycerol to high-purity hydrogen, Chemical Engineering Journal 286 (2016) 329-338.

[34] X. Zhang, Z. Li, Y. Peng, W. Su, X. Sun, J. Li, Investigation on a novel CaO–Y_2O_3 sorbent for efficient CO_2 mitigation, Chemical Engineering Journal 243 (2014) 297-304.

[35] S.F. Wu, L.L. Wang, Improvement of the stability of a ZrO_2-modified Ni–nano-CaO sorption complex catalyst for ReSER hydrogen production, International Journal of Hydrogen Energy 35 (2010) 6518-6524.

[36] A. Antzara, E. Heracleous, A.A. Lemonidou, Improving the stability of synthetic CaO-based CO_2 sorbents by structural promoters, Applied Energy 156 (2015) 331-343.

ACCEPTED MANUSCRIPT

[37] C. Luo, Y. Zheng, N. Ding, C. Zheng, Enhanced cyclic stability of CO_2 adsorption capacity of CaO-based sorbents using La_2O_3 or $Ca_{12}Al_{14}O_{33}$ as additives, Korean Journal of Chemical Engineering 28 (2011) 1042-1046.

[38] P.E. Sanchez-Jimenez, L.A. Perez-Maqueda, J.M. Valverde, Nanosilica supported CaO: A regenerable and mechanically hard CO_2 sorbent at Ca-looping conditions, Applied Energy 118 (2014) 92-99.

[39] R.T.K. Baker, The Relationship between Particle Motion on a Graphite Surface and Tammann Temperature, Journal of Catalysis 78 (1982) 473-476.

[40] A. Davidson, B. Morin, M Che, ESR determination of TiO_2 and SnO_2 Tammann temperatures Colloids and Surliwes A: Physicochemical and Engineerin Aspects 72 (1993) 245-255.

[41] P. Xu, Z. Zhou, C. Zhao, Z. Cheng, Catalytic performance of Ni/CaO-$Ca_5Al_6O_{14}$ bifunctional catalyst extrudate in sorption-enhanced steam methane reforming, Catalysis Today 259 (2016) 347-353.

[42] M. Xie, Z. Zhou, Y. Qi, Z. Cheng, W. Yuan, Sorption-enhanced steam methane reforming by in situ CO_2 capture on a CaO–$Ca_9Al_6O_{18}$ sorbent, Chemical Engineering Journal 207-208 (2012) 142-150.

[43] C.S. Martavaltzi, E.P. Pampaka, E.S. Korkakaki, A.A. Lemonidou, Hydrogen Production via Steam Reforming of Methane with Simultaneous CO_2 Capture over CaO−$Ca_{12}Al_{14}O_{33}$, Energy & Fuels 24 (2010) 2589-2595.

[44] R.-w. Liu, Z.-z. Qin, H.-b. Ji, T.-m. Su, Synthesis of Dimethyl Ether from CO_2 and H_2 Using a Cu–Fe–Zr/HZSM-5 Catalyst System, Industrial & Engineering Chemistry Research 52 (2013) 16648-16655.

ACCEPTED MANUSCRIPT

[45] Z.-z. Qin, T.-m. Su, H.-b. Ji, Y.-x. Jiang, R.-w. Liu, J.-h. Chen, Experimental and theoretical study of the intrinsic kinetics for dimethyl ether synthesis from CO_2 over Cu-Fe-Zr/HZSM-5, AIChE Journal 61 (2015) 1613-1627.

[46] Z.-z. Qin, X.-h. Zhou, T.-m. Su, Y.-x. Jiang, H.-b. Ji, Hydrogenation of CO_2 to dimethyl ether on La-, Ce-modified Cu-Fe/HZSM-5 catalysts, Catalysis Communications 75 (2016) 78-82.

[47] X. Zhou, T. Su, Y. Jiang, Z. Qin, H. Ji, Z. Guo, CuO-Fe_2O_3-CeO_2/HZSM-5 bifunctional catalyst hydrogenated CO_2 for enhanced dimethyl ether synthesis, Chemical Engineering Science 153 (2016) 10-20.

[48] B. Arstad, J. Prostak, R. Blom, Continuous hydrogen production by sorption enhanced steam methane reforming (SE-SMR) in a circulating fluidized bed reactor: Sorbent to catalyst ratio dependencies, Chemical Engineering Journal 189-190 (2012) 413-421.

[49] A.L. García-Lario, G.S. Grasa, R. Murillo, Performance of a combined CaO-based sorbent and catalyst on H_2 production, via sorption enhanced methane steam reforming, Chemical Engineering Journal 264 (2015) 697-705.

[50] M.A. Nieva, M.M. Villaverde, A. Monzón, T.F. Garetto, A.J. Marchi, Steam-methane reforming at low temperature on nickel-based catalysts, Chemical Engineering Journal 235 (2014) 158-166.

[51] C.-C. Chang, J.-W. Wang, C.-T. Chang, B.-J. Liaw, Y.-Z. Chen, Effect of ZrO_2 on steam reforming of methanol over CuO/ZnO/ZrO_2/Al_2O_3 catalysts, Chemical Engineering Journal 192 (2012) 350-356.

[52] R. Tesser, M. Di Serio, E. Santacesaria, Methanol steam reforming: A comparison of different kinetics in the simulation of a packed bed reactor, Chemical Engineering Journal 154 (2009) 69-75.

ACCEPTED MANUSCRIPT

[53] Y.J. Wu, P. Li, J.G. Yu, A.F. Cunha, A.E. Rodrigues, Sorption-enhanced steam reforming of ethanol on NiMgAl multifunctional materials: Experimental and numerical investigation, Chemical Engineering Journal 231 (2013) 36-48.

[54] R. Ma, B. Castro-Dominguez, I.P. Mardilovich, A.G. Dixon, Y.H. Ma, Experimental and simulation studies of the production of renewable hydrogen through ethanol steam reforming in a large-scale catalytic membrane reactor, Chemical Engineering Journal 303 (2016) 302-313.

[55] I. Rossetti, M. Compagnoni, M. Torli, Process simulation and optimization of H_2 production from ethanol steam reforming and its use in fuel cells. 2. Process analysis and optimization, Chemical Engineering Journal 281 (2015) 1036-1044.

[56] P.D. Vaidya, A.E. Rodrigues, Insight into steam reforming of ethanol to produce hydrogen for fuel cells, Chemical Engineering Journal 117 (2006) 39-49.

[57] V.P. Rathod, P. Bansal, P.V. Bhale, Analytical and Experimental Investigations for Hydrogen Rich Syngas Production by Biogas Reforming Processes, Energy Procedia 75 (2015) 728-733.

[58] P. Kolbitsch, C. Pfeifer, H. Hofbauer, Catalytic steam reforming of model biogas, Fuel 87 (2008) 701-706.

[59] H. Lee, J.K. Lee, U.G. Hong, Y. Yoo, Y.-J. Cho, J. Lee, H.-S. Jang, J.C. Jung, I.K. Song, Effect of oxygen capacity and oxygen mobility of supported $Mg_3(VO_4)_2$ catalysts on the performance in the oxidative dehydrogenation of n-butane, Journal of Industrial and Engineering Chemistry 18 (2012) 808-813.

[60] U. Izquierdo, V.L. Barrio, J. Requies, J.F. Cambra, M.B. Güemez, P.L. Arias, Tri-reforming: A new biogas process for synthesis gas and hydrogen production, International Journal of Hydrogen Energy 38 (2013) 7623-7631.

ACCEPTED MANUSCRIPT

[61] M. Sanchezsanchez, R. Navarro, J. Fierro, Ethanol steam reforming over $Ni/M_xO_y–Al_2O_3$ (M=Ce, La, Zr and Mg) catalysts: Influence of support on the hydrogen production, International Journal of Hydrogen Energy 32 (2007) 1462-1471.

[62] A. Djaidja, S. Libs, A. Kiennemann, A. Barama, Characterization and activity in dry reforming of methane on NiMg/Al and Ni/MgO catalysts, Catalysis Today 113 (2006) 194-200.

[63] F. Donat, N.H. Florin, E.J. Anthony, P.S. Fennell, Influence of high-temperature steam on the reactivity of CaO sorbent for CO_2 capture, Environmental science & technology 46 (2012) 1262-1269.

[64] K.S. Kin, N. Winograd, X-ray photoelectron spectroscopic studies of nickel-oxygen surfaces using oxygen and argon ion-bombardment, Surface Science 43 (1974) 625-643.

[65] J.C. Klein, D.M. Hercules, Surface Characterization of Model Urushibara Catalysts, Journal of catalysis 82 (1983) 424-441.

[66] R. Molina, G. Poncelet, r-Alumina-Supported Nickel Catalysts Prepared with Nickel Acetylacetonate. 2. A Study of the Thermolysis of the Metal Precursor, Journal of Physical Chemistry B 103 (1999) 11290-11296.

[67] T. Takeguchi, Y. kani, T. Yano, R. Kikuchi, K. Eguchi, K. Tsujimoto, Y. Uchida, A. Ueno, K. Omoshiki, M. Aizawa, Study on steam reforming of CH_4 and C_2 hydrocarbons and carbon deposition on Ni-YSZ cermets, Journal of Power Sources 112 (2002) 588–595.

[68] V. Nichele, M. Signoretto, F. Pinna, F. Menegazzo, I. Rossetti, G. Cruciani, G. Cerrato, A. Di Michele, Ni/ZrO_2 catalysts in ethanol steam reforming: Inhibition of coke formation by CaO-doping, Applied Catalysis B: Environmental 150-151 (2014) 12-20.

[69] A.S. Al-Fatesh, M.A. Naeem, A.H. Fakeeha, A.E. Abasaeed, Role of La_2O_3 as Promoter and Support in $Ni/\gamma\text{-}Al_2O_3$ Catalysts for Dry Reforming of Methane, Chinese Journal of Chemical Engineering 22 (2014) 28-37.

ACCEPTED MANUSCRIPT

[70] X. Yang, J. Da, H. Yu, H. Wang, Characterization and performance evaluation of Ni-based catalysts with Ce promoter for methane and hydrocarbons steam reforming process, Fuel 179 (2016) 353-361.

[71] C.E. Quincoces, S. Dicundo, A.M. Alvarez, M.G. Gonzalez, Effect of addition of CaO on Ni/Al_2O_3 catalysts over CO_2 reforming of methane, Materials Letters 50 (2001) 21-27.

ACCEPTED MANUSCRIPT

ACCEPTED MANUSCRIPT

Tables

Table 1 Properties of modified sorbents.

Sample	BET surface area (m^2/g)	Pore size (nm)	Pore volume (cm^3/g)	Crystallize size (nm)			
				CaO	$CaZrO_3$	CeO_2	La_2O_3
Zr-CaO (Fresh)	17.7	5.62	0.04	55.1	40.2	-	-
Zr-CaO (Used)	-	-	-	53.9	41.6	-	-
Ce-CaO (Fresh)	8.2	9.75	0.03	56.6	-	33.5	-
Ce-CaO (Used)	-	-	-	55.3	-	34.0	-
La-CaO (Fresh)	13.1	6.32	0.03	56.0	-	-	45.4
La-CaO (Used)	-	-	-	53.5	-	-	45.5

ACCEPTED MANUSCRIPT

Table 2 Oxygen storage capacities of Zr^{4+}, Ce^{4+} and La^{3+} modified CaO.

Sample	**OSC at low temperature (mmol/g)**	**OSC at high temperature (mmol/g)**	**Total O_2 OSC (mmol/g)**
Zr-CaO	0.04 (125 °C)	0.46 (520 °C)	0.50
Ce-CaO	1.76 (200 °C)	0.08 (530 °C)	1.84
La-CaO	-	2.08 (510 °C) 2.19 (615 °C)	4.28

*OSC refers to oxygen storage capacity (mmol/g)

ACCEPTED MANUSCRIPT

ACCEPTED MANUSCRIPT

Table 3 Atomic concentration of the elements at the surface of the multifunctional catalysts before and after reaction.

Sample	Binding energy of Ni (eV)	Atomic concentration at surface (%)					
		Ni	Zr	Ce	La	Ca	O
Ni-Zr-CaO (Fresh)	855.4	3.4	1.2	-	-	12.7	82.7
Ni-Zr-CaO (Used)	855.3 851.8	1.1 0.1	1.0	-	-	12.3	85.4
Ni-Ce-CaO (Fresh)	855.8	2.5	-	1.2	-	12.4	83.9
Ni-Ce-CaO (Used)	854.1	1.5	-	1.5	-	12.0	85.0
Ni-La-CaO (Fresh)	855.4	2.8	-	-	4.6	11.8	80.8
Ni-La-CaO (Used)	855.4 852.4	0.3 0.6	-	-	2.4	11.0	85.6

ACCEPTED MANUSCRIPT

ACCEPTED MANUSCRIPT

Figures

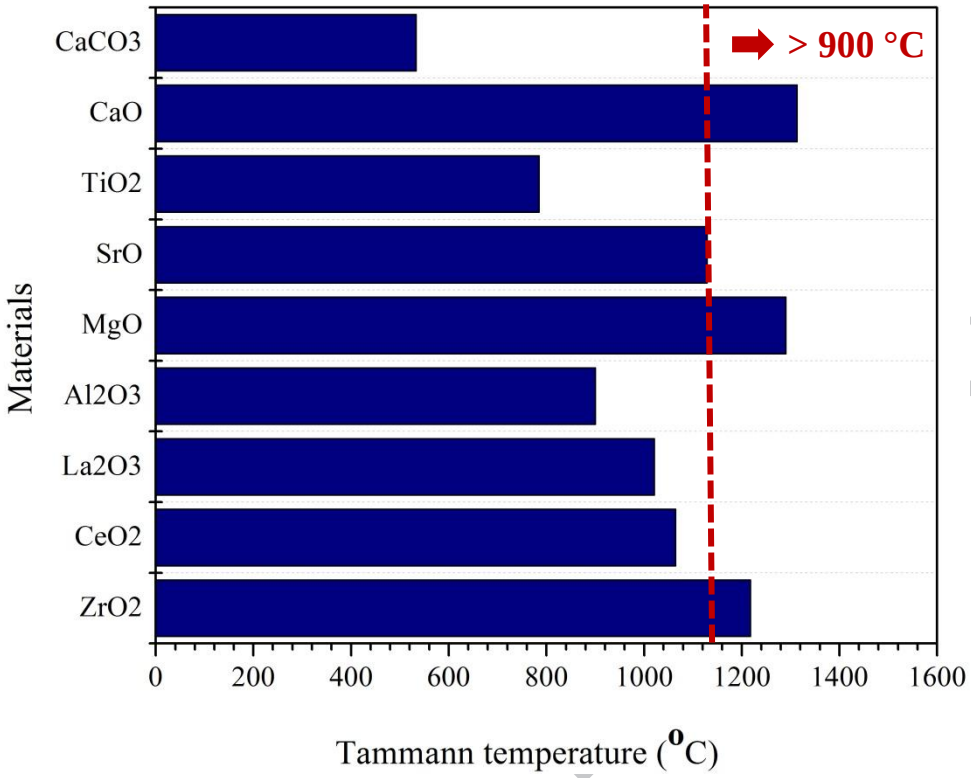

Fig. 1 Tammann temperatures of several materials.

ACCEPTED MANUSCRIPT

ACCEPTED MANUSCRIPT

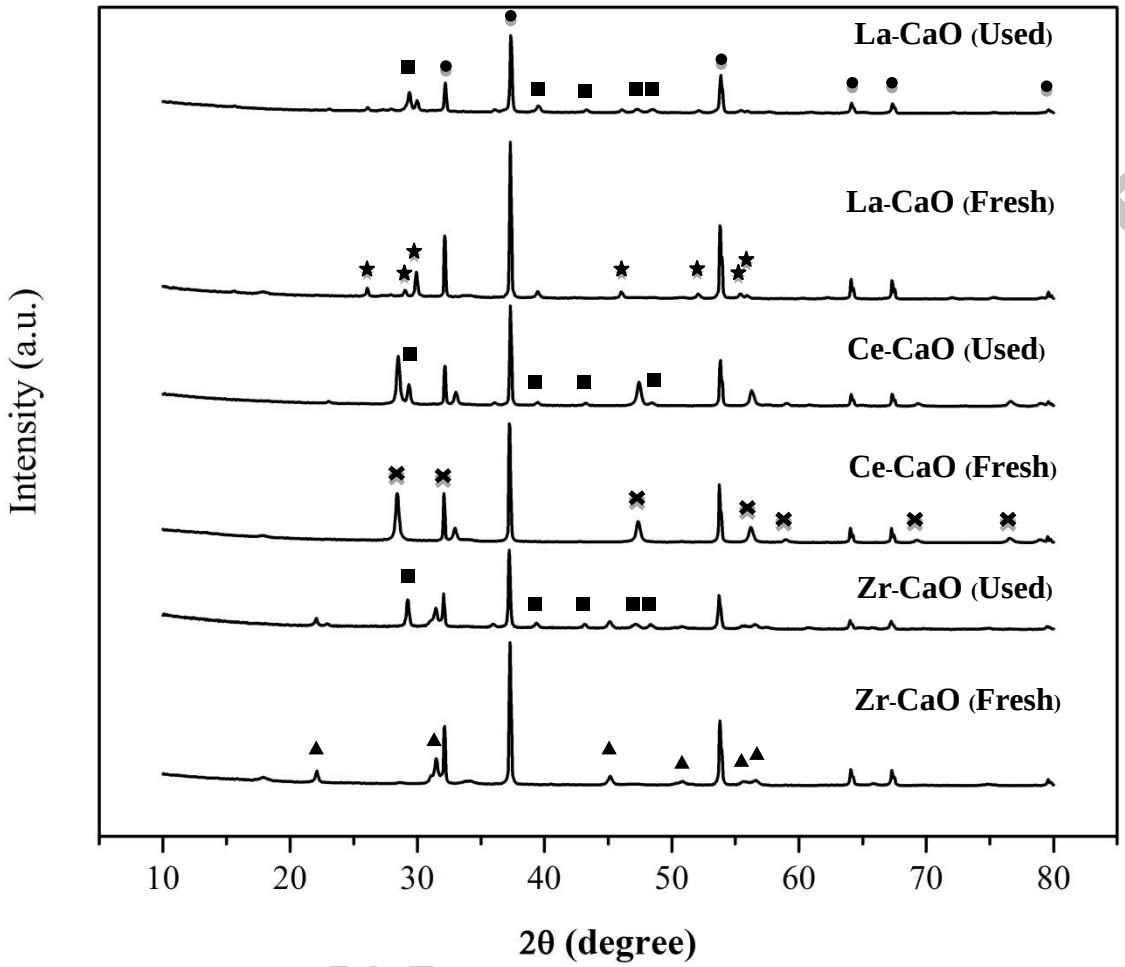

Fig. 2 XRD patterns of modified sorbents: ● CaO, ■ $CaCO_3$, ▲ $CaZrO_3$, ✕ CeO_2 and ★ La_2O_3.

ACCEPTED

ACCEPTED MANUSCRIPT

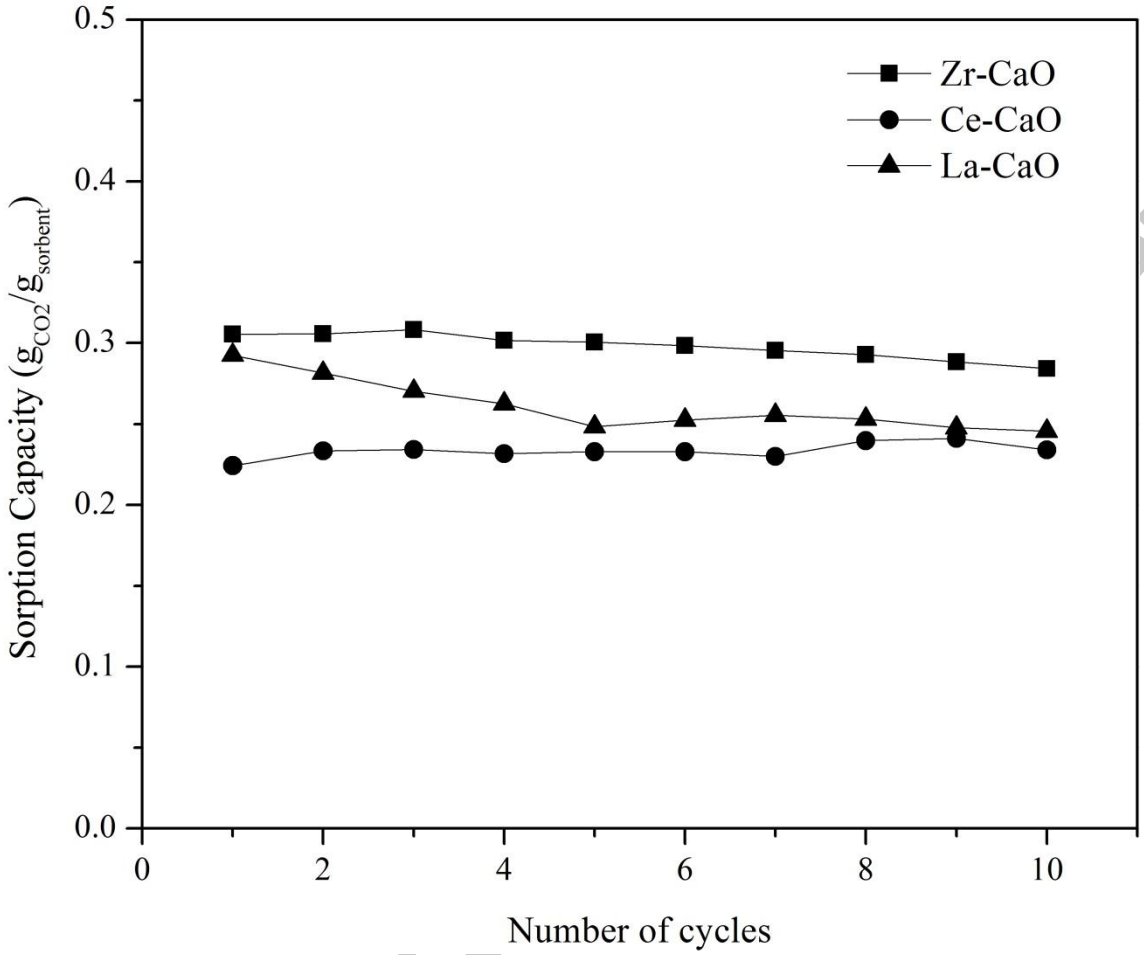

Fig. 3 CO_2 sorption capacities of Zr^{4+}, Ce^{4+} and La^{3+} modified CaO after the indicated number of sorption/desorption cycles.

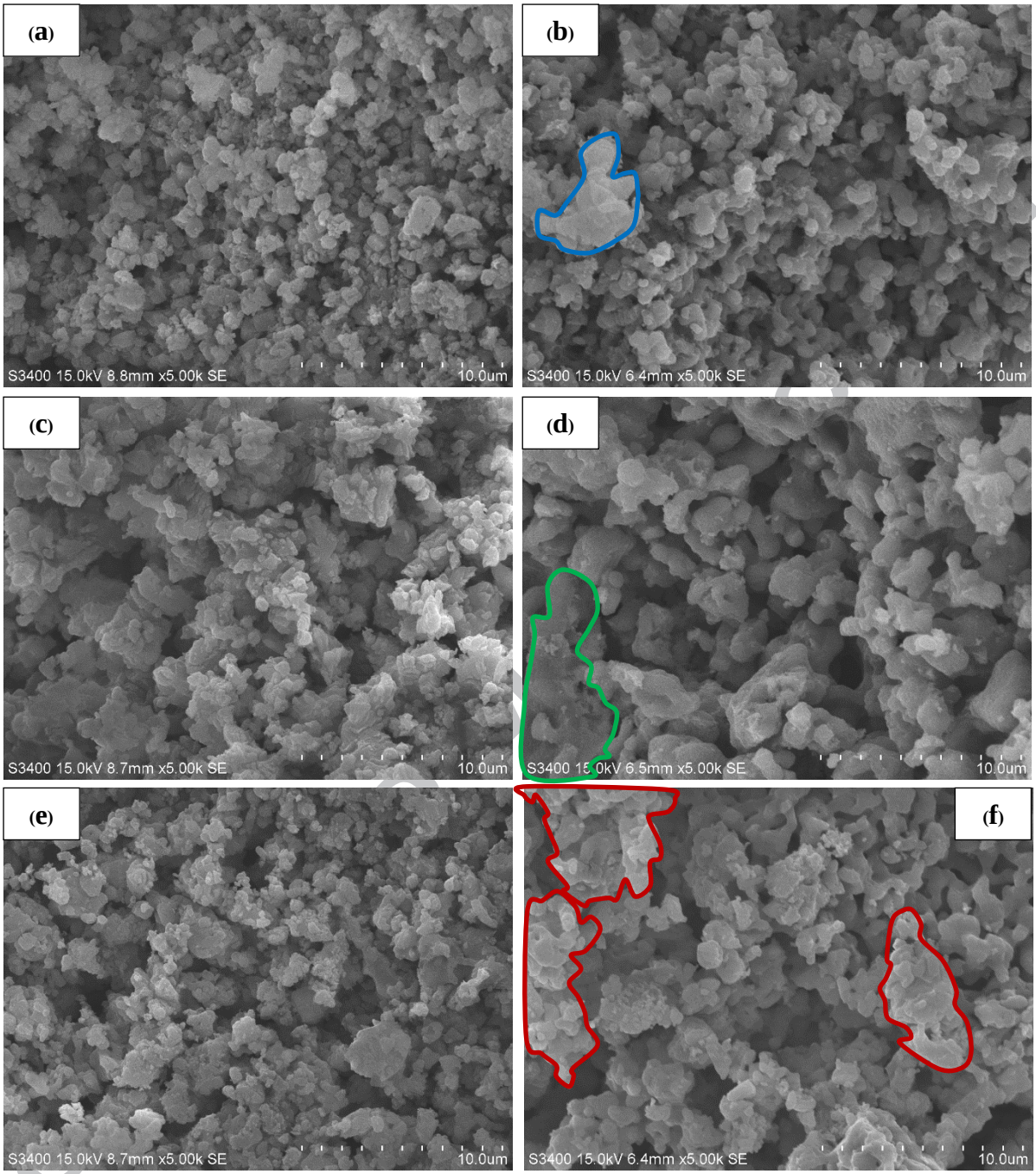

Fig. 4 SEM images of modified sorbents: (a) Zr-CaO (Fresh), (b) Zr-CaO (Used), (c) Ce-CaO (Fresh), (d) Ce-CaO (Used), (e) La-CaO (Fresh) and (f) La-CaO (Used).

ACCEPTED MANUSCRIPT

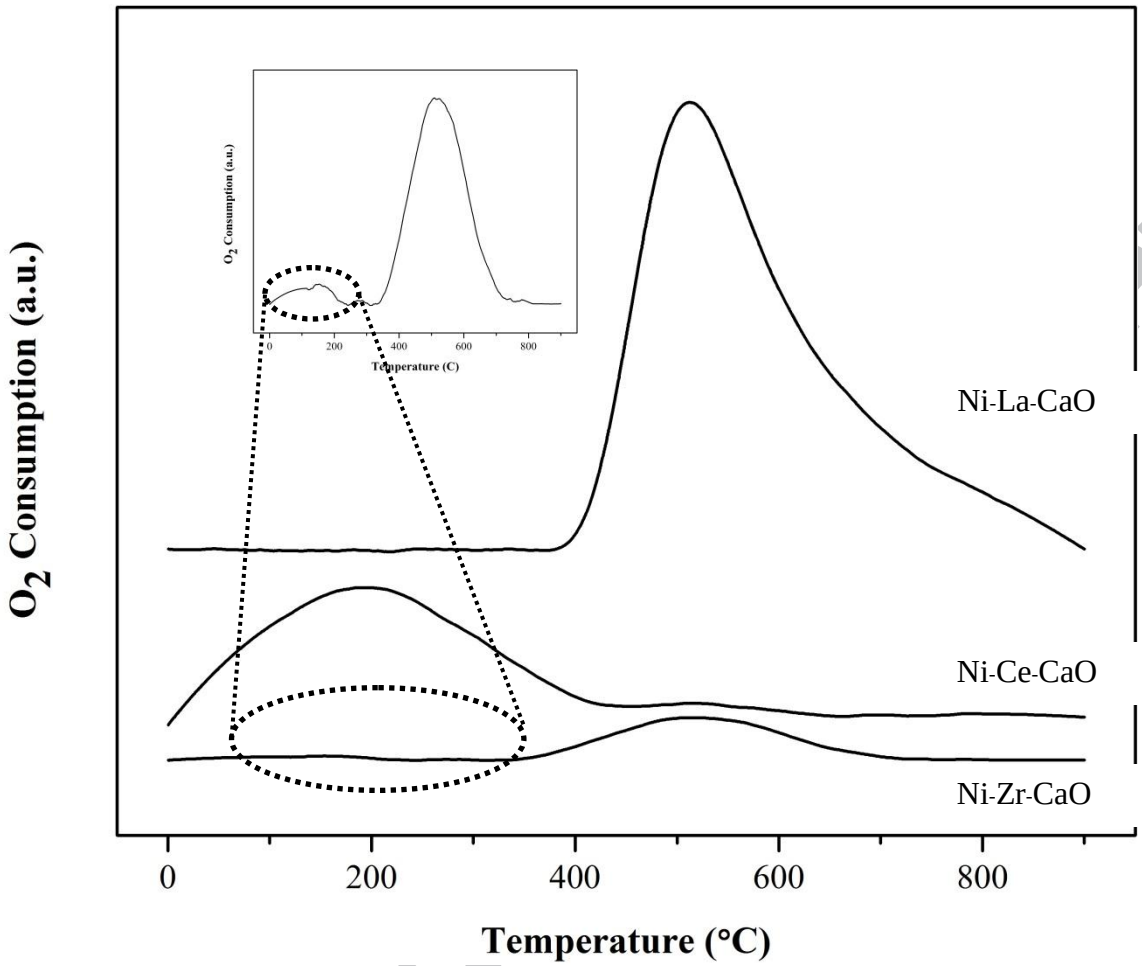

Fig. 5 O_2 consumption from the temperature-programmed reduction oxidation of Zr^{4+}, Ce^{4+} and La^{3+} modified CaO.

ACCEPTED MANUSCRIPT

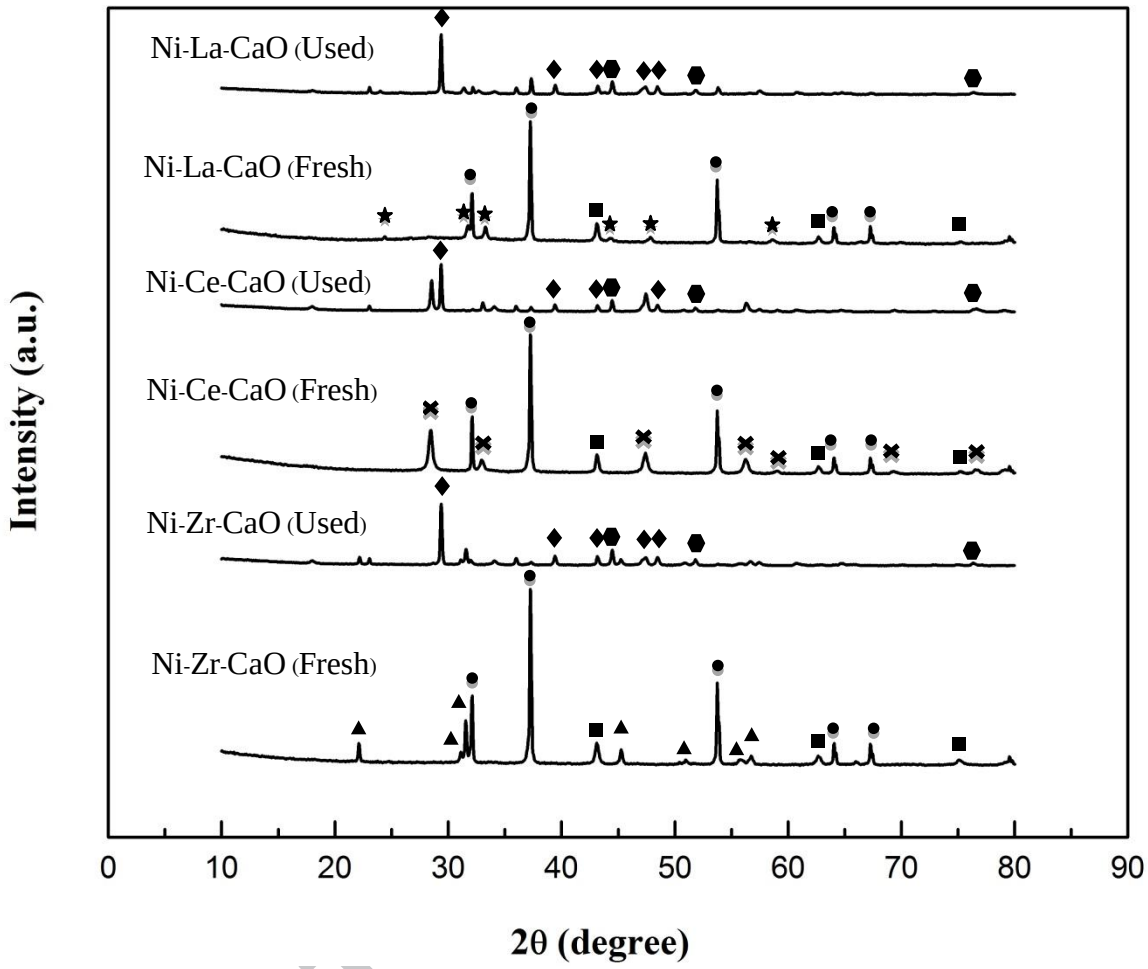

Fig. 6 XRD patterns of multifunctional catalysts: ● CaO, ■ NiO, ▲ $CaZrO_3$, ✕ CeO_2, ★ $(La_{1.7}Ca_{0.3})(NiO_4)$, ◆ $CaCO_3$ and ⬣ Ni.

ACCEPTED MANUSCRIPT

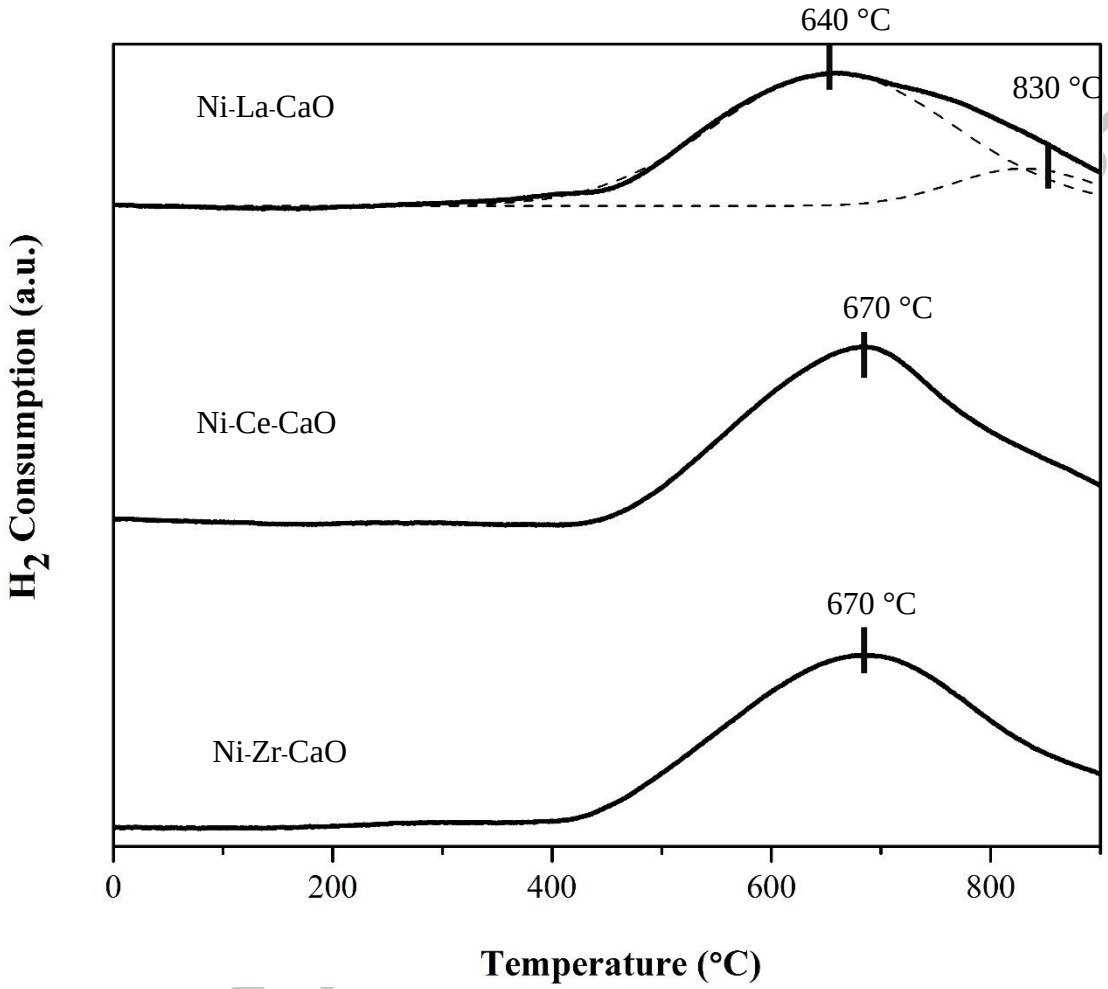

Fig. 7 H_2 consumption from the temperature-programmed reduction of Ni over Zr^{4+}, Ce^{4+} and La^{3+} modified CaO.

ACCEPTED MANUSCRIPT

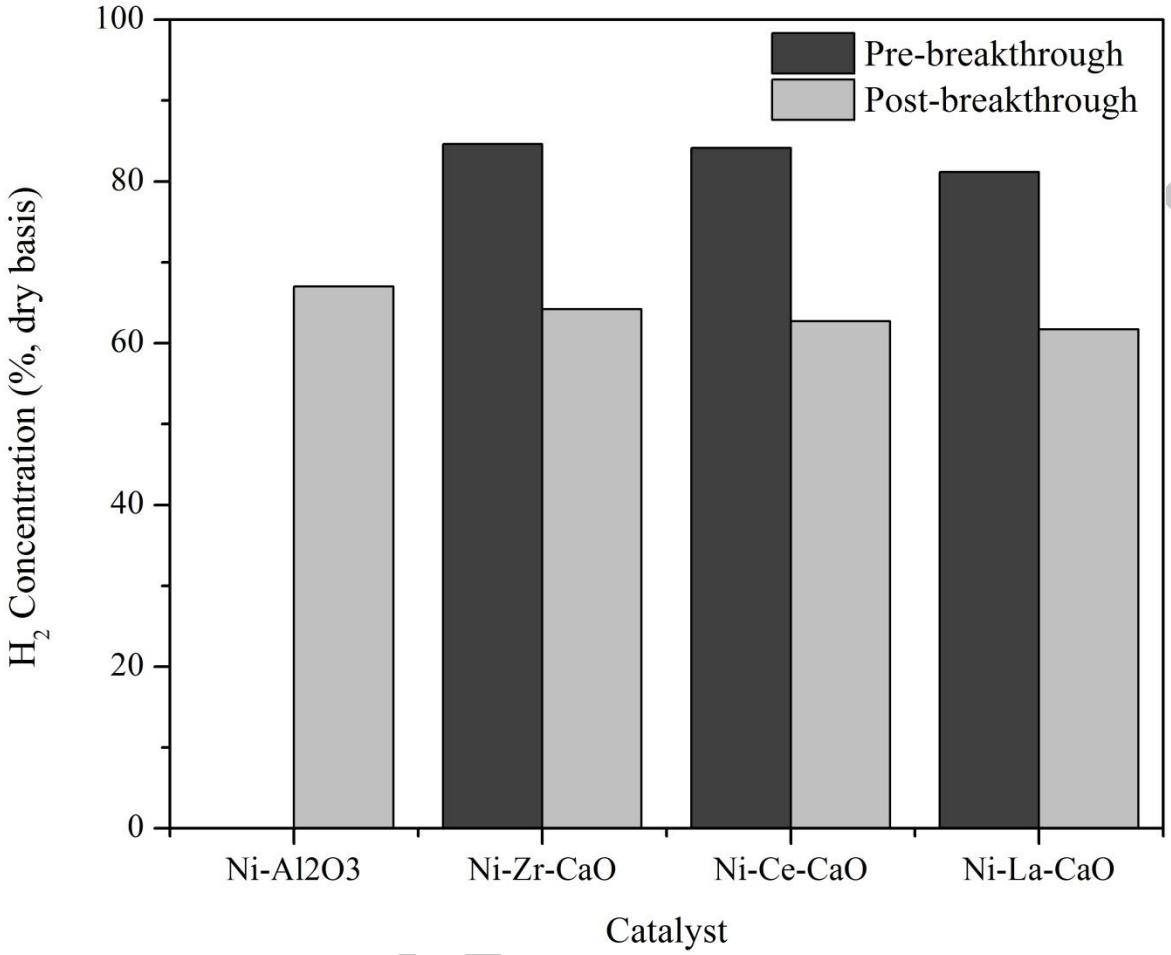

Fig. 8 H_2 concentrations from sorption enhanced steam reforming of biogas with various multifunctional catalysts.

ACCEPTED

ACCEPTED MANUSCRIPT

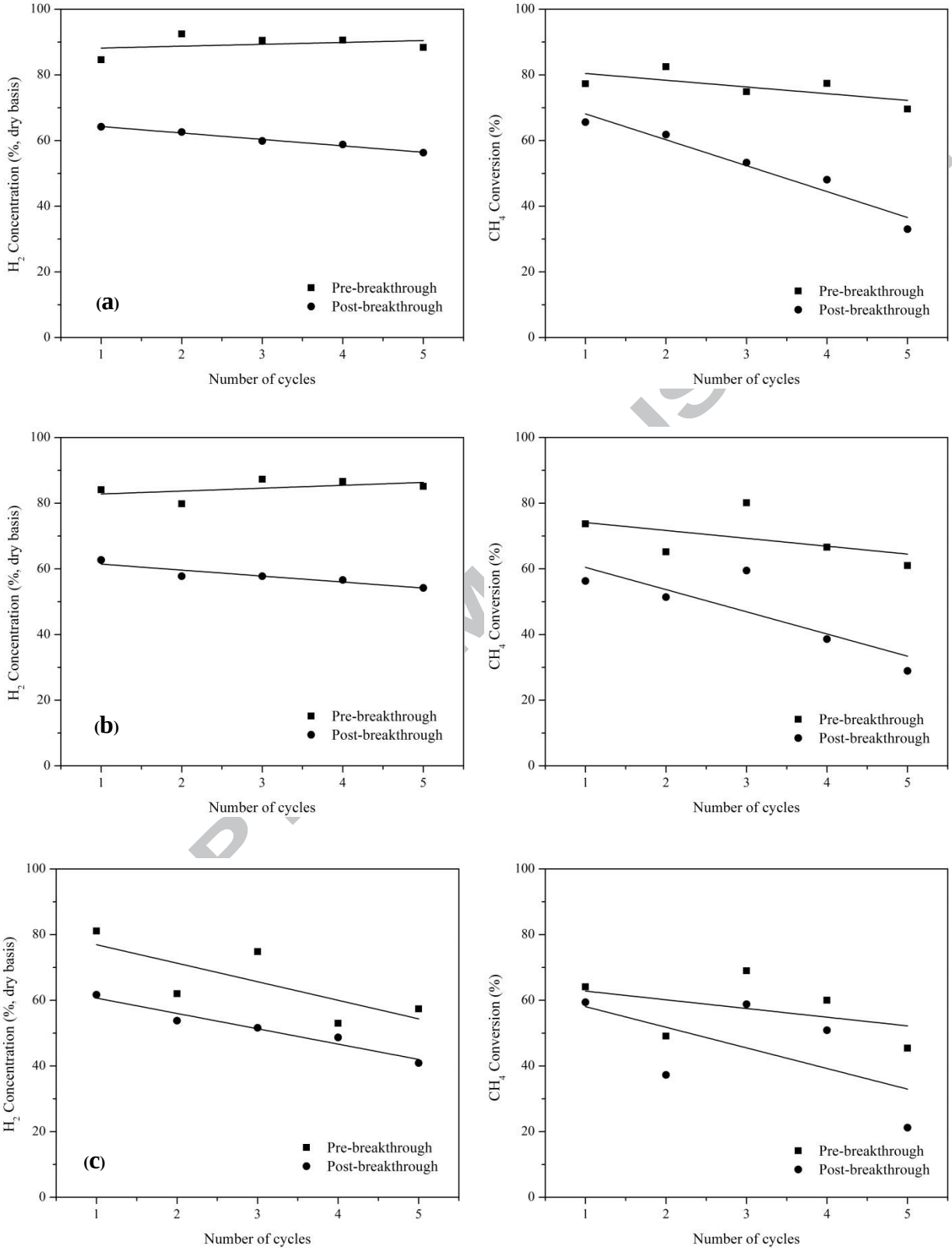

Fig. 9 H_2 purity and CH_4 conversion of multifunctional catalysts: (a) Ni-Zr-CaO, (b) Ni-Ce-CaO and (c) Ni-La-CaO.

ACCEPTED MANUSCRIPT

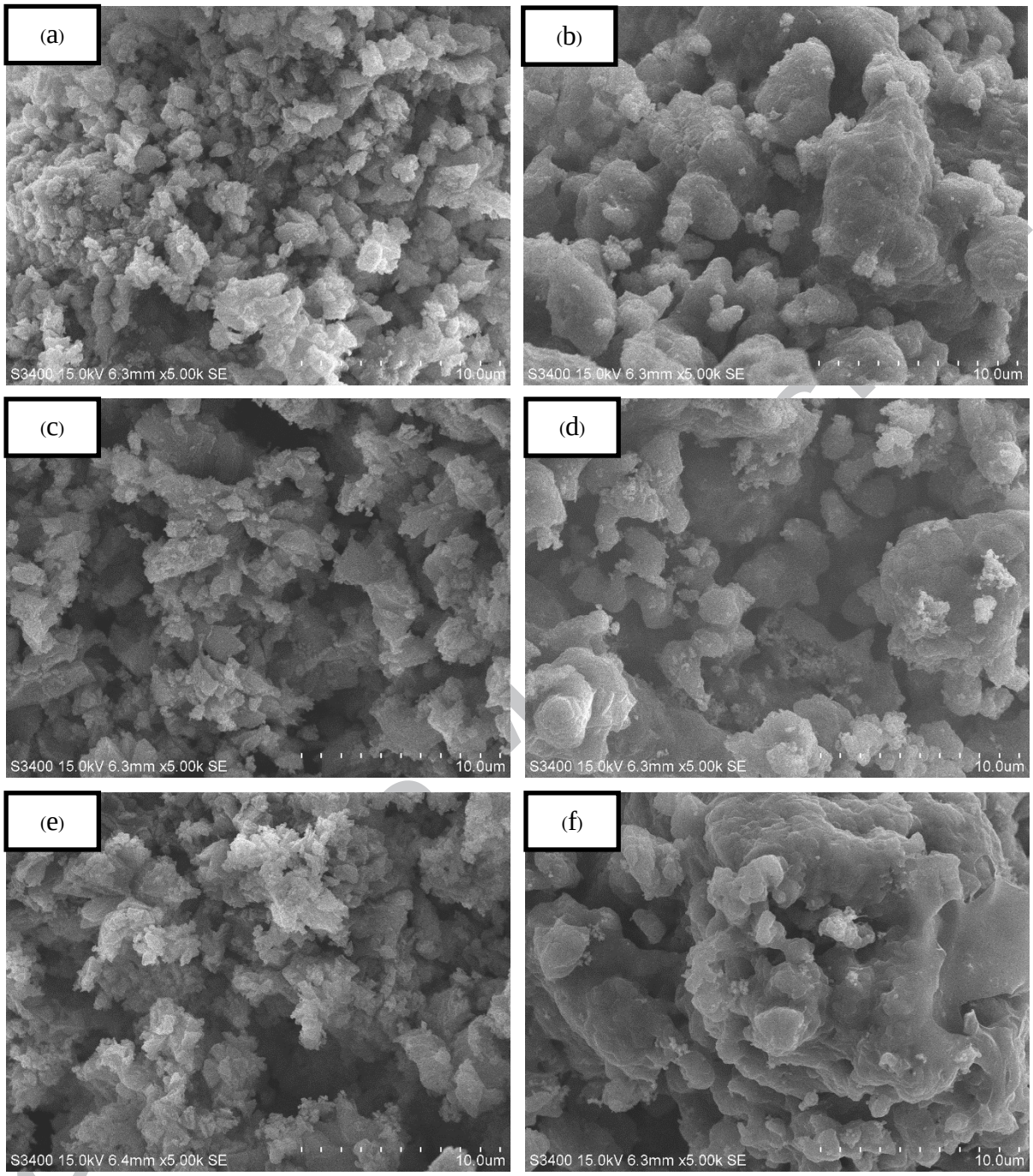

Fig. 10 SEM images of multifunctional catalysts: (a) Ni-Zr-CaO (Fresh), (b) Ni-Zr-CaO (Used), (c) Ni-Ce-CaO (Fresh), (d) Ni-Ce-CaO (Used), (e) Ni-La-CaO (Fresh) and (f) Ni-La-CaO (Used).

ACCEPTED MANUSCRIPT

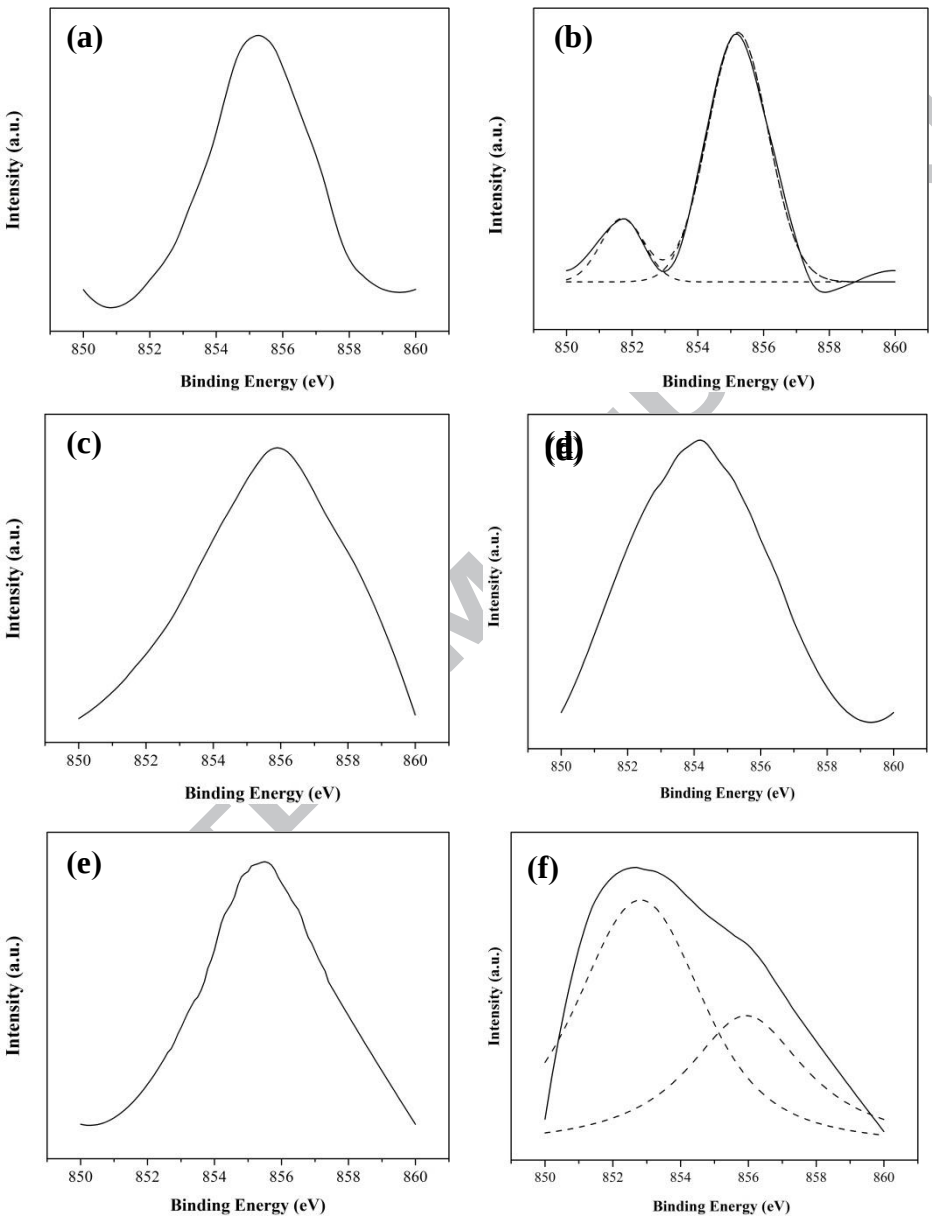

Fig. 11 XPS profile of multifunctional catalysts: (a) Ni-Zr-CaO (Fresh), (b) Ni-Zr-CaO (Used), (c) Ni-Ce-CaO (Fresh), (d) Ni-Ce-CaO (Used), (e) Ni-La-CaO (Fresh) and (f) Ni-La-CaO (Used).

ACCEPTED MANUSCRIPT

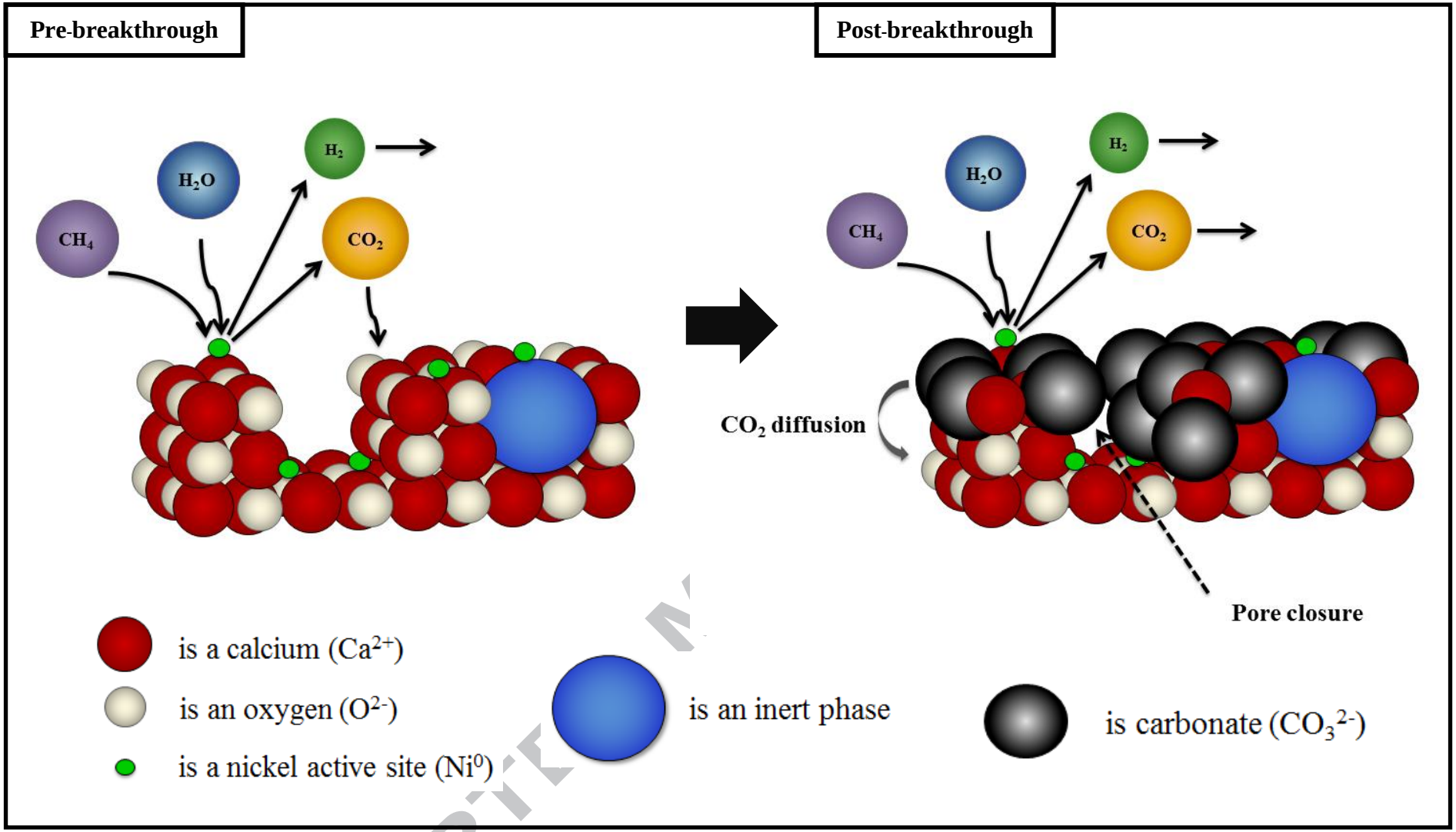

Fig. 12 Proposed mechanism of the densification of $CaCO_3$.

ACCEPTED MANUSCRIPT

Graphical abstract

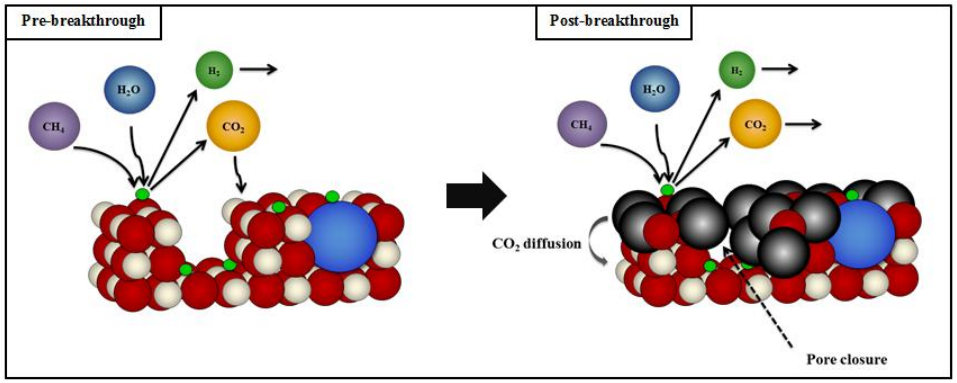

ACCEPTED MANUSCRIPT

ACCEPTED MANUSCRIPT

Highlights

- Zr^{2+}, Ce^{2+} and La^{3+} are doped on CaO for improving its CO_2 capture.
- Zr-CaO and Ce-CaO show stable CO_2 capture activity for at least 10 cycles.
- Their improved stability is enhanced by oxygen storage capacity at low temperatures.
- Multifunctional catalysts were tested for sorption enhanced biogas steam reforming.
- Ni-Zr-CaO and Ni-Ce-CaO deliver a stable H_2 purity over multiple cycle operations.

ACCEPTED MANUSCRIPT

Process Biochemistry xxx (2016) xxx–xxx

Contents lists available at ScienceDirect

Process Biochemistry

journal homepage: www.elsevier.com/locate/procbio

Enhanced effectiveness of *Rhizopus oryzae* by immobilization in a static bed fermentor for L-lactic acid production

Varunee Pimtong[a], Siriporn Ounaeb[a], Sitanan Thitiprasert[b], Vasana Tolieng[b], Sarintip Sooksai[b], Ruethairat Boonsombat[b], Somboon Tanasupawat[c], Suttichai Assabumrungrat[d], Nuttha Thongchul[b,*]

[a] *Biotechnology Program, Faculty of Science, Chulalongkorn University, Bangkok 10330, Thailand*
[b] *Institute of Biotechnology and Genetic Engineering, Chulalongkorn University, Bangkok 10330, Thailand*
[c] *Department of Microbiology, Faculty of Pharmaceutical Sciences, Chulalongkorn University, Bangkok 10330, Thailand*
[d] *Department of Chemical Engineering, Faculty of Engineering, Chulalongkorn University, Bangkok 10330, Thailand*

ARTICLE INFO

Article history:
Received 9 July 2016
Received in revised form 9 September 2016
Accepted 23 September 2016
Available online xxx

Keywords:
Static bed fermentor
Lactic acid
Continuous culture
Glucose tolerance
Hydrolysates
Toxic impurities

ABSTRACT

The static bed fermentor was successfully employed for cell immobilization in this study. By complete immobilization of *Rhizopus oryzae* on a fibrous matrix, cell-free fermentation broth resulted in improved mass transfer and easy operation compared with free cell fermentation in a typical stirred fermentor. Environmental conditions generated in this fermentor configuration favoring the immobilized *R. oryzae* to grow and produce lactic acid without substrate repression at high initial glucose concentration during batch cultivation. Approximately 67% of the theoretical lactate yield (0.50 g/g) with the productivity of 1.05 g/L h and the final titer of 75.28 g/L was obtained from fermentation with high glucose concentration (150 g/L). Complete cell immobilization supported the continuous operation of lactic acid production by *R. oryzae* since cell wash out was diminished. When operating the continuous culture at an appropriate dilution rate, a sufficiently high concentration of lactic acid (72.32 g/L) with a small amount of remaining glucose (<5 g/L) was obtained. Impurities remaining in the hydrolysates were generally considered toxic to microbial conversion; nevertheless, immobilized cells in the static bed fermentor exerted high tolerance to the salt impurities (Na^+, Cl^-) remaining in the cassava pulp hydrolysates to be used in lactate fermentation medium.

© 2016 Elsevier Ltd. All rights reserved.

1. Introduction

Lactic acid is recognised as a versatile chemical with multiple applications in food, pharmaceuticals, cosmetics, and household products [1]. The commercial production of lactic acid has long relied on bacterial fermentation because of its high final titer, yield, and productivity [2]. The potential application of lactic acid as the major building block in compostable plastic, polylactic acid, has recently driven market demand, while the product specifications for polymer grade lactic acid are of prime consideration [3,4]. Alternatively, lactic acid obtained from fungal fermentation holds great promise in producing polymer grade product because *Rhizopus oryzae* conveys only the *l-ldh* gene; therefore, optically pure L-lactic acid is obtained [5,6]. Lactic acid fermentation by *R. oryzae* is heterofermentative; therefore, ethanol is typically found to be the major byproduct, resulting in low lactate yield and productivity. To limit ethanol production, oxygen supply is necessary for growth and lactate production in fermentation by *R. oryzae*; therefore, sufficient mixing and aeration are mandatory.

Morphological diversity is a challenge in the submerged cultivation of *R. oryzae* for lactic acid. Change in morphology during cultivation is commonly observed as the effect of medium composition, pH, temperature, agitation, and so on [7]. It has been claimed that small pellets are preferable in cultivating *R. oryzae* for lactic acid as they enhance oxygen transfer in the fermentation broth and could be utilized for repeated batch operation. Nonetheless, increase in pellet size and density has typically been observed during fermentation.

Several techniques have been used to immobilize *R. oryzae* for proper morphology, good mass transfer, and homogeneity during fermentation in order to increase lactic acid production [8,9]. These techniques, for example, include entrapment in the polymeric matrices [10], mechanical containment in the microporous membrane filters [11], biofilm attachment on the support [12], and

* Corresponding author.
E-mail address: Nuttha.T@chula.ac.th (N. Thongchul).

http://dx.doi.org/10.1016/j.procbio.2016.09.020
1359-5113/© 2016 Elsevier Ltd. All rights reserved.

Please cite this article in press as: V. Pimtong, et al., Enhanced effectiveness of *Rhizopus oryzae* by immobilization in a static bed fermentor for L-lactic acid production, Process Biochem (2016), http://dx.doi.org/10.1016/j.procbio.2016.09.020

adsorption onto the fibrous matrices [13,14]. Several fermentors have been used for the immobilized cells of *R. oryzae* including air-lift fermentor, drum contactor, reciprocating jet fermentor, tower fermentor, and hollow fiber fermentor [15–18]. Generally, low lactic acid yields of approximately 0.65–0.78 g/g glucose with the final titer of 40–73 g/L were obtained in most immobilization studies [15,19–23]. Nonetheless, fibrous bed fermentors have been reported to enhance lactic acid production by fungal immobilization in the fibrous matrices, e.g., cotton cloth, affixed in the fermentors in batch, repeated batch, and fed-batch operations [13,14]. Through cell attachment on the flat sheet surface provided in this fermentor configuration, it was claimed that oxygen transfer was significantly improved, and therefore the lactic acid production increased.

A static bed fermentor, a type of fibrous bed fermentor, was investigated for its effectiveness in controlling the morphology of *R. oryzae* throughout fermentation. In typical batch fermentation, substrate repression was often troublesome when operating at high initial concentration. With proper morphological control in this fermentor configuration, it was believed that cultivation under this environmental stress was plausible. Long-term cultivation and the consumption of low cost substrates with acceptable fermentor productivity were desirable in fermentation operation especially at industrial level because of lowered operation costs. In this study, the immobilized *R. oryzae* on the cotton cloth in the static bed fermentor was tested according to three different aspects: susceptibility to grow and produce lactic acid at high initial glucose concentration; long-term stability during continuous culture; and tolerance to toxic impurities contained in the cellulosic hydrolysates to be used as the carbon source in fermentation.

2. Materials and methods

2.1. Culture, inoculum preparation, and media

The fungus *Rhizopus oryzae* NRRL395 used in this work was kindly provided by the Northern Regional Research Center, Peoria, IL, USA. The stock culture was maintained on potato dextrose agar (PDA) plates and subcultured every month to maintain viability and activity.

The sporangiospores were collected from the 7-day culture on PDA plates by shaving and extracting with sterile deionized water. The spore suspension was diluted to 10^6 spores/mL with sterile deionized water. The diluted spore suspension (10 mL) was inoculated into the fermentor containing the sterile growth medium of 4 L initial volume.

Unless otherwise noted, glucose was used as the sole carbon source in both growth and production media. A growth medium containing (per liter) 50 g glucose and 5 g yeast extract was used for germinating spores and initiating hyphal growth. The production medium for enhancing lactic acid production while maintaining metabolic activities with minimal cell growth of *R. oryzae* was composed of (per liter) 70 g glucose, 0.6 g KH_2PO_4, 0.25 $MgSO_4$, 0.088 g $ZnSO_4$, and 0.3 g urea [13,14]. The feeding medium used in continuous operation consisted solely of glucose at the concentration of 150 g/L while urea was intermittently added every 24 h at the concentration of 0.15 g/L.

To investigate the efficacy of immobilized *R. oryzae* to utilize cellulosic material for lactate production, cassava pulp hydrolysate was also prepared for use as the carbon source in both growth and production media. Fresh cassava pulp was pretreated by direct steam or NaOH explosion at 121 °C, 15 psig for 60 min. After that, the mixture was subjected to hydrolysis using enzymes (cellulase and amylases) or 1 M HCl. The detailed procedure can be found in Thongchul et al. (2010) [24]. Similar to the glucose based media previously mentioned, the initial total sugars in the hydrolysates were adjusted to approximately 50 g/L for growth medium and 70 g/L for production medium.

2.2. Fermentor design

Free cell fermentation was carried out in a 5 L stirred fermentor (Biostat B Plus, Sartorius, Germany) while immobilized cell fermentation was conducted in a static bed bioreactor modified from the 5 L stirred fermentor (Biostat B Plus, Sartorius, Germany). The static bed bioreactor was constructed with a perforated stainless steel matrix mounted with a 100% cotton cloth affixed to the top plate of the fermentor. A detailed configuration can be found elsewhere [13].

2.3. Fermentor set up and operation

The fermentor containing the 4 L growth medium was autoclaved at 121 °C for 30 min. After sterilization and cooling down, a dissolved oxygen (DO) probe was calibrated with sterile nitrogen and air. The fermentor was controlled at 30 °C with specified agitation and aeration rates. The fermentor was inoculated with 10 mL spore suspension (10^6/mL). The growth phase took approximately 48 h for spore germination and initial cell growth before the growth medium was discarded and the fermentor was filled with 4 L sterile production medium. During the production phase, the pH was automatically controlled at 6.0 by 5 M NaOH. During operation, antifoam was intermittently added to prevent foaming. For batch cultivation, fermentation finished when glucose depletion or lactate production stopped. In continuous culture, fermentation finished when lactate production ceased or glucose concentration exceeded 10 g/L. Fermentation broth samples were taken approximately every 6 h. In continuous operation, after changing the medium to production medium, batch operation was initiated until the remaining glucose in the fermentation reached 10–20 g/L when continuous operation started. The feed solution was continuously transferred into the static bed fermentor while the broth was taken out at the same volumetric flow rate at the specified dilution rate. Fermentation broth samples were also taken approximately every 6 h.

Batch operation was first conducted to reiterate the efficacy of immobilized *R. oryzae* in the fibrous bed fermentor over free cell culture in the stirred fermentor previously as claimed by Chotisubha-anandha et al. (2011) and Tay and Yang (2002) [13,14]. Additionally, the key factors that controlled lactate production by *R. oryzae* were described during batch operation in the static bed fermentor to further determine the operating conditions during long-term cultivation. Those included agitation, aeration, and initial glucose concentration. Later, the robustness of immobilized *R. oryzae* was tested during long-term cultivation under continuous operation. The effect of feed medium compositions on the fermentation kinetics was observed during the cultivation. Also, cultivation of the immobilized *R. oryzae* in the medium containing high salt content like those obtained from the hydrolysis products of cellulosic materials was investigated for its ability to grow and produce lactate compared to those in the base case cultivation in glucose medium.

2.4. Sample analyses

The amount of total sugars in cassava pulp hydrolysates was determined by completely hydrolyzing the hydrolysate sample (1 mL) with 1 M HCl (9 mL) for 1 h at 121 °C, 15 psig. Monosaccharides released in the samples (mainly glucose in all hydrolysates with trace amounts of xylose (less than 4 g/L) in the case of

Please cite this article in press as: V. Pimtong, et al., Enhanced effectiveness of *Rhizopus oryzae* by immobilization in a static bed fermentor for L-lactic acid production, Process Biochem (2016), http://dx.doi.org/10.1016/j.procbio.2016.09.020

HCl-treated cassava pulp hydrolysate) were analyzed by high performance liquid chromatography (HPLC).

Fermentation broth samples were centrifuged at 10,000 *g* for 7 min. The supernatant was collected for analyses of remaining glucose, lactic acid, fumaric acid, and ethanol by HPLC. Due to immobilization resulting in complete cell-free broth, cell biomass was harvested from the fermentor at the end of fermentation. This protocol was also applied to the free cell fermentation study for consistency. To avoid harvesting cell biomass during sampling in free cell cultivation, a cheesecloth was used as a cover at the end of the sampling tube. The biomass was thoroughly washed with deionized water to remove entrapped soluble salt particles until a neutral pH of the washed water was obtained. The biomass was then dried at 105 °C until constant weight was obtained.

Product yield was determined from the ratio of product formed to substrate consumed during fermentation. Volumetric productivity was defined as the total amount of product formed per unit volume per time.

For HPLC analysis, the samples were centrifuged, filtered through a cellulose acetate membrane (0.45 μm pore size), and diluted with double distilled water. A diluted particle-free sample (15 μL) was injected into an organic acid analysis column (Biorad, Aminex HPX-87H ion exclusion organic acid column; 300 mm×7.8 mm) maintained at 45 °C in a column oven. 0.005 M H_2SO_4 was used as an eluant at the flow rate of 0.6 mL/min. A refractive index detector was used to detect organic compounds. The standards containing glucose (GLC), xylose (XYL), lactate (LAC), fumarate (FUM), and ethanol (ETH) at different concentrations in between 0 and 2 g/L were injected into the column as references. The peak area was used for the comparison basis.

Cell morphology in the static bed bioreactor was examined by scanning electron microscopy (SEM). Immobilized cells attached on the cotton cloth matrix both inside and outside the bed were collected for SEM examination. The sample was cut into a small piece of 0.50.5 cm^2 then fixed by immersing into 2.5% glutaraldehyde in 0.1 M phosphate buffer (pH 7.2) overnight at 4 °C. The sample was thoroughly rinsed with 0.2 M phosphate buffer (pH 7.2) for 10 min twice, then soaked in deionized water for 10 min. Later the sample was progressively dehydrated in various concentrations of ethanol (from 30, 50, 70, 95, to 100%) for 10 min in each concentration with the triplicates at 100%. To prevent damage to the sample specimen, a critical point dryer (CPD 020, Balzer) was used to dry the specimen to the critical drying point. Before examination, the sample was coated with electrically conductive material (60% gold and 40% palladium) using a spotter coating machine (CPD 020, Balzer) in the presence of the medium containing gaseous argon. After the coating process, the sample was examined using the scanning electron microscope (JSM-5410LV, JEOL).

3. Results and discussions

In this work, *R. oryzae* immobilized in the static bed fermentor was tested for the ability to grow and ferment lactate under different environmental stresses such as high initial glucose concentration and high concentration of salt impurities in hydrolysis products. In addition, it was tested for the ability to run at similar fermentor performance over a long period compared with those operated in batch cultivation.

3.1. Free cells versus immobilized cells for lactic acid fermentation by R. oryzae

Like those typically found during the free cell cultivation of other fungi in a stirred tank fermentor, growing *R. oryzae* in this fermentor configuration resulted in diverse morphologies as seen in Fig. 1. The morphological diversity was responsible for fungal metabolism which resulted in different production rates and ratios of end metabolites [25]. Fig. 2(A) shows the fermentation kinetics of free cell *R. oryzae* cultivated in the stirred fermentor. The production phase started at 48 h when the growth medium was discarded and the production medium was transferred into the fermentor. In the production phase, the lag phase took approximately 5 h before lac-

Fig. 1. Diverse morphology of free cells of *R. oryzae* suspended in the fermentation medium during cultivation in the stirred fermentor. (A) after 24 h growth phase; (B) rigid biofilm attached on the fermentor wall; (C) pellets suspended in the fermentation medium; and (D) mycelial clumps attached at the baffle area.

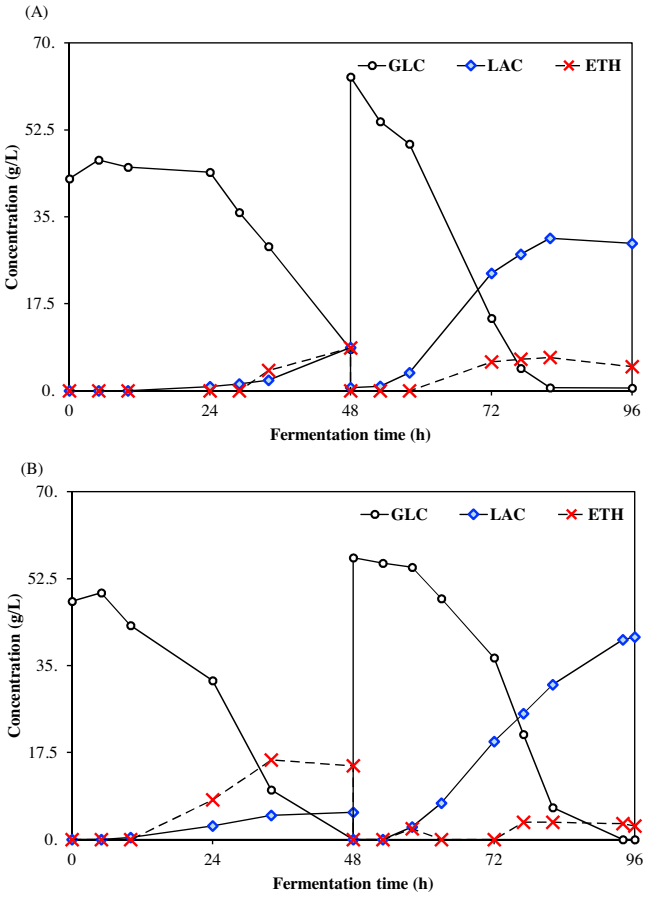

Fig. 2. Fermentation kinetics of (A) free cells of *R. oryzae* cultivated in the stirred fermentor and (B) immobilized cells of *R. oryzae* in the static bed fermentor. The fermentor was operated at 30 °C, 700 rpm, and 0.5 vvm air after inoculated with sporangiospores in the growth medium for 48 h. The growth medium was replaced by the production medium and the fermentation was carried out until 120 h. The pH was automatically controlled at 6.0 by 5 M NaOH during the production phase.

Please cite this article in press as: V. Pimtong, et al., Enhanced effectiveness of *Rhizopus oryzae* by immobilization in a static bed fermentor for L-lactic acid production, Process Biochem (2016), http://dx.doi.org/10.1016/j.procbio.2016.09.020

tate production began. Whilst glucose was noticeably consumed at the constant rate until almost depletion at 82 h. Low lactate yield of 0.46 g/g and productivity of 0.61 g/L·h together with the presence of ethanol at the corresponding yield of 0.08 g/g indicated unfavorable conditions in this fermentor configuration. Not only did the control and maintenance of the proper morphology for lactic acid production fail, but also operation at such a high agitation rate could also destroy fungal mycelia. This eventually led to change in the morphology during fermentation as the metabolic response to retain vitality and activity. The major problem in mass transfer was the diversity in morphology from pellets to clumps, especially as concerned oxygen limitation. The limiting oxygen eventually led to ethanol production [12,14,17,26–28]. Another major difficulty in operating the stirred fermentor for 2-phase lactate production by *R. oryzae* occurred during the medium change. The appearance of varied fungal growth everywhere hindered medium transfer as well as hampered sensor readings (pH, DO, and temperature, for example) (Fig. 1). As aforementioned, we could claim that the stirred fermentor was not appropriate for cultivating *R. oryzae* for lactate production.

For better control of the morphology of *R. oryzae*, the static bed fermentor was introduced in lactic acid fermentation [13]. By immobilizing the germinated spores and allowing them to grow in between the fibrous network of the cotton cloth, this resulted in complete cell immobilization (Fig. 3), higher cell density (Table 1) and a cell-free fermentation broth. Previous studies reported that complete cell immobilization in a thin layer allowed improved mass transfer especially oxygen transfer, simple control, and eventually enhanced lactic acid production (Table 1) [13,29]. Comparing the fermentation kinetics of lactate production in the static bed fermentor with those obtained in the stirred fermentor, ethanol production was apparently reduced by half when operating the 2 fermentor configurations at the same agitation and aeration rates (Fig. 2(A) and (B)). This strongly confirmed that immobilized cells in the form of a thin flat sheet in the static bed fermentor promoted a high cell density environment without limited oxygen transfer towards the center of the immobilized matrix. From Table 1, increased lactate production with lowered ethanol production was found when the agitation and aeration rates were increased. The highest lactate production was found when operating the static bed fermentor at 700 rpm and 0.5 vvm air. Evidence of balanced pyruvate fluxes towards the TCA cycle and lactate production route during cultivation was confirmed by the absence of fumarate and lowered ethanol concentration [5]. The results found in this study were similar to those previously reported in Chotisubha-anandha et al. (2011); Coban and Demirci (2016); and Thitiprasert et al. (2016) [13,29,30].

3.2. Improved performance on high glucose levels during lactate fermentation in the static bed fermentor

Although lactate production was improved with increasing agitation and aeration rates, the yield and productivity as well as the final titer were somewhat low when compared to those obtained from bacterial fermentation. The theoretical yield of lactate from glucose (75%) was nearly acquired from the culture in the static bed fermentor at 700 rpm and 0.5 vvm air; however, the final titer was only 40.79 g/L which was considered low for making downstream recovery become economically feasible (Table 2) [5]. Increasing the final titer could be simply done by using a high initial substrate concentration with the subsequently lower yield and productivity due to substrate repression [31]. In this study, the static bed fermentor was tested for its performance in controlling fungal morphology while at the same time manipulating fungal physiology and metabolism to grow and produce lactic acid at a high initial substrate concentration. As can be seen in Table 2, it was found that increasing the initial glucose concentration resulted in higher final lactate concentration without strong evidence of glucose repression. Complete glucose consumption was obtained at 96 h when using the initial glucose concentration of 100 g/L. At 150 g/L initial glucose, complete consumption occurred at 120 h. About 35.14 g/L glucose still remained in the fermentation broth at the end of fermentation (at 120 h) of 200 g/L glucose. It should be noted that the residual glucose would subsequently produce a larger load in the downstream recovery of lactate and wastewater treatment.

By applying the optimized operating conditions previously determined from the fermentation with initial glucose of 70 g/L, it was found that starting the fermentation with higher glucose concentration resulted in lower lactate yield (approximately 0.50 g/g glucose) but the productivity was improved. The ratio of medium compositions present in the production medium was somewhat responsible for the lower lactate yield. While increasing glucose concentration in the medium, the other compositions remained unchanged; therefore, the new proportion in the medium led to the deviation of glucose flux towards all possible routes in order to keep the metabolic balances within the cells [32]. Increase in the productivity could be explained by the high glucose concentration generated high metabolic fluxes in glycolysis that corresponded with the turnover rates of key enzymes responsible for lactate production [5,32]. Cell biomass production increased with the increasing initial glucose concentration when sufficient oxygen was present (Table 2). The same initial glucose concentration of 50 g/L was completely consumed during the growth phase, and this implied that the growth proceeded during the production phase when more glucose was available although the organic nitrogen source was limited with the presence of $ZnSO_4$, responsible for growth inhibition [24]. Nevertheless, cell biomass yield was not significantly affected by initial glucose concentration. Ethanol production also slightly increased with the increasing initial glucose concentration. This presumably confirmed that immobilizing *R. oryzae* in the form of a flat sheet promoted oxygen diffusion regardless of increasing the cell biomass concentration obtained from a high initial glucose concentration. Higher final lactate concentration was also achieved when the initial glucose concentration was increased. A similar finding was reported by Bulut et al. (2004) who focused on glucose repression in *R. oryzae* at concentrations higher than 200 g/L; however, the highest final lactate concentration obtained in their study was only 60 g/L with 150 g/L initial glucose concentration [31].

3.3. Efficacy of immobilized R. oryzae during the long-term continuous culture in the static bed fermentor

Continuous operation is recognised as a technique applied during cultivation that limits substrate repression and product inhibition; thus, prolonging the fermentation process at an acceptable targeted concentration, yield, and productivity under steady state condition [33]. Operating fermentation in continuous mode seems challenging due to the risk of wash out when a high dilution rate is applied for high productivity [8]. Cell wash out could be successfully avoided in a static bed fermentor where the cells have been fully immobilized onto the cotton cloth provided; therefore, continuous operation is feasible in this fermentor configuration. Fig. 4 shows the fermentation kinetics of immobilized *R. oryzae* cultivated in the static bed fermentor. Batch fermentation was primarily conducted as previously discussed. When the glucose concentration became low at 96 h, continuous operation was started by the feeding of glucose solution (150 g/L) at the volumetric flow rate of 0.04 L/h with the concurrent broth removal from the fermentor at the same flow rate. At the dilution rate of 0.01 h^{-1} studied, the operation rapidly approached a steady state within 11 h (at 107 h). High lactate concentration in between

Please cite this article in press as: V. Pimtong, et al., Enhanced effectiveness of *Rhizopus oryzae* by immobilization in a static bed fermentor for L-lactic acid production, Process Biochem (2016), http://dx.doi.org/10.1016/j.procbio.2016.09.020

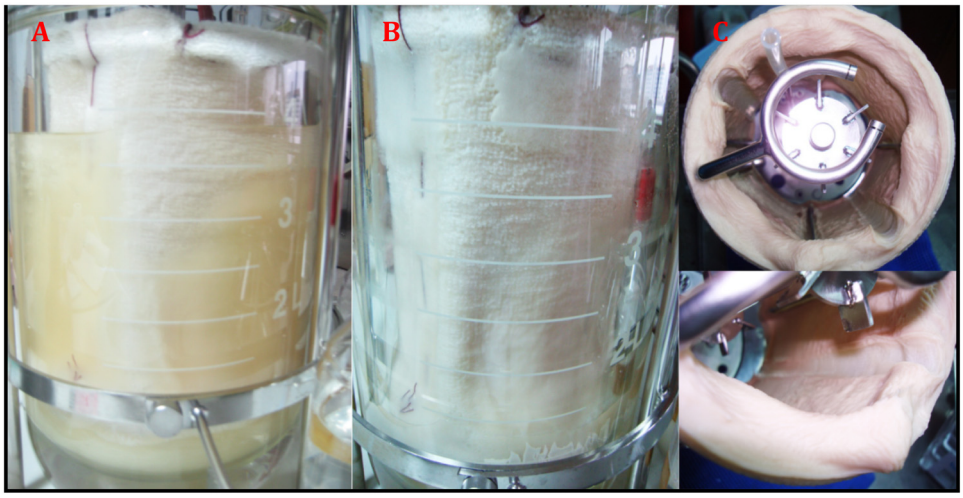

Fig. 3. Appearance of immobilized *R. oryzae* on the cotton sheet in the static bed fermentor. (A) At 24 h growth phase; (B) At 48 h growth phase; and (C) immobilized mycelia attached to both sides of the bed at the end of fermentation.

Table 1
Fermentation kinetics of both free cells and immobilized cells of *R. oryzae* cultivated in 2 fermentor configurations using different agitation and aeration rates at 96 h.

Conditions	CDW[a] (g)	Concentration (g/L)			Yield (g/g)			Productivity (g/L h)		
		LAC	GLC	CDW[a]	LAC	ETH	CDW[a]	LAC	ETH	CDW[a]
FC 700, 0.5	7.16 ± 1.95	29.67 ± 2.25	0.50 ± 0.02	2.39 ± 0.65	0.46 ± 0.04	0.08 ± 0.02	0.02 ± 0.00	0.61 ± 0.12	0.10 ± 0.04	0.02 ± 0.00
IM 300, 0.5	10.59 ± 2.02	29.66 ± 3.14	0.00 ± 0.00	3.53 ± 0.68	0.45 ± 0.06	0.04 ± 0.03	0.03 ± 0.01	0.62 ± 0.15	0.05 ± 0.01	0.02 ± 0.00
IM 300, 1.0	10.99 ± 1.76	31.84 ± 0.25	1.07 ± 0.15	3.66 ± 0.58	0.48 ± 0.02	0.00 ± 0.00	0.03 ± 0.00	0.66 ± 0.17	0.00 ± 0.00	0.03 ± 0.01
IM 500, 0.5	9.94 ± 1.43	29.66 ± 0.35	0.00 ± 0.00	3.31 ± 0.48	0.45 ± 0.01	0.04 ± 0.01	0.03 ± 0.01	0.62 ± 0.10	0.05 ± 0.01	0.02 ± 0.00
IM 500, 1.0	10.59 ± 1.38	39.59 ± 0.67	0.00 ± 0.00	3.53 ± 0.46	0.59 ± 0.01	0.00 ± 0.00	0.04 ± 0.01	0.82 ± 0.18	0.00 ± 0.00	0.03 ± 0.01
IM 700, 0.5	12.26 ± 2.19	40.79 ± 3.14	0.00 ± 0.00	4.09 ± 0.73	0.72 ± 0.06	0.05 ± 0.03	0.04 ± 0.00	0.85 ± 0.15	0.06 ± 0.02	0.03 ± 0.00
IM 700, 1.0	11.88 ± 1.87	40.66 ± 1.30	0.00 ± 0.00	3.96 ± 0.61	0.65 ± 0.02	0.00 ± 0.00	0.04 ± 0.01	0.85 ± 0.16	0.00 ± 0.00	0.04 ± 0.01

Remarks CDW represents total cell dry weight; LAC represents lactic acid; GLC represents glucose; ETH represents ethanol. FC means free cell culture in the stirred fermentor; IM means immobilized cell culture in the static bed fermentor. The numbers in the format of xxx, x.x appeared in the first column represent the agitation rate in rpm and aeration rate in vvm during cultivation.

[a] When reporting the values of CDW, the overall values were representing the values collected or calculated along both growth and production phases.

Table 2
Fermentation kinetics of batch cultivation of immobilized *R. oryzae* in the static bed fermentor at high glucose concentration during the production phase compared to the based case study (initial glucose of 70 g/L). The fermentation was operated at 30 °C, 700 rpm, and 0.5 vvm air. The pH was automatically controlled at 6.0 by 5 M NaOH.

Initial GLC (g/L)	CDW[a] (g)	Concentration (g/L)			Yield (g/g)			Productivity (g/L h)		
		LAC	GLC	CDW[a]	LAC	ETH	CDW[a]	LAC	ETH	CDW[a]
At 96 h										
70 (base case)	12.26 ± 2.19	40.79 ± 3.14	0.00 ± 0.00	4.09 ± 0.73	0.72 ± 0.06	0.05 ± 0.03	0.04 ± 0.00	0.85 ± 0.15	0.06 ± 0.02	0.03 ± 0.00
100	16.06 ± 1.26	48.86 ± 3.69	0.00 ± 0.00	5.35 ± 1.09	0.55 ± 0.03	0.05 ± 0.00	0.04 ± 0.01	1.02 ± 0.05	0.10 ± 0.02	0.04 ± 0.01
150	n/a	57.09 ± 4.28	27.62 ± 1.26	n/a	0.46 ± 0.01	0.08 ± 0.01	n/a	1.19 ± 0.16	0.20 ± 0.06	n/a
200	n/a	58.06 ± 1.33	80.60 ± 1.50	n/a	0.54 ± 0.07	0.09 ± 0.01	n/a	1.21 ± 0.08	0.19 ± 0.00	n/a
At 120 h										
150	21.61 ± 4.28	75.28 ± 1.48	0.00 ± 0.00	7.20 ± 0.22	0.50 ± 0.03	0.07 ± 0.00	0.04 ± 0.00	1.05 ± 0.09	0.15 ± 0.00	0.04 ± 0.00
200	27.02 ± 5.65	80.77 ± 1.50	35.14 ± 0.12	9.01 ± 1.15	0.53 ± 0.03	0.01 ± 0.00	0.04 ± 0.01	1.12 ± 0.08	0.02 ± 0.00	0.05 ± 0.01

Remarks CDW represents total cell dry weight; LAC represents lactic acid; GLC represents glucose; ETH represents ethanol.

[a] When reporting the values of CDW, the overall values were representing the values collected or calculated along both growth and production phases.

67 g/L and 79 g/L could be maintained with the remaining glucose lower than 5 g/L at steady state. Continuous operation was maintained at steady state until 220 h. After that, glucose accumulation was observed while lactate production slowly declined (data not shown). This revealed evidence of wash out as a result of lowering the metabolic rate of immobilized cells in the static bed fermentor. Sporulation was found at the end of fermentation strongly confirming lowered glucose consumption and the cessation of lactate production after 220 h operation (Fig. 5).

To further operate the continuous culture, a new steady state should have been attempted by reduction of the dilution rate; however, reducing the dilution rate gave the unwanted lower yield and productivity. Maintaining high yield and productivity could have been achieved by prevention of the sporulation that occurred under stress, i.e. limited nitrogen in this case. Therefore, urea was intermittently fed into the fermentor during continuous operation. The fermentation profile obtained in continuous operation with intermittent urea feeding was rather similar to that from the continuous culture with glucose solution feeding (Fig. 4(A)) except for the presence of fumaric acid (Fig. 4(B)). The fermentation approached a steady state at 104 h, only 12 h after the continuous operation started at 96 h. Nonetheless, when nitrogen was not limited, a steady state seemed difficult to maintain as could be observed from the slightly decreasing lactate concentration. Ethanol was

Please cite this article in press as: V. Pimtong, et al., Enhanced effectiveness of *Rhizopus oryzae* by immobilization in a static bed fermentor for L-lactic acid production, Process Biochem (2016), http://dx.doi.org/10.1016/j.procbio.2016.09.020

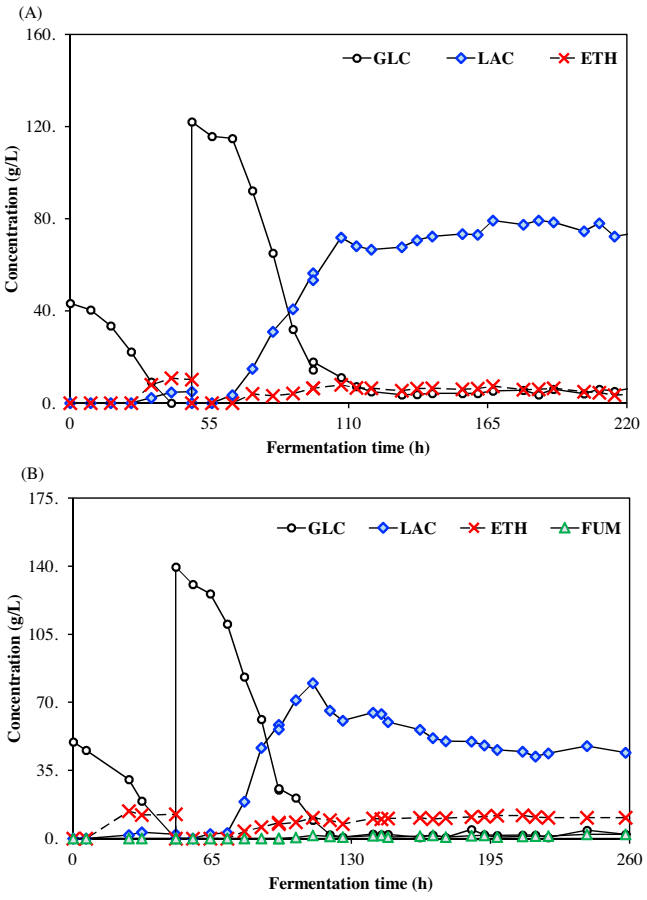

Fig. 4. Continuous culture of immobilized *R. oryzae* in the static bed fermentor. Fermentation was started with batch operation by inoculating spores for growth initiation for 48 h. After changing the medium, batch operation was continued until 96 h. Later continuous operation was started by 150 g/L glucose feeding at (A) the dilution rate of 0.01 h^{-1} and (B) the dilution rate of 0.01 h^{-1} with supplemented urea (0.15 g/L) every 24 h.

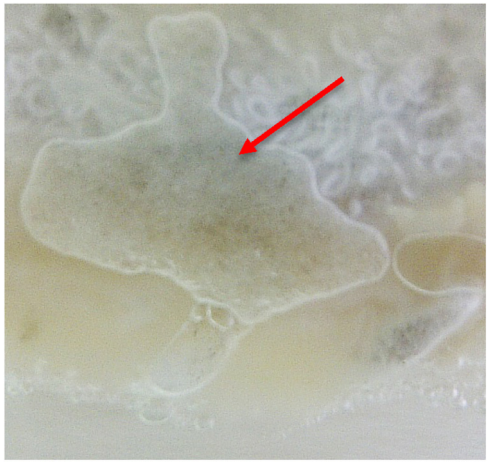

Fig. 5. Sporulation inside the immobilized sheet of *R. oryzae* in the static bed fermentation observed during continuous culture with sole glucose feeding (see arrow).

also found to a larger extent. The presence of fumaric acid and the larger amount of ethanol were caused by the supplemented nitrogen (urea). Immobilized *R. oryzae* responded to the existence of urea in the fermentation broth by shifting pyruvate flux towards biomass production as observed by the new branching and formation of new cells (Fig. 6). A second layer of immobilized cells further

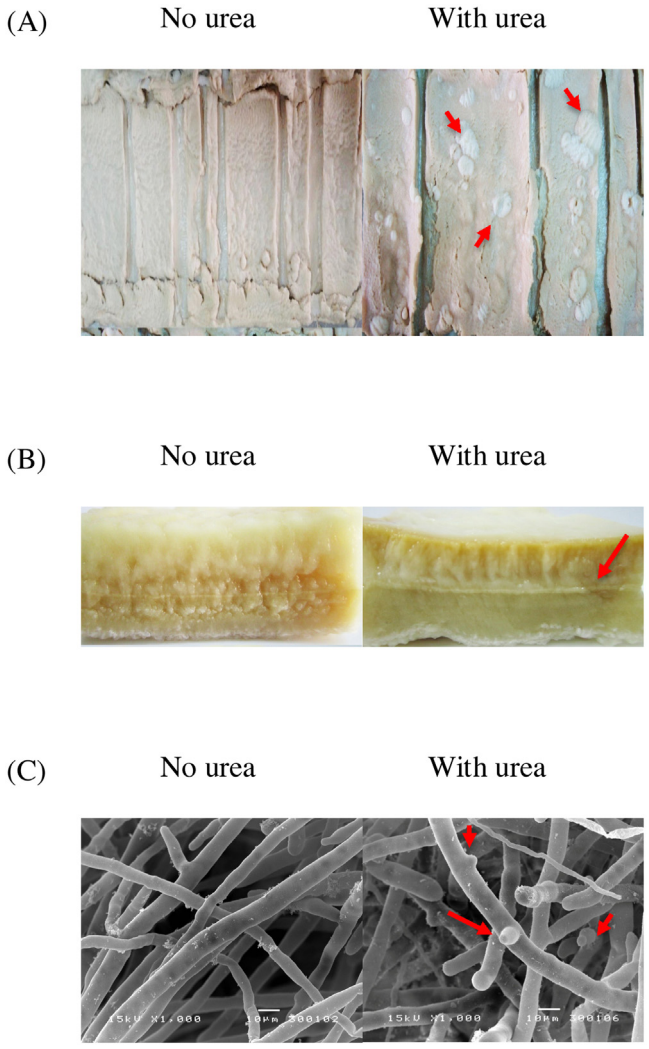

Fig. 6. Effect of intermittent urea feeding on growth behavior of immobilized *R. oryzae* during continuous culture; (A) morphology of immobilized cells showing new cells generated when urea was present; (B) cross-sectional area of immobilized sheet indicating 2-layer growth in the culture with intermittent urea feeding; and (C) from the scanning electron micrographs, branching was more evident in the culture with intermittent urea feeding.

grew on the flat sheet matrix (Fig. 6(B)) causing oxygen limitation; thus, increasing ethanol production [5,34].

The evidence of fumarate formation could be explained by the imbalanced C/N ratio of glucose and urea fed during continuous operation for biosynthesis towards the TCA cycle. As a result, fumarate, the key intermediate to cell biomass synthesis, was found [5,35]. Although urea proved to prevent sporulation during continuous operation, lactate production was not as good as operation with solely glucose feeding. Therefore, a balanced feeding ratio of urea should have been determined in order to maintain the proper metabolic rate for lactate production besides preventing sporulation.

Comparing the production performance in continuous operation with sole glucose feeding with that in batch culture, it was found that a sufficiently high lactate concentration could be maintained during continuous culture similar to the final concentration obtained from batch culture (approximately 70 g/L) (Table 3). Although similar yields were acquired from both batch and continuous cultures, productivity was slightly decreased in continuous fermentation. The results obtained in this work revealed the feasibility of operating a static bed fermentor in continuous mode

Please cite this article in press as: V. Pimtong, et al., Enhanced effectiveness of *Rhizopus oryzae* by immobilization in a static bed fermentor for L-lactic acid production, Process Biochem (2016), http://dx.doi.org/10.1016/j.procbio.2016.09.020

Table 3
Lactic acid production by *R. oryzae* acquired from different process operation.

Key conditions	Operating mode	Substrate	Final conc. (g/L)	Yield (g/g)	Productivity (g/L·h)	Fermentation time	References
Immobilized cells in the static bed fermentor	Batch	Glucose (150 g/L)	75.28	0.50	1.05	96 h	This work
	Continuous ($0.01\ h^{-1}$)	Glucose (150 g/L)	72.32	0.50	0.72	215 h	This work
Immobilized cells in a rotating bed fermentor	Repeated batch/fed-batch	Glucose	126.00	0.89	2.50	Within 100 h	Tay and Yang (2002)
Biofilm on honeycomb support in bubble column fermentor	Repeated batch	Glucose (80 g/L)	68.80	0.93	0.72	9 cycles (36 days)	Wang et al. (2010)
Multi-pulse feeding in a stirred fermentor (pelletized)	Fed-batch	Glucose	92.00	0.60	0.70	5.5 days	Liu et al. (2006)
Immobilized cells in polyurethane foam cubes	Continuous ($0.04–0.20\ h^{-1}$)	Glucose (102 g/L)	~38.00–58.00	0.60	1.00–6.20	33–90 h	Sun et al. (1999)
Microparticles with 10 g/L talcum addition	Batch	Glucose (126 g/L)	75.10	0.63	1.54	120 h	Coban and Demirci (2016)

for lactate production. Due to the stability of immobilized cells in the static bed fermentor, approximately, 67% of the theoretical lactate yield was achieved with reasonably high titer to that obtained from the batch culture over a long period. The main cuts in production cost could be achieved by reducing the seeding in every batch cycle, substrate/energy consumption, and labor. From Table 3, in the batch culture, high lactate yield and productivity were usually obtained with a low final product titer as the consequence of high specific product formation rates during the exponential growth phase and substrate repression. On the other hand, a high final lactate titer was acquired in repeated batch or fed-batch fermentation with slightly lower yield and productivity somewhat due to product inhibition as the fermentation proceeded and a larger amount of product was accumulated [36]. Continuous operation was generally introduced in fermentation in order to reduce both substrate repression and product inhibition, but this operating mode usually suffered from low yield and productivity in addition to being at higher risk of fermentor wash out when operating at a high dilution rate. Nonetheless, with a well optimized dilution rate and proper substrate compositions together with a remarkable cell immobilization technique like those determined in this work, it is believed that continuous culture could be successfully used in lactic acid fermentation by *R. oryzae*.

3.4. *Metabolic responses of immobilized* R. oryzae *to salt impurities in hydrolysis products*

Utilizing inexpensive cellulosic feedstocks or agricultural residues as the sole carbon substrates is another approach to lower lactic acid fermentation costs [37]. Pretreatment and hydrolysis are common techniques employed in sugar recovery from such feedstocks. Nonetheless, some impurities remain after pretreatment and hydrolysis such as salts, acetic acid, phenolic compounds, and furfurals are somewhat claimed to be responsible to lower fermentation efficacy due to their inhibitory effects on microbial metabolism [24,38,39]. To eliminate this problem, post-treatment after hydrolysis, e.g. resin adsorption, is required for impurity removal to obtain a sufficiently high purity of sugar solution for fermentation [40]. This undoubtedly results in cost contribution even if low-priced raw materials are used as foodstock [1]. An acceptable threshold of impurities remaining in the hydrolysate also depends on the robustness of the microbes to be used in fermentation. In this work, the performance of immobilized *R. oryzae* in the static bed fermentor was tested against the salt impurities remaining in the hydrolysates for its metabolic responses and lactate production. Similar to that observed in base case glucose fermentation, after inoculation, spore germination and immobilization on the cotton sheet occurred, generating complete immobilization on the cotton cloth and cell-free fermentation broth. Lactate yield and productivity as well as the final titer obtained from fermentations using cassava pulp hydrolysates were lower compared to those from glucose fermentation (Table 4). On the other hand, higher production of cell biomass and ethanol were acquired in fermentations of hydrolysates. This was presumably due to impurities including acetic acid, furfurals, and phenolic compounds from subsequent conversion of the hydrolysis products as well as salt ions including the Na^+ and Cl^- remaining in the NaOH explosion during pretreatment and acid hydrolysis. These impurities somehow caused fungal stress and impaired metabolic rate [41]. Scanning electron micrographs of the immobilized *R. oryzae* grown in the hydrolysate with NaOH explosion and HCl hydrolysate showed strong evidence of cell impairment as salt crystals were found attached to the growing mycelia immobilized on the cotton cloth (Fig. 7(A) and (B)). In order to withstand drastic conditions, adaptation occurred in the immobilized cell structure of *R. oryzae* in the static bed fermentor. More cell biomass was produced to substitute the impaired cells. With more cell biomass generation, the thick layer on the cotton sheet eventually caused oxygen limitation inside the immobilized cell structure. As a consequence, increasing ethanol production was observed. Although lower lactic acid production was obtained from cassava pulp hydrolysate compared with glucose, the lactate titer, yield, and productivity reported in this work were higher than those previously reported in Saito et al. (2012) [6]. The final lactate titer obtained from their study was lower than 10 g/L, while in this work with the steam pretreatment and enzymatic hydrolysis, a lactate production of 25.41 g/L final titer and 0.44 g/g yield were acquired. As aforementioned, the results in this work noticeably proved that growing *R. oryzae* in an immobilized flat sheet structure inside the static bed bioreactor helps the fungi to survive under drastic stress conditions. Thus, this would presumably confirm the effectiveness of this fermentor configuration.

4. Conclusion

Fungal fermentation usually suffers from diversity in morphology which directly affects the process performance. In this work, the static bed fermentor proved effective in controlling the proper morphology of *R. oryzae* during cultivation for lactic acid. With complete cell immobilization in this fermentor, cell-free broth was acquired; thus, generating the homogeneity with the increasing lactate production compared with free cell fermentation. Increase in tolerance under different environmental stresses including high glucose concentration and impurities remaining from cellulosic pretreatment and hydrolosis – considered toxic to microbial conversion—was observed from the immobilized culture in this fermentor configuration. In addition, long-term cultivation

Please cite this article in press as: V. Pimtong, et al., Enhanced effectiveness of *Rhizopus oryzae* by immobilization in a static bed fermentor for L-lactic acid production, Process Biochem (2016), http://dx.doi.org/10.1016/j.procbio.2016.09.020

Table 4
Metabolic responses of immobilized R. oryzae to salt impurities obtained from different pretreatment and hydrolysis of cassava pulp during batch cultivation in the static bed fermentor. The fermentation was operated at 30 °C, 700 rpm, and 0.5 vvm air. The pH was automatically controlled at 6.0 by 5 M NaOH.

Carbon substrate[a]	CDW[b] (g)	Final LAC conc. (g/L)	Yield (g/g)		Productivity (g/L h)	
			LAC	ETH	LAC	ETH
At 96 h						
Glucose	12.26 ± 2.19	40.79 ± 3.14	0.72 ± 0.06	0.05 ± 0.03	0.85 ± 0.15	0.06 ± 0.02
ECPHNP	57.26 ± 1.26	26.57 ± 0.10	0.42 ± 0.01	0.19 ± 0.01	0.66 ± 0.07	0.49 ± 0.06
ECPHSP	58.09 ± 1.04	25.41 ± 0.30	0.44 ± 0.01	0.16 ± 0.03	0.64 ± 0.11	0.38 ± 0.10
ECPHSNP	64.42 ± 1.35	7.63 ± 0.85	0.12 ± 0.02	0.21 ± 0.03	0.16 ± 0.04	0.27 ± 0.04
HACPH	76.81 ± 1.24	6.75 ± 0.74	0.13 ± 0.02	0.24 ± 0.02	0.14 ± 0.03	0.26 ± 0.03

Remarks:
ECPHNP—enzymatic cassava pulp hydrolysate without pretreatment.
ECPHSP—cassava pulp hydrylysate with steam pretreatment and enzymatic digestion.
ECPHSNP—cassava pulp hydrolysate with NaOH explosion and enzymatic digestion.
HACPH – HCl treated cassava pulp hydrolysate.
[a] Carbon substrate—initial glucose equivalent was set at approximately 70 g/L.
[b] CDW—cell dry weight collected at the end of fermentation.

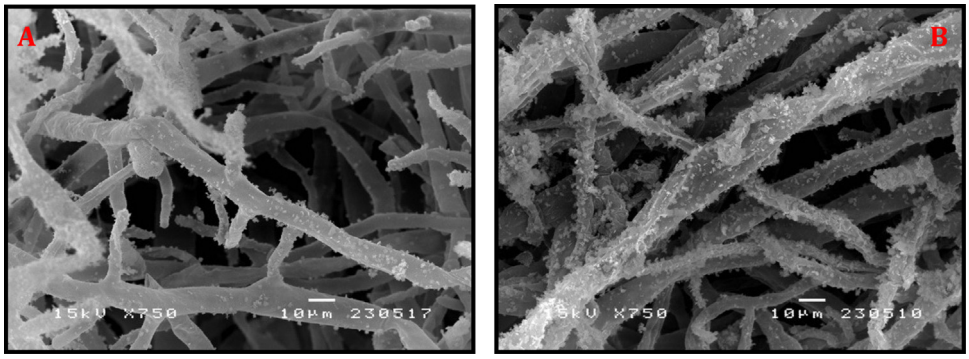

Fig. 7. Scanning electron micrographs showing salt crystals from hydrolysates attached on the mycelia of immobilized *R. oryzae* on the cotton cloth; (A) cassava pulp hydrolysate with NaOH explosion and enzymatic digestion; and (B) HCl-treated cassava pulp hydrolysate.

for lactic acid in this fermentor was proven to be feasible. With the constant cell density remaining in the fermentor, a steady state condition was easily approached and maintained for a long period with high lactate production. With the beneficial outcomes mentioned and the simple design, the significance of the static bed fermentor for fungal cultivation can be addressed.

Acknowledgments

This work was financially supported by the Grant for International Research Integration: Research Pyramid, Ratchadapiseksomphot Endowment Fund (GCURP_58_01_33_01) and Thailand Research Fund via the Distinguished Research Professor Grant (DPG5880003). The first author, Varunee Pimtong, was the recipient of the Ratchadapiseksomphot Endowment Fund via the 90th anniversary of Chulalongkorn University. The research facility support from the Chulalongkorn Academic Advancement into its 2nd Century Project (CUAASC) is also highly acknowledged.

References

[1] J. Wang, Q. Wang, Z. Xu, W. Zhang, J. Xiang, Effect of fermentation conditions on L-lactic acid production form soybean straw hydrolysate, J. Microbiol. Biotechnol. 25 (2015) 26–32.
[2] D.C. Vodnar, F.V. Dulf, O.L. Pop, C. Socaciu, L(+)-lactic acid production by pellet-form *Rhizopus oryzae* NRRL 395 on biodiesel crude glycerol, Microb. Cell Fact. 12 (2013) 1–9.
[3] G. Juodeikiene, D. Vidmantiene, L. Basinskiene, D. Cernauskas, E. Bartkiene, D. Cizeikiene, Green matrices for sustainability of biobased lactic acid from starchy biomass vs chemical synthesis, Catal. Today 239 (2015) 11–16.
[4] M. Taskin, N. Esim, S. Ortucu, Efficient production of L-lactic acid from chicken feather protein hydrolysate and sugar beet molasses by the newly isolated *Rhizopus oryzae* TS-61, Food Bioprod. Process. 90 (2012) 773–779.
[5] B.J. Meussen, L.H. de Graaff, J.P.M. Sanders, R.A. Weusthuis, Metabolic engineering of *Rhizopus oryzae* for the production of platform chemicals, Appl. Microbiol. Biotechnol. 94 (2012) 875–886.
[6] K. Saito, Y. Hasa, H. Abe, Production of lactic acid from xylose and wheat straw by *Rhizopus oryzae*, J. Biosci. Bioeng. 114 (2012) 166–169.
[7] T. Yamane, R. Tanaka, Highly accumulative production of L(+)-lactate from glucose by crystallization fermentation with immobilized *Rhizopus oryzae*, J. Biosci. Bioeng. 115 (2013) 90–95.
[8] M.A. Abdel-Rahman, Y. Tashiro, K. Sonomoto, Recent advances in lactic acid production by microbial fermentation processes, Biotechnol. Adv. 31 (2013) 877–902.
[9] E. Efremenko, O. Spiricheva, S. Varfolomeyev, V. Lozinsky, R*hizopus oryzae* fungus cells producing L(+)-lactic acid: kinetic and metabolic parameters of free and PVA-cryogel-entrapped mycelium, Appl. Microbiol. Biotechnol. 72 (2006) 480–485.
[10] Y. Sun, Y.-L. Li, S. Bai, Modeling of continuous L(+)-lactic acid production with immobilized *R. oryzae* in an airlift bioreactor, Biochem. Eng. J. 3 (1999) 87–90.
[11] H.N. Chang, N.J. Kim, J. Kang, C.M. Jeong, J.D. Choi, Q. Fei, B.J. Kim, S. Kwon, S.Y. Lee, J. Kim, Multistage high cell continuous fermentation for high productivity and titer, Bioprocess Biosyst. Eng. 34 (2011) 419–431.
[12] Z. Wang, Y. Wang, S.T. Yang, R. Wang, H. Ren, A novel honeycomb matrix for cell immobilization to enhance lactic acid production by *Rhizopus oryzae*, Bioresour. Technol. 101 (2010) 5557–5564.
[13] N. Chotisubha-anandha, S. Thitiprasert, V. Tolieng, N. Thongchul, Improved oxygen transfer and increased L-lactic acid production by morphology control of *Rhizopus oryzae* in a static bed bioreactor, Bioprocess Biosyst. Eng. 34 (2011) 163–172.
[14] A. Tay, S.T. Yang, Production of L-(+)-lactic acid from glucose and starch by immobilized cells of *Rhizopus oryzae* in a rotating fibrous bed bioreactor, Biotechnol. Bioeng. 80 (2002) 1–12.
[15] J.P. Lin, S.D. Ruan, P.L. Cen, Mathematical model of L-lactic acid fermentation in a RDC coupled with product separation by ion exchange, Chem. Eng. Commun. 168 (1998) 59–79.
[16] Y. Liu, W. Liao, C. Liu, S. Chen, Optimization of L-(+)-lactic acid production using pelletized filamentous *Rhizopus oryzae* NRRL395, Appl. Biochem. Biotechnol. 131 (2006) 844–853.
[17] E.Y. Park, Y. Kosakai, M. Okabe, Efficient production of L-(+)-lactic acid using mycelial cotton-like flocs of *Rhizopus oryzae* in an air-lift bioreactor, Biotechnol. Prog. 14 (1998) 699–704.

Please cite this article in press as: V. Pimtong, et al., Enhanced effectiveness of *Rhizopus oryzae* by immobilization in a static bed fermentor for L-lactic acid production, Process Biochem (2016), http://dx.doi.org/10.1016/j.procbio.2016.09.020

[18] Y. Sun, Y.L. Li, S. Bai, H. Yang, Z.D. Hu, Stability of immobilized *R. oryzae* in repetitive batch production of L-(+)-lactic acid: effect of inorganic salts, Bioprocess. Eng. 19 (1998) 155–157.
[19] X.Y. Dong, S. Bai, Y. Sun, Production of L(+)-lactic acid with *Rhizopus oryzae* immobilized in polyurethane foam cubes, Biotechnol. Lett. 18 (1996) 225–228.
[20] H. Hamamci, D.D. Ryu, Production of L(+)-lactic acid and using immobilized *Rhizopus oryzae*, reactor performance based on kinetic model simulation, Appl. Biochem. Biotechnol. 44 (1994) 125–133.
[21] Y.D. Hang, H. Hamamci, E.E. Woodams, Production of L(+)-lactic acid by *Rhizopus oryzae* immobilized in calcium alginate gels, Biotechnol. Lett. 11 (1989) 119–120.
[22] M. Tamada, A.A. Begum, S. Sadi, Production of L-(+)-lactic acid by immobilized cells of *Rhizopus oryzae* with polymer supports prepared by gamma-ray-induced polymerization, J. Ferment. Bioeng. 74 (1992) 379–383.
[23] L. Xuemei, L. Jianping, L. Moe, C. Peillin, L-lactic acid production using immobilized *Rhizopus oryzae* in a three-phase fluidized-bed with simultaneous product separation by electrodialysis, Bioprocess. Eng. 20 (1999) 230–237.
[24] N. Thongchul, S. Navankasattusas, S.T. Yang, Production of lactic acid and ethanol by *Rhizopus oryzae* integrated with cassava pulp hydrolysis, Bioprocess Biosyst. Eng. 33 (2010) 407–416.
[25] Y.-Q. Fu, L.-F. Yin, H.-Y. Zhu, R. Jiang, S. Li, Q. Xu, Effects of pellet characteristics on L-lactic acid fermentation by *R. oryzae*: pellet morphology, diameter, density, and interior structure, Appl. Biochem. Biotechnol. 174 (2014) 2019–2030.
[26] J.X. Du, N.J. Cao, C.S. Gong, G.T. Tsao, Production of L-lactic acid by *Rhizopus oryzae* in a bubble column fermentor, Appl. Biochem. Biotechnol. 7 (1998) 0–72, 323–329.
[27] J. Lin, M. Zhou, X. Zhao, S. Luo, Y. Lu, Extractive fermentation of L-lactic acid with immobilized *Rhizopus oryzae* in a three-phase fluidized bed, Chem. Eng. Process. 46 (2007) 369–374.
[28] B. Zhang, P.J. He, N.F. Ye, L.M. Shao, Enhanced isomer purity of lactic acid from the non-sterile fermentation of kitchen wastes, Bioresour. Technol. 99 (2008) 855–862.
[29] S. Thitiprasert, V. Pimtong, K. Kodama, S. Sooksai, S. Tanasupawat, S. Assabumrungrat, V. Tolieng, N. Thongchul, Correlative effect of dissolved oxygen and key enzyme inhibitors responsible for L-lactate production by immobilized *Rhizopus oryzae* NRRL395 cultivated in a static bed bioreactor, Process Biochem. 51 (2016) 204–212.
[30] H.B. Coban, A. Demirci, Enhancement and modeling of microparticle-added *Rhizopus oryzae* lactic acid production, Bioprocess Biosyst. Eng. 39 (2016) 323–340.
[31] S. Bulut, M. Elibol, D. Ozer, Effect of different carbon sources on L(+)-lactic acid production by *Rhizopus oryzae*, Biochem. Eng. J. 21 (2004) 33–37.
[32] W. Ke, S. Chang, X. Chen, S. Luo, S. Jiang, P. Yang, X. Wu, Z. Zheng, Metabolic control analysis of L-lactate synthesis pathway in *Rhizopus oryzae* As 3.2686, Bioprocess. Biosyst. Eng. 38 (2015) 2189–2199.
[33] X. Wu, S. Jiang, M. Zhang, S. Luo, X. Li, L. Pan, Z. Zheng, M. Liu, A new method studying the kinetics of L-lactic acid production by pellets *Rhizopus oryzae* in semi-continuous fermentation, Ann. Microbiol. 65 (2015) 1473–1480.
[34] N. Cao, J. Du, S. Gong, G.T. Tsao, Simultaneous production and recovery of fumaric acid from immobilized *Rhizopus oryzae* with a rotary biofilm contactor and an adsorption column, Appl. Environ. Microb. 62 (1996) 2926–2931.
[35] H. Wang, M. Seki, S. Furusaki, Characteristic of immobilized *L. delbrueckii* in liquid-solid fluidized bed bioreactor for lactic acid, J. Chem. Eng. Japan 28 (1995) 480–482.
[36] T. Gao, K.-P. Ho, L-lactic acid production by *Bacillus subtilis* MUR1 in continuous culture, J. Biotechnol. 168 (2013) 646–651.
[37] L. Zhang, X. Li, Q. Yong, S.-T. Yang, J. Ouyang, S. Yu, Simultaneous saccharification and fermentation of xylo-oligosaccharides manufacturing waste residue for L-lactic acid production by *Rhizopus oryzae*, Biochem. Eng. J. 94 (2015) 92–99.
[38] A. Pandey, C.R. Soccol, P. Nigam, V.T. Soccol, L.P.S. Vandenberge, R. Mohan, Biotechnological potential of agro-industrial residues. II: cassava bagasse, Bioresour. Technol. 74 (2000) 81–87.
[39] Y.J. Wee, J.S. Yun, D. Kim, H.W. Ryu, Batch and repeated batch production of L(+)-lactic acid by RKY1 using wood hydrolysate and corn steep liquor *Enterococcus faecalis*, J. Ind. Microbiol. Biotechnol. 33 (2006) 431–435.
[40] M.A. Abdel-Rahman, Y. Tashiro, K. Sonomoto, Lactic acid production from lignocellulose-derived sugars using lactic acid bacteria: overview and limits, J. Biotechnol. 156 (2011) 286–301.
[41] C.E. Wyman, B.E. Dale, R.T. Elander, M. Holtzapple, M.R. Ladisch, Y.Y. Lee, Coordinated development of leading biomass pretreatment technologies, Bioresour. Technol. 96 (2005) 1959–1966.

Please cite this article in press as: V. Pimtong, et al., Enhanced effectiveness of *Rhizopus oryzae* by immobilization in a static bed fermentor for L-lactic acid production, Process Biochem (2016), http://dx.doi.org/10.1016/j.procbio.2016.09.020

INTERNATIONAL JOURNAL OF HYDROGEN ENERGY XXX (2016) 1–12

Available online at www.sciencedirect.com

ScienceDirect

journal homepage: www.elsevier.com/locate/he

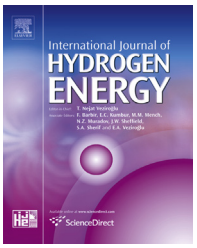

Optimal design of different reforming processes of the actual composition of bio-oil for high-temperature PEMFC systems

Suthida Authayanun [a,*], *Dang Saebea* [b], *Yaneeporn Patcharavorachot* [c], *Suttichai Assabumrungrat* [d], *Amornchai Arpornwichanop* [e]

[a] *Department of Chemical Engineering, Faculty of Engineering, Srinakharinwirot University, Nakhon Nayok 26120, Thailand*

[b] *Department of Chemical Engineering, Faculty of Engineering, Burapha University, Chonburi 20131, Thailand*

[c] *School of Chemical Engineering, Faculty of Engineering, King Mongkut's Institute of Technology Ladkrabang, Bangkok 10520, Thailand*

[d] *Center of Excellence in Catalysis and Catalytic Reaction Engineering, Department of Chemical Engineering, Faculty of Engineering, Chulalongkorn University, Bangkok 10330, Thailand*

[e] *Computational Process Engineering Research Unit, Department of Chemical Engineering, Faculty of Engineering, Chulalongkorn University, Bangkok 10330, Thailand*

ARTICLE INFO

Article history:
Received 24 July 2016
Received in revised form
18 October 2016
Accepted 21 October 2016
Available online xxx

Keywords:
Bio-oil
High-temperature PEMFC
Steam reforming
Autothermal reforming
Partial oxidation

ABSTRACT

Hydrogen production from bio-oil, a by-product of the pyrolysis of palm empty fruit bunches, using different reforming processes, i.e., steam reforming (SR), partial oxidation (POX) and autothermal reforming (ATR), is theoretically investigated using the actual composition of bio-oil. The effect of the reaction temperature, steam to carbon (S/C) ratio and oxygen to carbon (O/C) ratio on the hydrogen production and coke formation of the reformers is analysed. Favourable operating conditions to inhibit carbon formation, to produce low CO concentrations and to achieve high hydrogen yields for the hydrogen production processes coupled with a high-temperature water-gas shift reactor (HT-WGSR) in a high-temperature proton exchange membrane fuel cell (PEMFC) system is also investigated. The results show that an S/C ratio above two is preferred for the bio-oil steam reformer to keep the CO concentration below the maximum allowable limit of the high-temperature PEMFC. However, the CO concentration in the product gas from an HT-WGSR integrated with an autothermal reformer and a partial oxidation reactor is lower than the 5% limit at all temperatures (300–1000 °C), S/C ratios (1–2) and O/C ratios (0.3–1) considered. The efficiency of different bio-oil reforming processes integrated with high-temperature PEMFC systems is studied. The highest system efficiency is achieved from the integrated system consisting of a bio-oil steam reformer, an HT-WGSR and a high-temperature PEMFC with heat integration.

© 2016 Hydrogen Energy Publications LLC. Published by Elsevier Ltd. All rights reserved.

* *Corresponding author*. Fax: +66 3 732 2608.
E-mail address: suthidaa@g.swu.ac.th (S. Authayanun).

http://dx.doi.org/10.1016/j.ijhydene.2016.10.125
0360-3199/© 2016 Hydrogen Energy Publications LLC. Published by Elsevier Ltd. All rights reserved.

Please cite this article in press as: Authayanun S, et al., Optimal design of different reforming processes of the actual composition of bio-oil for high-temperature PEMFC systems, International Journal of Hydrogen Energy (2016), http://dx.doi.org/10.1016/j.ijhydene.2016.10.125

Introduction

Hydrogen is an energy carrier that is used to produce electricity via fuel cell applications. Most hydrogen is produced from natural gas through a steam reforming process due to the high performance and cost-effectiveness of this process. Biomass is one of the most interesting fuels for hydrogen production when environmental and availability aspects are considered [1]. Sources of biomass can be plants, residues from agriculture or forestry, and the organic components of household and industrial wastes. The best-known thermochemical processes for producing hydrogen from biomass are the pyrolysis and gasification processes. For the biomass gasification process, solid biomass is transformed to mainly gas phase products in a gasifier in the presence of oxygen or air. Alternatively, the biomass can be converted to hydrogen by using pyrolysis followed by the reforming process [2]. In the pyrolysis reactor, biomass is decomposed to liquid, gas and char in the absence of oxygen. The liquid product is called bio-oil and can be reformed to reformate gas in the reformer. The low energy density and high transportation cost of biomass are the main problems of hydrogen production from biomass gasification [3]. Because bio-oil is easier and less expensive to transport than biomass, the use of the biomass pyrolysis process to produce bio-oil, which is in turn reformed to hydrogen via reforming processes, is a promising way to produce hydrogen from biomass from different locations [3,4].

Many works focus on the development of bio-oil reforming processes using model compounds [5–7]. Gil et al. [8] studied the sorption-enhanced steam reforming using acetic acid as the model compound. They revealed that high steam to carbon ratio and low weight hourly space velocity (WHSV) in the feed stream can enhance hydrogen production and suppress methane, CO and CO_2 formation in the product gas. High hydrogen purities of up to 99.8% were obtained. Goicoechea et al. [9] analysed steam reforming using acetic acid as the model compound for bio-oil for a solid oxide fuel cell (SOFC) system. They revealed that steam reforming of acetic acid is thermodynamically feasible even at low steam to acetic acid ratios. To obtain a high hydrogen yield for the SOFC, a steam reformer should be operated at high temperatures and high steam to acetic acid ratios. However, lower steam to acetic acid ratios reduce the energy usage and improve the system efficiency. Zhang et al. [10] developed catalysts for steam reforming of acetic acid from bio-oil. They concluded that $Ni_{0.2}Co_{0.8}Mg_6O_{7\pm\delta}$ has more resistance to both carbon formation and oxidation of active metals compared to monometallic catalysts. Most previous works investigated only acetic acid as the model compound. However, actual bio-oil has a wide variety of components in addition to acetic acid. Many experimental studies of reforming of actual bio-oil have already been carried out [11–13]. Valle et al. [11] studied steam reforming of the aqueous fraction of bio-oil with pyrolytic lignin retention in a two-step reaction unit. For the first step, a pyrolytic lignin is deposited by repolymerization of certain bio-oil components, and the treated bio-oil is reformed in the second step. These authors concluded that the catalyst deactivation is low and the hydrogen yield and selectivity are improved by using a $Ni/La_2O_3–\alpha\ Al_2O_3$ catalyst. Additionally, the steam reforming of raw bio-oil in a fluidized bed reactor with CO_2 capture was studied by Remiro et al. [12] CO_2 was effectively captured by using dolomite as an adsorbent in the reforming reactor. The raw bio-oil was reformed at 600 °C without adding water. In addition, Remiro et al. [13] investigated the catalyst deactivation by coke deposition in the steam reforming of the bio-oil aqueous fraction. They concluded that the coke is gasified and Ni does not undergo sintering at 700 °C.

However, the theoretical study of hydrogen production from the mixture of different oxygenated components of real bio-oil is limited. Montero et al. [14] thermodynamically analysed the steam reforming of model compounds of real bio-oil and ethanol. They used components in the bio-oil resulting from the fast pyrolysis of pine sawdust as the model compounds. However, the performance analysis and comparison of different bio-oil reforming processes, steam reforming, partial oxidation and autothermal reforming has not been reported yet. In addition, the high molecular weight components in bio-oil tend to be reformed to carbon, which causes catalyst deactivation. Therefore, the study of reforming of actual bio-oil with consideration of carbon formation is an interesting topic.

The proton exchange membrane fuel cell (PEMFC) is a low-temperature fuel cell that plays a leading role in transportation, portable power and residential power applications. PEMFCs can be classified into two types, the low-temperature PEMFC (60–80 °C) and the high-temperature PEMFC (100–200 °C). For pure hydrogen operation, high-temperature PEMFCs show lower performance than low-temperature PEMFCs due to low oxygen permeability and strong phosphate adsorption [15]. However, high-temperature operation allows high-temperature PEMFCs to tolerate relatively high levels of fuel impurities. To utilize reformate gas for proton exchange membrane fuel cells, CO removal units are required to reduce the CO content in the reformate gas. For conventional PEMFCs, complex hydrogen purification units are typically needed to achieve CO concentrations below 10 ppm. For high-temperature PEMFCs, only a water-gas shift reactor is necessary due to the higher CO tolerance of this type of fuel cell [16].

Recently, the integration of the hydrogen production process with PEMFCs has received considerable attention. Because of increased power demand and environmental concerns, the development of a new sustainable feedstock for hydrogen production is necessary. Chutichai et al. [17] studied the integration of biomass gasification with the PEMFC system. They proposed that the system efficiency is enhanced up to 50% when waste heat is recovered to utilize in the system. Guan et al. [18] investigated a PEMFC system fuelled by bio-gas to cogenerate electricity and heat for a dairy farm and a biogas plant. They concluded that the total efficiency of the PEMFC – based combined heat and power system is 82%. In addition, this system can reduce CO_2 emissions by approximately 416 tons/year compared with a coal-fired combined heat and power plant. Recently, our previous work [19] analysed the performance of bio-ethanol steam reforming integrated with a PEMFC system by considering the environmental impact. The system integrating mixed bio-ethanol and methane reforming with the PEMFC system achieved a higher system

Please cite this article in press as: Authayanun S, et al., Optimal design of different reforming processes of the actual composition of bio-oil for high-temperature PEMFC systems, International Journal of Hydrogen Energy (2016), http://dx.doi.org/10.1016/j.ijhydene.2016.10.125

efficiency and a lower environmental impact than the system integrating dehydrated bio-ethanol reforming with the PEMFC because of the high energy consumption of the reformer, preheating unit and bio-ethanol distillation unit in the system using the dehydrated bio-ethanol reformer. In addition, our previous work also investigated the performance of a high-temperature PEMFC system fuelled by different non-renewable and renewable fuels (i.e., methane, methanol, ethanol, glycerol) [20]. The effect of CO poisoning on the high-temperature PEMFC performance and the necessity of a water-gas shift reactor as a CO removal unit were studied for each fuel type. The results showed that a water-gas shift is required to reduce the CO poisoning effect and to enhance the system efficiency. However, only limited work on high-temperature PEMFC systems that run on biomass-derived bio-oil has been published. In addition, the operational design of the reforming process coupled with the CO removal process for HT-PEMFCs should be investigated.

In this study, a thermodynamic analysis of hydrogen production from bio-oil, a by-product of pyrolysis of palm empty fruit bunches, using different reforming processes, i.e., steam reforming (SR), partial oxidation (POX) and autothermal reforming (ATR), is investigated using the Aspen Plus simulator and using the actual composition of the bio-oil. Simulation studies are performed to determine the influence of key operating parameters (e.g., reaction temperature, steam to carbon (S/C) molar feed ratio, oxygen to carbon (O/C) molar feed ratio) on the performance of a reformer in terms of hydrogen production and coke formation. The integration of the bio-oil reforming processes with the high-temperature water-gas shift reactor (HT-WGSR) to produce hydrogen for a high-temperature PEMFC was examined. The CO concentration at different reformer operating conditions is presented to find conditions to produce a sufficiently low CO concentration (<5%) for the HT-PEMFC. Subsequently, the optimal conditions for bio-oil steam reforming, autothermal reforming and partial oxidation processes integrated with an HT-WGSR to inhibit carbon formation, to achieve a low CO concentration and to maximize the hydrogen fraction are presented. In addition, the efficiency of the integrated high-temperature PEMFC systems at different reforming processes is studied and compared.

Process description

The integrated high-temperature PEMFC systems examined in this work are shown in Fig. 1. Each system consists of a fuel processing process and a high-temperature PEMFC. Steam reforming, autothermal reforming and partial oxidation are the hydrogen production processes and the high-temperature water-gas shift reactor is only used as a hydrogen purification process to decrease the CO concentration below 5%.

Fuel processing process

In this work, the composition of actual bio-oil produced from empty palm fruit bunch fast pyrolysis is used [21]. The composition of the bio-oil is shown in Table 1. The product compositions of the reformer and the water-gas shift reactor at equilibrium are calculated by minimization of the Gibbs free energy, as shown in Eq. (1):

$$\min_{n_i}(G^t)_{T,P} = \sum_{i=1}^{C} n_i \overline{G}_i = \sum_{i=1}^{C} n_i \left(G_i^{\circ} + RT \ln \frac{\overline{f}_i}{f_i^{\circ}} \right) \quad (1)$$

where C is the total number of components in the reaction system, and n_i is the amount of each gaseous component. Because of the conservation of atomic species, n_i must satisfy the element balance in Eq. (2):

$$\sum_i n_i a_{ik} - A_k = 0 \quad (k = 1, 2, \ldots, w) \quad (2)$$

where a_{ik} is the number of atoms of element k in component i, A_k is the total number of atoms of element k in the reaction mixture, and w is the total number of elements.

The reactions of oxygenates due to steam reforming, partial oxidation and autothermal reforming, along with the possible side reaction, are presented in Table 2. The components in the steam reforming system are the mixture of the actual components of bio-oil (see Table 1), CH_4, H_2, CO, CO_2, C (Graphite), C_2H_2, C_2H_4 and H_2O. The O_2 component is added to the reactive system for the partial oxidation and autothermal reforming processes. The structure and properties of the components in bio-oil (i.e., 1-hydroxy-2-butanone, 2(5H)-furanone, 2-cyclopenten-1-one, 2-hydroxy-3-methyl, 2-methoxy-(guaiacol), 2,6-dimethyoxy-(syringol), and Levoglucosan) are input to the Aspen Plus program since the thermodynamic properties of these components are not available in conventional thermodynamic databases.

The *Rgibbs* reactor module in Aspen Plus simulator is used to represent the steam reformer, the autothermal reformer, the partial oxidation reactor and the water-gas shift reactors. Methane is treated as an inert gas in the water-gas shift reactor. The equation of state used in the calculation is based on the Soave–Redlich–Kwong equation [9]. The HT-WGSR is operated at a temperature of 350 °C, and the ratio of steam to CO in the feed stream is greater than two. Additional steam is added if the steam to CO ratio of the reforming gas is lower than two. Table 3 shows the validation of the steam reforming of the acetic acid model compound using a steam reformer temperature of 800 °C, an S/C ratio of 6 and atmospheric pressure. The simulation results agree with the experimental data reported by Hu and Lu [22].

High-temperature PEMFCs

The high-temperature PEMFC model based on electrochemical reactions is coded in FORTRAN in the Aspen Plus simulator to predict the relation between voltage and current density. An ideal separator, *Sep*, is applied for the anode to separate the hydrogen from the reformate gas, and the cathode is modelled as an *Rgibbs* reactor. The cell temperature of the high-temperature PEMFC is specified as 175 °C. A PBI-doped phosphoric acid membrane is used as the electrolyte for the high-temperature PEMFC. The actual cell potentials or operating voltage of a fuel cell (E_{cell}) is always smaller than the reversible cell potential (E_r) due to irreversible losses. E_{cell} can be calculated from the activation loss at the anode ($\eta_{act,a}$), the activation loss at the cathode ($\eta_{act,c}$) and the ohmic loss (η_{ohmic}) as shown in Eq. (3).

Please cite this article in press as: Authayanun S, et al., Optimal design of different reforming processes of the actual composition of bio-oil for high-temperature PEMFC systems, International Journal of Hydrogen Energy (2016), http://dx.doi.org/10.1016/j.ijhydene.2016.10.125

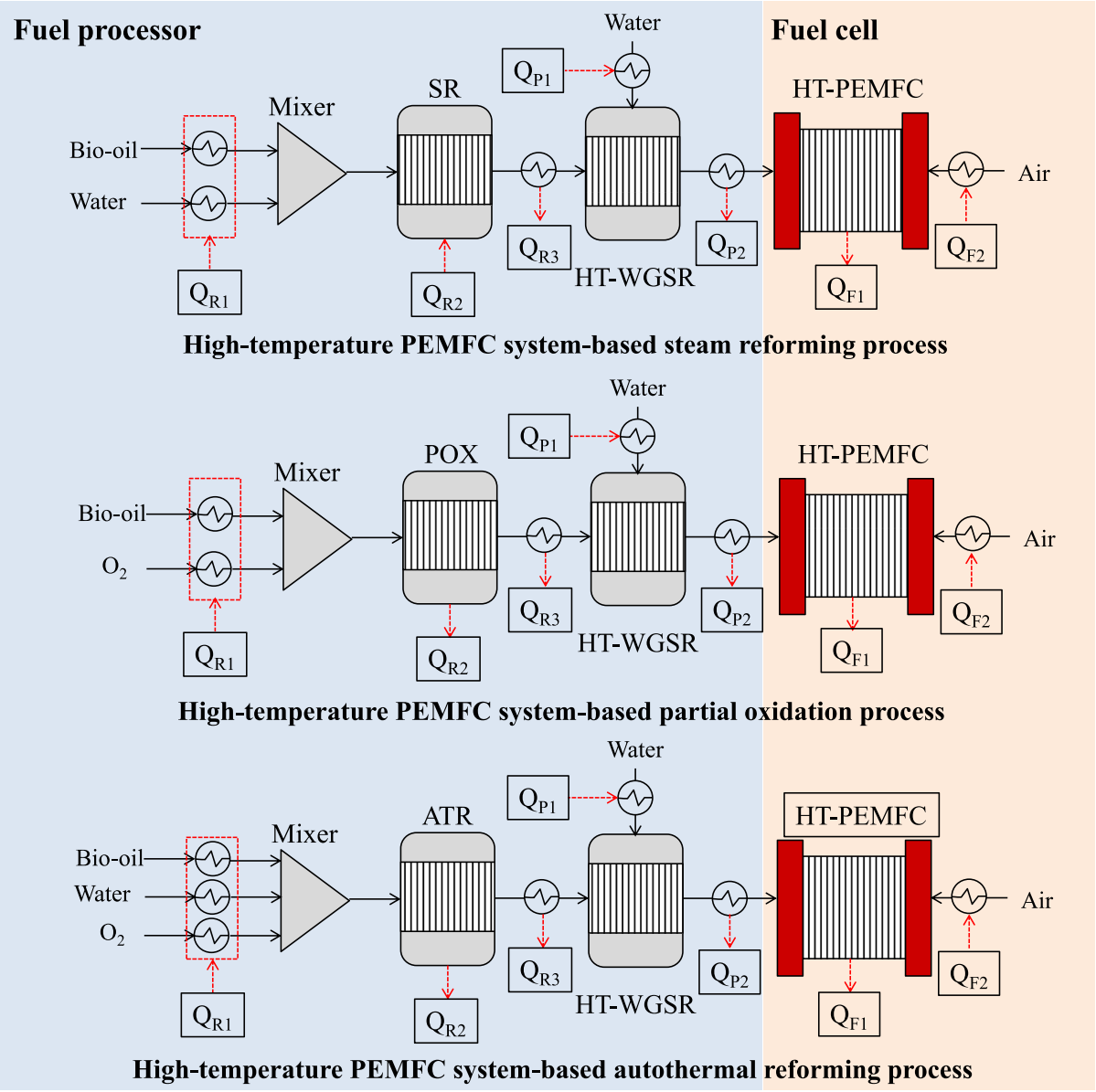

Fig. 1 – The integrated high-temperature PEMFC systems.

Table 1 – The composition of bio-oil from empty palm fruit bunch fast pyrolysis [21].

Components	Chemical formula	Composition (wt%)
Acetic acid	$C_2H_4O_2$	56.73
Propanoic acid (acetol)	$C_3H_6O_2$	1.09
1-hydroxy-2-butanone	$C_4H_8O_2$	3.49
2(5H)-furanone	$C_4H_4O_2$	0.33
2-cyclopenten-1-one, 2-hydroxy-3-methyl	$C_6H_8O_2$	7.90
Phenol	C_6H_6O	23.97
Phenol, 2-methoxy-(guaiacol)	$C_7H_8O_2$	1.70
Phenol, 2,6-dimethyoxy-(syringol)	$C_8H_{10}O_3$	2.90
Levoglucosan	$C_6H_{10}O_5$	1.88

$$E_{cell} = E_r - \eta_{act,a} - \eta_{act,c} - \eta_{ohmic} \quad (3)$$

The reversible cell potential is described by the Nernst equation.

$$E_r = -\left(\frac{\Delta H_T}{nF} - \frac{T\Delta S_T}{nF}\right) + \frac{RT}{nF}\ln\left[\frac{(RT)^{1.5}C_{Pt,a}C_{Pt,c}^{0.5}}{a_{H_2O}}\right] \quad (4)$$

where a_{H_2O} is the water activity defined by the ratio of water partial pressure to its saturation pressure ($P_{H_2O}^{sat}$), which is given in Eq. (5). $C_{Pt,a}$ and $C_{Pt,c}$ are the concentrations of hydrogen and oxygen at the anode and cathode catalyst surface, which are calculated by the Stefan–Maxwell equation and Fick's law, as shown in Table 4. D_{ij}^{eff} is calculated using the Slattery–Bird correlation [23] and corrected to account for the porosity/tortuosity effects using the Bruggeman correlation [24].

Please cite this article in press as: Authayanun S, et al., Optimal design of different reforming processes of the actual composition of bio-oil for high-temperature PEMFC systems, International Journal of Hydrogen Energy (2016), http://dx.doi.org/10.1016/j.ijhydene.2016.10.125

Table 2 – Reactions involved in the different hydrogen production processes.

Steam reforming

$C_nH_mO_k + (n-k)H_2O \rightarrow nCO + (n + m/2 - k)H_2$

$C_nH_mO_k + (2n-k)H_2O \rightarrow nCO_2 + (2n + m/2 - k)H_2$

Partial oxidation

$C_nH_mO_k + (n/2-k)O_2 \rightarrow nCO + (m/2)H_2$

$C_nH_mO_k + (n-k)O_2 \rightarrow nCO_2 + (m/2)H_2$

Autothermal reforming

$C_nH_mO_k + \frac{1}{2}(n/2-k)O_2 + \frac{1}{2}(n-k)H_2O \rightarrow nCO + \frac{1}{2}(n+m-k)H_2$

$C_nH_mO_k + \frac{1}{2}(n-k)O_2 + \frac{1}{2}(2n-k)H_2O \rightarrow nCO_2 + \frac{1}{2}(2n+m-k)H_2$

Additional side reactions for hydrogen production processes

Water–gas shift reaction

$CO + H_2O \leftrightarrow CO_2 + H_2$

Methanation reaction

$CO + 3H_2 \rightarrow CH_4 + H_2O$

Carbon formation reactions

$2CO \leftrightarrow CO_2 + C$

$CH_4 \leftrightarrow 2H_2 + C$

$CO + H_2 \leftrightarrow H_2O + C$

Table 3 – The validation of the acetic acid steam reforming process at a reformer temperature of 800 °C, S/C ratio of 6 and atmospheric pressure.

Component	% Conversion or yield		% Error
	Simulation	Experimental [22]	
Acetic acid	100	100	0.00
H_2	86	88	2.27
CO	12.7	13	2.31
CO_2	80.1	82	2.32
CH_4	0	0	0.00

$$P_{H_2O}^{sat} = (142.07682T^4 - 171026.12676T^3 + 78013638.11584T^2 - 15953375633.8471T + 1231888491801.45)*10^{-10} \quad (5)$$

Activation losses are governed by the Butler–Volmer equation (Eqs. (6) and (7)).

$$i_a = i_{0,a}\left(\exp\left(\frac{-\alpha_{Rd,a}F}{RT}(\eta_{act,a})\right) - \exp\left(\frac{-\alpha_{Ox,a}F}{RT}(\eta_{act,a})\right)\right) \quad (6)$$

$$i_c = i_{0,c}\left(\exp\left(\frac{-\alpha_{Rd,c}F}{RT}(\eta_{act,c})\right) - \exp\left(\frac{-\alpha_{Ox,c}F}{RT}(\eta_{act,c})\right)\right) \quad (7)$$

where i is the current density and α is the transfer coefficient. i_0 is the exchange current density, which can be calculated from Eqs. (8) and (9) for the anode and cathode, respectively.

$$i_{0,a} = i_{0,a}^{ref} a_{c,a} L_{c,a}\left(\frac{C_{Pt,a}}{C_{Pt,a}^{ref}}\right)^{\gamma} \exp\left[-\frac{E_{c,a}}{RT}\left(1 - \frac{T}{T_{ref,a}}\right)\right] \quad (8)$$

$$i_{0,c} = i_{0,c}^{ref} a_{c,c} L_{c,c}\left(\frac{C_{Pt,c}}{C_{Pt,c}^{ref}}\right)^{\gamma} \exp\left[-\frac{E_{c,c}}{RT}\left(1 - \frac{T}{T_{ref,c}}\right)\right] \quad (9)$$

Assuming $\alpha_{Rd} = \alpha_{Ox} = \alpha$, the hyperbolic sine function can be substituted in Eqs. (6) and (7), yielding the following relationship:

$$\eta_{act} = \frac{RT}{\alpha F}\sinh^{-1}\left(\frac{i}{2i_0}\right) \quad (10)$$

The effect of CO poisoning is included in the anode activation loss model of the high-temperature PEMFCs because hydrogen-rich gas from the fuel processor is used at the anode. The anode activation loss can be calculated from the exchange current density of hydrogen and the CO coverage

Table 4 – Diffusion models used in the simulation of the high-temperature PEMFC.

Diffusion models	Equations
Stefan Maxwell models	At the anode
	$\frac{dX_{CO_2}}{dz} = \frac{RT}{P}X_{CO_2}\left(\frac{N_{H_2,g}}{D_{H_2,CO_2}^{eff}}\right)$
	$\frac{dX_{H_2O}}{dz} = \frac{RT}{P}X_{H_2O}\left(\frac{N_{H_2,g}}{D_{H_2,H_2O}^{eff}}\right)$
	$\frac{dX_{CO}}{dz} = \frac{RT}{P}X_{CO}\left(\frac{N_{H_2,g}}{D_{H_2,CO}^{eff}}\right)$
	$\frac{dX_{CH_4}}{dz} = \frac{RT}{P}X_{CH_4}\left(\frac{N_{H_2,g}}{D_{H_2,CH_4}^{eff}}\right)$
	$X_{H_2} = 1 - X_{CO_2} - X_{H_2O} - X_{CO} - X_{CH_4}$
	At the cathode
	$\frac{dX_{N_2}}{dz} = \frac{RT}{P}X_{N_2}\left(\frac{N_{O_2}}{D_{N_2,O_2}^{eff}} + \frac{N_{H_2O,g}}{D_{N_2,H_2O}^{eff}}\right)$
	$\frac{dX_{H_2O}}{dz} = \frac{RT}{P}\left[X_{H_2O}\left(\frac{N_{O_2}}{D_{O_2,H_2O}^{eff}}\right) - N_{H_2O}\left(\frac{X_{O_2}}{D_{O_2,H_2O}^{eff}} + \frac{X_{N_2}}{D_{N_2,H_2O}^{eff}}\right)\right]$
	$X_{O_2} = 1 - X_{N_2} - X_{H_2O}$
Fick' law models	At the anode
	$\frac{N_{H_2}}{S_{Pt-anode}} = \frac{-D_{H_2}(C_{Pt,a} - C_{H_2(dissolve)})}{\delta_{anode}} C_{H_2(dissolve)} = C_{H_2}^{dissolved} \cdot X_{H_2} \cdot P$
	At the cathode
	$\frac{N_{O_2}}{S_{Pt-cathode}} = \frac{-D_{O_2}(C_{Pt,c} - C_{O_2(dissolve)})}{\delta_{cathode}} C_{O_2(dissolve)} = C_{O_2}^{dissolved} \cdot X_{O_2} \cdot P$

Please cite this article in press as: Authayanun S, et al., Optimal design of different reforming processes of the actual composition of bio-oil for high-temperature PEMFC systems, International Journal of Hydrogen Energy (2016), http://dx.doi.org/10.1016/j.ijhydene.2016.10.125

Table 5 – Parameters used for the high-temperature PEMFC [15].

Parameters	Value
Cell temperature, T (°C)	175
Operating pressure at anode, P_a (atm)	1
Operating pressure at cathode, P_c (atm)	1
Stoichiometric ratio at anode, S_a	1.25
Stoichiometric ratio at cathode, S_c	2
Membrane thickness, l_m (m)	4×10^{-5}
GDL thickness, z (m)	0.0002
Anode film thickness, δ_{anode} (m)	2.5×10^{-9}
Cathode film thickness,$\delta_{cathode}$ (m)	1.48×10^{-9}
Anode activation energy, $E_{c,a}$ (J mole^{-1} K^{-1})	16,900
Cathode activation energy, $E_{c,c}$ (J mole^{-1} K^{-1})	72,400
Anode reference cell temperature, $T_{ref,a}$ (°C)	160
Cathode reference cell temperature, $T_{ref,c}$ (°C)	100
Anode catalyst surface area, $a_{c,a}$ (m^2 g^{-1})	64
Cathode catalyst surface area, $a_{c,c}$ (m^2 g^{-1})	32.25
Anode catalyst loading, $L_{c,a}$ (mg cm^{-2})	0.2
Cathode catalyst loading, $L_{c,c}$ (mg cm^{-2})	0.4
Transfer coefficient at anode, α_a	0.5
Transfer coefficient at cathode, α_c	0.75
Reaction order at anode, γ_a	1
Reaction order at cathode, γ_c	1.375
Anode reference concentration, $C^{ref}_{Pt,a}$ (mol cm^{-3})	0.0002
Cathode reference concentration, $C^{ref}_{Pt,c}$ (mol cm^{-3})	0.0004

(θ_{CO}) [25] as shown in Eq. (11). The bridge model of CO adsorption on Pt and the anode activation loss of HT-PEMFC is represented by Eq. (12).

$$\eta_{act,a} = \frac{RT}{\alpha F}\sinh^{-1}\left(\frac{i}{2i_0(1-\theta_{CO})^2}\right) \quad (11)$$

$$\theta_{CO} = a*\ln\frac{[CO]}{[H_2]} + b*\ln(i)*\ln\frac{[CO]}{[H_2]} + c \quad (12)$$

where

$$a = -0.00012784*T^2 + 0.11717499*T - 26.62908873$$
$$b = 0.0001416*T^2 - 0.12813608*T + 28.852463626$$
$$c = -0.00034886*T^2 + 0.31596903*T - 70.11693333$$

The ohmic loss for a high-temperature PEMFC is described as follows:

$$\eta_{ohmic} = R_{mem}i = \left(\frac{\sigma_m}{l_m}\right)i \quad (13)$$

where R_{mem} is the membrane resistance, σ_m is the proton conductivity of the membrane and l_m is the membrane thickness.

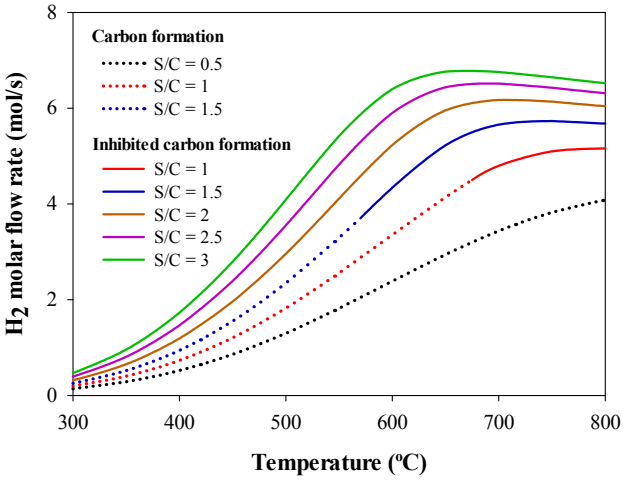

Fig. 2 – Effect of the reformer temperature and S/C ratio on the hydrogen molar flow rate of the steam reforming process.

The proton conductivity as a function of temperature and relative humidity [26] can be calculated from Eqs. (14)–(16).

$$\sigma_m = \frac{A}{T}\exp\left(\frac{-B}{R(T)}\right) \quad (14)$$

$$A = \exp\left(\left(k_1^a RH^3\right) + \left(k_2^a RH^2\right) + \left(k_3^a RH\right) + k_0^a\right) \quad (15)$$

$$B = \left(k_1^b RH^3\right) + \left(k_2^b RH^2\right) + \left(k_3^b RH\right) + k_0^b \quad (16)$$

The parameters used for the simulation of high-temperature PEMFCs are shown in Table 5. In addition, the detailed calculations of reformer efficiency, fuel processor efficiency, fuel cell efficiency and system efficiency can be found in Table 6. To calculate the system efficiency with heat integration, heat recovered from the high-temperature PEMFC is used to preheat the reactants for the fuel processing processes.

Results and discussion

Reforming processes

For the steam reforming process, the effect of the reformer temperature and S/C ratio on the hydrogen molar flow rate is shown in Fig. 2. The dashed lines show operating conditions to

Table 6 – The models of efficiency of high-temperature PEMFC systems.

Efficiency	Equations
Reformer efficiency (η_R)	$\eta_R = \frac{LHV_{H_2}\cdot(\dot{m}_{H_2})}{LHV_{fuel}\cdot(\dot{m}_{fuel})+Q_T}Q_T = Q_{R1} + Q_{R2} - Q_{R3}$
Fuel processor efficiency (η_{FP})	$\eta_{FP} = \frac{LHV_{H_2}\cdot(\dot{m}_{H_2})}{LHV_{fuel}\cdot(\dot{m}_{fuel})+Q_T}Q_T = Q_{R1} + Q_{R2} - Q_{R3} + Q_{P1}$
Fuel cell efficiency (η_{FC})	$\eta_{FC} = \frac{P_{FC}}{(\dot{m}_{H_2})\cdot LHV_{H_2}}$
System efficiency without heat integration (η_S)	$\eta_S = \frac{P_{FC}}{LHV_{fuel}\cdot(\dot{m}_{fuel})+Q_T}Q_T = Q_{R1} + Q_{R2} - Q_{R3} + Q_{P1} - Q_{P2} + Q_{F1}$
System efficiency with heat integration (η_{SC})	$\eta_{SC} = \frac{P_{FC}}{LHV_{fuel}\cdot(\dot{m}_{fuel})+Q_T}Q_T = Q_{R1} + Q_{R2} - Q_{R3} + Q_{P1} - Q_{P2} + Q_{F1} - Q_{F2}$

Please cite this article in press as: Authayanun S, et al., Optimal design of different reforming processes of the actual composition of bio-oil for high-temperature PEMFC systems, International Journal of Hydrogen Energy (2016), http://dx.doi.org/10.1016/j.ijhydene.2016.10.125

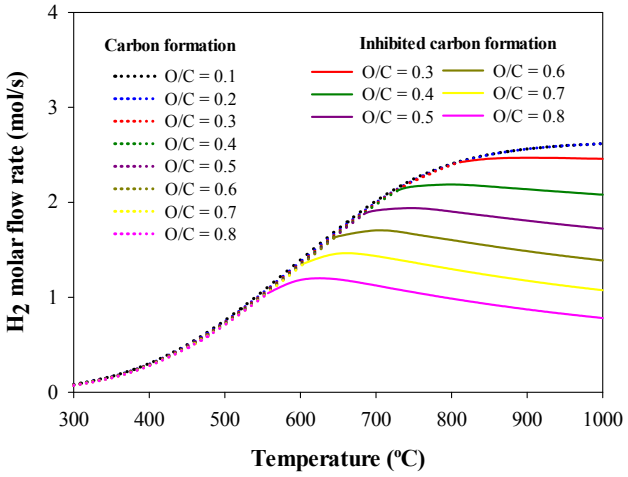

Fig. 3 – Effect of the reformer temperature and O/C ratio on the hydrogen molar flow rate of the partial oxidation process.

be avoided because carbon formation occurs, whereas the solid lines show the hydrogen production rate where carbon formation does not occur. The steam reformer should be operated at temperatures of 650–700 °C to maximize the hydrogen molar flow rate. Carbon formation is unfavourable at S/C ratios higher than two at all reformer temperatures considered. Compared to the steam reforming of the acetic acid model compound, higher S/C ratios are required for bio-oil steam reformer to prevent carbon formation due to the higher molecular weight compounds contained in actual bio-oil [27]. In addition, the simulation predictions of carbon formation for bio-oil steam reforming are in agreement with the results of Montero et al. [14]. Although carbon formation can be avoided by adding excess steam into the reformer, it still occurs at high temperatures, as observed from experimental data [13]. This is because the assumed graphite carbon in the simulation is not the complete representation of the carbon that is deposited, and it is a very complex task to thermodynamically model carbon deposition [14,28]. However, Hu and Lu [29], who experimentally investigated bio-oil steam

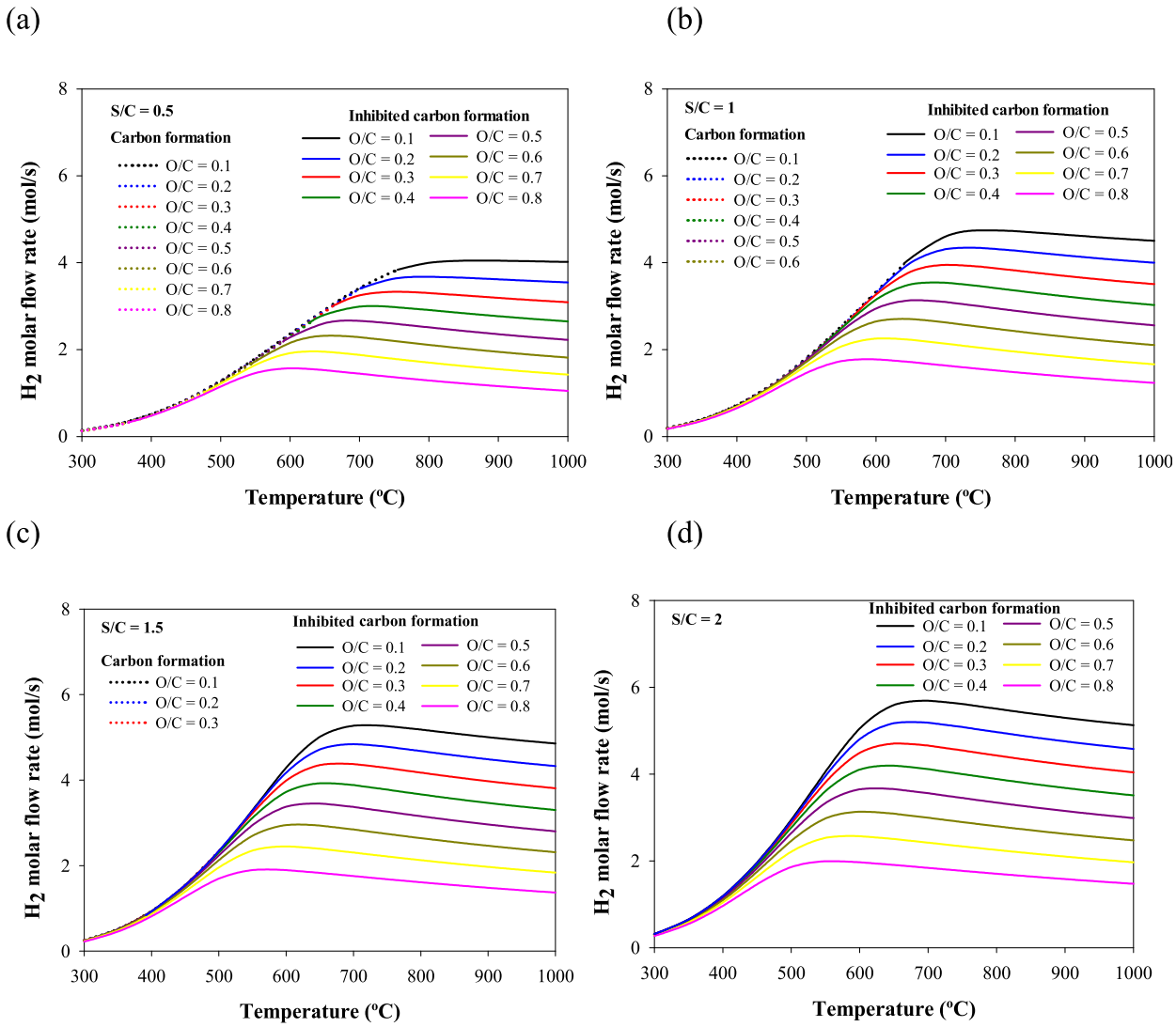

Fig. 4 – Effect of the reformer temperature and O/C ratio on the hydrogen molar flow rate of the autothermal reforming process at different S/C ratios: (a) S/C = 0.5, (b) S/C = 1, (c) S/C = 1.5 and S/C = 2.

Please cite this article in press as: Authayanun S, et al., Optimal design of different reforming processes of the actual composition of bio-oil for high-temperature PEMFC systems, International Journal of Hydrogen Energy (2016), http://dx.doi.org/10.1016/j.ijhydene.2016.10.125

reforming, partial oxidation and oxidative steam reforming with CO_2 utilization, proposed that high temperature has a positive effect on reducing coke formation. Therefore, further study and characterization of carbon is necessary, and it is an interesting topic for furthering the understanding of carbon formation in real systems [30]. In addition, it is noted that a high S/C ratio and high temperature are required to enhance hydrogen production and to prevent carbon formation.

Furthermore, the effect of reformer temperature and the O/C ratio on the hydrogen molar flow rate for the partial oxidation of actual bio-oil is presented in Fig. 3. The partial oxidation reactor is operated at atmosphere pressure and isothermal conditions. Additionally, the operating conditions represented by the dashed line and by the solid line show the hydrogen production with carbon formation and with inhibited carbon formation, respectively. According to the simulation results, carbon is formed at all O/C ratios (0.1–0.8) studied. At high O/C ratios (O/C ratio $\geq$ 0.3), the dashed lines become solid lines at higher temperatures. However, the hydrogen content decreases with increasing O/C ratio. From Fig. 3, the hydrogen molar flow rate increases with increasing temperature until reaching a maximum. Beyond that point, further increase in temperature slightly reduces the hydrogen production rate. The maximum hydrogen molar flow rate is observed at temperatures greater than 900 °C and O/C ratios of 0.1 and 0.2, but carbon formation is promoted at these conditions. Therefore, the optimal condition with inhibited carbon formation for partial oxidation of actual bio-oil is an O/C ratio of 0.3 and a temperature above 800 °C. Compared to the steam reforming process, the partial oxidation process provides a lower hydrogen content and needs to be operated at a higher temperature.

Next, the performance of autothermal reforming of actual bio-oil for hydrogen production is thermodynamically analysed under atmospheric pressure and at isothermal conditions. The effect of the operating parameters of autothermal reforming of actual bio-oil on the hydrogen molar flow rate is shown in Fig. 4. In this process, both steam and oxygen are used as agents to reform bio-oil into reformate gas. In Fig. 4(a), which shows the performance of autothermal reforming of the actual bio-oil composition at an S/C ratio of 0.5, the dashed lines appear at all operating O/C ratios. This means carbon formation is favourable at these conditions. However, the maximum hydrogen molar flow rate can be achieved at a reformer temperature of 800 °C and an O/C ratio of one with inhibited carbon formation.

In addition, the results further show that no dashed lines (meaning carbon formation did not occur) are found at high O/C ratios when the S/C ratio increases to 1 and 1.5, as shown in Fig. 4(b) and (c), respectively. For an autothermal reformer operated at an S/C ratio of one in Fig. 4(b), carbon did not appear in the products of the autothermal reformer at all operating temperatures when the O/C ratio was greater than 0.6. In addition, the O/C ratio needed to prevent carbon formation at all reformer temperatures should be greater than 0.3 when an S/C ratio of 1.5 is specified, as shown in Fig. 4(c). For an autothermal reformer operated at an S/C ratio of two, as shown in Fig. 4(b), carbon formation is avoided at all operating temperatures and O/C ratios studied. The hydrogen production of the autothermal reformer of actual bio-oil is enhanced at high S/C ratios, reformer temperatures of 700–800 °C and an O/C ratio of 0.1. However, it should be noted that operation at higher O/C ratios can reduce the requirement of external heat for the reformer.

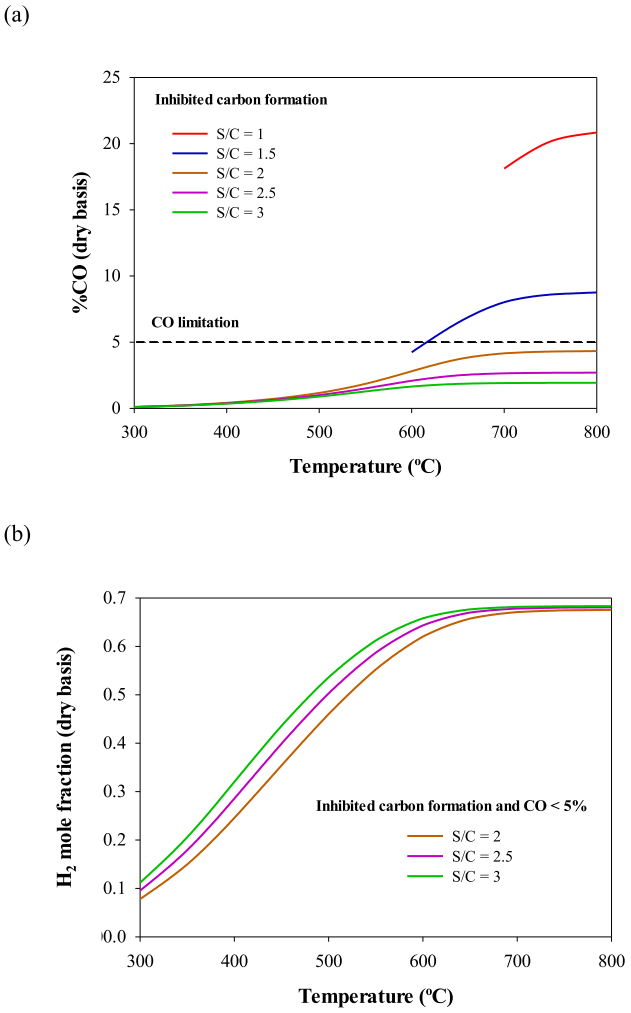

Fig. 5 – Effect of the reformer temperature and S/C ratio on the performance of the bio-oil steam reformer integrated with HT-WGSR at the carbon formation-inhibiting condition: (a) %CO (dry basis) and (b) Hydrogen mole fraction (dry basis).

Reforming processes integrated with a CO removal unit

The CO and hydrogen concentrations at different operating parameters of a steam reformer, a partial oxidation reactor and an autothermal reformer are investigated when the hydrogen production processes are integrated with a high-temperature water-gas shift reactor (HT-WGSR). It is noted that the optimal operating conditions for hydrogen production processes should not only maximize hydrogen concentration but also achieve a CO fraction lower than 5%. Therefore, the CO concentration in the product gases at various operating conditions is first studied and then the effect of operating conditions on the hydrogen fraction while avoiding carbon formation and achieving CO fractions <5% is investigated. For the bio-oil steam reformer integrated with an

Please cite this article in press as: Authayanun S, et al., Optimal design of different reforming processes of the actual composition of bio-oil for high-temperature PEMFC systems, International Journal of Hydrogen Energy (2016), http://dx.doi.org/10.1016/j.ijhydene.2016.10.125

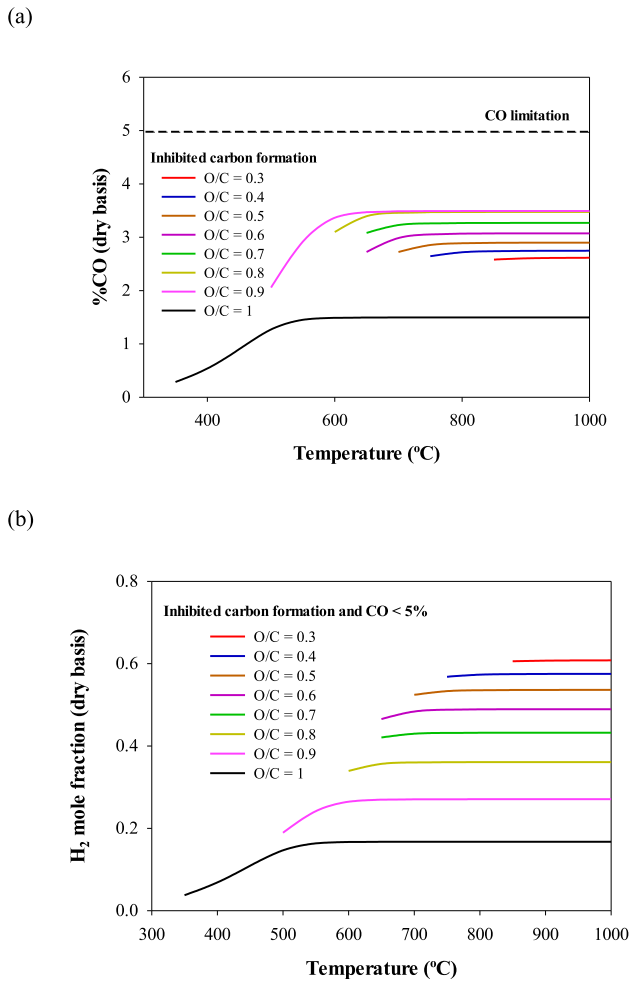

Fig. 6 – Effect of the reformer temperature and O/C ratio on the performance of the bio-oil partial oxidation reactor integrated with HT-WGSR at the carbon formation-inhibiting condition: (a) %CO (dry basis) and (b) Hydrogen mole fraction (dry basis).

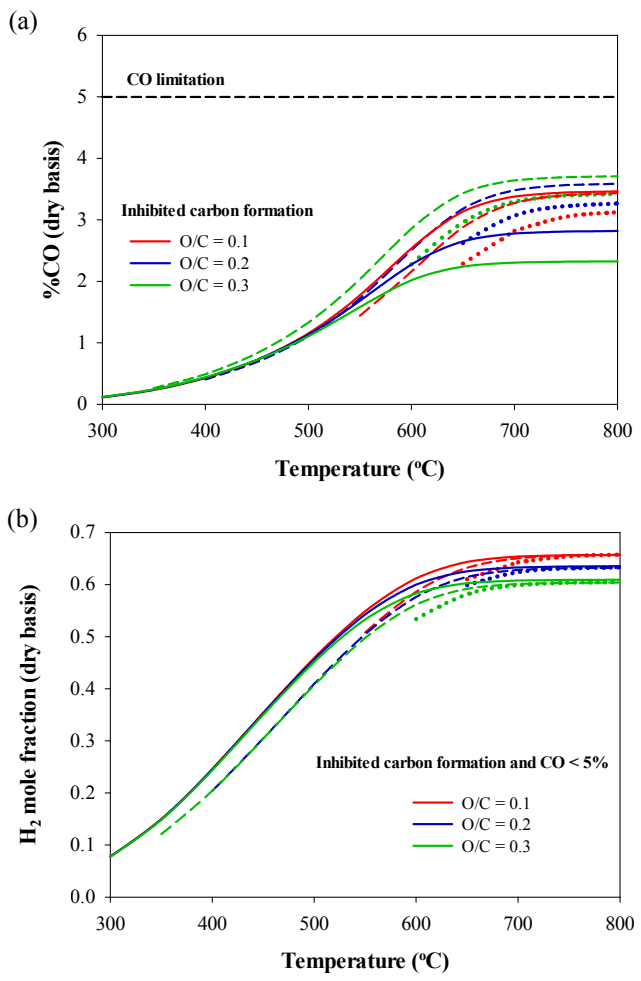

Fig. 7 – Effect of the reformer temperature and O/C ratio on the performance of the bio-oil autothermal reformer integrated with HT-WGSR at the carbon formation-inhibiting condition: (a) %CO (dry basis) and (b) Hydrogen mole fraction (dry basis). Dotted line – S/C = 1; Dashed line – S/C = 1.5; Solid line – S/C = 2.

HT-WGSR, the CO fraction increases with increasing temperature and with decreasing S/C ratio, as shown in Fig. 5(a). At S/C ratios of 1 and 1.5, the CO concentration is greater than 5% at almost all reformer temperatures studied. Therefore, the steam reformer should be operated at an S/C ratio $\geq$2 to keep the CO concentration below the maximum allowable limit of an HT-PEMFC. To find the optimal condition that maximizes hydrogen concentration, the effect of the S/C ratio and the reformer temperature on the hydrogen molar fraction from an HT-WGSR is studied at operating conditions that inhibit carbon formation and produced a CO concentration below 5%. The simulation results are presented in Fig. 5(b). The highest hydrogen concentration is obtained at reformer temperatures of 700–800 °C and S/C ratios of 2 or higher. However, it should be noted that operation at high temperature (above 700 °C) causes catalyst deactivation by sintering [2].

The partial oxidation reactor integrated with an HT-WGSR is examined next. The effect of the reformer temperature and the O/C ratio on CO fraction and hydrogen fraction in the product gas from the HT-WGSR is presented in Fig. 6(a) and (b). Fig. 6(a) shows that increasing the temperature from 300 to 600 °C increases the CO concentration. Further increase in temperature results in only small changes of the CO fraction. When the O/C ratio is lower than 0.9, the CO fraction increases with increasing O/C ratio. However, the CO concentration decreases when the O/C ratio increases from 0.9 to 1. The lowest CO concentration for a partial oxidation reactor integrated with an HT-WGSR is obtained at an O/C ratio of 1. This is because under conditions with a high amount of oxygen, fuel is converted to CO_2 instead of CO. The reactions for partial oxidation with different products (CO and CO_2) are shown in Table 2. Fig. 6(b) shows that a low O/C ratio is preferred to enhance hydrogen production. Increasing temperature improves the hydrogen concentration until it reaches an optimal value for each O/C ratio. In addition, it can be concluded that the CO fraction is below the limitation of the HT-PEMFC at all of the operating conditions studied.

The effect of temperature, the S/C ratio and the O/C ratio of an autothermal reformer integrated with an HT-WGSR on the fuel processor performance is shown in Fig. 7. These operating conditions have a significant effect on the CO and hydrogen

Please cite this article in press as: Authayanun S, et al., Optimal design of different reforming processes of the actual composition of bio-oil for high-temperature PEMFC systems, International Journal of Hydrogen Energy (2016), http://dx.doi.org/10.1016/j.ijhydene.2016.10.125

Table 7 – The optimal operating conditions and product compositions of the different reformers for high-temperature PEMFC systems at inhibited carbon formation and CO < 5%.

	Steam reformer	Autothermal reformer	Partial oxidation reactor
Temperature (°C)	700	700	850
S/C	2	1	–
O/C	–	0.1	0.3
Hydrogen fraction	0.67	0.64	0.61
%CO	4.15	2.82	2.58

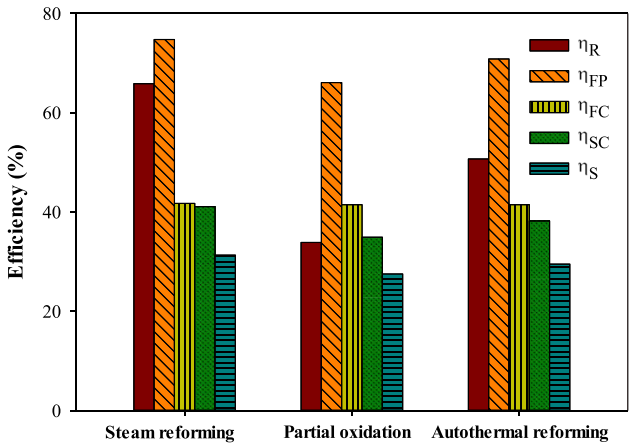

Fig. 8 – The efficiency of the different high-temperature PEMFC systems.

fractions, as shown in Fig. 7(a) and (b), respectively. At an S/C ratio of two, increasing the O/C ratio decreases the CO concentration. However, the CO fraction decreases with increasing O/C ratio at an S/C ratio lower than two. This is because the CO is still high at low S/C ratios, as seen in Fig. 5(a); therefore, the addition of oxygen has a significant effect on the CO concentration and can considerably reduce the CO content in the product gas. From Fig. 7(b), a high S/C ratio and a low O/C ratio are preferred for hydrogen production with a high hydrogen fraction (dry basis). The optimal operating temperature is 700 °C or higher. To apply the product gas for an HT-PEMFC, the optimal operating parameters of the steam reformer, autothermal reformer and partial oxidation reactor for an HT-PEMFC system to inhibit carbon formation, obtain a CO fraction <5%, and maximize the hydrogen fraction are shown in Table 7.

HT-PEMFC systems

The efficiency of the system and the efficiency of each unit of the different hydrogen production processes and HT-WGSR integrated with an HT-PEMFC are also studied, as shown in Fig. 8. The steam reforming process achieves the highest reformer efficiency (66%) and the partial oxidation process shows the lowest reformer efficiency (34%), whereas the reformer efficiency of the autothermal reforming process is approximately 51%. However, the fuel processor efficiency (efficiency of hydrogen production processes integrated with HT-WGSR) is enhanced from the reformer efficiency because additional hydrogen is produced from the HT-WGSR. The fuel processor efficiencies of the steam reformer, autothermal reformer and partial oxidation reactor are 75%, 71% and 66%, respectively. However, the fuel cell efficiency of each reforming process is quite similar due to the comparable hydrogen fraction, as seen in Table 7. In should be noted that the oxidant used in the autothermal reformer and the partial oxidation reactor is oxygen, and thus no nitrogen dilution effect occurs. The system efficiency improves when heat recovery from the HT-PEMFC is applied to the hydrogen production processes. The system using a steam reformer, HT-WGSR and HT-PEMFC with heat integration achieves the highest system efficiency (41%).

Conclusions

This study is focused on hydrogen production for HT-PEMFC systems to inhibit carbon formation and achieve a low CO concentration (CO < 5%). The actual components of bio-oil from fast pyrolysis of empty palm fruit bunch are used as the fuel for hydrogen production from steam reforming, partial oxidation and autothermal reforming processes. High reaction temperatures and high S/C ratios enhances hydrogen production, but hydrogen production decreases with increasing O/C molar ratio. However, reformer operation at high S/C molar ratios, high O/C molar ratios and high temperatures is required to prevent coke formation. It should be noted that graphite carbon does not fully represent carbon deposition and that further study of this critical issue is necessary. For a steam reformer integrated with HT-WGSR, the steam reformer should be operated at S/C $\geq$ 2 to keep the CO fraction below 5%, which is the requirement for HT-PEMFC. However, the CO concentration in the product gas from HT-WGSR is lower than 5% at all temperatures, S/C ratios and O/C ratios considered for the autothermal reformer and the partial oxidation reactor. In addition, the optimal operating conditions of the steam reformer, autothermal reformer and partial oxidation reactor for the HT-PEMFC system to maximize the hydrogen concentration, to inhibit carbon formation, and to maintain the CO fraction <5% are presented as well. When the different reforming options are compared, the HT-PEMFC system based on the steam reforming process achieved the highest system efficiency (41%), followed by the HT-PEMFC system based on autothermal reforming (38%) and the partial oxidation processes (35%).

Acknowledgements

Support from the Srinakharinwirot University and the Chulalongkorn Academic Advancement into its 2nd Century Project and the Thailand Research Fund (DPG5880003), is gratefully acknowledged.

Nomenclatures

a_c	Catalyst surface area, $m^2\ g^{-1}$
a_{H_2O}	Water activity

Please cite this article in press as: Authayanun S, et al., Optimal design of different reforming processes of the actual composition of bio-oil for high-temperature PEMFC systems, International Journal of Hydrogen Energy (2016), http://dx.doi.org/10.1016/j.ijhydene.2016.10.125

$C_{dissolve}$	Equilibrium concentration, mol cm^{-3}
C_{Pt}	Concentration on the catalyst surface, mol cm^{-3}
C_{Pt}^{ref}	Reference concentration on the catalyst surface, mol cm^{-3}
D_{ij}^{eff}	Binary diffusion coefficient, m^2 s^{-1}
E_c	Activation energy, J mol^{-1} K^{-1}
E_{cell}	Cell voltage, V
E_r	Reversible cell potential, V
F	Faraday constant, 96,485 C mol^{-1}
H	Enthalpy, J mol^{-1}
i	Current density, A m^{-2}
i_0	Exchange current density, A m^{-2}
i_0^{ref}	Reference exchange current density, A m^{-2}
L_c	Catalyst loading, mg cm^{-2}
l_m	Membrane thickness, m
m	Molar flow rate, mol s^{-1}
LHV	Lower heating value, kJ mol^{-1}
N	Molar flux, mol s^{-1} m^{-2}
P	Pressure, atm
P_{FC}	Power output of fuel cell, W
Q	Heat flow, J s^{-1}
Q_T	Total heat required for the hydrogen production process, J s^{-1}
R	Gas constant (=8.314), J mol^{-1} K^{-1}
S_{Pt}	Real platinum surface area
T	Cell temperature, K
X	Mole fraction

Greek letters

δ	Average film thickness, m
α	Transfer coefficient
γ	Reaction order
θ_{CO}	CO coverage
θ_H	H_2 coverage
σ_m	Proton conductivity, S cm^{-1}
η_{FP}	Fuel processor efficiency
η_{act}	Activation loss, V
η_{ohmic}	Ohmic loss, V
η_S	System efficiency without heat integration
η_{SC}	System efficiency with heat integration
η_R	Reformer efficiency
η_{FC}	Fuel cell efficiency

Subscripts and superscripts

a	Anode
c	Cathode
m	Membrane
i,j	Components "i" and "j"
in	Inlet stream
out	Outlet stream

REFERENCES

[1] Kan T, Xiong J, Li X, Ye T, Yuan L, Torimoto Y, et al. High efficient production of hydrogen from crude bio-oil via an integrative process between gasification and current-enhanced catalytic steam reforming. Int J Hydrogen Energy 2010;35:518–32.

[2] Medrano JA, Oliva M, Ruiz J, Garcia L, Arauzo J. Hydrogen from aqueous fraction of biomass pyrolysis liquids by catalytic steam reforming in fluidized bed. Energy 2011;36:2215–24.

[3] Braimakis K, Atsonios K, Panopoulos KD, Karellas S, Kakaras E. Economic evaluation of decentralized pyrolysis for the production of bio-oil as an energy carrier for improved logistics towards a large centralized gasification plant. Renew Sust Energ Rev 2014;35:57–72.

[4] Czernik S, Evans R, French R. Hydrogen from biomass-production by steam reforming of biomass pyrolysis oil. Catal Today 2007;129:265–8.

[5] Wiranarongkorn K, Authayanun S, Assabumrungrat S, Arpornwichanop A. Analysis of thermally coupling steam and tri-reforming processes for the production of hydrogen from bio-oil. Int J Hydrogen Energy 2016;41:18370–9.

[6] Esteban-Díez G, Gil MV, Pevida C, Chen D, Rubiera F. Effect of operating conditions on the sorption enhanced steam reforming of blends of acetic acid and acetone as bio-oil model compounds. Appl Energy 2016;177:579–90.

[7] Mei Y, Wu C, Liu R. Hydrogen production from steam reforming of bio-oil model compound and byproducts elimination. Int J Hydrogen Energy 2016;41:9145–52.

[8] Gil MV, Fermoso J, Pevida C, Chen D, Rubiera F. Production of fuel-cell grade H_2 by sorption enhanced steam reforming of acetic acid as a model compound of biomass-derived bio-oil. Appl Catal B Environ 2016;184:64–76.

[9] Goicoechea S, Ehrich H, Arias P, Kockmann N. Thermodynamic analysis of acetic acid steam reforming for hydrogen production. J Power Sources 2015;279:312–22.

[10] Zhang F, Wang N, Yang L, Li M, Huang L. Ni-Co bimetallic MgO-based catalysts for hydrogen production via steam reforming of acetic acid from bio-oil. Int J Hydrogen Energy 2014;39:18688–94.

[11] Valle B, Remiro A, Aguayo AT, Bilbao J, Gayubo AG. Catalysts Ni/α-Al2O3 and Ni/La2O3-α Al2O3 for hydrogen production by steam reforming of bio-oil aqueous fraction with pyrolytic lignin retention. Int J Hydrogen Energy 2013;38:1307–18.

[12] Remiro A, Valle B, Aguayo AT, Bilbao J, Gayubo AG. Steam reforming of raw bio-oil in a fluidized bed reactor with prior separation of pyrolytic lignin. Energy Fuels 2013;27:7549–59.

[13] Remiro A, Valle B, Aguayo AT, Bilbao J, Gayubo AG. Operating conditions for attenuating Ni/La_2O_3-α Al_2O_3 catalyst deactivation in the steam reforming of bio-oil aqueous fraction. Fuel Process Technol 2013;115:222–32.

[14] Montero C, Oar-Arteta L, Remiro A, Arandia A, Bilbao J, Gayubo AG. Thermodynamic comparison between bio-oil and ethanol steam reforming. Int J Hydrogen Energy 2015;40:15963–71.

[15] Authayanun S, Mamlouk M, Scott K, Arpornwichanop A. Comparison of high-temperature and low-temperature polymer electrolyte membrane fuel cell systems with glycerol reforming process for stationary applications. Appl Energy 2013;109:192–201.

[16] Authayanun S, Saebea D, Patcharavorachot Y, Arpornwichanop A. Evaluation of an integrated methane autothermal reforming and high-temperature proton exchange membrane fuel cell system. Energy 2015;80:331–9.

[17] Chutichai B, Authayanun S, Assabumrungrat S, Arpornwichanop A. Performance analysis of an integrated biomass gasification and PEMFC (proton exchange membrane fuel cell) system: hydrogen and power generation. Energy 2013;55:98–106.

[18] Guan T, Alvfors P, Lindbergh G. Investigation of the prospect of energy self-sufficiency and technical performance of an integrated PEMFC (proton exchange membrane fuel cell), dairy farm and biogas plant system. Appl Energy 2014;130:685–91.

Please cite this article in press as: Authayanun S, et al., Optimal design of different reforming processes of the actual composition of bio-oil for high-temperature PEMFC systems, International Journal of Hydrogen Energy (2016), http://dx.doi.org/10.1016/j.ijhydene.2016.10.125

[19] Authayanun S, Suwanmanee U, Arpornwichanop A. Enhancement of dilute bio-ethanol steam reforming for a proton exchange membrane fuel cell system by using methane as co-reactant: performance and life cycle assessment. Int J Hydrogen Energy 2015;40:12144–53.
[20] Authayanun S, Saebea D, Patcharavorachot Y, Arpornwichanop A. Effect of different fuel options on performance of high temperature PEMFC (proton exchange membrane fuel cell) systems. Energy 2014;68:989–97.
[21] Do TX, Lim Y, Yeo H. Techno-economic analysis of biooil production process from palm empty fruit bunches. Energy Convers Manage 2014;80:525–34.
[22] Hu X, Lu G. Investigation of the steam reforming of a series of model compounds derived from bio-oil for hydrogen production. Appl Catal B Environ 2009;88:376–85.
[23] Slattery JC, Bird RB. Calculation of the diffusion coefficient of dilute gases and of the self-diffusion coefficient of dense gases. AIChE J 1958;4:137–42.
[24] Scott K, Pilditch S, Mamlouk M. Modelling and experimental validation of a high temperature polymer electrolyte fuel cell. J Appl Electrochem 2007;37:1245–59.
[25] Authayanun S, Mamlouk M, Arpornwichanop A. Maximizing the efficiency of a HT-PEMFC system integrated with glycerol reformer. Int J Hydrogen Energy 2012;37:6808–17.
[26] Mamlouk M, Sousa T, Scott K. A high temperature polymer electrolyte membrane fuel cell model for reformate gas. Int J Electrochem 2011;2011:1–18.
[27] ECh Vagia, Lemonidou AA. Thermodynamic analysis of hydrogen production via steam reforming of selected components of aqueous bio-oil fraction. Int J Hydrogen Energy 2007;32:212–23.
[28] Vicente J, Montero C, Erena J, Azkoiti MJ, Bilbao J, Gayubo AG. Coke deactivation of Ni and Co catalysts in ethanol steam reforming at mild temperatures in a fluidized bed reactor. Int J Hydrogen Energy 2014;39:12586–96.
[29] Hu X, Lu G. Bio-oil steam reforming, partial oxidation or oxidative steam reforming coupled with bio-oil dry reforming to eliminate CO_2emission. Int J Hydrogen Energy 2010;35:7169–76.
[30] Alvarado FD, Gracia F. Steam reforming of ethanol for hydrogen production: thermodynamic analysis including different carbon deposits representation. Chem Eng J 2010;165:649–57.

Please cite this article in press as: Authayanun S, et al., Optimal design of different reforming processes of the actual composition of bio-oil for high-temperature PEMFC systems, International Journal of Hydrogen Energy (2016), http://dx.doi.org/10.1016/j.ijhydene.2016.10.125

Energy Conversion and Management 129 (2016) 189–199

Contents lists available at ScienceDirect

Energy Conversion and Management

journal homepage: www.elsevier.com/locate/enconman

Enhanced performance of solid oxide electrolysis cells by integration with a partial oxidation reactor: Energy and exergy analyses

Nuttawut Visitdumrongkul [a], Phanicha Tippawan [a], Suthida Authayanun [b], Suttichai Assabumrungrat [c], Amornchai Arpornwichanop [a,*]

[a] Computational Process Engineering Research Unit, Department of Chemical Engineering, Faculty of Engineering, Chulalongkorn University, Bangkok 10330, Thailand
[b] Department of Chemical Engineering, Faculty of Engineering, Srinakharinwirot University, Nakhon Nayok 26120, Thailand
[c] Center of Excellence in Catalysis and Catalytic Reaction Engineering, Department of Chemical Engineering, Faculty of Engineering, Chulalongkorn University, Bangkok 10330, Thailand

ARTICLE INFO

Article history:
Received 5 July 2016
Received in revised form 27 September 2016
Accepted 7 October 2016
Available online 15 October 2016

Keywords:
SOEC
Hydrogen production
Energy analysis
Exergy analysis
Partial oxidation

ABSTRACT

Hydrogen production without carbon dioxide emission has received a large amount of attention recently. A solid oxide electrolysis cell (SOEC) can produce pure hydrogen and oxygen via a steam electrolysis reaction that does not emit greenhouse gases. Due to the high operating temperature of SOEC, an external heat source is required for operation, which also helps to improve SOEC performance and reduce operating electricity. The non-catalytic partial oxidation reaction (POX), which is a highly exothermic reaction, can be used as an external heat source and can be integrated with SOEC. Therefore, the aim of this work is to study the effect of operating parameters of non-catalytic POX (i.e., the oxygen to carbon ratio, operating temperature and pressure) on SOEC performance, including exergy analysis of the process. The study indicates that non-catalytic partial oxidation can enhance the hydrogen production rate and efficiency of the system. In terms of exergy analysis, the non-catalytic partial oxidation reactor is demonstrated to be the highest exergy destruction unit due to irreversible chemical reactions taking place, whereas SOEC is a low exergy destruction unit. This result indicates that the partial oxidation reactor should be improved and optimally designed to obtain a high energy and exergy system efficiency.

© 2016 Elsevier Ltd. All rights reserved.

1. Introduction

Hydrogen is considered to be an important, clean energy carrier for the future since it can be used in fuel cells to generate electricity. However, conventional hydrogen production processes, such as reforming and gasification, emit carbon dioxide, which causes a global warming problem [1,2]. Electrolysis cells have received attention as a clean hydrogen technology because this technology can directly convert water to pure hydrogen and oxygen via an electrochemical reaction without carbon dioxide emission. Among the various types of electrolysis cells, the solid oxide electrolysis cell (SOEC) has received considerable attention because it has higher efficiency than other electrolysis cell types [3]. The SOEC is operated at high temperatures of approximately 1073–1273 K with thermal energy requirements. Ni et al. [4] studied the effects of electrode porosity, pore size and steam molar fraction on the SOEC performance. The results showed that increases in the electrode porosity, pore size and steam molar fraction can increase the SOEC performance. In addition, it was found that the electrical energy requirement was reduced at high operating temperatures (873–1273 K). This finding was similar to Udagawa's work [5] that the effect of intermediate temperatures on the SOEC performance was studied. Therefore, the use of thermal energy from external heat sources to supply the SOEC in high temperature operations is an attractive solution to reduce the requirement of electrical energy for SOEC operation [6]. As SOEC can produce pure oxygen, a combustion process that can provide thermal energy at a high temperature by using pure oxygen from SOEC has received attention [7,8].

The combustion process can be divided into two types: complete combustion and partial oxidation process (POX). Apart from heat, steam and carbon dioxide are produced in complete combustion. On the other hand, the partial oxidation process can produce carbon monoxide and hydrogen, which can be used as fuel in several processes. Therefore, the SOEC integrated with a partial oxidation system (SOEC-POX) can enhance the ability of hydrogen production and reduce the electrical requirement for SOEC operation [9].

To assess the SOEC-POX system performance and efficiency, energy and exergy analyses are used. The energy and exergy should be analyzed simultaneously to identify the sources of energy and exergy losses of the system by using the first law of

* Corresponding author.
E-mail address: Amornchai.A@chula.ac.th (A. Arpornwichanop).

http://dx.doi.org/10.1016/j.enconman.2016.10.023
0196-8904/© 2016 Elsevier Ltd. All rights reserved.

Nomenclature

B_g	permeability (m^2)
d_a	thickness of anode (m)
d_c	thickness of cathode (m)
$D_{H_2-H_2O}$	molecular diffusion
$D^{eff}_{H_2O}$	effective diffusion coefficient of steam ($m^2\ s^{-1}$)
$D_{H_2O,k}$	Knudsen diffusion
E^0	standard potential (V)
$E_{act,i}$	activation energy at cathode and anode ($J\ mol^{-1}\ K^{-1}$)
ex_{ch}	specific chemical exergy ($J\ mol^{-1}$)
$ex_{ch,i}$	standard chemical exergy of species *i* ($J\ mol^{-1}$)
$\dot{E}x_d$	exergy destruction (W)
ex_i	specific exergy ($J\ mol^{-1}$)
ex_{ph}	specific physical exergy ($J\ mol^{-1}$)
$\dot{E}x_Q$	exergy of thermal energy (W)
$\dot{E}x_w$	exergy of work (W)
F	Faraday's constant (96,485 C mol^{-1})
h_i	enthalpy of species *i* at general state ($J\ mol^{-1}$)
$h_{i,0}$	enthalpy of species *i* at reference environment state ($J\ mol^{-1}$)
J	current density ($A\ m^{-2}$)
$J_{0,a}$	exchange current density at anode ($A\ m^{-2}$)
$J_{0,c}$	exchange current density at cathode ($A\ m^{-2}$)
L	thickness of electrolyte (m)
LHV_{in}	lower heating value of inlet ($kJ\ kmol^{-1}$)
LHV_{out}	lower heating value of outlet ($kJ\ kmol^{-1}$)
LHV_{H_2}	lower heating value of hydrogen ($kJ\ mol^{-1}$)
M_{H_2}	molecular weight of hydrogen
M_{H_2O}	molecular weight of steam
n_e	number of electron for electrochemical reaction (2 electron)
n_p	electrode porosity
N_{cell}	number of cells
$\dot{N}_{CH_4 in}$	molar flow rate of inlet methane ($kmol\ h^{-1}$)
$\dot{N}_{H_2,out}$	outlet molar flow rate of hydrogen ($kmol\ h^{-1}$)
$\dot{N}_{H_2 produced}$	molar flow rate of produced hydrogen ($kmol\ h^{-1}$)
$\dot{N}_{H_2O,in}$	molar flow rate of steam ($kmol\ h^{-1}$)
$\dot{N}_{in}$	molar flow rate of inlet ($kmol\ h^{-1}$)
$\dot{N}_{out}$	molar flow rate of outlet ($kmol\ h^{-1}$)
P	operating pressure of SOEC (atm)
p_{H_2}	partial pressure of hydrogen ($N\ m^{-2}$)
p_{H_2O}	partial pressure of steam ($N\ m^{-2}$)
p_{O_2}	partial pressure of oxygen ($N\ m^{-2}$)
Q	heat of the system (W)
Q_{cell}	thermal energy input rate of SOEC (W)
Q_{out}	heat rate of the reaction ($kJ\ h^{-1}$)
Q_{ovp}	heat of overpotential (W)
r	average electrode pore radius (m)
R	gas constant ($8.314\ J\ mol^{-1}\ K^{-1}$)
s_i	entropy of species *i* at general state ($J\ mol^{-1}\ K^{-1}$)
$s_{i,0}$	entropy of species *i* at reference environment state ($J\ mol^{-1}\ K^{-1}$)
T	operating temperature (K)
T^*	dimensionless temperature
T_0	reference temperature (298.15 K)
U_f	utilization factor
W	electrical work (W)
W_{comp}	used energy for compressor (W)
W_{SOEC}	power of SOEC (W)
W_{SG}	used energy for steam generator (W)
y_i	composition of species *i*

Greek symbol

σ_{H_2}	collision diameter of hydrogen (m)
σ_{H_2O}	collision diameter of steam (m)
α	charge transfer coefficient
γ_i	pre-exponential factor at cathode and anode ($A\ m^{-2}$)
$\frac{\varepsilon_{H_2}}{K}$	Lennard-Jones Potentials of hydrogen
$\frac{\varepsilon_{H_2O}}{K}$	Lennard-Jones Potentials of steam
$\eta_{act,a}$	anode activation overpotential (V)
$\eta_{act,c}$	cathode activation overpotential (V)
$\eta_{con,a}$	anode concentration overpotential (V)
$\eta_{con,c}$	cathode concentration overpotential (V)
η_{en}	energy efficiency
η_{ex}	exergy efficiency
η_{ohm}	ohmic overpotential (V)
μ	dynamic viscosity ($kg\ m^{-1}\ s^{-1}$)
ξ	electrode tortuosity
Ω_D	dimensionless diffusion collision integral

thermodynamics and the second law of thermodynamics, respectively. Energy analysis is used to determine the energy requirement in forms of matter streams, heat and work; however, it cannot identify the real thermodynamic inefficiencies associated with the energy conversion system. In contrast, exergy analysis is a powerful tool that can be applied to a wide range of processes. It can be used to identify the location, quantity and quality of irreversible losses, as well as inefficient energy usage [10]. For this reason, there are currently many studies on energy and exergy analyses of the irreversible process. Ni et al. [11] conducted energy and exergy analyses of a proton exchange membrane electrolyzer plant to examine the effect of operating parameters on the performance and efficiency of the plant. Albrecht et al. [12] conducted exergy analysis of the partial oxidation of natural gas for a gas turbine plant. The result of this research showed that the most exergy loss occurred in the partial oxidation reactor (9.57%) and the air separation unit (6.21%). However, an exergy analysis of SOEC integrated with a partial oxidation system has not been reported yet.

The objective of this work is to study the SOEC integrated with a non-catalytic POX system in order to reduce the electrical energy and increase the SOEC system efficiency. The effects of the oxygen to carbon ratio, operating temperature, and pressure on the hydrogen yield and the efficiency of the POX reactor, as well as on the overpotentials and efficiency of the integrated SOEC system performance, are analyzed. In addition, energy and exergy analyses are applied to evaluate the performance of the SOEC-POX system, as well as the quality of energy usage within the system. The exergy destruction and efficiency of each unit of the SOEC-POX system are investigated to identify which unit should be improved.

2. Process description

2.1. Solid oxide electrolysis cell

A solid oxide electrolysis cell (SOEC) is an electrochemical device for hydrogen production via the electrochemical reaction of steam at high operating temperatures. The mechanism of SOEC operation is shown in Fig. 1(a). Fig. 1(b) presents the energy consumption in terms of electrical and thermal energies in water electrolysis. The steam is fed to a cathode channel where the electrochemical reaction takes place. The steam splits into a hydrogen molecule and an oxygen ion. Afterwards, the hydrogen is transported out of the cathode channel, while the oxygen ion

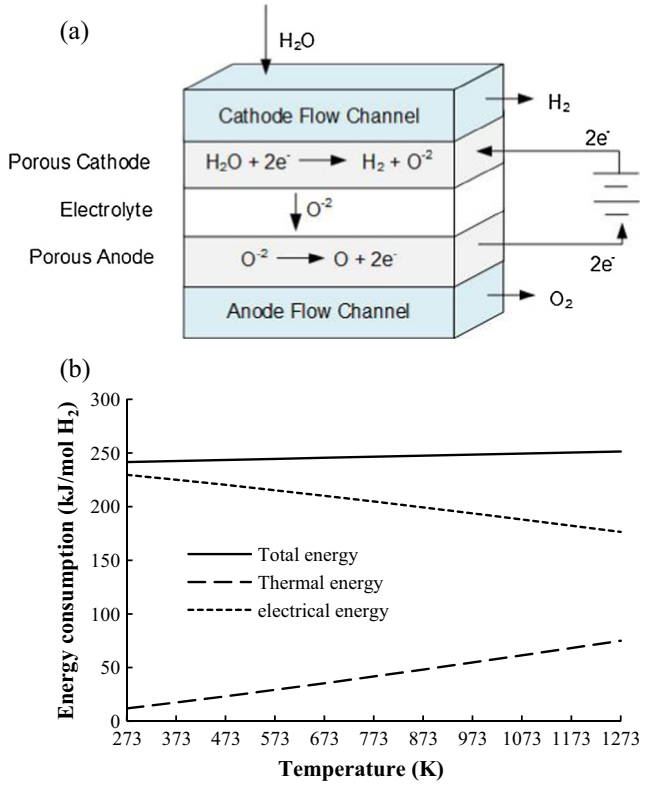

Fig. 1. (a) SOEC operation and (b) energy consumption of SOEC.

migrates through an electrolyte layer to the anode channel and combines into an oxygen molecule. The reactions need both electrical and thermal energies for operation. From the laws of thermodynamics, when the operating temperature is increased, the thermal energy is increased and the electrical energy is reduced; however, the total energy for operation is approximately constant [13]. It can be concluded that the increase in thermal energy can help to reduce the electrical energy and operating cost. Therefore, thermal energy is required for the SOEC operation, which can be provided by an exothermic process, for example, a partial oxidation process.

2.2. Partial oxidation

Partial oxidation (POX) of methane is a partial combustion reaction between methane and oxygen or air producing hydrogen and carbon monoxide as products. This process is an exothermic and complex reaction in which many side reactions can occur, as shown in Eqs. (R1)–(R5) [9].

$$CH_4 + 0.5O_2 \rightarrow CO + 2H_2 \quad (R1)$$

$$CH_4 + 2O_2 \rightarrow CO_2 + 2H_2O \quad (R2)$$

$$CH_4 + H_2O \leftrightarrow CO + 3H_2 \quad (R3)$$

$$CH_4 + CO_2 \leftrightarrow 2CO + 2H_2 \quad (R4)$$

$$CO + H_2O \leftrightarrow CO_2 + H_2 \quad (R5)$$

This process can be carried out via either catalytic or non-catalytic POX. The catalyst is added to the reactor to reduce the operating temperature. The operating temperature ranges of catalytic and non-catalytic POX are 1073–1273 K and 1273–1573 K, respectively [14,15]. The advantages of partial oxidation are fast reaction rates and fast start-up. Moreover, the process is exothermic; therefore, it does not require an external heat source and can provide heat to other processes [16]. However, the disadvantage of this process is that it is hard to control the temperature, thus resulting in coke and hot spot formation.

For the POX operation using pure oxygen, the addition of steam can reduce the maximum temperature of the flame within the reactor and thus prevent coke and hot spot formation. The suitable amount of steam for a POX reactor is approximately 10% of the volume of methane [16].

2.3. Solid oxide electrolysis cell integrated with partial oxidation process

In general, a furnace is used to provide external thermal energy for SOEC. However, the non-catalytic partial oxidation reactor is used as an external heat source for the SOEC in this work because this process not only supplies the necessary thermal energy but also can produce hydrogen. Therefore, the advantage of this process is the ability to increase the hydrogen production rate and reduce the operating cost. A flowsheet of the SOEC integrated with a non-catalytic partial oxidation process is shown in Fig. 2.

The procedures of this system are described as follows. First, water (*WATER* stream) is fed to a steam generator (*PUMP* and *HEATER1*), which is used to produce steam for the SOEC. Then, the generated steam (*STEAM* stream) is separated into two streams by a splitting unit (*SPLIT1*). One stream (*ST-POX* stream) is used in the POX reaction, and the other (*ST-SOEC* stream) is moved past the first heat exchanger (*HEATX1*) to increase the operation temperature of the SOEC by heat exchange with the product from the cathode channel (*HT-H2* stream). Next, the steam is mixed (*MIXING*) with some of the product from the cathode (*RECYCLE* stream) to adjust the steam to hydrogen ratio. The steam (*FEED-CA* stream) is already fed to the cathode of the SOEC (*CATHODE*). In order for oxygen to feed into the anode channel, oxygen in the standard state (*O2* stream) must increase its pressure at the first compressor (*COMP1*) which is operated in the isentropic mode. Then, the oxygen (*O2-PRESS* stream) must exchange heat with the anode product (*HT-O2* stream) at the second heat exchanger (*HEATX2*) and subsequently feed (*FEED-AN* stream) into the anode channel of the SOEC (*HEATER2* and *ANODE*). When the SOEC carries out the reaction, hydrogen and oxygen are produced in the cathode channel (*CA-PROD* stream). However, oxygen must be transported to the anode channel by passing electrolytes (*ELECTROL*). The hydrogen and some steam of the cathode channel are split into two streams (*SPLIT2*). One stream is used to adjust the steam to hydrogen ratio and the other is used to reduce the temperature by exchanging heat with the steam from the steam generator. For the produced oxygen at the outlet of the anode channel, the temperature is reduced by exchanging heat with oxygen, and then the temperature is reduced again at the third heat exchanger (*HEATX3*) by exchanging heat with methane (*CH4* stream), which is used as a reactant for the POX reaction. The oxygen with reduced temperature is split into two streams (*SPLIT3*). One stream (*O2-POX* stream) is used in the POX reaction, and the other is sent to the exit (*O2-PROD* stream). Methane (*CH4-POX* stream), oxygen (*O2-POX* stream) and steam (*ST-POX* stream) from the steam generator are pressurized at the second compressor (*COMP2*), which is operated in the isentropic mode, and then the pressurized stream (*FEED-POX* stream) is fed to a POX reactor *(POX)*.

3. Modeling of the solid oxide electrolysis cell

The process model of the SOEC is developed using Aspen plus software simulation. This software contains various basic unit operation modules and rigorous thermodynamic and physical

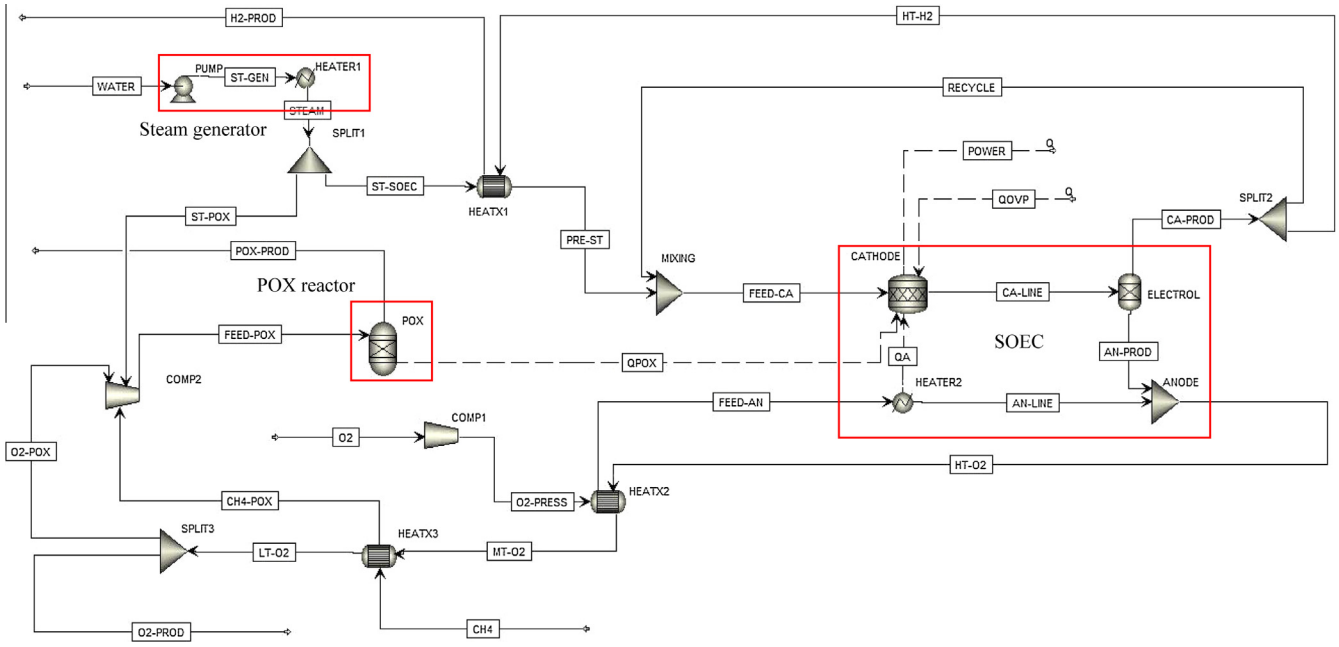

Fig. 2. Flowsheet of the SOEC integrated with a non-catalytic partial oxidation process.

property databases, as well as additional computational tools that can assist the designer for the process design and improvement. However, the SOEC module is not contained in the software. Therefore, the SOEC is developed by using existing functions and modules, and electrochemical characteristics are developed by using the FORTRAN language in a calculator block.

The electrochemical model of SOEC from Ni et al. [13] is applied for the electrical calculations in this work. Electrical energy is required to overcome the equilibrium voltage and irreversible losses. The equilibrium voltage, which is the minimum cell voltage, is needed to proceed the electrochemical reaction. It can be calculated from Eqs. (1) and (2) [13], which depend on the operating temperature and partial pressures of the gases:

$$E = E^0 + \frac{RT}{2F}\ln\left(\frac{P_{H_2}\cdot P_{O_2}^{1/2}}{P_{H_2O}}\right) \tag{1}$$

$$E^0 = 1.253 - 2.4516\times 10^{-4}T \tag{2}$$

The SOEC overpotentials are voltage losses and consist of the activation overpotential, ohmic overpotential, and concentration overpotential. The activation overpotential is related to the chemical kinetics of the electrochemical reactions at both the cathode and the anode and can be calculated by Eqs. (3) and (4), which are derived from the Butler-Volmer equation [13]:

$$\eta_{act,i} = \frac{RT}{F}\ln\left[\frac{J}{2J_{0,i}} + \sqrt{\left(\frac{J}{2J_{0,i}}\right)^2 + 1}\right] \tag{3}$$

$$J_{0,i} = \gamma_i \exp\left(-\frac{E_{act,i}}{RT}\right) \tag{4}$$

The ohmic overpotential is the voltage loss from the resistance of ion conductivity in the electrolyte layer and the transport of electrons through the electrode. The ohmic overpotential can be calculated by Ohm's law as shown in Eq. (5) [13]:

$$\eta_{ohm} = 2.99\times 10^{-5} JL \exp\left(\frac{10300}{T}\right) \tag{5}$$

The concentration overpotential is the transport resistance of reactant species that diffuse to reach the three phase boundary (TPB) at the cathode and the transport resistance of the product species leaving the TPB at the anode. The cathode and anode concentration overpotentials can be calculated by Eqs. (6) and (7), respectively. The concentration overpotential at the cathode is involved with the diffusion of steam and hydrogen from the cathode channel to the TPB. Fick's model is applied for the diffusion at the cathode because of its non-complicated nature and effective description of gas transport in the SOEC, whereas Darcy's law is used for the diffusion of oxygen at the interface of the electrolyte and the anode channel [13]:

$$\eta_{conc,c} = \frac{RT}{2F}\ln\left[\frac{\left(P_{H_2} + JRTd_c/2FD_{H_2O}^{eff}\right)\cdot P_{H_2O}}{\left(P_{H_2O} - JRTd_c/2FD_{H_2O}^{eff}\right)\cdot P_{H_2}}\right] \tag{6}$$

$$\eta_{conc,a} = \frac{RT}{4F}\ln\left(\frac{\sqrt{(P_{O_2})^2 + (JRT\mu d_a/2FB_g)}}{P_{O_2}}\right) \tag{7}$$

The effective diffusion coefficient of steam can be calculated by Eq. (8) [13]. Moreover, it is a function of Knudsen diffusion and molecular diffusion, which can be calculated with the kinetic theory and the Chapman-Enskog theory, as shown in Eqs. (9) and (10) [17], respectively:

$$\frac{1}{D_{H_2O}^{eff}} = \frac{\xi}{n_p}\left(\frac{1}{D_{H_2-H_2O}} + \frac{1}{D_{H_2O,k}}\right) \tag{8}$$

$$D_{H_2O,k} = \frac{4}{3}r\sqrt{\frac{8RT}{\pi M_{H_2O}}} \tag{9}$$

$$D_{H_2-H_2O} = 0.00133\left(\frac{1}{M_{H_2}} + \frac{1}{M_{H_2O}}\right)^{1/2}\frac{T^{3/2}}{P\sigma_{H_2-H_2O}^2\Omega_D} \tag{10}$$

$$\sigma_{H_2-H_2O} = \frac{\sigma_{H_2} + \sigma_{H_2O}}{2} \tag{11}$$

$$\Omega_D = \frac{1.06036}{(T^*)^{0.1561}} + \frac{0.193}{\exp(0.47635T^*)} + \frac{1.03587}{\exp(1.52996T^*)} + \frac{1.76474}{\exp(3.89411T^*)} \quad (12)$$

$$T^* = \frac{\kappa T}{\varepsilon_{H_2-H_2O}} \quad (13)$$

$$\frac{\varepsilon_{H_2-H_2O}}{\kappa} = \sqrt{\frac{\varepsilon_{H_2}}{\kappa} \cdot \frac{\varepsilon_{H_2O}}{\kappa}} \quad (14)$$

The permeability and dynamic viscosity of oxygen at the cathode can be calculated from Eqs. (15) and (17), respectively [18].

$$B_g = \frac{\varepsilon^3}{72\xi(1-\varepsilon)^2}(2r)^2 \quad (15)$$

$$\mu = -1.692 + 889.75\tau - 892.79\tau^2 + 905.98\tau^3 - 598.36\tau^4 + 221.64\tau^5 - 34.75\tau^6 \quad (16)$$

$$\tau = \frac{T(K)}{1000} \quad (17)$$

The SOEC overpotentials are converted into thermal energy, which can be used for the SOEC operation. This thermal energy is called the heat of overpotentials (Q_{ovp}) as shown in Eq. (18) [13]. The cell voltage of the SOEC can be calculated from Eq. (19).

$$Q_{ovp} = (\eta_{conc,c} + \eta_{conc,a} + \eta_{act,c} + \eta_{act,a} + \eta_{ohmic}) \cdot J \cdot Area \cdot N_{cell} \quad (18)$$

$$V = E + \eta_{conc,c} + \eta_{conc,a} + \eta_{act,c} + \eta_{act,a} + \eta_{ohmic} \quad (19)$$

In addition, the main parameters that affect the steam utilization factor (U_f) are the electrical current, number of cells and the inlet molar flow rate of steam, as shown in Eq. (20). The power of the SOEC, which represents the amount of electrical energy used for the reaction, is shown in Eq. (21).

$$U_f = \frac{I \cdot N_{cell}}{n_e \cdot F \cdot \dot{N}_{H_2O,in}} \quad (20)$$

$$W = I \cdot V \cdot N_{cell} \quad (21)$$

4. Energy analysis

The energy efficiency of the SOEC can be calculated using Eq. (22) [19]. The POX efficiency and hydrogen yield can be calculated from Eqs. (23) and (24), respectively.

$$\eta_{en,SOEC} = \frac{\dot{N}_{H_2,out} \cdot LHV_{H_2}}{W + Q_{cell}} \quad (22)$$

$$\eta_{en,POX} = \frac{\dot{N}_{out} \cdot LHV_{out} + Q_{out}}{\dot{N}_{in} \cdot LHV_{in}} \quad (23)$$

$$H_2 \text{ yield} = \frac{\dot{N}_{H_2 produced}}{\dot{N}_{CH_4\ in}} \quad (24)$$

The SOEC-POX system efficiency, which provides a performance index of this system, can be calculated by Eq. (25).

$$\eta_{en,SOEC-POX} = \frac{\left(\dot{N}_{H_2,out} \cdot LHV_{H_2}\right)_{SOEC} + \left(\dot{N}_{out} \cdot LHV_{out}\right)_{POX}}{W_{SOEC} + W_{SG} + W_{comp} + \left(\dot{N}_{in} \cdot LHV_{in}\right)_{POX}} \quad (25)$$

5. Exergy analysis

Exergy is the maximum theoretical useful work of the control volume of the system at a general state (T, P) when the system is brought into equilibrium at a reference environmental state (T_0, P_0) [11]. However, the exergy of the system can always be lost via two different ways: exhaust and destruction. Exhaust or external losses are caused by the exergy in unused streams, such as the purge stream, smoke, and cooling water. Destruction or internal losses is caused by the irreversibility of the unit or processes, such as the reaction and heat transfer. Therefore, the exergy destruction is an important parameter to investigate the energy quality and can be determined by an exergy balance as shown in Eq. (26) [20].

$$\sum \dot{E}x_Q + \sum_{in} \dot{n}_i ex_i - \sum_{out} \dot{n}_i ex_i + \dot{E}x_w - \dot{E}x_d = 0 \quad (26)$$

The exergy of thermal energy is dependent on the temperature and heat of the system as shown in Eq. (27) [21].

$$Ex_Q = \left(1 - \frac{T_0}{T}\right) Q \quad (27)$$

The specific exergy is the summation of the specific physical exergy and specific chemical exergy, which can be calculated by Eq. (28) [22]:

$$ex_i = ex_{ph} + ex_{ch} \quad (28)$$

The specific physical exergy is the maximum useful work obtained by passing a stream of matter from the general state to the environmental state. It can be determined by Eq. (29).

$$ex_{ph,i} = (h_i - h_{i,0}) - T_0(s_i - s_{i,0}) \quad (29)$$

The specific chemical exergy is the maximum useful energy that can be attained by passing from the environmental state to the dead state, by means of chemical processes with reactants and products at the environmental temperature and pressure. This type of exergy can be determined from Eq. (30).

$$ex_{ch} = \sum y_i \cdot ex_{ch,i} + RT_0 \sum y_i \cdot \ln y_i \quad (30)$$

The standard chemical exergy of each substance that is used in this work is presented in Table 1 [10].

The exergy of work associated with the shaft work performed by the system is shown in Eq. (31). The shaft work includes all terms of work, such as electrical work and mechanical work, but excludes the work performed by the system with volume change:

$$\dot{E}x_w = \dot{W} \quad (31)$$

Finally, the exergy efficiency of the system can be calculated from the matter inlet exergy and the exergy destruction, as shown in Eq. (32):

$$\eta_{ex} = 1 - \frac{\dot{E}x_d}{\dot{E}x_{in}} \quad (32)$$

Table 1
Standard chemical exergy.

Substances	Chemical exergy (kJ mol^{-1})
H_2	236.09
H_2O (l)	0.90
H_2O (g)	9.50
O_2	3.97
CH_4	831.20
CO_2	19.48
CO	274.71
N_2	0.72

Exergy analysis can predict the exergy destruction (inefficient use of useful work) of each unit operation in the considered process. For the exergy destruction calculation, an exergy balance equation can be used. The exergy destruction is always a positive value because it is calculated from the potential evaluation of energy that is used in each unit.

6. Model validation

To confirm the accuracy of the simulation, validation between the simulation and experimental data is presented. For the POX process, the experimental data from a patent of Texaco Development Corporation, which produces synthesis gas by using the direct partial oxidation of refinery gas with oxygen without catalysts [23], is used for the validation in this work. A temperature of 1700 K and a pressure of 31.03 bar are used, and this simulation assumes that the inlet gas does not contain sulfide. It is found that the product composition of the POX process from the simulation results and the experimental data are in good agreement, as shown in Fig. 3(a). In addition, the simulation results in this work are validated with the experimental data of the SOEC [24]. The electrolyte, cathode, and anode layers of the SOEC are made from yttria-stabilized zirconia (YSZ), nickel–YSZ (Ni–YSZ), and strontium-doped lanthanum-YSZ (LSM–YSZ), respectively. The operating conditions and the other parameters used in this simulation are shown in Table 2. The validation simulation and the experimental data at different temperatures are shown in Fig. 3(b). A good agreement between experimental and simulation data is observed.

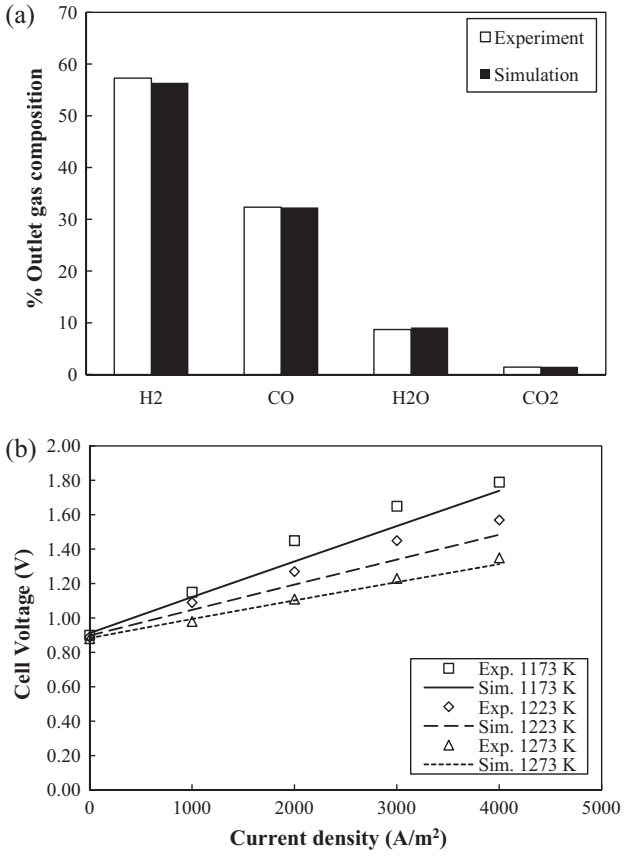

Fig. 3. (a) Comparison of the outlet gas composition between experimental and simulation data and (b) validation of current density versus voltage between simulation and experimental data at various operating temperatures.

7. Results and discussion

7.1. Effect of POX operating parameters on the performance and efficiency of POX and SOECs

Pure oxygen produced from SOECs and methane is used as the fuel for the non-catalytic partial oxidation reactor in this work. The operating conditions of SOECs used in this work are shown in Table 2. The operating temperature in the SOECs is varied by the heat of the exothermic reaction from the POX reactor. The effect of the oxygen to carbon ratio (O/C), operating pressure and temperature on the performance and efficiency of the POX reactor and SOECs is investigated. The obtained results of each stream are shown in Table 3.

7.1.1. Effect of the oxygen to carbon ratio

The simulation results of the hydrogen yield and POX efficiency at different O/C ratios, operated at a temperature and pressure of 1373 K and 5 bar, respectively, are shown in Fig. 4(a). It is found that the hydrogen yield is reduced with an increase in the O/C ratio because a portion of the methane fed to the reactor is used to generate heat via the methane oxidation reaction. In terms of the POX efficiency (Eq. (23)), it is slightly decreased with increasing O/C ratio because of low hydrogen and carbon monoxide production rates. For these reasons, it can be concluded that low O/C ratios are required to maximize hydrogen production for the methane partial oxidation reactor. However, the O/C ratios of the POX process affect the operating temperature of the SOEC as well. This is because the released heat from the partial oxidation reaction is used as the external heat for the SOEC system. From Fig. 4(b), it is observed that the performance of the SOEC, in terms of overall overpotential and equilibrium voltage, changes by varying the O/C ratio. The reduction of the overall overpotential and equilibrium voltage is observed at high O/C ratios. At these conditions, high external energy from the POX and SOEC operating temperature is present. This results in the reduction of heat of overpotential (internal heat requirement) and thus a low power requirement, leading to high cell efficiency at high O/C ratios as shown in Fig. 4(c).

Table 2
Input parameters and operating conditions.

Parameters	Values
Operating temperature, T (K)	1273
Operating pressure, P (bar)	5
Steam concentration (%)	90
Pre-exponential factor for anode exchange current density, γ_a ($A\,m^{-2}$)	2.051×10^9
Pre-exponential factor for cathode exchange current density, γ_c ($A\,m^{-2}$)	1.344×10^{10}
Activation energy for anode, $E_{act,a}$ ($J\,mol^{-1}$)	1.2×10^5
Activation energy for cathode, $E_{act,c}$ ($J\,mol^{-1}$)	1.0×10^5
Current density, J ($A\,m^{-2}$)	2500
Electrode porosity, n	0.4
Electrode tortuosity, ξ	5.0
Average pore radius, r (μm)	0.5
Cell area, A (m^2)	0.04
Number of cells, N_{cell} (cell)	1500
Sweep gas type	Oxygen
Anode-support	
Electrolyte thickness, L (μm)	50
Cathode thickness, d_c (μm)	50
Anode thickness, d_a (μm)	500
Model for validation [17]	
Electrolyte-support	
Electrolyte thickness, L (μm)	1000
Cathode thickness, d_c (μm)	100
Anode thickness, d_a (μm)	100
Steam concentration (%)	60

Table 3
Stream data of SOEC-POX system.

Streams	Temp. (K)	Press. (bar)	Flow rate (kmol h^{-1})	Molar composition					
				H_2	H_2O	O_2	CH_4	CO	CO_2
WATER	298.15	1	5.70	–	1.00	–	–	–	–
ST-GEN	298.15	5	5.70	–	1.00	–	–	–	–
STEAM	427.00	5	5.70	–	1.00	–	–	–	–
ST-POX	427.00	5	0.70	–	1.00	–	–	–	–
ST-SOEC	427.00	5	5.00	–	1.00	–	–	–	–
PRE-ST	1166.00	5	5.00	–	1.00	–	–	–	–
FEED-CA	1182.46	5	6.09	0.10	0.90	–	–	–	–
O2	298.15	1	5.00	–	–	1.00	–	–	–
O2-PRESS	529.57	5	5.00	–	–	1.00	–	–	–
FEED-AN	1272.00	5	5.00	–	–	1.00	–	–	–
CA-LINE	1273.00	5	7.49	0.45	0.36	0.19	–	–	–
AN-LINE	1273.00	5	5.00	–	–	1.00	–	–	–
CA-PROD	1273.00	5	6.09	0.56	0.44	–	–	–	–
RECYCLE	1273.00	5	1.09	0.56	0.44	–	–	–	–
HT-H2	1273.00	5	5.00	0.56	0.44	–	–	–	–
H2-PROD	428.00	5	5.00	0.56	0.44	–	–	–	–
AN-PROD	1273.00	5	1.40	–	–	1.00	–	–	–
HT-O2	1273.00	5	6.40	–	–	1.00	–	–	–
MT-O2	702.36	5	6.40	–	–	1.00	–	–	–
LT-O2	370.00	5	6.40	–	–	1.00	–	–	–
O2-POX	370.00	5	4.48	–	–	1.00	–	–	–
O2-PROD	370.00	5	1.92	–	–	1.00	–	–	–
CH4	298.15	1	6.93	–	–	–	1.00	–	–
CH4-POX	530.03	1	6.93	–	–	–	1.00	–	–
FEED-POX	719.10	5	12.10		0.057	0.370	0.573	–	–
POX-PROD	1373.00	5	21.46	0.576	0.102	–	–	0.297	0.025

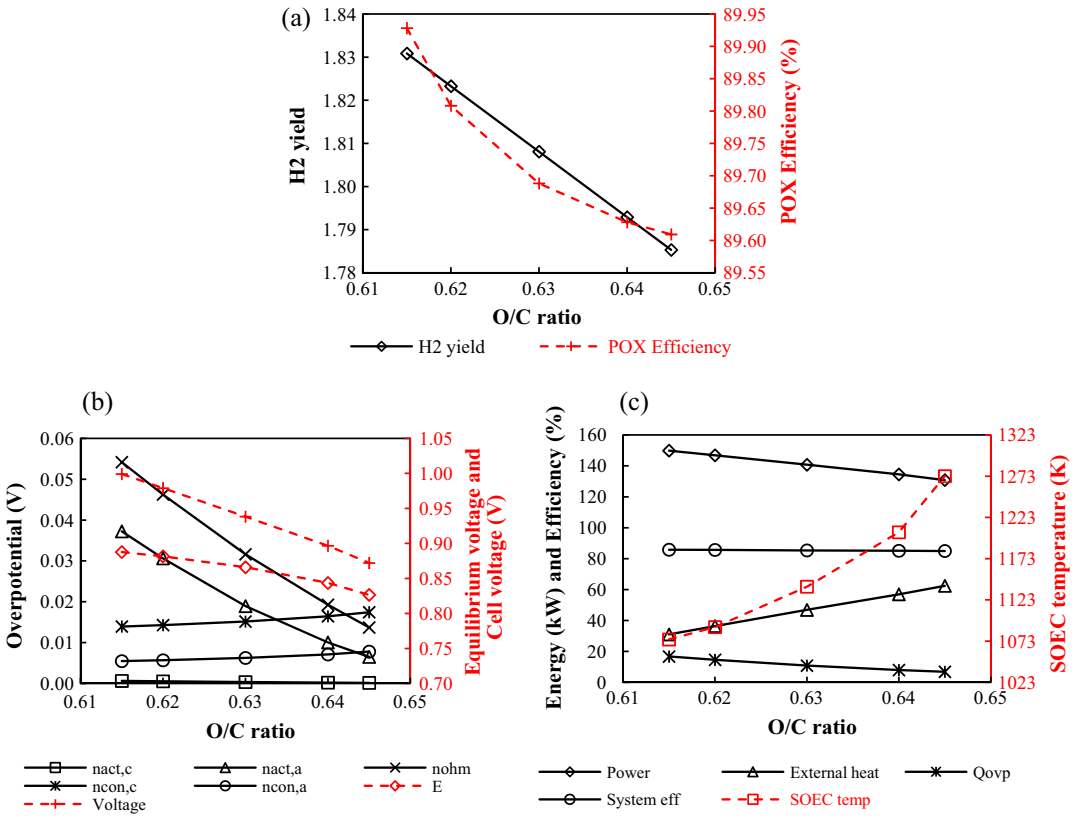

Fig. 4. Effect of O/C ratio on: (a) H_2 yield and POX efficiency; (b) equilibrium voltage, overpotential and cell voltage; and (c) power, external heat, and heat of overpotential, SOEC efficiency and SOEC temperature.

7.1.2. Effect of operating temperature of POX

The effect of operating temperature on the hydrogen yield and the efficiency of POX is shown in Fig. 5(a). In this work, the POX is operated at high temperatures (1373–1493 K) because SOECs require high external heat for the electrochemical reaction, and the oxygen reactant for the POX reactor is produced from SOECs. It is found that the operating temperature affects the performance of POX gradually. With the increase in operating temperature, the

exothermic reaction in the system is reversed, which results in a reduction of the reaction product. For this reason, the hydrogen yield is decreased with increasing operating temperature of the POX reaction. Therefore, the efficiency of the POX reactor decreases gradually with an increase in the operating temperature, as demonstrated in Fig. 5(a).

In terms of the thermal energy, an increase in POX operating temperature can reduce the external heat supplied to the SOEC because when the reactor requires an increase in temperature, the thermal energy produced from the POX reaction is used for adjusting the operating temperature of SOEC. Furthermore, the reactor does not receive thermal energy from an external source. For these reasons, it can be concluded that operation at high temperatures reduces the external energy supplied to the SOEC, which results in a decrease in the SOEC operating temperature, as shown in Fig. 5(c). Alternatively, the electrical energy of the SOEC is increased when the operating temperature of the POX reaction is increased due to a reduction in the SOEC operating temperature.

In terms of the electrical energy for the SOEC, it is worth mentioning that the operating temperature of the SOEC is reduced with the increasing operating temperature of the POX reaction; thus, both the equilibrium voltage and the overpotential are increased by increasing the POX reaction operating temperature, as shown in Fig. 5(b). This approach can increase both the cell voltage and the heat of overpotential of the SOEC. However, the efficiency of the system is reduced as shown in Fig. 5(c), due to increasing cell voltage from increasing the operating temperature of the POX reaction.

7.1.3. Effect of POX operating pressure

POX pressures in the range of 5–25 bar, which is the operating range for industry [16], are investigated when the temperature and O/C ratio of the POX reactor are 1333 K and 0.65, respectively. From Fig. 6(a), the hydrogen yield and the POX efficiency decrease with increasing operating pressure. However, high thermal energy is transferred as external energy for the SOEC operation when the POX reactor is operated at a high pressure. This is because the gas temperature is proportional to the gas pressure, which leads to an increase in the temperature at high operating pressures. In addition, an increase in pressure promotes the complete combustion of the reaction, which can increase the temperature of the product. For these reasons, an increase in the operating pressure of the POX reactor can reduce the equilibrium voltage and the overpotential, as shown in Fig. 6(b). This results in both a low electrical power and a low heat of overpotential at a high pressure, which are presented in Fig. 6(c). However, the produced hydrogen from the POX reaction is reduced with increasing operating pressure. Therefore, the system efficiency decreases with the POX pressure.

7.2. Comparison of the efficiency between a conventional SOEC system and a SOEC integrated with the POX reaction system (SOEC-POX)

The comparison of the efficiency between a conventional SOEC system and a SOEC integrated with the POX reaction system (SOEC-POX) is shown in Fig. 7(a). The conventional SOEC system is operated under the same conditions as the SOEC in SOEC-POX when the number of cells is equal to 1500 cells. That is, the operating temperature and current density are 1273 K and 2500 A m^{-2}, respectively, and steam at a concentration of 90% and oxygen (as the sweep gas) are applied. For the POX operation, because the SOEC cannot be operated at a high pressure, the POX reactor is operated at a pressure of 5 bar, with an operating temperature of 1373 K and an O/C ratio of 0.645. These operating parameters can enhance the SOEC performance, which results in a low electri-

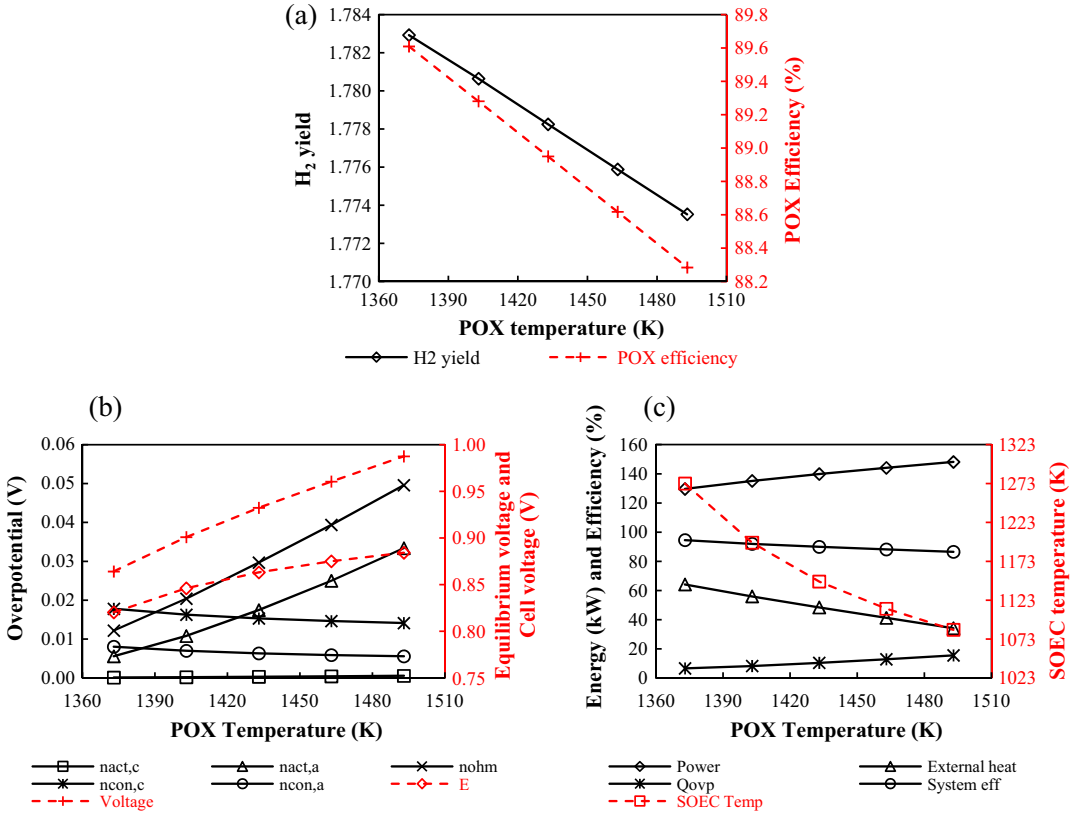

Fig. 5. Effect of operating temperature of POX reaction on: (a) H_2 yield and POX efficiency; (b) equilibrium voltage, overpotential and cell voltage; and (c) power, external heat, and heat of overpotential, SOEC efficiency and SOEC temperature.

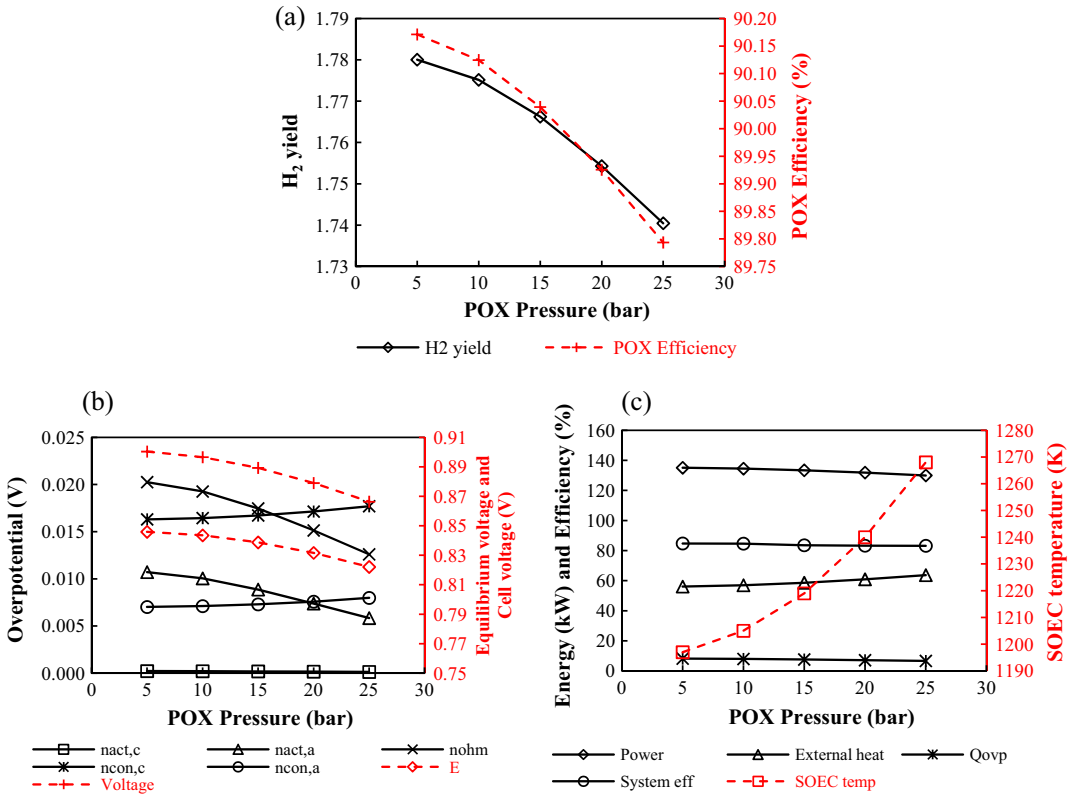

Fig. 6. Effect of operating pressure of the POX reaction on: (a) H_2 yield and POX efficiency; (b) equilibrium voltage, overpotential and cell voltage; and (c) power, external heat, and heat of overpotential, SOEC efficiency and SOEC temperature.

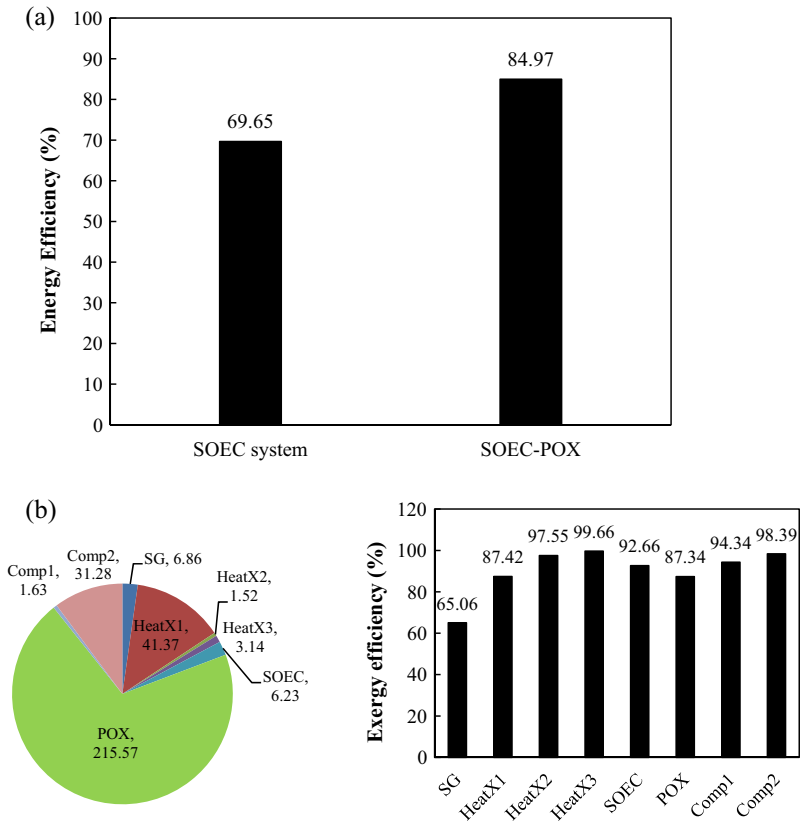

Fig. 7. (a) Comparison of efficiencies in the SOEC system, POX reactor and SOEC-POX and (b) exergy analysis of each unit in the process: Exergy destruction (left) and exergy efficiency (right).

cal energy requirement. From Fig. 7(a), the simulation results show that the SOEC system has lower energy efficiency than a SOEC integrated with a POX reactor system because the required energy for the SOEC is supplied by the thermal energy from the exothermic POX reaction.

7.3. Exergy analysis of each unit in the system

The exergy of the process, as shown in Fig. 7(b), is analyzed to examine the potentiality of energy consumption in each unit. The exergy destruction, which is the exergy loss from the change of entropy in each unit, is considered. The considered units for exergy analysis are the steam generator (SG), the first heat exchanger (*HEATX1*), the second heat exchanger (*HEATX2*), the third heat exchanger (*HEATX3*), the solid oxide electrolysis cell (SOEC), the POX reactor (POX), the first compressor (*COMP1*) and the second compressor (*COMP2*). Electrical and thermal energies are not used in the mixing unit and splitting units; thus, these units are not considered for the exergy analysis.

An evaluation of the exergy destruction of each unit operation is shown in Fig. 7(b). From the simulation results, it is found that the POX reactor has the highest exergy destruction compared to the other units because of the high chemical exergy of methane and low chemical exergy of the product gases. This results in a large difference in the chemical exergy between the inlet and the outlet streams. The lowest exergy destruction is obtained from *HEATX2*. *HEATX1* has higher exergy destruction compared with *HEATX2* and *HEATX3* because of the large difference in temperature exchange, which affects the physical exergy.

Although SOECs use both electrical and thermal energies for the electrochemical reaction, this unit has low exergy destruction as shown in Fig. 7(b). This is because the reduction reaction takes place in the SOEC, and hydrogen, which has a high standard chemical exergy value, is produced in this unit. Therefore, high exergy at the outlet of the SOEC is observed and the exergy destruction of this unit is quite small.

The third exergy destruction is *COMP2* because this unit is fed by three streams, which are the methane, oxygen and some steam streams, but the outlet is released in one stream. This leads to a compositional variation between the inlet and the outlet of this unit, which results in the chemical exergy of the outlet being lower than the inlet. In terms of the physical exergy, when gas is compressed, its volume will be small and its temperature will increase. Moreover, gas will always experience friction, resulting in some of the work that is supplied to the compressor being converted into heat. This results in energy loss from compression. For these reasons, *COMP2* has high exergy destruction. In *COMP1*, the pressure of the pure component, i.e., oxygen, is increased, and the quantity of this component in *COMP1* is lower than that in *COMP2*. This affects only the physical exergy, resulting in *COMP1* having lower exergy destruction than *COMP2*.

The exergy destruction of the steam generator results from the change in the substance phase from the liquid into the gas phase, as well as an increase in pressure. In addition, the thermal energy that is used for the phase change from water to steam is always lost. In terms of the chemical exergy, when water is converted into steam, the chemical exergy will always change due to compositional variations. In addition, a simple simulation of the steam generator may be another reason.

In addition, the exergy efficiency of each unit operation is shown in Fig. 7(b). Due to the high exergy destruction of the POX reactor, a low exergy efficiency (83.4%) is obtained. In addition, a high exergy efficiency (>90%) is obtained from *HEATX3*, *COMP2*, *HEATX2*, *COMP1* and the SOEC. *HEATX3* has the highest exergy efficiency because it has the lowest temperature exchange. Although *COMP2* has high exergy destruction, it also exhibits high exergy efficiency. This is because the exergy efficiency is dependent on the inlet exergy following Eq. (32), and *COMP2* also has three inlet streams resulting in high inlet exergy. For this reason, *COMP2* has high exergy destruction and efficiency.

8. Conclusions

SOEC integrated with a non-catalytic partial oxidation reactor can reduce the electrical energy requirement for SOEC operation, as well as increasing the hydrogen production rate. From the exergy analysis, the partial oxidation reactor is the highest exergy destruction unit, resulting in the lowest exergy efficiency, whereas the SOEC has low exergy destruction. For this reason, the partial oxidation reactor should be utilized. The results obtained can be helpful to further understand the optimal design and performance improvement of the SOEC integrated with the POX for hydrogen production.

Acknowledgments

Support from the 90th Anniversary of Chulalongkorn University Fund (the Ratchadaphiseksomphot Endowment Fund), the Thailand Research Fund (DPG5880003), The Institutional Research Grant (The Thailand Research Fund) (IRG 5780014) and Chulalongkorn University (RES_57_411_21_076) is gratefully acknowledged.

References

[1] Dincer I, Acar C. Review and evaluation of hydrogen production methods for better sustainability. Int J Hydrogen Energy 2015;40(34):11094–111.
[2] Yao J, Liu J, Hofbauer H, Chen G, Yan B, Shan R, Li W. Biomass to hydrogen-rich syngas via steam gasification of bio-oil/biochar slurry over $LaCo_{1-x}Cu_xO_3$ perovskite-type catalysts. Energy Convers Manage 2016;117:343–50.
[3] Millet P, Grigoriev S. Chapter 2 – water electrolysis technologies. In: Diéguez LMGAM, editor. Renewable hydrogen technologies. Amsterdam: Elsevier; 2013.
[4] Ni M, Leung MKH, Leung DYC. Parametric study of solid oxide steam electrolyzer for hydrogen production. Int J Hydrogen Energy 2007;32(13):2305–13.
[5] Udagawa J, Aguiar P, Brandon NP. Hydrogen production through steam electrolysis: model-based steady state performance of a cathode-supported intermediate temperature solid oxide electrolysis cell. J Power Sources 2007;166(1):127–36.
[6] Rivera-Tinoco R, Mansilla C, Bouallou C. Competitiveness of hydrogen production by high temperature electrolysis: impact of the heat source and identification of key parameters to achieve low production costs. Energy Convers Manage 2010;51:2623–34.
[7] Kato T, Kubota M, Kobayashi N, Suzuoki Y. Effective utilization of by-product oxygen from electrolysis hydrogen production. Energy 2005;30(14):2580–95.
[8] Patcharavorachot Y, Thongdee S, Saebea D, Authayanun S, Arpornwichanop A. Performance comparison of solid oxide steam electrolysis cells with/without the addition of methane. Energy Convers Manage 2016;120:274–86.
[9] Xu Y, Dai Z, Li C, Li X, Zhou Z, Yu G, Wang F. Numerical simulation of natural gas non-catalytic partial oxidation reformer. Int J Hydrogen Energy 2014;39(17):9149–57.
[10] Dincer I, Rosen MA. Exergy: energy, environment and sustainable development. 2nd ed. Elsevier Science; 2012.
[11] Ni M, Leung MK, Leung DY. Energy and exergy analysis of hydrogen production by a proton exchange membrane (PEM) electrolyzer plant. Energy Convers Manage 2008;49(10):2748–56;
Pavelka M, Klika V, Vágner P, Maršík F. Generalization of exergy analysis. Appl Energy 2015;137:158–72.
[12] Albrecht BA, Kok JBW, Veringa HJ. Generation of synthesis gas and power by partial oxidation of natural gas in a gas turbine. J Exergy 2002;4(4):357–70.
[13] Ni M, Leung MKH, Leung DYC. A modeling study on concentration overpotentials of a reversible solid oxide fuel cell. J Power Sources 2006;163(1):460–6.
[14] Chen W-H, Lin S-C. Characterization of catalytic partial oxidation of methane with carbon dioxide utilization and excess enthalpy recovery. Appl Energy 2016;162:1141–52.
[15] Wang R, Rohr D. Natural gas processing technologies for large scale solid oxide fuel cells. Fuel Chem Division Preprints 2002;47(2):507.

[16] Guo W, Wu Y, Dong L, Chen C, Wang F. Simulation of non-catalytic partial oxidation and scale-up of natural gas reformer. Fuel Process Technol 2012;98:45–50.
[17] Reid RC, Prausnitz JM, Poling BE. The properties of gases and liquids. New York: McGraw-Hill; 1987.
[18] Todd B, Young J. Thermodynamic and transport properties of gases for use in solid oxide fuel cell modelling. J Power Sources 2002;110(1):186–200.
[19] Zhang H, Lin G, Chen J. Evaluation and calculation on the efficiency of a water electrolysis system for hydrogen production. Int J Hydrogen Energy 2010;35 (20):10851–8.
[20] Tsatsaronis G. Definitions and nomenclature in exergy analysis and exergoeconomics. Energy 2007;32(4):249–53.
[21] Gundersen T. An introduction to the concept of exergy and energy quality. Trondheim, Norway: Department of Energy and Process Engineering, Norwegian University of Science and Technology; 2009. Version 3.
[22] Ghannadzadeh A, Thery-Hetreux R, Baudouin O, Baudet P, Floquet P, Joulia X. General methodology for exergy balance in ProSimPlus® process simulator. Energy 2012;44(1):38–59.
[23] Reynolds B, Conn R. Synthesis gas process. United States Patent Office Office; 1973.
[24] Momma A, Kato T, Kaga Y, Nagata S. Polarization behavior of high temperature solid oxide electrolysis cells (SOEC). J Ceram Soc Jpn 1997;105(5):369–73.

Journal of Industrial and Engineering Chemistry 43 (2016) 93–105

Contents lists available at ScienceDirect

Journal of Industrial and Engineering Chemistry

journal homepage: www.elsevier.com/locate/jiec

Optimal design and performance analyses of the glycerol ether production process using a reactive distillation column

Lida Simasatitkul[a], Punjawat Kaewwisetkul[b], Wisitsree Wiyaratn[c], Suttichai Assabumrungrat[d], Amornchai Arpornwichanop[b,*]

[a] Department of Industrial Chemistry, Faculty of Applied Science, King Mongkut's University of Technology North Bangkok, Bangkok 10800, Thailand
[b] Computational Process Engineering Research Unit, Department of Chemical Engineering, Faculty of Engineering, Chulalongkorn University, Bangkok 10330, Thailand
[c] Faculty of Industrial Education and Technology, King Mongkut's University of Technology Thonburi, Bangkok 10140, Thailand
[d] Center of Excellence in Catalysis and Catalytic Reaction Engineering, Department of Chemical Engineering, Faculty of Engineering, Chulalongkorn University, Bangkok 10330, Thailand

ARTICLE INFO

Article history:
Received 17 April 2016
Received in revised form 8 July 2016
Accepted 30 July 2016
Available online 9 August 2016

Keywords:
Reactive distillation
Glycerol ether
Design
Parametric analysis
Total annual cost

ABSTRACT

The use of glycerol from biodiesel industries to produce high value-added products would increase the competitive potential of biodiesel producers. The present work investigates the production of glycerol ethers, a diesel and biodiesel additive. A single reactive distillation is proposed to overcome the low glycerol conversion and product yield that limit a conventional process. The theoretical performance of the reactive distillation is analyzed taking glycerol conversion and the glycerol ether yield into consideration. The simulation results show that the glycerol and mono-*tert*-butyl ether of glycerol are completely used in the reactive stages and thus, the recycle section by which glycerol and the mono-*tert*-butyl ether of glycerol are recovered is unessential. The parametric analysis for the reactive distillation is reported. Based on the process economic analysis from a total annual cost, the optimal reactive distillation configuration for glycerol ether production consists of two rectifying stages, eight reactive stages and one stripping stage.
© 2016 The Korean Society of Industrial and Engineering Chemistry. Published by Elsevier B.V. All rights reserved.

Introduction

Using biomass to produce biodiesel provides a possible alternative to fossil fuels, particularly given that diesel and biodiesel are important fuels for both industrial and agricultural product transportation. Biodiesel can be used instead of diesel fuel without requiring modification to diesel engines because the properties of biodiesel are similar to those of conventional diesel fuel [1,2]. Transesterification is the most common process used to produce biodiesel from methanol and vegetable oil, such as palm oil, soybean oil, rapeseed oil, mustard oil, canola oil, waste cooking oil or animal fat [3]. However, this process converts 10% of the vegetable oil used to crude glycerol. Because of the large amount of biodiesel production in many countries as a result of increasing energy demands and limiting reserves of conventional fossil fuel, a large quantity of crude glycerol is generated world-wide. The current demand for glycerol is substantially less than the excess of glycerol generated via biodiesel production, and the trend toward glycerol production is expected to increased continually in future years [4]. This oversupply of glycerol has already resulted in decreased glycerol prices and rising environmental concerns with regard to contaminated glycerol disposal, prompting the search for new glycerol uses, such as converting glycerol into value-added products.

Some simple value-added products produced using glycerol have been discovered, including acrolein (used in acrylic acid ester and acylic acid synthesis) and 1,3-propanediol (used to produce polymers, cosmetics, foods and lubricants) [5,6]. Moreover, using glycerol to produce high value-added products should reduce biodiesel production costs and increase the competitiveness of biodiesel producers [2,7]. Glycerol is known to be a versatile chemical that can be converted into numerous chemicals or bio-based products, such as drugs, personal products, oral care products, cosmetics, emulsifiers, skin protectants, asphalt, ceramics, adhesives, food and beverages, polyether, alkyd resins, and

Abbreviations: DTBG, Di-*tert*-butyl ether of glycerol; G, Glycerol; MTBG, Mono-*tert*-butyl ether of glycerol; TTBG, Tri-*tert*-butyl ether of glycerol.

* Corresponding author. Fax: +66 2 218 6877.
E-mail address: Amornchai.A@chula.ac.th (A. Arpornwichanop).

http://dx.doi.org/10.1016/j.jiec.2016.07.052
1226-086X/© 2016 The Korean Society of Industrial and Engineering Chemistry. Published by Elsevier B.V. All rights reserved.

Nomenclature

a_i	Activity of species i (−)
k_i	Rate constant of reaction I ($mol\,s^{-1}\,kg^{-1}$)
$K_{eq,i}$	Equilibrium constant of reaction I (−)
r_i	Reaction rate of reaction i ($mol\,s^{-1}\,kg^{-1}$)
T	Temperature (K)
x_D	Purity of product (−)

triacetin [5]. Alternatively, glycerol can be used to produce value-added products like fuel additives, such as the di- and tri-*tert*-butyl ethers of glycerol [8]. Such fuel additives increase the cetane numbers of diesel fuels and decrease pollutants emissions, including smoke, dust, carbon dioxide, hydrocarbon compounds and aldehydes. Moreover, these additives can reduce the cloud points of the fuels to which they are added and increase the performances and volumes of diesel or bio-diesel products [9].

Researchers have previously used isobutylene and glycerol to produce fuel additives; however, isobutylene is costly and requires additional purification procedures, i.e., sulfuric acid extraction or molecular sieves, to separate the fuel additive from the by-product (C_8–C_{16}) produced by an oligomerization reaction between glycerol and isobutylene [10]. A few studies have focused on using butylene instead of isobutylene; however, butylene use is challenging because of the unstable catalyst required by the process. Bio-alcohols, such as ethanol and butanol, are also used to synthesize fuel additives. The main disadvantage to using these two chemicals is the greater production of the mono-*tert*-butyl ether of glycerol (by-product) compared to the di- and tri-*tert*-butyl ethers of glycerol (the desired fuel additives). Presently, *tert*-butyl alcohol and glycerol are preferred for producing fuel additives, particularly given the lower cost of *tert*-butyl alcohol compared to isobutylene. Furthermore, *tert*-butyl alcohol can be produced from biomass, such as starch, lignocellulosic and straw, but isobutylene is produced by catalytic cracking and steam cracking fractions of refining petroleum. In addition, *tert*-butyl alcohol is a by-product of propylene oxide production. Furthermore, the use of *tert*-butyl alcohol can prevent disadvantageous oligomerization reactions (C_8–C_{16} hydrocarbon), and *tert*-butyl alcohol can be dissolved in glycerol, whereas isobutylene requires solvents or must be used at high pressures. However, because the catalyst is deactivated by water as a by-product, the etherification reaction of glycerol with *tert*-butyl and alcohol exhibits lower conversion and selectivity compared to the etherification reaction between glycerol and isobutylene [11].

Many studies have been published regarding the synthesis of fuel additives from glycerol and *tert*-butyl alcohol. Ozbay et al. [12] compared the use of various solid acid catalysts (in the etherification reaction), such as Amberlyst-15, Amberlyst-16, Amberlyst-35, Nafion-SAC-13 and gamma-alumina. The results indicated that Amberlyst-15 had the highest activity at 110 °C, but A-16 showed higher selectivity for the di-*tert*-butyl ether of glycerol. Frusteri et al. [13] found that water, a by-product, can inhibit the etherification reaction; thus, separating water from the reactor can improve the conversion of glycerol.

Vlad et al. [14] developed a fuel-additive production process using a plug flow reactor, and separation and recycling were included in this process. However, a high amount (up to 60% of total product) of the mono-*tert*-butyl ether of glycerol, a by-product of the etherification reaction between *tert*-butyl alcohol and glycerol, was generated. Thus, high energy and a large distillation column were required to redirect/recycle this mono-*tert*-butyl ether to the reactor. Moreover, the process developed in this study generated a substantial amount of water, used a high TBA-to-glycerol ratio and required high energy consumption and many distillation columns to separate water and TBA from the final product. Furthermore, the conversion of glycerol was low so that a process development to to improve the productivity is required.

Due to its advantages over the conventional process, reactive distillation is considered a potential means of enhancing the production of fuel additives [15]. For example, both the reaction and separation tasks can be performed in a single unit, so that capital and operating costs can be reduced. Moreover, reactive distillation provides high conversion, improves product yields, and reduces energy consumption [16,17]. However, optimizing the design for reactive distillation is difficult and involves many design variables, such as the number of rectifying stages, the number of reactive stages, and the number of stripping stages. A reactive distillation for etherification of glycerol with *tert*-butyl alcohol was investigated by Vlad and Bildea [18]. However, in their system design, the reactants were fed into the reactive distillation as the vapor phase below the reactive zone, resulting in low liquid accumulation in the reactive stages. Moreover, there is no detail in the steady-stage design of a reactive distillation for glycerol etherification in term of the economic evaluation.

The present study is to design a reactive distillation for the etherification reaction between glycerol and *tert*-butyl alcohol to produce glycerol ether. The total annual cost is the criterion used to determine a suitable design for the reactive distillation. Simulations of the reactive distillation are performed using an Aspen Plus simulator. The effects of primary design operating parameters, such as the numbers of reactive, rectifying and stripping stages, the molar reflux ratio, the reboiler duty, and the molar ratio of reactant, on fuel additive production are investigated.

Kinetic model of the etherification reaction between *tert*-butyl alcohol and glycerol

This study is focused on the production of glycerol ether (the di- and tri-*tert*-butyl ethers of glycerol). Di- and tri-*tert*-butyl ethers of glycerol are produced via an etherification reaction between *tert*-butyl alcohol and glycerol that consists of the following three steps (Eqs. (1)–(3)):

$$\text{Glycerol} + \text{TBA} \underset{k_{-1}}{\overset{k_1}{\leftrightarrow}} \text{MTBG} + H_2O \quad (1)$$

$$\text{MTBG} + \text{TBA} \underset{k_{-2}}{\overset{k_2}{\leftrightarrow}} \text{DTBG} + H_2O \quad (2)$$

Table 1
Equilibrium constants and rate constants for the etherification reaction between *tert*-butyl alcohol and glycerol [19].

Equilibrium constant	Rate constant ($mol^{-1}\,kg^{-1}$)
$K_{eq1} = \exp(2.534 - 1005.5/T)$	$k_1 = \exp(16.114 - 6641.5/T)$
$K_{eq2} = \exp(2.087 - 1051.1/T)$	$k_2 = \exp(26.511 - 10{,}305/T)$
$K_{eq3} = \exp(0.978 - 2212/T)$	$k_3 = \exp(5.462 - 3715/T)$

Table 2
Standard conditions for reactive distillation.

Condition of feed		Column specification	
Temperature (K)	298	Rectifying stages	5
Feed flow rate (kmol/h)		Reaction stages	5
Glycerol	2	Stripping stages	0
tert-Butyl alcohol	10	Reboiler duty (kW)	80
Feed stage		Reflux ratio	1
Glycerol	7		
tert-Butyl alcohol	11		

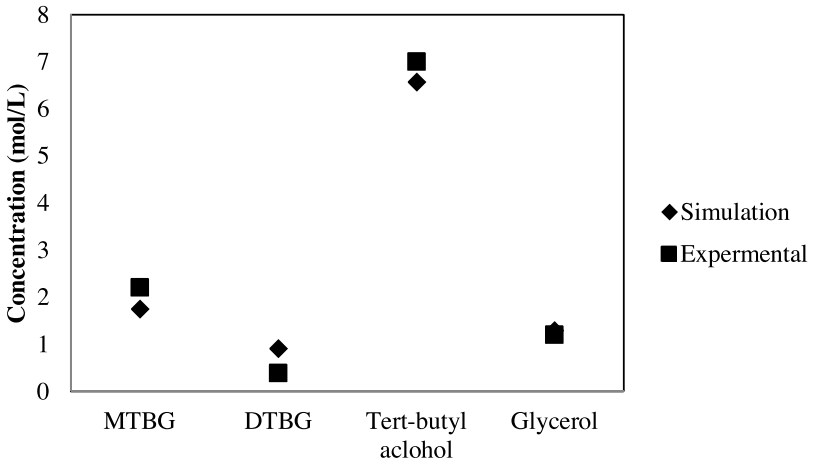

Fig. 1. Comparison of simulated results this work and experimental result from Kiatkittipong et al. [19].

$$DTBG + TBA \underset{k_{-3}}{\overset{k_3}{\leftrightarrow}} TTBG + H_2O \quad (3)$$

In the above reactions, the di-*tert*-butyl ether of glycerol (DTBD) and the tri-*tert*-butyl ether of glycerol (TTBG) are the major products (fuel additives) that can be added to diesel and biodiesel fuels, while the mono-*tert*-butyl ether of glycerol (MTBG) and

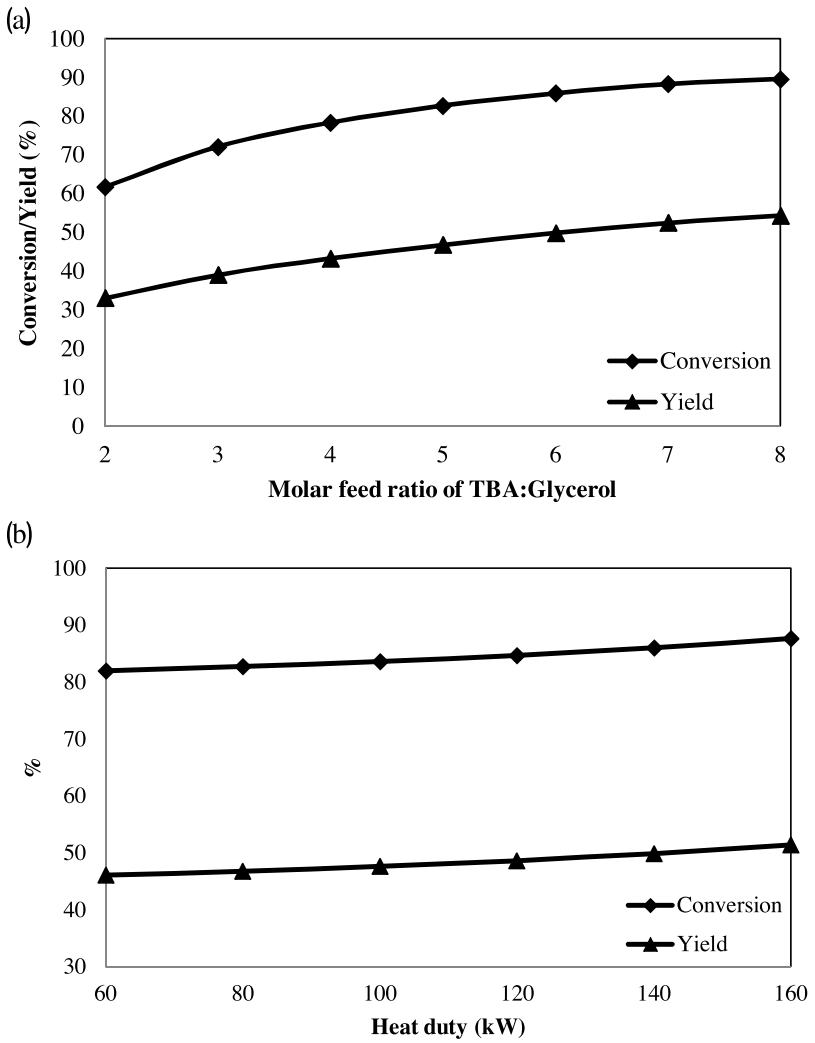

Fig. 2. Effects of (a) molar feed ratios of *tert*-butyl alcohol to glycerol and (b) reboiler duty on the conversion of glycerol and the yields of di- and tri-*tert*-butyl ethers of glycerol.

water are by-products. All of the reactions are reversible and can be catalyzed by amberlyst 15 (acidic cation-exchange resin), and the three reversible reactions are exothermic. The kinetic models of each reaction provide important information for process simulation and have been studied by Kiatkittipong et al. [19]. The rate constants and equilibrium constants for etherification reactions of glycerol with *tert*-butyl alcohol are given in Table 1. The rate expressions for each reaction step are as follows (Eqs. (4)–(6)):

$$r_1 = k_1\left(a_G a_{TBA} - \frac{1}{K_{eq1}} a_{MTBG} a_{H_2O}\right) \quad (4)$$

$$r_2 = k_2\left(a_{MTBG} a_{TBA} - \frac{1}{K_{eq2}} a_{DTBG} a_{H_2O}\right) \quad (5)$$

$$r_3 = k_3\left(a_{DTBG} a_{TBA} - \frac{1}{K_{eq3}} a_{TTBG} a_{H_2O}\right) \quad (6)$$

The NRTL-Redich Kwong model is used to predict the thermodynamic properties of substances in the system. The interaction parameters are taken from the Aspen Plus database or estimated using the UNIFAC method.

Reactive distillation for glycerol ether production

The reactive distillation column is utilized under standard conditions, and it consists of 12 stages, which include a partial reboiler and a total condenser, for which the numbering of stages is top downward. The column pressure is 1 bar. The feed conditions under standard conditions are as follows: 2 kmol/h glycerol and 10 kmol/h *tert*-butyl alcohol, a reflux ratio of 1, a reboiler duty at 80 kW and a feed location of glycerol and *tert*-butyl alcohol at stage 1 and at the bottom of the reactive stages, respectively. Stages 7–11 constitute the reactive stages. The standard conditions for reactive distillation are given in Table 2.

Simulation of the production of glycerol ether in the reactive distillation is carried out by using the RADFRAC model in Aspen

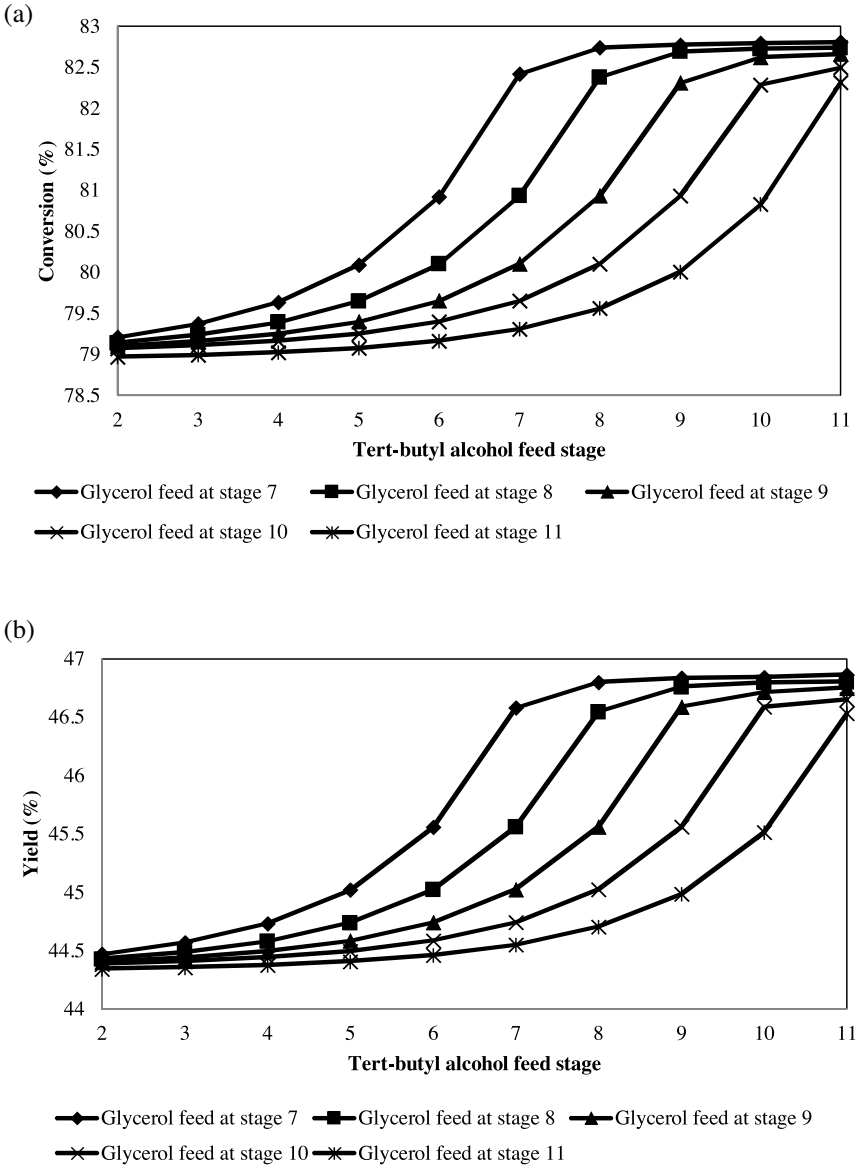

Fig. 3. Effects of *tert*-butyl alcohol feed stages locations on (a) the conversion of glycerol and (b) the yields of di- and tri-*tert*-butyl ethers of glycerol at various glycerol feed stage locations.

Plus simulation package. All system performances pertaining to reactive distillation for glycerol ether production are considered in terms of the resulting conversion of glycerol and yields of di- and tri-*tert*-butyl ethers of glycerol. The conversion of glycerol and yields of di and tri-*tert*-butyl ethers of glycerol are defined according to the equations below (Eqs. (7) and (8)).

$$\%\,\text{Conversion} = \frac{\text{Difference of glycerol in molar flow rate of inlet and outlet}}{\text{Molar feed flow rate of glycerol to reactive distillation}} \times 100\% \quad (7)$$

$$\%\text{Yield} = \frac{\text{Molar flow rate of outlet of di} - \text{ and tri}-\textit{tert}-\text{butyl ethers of glycerol}}{\text{Difference in molar flow rate of inlet and outlet of glycerol}} \times 100\% \quad (8)$$

Model validation

In order to validate the simulation model of the reactive distillation for glycerol ether production, the reliability of the reactive distillation model coupled with the kinetic model as mentioned in the previous section is tested by comparing the simulated results obtained from Aspen Plus with the experimental data from Kiatkittipong et al. [19]. For comparison, the reactive distillation column consisting of six rectifying stages and six reactive stages is operated at the pressure of 1 bar with reflux ratio at 2. Feed streams of *tert*-butyl alcohol and glycerol at temperature 298 °C and feed ratio of four by volume are fed to the bottom and first stage of reactive stages in reactive distillation. The bottom products of the reactive distillation obtained from the model prediction and experiment are compared as shown in Fig. 1 and the simulated results are in good agreement with the experimental data.

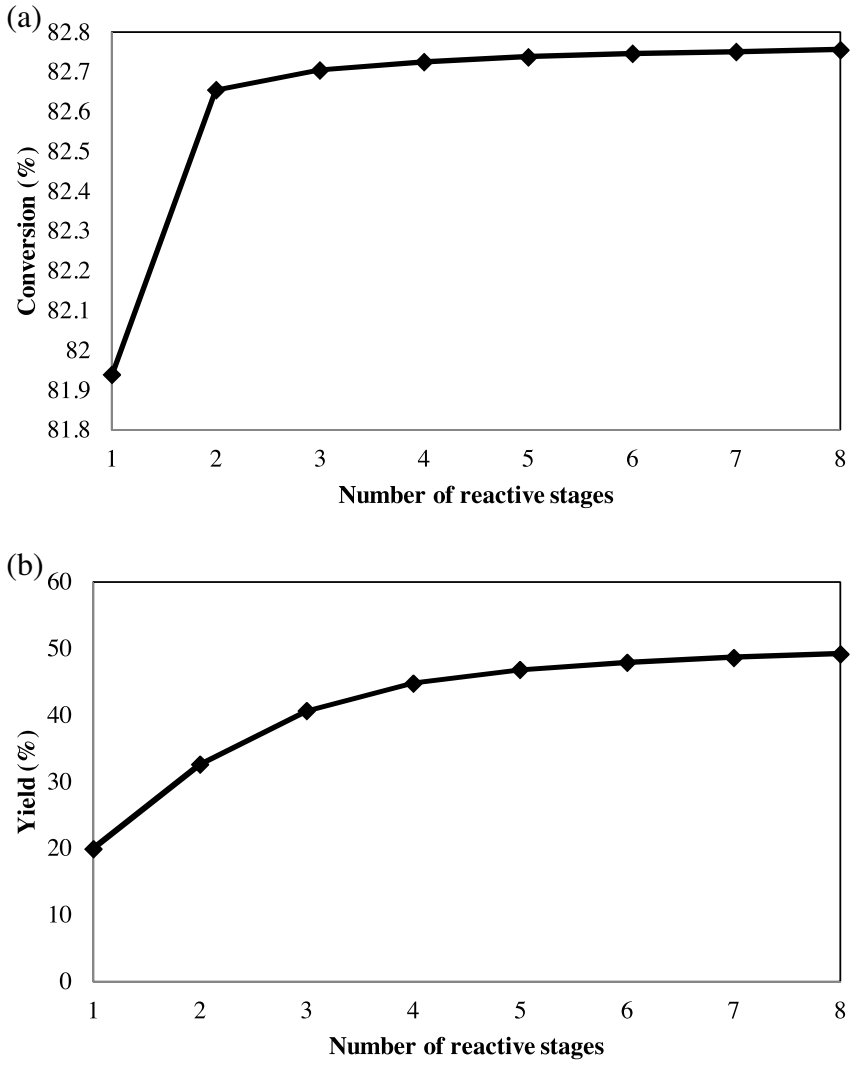

Fig. 4. Effects of reactive stages on (a) the conversion of glycerol and (b) the yields of di- and tri-*tert*-butyl ethers of glycerol.

Results and discussion

Effects of feed ratio of tert*-butyl alcohol to glycerol*

The molar feed ratio of *tert*-butyl alcohol to glycerol is an important parameter related to reactive distillation performance. The molar ratios of *tert*-butyl alcohol to glycerol studied herein are 2:1 to 8:1. Fig. 2(a) shows the effects of the feed molar ratio of *tert*-butyl alcohol to glycerol on the conversion of glycerol and yields of di- and tri-*tert*-butyl ethers of glycerol. The simulation results show that the conversion of glycerol and yields of di- and tri-*tert*-butyl ethers of glycerol increase as the molar feed ratio of *tert*-butyl alcohol to glycerol increases. This is because *tert*-butyl alcohol is the reactant of three etherification reactions of glycerol and *tert*-butyl alcohol, such that *tert*-butyl alcohol forces etherification forward.

Effects of reboiler heat duty

Fig. 2(b) shows the effects of reboiler duty on the conversion of glycerol and yields of di- and tri-*tert*-butyl ethers of glycerol within a range of 60–160 kW. As the heat duty increases, more unreacted reactants, such as glycerol and the mono-*tert*-butyl ether of glycerol, react in the reactive stages. For this reason, increasing the reboiler duty increases both the conversion of glycerol and the yields of di- and tri-*tert*-butyl ethers of glycerol.

Effects of feed stage location

The two feed locations also constitute an important design variable. The feed stage locations are adjusted to optimize the performance of the reactive distillation in terms of the conversion of glycerol and the yields of di- and tri-*tert*-butyl ethers of glycerol. Feeding *tert*-butyl alcohol (lighter reactant) at the bottom of the reactive stages and feeding glycerol (heavier reactant) at the top of the reactive stages results in the greatest reactive reaction performance. The amount of glycerol in the reactive stages decreases as the feed location of glycerol is changed from the top to the bottom of the reactive stages. On the other hand, the amount of *tert*-butyl alcohol decreases when the feed location of methanol is changed from the bottom to the top of the reactive stages. For this reason, *tert*-butyl alcohol (lighter reactant) and glycerol (heavier reactant) must be fed at the bottom and the top of the reaction stages, respectively. The effects of the feed stage locations of glycerol and *tert*-butyl alcohol on the conversion of glycerol and the yields of di- and tri-*tert*-butyl ethers of glycerol resulting from the reactive distillation are shown in Fig. 3.

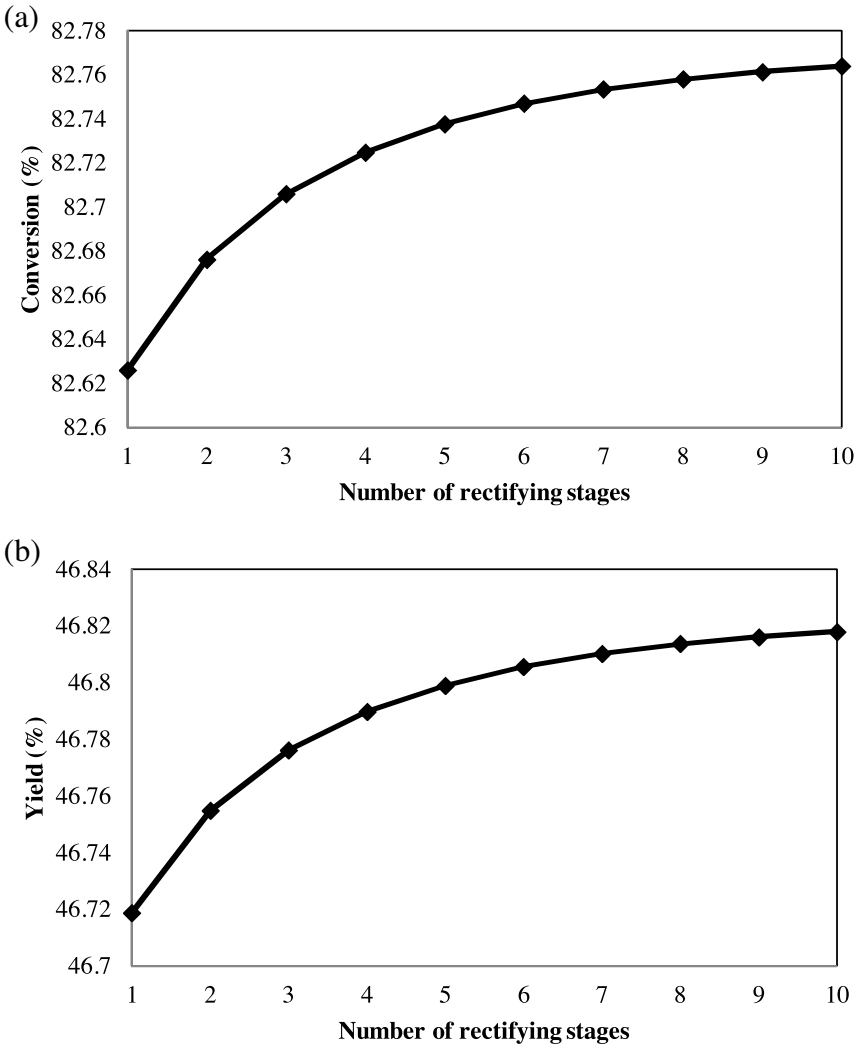

Fig. 5. Effects of rectifying stages on (a) the conversion of glycerol and (b) the yields of di- and tri-*tert*-butyl ethers of glycerol.

Effects of the number of reactive stages

Fig. 4 demonstrates the effects of changing the number of reactive stages in terms of the resulting conversion of glycerol and yields of di- and tri-*tert*-butyl ethers of glycerol under standard conditions. The number of reactive stages is varied from 1 to 8. The conversion of glycerol and the yields of di- and tri-*tert*-butyl ethers of glycerol increase as the number of reactive stages increases from 1 to 8. This is because increasing the number of reactive stages can improve the space time of the reactant during the reactive stages. Fig. 4 shows that both the conversion of glycerol and the yields of di- and tri-*tert*-butyl ethers of glycerol increase as the number of reactive stages increases. This is because increasing the number of reactive stages can increase the space time of the reactant (i.e., *tert*-butyl alcohol) and the intermediate (i.e., the mono-*tert*-butyl ether of glycerol) during the reactive stages. For this reason, *tert*-butyl alcohol and the mono-*tert*-butyl ether of glycerol are reacted and converted to the di- and tri-*tert*-butyl ethers of glycerol.

Effects of the number of rectifying stages

Fig. 5 demonstrates how the number of rectifying stages affects the performance of the reactive distillation under standard conditions. The number of rectifying stages is varied from 1 to 10. Increasing the number of rectifying stages can help separate water, which inhibits the etherification reaction of *tert*-butyl alcohol and glycerol during the reactive stages, so the conversion of glycerol and the yields of di- and tri-*tert*-butyl ethers of glycerol increase accordingly.

Effects of the number of stripping stages

Fig. 6 shows how the number of stripping stages affects the performance of the reactive distillation. The number of stripping stages is varied from 0 to 8. As the number of stages in the stripping section increases, more unreacted glycerol and mono-*tert*-butyl ether of glycerol cannot separate from the bottom of the reactive distillation and, therefore, cannot return to the reactive stages. For this reason, the conversion of glycerol and the yields of di- and tri-*tert*-butyl ethers of glycerol decrease.

Effects of reflux ratio

Fig. 7 shows how the reflux ratio affects the reactive distillation in terms of the conversion of glycerol and the yields of di- and tri-*tert*-butyl ethers of glycerol. The results demonstrate that the conversion of glycerol and the yields of di- and tri-*tert*-butyl ethers

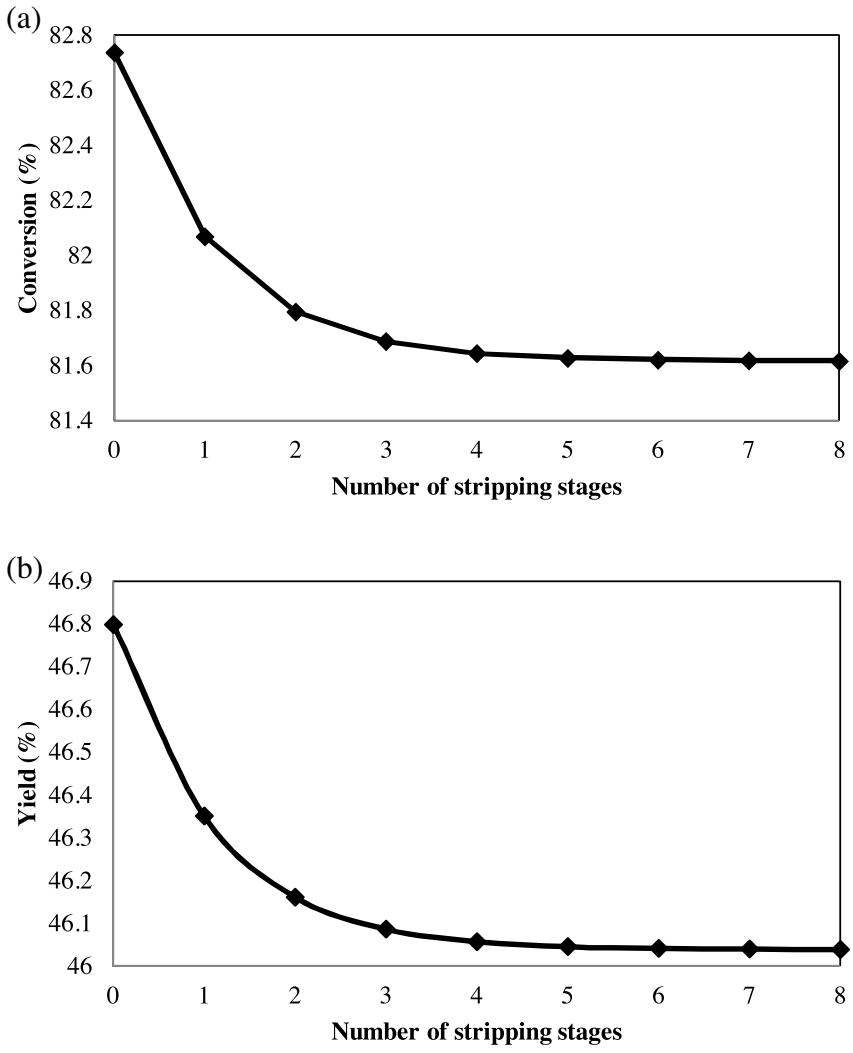

Fig. 6. Effects of stripping stages on (a) the conversion of glycerol and (b) the yields of di- and tri-*tert*-butyl ethers of glycerol.

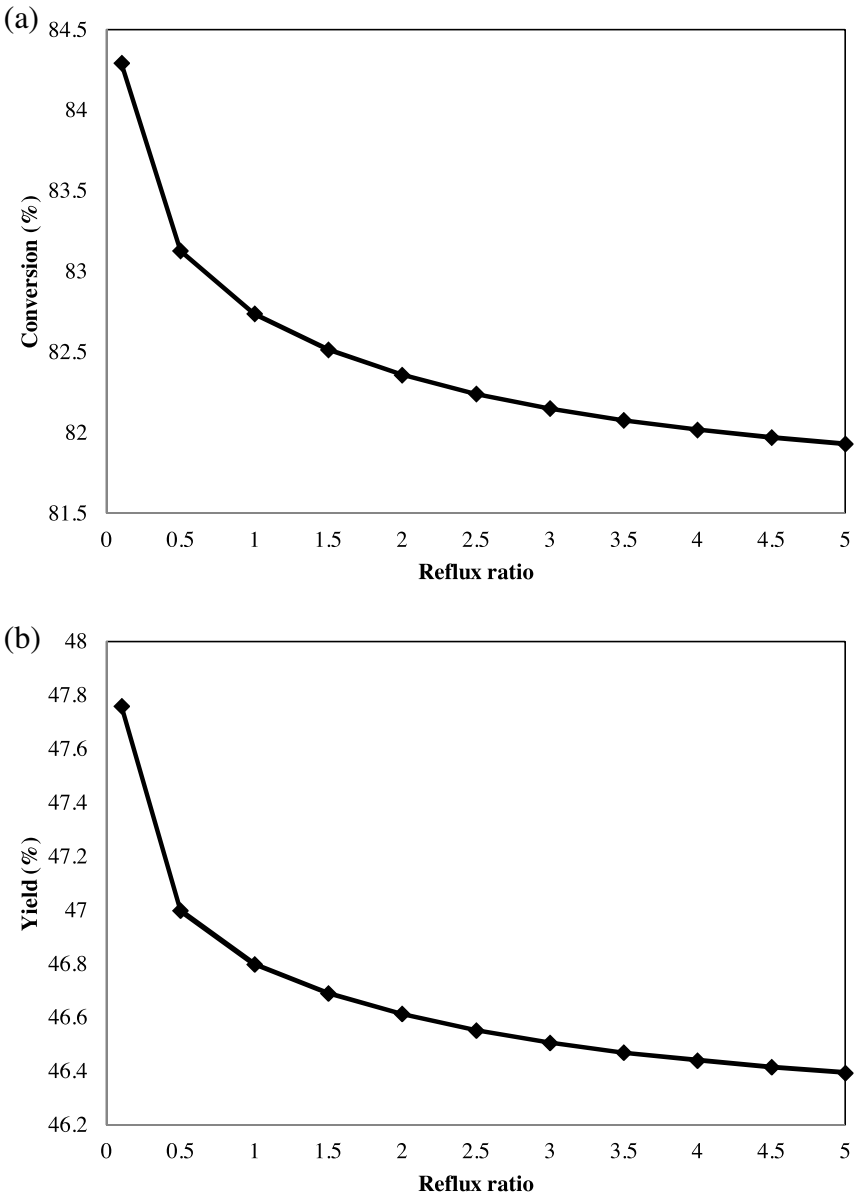

Fig. 7. Effects of reflux ratio on (a) the conversion of glycerol and (b) the yields of di- and tri-*tert*-butyl ethers of glycerol.

of glycerol decrease as the reflux ratio increases. This is because increasing the reflux ratio increases the amount of water in the reactive stages. Because water can inhibit the etherification reaction of *tert*-butyl alcohol and glycerol, the reflux ratio should be minimized as much as possible.

Economic assessment of reactive distillation for glycerol ether production

This section investigates the steady-state economics of reactive distillation for glycerol ether (di- and tri-*tert*-butyl ethers of glycerol) production and optimizes the single reactive distillation requirements for glycerol ether production based on total annual costs, including operating cost and annualized capital cost. The tray sizing function in the Aspen Plus simulation is used to estimate the diameter of the reactive distillation. The distance between trays is maintained at 2 ft. The annualized capital cost is calculated using a payback period of 3 years and the cost data from Appendix B of Douglas's book [20]. The total annual cost (TAC) is defined as shown in Eq. (9) below.

$$\mathrm{TAC} = \mathrm{TAC_{ope}} + \frac{\mathrm{TAC_{cap}}}{\text{Payback Period}} \tag{9}$$

The optimal design configuration of a reactive distillation is determined by minimizing the total annual cost (Eq. (10)).

$$\begin{aligned} &\underset{x}{\text{Minimize}} \quad \mathrm{TAC} \\ &\text{Subject to :} \quad \text{Conversion} = 99\% \\ &\qquad\qquad\quad \text{Yield} = 99\% \\ &\qquad\qquad\quad \text{Production rate} = 2.12\ \text{kmol/h} \\ &\qquad\qquad\quad x_D = 98\% \end{aligned} \tag{10}$$

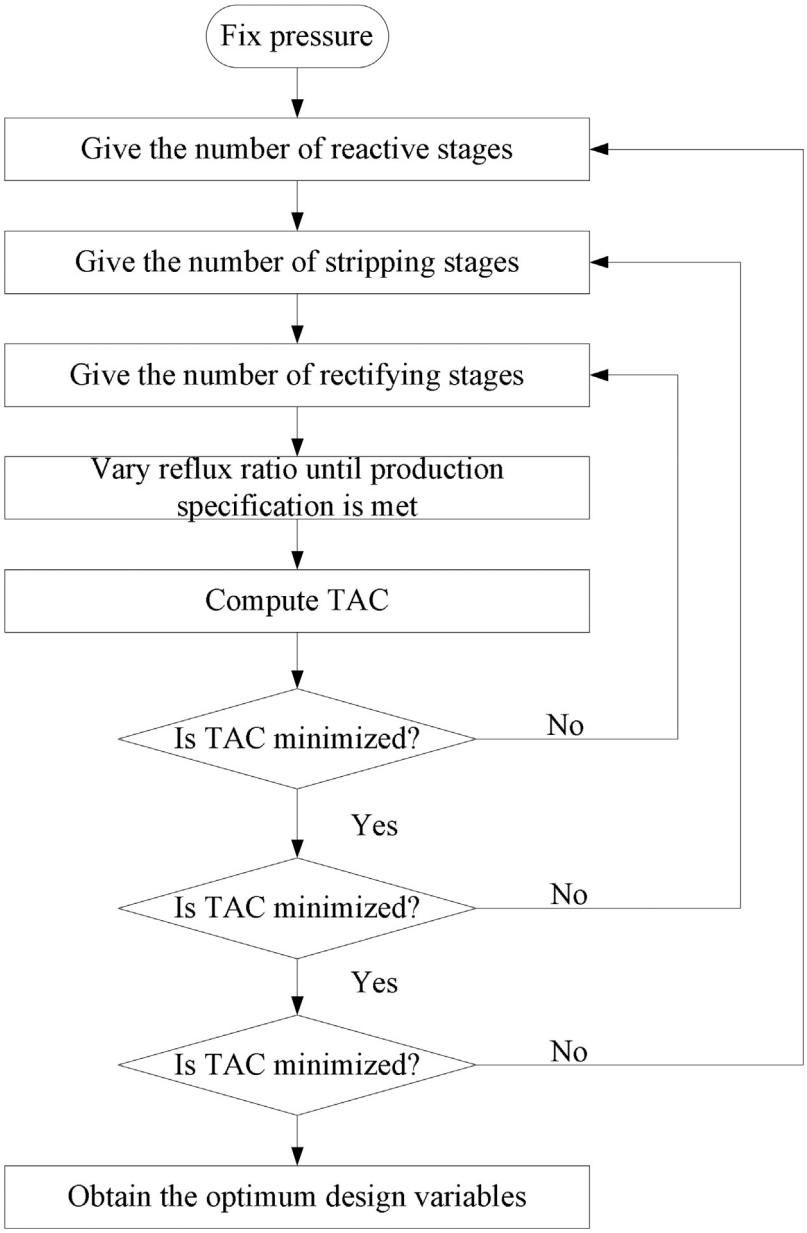

Fig. 8. Design procedure for reactive distillation for glycerol ether production.

where x is the vector of design variables (i.e., the number of reactive stages, the number of rectifying stages and the number of stripping stages).

The capital cost calculation includes the cost of reactive distillation column, trays, reboiler and condenser. The operating cost calculation includes costs associated with water cooling for condenser and steam for reboiler. In all cases in the present study, the molar ratio of *tert*-butyl alcohol to glycerol is 6:1.

Assumptions and specifications for the glycerol ether stream and the reactive distillation design

The annualized capital cost is calculated with a payback period of 3 years and using the cost data from Appendix B of Douglas's book [20]. The assumptions and specifications of the reactive distillation design and glycerol ether stream are as follows:

1. The design objective is to obtain a 99 mol% conversion of glycerol.
2. The design objective is to obtain a 99 mol% yield of fuel additive (di- and tri-*tert*-butyl ethers of glycerol).
3. The design specification is to obtain 2.124 kmol/h of fuel additive (di- and tri-*tert*-butyl ethers of glycerol) at the glycerol ether stream.
4. The purity of the product stream is 98 mol%.
5. The feed stages locations of glycerol and *tert*-butyl alcohol are fixed at the top and bottom of the reactive stages, respectively.
6. The molar ratio of *tert*-butyl alcohol to glycerol is fixed at 6:1.
7. There is no pressure drop and the pressure column is fixed at 9 bar.
8. A plant availability of 8150 h/year is assumed.

Based on these assumptions and specifications, the following three variables require optimization: (1) number of rectifying

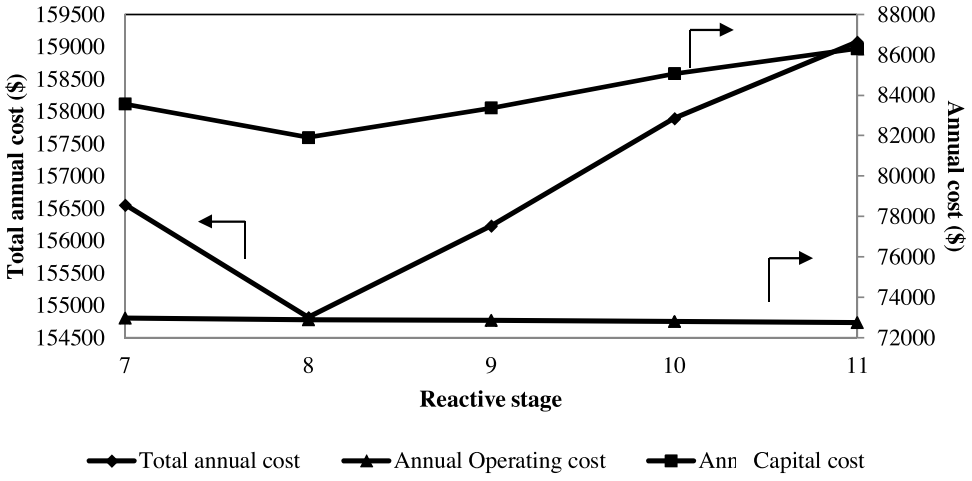

Fig. 9. Effects of reactive stages on total annual costs.

stages, (2) number of stripping stages, and (3) number of reactive stages. The reactive distillation design procedure is shown in Fig. 8. The range of design variables is chosen depending the assumptions and product specifications.

Fig. 9 demonstrates the importance of the number of reactive stages as a parameter. Increasing the number of reactive stages provides many benefits. First, increasing the number of reactive stages correspondingly increases the space time of the reactant during the reactive stages, thereby increasing conversion of glycerol and fuel additive yields. Furthermore, the liquid holdup is increased with an increase in the number of reactive stages and thus, the reaction rates are increased. Second, increasing the number of reactive stages results in better separation performance, such as the separation of a heavy product from a light unreacted reactant and by-product. Thus, the operating and capital costs associated with the reboiler can be reduced by increasing the number of reactive stages. However, increasing the number of reactive stages to more than eight stages results in higher capital costs and it is insignificant in the production yield, leading us to conclude that 8 is the optimum number of reactive stages for the conditions utilized in the present study.

The effects of reactive stages, the rectifying stage and the stripping stage on the total annual cost of reactive distillation are demonstrated in Fig. 10. Because glycerol and the mono-*tert*-butyl ether of glycerol are used completely during the reactive stages, all of the components remaining during the rectifying and stripping stages are fuel additives (di- and tri-*tert*-butyl ethers of glycerol), *tert*-butyl alcohol and water. The boiling point of glycerol ether is higher than those of *tert*-butyl alcohol and water, so separating fuel additives from *tert*-butyl alcohol and water requires a few rectifying and stripping stages to achieve purity specifications.

Increasing the number of rectifying stage provides many benefits. First, increasing the number of rectifying stages can help to separate water from the reactive stages, such that the reboiler duty is reduced. Secondly, increasing the number of rectifying stages increases both the conversion of glycerol and the yields of di- and tri-*tert*-butyl ethers of glycerol. However, increasing the number of rectifying stages increases capital costs.

Increasing the number of stripping stages can help to separate *tert*-butyl alcohol from glycerol ether to meet the purity specifications of the product. Fig. 10 shows that the number of stripping stages is more sensitive than the number of rectifying stages. However, increasing the number of stripping stages enhances already high capital costs due to increased trays and heat exchanger area. Furthermore, both the conversion of glycerol and the yields of di- and tri-*tert*-butyl ethers of glycerol are reduced, leading to a high accumulation of *tert*- butyl alcohol in the stripping stages.

However, product purity cannot increase to 99% without stripping stages. For this reason, stripping stages are among the most essential considerations regarding reactive distillation (due to specifications related to product contamination). Fig. 10 shows that the optimum number of rectifying stages is 2 and the optimum number of stripping stages is 1. Regarding the boiling point ranking of the components in this system, *tert*-butyl alcohol is the lightest component and thus, a few number rectifying stages and stripping stages are required.

With regard to the reboiler duty, increasing the reboiler duty can increase conversion and selectivity for di- and tri-*tert*-butyl alcohol. This is because unreacted glycerol is available and reacts during the reactive stages. The reboiler duty must be high enough to separate all of the unreacted glycerol in the bottom of the reactive distillation apparatus, such that this glycerol can be utilized during the reactive stages. In addition, the reboiler duty separates all of the water (as by product) as well as the excess *tert*-butyl alcohol from the product (di- and tri-*tert*-butyl ethers of alcohol). However, a higher reboiler duty means higher operating costs. Thus, the optimal operating reboiler duty determined herein is 260.1 kW.

Increasing the reflux ratio reduces both the conversion of glycerol and the yields of di- and tri-*tert*-butyl ethers of glycerol. This is because increasing the reflux ratio increases the amount of water that can inhibit the etherification reaction of *tert*-butyl alcohol and glycerol during the reactive stages. Furthermore, increasing the reflux ratio results in higher total annual costs. For these reasons, the reflux ratio must be kept as low as possible. Considering the minimization of the total annual cost, the optimal design and operating parameters of reactive distillation are summarized in Table 3. The optimal configuration of reactive distillation is shown in Fig. 11.

Conclusions

The present study investigates using reactive distillation to produce glycerol ether from the etherification reaction of *tert*-butyl alcohol and glycerol. Reactive distillation is used to improve

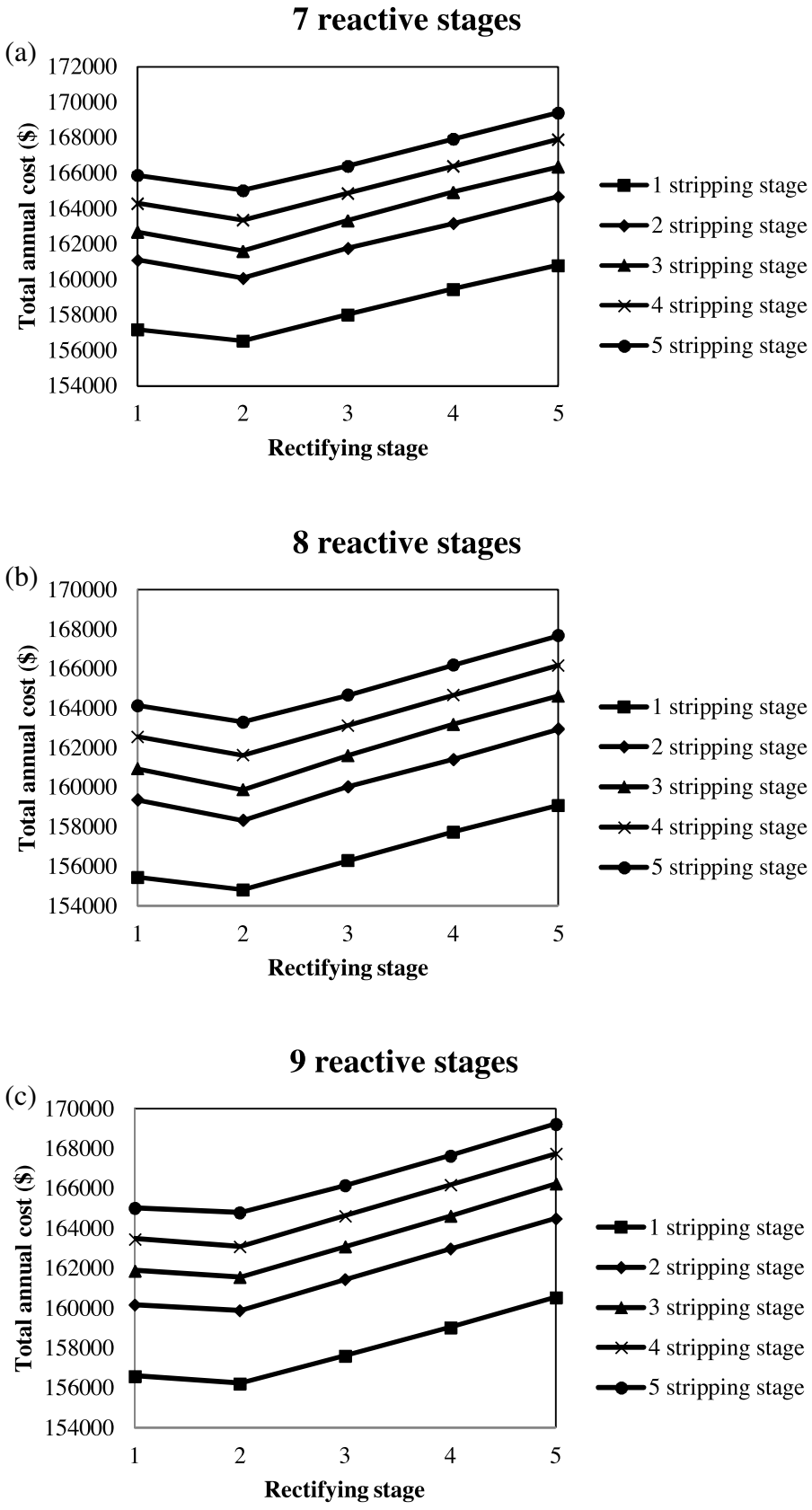

Fig. 10. Effects of rectifying and stripping stages on the total annual cost of reactive distillation, when the number of reactive stages is fixed at (a) 7, (b) 8 and (c) 9.

Table 3
Optimal operating parameters for reactive distillation for glycerol ether production.

Condition of feed		Column specification	
Temperature (K)	298	Rectifying stages	2
Feed flow rate (kmol/h)		Reaction stages	8
Glycerol	2.15	Stripping stages	1
tert-Butyl alcohol	12.9	Reboiler duty (kW)	260.1
Feed stage		Reflux ratio	0.05
Glycerol	4		
tert-Butyl alcohol	11		

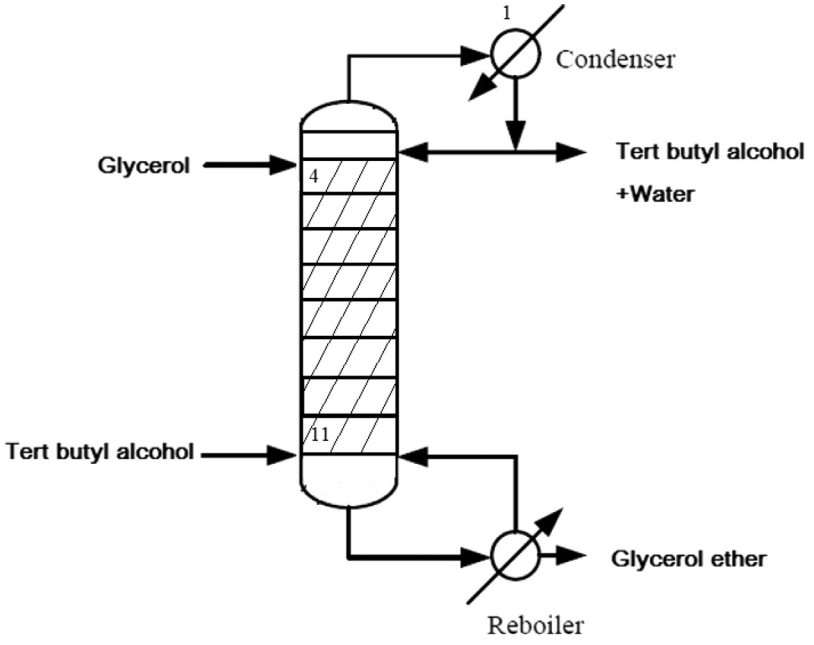

Fig. 11. Optimal configuration of a reactive distillation for glycerol etherification.

the performance of fuel additive production in terms of the resulting conversion of glycerol and the yields of di- and tri-*tert*-butyl ethers of glycerol. RADFRAC module in Aspen Plus is used to study the parameters of reactive distillation, including the reflux ratio, the reboiler duty, the number of stages on performance of reactive distillation in terms of conversion of glycerol and yields of di- and tri-*tert*-butyl ethers of glycerol. The optimal reactive distillation configurations can also be found by optimizing the total annual cost. The glycerol and mono-*tert*-butyl ether of glycerol are completely used in the reactive stages. Therefore, the recycle section by which glycerol and the mono-*tert*-butyl ether of glycerol are recovered is unessential.

In conclusion, reactive distillation can reduce energy requirements. The simulation results herein show that increasing the feed ratio of *tert*-butyl alcohol to glycerol, the number of reactive stages, the number of rectifying stages, and the reboiler duty improves both the conversion of glycerol and the yields of di- and tri-*tert*-butyl ethers of glycerol. However, increasing the number of stripping stages and the reflux ratio causes an opposite trend, although increasing the number of stripping stages benefits separation performance. Suitable feed stage locations of *tert*-butyl alcohol and glycerol are the bottom and the top, respectively, of the reactive stages. The optimal reactive distillation configuration for glycerol ether production consists of two rectifying stages, eight reactive stages and one stripping stage.

Acknowledgments

Support from the Ratchadaphiseksomphot Endowment Fund, Chulalongkorn University, and the Thailand Research Fund (DPG5880003) is gratefully acknowledged.

References

[1] W. Liu, P. Yin, X. Liu, S. Zhang, R. Qu, J. Ind. Eng. Chem. 21 (2015) 893.
[2] A. Singhabhandhu, T. Tezuka, Energy 35 (6) (2010) 2493.
[3] K. Neumann, K. Werth, A. Martín, A. Górak, Chem. Eng. Res. Des. 107 (2016) 52–62.
[4] M. Ayoub, A.Z. Abdullah, Renew. Sustainable Energy Rev. 16 (5) (2012) 2671.
[5] H.W. Tan, A.R. Abdul Aziz, M.K. Aroua, Renew. Sustainable Energy Rev. 27 (2013) 118.
[6] L. Bueno, C. Toro, M. Martín, Chem. Eng. Res. Des. 93 (2015) 432.
[7] H. Rastegari, H.S. Ghaziaskar, J. Ind. Eng. Chem. 21 (2015) 856.
[8] Z. Gholami, A.H. Abdullah, K. Lee, Renew. Sustainable Energy Rev. 39 (2014) 327.
[9] N. Rahmat, A.Z. Abdullah, A.R. Mohamed, Renew. Sustainable Energy Rev. 14 (2010) 987.
[10] O.D. Bozkurt, F.M. Tunc, N. Baglar, S. Celebi, D. Gunbas, A. Uzun, Fuel Process. Technol. 138 (2015) 780.
[11] N. Viswanadham, S.K. Saxena, Fuel 103 (2013) 980.

[12] N. Ozbay, N. Oktar, G. Dogu, T. Dogu, Int. J. Chem. React. Eng. 8 (1) (2010), doi: http://dx.doi.org/10.2202/1542-6580.2149.
[13] F. Frusteri, F. Arena, G. Bonura, C. Cannilla, L. Spadaro, O. Di Blasi, Appl. Catal. A: Gen. 367 (1–2) (2009) 77.
[14] E. Vlad, C.S. Bildea, G. Bozga, Sci. World J. 2012 (2012).
[15] P. Lutze, A. Gorak, Chem. Eng. Res. Des. 91 (2013) 1978.
[16] A. Arpornwichanop, K. Koomsup, S. Assabumrungrat, J. Ind. Eng. Chem. 14 (6) (2008) 796.
[17] L. Zhang, H. Chen, Y. Yuan, J. Yu, S. Wang, K. Huang, Chem. Eng. Res. Des. 100 (2015) 311.
[18] E. Vlad, C.S. Bildea, Chem. Eng. Trans. 29 (2012) 589.
[19] W. Kiatkittipong, P. Intaracharoen, N. Laosiripojana, C. Chaisuk, P. Praserthdam, S. Assabumrungrat, Comput. Chem. Eng. 35 (10) (2011) 2034.
[20] J.M. Douglas, Conceptual Design of Chemical Processes, McGraw-Hill, New York, USA, 1988.

Energy Conversion and Management 124 (2016) 325–332

Contents lists available at ScienceDirect

Energy Conversion and Management

journal homepage: www.elsevier.com/locate/enconman

Using glycerol for hydrogen production via sorption-enhanced chemical looping reforming: Thermodynamic analysis

Phanicha Tippawan [a], Tidtaya Thammasit [a], Suttichai Assabumrungrat [b], Amornchai Arpornwichanop [a,*]

[a] Computational Process Engineering Research Unit, Department of Chemical Engineering, Faculty of Engineering, Chulalongkorn University, Bangkok 10330, Thailand
[b] Center of Excellence in Catalysis and Catalytic Reaction Engineering, Department of Chemical Engineering, Faculty of Engineering, Chulalongkorn University, Bangkok 10330, Thailand

ARTICLE INFO

Article history:
Received 12 April 2016
Received in revised form 5 July 2016
Accepted 6 July 2016
Available online 19 July 2016

Keywords:
Sorption enhanced-chemical looping reforming
Glycerol
Hydrogen production
Thermodynamic analysis
Self-sufficient energy

ABSTRACT

Sorption enhanced-chemical looping reforming (SECLR), which combines a chemical looping reforming method (CLR) and a sorption-enhanced reforming method (SER) in a single-stage process, is proposed for the hydrogen production from glycerol. The model of the SECLR process using a solid oxygen carrier and CO_2 absorbent is developed using a flowsheet simulator. The comparison between chemical looping reforming (CLR) with/without CaO sorbent is investigated. The results show that the addition of CaO sorbent provides an increase in a hydrogen concentration. The SECLR process is then deeply analyzed by considering the effect of the primary parameters on its performance in terms of hydrogen production, carbon formation and net energy requirements. The parametric analysis indicates that operating the SECLR at a steam-to-glycerol molar ratio higher than two and a sufficient calcium oxide-to-glycerol molar ratio of three can inhibit the formation of carbon. The hydrogen yield increases significantly upon increasing the reforming temperature. The required energy of the process varies with the amount of nickel oxide used as a solid oxygen carrier. The exergy analysis is considered to identify the optimal operation for self-sufficient energy and the results show that the operation of the SECLR at the nickel oxide-to-glycerol molar ratio of 1.87 is sufficient to be the most optimal condition with regard to both energy and exergy considerations.

© 2016 Elsevier Ltd. All rights reserved.

1. Introduction

The ever-increasing energy demand and the limited amount of conventional fossil fuels coupled with the growing concerns of global warming have stimulated a number of researchers to search for alternative energy. Among the various alternative energy forms, hydrogen is considered an important energy carrier in the future [1]. It is also an important raw material in the chemical and petrochemical industries and can be used as a fuel in fuel cells to produce electrical energy. For reasons of sustainability, the use of renewable fuel sources for hydrogen production has received considerable attention [2].

Glycerol is an important renewable fuel that can be reformed into hydrogen by different methods, e.g., the steam reforming process [3], partial oxidation process [4], auto-thermal reforming process [5], aqueous-phase reforming process [6] and supercritical water reforming process [7]. Moreover, the use of glycerol as a hydrogen source can reduce a glut of glycerol from biodiesel production and consequently reduce its operating cost [8,9]. Presently, although many studies show that the catalytic steam reforming of glycerol is feasible for hydrogen production [10–13], the demand for high-purity hydrogen production is rapidly growing in the electronic, ceramic, and chemical industries. Hence, an improved process for high-purity hydrogen production is needed in terms of the better energy usage and control CO_2 emissions [14].

To enhance the performance of a hydrogen production process, the use of the concept of a multi-functional unit operation is interesting. Recently, a sorption-enhanced chemical looping reforming (SECLR) that combines a chemical looping reforming method (CLR) and a sorption-enhanced reforming method (SER) in one process stage was proposed by Rydén and Ramos [15]. The chemical looping reforming method is used for the production of hydrogen via the cyclic reduction and oxidation of a solid oxygen carrier [16–18], whereas the sorption-enhanced reforming method with in situ CO_2 removal is employed for the production and enhancement of the hydrogen purity. The sorption-enhanced chemical looping reforming process uses three interconnected fluidized bed reactors (i.e., reforming reactor, calcination reactor and air

* Corresponding author.
E-mail address: Amornchai.A@chula.ac.th (A. Arpornwichanop).

http://dx.doi.org/10.1016/j.enconman.2016.07.018
0196-8904/© 2016 Elsevier Ltd. All rights reserved.

reactor) to produce high-purity hydrogen, carbon dioxide and nitrogen without the need for an additional gas separation unit.

In recent years, most studies on the sorption-enhanced chemical looping reforming have focused heavily on using methane as a fuel [19–22], whereas a few works have been done on glycerol. Dou et al. [23] showed that the continuous sorption-enhanced steam reforming of glycerol using two moving-bed reactors with a Ni-based catalyst and CaO sorbent can produce hydrogen with 93.9% purity. Dou et al. [24] designed the moving bed reactors to achieve that the catalyst oxidation and sorbent regeneration was taken place under the same conditions in the reactor. By combining different units in one stage, this process has a great potential for low cost hydrogen production and high efficiency. Recently, they have succeeded in studying the sorption-enhanced steam reforming of glycerol in a fixed-bed reactor [25]. The literatures also revealed the benefits of using NiO as a solid oxygen carrier for SECLR because of its high reactivity and strong catalytic properties. Once NiO is reduced, some metallic Ni obtained has the excellent catalytic properties for steam reforming and water gas shift reaction [24,26]. In general, transition metals have been used as oxygen carriers in chemical looping processes, such as iron, copper, nickel, cobalt and manganese. Zafar et al. [27] examined different solid oxygen carriers in a fluidized bed reactor and concluded that NiO appeared the most promising active metal. Fernandez et al. [28] reported that Ca/Cu chemical looping process is feasible for hydrogen production but it is only favored to operate under conditions of moderate temperature, low pressure and high steam/carbon molar ratio. To determine the optimal operating conditions, the theoretical and experimental study by Wang [29] was presented by considering the effects of reforming temperatures and reactants ratios; however, this work did not describe the energy management in each unit in details and completed thermodynamic analysis is not included.

In this work, the sorption enhanced-chemical looping reforming process (SECLR) of glycerol is studied. A thermodynamic approach is used to investigate the effects of the operating parameters on the SECLR under steady-state condition. The effects of the primary operating parameters, i.e., temperature (T), calcium oxide-to-glycerol ratio (CaO/G), nickel oxide-to-glycerol ratio (NiO/G) and steam-to-glycerol ratio (S/G), on the performance of the SECLR process are analyzed in terms of the hydrogen production, carbon formation, energy demand of each unit and the overall process. To determine the thermally self-sufficient condition, the result is discussed based on energy and exergy considerations.

2. Description of the sorption-enhanced chemical looping glycerol steam reforming (SECLR)

The flow diagram of the sorption-enhanced chemical looping reforming process (SECLR) for hydrogen production from glycerol is shown in Fig. 1. The process consists of three reactors: reforming reactor, calcination reactor and air reactor, three cyclones and two heaters. The reactant feed stream consists of glycerol ($C_3H_8O_3$) and water (H_2O) at 25 °C and 1 atm. Before feeding to the reforming reactor, the reactant stream is preheated in order to vaporize into vapor phase at 1 atm. The reactant stream in vapor phase and the solids (NiO + CaO) stream from Cyclone3 are sent to the reforming reactor. The feed flow rates of the glycerol and water streams, and the NiO + CaO stream are tested to assess the condition which gives the optimum hydrogen production. In the reforming reactor, glycerol is oxidized with NiO and H_2O together with CO_2, which is adsorbed by CaO. The product stream contains hydrogen as a major product and other gases and solids is sent to Cyclone1 to separate the solids from the gases. The solid product stream which consists of nickle (Ni) and calcium carbonate ($CaCO_3$) is sent to the calcination reactor operated at 900 °C and 1 atm in order to regenerate calcium oxide (CaO) and release pure CO_2 gas. The product stream from the calcination reactor is sent to Cyclone2 where CO_2 is separated gas from solid particles (Ni and CaO). Without separation of CaO, the CaO, Ni and air at temperature of 900 °C and 1 atm can be sent to the air reactor [24] in order to regenerate Ni to NiO via the oxidation reaction. The gases and solids produced from the air reactor are fed to Cyclone3 where N_2 and O_2 off-gas is separated from NiO and CaO solid. Finally, both NiO and CaO solids are recycled to the reforming reactor. In this study, the air flow rate is specified at 17 mol/s to regenerate the NiO completely. Dashed-line boxes represented in Fig. 1 are referred to the heat requirement inside reforming process (evaporator and reforming reactor), calcination reactor, and air reactor (heater and air reactor). All product streams released at high temperatures are cooled down to 150 °C, therefore the heat from hot gaseous products can be used as useful heat for the heat requiring units such as heaters and reactors. To compare with CLR process, hydrogen production by chemical looping reforming is operated without carbon dioxide sorption. The process flowsheet is similar to Fig. 1 but there is no CaO and $CaCO_3$ as the components Therefore, calcination reactor and its heat duty are also absent. The CLR process only uses two interconnected reactors: reforming reactor and air reactor, two cyclones and two heaters.

3. Thermodynamic analysis

Thermodynamic analysis is performed by using Aspen Plus simulator in which unit operations including reactors, cyclones and heaters in the process are modelled with equilibrium RGIBBS reactors, HEATERs, and SSPLIT, respectively. The minimization of Gibbs free energy can calculate the equilibrium compositions of gaseous and solid products without specification of the possible reactions. However, the potential of this approach is limited if the concern compositions are not completely added. In this study, pure glycerol and water are the main reactants for hydrogen production via the SECLR process or CLR process using NiO as the oxygen carrier and CaO as the CO_2 adsorbent. Therefore, the possible components in the process consist of gaseous components (H_2, H_2O, CO, CO_2, CH_4 and unreacted $C_3H_8O_3$) and solid components (NiO, Ni, CaO, $CaCO_3$, $Ca(OH)_2$ and C) [29]. The reactors are analyzed at a steady state operation with isothermal and isobaric conditions. The Aspen Plus simulation is set up with a stream class of MIXCIPSD, to allow for the perfect separation between solids and gases in the cyclones. The physical property method for thermodynamic calculation is based on the SOLIDS property. Other assumptions made are (1) kinetic effects are not considered in the simulation and thermodynamic assessments, (2) the deactivation of solid materials is not taken into account, (3) pressure drops are neglected during operation in all units, (4) all gaseous components behave as an ideal gas, and (5) heat transfer between the unit operation ideally occurs.

The sensitivity analysis in Aspen Plus is used to examine the effects of the operating conditions. The simulation is run by varying the reforming temperature (T), CaO/G ratio, S/G ratio and NiO/G ratio, with the objective of studying these parameters' effects on the gas production yield, hydrogen purity, carbon formation, and heat duty. The possible reactions in the SECLR process are shown in Table 1 [24,29]. The performance of the process is expressed in terms of yield of product i (Eq. (1)), purity of product i on dry basis (Eq. (2)), carbon formation (Eq. (3)), and net heat duty (Eq. (4)) which can be positive (endothermic process), negative (exothermic process), or zero (self-sufficient process), depending on the operating conditions. In all simulations the glycerol feed rate and operating pressure are kept at 1 mol/s and 1 atm, respectively. The key operating parameters for investigation are reforming temperatures (T), CaO/G ratio (Eq. (5)), S/G ratio (Eq. (6)) and NiO/G ratio (Eq. (7)).

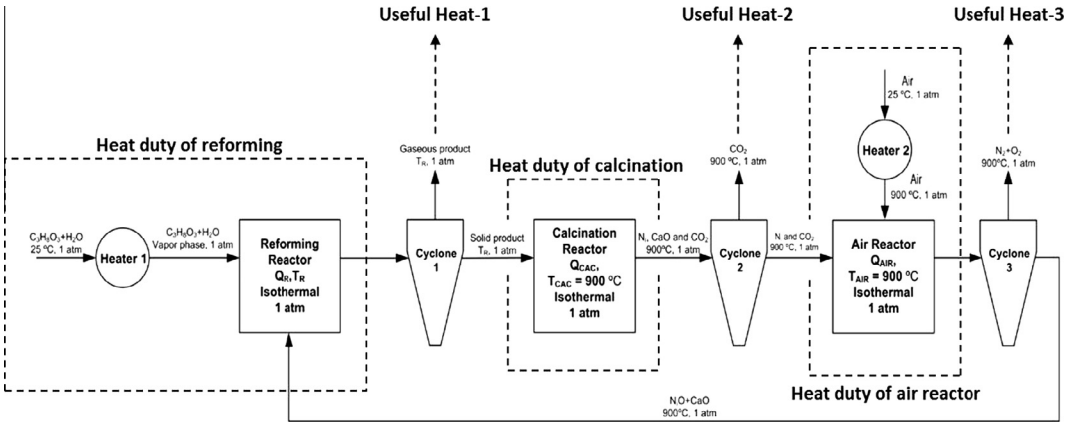

Fig. 1. The block flow diagram of the sorption-enhanced chemical looping reforming (SECLR) of glycerol.

Table 1
Possible reactions in SECLR process of glycerol [24,29].

In reforming reactor		
Oxidization:	$C_3H_8O_3 + H_2O + NiO \rightarrow CO + 2CO_2 + 5H_2 + Ni$	(R1)
Steam reforming:	$C_3H_8O_3 \overset{steam}{\longrightarrow} 3\ CO + 4H_2$	(R2)
WGS:	$CO + H_2O \rightarrow CO_2 + H_2$	(R3)
Carbonation:	$CaO + CO_2 \rightarrow CaCO_3$	(R4)
Overall:	$C_3H_8O_3 + 2H_2O + NiO + 3CaO \rightarrow 6H_2 + 3CaCO_3 + Ni$	(R5)
In calcination reactor		
Calcination:	$CaCO_3 \rightarrow CaO + CO_2$	(R6)
In air reactor		
Oxidation:	$2Ni + O_2 \rightarrow 2NiO$	(R7)
	$2C + O_2 \rightarrow 2CO$	(R8)
	$C + O_2 \rightarrow CO_2$	(R9)
Side reactions		
Methanations:	$CO + 3H_2 \rightarrow CH_4 + H_2O$	(R10)
	$CO_2 + 4H_2 \rightarrow CH_4 + 2H_2O$	(R11)
Boudouard:	$2CO \rightarrow C + CO_2$	(R12)
Reduction of CO:	$CO + H_2 \rightarrow C + H_2O$	(R13)
Reduction of CO_2:	$CO + H_2 \rightarrow C + H_2O$	(R14)
Methane creacking:	$CH_4 \rightarrow C + 2H_2$	(R15)
$Ca(OH)_2$ decomposition:	$Ca(OH)_2 \rightarrow CaO + H_2O$	(R16)

$$\text{Yield of product } i = \frac{n_{i,\text{out}}}{n_{\text{glycerol,feed}}} \quad (1)$$

$$\text{Purity of product } i\ (\%\ \text{dry basis}) = \frac{n_{i,\text{out}}}{(n_{\text{total,out}} - n_{\text{H}_2\text{O,out}})} \times 100 \quad (2)$$

$$\text{Carbon formation } (\text{mol/s}) = n_c \quad (3)$$

$$\text{Net heat duty}\left(\sum Q\right) = Q_{\text{reformer}} + Q_{\text{calcine}} + Q_{\text{air}} + Q_{\text{useful}} \quad (4)$$

$$\text{CaO/G ratio} = \frac{\text{Molar flow rate of feeding CaO}}{\text{Molar flow rate of feeding glycerol}} \quad (5)$$

$$\text{S/G ratio} = \frac{\text{Molar flow rate of feeding water}}{\text{Molar flow rate of feeding glycerol}} \quad (6)$$

$$\text{NiO/G ratio} = \frac{\text{Molar flow rate of feeding NiO}}{\text{Molar flow rate of feeding glycerol}} \quad (7)$$

where $n_{i,\text{out}}$ is the molar flow rate of product gas i from the reforming reactor, $n_{\text{glycerol,feed}}$ is the molar flow rate of feeding glycerol, $n_{\text{total,out}}$ is the molar flow rate of geseous product stream from the reforming reactor, n_c is the molar flow rate of carbon solid, Q_{reformer} is the heat duty of the reforming reactor including heat duty of Heater 1, Q_{calcine} is the heat duty of the calcination reactor, Q_{air} is the heat duty of the air reactor including heat duty of air pre-heater, Q_{useful} is the heat duty of product streams, i.e., H_2, CO_2 and $N_2 + O_2$, which are cooled to 150 °C.

This study aims to achieve the net heat duty at zero; however, it is the preliminary assessment. Because the calculated heat is based on only the quantity of energy, estimating the heat transfer in an exergy form can reveal more reliable results with the real magnitude of the useful heat to determine the optimal self-sufficient condition. The exergy associated with the heat transfer is governed as follows:

$$\text{Exergy of heat } (EX_Q) = Q_j \cdot \left(1 - \frac{T_0}{T_j}\right) \quad (8)$$

where Q_j is the heat duty of unit operation j, T_0 is the reference temperature of 298.15 K and T_j is the temperature of unit operation j.

For model validation, the simulation results are divided into two parts in order to compare with the experimental data under the same conditions. As shown in Table 2, firstly, the results from the steam reforming of glycerol without CO_2 sorption are compared with the experimental results of Dou et al. [23]. The experiment is carried out at a temperature of 600 °C, inlet gas velocity of 0.5 m/s, S/C ratio of 2 and NiO/Al_2O_3 as a catalyst. Secondly, the result from the SECLR of glycerol is compared with the experimental results of Dou et al. [24]. The experiment is carried out at a temperature of 500 °C, feeding velocity of 4 ml/h, S/C ratio

Table 2
Comparison between the simulation results and experimental data [23,24].

		Simulation	Reference
CLR (without CaO)	H_2 (vol%)	60.700	59.1
	CO_2 (vol%)	27.596	27.2
	CH_4 (vol%)	2.216	5.9
	CO (vol%)	9.489	7.8
SECLR (with CaO)	H_2 (vol%)	94.312	94.6

of 3 and NiO/CaO ratio of 1. Table 2 indicates that the model prediction of steam reforming without CaO shows some errors obtained on the product gas compositions. This may be due to the effect of catalyst that thermodynamic simulation might have a little loss of sensitivity. However, the simulation result agrees very well with the amount of CO_2 reported data and on account of this, removing CO_2 by using SECLR process is shown to be a promising way to enhance the hydrogen purity. In the SECLR case, the model prediction shows a good agreement with experimental data reported in literature with only 0.3% error.

4. Results and discussion

4.1. Comparison between the CLR and the SECLR processes

A comparison between the chemical looping reforming (CLR) without CaO sorbent and the sorption-enhanced chemical looping reforming (SECLR) with CaO sorbent for carbon dioxide sorption is presented in Table 3. For the conditions that are studied, the temperature and pressure of the reforming reactor are constantly specified at 500 °C and 1 atm, respectively. According to the stoichiometric of the overall reaction (R5) in the reforming reactor, all conditions are operated with glycerol and NiO molar flow rates of 1 mol/s to study the enhancement effects of the CaO sorbent and steam.

Table 3 shows that the SECLR with carbon dioxide sorption can achieve a higher hydrogen yield and hydrogen concentration than the process without carbon dioxide sorption (CLR). This is because the addition of CaO sorbent captures CO_2 as $CaCO_3$ via a carbonation reaction (R4), which can shift the equilibrium forward to the product side and promote the hydrogen yield via the oxidization reaction (R1) and water gas shift reaction (R3). In addition, the presence of CaO sorbent leads to reduced methane formation from 0.730 to 0.686 for a constant S/G ratio of one, as the smaller amounts of CO and CO_2 that result from the carbon dioxide capture can inhibit the methanation reactions (R10 and R11). Consequently, the reductions of CO, CO_2 and CH_4 gaseous products are also advantageous to lower carbon formation via the reverse direction of Boudouard reaction (R12), reduction of CO (R13), reduction of CO_2 (R14), and methane cracking reaction (R15). Moreover, the hydrogen yield increases when increasing the S/G ratio for all cases because the addition of water relates the oxidization reaction (R1), the glycerol steam reforming reaction (R2) and the water gas shift reaction (R3) which all reactions enhance the hydrogen production. The combination of the steam reforming, water gas shift and carbonation reactions with the increasing S/G ratio causes decreases in the methane, carbon monoxide, carbon dioxide and carbon formation because they lead to CO_2 reduction as well as CO, CH_4 and solid carbon reduction.

From these results, it can be concluded that the hydrogen yield and concentration can be enhanced by adding CaO sorbent and water. Moreover, the excess of CaO and steam can help prevent carbon formation in the reforming reactor, as shown in Fig. 2.

In the SECLR process, the carbon formation with different CaO/G ratios and S/G ratios is shown in Fig. 2. The carbon formation depends on the operating conditions and the compositions of the feed stream. The side reactions leading to carbon formation are the Boudouard reaction (R12), reduction of CO (R13), and reduction of CO_2 (R14), which are exothermic, and methane cracking reaction (R15), which is endothermic. The results from Fig. 2(a) show that upon increasing the CaO/G ratio and S/G ratio, the carbon formation decreases because the presence of CaO and water can reduce the amounts of CO and CO_2 and inhibit the methane formation. Therefore, side reactions are unfavorable in these conditions. The result from Fig. 2(b) shows that the carbon formation increases with the increasing temperature but decreases as the temperature exceeds 670 °C. The carbon formation is favorable at low S/G ratios because the methane production yield is high at this condition. Therefore, the methane cracking reaction (R15), which is endothermic, stimulates the carbon formation at high temperature and a low S/G ratio. However, the carbon formation decreases when the temperature exceeds 670 °C because the carbon dioxide sorption and water gas shift reaction are unfavorable at high temperatures. Therefore, the exothermic reactions (R12, R13 and R14) that govern the CO and CO_2 content are shifted backward when the temperature exceeds 670 °C.

As the formation of carbon leads to catalyst deactivation and pipeline blockage, it is necessary to keep it under control and avoid the carbon formation region in the operation. Using excess CaO/G and S/G ratios can help prevent carbon formation, namely, a CaO/G ratio of three and an S/G ratio of two.

4.2. Effect of operating temperature on the SECLR process

The effect of the operating temperature in the reforming reactor is investigated at 1 atm for a S/G ratio of two, a NiO/G ratio of one, and a CaO/G ratio of three, with a glycerol feed rate of 1 mol/s. The gas production yields are shown in Fig. 3(a) at four different temperatures of 400 °C, 500 °C, 600 °C, and 700 °C. For each temperature, there is no carbon formation (data not shown) because the condition has sufficient steam and carbon dioxide sorbent. It may be observed that the hydrogen yield increases with the increasing temperature. As the temperature increases, the glycerol steam reforming reaction (R2), which is highly endothermic, is intensified to produce hydrogen and carbon dioxide. The carbon dioxide produced in the reforming reactor is simultaneously adsorbed by CaO sorbent. However, the carbonation reaction (R4), which converts CO_2 to $CaCO_3$, is less pronounced at high temperature. The high

Table 3
Yields of products and H_2 concentration at 500 °C and 1 atm obtained in the reforming reactor for a glycerol flow rate of 1 mol/s and a NiO flow rate of 1 mol/s at different conditions.

	Yield of products (mol of product/mol of glycerol feed)						H_2 concentration
	H_2	CH_4	H_2O	CO	CO_2	C	(% dry basis)
CLR (without CaO) + S/G of one	1.422	0.730	2.119	0.176	1.352	0.742	38.64
CLR (without CaO) + S/G of two	1.706	0.875	2.543	0.212	1.623	0.290	38.64
SECLR (with CaO) + S/G of one	3.254	0.686	0.374	0.001	0.001	0.000	82.54
SECLR (with CaO) + S/G of two	4.413	0.397	0.794	0.001	0.001	0.000	91.72

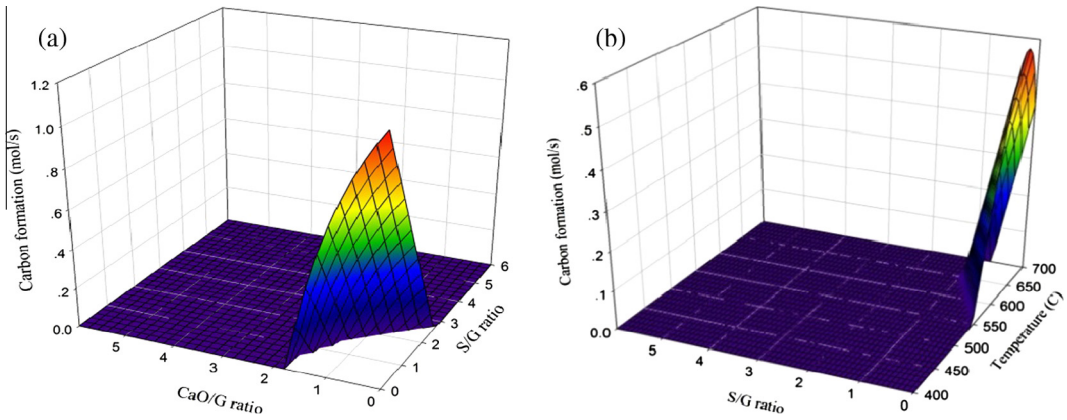

Fig. 2. Carbon formation as a function of (a) the CaO/G ratio and S/G ratio at a reforming temperature of 500 °C and (b) the S/G ratio and reforming temperature with a CaO/G ratio of 3 obtained in a reforming reactor with 1 mol/s of glycerol and 1 mol/s of NiO.

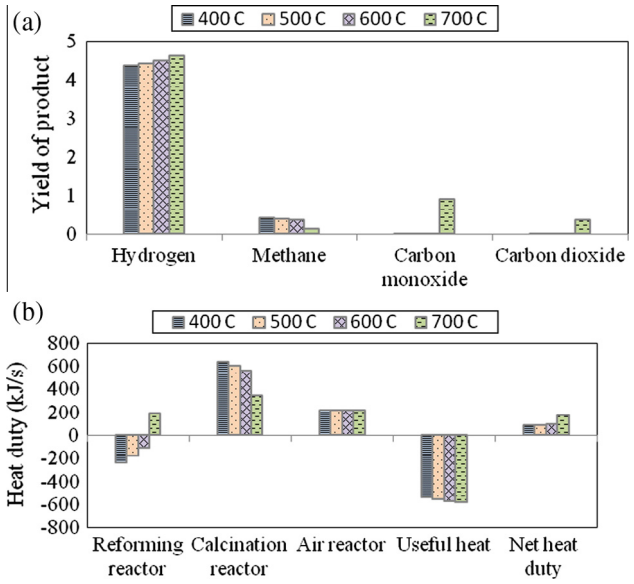

Fig. 3. (a) Gas production yields in the reforming reactor and (b) heat duty of process at different temperatures for a glycerol flow rate of 1 mol/s with an NiO/G ratio of 1, S/G ratio of 2 and CaO/G ratio of 3.

temperature also discourages the water gas shift reaction (exothermic reaction), which leads to the highest carbon monoxide yield and concentration at a temperature of 700 °C. The methane formation is unfavorable at high temperature due to the exothermicity of the methanation reactions (R10 and R11). It is necessary to be noted that in this study $Ca(OH)_2$ is just found on traces. The calcium hydroxide decomposition (R16) strongly proceeds in forward direction due to the high temperature operation.

The energy demand at different temperatures in the SECLR process is presented in Fig. 3(b). From the simulation results, it can be observed that the heat duty of the reforming reactor is more positive because of the high amount of energy required for the highly endothermic steam reforming (R2). In addition, the adsorption of carbon dioxide by CaO to form $CaCO_3$ is inhibited at high temperature, so increasing temperatures leads to a lower amount of $CaCO_3$ to regenerate via the calcination reaction (R6) in the calcination reactor. Therefore, the heat duty of the calcination reactor is reasonably decreased with the increasing temperature. When the temperature in the reforming reactor increases; the product streams which have a higher temperature can provide more useful heat duty, but due to no carbon formation and constant NiO/G ratio it is not affected on the heat duty of the air reactor via the oxidation reaction (R7 to R9). From the different temperatures, it is concluded that the net heat duty of the process is more positive with the increasing temperature.

4.3. Effect of nickel oxide-to-glycerol molar ratio (NiO/G) on the SECLR process

The effect of the NiO/G ratio on yields of the products and hydrogen purity is presented in Fig. 4(a). In the first period, the hydrogen yield is enhanced from 4.01 to 4.48 mol H_2/mol glycerol feed upon increasing the NiO/G ratio from 0 to 1.8. This is because the oxidization reaction (R1) produces more hydrogen. A NiO/G ratio higher than 1.8 shows less improvement on the hydrogen yield because the glycerol is completely combusted to produce carbon dioxide and steam instead of producing hydrogen. However, the carbon dioxide is adsorbed by the CaO sorbent, so the purity of the hydrogen is further enhanced. The energy demand in the SECLR process with various NiO/G ratios is presented in Fig. 4(b). In the oxidization reaction, glycerol is oxidized with steam and NiO to produce H_2, CO, CO_2, and Ni, which becomes more favorable in the presence of more NiO and then releases more heat.

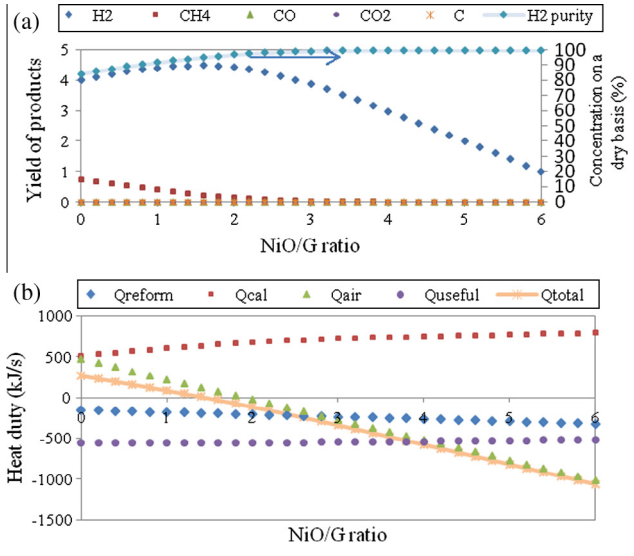

Fig. 4. (a) Yields of products and H_2 purity in the reforming reactor, (b) heat duty of process with different NiO/G ratios for a glycerol flow rate of 1 mol/s, S/G ratio of 2 and CaO/G ratio of 3 at a reforming temperature of 500 °C.

Therefore, the heat duty of the reforming reactor becomes more negative when increasing the NiO/G ratio. Nevertheless, the carbon dioxide produced in the reforming reactor is captured by sufficient CaO sorbent to form $CaCO_3$ via the carbonation reaction (R4), so the heat duty of the calcination (R6) is positive because a high amount of energy is required to release the carbon dioxide from the calcium carbonate and regenerate calcium oxide. In the air reactor, the heat duty is generally negative because the Ni is oxidized by oxygen providing more heat from the exothermic reactions of oxidation (R7 to R9). Therefore, the net heat duty becomes negative with the increasing NiO/C ratio. The use of NiO as an oxygen carrier can help produce energy by a partial oxidization reaction or complete combustion, depending on the amount of oxygen carrier. However, it is found that at low NiO/G ratios, the heat duty of the air reactor is positive. In other words, at low NiO/G ratios between 0 and 1.6 the external heat for the air reactor operated at 900 °C is required. To operate without energy input from external sources, it can be concluded that the process should have a higher NiO/G ratio feed.

4.4. Effect of calcium oxide-to-glycerol molar ratio (CaO/G) on the SECLR process

Fig. 5(a) shows the effect of the CaO/G ratio on the yields of products and hydrogen purity. The carbon dioxide gas is adsorbed by the CaO sorbent via the carbonation reaction (R4), which involves the carbon monoxide reduction via the water gas shift reaction (R3). For this reason, a higher hydrogen purity is obtained by increasing the CaO/C ratio. However, it is found that the hydrogen yield and purity first increase sharply with the increasing CaO/G ratio and then stabilize as the CaO/C ratio exceeds 2.6. The lower CaO/C ratio could not totally adsorb the produced CO_2 gas from the oxidization (R1) and water gas shift reactions (R3), so the carbon dioxide yield is still high. Furthermore, the methane yield is high at low CaO/C ratios because carbon monoxide and carbon dioxide can react with hydrogen to produce methane via the methanation reactions (R10 and R11). The energy demand of the SECLR process with various CaO/G ratios is presented in Fig. 5(b). Upon increasing CaO/G ratio, the carbonation reaction, which is exothermic, is shifted forward, so the heat duty of the reforming reactor becomes more negative. However, more energy is required to regenerate $CaCO_3$ to CaO and release CO_2, so the heat duty of the calcination reactor is more positive with a large amount of $CaCO_3$.

4.5. Effect of steam-to-glycerol molar ratio (S/G) on the SECLR process

The effect of the S/G molar ratio on the yield of products and hydrogen purity in the reforming reactor is shown in Fig. 6(a). The hydrogen yield and purity increase with the addition of excess water to the reforming reactor because the higher amount of water favorably reacts with carbon monoxide and shifts the equilibrium of the water gas shift reaction (R3) forward, leading to a lower amount of carbon monoxide together with carbon dioxide adsorption to enhance the hydrogen yield and purity. Moreover, it can be noted that the yield of methane slightly decreases upon increasing the S/G ratio because the water can obstruct the formation of methane and carbon via the methanation reactions (R10 and R11) and methane cracking (R15), respectively. However, the disadvantage of adding more water is that the product of hydrogen is diluted with excess steam, resulting in the need for high energy consumption to separate the water and hydrogen. In addition, a higher water feed requires a higher amount of energy for evaporation into the vapor phase for the glycerol steam reforming reaction, as is shown in Fig. 6(b). The net heat duty of the process becomes positive with the increasing S/G ratio because more energy is consumed to generate steam with a higher amount of water feed. For this reason, the heat duty of the reforming reactor increases with the increasing S/G ratio. Moreover, at a higher S/G ratio, the water-gas shift reaction is shifted forward, and thus a higher amount of CO_2 is produced. Therefore, it is found that more energy is needed to release the carbon dioxide in the calcination reactor, so the heat duty of the calcination reactor increases upon increasing the S/G ratio.

4.6. Optimal self-sufficient operation

From the results of the parametric analysis, S/G ratios higher than two and a sufficient CaO/G ratio of three can inhibit the carbon formation in the operation. The hydrogen yield increases significantly upon increasing the reforming temperature. However, the more the temperature increases, the more energy is required. The required energy of the process varies with the amount of NiO used as a solid oxygen carrier. Therefore, the objective function

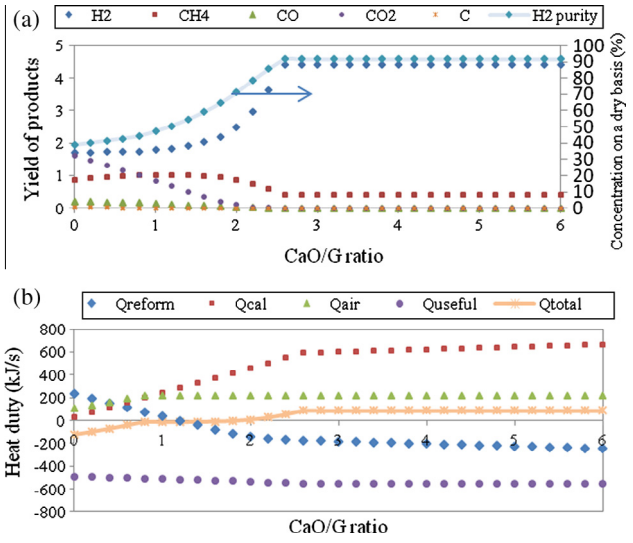

Fig. 5. (a) Yields of products and H_2 purity in the reforming reactor, (b) heat duty of the process with different CaO/G ratios for a glycerol flow rate of 1 mol/s, NiO/G ratio of 1 and S/G ratio of 2.

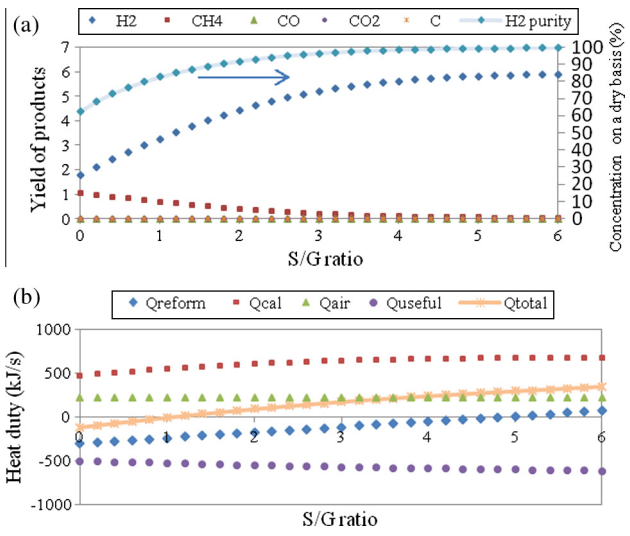

Fig. 6. (a) Yields of products and H_2 purity in the reforming reactor, (b) heat duty of the process with different S/G ratios for a glycerol flow rate of 1 mol/s, NiO/G ratio of 1 and CaO/G ratio of 3.

of this process is the highest hydrogen production yield and no carbon formation at self-sufficient conditions. The decision variable is the reforming temperature, S/G ratio and NiO/G ratio to achieve the objective function. The study is made by considering the use of a CaO/G ratio of three because it is sufficient for totally adsorbing the carbon dioxide. As the energy balance of the SECLR process mainly depends on the NiO content in the feed stream, the suitable NiO/G ratio is determined to optimize the hydrogen production yield with the constraint of a net heat duty of the process equal to zero.

The result of the optimization is shown in Fig. 7. It is found that the hydrogen yield increases with the increasing temperature and S/G ratio and then decreases when the temperature and S/G ratio exceed optimum points. The optimum operating point is a reforming temperature of 580 °C and a S/G molar ratio of 3.2, adjusting the NiO/G ratio to 1.84 to operate at self-sufficient conditions with the net heat duty of the process near zero.

However, when the exergy of heat is concerned, the net heat duty of the process including the heat duties of the reforming reactor, calcination reactor, air reactor and the useful heat duty of the product streams after cooling at 150 °C cannot be assured that the thermal energy will be self-sufficient on this condition. The net exergy of heat which shows the real magnitude of useful energy is calculated as shown in Table 4. It indicates that based on the previous optimal condition the net exergy of heat still positive. This means that the exhaust heat from reformer, air reactor, and product stream cannot be transferred the enough heat into the heat requiring units. Some amount of heat in the process is actually lost its quality by mismatch heat transfer and temperature gradient as shown in Eq. (8). In this work, additional heat is needed by increasing the NiO/G ratio to 1.87. Therefore, the final result points that the NiO/G ratio of 1.87 is sufficient to be the most optimal condition with regard to both energy and exergy considerations. Fig. 8 shows the optimal SECLR process with heat integration in Aspen Plus simulator. Based on the energy and exergy calculations, the useful heat duties from the product stream can be recovered to pre-heat the reactants and air while the exhaust heats from the reforming reactor and air reactor can be utilized for the calcination reactor.

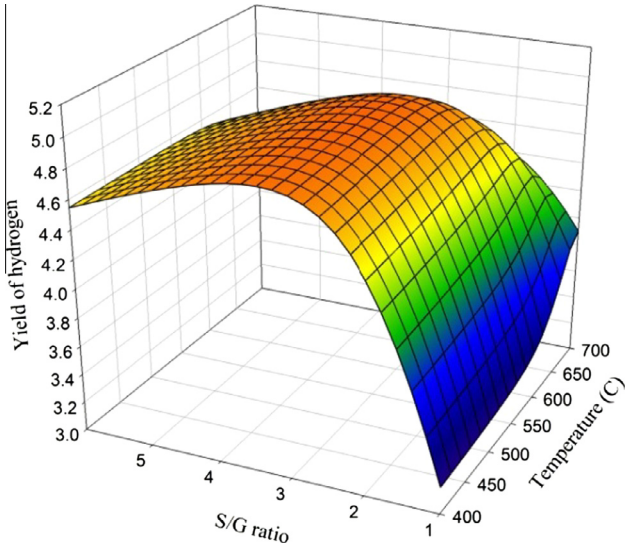

Fig. 7. Optimization results at the self-sufficient condition without carbon formation.

Table 4
Heat duty and exergy of heat for each unit operation and overall process.

NiO/G ratio	1.84		1.87	
Unit operation	Q (kJ/s)	EX_Q (kJ/s)	Adjusted Q (kJ/s)	Adjusted EX_Q (kJ/s)
Reformer	−354.75	−230.78	−355.50	−231.26
Calcinator	648.77	483.89	649.81	484.66
Air reactor	−454.33	−338.86	−461.74	−344.39
Evaporator	284.01	119.00	284.01	119.00
Heater	468.17	349.18	468.17	349.18
Useful heat-1	−98.35	−62.87	−98.43	−62.93
Useful heat-2	−110.44	−70.60	−110.53	−70.66
Useful heat-3	−382.80	−244.73	−382.42	−244.49
SUM	0.29	4.23	−6.63	−0.88

5. Conclusions

The thermodynamic analysis of the sorption-enhanced chemical looping reforming process using glycerol and water as the reactants has been performed by the minimization of the Gibbs free energy. From the simulation results and the studied effects of the parameters, it is found that the hydrogen yield and purity can be enhanced by carbon dioxide sorption and the addition of water. The excess CaO sorbent and water can also inhibit the carbon formation in the SECLR process. Carbon formation could be avoided by using a CaO/G ratio of three and a S/G ratio of two. The hydrogen

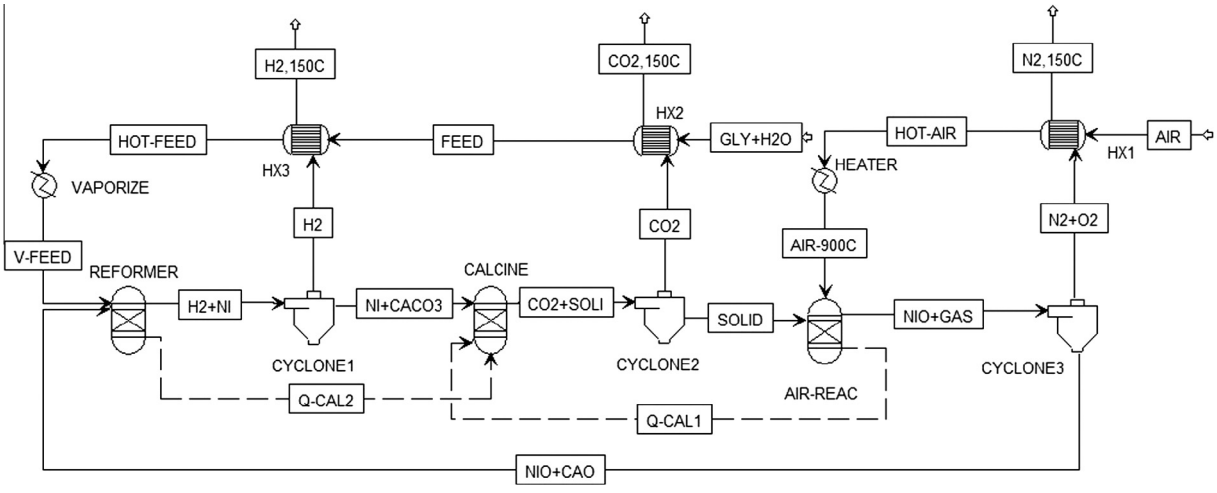

Fig. 8. The SECLR process with heat integration in Aspen Plus simulator .

yield can be obtained at a high temperature and low NiO/G ratio. The highest hydrogen purity can be obtained at a temperature of 500 °C and a CaO/G ratio higher than 2.6 is sufficient for total CO_2 adsorption. The net heat duty has a negative value at a high NiO/G ratio while the more increases the CaO/G ratio and S/G ratio, the more energy is required. Regarding heat duty calculation, the self-sufficient condition can be achieved without carbon formation when the reforming temperature is 580 °C at atmospheric pressure, the S/G molar ratio is 3.2 and the NiO/G molar ratio is 1.84. However, when the exergy of heat is concerned, the net exergy of heat still positive. This means that the exhaust heat from exothermic units cannot be transferred enough heat into the heat requiring units. Therefore, the additional heat is needed by increasing the NiO/G ratio to 1.87. In this condition, a hydrogen production yield of 4.90 mol H_2/mol $C_3H_8O_3$ and a hydrogen purity of 98.31% on a dry basis can be produced in the reforming reactor.

Acknowledgments

Support from the Chulalongkorn Academic Advancement into Its 2nd Century Project and the Thailand Research Fund (DPG5880003) is gratefully acknowledged. P. Tippawan would also like to acknowledge the Postdoctoral fellowship, Chulalongkorn University.

References

[1] Nicoletti G, Arcuri N, Nicoletti G, Bruno R. A technical and environmental comparison between hydrogen and some fossil fuels. Energy Convers Manage 2015;89:205–13.
[2] Demirbas A. Biofuels securing the planet's future energy needs. Energy Convers Manage 2009;50:2239–49.
[3] Dou B, Wang C, Song Y, Chen H, Xu Y. Activity of Ni–Cu–Al based catalyst for renewable hydrogen production from steam reforming of glycerol. Energy Convers Manage 2014;78:253–9.
[4] Wang W. Thermodynamic analysis of glycerol partial oxidation for hydrogen production. Fuel Process Technol 2010;91:1401–8.
[5] Leal AL, Soria MA, Madeira LM. Autothermal reforming of impure glycerol for H_2 production: thermodynamic study including in situ CO_2 and/or H_2 separation. Int J Hydrogen Energy 2016;41:2607–20.
[6] Remón J, Giménez JR, Valiente A, García L, Arauzo J. Production of gaseous and liquid chemicals by aqueous phase reforming of crude glycerol: influence of operating conditions on the process. Energy Convers Manage 2016;110:90–112.
[7] Galera S, Gutiérrez Ortiz FJ. Life cycle assessment of hydrogen and power production by supercritical water reforming of glycerol. Energy Convers Manage 2015;96:637–45.
[8] Parawira W. Biodiesel production from Jatropha curcas: a review. Sci Res Essays 2010;5(14):1796–808.
[9] Anitha M, Kamarudin SK, Kofli NT. Review: the potential of glycerol as a value-added commodity. Chem Eng J 2016;295:119–30.
[10] Czernik S, French R, Feik C, Chornet E. Hydrogen by catalytic steam reforming of liquid byproducts from biomass thermoconversion processes. Ind Eng Chem Res 2002;41(17):4209–15.
[11] Adhikari S, Fernando SD, Haryanto A. Hydrogen production from glycerin by steam reforming over nickel catalysts. Renewable Energy 2008;33:1097–100.
[12] Adhikari S, Fernando SD, Haryanto A. Hydrogen production from glycerol: an update. Energy Convers Manage 2009;50:2600–4.
[13] Cheng CK, Foo SY, Adesina AA. Steam reforming of glycerol over Ni/Al_2O_3 catalyst. Catal Today 2011;178:25–33.
[14] Dou B, Song Y, Wang C, Chen H, Xu Y. Hydrogen production from catalytic steam reforming of biodiesel byproduct glycerol: issues and challenges. Renew Sustain Energy Rev 2014;30:950–60.
[15] Rydén M, Ramos P. H_2 production with CO_2 capture by sorption enhanced chemical-looping reforming using NiO as oxygen carrier and CaO as CO_2 sorbent. Fuel Process Technol 2012;96:27–36.
[16] Rydén M, Lyngfelt A, Mattisson T. Two novel approaches for hydrogen production chemical-looping reforming and steam reforming with carbon dioxide capture by chemical-looping combustion. In: Paper presented at the proceedings of the 16th world hydrogen energy conference, Lyon, France.
[17] Diego LF, Ortiz M, García-Labiano F, Adánez J, Abad A, Gayán P. Hydrogen production by chemical-looping reforming in a circulating fluidized bed reactor using Ni-based oxygen carriers. J Power Sources 2009;192:27–34.
[18] Jiang B, Dou B, Song Y, Zhang C, Du B, Chen H, et al. Hydrogen production from chemical looping steam reforming of glycerol by Ni-based oxygen carrier in a fixed-bed reactor. Chem Eng J 2015;280:459–67.
[19] Yahom A, Powell J, Pavarajarn V, Onbhuddha P, Charojrochkul S, Assabumrungrat S. Simulation and thermodynamic analysis of chemical looping reforming and CO_2 enhanced chemical looping reforming. Chem Eng Res Des 2014;92:2575–83.
[20] Anderson DM, Kottke PA, Fedorov AG. Thermodynamic analysis of hydrogen production via sorption-enhanced steam methane reforming in a new class of variable volume batch-membrane reactor. Int J Hydrogen Energy 2014;39:17985–97.
[21] Antzara A, Heracleous E, Bukur DB, Lemonidou AA. Thermodynamic analysis of hydrogen production via chemical looping steam methane reforming coupled with in situ CO_2 capture. Energy Procedia 2014;63:6576–89.
[22] Antzara A, Heracleous E, Bukur DB, Lemonidou AA. Thermodynamic analysis of hydrogen production via chemical looping steam methane reforming coupled with in situ CO_2 capture. Int J Greenhouse Gas Control 2015;32:115–28.
[23] Dou B, Wang C, Chen H, Song Y, Xie B. Continuous sorption-enhanced steam reforming of glycerol to high-purity hydrogen production. Int J Hydrogen Energy 2013;38:11902–9.
[24] Dou B, Song Y, Wang C, Chen H, Yang M, Xu Y. Hydrogen production by enhanced-sorption chemical looping steam reforming of glycerol in moving-bed reactors. Appl Energy 2014;130:342–9.
[25] Dou B, Jiang B, Song Y, Zhang C, Wang C, Chen H, et al. Enhanced hydrogen production by sorption-enhanced steam reforming from glycerol with in-situ CO_2 removal in a fixed-bed reactor. Fuel 2016;166:340–6.
[26] Dueso C, Ortiz M, Abad A, García-Labiano F, Diego LF, Gayán P, et al. Reduction and oxidation kinetics of nickel-based oxygen- carriers for chemical-looping combustion and chemical-looping reforming. Chem Eng J 2012;188:142–54.
[27] Zafar Q, Mattisson T, Gevert B. Integrated hydrogen and power production with CO_2 capture using chemical-looping reforming redox reactivity of particles of CuO, Mn_2O_3, NiO, and Fe_2O_3 using SiO_2 as a support. Ind Eng Chem Res 2005;44(10):3485–96.
[28] Fernandez JR, Abanades JC, Grasa G. Modeling of sorption enhanced steam methane reforming—Part II: simulation within a novel Ca/Cu chemical loop process for hydrogen production. Chem Eng Sci 2012;84:12–20.
[29] Wang W. Hydrogen production via sorption enhanced chemical looping reforming Hydrogen production via sorption enhanced chemical looping reforming Theoretical and experimental study. Korean J Chem Eng 2014;31(2):230–9.

Energy Conversion and Management 140 (2017) 228–239

Contents lists available at ScienceDirect

Energy Conversion and Management

journal homepage: www.elsevier.com/locate/enconman

Exergoeconomics of hydrogen production from biomass air-steam gasification with methane co-feeding

Teeranun Nakyai [a], Suthida Authayanun [b], Yaneeporn Patcharavorachot [c], Amornchai Arpornwichanop [d], Suttichai Assabumrungrat [e], Dang Saebea [a,*]

[a] Department of Chemical Engineering, Faculty of Engineering, Burapha University, Chonburi 20131, Thailand
[b] Department of Chemical Engineering, Faculty of Engineering, Srinakharinwirot University, Nakorn Nayok 26120, Thailand
[c] School of Chemical Engineering, Faculty of Engineering, King Mongkut's Institute of Technology Ladkrabang, Bangkok 10520, Thailand
[d] Computational Process Engineering, Chulalongkorn University, Bangkok 10330, Thailand
[e] Center of Excellence in Catalysis and Catalytic Reaction Engineering, Department of Chemical Engineering, Faculty of Engineering, Chulalongkorn University, Bangkok 10330, Thailand

ARTICLE INFO

Article history:
Received 20 December 2016
Received in revised form 14 February 2017
Accepted 1 March 2017

Keywords:
Biomass
Air–steam gasification
Exergy
Exergoeconomic
Methane co-feeding

ABSTRACT

Biomass is one of the most promising energy sources for hydrogen production. However, biomass gasification has a low hydrogen content in the producer gas. To increase the hydrogen yield, the co-feeding of methane into biomass gasification is proposed in this study. The type of gasifying agent is a key factor in the determination of the content of the hydrogen product. To compare the designs and find the best performance criteria of a process, not only energy and exergy analyses but also a cost analysis of the process should be investigated. In the present study, the effects of various types of gasifying agent, i.e., air and both steam and air, for the biomass gasification with/without methane co-feeding are investigated through an exergoeconomic analysis. It is observed that the air-steam used as an agent achieves high energy and exergy efficiency. Methane co-feeding can improve the energy and exergy efficiency. In exergoeconomic analysis, the specific exergy cost (SPECO) method is applied to investigate the unit cost of hydrogen. The economic reveal that the biomass gasification using air-steam as an agent with methane co-feeding also presented the lowest unit hydrogen cost of 2.69 $/kg. The unit exergy cost of hydrogen is 0.068 $/kW h.

© 2017 Elsevier Ltd. All rights reserved.

1. Introduction

The consumption of fuels and chemicals continuously grows. Hydrogen plays an important role in the chemical industry as a fuel and chemical reactant due to its high energy density and low emission [1–3]. Most synthesis gas is produced from fossil sources. The combustion of fossil fuel leads to environmental problems such as the greenhouse effect and air pollution [4–6]. Additionally, fossil sources are limited in quantity. To develop sustainable strategies for energy production, renewable resources have been investigated as substitutes for fossil sources [7]. Biomass has been considered to be an alternative fuel for hydrogen production because it is an organic material that comes from various green sources including agricultural residues and waste from industrial production processes [8,9]. Although conversion biomass into fuels releases carbon dioxide in the atmosphere, biomass utilization is carbon dioxide neutral due to growth of the crops taking carbon dioxide out of the atmosphere.

Biomass can be converted to synthesis gas via a gasification process. The main challenges regarding large-scale biomass gasification are the low hydrogen content in the synthesis gas product and the high energy input required. The quality of the hydrogen content in the syngas depends upon the type of biomass used, the gasifier reactor, gasifying agent, and operating condition of the gasifier. To increase the hydrogen content and reduce the tar content in the fuel gas, preheating of the gasification agent was proposed in publications [10,11].

The most common gasifying agent is air because of its abundance and inexpensiveness. However, the large proportion of inert nitrogen gas in ambient air directly causes the low quality, with a higher heating value (HHV) of 4–6 MJ per cubic metre at standard temperature and pressure (m^3 stp; 25 °C, 1 atm). Furthermore, the use of air as a gasification agent obtains low hydrogen content of the product gas. The gas product from biomass gasification with pure oxygen has a higher product gas quality than that with air (HHV = 10–15 MJ/m^3 stp.), but the separation cost of pure oxygen

* Corresponding author.
E-mail address: dangs@eng.buu.ac.th (D. Saebea).

http://dx.doi.org/10.1016/j.enconman.2017.03.002
0196-8904/© 2017 Elsevier Ltd. All rights reserved.

Nomenclature

a, b, c, d	empirical coefficients
ex	standard exergy (kJ/kmol)
i	interest rate
E	energy (kJ/kg)
Ex	exergy (kJ/kg)
$\dot{E}x$	exergy rate (MW)
m	mole of air to mass of biomass ratio (mol/kg)
$\dot{m}$	mass flow rate of the biomass (kg/s)
c	unit exergy cost ($/GJ)
$\bar{c}_p$	constant pressure specific heat capacity (kJ/kmol K)
C	initial investment cost ($)
$\dot{C}$	cost rate ($/h)
$C\dot{A}$	annual capital cost ($/yr)
n	molar yield (mol/kg), lifetime of equipment (yr)
T	temperature (K)
P	pressure (Pa)
R	universal gas constant (kJ/kmol K)
h	specific enthalpy (kJ/kmol)
s	specific entropy (kJ/kmol K)
S	salvage value ($)
y	mole fraction of gas component
$\dot{Z}$	sum of capital investment and operation and maintenance cost rates ($/h)

Greek letters

β	correlation factor
η	efficiency (%)
τ	annual operating time of equipment (h)
ϕ	operating and maintenance factor

Superscripts

ki	kinetic
ep	potential
ph	physical
ch	chemical
CI	capital cost investment
OM	operating and maintenance
T	total

Subscripts

i	component gases
0	dead state
air	air
agent	gasifying agent
ash	ash
biomass	biomass
en	energy
ex	exergy
gas	product gases
methane	methane
n	life time of the process (yr)
process	process
p	product
total	total
F	feed
kth	kth equipment
w	water

Abbreviations

ER	equivalence ratio
CRF	capital recovery factor
PEC	purchased equipment cost ($)
PW	present worth ($)
PWF	present worth factor
LHV	lower heating value (MJ/kg or kJ/kg)
HHV	higher heating value (MJ/kg or kJ/kg)
SPECO	specific exergy cost

is relatively high [12]. The gas product of the steam reforming process has a medium caloric value and higher heating value (15–20 MJ/m^3 stp.). Although the gas product from the biomass steam gasification process is of high quality, a high energy input is required [13].

The type of feedstock is an important factor regarding the gas product quality. Several studies have been conducted by concurrently co-feeding methane or natural gas together with a carbonaceous solid [14–16]. Aaron et al. [14] reported that the addition of methane to the gasification of rice hulls affects the contents of hydrogen and carbon dioxide in the fuel gas. Moreover, some research topics have studied the addition of natural gas into the biomass gasification to generate the electricity. Pantaleo et al. [15] performed a micro gas turbine (MGT) cycle using natural gas and biomass as fuel. The combined cooling, heating and power system (CCHP) integrating biomass gasification and the co-firing of natural gas was investigated by Wang et al. [16]. Their results found that the energy efficiency of the electric power system with co-feeding of natural gas and biomass is higher than that with the use of biomass alone.

The process of biomass gasification requires a high energy input. The assessment of the energy conversion of biomass gasification systems using energy and exergy analyses should be considered to determine the optimum system and conditions [17,18]. The types of feedstocks, gasification agents, and gasifiers have the important influence on the energy and exergy efficiencies. The energy and exergy values of the biomass gasification system depend on the ultimate analysis and moisture content of feedstock [19,20]. The study of the different gasification agents on the energy and exergy efficiencies was obtained [19,21,22]. Hosseini et al. [19] found that the air used as a gasifying agent achieves higher energy efficiency than the use of steam. However, the exergy efficiency of the steam gasification is higher than that from partial oxidation gasification [22]. Moreover, the energy and exergy analyses to find the optimum condition of several gasifiers have been studied. The results of Loha et al. [23] indicated that the energy and exergy efficiencies have a maximum at the carbon boundary point. For the gasification of rice husks in an entrained flow gasifier, Zhang et al. [22] reported that the highest energy and exergy of syngas product are achieved at the gasifier temperature and equivalence ratio of 1000 °C and 0.25, respectively.

The cost of hydrogen production is also an important criterion. In an exergoeconomic analysis, the exergy and economics are combined to study a thermochemical system [24]. Various studies have been conducted on the exergoeconomic analysis of hydrogen production from biomass [25–27]. The parameters for considering the unit cost of hydrogen production are the capital investment, operation and maintenance costs. Also, the results of Lv et al. [25] indicated that the costs of electricity and the catalyst in the combined system of downdraft gasifier and a CO-shift reactor have a major impact on the hydrogen production cost. A comparison of the costs of hydrogen production from three types of gasifier reactor, i.e., downdraft, circulating fluidized bed, and plasma gasifier, was performed by Kalinci et al. [27]. They stated that the circulating

fluidized bed achieves the highest hydrogen product. However, the cost of hydrogen production from the downdraft process is the lowest due to the highest exergy efficiency for three different hydrogen production processes.

As described above, the effect of methane co-feeding and the use of different agents for biomass gasification on the hydrogen content have been widely reported. However, the energy and cost analysis of the hydrogen production of biomass gasification, which provides important indicators for the decision to select the proper guidelines, is still a matter for further investigation. Thus, the main objectives of this work are to study the impact of methane co-feeding in biomass gasification and the suitable gasifying agents using an exergoeconomic analysis. The effects of the preheating temperature of the agents, equivalence ratio and steam to biomass ratio are considered first to find the proper conditions for biomass gasification. In the next section, a comparison of different gasifying agents and the addition of methane for the exergy and economic analysis are investigated.

2. Simulation and model

2.1. Assumptions of the model

Biomass gasification is considered in the downdraft reactor. The downdraft fixed bed gasification includes four zones; drying, pyrolysis, combustion, and gasification. In this study, the combustion and gasification were combined in same zone. The flowsheet of the biomass gasification is shown in Fig. 1. The basic assumptions for the simulation of the biomass gasification are as follows:

(1) biomass gasification operates at steady-state conditions;
(2) the system is assumed to be adiabatic;
(3) all gases behave as ideal gases; and
(4) the reactions in the gasifier are at an equilibrium state.

2.2. Aspen Plus model description

The biomass used in this study is rubber wood. The proximate and ultimate analyses of the rubber wood are shown in Table 1 [28]. The proximate analysis reveals the contents of fixed carbon (FC), volatile matter (VM), moisture content (MC), and ash (ASH). The ultimate analysis reveals the elemental contents of carbon, hydrogen, nitrogen, oxygen, and ash. Fig. 1 shows the unit operations of the biomass gasification process simulated in an Aspen Plus flowsheet. For the downdraft gasification process, the biomass is fed into a drying zone. RSTOIC and FLASH3 blocks were used for drying zone. An RSTOIC block was used to convert the raw biomass into dry biomass and steam. The reaction for biomass drying is as follows.

Table 1
Proximate and ultimate analyses of dry basis biomass.

Proximate analysis	(wt% dry basis)	Ultimate analysis	(wt% dry basis)
FC	19.20	C	50.60
VM	80.10	H	6.50
ASH	0.70	O	42.00
		N	0.20
		ASH	0.70

$$\text{Biomass (wet)} \rightarrow \text{Biomass (dry)} + H_2O\ \text{(steam)} \quad (1)$$

The dry biomass and steam was separated with the FLASH3 block. In the decomposition or pyrolysis zone, the RYIELD block was used to convert the nonconventional component into the constituent elements of carbon, nitrogen, oxygen, hydrogen, sulphur, and ash. The yield distribution is highly dependent on the biomass feedstock as evaluated by the ultimate analysis. Before feeding the dry biomass into the RGIBBS block, the heat of reaction (QDCOMP) associated with the decomposition of the biomass must be considered in the biomass gasification. In the gasification zone, the RGIBBS block based on the chemical and phase equilibria was used as a reactor. The reactions occurring in the gasification zone were included in Table 2 [29]. The dry biomass was fed with various gasification agents and fuel, such as air, steam, and methane. To preheat the gasifying agent and fuel, the HEATER block was employed. In the final zone, the separation of the syngas product from the ash used the SSPLIT block.

According to the Aspen Plus simulator, the physical properties of the conventional component can be calculated using the Peng-Robinson-Boston-Mathias (PR-BM) model. This thermodynamic property model can describe both pure and mixed components. Naveed et al. [30] showed that this model is quite appropriate for high ranges of temperature and pressure. In this simulation, the HCOALGEN and DCOALIGT property models were used to calculate the enthalpy and density of the biomass and ash, which are non-conventional components.

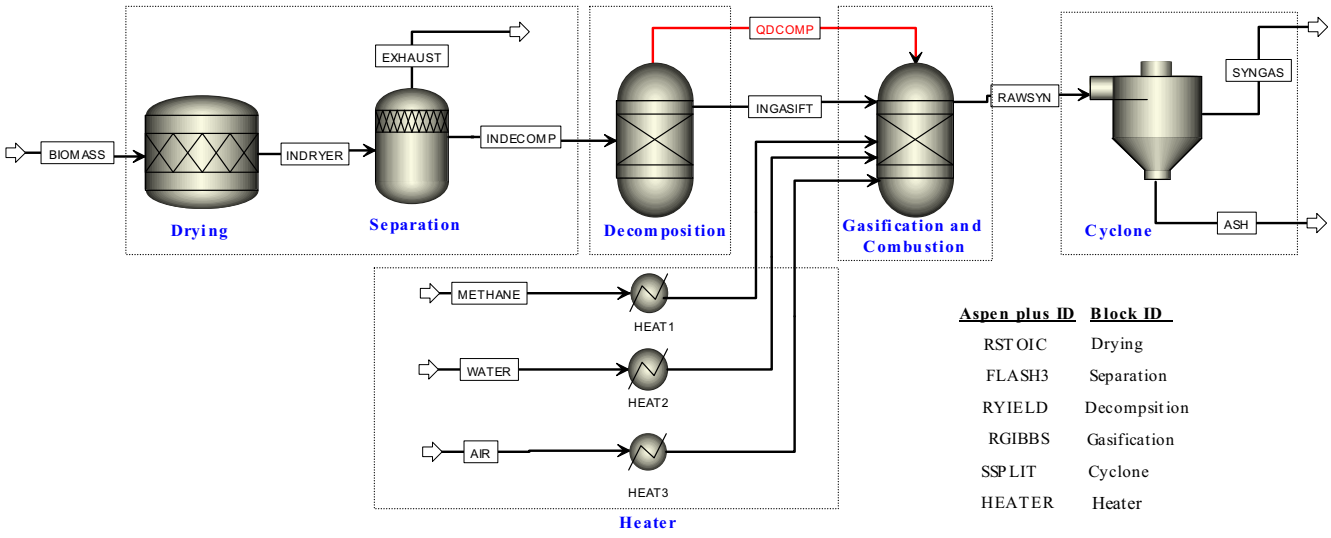

Fig. 1. Aspen Plus flowsheet used for simulation of biomass gasification process in downdraft fixed bed.

Table 2
Reactions in the gasifier.

Reaction number	Reaction name	Chemical equation	Heat of reaction (MJ/kmol)
R1	Char gasification	$C + H_2O \leftrightarrow CO + H_2$	+131
R2	Methanation	$C + 2H_2 \leftrightarrow CH_4$	−75
R3	Boudouard	$C + CO_2 \leftrightarrow 2CO$	+172
R4	Char partial oxidation	$C + 0.5O_2 \leftrightarrow CO$	−283
R5	Char combustion	$C + O_2 \leftrightarrow CO_2$	−393
R6	Methane shift	$CH_4 + H_2O \leftrightarrow CO + 3H_2$	+206
R7	Water gas shift	$CO + H_2O \leftrightarrow CO_2 + H_2$	−41
R8	Hydrogen partial oxidation	$H_2 + 0.5O_2 \leftrightarrow H_2O$	−242

3. Energy and exergy analysis

3.1. Energy analysis

The energy analysis consists of four types of energy, which are kinetic energy (E^{ki}), potential energy (E^{ep}), physical energy (E^{ph}), and chemical energy (E^{ch}), as follows:

$$E_{total} = E^{ki} + E^{ep} + E^{ph} + E^{ch} \quad (2)$$

The kinetic and potential energies have very low values compared with the total energy [22,31] so they can be neglected. The simplified equation for the total energy is shown below.

$$E_{total} = E^{ph} + E^{ch} \quad (3)$$

$$E^{ph} = \sum_{i=1} n_i h_i \quad (4)$$

In Eqs. (3) and (4), h_i is the specific enthalpy (kJ/kmol) and n_i is the molar yield of gas component i (mol/kg). The specific enthalpy, specific entropy, standard chemical exergy, and higher heating value of the component of gases at the dead state (temperature T_0 = 25 °C and pressure P_0 = 1 atm) are shown in Table 3.

The chemical energy is calculated from the higher heating value (HHV) of gas component i, which can be obtained from Eq. (5).

$$E^{ch} = \sum_{i=1} n_i \mathrm{HHV}_i \quad (5)$$

The energy of the biomass is calculated from the equation as follow:

$$E^{ch} = \dot{m}\mathrm{HHV}_{biomass} \quad (6)$$

where $\dot{m}$ is the mass flow rate of the biomass in kg/s and $\mathrm{HHV}_{biomass}$ represents the higher heating value of the biomass in MJ/kg. The higher heating value of rubber wood is 19.6 MJ/kg [28].

3.2. Exergy analysis

Based on the second law of thermodynamics, the exergy can be defined as the maximum work obtainable between the system and reference states. In this section, the evaluation of the exergy for biomass gasification is obtained from Eq. (7).

$$Ex_{total} = Ex^{ki} + Ex^{ep} + Ex^{ph} + Ex^{ch} \quad (7)$$

where Ex_{total} is the total exergy of the gas product (kJ/kg) and Ex^{ki}, Ex^{ep}, Ex^{ph}, and Ex^{ch} are the kinetic exergy, potential exergy, physical exergy, and chemical exergy, respectively. Previous studies have been reported that the values of the kinetic and potential exergies are very low and can be neglected [22]. Thus, the simplified total exergy can be written as:

$$Ex_{total} = Ex^{ph} + Ex^{ch} \quad (8)$$

The physical exergy can be calculated as:

$$Ex^{ph} = \sum_{i=1} n_i Ex_i^{ph} \quad (9)$$

where Ex_i^{ph} denotes the physical exergy of component i in the gas product, which can be obtained Eq. (10) [18,32].

$$Ex_i^{ph} = (h - h_0) - T_0(s - s_0) \quad (10)$$

where h_0 and s_0 are the specific enthalpy and entropy at the reference state.

$$h - h_0 = \int_{T_0}^{T} \bar{c}_p dT \quad (11)$$

and

$$s - s_0 = \int_{T_0}^{T} \frac{\bar{c}_p}{T} dT - R \ln \frac{P}{P_0} \quad (12)$$

where $\bar{c}_p$ is the specific heat capacity at constant pressure (kJ/kmol K). The coefficient of the heat capacity for each component can be obtained from [33], as shown in Table 3.

$$\bar{c}_p = a + bT + cT^2 + dT^3 \quad (13)$$

where a, b, c, and d are empirical coefficients.

The chemical exergy is similarly calculated as

$$Ex^{ch} = \sum_i n_i (ex_i^{ch} + RT_0 \ln y_i) \quad (14)$$

where ex_i^{ch} is the standard chemical exergy of gas component i as shown in Table 3 and y_i is the mole fraction of gas component i.

The feed exergy of the biomass is given by the correlation equation as below [34]:

$$Ex_{biomass} = \beta(\mathrm{LHV}_{biomass} + [\mathrm{MC}]h_w) + 9683[\mathrm{S}] + ex_{ash}[\mathrm{ASH}] + ex_{H_2O}[\mathrm{MC}] \quad (15)$$

Table 3
Specific enthalpy, specific entropy, standard chemical exergy, and higher heating value of the components at the dead state.

Component	Enthalpy, h_0 (kJ/kmol)	Entropy, s_0 (kJ/kmol K)	Exergy, ex_i^{ch} (kJ/kmol)	Higher heating value, HHV_i (kJ/kmol)	Empirical coefficients for specific heat capacities				Temperature range (K)
					a	$b \times 10^{-2}$	$c \times 10^{-5}$	$d \times 10^{-9}$	
H_2	8468	130.57	236,100	285,840	29.11	−0.19	0.40	−0.87	273–1800
CO	8669	197.54	275,100	282,990	28.16	0.17	0.53	−2.22	273–1800
CO_2	9364	213.69	19,870	–	22.26	5.98	−3.50	7.47	273–1800
CH_4	–	186.16	831,650	890,360	19.89	5.02	1.27	−11.01	273–1800
N_2	8669	191.50	720	–	28.90	−0.16	0.81	−2.87	273–1800
O_2	8682	205.03	3970	–	25.48	1.52	−0.72	1.31	273–1800
H_2O (g)	9904	188.72	9500	–	32.24	0.19	1.06	−3.60	273–1800
Air	–	69.94	900	–	28.11	0.20	0.48	−1.97	273–1800

where h_w is the evaporation enthalpy of moisture in the biomass, β is a correlation factor, which can be defined as Eq. (16). However, according to Eq. (15) the exergy of ash is neglected. This is due to there is relatively small effect on the total exergy.

$$\beta = \frac{1.0412 + 0.2160[H/C] - 0.2499[O/C]\{1 + 0.7884[H/C]\} + 0.0450[N/C]}{1 - 0.3035[O/C]}, \quad \text{for } [O/C] \leqslant 2.67 \tag{16}$$

$LHV_{biomass}$ is the lower heating value of the biomass in MJ/kg. This parameter is calculated from the following equation:

$$LHV_{biomass} = 425.73849\,[C] + 91.51107\,[H] - 199.15224\,[O] + 297.0116\,[S] \tag{17}$$

The mass percentages of the C, H, O, and S elements in the biomass can be obtained from ultimate analysis, as shown in Table 1. The relationship between the lower heating value (LHV) and the higher heating value (HHV) can be calculated using the following equation [35]:

$$HHV = LHV + 21.978\,[H] \tag{18}$$

The physical exergy of the biomass at the initial state is zero [20].

The physical exergy and chemical exergy of the gasification agent are evaluated using equation Eqs. (9) and (14). The physical exergy and the chemical exergy of air can be calculated from Eq. (19).

$$Ex^{ch}_{air} = m_{air/biomass}\left[ex^{ch}_{O_2} + 3.76 ex^{ch}_{N_2} + RT_o\{\ln y_{O_2} + \ln y_{N_2}\}\right] \tag{19}$$

where $m_{air/biomass}$ is the moles of air to mass of biomass ratio, $ex^{ch}_{O_2}$ and $ex^{ch}_{N_2}$ are the standard chemical exergies of oxygen and nitrogen, respectively, y_{O_2} and y_{N_2} are moles fraction of oxygen and nitrogen in air and R is the universal gas constant.

3.3. Energy and exergy efficiencies

The energy and exergy efficiencies of the product gas in a biomass gasification are calculated using the following equations:

$$\eta_E = \frac{E_{gas}}{E_{biomass} + E_{agent} + E_{methane}} \times 100\% \tag{20}$$

$$\eta_{Ex} = \frac{Ex_{gas}}{Ex_{biomas} + Ex_{agent} + Ex_{methane}} \times 100\% \tag{21}$$

The overall energy efficiency is defined as the ratio of the energy of the syngas at the output to the energy inputs which comprise the energy flow in with gasified fuels and agents. In addition, the energy efficiency of system is considered as follows:

$$\eta_{E,sys} = \frac{E_{gas}}{E_{Fuel} + Q_{sup}} \times 100\% \tag{22}$$

where Q_{sup} is the heat supplied in the preheating of gasifying agents and fuels. Similarly, the exergy efficiency of the overall system is presented as the following equations:

$$\eta_{Ex,sys} = \frac{Ex_{gas}}{Ex_{Fuel} + Ex_q} \times 100\% \tag{23}$$

where Ex_q is the exergy due to the heat transfer for each equipment and according to the following equation:

$$Ex_q = \left(1 - \frac{T_o}{T}\right) Q_{sup} \tag{24}$$

3.4. Exergoeconomic analysis

The cost balance for downdraft gasification operating at steady state is calculated by Eq. (25) [5,36,37].

$$\dot{C}_P = \dot{C}_F + \dot{Z}^T_k \tag{25}$$

where $\dot{C}_P$ is cost rate of the product stream ($/h), $\dot{Z}$ is sum of capital investment cost and the operating and maintenance costs of the system ($/h) of component k, and $\dot{C}_F$ is the cost rate of the feed stream ($/h), calculated from following equation.

$$\dot{C}_F = c\dot{E}x \tag{26}$$

where c is the unit exergy cost of the stream (heat, or work stream) at the inlet and outlet in the biomass gasification system and $\dot{E}x$ is the exergy rate.

The total cost rate of operation and maintenance can be obtained as follows ($\dot{Z}^T_k$) [38,39].

$$\dot{Z}^T_k = \dot{Z}^{CI}_k + \dot{Z}^{OM}_k \tag{27}$$

According to Eq. (27), the total operation and maintenance cost for the kth equipment in a gasification process is the sum of the capital investment cost ($\dot{Z}^{CI}_k$) and the hourly operating and maintenance cost ($\dot{Z}^{OM}_k$), which can be determined using Eqs. (28) and (29).

$$\dot{Z}^{CI}_k = \frac{\phi C\dot{A}^{CI}_{process}}{\tau} \frac{PEC}{\sum_{process} PEC_k} \tag{28}$$

$$\dot{Z}^{OM}_k = \frac{\phi C\dot{A}^{OM}_{process}}{\tau} \frac{PEC}{\sum_{process} PEC_k} \tag{29}$$

where $C\dot{A}^{CI}_{process}$ is the annual capital investment cost, $C\dot{A}^{OM}_{process}$ is the annual operating and maintenance costs, ϕ is the operating and maintenance factor, PEC is the purchased equipment cost, and τ is the annual operation time of equipment kth.

In Eqs. (28) and (29), the annualized capital cost ($C\dot{A}$) can be calculated using the capital recovery factor (CRF) and present worth (PW) of the process.

$$C\dot{A}_{process} = PW_{process} CRF \tag{30}$$

Using the interest rate i, the capital cost recovery factor (CRF) is

$$CRF = \frac{i(i+1)^n}{(1+i)^n - 1} \tag{31}$$

The present worth of the considered process (PW) is

$$PW_{process} = C - S_n PWF \tag{32}$$

where C is the initial investment cost of equipment.

The present worth factor (PWF) is

$$PWF = \frac{1}{(1+i)^n} \tag{33}$$

where i is the interest rate, n is the lifetime of the equipment in years, and S_n is the salvage value at the end of the equipment life. In this study, both the interest rate and salvage value are taken to be 10% [26]. The economic data based on the biomass gasification process and the criteria for calculating the operation annualized costs are shown in Tables 4 and 5. The annual labor cost estimation assumes fulltime operation [25,40].

The cost rate of fuel can be calculated using the following equation [41]:

$$\dot{C}_{Fuel} = \dot{m}\dot{c}_{Fuel} LHV_{Fuel} \tag{34}$$

Table 4
Economic analysis data.

Parameter	Value
Capital recovery period (yr)	25
Interest rate (%)	10
Annual operating time (h)	8000
Operating and maintenance factor	1

Table 5
Criteria for calculating the annualized operating and gasification agent and fuel costs.

Parameter	Value
Operating cost	
Labour[a] ($)	35,000
Catalyst[b]	2
Interest[b]	10
Insurance[b]	3
Maintenance[b]	10
Overheads/other[b]	1
Gasification agent and fuel cost	
Air	–
Water ($/t)	4.59
Methane ($/GJ)	3.04
Biomass ($/GJ)	2.00

[a] Full-time operation.
[b] % of capital cost investment.

where LHV_{Fuel} is the lower heating value of fuels (biomass and methane). The lower heating value of the methane is 50,050 kJ/kg [42], while the lower heating value of biomass can be calculated from Eq. (17).

The unit cost of gasification agents, including air and steam, are shown in Table 5 [24,25]. The unit of methane cost is taken from the U.S. Energy Information Administration as 3.04 $/GJ (as of 10 August 2016) [43]. The unit cost of biomass and water obtained from literatures are 2 $/GJ and 4.59 $/t, respectively [26,27].

The total capital investment cost of equipment in each system depends on the size and capacity of the equipment. Thus, the rule of six-tenths method was applied for calculating the total capital investment cost, which is given by:

$$C_i = C_0\left(\frac{S_i}{S_0}\right)^f \tag{35}$$

where C_i is actual cost of component, C_0 is the reference cost having size S_0, and f is scaling factor. The scaling factor is commonly used in the range of 0.3–1. In this work, the value of scaling factor assumed to be 0.6 [44]. Additionally, not only the size and capacity of equipment have effect on the total capital investment cost, but also the reference year should be regarded. The cost at the reference year can be calculated from the Chemical engineering Plant cost index (CEPCI). In this study, the reference year was 2016. The cost at reference year can be obtained as the following equation:

$$\text{Cost at the reference year} = \text{Original cost} \times \left(\frac{\text{CI for reference year}}{\text{CI when original cost was obtained}}\right) \tag{36}$$

The values of CI are 390.6, 395.6 and 536.5 for years 1999, 2002, and 2016, respectively [45]. The case-based cost of gasifier and heater were adapted from previous work [46].

3.5. Model validation

The rubber wood chips as biomass and an air gasification agent are fed into a downdraft gasifier to produce the syngas. The downdraft gasification for syngas production was validated with the experimental data of Jayah et al. [28]. The ultimate and proximate analyses of the biomass fuel are given in Table 1. The operating conditions of the biomass gasification process for the validation of the model are included in Table 6. Table 7 shows the predicted syngas composition, including hydrogen, carbon monoxide, carbon dioxide, and methane, compared the experimental data at the equivalence ratios of 0.35 and 0.38 [28]. It can indicate that the results from the model and experiment are in good agreement.

Table 6
Gasification operating conditions.

Gasification conditions	Values
Biomass flow rate (kg/h)	27.38
Equivalence ratio (–)	0.35, 0.38
Gasification pressure (bar)	1.01
Gasification temperature (K)	1000.00

Table 7
Simulation and experimental results for rubber wood gasification.

Syngas composition (% vol)	Experimental		Model data	
	ER (0.35)	ER (0.38)	ER (0.35)	ER (0.38)
H_2	19.60	20.20	20.86	21.31
CO	17.20	18.30	21.04	20.83
CO_2	9.90	9.70	10.07	9.70
CH_4	1.40	1.10	0.09	0.04

4. Results and discussion

4.1. Gasification of biomass

4.1.1. Influence of the preheating temperature of the gasification agent and equivalence ratio on the syngas composition

The influences of the equivalence ratio (ER) and preheating temperature on the syngas composition are illustrated in Fig. 2(a)–(d). In this study, the inlet mass flow rate of biomass to the gasifier is 266.7 kg/h. The preheating temperature was varied from 100 to 1000 °C, while the equivalence ratio (ER) was studied in the range of 0.15 –0.45. Fig. 2(a) shows the effects of the preheating temperature and ER on hydrogen production. As seen, increasing the preheating temperature can enhance hydrogen production and decrease methane and carbon dioxide production. This is because the char gasification reaction (R1), Boudouard reaction (R3), and methane shift reaction (R6) as endothermic reactions are favoured at higher preheating temperatures. Additionally, the carbon monoxide content gradually increases from 19.88% to 22.88% as the preheating temperature is elevated from 100 to 1000 °C.

The ER is the ratio of the air flow supplied relative to the air flow needed for the stoichiometric complete combustion of the biomass. From Fig. 2(a)–(d), the yield of hydrogen slightly increases upon increasing the ER from 0.15 to 0.21. However, increasing the ER from 0.21 to 0.45 causes the yield of hydrogen to be reduced from 24.11% to 9.66%. The increment of the ER over 0.21 provides excess air to the system, resulting in the enhancement of the char partial oxidation (R4) and hydrogen partial oxidation (R8) reactions. Thus, the composition of the combustible gases, including hydrogen, carbon monoxide, and methane, are diminished as the ER is raised (see Fig. 2(b)–(d)). For the content of carbon dioxide in product gas, the carbon dioxide can be produced from the char combustion reaction (R5). However, the content of the carbon dioxide decreases at higher ER, resulting from carbon dioxide consumed in the Boudouard reaction (R3). It can be explained that the

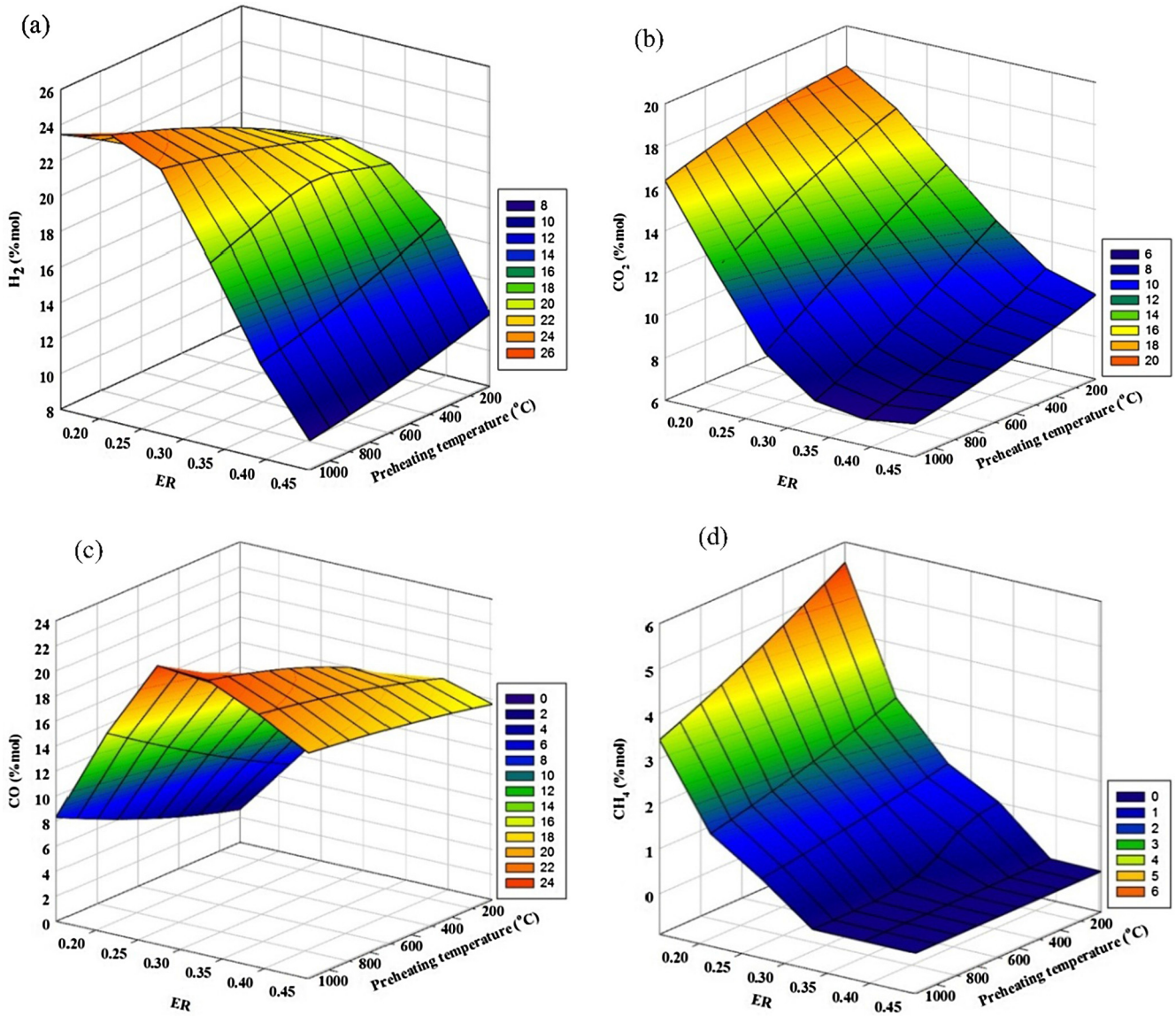

Fig. 2. Influences of preheating temperature and ER on (a) hydrogen, (b) carbon monoxide, (c) carbon dioxide, and (d) methane fractions.

increasing of the ER raises the oxidation and combustion taken place in the gasification process. This leads to the increase in the temperature of the biomass gasification system due to the biomass gasification as adiabatic process. Therefore, the increase in the ER drives the Boudouard reaction (R3) as the endothermic reaction in forward direction. Simultaneously considering the effects of the preheating temperature and the equivalence ratio, the maximum hydrogen production that can be achieved is 24.11% at the preheating temperature of 1000 °C and ER of 0.21.

4.1.2. Influence of the steam to biomass ratio on the syngas composition

The addition of steam to biomass gasification can enhance the hydrogen yield. Therefore, the influence of additional steam on the product composition was studied in this section. The optimum preheating temperature and ER are 1000 °C and 0.21, respectively. Fig. 3 presents the additional steam to biomass ratio from 0 to 2.0 at a preheating temperature of 1000 °C and an ER of 0.21. In the steam to biomass ratio (S/B) range of 0–1.0, the hydrogen, carbon

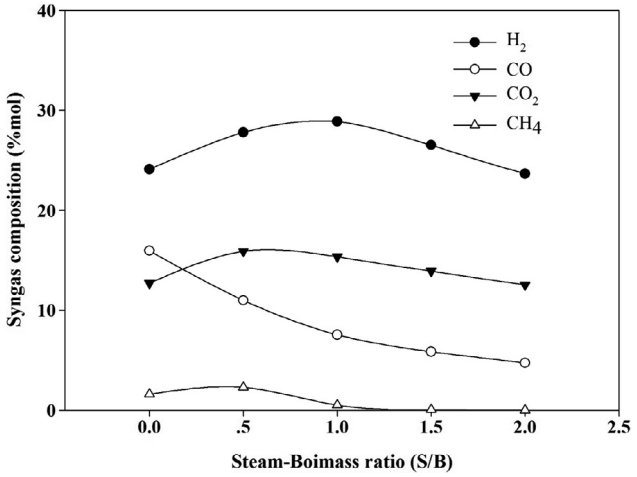

Fig. 3. Influence of steam to biomass ratio on syngas composition at ER = 0.21, T = 1000 °C.

Table 8
Influence of air and steam gasification agents and methane co-feeding on product gas composition.

Cases	Gasification agents	Fuels	Gas composition (mol/kg biomass)			
			H_2	CO	CO_2	CH_4
A	Air	Biomass	23.26	15.48	12.22	1.53
A + S	Air-steam	Biomass	46.82	12.29	24.84	0.78
A + M	Air	Biomass with methane co-feeding	49.07	16.54	11.55	10.04
A + S + M	Air-steam	Biomass with methane co-feeding	67.31	14.06	25.46	14.81

dioxide and methane increase, whereas the carbon monoxide decreases. This can be explained by steam driving the char gasification (R1), methane shift (R6), and water gas shift (R7) reactions. In the char gasification, the solid carbon reacts with steam to form hydrogen and carbon monoxide, leading to the enhancement of the hydrogen yield. In addition, the methane produced in the gasification chamber can be reacted with the steam to produce the hydrogen and carbon monoxide in the syngas product from the methane shift reaction (R6). However, the carbon monoxide content in the syngas is decreased with increasing S/B owing to the water gas shift reaction. In the S/B range of 1.0–2.0, it can be observed that the component contents of hydrogen, carbon monoxide, carbon dioxide, and methane decrease. This is because the introduction of excessive steam to the biomass gasification results in the decrease in the reaction temperature, leading to the reduction in the syngas contents in product gas. Moreover, the decrease in all components in the product also arises from the dilution due to the excessive steam in the biomass gasification. Thus, the optimum ratio of steam to biomass at the maximum yield of hydrogen is 1.0.

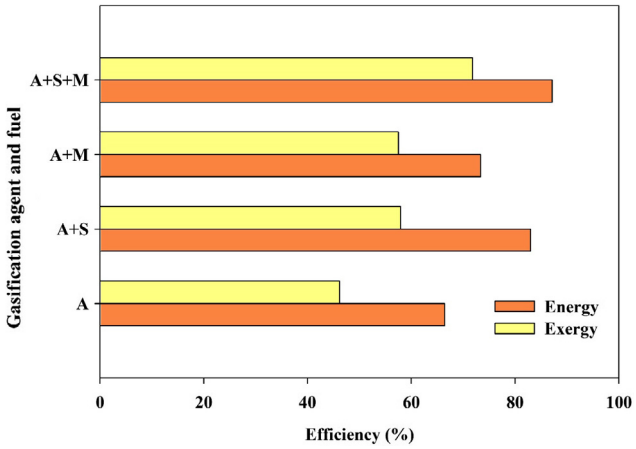

Fig. 4. Energy and exergy efficiencies of biomass gasification using various gasification agents and methane co-feeding; A (air), S (steam), and M (methane).

4.2. Gasification of biomass at different gasifying agents with and without methane co-feeding

4.2.1. Influence of different gasifying agents with and without methane co-feeding on H_2/CO ratio

In this section, the influence of the use of air and/or steam as the gasifying agent with the co-feeding of methane on the yield of the gas product was studied. The various gasifying agents in four cases are used at a preheating temperature of 1000 °C and equivalence ratio of 0.21. The steam and methane to biomass ratios were set to 1.0 and 0.36 kg/kg biomass, respectively. Table 8 compares the product gas compositions using different agents in biomass gasification with and without methane co-feeding. The various gasifying agents are divided into four cases: air (A), air with methane co-feeding (A + M), air and steam (A + S), and air and steam with methane co-feeding (A + S + M). It can be observed that utilizing a mixture of air and steam as a gasifying agent can improve the syngas quality compared to the case of using air alone, without methane co-feeding. This is because the oxygen content in the air provides the energy for exothermic reactions in biomass gasification. The addition of steam also has the effect of driving the water gas shift reaction (R7), resulting in increases in the hydrogen and carbon dioxide contents. The hydrogen production can be also increased with adding steam from the char gasification reaction (R1).

In addition, the influence of the C species of CH_4 can be divided to two cases: the air as gasification agent with co-feeding of methane (A + M) and air-steam with co-feeding of methane (A + S + M). Firstly, the Boudouard (R3) and char partial oxidation (R4) reactions can occur when using the methane co-feeding with biomass for the gasification with air. This result leads to the increase in the carbon monoxide, whereas the concentration of carbon dioxide becomes lower. Secondly, when using steam with methane co-feeding, the contents of hydrogen and carbon monoxide increase as a result of the char gasification (R1) and methane shift reaction (R6) reactions. Furthermore, the carbon dioxide and hydrogen are increased by the reaction between carbon monoxide and steam from the water gas shift (R7). The mixture of air and steam as an agent with methane co-feeding can enhance the hydrogen yield from 23.26 to 67.31 mol/kg biomass.

4.2.2. Influence of different gasifying agents with and without methane co-feeding on system performance

The performances of biomass gasification processes are indicated by the energy and exergy efficiencies. The total energy can be determined from the physical and chemical energy. Physical energy is the change of enthalpy from the environmental state, while the chemical energy values of the product gases are evaluated from Eq. (5). The energy efficiency is the ratio of energy outputs to energy inputs.

A comparison of the energy and exergy efficiencies of different gasifying agents for biomass gasification is illustrated in Fig. 4. From Fig. 4, the exergy efficiency is lower than the energy efficiency because the entropy occurred in the system is taken into consideration of exergy efficiency. The range of energy efficiency of the product gas with various gasifying agents is 66.41–87.14%. The air-steam with co-feeding of methane has the highest energy efficiency of the product gas because of the high yields of hydrogen, carbon dioxide, and methane in this case.

According to the second law of thermodynamics, the exergy efficiency in the product gas can be investigated using Eq. (21), which is the work output compared to the potential of the input to do work. As can be seen Fig. 4, the exergy efficiency shows similar trend with the energy analysis. The exergy efficiency of product gas is 46.16%, 57.90%, 57.52% and 71.80% for air (A), air with methane co-feeding (A + M), air and steam (A + S), and air and steam with methane co-feeding (A + S + M), respectively. The use of air-steam as a gasifying agent with methane co-feeding shows the highest exergy efficiency. This is because this case produces the highest yields of hydrogen of all of the agents as shown in

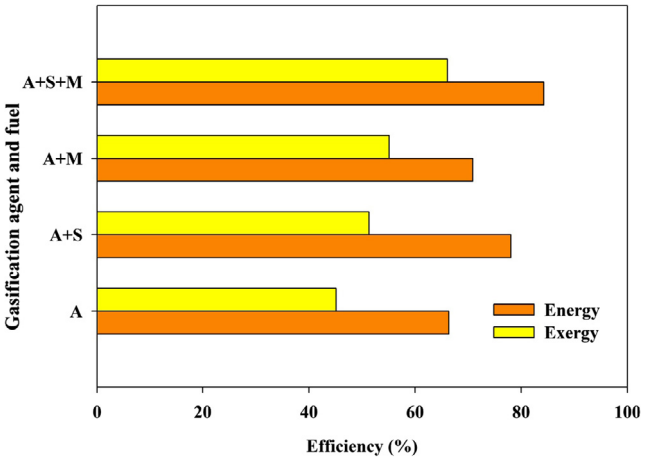

Fig. 5. Overall energy and exergy efficiencies of biomass gasification using various gasification agents and methane co-feeding; A (air), S (steam), and M (methane).

Table 8. The increased amount of syngas product in the process can improve the chemical exergy as well and thereby the total exergy.

The addition of steam and methane to the gasifier requires more energy consumption for the preheating. Thus, the energy and exergy efficiencies of the overall system using various gasification agents and methane co-feeding should be considered. Fig. 5 shows the overall energy and exergy efficiencies of A, A + S, A + M, and A + S + M, which are in the range of 66.36–84.25% for energy efficiency and in the range of 45.12–66.12% for exergy efficiency. The results indicate that the tendencies of the overall energy and exergy efficiencies are the same as the energy and exergy efficiencies of product gas. The air-steam co-feeding of methane also has the highest energy and exergy efficiencies of the overall system. This result indicates that the increment of energy consumption for the preheating of steam and methane has less influence on the energy and exergy efficiencies of overall system.

4.3. SPECO analysis

The specific exergy cost (SPECO) was used to calculate the hydrogen unit costs using the exergy-related costs in thermal systems. In this study, the unit costs of the four cases using different gasifying agents with and without methane co-feeding were obtained. To calculate the cost rate of the input stream, the exergy of the steam input in Section 4.2 was used. The mass flow rate, temperature, pressure, unit cost rate, and cost rate of the input stream are given in Table 9. It can be seen that the exergy rate stream has a direct effect on its cost rate. From Table 9, the cost rate of biomass and methane as fuel are higher than that of the gasifiying agent due to the high exergy rate of the biomass and methane streams.

For the capital investment cost, the main equipment in the biomass gasification process, including the downdraft gasifier and heat exchanger, were calculated using Eqs. (27)–(33). An interest rate of 10% was specified. Therefore, the CRF can be determined using Eq. (31) and a value of 0.11. Consequently, the purchased equipment, operation and maintenance, and total costs of the biomass gasification and its components are shown in Table 10. The results were found that the cost rate of the capital investment cost is lower than operating and maintenance cost. The largest cost rate of capital investment, operating, and maintenance are the gasifier about 53% of total cost rate of the process. Considering the cost rate of the heaters, which are used to preheat the gasifying agents and fuels, the cost rate of heater (Heat Ex 2) for preheating of steam is higher than that for preheating the air and methane (Heat Ex 1 and Heat Ex 3). This can be described that the preheating of steam needs more energy than air and methane at the same temperature. In addition, the operating cost rate depends on the several parameters such as the labor cost, catalyst, interest rate, maintenance, and other. Also, the interest and maintenance mainly affect the operating and maintenance cost rate.

Fig. 6 displays the total cost rate of capital investment, operation and maintenance, fuel, and gasifying agent of various gasification agents with and without methane co-feeding. It can be observed that the mixture of air and steam as an agent with

Table 9
Exergy and cost rate of input stream components.

Stream	Mass flow rate (kg/s)	Temperature (K)	Pressure (kPa)	$\dot{E}x$ (MW)	c ($/GJ)	$\dot{C}$ ($/h)
Biomass	0.074	298.15	101.325	1.63	1.78	10.45
Air	0.097	298.15	101.325	–	–	–
Water	0.074	298.15	101.325	0.04	8.47	1.22
Methane	0.027	298.15	101.325	1.40	2.90	14.61
Pre-air	0.097	1273.15	101.325	0.07	23.33	5.53
Pre-steam	0.074	1273.15	101.325	0.13	27.52	12.64
Pre-methane	0.027	1273.15	101.325	1.46	3.80	20.03

Table 10
Purchased equipment, operating and maintenance, and total costs of the biomass gasification.

Capital investment	*PEC* ($)	*PEC*%	$\dot{Z}_k^{CI}$ ($/h)	$\dot{Z}_k^{OM}$ ($/h)	$\dot{Z}_k^{T}$ ($/h)
Gasifier	501228.16	0.53	6.84	18.62	25.46
Heat Ex 1	106763.99	0.11	1.46	3.97	5.42
Heat Ex 2	224773.40	0.24	3.07	8.35	11.42
Heat Ex 3	108653.02	0.12	1.50	4.04	5.53
Total	941418.57	1.00	12.86	34.97	47.83
Operation ($/yr)					
Labor cost	35000.00				
Catalyst	18828.37				
Interest	94141.86				
Insurance	28242.56				
Maintenance	94141.86				
Overheads/other	9414.19				
Total	279768.83				

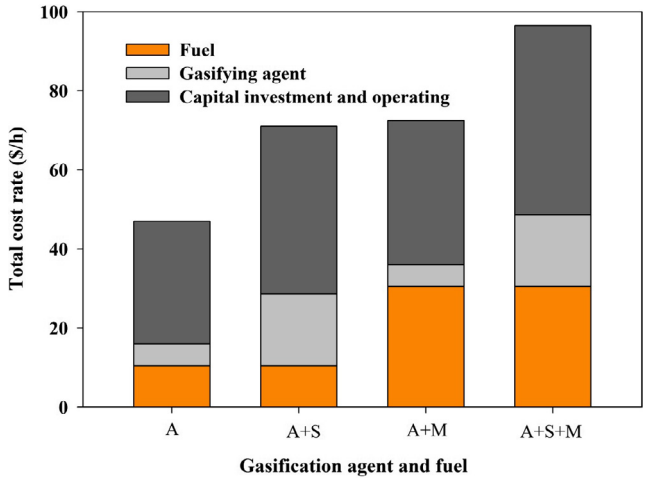

Fig. 6. Total cost rate of fuel, gasifying agent and capital investment and operation and maintenance using various gasification agents.

methane co-feeding (A + M + S) is highest of total cost rate. This is due to a high cost of the heater that is used to preheat the gasifying agent and fuel. Moreover, the cost rate of operation and maintenance in case of the using air-steam as a gasification agent is higher than that of using only air as a gasification agent. This situation can be described that the steam production consumes the energy more than the preheating of air and methane. The cost rate of the preheating temperature for steam is higher than that for air and methane about 16.47 and 36.85%, respectively.

In addition, the cost rates of fuel have also directly effect on the cost of hydrogen production. The case of air and steam as an agent with methane co-feeding is the highest of the cost rate for fuel cost because of the price of methane. Comparing to the gasifying agent for all case study, the cost rate of steam also prominent when compare with air. As a result, it can be indicated that the total cost rate of air-steam as an agent with methane co-feeding gives the highest total cost rate. In comparison to using air as the gasification agent, the total cost rate of using only air as an agent without methane co-feeding are lower than those of the cases of a mixture of air and steam (A + S) and air with methane co-feeding (A + M). The total cost rate of four cases are 46.98, 71.43, 72.41, and 96.43 $/h for air (A), air and steam (A + S), air with methane co-feeding (A + M) and air-steam as an agent with methane co-feeding (A + S + M).

Table 11 shows the costs of hydrogen using different gasification agents. The cost of hydrogen production can be estimated from the cost balance at steady state from Eqs. (25) and (26). The values of the cost of hydrogen in the four cases are evaluated as 3.79, 2.84, 2.77, and 2.69 $/kg for air (A), air and steam (A + S), air with methane co-feeding (A + M), and air-steam with methane co-feeding (A + S + M), respectively. As mentioned above, the use of air as a gasification agent gives the highest cost of hydrogen production. Nevertheless, the total cost rates of the capital investment as well as the operation and maintenance are the lowest, as seen in Fig. 6. This is mainly due to the low hydrogen yield produced from the gasifier (see Table 8). The cost can be reduced by increasing the hydrogen content in the syngas. Thus, the use of air-steam with methane co-feeding (A + S + M) gives the lowest cost of hydrogen because it has the maximum mass flow rate of hydrogen of 26.17 kg/h.

Table 11
Unit hydrogen costs from different gasifying agents and methane co-feeding.

Gasification agent	A	A + S	A + M	A + S + M
$\dot{Z}_k^T$ ($/h)	30.99	42.41	36.41	47.83
$\dot{C}_{Biomass}$ ($/h)	10.45	10.45	10.45	10.45
$\dot{C}_{Air}$ ($/h)	5.53	5.53	5.53	5.53
$\dot{C}_{Water}$ ($/h)	–	12.64	–	12.64
$\dot{C}_{Methane}$ ($/h)	–	0.00	20.03	20.03
$\dot{C}_T$ ($/h)	46.98	71.03	72.43	96.48
H_2 (kg/h)	12.40	24.98	26.18	35.90
C_{H_2} ($/kg)	3.79	2.84	2.77	2.69
C_{H_2} ($/kWh)	0.096	0.072	0.070	0.068

Table 12
Unit hydrogen cost from different studies.

Unit hydrogen cost ($/kg)	Energy source	Process	Reference
1.50[a], 3.57[b]	Natural gas	Steam reforming of natural gas	[47]
1.36	Coal	Coal gasification	[48]
3.50	Wind	Electrolysis	[49]
5.10[c]	Solar	Power tower electrolysis	[50]
2.69	Biomass and methane	Biomass air-steam gasification with methane co-feeding	This study

[a] Capacity of 1.2 Gg/day.
[b] Capacity of 500 kg/day.
[c] Based on electrolyzer cost of 500 $/kW.

In this section, the unit hydrogen production cost via different process was compared, which is the non-renewable and renewable energy sources. The non-renewable energies are the reforming of natural gas and coal gasification processes. Also, the alternative or renewable energies for the hydrogen production are electrolysis and power tower electrolysis processes [47–50]. From Table 12, it indicates that the cost of hydrogen production via the steam reforming of natural gas, which is conventional process, in the small scale (500 kg/day) is higher than that via the biomass air-steam gasification with methane co-feeding. In contrast, the hydrogen cost from the biomass air-steam gasification with methane co-feeding is not competitive with the steam reforming of natural gas process at large-scale facility (1.2 Gg/day). For coal gasification, the cost of the hydrogen production is the lowest because of a low price of the feedstock. Although the hydrogen production cost via coal gasification process is the cheapest, using coal as fuel can lead to serious environmental impacts.

Apart from the hydrogen production from the thermal process, the water electrolysis combined with wind or solar energy resource to produce hydrogen is also considered. The hydrogen production costs from these technologies are still currently high priced. The cost of hydrogen production from the water electrolysis combined with wind resource is 3.50 $/kg which is not included the capital cost of turbine. For the hydrogen cost from the water electrolysis combined with solar resources, this process is the highest production cost per kilogram of hydrogen (5.10 $/kg), when compared to the other sources. The cost of hydrogen production from the water electrolysis combined with the solar energy is more than 1.89 times the biomass air-steam gasification with methane co-feeding. It is clear that the hydrogen production cost via solar energy is not competitive in this time and needs to be developed for completion in the future. As mentioned in Table 12, it can be concluded that the hydrogen production costs from this study are practically application in the area of hydrogen production.

Also, in order to reduce the cost of the hydrogen production and increase the efficiency of the system, some researcher has been conducted the hydrogen and power production to reduced cost of hydrogen production [27]. The hydrogen cost from such system of 1.16 $/kg for biomass gasification process. Kohl et al. [51] investigated the performance of three different biomass upgrading process (wood pellets, torrefied wood pellets, and fast pyrolysis slurry) with a combined heat and power plant. They reported that the

exergetic efficiencies of the system are improved. In addition, as mention before, the operation of the biomass with air-steam as agent with methane co-feeding in the large scale process similar to reforming of natural gas may reduce the hydrogen production cost.

5. Conclusions

The hydrogen production from biomass gasification using different gasifying agent and adding methane as co-feeding studied though energy, exergy, and economic analysis has been presented. The effects of the operating parameters of biomass gasification without methane co-feeding i.e., preheating temperature, equivalence ratio, and steam to biomass, were studied in the first part. The simulation results showed that increasing the preheating temperature of the gasification agent and fuel can positively affect the hydrogen product. The equivalence ratio (ER) is affected to biomass gasification process comprising syngas compositions. High ER leads to decrease in the hydrogen yield of product gas. Additionally, the hydrogen content in syngas can be enhanced with adding steam to the biomass gasification. However, the excessive steam results in the dilution of syngas product. Considering the effect of using methane co-feeding, the addition of methane to the air-steam biomass gasification can raise the hydrogen yield and steam to the gasifier requires higher energy input, the air-steam biomass gasification with methane co-feeding achieves the highest energy and exergy efficiencies of product gas at 87.14% and 71.80%, respectively.

Considering the overall system, the overall energy and exergy efficiencies in case of the air-steam biomass gasification with methane co-feeding are also higher than other cases. It has been shown that the increment of hydrogen yield in case of adding methane and steam into the biomass gasification has significant impact on the increase in the energy and exergy efficiencies in spite of higher energy input. In the exergoeconomic analysis, the SPECO method was obtained to estimate the unit cost of hydrogen. According to the results of hydrogen unit cost, the air-steam biomass gasification with methane co-feeding provides the lowest hydrogen production cost of 2.69 $/kg which is practically application in the area of hydrogen production. Moreover, the hydrogen unit cost of the biomass air-steam gasification with methane co-feeding is lower than that of the steam reforming of natural gas in the small scale which is the conventional process of hydrogen production. Therefore, the air-steam biomass gasification with methane co-feeding is an attractive process for the hydrogen production.

Acknowledgements

The authors would like to express their gratitude for financial support from Burapha University (No. 152/2559) and the Thailand Research Fund (No. DPG5880003).

References

[1] Chum HL, Overend RP. Biomass and renewable fuels. Fuel Process Technol 2001;71:187–95.
[2] Panagiotopoulos IA, Karaoglanoglou LS, Koullas DP, Bakker RR, Claassen PAM, Koukios EG. Technical suitability mapping of feedstocks for biological hydrogen production. J Clean Prod 2015;102:521–8.
[3] Abuşoğlu A, Demir S, Özahi E. Energy and economic analyses of models developed for sustainable hydrogen production from biogas-based electricity and sewage sludge. Int J Hydrogen Energy 2016;41:13426–35.
[4] Nguyen TLT, Hermansen JE, Nielsen RG. Environmental assessment of gasification technology for biomass conversion to energy in comparison with other alternatives: the case of wheat straw. J Clean Prod 2013;53:138–48.
[5] Rahman MM, Mostafiz SB, Paatero JV, Lahdelma R. Extension of energy crops on surplus agricultural lands: a potentially viable option in developing countries while fossil fuel reserves are diminishing Renew Sustain. Renew Energy 2014;29:108–19.
[6] Zhang L, Xu C, Champagne P. Overview of recent advances in thermo-chemical conversion of biomass. Energy Convers Manage 2010;51:969–82.
[7] Sharma S, Sheth PN. Air–steam biomass gasification: experiments, modeling and simulation. Energy Convers Manage 2016;110:307–18.
[8] Caputo AC, Palumbo M, Pelagagge PM, Scacchia F. Economics of biomass energy utilization in combustion and gasification plants: effects of logistic variables. Biomass Bioenergy 2005;28:35–51.
[9] Tozlu A, Özahi E, Abuşoğlu A. Waste to energy technologies for municipal solid waste management in Gaziantep. Renew Sustain Energy Rev 2016;54:809–15.
[10] Skoulou VK, Efthymio K, Stylianos A, Yang W, Zabaniotou A. Effect of biomass leaching on H_2 production, ash and tar behavior during high temperature steam gasification (HTSG) process. Int J Hydrogen Energy 2009;34(14):5666–73.
[11] Guangul FM, Sulaiman SA, Ramli A. Gasifier selection, design and gasification of oil palm fronds with preheated and unheated gasifying air. Bioresource Technol 2012;126:224–32.
[12] Li XT, Grace JR, Lim CJ, Watkinson AP, Chen HP, Kim JR. Biomass gasification in a circulating fluidized bed. Biomass Bioenergy 2004;26(2):171–93.
[13] Parthasarathy P, Narayanan KS. Hydrogen production from steam gasification of Biomass: influence of process parameters on hydrogen yield – a review. Renew Energy 2014;66:570–9.
[14] Aaron WP, Erica LJ, Jeni C, Alan WW. Co-processing methane in high temperature steam gasification of biomass. Bioresource Technol 2012;128:553–9.
[15] Pantaleo AM, Camporeale S, Shah N. Natural gas–biomass dual fuelled microturbines: comparison of operating strategies in the Italian Residential Sector. Appl Therm Eng 2014;71(2):686–96.
[16] Wang J, Tianzhi M, Jun S, Hongguang J. Modeling and performance analysis of CCHP (Combined Cooling, Heating and Power) system based on co-firing of natural gas and biomass gasification gas. Energy 2015;93:801–15.
[17] Ometto AR, Roma WNL. Atmospheric impacts of the life cycle emissions of fuel ethanol in Brazil: based on chemical exergy. J Clean Prod 2010;18(1):71–6.
[18] Iribarren D, Susmozas A, Petrakopoulou F, Dufour J. Environmental and exergetic evaluation of hydrogen production via lignocellulosic biomass gasification. J Clean Prod 2014;69:165–75.
[19] Hosseini M, Dincer I, Rosen MA. Steam and air fed biomass gasification: comparisons based on energy and exergy. Int J Hydrogen Energy 2012;37(21):16446–52.
[20] Zhang Y, Li B, Li H, Liu H. Thermodynamic evaluation of biomass gasification with air in autothermal gasifiers. Thermochim Acta 2011;519(1–2):65–71.
[21] Abuadala A, Dincer I, Naterer GF. Exergy analysis of hydrogen production from biomass gasification. Int J Hydrogen Energy 2010;35:4981–90.
[22] Zhang Y, Zhao Y, Gao X, Li B, Huang J. Energy and exergy analyses of syngas produced from rice husk gasification in an entrained flow reactor. J Clean Prod 2015;95:273–80.
[23] Loha C, Chattopadhyay H, Chatterjee PK. Thermodynamic analysis of hydrogen rich synthetic gas generation from fluidized bed gasification of rice husk. Energy 2011;36:4063–71.
[24] Lazzaretto A, Tsatsaronis G. SPECO: a systematic and general methodology for calculating efficiencies and costs in thermal systems. Energy 2006;31:1257–89.
[25] Lv P, Yuan Z, Ma L, Wu C, Chen Y, Zhu J. Hydrogen-rich gas production from biomass air and oxygen/steam gasification in a downdraft gasifier. Renew Energy 2007;32(13):2173–85.
[26] Abuadala A, Dincer I. Exergoeconomic analysis of a hybrid system based on steam biomass gasification products for hydrogen production. Int J Hydrogen Energy 2011;36:12780–93.
[27] Kalinci Y, Hepbasli A, Dincer I. Exergoeconomic analysis and performance assessment of hydrogen and power production using different gasification systems. Fuel 2012;102:187–98.
[28] Jayah TH, Aye L, Fuller RJ, Stewart DF. Computer simulation of a downdraft wood gasifier for tea drying. Biomass Bioenergy 2003;25:459–69.
[29] Zhang X, Li H, Liu L, Zeng R, Zhang G. Analysis of a feasible trigeneration system taking solar energy and biomass as co-feeds. Energy Convers Manage 2016;122:74–84.
[30] Naveed R, Ashraf A, Naveed S, Malik A. Simulation of hybrid biomass gasification Using Aspen plus: a comparative performance analysis for food, municipal solid and poultry waste. Biomass Bioenergy 2011;35:3962–9.
[31] Tapasvi D, Kempegowda RS, Tran KQ, Skreiberg O, Gronli M. A simulation study on the torrefied biomass gasification. Energy Convers Manage 2015;90:446–57.
[32] Zhang Y, Li B, Li H, Zhang B. Exergy analysis of biomass utilization via steam gasification and partial oxidation. Thermochim Acta 2012;538:21–8.
[33] Cengel YA, Boles MA. Thermodynamics: an engineering approach. 6th ed. New York: Mc Graw Hill Companies, Inc.; 2008.
[34] Szargut J, Morris DR, Stewart FR. Exergy analysis of thermal, chemical, and metallurgical processes. 1st ed. Edwards Brothers, Inc.; 1988.
[35] Bilgen S, Kaygusuz K, Sari A. Second law analysis of various types of coal and woody biomass in Turkey. Energy Source 2004;26(11):1083–94.
[36] Wang J, Mao T. Cost allocation and sensitivity analysis of multi-products from biomass gasification combined cooling heating and power system based on

the exergoeconomic methodology. Energy Convers Manage 2015;105 (4811):230–9.
[37] Yılmaz C, Kanoğlu M, Abuşoğlu A. Exergetic cost evaluation of hydrogen production powered by combined flash-binary geothermal power plant. Int J Hydrogen Energy 2015;40:14021–30.
[38] Yılmaz C, Kanoğlu M, Abuşoğlu A. Thermoeconomic cost evaluation of hydrogen production driven by binary geothermal power plant. Geothermics 2015;57:18–25.
[39] Soltani S, Mahmoudi SMS, Yari M, Morosuk T, Rosen MA, Zare V. A comparative exergoeconomic analysis of two biomass and co-firing combined power plants. Energy Convers Manage 2013;76:83–91.
[40] Gim B, Yoon WL. Analysis of the economy of scale and estimation of the future hydrogen production costs at on-site hydrogen refueling stations in Korea. Int J Hydrogen Energy 2012;37(24):19138–45.
[41] Memona AG, Memona RA, Harijan K, Uqaili MA. Parametric based thermo-environmental and exergoeconomic analyses of a combined cycle power plant with regression analysis and optimization. Energy Convers Manage 2015;92:19–35.
[42] Memon AG, Memon RA, Harijan K, Uqaili MA. Thermo-environmental analysis of an open cycle gas turbine power plant with regression modeling and optimization. J Energy Inst 2014;87:81–8.
[43] Unit Methane cost. <http://www.eia.gov/dnav/ng/ng_pri_sum_dcu_nus_m.htm>; 2016 [accessed 10.08.2016].
[44] Kalinci Y, Hepbasli A, Dincer I. Exergoeconomic analysis of hydrogen production from plasma gasification of sewage sludge using specific exergy cost method. Int J Hydrogen Energy 2011;36(17):11408–17.
[45] Cost Index. Chemical engineering report features report Guidebook. <www.chemengonline.com>; 2016 [accessed 10.08.2016].
[46] Im-orb K, Simasatitkul L, Arpornwichanop A. Techno-economic analysis of the biomass gasification and Fischer-Tropsch integrated process with off-gas recirculation. Energy 2016;94:483–96.
[47] Williams RB, Kornbluth K, Erickson PA, Jenkins BM, Gildart M. Estimates of hydrogen production potential and costs from California Landfill Gas. In: proceedings of 15th European Biomass Conference and Exhibition, Berlin, Germany; May 7–11, 2007.
[48] Kreutz T, Williams R, Consonni S, Chiesa P. Co-production of hydrogen, electricity and CO_2 from coal with commercially ready technology. Part B: economic analysis. Int J Hydrogen Energy 2005;30:769–84.
[49] Bockris JO, Veziroglu TN. Estimates of the price of hydrogen as a medium for wind and solar sources. Int J Hydrogen Energy 2007;32:1605–10.
[50] Kolb GJ, Diver RB, Siegel N. Central-station solar hydrogen power plant. J Solar Energy Eng 2007;129:179–83.
[51] Kohl T, Teles M, Melin K, Laukkanen T, Järvinen M, Park SW. Exergoeconomic assessment of CHP-integrated biomass upgrading. Appl Energy 2015;156:290–305.

Available online at www.sciencedirect.com

ScienceDirect

journal homepage: www.elsevier.com/locate/he

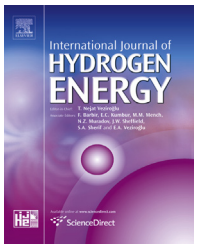

Analysis of thermally coupling steam and tri-reforming processes for the production of hydrogen from bio-oil

Kunlanan Wiranarongkorn [a], *Suthida Authayanun* [b], *Suttichai Assabumrungrat* [c], *Amornchai Arpornwichanop* [a,*]

[a] *Computational Process Engineering Research Unit, Department of Chemical Engineering, Faculty of Engineering, Chulalongkorn University, Bangkok 10330, Thailand*

[b] *Department of Chemical Engineering, Faculty of Engineering, Srinakharinwirot University, Nakhon Nayok 26120, Thailand*

[c] *Center of Excellence in Catalysis and Catalytic Reaction Engineering, Department of Chemical Engineering, Faculty of Engineering, Chulalongkorn University, Bangkok 10330, Thailand*

ARTICLE INFO

Article history:
Received 26 March 2016
Received in revised form
16 August 2016
Accepted 19 August 2016
Available online 15 September 2016

Keywords:
Bio-oil
Steam reforming
Tri-reforming
Thermal coupling
Hydrogen production

ABSTRACT

This paper presents the thermodynamic analysis of thermally coupling steam and tri-reforming processes using a bio-oil aqueous fraction for hydrogen production. The total energy efficiency is investigated to evaluate the overall performance of the proposed system. It is found that the operating temperature, steam-to-bio-oil feed (S/F) ratio and split ratio of waste gas recovery have a positive effect on hydrogen yield; the optimal values are as follows: operating temperature of the steam reforming, 650 °C; tri-reforming operating temperature, 580 °C; S/F ratio, 6; and split ratio, 0.5. However, an increase in such parameters increases the energy requirement for the steam reformer. The new proposed system combining thermally coupled steam and tri-reforming processes with a membrane water gas shift reactor offers higher energy efficiency than a conventional steam reforming process.

© 2016 Hydrogen Energy Publications LLC. Published by Elsevier Ltd. All rights reserved.

Introduction

Hydrogen is an important chemical that is widely used in the petroleum and chemical industries. It is considered a clean energy carrier and can be employed in fuel cells for electricity generation [1,2]. Presently, hydrogen is produced from fossil fuels, such as natural gas and coal, through thermo-chemical processes. However, due to environmental concerns and the limited availability of fossil fuels, it is advantageous to use renewable resources for hydrogen production, which could also limit greenhouse gas emissions [1–4].

Among the various renewable energy sources that have potential use in hydrogen production, bio-oil obtained from a biomass pyrolysis process has received considerable attention. Bio-oil is derived from plants that use CO_2 for their growth; this has positive effects, including CO_2 balance and the easy transport and storage of liquid fuel. In general, bio-oil

* *Corresponding author*. Fax: +66 2 218 6877.
E-mail address: Amornchai.A@chula.ac.th (A. Arpornwichanop).

http://dx.doi.org/10.1016/j.ijhydene.2016.08.148

0360-3199/© 2016 Hydrogen Energy Publications LLC. Published by Elsevier Ltd. All rights reserved.

consists of a complex mixture of oxygenated compounds, depending on the biomass feedstock and the fast pyrolysis technology used. The major components of bio-oil are acid, alcohol, ketone, aldehyde and phenol [5–7]. Bio-oil can be separated into an aqueous fraction and an organic fraction by adding water. The aqueous fraction of bio-oil contains light carbohydrate-derived compounds, including acetic acid, formic acid, hydroxylacetaldehyde, acetol and levoglucosan; these compounds can be easily converted to hydrogen [7]. The organic fraction of bio-oil contains lignin-derived compounds, which cause catalyst deactivation in a steam reforming process [8,9].

To date, hydrogen is primarily produced from a steam reforming process in which steam reacts with fossil fuels or biofuels at high temperatures to produce hydrogen rich gas [10,11]. This process involves a strongly endothermic reaction in the presence of reforming catalysts. For a conventional process, a portion of the fuel is combusted to generate heat for the steam reforming reaction, which requires the use of a huge fired furnace and results in low energy efficiency [12,13]. The use of bio-oil as a fuel for bio-oil combustion in a burner or furnace is not suitable because of bio-oil's high viscosity, high water content, poor volatility and corrosiveness [6,14]. Tzanetakis et al. [15] studied the spray combustion characteristics and emissions of 80% bio-oil blended with 20% ethanol in comparison to conventional fuel oils. They found that a bio-oil blend has a lower combustion efficiency than petroleum fuel oils.

A tri-reforming process is the combination of endothermic steam reforming, dry reforming, and exothermic partial oxidation. The advantage of the tri-reforming process is that heat produced by the exothermic oxidation reaction can be used to supply energy for the steam and dry reforming reactions. As the tri-reforming process utilizes CO_2, some researchers have studied its use with biogas feedstock to produce synthesis gas [16,17]. In addition, the tri-reforming process is a method for reducing CO_2 emissions in flue stack gases [18,19]. Because of the wide range of H_2/CO ratios in synthesis gas produced from a tri-reforming process, many studies have focused on finding the optimum H_2/CO ratios for synthesis of methanol and dimethyl ether via a methane tri-reforming process [19–22]. As the tri-reformer behaves as an exothermic reactor under some operating conditions, it can be integrated with a steam reformer for heat supply and additional hydrogen production [23]. Consequently, the efficiency of bio-oil steam reforming may be improved by using integrating both as reforming and tri-reforming via thermal coupling. Such an integrated process may decrease external heat requirements and result in an enhancement of hydrogen production. In addition, such an approach may also reduce environmental impact by using CO_2 as a co-reactant.

At present, the concept of coupling of endothermic and exothermic reactions has been applied to many processes. Bayat et al. [24] analyzed the two different configurations of exothermic-endothermic heat exchanger reactor for methanol production; the necessary heat for the endothermic methanol synthesis reaction was provided by the catalytic dehydrogenation of cyclohexane. The result revealed that the thermally coupling process increases the methanol production rate in comparison with a conventional process. Karimipourfard et al. [25] studied the integrated thermal coupling of endothermic steam reforming and dehydrogenation reaction, and exothermic methane oxidation for synthesis gas, hydrogen and propylene productions. The results proved that the thermally coupled reactor enhances the process in terms of the production rate, costs and energy efficiency. Bruschi et al. [26] investigated the thermal coupling of ethanol steam reforming and ethanol combustion in a microreformer for hydrogen production and found that the moderately high hydrogen yield was obtained. Mirvakili et al. [27] studied the thermally coupled reactors for styrene production. The results showed that styrene production in the thermally coupled reactor is higher than the conventional reactor (5% increase). Some researchers have applied the tri-reforming process to be a heat source for the thermally coupling reactor. Farniaei et al. [28] investigated a syngas production with thermally coupled reactor of methane dry reforming and tri-reforming. The results indicated that the proposed process can produce two types of syngas with different quality and reduce the energy consumption.

To obtain a higher hydrogen content and a high-purity product, a water gas shift reactor and separation units are added to the hydrogen production process; examples of separation units include pressure swing adsorption (PSA) and cryogenic distillation units [13]. Because the water gas shift reaction is exothermic and reversible, it is a strongly equilibrium-limited reaction when performed at high operating temperatures. One promising method for reducing the complexity of the hydrogen production process is to combine both the generation and separation of hydrogen in a membrane water-gas shift (MWGS) reactor. In addition, the removal of H_2 via a membrane enhances the water gas shift reaction and thus improves both H_2 yield and conversion efficiency [11,29].

The objective of this work is to study the thermodynamic effects of thermally coupling steam and tri-reforming processes with a membrane water-gas shift reactor while using a bio-oil aqueous fraction for hydrogen production. The retentate gas formed from the membrane water-gas shift reactor is recycled to the tri-reformer to improve the overall process efficiency by producing more hydrogen and heat for the steam reformer. The effects of the tri-reformer and steam reformer temperature, the steam-to-feed ratio, and the split ratio of waste gas recovery are investigated to determine the optimal condition of this process. Furthermore, the energy efficiency of thermally coupling steam and tri-reforming processes is investigated and compared with the conventional steam reforming process.

Methodology

Process description

In this work, hydrogen production is studied using the thermal coupling of steam and tri-reforming processes with a membrane water-gas shift reactor. A bio-oil aqueous fraction is used as feedstock for the steam and tri-reforming processes. The physical properties and elemental compositions of the aqueous fraction of bio-oil are shown in Table 1. The main

Table 1 – Characteristics of the aqueous fraction of bio-oil [30,33–36].

Element analysis (wt. %)	
Carbon	29.8–49.2
Hydrogen	6.1–9.9
Oxygen	45–59.7
Nitrogen	0.1–2.6
Sulfur	<0.1
pH	2.2–3.8
Water content (wt. %)	70–85
LHV (MJ/kg)	13–19

elemental compositions are carbon, hydrogen and oxygen. Table 2 shows the chemical compositions of the bio-oil aqueous fraction [31]. It is shown that acetic acid is the major component, therefore, it is used as a model compound to represent the bio-oil aqueous fraction in this simulation study. Due to the addition of water during the preparation of the bio-oil aqueous fraction, the amount of water in the bio-oil aqueous phase is 70–85%. In this study, the amount of water in the bio-oil aqueous fraction at the base case condition in term of the steam-to-fuel (bio-oil) molar ratio is 5.58 [32].

Fig. 1 illustrates the thermal coupling of steam and tri-reforming processes in conjunction with a membrane water-gas shift reactor; a bio-oil aqueous fraction is used for hydrogen production. This process has two sections: the thermal coupling of steam and tri-reforming processes and the membrane water-gas shift (MWGS) reactor. The first section is used to produce hydrogen, and the second is used to enhance hydrogen production and reduce carbon monoxide. The gases produced from the reforming section are cooled at a temperature of 300 °C before being fed into the MWGS reactor. The MWGS reactor also acts as separator where pure hydrogen is separated from other products. In this work, the permeate stream is called hydrogen stream (HYDROGEN), whereas the waste gas stream which separates from the MWGS reactor is called retentate stream (RETENT). The waste gases in retentate stream, which consist of steam and CO_2, are recycled back to the tri-reformer as co-reactants. The thermally coupled steam and tri-reforming processes consist of an endothermic reactor (steam reformer) and an exothermic reactor (tri-reformer). The main reactions taken place in the steam reformer are steam reforming (Eq. (1)) and water-gas shift (Eq. (2)) reactions [10].

Table 2 – Chemical compositions of bio-oil aqueous fraction [31].

Compounds	wt. %	Compounds	wt. %
Acetaldehyde	0.27	Caproic acid	0.01
Furan	0.04	Guaiacol	0.05
Acetone	0.11	4-Methylguaiacol	0.03
Methanol	1.98	o-Cresol	<0.01
2-Butanone	0.04	Phenol	0.02
Isopropanol	0.02	4-Ethylguaiacol	<0.01
Ethanol	<0.01	m-Cresol	0.01
2-Pentanone	0.01	2-Propylphenol	<0.01
n-Propanol	0.01	Eugenol	<0.01
1-Hydroxy-2-Propanone	2.66	4-Ethylphenol	0.01
Glycolaldehyde	0.78	o-Vanillin	0.02
1-Hydroxy-2-butanone	0.08	Syringol/4-Propylphenol	0.01
Acetic acid	11.6	Isoeugenol	0.02
Furfural	0.34	5-(Hydroxymethyl)furfural	0.04
2-Acetylfuran	0.02	4-Methylcatechol	<0.01
Propanoic acid	0.02	4-Ethylcatechol	0.02
Isobutyric acid	0.02	Sugars	4.3
5-Methylfurfural	0.02	Unknown GC-detectable compounds	4.7
Butyric acid	0.06	Water	72.7
Valeric acid	0.03		

$$C_nH_mO_p + (n-p)H_2O \rightarrow nCO + \left(n - p + \frac{m}{2}\right)H_2 \quad (1)$$

$$CO + H_2O \rightarrow CO_2 + H_2 \quad (2)$$

In the tri-reformer, steam reforming (Eq. (1)), CO_2 reforming (Eq. (3)), and oxidation (Eqs. (4) and (5)) reactions are coupled in a single reactor [20,37]. At the suitable condition, the tri-reformer generates heat for the steam reformer and produces additional hydrogen at the same time.

$$C_nH_mO_p + CO_2 \rightarrow CO + H_2 \quad (3)$$

$$C_nH_mO_p + \frac{(n-p)}{2}O_2 \rightarrow nCO + \left(\frac{m}{2}\right)H_2 \quad (4)$$

$$C_nH_mO_p + \left(n - \frac{p}{2} + \frac{m}{4}\right)O_2 \rightarrow nCO_2 + \left(\frac{m}{2}\right)H_2O \quad (5)$$

In this process, steam and acetic acid (a model compound of bio-oil aqueous fraction) are fed into the steam reformer to produce hydrogen-rich gas; while combustion air and bio-oil fuel at 25 °C is fed into the tri-reformer for the combustion reaction. A portion of the retentate stream from the MWGS reactor, which consists of CO_2 and steam, is recycled to the tri-reformer to produce more hydrogen via steam reforming and dry reforming reactions. In the tri-reformer, major products consist of a useful gas mixture of H_2, CO, CO_2 and CH_4.

Process model

In this study, simulation studies based on a thermodynamic analysis are performed using an Aspen Plus simulator (Fig. 1). The bio-oil flowrate is fixed at 150 kmol/h. Bio-oil is fed into the steam reformer at a rate of 100 kmol/h, and the remainder is fed into the tri-reformer. *Rgibbs* reactor (ST-REFO, TRI-REFO) models based on minimization of Gibbs free energy are applied for the steam and tri-reformers. The operating conditions and the types of MWGS reactors used are summarized in Table 3. The operating temperatures of the steam and tri-reformers are in the range of 400–800 °C. For the standard conditions, the steam to fuel ratio (S/F), which is the molar ratio of steam to bio-oil fuel in the feed stream, is 5.58, and the split ratio of retentate stream, the ratio of the stream recycled to the tri-reformer and the stream purged from the process, is 0.5. In addition, sub-water-gas shift reactors and sub-separators are combined to simulate the MWGS reactor [38]. An *R-Equill* reactor model is used to simulate the water gas shift reaction wherein the water gas shift reaction is assumed to reach the thermodynamic equilibrium locally. The ideal separator model (*Sep*) is used to separate pure hydrogen. In this work, the experimental data of Mendes et al. [39], which

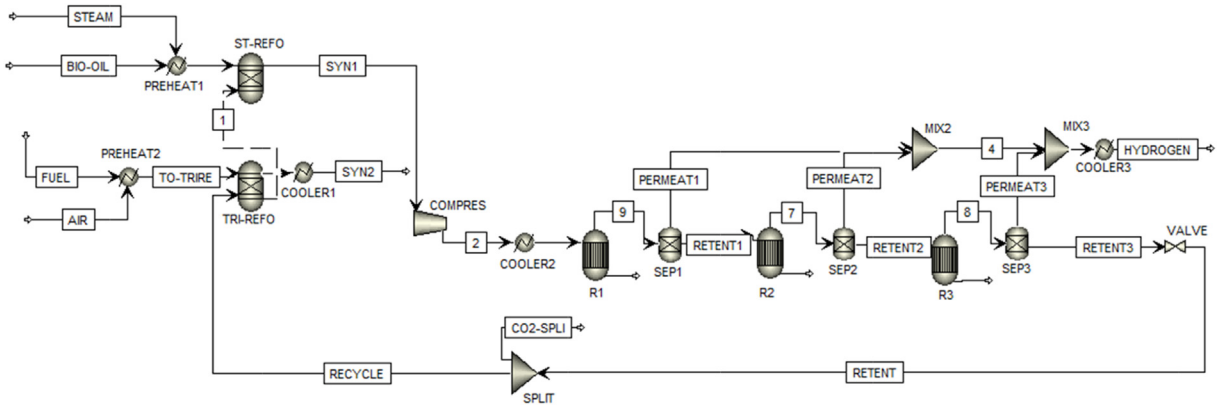

Fig. 1 – A schematic diagram of thermally coupling steam and tri-reforming with membrane water-gas shift reactor of bio-oil aqueous fraction for hydrogen production.

studied the performance of a Pd–Ag membrane reactor, is used to determine the operating conditions of the MWGS reactor. They presented that the optimal conditions to produce high H_2 purity of 90% are as follows: a temperature of 300 °C, an operating pressure of 2.026 bar and a permeate pressure of 1.013 bar.

System analysis

The hydrogen yield is defined as a ratio of the molar flow rate of hydrogen to the molar flow rate of bio-oil feed (Eq. (6)); it is used to evaluate the performance of thermally coupled steam and tri-reforming of bio-oil.

$$Y_{H_2} = \frac{\text{Hydrogen molar flow rate}}{\text{Bio} - \text{oil molar flow rate}} \quad (6)$$

The hydrogen efficiency of the overall process can be calculated from hydrogen production and bio-oil consumption in terms of lower heating values (LHV) as shown in Eq. (7) [30]. The thermal efficiency is calculated from the net energy output and the net energy input as shown in Eq. (8). The energy consumption is calculated from the electrical energy demand from unit operations such as preheaters, compressors and coolers [30].

$$\text{Hydrogen efficiency} = \frac{m_{H_2} \cdot LHV_{H_2}}{m_{bio-oil} \cdot LHV_{bio-oil}} \quad (7)$$

$$\text{Thermal efficiency} = \frac{m_{H_2} \cdot LHV_{H_2}}{m_{bio-oil} \cdot LHV_{bio-oil} + \text{Energy consumption(MW)}} \quad (8)$$

Results and discussion

Operating parameters are important factors that affect hydrogen production and energy efficiency. This study analyzes the effects of temperature, steam to fuel ratio (S/F) and split ratio on hydrogen yield, gas composition and energy consumption. The major products in the retentate stream of the MWGS reactor are CO_2 and steam. This stream is recycled to the tri-reformer for steam reforming, dry reforming and partial oxidation reactions. This affects energy consumption and hydrogen production from the tri-reformer. The energy efficiency at optimal operating conditions of the thermally coupled steam and tri-reforming processes are compared with conventional reforming processes. The simulation results using a steam reformer model are compared with experimental data [32] as shown in Fig. 2. The model prediction is in agreement with experimental data. In addition, the MWGS model is validated with the experimental results of Mendes et al.' s work [39], it is found that at a temperature of 300 °C, an operating pressure of 2.026 bar, and a permeate pressure of 1.013 bar, the model can reasonably predict the hydrogen purity with an average error of 3.7%.

Effect of tri-reforming temperature

Fig. 3 presents the effect of the temperature of the tri-reformer on hydrogen yield and energy consumption. The temperature of the steam reformer, the S/F ratio and the split ratio of retentate stream are fixed at 650 °C, 5.58 and 0.5, respectively. It is found that hydrogen yield increases with increasing temperature and reaches its maximum value at 580 °C. Energy is considerably consumed when the temperature of the tri-reformer is high; this is due to the endothermic steam and dry reforming reactions. At 580 °C, the highest hydrogen yield and the reactor's net heat duty are obtained at 2 and −1.8 MW, respectively. However, the hydrogen yield slightly decreases at temperatures higher than 600 °C because of a favorable reverse water-gas shift reaction at high reaction

Table 3 – Operating conditions for hydrogen production.

Flowsheet element	Parameter	Value
Bio-oil feed (acetic acid model compound)	Flow rate (kmol/h)	150
	Temperature, °C	25
	Pressure (bar)	1.013
Steam feed	Flow rate (kmol/h)	558
	Temperature (°C)	100
	Pressure (bar)	1.013
Steam reformer (*Rgibbs* reactor model)	Operating temperature (°C)	400–800
	Operating pressure (bar)	1.013
Tri-reformer (*Rgibbs* reactor model)	Operating temperature (°C)	400–800
	Operating pressure (bar)	1.013
MWGS reactor (*R-Equill* reactor model and Separator model)	Operating temperature (°C)	300
	Operating pressure (bar)	2.026
	Permeate pressure (bar)	1.013
	Hydrogen recovery (%)	90

temperatures. Therefore, high CO and low hydrogen production are obtained at a high operating temperature, as shown in Fig. 4. In addition, the composition of methane and CO_2 decreases with increasing temperature because dry reforming and steam reforming reactions are promoted at high temperatures.

Effect of steam reformer temperature

The effects of temperature on product composition are studied in the thermally coupled steam and tri-reforming processes. The tri-reforming temperature is fixed at optimal conditions (580 °C). Fig. 5 shows the effects of different temperatures on hydrogen production from steam reformer and tri-reformers. These results show that hydrogen production from the steam reformer initially increases as temperature increases and then plateaus at temperatures above 650 °C. The hydrogen fraction produced from the tri-reformer decreases with temperature; this is because the steam reforming reaction, which converts steam and bio-oil to hydrogen and CO, is favored at high temperature. However, it has an insignificant effect on hydrogen yield at temperatures higher than 650 °C, as a limitation of the exothermic water-gas shift reaction. Regarding the energy consumption, the steam

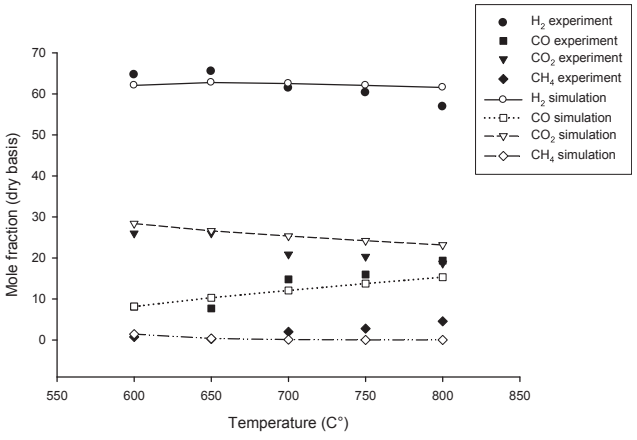

Fig. 2 – Validation of the steam reformer model on product composition with S/F ratio = 5.58 and pressure = 1.013 bar.

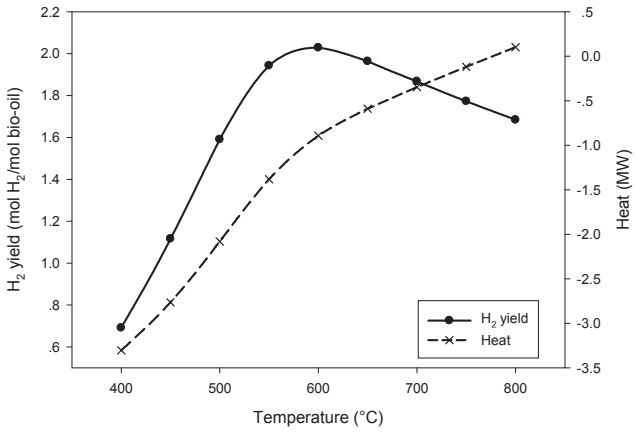

Fig. 3 – Effect of tri-reforming temperature on H_2 yield and reactor net heat duty with a steam reforming temperature of 650 °C and an S/F ratio of 5.58.

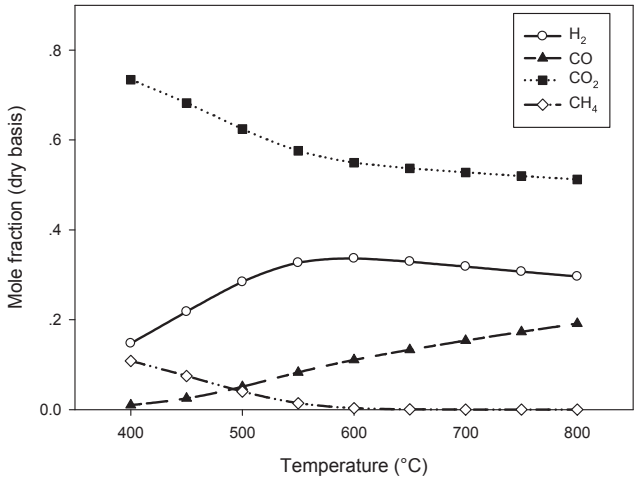

Fig. 4 – Effect of tri-reforming temperature on product composition (dry basis) at steam reforming temperature = 650 °C and S/F ratio = 5.58.

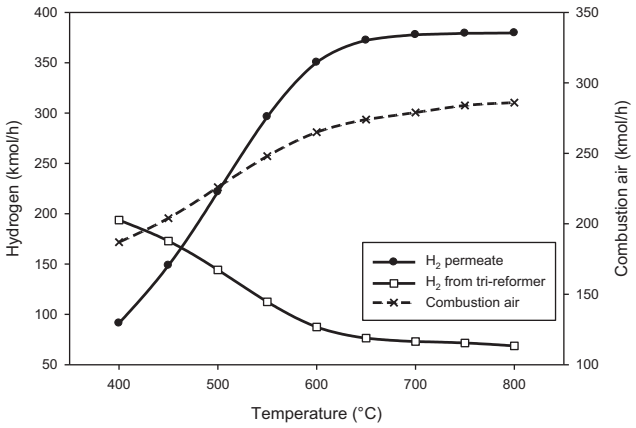

Fig. 5 – Effect of steam reforming temperature on hydrogen production and combustion air at tri-reforming temperature = 580 °C and S/F ratio = 5.58.

reformer needs more energy at higher temperatures; thus, some part of the bio-oil is combusted with air to meet the energy demands of the steam reformer which decreases hydrogen production via steam reforming. In addition, the steam reformer demands a higher air feed flow rate at high operating temperatures. Fig. 6 shows product compositions from the tri-reformer; an increase in temperature increases CO_2 and decreases hydrogen because of the increased combustion reaction in the tri-reformer. Further, Fig. 7 shows the hydrogen yield from two reactors at variable steam reformer temperatures. The results show that the hydrogen yield of the overall process increases with temperature initially and then plateaus after 650 °C.

Effect of steam to fuel ratio (S/F)

The steam to fuel ratio affects both hydrogen yield and energy consumption in the steam reformer. Fig. 8 illustrates the hydrogen production from both the steam reformer and tri-

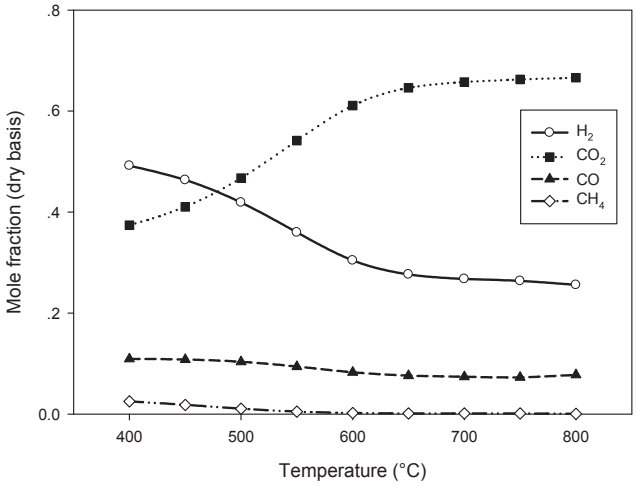

Fig. 6 – Effect of steam reforming temperature on product composition of tri-reformer at tri-reforming temperature = 580 °C and S/F ratio = 5.58.

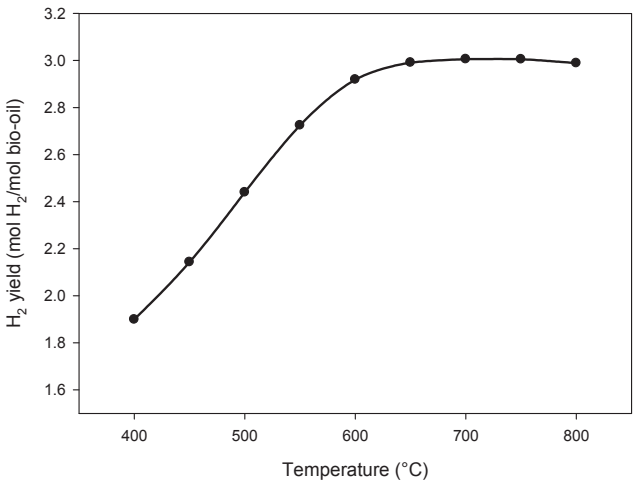

Fig. 7 – Effect of steam reforming temperature on hydrogen yield at tri reforming temperature = 580 °C and S/F ratio = 5.58.

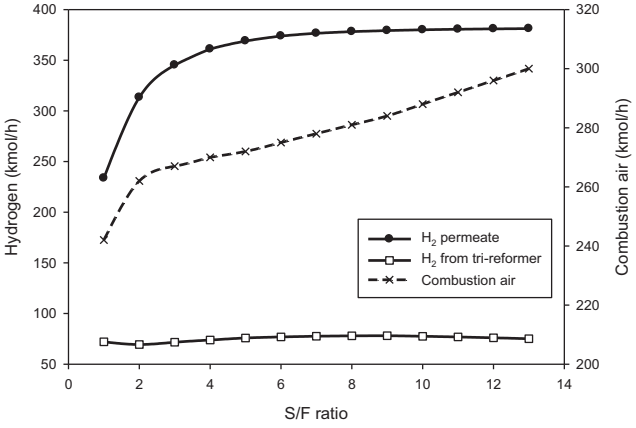

Fig. 8 – Effect of S/F ratio on hydrogen production and combustion air at steam and tri-reforming temperature of 650 and 580 °C, respectively.

reformer when the steam to fuel ratio increases from 1 to 13. It is observed that hydrogen production in the steam reformer increases as the S/F ratio increases from 1 to 6 because excess steam favors both steam reforming and the water-gas shift reaction. However, the S/F ratio does not have a significant effect on hydrogen production for S/F ratios above 6. For the tri-reformer, increasing the amount of steam increases steam in the waste gas recovery, which reduces the amount of CO in the gas product of the tri-reformer (Fig. 9). However, this increases the energy requirement for the steam reformer which is supplied by the combustion reaction of combustion air and bio-oil inside the tri-reformer. Consequently, hydrogen production from the tri-reformer is not significantly increased when the S/F ratio is increased.

Fig. 10 presents the hydrogen yield from the integrated process at various S/F ratios. It should be noted that changes in the S/F ratio only affect hydrogen production from the steam reformer. Fig. 9 shows the simulation results that hydrogen yield reaches the maximum value at an S/F ratio of

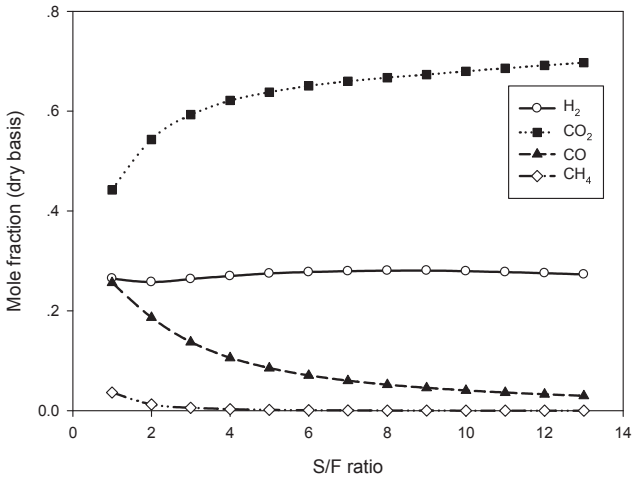

Fig. 9 – Effect of S/F ratio on product composition of tri-reformer at steam and tri-reforming temperature of 650 and 580 °C, respectively.

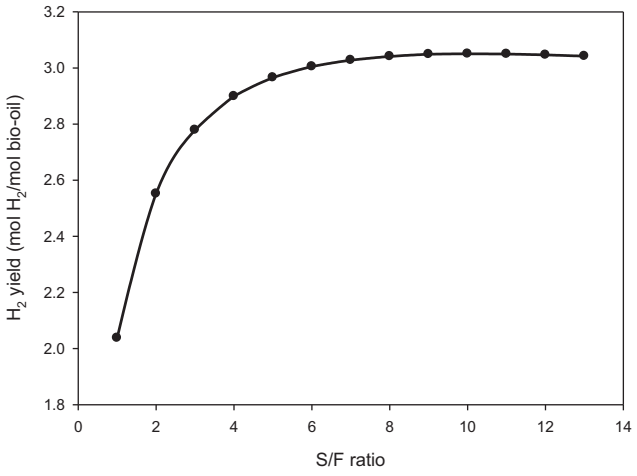

Fig. 10 – Effect of S/F ratio on hydrogen yield at steam and tri-reforming temperature of 650 and 580 °C, respectively.

6. It is noted that the amount of steam is also important to a carbon formation affecting the catalyst deactivation; an increase in steam (S/F ratio > 3) fed to the reforming process can suppress the formation of carbon [40].

Effect of split ratio of the retentate stream

In this work, the steam and carbon dioxide produced in waste gases from the MWGS reactor are recycled to the tri-reformer as reactants for steam reforming, dry reforming, and partial oxidation reactions. The feed ratio of Fuel (H_2O:CO_2:O_2) significantly affects hydrogen production and energy consumption. In this process, CO_2 and steam recovery are varied by the split ratio of the retentate stream when the bio-oil molar feed flow rate is fixed. Consequently, the rate of the combustion reaction and air addition are controlled by the ratio of the waste gas recovery in order to maintain energy for the steam reformer. Fig. 11 shows the effect of the split ratio of the retentate stream on hydrogen yield and molar flow of air

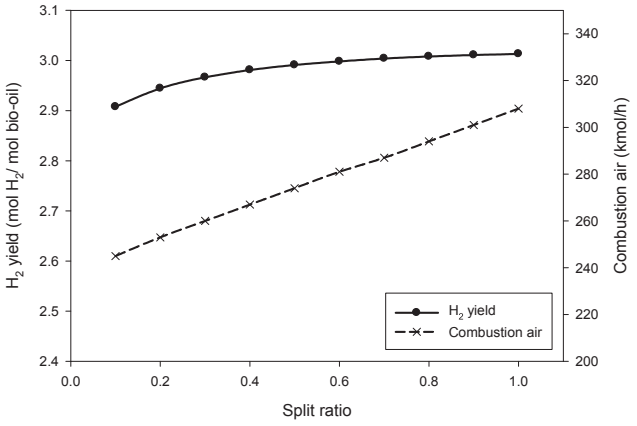

Fig. 11 – Effect of split ratio of retentate stream on hydrogen yield and combustion air at steam and tri-reforming temperature = 650 and 580 °C, respectively, and S/F ratio = 5.58.

for the combustion reaction. The results show that the hydrogen yield increases with an increasing split ratio until a split ratio of 0.5 is reached. This is because the fractions of H_2O and CO_2 in fuel stream increase (Fig. 12). However, higher amounts of steam and CO_2 consume energy from the combustion reaction. To maintain the temperature of the steam reformer, more combustion air is fed into the tri-reformer when the split ratio increases, resulting in an insignificant change in the O_2/fuel ratio in feed stream. At a split ratio higher than 0.5, the hydrogen yield plateaus because of the limited fuel feed.

From the parametric analysis of the process presented above, the optimal operating parameters of the thermally coupling steam and tri-reforming of the bio-oil aqueous fraction with MWGS reactor is shown in Table 4. The simulation results of the process under the optimal operation are presented in Table 5. It is found that pure hydrogen obtained from the MWGS reactor in the permeate stream is 372.28 kmol/h. In

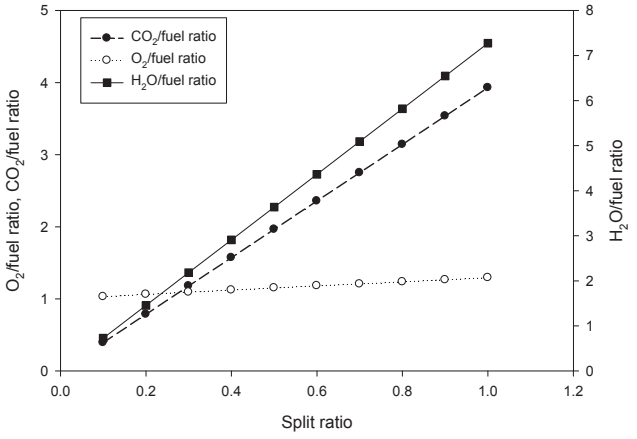

Fig. 12 – Effect of split ratio of retentate stream on the feed ratio of tri-reformer (O_2/fuel, CO_2/fuel, and H_2O/fuel ratios) at steam and tri-reforming temperatures = 650 and 580 °C, respectively, and S/F ratio = 5.58.

Table 4 – The optimal conditions of the thermally coupling steam and tri-reforming with MWGS reactor of bio-oil aqueous fraction.

Operating temperature of steam reformer (°C)	650
Operating temperature of tri-reformer (°C)	580
Steam/fuel ratio	6
split ratio of retentate stream	0.5

addition, more synthesis gas with hydrogen of 76.39 kmol/h is produced from the tri-reformer.

Energy efficiency

Table 6 shows the comparison of energy efficiency between a conventional steam reforming process that uses a conventional combustor to generate heat for the process and the thermally coupled steam and tri-reforming processes integrated with the MWGS reactor. Greater hydrogen production is observed in the thermally coupled process; hydrogen production of the thermally coupled steam and tri-reforming processes and the conventional steam reforming process were 30.15 and 25.09 MW_{LHV}, respectively. This difference is due to the tri-reformer generating energy for the steam reformer and increased hydrogen production for the overall process; whereas, a conventional combustor only generates heat for the conventional steam reforming process. Consequently, the hydrogen efficiency of the thermally coupled steam and tri-reforming process (0.77) is greater than the hydrogen efficiency of the conventional steam reforming process (0.64).

The configuration of the system comprises the following parts: preheater, coolers, compressor, and MWGS reactor. Energy consumption for these units differs in two different processes. The amount of energy consumption in the thermally coupled steam and tri-reforming processes is less than the conventional steam reforming process because the thermally coupled process provides the useful energy from syngas producing from the tri-reformer. Considering the energy consumption, the total efficiency of the thermally coupled steam and tri-reforming processes and the conventional steam reforming processes are 0.69 and 0.52, respectively (32.7% increase).

Table 5 – The results of simulation of the thermally coupling steam and tri-reforming with MWGS reactor of bio-oil aqueous fraction.

	Waste gas (retentate stream)	Pure hydrogen (permeate stream)	Synthesis gas from tri-reformer
Temperature (°C)	300	25	25
Pressure (bar)	1.013	1.013	1.013
Molar flow (kmol/h)			
H_2	18.13	372.278	76.39
CO	1.67		21.01
CO_2	196.35		178.65
H_2O	363.63		215.78
CH_4	1.98		0.35
N_2			216.46
Mole fraction			
H_2	0.0311	1	0.1078
CO	0.0029		0.0296
CO_2	0.3375		0.2521
H_2O	0.6250		0.3045
CH_4	0.0034		0.0005
N_2			0.3045

Table 6 – Comparison of energy efficiency between thermally coupling steam and tri-reforming process and conventional steam reforming process.

	Thermally coupling steam and tri-reforming		Conventional steam reforming	
	Mass flow (kg/h)	MW_{LHV}	Mass flow (kg/h)	MW_{LHV}
Input				
Bio-oil feed[a]	9007.89	39.28	9007.89	39.28
Output				
Hydrogen production[b]	904.46	30.15	752.66	25.09
Hydrogen efficiency		0.77		0.64
Heat demand/supply (+/−)				
PREHEAT1		12.79		12.79
PREHEAT2		2.7		1.05
COOLER		−12.63		−6.12
COMPRES (compressor)		1.9		1.9
MWGS reactor		−0.59		−0.59
Total energy consumption		4.17		9.03
Total efficiency		0.69		0.52

[a] $LHV_{bio\text{-}oil}$ = 15.7 MW/kg [36].
[b] LHV_{H2} = 120 MW/kg [41].

Conclusions

The thermally coupled steam and tri-reforming processes integrated with a membrane water-gas shift (MWGS) reactor and using a bio-oil aqueous fraction take advantage of the fact that the tri-reformer generates heat for the steam reformer and produces hydrogen at the same time. Thermodynamic analysis of the operating conditions of this process is performed. The results indicate that hydrogen yield increases as the temperature increases with maxima at steam reforming temperature of 650 °C and tri-reforming temperature of 580 °C, and hydrogen yield increases with the S/F ratio with a maximum S/F = 6. Moreover, increasing the split ratio of retentate stream increases hydrogen yield, but reaches a plateau at a ratio = 0.5. At the optimal conditions, the hydrogen yield of 3 mol H_2/mol bio-oil is obtained from the process. However, increasing the steam reforming temperature, steam, and split ratio of retentate stream requires more air combustion for the exothermic reaction. The energy efficiency from using the thermally coupled steam and tri-reforming processes with a MWGS reactor is greater than using conventional steam reforming. In conclusion, a tri-reformer can replace huge fire furnaces by recycling flue gas in order to increase energy efficiency. However, the high investment cost of membrane technology is the big challenge

for commercial process [42]. In addition, to achieve greater efficiency, heat integration analysis should be investigated further.

Acknowledgments

Support from The Royal Golden Jubilee Ph.D. Program (The Thailand Research Fund), the National Research University Project (Office of Higher Education Commission) and Chulalongkorn Academic Advancement into Its 2nd Century Project is gratefully acknowledged.

REFERENCES

[1] Ogden JM. Hydrogen as an energy carrier: outlook for 2010, 2030, and 2050. Institute of Transportation Studies. UC Davis: Institute of Transportation Studies (UCD). 2004.
[2] Conte M, Mario FD, Iacobazzi A, Mattucci A, Moreno A, Ronchetti M. Hydrogen as future energy carrier: thee ENEA point of view on technology and application prospects. Energies 2009;2:150–79.
[3] Züttel A, Remhof A, Borgschulte A, Friedrichs O. Hydrogen: the future energy carrier. Math Phys Eng Sci 2010;368:3329–42.
[4] Corbo P, Migliardini F, Veneri O. Hydrogen fuel cell for road vehicles. London: Springer; 2011.
[5] Mohan D, Pittman Jr CU, Steele PH. Pyrolysis of wood/biomass for bio-oil: a critical review. Energy Fuels 2006;20:848–89.
[6] Czernik S, Bridgwater AV. Overview of applications of biomass fast pyrolysis oil. Energy Fuels 2004;18:590–8.
[7] Blasi A, Fiorenza G, Freda C, Calabro V. Steam reforming of biofuels for the production of hydrogen rich gas. In: Membranes for clean and renewable power applications. Elsevier; 2013. p. 145–81.
[8] Garcia L, French R, Czernik S, Chornet E. Catalytic steam of bio-oils for production of hydrogen: effects of catalyst composition. Appl Catal A General 2000;201:225–39.
[9] Valle B, Remiro A, Aguayo AT, Bilbao J, Gayubo AG. Catalysts of Ni/α-Al_2O_3 and Ni/La_2O_3-αAl_2O_3 for hydrogen production by steam reforming of bio-oil aqueous fraction with pyrolytic lignin retention. Int J Hydrogen Energy 2013;38(3):1307–18.
[10] Trane R, Dahl S, Skjøth-Rasmussen MS, Jensen AD. Catalytic steam reforming of bio-oil. Int J Hydrogen Energy 2012;37(8):6447–72.
[11] Blasi A, Giorenza G, Enea CF. Steam reforming of biofuels for the production of hydrogen-rich gas. Woodhead Publishing Limited; 2014.
[12] Martínez I, Romano MC, Chiesa P, Grasa G, Murillo R. Hydrogen production through sorption enhanced steam reforming of natural gas: thermodynamic plant assessment. Int J Hydrogen Energy 2013;38:15180–99.
[13] Molburg JC, Doctor RD. Hydrogen from steam-methane reforming with CO2 capture, 20th Annual International Pittsburgh Coal Conference, Pittsburgh, PA, 2003.
[14] No S. Application of bio-oils from lignocellulosic biomass to transportation, heat and power generation-a review. Renew Sustain Energy Rev 2014;40:1108–25.
[15] Tzanetakis T, Moloodi S, Farra N, Nguyen B, McGrah A, Thomson M. Comparison of the spray combustion characteristics and emissions of a wood-derived fast pyrolysis liquid-ethanol blend with number2 and number4 fuel oils in a pilot-stabilized swirl burner. Energy Fuels 2011;25:4305–21.
[16] Faro ML, Vita A, Pino L, Arico AS. Performance evaluation of a solid oxide fuel cell coupled to an external biogas tri-reforming process. Fuel Process Technol 2013;115:238–45.
[17] Pino L, Vita A, Lagana M, Recupero V. Hydrogen from biogas: catalytic tri-reforming process with Ni/La Ce O mixed oxides. Appl Catal B Environ 2014;148–149:91–105.
[18] Halmann M, Steinfeld A. Hydrogen production and CO_2 fixation by flue-gas treatment using methane tri-reforming or coke/coal gasification combined with lime carbonation. Int J Hydrogen Energy 2009;34:8061–6.
[19] Zhang Y, Cruz J, Zhang S, Lou HH, Benson TJ. Process simulation and optimization of methanol production coupled to tri-reforming process. Int J Hydrogen Energy 2013;38:13617–30.
[20] Aboosadi ZA, Jahanmiri AH, Rahimpour MR. Optimization of tri-reformer reactor to produce synthesis gas for methanol production using differential evolution (DE) method. Appl Energy 2011;88:2691–701.
[21] Majewski AJ, Wood J. Tri-reforming of methane over Ni@SiO2 catalyst. Int J Hydrogen Energy 2014;39:12578–85.
[22] García-Vargas JM, Valverde JL, Lucas-Consuegra A, Dorado F, Sánchez P. Methane tri-reforming over a Ni/β-SiC-based catalyst: optimizing the feedstock composition. Int J Hydrogen Energy 2013;38:4524–32.
[23] Rahnama H, Farniaei M, Abbasi M, Rahimpour MR. Modeling of synthesis gas and hydrogen production in a thermally coupling of steam and tri-reforming of methane with membranes. J Ind Eng Chem 2014;20:1779–92.
[24] Bayat M, Rahimpour MR, Taheri M, Pashaei M, Sharifzadeh S. A comparative study of two different configurations for exothermic-endothermic heat exchanger reactor. Chem Eng Process 2012;52:63–73.
[25] Karimipourfard D, Kabiri S, Rahimpour MR. A novel integrated thermally double coupled configuration for methane steam reforming, methane oxidation and dehydrogenation of propane. J Nat Gas Sci Eng 2014;21:134–46.
[26] Bruschi YM, López E, Pedermera MN, Borio DO. Coupling exothermic and endothermic reactions in an ethanol microreformer for hydrogen production. Chem Eng J 2016;294:97–104.
[27] Mirvakili A, Heravi M, Karimipourfard D, Rahimpour MR. Simultaneous synthesis gas and styrene production in the optimized thermally coupled reactor. J Nat Gas Sci Eng 2014;16:18–30.
[28] Farniaei M, Abbasi M, Rahnama H, Rahimpour MR, Shariati A. Syngas production in a novel methane dry reformer by utilizing of tri-reforming process for energy supplying: modeling and simulation. J Nat Gas Sci Eng 2014;20:132–46.
[29] Gosiewski K, Warmuzinski K, Tanczyk M. Mathematical simulation of WGS membrane reactor for gas from coal gasification. Catal Today 2010;156:229–36.
[30] Yao D, Wu C, Yang H, Hu Q, Nahil MA, Chen H, et al. Hydrogen production from catalytic reforming of the aqueous fraction of pyrolysis bio-oil with modified Ni-Al catalysts. Int J Hydrogen Energy 2014;39:14642–52.
[31] Paasikallio V, Kihlman J, Sánchez CA, Simell P, Solantausta Y, Lehtonen J. Steam reforming of pyrolysis oil aqueous fraction obtained by one-step fractional condensation. Int J Hydrogen Energy 2015:1–9.
[32] Bimbela F, Oliva M, Carcia L, Arauzo J. Hydrogen production via catalytic steam reforming of the aqueous fraction of bio-oil using nickel-based coprecipitated catalysts. Int J Hydrogen Energy 2013;38:14476–87.
[33] Liu S, Chen M, Hu Q, Wang J, Kong L. The kinetics model and pyrolysis behavior of the aqueous fraction of bio-oil. Bioresour Technol 2013;129:381–6.

[34] Lindfors C, Kuoppala E, Oasmaa A, Solantausta Y, Arpiainen V. Fractionation of bio-oil. Energy Fuels 2014;28:5785–91.
[35] Remón J, Broust F, Valette J, Chhiti Y, Alava I, Fernandez-Akarregi AR, et al. Production of a hydrogen-rich gas from fast pyrolysis bio-oils: composition between homogeneous and catalytic steam reforming routes. Int J Hydrogen Energy 2014;39:171–82.
[36] Lehto J, Oasmaa A, Solantausta Y, Kytö M, Chiaramonti D. Review of fuel oil quality and combustion of fast pyrolysis bio-oils from lignocellulosic biomass. Appl Energy 2014;116:178–90.
[37] Vagia E Ch, Lemonidou AA. Thermodynamic analysis of hydrogen production via autothermal steam reforming of selected components of aqueous bio-oil fraction. Int J Hydrogen Energy 2008;33:2489–500.
[38] Authayanun S, Aunsup P, Patcharavorachot, Arpornwichanop A. Theoretical analysis of a biogas-fed PEMFC system with different hydrogen purification: conventional and membrane-based water gas shift processes. Energy Convers Manag 2014;86:60–9.
[39] Mendes D, Sá S, Tosti S, Sousa JM, Madeira LM, Mendes A. Experimental and modeling studies on the low-temperature water-gas shift reaction in a dense Pd–Ag packed-bed membrane reactor. Chem Eng Sci 2011;66:2356–67.
[40] Goyal N, Pant KK, Gupta R. Hydrogen production by steam reforming of model bio-oil using structured Ni/Al_2O_3 catalyst. Int J Hydrogen Energy 2013;38:921–33.
[41] Dutta S. A review on production, storage of hydrogen and its utilization as energy resource. J Ind Eng Chem 2014;20:1148–56.
[42] Dijkstra JW, Raju G, Peppink G, Jansen D. Techno-economic evaluation of membrane technology for pre-combustion decarbonisation: water-gas shift versus reforming. Energy Procedia 2011;4:723–30.

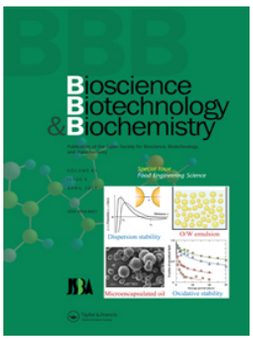

Bioscience, Biotechnology, and Biochemistry

ISSN: 0916-8451 (Print) 1347-6947 (Online) Journal homepage: http://www.tandfonline.com/loi/tbbb20

Encapsulation of lemongrass oil with cyclodextrins by spray drying and its controlled release characteristics

Sarunya Phunpee, Uracha Rangsadthong Ruktanonchai, Hidefumi Yoshii, Suttichai Assabumrungrat & Apinan Soottitantawat

To cite this article: Sarunya Phunpee, Uracha Rangsadthong Ruktanonchai, Hidefumi Yoshii, Suttichai Assabumrungrat & Apinan Soottitantawat (2017) Encapsulation of lemongrass oil with cyclodextrins by spray drying and its controlled release characteristics, Bioscience, Biotechnology, and Biochemistry, 81:4, 718-723, DOI: 10.1080/09168451.2016.1277942

To link to this article: http://dx.doi.org/10.1080/09168451.2016.1277942

Published online: 17 Jan 2017.

Submit your article to this journal

Article views: 70

View related articles

View Crossmark data

Full Terms & Conditions of access and use can be found at
http://www.tandfonline.com/action/journalInformation?journalCode=tbbb20

Download by: [Chulalongkorn University] **Date:** 28 May 2017, At: 17:08

Bioscience, Biotechnology, and Biochemistry, 2017
Vol. 81, No. 4, 718–723

Encapsulation of lemongrass oil with cyclodextrins by spray drying and its controlled release characteristics

Sarunya Phunpee[1,2], Uracha Rangsadthong Ruktanonchai[2], Hidefumi Yoshii[3], Suttichai Assabumrungrat[1] and Apinan Soottitantawat[1,*]

[1]*Faculty of Engineering, Department of Chemical Engineering, Chulalongkorn University, Bangkok, Thailand;*
[2]*National Nanotechnology Center, National Science and Technology Development Agency, Patumthani, Thailand;*
[3]*Department of Applied Biological Science, Kagawa University, Kagawa, Japan*

Received October 27, 2016; accepted December 23, 2016
http://dx.doi.org/10.1080/09168451.2016.1277942

Inclusion of the two isomers of citral (*E*-citral and *Z*-citral), components of lemongrass oil, was investigated within the confines of various cyclodextrin (*α*-CD, *β*-CD and *γ*-CD) host molecules. Aqueous complex formation constants for *E*-citral with *α*-CD, *β*-CD and *γ*-CD were determined to be 123, 185, and 204 L/mol, respectively, whereas *Z*-citral exhibited stronger affinities (157, 206, and 253 L/mol, respectively). The binding trend *γ*-CD > *β*-CD > *α*-CD is a reflection of the more favorable geometrical accommodation of the citral isomers with increasing cavity size. Encapsulation of lemongrass oil within CDs was undertaken through shaking citral:CD (1:1, 1.5:1, and 2:1 molar ratio) mixtures followed by spray drying. Maximum citral retention occurred at a 1:1 molar ratio with *β*-CD and *α*-CD demonstrating the highest levels of total *E*-citral and *Z*-citral retention, respectively. Furthermore, the *β*-CD complex demonstrated the slowest release rate of all inclusion complex powders.

Keywords: cyclodextrins; lemongrass oil; inclusion complex; spray drying; citral

Lemongrass (*Cympopogon citratus Stapf*) is widely cultivated in Thailand and is extensively employed as an ingredient in Thai cuisine. Citral (3,7-dimethyl-2,6-octadienal), the major component of extracted lemongrass oil (65–80% by weight) is a mixture of two geometric isomers, geranial (*trans*-citral, *E*-citral) and neral (*cis*-citral, *Z*-citral). Although citrals have been reported to exhibit high antimicrobial activities, they are poorly water soluble[1–3] and lose their therapeutic properties on oxidation when exposed to heat, air, and light[4,5]. Encapsulation of citral is thus a potential method for enhancing its stability and enabling its biological properties to be retained over time[6–8].

Encapsulation is a process in which core materials are enclosed within the confines of a coating material, most often a molecular container[9,10]. Cyclodextrins (CDs), cyclic oligosaccharides produced by enzymatic degradation of starch and possessing a doughnut-shaped ring structure,[11,12] have been widely utilized in encapsulation studies. The most commonly used CDs are *α*-CD, *β*-CD, and *γ*-CD, which consist of cyclic arrangements of 6, 7, or 8 glucopyranose units, respectively. While the exterior of CDs is hydrophilic allowing for a degree of water solubility, the central cavity is hydrophobic and permits inclusion complex formation when guest molecules, or part thereof, can fit appropriately and bind inside the cavity. The ability of the CDs to form an inclusion complex with the guest molecule depends upon matching of the cavity size and guest dimensions, and the occurrence of intermolecular forces such as van der Waals forces, hydrophobic interactions, and hydrogen bonds to enable host–guest binding[13,14]. For the three CDs mentioned above, the cavity sizes follow the order *α*-CD < *β*-CD < *γ*-CD, so it is necessary to consider carefully the dimensions of CD and guest to enable prediction of complexation behavior. For example, guest molecules having low molecular weights may be comfortably accommodated inside any of these CDs although it is possible that more than one guest molecule may reside inside the cavity. In contrast, guest molecules with higher molecular weights may be bound by more than one CD molecule, or have only one guest per cavity. Inclusion may also enable the reactivity of guest molecules to be tailored in the absence of chemical modifications[15,16].

The aim of this study was to investigate inclusion complex formation between two isomers of citral within CD host molecules, and assess the effect of citral:CDs molar ratio on total citral retention. Furthermore, probing the release characteristics and antimicrobial activities of the spray dried complexes was undertaken with a view toward assessing their utility in practical applications.

Materials and methods

Materials. *α*-CD, *β*-CD, and *γ*-CD were purchased from Ensuiko Sugar Chemical Co. (Yokohama, Japan).

*Corresponding author: Email: apinan.s@chula.ac.th

© 2017 Japan Society for Bioscience, Biotechnology, and Agrochemistry

Citral was purchased from Sigma-Aldrich Co. Ltd., (St. Louis, USA). Lemongrass oil was purchased from Thai-China Flavors and Fragrances Industry (Nonthaburi, Thailand). Chloroform and cyclohexanone were purchased from Wako Pure Chemical Industry (Osaka, Japan). The micro-organism used in antimicrobial testing was *Candida albicans* ATCC 10231, which was obtained from the Department of Medical Sciences (Ministry of Public Health, Thailand). Sabouraud dextrose broth (SDB) and Sabouraud dextrose agar (SDA) were from Difco (New Jersey, USA). Tween 80 (Polyoxyethylene sorbitan mono-oleate) was from VWR International Co. Ltd. (Pennsylvania, USA). Sodium chloride (NaCl) was obtained from Fisher Scientific (Leicestershire, UK). The deionized (DI) water was produced using a MilliQ Plus system (Millipore, Schwalbach, Germany).

Phase solubility study. The phase solubility study was conducted as described by Higuchi and Connors[17]. An excess amount of lemongrass oil (80 μL) was added, in separate experiments, into gas-tight vials containing an aqueous solution of CD (α-CD, β-CD, or γ-CD, concentration 0–10 mmol/L). The vials were shaken at 45 °C for 48 h to ensure equilibrium, and then the supernatants were separated by centrifugation (Kubota, Japan) at 10,000 rpm for 15 min. The supernatants (4 mL) were mixed with chloroform solution (1 mL, 1 μL/mL in cyclohexanone) in a sealed glass tube. The solutions were heated in a water bath at 90 °C for 30 min, with vortexing for 30 s after each 10-min interval. After this time, a 1-μL aliquot of the organic phase containing citrals was analyzed by gas chromatography (GC 2010, Shimadzu Corporation, Japan). Gas chromatography conditions were as follows: injector and detector temperatures 210 and 230 °C, respectively, initial column temperature 50 °C for 1 min followed by heating (10 °C/min) to 230 °C. From the phase solubility diagram the complex formation constant, K_C, could be calculated in accordance with Equation (1), as applied for the formation of a 1:1 inclusion complex.

$$K_C = \frac{\text{Slope}}{\text{Intercept} \times (1 - \text{Slope})} \quad (1)$$

Preparation of encapsulated spray-dried powder. All encapsulated powders were produced by spray drying, using α-CD, β-CD, or γ-CD as encapsulating agents. The inclusion complexes between CDs and citrals were prepared from a CD slurry (20 wt% solid in water). Lemongrass oil was added into the CD slurry at such a quantity to afford a predetermined citrals:CD molar ratio (1:1, 1.5:1, or 2:1). The mixtures were then shaken at 250 rpm, 45 °C for 12 h, followed by homogenization at 8000 rpm for 3 min using a high-speed homogenizer (Polytron PT 3100, Kinematica, Japan) affording the liquid feed for spray drying. The encapsulated powders were formulated using a spray dryer (Ohkawara Kakouki, Yokohama, Japan) operating under the following conditions: atomizer rotary speed 30,000 rpm, feed rate 30 mL/min, air flow rate 110 kg/h, inlet temperature 160 °C.

Determination of total citrals retention. The citrals content in each spray-dried powder was determined by solvent extraction with chloroform. The spray-dried powder (50 mg) was dissolved in distilled water (4 mL) and chloroform (1 mL), in a sealed glass tube. The solutions were heated in a water bath at 90 °C for 30 min, with vortexing for 30 s after every 10-min interval. The organic phase (1 μL) containing volatile compounds was analyzed by gas chromatography (GC 2010, Shimadzu Corporation, Japan) with quantification of citrals levels being determined as in the phase solubility study. The total citrals retention during spray drying is defined as the ratio of the quantity of citrals in the encapsulated powder on a dry basis relative to the original citrals level in the feed liquid.

SEM morphology investigations. A scanning electron microscope (JEOL JSM 6060, EVISA, Japan) was used to investigate the microstructure of the inclusion complexes. Spray-dried powders were placed on the SEM holder and coated with Pt–Pd using a magnetron sputter coater. The samples were then analyzed with the SEM operating at an accelerating voltage of 15 kV.

Release characteristics of citrals from spray-dried powders. The spray-dried powder (50 mg) were kept in an open bottle and placed in the chamber (BTL-433, Espec, United Kingdom) for 7 days at 37 °C and 52% RH. After this time, the powder was analyzed for residual amounts of citrals using the extraction method as described above. The citrals retention in the control release experiment was defined as the percentage of citrals content at each time relative to the initial citrals content, and the release rate constant of citrals under the experimental conditions could be derived from the Avrami equation (Equation (2)).

$$R = \exp[-(kt)^n] \quad (2)$$

In this equation, R represents the retention of the volatile, t is the release time, k is the release mechanism, and n is a parameter representing the release mechanism.

In vitro antimicrobial activity. The minimum inhibitory concentration (MIC) and the minimum bactericidal concentration (MBC) of citrals and lemongrass oil were firstly determined by microdilution broth testing against *C. albicans* ATCC 10231. Briefly, stock solutions of citrals and lemongrass oil were prepared at a concentration of 2,000 μg/mL (in 0.05% v/v Tween 80). All samples were transferred into 96-well plates and serial dilutions performed. Inoculums consisting of 10^6 CFU/mL were added into each well, followed by incubation at 37 °C for 48 h. Microbial growth was measured using a microplate reader (Molecular Devices, California, USA) at 600 nm. The MIC is defined as the lowest concentration of an antibacterial agent inhibiting visible growth, whereas MBC represents the lowest concentration of an antibacterial agent required for lethality. Following MIC/MBC

determination, the antimicrobial activities of spray-dried powders (at the highest total citrals retention) against *C. albicans* ATCC 10231 were assessed. The spray-dried powders were sterilized with UV irradiation for 1 h and then dissolved in SDB (0.05% v/v Tween 80) at a quantity corresponding to the MIC value. Inoculums consisting of 10^6 CFU/mL were added to the samples, and the treatment efficiency analyzed after incubation for 0, 1, 3, 5, and 7 h at 37 °C. At each of these times, inoculums were diluted with aqueous NaCl solution (0.85 wt% solid) and each dilution was spread onto SDA by spiral plattering (Spiral Biotech Autoplate 4000, USA), followed by further incubation at 37 °C for 48 h. Antimicrobial activities were measured by counting of viable colonies on the SDA surface. The treatment efficiency was defined as the percentage reduction (% Reduction) in bacterial growth, as expressed by Equation (3):

$$\%\text{Reduction} = \frac{(A-B)}{A} \times 100 \qquad (3)$$

where % Reduction represents the percentage reduction in microbial population. A is the number of colonies on media inoculated with microbes and B is the number of colonies on media with containing microbes and spray-dried powder.

Results and discussion

Phase solubility study

Phase solubility studies are useful for allowing fundamental predictions of inclusion complex formation to be made. Using this method, as reported by Higuchi and Connors,[17] the stoichiometry of the inclusion complex and its formation constant were determined in water at various CD concentrations. From this protocol, two types of phase solubility diagram can be obtained: type A (A_L, A_N, A_P solubility curves) when the solubility of the guest molecule increases with increasing CD concentration and type B (B_s, and B_i solubility curves) representing the formation of complexes having limited solubility in aqueous media. The phase solubility profiles for complexes formed between citrals (*E*-citral and *Z*-citral) and CDs at 45 °C are illustrated in Fig. 1. The aqueous solubilities of *E*-citral and *Z*-citral alone are approximately 4 mmol/L. Addition of CDs (2–10 mmol/L) to citrals resulted in enhancements in their water solubility, a consequence of inclusion complex formation. Complexation between α-CD and citrals afforded a linear solubility diagram defined as A_L type[17], with 1:1 complex stoichiometry. As the relationship is linear the formation constant can be calculated from the slope of the phase solubility diagram (Equation 1). Solubility profiles for citral complex formation with β-CD or γ-CD are consistent with the B_S type,[17] as the solubilities of both *E*-citral and *Z*-citral increased with β-CD and γ-CD concentration up to 4 mmol/L, and subsequently remained constant. Haiyee et al.[18] and Waleczek et al.[19] previously reported the stoichiometry of B_S type interactions could be assumed as being 1:1, with the complex formation constant derivable from the initial slope. The formation constants between *E*-citral and α-CD, β-CD, and γ-CD at 45°C were 123, 185, and 204 L/mol, respectively, although *Z*-citral showed slightly higher affinity for CD binding (157, 207, and 253 L/mol, respectively) under identical conditions. The binding strength trend implies that larger cavities allow for more favorable geometrical accommodation of the citrals, as reflected by the order γ-CD > β-CD > α-CD. Our formation constant results are the binding trend similar to those reported by Decock et al.[20], who report the formation constant between *E*-citral and α-CD and β-CD were 66 and 728 L/mol, respectively. Moreover, the complex formation constants between *Z*-citral and α-CD and β-CD were 93 and 693 L/mol, respectively.

The effect of CD type and citrals:CD mole ratio on total citrals retention

As reported earlier the major components of extracted lemongrass oil are *E*-citral (41.6% w/w) and *Z*-citral (31.78% w/w)[21] although these components are poorly water soluble and volatile. Accordingly, it was of interest to investigate the level of citral retention after encapsulation and this was achieved by varying the citrals:CD molar ratio during the fabrication process prior to quantification of citrals levels using gas chromatography. Figure 2 indicates that the total citrals retention decreased as loading levels increased, consistent with citrals being fully bound at low loadings and the presence of unbound citral in the powder at high citral:CD molar ratios. Higher citral:CD ratios result in CD cavities exhibiting full occupancy[22,23] with excess citrals being loosely held within the powder structure, resulting in loss during spray drying[24]. The maximum total citrals retention was observed at a citrals:CD molar ratio of 1:1. Furthermore, the degree of total retention of *E*-citral in CDs follows the order β-CD > γ-CD > α-CD, different to that of *Z*-citral (α-CD >

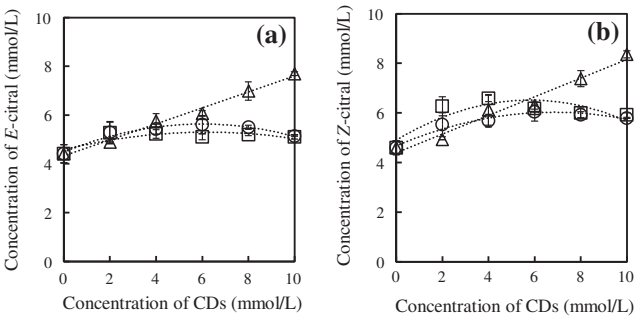

Fig. 1. Phase solubility study of *E*-citral (a) and *Z*-citral (b) within different CDs; α-CD (△), β-CD (○), γ-CD (□) at 45 °C.

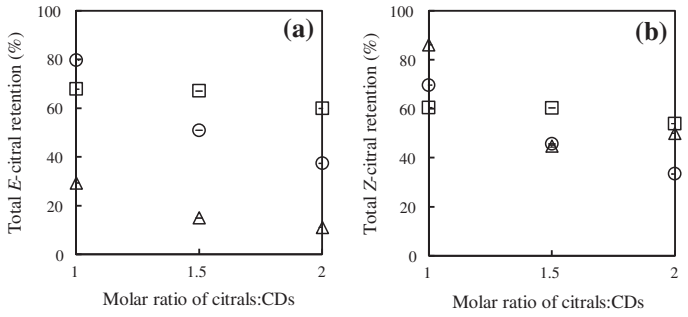

Fig. 2. Total *E*-citral retention (a) and *Z*-citral retention (b) within different CDs; *α*-CD (△), *β*-CD (○), *γ*-CD (□).

β-CD > *γ*-CD)[25]. According to the phase solubility results, the aqueous complex formation constants between citrals and CDs follow the order *γ*-CD > *β*-CD > *α*-CD, implying that *γ*-CD best accommodates citral guest molecules. However, the lower retention in *γ*-CD is a consequence of the less than optimal fit of the entire citral molecule within the cavity[25], resulting in their loss during spray drying and accounting for the lower total retention in this host system.

Scanning electron microscopy

The morphologies of all particles were investigated using scanning electron microscopy (SEM). Figure 3(a)–(c) shows SEM images of native *α*-CD, *β*-CD, and *γ*-CD particles, respectively. While the crystalline structure of native CDs is evident the encapsulated spray-dried powders prepared from *α*-CD and *γ*-CD resemble spherical aggregates (Fig. 3(d)–(f)), which occur as a result of agglomeration during spray drying. It is possible that the water solubility of CDs (*γ*-CD > *α*-CD > *β*-CD) may play a role in their dissolution, and the formation of inter-particle bridges at particle contact points on re-drying[26]. In contrast, spray-dried powder prepared from *β*-CD is observed to form crystalline particles, possibly due to the lower solubility of this host in comparison to other CDs.

Release characteristics of spray-dried powders

The controlled-release behavior of the encapsulated spray-dried powders (1:1 citrals:CD) was examined at

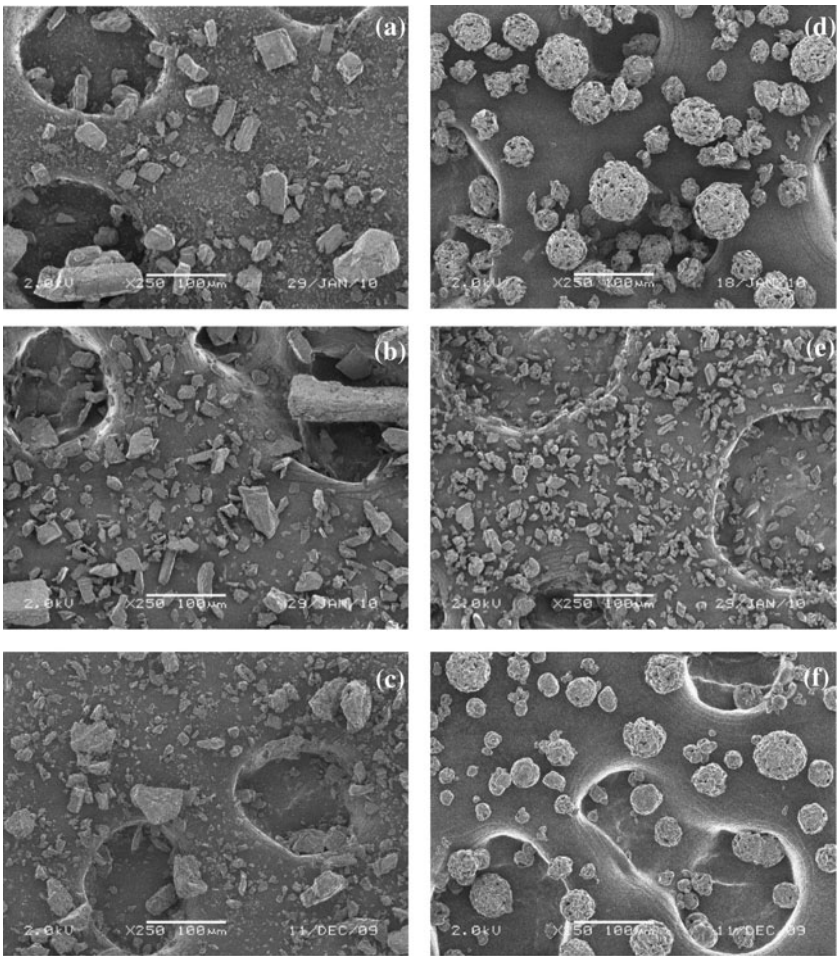

Fig. 3. SEM photographs of native *α*-CD (a), *β*-CD (b), *γ*-CD (c), and spray-dried 1:1 M ratio citral:CD powders (*α*-CD (d), *β*-CD (e), *γ*-CD (f)).

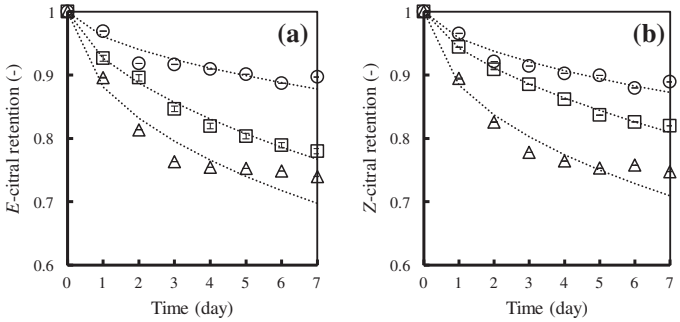

Fig. 4. Release behavior of *E*-citral (a) and *Z*-citral (b) from CD inclusion complexes at 37 °C, 52% relative humidity. α-CD (△), β-CD (○), γ-CD (□). Dashed lines represent calculated values by Avrami Equation.

37 °C and 52% relative humidity. Figure 4 highlights citrals release being more rapid in all CD systems during the first day of storage, with the release rate subsequently slowing and reaching a near plateau toward the end of the study period (c.a. 5 days). Considering the effect of CD type on citrals retention, the release rate of both citrals included in β-CD was lower than for that bound in other CDs. These results are consistent with those of total citral retention as discussed earlier, and indicate preferential inclusion of citrals within β-CD over the other systems[27]. Moreover, *E*-citral had a higher release rate than *Z*-citral. This result may be due to *Z*-citral could perfectly fit inside CDs cavity better than *E*-citral, similarly results with Ruktanonchai et al.[21].

Although both geometrical isomers of citral have the same molecular weight, their size difference may impart some effects on the release mechanism. The Avrami equation[28,29] (Equation 2) was used to evaluate the release rate constant, and hence the mechanism, of citrals release. Plotting ln(–ln*R*) (*y*-axis) against ln*t* (*x*-axis) afforded the Avrami parameters *n* and *k*, which are given in Table 1. Values of $n < 1$ indicated that release of included citrals from the complexes corresponds to the diffusion-limited kinetic model. The mechanism of molecular diffusion can be explained by the presence of water in the powder, which interacts with the polar surface of the CDs. Over time, citral molecules can undergo replacement by water which represents a reverse situation to that of inclusion complex formation. The higher values of *k* for α-CD and γ-CD complexes than β-CD complexes indicate greater levels of diffusion in the former systems, which is consistent with β-CD being able to encapsulate citrals more effectively as discussed earlier.

Table 1. Release rate constants (*k*) and parameters representing the release mechanism (*n*) of *E*-citral and *Z*-citral in lemongrass oil from CD inclusion complexes at 37 °C and 52% RH.

	n (–)		*k* (10^{-5}/day)	
Cyclodextrin	*E*-citral	*Z*-citral	*E*-citral	*Z*-citral
α-CD	0.54	0.52	21.4	18.6
β-CD	0.60	0.60	4.8	5.1
γ-CD	0.64	0.65	17.9	13.2

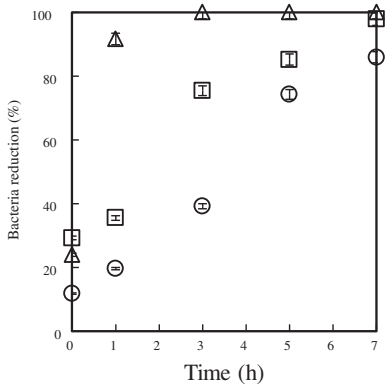

Fig. 5. Reductions in bacterial growth (*C. albicans*) as a function of time for media containing spray-dried powder; α-CD (△), β-CD (○), γ-CD (□).

Antimicrobial activities of spray-dried powders

As the minimum inhibitory (MIC) and MBCs obtained from pure citrals (250 and 1000 µg/mL, respectively) proved similar to those of lemongrass oil this suggests that these are the major antimicrobial components in the oil itself. Figure 5 highlights the impact of included citrals on the percentage reduction in growth of *C. albicans* as a function of time. Based on these results, α-CD complexes show the most pronounced antimicrobial effects, with 91.65% reduction in microbial levels after 1 h, and 100% after 3 h exposure. These results are consistent with the release rate order for included citrals (α-CD < γ-CD < β-CD), and indicate that the antimicrobial activities of both *E*-, and *Z*-citral are retained during the encapsulation process. In related work, Leimann et al.[1] have reported the MIC values of microencapsulated citrals toward *E. coli* (22.32 mg/mL), and *S. aureus* (2.79 mg/mL).

Conclusion

Molecular encapsulation within the cavity of CDs is an effective method for preventing the loss of citrals during spray drying. α-, and β-CDs proved most efficient for the encapsulation of *E*-citral and *Z*-citral, respectively, with all CDs showing maximum total citrals retention at a 1:1 M ratio of citrals:CD. The encapsulation efficiency was found to not be solely dependent on the complex formation constant, but was also influenced by the spray drying process. On storage, β-CD complexes exhibited slower release rates

than the γ-CD, and α-CD complexes, with citral release being consistent with the limited diffusion kinetic model.

Acknowledgment

We acknowledge the Center of Excellence in Particle Technology, Chulalongkorn University, Kagawa University, and National Nanotechnology Center, National Science and Technology Development Agency for providing facilities for this work.

Disclosure statement

No potential conflict of interest was reported by the authors.

Funding

The work was financially supported by the Chulalongkorn University [Contract No. RES_57_411_21_076]; The Thailand Research Fund [grant number DPG5880003], [grant number IRG5780014].

References

[1] Leimann FV, Gonçalves OH, Machado RAF, et al. Antimicrobial activity of microencapsulated lemongrass essential oil and the effect of experimental parameters on microcapsules size and morphology. Mat Sci Eng. 2009;29:430–436.
[2] Silva CB, Guterres SS, Weisheimer V, et al. Antifungal activity of the lemongrass oil and citral against *Candida* spp. Braz J Infect Dis. 2008;12(1):63–66.
[3] Tzortzakis NG, Economakis CD. Antifungal activity of lemongrass (*Cympopogon citratus* L.) essential oil against key postharvest pathogens. Innov Food Sci Emerg Technol. 2007;8:253–258.
[4] Ueno T, Masuda H, Ho CT. Formation mechanism of *p*-methylacetophenone from citral via a *tert*-alkoxy radical intermediate. J Agric Food Chem. 2004;52:5677–5684.
[5] Kimura K, Nishimura H, Iwata I, et al. Deterioration mechanism of lemon flavor. 2. Formation mechanism of off-odor substances arising from citral. J Agric Food Chem. 1983;31:801–804.
[6] Lu Z, Cheng B, Hu Y, et al. Complexation of resveratrol with cyclodextrins: solubility and antioxidant activity. Food Chem. 2009;113:17–20.
[7] Jafari SM, Assadpoor E, He Y, et al. Encapsulation efficiency of food flavours and oils during spray drying. Drying Tech. 2008;26:816–835.
[8] Zhang A, Liu W. Inclusion effect of alpha-cyclodextrin on chemical degradation of malathionin water. Arch Environ Contam Toxicol. 2008;54(3):355–362.
[9] Jafari SM, Assadpoor E, Bhandari B, et al. Nano-particle encapsulation of fish oil by spray drying. Food Res Int. 2009;41:172–183.
[10] Madene A, Jacquot M, Scher J, et al. Flavour encapsulation and controlled release – a review. Int J Food Sci Tech. 2006;41:1–21.
[11] Szejtli J. Past, present, and future of cyclodextrin research. Pure Appl Chem. 2004;76:1825–1845.
[12] Li Z, Wang M, Wang F, et al. γ-cyclodextrin: a review on enzymatic production and applications. Appl Microbiol Biotechnol. 2007;77:245–255.
[13] Astray G, Gonzalez-Barreiro C, Mejuto JC, et al. A review on the use of cyclodextrins in foods. Food Hydrocolloids. 2009;23:1631–1640.
[14] Del Valle EMM. Cyclodextrins and their uses: a review. Process Biochem. 2004;39:1033–1046.
[15] Karathanos VT, Mourtzinos I, Yannakopoulou K, et al. Study of the solubility, antioxidant activity and structure of inclusion complex of vanillin with β-cyclodextrin. Food Chem. 2007;101:652–658.
[16] Sajeesh S, Sharma CP. Cyclodextrin–insulin complex encapsulated polymethacrylic acid based nanoparticles for oral insulin delivery. Int J Pharm. 2006;325:147–154.
[17] Higuchi T, Connors KA. Phase-solubility techniques. Adv Anal Chem Inst. 1965;4:117–212.
[18] Haiyee ZA, Saim N, Said M, et al. Characterization of cyclodextrin complexes with turmeric oleoresin. Food Chem. 2009;114:459–465.
[19] Waleczek KJ, Marques HMC, Hempel B, et al. Phase solubility studies of pure (−)-α-bisabolol and camomile essential oil with β-cyclodextrin. Euro J Pharm Biopharm. 2003;55:247–251.
[20] Decock G, Landy D, Surpateanu G, et al. Study of the retention of aroma components by cyclodextrins by static headspace gas chromatography. J Inclusion Phenom Macrocyclic Chem. 2008;62:297–302.
[21] Ruktanonchai UR, Srinuanchai W, Saesoo S, et al. Encapsulation of citral isomers in extracted lemongrass oil with cyclodextrins: molecular modeling and physicochemical characterizations. Biosci Biotech Biochem. 2011;75:2340–2345.
[22] Toro-Sanchez CL, Ayala-Zavala JF, Machi L, et al. Controlled release of antifungal volatiles of thyme essential oil from β-cyclodextrin capsules. J Inclusion Phenom Macrocycl Chem. 2010;67:431–441.
[23] Fernandes LP, Oliveira WP, Sztatisz J, et al. Solid state studies on molecular inclusions of *Lippia sidoides* essential oil obtained by spray drying. J Therm Anal Cal. 2009;95:855–863.
[24] Liu XD, Furuta T, Yoshii H, et al. Cyclodextrin encapsulation to prevent the loss of l -menthol and its retention during drying. Biosci Biotechnol Biochem. 2000;64:1608–1613.
[25] Reineccius TA, Reineccius GA, Peppard TL. Encapsulation of flavors using cyclodextrins: comparison of flavor retention in Alpha, Beta, and Gamma types. J Food Sci. 2002;67:219–225.
[26] Buffo RA, Probst K, Zehentbauer G, et al. Effects of agglomeration on the properties of spray-dried encapsulated flavours. Flavour Fragr J. 2002;17:292–299.
[27] Reineccius TA, Reineccius GA, Peppard TL. Comparison of flavor release from alpha-, Beta- and Gamma-cyclodextrins. J Food Sci. 2003;68:1234–1239.
[28] Yoshii H, Soottitantawat A, Liu XD, et al. Flavor release from spray dried maltodextrin/gum arabic or soy matrices as a function of storage relative humidity. Innovative Food Sci Emerg Tech. 2001;2:55–61.
[29] Soottitantawat A, Takayama K, Okamura K, et al. Microencapsulation of l-menthol by spray drying and its release characteristics. Innovative Food Sci Emerg Tech. 2005;6:163–170.

Available online at www.sciencedirect.com

ScienceDirect

journal homepage: www.elsevier.com/locate/he

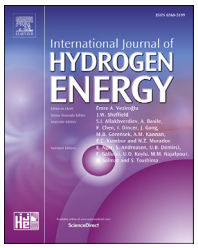

Modeling of thermally-coupled monolithic membrane reformer for vehicular hydrogen production

Tara Jiwanuruk [a], *Sompong Putivisutisak* [b,c], *Paravee Vas-Umnuay* [d], *Palang Bumroongsakulsawat* [a], *Chin Kui Cheng* [e], *Suttichai Assabumrungrat* [a,*]

[a] *Center of Excellence in Catalysis and Catalytic Reaction Engineering, Department of Chemical Engineering, Faculty of Engineering, Chulalongkorn University, Bangkok 10330, Thailand*

[b] *Department of Mechanical Engineering, Faculty of Engineering, Chulalongkorn University, Bangkok 10330, Thailand*

[c] *Advanced Computational Fluid Dynamics Research Unit, Faculty of Engineering, Chulalongkorn University, Phayathai, Bangkok 10330, Thailand*

[d] *Center of Excellence in Particle Technology, Department of Chemical Engineering, Faculty of Engineering, Chulalongkorn University, Bangkok 10330, Thailand*

[e] *Faculty of Chemical & Natural Resources Engineering, Universiti Malaysia Pahang, Lebuhraya Tun Razak, 26300 Gambang, Kuantan, Pahang, Malaysia*

ARTICLE INFO

Article history:
Received 18 June 2017
Received in revised form
29 August 2017
Accepted 31 August 2017
Available online 25 September 2017

Keywords:
Monolith
Heat integration
Membrane reactor
Hydrogen production

ABSTRACT

A thermally-coupled monolithic membrane reformer (TMMR) is a heat and membrane integrated reformer for portable hydrogen production. This study simulates the TMMR using Aspen Plus software to find the appropriate monolith design and operation parameters to achieve optimal energy efficiency and hydrogen production within a small volume reactor. Different types of fuels, *i.e.* methane, methanol and ethanol, and various operating conditions, including molar flow rate of fuel (0.01–0.05 mol/s for combustion and 0.1–0.5 mol/s for reforming) and reforming pressure (3–5 atm), were investigated via thermodynamic equilibrium analysis. When methanol and ethanol were used as feedstocks, a reverse water-gas-shift reaction occurred, resulting in a decrease of energy efficiency. While using methane as a feedstock with a specific molar flow rate of 0.03 mol/s for the combustion reaction, 0.30 mol/s for the reforming reaction, and a reforming pressure of 4 atm, significant improvement of efficiency was observed. At the same time, the performance of the TMMR design was simulated based on the surface area of different sizes and configurations of monolith, *i.e.* parallel and checked arrangements, by using a kinetic-based model approach. The highest efficiency achieved was from the checked arrangement of monolith with 200 cpsi of cell density, 150 mm of diameter and length, and

* *Corresponding author.*
E-mail address: suttichai.a@chula.ac.th (S. Assabumrungrat).

http://dx.doi.org/10.1016/j.ijhydene.2017.08.210

0360-3199/© 2017 Hydrogen Energy Publications LLC. Published by Elsevier Ltd. All rights reserved.

exchange area of around 1.5 m^2. This design requires a small space of only 2.65 L in volume to provide 129 kW of hydrogen energy production with 44.0% efficiency. In conclusion, the proposed design and conditions could be a benchmark for future research on efficient compact reformers for vehicular applications.

© 2017 Hydrogen Energy Publications LLC. Published by Elsevier Ltd. All rights reserved.

Introduction

Hydrogen is an energy carrier considered as an alternative fuel for renewable energy. Hydrogen fuel can potentially replace fossil fuels in vehicles leading to markedly reduced CO_2 emissions from the traditional combustion engine. The utilization of hydrogen fuel via fuel cells produces electricity for driving the vehicles and the fuel cell technology has been used recently in conventional vehicles [1–4]. As a result, the demand for hydrogen has been increasing significantly, leading to the development of the production and usage. Since the low density of hydrogen leads to an expensive transportation cost of the compressed or liquefied hydrogen fuel, on-site hydrogen production deflates the cost and increases economic feasibility [5–7], leading to an interest of portable hydrogen production using alternative fuels as a hydrogen source. Alternative fuels including methane, methanol, and ethanol have been utilized as feedstocks for hydrogen production in various industries [8,9]. These fuels can be produced from conventional industrial processes and bio-processes such as waste fermentation, gasification and pyrolysis of biomasses [10–16]. Moreover, methane and methanol can also be produced from recycling of carbon dioxide directly [17–19], resulting in the decrease of CO_2 emissions.

In conventional processes, hydrogen production comprises three main sections, *i.e.* heat supply, reforming and hydrogen separation. However, the conventional processes are not suitable for a portable system because of the size and weight limitations. For this reason, micro-channel reformers have been considered especially for vehicle applications [20–22]. Micro-channel reformers have several advantages over conventional reformers such as low pressure drop, low mass and heat transfer resistance and fast start-up. Monoliths have been used in several systems [23–27] to serve as the micro-channel structure as it is commercially available. Monoliths can integrate various processes within its structure, which consequently can lead to a compact micro-channel reformer. All the three main units required in the conventional hydrogen production processes can be integrated within the monolith to form a "thermally-coupled monolithic membrane reformer (TMMR)".

The integrated reformer has been studied separately in thermally-coupled reformers [28–30] and membrane reformers [26,31–38]. With heat being integrated, the diesel reformer in micro-scale combined with a heat exchanger of combustion gases was investigated by O'Connell et al. [28,29]. When operated at 1023 K and a steam to carbon molar ratio of 3.17, 98% of diesel was converted with successful hydrogen production for a 5-kW fuel cell. Zanfir and Gavriilidis simulated two channels of thermally-coupled reformers of methane using numerical methods [30]. It was found that the temperature gradient of the gas phase was 40 K which was significantly lower than those in conventional reformers.

The membrane integrated reformer has been investigated for a couple of decades. Membrane reactors showed remarkably high performance improvement over traditional reactors for hydrogen production [32–40]. The performance of membrane reactors depends on hydrogen separation rate increasing with the operating parameters such as temperature, pressure, sweep gas flow rate, etc. [41–43]. For the palladium membrane fabrication, Kim et al. successfully coated a palladium membrane with 8 μm of thickness within the cordierite monolith by electroless plating [26]. At the optimum operating condition, the selectivity of hydrogen per helium of 360 was achieved. Palladium membrane integrated with a water-gas-shift reactor was also investigated by Karnik et al. [31]. The membrane-supported copper catalyst yielded a hydrogen permeation flux of 5.2 mol m^{-2} s^{-1} when operated at 373 K. Additionally, a Pd-Au membrane was investigated for long term operation of methane steam reforming reaction [44]. Permeate purity of the membrane remained above 99.2% when operated continuously for 530 h. To simulate the membrane reactor, Aspen Plus using sequential modular approach was proposed [39,45,46]. In the study of Ye et al., a fluidized-bed membrane reformer was simulated via this method. Their simulation results were similar to the experimental results at various operating temperatures [39].

In this study, hydrogen production using TMMR was investigated using Aspen Plus with a sequential modular approach. The simulation was divided into two sections: thermodynamic study and TMMR design. In the thermodynamic study, methane, methanol and ethanol were used as feedstocks and the reformer was operated under various operating conditions. The TMMR design was optimized based on the surface area which depends on the monolith configuration, diameter, length, and cell density. The flow arrangement in the TMMR was also explored. The optimal design and operating conditions of TMMR as well as flow arrangement show great promise in terms of energy requirements for vehicular applications. This configuration of TMMR is proposed as a portable reformer and a guideline for TMMR fabrication in further studies.

Modeling and simulation

Model characteristics

For hydrogen utilization in vehicles, proton exchange membrane fuel cell (PEMFC) and recovering system of the process

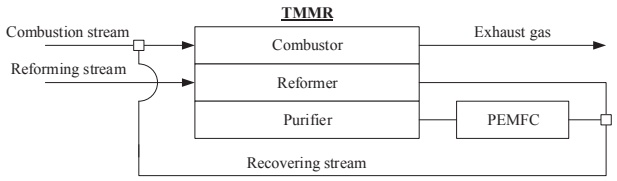

Fig. 1 – Hydrogen production system for vehicles.

were included in the model simulation, as shown in Fig. 1. Hydrogen produced from TMMR was directly fed into PEMFC. A half of moles of hydrogen was consumed and converted into electricity by PEMFC, giving the membrane a 50% efficiency [47,48]. After the conversion in PEMFC, unreacted hydrogen (the remaining 50%) mixed with the residue from the reforming streams and the gas mixture was fed as a recovering stream into the combustor of the TMMR.

As shown in Fig. 1, the model of TMMR was simplified into three sections comprised of combustor, reformer and purifier. Reactants including fuel and 3 mol/s of air were fed in excess into the combustor where the gases underwent a near complete combustion due to the fast reaction rate. Hot combusted gas was used to supply to the reforming section. No pressure drop was assumed for the flows in all sections.

In the reformer section, fuel and water reacted over a Ni based catalyst which was coated on the reformer wall inside this channel. The reactions were simulated based on thermodynamic equilibrium calculations and kinetic-based models under adiabatic and isobaric condition. Hydrogen gas and other by-products were produced and hydrogen obtained in the product stream was then separated using a membrane in the purifier section.

For hydrogen separation in the purifier, palladium and palladium alloy membranes were employed because of the high hydrogen solubility of palladium [49]. Hydrogen permeation flux through membrane was adopted from Gallucci et al. [50], as shown in Eq. (1), where the pressure inside the purifier was specified at 1 atm. Membrane thickness was fixed at 8 μm according to the experiment from Kim et al. [26]. Hydrogen can be permeated specifically from the reformer section into the purifier section without reversion.

$$H_2\text{flux} = \frac{1.12e^{-5}\left(\text{mol/m}\cdot\text{s}\cdot\text{Pa}^{0.5}\right)}{\text{Membrane thickness}} \cdot e^{\frac{-29.16(\text{kJ/mol})}{R\cdot T}} \cdot \left(p^{0.5}_{H_2,\text{Reforming}} - p^{0.5}_{H_2,\text{Purifier}}\right) \quad (1)$$

In this study, square channel monolith structures with parallel and checked arrangements were considered, as depicted in Fig. 2. Based on the TMMR design, surface area, which was used for exchanging heat, hydrogen separation, and calculation of catalyst weight in the reformer, and the flow arrangement were calculated. The ratios of surface area in the reformer, heat exchanger and separator are 0.5:0.125:0.125 for the parallel arrangement and 0.5:0.25:0.25 for the checked arrangement. Jiwanuruk et al. reported that the reformer with checked arrangement offered higher heat exchange ability in thermally coupled reformer and higher performance in a micro membrane reformer [24,25]. Thus, the checked arrangement was applied as a base case of this study.

Hydrogen energy and energy efficiency were used as an indicator of the TMMR performance. Hydrogen energy was computed from hydrogen consumption, and energy efficiency was calculated, as shown in Eqs. (2) and (3), respectively.

$$\text{Hydrogen energy(kW)} = n_{H_2} \cdot \Delta\widehat{H}^0_{c,H_2} \quad (2)$$

$$\text{Energy efficiency(\%)} = \frac{n_{H_2} \cdot \Delta\widehat{H}^0_{c,H_2}}{n_{fuel} \cdot \Delta\widehat{H}^0_{c,fuel}} \times 100 \quad (3)$$

Simulation with Aspen Plus

Aspen Plus is a commercial software which is widely used in process simulation. However, the model of TMMR does not exist in the program, therefore a sequential modular approach was required for the TMMR process simulation. This method has been conducted in several Aspen Plus simulations [39,45,46]. As illustrated in Fig. 3, TMMR was divided into sub-combustors, sub-reformers, and sub-purifiers. Sub-combustors performed as heat exchanger units that supplied heat to the reforming stream where the reactions took place in the sub-reformer. The heat exchanger was simplified using a constant overall heat transfer coefficient at 130 W m^{-2} K^{-1} [51]. Then, hydrogen obtained in the product stream was separated via sub-purifier. FORTRAN code for hydrogen separation based on Eq. (1) was incorporated into Aspen Plus. The permeated hydrogen was fed into the next sub-purifier, while the residue was fed as a reforming stream into the next sub-units. Peng–Robinson equation was applied as the equation of state for the calculations.

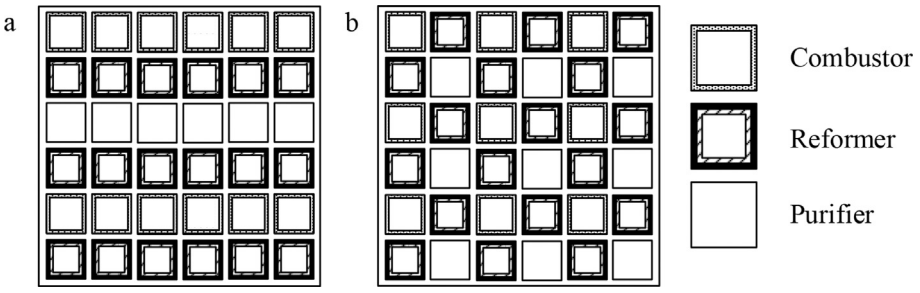

Fig. 2 – Illustrations of two different types of flow arrangements of TMMR; a) parallel arrangement and b) checked arrangement.

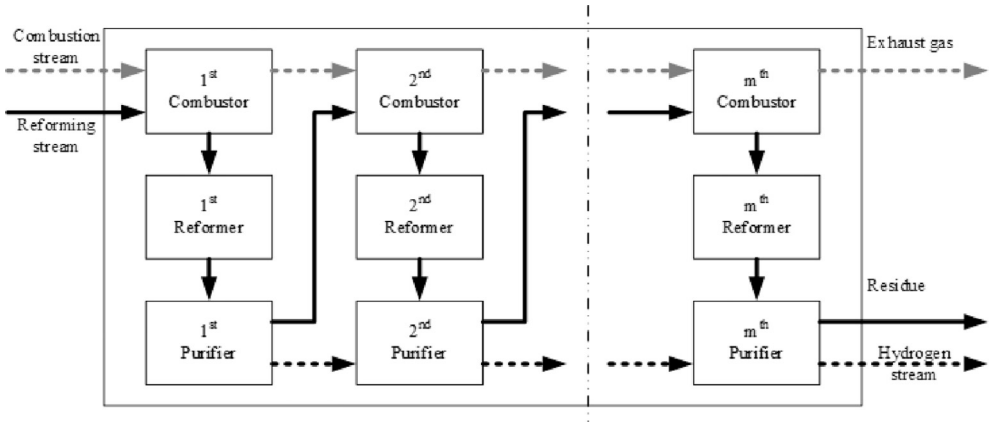

Fig. 3 – Schematic diagram of sequential modular simulation of TMMR.

Results and discussion

Model validation

The model for membrane reactors was validated with the experimental results from methane steam reforming reactions based on thermodynamic equilibrium and kinetic-based models. For this study, the number of sub-units (m) was varied from 1 to 40 to assure the model was fully integrated between reactor and membrane separator. Methane conversion was used as the indicator to estimate the reasonable value of m. The increment of m has led to increasing methane conversion because the system was operated almost similar to the integrated reformer. When m of 40 was used in both models, the system was completely integrated and the variation of methane conversion became inconsequential. Therefore, the value of m was suitable at 40 which was employed in both model studies.

To verify the simulation results, the experimental data obtained in a traditional reactor (TR) and a membrane reactor (MR) from Shu et al. [52] and Gallucci et al. [53] were adopted. In the thermodynamic equilibrium model, comparison of methane conversion at different temperatures from simulated and experimental data from Shu et al. are shown in Fig. 4a, while those of the kinetic model and experiments from Gallucci et al. are shown in Fig. 4b. Similar trend curves were observed for simulated and experimental results in both models. The related results of experiment and simulation proved the accuracy of the calculation and the models can represent the system of membrane reactors. As a result, both models were qualified and applicable for further study.

Thermodynamic-based study

Thermodynamic-based approach was a preliminary study of TMMR based on thermodynamic equilibrium. For each sub-reformer, the Gibbs reactor model in Aspen Plus was employed and free energy minimization was calculated to determine the products at equilibrium state. The total Gibbs function for the system is given as follows.

$$nG = \sum\left(n_i G_i^0\right) + RT\sum\left(n_i \ln\frac{y_i p\widehat{\phi}}{f_i^0}\right) \quad (4)$$

Methane, methanol and ethanol were examined as different hydrogen sources and possible products of these fuels from steam reforming reactions must be specified in the Gibbs reactor. Based on the experiments [54–57], by-products such as formaldehyde, dimethyl ether, acetaldehyde, ethylene and acetone were obtained from steam reforming reactions of methanol and ethanol. However, these by-products are not thermodynamically stable; hence they were excluded from the simulation [54–57]. Therefore, $CH_3OH, C_2H_5OH, CH_4, H_2O, H_2, CO$ and CO_2 were considered as the products in this model.

In the preliminary study, the monolith with cell density of 300 cpsi, diameter of 100 mm and length of 200 mm was used as a based model. Various operating conditions were investigated to achieve the energy requirement of commercial vehicles approximately at 100 kW. Different alternative fuels, including methane, methanol and ethanol, are fed into the combustion section with molar flow rates ranging from 0.01 to 0.05 mol/s. While in the reforming section, flow rates of methane and methanol were in the range of 0.10–0.50 mol/s. However, due to higher hydrogen content of ethanol, flow rate of ethanol was in the range of 0.10–0.30 mol/s. Steam to carbon molar ratio was fixed at 2.0 for methane, 1.0 for methanol and 3.0 for ethanol according to their stoichiometry. Reforming pressure was operated between 3 and 5 atm.

Effects of feed flow rate of alternative fuels

To investigate the effects of feed flow rate of the alternative fuels, the reforming pressure was fixed at 4 atm. According to previous studies, steam reforming of ethanol and methanol could reach nearly 100% conversion in the first sub-reformer due to their thermodynamic properties at equilibrium state [54–57]. Energy efficiency which was limited to 50% by the efficiency of PEMFC can be seen in Fig. 5(a – c). With increasing flow rate in the reforming and combustion sections, the temperature profile in the TMMR was raised, resulting in enhanced reaction rate and hydrogen separation. Similarly, the conversion of fuel and hydrocarbon by-products was also

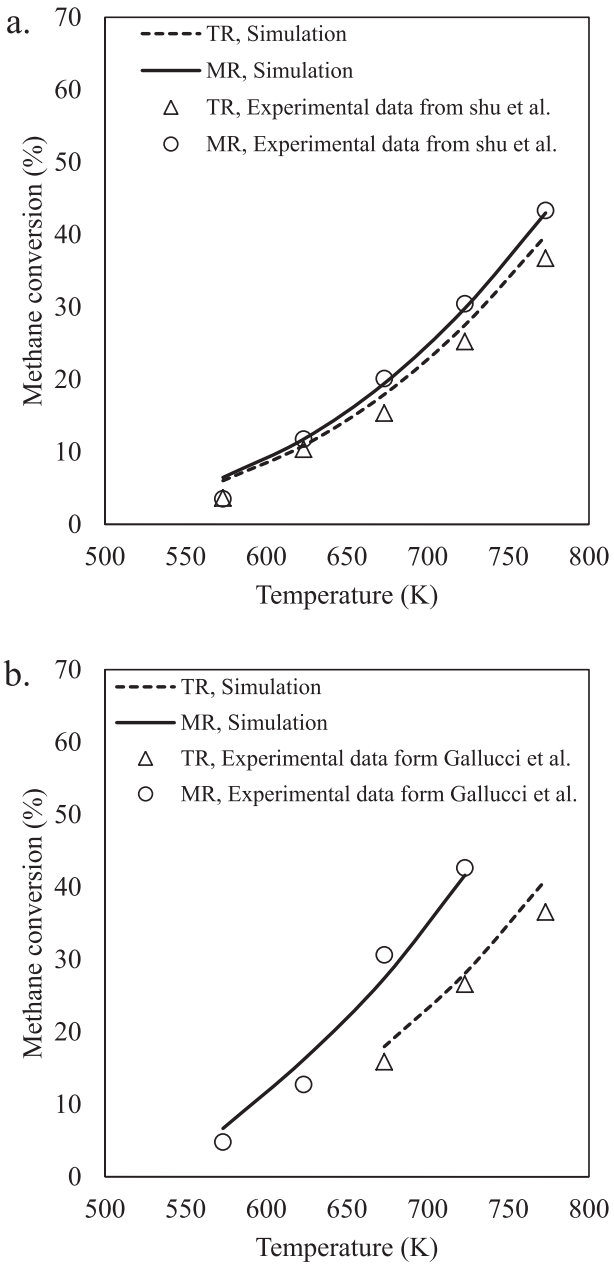

Fig. 4 – Relationship between methane conversion and temperature in traditional reactor and membrane reactor; a) thermodynamic equilibrium and b) kinetic-based models. Solid and dash lines indicate simulated results from both reactors, while ○ and △ are experimental results from both reactors from Shu et al. [52] and Gallucci et al. [53].

increased, leading to higher energy efficiency. After a complete conversion, a further increase of the flow rate promoted a reverse water-gas-shift reaction. Thus, hydrogen product was reduced in the reforming section, which consequently decreased the energy efficiency. Therefore, the TMMR performed effectively when operated at high temperature with less presence of reverse water-gas-shift reaction.

When comparing the efficiency derived among different hydrogen sources, the highest energy efficiency achieved at various molar flow rates of combustion and reforming streams was obtained from methane (Fig. 5a), followed by ethanol (Fig. 5c) and methanol (Fig. 5b). It should be noted that the shades of color in the figures represent the efficiency profile. Since the conversion was complete in the inlet section, methanol and ethanol were mainly converted into methane and syngas. When reforming temperature was increased along the reformer, methane steam reforming and reverse water-gas-shift reactions occurred. Upon completion of methane conversion, the reverse water-gas-shift reaction occurred resulting in lower energy efficiency. It was found that the reverse water-gas-shift reaction was more apparent when using methanol and ethanol. Therefore, methanol and ethanol, which were sensitive at high temperature, were not suitable as feedstocks for TMMR. As a consequence, methane was proposed to be used as the fuel of choice for TMMR in this study.

Effect of reforming pressure

As presented in Eq. (1), increasing reforming pressure enhanced the driving force of hydrogen separation. The highest energy efficiencies derived from TMMR when reforming pressure was operated at 3, 4, and 5 atm were 39.14%, 43.02%, and 45.12%, which can be seen in Figs. 6a, 5a and 6b, respectively. Reforming pressure of 4 atm offered over 40% of energy efficiency and a further increase of reforming pressure provided an unnoticeable improvement. In this study, the reforming pressure of 4 atm was used consequently in the calculations.

According to the simulation, hydrogen energy produced from the TMMR system with various molar flow rates of combustion and reforming streams is demonstrated in Fig. 7, where the shades of color represent the hydrogen energy profile. For commercial vehicles, the energy requirement was approximately about 100 kW which was considered as the energy production target in this study. The condition that can achieve the target was methane flow rate beyond 0.30 mol/s for the reforming stream and 0.01 mol/s for the combustion stream. The high energy efficiency which was close to the target was performed at 0.30 and 0.03 mol/s for the reforming and combustion sections respectively. This operating condition successfully provided 126.10 kW of energy with 42.92% energy efficiency.

Furthermore, the increase of feed flow rate of fuel resulted in increasing operating temperature of TMMR. Even though the energy efficiency was increased with increasing temperature, the efficiency was decreased because of the presence of reverse water-gas-shift reaction. As a result, the suitable operating conditions using methane as a fuel were implemented as following; reforming pressure of 4 atm with the feed flow rate of 0.30 mol/s for reforming reaction and 0.03 mol/s for the combustion reaction.

TMMR design

In this section, a plug flow reactor model was used to simulate the reaction occurring in the reforming channel whereby the catalyst weight was specific at 0.04 kg/m^2. Since the catalyst was fabricated over the reformer wall, the catalyst weight was calculated based on the surface area of the reforming channel

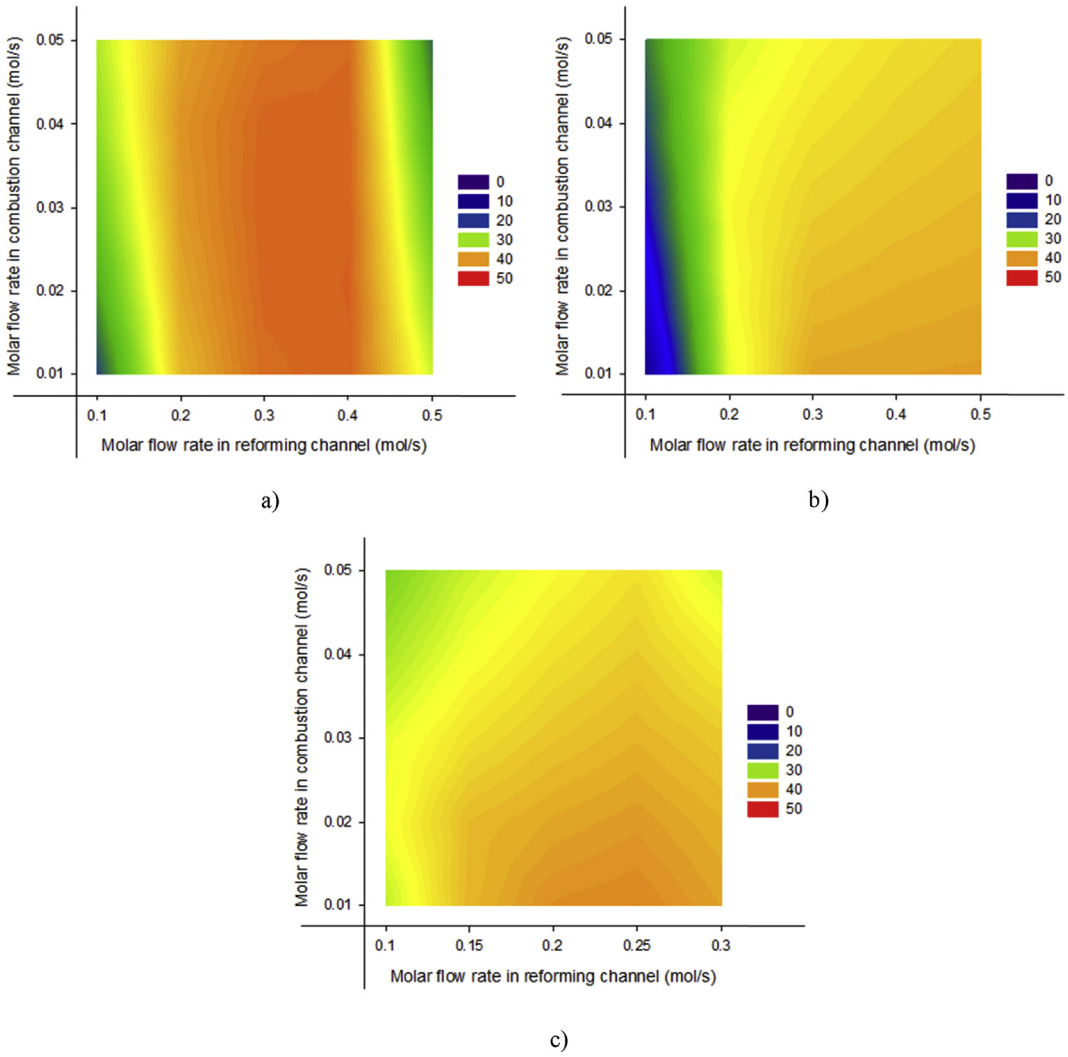

Fig. 5 – Energy efficiency profiles of different green fuels; a) methane, b) methanol, and c) ethanol, obtained from various molar flow rates of combustion and reforming streams at reforming pressure of 4 atm. (For interpretation of the references to color in this figure legend, the reader is referred to the web version of this article.)

in the monolith structure. According to thermodynamic-based study, methane, which provided the highest efficiency, was used for designing the TMMR in terms of a kinetic-based model. All of methane steam reforming reactions are shown in R1 to R3 and their kinetic expressions obtained from Xu and Froment are presented in Eqs. (5)–(7), respectively [58].

$$CH_4 + H_2O \leftrightarrow CO + 3H_2 \quad (R1)$$

$$CO + H_2O \leftrightarrow CO_2 + H_2 \quad (R2)$$

$$CH_4 + 2H_2O \leftrightarrow CO_2 + 4H_2 \quad (R3)$$

$$r_{R1} = \frac{\frac{k_1}{p_{H_2}^{2.5}}\left(p_{CH_4}p_{H_2O} - \frac{p_{H_2}^3 p_{CO}}{K_{eq1}}\right)}{\left(1 + K_{CO}p_{CO} + K_{H_2}p_{H_2} + K_{CH_4}p_{CH_4} + \frac{K_{H_2O}p_{H_2O}}{p_{H_2}}\right)^2} \quad (5)$$

$$r_{R2} = \frac{\frac{k_2}{p_{H_2}}\left(p_{CO}p_{H_2O} - \frac{p_{H_2}p_{CO_2}}{K_{eq2}}\right)}{\left(1 + K_{CO}p_{CO} + K_{H_2}p_{H_2} + K_{CH_4}p_{CH_4} + \frac{K_{H_2O}p_{H_2O}}{p_{H_2}}\right)^2} \quad (6)$$

$$r_{R3} = \frac{\frac{k_3}{p_{H_2}^{3.5}}\left(p_{CH_4}p_{H_2O}^2 - \frac{p_{H_2}^4 p_{CO_2}}{K_{eq3}}\right)}{\left(1 + K_{CO}p_{CO} + K_{H_2}p_{H_2} + K_{CH_4}p_{CH_4} + \frac{K_{H_2O}p_{H_2O}}{p_{H_2}}\right)^2} \quad (7)$$

where K_{eq} are equilibrium constants of each reaction according to their numbers. All of the kinetic parameters are listed in Table 1. The reaction rate constants are expressed in Eqs. (8) and (9) as follows.

$$k_i = A_i \exp\left(\frac{-E_a}{RT}\right) \quad (8)$$

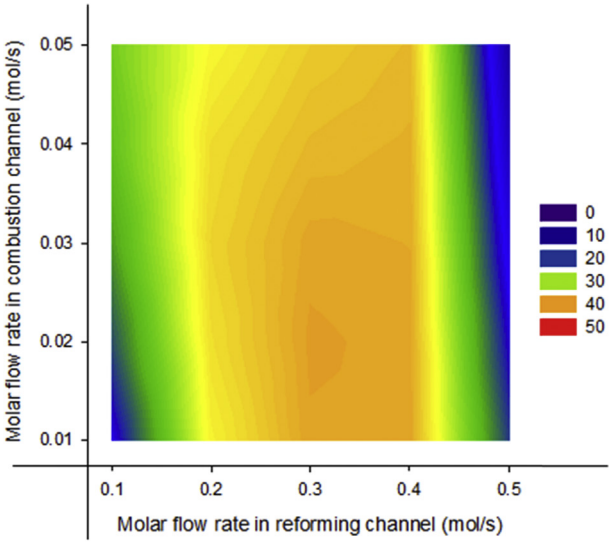

a)

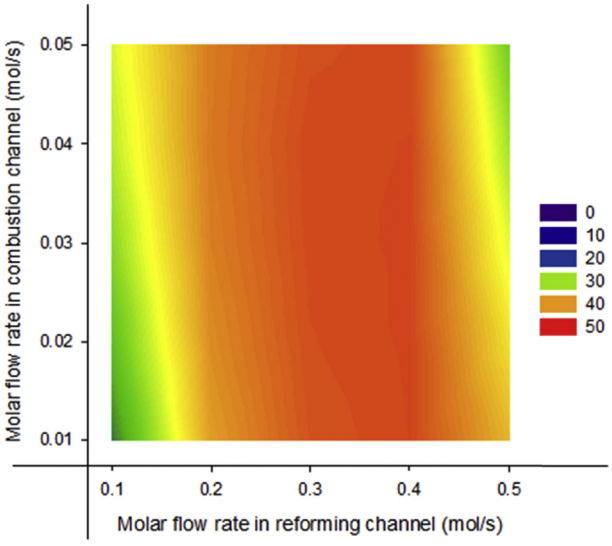

b)

Fig. 6 – Energy efficiency profiles of methane as fuel obtained from various molar flow rates of combustion and reforming streams when reforming at a) 3 atm and b) 5 atm.

$$K_i = A_i \exp\left(\frac{-\Delta H}{RT}\right) \quad (9)$$

where E_a and ΔH are activated energy and enthalpy change of reaction, respectively.

To design the TMMR, selected operating conditions derived from the thermodynamic-based study were employed. The configuration of monolith was specified as follows; cell density of 200, 300 and 400 cpsi and diameter and length between 100 and 200 mm. The monolith with checked arrangement was conducted with the area ratio of 0.25:0.25:0.50 for heat exchange, hydrogen separation and reaction, respectively.

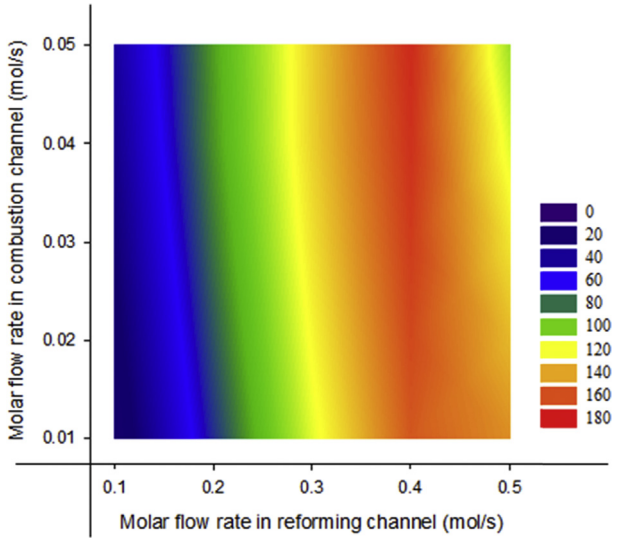

Fig. 7 – Hydrogen energy profile of methane steam reforming at 4 atm obtained from various molar flow rates of combustion and reforming streams.

Table 1 – Lists of reaction rate constants and kinetic parameters in Eqs. (5)–(7) [58].

Parameters	Pre-exponential factors	Activated energy (kJ/mol)	Enthalpy change (kJ/mol)
k_1	4.225×10^{15}	240.10	–
k_2	1.955×10^{6}	67.13	–
k_3	1.020×10^{15}	243.90	–
K_{CO}	8.23×10^{-5}	–	−70.65
K_{H2}	6.12×10^{-9}	–	−82.90
K_{CH4}	6.65×10^{-4}	–	−38.28
K_{H_2O}	1.77×10^{5}	–	88.68

For a small surface area of monolith (with 100 mm in diameter, 200 mm long, and 200 cpsi of cell density), temperature profile and molar flow rate of reforming products along the TMMR length are shown in Fig. 8(a – b), respectively. It can be explained that small surface area of monolith provided low heat transfer, resulting in high energy loss in the exhaust gas at the outlet stream. Due to the lower temperature at the inlet, lower rate of reaction was obtained, leading to a low content of hydrogen and an absence of hydrogen separation. However, when the partial pressure of hydrogen, operated in the reformer with 65 mm long, was higher than 1 atm, hydrogen separation appeared and the reaction shifted forward. Consequently, methane conversion obtained was about 82% at the outlet of TMMR. On the other hand, the incomplete conversion and low hydrogen separation could lead to energy efficiency as low as 32.84%.

In comparison, for a high surface area of monolith (with 200 mm in diameter, 200 mm long, and 200 cpsi of cell density), temperature profile and molar flow rate of reforming products are presented in Fig. 9(a – b), respectively. Fig. 9a shows a sharp decrease of the combustion gas temperature, indicating that heat could transfer to the

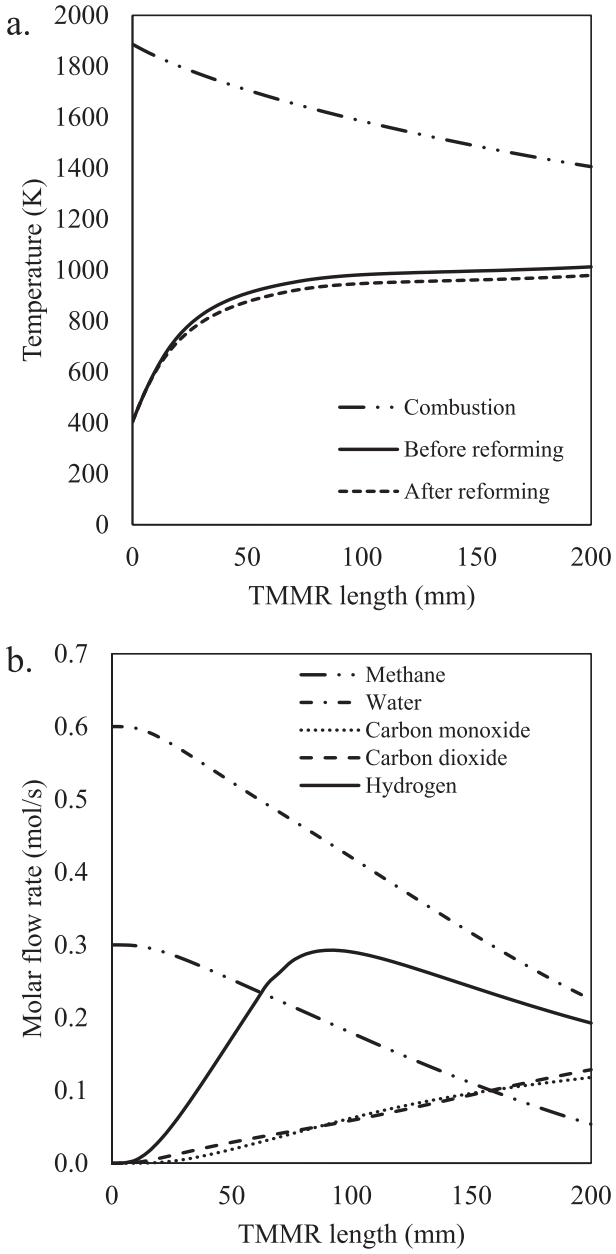

Fig. 8 – Plots of (a) temperature profiles of combustion, before reforming, and after reforming streams versus TMMR length and (b) molar flow rates of reforming products versus TMMR length, obtained from monolith with small surface area (100 mm in diameter, 200 mm long, and 200 cpsi of cell density).

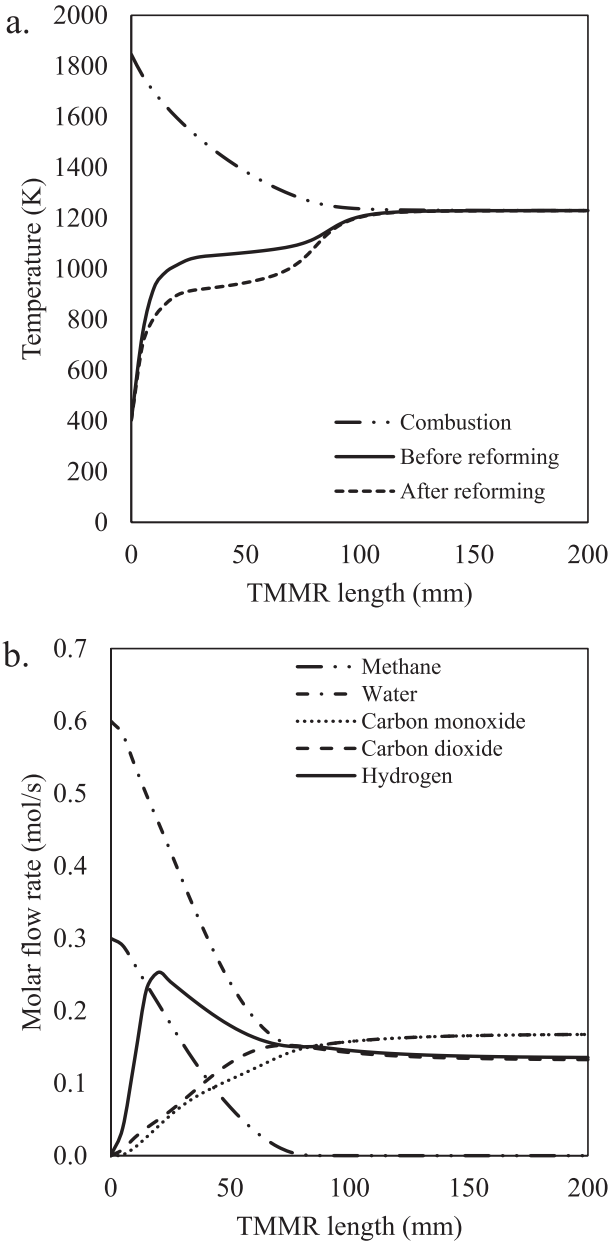

Fig. 9 – Plots of (a) temperature profiles of combustion, before reforming, and after reforming streams versus TMMR length and (b) molar flow rates of reforming products versus TMMR length, obtained from monolith with large surface area (200 mm diameter, 200 mm long, and 200 cpsi).

reforming gas efficiently. The reforming temperature rapidly increased and approached the combustion gas temperature when the reactor length was beyond 100 mm, resulting in the apparently high reaction rate. Furthermore, hydrogen separation started at the reformer length of 15 mm. The complete conversion of methane was also obtained when the reformer length was higher than 85 mm. After the conversion has completed, reverse water-gas-shift reaction occurred at high temperature, resulting in lower partial pressure of hydrogen, which limited the separation process. Consequently, the energy efficiency of 43.63% for this design was obtained.

It is obvious that the exchange area of monolith has a significant influence on the energy efficiency and hydrogen production. It can be seen from Fig. 10 that the hydrogen energy increases sharply until it reaches the maximum at the exchange area of 1.5 m^2. However, further increase of the exchange area led to a slight decrease of hydrogen energy as a result of the presence of reverse water-gas-shift reaction from the excessive heat for reforming reaction. From this study, the

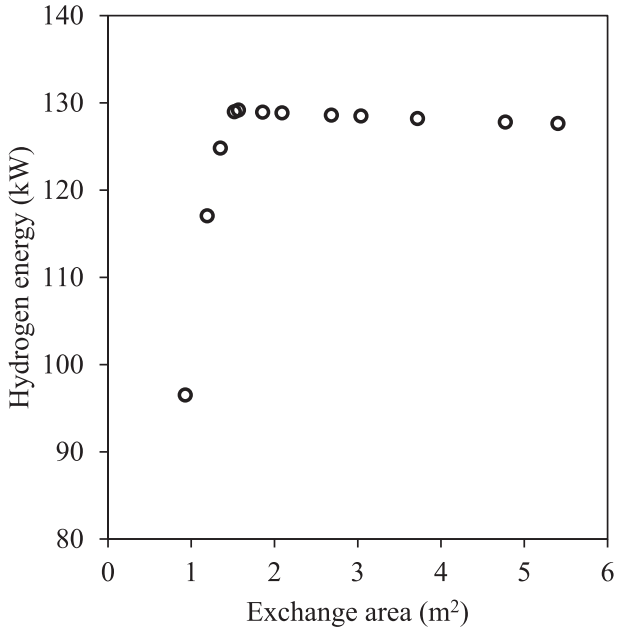

Fig. 10 – Plot of hydrogen energy production versus exchange area of monolith.

design of monolith with 200 cpsi of cell density and 150 mm in diameter and length, which resulted in a small volume of only 2.65 L required, which under optimal conditions used in conjunction with the TMMR, produced 129 kW of hydrogen energy at 43.96% efficiency.

Effect of the flow arrangement on the TMMR

In this part, the effect of different TMMR configurations on flow arrangements in the monolith and corresponding operating conditions was investigated. It should be noted that the exchange area of the parallel arrangement was half of that of the checked arrangement. According to Table 2 which shows the energy efficiency and hydrogen energy production rate obtained from both arrangements, it is revealed that the monolith with checked arrangement provided almost complete conversion of methane and higher hydrogen energy production and energy efficiency, compared to that of the parallel arrangement. For further study of the effect of different arrangements on the heat transfer, temperature profile and hydrogen permeation were investigated along the TMMR length, which is shown in Fig. 11(a – b). It is observed that the reforming temperature in the parallel arrangement

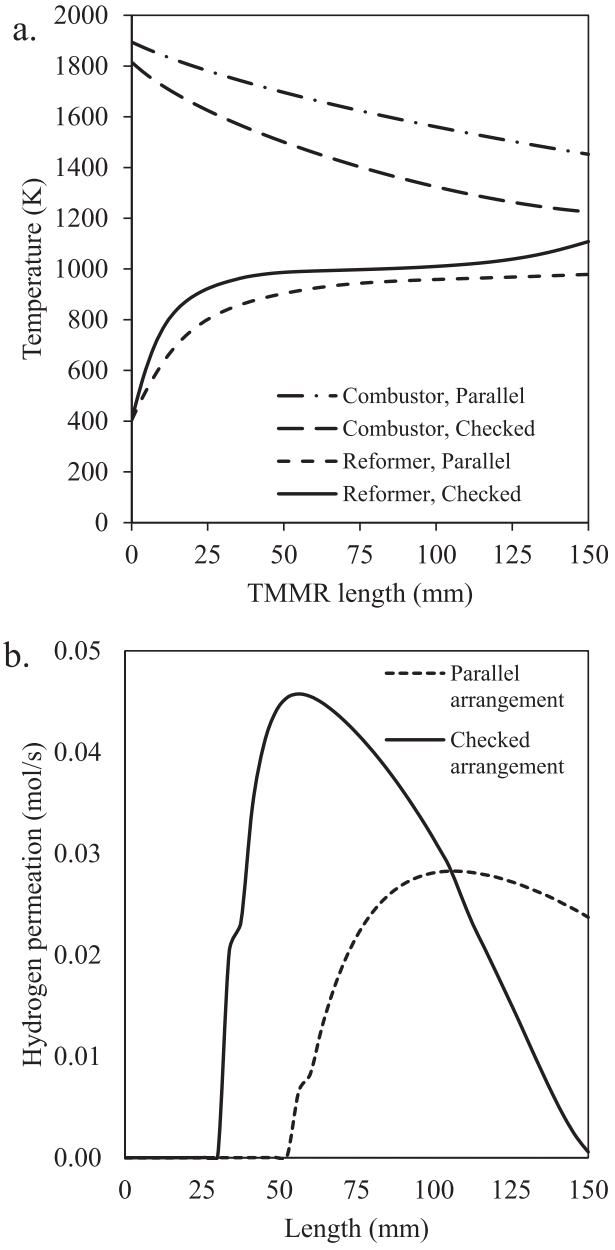

Fig. 11 – Relationships between (a) temperature profiles of streams in the combustor and reformer with parallel and checked arrangements and TMMR length, and (b) hydrogen permeation in the parallel and checked arrangements of monolith along the TMMR length.

was lower than that of the checked arrangement, due to the poorer heat transfer within the configuration. Moreover, hydrogen separation rate was slower while the reforming stream still contained a high content of hydrogen, as shown in Fig. 11b. As a result, a larger area was required to complete the separation process of the parallel arrangement. Total hydrogen permeation in the parallel arrangement was 0.62 mol/s which was lower than that in the checked arrangement which was 0.28 mol/s. Low heat transfer and separation rate led to a decrease in equilibrium shift effect. Hence, methane conversion was reduced to 77%.

Table 2 – Comparison of methane conversion, hydrogen energy production, and energy efficiency obtained from the parallel arrangement and the checked arrangement.

Flow arrangement	Methane conversion (%)	Hydrogen production (kW)	Energy efficiency (%)
Parallel arrangement	77.1	88.2	30.0
Checked arrangement	99.7	129.2	44.0

Since the monolith with checked arrangement provided more efficient heat transfer and higher hydrogen separation, resulting in 40 kW of hydrogen energy higher and 14% of energy efficiency higher than those obtained from the parallel arrangement, therefore the checked arrangement was applied in the TMMR. According to the proposed TMMR configuration and operating condition, the working temperature which averaged 973 K was obviously high when compared with the conventional palladium membrane reactor operations. However, there are several studies on palladium membranes with evidence of hydrogen permeation at the temperatures of up to 1173 K, proving the availability of palladium membrane for high working temperature [59–61].

Conclusion

A thermally coupled monolithic membrane reformer, TMMR, for portable system applications was studied using Aspen Plus software by using a sequential method for 40 sub-units. Various operating conditions and different types of hydrogen sources were examined via thermodynamic equilibrium approach. The operating temperature was increased with increasing molar flow rate of fuel. Among methane, methanol, and ethanol as fuels, methane provided the highest energy efficiency, which is suitable for TMMR. This is because the reverse water-gas-shift reaction persisted when methanol and ethanol were used as fuels, resulting in lower hydrogen production and energy efficiency. Moreover, the efficiency was enhanced by the increase of the reforming pressure, and it was appropriate at 4 atm. For the design of TMMR with different configurations of monolith, the simulations were calculated based on the kinetic-based model by using methane as a fuel. It was found that the energy efficiency depended on the exchange area of the monolith, resulting in higher performance with the checked arrangement configuration. The monolith with checked arrangement of 200 cpsi of cell density, 150 mm in diameter and length, and 1.5 m^2 of exchange area provided the best performance of the TMMR. This design, which requires only 2.65 L of volume, could offer 129 kW of hydrogen energy and 43.96% efficiency, can perform as a compact reformer for vehicular system applications. This model of TMMR can be a guideline for further studies on compact reactor fabrication.

Acknowledgement

This work is financially supported by the Thailand Research Fund (DPG5880003) and the Royal Golden Jubilee PhD Program from the Thailand Research Fund and Chulalongkorn University.

REFERENCES

[1] Yetano Roche M, Mourato S, Fischedick M, Pietzner K, Viebahn P. Public attitudes towards and demand for hydrogen and fuel cell vehicles: a review of the evidence and methodological implications. Energy Policy 2010;38:5301–10.
[2] Fayaz H, Saidur R, Razali N, Anuar FS, Saleman AR, Islam MR. An overview of hydrogen as a vehicle fuel. Renew Sustain Energy Rev 2012;16:5511–28.
[3] Eberle U, Müller B, von Helmolt R. Fuel cell electric vehicles and hydrogen infrastructure: status 2012. Energy Environ Sci 2012;5:8780.
[4] Contestabile M, Offer GJ, Slade R, Jaeger F, Thoennes M. Battery electric vehicles, hydrogen fuel cells and biofuels. Which will be the winner? Energy Environ Sci 2011;4:3754.
[5] Melaina M, Penev M. Hydrogen station cost estimates: comparing hydrogen station cost calculator results with other recent estimates. NREL (National Renewable Energy Laboratory (NREL), Golden, CO (United States)); 2013.
[6] Shayegan S, Pearson PJG, Hart D. Hydrogen for buses in London: a scenario analysis of changes over time in refuelling infrastructure costs☆. Int J Hydrogen Energy 2009;34:8415–27.
[7] Gim B, Yoon WL. Analysis of the economy of scale and estimation of the future hydrogen production costs at on-site hydrogen refueling stations in Korea. Int J Hydrogen Energy 2012;37:19138–45.
[8] Katayama Y, Tamaura Y. Development of new green-fuel production technology by combination of fossil fuel and renewable energy. Energy 2005;30:2179–85.
[9] Lv H, Geletii YV, Zhao C, Vickers JW, Zhu G, Luo Z, et al. Polyoxometalate water oxidation catalysts and the production of green fuel. Chem Soc Rev 2012;41:7572–89.
[10] Sutton D, Kelleher B, Ross JR. Review of literature on catalysts for biomass gasification. Fuel Process Technol 2001;73:155–73.
[11] Sun Y, Cheng J. Hydrolysis of lignocellulosic materials for ethanol production: a review. Bioresour Technol 2002;83:1–11.
[12] Yadvika Santosh, Sreekrishnan TR, Kohli S, Rana V. Enhancement of biogas production from solid substrates using different techniques–a review. Bioresour Technol 2004;95:1–10.
[13] Brethauer S, Wyman CE. Review: continuous hydrolysis and fermentation for cellulosic ethanol production. Bioresour Technol 2010;101:4862–74.
[14] Carpenter D, Westover TL, Czernik S, Jablonski W. Biomass feedstocks for renewable fuel production: a review of the impacts of feedstock and pretreatment on the yield and product distribution of fast pyrolysis bio-oils and vapors. Green Chem 2014;16:384–406.
[15] Taherzadeh MJ, Karimi K. Pretreatment of lignocellulosic wastes to improve ethanol and biogas production: a review. Int J Mol Sci 2008;9:1621–51.
[16] Mohan D, Pittman CU, Steele PH. Pyrolysis of wood/biomass for bio-oil: a critical review. Energy Fuels 2006;20:848–89.
[17] Centi G, Perathoner S. Opportunities and prospects in the chemical recycling of carbon dioxide to fuels. Catal Today 2009;148:191–205.
[18] Olah GA, Goeppert A, Prakash GS. Chemical recycling of carbon dioxide to methanol and dimethyl ether: from greenhouse gas to renewable, environmentally carbon neutral fuels and synthetic hydrocarbons. J Org Chem 2008;74:487–98.
[19] Roy SC, Varghese OK, Paulose M, Grimes CA. Toward solar fuels: photocatalytic conversion of carbon dioxide to hydrocarbons. Acs Nano 2010;4:1259–78.
[20] Sanz O, Echave FJ, Romero-Sarria F, Odriozola JA, Montes M. Chapter 9-advances in structured and microstructured catalytic reactors for hydrogen production. In: Gandía LM, Arzamendi G, Diéguez PM, editors. Renewable hydrogen technologies. Amsterdam: Elsevier; 2013. p. 201–24.
[21] Kolb G. Review: microstructured reactors for distributed and renewable production of fuels and electrical energy. Chem Eng Process Process Intensif 2013;65:1–44.

[22] Holladay JD, Wang Y, Jones E. Review of developments in portable hydrogen production using microreactor technology. Chem Rev 2004;104:4767–90.
[23] Frauhammer J, Eigenberger G, Hippel Lv, Arntz D. A new reactor concept for endothermic high-temperature reactions. Chem Eng Sci 1999;54:3661–70.
[24] Jiwanuruk T, Putivisutisak S, Ponpesh P, Kositanont C, Tagawa T, Yamada H, et al. Comparison between parallel and checked arrangements of micro reformer for H_2 production from methane. Chem Eng J 2015;268:135–43.
[25] Jiwanuruk T, Putivisutisak S, Ponpesh P, Bumroongsakulsawat P, Tagawa T, Yamada H, et al. Effect of flow arrangement on micro membrane reforming for H_2 production from methane. Chem Eng J 2016;293:319–26.
[26] Kim D, Kellogg A, Livaich E, Wilhite BA. Towards an integrated ceramic micro-membrane network: electroless-plated palladium membranes in cordierite supports. J Membr Sci 2009;340:109–16.
[27] Moreno AM, Damodharan S, Wilhite B. Influence of two-dimensional distribution schemes upon reactor performance in a ceramic microchannel network for autothermal methanol reforming. Ind Eng Chem Res 2010;49:10956–64.
[28] O'Connell M, Kolb G, Schelhaas KP, Schuerer J, Tiemann D, Ziogas A, et al. Development and evaluation of a microreactor for the reforming of diesel fuel in the kW range. Int J Hydrogen Energy 2009;34:6290–303.
[29] O'Connell M, Kolb G, Schelhaas KP, Schürer J, Tiemann D, Ziogas A, et al. An investigation into the transient behavior of a microreactor system for reforming of diesel fuel in the kW range. Chem Eng Technol 2009;32:1790–8.
[30] Zanfir M, Gavriilidis A. Catalytic combustion assisted methane steam reforming in a catalytic plate reactor. Chem Eng Sci 2003;58:3947–60.
[31] Karnik SV, Hatalis MK, Kothare MV. Towards a palladium micro-membrane for the water gas shift reaction: microfabrication approach and hydrogen purification results. J Microelectromech Syst 2003;12:93–100.
[32] Fernandez E, Helmi A, Medrano JA, Coenen K, Arratibel A, Melendez J, et al. Palladium based membranes and membrane reactors for hydrogen production and purification: an overview of research activities at Tecnalia and TU/e. Int J Hydrogen Energy 2017;42:13763–76.
[33] Adrover ME, Borio D, Pedernera M. Comparison between WGS membrane reactors operating with and without sweep gas: limiting conditions for co-current flow. Int J Hydrogen Energy 2017;42:5139–49.
[34] Yan Y, Cui Y, Zhang L, Li L, Zhang J, Chen Y, et al. Experimental investigation of methane auto-thermal reforming in hydrogen-permeable membrane reactor for pure hydrogen production. Int J Hydrogen Energy 2016;41:13069–76.
[35] Sumrunronnasak S, Tantayanon S, Kiatgamolchai S, Sukonket T. Improved hydrogen production from dry reforming reaction using a catalytic packed-bed membrane reactor with Ni-based catalyst and dense PdAgCu alloy membrane. Int J Hydrogen Energy 2016;41:2621–30.
[36] Silva JD, de Abreu CAM. Modelling and simulation in conventional fixed-bed and fixed-bed membrane reactors for the steam reforming of methane. Int J Hydrogen Energy 2016;41:11660–74.
[37] Ghasemzadeh K, Andalib E, Basile A. Evaluation of dense Pd–Ag membrane reactor performance during methanol steam reforming in comparison with autothermal reforming using CFD analysis. Int J Hydrogen Energy 2016;41:8745–54.
[38] Brunetti A, Caravella A, Fernandez E, Pacheco Tanaka DA, Gallucci F, Drioli E, et al. Syngas upgrading in a membrane reactor with thin Pd-alloy supported membrane. Int J Hydrogen Energy 2015;40:10883–93.
[39] Ye G, Xie D, Qiao W, Grace JR, Lim CJ. Modeling of fluidized bed membrane reactors for hydrogen production from steam methane reforming with Aspen Plus. Int J Hydrogen Energy 2009;34:4755–62.
[40] Patel KS, Sunol AK. Modeling and simulation of methane steam reforming in a thermally coupled membrane reactor. Int J Hydrogen Energy 2007;32:2344–58.
[41] Vásquez Castillo JM, Sato T, Itoh N. Effect of temperature and pressure on hydrogen production from steam reforming of biogas with Pd–Ag membrane reactor. Int J Hydrogen Energy 2015;40:3582–91.
[42] Ghasemzadeh K, Zeynali R, Basile A. Theoretical study of hydrogen production using inorganic membrane reactors during WGS reaction. Int J Hydrogen Energy 2016;41:8696–705.
[43] Saidi M. Performance assessment and evaluation of catalytic membrane reactor for pure hydrogen production via steam reforming of methanol. Int J Hydrogen Energy 2017;42:16170–85.
[44] Abu El Hawa HW, Lundin S-TB, Patki NS, Douglas Way J. Steam methane reforming in a PdAu membrane reactor: long-term assessment. Int J Hydrogen Energy 2016;41:10193–201.
[45] Jin Y, Rui Z, Tian Y, Lin Y, Li Y. Sequential simulation of dense oxygen permeation membrane reactor for hydrogen production from oxidative steam reforming of ethanol with ASPEN PLUS. Int J Hydrogen Energy 2010;35:6691–8.
[46] Shafiee A, Arab M, Lai Z, Liu Z, Abbas A. Modelling and sequential simulation of multi-tubular metallic membrane and techno-economics of a hydrogen production process employing thin-layer membrane reactor. Int J Hydrogen Energy 2016;41:19081–97.
[47] Cutillo A, Specchia S, Antonini M, Saracco G, Specchia V. Diesel fuel processor for PEM fuel cells: two possible alternatives (ATR versus SR). J Power Sources 2006;154:379–85.
[48] Ersoz A, Olgun H, Ozdogan S. Reforming options for hydrogen production from fossil fuels for PEM fuel cells. J Power Sources 2006;154:67–73.
[49] Yun S, Oyama ST. Correlations in palladium membranes for hydrogen separation: a review. J Membr Sci 2011;375:28–45.
[50] Gallucci F, Paturzo L, Basile A. Hydrogen recovery from methanol steam reforming in a dense membrane reactor: simulation study. Ind Eng Chem Res 2004;43:2420–32.
[51] Hall SM. Rules of thumb for chemical engineers. Elsevier Science; 2011.
[52] Shu J, Grandjean BPA, Kaliaguine S. Methane steam reforming in asymmetric Pd- and Pd-Ag/porous SS membrane reactors. Appl Catal A General 1994;119:305–25.
[53] Gallucci F, Paturzo L, Basile A. A simulation study of the steam reforming of methane in a dense tubular membrane reactor. Int J Hydrogen Energy 2004;29:611–7.
[54] Faungnawakij K, Kikuchi R, Eguchi K. Thermodynamic evaluation of methanol steam reforming for hydrogen production. J Power Sources 2006;161:87–94.
[55] Lwin Y, Daud WRW, Mohamad AB, Yaakob Z. Hydrogen production from steam–methanol reforming: thermodynamic analysis. Int J Hydrogen Energy 2000;25:47–53.
[56] Rabenstein G, Hacker V. Hydrogen for fuel cells from ethanol by steam-reforming, partial-oxidation and combined auto-thermal reforming: a thermodynamic analysis. J Power Sources 2008;185:1293–304.
[57] Lima da Silva A, Malfatti CdF, Müller IL. Thermodynamic analysis of ethanol steam reforming using Gibbs energy minimization method: a detailed study of the conditions of carbon deposition. Int J Hydrogen Energy 2009;34:4321–30.

[58] Xu J, Froment GF. Methane steam reforming, methanation and water-gas shift: I. Intrinsic kinetics. AlChE J 1989;35:88–96.
[59] Paglieri SN, Foo KY, Way JD, Collins JP, Harper-Nixon DL. A new preparation technique for Pd/alumina membranes with enhanced high-temperature stability. Ind Eng Chem Res 1999;38:1925–36.
[60] Katsuta H, Farraro R, McLellan R. The diffusivity of hydrogen in palladium. Acta Metall 1979;27:1111–4.
[61] Morreale BD, Ciocco MV, Enick RM, Morsi BI, Howard BH, Cugini AV, et al. The permeability of hydrogen in bulk palladium at elevated temperatures and pressures. J Membr Sci 2003;212:87–97.

Nomenclature

p: Pressure (Pa)
T: Temperature (K)
R: Gas constant (J mol^{-1} K^{-1})
n: Total molar flow rate (mol s^{-1})
n_i: Molar flow rate of species i (mol s^{-1})
$\Delta\widehat{H}^0_{c,i}$: Heat of combustion of species i (kW mol^{-1})
G: Molar Gibbs free energy (J mol^{-1})
G^0_i: Gibbs free energy of species i at its standard state (J mol^{-1})
y_i: Mole fraction of compound i in the gas mixture (–)
f^0_i: Fugacity of species i at its standard state (Pa)
r_j: Rate of reaction j (mol s^{-1} m^{-2})
A_i: Pre-exponential factor
E_a: Activation energy (kJ/mol)
$-\Delta H$: enthalpy change of reaction (kJ/mol)

Greek symbols

$\widehat{\varphi}$: Fugacity coefficient of species i in the gas mixture

Abbreviations

TMMR: Thermally coupled monolithic membrane reformer
TR: Traditional reactor
MR: Membrane reactor

Energy Conversion and Management 153 (2017) 493–503

Contents lists available at ScienceDirect

Energy Conversion and Management

journal homepage: www.elsevier.com/locate/enconman

Process design of biodiesel production: Hybridization of ester-and transesterification in a single reactive distillation

Nattawat Petchsoongsakul[a], Kanokwan Ngaosuwan[b], Worapon Kiatkittipong[c], Farid Aiouache[d], Suttichai Assabumrungrat[a,*]

[a] Center of Excellence in Catalysis and Catalytic Reaction Engineering, Department of Chemical Engineering, Faculty of Engineering, Chulalongkorn University, Bangkok 10330, Thailand
[b] Chemical Engineering Division, Engineering Faculty, Rajamangala University of Technology Krungthep, Bangkok 10120, Thailand
[c] Department of Chemical Engineering, Faculty of Engineering and Industrial Technology, Silpakorn University, Nakhon Pathom 73000, Thailand
[d] Engineering Department, Lancaster University, United Kingdom

ARTICLE INFO

Keywords:
Transesterification
Esterification
Hybridized reactive distillation
Biodiesel
Waste cooking oil

ABSTRACT

A novel hybridization of esterification and transesterification processes in a single reactive distillation column was proposed for biodiesel production from waste cooking oil. Continuous process operation was designed in a single reactive distillation column using two different types of heterogeneous catalyst. Amberlyst-15 was loaded on the top of reactive section to eliminate free fatty acid via esterification and CaO/Al_2O_3 was loaded at the lower section for biodiesel synthesis via transesterification. Suitable design parameters and operating conditions were determined by process simulation using commercial Aspen Plus program. The hybridized process via reactive distillation could reduce the number of equipment, methanol to oil in feed and energy consumption compared to the conventional alkaline catalyzed process and the process of two reactive distillation columns in series (packing with Amberlyst-15 and CaO/Al_2O_3). Net specific energy requirement was achieved to the lower value as 216 kWhr/kmol biodiesel (or 197 kWhr/kmol biodiesel with allocation to 98% purity of glycerol by-product). This value is lower than that from the conventional process and also the two reactive distillation columns in series of 665 and 224 kWhr/kmol biodiesel, respectively. Moreover, increasing pressure in the hybridized column from 1 to 3 bar decreased the number of reactive stage from 24 stages (4 esterification and 20 transesterification) to 8 stages (3 esterification and 5 transesterification). Several feedstocks with different FFA content can be operated in this hybridization ester- and transesterification column within the 8 reactive stages with flexible of number of catalyst packing stage (acid and alkali catalysts) under column pressure of 3 bar.

1. Introduction

The demand for fossil resources in all sectors such as transportation, power production and various industries is steadily increasing. For instance, it is anticipated that consumption of petroleum in the USA, a reference country for worldwide demand and consumption of fossil fuels, will rise from 84.4 to 116 million barrels per day in 2030 [1,2]. Energy from fossil resources will therefore remain the main contributor to various pollutions, including CO_2 emissions and global warming consequences [3]. Because of the environmental concern, the exploration and development of alternative energies for sustainable developments, are therefore very crucial in term of energy security.

Vegetable oil can be used as liquid fuel by different modification methods such as dilution, thermal cracking (pyrolysis), transesterification, and microemulsification. However, transesterification is so far the most competitive method for producing higher quality of biodiesels [4–6]. Biodiesel is defined as a mono alkyl ester of a fatty acid that is produced from vegetable oils or animal fats, reacting with short chain alcohol such as methanol [7].

However, production of biofuels from human nutrition sources can cause a food crisis. Consequently, using non-edible oil or waste cooking oil as feedstock for biodiesel production such as algae oil [8–10], microalgae [11–15], jatropha oil [16] and grease oil [17] are of interest. Moreover, the use of waste edible oil as feedstocks can reduce biodiesel production costs by 60–90% [18–20]. However, water and free fatty acid (FFA) content in the waste cooking oil have a negative influence on the transesterification rate [21,22]. Hydrolysis of triglyceride can also take place in the presence of heat and water, resulting in an increase of percentage of FFA in the oil [23]. Therefore, in order to produce economical biodiesel, the amount of FFA and water must be eliminated or

* Corresponding author.
E-mail address: Suttichai.A@chula.ac.th (S. Assabumrungrat).

http://dx.doi.org/10.1016/j.enconman.2017.10.013
Received 27 June 2017; Received in revised form 21 September 2017; Accepted 5 October 2017
0196-8904/ © 2017 Elsevier Ltd. All rights reserved.

reduced before transesterification. The conventional technology (using continuous reactor) was found not compatible with FFA content oils threshold value of about 0.5 wt% [24]. Otherwise, alternative approaches e.g. sub- and supercritical methanol [25] or superheated methanol technology is suggested [26,27].

Reactive distillation (RD) is a process that includes a chemical reaction and a distillation, occurring simultaneously in single equipment. A variety of reactions with homogenous catalyst or heterogeneous catalyst or without catalyst have been tested via the RD process, mainly driven by advantages such as, a continuous removal of product from reaction zone for shifting the chemical equilibrium limitation, a decrease in capital costs by using a single reaction-separation unit, reduction in complexity of the piping and instrumentation design, resulting in suitable heat integration and utilities utilizations. RD design has been currently cited for biodiesel production by esterification [28,29] and transesterification [30,31]. Recently, Pérez-Cisneros et al. [32] proposed an integration of two heterogeneous RD processes for biodiesel production. FFA in the feed was pretreated by esterification in the first RD and a decanter was employed to separate non-converted triglycerides before being sent to the second RD for transesterification. The process design, however, was carried out solely for one reaction (i.e. esterification or transesterification) per column of RD.

The aim of this work is to hybridize the esterification and transesterification processes into a single RD column for biodiesel production. The concept of this RD design consists of an upper section for the pretreatment of waste cooking oil to eliminate FFA and a lower section for conversion of triglyceride into biodiesel.

2. Methodology

In this work, Dortmund modified UNIFAC model [33] was selected to predict vapor-liquid equilibrium (VLE) and liquid-liquid equilibrium (LLE). VLE of mixtures of methanol-biodiesel and methanol-glycerol systems, and LLE of mixtures of water-biodiesel, methanol-biodiesel-glycerol, and methanol-water-biodiesel systems have been experimentally investigated by Kuramochi et al. [34]. They reported that the Dortmund modified UNIFAC model was the most suitable for prediction of the physical equilirbia properties of various mixtures associated with the design of biodiesel processes.

Steady state process simulation has been performed with Aspen Plus® version 8.0. The continuous stirred tank reactor (CSTR) model was employed for the conventional process. The RADFRAC model has been extensively used in the design of RD columns. RADFRAC relies on an equilibrium stage model and is capable to deal with ideal and non-ideal vapor-liquid equilibrium (VLE) and vapor-liquid (I)-liquid (II) equilibrium (VLLE). Note that although thermodynamic model used in the previous works for the prediction of VLE were accurate enough for esterification [35] and transesterification [36] in reactive distillation at atmospheric pressure, at pressure higher than atmosphere, however, mixtures containing glycerol, FAME, methanol and water lead to the presence of a second liquid phase, and therefore, a VLLE should be taken into account (as can be illustrated in Fig. S1(a)–(c)). Therefore, a VLLE model was implemented in the simulations of this study. Moreover, the RADFRAC model does not require the need to set details about the packing and the size of the column, leading to assumed preliminary values of stage efficiency [30]. Oleic acid and triolein were used as a model compound of FFA and triglyceride, respectively. Amberlyst-15 was chosen to catalyze esterification of FFA as it was demonstrated to produce high yield of biodiesel [32]. Pal et al. [37] reported that this catalyst has a long life time, is widely used in important industrial processes and is also cost-effective. Boz et al. [38] also reported that this catalyst did not deteriorate after reuse at least for three cycles of 9 h reaction time each at laboratory scale.

Calcium oxide supported on alumina (CaO/Al_2O_3) was selected to catalyze transesterification of triglyceride. This catalyst was demonstrated to offer an economic merit for biodiesel production by the RD process [39]. Kesic et al. [40] reported that CaO catalyst has a long catalyst lifetime and could maintain activity even after being reused. Moreover, Liu et al. [41] has confirmed by their experimental results that CaO can be repeatedly used for 20 cycles for transesterification of soybean oil and methanol. However, it should be noted that the time stream of catalysts was not included in the simulation since the process was assumed to run under steady state operation.

The performance of processes was determined by observing the yield and purity of biodiesel. A standard purity of biodiesel or fatty acid methyl ester (FAME) of 96.5 wt% was used as criteria of performance. The yield of biodiesel is defined by Eq. (1):

$$\text{Biodiesel yield, \%} = \frac{F_{\text{Methyl oleate}}}{(3 \times F_{\text{Triolein,initial}}) + F_{\text{Oleic acid,initial}}} \times 100\% \quad (1)$$

where $F_{\text{Methyl oleate}}$ is the molar flow rate of methyl oleate in product stream, $F_{\text{Triolein,initial}}$ and $F_{\text{Oleic acid,initial}}$ are molar flow rate of triolein and oleic acid in feed stream, respectively.

3. Results and discussion

3.1. Kinetic data validation

Model validations of kinetic parameters of the reaction catalyzed by sodium hydroxide as homogeneous base catalyst [42] and CaO/Al_2O_3 as solid base catalyst [43], which were performed in a batch reactor, are shown in Fig. 1(a) and (b), respectively. The results for both kinetic data were in good agreement with the experimental data as shown herein.

The kinetic data for esterification pretreatment step by using Amberlyst-15 catalyst were validated by using the work of Steinigeweg and Gmehling [29], who employed this catalyst for the RD process. The validation results in terms of FFA conversion as a function of reflux ratio are provided in Fig. 2. The results of our simulation show close trends of conversion along with the reflux ratio with the maximum deviation of less than 10% than aforementioned work [29]. It should be noted that the pseudo-homogeneous kinetic model did not fit well the experimental data, especially at values of low reflux ratio. Moreover, the swelling parameter of Amberlyst-15 data (as present in Langmuir-Hinshelwood model) could not be included in the kinetic model that was implemented in the RADFRAC model, which is a ready-to-use and compatible with the RADFRAC model, was therefore not applied in this study. It is worth to note that the comparison among three process configurations (conventional process, integrated two RDs in series and hybridized RD which will be mentioned later), waste cooking oil containing 6% FFA was employed as a feedstock. With low FFA content, the amount of produced water via esterification was not significant, and therefore the effect of water adsorption on Amberlyst 15 can be negligible and pseudo-homogeneous kinetic models were effectively employed in the calculations. However for high FFA content ca. 80–100% which will be considered in the hybridized RD, the effect of water inhibition should be taken into account which will be discussed later.

3.2. Conventional process for biodiesel production

The conventional process of biodiesel production by using waste cooking oil is presented in Fig. 3(a) esterification and acid removal and (b) transesterification, water washing, methanol recovery, glycerol purification and biodiesel purification. [44] A molar flow of waste cooking oil (6% FFA content) was preheated (E-111) to 60 °C before feeding the pretreatment reactor (R-111) in order to eliminate FFA by esterification. The fresh methanol was mixed with the sulfuric acid (H_2SO_4) before feeding to R-111 reactor. All FFA was converted to FAME and the exit stream (stream-7) was cooled before feeding to the glycerol washing column (T-110) to remove the catalyst and some water from the triglyceride. The washing stream was fed into

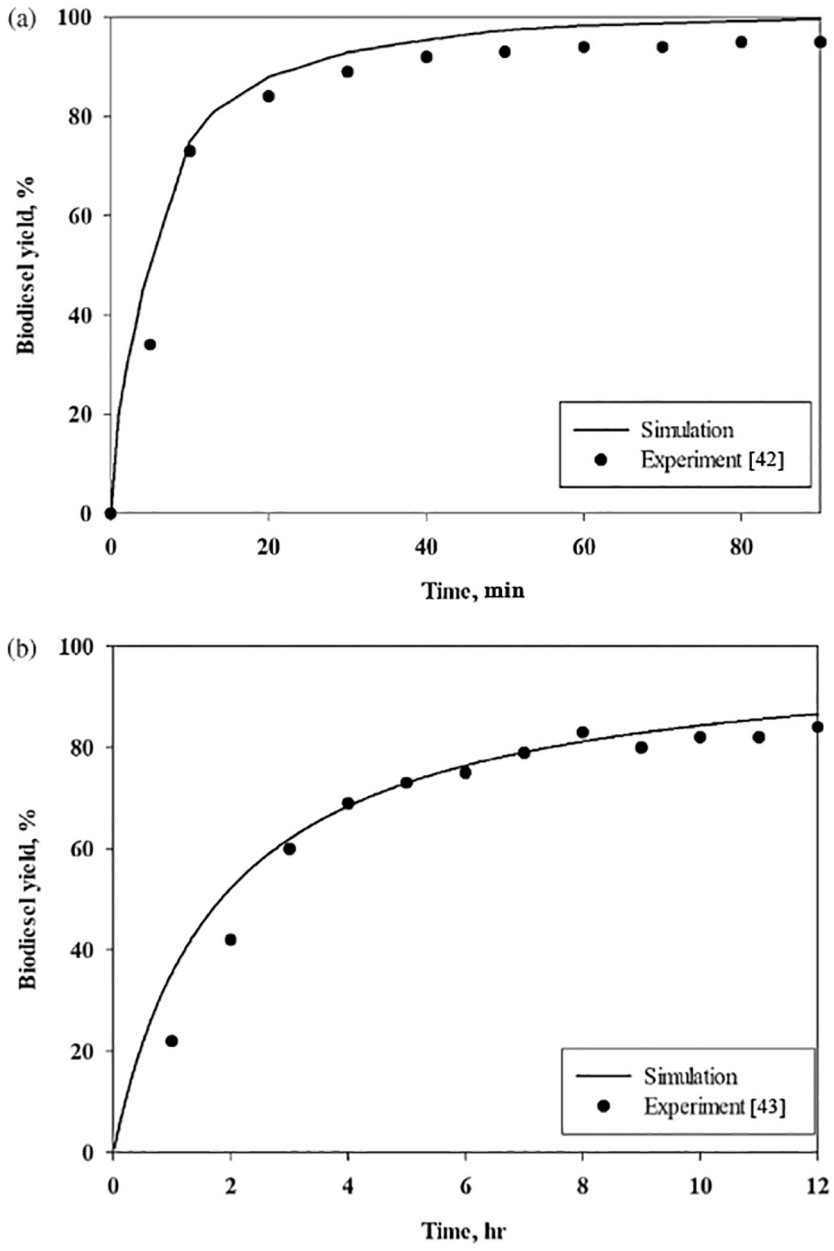

Fig. 1. Model validations of (a) kinetic model catalyzed by sodium hydroxide in batch reactor (data adapted from Noureddini and Zhu [42], T = 50 °C, methanol to oil = 6:1 at atmospheric pressure) and (b) kinetic model catalyzed by CaO/Al_2O_3 in batch reactor (data adapted from Pasupulety et al. [43], T = 150 °C, methanol to oil = 9:1 at pressure = 1 bar).

distillation column (T-111) to recover unreacted methanol and further recycle back to the reactor. Sodium hydroxide (NaOH), as homogeneous catalyst in the alkali catalyzed transesterification unit, was mixed with the fresh methanol (Methanol-2 or stream-15) and fed to transesterification reactor (R-121). Meanwhile, the pretreated oil stream was preheated (E-121) to 60 °C before feeding the reactor. In R-121, 97% of triglyceride was converted to FAME. After completing the reaction, product stream was fed to distillation column (T-121) with the optimal reflux ratio of 1.0 to recover the unreacted methanol (Fig. 3(a)). The overhead stream, mainly of unreacted methanol, was recycled back to the reactor while the bottom stream of mainly biodiesel, glycerol and catalyst was processed by water washing in the purification unit (T-133) with the optimal reflux ratio of 1.0 to reach a high-quality biodiesel product conforming to ASTM/EN specification (i.e. composition greater than 97%). The bottom effluent stream (stream-21) was sent to the neutralization column (T-131) to remove catalyst by adding phosphoric acid (H_3PO_4), and to produce sodium phosphate (Na_3PO_4). Sodium phosphate as solid material was then removed by filtration. The filtrate (76% glycerol) was fed to the distillation column (T-132) for purification of glycerol. Crude glycerol (i.e. composition higher than 85%) can be achieved in T-132 with the reflux ratio of 1.0. However, the standard of technical grade glycerol for washing column was preferred (i.e. composition higher than 92%) [44]. In order to obtain technical grade glycerol, a high reflux ratio (i.e. higher than 2.0) was required and hence energy consumption of T-132 was increased from 31 to 48 kW. As summarized in Table 1, under this design condition, the purity and yield of biodiesel were 99.97% and 99.70%, respectively. Glycerol purity was 85.01% (with a low reflux, i.e. value of 1.0) and 92.01% (with a reflux of 2.0) which could meet the specifications of the crude and the technical grade glycerol, respectively.

Since the technical grade of glycerol could be obtained as a valuable by-product, the allocation of this energy consumption to glycerol should be taken into account. Based on this allocation (by mass) to glycerol production, energy requirement is attributed to 605 kWhr/kmol biodiesel productions. In order to compare with the real experimental or commercial data, the energy requirement in the transesterification process ((Fig. 3(b)), including transesterification, water

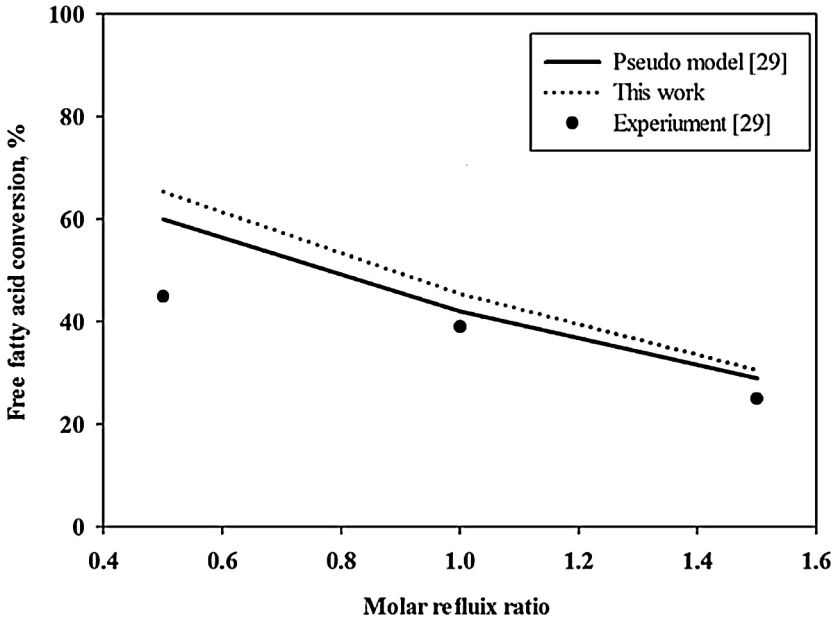

Fig. 2. Model validation of kinetic data using Amberlyst-15 in term of free fatty acid conversion as a function of reflux ratio using packing of Katapak-SP.

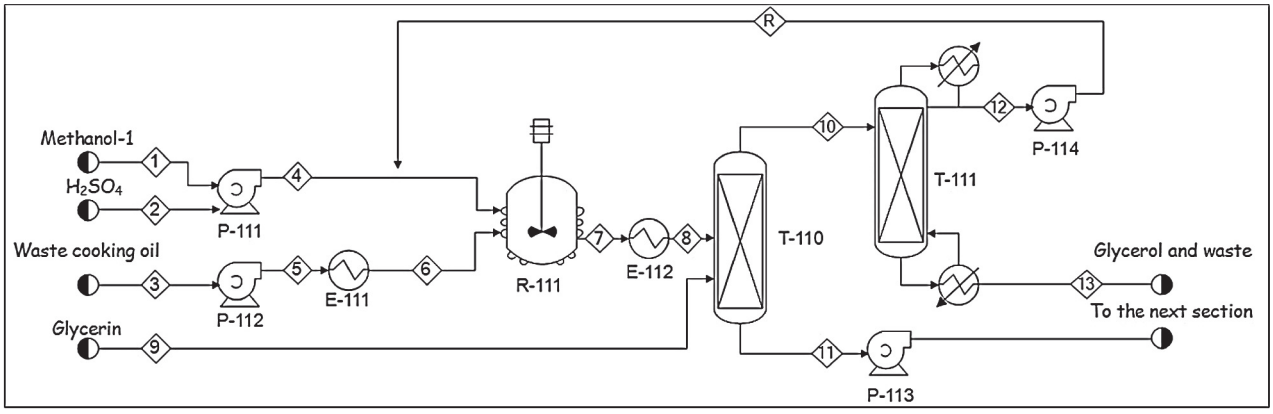

(a) Part 1: Esterification and acid removal

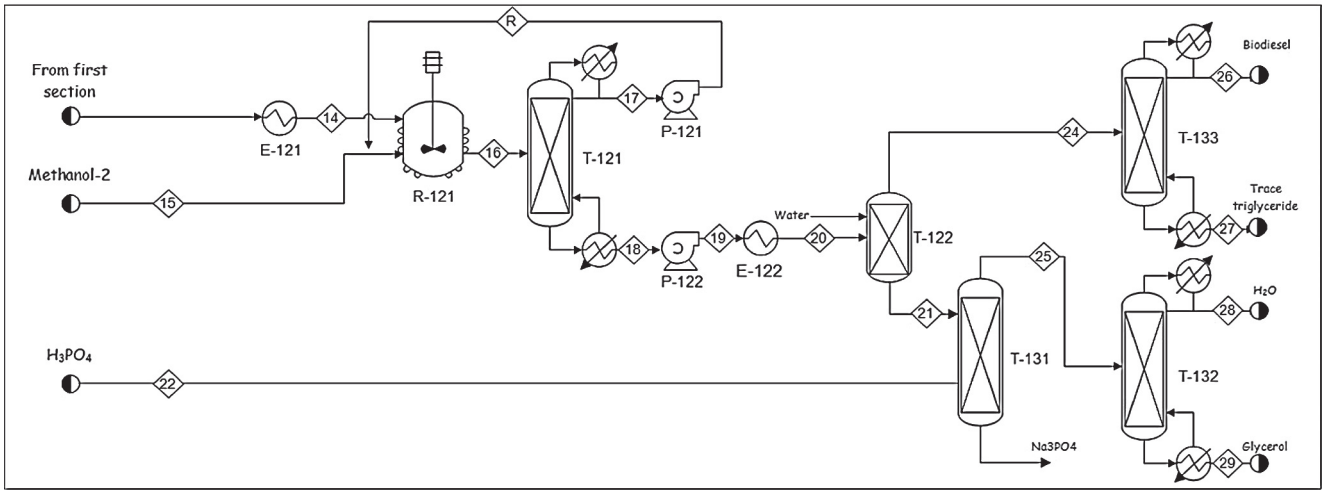

(b) Part 2: Transesterification, water washing, methanol recovery, glycerol purification and biodiesel purification

Fig. 3. Simplified conventional processes for biodiesel production using waste cooking oil as feedstock. (a) Part 1 and (b) Part 2.

Table 1
Performance comparison of different biodiesel production processes.

	Conventional process	Integrated two RDs	Hybridization of RD
Overall methanol to oil feed molar ratio	8:1	6.5:1	4:1
Biodiesel purity, wt%	99.70	97.49	97.61
Overall biodiesel yield, %	99.97	98.32	99.87
Heat exchanger duty, kW			
Preheat or cool-down heat exchanger	*(E-111)* 21	24	22
	(E-112) 12 *(E-121)* −36 *(E-122)* 46		
Reactor heat duty, kW			
Pretreatment reactor	21		
Neutralization reactor	20	–	–
Transesterification reactor	−24		
Distillation column duty, kW			
Methanol recovery	−407/385.5	–	–
Biodiesel purification	−568/523.8	–	–
Reactive distillation column, kW			
Column-1	–	−127/213	−138/229
Column-2	–	−112/187	–
Total reactive distillation column, kW			
Make up glycerol usage, kg/hr	110	–	–
Make up water usage, kg/hr	11	–	–
Make up acid usage, kg/hr	9.8	–	–
Glycerol purity before purified, wt%	76.78	84.61	87.44
Glycerol purity after purified, wt%			
Low reflux ratio	85.01	96.80	96.38
High reflux ratio	92.01	–	–
Energy requirement for glycerol purified, kW			
Low reflux ratio	−26/30	−4/10	−4/10
High reflux ratio	−34/48	–	–
Total net specific energy requirement (kWhr/kmol biodiesel)	665	224	216
Total net specific energy requirement allocates with technical grade glycerol production (kWhr/kmol biodiesel)	605	216	197
Number of unit operation			
Reactor	3	–	–
Reactive distillation column	–	2	1
Distillation column	4	–	–
Decanter	–	1	1
Extraction column	2	–	–
Total number of unit operation	9	3	2

washing, methanol recovery, glycerol purification and biodiesel purification unit, was calculated as 393 kWhr/kmol biodiesel which is in a good agreement to the energy consumption for biodiesel production via transesterification process of 360 kWhr/kmol biodiesel reported by Smith et al. [45].

Despite the reduction of raw material cost by using waste cooking oil, the process was found complex, necessitating a large number of operating units. This is because of the addition of a pretreatment unit to remove FFA, separation of catalyst out from the system (neutralization unit), and purification of biodiesel and glycerol. RD process was chosen as alternative option to reduce the number of unit operation as discussed in the next section.

3.3. An integrated unit of two reactive distillation columns for biodiesel production

An integrated process by two RD columns for the esterification and the transesterification has been proposed (Fig. 4) [32]. Fresh methanol and waste cooking oil (containing 6% FFA) was fed in the first RD (T-211) with molar ratio of 2.5:1. T-211 was loaded with Amberlyst-15 as solid catalyst for esterification. In order to eliminate FFA to less than 0.5 wt%, the configuration design for reactive distillations was shown in Table 2. The result indicated that 3 reactive stages are required. Methanol and water were vaporized out at top column while triglyceride and FAME (from esterification) were retrieved from the bottom of this column. Triglycerides were separated by using decanter (D-211) before proceeding to next RD column for transesterification. Methanol (stream-7) and triglyceride (stream-6) were fed to the second stage of the second RD column (T-221) which was loaded with alkali solid catalyst (CaO/Al_2O_3). In this column, 18 reactive stages and a reflux ratio of 1.0 were used to obtain a good separation and high biodiesel production. Unreacted methanol was vaporized in overhead stream (stream-8) while downstream, mainly FAME and glycerol, was processed by the decanter (D-221) to separate glycerol and reached a final biodiesel product, adhering to ASTM/EN specification. Glycerol obtained from the decanter is marginal on crude glycerol specification (84.6%). Purification of glycerol to technical grade could be achieved with further glycerol distillation.

This process can produce high purity biodiesel by using heterogeneous catalyst system for both reactions, thus, the number of operating equipment unit was reduced (no requirement of catalyst separation). However, this process required at least two RD columns (T-211 for esterification and T-221 for transesterification) to produce biodiesel from waste cooking oil. Under the optimal condition, biodiesel yield of 98.3% with purity of 97.5% was achieved with energy consumption of 224 kWhr/kmol of biodiesels. The energy consumption is higher than the value reported Pérez-Cisneros [32] (138 kWhr/kmol) who employed Amberlyst-15 and MgO catalyst in esterification and transesterification. This might be due to CaO/Al_2O_3 catalyst that exhibited slower kinetic rate than MgO and was driven by less surface basic sites in the former catalyst, resulting in requirement of higher number of reactive stages [46].

As summarized in Table 1, the conventional process was very energy intensive due to energy consumption of the distillation column for the purification and the recovery processing. An integration of two RD columns would reduce the number of unit operations along with significantly low energy consumption.

3.4. Hybridization of esterification and transesterification in a single reactive distillation column for biodiesel production

The hybridization of esterification and transesterification in a single RD was proposed as shown in Fig. 5. The upper section of column was packed with Amberlyst-15 for esterification. After FFA content (6% FFA content) was reduced, the resulting reactants flow down to the lower section which was packed with CaO/Al_2O_3 for transesterification. Methanol and waste cooking oil were co-fed at the second stage. In order to meet the specification of biodiesel standard, the RD configuration with minimum stage requirement was determined as shown in Table 2.

The suitable RD configuration to produce biodiesel by hybridized RD using Amberlyst-15 and CaO/Al_2O_3 catalyst consist of 24 reactive stages (4 stages for the esterification and 20 stages for the transesterification). Reflux ratio did not affect product purity and yield, leading such low reflux ratio to be considered sufficient. This was due to large difference in the boiling temperatures between overhead products, mainly methanol and water (methanol: 69 °C, water: 100 °C) and other components of the reaction mixture (glycerol: 290 °C, methyl oleate biodiesel: 351 °C, oleic acid: 360 °C, triolein: 554 °C).

The optimum condition was found to be 4:1 of methanol to oil molar

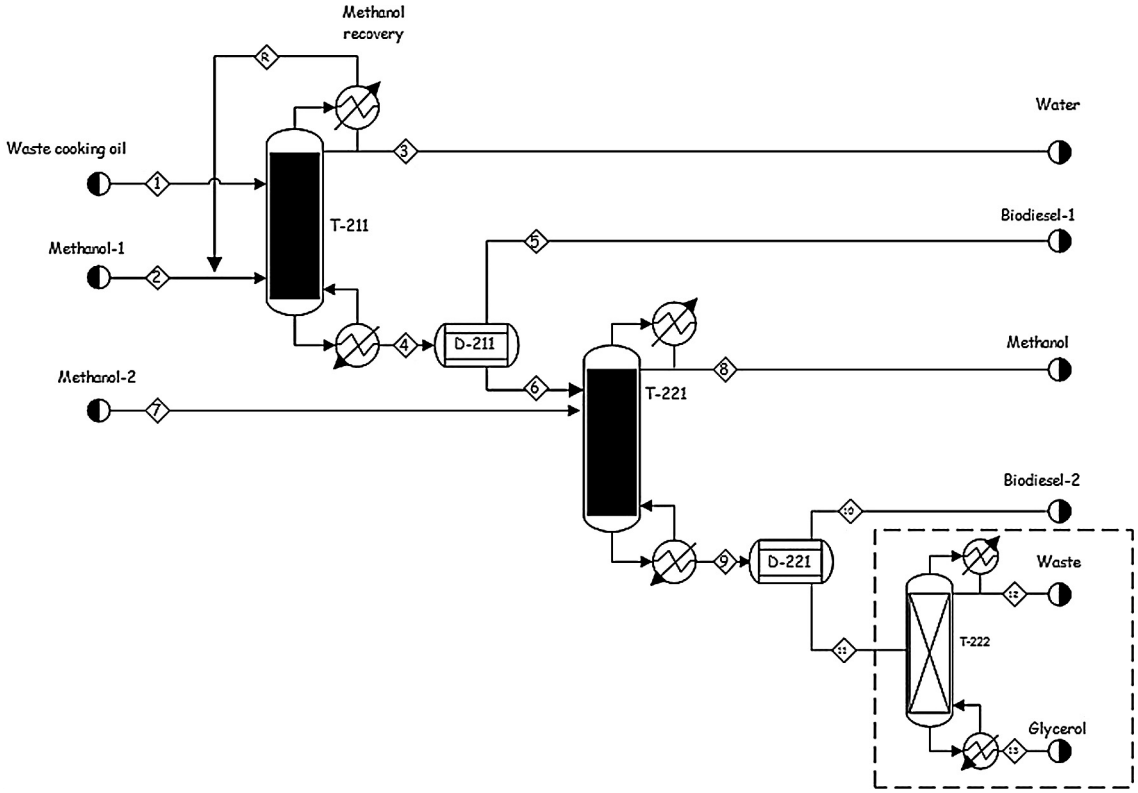

Fig. 4. An integrated reactive distillation for biodiesel production (dashed frame represents optional distillation column to obtain technical grade glycerol).

Table 2
Details of simulation design for integrated and hybridized reactive distillation processes.

Parameter	Integrated two RDs		Hybridization of RD	
	Esterification column (T-211)	Transesterification column (T-221)	Column pressure 1 bar	Column pressure 3 bar
Column diameter (m)	0.24	0.96	0.82	0.30
Column height (m)	3.00	12.00	15.60	6.00
Number of reactive stage	3	18	24	8
Catalyst loading	Acid catalyst 2.5 wt%[a]	Alkali catalyst 3 wt%[b]	Acid 2.5 wt%[a] and alkali catalyst 3 wt%[b]	
Biodiesel production rate (kg/h)	1000		1000	

[a] Steinigeweg and Gmehling [29].
[b] Pasupulety et al. [43].

feed ratio, reflux ratio of 0.1 and reboiler heat duty of 216 kWhr/kmol biodiesel.

The downstream product from the RD column, mainly FAME and glycerol, was fed into the purification step using only decanter (D-311) to separate biodiesel from glycerol. In comparison with the two RD columns in series, the hybridized RD column can reduce methanol feed ratio and consume lower energy requirement as illustrated in Table 1.

It can be concluded that the hybridization of esterification and transesterification in a single RD to produce biodiesel from waste cooking oil is a very promising process. It exhibits several advantages over conventional process and two RD columns in series e.g. lower amount of methanol to oil ratio and reduced process steps to obtain high purity biodiesel and glycerol, resulting in lower number of unit operation and energy consumption. Therefore, the next section will provide the optimum operating parameters to produce biodiesel in the single hybridization of ester-transesterification RD column.

3.4.1. Hybrid ester- and transesterification RD process under pressurized condition

Gaurav et al. [47] revealed that the process design for biodiesel production via transesterification using RD column at high pressure column of 3 bar would provide higher biodiesel yield than that operated at normal pressure. The effect of operating pressure for biodiesel production on the number of stage in the single hybridization ester-transesterification RD were therefore investigated. To elucidate the influence of column pressure on the reaction performance, the extent of reaction was plotted as shown in Fig. 6.

Our finding suggests that an increase in the column pressures not only enhances the rate of transesterification but also improves the rate of esterification, owing to promoted miscibility of triglycerides and FFA in methanol at high temperatures and pressures. The polarity of methanol increases at high pressure and temperature, resulting in acceleration of the reaction rate [48]. Moreover, it was found that increasing the operating pressure would provide the highest biodiesel production because the highest temperature profile (i.e. bottom temperature was 173, 184, 205 and 247 °C under pressure column 1, 2, 3 and 4 bar, respectively) along the column was obtained and also would pressurize more methanol in liquid phase. This led to higher reaction rate than that obtained at atmospheric pressure. However, the optimum column pressure should be set no more than 3 bar since no significant difference in biodiesel yield was found at column pressure of 4 bar (as shown in Fig. 6). The required number of stages for esterification and

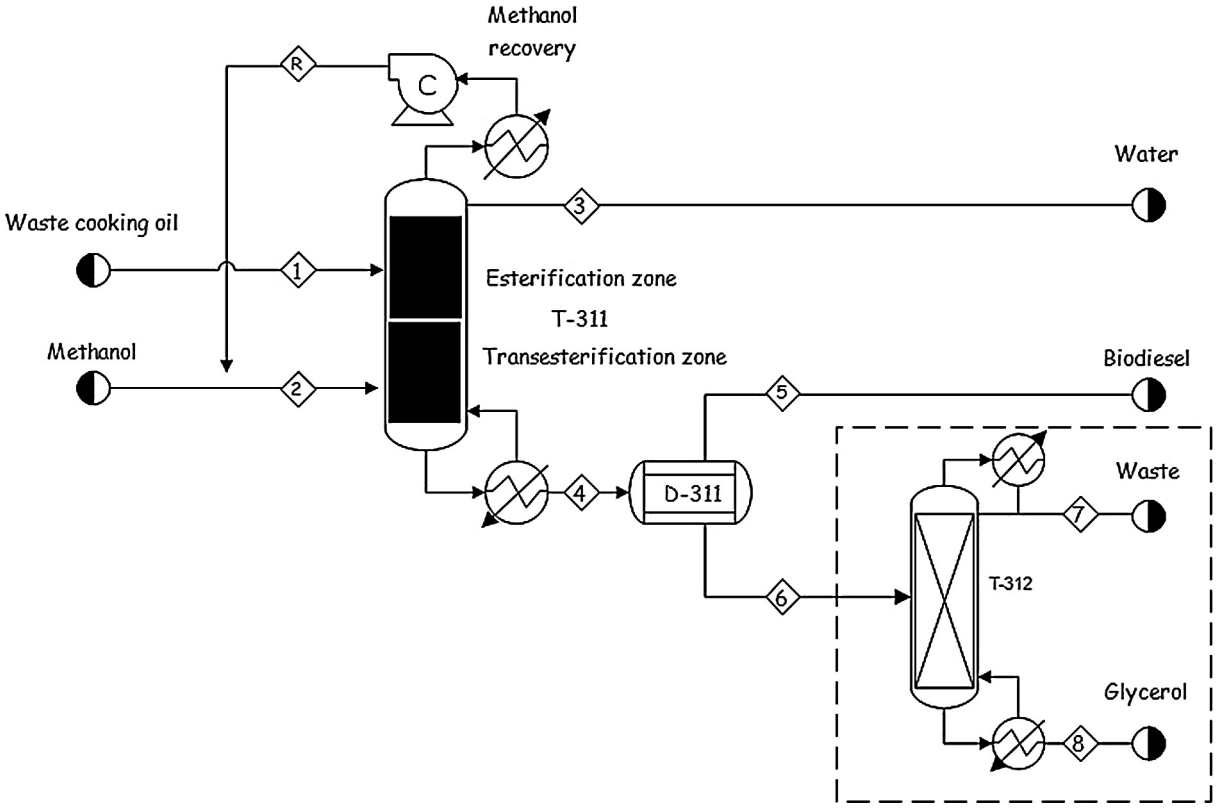

Fig. 5. Hybridization of ester-and transesterification in a single reactive distillation for biodiesel production (dashed frame represents optional distillation column to obtain technical grade glycerol).

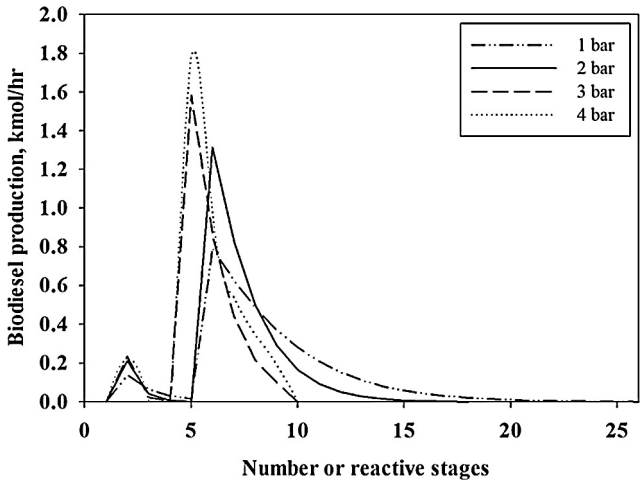

Fig. 6. Reaction rate profiles with in the reactive distillation column using methanol to oil ratio of 4:1 and reflux ratio 0.1 for waste cooking oil with 6% FFA.

Table 3
Required number of stages for achieving biodiesel yield greater than 97% at different column pressures.

Column pressure [bar]	1	2	3	4
Total number of stages[a]	26	18	10	10
Esterification stages	4	4	3	3
Transesterification stages	20	12	5	5

[a] Total number of stage = reactive stage + rectifying stage + stripping stage.

transesterification under different operating pressures are summarized in Table 3. Lower number of stages for esterification and transesterification are required at high operating pressure. The amount of catalyst loading and the sizing of RDs are summarized in Table 2.

3.4.2. Effects of rectifying and stripping stages

Other configurations and operating parameters were fixed while the number of stages in rectifying and stripping sections was varied to determine the suitable operating conditions. It was found that this hybridization would not require more rectifying and stripping stages to provide more separation of each component from the main product, due to their relevant relative volatilities (result is not shown).

3.4.3. Effects of reflux ratio and reboiler duty

Fig. 7 shows the purity of biodiesel (bottom stream), biodiesel yield and reboiler heat duty with different reflux ratio. Total feed flow rate, methanol to oil molar ratio and specification of biodiesel yield (i.e. composition higher than 97%) were fixed while reflux ratio was varied from 0.1 to 3. The results show that the purity and the yield of biodiesel did not change when reflux ratio was increased from 0.1 to 3, at methanol to oil feed ratio of 4:1. However, increasing the reflux ratio led to higher energy consumption due to more amount of methanol being refluxed back into the column, requiring thus more duties for the condenser and the reboiler duty to condense and vaporize, respectively. It was found that a value of reflux ratio of 0.1 was enough to produce high purity biodiesel but was not enough to reach a purity of biodiesel that is conform to the standard. This is due to large differences in the boiling temperature between methanol and other component of the reaction mixture as mentioned earlier. Low reflux ratio was enough for catalytic distillation to produce biodiesel via transesterification as reported by others researcher [30,47].

3.4.4. Effects of methanol excess, reactive stages and methanol feed location

Effects of number of reactive stages and methanol excess on biodiesel yield, biodiesel purity and reboiler duty requirement are shown

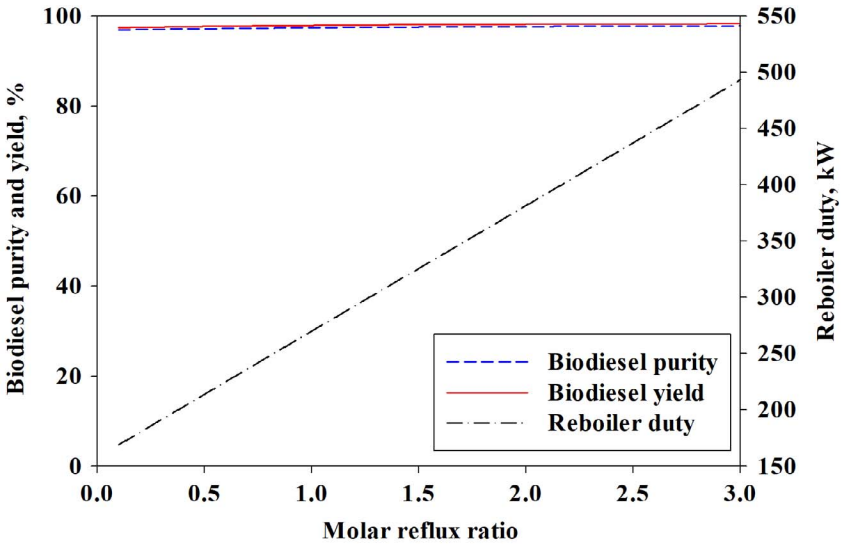

Fig. 7. Yield of biodiesel, purity of biodiesel and reboiler duty of reactive distillation at various molar reflux ratio by using methanol to oil ratio of 4:1 under column pressure of 3 bar.

in Fig. 8(a)–(c), respectively. In the case of 6% FFA in oil feed, a number of three esterification stages was found enough to diminish FFA even with no methanol excess; therefore, the number of reactive stages in this hybridization RD would be a function of the transesterification stage when a number of three stages of esterification was fixed. Biodiesel yield and purity increased significantly by increasing the number of reactive stages or using higher methanol excess, owing to more contacting area of methanol to drive forward reaction in the reactive zone. However, reboiler duty was increased too due to additional energy consumed to heat methanol and the nature of endothermic reaction in the reactive section. The optimal conditions for hybridization RD with 6%FFA were found to be 8 reactive stages (3 for esterification and 5 for transesterification), 22% methanol excess and reboiler duty of 141 kWhr/kmol of biodiesel.

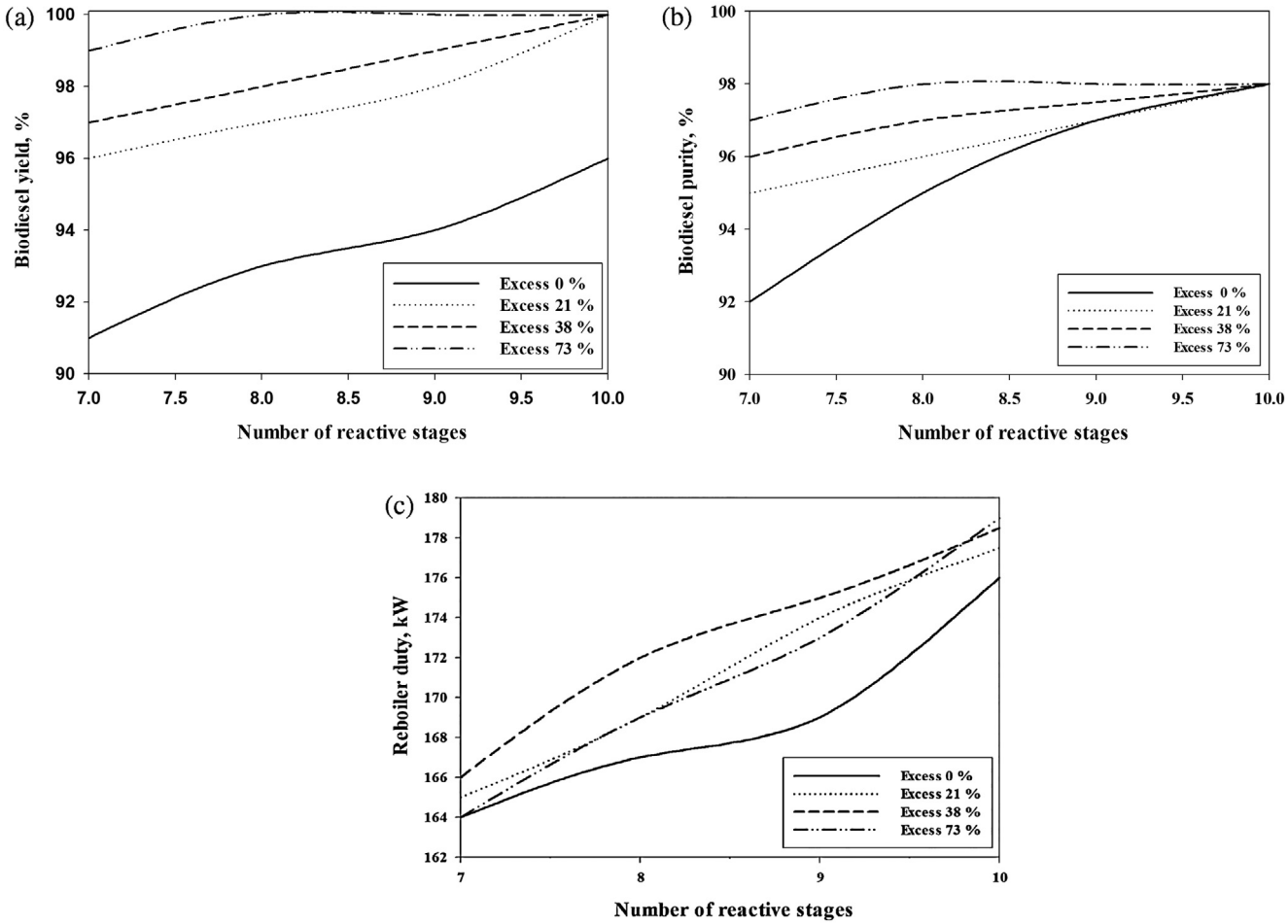

Fig. 8. Yield of biodiesel (a), purity of biodiesel (b) and reboiler duty of reactive distillation (c) at various reactive stages by using different methanol to oil ratio under column pressure of 3 bar.

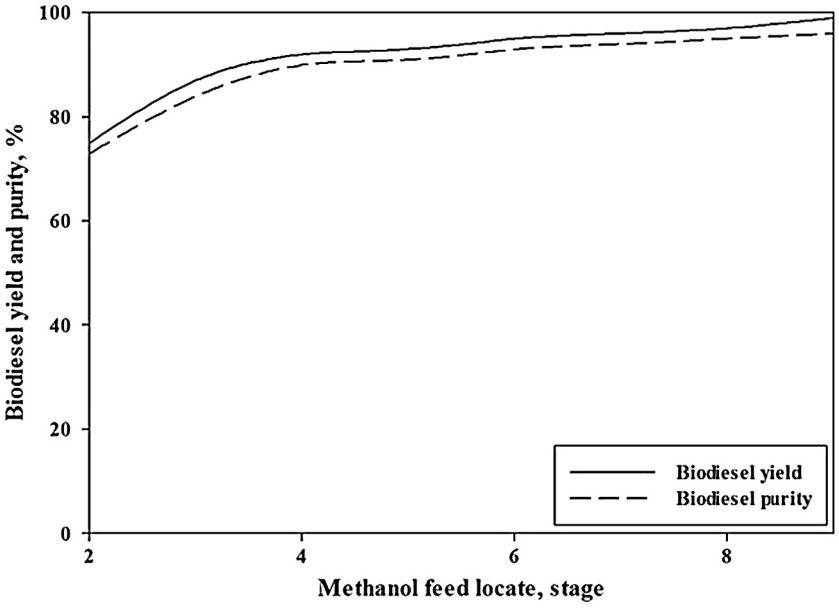

Fig. 9. Yield and purity of biodiesel at various methanol feed location by fixed oil feed stage at first stage of reaction zone and under column pressure of 3 bar.

Fig. 9 shows effect of methanol feed location on biodiesel yield and purity. Waste cooking oil, as heavier reactant, was fed at the first of reactive stage (2nd stage). Methanol, as a lighter reactant, was fed at the last reactive stage (9th stage), agreeing with typical design of RD. The result of feed location for the hybridized RD column was in agreement with the reactive distillation catalyzed by heterogeneous catalyst for a single reaction of esterification and transesterification [30,32]. Finally, impact of the free fatty acid on the design column will be discussed in the following section.

3.4.5. *Effect of FFA content in feedstock*

Amount of FFA content is typically function of the source of feedstocks. Therefore, effect of FFA content must be considered to determine the suitable operating condition for this hybridized RD column. Moreover, if the number of stage for esterification was not sufficient to eliminate all amount of FFA, biodiesel production rate would be decreased because of side reactions (i.e. saponification). It is illustrated in Table 4 for six cases; 0 (Pure TG), 20, 40, 60, 80 and 100% (pure FFA).

Table 4 summarizes the requirement for the number of reactive stages and operating conditions to obtain design specifications for different FFA content in the feedstock. It can be concluded that the advantage of hybridization of ester-and transesterification RD is reflected by a flexible design of biodiesel production from different feedstocks (various FFA contents). The requirement of maximum number of reactive stages was found not exceeding eight reactive stages (i.e. three stages for esterification and five stages for transesterification) to meet FFA composition (ca. 20%FFA). The requirements for number of stages and energy could be reduced, depending on feed composition as shown in Table 4. This implied a column to be fabricated with ten total stages; one stripping stage, one rectifying stage and eight reactive stages. The packing of acid and base catalysts could be adjusted, depending on free fatty acid content in waste cooking oil feed, to obtain a biodiesel of high yield and purities of biodiesel. However, as mentioned earlier, in case of high FFA content ca. 80–100% of hybridized RD, the effect of water inhibition should not be neglected. The recalculation was performed by decreasing rate of reaction of pseudo-homogeneous kinetic model approx. 30% (to fit with experimental data of low reflux ratio in Fig. 2) and the calculation results show that 4 reactive stages (instead of 3 reactive stages as shown in Table 4) are recommended to ensure the complete conversion of FFA.

Note that our simulation results were based on a design that relied on the equilibrium model between the phases along with reaction kinetics. It simplified the anticipated challenging calculations of the non-equilibrium model that would have required detailed physical properties, prediction of missing mass and heat transfer characteristics and extended computational time. It is a typical approach to obtain a preliminary design. In order to design real column for actual plant, a more complex model taking into account more realistic phenomena such as non-equilibrium with mass transfer limitation, and other issues such as dynamic controllability need to be taken into account.

4. Conclusion

The hybridization of ester- and transesterification for biodiesel production in a single reactive distillation column was investigated in this study. Heterogeneous catalysts, Amberlyst-15 was loaded at the upper part of the reactive section to eliminate free fatty acid (via esterification), while CaO/Al_2O_3 was loaded at the lower part for biodiesel synthesis (via transesterification). The hybridized RD column not only combined the step of esterification pretreatment,

Table 4
Number of required reactive stage and operating conditions for achieving design specification for different free fatty acid contents.

Oil specification	Number of required reactive stage		Methanol excess (%)	Energy requirement, kWhr/kmol biodiesel
	Esterification	Transesterification		
Pure TG	–	5	33	117
FFA 20%	3	5	24	144
FFA 40%	3	4	19	138
FFA 60%	3	3	16	132
FFA 80%	3	3	14	136
Pure FFA	3	–	0	124

transesterification and separation/purification of the products into a single RD but also improved the biodiesel yield with lower methanol in feed, hence lower energy requirement compared to the conventional alkaline catalyzed process, or even with the process of two RD columns in series. The suitable design of the hybridized RD column consisted of 4 stages of esterification and 20 stages of transesterification with optimum condition of 4:1 of methanol to oil molar feed ratio and reflux ratio of 0.1. The net energy requirement for the hybridized RD, catalyzed by Amberlyst 15 and CaO/Al_2O_3, reached a value of s 216 kWhr/kmol biodiesel (or 197 kWhr/kmol biodiesel with an allocated purity of 98 wt% to glycerol by-product). Moreover, increasing the operating pressure of the hybridized column from 1 to 3 bar decreased the number of reactive stages from 24 stages to 8 stages. Effect of FFA content in feed has shown that a maximum number of 8 stages was enough to cope with all FFA contents. By adjusting the ratio of acid catalyst and base catalyst packed stage, the design eliminated FFA for different feedstock, and thus reached high values of yield and purity of biodiesel.

Acknowledgements

This work was financially supported by the Thailand Research Fund (DPG5880003). Department of Chemical Engineering, Faculty of Engineering, Chulalongkorn University would like to acknowledge The Institutional Research Grant (The Thailand Research Fund), IRG 5780014, and Chulalongkorn University, Contract No. RES_57_411_21_076.

Appendix A. Supplementary material

Supplementary data associated with this article can be found, in the online version, at http://dx.doi.org/10.1016/j.enconman.2017.10.013.

References

[1] E. Department, Energy Department www.energy.gov (n.d.).
[2] B.R. Inc., Bioengineering Resource www.brienergy.com (n.d.).
[3] Maceiras R, Rodríguez M, Cancela A, Urréjola S, Sánchez A. Macroalgae: raw material for biodiesel production. Appl Energy 2011;88:3318–23. http://dx.doi.org/10.1016/j.apenergy.2010.11.027.
[4] Lian S, Li H, Tang J, Tong D, Hu C. Integration of extraction and transesterification of lipid from jatropha seeds for the production of biodiesel. Appl Energy 2012;98:540–7. http://dx.doi.org/10.1016/j.apenergy.2012.04.029.
[5] Yusuf NNAN, Kamarudin SK, Yaakub Z. Overview on the current trends in biodiesel production. Energy Convers Manage 2011;52:2741–51. http://dx.doi.org/10.1016/j.enconman.2010.12.004.
[6] Knothe G, Razon LF. Biodiesel fuels. Prog Energy Combust Sci 2017;58:36–59. http://dx.doi.org/10.1016/j.pecs.2016.08.001.
[7] Miladinovi MR, Stamenkovi OS, Bankovi PT, Milutinovi Nikoli AD, Jovanovi DM, Veljkovi VB. Modeling and optimization of sunflower oil methanolysis over quicklime bits in a packed bed tubular reactor using the response surface methodology. Energy Convers Manage 2016;130:25–33. doi: http://dx.doi.org/10.1016/j.enconman.2016.10.020.
[8] Karatay SE, Dönmez G. Microbial oil production from thermophile cyanobacteria for biodiesel production. Appl Energy 2011;88:3632–5. http://dx.doi.org/10.1016/j.apenergy.2011.04.010.
[9] Rasoul-Amini S, Montazeri-Najafabady N, Mobasher MA, Hoseini-Alhashemi S, Ghasemi Y. Chlorella sp.: A new strain with highly saturated fatty acids for biodiesel production in bubble-column photobioreactor. Appl Energy 2011;88:3354–6. http://dx.doi.org/10.1016/j.apenergy.2010.12.040.
[10] Chisti Y, Yan J. Energy from algae: current status and future trends: algal biofuels–a status report. Appl Energy 2011;88:3277–9. http://dx.doi.org/10.1016/j.apenergy.2011.04.038.
[11] Abou-Shanab RAI, Hwang J-H, Cho Y, Min B, Jeon B-H. Characterization of microalgal species isolated from fresh water bodies as a potential source for biodiesel production. Appl Energy 2011;88:3300–6. http://dx.doi.org/10.1016/j.apenergy.2011.01.060.
[12] Gao C, Zhai Y, Ding Y, Wu Q. Application of sweet sorghum for biodiesel production by heterotrophic microalga Chlorella protothecoides. Appl Energy 2010;87:756–61. http://dx.doi.org/10.1016/j.apenergy.2009.09.006.
[13] Lam MK, Lee KT. Potential of using organic fertilizer to cultivate Chlorella vulgaris for biodiesel production. Appl Energy 2012;94:303–8. http://dx.doi.org/10.1016/j.apenergy.2012.01.075.
[14] Sánchez Á, Maceiras R, Cancela Á, Pérez A. Culture aspects of Isochrysis galbana for biodiesel production. Appl Energy 2013;101:192–7. http://dx.doi.org/10.1016/j.apenergy.2012.03.027.
[15] Huang G, Chen F, Wei D, Zhang X, Chen G. Biodiesel production by microalgal biotechnology. Appl Energy 2010;87:38–46. http://dx.doi.org/10.1016/j.apenergy.2009.06.016.
[16] Ganapathy T, Murugesan K, Gakkhar RP. Performance optimization of Jatropha biodiesel engine model using Taguchi approach. Appl Energy 2009;86:2476–86. http://dx.doi.org/10.1016/j.apenergy.2009.02.008.
[17] Montefrio MJ, Xinwen T, Obbard JP. Recovery and pre-treatment of fats, oil and grease from grease interceptors for biodiesel production. Appl Energy 2010;87:3155–61. http://dx.doi.org/10.1016/j.apenergy.2010.04.011.
[18] Marchetti JM, Miguel VU, Errazu AF. Techno-economic study of different alternatives for biodiesel production. Fuel Process Technol 2008;89:740–8. http://dx.doi.org/10.1016/j.fuproc.2008.01.007.
[19] Mansir N, Taufiq-Yap YH, Rashid U, Lokman IM. Investigation of heterogeneous solid acid catalyst performance on low grade feedstocks for biodiesel production: a review. Energy Convers Manage 2017;141:171–82. http://dx.doi.org/10.1016/j.enconman.2016.07.037.
[20] Nurfitri I, Maniam GP, Hindryawati N, Yusoff MM, Ganesan S. Potential of feedstock and catalysts from waste in biodiesel preparation: a review. Energy Convers Manage 2013;74:395–402. http://dx.doi.org/10.1016/j.enconman.2013.04.042.
[21] Jacobson K, Gopinath R, Meher LC, Dalai AK. Solid acid catalyzed biodiesel production from waste cooking oil. Appl Catal B Environ 2008;85:86–91. http://dx.doi.org/10.1016/j.apcatb.2008.07.005.
[22] Utlu Z. Evaluation of biodiesel fuel obtained from waste cooking oil, energy sources. Part A Recover Util Environ Eff 2007;29:1295–304. http://dx.doi.org/10.1080/00908310500434564.
[23] Marmesat S, Rodrigues E, Velasco J, Dobarganes C. Quality of used frying fats and oils: comparison of rapid tests based on chemical and physical oil properties. Int J Food Sci Technol 2007;8.
[24] Demirbas A. Biodiesel from waste cooking oil via base-catalytic and supercritical methanol transesterification. Energy Convers Manage 2009;50:923–7. http://dx.doi.org/10.1016/j.enconman.2008.12.023.
[25] Laosiripojana N, Kiatkittipong W, Sutthisripok W, Assabumrungrat S. Synthesis of methyl esters from relevant palm products in near-critical methanol with modified-zirconia catalysts. Biores Technol 2010;101:8416–23. http://dx.doi.org/10.1016/j.biortech.2010.05.076.
[26] Ang GT, Tan KT, Lee KT, Mohamed AR. Biodiesel production via injection of superheated methanol technology at atmospheric pressure. Energy Convers Manage 2014;87:1231–8. http://dx.doi.org/10.1016/j.enconman.2014.02.037.
[27] Ang GT, Tan KT, Lee KT, Mohamed AR. Kinetic studies of sea mango (*Cerbera odollam*) oil for biodiesel production via injection of superheated methanol vapour technology. Energy Convers Manage 2015;105:1213–22. http://dx.doi.org/10.1016/j.enconman.2015.08.076.
[28] Dimian AC, Bildea CS, Omota F, Kiss AA. Innovative process for fatty acid esters by dual reactive distillation. Comput Chem Eng 2009;33:743–50. http://dx.doi.org/10.1016/j.compchemeng.2008.09.020.
[29] Steinigeweg S, Gmehling J. Esterification of a fatty acid by reactive distillation. Ind Eng Chem Res 2003;42:3612–9. http://dx.doi.org/10.1021/ie020925i.
[30] Boon-anuwat N, Kiatkittipong W, Aiouache F, Assabumrungrat S. Process design of continuous biodiesel production by reactive distillation: comparison between homogeneous and heterogeneous catalysts. Chem Eng Process Process Intensif 2015;92:33–44. http://dx.doi.org/10.1016/j.cep.2015.03.025.
[31] Prasertsit K, Mueanmas C, Tongurai C. Transesterification of palm oil with methanol in a reactive distillation column. Chem Eng Process Process Intensif 2013;70:21–6. http://dx.doi.org/10.1016/j.cep.2013.05.011.
[32] Pérez-Cisneros ES, Mena-Espino X, Rodríguez-López V, Sales-Cruz M, Viveros-García T, Lobo-Oehmichen R. An integrated reactive distillation process for biodiesel production. Comput Chem Eng 2016;91:233–46. http://dx.doi.org/10.1016/j.compchemeng.2016.01.008.
[33] Lohmann J, Joh R, Gmehling J. From UNIFAC to Modified UNIFAC (Dortmund). Ind Eng Chem Res 2001;40:957–64. http://dx.doi.org/10.1021/ie0005710.
[34] Kuramochi H, Maeda K, Kato S, Osako M, Nakamura K, Sakai S. Application of UNIFAC models for prediction of vapor–liquid and liquid–liquid equilibria relevant to separation and purification processes of crude biodiesel fuel. Fuel 2009;88:1472–7. http://dx.doi.org/10.1016/j.fuel.2009.01.017.
[35] Banchero M, Gozzelino G. Nb_2O_5-catalyzed kinetics of fatty acids esterification for reactive distillation process simulation. Chem Eng Res Des 2015;100:292–301. http://dx.doi.org/10.1016/j.cherd.2015.05.043.
[36] Xiao Y, Li H, Xiao G, Gao L, Pan X. Simulation of the catalytic reactive distillation process for biodiesel production via transesterification, ICMREE 2013 – Proc. 2013 Int. Conf. Mater. Renew. Energy Environ. 2013;1:196–9. http://dx.doi.org/10.1109/ICMREE.2013.6893646.
[37] Pal R, Sarkar T, Khasnobis S. Amberlyst-15 in organic synthesis. Arkivoc 2012;2012:570–609. http://dx.doi.org/10.3998/ark.5550190.0013.114.
[38] Boz N, Degirmenbasi N, Kalyon DM. Esterification and transesterification of waste cooking oil over Amberlyst 15 and modified Amberlyst 15 catalysts. Appl Catal B Environ 2015;165:723–30. http://dx.doi.org/10.1016/j.apcatb.2014.10.079.
[39] Jaeger WK, Egelkraut TM. Biofuel economics in a setting of multiple objectives and unintended consequences. Renew Sustain Energy Rev 2011;15:4320–33. http://dx.doi.org/10.1016/j.rser.2011.07.118.
[40] Kesic Z, Lukic I, Zdujic M, Mojovic L, Skala D. Calcium oxide based catalysts for biodiesel production: a review. Chem Ind Chem Eng Q 2016;22. http://dx.doi.org/10.2298/CICEQ160203010K. 10-10.
[41] Liu X, He H, Wang Y, Zhu S, Piao X. Transesterification of soybean oil to biodiesel using CaO as a solid base catalyst. Fuel 2008;87:216–21. http://dx.doi.org/10.1016/j.fuel.2007.04.013.

[42] Noureddini H, Zhu D. Kinetics of transesterification of soybean oil. J Am Oil Chem Soc 1997;74:1457–63.
[43] Pasupulety N, Gunda K, Liu Y, Rempel GL, Ng FTT. Production of biodiesel from soybean oil on CaO/Al_2O_3 solid base catalysts. Appl Catal A Gen 2013;452:189–202. http://dx.doi.org/10.1016/j.apcata.2012.10.006.
[44] Zhang Y, Dubé MA, McLean DD, Kates M. Biodiesel production from waste cooking oil: 1. Process design and technological assessment. Biores Technol 2003;89:1–16. http://dx.doi.org/10.1016/S0960-8524(03)00040-3.
[45] Smith EG, Janzen HH, Newlands NK. Energy balances of biodiesel production from soybean and canola in Canada. Can J Plant Sci 2007;87:793–801. http://dx.doi.org/10.4141/CJPS06067.
[46] Moradi G, Davoodbeygi Y, Mohadesi M, Hosseini S. Kinetics of transesterification reaction using CAO/AL_2O_3 catalyst synthesized by sol-gel method. Can J Chem Eng 2015;93:819–24. http://dx.doi.org/10.1002/cjce.22158.
[47] Gaurav A, Leite ML, Ng FTT, Rempel GL. Transesterification of triglyceride to fatty acid alkyl esters (biodiesel): comparison of utility requirements and capital costs between reaction separation and catalytic distillation configurations. Energy Fuels 2013;27:6847–57. http://dx.doi.org/10.1021/ef401790n.
[48] Glišić S, Lukic I, Skala D. Biodiesel synthesis at high pressure and temperature: analysis of energy consumption on industrial scale. Biores Technol 2009;100:6347–54. http://dx.doi.org/10.1016/j.biortech.2009.07.024.

Ann Microbiol (2017) 67:763–778
https://doi.org/10.1007/s13213-017-1306-y

ORIGINAL ARTICLE

Characterization of D-lactic acid, spore-forming bacteria and *Terrilactibacillus laevilacticus* SK5-6 as potential industrial strains

Budsabathip Prasirtsak[1] · Sitanan Thitiprasert[2] · Vasana Tolieng[2] · Suttichai Assabumrungrat[3] · Somboon Tanasupawat[4] · Nuttha Thongchul[2]

Received: 4 July 2017 / Accepted: 11 October 2017 / Published online: 24 October 2017
© Springer-Verlag GmbH Germany and the University of Milan 2017

Abstract In this study, we screened and isolated D-lactic acid-producing bacteria from soil and tree barks collected in Thailand. Among the isolates obtained, *Terrilactibacillus laevilacticus* SK5-6 exhibited good D-lactate production in the primary screening fermentation (99.27 g/L final lactate titer with 0.90 g/g yield, 1.38 g/L·h, and 99.00% D-enantiomer equivalent). *Terrilactibacillus laevilacticus* SK5-6 is a Gram-positive, endospore-forming, homofermentative D-lactate producer that can ferment a wide range of sugars to produce D-lactate. Unlike the typical D-lactate producers, such as catalase-negative *Sporolactobacillus* sp., *T. laevilacticus* SK5-6 possesses catalase activity; therefore, a two-phase fermentation was employed for D-lactate production. During an aerobic preculture stage, a high-density cell mass was rapidly obtained due to aerobic respiration. When transferred to the fermentation stage at the correct physiological stage (inoculum age) and proper concentration of cell mass (inoculum size), *T. laevilacticus* rapidly converted glucose into D-lactate under anaerobic conditions, resulting in a high final lactate titer (102.22 g/L), high yield (0.84 g/g), and high productivity (2.13 g/L·h). When the process conditions were shifted from an aerobic to an anaerobic environment, unlike other lactate-producing bacteria, the mixed acid fermentation route was not activated in the culture of *T. laevilacticus* SK5-6 during the fermentation stage when some trace oxygen still remained. Our study demonstrates the excellent characteristics of this isolate for D-lactate production; in particular, a high product yield was obtained without byproduct formation. Based on these key characteristics of *T. laevilacticus* SK5-6, we suggest that this isolate is a novel D-lactate producer for use in industrial fermentation.

Keywords *Terrilactibacillus laevilacticus* · Two-phase fermentation · D-lactic acid · Catalase positive · Homofermentative

The GenBank/EMBL/DBBJ accession number for the 16S rRNA of strain SK5-6 is LC222555; for strain BRY67-1, LC222556; for strain BRY67-2, LC222557; for strain BRY67-3, LC222558; for strain NK44-2, LC222559; for strain SP43-2, LC222560.

✉ Nuttha Thongchul
Nuttha.T@chula.ac.th

[1] Program in Biotechnology, Faculty of Science, Chulalongkorn University, Phayathai Road, Wangmai, Pathumwan, Bangkok 10330, Thailand

[2] Institute of Biotechnology and Genetic Engineering, Chulalongkorn University, Phayathai Road, Wangmai, Pathumwan, Bangkok 10330, Thailand

[3] Department of Chemical Engineering, Faculty of Engineering, Chulalongkorn University, Phayathai Road, Wangmai, Pathumwan, Bangkok 10330, Thailand

[4] Department of Microbiology and Biochemistry, Faculty of Pharmaceutical Sciences, Chulalongkorn University, Phayathai Road, Wangmai, Pathumwan, Bangkok 10330, Thailand

Introduction

Lactic acid is widely used in the pharmaceutical and chemical industries as well as for many other applications including, for example, as an acidulant, a flavor enhancer, and a food preservative. The relatively recent global awareness of the large consumption of non-renewable plastic products has driven the development of compostable plastics from the renewable resources as an alternative. Polylactic acid (PLA) is one of the more promising bio-based plastics drawing interest in research and development. During its early developmental stage, PLA was synthesized from the optically pure L-lactic acid owing to the availability of L-lactic acid in the market. The first generation of PLA products has limited uses since their mechanical

and thermal properties were not competitive with the available commodity plastics. The mechanical and thermal properties of PLA can be improved by incorporating the stereoblock structure that yields an increasing melting temperature. Both optically pure L- and D-lactic acid are required to synthesize the stereoblock PLA. However, unlike L-lactic acid with its wide range of applications, the production of D-lactic acid is currently limited (Li et al. 2013).

Lactic acid is currently produced via microbial fermentation under mild conditions and low energy consumption. Microbial fermentation utilizes low-cost, renewable feedstocks to produce a racemic mixture or an optically pure isomer of lactic acid (L- and D-lactic acid), depending on the microbes employed (Wee et al. 2006; John et al. 2009; Xu et al. 2010). D-lactic acid is only produced in some bacteria, including *Lactobacillus delbrueckii*, *Leuconostoc* sp., and *Sporolactobacillus* sp., as a metabolic response to environmental stress (Panesar et al., 2010; Tashiro et al. 2011; Mimitsuka et al. 2012; Li et al. 2013; Zhao et al. 2014; Bai et al. 2016). It has been noted that D-lactate production with the aforementioned strains usually results in poor fermentation performance, which has led to genetic engineering being employed for strain development to specifically produce optically pure D-lactate; however, the genetically modified microbes have limited industrial applications due to biosafety regulation limits and genetic instability (Feng et al. 2014; Tsuge et al. 2014; Baek et al. 2016). Therefore, wild strains are still preferred in industrial D-lactate production facilities.

Previous screening studies in Thailand have isolated novel D-lactate-producing strains from natural samples. Thamacharoensuk et al. (2015) recently isolated two D-lactate producers from tree barks which they subsequently identified as the novel species *Sporolactobacillus spathodeae* and *S. shoreae*. Prasirtsak et al. (2016) isolated the novel bacterial genus *Terrilactibacillus* from soil samples collected in Thailand, which they later identified as *Terrilactibacillus laevilacticus* NK26-11^T, a catalase-positive D-lactate producer. This species has attracted researchers' attention due to its good fermentation performance (high yield, high productivity, and high optical purity). Based on these findings, Thailand would appear to be a good source of natural material for bacterial screening. The aim of the study reported here was to obtain robust D-lactate producers through a process of bacterial screening of natural samples and subsequent isolation, and identification of D-lactate producers. Among the D-lactate producers screened in this study, we identified one as *T. laevilacticus* SK5-6, a novel genus, which exhibited a good fermentation performance in the primary screening. Little is known about D-lactate production by this genus. Consequently, we report here the preliminary fermentation optimization for D-lactate production by *T. laevilacticus* SK5-6 and propose that this novel genus is a promising D-lactate-producing strain for use in industrial fermentation.

Material and methods

Sample collection

A total of 76 samples of soil and tree barks were collected from December 2014 to August 2015 in the northern, eastern, and central provinces of Thailand (3 samples from Chiangmai, 5 from Phitsanulok, 11 from Rayong, 4 from Suphanburi, 5 from Saraburi, 8 from Ayutthaya, 33 from Nakhonpathom, and 7 from Bangkok). The isolate SK5-6 was screened from a soil sample collected at the Faculty of Pharmaceutical Sciences, Chulalongkorn University, Bangkok.

Bacterial isolation

Natural samples (approx. 200–300 mg) were collected from soil and tree barks. To selectively revive the growth of bacteria, we transferred a portion of the collected sample (0.25 g)into 5 mL sterile enrichment medium [composition per liter: 10 g glucose, 5 g yeast extract, 5 g peptone, 0.25 g KH_2PO_4, and 0.25 g K_2HPO_4, supplemented with 10 mL salt solution (composition per 10 mL: 400 mg $MgSO_4{\cdot}7H_2O$, 20 mg $MnSO_4{\cdot}5H_2O$, 20 mg $FeSO_4{\cdot}7H_2O$, and 20 mg NaClpH 4.4), pH 4.4], followed by heat shock at 80 °C for 10 min. The suspension was subsequently incubated at 37 °C until growth was observed and then transferred onto a glucose–yeast extract–peptone (GYP) agar (composition per liter: 10 g glucose, 5 g yeast extract, 5 g peptone, 0.25 g KH_2PO_4, 0.25 g K_2HPO_4, 20 g agar, 5 g $CaCO_3$, 10 mL salt solution) plate containing $CaCO_3$ as the acid production indicator. The pH of the GYP agar medium was adjusted to 6.80.

The GYP agar plate was incubated at 37 °C until colonies developed. The colonies that formed in a large clear zone were transferred onto a new GYP agar plate for single colony purification. A single colony was transferred into a new GYP agar slant. To maintain the activity of the selected colony, the colony was subcultured into a new GYP agar slant every 10 days. The single colony was ultimately transferred into a sterile skim milk solution and kept at −80 °C for long-term storage.

Phenotypic characterization

The bacterial isolates were cultured in a phenotypic medium (composition per liter: 10 g glucose, 10 g yeast extract, 10 g peptone, 10 g CH_3COONa, 5 mL salt solution) at 37 °C under anaerobic conditions for phenotypic characterization. Cell form and cell size were examined under the microscope. The Hucker–Conn modification method was used for Gram staining (Tanasupawat et al. 1992. 1998). Spore formation was examined by scanning electron microscopy. The effects of temperature, initial pH, and NaCl concentration on growth were observed in the culture grown in the phenotypic medium. Catalase and oxidase activities, nitrate reduction, and

hydrolysis of arginine and starch were tested following the methods previously described in Tanasupawat et al. (1998). Additional biochemical characteristics of the isolates were determined after incubation for 2 days at 37 °C under aerobic conditions using API 50 CH strips (bioMérieux, Marcy-l'Étoile, France) according to the manufacturer's instructions.

Genotypic characterization

DNA was extracted from the cells grown in the GYP broth for 2 days and purified using the method described by Saito and Miura (1963). The 16S rRNA gene of the isolate was amplified and the PCR product purified and sequenced as previously described (Saito and Miura 1963; Tanasupawat et al. 2004). The sequence of the isolate was aligned with the selected sequences obtained from GenBank using CLUSTAL_X version 1.81. The alignment was manually edited to remove gaps and ambiguous nucleotides before the construction of a phylogenetic tree with the neighbor-joining method and the maximum-likelihood method using MEGA version 6 (Felsenstein 1981; Saitou and Nei 1987; Tamura et al. 2013). The confidence values of the individual branches in the phylogenetic tree were determined using the bootstrap analysis of Felsenstein (1985) based on 1000 replications. The values for the sequence similarity among the closest strains were determined using the EzTaxon server (Kim et al. 2012).

Primary screening for D-lactate-producing isolates

The bacterial isolates were categorized into two groups based on the presence of catalase activity in the primary screening for D-lactate production. Each isolate was subcultured onto a fresh new GYP agar slant and incubated anaerobically at 37 °C for 48 h. To prepare the bacterial suspension, we first transferred 2 mL of sterile preculture medium into the culture slant and then thoroughly mixed the contents of the slant. The bacterial suspension was then inoculated in a preculture flask containing 48 mL sterile preculture medium.

For the catalase-negative isolate, we inoculated 2 mL of the bacterial suspension into the preculture medium (pH 6.8) containing (per liter) 10 g glucose, 5 g yeast extract, 5 g peptone, 0.25 g KH_2PO_4, 0.25 g K_2HPO_4, 10 mL salt solution, and 5 g $CaCO_3$. The culture was incubated at 37 °C under anaerobic conditions for 26 h [in a flask plugged with a T-type silicone stopper and placed into a W-zip pouch containing AnaeroPack-Anaero (Mitsubishi Gas Chemical, Tokyo, Japan)], following which 1 mL of the preculture broth was transferred into 49 mL of sterile fermentation medium (composition per liter: 120 g glucose, 10 g yeast extract, 5 g peptone, 0.25 g KH_2PO_4, 0.25 g K_2HPO_4, 10 mL salt solution, 80 g $CaCO_3$). The culture was incubated at 37 °C under anaerobic conditions for 72 h [in a flask plugged with a T-type silicone stopper and placed into a W-zip pouch containing AnaeroPack-Anaero (Mitsubishi Gas Chemical)]. At the end of the fermentation, the sample was collected for analyses of the remaining glucose, D-lactate, byproducts, and optical purity of D-lactate.

For the catalase-positive isolate, the bacterial suspension was inoculated in preculture medium (pH 6.8) containing (per liter) 10 g glucose, 15 g yeast extract, 4 g NH_4Cl, 0.5 g KH_2PO_4, 0.5 g K_2HPO_4, 20 mL salt solution, and 5 g $CaCO_3$ and incubated at 37 °C, 200 rpm for 5 h in a flask plugged with a C-type silicone stopper. Thereafter, 25 mL of the preculture broth was transferred into 25 mL of the sterile fermentation medium containing (per liter) 240 g glucose and 80 g $CaCO_3$. The culture was then incubated at 37 °C for another 72 h in a flask plugged with a T-type silicone stopper and placed into a W-zip pouch containing AnaeroPack-Anaero (Mitsubishi Gas Chemical). At the end of the fermentation, the sample was collected for analyses of the remaining glucose, D-lactate, byproducts, and optical purity of D-lactate.

Effects of inoculum size, oxygen, and mixing on growth of *T. laevilacticus* SK5-6 during the preculture stage

The operating conditions during both the preculture and fermentation stages of the catalase-positive isolate *T. laevilacticus* SK5-6 were further optimized in flask cultivation. The growth profile during the preculture stage was determined. *T. laevilacticus* SK5-6 was subcultured onto fresh new GYP agar slants and incubated at 37 °C for 24 h to prepare the bacterial suspension. The preculture medium was inoculated with the bacterial suspension [optical density at 600 nm (OD_{600}) of 30-40, where OD_{600} of 1 is equivalent to 0.12 g/L cell dry weight] of *T. laevilacticus* SK5-6 at different inoculum sizes (0.5, 1, and 2%). The culture was incubated in an Erlenmeyer flask at 37 °C under different mixing (no mixing and mixing at 200 rpm) and gas permeability (to generate an aerobic/anaerobic culture environment) conditions. To manipulate the air permeability of the culture flask in order to initiate an aerobic condition, we plugged the flask with a C-type silicone stopper to allow good air permeability. To generate anaerobic conditions, we plugged the flask with a T-type silicone stopper and placed it into a W-zip pouch containing AnaeroPack-Anaero (Mitsubishi Gas Chemical). Samples were taken at 1-h intervals for 8 h for the analyses of cell mass, the remaining glucose, and product formation.

Effect of the preculture seed on D-lactate fermentation

Terrilactibacillus laevilacticus SK5-6 was subcultured onto GYP agar slants and incubated at 37 °C. The bacterial suspension of OD_{600} of 30-40 was prepared for inoculation into the preculture medium at 1% inoculum size. The preculture flask was incubated at 37 °C under different mixing (no mixing and

mixing at 200 rpm) and gas permeability [using a C-type silicone stopper or a T-type silicone stopper and placing the flask in a W-zip pouch containing AnaeroPack-Anaero (Mitsubishi Gas Chemical)] conditions. The preculture time was varied between the mid log phase (4 h) and the late log phase (5 h). Following preculture,, the preculture broth was transferred into the fermentation medium at 50% inoculum size. The fermentation culture was incubated at the same temperature for 48 h under varied mixing (no mixing and mixing at 150 rpm) and gas permeation [with either a C-type silicone stopper or a T-type silicone stopper and placing the flask in a W-zip pouch containing AnaeroPack-Anaero (Mitsubish Gas Chemical) conditions. Samples were taken every 12 h for analyses of OD_{600} readings, the remaining glucose, and lactate and byproduct formation.

D-lactate fermentation by *T. laevilacticus* SK5-6 in a 5-L stirred fermenter

The fermentation platform of *T. laevilacticus* SK5-6 was preliminarily determined in a 5-L stirred fermenter. A 24-h GYP agar slant was used to prepare the bacterial suspension. The bacterial suspension (1% inoculum size) was inoculated in a preculture flask plugged with a C-type silicone stopper. The preculture flask was incubated at 37 °C, 200 rpm for 4 h. After that, the preculture flask was transferred into a 5-L stirred fermenter that contained 2.5 L of the sterile preculture medium at 10% inoculum size. The fermenter was operated at 37 °C, agitated at 300 rpm, with 1.0 vvm air. After 3 h, 0.5 L of the fermentation medium containing (per liter) 720 g glucose and 480 g $CaCO_3$ was added into the fermenter. Aeration was stopped and the agitation speed was varied at 200 and 300 rpm to obtain the optimal D-lactate production rate. Samples were taken every 6 h for 48 h for analyses of cell mass, remaining glucose, and lactate and byproduct formation.

Analytical methods

A sample of fermentation broth was centrifuged at 10,000 *g* for 5 min to separate the cell-free supernatant from the cell mass. The supernatant was collected for further analyses of the remaining glucose, lactic acid, byproducts, and the optical purity of D-lactate. The cell mass was acidified with 1 M HCl to remove any insoluble $CaCO_3$ remaining in the sample. The acidified sample was centrifuged and the particles resuspended in deionized water for the OD reading. Spectrophotometry was used to determine the OD_{600} of the cell mass present in the fermentation broth. Cell mass concentration was then calculated from the correlation between OD_{600} and cell dry weight (where an OD_{600} of 1 is equivalent to 0.12 g/L).

The concentration of products formed and glucose substrate remaining during the fermentation were analyzed using high-performance liquid chromatography (HPLC). Fermentation samples were centrifuged, filtered through a PTFE (hydrophilic) membrane, and diluted with double deionized water. For analyses of the remaining glucose, total lactic acid (both L- and D-lactic acid), and acetic acid, 15 μL diluted particle-free samples were automatically injected (SIL-10A HPLC autosampler (Shimadzu Corp., Kyoto, Japan) into an organic acid analysis column (Aminex HPX-87H ion exclusion organic acid column; 300 mm × 7.8 mm; Bio-Rad, Hercules, CA), and maintained at 45 °C in a column oven (CTO-10A; Shimadzu Corp.). H_2SO_4 (0.005 M) was pumped through the system at a flow rate of 0.6 mL/min (LC-10Avp System Controller; Shimadzu Corp.). A refractive index detector (RID-10A; Shimadzu Corp.) was used to detect the organic compounds. The standards containing 0–2 g/L of each component (glucose, lactate, and acetate) were injected as references to determine sample concentration. The chromatogram peak area was used as the comparison basis in determining the concentration. To determine the optical purity of lactic acid, 5 μL diluted particle-free samples were automatically injected into a chiral column (Sumipack, Sumichiral OA5000) and maintained at 40 °C. $CuSO_4$ (0.001 M) was used as the eluent at a flow rate of 1.0 mL/min. A UV detector was used to detect the lactate isomers at 254 nm. The standards containing 0–2 g/L of D- and L-lactic acid were injected as references to determine sample concentration.

Product yield ($Y_{p/s}$) was determined from the ratio of the product formed to carbon substrate consumed during the fermentation stage. Volumetric productivity was defined as the total amount of product formed per unit volume per time. The optical purity of the D-lactate was defined from the peak areas of the chromatogram as follows (Zhao et al. 2014).

$$Optical\ purity = \frac{\mathrm{D}-lactate-\mathrm{L}-lactate}{\mathrm{D}-lactate+\mathrm{L}-lactate} \times 100\%$$

Results and discussion

Isolation, identification, characterization, and screening of D-lactic acid producers

A total of 116 bacterial isolates were obtained from 76 natural samples, of which only six, including SK5-6, SP43-2, NK44-2, BRY67-1, BRY67-2, and BRY67-3, produced D-lactic acid. The neighbor-joining phylogenetic tree based on the 16S rRNA gene sequences suggested that the isolate SK5-6 was 100% related to the novel *Terrilactibacillus laevilacticus* NK26-11^T (= LMG27803^T = TISTR2241^T = PCU335^T) previously reported by Prasirtsak et al. (2016). The isolate SP43-2 demonstrated a high similarity in 16S rRNA sequence to *Sporolactobacillus nakayamae* subsp. *nakayamae* DSM11696^T (99.6%) (Yanagida

et al. 1997). The other isolates, including NK44-2, BRY67-1, BRY67-2, and BRY67-3, had similar percentages of 99.2–99.7% to *Sporolactobacillus laevolacticus* DSM442^T (Hatayama et al. 2006). (Table 1; Fig. 1).

The morphological and biochemical characterization revealed that all six isolates were Gram-positive, facultative anaerobic, spore-forming, rod-shaped bacteria. None were able to hydrolyze starch and arginine. All isolates lacked oxidase and catalase with the exception of SK5-6 which exhibited a positive result for catalase activity. As a result, oxygen was not restricted in the cultivation of SK5-6 while the others required an anaerobic environment for growth. All six isolates produced D-lactate from glucose via a homofermentative route. They grew at 20–40 °C, at a pH of 5.5–8.5. They tolerated a salt concentration of up to 3%. These isolates utilized various substrates in addition to glucose (Table 1).

Based on the results of the primary screening fermentation, all six isolates exhibited a high D-lactate production compared with the type strain *T. laevilacticus* NK26-11^T previously identified by our research group (Table 2). All six isolates also produced D-lactate from glucose at high yields of approximately 0.83–1.00 g/g glucose. Productivity in flask culture was in an acceptable range of 1.06–1.42 g/L·h, with a sufficiently high final titer of 76.01–102.43 g/L from an initial glucose concentration of 120 g/L. While isolates SK5-6, SP43-2, and NK44-2 yielded D-lactate of a high optical purity, the D-lactate produced by isolates BRY67-1, BRY67-2, and BRY67-3 had an optical purity of < 99.0% D-enantiomer equivalent (ee), thereby necessitating a more complicated recovery and purification process to acquire a sufficiently higher purity than 99.0% for the polymer-grade lactic acid. As a result, fermentation optimization by these latter three isolates was not continued. Comparison of isolates SK5-6, SP43-2, and NK44-2 showed that SK5-6 exhibited strong catalase activity while the other two isolates were catalase negative. Therefore, it was possible to implement a two-phase fermentation process (aerobic preculture and subsequent anaerobic fermentation) using SK5-6, with high cell densities of SK5-6 obtained during the aerobic preculture stage, which enabled the production of D-lactate during the anaerobic fermentation stage at a high production rate (Qin et al. 2010; Ma et al. 2014). *Terrilactibacillus laevilacticus* is a novel bacterial genus capable of producing D-lactate, as previously identified by Prasirtsak et al. (2013) and Prasirtsak et al. (2016), but to date optimization of the fermentation process by this bacterial genus has not been reported. Therefore, we attempted to determine the key process parameters that modify D-lactate fermentation by this novel genus.

Determination of the correct physiological stage of preculture seed for D-lactate fermentation by *T. laevilacticus* SK5-6

We next investigated the metabolic response of SK5-6 under both aerobic and anaerobic conditions, as well as the effect of mixing to allow a good gas diffusion and homogeneity in the culture. Without mixing, a similar growth rate was obtained from the cultures incubated under anaerobic/aerobic conditions (Fig. 2). With mixing at 200 rpm, the culture incubated under the aerobic conditions yielded a slightly higher growth rate, resulting in a higher final cell concentration when the growth reached stationary phase (5 h). With sufficient mixing, the lag phase was shortened and the growth rate was higher. Therefore, comparing the two parameters studied, mixing would appear to have had a stronger effect on the growth of SK5-6. In addition, a higher growth rate and maximum cell dry weight were achieved from the culture grown under the aerobic conditions. In the presence of oxygen, SK5-6 generated more ATP via glycolysis, citric acid cycle (TCA), and the electron transport chain (ETC). which eventually resulted in a higher growth rate, although the difference between the growth rate under anaerobic and aerobic conditions, respectively, was not dramatically different.

The effects of inoculum size were also investigated (Fig. 3). It was found that a small inoculum size (0.5%) resulted in a longer lag phase (Fig. 3a) and that, conversely, increasing the inoculum size to 1 and 2%, respectively, shortened the lag phase. However, with respect to the log phase, the growth rate during the log phase of SK5-6 was similar for all three inoculum sizes studied. Changing the culture from an aerobic to an anaerobic environment did not affect cell growth to any great degree regardless of inoculum size. Glucose consumption (Fig. 3b) was consistent with the growth profile. The formation of lactate was observed during the preculture stage (Fig. 3c), indicating that the expression of lactate dehydrogenase for lactate production when the metabolic flux shifted toward the anaerobic route. As shown in Fig. 3a, c, lactate started to accumulate when growth entered the log phase. At a small inoculum size (0.5%), lactate formation appeared when growth was in mid log phase; at a larger inoculum size (1 and 2%), lactate started to form from the early log phase. At the 2% inoculum size, a high concentration of lactate (8.89–10.60 g/L) accumulated in the preculture broth; this acted as a stressor on the cells and later had diverse effects on lactate formation during the fermentation stage. At the 1% inoculum size used to inoculate the preculture flask, a shortened lag phase was observed with rapid growth, high cell mass concentration, and slight lactate formation. This indicates that inoculation of the new medium with the proper density of cells induced high biosynthetic rates within a short time frame (Egervarn et al. 2007). Based on these results, we considered the 1% inoculum size to be suitable for use in further optimization studies.

Not only did a sufficiently high concentration of the inoculum enhance the metabolic rate, the proper physiological stage also played a role in modifying the performance of SK5-6 during fermentation. Zagari et al. (2013) reported that the inoculum promptly metabolized glucose to D-lactate at a

Table 1 Selected characteristics of six D-lactate-producing isolates and their closely related type strains.

Characteristic	Isolate SK5-6	*Terrilactibacillus laevilacticus* NK26-11^T	Isolate SP43-2	*Sporolactobacillus nakayamae* subsp. *nakayamae* DSM1196^T	Isolate NK44-2	Isolate BRY67-1	Isolate BRY67-2	Isolate BRY67-3	*Sporolactobacillus laevolacticus* DSM442^T
Cell shape	Rod	Rod	Rod	Rod	Rod	Rod	Rod	Rod	Rod
Spore formation	+	+	+	+	+	+	+	+	+
Temperature range (°C)	25–40	20–45	20–40	20–40	20–40	20–40	20–40	20-40	20–40
NaCl range (%)	0–3	0–3	0–3	0–3	0–3	0–3	0–3	0–3	0–2
pH range	5.5–8.5	5.0–8.5	4.0–9.0	4.5–8.5	4.0–8.5	4.0–9.0	4.0–9.0	4.0–9.0	4.0–9.0
Catalase activity	+	+	-	-	-	-	-	-	-
Lactate isomer produced	D	D	D	D	D	D	D	D	D
Acid production from:									
Glycerol	+	+	-	-	-	-	-	-	-
Erythritol	+	+	-	-	-	-	-	-	-
D-Galactose	+	+	-	-	+	+	+	+	W
D-Glucose	+	+	+	+	+	+	+	+	+
D-Fructose	+	+	+	+	+	+	+	+	+
D-Lyxose	+	+	-	-	-	-	-	-	-
D-Mannose	+	+	+	+	+	+	+	+	+
D-Saccharose	+	+	+	+	+	+	+	+	+
D-Turanose	+	+	-	W	-	-	-	-	-
D-Ribose	-	-	-	-	-	-	-	-	-
D-Xylose	-	-	-	-	-	-	-	-	-
Origin	Soil	-	Bark	-	Bark	Bark	Bark	Bark	-

+, Positive; -, negative; W, weakly positive

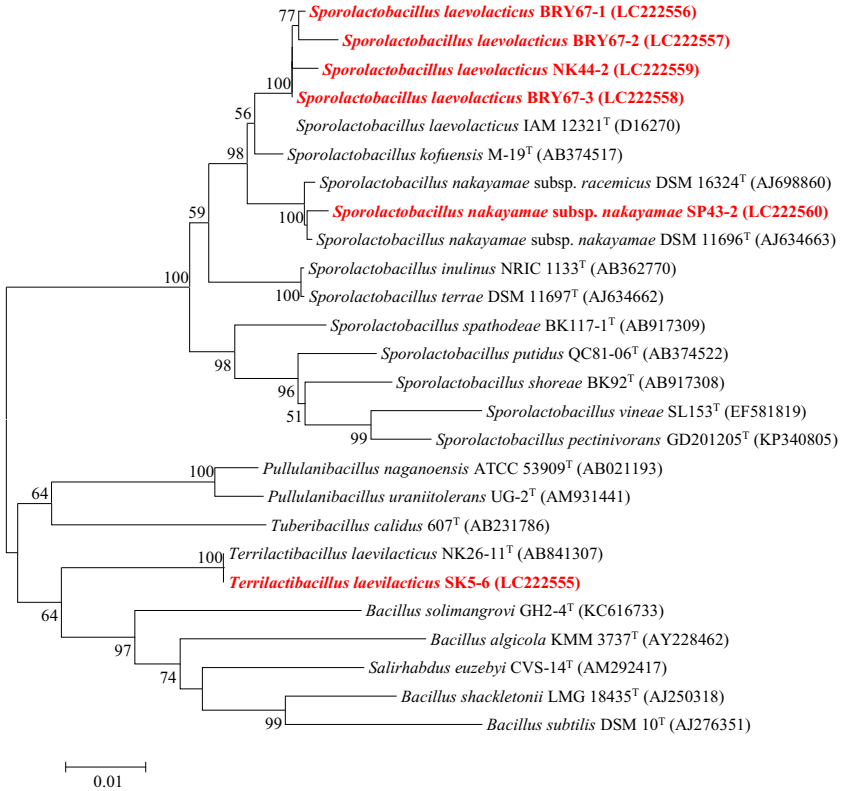

Fig. 1 Neighbor-joining tree, based on 16S rRNA gene sequences, showing the phylogenetic relationship of the isolated strains SK5-6, SP43-2, NK44-2, BRY67-1, BRY67-2, BRY67-3, and related species. Bar represents sequence divergence (1%) (color figure online)

high rate during the log phase. In our study, we observed the effect of inoculum size on D-lactate production in the culture during the mid log phase (4 h) and during the late log phase when the cell concentration was higher (5 h). The results showed that there was no difference in D-lactate production performance from both inoculum seeds studied. This result can be explained by fact that the specific growth rate of SK5-6 at the mid log phase was higher than that at the late log phase when cells were approaching the stationary phase, although the cell concentration at the mid log phase was about half that at the late log phase (Figs. 2, 3a). More specifically, the high growth rate could have compensated for with a high cell concentration. This finding suggested that the seed train development for SK5-6 was rather flexible and effective as it could occur at times between the mid log and the late log phases.

Investigation of the metabolic behavior of T. laevilacticus SK5-6 during the fermentation stage

The preculture seed obtained during the preculture stage under different culture conditions was used as inoculum for the

Table 2 D-lactic acid production from six isolates selected in the primary screening compared with the type strain *Terrilactibacillus laevilacticus* NK26-11

Isolate	D-lactate				Remaining glucose (g/L)
	Final concentration (g/L)	Optical purity (%ee)	Yield (g/g)	Productivity (g/L·h)	
NK26-11T	60.52 ± 0.44	96.44 ± 0.68	0.50 ± 0.01	0.84 ± 0.02	0.00 ± 0.00
SK5-6	99.27 ± 0.71	99.00 ± 0.70	0.90 ± 0.00	1.38 ± 0.00	9.74 ± 0.14
SP43-2	102.43 ± 2.71	100.00 ± 0.00	0.85 ± 0.01	1.42 ± 0.02	0.00 ± 0.00
NK44-2	90.84 ± 2.57	100.00 ± 0.00	0.83 ± 0.01	1.26 ± 0.01	10.93 ± 0.08
BRY67-1	101.12 ± 0.72	98.76 ± 0.70	1.00 ± 0.01	1.40 ± 0.01	18.75 ± 0.13
BRY67-2	83.68 ± 0.59	98.30 ± 0.70	0.86 ± 0.01	1.16 ± 0.01	22.84 ± 0.16
BRY67-3	76.01 ± 1.07	98. 56 ± 1.39	0.85 ± 0.01	1.06 ± 0.01	30.41 ± 0.43

The fermentation was conducted in a shake flask culture with an initial glucose concentration of 120 g/L

Values in table are presented as the mean ± standard deviation (SD)

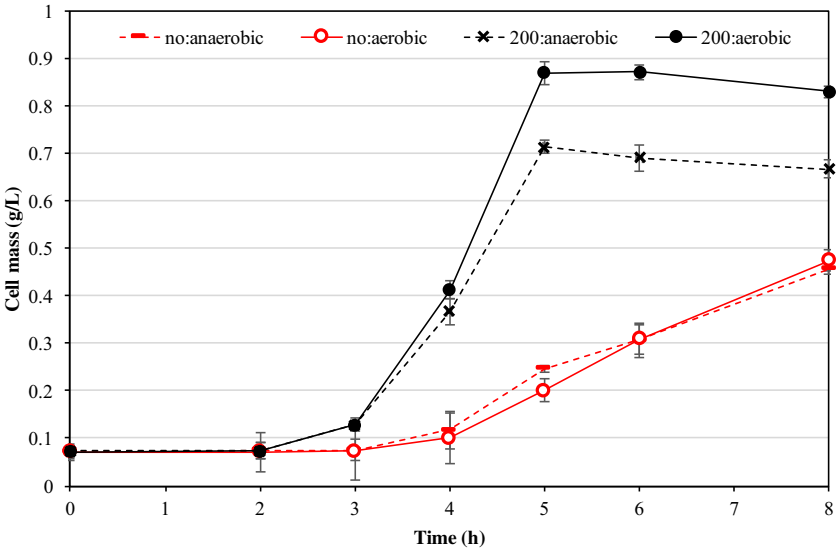

Fig. 2 Effect of mixing [no mixing (no) vs. mixing at 200 rpm (200)] and oxygen (anaerobic vs. aerobic conditions) on growth of isolate SK5-6 during the preculture stage in the flask culture (color figure online)

fermentation medium for D-lactate production. The metabolic response of SK5-6 under different cultivation conditions and its production performance during the fermentation stage are shown in Table 3. It is clear that mixing and anaerobic conditions were necessary for D-lactate production, as indicated by the higher final lactate titer, yield, and productivity and lower glucose levels remaining in the fermentation broth. No significant difference ($P \leq 0.05$) in D-lactic acid production was observed when the fermentation was carried out at 150 rpm under anaerobic conditions, although varied preculture seeds were used as inoculum for the fermentation stage (Table 3, see footnotes a and b). The high yield indicates that SK5-6 successfully utilized glucose for the production of lactate during the anaerobic respiration process when oxygen was limited, unlike the process previously reported during the preculture stage where mixing played a significant role in promoting growth while aerobic/anaerobic conditions appeared to have less effect on growth. During the fermentation stage, anaerobic conditions had a positive effect on lactate production irregardless of mixing (Fig. 2; Table 3).

When the fermentation medium was inoculated with the aerobic preculture seed (both at the mid log and late log phases) and the fermentation stage proceeded under aerobic conditions with mixing (Table 3, see footnote c), cells grew rapidly and approached a stationary phase within 24 h (Table 3). These cells subsequently entered the declining phase, resulting in lower cell dry weight compared with that obtained under the other fermentation conditions (data not shown). As a result, low lactate production was obtained. Transferring the anaerobic preculture seed (both at the mid log and late log phases) to the fermentation stage with mixing and aeration (Table 3, see footnote d) caused adverse effects on cell growth which resulted in low lactate production (Table 3). Cell mass slowly increased (data not shown). One explanation is that anaerobic cells being transferred into the fermentation medium contained only high concentrations of glucose and $CaCO_3$. The fermentation operated at 150 rpm under aerobic conditions, then the cells entered their lag phase as they required the expression of catalase activity to break down hydrogen peroxide (H_2O_2). As a result, the growth rate was low when the metabolic pathway was shifted from the anaerobic preculture seed to the aerobic fermentation with sufficient mixing.

With respect to the effect of preculture seed being transferred to the fermentation stage, changing the inoculum age from the mid log to late log phases did not cause a dramatic change in the fermentation performance during the fermentation stage conducted under the same conditions (Table 3, see footnote a). The aerobic and anaerobic preculture seeds also demonstrated a similar performance (Table 3, see footnote a). More interestingly, no byproduct was found during the fermentation stage, indicating that SK5-6 converted glucose to D-lactate through homofermentation. This preliminary finding indicates that high lactate production can be achieved when the fermentation is performed at 150 rpm under anaerobic conditions. The preculture seed of SK5-6 transferred to the fermentation stage can be prepared under both aerobic and anaerobic conditions. Therefore, we can conclude that the fermentation process using SK5-6 is relatively simple compared with conventional lactate production which usually leads to problems in terms of byproduct formation, low yield, and low productivity.

Effect of agitation on D-lactate fermentation by *T. laevilacticus* SK5-6 in the 5-L stirred fermenter

The time course kinetics of SK5-6 during the fermentation stage are shown in Fig. 4. We found that increasing the agitation speed from 200 to 300 rpm significantly enhanced lactate production. With adequate mixing, glucose was rapidly

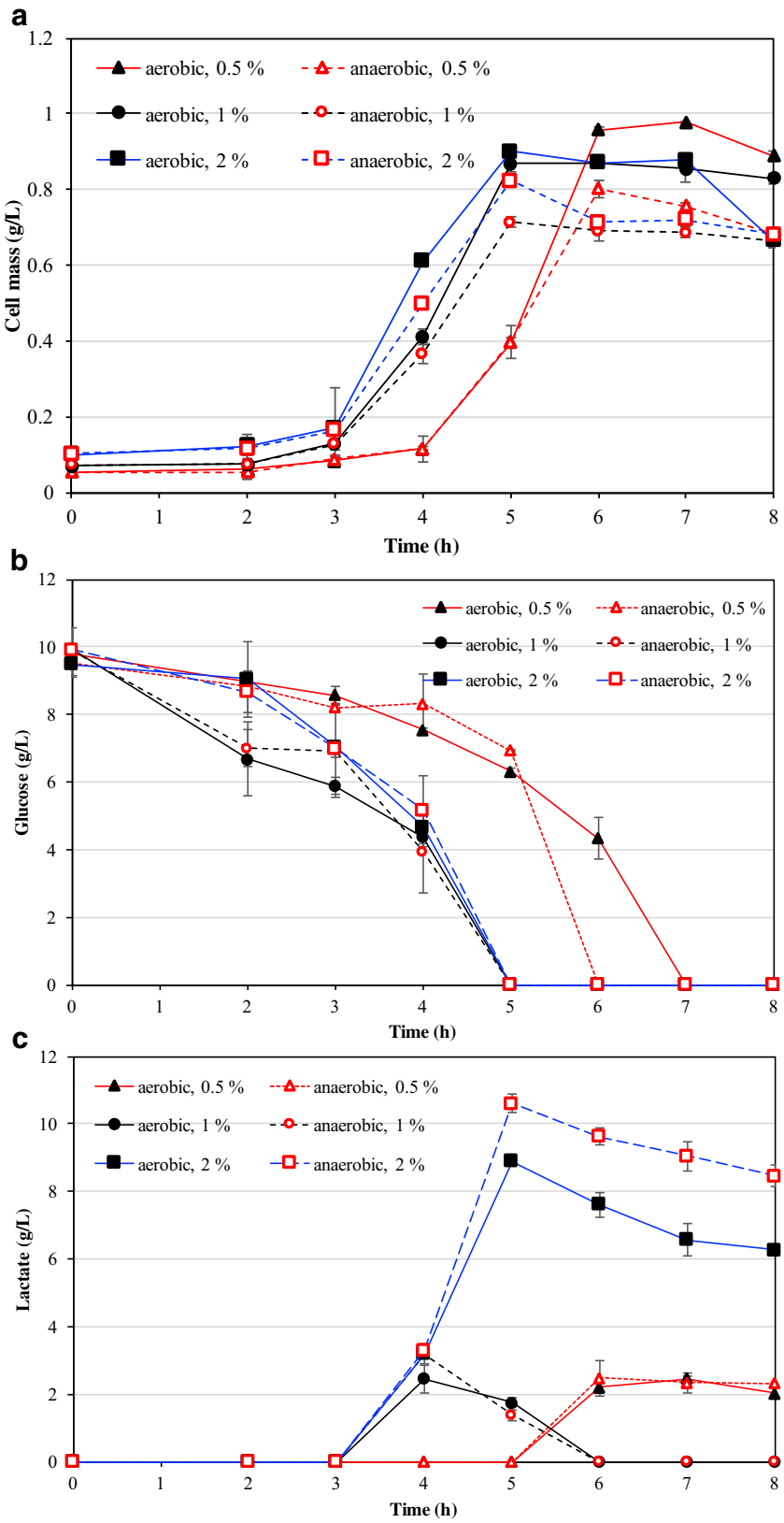

Fig. 3 Effect of inoculum size (0.5, 1, 2%) on the growth, glucose consumption, and lactate formation of isolate SK5-6 during the preculture stage in flask culture under aerobic and anaerobic conditions. The cultures were incubated at 37 °C, 200 rpm under either aerobic or anaerobic conditions. **a** Cell mass, **b** glucose concentration, **c** lactate concentration (color figure online)

consumed via the anaerobic fermentative pathway, resulting in increasing cell mass and increasing levels of lactate as the growth-associated product. The final cell mass obtained from the fermentation culture at 300 rpm (2.066 g/L) was almost fourfold higher than that in the culture at 200 rpm (0.564 g/L). This subsequently resulted in high lactate production in the

Table 3 D-lactate production during the fermentation stage in relation to preculture seed and cultivation conditions during the fermentation stage

Preculture seeds[a]	Fermentation conditions[b]	At 48 h			Fermentation performance		
		Cell mass (g/L)	Glucose (g/L)	Lactate (g/L)	Yield (g/g)	Productivity (g/L·h)	Optical purity (%ee)
Mid log (4 h) and aerobic conditions	No mixing, aerobic	1.445 ± 0.012	32.97 ± 3.31	67.54 ± 0.94	0.75 ± 0.04	1.41 ± 0.02	98.76 ± 1.40
	No mixing, anaerobic	1.798 ± 0.001	16.63 ± 0.92	85.46 ± 0.89	0.79 ± 0.03	1.78 ± 0.02	98.87 ± 0.35
	150 rpm, aerobic	0.450 ± 0.004[c]	17.05 ± 2.09	66.84 ± 2.22	0.62 ± 0.03	1.39 ± 0.05	98.22 ± 0.14
	150 rpm, anaerobic	1.475 ± 0.011	2.74 ± 3.88	102.22 ± 4.48	0.84 ± 0.00	2.13 ± 0.09	99.64 ± 0.07
Mid log (4 h) and anaerobic conditions	No mixing, aerobic	1.552± 0.001	14.57 ± 0.09	84.62 ± 3.26	0.78 ± 0.01	1.76 ± 0.07	98.68 ± 0.14
	No mixing, anaerobic	1.546 ± 0.004	22.55 ± 3.56	81.05 ± 1.21	0.81 ± 0.05	1.69 ± 0.03	98.69 ± 0.28
	150 rpm, aerobic	0.372 ± 0.004[d]	44.79 ± 3.74	35.43 ± 3.08	0.46 ± 0.06	0.74 ± 0.06	98.60 ± 0.35
	150 rpm, anaerobic	1.289 ± 0.003	0.00 ± 0.00	101.76 ± 5.81	0.82 ± 0.06	2.12 ± 0.12	99.63 ± 0.07
Late log (5 h) and aerobic conditions	No mixing, aerobic	1.609 ± 0.001	22.63 ± 1.51	71.98 ± 1.75	0.71 ± 0.04	1.50 ± 0.04	99.32 ± 0.14
	No mixing, anaerobic	1.756 ± 0.001	37.87 ± 1.17	71.88 ± 1.42	0.84 ± 0.01	1.50 ± 0.03	99.37 ± 0.21
	150 rpm, aerobic	0.663 ± 0.003[c]	94.60 ± 2.10	18.98 ± 2.22	0.69 ± 0.04	0.40 ± 0.05	98.85 ± 0.35
	150 rpm, anaerobic	1.356 ± 0.005	6.88 ± 0.44	99.22 ± 1.01	0.86 ± 0.01	2.07 ± 0.02	99.69 ± 0.28
Late log (5 h) and anaerobic conditions	No mixing, aerobic	1.463 ± 0.002	12.12 ± 0.64	69.90 ± 0.45	0.62 ± 0.01	1.46 ± 0.01	99.35 ± 0.14
	No mixing, anaerobic	1.498 ± 0.006	19.65 ± 0.49	79.67 ± 0.99	0.71 ± 0.03	1.66 ± 0.01	99.26 ± 0.07
	150 rpm, aerobic	0.759 ± 0.018[d]	92.43 ± 1.83	18.68 ± 0.33	0.61 ± 0.07	0.39 ± 0.01	99.80 ± 0.58
	150 rpm, anaerobic	1.262 ± 0.002	6.61 ± 0.48	101.02 ± 0.91	0.85 ± 0.02	2.10 ± 0.02	99.67 ± 0.25

Values in table are presented as the mean ± SD

[a] There was no significant difference at $P \leq 0.05$ in D-lactic acid production when preculture conditions were varied (age and oxygen) during fermentation carried out with 150 rpm (mixing) under anaerobic conditions

[b] Changing the fermentation conditions [mixing (no mixing/200 rpm) and oxygen (aerobic/anaerobic)] resulted in significant changes at $P \leq 0.05$ in cell growth, glucose consumption, and D-lactic acid production

[c] Cell mass during the aerobic fermentation at 150 rpm reached the maximum concentration at 24 h (data not shown), followed by a subsequent drop in cell mass, resulting in the low cell concentration

[d] Cell mass slowly increased because of the long lag phase when shifting from anaerobic preculture to aerobic fermentation

fermentation system at 300 rpm (final titer of 92.60 g/L, yield of 0.94, and productivity of 1.93 g/L·h). On the other hand, a low mixing rate (200 rpm) rather limited the bioconversion process; therefore, a lower glucose consumption rate resulted, with a large amount of residual glucose (58.49 g/L, only half was consumed during fermentation) and subsequently low lactate production (final titer of 46.05 g/L, with a yield of 0.71 and productivity of 0.96 g/L·h). From the fermentation profiles shown in Fig. 4, it should be noted that the pH was successfully maintained during the fermentation by adding $CaCO_3$ at the beginning of the fermentation stage. The results suggested that with sufficient mixing, the homogeneous system generated the proper heat and mass transport which in turn facilitated the bioconversion of glucose to D-lactate (Aguirre-Ezkauriatza et al. 2008; Ibrahim et al. 2010; Watanabe et al. 2012).

Mixing is another key parameter controlling the fermentation performance as it modifies both broth homogeneity and transport in the fermentation system. With sufficient mixing, glucose uptake rate was rapid, resulting in a large pool of pyruvate being converted to D-lactate by lactate dehydrogenase (Hou et al. 2000). Mixing is typically employed for gas distribution in the culture. It has been reported that the microaeration condition generated by sufficient mixing enhanced the cell growth of *Lactococcus lactis* MG1363 (Nordkvist et al. 2003; Neves et al. 2005). It has also been reported that combining mixing with aeration resulted in better growth of *L. lactis* than no mixing (Ishizaki and Ueda 1995; Pedersen et al. 2008). In typical lactate fermentation, a calcium base is used to control pH. Without adequate mixing, heterogeneity is generated in the culture broth due to $CaCO_3$ and cell sedimentation, eventually affecting the overall process kinetics (Qin et al. 2010; Ma et al. 2014).

A comparison of the preliminary fermentation optimization from the primary screening of the flask and fermenter culture revealed that under our preliminary optimized process conditions, the catalase-positive strain *T. laevilacticus* SK5-6 performed promisingly in terms of D-lactate production. We therefore considered this strain to be a novel industrial producer in addition to the typical catalase-negative *Sporalactobacillus* sp. (Table 4). We believe that further process optimization can provide greater improvement in the production performance of SK5-6 and the subsequent effective fermentation platform for large-scale production operations.

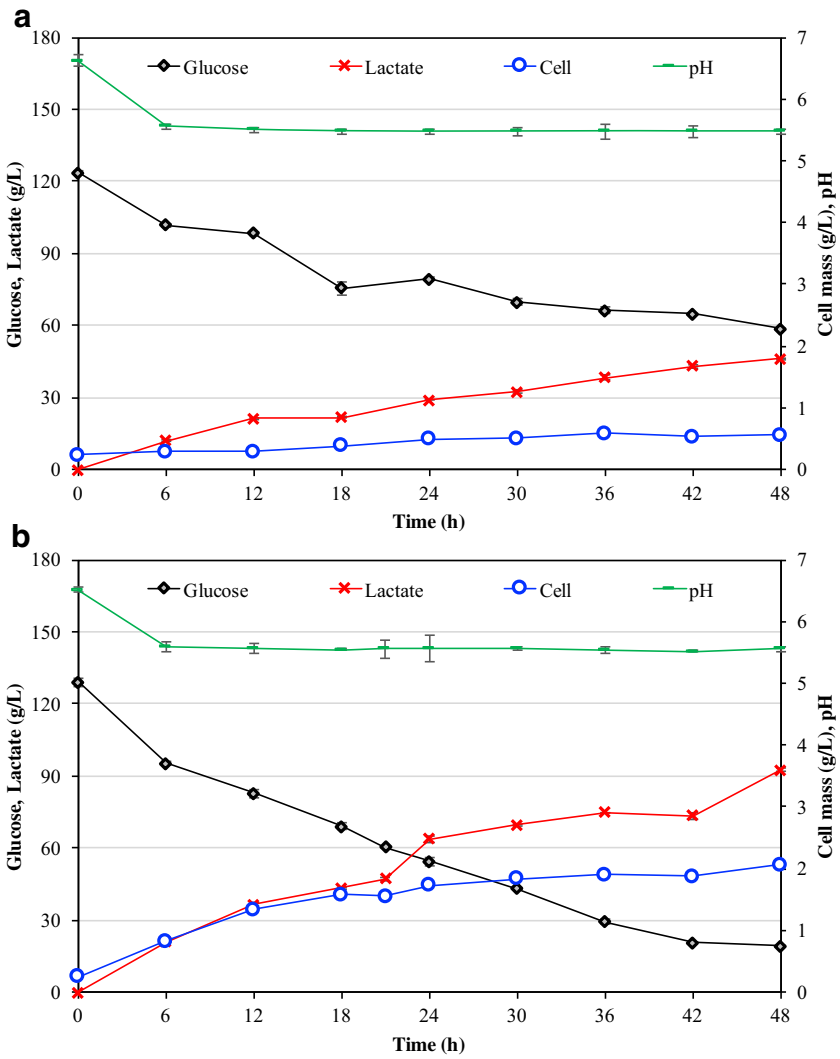

Fig. 4 Effect of mixing during the fermentation stage of isolate SK5-6 cultivated under anaerobic conditions in the 5-L stirred fermenter. **a** 200 rpm, **b** 300 rpm (color figure online)

Terrilactibacillus sp. as a promising industrial D-lactate producing isolate

The origin of the major D-lactate producers previously reported in the literature as well as those isolated in this study is shown in Table 5. It appears that D-lactate producers are distributed in limited sources and that their preferred environment is a rather acidic pH (Sanders et al. 2003). Currently, *Sporolactobacillus* sp. is known as the key producer of D-lactate in industrial fermentation processes. *Sporolactobacillus* sp. can be found in soil, tree bark, and fermented food and feed. Previous studies have reported the isolation of *Sporolactobacillus inulinus* from chicken feed and the isolation of *S. nakayamae* subsp. *nakayamae*, *S. nakayamae* subsp. *racemicus*, *S. lactosus*, *S. kofuensis*, and

Table 4 Preliminary optimization of fermentation conditions for D-lactate production by isolate SK5-6 resulted in improved fermentation performance.

Optimized conditions	Time (h)	Residual glucose (g/L)	Final lactate (g/L)	Optical purity (%ee)	Yield (g/g)	Productivity (g/L·h)
Flask culture						
Primary screening	72	9.74 ± 0.14	99.27 ± 0.71	99.00 ± 0.70	0.90 ± 0.00	1.38 ± 0.02
Flask culture						
Aerobic preculture, anaerobic fermentation	48	2.74 ± 3.88	102.22 ± 4.48	99.64 ± 0.07	0.84 ± 0.00	2.13 ± 0.09
Fermenter culture						
Aerobic preculture, anaerobic fermentation agitated at 300 rpm	48	19.20 ± 0.03	92.60 ± 0.65	99.56 ± 0.07	0.84 ± 0.00	1.93 ± 0.01

Values in table are presented as the mean ± SD where appropriate

Table 5 Origin of the major D-lactate producers reported in the literature and those isolated in this study

Sample origin	Microorganism	References
Chicken feed, soil, fermentation starter	*Sporolactobacillus inulinus* *S. nakayamae* subsp. *nakayamae*	Yanagida et al. 1997
	S. nakayamae subsp. *racemicus*	
	S. lactosus	
	S. kofuensis	
	S. terrae	
Vineyard soil	*S. vineae*	Chang et al. 2008
Spoiled orange juice	*S. putidas*	Fujita et al. 2010
Bark of *Spathodea campanulata* P. *Beauv.*	*S. spathodeae*	Thamacharoensuk et al. 2015
Bark of *Shorea talura* Roxb	*S. shoreae*	Thamacharoensuk et al. 2015
Bark of *Lagerstroemia floribunda* Jack ex Blume.	*S. terrae* CU68-2	Prasirtsak et al. 2013
Bark of *Samanea saman*	*S. nakayamae* subsp. *nakayamae* SP43-2	This study
Bark of *Musa sapientum* Linn.	*S. laevolacticus* NK44-2	This study
Bark of *Sterculia foetida* L.	*S. laevolacticus* BRY67-1	This study
Bark of *Sterculia foetida* L.	*S. laevolacticus* BRY67-2	This study
Bark of *Sterculia foetida* L.	*S. laevolacticus* BRY67-3	This study
Soil	*Terrilactibacillus laevilacticus* NK26-11^T	Prasirtsak et al. 2016
Soil	*T. laevilacticus* SK5-6	This study

S. terrae from soil samples and fermentation starters (Yanagida et al. 1997). *Sporolactobacillus vineae* and *S. putidas* were found in vineyard soil in Korea and in spoiled orange juice, respectively (Chang et al. 2008; Fujita et al. 2010). *Sporolactobacillus* sp. is a Gram-positive, facultatively anaerobic, motile, and endospore-forming microbe. This genus lacks the activities of oxidase and catalase. In addition, it cannot reduce nitrate. The members of this bacterial genus produce D-lactate from glucose and other carbon substrates depending on the specific characteristics of the type strains belonging to this genus (Yanagida et al. 1997; Fujita et al. 2010). Cultivation of *Sporolactobacillus* is restricted under anaerobic conditions when the oxygen is limited because of the lack of catalase activity and a cytochrome system (Holzapfel and Botha 1988; Watanabe et al. 2012), which results in low ATP generation and a subsequently low metabolic rate compared to aerobic culture.

Respiratory metabolism results in the conversion of glucose into ATP via glycolysis, the TCA, and oxidative phosphorylation. The ATP is generated in this metabolic process because of the activity of the electron transport system. As the electrons are passed down through the ETC, each molecule in the chain alternates between its reduced and oxidative forms. Cytochrome oxidase, which appears at the end of the chain, catalyzes the oxidation of the last cytochrome molecule by molecular oxygen. This final process results in the reduction of the molecular oxygen to water. The incomplete reduction of oxygen often leads to the production of H_2O_2 or the superoxide free radical (O_2^-), both of which are toxic to the cell. Many aerobic or facultatively anaerobic cells produce the enzymes catalase and superdismutase that remove these toxic compounds, respectively, while strict anaerobes usually lack these enzymes and are therefore restricted to an oxygen-free environment (Hassan and Fridovich 1977; Pedersen et al. 2008).

Based on its biochemical characterization, our novel *Terrilactibacillus* isolate exhibits catalase activity, thus confirming that the bacteria in this genus can survive in the presence of oxygen—unlike species of the genus *Sporolactobacillus*. Since bacteria belonging to the genus *Terrilactibacillus* possess catalase activity, they generate more ATP and grow rapidly in the presence of oxygen, which subsequently results in a high cell mass concentration and lactate productivity (Watanabe et al. 2012; Prasirtsak et al. 2016).

It should be noted that *Terrilactibacillus* sp. is also a Gram-positive and endospore-forming D-lactate producing microbe; therefore, it can survive exposure to harsh conditions, such as low pH (Sanders et al. 2003). As seen in Table 1, *Terrilactibacillus* sp. consumed a wide range of carbon sugars, especially glycerol, for D-lactate production, while *Sporolactobacillus* sp. demonstrated a limited ability to convert several sugars. The ability of *Terrilactibacillus* sp. to metabolize glycerol is a consequence of the catalase activity possessed by these bacteria. Hassan and Fridovich (1977) claimed that oxygen is involved in the consumption of polyhydroxy alcohols by some lactate producers as in their study 1 mole of oxygen was required to convert 1 mole of glycerol substrate into 1 mole of lactate and 1 mole of H_2O_2.

Table 6 D-lactate production by the potential strains reported in the literature and in this study

Strain	Operation	pH control	Lactate (g/L)	Yield (g/g)	Productivity (g/L·h)	Optical purity (%ee)	References
Sporolactobacillus sp. CASD	Batch	$CaCO_3$	80–90	0.86–0.97	1.77	-	Zhao et al. 2010
Sporolactobacillus sp. CASD	Fed-batch	$CaCO_3$	207	0.93	3.80	99.3	Wang et al. 2011
S. laevolacticus JCM2513	Continuous	$Ca(OH)_2$	67.3	0.98	11.20	-	Mimitsuka et al. 2012
Sporolactobacillus sp. Y2-8	Batch	$CaCO_3$	122	0.81	1.00	99.1	Zheng et al. 2012
S. laevolacticus DSM442	Fed-batch	$CaCO_3$	144.2	0.96	4.13	99.3	Li et al. 2013
Lactobacillus coryniformis	Flask	NH_4OH	186.4	0.85	3.11	-	Nguyen et al. 2013
Klebsiella pneumoniae ATCC25955	Fed-batch	NH_4OH	142.1	0.82	2.96	100	Feng et al. 2014
Escherichia coli HBUT-D	Pilot scale	$Ca(OH)_2$	127	0.93	6.35	99.5	Liu et al. 2014
Sporolactobacillus inulinus Y2-8	Fed-batch	NH_4OH	218.8	-	1.65	>99.0	Zhao et al. 2014
Sporolactobacillus sp. Y2-8	Batch	$CaCO_3$	125.0	-	1.39	99	Sun et al. 2015
S. inulinus NBRC13595	Batch	$CaCO_3$	189.0	0.94	5.25	>98	Tadi et al. 2017
S. inulinus YBS1-5	Fed-batch	$CaCO_3$	107.2	0.85	1.19	99.2	Bai et al. 2016
Terrilactibacillus laevilacticus SK5-6	Flask	$CaCO_3$	102.2	0.84	2.13	99.6	This study
T. laevilacticus SK5-6	Batch	$CaCO_3$	96.6	0.84	1.93	99.6	This study

Based on the taxonomical and biochemical characteristics mentioned here, we conclude that our novel *Terrilactibacillus* sp. shows a promising performance as an industrial D-lactate-producing strain.

Establishing a D-lactate fermentation platform by *Terrilactibacillus* sp.

Understanding the metabolic behavior of the microbe is mandatory in fermentation process optimization to achieve the targeted production performance. In this study, we have identified the key parameters that controlled the growth and synthesis of metabolites during the cultivation of SK5-6 and successfully introduced a two-phase fermentation process for cultivating SK5-6 under aerobic conditions and fermenting homo D-lactate under anaerobic conditions. The major advantage of this two-phase fermentation procedure is that the high cell density obtained during the preculture stage accelerates the anaerobic conversion of glucose to lactate during the fermentation stage. However, previous studies have reported drawbacks of this process when the process condition is switched from an aerobic to an anaerobic environment (Qin et al. 2010; Ma et al. 2014). It has been observed that byproducts often appear as the metabolic pathway shifts from aerobic respiration to the mixed acid fermentation, when a high glucose concentration is present, with the remaining oxygen available at the initial stage of the fermentation. Expelling the remaining oxygen from the preculture stage by flushing the fermenter with inert gas to obtain a strictly anaerobic condition is considered to be cumbersome. Nevertheless, we did not observe this phenomenon in the two-phase fermentation process with SK5-6 for D-lactate production, which strongly indicates the robustness of SK5-6 as a suitable industrial-scale D-lactate producer.

Comparing D-lactate production performance by *Terrilactibacillus* sp. with other species

D-Lactate production has been reported in a number of bacteria, including *Sporolactobacillus inulinus*, *S. laevolacticus*, *Lactobacillus delbrueckii*, and *Leuconostoc* sp. Among these genera, *Sporolactobacillus* sp. has been claimed to be the promising candidate for industrial fermentation. Tashiro et al. (2011) reported that fermentation by wild-type strains, such as thermotolerant *L. delbrueckii* subsp. *lactis* QU41, yielded 87.4 g/L D-lactate with a high optical purity of 99.9%ee using MRS medium containing 100 g/L glucose. Mimitsuka et al. (2012) conducted batch fermentation with *S. laevolacticus* JCM2513 and reported a final titer of D-lactate of 55.7 g/L, with a yield of 0.89 g/g and productivity of 0.25 g/L·h.

Comparison of the production performance of D-lactate to that obtained from the well-established L-lactate production process revealed that the final titer along with yield and productivity were still relatively low using D-lactate, thus making the former process economically uncompetitive. Li et al. (2013) claimed that the poor efficiency of D-lactate fermentation was the result of inhibition due to high substrate concentration. In batch fermentation by *S. laevolacticus* DSM442 using a high initial glucose concentration (>100 g/L)

supplemented with cottonseed as the nitrogen source, these authors found that lactic acid production was inhibited. Improved fermentation efficiency was obtained by a fed-batch process, with an increasing final titer of 144.4 g/L, yield of 0.96 g/g, productivity of 4.13 g/L·h, and optical purity of 99.3%ee (Li et al. 2013). D-lactate production by *S. inulinus* Y2-8 in batch fermentation in a fibrous bed bioreactor using corn flour hydrolysate was reported by Zhao et al. (2014). In that process, a high yield of 0.98 g/g, with a productivity of 1.62 g/L·h and optical purity of 99.0%ee was obtained. In another study, Bai et al. (2016) used fed-batch D-lactate fermentation by *S. inulinus* YBS1-5 with simultaneous utilization of cottonseed meal and corncob residue to produce a high D-lactate concentration (107.2 g/L), high productivity (1.19 g/L.h), and high yield (0.85 g/g). These authors also reported an optical purity of D-lactate of 99.2%ee.

As seen in Table 6, wild strains, such as *Sporolactobacillus* sp. and *Lactobacillus* sp., have been found to exhibit slightly low productivity in batch and fed-batch processes (de Franca et al. 2009). Improved production performance was obtained during continuous culture incorporated with the separation system (Koutinas et al. 2014). For example, by incorporating an electrodialysis membrane unit with the fermentation system, an improved productivity of 8 g/L·h was obtained (Mintian et al. 2005). Improved productivity has also been obtained in metabolically engineered strains of *Escherichia coli* and *Klebsiella pneumoniae* (Feng et al. 2014; Tsuge et al. 2014; Baek et al. 2016). Nevertheless, the engineered strains are usually of limited use, especially in large-scale operations, due to biosafety regulations, need for large investment in production facilities, and genetic instability of the strains. As a result, wild strains are still preferable. Comparing the production performance of SK5-6 to that of the other D-lactate producers, as reported in Table 6, we suggest that with further process optimization and fermentation platform development, SK5-6 can become a promising industrial strain for D-lactate fermentation.

Conclusion

In this study, D-lactate producers were isolated from natural samples collected in Thailand. Among the six isolates which produced D-lactate, *T. laevilacticus* SK5-6 showed the best characteristics in comparison to other D-lactate producers previously reported in the literature. Strain SK5-6 demonstrated the ability to utilize several carbon substrates for D-lactate production. The optical purity of D-lactate was sufficiently high for polymer-grade specification (>99.5%ee). Unlike *Sporolactobacillus* sp., the most common D-lactate-producing strain, SK5-6 produced catalase; thus, oxygen was not restricted during the cultivation. Using a simple two-phase fermentation process, we introduced an aerobic preculture to generate robust, high-cell-density cell mass of SK5-6 for D-lactate production during the anaerobic fermentation stage without byproducts. This resulted in high yield and high productivity. The results of this research therefore confirm the potential of using *Terrilactibacillus* sp. as a D-lactate producer.

Acknowledgements Financial supports from the Grant for International Research Integration: Research Pyramid, Ratchadapiseksomphot Endowment Fund (GCURP_58_01_33_01) and Thailand Research Fund via the Distinguished Research Professor Grant (DPG5880003) are gratefully acknowledged. Research facility support through the Chulalongkorn Academic Advancement into its 2nd Century Project (CUAASC) is also appreciated.

Compliance with ethical standards

Conflict of interest The authors declare no conflict of interest.

Ethical approval This article does not contain any studies with human participants or animals performed by any of the authors.

References

Aguirre-Ezkauriatza EJ, Galarza-Gonzalez MG, Uribe-Bujanda AI, Rios-Licea M, Lopez-Pacheco F, Hernandez-Brenes CM, Alvarez MM (2008) Effect of mixing during fermentation in yoghurt manufacturing. J Dairy Sci 91:4454–4465

Baek SH, Kwon EY, Kim YH, Hahn JS (2016) Metabolic engineering and adaptive evolution for efficient production of D-lactic acid in *Saccharomyces cerevisiae*. Appl Microbiol Biotechnol 100:2737–2748

Bai Z, Gao Z, Sun J, Wu B, He B (2016) D-lactic acid production by *Sporolactobacillus inulinus* YBS1-5 with simultaneous utilization of cottonseed meal and corncob residue. Bioresour Technol 207: 346–352

Chang YH, Jung MY, Park IS, Oh HM (2008) *Sporolactobacillus vineae* sp. nov., a spore-forming lactic acid bacterium isolated from vineyard soil. Int J Syst Evol Microbiol 58:2316–2320

Egervarn M, Lindmark H, Roos S, Huys G, Lindgren S (2007) Effects of inoculum size and incubation time on broth microdilution susceptibility testing of lactic acid bacteria. Antimicrob Agent Chemother 51:394–396

Felsenstein J (1981) Evolutionary trees from DNA sequences: a maximum likelihood approach. J Mol Evol 1:368–376

Felsenstein J (1985) Confidence limits on phylogenies: an approach using the bootstrap. Evolution 39:783–791

Feng X, Ding Y, Xian M, Xu X, Zhang R, Zhao G (2014) Production of optically pure D-lactate from glycerol by engineered *Klebsiella pneumoniae* strain. Bioresour Technol 172:269–275

de Franca FP, de Jesus AM, Oliveira FJS (2009) Enhancement of lactic acid fermentation by *Lactobacillus delbrueckii* ATCC6949 using sugarcane molasses. Can J Pure Appl Sci 3:773–778

Fujita R, Mochida K, Kata M, Goto K (2010) *Sporolactobacillus putidus* sp. nov., an endospore-forming lactic acid bacterium isolated from spoiled orange juice. Int J Syst Evol Microbiol 60:1499–1503

Hassan HM, Fridovich I (1977) Physiological function of superoxidase dismutase in glucose-limited chemostat cultures of *Escherichia coli*. J Bacteriol 130:805–811

Hatayama K, Shoun H, Ueda Y, Nakamura A (2006) *Tuberibacillus calidus* gen. nov., sp. nov., isolated from a compost pile and reclassification of *Bacillus naganoensis* Tomimura *et al.* 1990 as

Pullulanibacillus naganoensis gen. nov., comb. nov. and *Bacillus laevolacticus* Andersch *et al.* 1994 as *Sporolactobacillus laevolacticus* comb. nov. Int J Syst Evol Microbiol 56:2545–2551

Holzapfel WH, Botha SJ (1988) Physiology of *Sporolactobacillus* strains isolated from different habitats and the indication of in vitro antagonism against *Bacillus* species. Int J Food Microbiol 7:161–168

Hou R, Chen Z, Yi X, Bi-An J, Xu G (2000) Catalytic reaction mechanism of L-lactate dehydrogenase: an ab initio study. Sci China Ser B Chem 43:587–599

Ibrahim SB, Rahman NAA, Mohamad R, Rahim RA (2010) Effects of agitation speed, temperature, carbon and nitrogen sources on the growth of recombinant *Lactococcus lactis* NZ9000 carrying domain 1 of aerolysin gene. Afr J Biotechnol 9:5392–5398

Ishizaki A, Ueda T (1995) Growth kinetics and product inhibition of *Lactococcus lactis* IO-1 culture in xylose medium. J Ferment Bioeng 80:287–290

John RP, Anisha GS, Nampoothiri KM, Pandey A (2009) Direct lactic acid fermentation: focus on simultaneous saccharification and lactic acid production. Biotechnol Adv 27:145–152

Kim OS, Cho YJ, Lee K, Yoon SH, Kim M, Na H, Park SC, Jeon YS, Lee H, Yi H, Won S, Chun J (2012) Introducing EzTaxon-e: a prokaryotic 16S rRNA gene sequence database with phylotypes that represent uncultured species. Int J Syst Evol Microbiol 62:716–721

Koutinas AA, Vlysidis A, Pleissner D, Kopsahelis N, Garcia IL, Kookos IK, Papanikolaou S, Kwan TH, Lin CSK (2014) Valorization of industrial waste and byproduct streams via fermentation for the production of hemicals and biopolymers. Chem Soc Rev 43:2587–2627

Li Y, Wang L, Ju J, Yu B, Ma Y (2013) Efficient production of polymer-grade D-lactate by *Sporolactobacillus laevolacticus* DSM442 with agricultural waste cottonseed as the sole nitrogen source. Bioresour Technol 142:186–191

Liu Y, Gao W, Zhao X, Wang J, Garza E, Manow R, Zhou S (2014) Pilot scale demonstration of D-lactic acid fermentation facilitated by $Ca(OH)_2$ using a metabolically engineered *Escherichia coli*. Bioresour Technol 169:559–565

Ma KD, Maeda T, You HY, Shirai Y (2014) Open fermentative production of L-lactic acid with high optical purity by thermophilic *Bacillus coagulans* using excess sludge as nutrient. Bioresour Technol 151: 28–35

Mimitsuka T, Na K, Morita K, Sawai H, Minegishi S, Henmi M, Yamada K, Shimizu S, Yonehara T (2012) A membrane-integrated fermentation reactor system: its effects in reducing the amount of sub-raw materials for D-lactic acid continuous fermentation by *Sporolactobacillus laevolacticus*. Biosci Biotechnol Biochem 76: 67–72

Min-tian G, Koide M, Gotou R, Takanashi H, Hirata M, Hano T (2005) Development of a continuous electrodialysis fermentation system for production of lactic acid by *Lactobacillus rhamnosus*. Process Biochem 40:1033–1036

Neves AR, Pool WA, Kok J, Kuipers OP, Santos H (2005) Overview on sugar metabolism and its control in *Lactococcus lactis*—the input from in vivo NMR. FEMS Microbiol Rev 29:531–554

Nguyen CM, Choi GJ, Choi YH, Jang KS, Kim JC (2013) D- and L-lactic acid production from fresh sweet potato through simultaneous saccharification and fermentation. Biochem Eng J 81:40–46

Nordkvist M, Jensen NBS, Villadsen J (2003) Glucose metabolism in LACTOCOCCUS LACTIS MG1363 under different aeration conditions: requirement of acetate to sustain growth under microaerobic conditions. Appl Environ Microbiol 69:3462–3468

Panesar PS, Kennedy JF, Knill CJ, Kosseva M (2010) Production of L(+) lactic acid using *Lactobacillus casei* from whey. Braz Arch Biol Technol 53:219–226

Pedersen MB, Garrigues C, Tuphile K, Brun C, Vido K, Bennedsen M, Mollgaard H, Gaudu P, Gruss A (2008) Impact of aeration and heme-activated respiration on *Lactococcus lactis* gene expression: identification of a heme-responsive operon. J Bacteriol 19:4903–4911

Prasirtsak B, Tanasupawat S, Boonsombat R, Kodama K, Thongchul N (2013) Characterization of lactic acid producing bacteria from Thai sources. J Appl Pharm Sci 3:33–38

Prasirtsak B, Thongchul N, Tolieng V, Tanasupawat S (2016) *Terrilactibacillus laevilacticus* gen. nov., sp. nov., isolated from soil. Int J Syst Evol Microbiol 66:1311–1316

Qin JY, Wang XW, Zheng ZJ, Ma CQ, Tang HZ, Xu P (2010) Production of L-lactic acid by a thermophilic *Bacillus* mutant using sodium hydroxide as neutralizing agent. Bioresour Technol 101:7570–7576

Saito H, Miura KI (1963) Preparation of transforming deoxyribonucleic acid by phenol treatment. Biochim Biophys Acta 72:619–629

Saitou N, Nei M (1987) The neighbor-joining method: a new method for reconstructing phylogenetic trees. Mol Biol Evol 4:406–425

Sanders ME, Morelli L, Tompkins TA (2003) Sporeformers as human probiotics: *Bacillus*, *Sporolactobacillus*, and *Brevibacillus*. Compr Rev Food Sci Food Saf 2:101–110

Sun J, Wang Y, Wu B, Bai Z, He B (2015) Enhanced production of D-lactic acid by *Sporolactobacillus* sp. Y2-8 mutant generated by atmospheric and room temperature plasma. Biotechnol Appl Biochem 62:287–292

Tadi SRR, Arun EVR, Limaye AM, Sivaprakasam S (2017) Enhanced production of optically pure D(-) lactic acid from nutritionally rich *Borassus flabellifer* sugar and whey protein hydrolysate based-fermentation medium. Biotechnol Appl Biochem 64:279–289

Tamura K, Stecher G, Peterson D, Filipski A, Kumar S (2013) MEGA6: molecular evolutionary genetics analysis version 6.0. Mol Biol Evol 30:2725–2729

Tanasupawat S, Ezaki T, Suzuki KI, Okada S, Komagata K, Kozaki M (1992) Characterization and identification of *Lactobacillus pentosus* and *Lactobacillus plantarum* strains from fermented foods in Thailand. J Gen Appl Microbiol 38:121–134

Tanasupawat S, Okada S, Komagata K (1998) Lactic acid bacteria found in fermented fish in Thailand. J Gen Appl Microbiol 4:193–200

Tanasupawat S, Thawai C, Yukphan P, Moonmangmee D, Itoh T, Adachi O, Yamada Y (2004) *Gluconobacter thailandicus* sp. nov., an acetic acid bacterium in the α-*Proteobacteria*. J Gen Appl Microbiol 50: 159–167

Tashiro Y, Kaneko W, Sun Y, Shibata K, Inokuma K, Zendo T, Sonomoto K (2011) Continuous D-lactic acid production by a novel thermotolerant *Lactobacillus delbrueckii* subsp. *lactis* QU 41. Appl Microbiol Biotechnol 89:1741–1750

Thamacharoensuk T, Kitahara M, Ohkuma M, Thongchul N, Tanasupawat S (2015) *Sporolactobacillus shoreae* sp. nov. and *Sporolactobacillus spathodeae* sp. nov., two spore-forming lactic acid bacteria isolated from tree barks in Thailand. Int J Syst Evol Microbiol 65:1220–1226

Tsuge Y, Kawaguchi H, Sasaki K, Tanaka T, Kondo A (2014) Two-step production of D-lactate from mixed sugars by growing and resting cells of metabolically engineered *Lactobacillus plantarum*. Appl Microbiol Biotechnol 98:4911–4918

Wang L, Zhao B, Li F, Xu K, Ma C, Tao F, Li Q, Xu P (2011) Highly efficient production of D-lactate by *Sporolactobacillus* sp. CASD with simultaneous enzymatic hydrolysis of peanut meal. Appl Microbiol Biotechnol 89:1009–1017

Watanabe M, van der Veen S, Nakajima H, Abee T (2012) Effect of respiration and manganese on oxidative stress resistance of *Lactobacillus plantarum* WCFS1. Microbiology 158:293–300

Wee YJ, Kim JN, Ryu HW (2006) Biotechnological production of lactic acid and its recent applications. Food Technol Biotech 44:163–172

Xu TT, Bai ZZ, Wang LJ, He BF (2010) Breeding of D(-)-lactic acid high producing strain by low-energy ion implantation and preliminary analysis of related metabolism. Appl Biochem Biotechnol 160: 314–321

Yanagida F, Suzuki KI, Kozaki M, Komagata K (1997) Proposal of *Sporolactobacillus nakayamae* subsp. *nakayamae* sp. nov., subsp. nov., *Sporolactobacillus nakayamae* subsp. *racemicus* subsp. nov.,

Sporolactobacillus terrae sp. nov., *Sporolactobacillus kofuensis* sp. nov., and *Sporolactobacillus lactosus* sp. nov. Int J Syst Bacteriol 47:499–504

Zagari F, Jordan M, Stettler M, Broly H, Wurn FM (2013) Lactate metabolism shift in CHO cell culture: the role of mitochondrial oxidative activity. New Biotech 30:238–245

Zhao B, Wang L, Li F, Hua D, Ma C, Ma Y, Xu P (2010) Kinetics of D-lactic acid production by *Sporolactobacillus* sp. strain CASD using repeated batch fermentation. Bioresour Technol 101:6499–6505

Zhao T, Liu D, Ren H, Shi X, Zhao N, Chen Y, Ying H (2014) D-lactic acid production by *Sporolactobacillus inulinus* Y2-8 immobilized in fibrous bed bioreactor using corn flour hydrolyzate. J Microbiol. Biotechnol 24:1664–1672

Zheng L, Bai Z, Xu T, He B (2012) Glucokinase contributes to glucose phosphorylation in D-lactic acid production by *Sporolactobacillus inulinus* Y2-8. J Ind Microbiol Biotechnol 39:1685–1692

Bioprocess Biosyst Eng (2017) 40:1787–1799
DOI 10.1007/s00449-017-1833-8

RESEARCH PAPER

A homofermentative *Bacillus* sp. BC-001 and its performance as a potential L-lactate industrial strain

Sitanan Thitiprasert[1] · Kentaro Kodama[1] · Somboon Tanasupawat[2] · Phatthanon Prasitchoke[3] · Tanapawarin Rampai[4] · Budsabathip Prasirtsak[4] · Vasana Tolieng[1] · Jiraporn Piluk[1] · Suttichai Assabumrungrat[5] · Nuttha Thongchul[1]

Received: 15 May 2017 / Accepted: 16 August 2017 / Published online: 22 August 2017
© Springer-Verlag GmbH Germany 2017

Abstract *Bacillus* sp. BC-001 was first reported as a potent thermotolerant and homofermentative strain for an industrial-scale L-lactate production. In a flask culture, this isolate fermented both glucose and sucrose to lactate with high yield (0.96 and 0.87 g/g) and productivity (2.8 and 2.6 g/L h), respectively. The higher lactate production performance was obtained in the simultaneous saccharification and fermentation of liquefied starch (150.1 g/L final titer, 0.98 g/g yield, 3.2 g/L h productivity) and the fed-batch glucose fermentation (139.9 g/L final titer, 0.96 g/g yield, 2.9 g/L h productivity). Significant increase in lactate productivity (5.5–6.1 g/L h) was obtained from the high/heavy-inoculum seed in the stirred tank fermentor. Both calcium bases and monovalent bases were successfully employed for pH control during lactate fermentation by this isolate resulting in a versatile and simple operation. By the two-phase fermentation using the high/heavy-inoculum seed of BC-001, the fermentation reproducibility was acquired toward the pilot-scale fermentors.

✉ Nuttha Thongchul
Nuttha.T@chula.ac.th

[1] Institute of Biotechnology and Genetic Engineering, Chulalongkorn University, Institute Building 3, Phayathai Road, Wangmai, Pathumwan, Bangkok 10330, Thailand

[2] Department of Biochemistry and Microbiology, Faculty of Pharmaceutical Sciences, Chulalongkorn University, Bangkok, Thailand

[3] Science and Innovation, PTT Global Chemical Public Company Limited, Rayong, Thailand

[4] Program in Biotechnology, Faculty of Science, Chulalongkorn University, Bangkok, Thailand

[5] Department of Chemical Engineering, Faculty of Engineering, Chulalongkorn University, Bangkok, Thailand

Keywords *Bacillus* sp. BC-001 · Lactic acid · Heavy-inoculum seed · Fermentation scale-up

Introduction

In addition to the existing applications in food, pharmaceutical, and chemical industries, lactic acid is used as the building block in polymerization to a compostable plastic (polylactic acid) [1, 2]. The demand of lactic acid in food and pharmaceutical applications is comparatively low when it is used as product supplement. On the other hand, the mass production of lactic acid at low cost is necessary that the sale price of polylactic acid can be competitive with the commercially available petroleum-based plastics. Moreover, the high optical purity of lactic acid product is essential in the polymerization process. Therefore, seeking the microbe that yields both high product titer and optical purity is mandatory.

Rhizopus sp., *Lactobacillus* sp., and several genetically modified microbes have been proven for the ability to produce lactic acid with the sufficiently high yield, productivity, and optical purity [1–6]. Using the low-cost feedstocks is usually employed for the production cost reduction. Lactate fermentation from cellulosic materials, agro-industrial residues, and household wastes by the genetically modified microbes has been widely reported [7–14]. Besides, the thermotolerant bacteria have been introduced as the industrial strains to produce lactic acid via the simultaneous saccharification and fermentation (SSF) process to lower the overall process cost [15–17]. Among those microbes, *Bacillus coagulans* has been proven for its ability to ferment both pentoses and hexoses via the homolactic acid fermentative pathway at a high temperature to reduce the production cost [12, 13, 18–20].

Nonetheless, lactate fermentation by *B. coagulans* rather experienced low productivity during the anaerobic fermentation. The productivity could be increased in the fermentation in the presence of oxygen but this would result in a low lactate yield along with the presence of byproducts such as acetate, acetoin, and 2,3-butanediol [21].

Lactic acid production by the conventional lime process generally experiences the high sulfuric acid consumption and the handling of the solid gypsum byproduct. Approximately one ton of crude gypsum is produced for a ton of lactic acid product in the conventional production plants. The disposal of gypsum byproduct generates considerable economic and ecological problems in a large-scale operation [22]. Lactic acid recovery by the membrane separation processes, such as microfiltration, ultrafiltration, and electrodialysis, is a promising alternative to the lime process because the solid salt residues discharged from acidification can be avoided. Nonetheless, the major drawback of the membrane process is the presence of multivalent cations such as calcium and magnesium that are unfavorable since they form insoluble hydroxides at the interface where ion separation occurs. Therefore, this is considered as the major drawback in the calcium base process for lactic acid fermentation. On the other hand, several studies have reported the success in controlling the pH in lactic acid fermentation by NH_4OH but it should be noted that the ammonium handling in the large-scale operation must be conducted with caution due to a high evaporation rate and health risks [4, 23–25]. More stable bases such as NaOH and KOH are preferable but only a few reports are available on bacterial lactic acid fermentation using these two bases since both sodium and potassium ions typically generate bacterial stress resulting in a slow growth and a low lactate productivity [22].

In this study, the novel homofermentative *Bacillus* sp. BC-001 was isolated and first time reported for its performance to produce an optically pure L-lactic acid at a remarkably high production rate, without any byproducts, from different carbon substrates including glucose, sucrose, and hydrolyzed starch derived from sugarcane- and cassava-based feedstocks. The high/heavy-inoculum seed developed during the aerobic preculture stage enhanced lactate production rate and yield during the anaerobic fermentation. Unlike the typical lime process previously reported in the fermentation of other lactate producers, the pH during lactate fermentation by *Bacillus* sp. BC-001 could be simply controlled by the alkaline solutions including NH_4OH, NaOH, and KOH while the high lactate production rate and yield were still acquired. The optimized production platform determined in the small-scale fermentations has been successfully reproducible in the pilot-scale operation in the 30, 300, and 3000 L fermentors. From the findings reported in this study, we can claim that the novel *Bacillus* sp. BC-001 can be considered as the potent industrial lactate-producing strain.

Materials and methods

Bacterial isolate and stock maintenance

All experiments in this study were performed with an in-house isolate, *Bacillus* sp. BC-001, screened by Dr. Kentaro Kodama. This isolate is deposited as the patented strain at the NITE Patent Microorganisms Depository as NITE BP-01943 for its industrial purpose.

Bacillus sp. BC-001 was isolated from the soil samples in Thailand and primarily identified by the analytical profile index system using biochemical API test kits (bioMerieux SA, France) according to the manufacturer's instruction. The DNA was isolated from the cells grown in the glucose–yeast extract–peptone (GYP) culture medium after incubation for 2 days, and was purified by the method described by Saito and Miura [26]. The DNA base comparison was determined from the analysis of the DNA contents of the samples by the reversed-phase high-performance liquid chromatography [27]. The DNA was hydrolyzed with nuclease P1 and bacterial alkaline phosphatase into nucleosides. The mixture of nucleosides (2 μg) was injected into the high-performance liquid chromatography (HPLC) system without prior purification. This method gave the relative standard errors of nucleoside analysis less than 1%. The 16S rRNA gene of the isolate was amplified and the PCR product was purified and sequenced as previously described by Tanasupawat et al. [28]. The sequence of the isolate was aligned with the selected sequences obtained from GenBank using CLUSTAL_X version 1.81. The alignment was manually edited to remove the gaps and the ambiguous nucleotides before the construction of a phylogenetic tree by the neighbor-joining method using MEGA program (version 5.05) [29]. The confidence values of the individual branches in the phylogenetic tree were determined by the bootstrap analysis of Felsenstein [30] based on 1000 replications. The values for the sequence similarity among the closest strains were determined by the EzTaxon server [31].

The data of the 16S rRNA gene sequence of *Bacillus* sp. BC-001 have been deposited at the DNA DataBank of Japan (DDBJ) and the accession number is LC223101.

The stock culture of *Bacillus* sp. BC-001 was maintained in the skim milk at −80 °C. The active culture was transferred onto the fresh new GYP agar slant every 10 days.

Medium and inoculum preparation

The GYP agar medium contained (per liter) 10 g of glucose, 5 g of yeast extract, 5 g of peptone, 0.25 g of KH_2PO_4, 0.25 g of K_2HPO_4, 20 g of agar, 5 g of $CaCO_3$, and 10 mL of salt solution. The pH of the GYP agar medium was adjusted to 6.80. The compositions of the salt solution consisted of (per 10 mL) 400 mg of $MgSO_4 \cdot 7H_2O$, 20 mg of $MnSO_4 \cdot 5H_2O$, 20 mg of $FeSO_4 \cdot 7H_2O$, and 20 mg of NaCl. The preculture medium contained (per liter) 10 g of glucose, 15 g of yeast extract, 4 g of NH_4Cl, 0.5 g of KH_2PO_4, 0.5 g of K_2HPO_4, 5 g of $CaCO_3$, and 20 mL of salt solution. The pH of the preculture medium was initially adjusted to 6.80. The compositions of the seed medium to be used in the stirred fermentor were like those present in the preculture medium except for the higher initial glucose concentration of 15 g/L and $Ca(OH)_2$ substituting $CaCO_3$. The initial pH of the seed medium was set at 6.50. The fermentation medium contained solely carbon substrates to be tested, e.g., glucose, sucrose, and liquefied cassava starch at the different concentrations. Liquefied cassava starch was prepared from the starch slurry (30% w/v). The pH of the starch slurry was adjusted to 5.80 before digestion by 120 μL of α-amylase (Spezyme Ethyl (6700–7300 AAU/g, 1.18–1.22 g/mL), Genencor, USA) at 100 °C for 90 min. After that the pH was adjusted to 6.50.

Before use, *Bacillus* sp. BC-001 was subcultured onto the fresh new GYP agar slant and incubated at 50 °C for 24 h. After that 1 mL of sterile deionized water was added into the slant before thoroughly vortexing to obtain the bacterial suspension. The suspension was collected for the OD600 reading. Then the bacterial suspension was diluted with sterile deionized water to obtain the OD600 of 30–40 for inoculation into the preculture medium at 1% inoculum size.

Two-phase L-lactate fermentation from the different carbon substrates in a flask culture

Figure 1 shows the process flow diagram of the two-phase fermentation study in the flask culture from the different carbon substrates. Different fermentation modes, e.g., batch, fed-batch, and SSF processes were employed. The production process consisted of preculture and fermentation phases. The preculture phase was started by transferring the bacterial suspension (OD600 of 30–40) at 1% inoculum size into the 250-mL Erlenmeyer flask containing 50 mL of sterile preculture medium. The culture flask was plugged with the C-type silicone stopper (Silicosen®) (to allow good air permeability) and incubated at 50 °C, 200 rpm (to provide sufficient mixing) for 5 h.

During batch cultivation, the fermentation phase started by inoculating the sterile concentrated carbon substrates, e.g., glucose (240 g/L), sucrose (300 g/L), and liquefied cassava starch (300 g/L) with the 5-h preculture broth at 50% inoculum size. The sterile $CaCO_3$ powder was added into the culture for pH control during fermentation. The culture flask was plugged with the T-type silicone stopper (Silicosen®) to provide an anaerobic environment. The culture was incubated at 50 °C for 48 h.

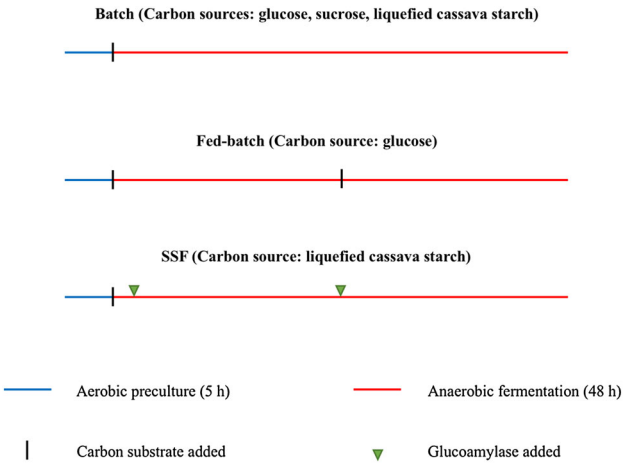

Fig. 1 Process scheme showing the key operating conditions in the two-phase L-lactate fermentation by *Bacillus* sp. BC-001. The bacterial suspension was inoculated into the preculture medium containing glucose as the sole carbon substrate. Later, L-lactate was produced during the fermentation stage using different carbon substrates under the different modes of operation

In fed-batch operation, the fermentation began similar to the batch cultivation of glucose. After 24 h, glucose powder (5 g) was added to the fermentation broth to bring up the total glucose concentration added into the culture to 150 g/L. The culture was incubated at 50 °C for 48 h.

Lactate production from liquefied starch was conducted by SSF process. The fermentation phase started by inoculating the fermentation medium containing a mixture of 300 g/L liquefied starch and 40 g/L glucose with the 5-h preculture broth at 50% inoculum size. After 2 h and 24 h, 200 μL of glucoamylase (Glucozyme #20000 (40 U/mg, 37.5 g/L), Nagase ChemteX Corp., Japan) was added into the culture. The culture was incubated at 50 °C for 48 h.

At the end of the fermentation, the broth was collected for analyses of the remaining carbon substrates, lactic acid, byproducts, and the optical purity of lactate product.

Effect of inoculum, mixing, and air permeability on lactate production in a flask culture

The operating conditions during the preculture and fermentation stages were optimized in the flask culture cultivation. The preculture medium was inoculated with the suspension of *Bacillus* sp. BC-001 at 1% inoculum

size (OD600 of 30–40). The culture was incubated into the Erlenmeyer flask plugged with the C-type silicone stopper at 50 °C, 200 rpm. To determine the suitable stage of seed starter for lactate fermentation, the preculture time was varied from 3 to 5 h (during the log phase growth). After that the preculture broth was transferred into the sterile fermentation medium containing 200 g/L glucose at 50% inoculum size. The sterile $Ca(OH)_2$ powder was added for pH control. The culture broth was incubated at 50 °C.

The effect of mixing and oxygen (air permeability) on lactate production during the fermentation was also investigated. To observe the effect of mixing, the fermentation was conducted with 200 rpm or without mixing. The effect of oxygen was observed from the metabolic response of *Bacillus* sp. BC-001 cultivated in the flask plugged with the two different silicone stoppers that allowed the different pattern of air permeability. Those include the culture flask plugged with the T-type silicone stopper placed into the W-zip pouch containing the AnaeroPack-Anaero (Mitsubishi Gas Chemical) and the culture flask plugged with the C-type silicone stopper.

The fermentation time was 24 h. The sample broth was collected for the OD reading, and analyses of the remaining glucose, lactic acid, byproducts, and the optical purity of lactate product.

L-Lactate production by two-phase fermentation in a 5-L stirred fermentor using high-inoculum seed

Further increase of L-lactate production by process optimization was conducted in the 5-L stirred fermentor. Initially, the bacterial suspension (1% inoculum size, OD600 of 30–40) was inoculated into the preculture medium. The culture (50 mL each, five flasks) was incubated into the Erlenmeyer flask plugged with the C-type silicone stopper at 50 °C, 200 rpm for 3 h. The preculture broth was transferred into the 5-L stirred fermentor containing 2.25 L of seed medium (10% inoculum size). The fermentor was controlled at 50 °C, 300 rpm, and 1.0 vvm air for 3 h without pH control. After that, 1 L of concentrated glucose solution (350 g/L) was added into the fermentor to obtain 100 g/L initial glucose concentration. The aeration was stopped. The fermentation was further conducted at the same temperature and agitation rate. The pH was automatically controlled at 6.50. The different base solutions including 7 M NH_4OH, 10 M NaOH, and 10 M KOH were tested for pH control during lactate fermentation. The samples were periodically collected for the OD reading, the remaining glucose, lactate, and byproducts. The fermentation continued until glucose depletion.

Intermittent glucose feeding for heavy-inoculum seed preparation for enhanced L-lactate production

L-Lactate fermentation by heavy-inoculum *Bacillus sp.* BC-001 was investigated in the 5-L stirred fermentor. The bacterial suspension (1% inoculum size with the OD600 of 30–40) was inoculated into the Erlenmeyer flask containing the sterile preculture medium plugged with the C-type silicone stopper. The culture was incubated at 50 °C, 200 rpm for 3 h. The 3-h preculture was used to inoculate into the fermentor containing 2.25 L of sterile seed medium. To prepare the heavy-inoculum seed (86% inoculum size), the fermentor was operated at 50 °C, 300 rpm, and 1.0 vvm air for 2 h. After that 0.5 L of glucose solution (30 g/L) was added into the fermentor. The fermentor was further operated at the same conditions for another 2 h. Later, the aeration was stopped and 0.5 L of concentrated glucose solution was added into the fermentor to bring up the glucose concentration to 100 g/L where the fermentation stage was started. The fermentation was further conducted at the same temperature and agitation rate. The pH was controlled at 6.50 using different bases including 7 M NH_4OH, 10 M NaOH, and 10 M KOH. The samples were periodically collected for the OD reading, the remaining glucose, lactate, and byproducts. The fermentation continued until glucose depletion.

Fermentation scale-up of *Bacillus* sp. BC-001 in the pilot stirred fermentors

High-inoculum seed approach was used to prepare the seed train for the pilot-scale fermentation in the stirred tank fermentors (30, 300, and 3000 L). The pilot production fermentors were operated at 50 °C and the pH was automatically controlled at 6.50 by 10 M NaOH. The agitation rates of the pilot fermentors were predicted using the constant power input per unit volume criterion and the fermentor configurations. The fermentation was carried out until glucose depletion. The samples were periodically taken for the OD reading, and the analyses of the remaining glucose and product formation.

Analytical methods

Fermentation broth sample was centrifuged at 10,000*g* for 5 min to separate the cell-free supernatant from the biomass. The supernatant was collected for further analyses of the remaining substrates, lactic acid and byproduct formation, and the optical purity of lactate product. The solid cell biomass was acidified with 1 M HCl to remove insoluble calcium bases remaining in the sample. The acidified sample was centrifuged and the obtained solid

particles were resuspended in deionized water for the OD reading. Spectrophotometry was used to determine the OD at 600 nm of the cell biomass present in the fermentation broth.

The concentration of the products formed and carbon substrates remained during the fermentation was analyzed by HPLC. Fermentation samples were centrifuged, filtered through the PTFE (hydrophilic) membrane, and diluted with double-deionized water. For analyses of remaining glucose, fructose, sucrose, total lactic acid (both L- and D-lactate), and acetic acid, 15 μL of diluted particle-free samples was automatically injected (Shimadzu-SIL-10A) into an organic acid analysis column (Biorad, Aminex HPX-87H ion exclusion organic acid column; 300 mm × 7.8 mm) maintained at 45 °C in a column oven (Shimadzu-CTO-10A). A 0.005 M H_2SO_4 was pumped through the system at the flowrate of 0.6 mL/min (Shimadzu-LC-10Avp). A refractive index detector (Shimadzu-RID-10A) was used to detect the organic compounds. The standards containing 0–2 g/L of each component (glucose, fructose, sucrose, lactate, and acetate) were injected as the references to determine the sample concentration. The peak area was used in determining the concentration. For determining the optical purity of lactic acid produced, 5 μL of diluted particle-free samples was automatically injected into a chiral column (Sumipack, Sumichiral OA5000) maintained at 40 °C. A 0.001 M $CuSO_4$ was used as eluant at the flowrate of 1.0 mL/min. The UV/Vis (Shimadzu-SPD-10Avp) detector was used to detect the lactate isomers at 254 nm. The standards containing 0–2 g/L of D- and L-lactate were injected as the references to determine the sample concentration [1].

Product yield ($Y_{p/s}$) was determined from the conversion ratio of product to carbon substrate consumed during fermentation, while $Y_{p/x}$ indicates the ratio of product generated to the increasing optical density during fermentation. Volumetric productivity was defined as the total amount of product formed per unit volume per time. The optical purity of L-lactate was defined as follows [32]:

$$\text{Optical purity} = \frac{\text{L}-\text{lactic acid} - \text{D}-\text{lactic acid}}{\text{L-lactic acid} + \text{D-lactic acid}} \times 100\%$$

Results

Bacillus sp. BC-001 as a novel L-lactate producer

Among the screened isolates obtained from the natural samples in Thailand, *Bacillus* sp. BC-001 produced an optically pure L-lactate at a high production rate. This isolate was identified as a novel *Bacillus* strain based on the 16S rRNA gene sequence analysis and the DNA–DNA hybridization (Fig. 2; Table 1). From the phylogeny analysis, the sequence similarity among the closest strains of the available database on EzTaxon server [30] revealed that *Bacillus* sp. BC-001 is the novel species closely related to *Bacillus acidiproducens* SL213^T identified by Jung et al. [33], and *Bacillus coagulans* ATCC7050^T, a commonly known industrial L-lactate producer, with the similarity percentages of 98 and 97%, respectively (Fig. 2). From the DNA–DNA hybridization data, the similarity percentages of the DNA pools to the two closely related type strains were less than 70%; thus, confirming that *Bacillus* sp. BC-001 is the novel *Bacillus* species (Table 1).

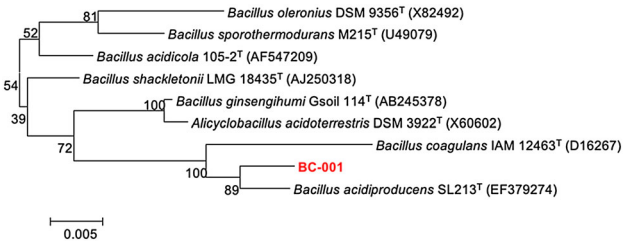

Fig. 2 A phylogenetic tree, based on 16s rRNA gene sequence, showing the position of *Bacillus* sp. BC-001 compared with its closely related type strains *B. acidiproducens* SL213^T and *B. coagulans* IAM12463^T

From the phenotypic characterization using the analytical profile index system (API test kits), it was found that *Bacillus* sp. BC-001 was potent to ferment several carbon substrates for lactic acid. Comparing the acid production from the different carbon sources, unlike *B. coagulans* ATCC7050^T, both *Bacillus* sp. BC-001 and *B. acidiproducens* SL213^T could utilize a wide range of carbon substrates derived from plant biomass (mainly arabinose and xylose), sugar crops (sucrose, glucose, and fructose), and starchy materials (starch) (Table 2). In addition, *Bacillus* sp. BC-001 was found as the novel thermotolerant strain which could grow at the optimal temperature of 50 °C.

Further investigation on *Bacillus* sp. BC-001 was conducted in a flask culture. Table 3 reports the fermentation performance of *Bacillus* sp. BC-001 grown on glucose, sucrose, and liquefied starch under the different operation modes. Batch fermentation of glucose gave the highest lactate yield among the three substrates tested. But the highest lactate titer was achieved from the sucrose fermentation. The productivity of both glucose and sucrose fermentations was similar while batch fermentation of liquefied starch resulted in the low lactate production. This implied that *Bacillus* sp. BC-001 lacked amylase to digest the oligosaccharides into monosugars. The fermentation of the concentrated substrates for high final lactate titer by *Bacillus* sp. BC-001 was also investigated. Compared with the base case fermentation with the initial glucose

Table 1 Similarity percentage of *Bacillus* sp. BC-001 to its closely related type strains, *B. acidiproducens* SL213^T and *B. coagulans* ATCC7050^T determined by the DNA–DNA hybridization technique

Isolates	DNA probe	
	Bacillus sp. BC-001 (%)	*B. acidiproducens* SL213^T (%)
Bacillus sp. BC-001	100	30.71
B. acidiproducens SL213^T	58.70	100
B. coagulans ATCC7050^T	48.14	34.74

Table 2 Comparison of key characteristics and acid production from selected carbon substrates by *Bacillus* sp. BC-001 and its closely related type strains *B. acidiproducens* SL213^T and *B. coagulans* ATCC7050^T

Characteristics	BC-001	*B. acidiproducens* SL213^T	*B. coagulans* ATCC7050^T
T for growth (°C)			
Range	25–55	25–55	30–55
Optimum	50	37	30
Lactic acid production at optimum T	+	+	+
Acid production from			
Glycerol	w	+	+
L-Arabinose	+	+	–
Ribose	+	+	–
D-Xylose	+	+	–
Galactose	+	+	+
Glucose	+	+	+
Fructose	+	+	+
Mannose	+	+	+
Rhamnose	+	+	–
Mannitol	–	+	–
Lactose	+	–	+
Sucrose	+	+	–
Starch	+	–	w

w represents weak (low production)

Table 3 Lactic acid production by *Bacillus* sp. BC-001 from glucose, sucrose, and liquefied starch in the flask culture under the different operation modes

Operation mode	Carbon substrate (total conc. in g/L)[a]	L-Lactate				Acetate titer (g/L)	Remaining glucose (g/L)
		Final titer (g/L)	Yield (g/g)	Productivity (g/L h)	Optical purity (%ee)[b]		
Batch	Glucose (120)	84.2 ± 4.8[c]	0.96 ± 0.06	2.8 ± 1.2	100.0 ± 0.0	ND[d]	0
	Sucrose (150)	126.9 ± 6.1	0.87 ± 0.03	2.6 ± 0.2	100.0 ± 0.0	ND	0
	Liquefied starch[e](150)	13.3 ± 4.7	0.09 ± 0.03	0.3 ± 0.1	100.0 ± 0.0	ND	0
Fed-batch	Glucose (100 + 50)	139.9 ± 6.3	0.96 ± 0.04	2.9 ± 0.1	100.0 ± 0.0	ND	3.9 ± 0.1
Simultaneous saccharification and fermentation	Liquefied starch (150) and glucose (20)	150.1 ± 1.8	0.98 ± 0.08	3.2 ± 0.1	99.7 ± 0.0	ND	0

[a] Total concentration of carbon substrates added into the fermentation medium

[b] Percentage of enantiomer excess representing the optical purity of lactate

[c] Each data point represents the mean of triplicate determinations ± standard deviation

[d] Not detected

[e] Liquefied starch

concentration of 120 g/L, fermenting sucrose at a high initial concentration of 150 g/L gave a slightly lower yield but a higher lactate titer and the similar productivity, while the higher final titer, yield, and productivity were achieved in the fed-batch glucose fermentation as well as the SSF process. The findings indicated that the operation mode

played a role in controlling the fermentation performance of *Bacillus* sp. BC-001.

Optimizing the conditions for preculture seed to enhance lactate production

To develop the simple but reliable process for industrial fermentation, the seed starter is one of the key factors controlling process efficiency and economy. Generating the seed starter at the correct physiological stage with a sufficiently high concentration for passage to the production fermentor helps improve the fermentation productivity. One advantage of growing *Bacillus* spp. including *Bacillus* sp. BC-001 is that this genus produces catalase; thus, it rapidly grows under the aerobic condition [22]. Both the physiological stage and the seed concentration for passage to the fermentation stage were varied in the preculture stage (Table 4). The preculture stage was started by inoculating the cell suspension to obtain the initial OD600 of 0.4. The increasing OD600 of approximately 10 times was obtained within 3–5 h (with the doubling time of approximately 0.9–1.5 h) indicating that *Bacillus* sp. BC-001 rapidly grew in the simple glucose preculture medium. The longer preculture time resulted in the higher final OD and lactate accumulation in the preculture broth. The similar final titer, yield, and productivity of lactate during the fermentation stage indicated that the change in age of the preculture seed did not strongly affect the fermentation behavior of *Bacillus* sp. BC-001 cultivated at the same conditions (Table 4). With 50% inoculum size, the correct physiological stage of the seed starter, the sufficient mixing, and the proper air permeability, *Bacillus* sp. BC-001 rapidly fermented glucose for lactate within 24 h, without any byproduct observed. This led to both high yield and productivity (Table 4). Among the four conditions studied, the fermentation with 200 rpm mixing and the suitable air permeability (the flask plugged with the C-type silicone stopper) yielded the highest lactate productivity. This is almost twice higher than the anaerobic fermentation (the flask plugged with the T-type silicone stopper placed into the W-zip pouch containing the AnaeroPack-Anaero without mixing). The higher lactate yield was above 1.00 g/g with lower final lactate titer, and productivity obtained from the fermentations without mixing and those under the anaerobic condition resulted from incomplete glucose consumption (glucose remained at 24 h). This indicated that *Bacillus* sp. BC-001 consumed glucose at lower rate under insufficient mixing and oxygen availability during fermentation. Contrary to the typical fermentation by *B. coagulans*, *Bacillus* sp. BC-001 rapidly grew under the aerobic condition yielding a relatively high concentration of the seed culture. During the aerobic preculture, lactate production was considerably low and no byproduct was observed from the HPLC chromatograms (data not shown). With the relatively high inoculum concentration of the active seed culture obtained from the preculture stage, the high lactate production was obtained in the fermentation stage with adequate mixing and sufficiently high air permeability (200 rpm, with C-type stopper). This finding revealed that the strictly anaerobic

Table 4 Effects of the inoculum size and age of the preculture seed and mixing/air permeability on lactate fermentation by *Bacillus* sp. BC-001 cultivated in the flask culture

Preculture			Fermentation				
Time/age	Final OD	Lactate produced (g/L)	Mixing/Air permeability	Final OD	Final lactate titer (g/L)	Yield (g/g)	Productivity (g/L h)
3 h/early log	3.1 ± 0.2	1.4 ± 0.1	No mixing, with T-type stopper	13.2 ± 1.2[a]	53.7 ± 6.3	1.13 ± 0.10	2.2 ± 0.3
			No mixing, with C-type stopper	19.7 ± 1.8	73.1 ± 3.7	1.06 ± 0.10	3.0 ± 0.2
			200 rpm, with T-type stopper	13.2 ± 0.9	59.3 ± 4.8	1.11 ± 0.05	2.5 ± 0.2
			200 rpm, with C-type stopper	22.6 ± 1.5	92.4 ± 6.8	0.93 ± 0.07	3.9 ± 0.3
4 h/mid-log	4.1 ± 0.3	2.4 ± 0.1	No mixing, with T-type stopper	13.8 ± 0.8	54.4 ± 0.5	1.24 ± 0.09	2.3 ± 0.0
			No mixing, with C-type stopper	21.3 ± 2.3	75.1 ± 2.0	1.06 ± 0.12	3.1 ± 0.1
			200 rpm, with T-type stopper	13.2 ± 0.4	58.9 ± 5.1	1.21 ± 0.11	2.5 ± 0.2
			200 rpm, with C-type stopper	25.3 ± 0.1	92.2 ± 6.7	0.93 ± 0.07	3.8 ± 0.3
5 h/late log	4.6 ± 0.1	2.4 ± 0.1	No mixing, with T-type stopper	13.8 ± 0.8	51.2 ± 3.2	1.22 ± 0.21	2.1 ± 0.1
			No mixing, with C-type stopper	20.2 ± 1.7	71.1 ± 8.2	1.06 ± 0.06	3.0 ± 0.3
			200 rpm, with T-type stopper	15.0 ± 3.2	67.5 ± 15.4	1.10 ± 0.23	2.8 ± 0.6
			200 rpm, with C-type stopper	24.6 ± 0.5	95.5 ± 0.7	0.96 ± 0.01	4.0 ± 0.0

The preculture medium was inoculated with 1% inoculum size. Fermentation was started by transferring the preculture broth into the fermentation medium containing 200 g/L glucose. $Ca(OH)_2$ was added for pH control during the fermentation

[a] Each data point represents the mean of triplicate determinations ± standard deviation

environment was not mandatory in lactic acid production by *Bacillus* sp. BC-001 during the fermentation stage.

Generating the robust microbes by the heavy inoculum for lactate fermentation in the stirred fermentor

The fermentation results obtained from the flask culture indicated that the large inoculum size and the correct physiological stage of the preculture broth provided the robust high-inoculum-concentration seed that enhanced lactate production in the fermentation stage. The high-inoculum-concentration seed culture prepared by the heavy-inoculum approach was observed for lactate fermentation performance in a 5-L stirred fermentor. Table 5 shows the fermentation performance of *Bacillus* sp. BC-001. Compared with the results shown in Table 4 (50% inoculum size), the significantly high productivity (5.1–5.7 g/L h) was obtained by the high-inoculum seeding approach (71% inoculum size). More interestingly, *Bacillus* sp. BC-001 exhibited the high lactate production performance during the fermentation using the monovalent base solutions, e.g., NH_4OH, NaOH, and KOH. This eased the fermentation control and operation especially in the large-scale production. It should be noted that the monovalent base solutions are reported as toxic to other *Bacillus* strains.

Further improving lactate yield and productivity was conducted by the heavy-inoculum seed (86% inoculum size) during the preculture stage. To prepare the heavy inoculum, glucose was intermittently fed during the aerobic preculture stage to prevent glucose repression. The higher OD transfer but the slightly similar final OD was obtained from the fermentation using heavy inoculum. The improved lactate yield and productivity were confirmed by the higher $Y_{p/x}$ during the fermentation stage indicating the lower substrate consumption for cell biomass (Table 5).

Pilot-scale lactate fermentation by *Bacillus* sp. BC-001

The production test runs were conducted in a series of the 30, 300, and 3000 L stirred fermentors using the optimized fermentation platform obtained from the 5-L stirred fermentor. All fermentors were operated at 50 °C, and the pH during the fermentation stage was controlled at 6.5 by 10 M NaOH. The preculture/seed preparation followed the protocol previously determined for lactate production by *Bacillus* sp. BC-001 in the 5-L stirred fermentor. The power input per unit volume was selected as an engineering criterion to predict the agitation rates in all pilot fermentors. Table 6 represents the repeatability of the fermentation kinetics obtained in all production scales being tested. It was observed that the similar growth rate and lactate production were obtained in all fermentor scales compared with the base case fermentation in the 5-L stirred fermentor. The findings here confirmed that the power input per unit volume was an appropriate scale-up criterion for lactate production by *Bacillus* sp. BC-001. Particularly, the results in Table 6 revealed that the growth-associated product kinetics model for lactate formation by *Bacillus* sp. BC-001 was well correlated with the mass transport pattern manipulated by the power input per unit volume to all fermentor scales. It was also reported in many works that the power input per unit volume was successfully used in fermentation scale-up [34].

Table 5 Lactate production by heavy-inoculum fermentation of *Bacillus* sp. BC-001

Inoculum size	Base used during fermentation	Fermentation time (h)	Initial OD	Final OD	Final lactate titer (g/L)	Lactate yield (g/g)	Lactate productivity (g/L h)	$Y_{p/x}$[a]
71% (high inoculum)	7 M NH_4OH	17	5.5 ± 0.2[b]	20.7 ± 2.6	87.3 ± 4.6	0.87 ± 0.04	5.1 ± 0.3	6.7
	10 M NaOH	19	5.0 ± 2.9	22.0 ± 1.6	99.9 ± 15.0	0.94 ± 0.01	5.6 ± 1.1	6.6
	10 M KOH	18	8.1 ± 2.8	25.1 ± 2.2	102.9 ± 3.1	0.95 ± 0.00	5.7 ± 0.2	7.5
86% (heavy inoculum)	7 M NH_4OH	17	8.6 ± 1.1	21.1 ± 1.7	99.1 ± 8.1	0.99 ± 0.09	5.9 ± 0.7	8.2
	10 M NaOH	18	9.7 ± 1.6	22.6 ± 2.8	108.9 ± 12.4	1.04 ± 0.15	6.1 ± 0.7	8.8
	10 M KOH	19	10.8 ± 1.7	23.7 ± 6.9	102.0 ± 3.0	0.92 ± 0.04	5.5 ± 0.1	9.1
50% (Ma et al. [21])	10% NH_3	38	5.6 ± 0.1	NA[c]	98.6 ± 0.6	0.98 ± 0.01	2.6 ± 0.0	NA
10% (Qin et al. [22])	10 M NaOH	30	NA	NA	108.0 ± 2.0	0.92 ± 0.01	3.6 ± 0.07	NA

High/Heavy-inoculum approach was introduced in the final aerobic seed preparation stage to generate high cell density during fermentation phase

[a] An amount of lactate produced per amount of cell generated (in term of OD) during fermentation phase

[b] Each data point represents the mean of triplicate determinations ± standard deviation

[c] Not available

Table 6 Performance of *Bacillus* sp. BC-001 on lactate fermentation in the pilot fermentors

Tank size	5 L (base case)	30 L	300 L	3000 L
Working volume (L)	3.5	20	200	2000
Impeller diameter (mm)	76	113	296	430
Agitation rate (rpm)	300	230	132	95
Inoculum				
OD transfer	30–40	38.90 ± 0.00	36.80 ± 0.00	38.70 ± 0.71
Inoculum age (h)	24	24	24	24
Seed 1				
OD transfer	3–4	4.22 ± 0.33[a]	5.43 ± 0.01	4.57 ± 0.46
Seed 2				
OD transfer	3–4	4.91 ± 1.42	3.35 ± 0.03	5.63 ± 0.03
Seed 3				
OD transfer		3.05 ± 0.11	9.08 ± 0.07	8.24 ± 0.85
Lactate accumulation (g/L)		0.87 ± 1.22	2.42 ± 0.00	1.55 ± 0.05
Fermentation				
Time (h)	18	18	18	16.5
Final OD	22.00	25.75 ± 3.00	21.20 ± 0.35	27.73 ± 7.07
Final lactate (g/L)	100	120.60 ± 9.99	90.92 ± 0.00	104.11 ± 0.00
Lactate yield (g/g)	0.94	1.05 ± 0.07	0.91 ± 0.00	0.87 ± 0.00
Lactate productivity (g/L h)	5.60	6.70 ± 0.55	5.05 ± 0.00	6.31 ± 0.00
Remaining glucose (g/L)	<5.00	1.51 ± 2.14	0.00 ± 0.00	2.25 ± 0.00

The power input per unit volume was selected as the constant criterion to predict the mixing pattern in the pilot fermentors compared with that of the base case fermentation in the 5-L stirred fermentor

[a] Each data point represents the mean of triplicate determinations ± standard deviation

Discussion

Advantages of using *Bacillus* sp. BC-001 for L-lactate production

From the results shown in Tables 2 and 3, it can be stated that the novel thermotolerant catalase-positive *Bacillus* sp. BC-001 exhibited a remarkable ability to produce the optically pure L-lactic acid from different carbon sources (glucose and sucrose). In addition, this strain provided the favorable outcomes in the SSF process using the hydrolysis products from cassava starch operating at a relatively high temperature (Table 2) [6]. The major merit of using this novel thermotolerant strain for lactate fermentation is the high fermentation temperature; thus, medium sterilization can be omitted [10, 32]. By this, the energy consumption is lower. In addition, lactate fermentation at the high temperature favors the SSF process of lignocellulosic feedstocks and starch crops because the cellulosic enzymes including amylases and cellulases usually work well at high temperature [6, 20]. From the result in Table 3, *Bacillus* sp. BC-001 showed the potential on sucrose utilization for lactate production as observed from the highest lactate titer compared to the fermentation of glucose and starch. The low lactate production observed from starch fermentation indicated that *Bacillus* sp. BC-001 lacked amylases. Therefore, starch substrate pretreatment and hydrolysis prior to the fermentation process are required.

Fermentation using the high initial substrate concentration is necessary to get the high lactate titer so that the equipment sizes in both upstream and downstream processes along with the production cost can be subsequently reduced. Such fermentation process requires microbes that can tolerate to the high substrate concentration [20]. It was observed that *Bacillus* sp. BC-001 was rather tolerant to the high initial sucrose concentration although the yield was slightly low (Table 3). The evidence of low yield could be explained by the consumption of sucrose for enzyme production to convert sucrose into glucose and fructose before assimilation into the cell for growth and lactate production. The similar productivity to the glucose fermentation revealed the sufficiently high rate of sucrose conversion to glucose and fructose and the rapid uptake rate of fructose comparable to glucose uptake rate for lactic acid production. Therefore, fermentation of the highly concentrated sucrose syrup or even the byproducts from sugar mills such as molasses is plausible. This reveals another key promising performance of *Bacillus* sp. BC-001 over *B. coagulans* to ferment sugarcane-based substrates for lactate [12, 33]. When glucose was used as the sole carbon substrate in the fermentation, the inhibition by high concentration is generally of concern. However, with the suitable glucose

feeding program during the fed-batch fermentation, the inhibition by high concentration during lactate fermentation by *Bacillus* sp. BC-001 was well manipulated [18]. The inhibition by high substrate concentration was reduced in the SSF process where the enzymatic starch hydrolysis and glucose uptake for lactate fermentation were properly controlled. It is noted that the optical purity of lactate products obtained was about 100%ee regardless of the carbon substrates and the operation modes applied during the cultivation. From the preliminary findings in the flask culture, it can be stated that *Bacillus* sp. BC-001 is one of the promising L-lactate producers for the industrial applications as it can ferment a variety of carbon substrates for the optically pure L-lactate with the high titer, yield, and productivity at the high temperature [6, 18].

Optimal preculture seed promoted lactate production

The fermentation process optimization results in the 5-L stirred fermentor revealed that both the inoculum size and age were the key factors controlling the metabolic activity of *Bacillus* sp. BC-001. It was found that the preculture age in between the mid-log and the late-log phase yielded the suitable physiological stage for lactate fermentation in the production fermentor. By the correct physiological stage and the proper concentration of the seed culture, the lag phase was shortened during the fermentation stage. Although aeration was instantly stopped, which diverted the pyruvate flux to the anaerobic fermentation, the vegetative cells being transferred into the fermentation stage could continue the metabolic activities by converting glucose to cell biomass and the final lactic acid product (Table 5) [19]. During seed preparation, it is crucial to control the age of the preculture so that the high yield and overall batch productivity can be acquired. In this study, the short-duration, high/heavy-inoculum-concentration preculture was proven to be effective for lactate production during the fermentation stage. By this approach, the seed starter had a low metabolic stress as the cell population was still at the exponential growth phase with the sufficient substrates available [35]. The evidence of a small amount of lactate formed during the preculture stage implied the expression of lactate dehydrogenase (Tables 4, 6). Thus, when the fermentation stage was started, *Bacillus* sp. BC-001 promptly converted the substrate into lactate.

From the growth and product formation kinetics of *Bacillus* sp. BC-001 obtained from the fermentations in all production scales, this novel isolate grew rapidly under the aerobic condition as observed from the increasing OD up to ten times within 3–5 h. When the aeration was immediately stopped, the homolactic acid fermentation process was triggered by a lack of sufficient amount of oxygen. This process yielded lactate as the final product. The byproducts including acetate, acetoin, and 2,3-butanediol are often found during the aerobic fermentation by *Lactobacillus* sp. or *B. coagulans* due to the metabolic shift to the mixed acid fermentation pathway when the fermentation was failed to be maintained under the strictly anaerobic condition [20]. To limit the byproduct formation, the anaerobic lactate fermentation was usually employed which resulted in the low productivity (Table 5; Fig. 3) [21, 22]. In contrast, *Bacillus* sp. 001 was unlike *Lactobacillus* sp. and *B. coagulans*. The evidence for lack of byproduct observed during the two-phase fermentation by *Bacillus* sp. BC-001 confirmed that this isolate grew well during the aerated stage and fermented the carbon substrates to lactate by the homofermentative pathway while the strictly anaerobic environment was not necessitated (no requirement for air elimination from the fermentor when switching from preculture to fermentation stages). In addition, the growth and lactate production profiles indicated that the production performance followed the growth-associated product formation kinetics model. As a result, the two-phase fermentation platform could be simply employed for lactate production by this isolate.

Effect of mixing in L-lactate fermentation by *Bacillus* sp. BC-001

It should be noted that mixing is considered as the important factor that impacts the fermentation process scale-up. Mixing not only provides the broth homogeneity but it is also the key facilitating mass transport especially oxygen in the aerobic culture [1]. The previous studies on lactate fermentation by *B. coagulans* reported that mixing and oxygen level played a role in manipulating the metabolic fluxes and, therefore, controlling growth, lactate, and byproduct formation [4, 21, 22]. *B. coagulans* generally required the high oxygen level during the growth stage to provide sufficiently high cell biomass for the fermentation stage where oxygen was strictly prohibited. The two-phase culture of *B. coagulans* usually resulted in byproduct formation because of the high-inoculum-concentration seed culture that failed to switch from the aerobic respiration metabolism to the homolactic acid fermentative pathway. Thus, the excess pyruvate flux entered the mixed acid fermentation pathway. This resulted in the lower product yield although the high productivity could be obtained. To prevent byproduct formation, the strictly anaerobic fermentation process which gave the lower biomass production and the low lactate productivity was typically employed in lactate production by *B. coagulans*. Unlike *B. coagulans*, with the high-carbon substrate added into the culture and the trace amount of oxygen remaining in the fermentation broth at the initial fermentation stage

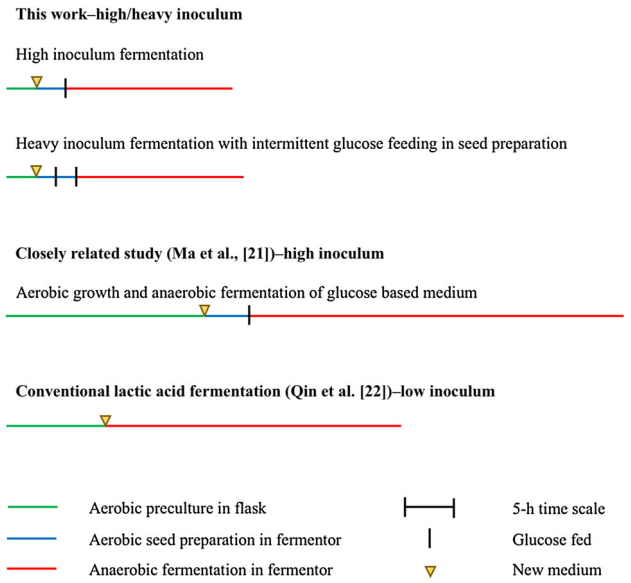

Fig. 3 Schematic diagram representing high/heavy-inoculum fermentation to produce lactate developed in this study compared with other key batch fermentation processes reported in the literature

(approximately 2–3% DO, data not shown), *Bacillus* sp. BC-001 simultaneously grew and produced lactate via the homolactic acid fermentative pathway. This resulted in both the high yield and productivity of lactic acid with the increasing cell biomass during the fermentation stage [5].

The merits of high/heavy inoculum in two-phase fermentation

It was reported that *Lactobacillus* spp. and *Bacillus* spp. have high susceptibility to stress by the monovalent ions. Therefore, the fermentation by these isolates using the monovalent bases for pH control usually gave low productivity. Although the strain improvement has been conducted to improve the tolerance to the monovalent ions, to date only a little accomplishment has been reported in the genetically modified yeast and the bacterial mutants [21, 22, 36]. Hence, the typical lime process for lactate production by *Lactobacillus* sp. and *B. coagulans* is still widely available [37]. On the other hand, *Bacillus* sp. BC-001 could utilize both the monovalent bases, e.g., NH_4OH, NaOH, and KOH and the typical lime base ($Ca(OH)_2$) for pH control during the two-phase lactate fermentation with the acceptably high product yield and productivity. More explanation on the stress from the monovalent ions during lactate fermentation by *Lactobacillus* sp. and *Bacillus* sp. previously reported was mentioned by Bakker [38]. It was claimed that the stress from the monovalent ions resulted from an increase in cytoplasmic concentration of such ions. Bacteria protect themselves by turning on the two-ion extrusion systems to transport the ions across the cytoplasmic membrane. The primary systems are those catalyzing the active transport. These systems are energy driven and the energy source can originate from ATP, respiration, and metabolic conversion. One way to increase the metabolic energy is to conduct the bioconversion under the oxidative conditions. The secondary systems are mainly the proton antiporters which catalyze an ion efflux in exchange for proton. As a result, the efficiency of the secondary systems relies on the physiological pH and the culture pH [22, 38].

The results shown in Table 6 revealed that *Bacillus* sp. BC-001 was the potential industrial lactate producer. Fermentation repeatability was achieved when the two-phase fermentation platform was employed for lactate production in all fermentors. By the two-phase fermentation using the high/heavy-inoculum seed, the remarkably high lactate yield and productivity were achieved from the fermentations using monovalent bases including NH_4OH, NaOH, and KOH besides the typical calcium bases for pH control (Tables 4, 5). Compared to the conventional lactate fermentation using lime-based process, this fermentation platform developed in this study provided several advantages including the simple operation and the easy downstream recovery process.

Conclusions

A novel thermotolerant, catalase-positive *Bacillus* sp. BC-001 exhibited a remarkable ability to produce the optically pure L-lactic acid from both glucose and sucrose at the high production rate. Cassava starch after pretreatment and hydrolysis could be also an alternated carbon feedstock for lactate fermentation by this isolate. *Bacillus* sp. BC-001 grew rapidly under the aerobic condition while the strictly anaerobic condition was not restricted for lactate fermentation by this isolate. As a consequence, a simple two-phase fermentation was simply applied for lactate fermentation inoculated with a high/heavy-inoculum seed culture which resulted in high lactate yield and productivity. During the fermentor operation, high/heavy-inoculum approach was introduced in the two-phase lactate fermentation. High/heavy inoculum obtained from the aerobic preculture stage led to the high product to cell biomass yield during the fermentation stage. This indicated an effective substrate consumption for lactate in the fermentation using the high/heavy-inoculum seed culture. From the low nutrient requirement, no byproduct, and the reproducible fermentation platform developed for this novel *Bacillus* isolate, we can claim that *Bacillus* sp. BC-001 can be a promising industrial lactate producer.

Acknowledgements This work was financially supported by PTT Global Chemical Public Company Limited and Chulalongkorn University under an industrial-university linkage program. Partial supports from the Grant for International Research Integration: Research Pyramid, Ratchadapiseksomphot Endowment Fund (GCURP_58_01_33_01) and Thailand Research Fund via the Distinguished Research Professor Grant (DPG5880003) are also acknowledged. The pilot research facility support from the Chulalongkorn Academic Advancement into its 2nd Century Project (CUAASC) is highly appreciated.

Compliance with ethical standards

Conflict of interest The authors declare that they have no conflict of interest.

Ethical approval This article does not contain any studies with human participants or animals performed by any of the authors.

References

1. Chotisubha-anandha N, Thitiprasert S, Tolieng V, Thongchul N (2011) Improved oxygen transfer and increased L-lactic acid production by morphology control of *Rhizopus oryzae* in a static bed bioreactor. Bioprocess Biosyst Eng 34:163–172
2. Phrueksawan P, Kulpreecha S, Sooksai S, Thongchul N (2012) Direct fermentation of L(+)-lactic acid from cassava pulp by solid state culture of *Rhizopus oryzae*. Bioprocess Biosyst Eng 35:1429–1436
3. Gao T, Wong Y, Ng C, Ho K (2012) L-lactic acid production by *Bacillus subtilis* MUR1. Bioresour Technol 121:105–110
4. Gao T, Ho K-P (2013) L-lactic acid production by *Bacillus subtilis* MUR1 in continuous culture. J Biotechnol 168:646–651
5. Michelson T, Kask K, Jogi E, Talpsep E, Suitso I, Nurk A (2006) L(+)-lactic acid producer *Bacillus coagulans* SIM-7 DSM 14043 and its comparison with *Lactobacillus delbrueckii* ssp *lactis* DSM 20073. Enzyme Microb Technol 39:861–867
6. Wang LM, Xue ZW, Zhao B, Yu B, Xu P, Ma YH (2013) Jerusalem artichoke powder: a useful material in producing high-optical-purity L-lactate using an efficient sugar-utilizing thermophilic *Bacillus coagulans* strain. Bioresour Technol 130:174–180
7. Maas RHW, Bakker RR, Jansen MLA, Visser D, De Jong E, Eggink G, Weusthuis RA (2008) Lactic acid production from lime-treated wheat straw by *Bacillus coagulans*: neutralization of acid by fed-batch addition of alkaline substrate. Appl Microbiol Biotechnol 78:751–758
8. Patel MA, Ou MS, Harbrucker R, Aldrich HC, Buszko ML, Ingram LO, Shanmugam KT (2006) Isolation and characterization of acid-tolerant, thermophilic bacteria for effective fermentation of biomass-derived sugars to lactic acid. Appl Environ Microbiol 72:3228–3235
9. Peng LL, Wang LM, Che CC, Yang G, Yu B, Ma YH (2013) *Bacillus* sp strain P38: an efficient producer of L-lactate from cellulosic hydrolysate, with high tolerance for 2-furfural. Bioresour Technol 149:169–176
10. Sakai K, Ezaki Y (2006) Open L-lactic acid fermentation of food refuse using thermophilic *Bacillus coagulans* and fluorescence in situ hybridization analysis of microflora. J Biosci Bioeng 101:457–463
11. Tashiro Y, Matsumoto H, Miyamoto H, Okugawa Y, Pramod P, Miyamoto H, Sakai K (2013) A novel production process for optically pure L-lactic acid from kitchen refuse using a bacterial consortium at high temperatures. Bioresour Technol 146:672–681
12. Xu K, Xu P (2014) Efficient production of L-lactic acid using co-feeding strategy based on cane molasses/glucose carbon sources. Bioresour Technol 153:23–29
13. Ye LD, Zhou XD, Bin Hudari MS, Li Z, Wu JC (2013) Highly efficient production of L-lactic acid from xylose by newly isolated *Bacillus coagulans* C106. Bioresour Technol 132:38–44
14. Zhang B, He PJ, Ye NF, Shao LM (2008) Enhanced isomer purity of lactic acid from the non-sterile fermentation of kitchen wastes. Bioresour Technol 99:855–862
15. Ou MS, Mohammed N, Ingram LO, Shanmugam KT (2009) Thermophilic *Bacillus coagulans* requires less cellulase for simultaneous saccharification and fermentation of cellulose to products than mesophilic microbial catalysts. Appl Biochem Biotechnol 155:76–82
16. Ouyang J, Cai C, Chen H, Jiang T, Zheng ZJ (2012) Efficient non-sterilized fermentation of biomass-derived xylose to lactic acid by a thermotolerant *Bacillus coagulans* NL01. Appl Biochem Biotechnol 168:2387–2397
17. Ye LD, Bin Hudari MS, Li Z, Wu JC (2014) Simultaneous detoxification, saccharification and co-fermentation of oil palm empty fruit branch hydrolysate for L-lactic acid production by *Bacillus coagulans* JI12. Biochem Eng J 83:16–21
18. Ou MS, Ingram LO, Shanmugam KT (2011) L(+)-lactic acid production from non-food carbohydrates by thermotolerant *Bacillus coagulans*. J Ind Microbiol Biotechnol 38:599–605
19. Rosenberg M, Rebros M, Kristofikova L, Malatova K (2005) High temperature lactic acid production by *Bacillus coagulans* immobilized in LentiKats. Biotechnol Lett 27:1943–1947
20. Zhou XD, Ye LD, Wu JC (2013) Efficient production of L-lactic acid by newly isolated thermophilic *Bacillus coagulans* WCP10-4 with high glucose tolerance. Appl Microbiol Biotechnol 97:4309–4314
21. Ma KD, Maeda T, You HY, Shirai Y (2014) Open fermentative production of L-lactic acid with high optical purity by thermophilic *Bacillus coagulans* using excess sludge as nutrient. Bioresour Technol 151:28–35
22. Qin JY, Wang XW, Zheng ZJ, Ma CQ, Tang HZ, Xu P (2010) Production of L-lactic acid by a thermophilic *Bacillus* mutant using sodium hydroxide as neutralizing agent. Bioresour Technol 101:7570–7576
23. Bai DM, Yan ZH, Wei Q, Zhao XM, Li XG, Xu SM (2004) Ammonium lactate production by *Lactobacillus lactis* BME5-18M in pH-controlled fed-batch fermentations. Biochem Eng J 19:47–51
24. Ding SF, Tan TW (2006) L-lactic acid production by *Lactobacillus casei* fermentation using different fed-batch feeding strategies. Process Biochem 41:1451–1454
25. Zhu Y, Eiteman MA, DeWitt K, Altman E (2007) Homolactate fermentation by metabolically engineered *Escherichia coli* strains. Appl Environ Microbiol 73:456–464
26. Saito H, Miura KI (1963) Preparation of transforming deoxyribonucleic acid by phenol treatment. Biochim Biophys Acta 72:619–629
27. Tamaoka J, Komagata K (1984) Determination of DNA base composition by reversed-phase high-performance liquid chromatography. FEMS Microbiol Lett 25:125–128
28. Tanasupawat S, Thawai C, Yukphan P, Moonmangmee D, Itoh T, Adachi O, Yamada Y (2004) *Gluconobacter thailandicus* sp nov., an acetic acid bacterium in the alpha-proteobacteria. J Gen Appl Microbiol 50:159–167
29. Saitou N, Nei M (1987) The neighbor-joining method: a new method for reconstructing phylogenetic trees. Mol Biol Evol 4:406–425
30. Felsenstein J (1985) Confidence limits on phylogenies: an approach using the bootstrap. Evolution 39:783–791

31. Chun J, Lee JH, Jung Y, Kim M, Kim S, Kim BK, Lim YW (2007) EzTaxon: a web-based tool for the identification of prokaryotes based on 16S ribosomal RNA gene sequences. Int J Syst Evol Microbiol 57:2259–2261
32. Zhao B, Wang LM, Ma CQ, Yang CY, Xu P, Ma YH (2010) Repeated open fermentative production of optically pure L-lactic acid using a thermophilic *Bacillus* sp strain. Bioresour Technol 101:6494–6498
33. Jung MY, Kim JS, Chang YH (2009) *Bacillus acidiproducens* sp nov., vineyard soil isolates that produce lactic acid. Int J Syst Evol Microbiol 59:2226–2231
34. Miura S, Arimura T, Hoshino M, Kojima M, Dwiarti L, Okabe M (2003) Optimization and scale-up of L-lactic acid fermentation by mutant strain *Rhizopus* sp MK-96-1196 in airlift bioreactors. J Biosci Bioeng 96:65–69
35. Serrazanetti DI, Ndagijimana M, Sado-Kamdam SL, Corsetti A, Vogel RF, Ehrmann M, Guerzoni ME (2011) Acid stress-mediated metabolic shift in *Lactobacillus sanfranciscensis* LSCE1. Appl Environ Microbiol 77:2656–2666
36. Saitoh S, Ishida N, Onishi T, Tokuhiro K, Nagamori E, Kitamoto K, Takahashi H (2005) Genetically engineered wine yeast produces a high concentration of L-lactic acid of extremely high optical purity. Appl Environ Microbiol 71:2789–2792
37. Payot T, Chemaly Z, Fick M (1999) Lactic acid production by *Bacillus coagulans*–kinetic studies and optimization of culture medium for batch and continuous fermentations. Enzyme Microb Technol 24:191–199
38. Bakker EP (1990) The role of alkali-cation transport in energy coupling of neutrophilic and acidophilic bacteria: an assessment of methods and concepts. FEMS Microbiol Lett 75:319–334

SCIENTIFIC PAPER

ALTERNATIVE REVERSE OSMOSIS TO PURIFY LACTIC ACID FROM A FERMENTATION BROTH

Natnirin Phanthumchinda[1], Tanapawarin Rampai[1], Budsabathip Prasirtsak[1], Sitanan Thitiprasert[2], Somboon Tanasupawat[3], Suttichai Assabumrungrat[4], Nuttha Thongchul[2*]

[1]Program in Biotechnology, Faculty of Science, Chulalongkorn University, Phayathai Road, Wangmai, Bangkok 10330, Thailand
[2]Institute of Biotechnology and Genetic Engineering, Chulalongkorn University, Phayathai Road, Wangmai, Bangkok 10330, Thailand
[3]Department of Biochemistry and Microbiology, Faculty of Pharmaceutical Sciences, Phayathai Road, Wangmai, Bangkok 10330, Thailand
[4]Department of Chemical Engineering, Faculty of Engineering, Chulalongkorn University, Phayathai Road, Wangmai, Pathumwan, Bangkok 10330, Thailand

Received 14.3.2017.
Revised 15.8.2017.
Accepted 29.8.2017.

[*] Corresponding author: Nuttha Thongchul, Phone: +66-2-2188073; Fax: +66-2-2533543; E-mail: Nuttha.T@chula.ac.th

Abstract

Brackish water reverse osmosis (BWRO) and seawater reverse osmosis (SWRO) membranes were used in the 2-stage reverse osmosis (RO) unit to recover, pre-purify, and pre-concentrate lactic acid. Calcium lactate, sodium lactate, and ammonium lactate were used as model feed solutions. The operating pressure showed a pronounced effect on lactate passage through the first BWRO unit, and the Donnan exclusion effect and hydrogen bonding were responsible for cation rejection. Calcium ions were rejected at the BWRO unit because of low diffusion rate and charge interaction at the surface. However, monovalent ions formed hydrogen bonds with the carbonyl group of the membrane that allowed passage across the membrane. The second SWRO unit was for pre-concentrating lactic acid. A high lactate purity of 99.2% with a total recovery of 50.5% was acquired from calcium lactate feed solution. Lower purity with higher lactate recovery was obtained when the feed solution was sodium lactate and ammonium lactate. When the actual fermentation broth was used in the 2-stage RO unit, a slightly lower recovery and purity of lactic acid were obtained. It was claimed that the total ions present in the fermentation broth were responsible for the low efficiency of the 2-stage RO unit.

Keywords: Lactic acid; Fermentation broth; Reverse osmosis; Donnan exclusion effect; Ionic strength

Highlights

- Reverse osmosis was used to recover and purify lactic acid from fermentation broth
- Cation rejection occurred at the first BWRO unit, where lactic acid was separated
- Concentration of lactic acid occurred at the second SWRO unit
- Sufficiently high lactate purity and recovery was obtained from 2-stage RO units
- Donnan potential, pH, and operating pressure controlled ion rejection

Graphical Abstract

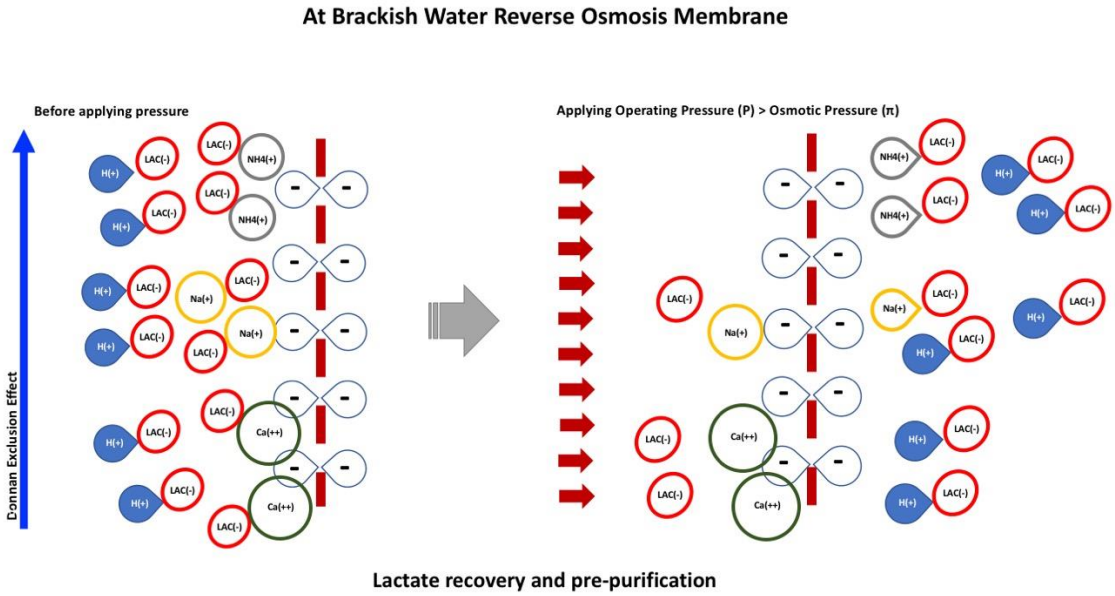

Introduction

Owing to its chiral structure, consisting of both carboxyl and hydroxyl groups, lactic acid has been extensively used in the food, cosmetic, and pharmaceutical industries. To date, the market demand for lactic acid has increased considerably because of the global trend toward environmental protection that accelerated the supply of biodegradable plastics. Currently, bacterial fermentation is widely used in industrial lactic acid production. During production, the pH is typically decreased as the acid is produced, and the proper operating pH must be maintained at 5.5–6.5 [1]. pH control is carried out by the addition of bases such as calcium bases ($CaCO_3$ and $Ca(OH)_2$), NaOH, and NH_4OH [2,3]. This generates 2 lactate species (free lactic acid and lactate salt) in the fermentation broth depending on the operating pH control. At the end of the fermentation, lactate salts and free lactic acid must be recovered in the form of free acid in the downstream operation units.

In the recovery and purification of lactic acid from the fermentation broth, many major process steps are involved: e.g., primary recovery, product purification, and finishing processes [4]. The first step in primary recovery units involves cell separation by centrifugation or microfiltration [4-7]. Several downstream techniques have been used for recovering and separating lactic acid, including reactive distillation, reactive extraction, adsorption (ion exchange), and membrane separation (electrodialysis) [8]. Both distillation and electrodialysis have high energy consumption in a large-scale operation because of the low volatility of lactic acid and high electricity loading, respectively [9]. When charged compounds such as amino acids and other organic acids are present, the separation efficiency of electrodialysis decreases as a result of membrane fouling. Electrodialysis fails to reject divalent ions such as calcium and magnesium; therefore, it is not suitable for recovering lactic acid from the conventional calcium base fermentation process where lactate species are present in the form of calcium lactate and lactic acid [10,11]. In reactive extraction, toxicity of solvent and final product contamination are usually of concern [12]. Using ion exchangers to recover lactic acid requires large amounts of chemicals, enzymes, and process water during the resin regeneration and washing steps. This eventually generates a large effluent loading in wastewater treatment. In addition, precautions should be taken in the pretreatment steps before feed enters the ion exchangers so as to avoid fouling and resin deterioration [13]. Purified lactic acid then enters the evaporator where water is removed, resulting in concentrated lactic acid as the finished product [14-16]. As previously mentioned, process

integration is necessary in order to achieve good recovery and purification performance as well as cost effectiveness.

Membrane separation provides advantages of low energy consumption and low toxicity. Nevertheless, a single membrane unit cannot fulfill lactate recovery, purification, and concentration of lactic acid [7]. Typically, nanofiltration is used prior to the product finishing step (evaporation in case of lactic acid recovery and purification). Nanofiltration is applied for removal of trace ions and small, neutral molecules from free lactic acid solution [14]. On the other hand, reverse osmosis (RO) is generally applied for removal of water in previous literatures [7]. In this study, a 2-stage RO membrane-based process was developed for recovering, purifying, and concentrating lactic acid from the model solution and the cell-free fermentation broth by applying the appropriate pressure higher than the osmotic pressure of the species of interest. From the principle of the RO process, solute transport occurs by diffusion through the membrane depending on molecular size and charge [17]. With smaller pore sizes than the nanofiltration membrane, the RO membrane provides high efficiency in the rejection of monovalent ions [18]. It was also reported that some trace organic compounds, such as neutral molecules smaller than the molecular weight cut-off of the membrane, leaked and passed through the membrane [19]. By applying an operating pressure sufficiently higher than the osmotic pressure of the molecules, such molecules can pass through the RO membrane. At the proper pH, free lactic acid passed across the first RO membrane to the permeate side whilst the cation salts remained in the retentate. The second RO unit was for pre-concentrating lactic acid solution. Compared with the other techniques mentioned previously, RO filtration did not require chemicals, enzymes, and process water during the operation. The low volumetric rate of the exit stream from this 2-stage RO unit resulted in size reduction of the evaporator and lower capital and operating expenditures.

Materials and Methods

Chemicals

Calcium lactate (CaLAC), sodium lactate (NaLAC), and ammonium lactate (NH_4LAC) purchased from Sigma-Aldrich were used in this study as model solutions. These chemicals were dissolved directly in deionized water to the specified concentration (5 g/L lactic acid equivalent). This equivalent mass concentration of lactic acid resulted in different pH values of the solution, e.g., 4, 4, and 9 for CaLAC, NaLAC, and NH_4LAC solutions,

respectively. To obtain the specific tested pH at 4 and 6, the pH of the model solution was adjusted by 5 M NaOH or 1 M H_2SO_4. The concentrations of the lactate species at equilibrium (both free lactic acid and its salts) were dependent on the pH. The following stoichiometry describes the presence of lactate species mimicking those that appear in the fermentation processes.

When $CaCO_3$ was used for pH control during the fermentation, both lactic acid and calcium lactate were present in the solution.

$$2CH_3CHOHCOOH + CaCO_3 \rightleftharpoons (CH_3CHOHCOO)_2Ca + H_2O + CO_2$$

When NaOH was used for pH control during the fermentation, both lactic acid and sodium lactate were present in the solution.

$$CH_3CHOHCOOH + NaOH \rightleftharpoons (CH_3CHOHCOO)Na + H_2O$$

When NH_4OH was used for pH control during the fermentation, both lactic acid and ammonium lactate were present in the solution.

$$CH_3CHOHCOOH + NH_4OH \rightleftharpoons (CH_3CHOHCOO)NH_4 + H_2O$$

Fermentation broth preparation

Lactate fermentation broth was prepared from the cultivation of *Bacillus coagulans* BC-013 in a 5 L stirred fermentor. An active 24-h glucose–yeast extract–peptone slant was used to prepare the bacterial suspension. The bacterial suspension (1% inoculum size) was inoculated in a preculture flask containing the preculture medium. The preculture medium contained (per liter) 10 g glucose, 15 g yeast extract, 4 g NH_4Cl, 0.5 g KH_2PO_4, 0.5 g K_2HPO_4, 5 g $CaCO_3$, and 20 mL salt solution. The compositions of the salt solution consisted of (per 10 mL) 400 mg $MgSO_4 \cdot 7H_2O$, 20 mg $MnSO_4 \cdot 5H_2O$, 20 mg $FeSO_4 \cdot 7H_2O$, and 20 mg NaCl. The preculture flask was incubated at 50 °C, 200 rpm for 3 h. After that, the preculture flask was transferred into the 5 L stirred fermenter containing 2.5 L sterile preculture medium at 10% inoculum size. The fermenter was operated at 50 °C and agitated at 300 rpm with 1 vvm air. After 3 h, 0.5 L of the fermentation medium containing (per liter) 720 g glucose was

added into the fermenter. Aeration was then stopped. Three different bases, i.e., $CaCO_3$, NaOH, and NH_4OH, were used for pH control at 6.5. As a result, 3 different lactate salts, i.e., CaLAC, NaLAC, and NH_4LAC, were obtained in the fermentation. Fermentation was continued for 48 h until glucose depletion. Next, the fermentation broth was harvested. Cell biomass and soluble, neutral macromolecules such as proteins, sugars, etc. were removed from the fermentation broth by microfiltration and ultrafiltration. The cell-free broth obtained was later used in the 2-stage RO unit.

Designing and setting up the RO apparatus design

An in-house RO unit was constructed by a local Thai company (Icrotech Co., Ltd.) for use in this study. The apparatus set-up is illustrated in Fig. 1.

Please place Fig. 1 here.

Two RO membrane filtration units were subsequently connected with auxiliary instruments, including boost pumps, pressure gauges, flowmeters for feed, concentrate, and permeate, valves, and storage vessels. Negatively charged brackish water RO (BWRO) elements (DOW FILMTEC^{TM} BW60-1812-75) were installed at the first RO unit for recovering lactate from the model solution while allowing some salts to pass through the membrane at a rejection percentage of 97–99% (Table 1). In the second RO unit, positively charged seawater RO (SWRO) elements (DOW FILMTEC^{TM} SW30-2521) were installed for pre-concentrating recovered lactate obtained from the first RO unit where water was expelled. The rejection percentage was higher than 99.4% (Table 1). As a result, lactate was passed through the BWRO unit to the permeate side and later entered the SWRO unit. Lactic acid was then concentrated in the following SWRO unit and remained in the retentate.

Please place Table 1 here.

Batch operation was used in the first RO unit where the feed solution entered the unit and the permeate discharged from the first unit to enter the second RO unit later on. In the second RO unit, the retentate was recycled so that most of the remaining water in the retentate was discharged into the permeate. The maximum operating pressure for the BWRO

and SWRO units was set at 6 and 15 bar, respectively, owing to the pressure limit of apparatus housing, pumps, and piping systems.

Determining the operating conditions

To utilize the principle of RO in the recovery of lactic acid, osmotic pressure was introduced as a key factor determining the process conditions. The operating pressure was adjusted over the osmotic pressure of lactic acid so that lactic acid could pass through the BWRO membrane to the permeate, with other fermentation impurities remaining in the retentate. Eq. (1) expresses osmotic pressure as a function of molarity and temperature.

$$\pi = iMRT \quad (1)$$

where π is the osmotic pressure (bar), i is the dimensionless van't Hoff factor, M is the molar concentration of the solution/species of interest (in this case, lactic acid and its salts), R is the gas constant (0.082 L·bar/K·mol), and T is the temperature in K.

From Eq. (1), the osmotic pressures of the 3 model solutions, e.g., CaLAC, NaLAC, and NH_4LAC with 5 g/L lactate equivalent to be studied are 2.12 bar, 2.82 bar, and 2.81 bar, respectively. The osmotic pressure of lactic acid solution at 5 g/L is 1.41 bar.

The effects of pH and operating pressure on lactate separation efficiency at the BWRO unit were investigated. The lactate model solution (2 L) at 5 g/L LAC equivalent was adjusted to the tested pH values of 4 and 6 using either NaOH or H_2SO_4. The operating pressure was varied at 4 and 6 bar. Further increasing the concentration of the lactate model solution to higher than 5 g/L LAC equivalent resulted in higher osmotic pressure that exceeded the maximum pressure threshold in the BWRO apparatus (7 bar) and consequently led to reduced mass flux and separation efficiency. Therefore, the tested concentration of the model solution was limited at 5 g/L LAC equivalent.

The model solution (2 L) in the feed tank was fed into the first BWRO unit where free lactic acid was supposed to be separated from other impurity species, including Ca^{2+}, Na^+, NH_4^+, and SO_4^{2-} (in case the model solution was adjusted to the desired pH by H_2SO_4). The operating temperature was set at 30 °C. The apparatus was run until the collected volume of the permeate of 1.6 L was obtained. Samples (20 mL) were periodically collected from both permeate and retentate for analyses of free lactic acid concentration and ion species.

The permeate that left the BWRO unit and collected in the SWRO feed tank (1.6 L) was passed through the SWRO unit where water separation occurred, which resulted in lactate concentration in the retentate. The operating temperature was also set at 30 °C. The effects of pH and pressure on separation efficiency were determined. The tested pressure was set at 13 and 15 bar. At the first 5 min of operation, the retentate was recycled into the SWRO feed tank. After the recycling was stopped, the operation was continued until the permeate flux became zero. Samples (20 mL) were periodically collected for analyses of lactic acid and all the major remaining impurities.

Sample analyses

During the runs, samples from the permeate and retentate obtained in each RO unit were collected periodically for determining discharge volume, measuring pH, and analyzing substances that remained. For ion analyses, the collected samples were analyzed for concentrations of lactic acid and major impurity ions, including Ca^{2+}, Na^{+}, N (representing NH_4^{+}), SO_4^{2-}, Cl^{-}, P, and Mg^{2+}.

L-lactate ion in the sample was analyzed with a glucose–lactate analyzer (YSI2700, Yellow Spring Instruments Inc.) within the detection range of 0–2.67 g/L. The sample size of 25 μL was automatically injected into the reaction chamber where the enzymatic reaction occurred. The reading of L-lactate concentration was explained by the action of L-lactate oxidase immobilized at the membrane sensor.

An atomic absorption spectrophotometer was used to determine the metal concentration, including Ca^{2+} and Na^{+}, in the sample. The sample was prepared by dilution with 5% v/v HNO_3 solution. An air flame of 13.60 L/min along with an acetylene flame of 2 L/min was used for metal atomization of the sample before reading the atomic absorption with the atomic absorption spectrophotometer (AA280FS, Varian Inc.). Aqueous standard solutions were prepared by dilution to appropriate concentrations (2, 4, 6, and 8 mg/L for Ca^{2+}, and 5, 10, 20, and 30 mg/L for Na^{+}). The concentration of Ca^{2+} and Na^{+} in the sample was calculated by comparing the spectra with the standard calibration curves.

Nitrogen content was determined by the total Kjeldahl nitrogen technique. Nitrogen in the sample was first converted to NH_3 by metal-catalyzed acid digestion. The resulting NH_3 was separated from the sample by distillation. Released NH_3 was captured in a diluted H_2SO_4 solution. The result represented organic nitrogen after digestion and distillation in the sample.

The digestion reagent (catalyst) was prepared by mixing 134 g K_2SO_4 and 7.3 g $CuSO_4$ in 134 mL concentrated H_2SO_4. After that, the volume was made up to 1 L. Digestion reagent (50 mL) was added into the sample, and digestion proceeded for 30 min (Buchi, K499). Later, 50 mL boric acid was added into the reaction mixture as the absorbent solution during NH_3 distillation (Buchi, K375). Finally, NH_3 was determined by titration with a standard solution (Buchi, K376) [20].

Chloride was analyzed by the potentiometric method. The solubilized chloride ion in the sample was measured by a chloride ion-selective electrode during titration (Orion 720A, Labx Inc.). The sample was mixed with concentrated HNO_3 before dilution to the proper concentration. Titration was performed with a standard $AgNO_3$ solution as the reference.

Phosphorus was determined by the total phosphorus method using persulfate digestion. The sample (50 mL) was mixed with 11 N H_2SO_4 (1 mL). Next, dissolved and particulate phosphorus in the sample was digested with $(NH_4)_2S_2O_8$ (0.4 g) to convert phosphorus into orthophosphate (mixed and boiled to obtain a final volume of 40 mL). The orthophosphate concentration was measured by a spectrophotometer (Nova Spec 2, Pharmacia Biotech Inc.) using a standard calibration curve. The calibration curve was prepared from a standard phosphorus solution (0.3–1.2 mg P/L).

Sulfate ion in the sample was determined by the turbidimetric method. Sulfate ion present in the sample was converted into a $BaSO_4$ suspension under controlled conditions. The sample (80 mL) was mixed with 20 mL buffer solution containing (per liter) 30 g $MgCl_2{\cdot}6H_2O$, 5 g $CH_3COONa{\cdot}3H_2O$, 1 g KNO_3, and 20 mL acetic acid (99%). Then, $BaCl_2$ was added into the reaction mixture to obtain $BaSO_4$ precipitate. The turbidity was measured by a spectrophotometer (2100P, HACH). The concentration was determined using the calibration curve of the standard sulfate solution [20].

Investigating the performance of the 2-stage RO unit

The performance of the 2-stage RO unit was evaluated using 6 criteria: mass flux of lactic acid, lactic acid separation, ion separation, lactic acid recovery, overall recovery, and purity.

The mass flux of lactic acid (J_{LA}) at the BWRO unit was calculated by the following equation.

$$J_{LA} = \frac{m_{LA,BWP}}{A \cdot t} \quad (2)$$

where $m_{LA,BWP}$ is the lactic acid mass (g) passing through the membrane, A is effective membrane surface area (m^2), and t is time (h).

The efficiency of the BWRO unit to separate lactic acid from other ions can be explained by lactic acid separation (S_{LA}) in percentage defined by Eq. (3).

$$S_{LA} = \frac{m_{LA,BWP}}{F_{LA}} \cdot 100 \quad (3)$$

where $m_{LA,BWP}$ is the lactic acid mass (g) passing through the BWRO unit and F_{LA} is the initial mass of lactic acid present in the feed solution (g).

The ion (i) leakage at the BWRO unit can be described by the separation percentage (S_i) as seen in Eq. (4).

$$S_i = \frac{m_{i,BWP}}{F_i} \cdot 100 \quad (4)$$

where $m_{i,BWP}$ is the mass of ion i (g) moving through the BWRO unit and F_i is the initial mass of the ion (g) present in the feed solution.

The efficiency of the SWRO unit to pre-concentrate lactic acid can be represented by lactic acid recovery in percentage (R_{LA}) described by Eq. (5).

$$R_{LA} = \frac{C_{LA,SWF} - C_{LA,SWP}}{C_{LA,SWF}} \cdot 100 \quad (5)$$

where $C_{LA,SWF}$ and $C_{LA,SWP}$ are lactic acid concentrations (g/L) present in the feed solution entering the SWRO unit and the permeate leaving the SWRO unit.

The overall recovery ($R_{overall}$) of lactic acid product obtained from the 2-stage RO unit can be described by Eq. (6).

$$R_{overall} = S_{LA} \cdot R_{LA} \cdot 100 \quad (6)$$

where S_{LA} and R_{LA} were defined from Eqs. (3) and (5), respectively.

The purity of lactic acid product (P_{LA}) obtained from the 2-stage RO unit can be described by the mass ratio of lactic acid and the total ions that remained in the retentate of the SWRO unit (Eq. (7)).

$$P_{LA} = \frac{m_{LA,SWR}}{m_{T,SWR}} \cdot 100 \quad (7)$$

where $m_{LA,SWR}$ and $m_{T,\,SWR}$ represent the mass of lactic acid product and the total mass of ions that remained in the retentate leaving the SWRO unit.

Results and Discussion

Lactate separation at the BWRO unit

A feed solution of different lactate salts, including CaLAC, NaLAC, and NH_4LAC, was prepared at an equivalent lactate concentration of 5 g/L. To obtain the specific tested pH at 4 and 6, NaOH and H_2SO_4 were added into the solution to adjust to the desired tested pH, which eventually resulted in changes in the molar concentration of chemical ions present in the model solutions (Table 2).

Please place Table 2 here.

The obtained model solutions were then transferred into the feed tank to be pumped into the BWRO unit at different operating pressures (4 and 6 bar) where lactic acid presumably passed through whereas the other cations remained in the retentate. Fig. 2 shows the lactate mass flux passing through the BWRO membrane. The lactate mass flux increased with increasing operating pressure. It appears that the pH strongly influenced lactate transport through the BWRO membrane for CaLAC and NaLAC. On the other hand, pH showed less effect on lactate transport when compared with the operating pressure for NH_4LAC.

Please place Fig. 2 here.

The separation efficiency of the BWRO unit is expressed by Eqs. (3) and (4) and displayed in Fig. 3. It was observed that the operating pressure exhibited a strong effect on lactate separation in the BWRO unit. High lactate separation efficiency (% lactate passage) was obtained from all 3 model solutions at 6 bar regardless of changes in pH compared with the runs using an operating pressure of 4 bar. It was suggested that increasing the operating pressure from 4 to 6 bar improved lactate separation owing to the larger difference in operating pressure and the osmotic pressure of lactic acid generating a larger driving force across the membrane, which eventually resulted in a higher diffusion rate (high lactate flux as seen in Fig. 2). Operating pressures higher than the osmotic pressure of the solution resulted in an increasing mass flux throughout the membrane and thus the separation efficiency [21]. It should be noted that the osmotic pressure of the solution was increased with increasing concentration of the feed solution [22]. Therefore, operation at a certain pressure with varied feed concentrations resulted in a different permeate flux, and eventually lactate separation efficiency, in the 3 model solutions studied.

Please place Fig. 3 here.

From Fig. 3, pH was found to be responsible for lactate separation in the BWRO unit. This was related to the amount of total ions present in the feed solution, which played a role in mass transport across the membrane (Table 2). Liew et al. claimed that as the ionic strength of the feed solution increased, the permeate flux decreased as a result of increases in osmotic pressure and viscosity [23]. It was observed that the higher total ion concentration lowered the lactate flux (Figs. 2 and 3). At the same operating pressure, higher permeate flux resulting in significantly higher lactate separation at the BWRO unit was achieved at a lower pH with a rapid diffusion rate (pH 4 compared with pH 6) in the case of CaLAC and NaLAC feed solutions, when the total ion concentration of the feed solution was lower (Table 2). On the other hand, in the case of NH_4LAC, slightly increasing permeate flux and lactate separation were obtained at pH 6. This was presumably due to the slight change in total ion concentration, resulting in a similar ionic strength between the 2 pH values studied. The findings in this work confirmed that the pH and the total ion concentration of the feed solution played a role in controlling permeate flux, and thus separation efficiency, at the BWRO unit.

Ion rejection by the BWRO membrane

As previously mentioned, the separation of lactate from other ions was expected at the BWRO unit. Nonetheless, not only lactate species but also calcium, sodium, and ammonium ions could pass through the BWRO membrane (Fig. 2). Several interaction mechanisms of salt passage through the membrane have been investigated, including convection, diffusion, and charge repulsion. It was claimed that both membrane charge and feed ionic strength played a significant role in salt rejection [24]. When a typical feed solution interacted at the surface of the negatively charged membrane, the ion shift was generated at the boundary between the membrane and the solution, resulting in an electrical potential known as the Donnan exclusion effect [22]. In the case of uncharged solutes such as undissociated lactic acid, solution transport mainly occurred through diffusion and convection. The larger the difference between the operating pressure and the osmotic pressure, the larger the percentage of undissociated lactic acid that passed through the BWRO membrane. When lactic acid species were present in the dissociated form at an operating pH higher than the pK_a value (3.86), the Donnan exclusion effect governed the transport of ion species through the BWRO membrane [25]. Thus, higher lactate rejection was observed in all 3 model solutions at pH 6 owing to a larger electric repulsive force by the negatively charged surface (Fig. 3).

Considering the passage of Ca^{2+}, Na^{+}, NH_4^{+}, and H^{+} through the BWRO membrane, these cations typically bind at the membrane surface. The higher the pH, the more the dissociated lactate and the more the negatively charged membrane brings larger cations to the membrane surface [21]. It was suggested that the larger ions had lower diffusion rates and thus were expected to have lower concentrations in the permeate. Size controlled ion diffusion, and the ability of ions to form hydrogen bonds with the carbonyl group of the polyamide membrane facilitated the passage of such ions [22,23]. In addition, Tu et al. and Zaidi et al. confirmed that salt rejection by the BW30 membrane was dominated mostly by size exclusion [26,27]. Thus, in our work, most of the Ca^{2+} ions were retained whereas Na^{+} and NH_4^{+} apparently passed through the BWRO membrane.

Water permeability and solute rejection at the SWRO unit

Lactate concentration was determined in the SWRO unit under different operating pressures. After passing through the BWRO unit, the model solution was passed through and

recirculated in the SWRO unit for 5 min. The sample was collected for analyses of lactate in both the retentate and permeate. The performance of the SWRO unit in terms of lactate recovery and water permeation is shown in Table 3.

Please place Table 3 here.

Slightly increasing the pressure from 13 to 15 bar did not result in significant changes in SWRO performance. A slight increase in lactate concentration at the retentate with a higher water permeable flux was obtained at 15 bar. From Table 3, it is apparent that a relatively high rejection percentage of 95-99% was obtained at the SWRO unit operated at 13 bar. Therefore, running SWRO at this pressure not only gave an increasing concentration of lactic acid product at the retentate, but the operating cost could also be reduced [28]. Although the operating pressure used in this study did not show a significant effect on lactate recovery owing to the limited applied pressure to the apparatus up to 15 bar, it is believed that with higher operating pressure, higher lactate rejection rate and water flux should have been obtained, and eventually resulting in increasing concentration of lactic acid product at the retentate [28].

A typical RO operation involved the removal of inorganic and organic salts from the aqueous solution [29]. The SWRO membrane used in this work was the positively charged membrane containing free amine groups; therefore, high cation rejection was expected, especially at the lower pH (pH 4) when the feed solution was more protonated and lactic acid was present more in the undissociated form. Similar to observations in the BWRO unit, evidence of some NH_4^+ leaking out from the SWRO membrane could be explained by hydrogen bonding to the carbonyl group of the polyamide membrane facilitating the passage of NH_4^+ through the permeate although Ca^{2+} and Na^+ ions were strongly rejected because of the repulsive force of the positively charged surface [22,23]. Evidence of high rejection percentages of both cations (Ca^{2+}, Na^+, and NH_4^+) and lactate ions confirmed that the SWRO unit was successfully utilized to concentrate lactate at the retentate by expelling water through the membrane (Table 3).

Total mass balance and efficiency of lactate recovery at the 2-stage RO units

Fig. 4 presents the total mass balance over the 2-stage RO units. The first BWRO unit was considered as the key operating unit where lactate ions were separated from the cations, and the second SWRO unit was for concentrating the product remaining in the retentate.

Please place Fig. 4 here.

From the 3 model solutions studied, it was found that more than 50% of lactic acid from the feed stream was recovered from the 2-stage RO units (Table 4). Compared with the other 2 feed solutions, when the feed stream was CaLAC, a lactic acid purity of 99.2% was obtained. Nonetheless, the total recovery seemed to be slightly low (50.5%). It should also be noted that the highest lactic acid purity was obtained with the lowest recovery percentage.

Please place Table 4 here.

In addition, the efficiency of the 2-stage RO unit was tested with the actual lactic acid fermentation broth. The fermentation broths, including CaLAC broth, NaLAC broth, and NH_4LAC broth, primarily passed through the microfiltration and ultrafiltration units where cells and proteins were separated. The solutions were then diluted to obtain the equivalent concentration of lactic acid of 5 g/L before entering the RO units operated at optimized conditions determined before allowing lactic acid recovery and purification. Table 5 presents the efficiency of the 2-stage RO units constructed in this study on lactic acid separation and purification from the actual fermentation broths. Compared with the model solutions, the overall lactate recovery was similar whereas the purity was lower.

Please place Table 5 here.

Various ions present in the actual fermentation broth were claimed to be responsible for the lower purity (Fig. 5). The amount of total ions present in the feed fermentation broth was higher than that of the model solution; therefore, the Donnan exclusion effect was lowered, resulting in increasing ion passage across the BWRO membrane [24].

From the findings in this study, it can be presumably concluded that the membrane based process to recover and purify lactic acid from the fermentation broth has 2 major advantages. The first one is that no pretreatment is required for the cell-free fermentation broth before entering the 2-stage RO unit to recover, purify, and concentrate lactic acid. In

general, pretreatment of the cell-free fermentation broth by acidification using H_2SO_4 is necessary for lactate recovery by the typical ion exchange resin based process. Furthermore, using the typical ion exchanger to separate lactic acid from the fermentation broth requires 3 main steps including feed stream loading (adsorption), washing (to remove unbound solution from the resins), and lactic acid elution by proper eluant (desorption) [8]. This resulted in the increasing consumption of chemicals, wastewater treatment, and eventually dilution of the fermentation broth after acidification. Secondly, without pretreatment of the cell-free fermentation broth and applying the 2-stage RO unit for lactic acid recovery, the volume of cell-free fermentation broth remained unchanged. Therefore, the downstream equipment sizing can be smaller compared with the typical downstream process using ion exchange resins. Although the broth had to be diluted to 5 g/L before entering the 2-stage RO unit, the performance of this unit to recover, pre-purify, and pre-concentrate lactic acid was evident. This strongly indicated the beneficial outcome of this process, especially when we could operate without the pressure limit as experienced in this work with our in-house apparatus.

Please place Fig. 5 here.

It is suggested that lactic acid loss in the retentate at the BWRO unit can be reduced by stream recycling at the feed tank. In addition, to increase the purity of lactic acid product, the retentate from the SWRO unit is recommended to pass through another membrane unit, i.e., a nanofiltration unit, to eliminate the remaining trace ions. By selecting the proper membrane, it is believed that the purity of lactic acid product can be increased [30]. From the findings of this study, it can be claimed that the 2-stage RO membrane process has for the first time been reported as a simple operation but effective in recovering and purifying lactic acid from the fermentation broth.

Conclusions

The in-house 2-stage RO unit constructed in this study was used to recover and purify lactic acid. The acceptable amount of free lactic acid recovered with sufficiently high purity was obtained under optimized operating conditions. This unit was applicable to different fermentation broth solutions, including calcium lactate, sodium lactate, and ammonium lactate. Although the operating pressure was set at a higher value than the lactate osmotic pressure, lactate rejection was still observed at the BWRO unit where most of the lactate was

expected to pass through the membrane while other ions remained in the retentate. It was found that the total ion concentration of the feed solution and the operating pH both played a crucial role in controlling ion leakage across the membrane, thereby controlling both lactate recovery and purity of this RO membrane system. From the results obtained in this study, it is suggested that by coupling this 2-stage RO unit with the upstream fermentation and primary cell and protein separation (microfiltration and ultrafiltration) units, the simple design of continuous fermentation and lactic acid recovery to achieve high productivity in long-term operations is feasible.

Acknowledgments

This work was conducted under the University–Industry Linkage Program with the collaboration of researchers from Chulalongkorn University and PTT Global Chemical Public Company Limited. Partial support by Grant for International Research Integration: Research Pyramid, Ratchadapiseksomphot Endowment Fund (GCURP_58_01_33_01) and Thailand Research Fund via the Distinguished Research Professor Grant (DPG5880003) was highly appreciated. Research facility supported by Chulalongkorn Academic Advancement into its 2nd Century Project (CUAASC) is highly acknowledged.

References

[1] A.N. Vaidya, R.A. Pandey, S. Mudliar, M.S. Kumar, T. Chakrabarti, S. Devotta, Crit. Rev. Environ. Sci. Technol. 35 (2005) 429-467.

[2] K. Hetenyi, A. Nemeth, B. Sevella, Chem. Eng. Process. 50 (2011) 293-299.

[3] S. Nakano, C.U. Ugwu, Y. Tokiwa, Bioresour. Technol. 104 (2012) 791-794.

[4] P.F. Stanbury, A. Whitaker, S. J. Hall, In Fermentation Technology Handbook. Pergamon Press, Oxford (2017) p. 619.

[5] Y. Li, A. Shahbazi, C.T. Kadzere, Food. Eng. (2006) 574-580.

[6] M.A.A. Rahman, Y. Tashiro, K. Sonomoto, Biotechnol. Adv. (2013) 877–902.

[7] P. Pal, J. Sikder, S. Roy, L. Giorno, Chem. Eng. Process. 48 (2009) 1549–1559.

[8] C. Rodrigues, L.P.S. Vandenberghe, A.L. Woiciechowski, J. de Oliveira, L.A.J. Letti, C.R. Soccol, Biotechnol. Bioeng. (2017) 543-556.

[9] P. Khunnonkwao, P. Boontawan, D. Haltrich, T. Maischberger, A. Boontawan, Process. Biochem. 47 (2012) 1948-1956.

[10] J.H. Kim, J.-G. Na, H.J. Shim, Y.K. Chang, J. Membr. Sci. 396 (2012) 110-118.

[11] E.G. Lee, S.H. Kang, H.H. Kim, Y.K. Chang, Biotechnol. Bioproc. Eng. 11 (2006) 313–318.

[12] K.L. Wasewar, A.A. Yawalkar, J.A. Moulijn, V.G. Pangarkar, Ind. Eng. Chem. Res. 43 (2004) 5969-5982.

[13] H.G. Joglekar, I. Rahman, S. Babu, B.D. Kulkari, A. Joshi, Sep. Purif. Technol. 52 (2006) 1-17.

[14] T. Ghaffar, M. Irshad, Z. Anwar, T. Aqil, Z. Zulifqar, A. Tariq, M. Kamran, N. Ehsan, S. Mehmood, J. Radiat. Res. Appl. Sci. (2014) 222-229.

[15] C.S.L. Garzon, A.J.J. Straathof, Biotechnol. Adv. (2014) 873-904.

[16] B. Wojtyniak, J. Kołodziejczyk, D. Szaniawska, Chem. Eng. (2016) 28-36.

[17] C. Bellona, J.E. Drewes, P. Xu, G. Amy, Water. Res. 38 (2004) 2795-2809.

[18] S.S. Sablani, R.M. Shafiur, A.K. Datta, A.S. In Food and Bioprocesses Modeling Techniques Handbook, CRC press (2007).

[19] K. Kosutic, B. Kunst, Desalination. 142 (2002) 47-56.

[20] D.E Andrew, S.C. Lenore, W.R Eugene, E.G. Arnold, In Water and Wastewater Handbook, A.H.F Mary Ed., American Public Health Association and Water Environment Federation, Washington (2005), p. 131.

[21] V. Freger, T.C. Arnot, J.A. Howell, J. Membr. Sci. 178 (2000) 185-193.

[22] M.I. Gonzalez, S. Alvarez, F.A. Riera, R. Alvarez, Desalination. 228 (2008) 84-96.

[23] M.K.H. Liew, S. Tanaka, M. Morita, Desalination. 101 (1995) 269-277.

[24] C. Bartels, R. Franks, S. Rybar, M. Schierach, M. Wilf, Desalination. 184 (2005) 185-195.

[25] P. Dey, L. Linnanen, P. Pal, Desalination. 288 (2012) 47-57.

[26] K.L. Tu, L.D. Nghiem, A.R. Chivas, Chem. Eng. J. 168 (2011) 700-706.

[27] S.M.J. Zaidi, F. Fadhillahb, Z. Khanc, A.F. Ismail, Desalination. 368 (2015) 202-213.

[28] M.H. Oo, L. Song, Desalination. 246 (2009) 605-612.

[29] R.A. Diltz, T.V. Marolla, M.V. Henley, L. Li, Bioresour. Technol. 98 (2007) 686-695.

[30] M.-S. Kim, J.-G. Na, M.-K. Lee, H. Ryu, Y.-K. Chang, J.M. Triolo, Y.-M. Yun, D.-H. Kim. Water. Res. 96 (2016) 208-216.

Figure Captions

Fig. 1 Schematic diagram of the in-house RO unit for recovery and purification of lactic acid.

Fig. 2 Lactate flux at the permeate of the BWRO unit operated at 30 °C. CaLAC, NaLAC, and NH_4LAC containing the initial lactate equivalent of 5 g/L at different pH values were passed through the BWRO unit at different operating pressures.

Fig. 3 Lactic acid separation at the BWRO unit operated at 30 °C. CaLAC, NaLAC, and NH_4LAC with the initial lactate equivalent of 5 g/L were passed through the BWRO unit at different operating pressures (a: 4 bar; b: 6 bar).

Fig. 4 Total mass balance over the 2-stage RO units. The model solution (a: CaLAC; b: NaLAC; c: NH_4LAC) was fed into the apparatus operated under optimized pH and pressure.

Fig. 5 Percentage of ion leakage into the permeate. The different cell-free lactate broth solutions, including CaLAC broth, NaLAC broth, and NH_4LAC broth, entered the BWRO unit operated under the optimized conditions previously determined.

Table 1 Characteristics of DOW FILMTEC™ RO membrane elements used in this study.

Product name	DOW FILMTEC™ BW60	DOW FILMTEC™ SW30
Model	BW60-1812-75	SW30-2521
Membrane type	Polyamide thin-film composite	Polyamide thin-film composite
Membrane surface area (m^2)	0.77	1.20
Membrane surface charge	Negative	Positive
Dimension (mm × mm)	44.5 × 305	63.5 × 533
Permeate flow rate (L/h)	12	45
Average NaCl rejection (%)	97–99	99.4
Maximum applied pressure (bar)	10	55
Maximum applied temperature (°C)	45	45
pH range	2–11	2–11

Table 2 Molar concentration of chemical species present in different lactate model solutions containing a lactic acid equivalent of 5 g/L at pH 4 and pH 6.

Species (mol/L)	pH 4			pH 6		
	CaLAC	NaLAC	NH_4LAC	CaLAC	NaLAC	NH_4LAC
Total	0.056	0.056	0.056	0.056	0.056	0.056
LAC^-	0.024	0.025	0.018	0.024	0.025	0.018
Free $LA_{(cal)}$	0.032	0.031	0.038	0.032	0.031	0.038
$LAC^-_{(cal)}$						
Ca^{2+}	0.016	-	-	0.016	-	-
Na^+	-	0.031	-	0.050	0.086	-
NH_4^+	-	-	0.038	-	-	0.038
SO_4^{2-}	-	-	0.015	-	-	0.007
H_3O^+	10^{-4}	10^{-4}	10^{-4}	10^{-6}	10^{-6}	10^{-6}
OH^-	10^{-10}	10^{-10}	10^{-10}	10^{-8}	10^{-8}	10^{-8}
Total ions	0.0721	0.0821	0.1091	0.1220	0.1420	0.1010

Table 3 Effect of operating pressure on lactate recovery at the SWRO unit. Permeates from the BWRO unit passed through the SWRO unit at 30 °C where water was expelled yielding concentrated lactic acid solution.

Starting feed	CaLAC	NaLAC	NH_4LAC
At 13 bar			
Lactate at permeate (g/L)	0.05	0.20	0.09
Lactate at retentate (g/L)	6.45	9.68	7.97
Lactate rejection (%)	98	95	99
Cation rejection (%)	99	99	99
Water flux (L/m^2 h)	11.4	10.8	8.4
At 15 bar			
Lactate at permeate (g/L)	0.07	0.22	0.11
Lactate at retentate (g/L)	7.47	11.50	9.54
Lactate rejection (%)	98	95	100
Cation rejection (%)	99	99	90
Water flux (L/m^2 h)	13.2	12.0	10.8

Table 4 Overall recovery and purity of lactic acid from the 3 different model solutions after passing through the 2-stage RO units operated at optimized conditions.

Feed solution	CaLAC	NaLAC	NH_4LAC
Operating conditions	pH 4, 6 bar at BWRO pH 4.6, 15 bar at SWRO	pH 4, 6 bar at BWRO pH 4.5, 15 bar at SWRO	pH 6, 6 bar at BWRO pH 5.9, 15 bar at SWRO
Total lactic acid recovery	50.5%	66.4%	70.3%
Purity	99.2%	89.9%	89.7%

Table 5 Performance of the 2-stage RO unit to recover and purify lactic acid from the fermentation broth.

Feed solution	CaLAC broth	NaLAC broth	NH_4LAC broth
Operating conditions	pH 6, 6 bar at BWRO pH 5.39, 15 bar at SWRO	pH 6, 6 bar at BWRO pH 5.81, 15 bar at SWRO	pH 6, 6 bar at BWRO pH 5.96, 15 bar at SWRO
Lactate passage at BWRO	54.2%	66.9%	72.0%
Lactate rejection at SWRO	100%	97.4%	99.6%
Total lactic acid recovery	54.2%	65.2%	71.7%
Purity	86.1%	73.3%	74.7%

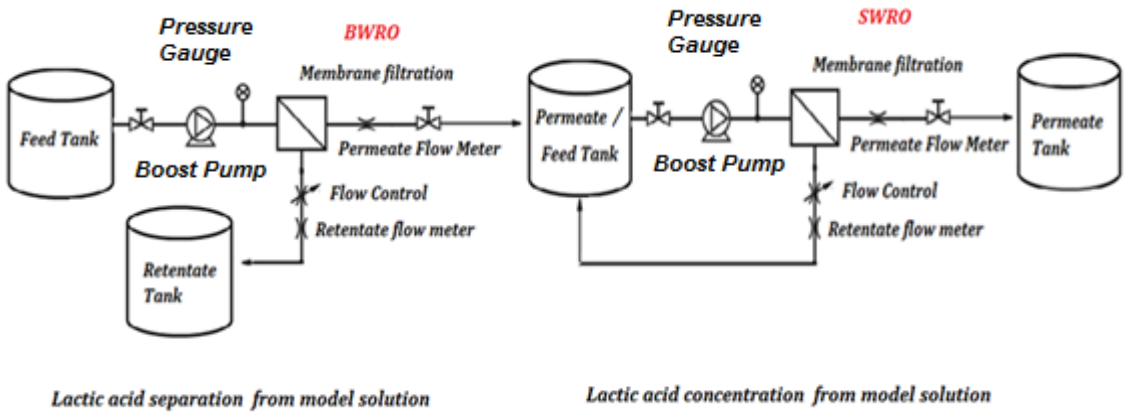
Pressure Gauge
BWRO
Membrane filtration
Feed Tank
Boost Pump
Permeate Flow Meter
Flow Control
Retentate flow meter
Retentate Tank
Lactic acid separation from model solution
Pressure Gauge
SWRO
Membrane filtration
Permeate / Feed Tank
Boost Pump
Permeate Flow Meter
Permeate Tank
Flow Control
Retentate flow meter
Lactic acid concentration from model solution

Fig. 1

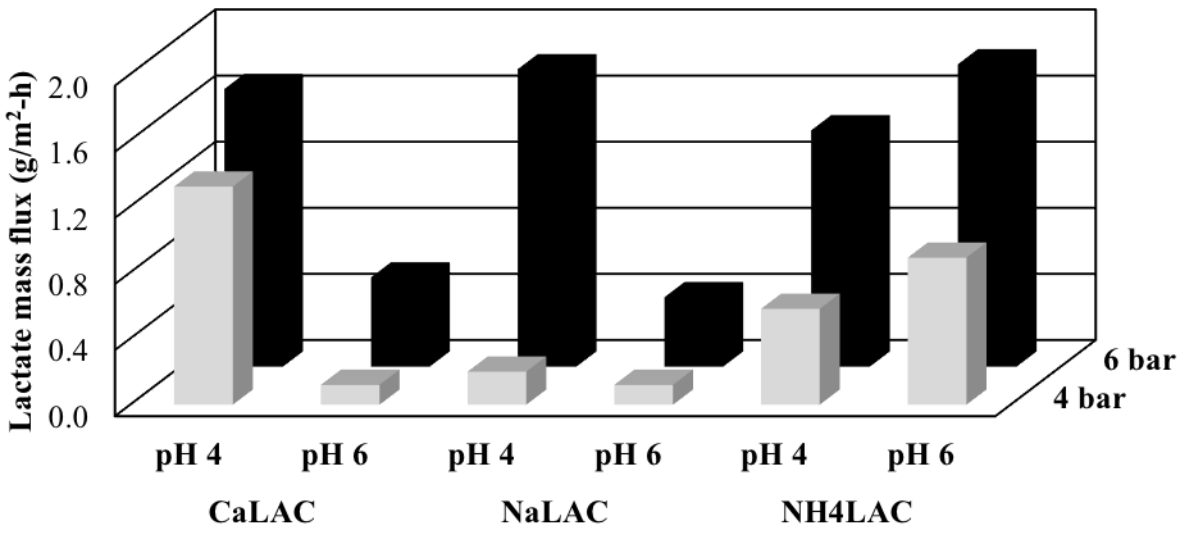
Lactate mass flux (g/m²-h)
2.0
1.6
1.2
0.8
0.4
0.0
6 bar
4 bar
pH 4
pH 6
pH 4
pH 6
pH 4
pH 6
CaLAC
NaLAC
NH4LAC

Fig. 2

a

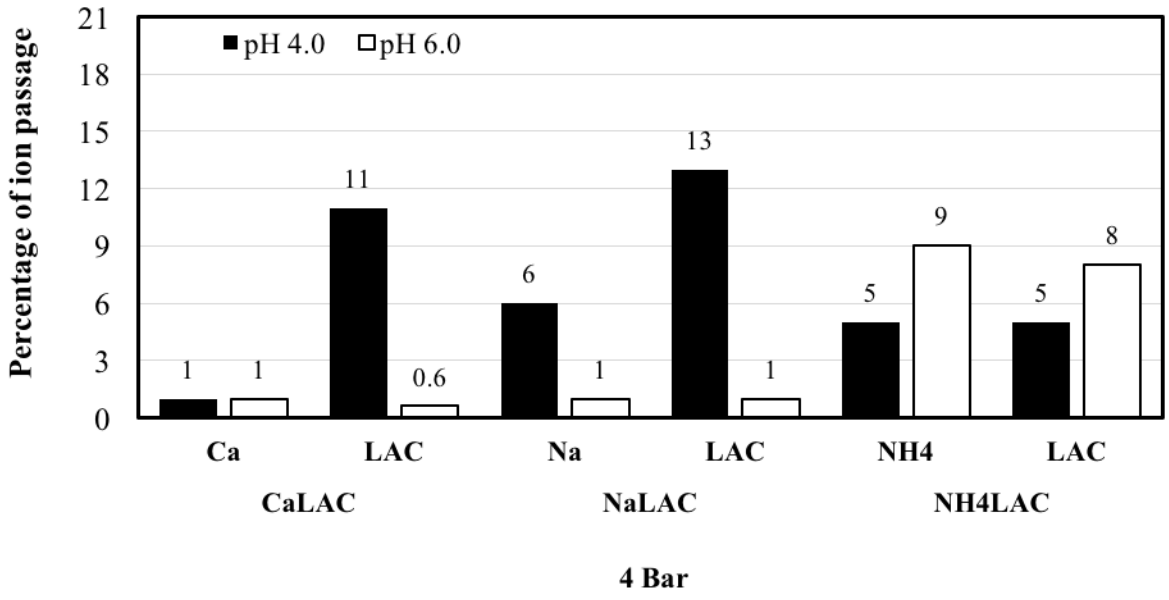
Percentage of ion passage
pH 4.0
pH 6.0
21
18
15
12
9
6
3
0
1
1
11
0.6
6
1
13
1
5
9
5
8
Ca
LAC
Na
LAC
NH4
LAC
CaLAC
NaLAC
NH4LAC
4 Bar

b

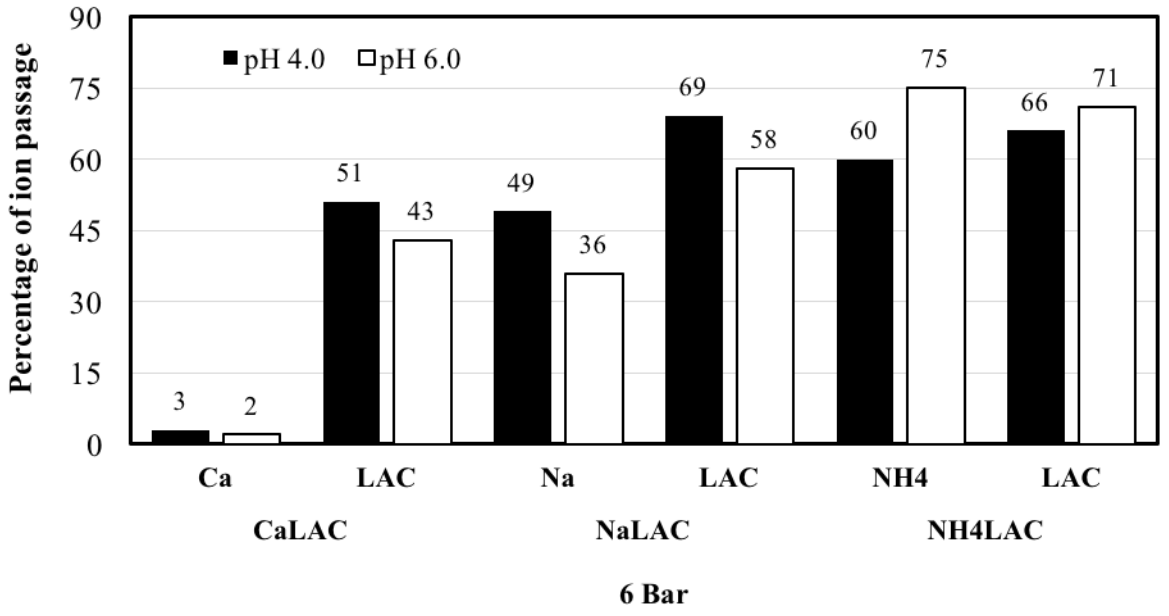
Percentage of ion passage
pH 4.0
pH 6.0
90
75
60
45
30
15
0
3
2
51
43
49
36
69
58
60
75
66
71
Ca
LAC
Na
LAC
NH4
LAC
CaLAC
NaLAC
NH4LAC
6 Bar

Fig. 3

a

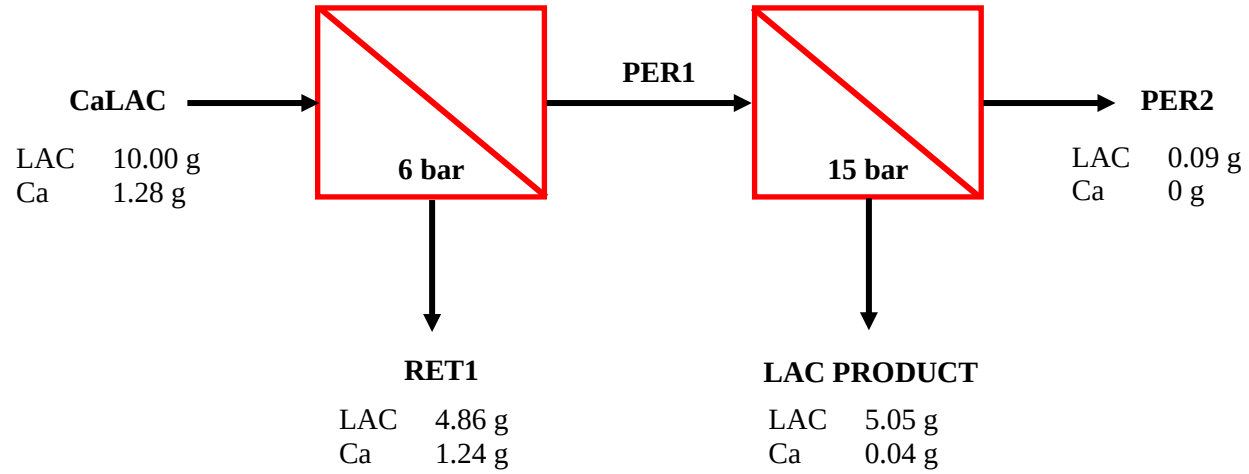
CaLAC
LAC 10.00 g
Ca 1.28 g
6 bar
PER1
15 bar
PER2
LAC 0.09 g
Ca 0 g
RET1
LAC 4.86 g
Ca 1.24 g
LAC PRODUCT
LAC 5.05 g
Ca 0.04 g

b

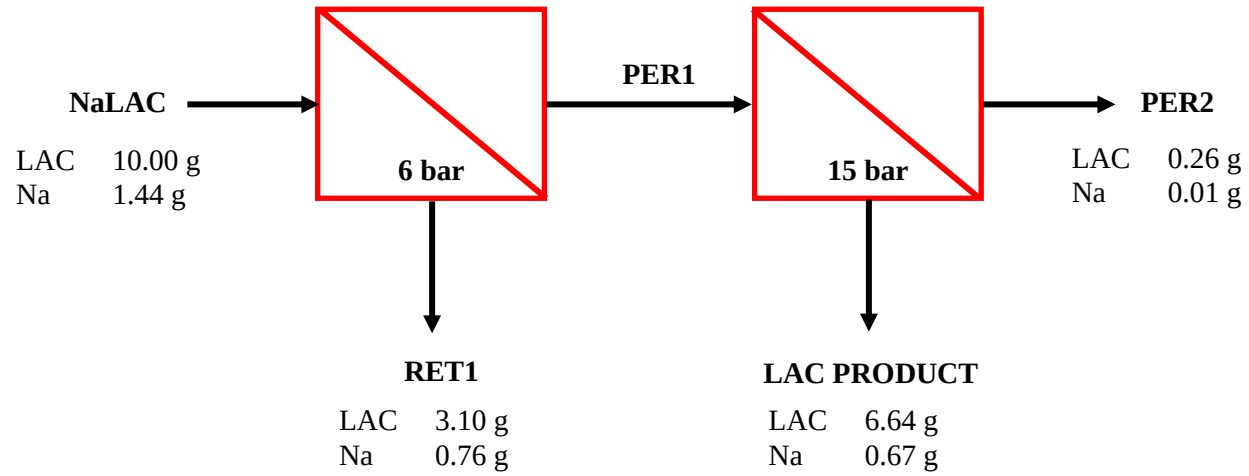
NaLAC
LAC 10.00 g
Na 1.44 g
6 bar
PER1
15 bar
PER2
LAC 0.26 g
Na 0.01 g
RET1
LAC 3.10 g
Na 0.76 g
LAC PRODUCT
LAC 6.64 g
Na 0.67 g

c

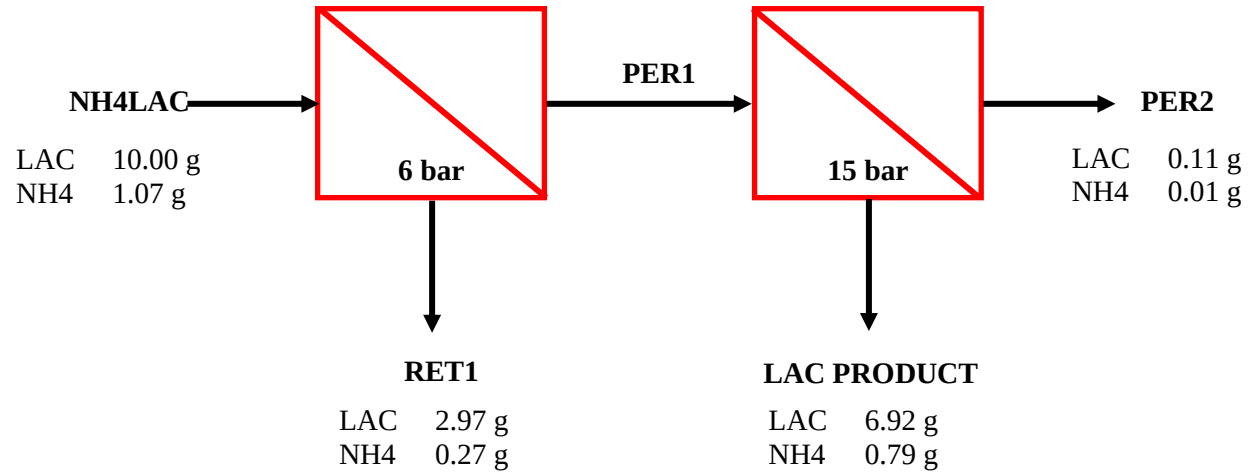
NH4LAC
LAC 10.00 g
NH4 1.07 g
6 bar
PER1
15 bar
PER2
LAC 0.11 g
NH4 0.01 g
RET1
LAC 2.97 g
NH4 0.27 g
LAC PRODUCT
LAC 6.92 g
NH4 0.79 g

Fig. 4

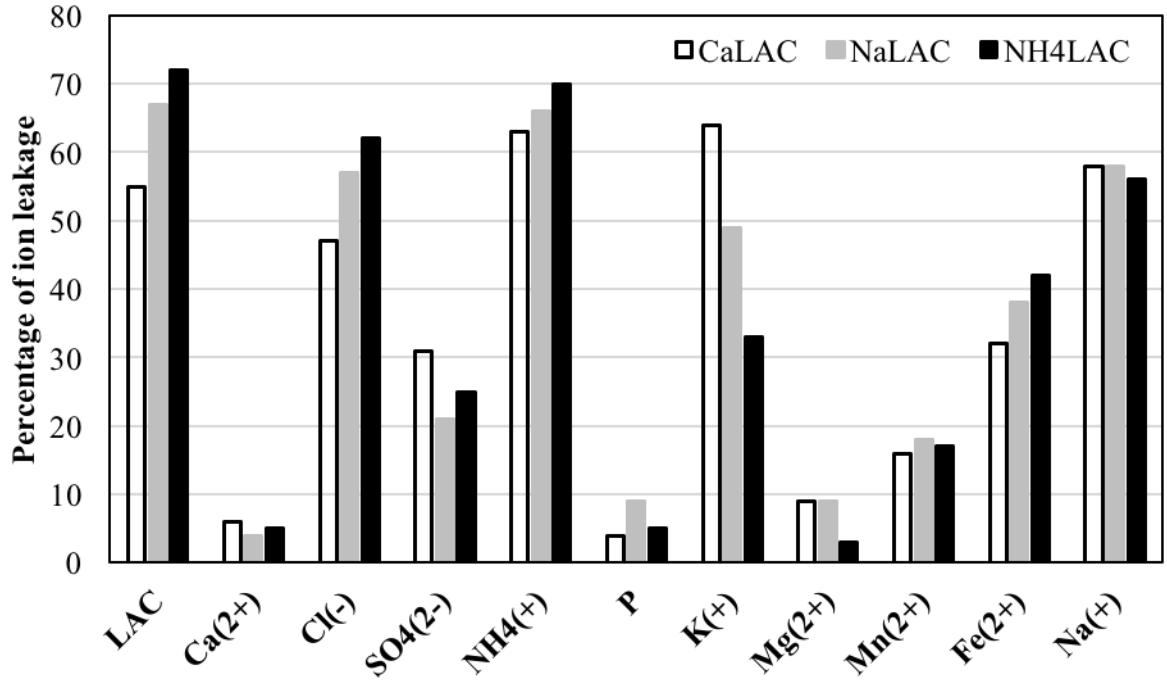
80
70
60
50
40
30
20
10
0
Percentage of ion leakage
CaLAC
NaLAC
NH4LAC
LAC
Ca(2+)
Cl(-)
SO4(2-)
NH4(+)
P
K(+)
Mg(2+)
Mn(2+)
Fe(2+)
Na(+)

Fig. 5

Journal of Environmental Chemical Engineering 5 (2017) 3115–3121

Contents lists available at ScienceDirect

Journal of Environmental Chemical Engineering

journal homepage: www.elsevier.com/locate/jece

Reduction of carbon dioxide via catalytic hydrogenation over copper-based catalysts modified by oyster shell-derived calcium oxide

Wilasinee Wisaijorn[a,c], Yingyot Poo-arporn[b], Pablo Marin[c], Salvador Ordóñez[c], Suttichai Assabumrungrat[d], Piyasan Praserthdam[d], Dang Saebea[a], Soipatta Soisuwan[a,*]

[a] Department of Chemical Engineering, Faculty of Engineering, Burapha University, 169 Long-Hard Bangsaen Road, Saensuk Sub-district, Muang District, Chonburi, 20131, Thailand
[b] Synchrotron Light Research Institute (Public Organization), 111 University Avenue, Muang District, Nakhon Ratchasima, 30000, Thailand
[c] Department of Chemical and Environmental Engineering, University of Oviedo, Julián Claveria s/n, 33006 Oviedo, Spain
[d] Center of Excellence in Catalysis and Catalytic Reaction Engineering, Department of Chemical Engineering, Faculty of Engineering, Chulalongkorn University, Patumwan District, Bangkok, 10330, Thailand

ARTICLE INFO

Keywords:
Methanol synthesis
Calcium oxide
Copper-based catalysts
Basicity

ABSTRACT

This research aims to investigate the effects of CaO and modified CaO on copper-based catalysts for methanol synthesis. The CaO and modified CaO were derived from oyster shell and employed as an additive in a zirconia-supported copper catalyst (Cu/ZrO_2). The physical and chemical properties of the catalysts were characterized by XRD, BET, CO_2-TPD, H_2-TPD and XANES. The addition of oyster shell-derived calcium oxide promoters to the catalysts significantly improved their chemical properties and methanol synthesis possibly owing to impurities and defects in the crystal structure of natural calcium oxide.

1. Introduction

The demand for fossil fuels has increased in the last few decades, especially in Asia. This results in the emission of carbon dioxide to the atmosphere, which accelerates global warming [1]. The capture and chemical transformation of this carbon dioxide into high-value products, such as methanol or dimethyl ether, has been extensively investigated. Carbon dioxide is a thermodynamically stable compound and, thereby, typically operated under a catalytic process. Since the stoichiometric equation for the synthesis of methanol produces fewer gas molecules and the reaction is highly exothermic [2], catalytic carbon dioxide hydrogenation can be enhanced under high pressure and low temperature [2,3]. In addition, the proper catalyst should provide high selectivity towards methanol so as to avoid considerable side products from a reverse water gas shift, such as carbon monoxide and hydrocarbons [4,5].

Several types of the catalysts have been studied under a range of pressures to optimize their methanol selectivity and to identify the catalytic function in the methanol pathway of interest [6–8]. Despite their identical compositions, the catalysts that were calcined at different temperatures led to different metal/oxide dispersions, which eventually caused variations in the final products and catalytic activities [9,10]. It was known that the methanol could selectively be synthesized by increasing the proportion of basic sites in the catalysts such as F-, Mg- or La-modified copper-based catalysts [11–13]. Incorporating La (up to 5%) into the copper-based catalyst enabled the CO_2 desorption temperature to reach c.a. 300 °C, making the methanol selectivity more favorable [12].

Calcium oxide, a highly abundant natural oxide, is capable of adsorbing the starting material, carbon dioxide, and possesses remarkably strong basic sites [14,15]. Calcium oxide has been applied in many processes, ranging from carbon dioxide storage [16] to biodiesel catalysis [17] to carbon monoxide synthesis via a reverse water gas shift [18]. In this work, calcium oxide was derived from the oyster shell and subsequently used as an additive in the preparation of the copper-based catalysts. Basicity of these calcium oxides were modified by titanium ethoxide ($Ti(OC_2H_5)_4$) [19]. The catalysts were characterized by N_2-physisorption, X-ray diffraction, temperature-programmed H_2 and CO_2 desorptions, and in situ measurement of the Cu K-edge X-ray Adsorption Near Edge Structure (XANES) spectrum following the thermally controlled H_2 reduction. Furthermore, the methanol synthesis over the copper catalysts with or without calcium oxide modification were extensively investigated.

* Corresponding author.
E-mail addresses: soipatta@eng.buu.ac.th, soipatta@buu.ac.th (S. Soisuwan).

http://dx.doi.org/10.1016/j.jece.2017.06.018
Received 13 April 2017; Received in revised form 27 May 2017; Accepted 11 June 2017
Available online 12 June 2017
2213-3437/ © 2017 Elsevier Ltd. All rights reserved.

2. Experimental

2.1. Preparation of copper-based catalysts and modification by calcium oxide

Calcium oxide was derived from the dried oyster shell that was mostly composed of cubic calcium carbonate. The shell was ground to sizes ranging from 250 to 300 μm and was calcined at 850 °C to obtain calcium oxide powder. The modification of calcium oxide was carried out by an incipient wetness impregnation of titanium ethoxide (Ti $(OC_2H_5)_4$) (Sigma-Aldrich) solution to adjust the basicity of the calcium oxide. Approximately 7 mol% Ti was dispersed onto calcium oxide. These calcium oxides were named CaO and CaO_Ti, and they were employed as additives at 10 wt% in Y-stabilized ZrO_2 supports (Tosoh ZrO_2, Nanyo Manufacturing Complex). Tosoh ZrO_2 powder was physically mixed with the resulting calcium oxide. The mixture was then gradually impregnated by a copper nitrate solution to obtain a 10 wt% copper-based catalyst. The catalyst was dried overnight and calcined at 650 °C for 3 h to obtain the products, namely, Cu/ZrO_2_CaO and Cu/ZrO_2_CaO_Ti. The physicochemical properties of all of the catalysts were investigated in comparison to copper-based catalysts modified either with commercial calcium oxide (Labochem) (Cu/ZrO_2_CaOcom) or without calcium oxide (Cu/ZrO_2).

2.2. Catalyst characterizations

Powder diffraction were investigated with an X-ray diffractometer (SEIMENS D5000) equipped with Cu-Kα radiation and a Ni filter to record the 2θ diffraction angle from λ = 0.154 nm. The N_2 physisorption at 77 K (liquid nitrogen temperature) was carried out by a Quantachrome NOVA 1200 to obtain the N_2 adsorption results at different relative pressures (P/P_0) in the range of 0.05–0.35. Prior to N_2 physisorption, the sample was outgassed at 300 °C for 3 h. A Micromeritics ChemiSorb 2750 instrument was used for temperature-programmed desorption (TPD) of H_2 and CO_2. The catalyst (0.5 g) was cleaned under a flow of helium for 1 h, then reduced under a flow of 50/50 H_2/N_2 for 6 h (30 ml/min, 400 °C), and finally saturated under a 50/50 H_2/N_2 mixture. To remove any physically adsorbed H_2, helium was flowed over the catalyst for 1 h. The temperature of H_2desorption was ramped from 100 to 800 °C at a rate of 10 °C/min, and the effluent gases were passed through a dry ice trap to remove water vapor. The desorption was detected by a thermal conductivity detector [11,13]. The temperature-programmed CO_2 desorption was run for the fresh catalyst, before or after the hydrogen reduction at 400 °C for 6 h, to determine the number of the basic sites and their strength. Prior to the CO_2 desorption, the catalyst was cleaned using a similar procedure to the H_2 desorption, and the saturation of CO_2 was operated at room temperature for 6 h. The system was heated to 800 °C after the removal of excess physically adsorbed CO_2. The reduced catalyst, was produced under the same condition as H_2-TPD [8,13]. The H_2-temperature programmed reduction (H_2-TPR) along with the in situ X-ray Absorption Near Edge Structure (XANES) spectroscopy was used to examine the reduction behavior of the copper-based catalysts modified by three types of calcium oxide. The in situ measurements of Cu K-edge XANES spectra were taken at BL2.2: TRXAS, SLRI, Thailand [20]. The catalyst was reduced under a 50/50 H_2/N_2 mixture using a gradual ramp of temperature to 400 °C (5 °C/min). The Cu K-edge XANES were recorded at room temperature and every 5 °C interval until 400 °C. The total heating period was 75 min and resulting spectra was taken for every 5 °C interval. The reduction temperature was held at 400 °C for 6 h where Cu K-edge XANES spectra were lastly performed. Linear combination fitting of Cu K-edge XANES was applied to estimate the phase fractions of $Cu^0/Cu^{1+}/Cu^2$.

2.3. CO_2 hydrogenation

A solid mixture of 0.5 g of the copper-based catalyst (80–100 μm) and 1.0 g of glass beads (250–300 μm) was mounted onto a stainless steel tubular fixed bed reactor. Prior to testing, the catalysts were reduced at 300 °C for 4 h. The CO_2 hydrogenation was tested at 250 °C and 30 bar for 4 h [GHSV 79,900 h^{-1} and $CO_2/H_2/N_2$, 9/27/9]. The reactor effluent was analyzed on-line by a gas chromatograph (HP Plot Q and MolSieve columns) equipped with flame-ionization and thermal conductivity detectors. The rate of methanol production was calculated from the fraction of CO_2 converted as follows:

$$\text{Rate of methanol production (mol } h^{-1} \text{ kg catalyst}^{-1}) = \frac{x_{CO_2} F_{CO_{2input}}}{w}$$

where, x_{CO_2}: fraction of carbon dioxide conversion to methanol
$F_{CO_{2input}}$: molar flow rate of carbon dioxide input (mol h^{-1}),
w : weight of catalyst (kg)

3. Results and discussion

3.1. X-ray diffraction (XRD) and specific BET surface area

The X-ray diffraction patterns of all catalysts are shown in Fig. 1. Peaks at 2θ = 30°, 35°, 50° and 60° corresponded to tetragonal zirconia [21]. A small peak at 38° was attributed to crystalline copper oxide although the catalyst was composed of only 10 wt% copper oxide. No significant crystalline signal of calcium species was observed, suggesting good dispersion of calcium species throughout the catalysts. All of the catalysts exhibit identical X-ray diffraction patterns and specific surface areas, indicating that they were comparable in physical properties and the catalytic properties were apparently dependent of the surface chemistry. The catalyst surface area in systems with additive-mixed supports improved over bare Tosoh-ZrO_2 systems, which only had 14 m^2/g.

3.2. Temperature programmed desorption (TPD)

The surface chemistry of the catalysts, both fresh and reduced ones, was characterized by the temperature-programmed H_2 and CO_2 desorption as shown in Figs. 2–4Figure 2 . The H_2 desorption (conducted after 6-h of reduction at 400 °C) shows the adsorption of hydrogen onto the catalyst structure over a wide range of temperatures. According to our previous results with the thermal gravimetric analysis [15], the weight decomposition of catalysts occurred only at 400 °C due to the loss of hydroxyl groups incorporated into the calcium species, and the catalyst weight itself was stable up to 800 °C. The decomposition of these hydroxyl groups disappeared during the 6 h-long hydrogen reduction at 400 °C. The broad signal located in the high temperature range (400–800 °C) was attributed to spillover hydrogen atoms bonding to the electronic surface of oxides, such as ZrO_2, CaO or modified CaO,

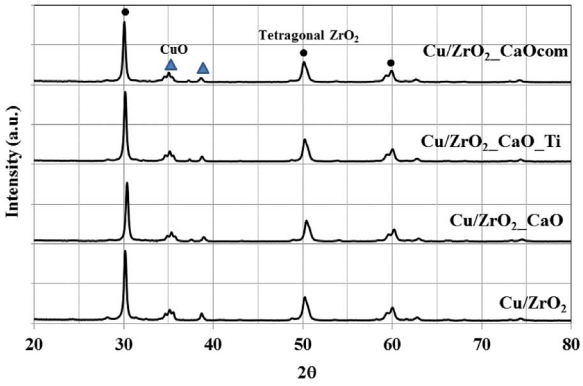

Fig. 1. X-ray diffraction patterns of fresh copper-based catalysts.

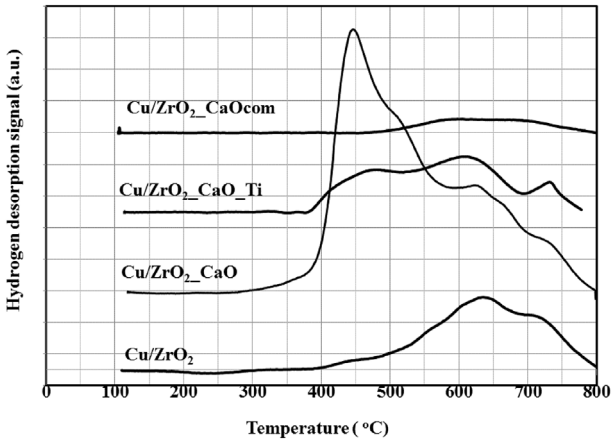

Fig. 2. Hydrogen temperature programmed desorption profiles after reduction at 400 °C for 6 h.

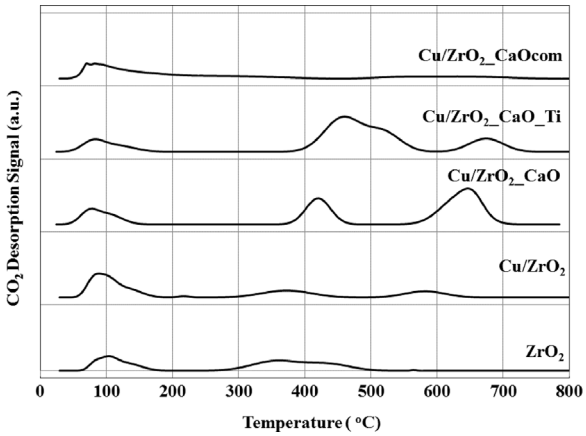

Fig. 3. CO_2 Temperature Programmed Desorption profiles of all fresh catalysts compared to ZrO_2 support.

as shown in Fig. 2 [13]. However, hydrogen adsorption was saturated at 100 °C and the desorption process was investigated up to 800 °C, so no hydrogen atoms were found to desorb from copper metal sites at low temperatures (< 100 °C). Cu/ZrO_2_CaO desorbed the more hydrogen from the active surface, 1.2 mmol g $catalyst^{-1}$, whereas Cu/ZrO_2_CaOcom, i.e. with commercial CaO, gave only 0.1 mmol g $catalyst^{-1}$. Surface defects in CaO derived from the oyster shell may facilitate the adsorption of hydrogen spillover compared to commercial CaO, which has fewer defects, as determined by S. Xia et al. and K. Prins [22,23].

The elements on the calcium oxide surface were determined by SEM-EDXS (Table 3). All of the catalysts showed a low-temperature CO_2 desorption at approximately 100 °C, similar to the Tosoh zirconium dioxide support, but this desorption was higher than that observed for the sole ZrO_2 support, suggesting that carbon dioxide adsorbed onto copper oxide [8]. However, this ability was lost after the reduction with hydrogen, as shown in Table 1. The CO_2-TPD profiles of the natural or commercial CaO-modified catalysts exhibited CO_2 desorption between 400 and 600 °C, as shown in Figs. 3 and 4 (below), while more CO_2 adsorption sites appeared above 600 °C. This indicated that CO_2 strongly bonded to the catalytic surface formed during hydrogen reduction. In contrast, the catalyst containing the commercial CaO showed no significant desorption of CO_2 at the high temperatures, indicating the lack of defect formation in crystalline CaO or in its amorphous structure. The structure of calcium oxide was rich in defects, including impurities, oxygen vacancies, and surface-level oxygen atoms, [24] which can strongly bond to carbon dioxide as monodentate or bidentate carbonates, as shown in Fig. 4 (below). However,

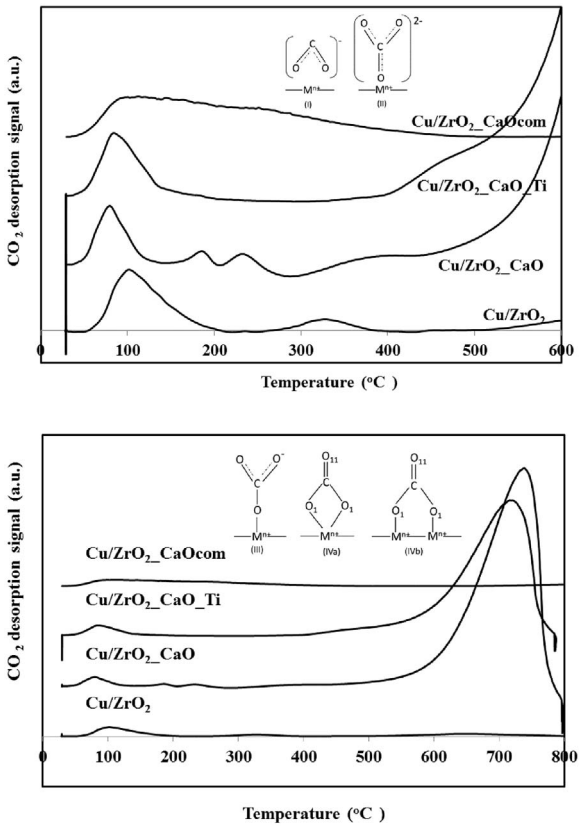

Fig. 4. CO_2 Temperature Programmed Desorption profiles of the catalysts after reduction at 400 °C for 6 h (top − low temperature and below − low and high temperature).

carboxylate (CO_2^-) and non-coordinated carbonate are observed on weak basic sites, as shown in Fig. 4 (top). The catalyst composed of oyster shell-derived calcium oxide contained a higher number of carbon dioxide adsorption sites, as shown in Table 1. The impurities (cation sites) and oxygen vacancies are possible key factors for CO_2 adsorption. The loss of oxygen atoms during hydrogen reduction can cause more oxygen vacancies and in turn increase the amount of carbon dioxide adsorption for all catalysts. The carbon dioxide adsorption was increased sharply in case of copper-based catalysts modified by the oyster shell-derived calcium oxide, likely from the charge imbalance in the presence of its impurities, such as Pb, Sr or Mg, and more oxygen vacancies.

3.3. *In situ X-ray absorption near edge structure*

The in-situ measurement of Cu K-edge XANES of the copper-based catalysts after the H_2 reduction in Fig. 5. Fig. 6 exhibited fraction of $Cu^0/Cu^{1+}/Cu^{2+}$ after hydrogen reduction from room temperature to 400 °C. The linear combination of Cu^0, Cu^{1+} and Cu^{2+} spectra were fitted to the resulting spectra by Athena program in order to obtain fraction of $Cu^0/Cu^{1+}/Cu^2$ existing during hydrogen reduction until 400 °C as shown in Fig. 6 and Table 2. Cu/ZrO_2 gave the amount of reduction to only 12%, whereas the calcium oxide in the copper − based catalysts may facilitate the reduction. However, it may prevent sintering during calcination and cause the copper species to be well-dispersed on zirconium oxide support [13,25]. The copper species consisting in Cu/ZrO_2_CaO, Cu/ZrO_2_CaO_Ti, and Cu/ZrO_2_CaOcom catalysts were considerably converted to a copper metal after reduction at 400 °C at which H_2 can be adsorbed. However, promising catalysts for hydrogen adsorption were Cu/ZrO_2_CaO, representing in Table 2. This hydrogen adsorption was likely attributed to hydrogen spillover on boundary of copper species (Cu^0, Cu^{1+}, Cu^{2+}), calcium oxide or zirconium oxide [23,25]. The XAS patterns after reduction at 300 °C and

Table 1
The number of CO_2 desorption sites of fresh catalysts and after reduction at 400 °C and methanol synthesis.

Catalyst	Amount of CO_2 desorption (mmol/g catalyst)				Average rate of methanol synthesis (g CH_3OH kg^{-1} h^{-1})
	Temperature Range 30–600 °C		Temperature Range 30–800 °C		
	before reduction	after reduction	before reduction	after reduction	
Cu/ZrO_2	3.33	1.87	4.10	2.65	4.1
Cu/ZrO_2_CaO	11.96	0.97	16.33	53.18	19.4
Cu/ZrO_2_CaO_Ti	5.21	1.34	6.23	40.53	6.3
Cu/ZrO_2_CaOcom	2.84	1.48	3.48	3.98	2.8

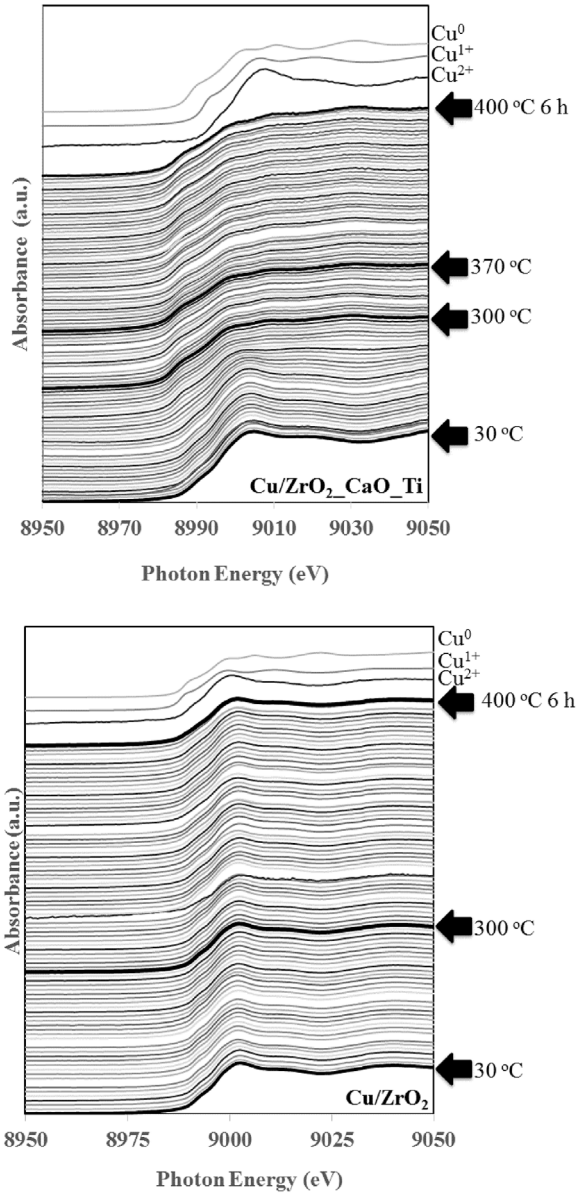

Fig. 5. Time resolved XANES reduction spectra of Cu/ZrO_2_CaO_Ti and Cu/ZrO_2 from 30 to 400 °C holding until 6 h and then cooled down to room temperature.

400 °C were similar for all catalysts, suggesting that physicochemical properties of the catalysts after the hydrogen reduction at these temperatures are identical, so as to pre-treating temperature for reduction prior to testing CO_2 hydrogenation was absolutely determined at 300 °C for 4 h where copper oxide dispersed on zirconia and modified calcium oxide supports was mostly transformed to copper metal, while copper oxide dispersed on sole zirconia support (Cu/ZrO_2) was hardly converted to copper metal at this temperature.

3.4. CO_2 hydrogenation testing and surface sites

Carbon dioxide hydrogenation was carried out at 250 °C under 30 bar and gas hourly space velocity was 79,000 h^{-1} or 460 NL/min. Fig. 7 on left and right depicts the catalytic performance for different types of calcium oxide. All catalysts produced three products i.e. carbon monoxide, methanol and methane. The catalysts were highly selective to carbon monoxide (87%–99%), suggesting that they were favorable towards a reverse water gas shift reaction in similar to the copper-based catalysts [13,26] which were also selective to carbon monoxide (40–80%). The carbon monoxide can subsequently react to generate higher hydrocarbon or methanol. The production of CH_4 from CO_2 hydrogenation is considered as thermodynamically favorable [27]. The copper-based catalysts gave the methane selectivity lower than 0.5%. The Cu/ZrO_2_CaO provided the highest selectivity towards methanol. Note that the methanol synthesis rate increased from 4.1 g CH_3OH kg^{-1} h^{-1} to 19.4 g CH_3OH kg^{-1} h^{-1} with 10 wt% additional oyster shell-derived calcium oxide (Fig. 8) despite the fact that the catalyst gave the lowest%CO_2 conversion. The rates of methanol production were dependent on the differences in the catalyst surfaces, including both the number of H_2 and CO_2 adsorption sites. The observed methanol synthesis substantiates the occurrence of the dual-sites mechanism, which relies on basic oxide sites and hydrogenation sites [28].

However, the metal/oxide interface has a fundamental role in promoting ZrO_2's ability to form intermediates via CO_2 adsorption [27,29] due to their ability to adsorb carbon dioxide and act as carbon sources. These carbon sources on weak and strong basic sites can be hydrogenated to an intermediate and eventually to methanol [12,13]. According to Table 3, the specific activities, as referred to total basic sites, weak basic sites and hydrogen chemisorption sites (TOF1, TOF2 and TOF3) are high for Cu/ZrO_2_CaO, which is in good agreement with the ability of CO_2 and H_2 adsorption. The wide dispersion of copper metal hydrogenation sites can contribute to methanol formation, however the ability to adsorb carbon dioxide onto basic sites more strongly encourages methanol formation than does the ability to adsorb hydrogen onto copper metal sites [30,31].

The catalyst with oyster shell-derived calcium oxide had a large number of strong basic sites, but the rate of methanol production was only slightly higher than that of Cu/ZrO_2 and Cu/ZrO_2_CaOcom. Although methanol formation tends to occurs at strong basic sites, it did not show high activity because the strong basic sites may inhibit product desorption. The oyster shell-derived calcium oxide modification by titanium ions can aid electron transfer on the copper-based catalysts [32] leading to a facile hydrogen reduction that results in 100% of the copper being metallic, as shown by XANES (Table 4).

4. Conclusions

The calcium oxide can prevent sintering resulting in a good dispersion of active metal sites on catalyst support. The oyster shell-derived calcium oxide can facilitate the CO_2 adsorption owning to its

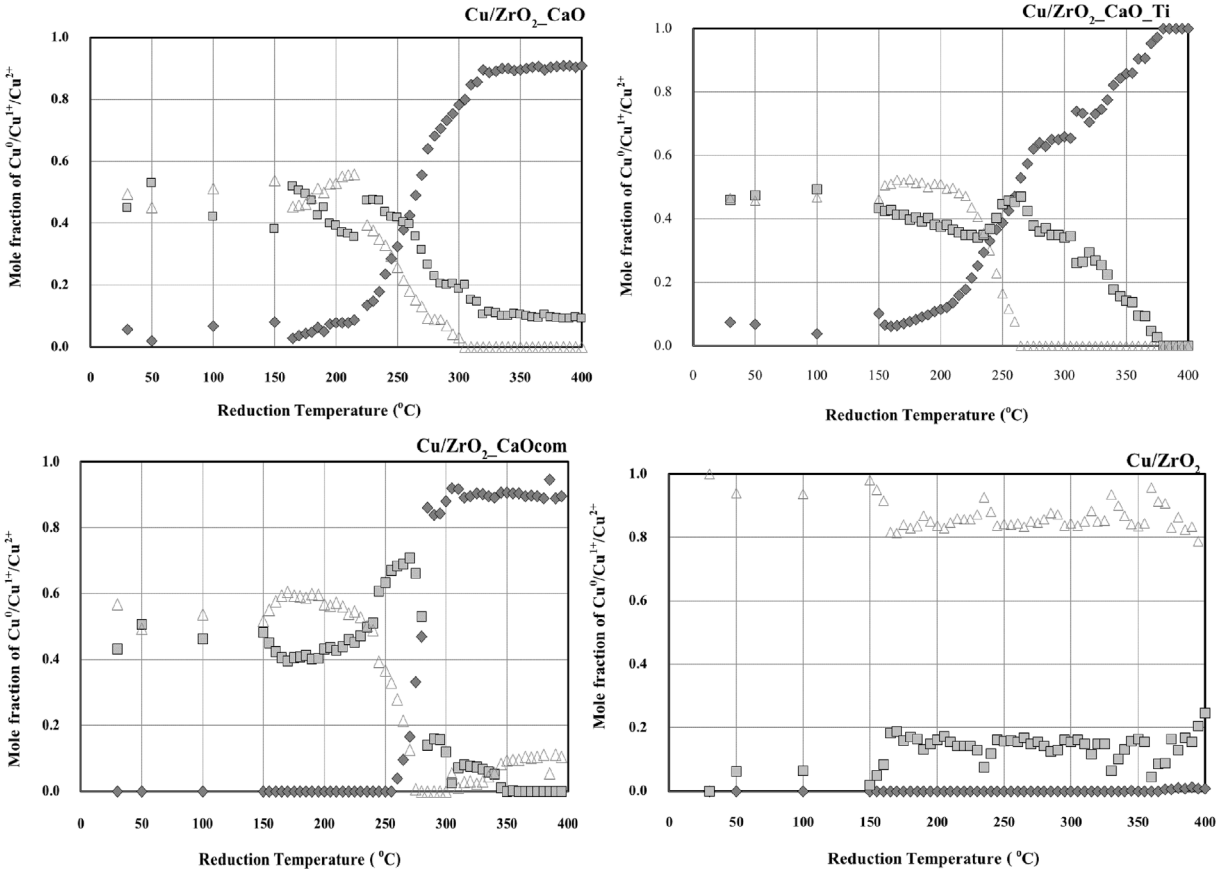

Fig. 6. Mole fraction of Cu^0(♦)/Cu^{1+}(■)/Cu^{2+}(Δ) from linear combination fitting from time resolved XANES reduction spectra in Fig. 5 as a function of temperature.

Table 2
Catalytic properties of copper-based catalysts modified by various types of calcium oxide.

Catalyst	H_2 desorption (mmol/g catalyst)	SSA (m^2/g)	$Cu^0/Cu^{1+}/Cu^{2+}$		% Reducibility
			at 30 °C	After reduction at 400 °C (%Cu^0)	
Cu/ZrO_2	0.38	15.7 ± 0.1	0/0/100	0/25/75 (0%)	13
Cu/ZrO_2_CaO	1.20	15.7 ± 0.1	6/45/49	91/9/0 (91%)	94
Cu/ZrO_2_CaO_Ti	0.40	15.8 ± 0.1	7/46/47	100/0/0 (100%)	100
Cu/ZrO_2_CaOcom	0.10	15.7 ± 0.1	0/43/57	90/0/10 (90%)	87

SSA: specific surface area.

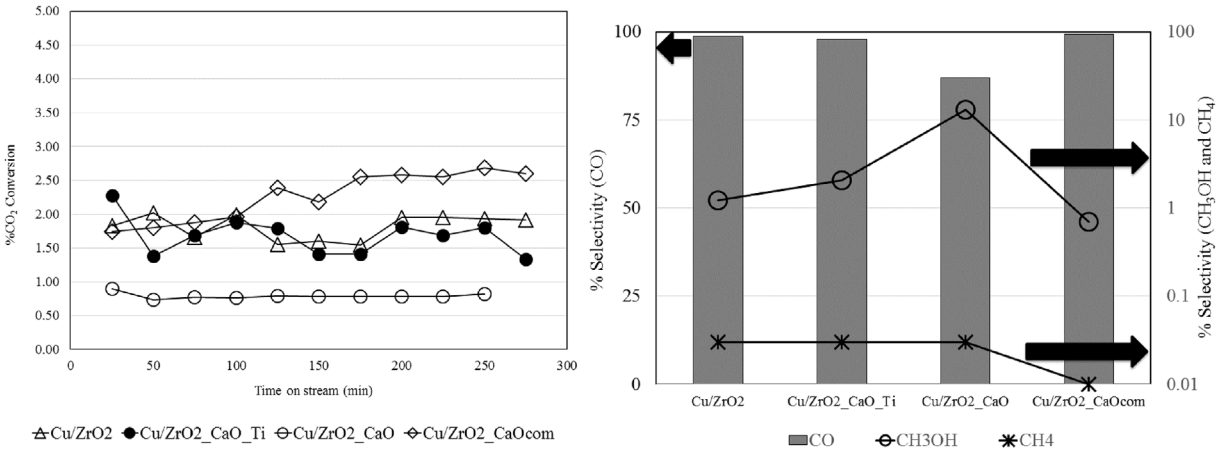

Fig. 7. Time on stream of%CO_2 conversion and%product selectivity under 3 MPa and 250 °C (GHSV 79,900 h^{-1}).

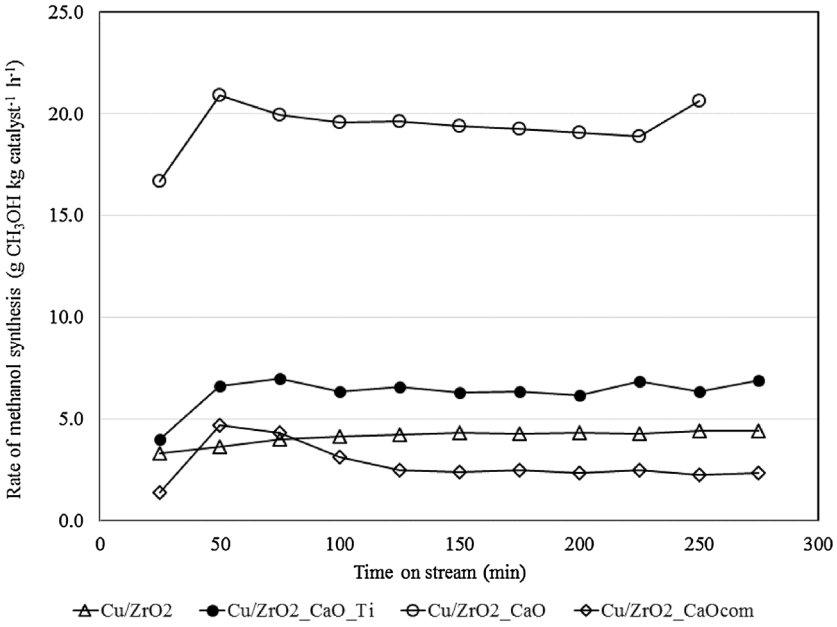

Fig. 8. Rate of methanol synthesis (g CH_3OH kg catalyst^{-1} h^{-1}).

Table 3
Elements dispersion on oyster shell surface by SEM-EDXS.

Raw Materials	% Mole of element dispersion on oyster shell surface									
	C	O	Na	Mg	Al	Sr	Pb	Ca	Fe	Cl
Oyster Shell	7.5	51.3	3.8	2.9	2.0	1.5	1.9	23.6	0.4	5.4

Table 4
Turnover Frequency (1/h) of methanol formation.

Catalyst	Turnover frequency (1/h)		
	TOF1 (total basic sites)	TOF2 (weak basic sites)	TOF3 (H_2 adsorbing sites)
Cu/ZrO_2	0.019	0.027	0.133
Cu/ZrO_2_CaO	0.048	2.606	2.107
Cu/ZrO_2_CaO_Ti	0.003	0.099	0.331
Cu/ZrO_2_CaOcom	0.005	0.014	0.212

Note

Turn over frequency 1 (TOF 1)

$$= \frac{\text{Rate of methanol synthesis (mmol kg cat}^{-1}\,\text{h}^{-1})}{\text{Total amount of carbon dioxide absorbing sites (30 – 800 °C) (mmol kg cat}^{-1})}$$

Turn over frequency 2 (TOF 2)

$$= \frac{\text{Rate of methanol synthesis (mmol kg cat}^{-1}\,\text{h}^{-1})}{\text{Amount of carbon dioxide absorbing sites (30 to 600 °C) (mmol kg cat}^{-1})}$$

surface defect. This leads to a higher rate of methanol production, whereas strong base sites may inhibit the methanol desorption. Titanium consisting in the oyster-derived calcium oxide can promote reducibility of copper-based catalyst.

Acknowledgements

The authors would like to give their gratitude to Assist. Prof. Dr. Pichan Sawangwong and ERASMUS MUNDUS (SAT) for their financial support to S.S and W.W. in 2015. Additional thanks to the Faculty of Engineering, Burapha University, Synchrotron Light Research Institute (Public Organization) (Thailand), The University of Oviedo (Spain), Miss Sutarat Thongratkeaw and the Center of Excellence in Catalysis and Catalytic Reaction Engineering, Chulalongkorn University and the Thailand Research Fund for grant No. DPG5880003.

References

[1] G.A. Olah, A. Goeppert, G.K. Surya Prakash, Chemical recycling of carbon dioxide to methanol and dimethyl ether: from greenhouse gas to renewable, environmentally carbon neutral fuels and synthetic hydrocarbons, J. Org. Chem. 74 (2) (2009) 487–498.
[2] S.G. Jadhav, P.D. Vaidya, B.M. Bhanage, J.B. Joshi, Catalytic carbon dioxide hydrogenation to methanol: a review of recent studies, Chem. Eng. Res. Des. 92 (2014) 2557–2567.
[3] B. Tidona, C. Koppold, A. Bansode, A. Urakawa, P. Rudolf von Rohrm, CO_2 hydrogenation to methanol at pressure up to 950 bar, J. Supercrit. Fluids 78 (2013) 70–77.
[4] Y. Wu, H. Xie, Y. Kou, N. Tsubaki, Y. Han, Y. Tan, The mechanism of higher alcohol formation on ZrO_2-based catalyst from syngas, Korean J. Chem. Eng. 32 (3) (2015) 406–412.
[5] F. Gallucci, L. Paturzo, A. Basile, An experimental study of CO_2 hydrogenation into methanol involving a zeolite membrane reactor, Chem. Eng. Process.: Process Intensif. 43 (8) (2004) 1029–1036.
[6] J. Weigel, R.A. Koeppel, A. Baiker, A. Wokaun, Surface species in CO and CO_2 hydrogenation over copper/zirconia: on the methanol synthesis mechanism, Langmuir 12 (1996) 5319–5329.
[7] H.Y. Chen, S.P. Lau, L. Chen, J. Lin, C.H.A. Huan, K.L. Tan, J.S. Pan, Synergism between Cu and Zn sites in Cu/Zn catalysts for methanol synthesis, Appl. Surf. Sci. 152 (1999) 193–199.
[8] W.N. Roslam, W. Isahak, Z.A.C. Ramli, M.W. Ismail, K. Ismail, R.M. Yusop, M.W. Mohamed Hisham, M.A. Yarmo, Adsorption-desorption of CO_2 on different type of copper oxides surfaces: physical and chemical attractions studies, J. CO_2 Util. 2 (2013) 8–15.
[9] S. Soisuwan, W. Wisaijorn, C. Nimnul, O. Maunghimapan, P. Prasertdam, The combination of calcium oxide and their selective products for CO_2 hydrogenation, Eng. J. 20 (2) (2016) 39–48.
[10] J. Yu, Q. Ge, W. Feng, H. Xu, Influence of calcination on the efficiency of CaO promotion over CaO modified Pt/γ-Al_2O_3 catalyst, Appl. Catal. A-Gen. 395 (2011) 114–119.
[11] P. GaO, F. Li, L. Zhang, N. Zhao, F. Xiao, W. Wei, L. Zhong, Y. Sun, Influence of fluorine on the performance of fluorine-modified Cu/Zn/Al catalysts for CO_2 hydrogenation to methanol, J. CO_2 Util. 2 (2013) 16–23.
[12] X. Guo, D. Mao, G. Lu, S. Wang, G. Wu, The influence of La doping on the catalytic behavior of Cu/ZrO_2 for methanol synthesis from CO_2 hydrogenation, J. Mol. Catal. A-Chem. 345 (2011) 60–68.
[13] H. Ren, C.H. Xu, H.Y. Zhao, Y.X. Wang, J. Liu, J.Y. Liu, Methanol synthesis from CO_2 hydrogenation over Cu/γ- Al_2O_3 catalysts modified by ZnO, ZrO_2 and MgO, J. Ind. Eng. Chem. 28 (2015) 261–267.

[14] S. Soisuwan, J. Prammachant, W. Wisaijorn, P. Praserthdam, The characteristics of green calcium oxide derived from aquatic materials, Procedia Chem. 2 (2014) 53–61.
[15] W. Wisaijorn, P. Praserthdam, S. Assabumrungrat, Modification of green calcium oxide and characteristics for clean energy catalysts, Energy Procedia 79 (2015) 685–690.
[16] T. Witoon, Characterization of calcium oxide derived from egg shell and it application of CO_2 sorbent, Ceram. Int. 37 (2011) 3291–3298.
[17] D.M. Marinković, M.V. Stanković, A.V. Veličković, J.M. Avramović, M.R. Miladinović, O.O. Stamenković, V.B. Veljković, Calcium oxide as a promising heterogeneous catalyst for biodiesel, Renew. Sustain. Energy Rev. 56 (2016) 1387–1408.
[18] M.C. Román-Martínez, D. Cazorla-Amorós, A. Linares-Solano, C. Salinas-Martínez de Lecea, CO_2 hydrogenation under pressure on catalysts Pt-Ca/C, Appl. Catal. A-Gen. 134 (1) (1996) 159–167.
[19] L. Vieille, A. Govin, P. Grosseau, Improvements of calcium oxide based sorbents for multiple CO_2 capture cycles, Powder Technol. 228 (2012) 319–323.
[20] Y. Poo-arporn, P. Chirawatkul, W. Saengsui, S. Chotiwan, S. Kityakarn, S. Klinkhieo, J. Hormes, P. Songsiriritthigul, Time-resolved XAS (Bonn-SUT-SLRI) beamline at SLRI, J. Synchrotron Radiat. 19 (2012) 937–943.
[21] H. Zhou, S. Pu, J. Huo, W. Cao, B. Wang, J. Li, Facile corrosion synthesis and sintering of disperse pure tetragonal zirconia nanoparticles, Ceram. Int. 42 (2016) 15005–15011.
[22] S. Xia, R. Nie, X. Lu, L. Wang, P. Chen, Z. Hou, Hydrogenolysis of glycerol over $Cu_{0.4}/Zn_{5.6-x}Mg_xAl_2O_{8.6}$ catalysts: the role of basicity and hydrogen spillover, J. Catal. 296 (2012) 1–11.
[23] K. Prins, Hydrogen spillover, Chem. Rev. 112 (2012) 2714–2738.
[24] A. Davydov, Molecular Spectroscopy of Oxide Catalyst Surfaces, John Wiley & Sons Ltd, England, 2003.
[25] I.U. Din, M.S. Shaharun, D. Subbarao, A. Naeem, F. Hussain, Influence of niobium on carbon nanofibers based Cu/ZrO_2 catalysts for liquid phase hydrogenation of CO_2 to methanol, Catal. Today 259 (2) (2016) 303–311.
[26] Z. Hui-ding, B. Shao-fen, L. Xin-mei, Y. Zi-feng, Structure and performance of Cu/ZrO_2 catalyst for the synthesis of methanol from CO_2 hydrogenation, J. Fuel Chem. Technol. 38 (4) (2010) 462–467.
[27] C. Jia, J. Gao, Y. Dai, J. Zhang, Y. Yang, The thermodynamics analysis and experimental validation for complicated systems in CO_2 hydrogenation process, J. Energy Chem. 25 (2016) 1027–1037.
[28] F. Arena, G. Mezzatesta, G. Zafarana, G. Trunfio, F. Frusteri, L. Spadaro, Effect of oxide carrier on surface functionality and process performance of the Cu-ZnO system in the synthesis of methanol via CO_2 hydrogenation, J. Catal. 300 (2013) 141–151.
[29] B.S. Clausen, J. Schiotz, L. Grabaek, C.V. Ovesen, K.W. Jacobsen, J.K. Norskov, H. Topsoe, Wetting/non-wetting phenomena during catalysis: evidence from in situ on-line EXAFS studies of Cu-based catalysts, Top. Catal. 1 (1994) 367–376.
[30] T. Fujitani, J. Nakamura, The chemical modification seen in the Cu/ZnO methanol synthesis catalysts, Appl. Catal. A-Gen. 191 (2000) 111–129.
[31] G. Meitzner, E. Iglesia, New insights into methanol synthesis catalysts from X-ray absorption spectroscopy, Catal. Today 53 (3) (1999) 433–441.
[32] T. Engel, P. Reid, Physical Chemistry, second edition, Prentice Hall, New Jersey, 2010.

Process Biochemistry 68 (2018) 205–213

Contents lists available at ScienceDirect

Process Biochemistry

journal homepage: www.elsevier.com/locate/procbio

Process and cost modeling of lactic acid recovery from fermentation broths by membrane-based process

Natnirin Phanthumchinda[a], Sitanan Thitiprasert[b], Somboon Tanasupawat[c], Suttichai Assabumrungrat[d], Nuttha Thongchul[b,*]

[a] Program in Biotechnology, Faculty of Science, Chulalongkorn University, Phayathai Road, Wangmai, Bangkok 10330, Thailand
[b] Institute of Biotechnology and Genetic Engineering, Chulalongkorn University, Phayathai Road, Wangmai, Bangkok 10330, Thailand
[c] Department of Biochemistry and Microbiology, Faculty of Pharmaceutical Sciences, Phayathai Road, Wangmai, Bangkok 10330, Thailand
[d] Department of Chemical Engineering, Faculty of Engineering, Chulalongkorn University, Phayathai Road, Wangmai, Pathumwan, Bangkok 10330, Thailand

ARTICLE INFO

Keywords:
Lactic acid
Fermentation broth
Downstream recovery
Membrane filtration
Process simulation
Economic analysis

ABSTRACT

Process and cost models for lactic acid recovery from fermentation broths at an annual capacity of 100,000 kg were developed as a research tool to evaluate an alternate process technology. The models were developed using SuperPro® Designer software by gathering the optimized data from the laboratory scale experiments. Sizing of unit operations, chemicals and utility consumptions, and estimation of capital and operating costs with the cost breakdown analysis were acquired from the simulation. A membrane-based process design was proposed in this study. The processes mainly consisted of microfiltration for cell removal, a series of ultrafiltration for eliminating proteins, and the integrated reverse osmosis systems to recover, pre-concentrate, and pre-purify lactic acid. Among the 3 proposed process designs, the in-parallel membrane-based process exhibited the highest lactic acid recovery yield, while the purity remained sufficiently high compared to commercial-grade products. The number of unit operations was found to be responsible for high production cost, in terms of both investment and operating costs. Omitting centrifugation and ultrafiltration at a 30-kDa molecular weight cut-off and use of the in-parallel integrated brackish water reverse-osmosis membrane units could lower operating costs by 23–31% for various fermentation broths that entered the downstream processing units.

1. Introduction

Lactic acid has been extensively used in the food, cosmetic, and pharmaceutical industries due to its chiral structure, containing both carboxyl and hydroxyl groups that can be converted into many useful chemicals. It was suggested that recent increasing demand of lactic acid was due to the production of biodegradable polylactic acid (PLA). According to the "Lactic Acid Market by Application (Biodegradable Polymer, Food, & Beverage, Personal Care & Pharmaceutical) & Polylactic Acid Market by Application (Packaging, Agriculture, Automobile, Electronics, Textile), & by Geography – Global Trends & Forecast to 2020", the global PLA market is projected to reach USD 5.16 billions by 2020 with growth at a CAGR of 20.9% during the forecast period. Europe is estimated as the largest market for PLA, while Asia-Pacific is projected to be the fastest growing market. It was suggested that government regulations and growing environmental concerns are the key drivers of the PLA market. The expansion of the PLA market thus drives the continual growth of the lactic acid market to serve as a building block in PLA synthesis. From the report, the global lactic acid market is projected to reach USD 3.82 billions by 2020, growing at a CAGR of 18.6% during the forecast period [1].

Lactic acid can be produced from renewable feedstocks via microbial fermentation with high yield and production performance, and thus, the process is considered green [2]. Currently, bacterial fermentation is widely used in industrial lactic acid production. During production, the pH is typically decreased as acid is produced, and the proper operating pH must be maintained at 5.5–6.5. Typically, pH control is performed by the addition of bases such as calcium bases ($CaCO_3$ and $Ca(OH)_2$), NaOH, and NH_4OH. This generates 2 lactate species (free lactic acid and its salt) in the fermentation broth. The concentration ratio of the 2 species depends on the operating pH during fermentation cultivation. The selection of neutralizing agents varies from process to process and primarily depends on the tolerance of microbial strains to the cations of the neutralizing agents and the production process performance [3,4]. It should be noted that the lactic acid fermentation broth contains several components; therefore, the

* Corresponding author.
E-mail address: Nuttha.T@chula.ac.th (N. Thongchul).

https://doi.org/10.1016/j.procbio.2018.02.013
Received 26 October 2017; Received in revised form 10 February 2018; Accepted 13 February 2018
Available online 17 February 2018
1359-5113/ © 2018 Elsevier Ltd. All rights reserved.

downstream recovery and purification of lactic acid after fermentation is of concern [5,6]. Many downstream units have been developed to recover and purify lactic acid, either for single-unit operation or the combined units to achieve the targeted product purity and recovery yield. The typical downstream units in lactic acid recovery include centrifugation [7], extraction [8], distillation [9], adsorption (ion exchanger) [10], membrane filtration (microfiltration (MF), ultrafiltration (UF), nanofiltration (NF), electrodialysis (ED), and reverse osmosis (RO)) [11–15], evaporation, and crystallization [16,17]. Each unit provides the specific function, operating conditions, cost spending, and drawbacks of lactic acid recovery. Therefore, most downstream process design involves many steps to achieve the desirable product specifications. Nonetheless, the production cost increases, as there are many unit operations and steps involved in the recovery process. Ideally, the downstream lactic acid recovery process should provide simple operation, high process performance, good cost effectiveness, and low environmental impact. In addition, the integrated design should be able to accept a variety of lactic acid fermentation broths that might be obtained from various fermentation processes.

Many process simulation tools have been continuously applied in chemical industries for developing and optimizing the design and operation of integrated processes since the 1960s. When a new process model is proposed, process simulators can generate the model that predicts equipment sizing, process scheduling, and economic evaluation [18]. Thus, the simulation results are often used as a tool to guarantee process feasibility at the initial stage of process design.

Among the unit operations mentioned above, membrane filtration provides beneficial outcomes with a low energy requirement, low chemical consumption, and low effluent generation; it is thus considered a green process. The objective of this study was to provide technical insights into membrane-based process technology as an alternative to recover lactic acid from fermentation broths. SuperPro® designer software was used as the simulation tool. The simulation data obtained in this study suggested that the membrane-based processes had good process performance, with lower investment and operating costs compared to the base case design. The proposed membrane-based processes reflect the fact that the modified process can be employed in developing process integration and intensification, for enhanced productivity and cost effectiveness in lactic acid recovery from the fermentation broth.

2. Material and methods

Process simulation was conducted in this study to compare 3 different downstream processes to separate and recover lactic acid from the fermentation broth. The operating data was applied from our previous experimental results performed using the laboratory-scale apparatus. Details are described elsewhere in this paper.

2.1. Feed properties

The fermentation broth was obtained from the cultivation of thermotolerant *Bacillus* sp. in a 5-L stirred fermentor. An active 24-h glucose-yeast extract-peptone slant was used to prepare the bacterial suspension. The bacterial suspension (1% inoculum size) was inoculated in a preculture vessel containing the preculture medium. The preculture medium contained (per liter) 10 g glucose, 15 g yeast extract, 4 g NH_4Cl, 0.5 g KH_2PO_4, 0.5 g K_2HPO_4, 5 g $CaCO_3$, and 20 mL salt solution. The compositions of the salt solution consisted of (per 10 mL) 400 mg $MgSO_4{\cdot}7H_2O$, 20 mg $MnSO_4{\cdot}5H_2O$, 20 mg $FeSO_4{\cdot}7H_2O$, and 20 mg NaCl. The preculture flask was incubated at 50 °C, 200 rpm for 3 h. The preculture flask was then transferred into the 5-L stirred fermentor containing 2.5 L sterile preculture medium at the 10% inoculum size. The fermentor was operated at 50 °C and agitated at 300 rpm with 1.0 vvm air. After 3 h, 0.5 L of the fermentation medium containing (per liter) 720 g glucose was added to the fermentor. Aeration was stopped [2].

Table 1
Feed compositions in lactate fermentation broths from cultivation of *Bacillus* sp. in 5-L stirred fermentor for use in simulation.

Species/Ions present in g/L	Fermentation broth		
	CaLAC	NaLAC	NH_4LAC
Lactate	86.40	84.30	84.70
Monovalent cation			
Na^+	0.15	22.83	0.17
NH_4^+	2.19	2.23	15.59
K^+	0.67	0.86	0.82
Monovalent anion			
Cl^-	2.35	2.74	2.52
Divalent cation			
Ca^{2+}	8.35	0.35	0.38
Fe^{2+}	0.02	0.01	0.01
Mn^{2+}	0.02	0.01	0.02
Mg^{2+}	0.07	0.07	0.08
Divalent anion			
SO_4^{2-}	0.29	0.25	0.26
Multivalent cation			
P^{3+} (representing PO_4^{3-})	0.06	0.05	0.05

Three different bases, i.e., $CaCO_3$, NaOH, and NH_4OH, were used for pH control at 6.5. As a result, 3 different lactate salts, i.e., CaLAC, NaLAC, and NH_4LAC, with different feed compositions were obtained in the fermentation, and fermentation continued for 48 h until glucose depletion. The fermentation broth was harvested, and composition analysis was performed to determine the feed properties for the downstream operation (Table 1).

2.2. Process description

Three process schemes were proposed for recovering, pre-purifying, and pre-concentrating lactic acid from the fermentation broth. The simplified lactic acid recovery process schemes are shown in Fig. 1. The general process scheme included (1) cell biomass removal from the fermentation broth, which left the fermentation process in the primary recovery unit. In a typical primary recovery stage, centrifugation with subsequent microfiltration is generally used for cell removal. Later, (2) the proteins retained in the cell-free broth were removed during the clarification step by a series of ultrafiltrations. Then, (3) the reverse osmosis (RO) units were applied to recover free lactic acid from other ions and to pre-concentrate before transfer to the final purification and finishing processes.

In the base process, cell biomass was removed by centrifugation (CF) and microfiltration (MF). Proteins were removed from the cell-free broth by a series of ultrafiltrations (UF1, UF2, and UF3) installed with different molecular weight cut-off (MWCO) membranes (30 kDa, 5 kDa, and 1 kDa, respectively). Lactic acid was separated from other ions and pre-concentrated in a series of RO membrane filtration steps, where the brackish water RO (BWRO) membrane (Dow FilmTec™, USA) and the sea water RO (SWRO) membrane (Dow FilmTec™, USA) were installed at the RO1 and RO2 units, respectively (Fig. 1(A)).

For cost-effectiveness, the number of unit operations involved in the primary recovery stage was reduced. From the data obtained from the laboratory scale experiment, when the centrifugation and ultrafiltration at 30 kDa MWCO membrane were omitted, the properties of the cell-free broth entering the RO units remained unchanged compared to those obtained from the base operation. In the membrane-based process, cell biomass was removed by MF. Later, the cell-free broth was clarified by UF1 and UF2 and installed with 5 kDa MWCO and 1 kDa MWCO membranes, respectively. Similar to those in Fig. 1(A), lactic acid was then separated and pre-concentrated by the series of RO membrane filtrations (Fig. 1(B)).

To improve the recovery efficiency, an in-parallel membrane-based process was proposed (Fig. 1(C)). The unit operations employed in the

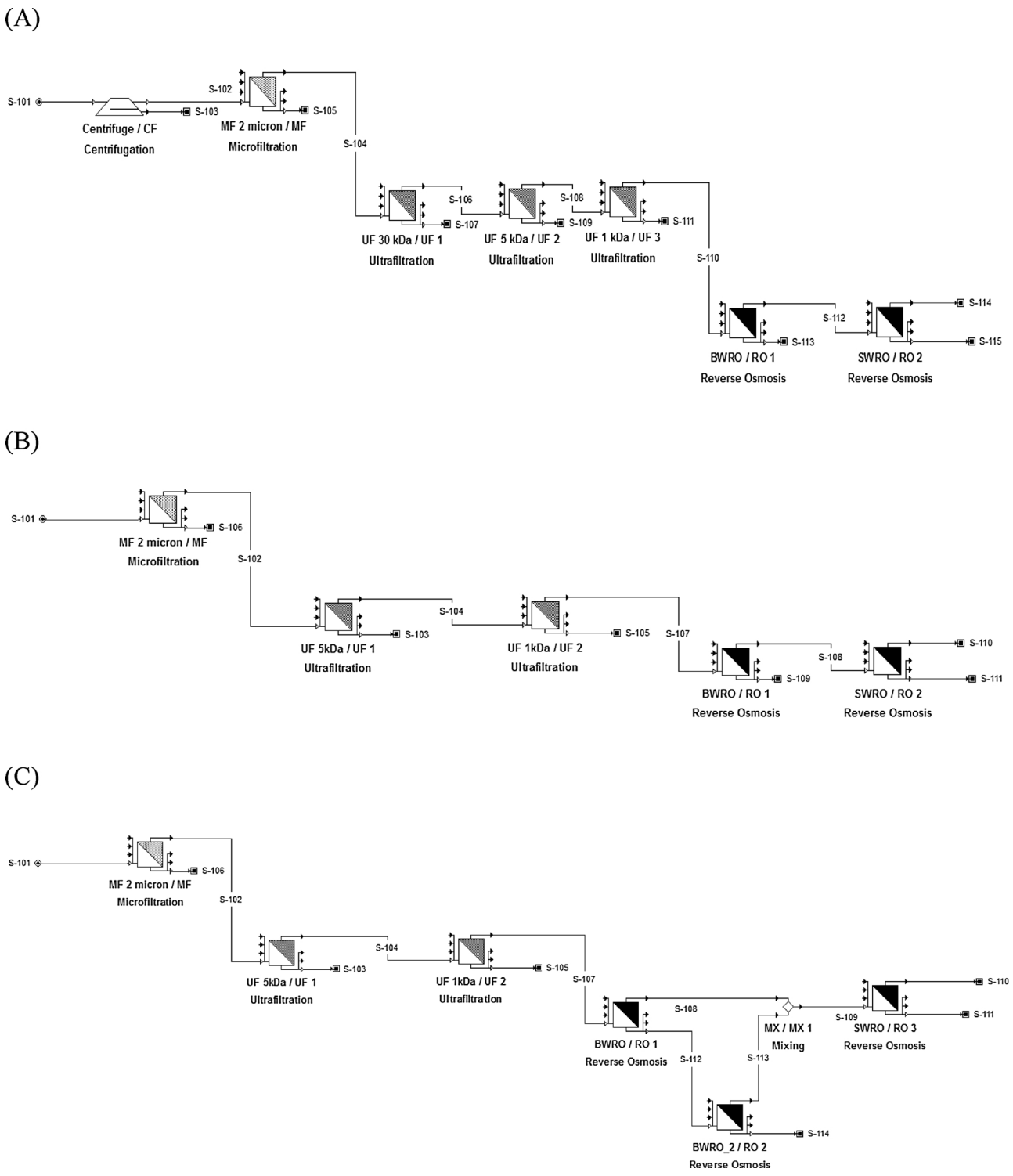

Fig. 1. Simplified process flow diagrams displaying major process equipment in lactic acid recovery from fermentation broth. (A) base process; (B) membrane-based process; and (C) in-parallel membrane-based process.

in-parallel membrane-based process for cell biomass removal and broth clarification were similar to those in the membrane-based process flow diagram. For better recovery of lactic acid from the clarified broth, 2 BWRO membrane units were installed in parallel. The permeates from both RO1 and RO2 were combined in the mixer (MX1) before entering the SWRO membrane unit (RO3) for pre-concentration.

The process simulator (SuperPro Designer®, Intelligen, Inc., USA) quantified the process characteristics, energy requirements, and equipment parameters of each major equipment for the specified operating scenarios. The volumes, compositions, and other physical characteristics of the input and output streams for each unit were identified. The obtained information was set as the basis of utility consumption and purchased equipment costs for each unit item.

2.3. Operating conditions and experimental results at laboratory scale

The equipment models and the key operating conditions employed in the laboratory scale experiments are summarized in Table 2. Among

Table 2
Major unit operations and their operating conditions in laboratory-scale experiments.

Unit	Centrifuge	MF	UF			RO	
						BWRO	SWRO
Manufacturer	Kubota Corporation (Japan)	TangenX Technology Corporation (USA)				Local company in Thailand	
Configuration	Refrigerated	Flat sheet				Spiral wound	
Material	Stainless steel	Polyethersulfone				Polyamide thin-film composite	
Dimension (mm × mm)	–	210 × 475				44.5 × 305	63.5 × 533
Model	KR-20000T	XPM20A01S	XP030A01S	XP005A01S	PP001A01L	BW60-1812-75	SW30-2521
Speed (rpm)	20000	–	–	–	–	–	–
Pore size	–	0.2 µm	30 kDa	5 kDa	1 kDa	0.001 µm	0.001 µm
Surface charge	–	–	–	–	–	Negatively	Positively
Surface area (m^2)	–	0.1	0.1	0.1	0.1	0.77	1.2
Pressure (bar) at 30 °C	–	2	2	2	2	6	15
pH range	6	6	6	6	6	6	6
Temperature (°C)	30	30	30	30	30	30	30
Average NaCl rejection (%)	–	–	–	–	–	97–99%	99.4%

Table 3
Experimental results showing ion rejection coefficient for laboratory-scale BWRO membrane unit to be defined in the process description in the simulation model.

Rejection coefficient	Fermentation broth		
	CaLAC broth	NaLAC broth	NH_4LAC broth
Lactic acid	0.748	0.546	0.417
Na^+	0.657	0.685	0.750
NH_4^+	0.666	0.641	0.469
K^+	0.673	0.768	0.891
Cl^-	0.770	0.733	0.557
Ca^{2+}	0.987	0.988	0.988
Fe^{2+}	0.855	0.852	0.750
Mn^{2+}	0.800	0.834	0.834
Mg^{2+}	0.979	0.977	0.981
SO_4^{2-}	0.914	0.931	0.917
P^{3+}	0.968	0.972	0.971

Table 4
Simulated operational data for lactic acid recovery via base case process at annual capacity of 100,000 kg.

Feed stream	CaLAC broth	NaLAC broth	NH_4LAC broth
Overall process data			
Batch capacity (kg/batch)	75.87	50.56	63.21
Number of batch runs	1318	1978	1582
Annual operating time (h)	7917	7919	7918
Batch time (h)	15.42	11.42	13.42
Cycle turnaround time (h)	6	4	5
Equipment sizing, number of units, and operating conditions			
Centrifuge	4 units, 30 °C, 15,900 g, 30 min		
	94.91 L/h	90.37 L/h	96.20 L/h
MF	2 units, 30 °C, 2 bar, 10 min, 36.09 m^2		
UF (30 kDa)	2 units, 30 °C, 2 bar, 10 min, 36.09 m^2		
UF (5 kDa)	2 units, 30 °C, 2 bar, 60 min, 36.09 m^2		
UF (1 kDa)	2 units, 30 °C, 2 bar, 120 min, 36.09 m^2		
BWRO	2 units, 30 °C, 6 bar, 3.17 m^2		
SWRO	2 units, 30 °C, 15 bar, 5 min, 3.17 m^2		

the major unit equipment, the BWRO membrane unit played a key role in separating lactic acid from other ions; and thus, the overall process performance relied on the operation during this process step. Notably, the clarified broth after passing through the UF units was diluted to a low concentration of lactic acid at 5 g/L, due to the limitation of the small-scale membrane apparatus. However, the dilution step was neglected in the simulation model. Table 3 shows the experimental results for the ion rejection coefficient (RC) obtained from the BWRO membrane unit in the laboratory-scale apparatus. The information in this table was input in the simulation model to calculate mass and energy balances.

3. Results and discussion

Based on the experimental data describing the composition of the fermentation broths, the operating conditions, and the performance of the proposed unit operations, the lactic acid recovery yield and the product purity were estimated by the simulation model. Tables 3 and 4 give an overview of the key operational data in the base case process and the membrane-based process (Fig. 1(A) and (B)) for various feed compositions (CaLAC broth, NaLAC broth, and NH_4LAC broth). The batchwise operation was performed at 30 °C and pH 6. By assuming an annual production of 100,000 kg lactic acid, the model predicted the overall process data, the number of each unit required and its sizing. More details on the simulated mass balance for each process flow diagram are presented in Appendix A (Tables S.1–S.3).

3.1. Process analysis

In the base case operation, the cell and insoluble materials remaining in the fermentation broth were removed in the primary recovery section using centrifuge and microfiltration, while only microfiltration was used in the membrane-based process for removing cell biomass and insoluble materials. From the experimental data, it was found that both cell biomass and insoluble materials were completely removed from the fermentation broth, and thus the cell-free broth was further clarified by UF. This resulted in clarified cell-free broth, without the presence of cell biomass and soluble proteins that were carried over to subsequent unit operations. The simulated data show that the unit operation, including 1 unit of MF and 2 units of UF installed with the 5 kDa and 1 kDa MWCO membranes in the primary recovery section of the membrane-based process, effectively removed cell mass, insoluble materials, and proteins in acceptable ranges, similar to those obtained from our previous experimental data, which has been reported elsewhere. From the simulated data representing the mass balance of ions/species remaining in the feed stream, less lactate loss was observed in the membrane-based process (See Appendix A, Tables S.1–S.3). Li et al. [19] reported that most proteins could be separated by the UF membranes with MWCOs of 5 kDa and 20 kDa [19]. From the findings mentioned above, it was confirmed that the centrifugation and ultrafiltration with the 30 kDa MWCO membrane shown in the base case process flow diagram could be omitted. This lowered the capital cost and subsequently the operating cost in the membrane-based process, since no centrifuge was required and the number of UF units were reduced by 2 units (Tables 4 and 5).

The stream left the primary recovery section and entered the recovery section, where lactic acid was separated and pre-concentrated in the BWRO and SWRO membrane units. Fig. 2 compares the simulated

Table 5
Simulated operational data for lactic acid recovery via membrane-based process at annual capacity of 100,000 kg.

Feed stream	CaLAC broth	NaLAC broth	NH_4LAC broth
Overall process data			
Batch throughput (kg/batch)	75.82	50.56	63.17
Number of batches per year	1319	1978	1583
Annual operating time (h)	7918	7916	7919
Recipe batch time (h)	10.08	8.08	9.08
Recipe cycle time (h)	6	4	5
Equipment sizing, number of units, and operating conditions			
MF	2 units, 30 °C, 2 bar, 60 min, 36.0 m^2		
UF (5 kDa)	2 units, 30 °C, 2 bar, 60 min, 36.0 m^2		
UF (1 kDa)	2 units, 30 °C, 2 bar, 120 min, 36.0 m^2		
BWRO	2 units, 30 °C, 6 bar, 3.70 m^2		
SWRO	2 units, 30 °C, 15 bar, 5 min, 3.70 m^2		

results for lactic acid recovery from the lactate fermentation broths (CaLAC broth, NaLAC broth, and NH_4LAC broth) in the base case, membrane-based, and in-parallel membrane-based processes. It was found that lactic acid left the SWRO membrane unit at a high concentration (~1000 g/L), regardless of the recovery process and the feed stream (Fig. 2(A)). Changing the feed streams resulted in different lactic acid product purity from the final SWRO membrane unit, while the different recovery processes did not have a strong effect on the product purity (Fig. 2(B)). Nevertheless, the recovery process strongly impacted the overall lactic acid product recovery (Fig. 2(C)). Higher lactate loss was observed in the base process, while the overall recovery yield was improved by the membrane-based and in-parallel membrane-based processes, respectively. Via the in-parallel membrane-based process, the overall lactic acid recovery increased by 48% for CaLAC broth, 31% for NaLAC broth, and 28% for NH_4LAC broth, respectively, compared to the membrane-based process.

In general, the unit operations involved in downstream product recovery are responsible for the loss of a desirable product (in this case "lactic acid"). Lactic acid loss was observed due to the cell removal and clarification step. Minimizing the unit installation in this section could help prevent such loss. As a consequence, lower lactic acid loss was obtained in the membrane-based process, compared to the base process (Tables S.1–S.3 and Fig. 2(C)).

In this study, major lactic acid loss occurred at the BWRO membrane unit (RO1) (Tables S.1–S.3 and Fig. 1). To prevent product loss, another BWRO membrane unit was installed (RO2), wherein lactic acid was further recovered from the retentate stream left RO1 (Fig. 1(C)). The permeate streams from both RO1 and RO2 in the in-parallel membrane-based process were then mixed and passed across the SWRO membrane unit (RO3), where lactic acid with sufficiently high purity was pre-concentrated. To be more specific, compared to the commercial-grade lactic acid available, i.e., FCC88 with 87.5–88.5% purity, FCC80 with 79.5–80.5% purity, and FCC50 with 49.5–50.5% purity, the process flow diagrams proposed in this study provided the simulated lactic acid product at higher purity than the commercially available products (Fig. 2(B)) [20].

It should be noted that of all 3 recovery processes proposed in this study, the highest lactic acid purity with the lowest recovery was obtained for the CaLAC feed stream. When the feed stream was NaLAC broth or NH_4LAC broth, high lactic acid recovery was obtained with the lower product purity. When a typical feed solution interacted at the surface of the negatively charged membrane, the ion shift was generated at the boundary between the membrane and the solution, resulting in an electrical potential known as the Donnan exclusion effect [21]. In the case of uncharged solutes, such as undissociated lactic acid, solution transport mainly occurred through diffusion and convection. A larger difference between the operating pressure and the osmotic pressure correlates to a larger percentage of undissociated lactic acid that passed through the BWRO membrane. When lactic acid species were present in the dissociated form at an operating pH above the pKa (3.86), the Donnan exclusion effect governed the transport of ion species through the BWRO membrane [22]. In the passage of Ca^{2+}, Na^+, NH_4^+, and H^+ through the BWRO membrane, these cations typically bind at the membrane surface. It was suggested that larger ions had lower diffusion rates and thus were expected to have lower concentrations in the permeate. Size-controlled ion diffusion, and the ability of ions to form hydrogen bonds with the carbonyl group of the polyamide membrane facilitated the passage of such ions [21,23]. Therefore, most Ca^{2+} ions were retained, whereas Na^+ and NH_4^+ apparently passed through the BWRO. This eventually resulted in the lower product purity in case of NaLAC and NH_4LAC.

Table 6 shows the performance of the designed process flow diagrams to recover lactic acid in this study, compared to previous literature. The typical downstream recovery of lactic acid primarily includes centrifugation, filtration, extraction, and distillation. Simple operation, low capital expenditure (CAPEX) and operating expenditure (OPEX), and reduced product contamination are always considered key controlling factors in process performance. To achieve high product purity, many downstream units are installed to remove impurities, while this eventually leads to low product recovery, due to loss between unit operations [10,12]. In typical recovery processes such as extraction and ion exchange, high consumption of solvent and adsorbent with a large amount of wastewater generated from each unit are usually the design constrains. However, the membrane-based processes proposed in this study not only gave a high final product concentration with high purity comparable to the commercially available product (FCC80); membrane operation was also a simple process, with low chemical consumption and wastewater generation [26]. Although low lactic acid recovery was observed in the base case and membrane bases processes, this could be improved by the additional BWRO membrane unit to minimize product loss. It is believed that recovery can be further improved with stream recycle or unit integration in the BWRO membrane units. In addition, further purification to remove the monovalent ions from the lactic acid product leaving the SWRO membrane unit can be achieved by installation of a nanofiltration unit after the SWRO membrane unit.

3.2. Economic evaluation

The cost model integrated the data developed in the lactic acid recovery process simulation model using information from material and energy balances to describe the economic impact of the membrane-based process compared to the base process and those previously reported in the literature [27]. By assuming batchwise operation with an annual capacity of 100,000 kg lactic acid product, a basis operating time of 330 days per year (7920 h) was used in the model. Detailed operation durations and scheduling to visualize the process are presented in the Gantt chart (See Appendix A, Fig. S.1–S.3). The purchased costs for the major equipment and the operating costs including utilities and labor were estimated from the default values from SuperPro Designer®. The raw material costs were obtained from quotations from suppliers. Considering the financial investment, the project lifetime was estimated for 15 years, with a construction period of 30 months and a startup period of 4 months at the inflation rate of 4%. The total fixed investment costs were estimated in Table 7. It was observed that both membrane-based process and the in-parallel membrane-based process required lower investment costs than the base process, with cost reductions of 72% and 71%, respectively. The results suggested that the installation of centrifuge and ultrafiltration with a 30 kDa MWCO membrane primarily contributed to process investment, while installation of the extra BWRO unit in the in-parallel membrane-based process resulted in an increasing investment cost of only 6% compared to the membrane-based process.

The annual operating cost was estimated a specific downstream recovery process with 3 different broths (Fig. 3). The reduction of

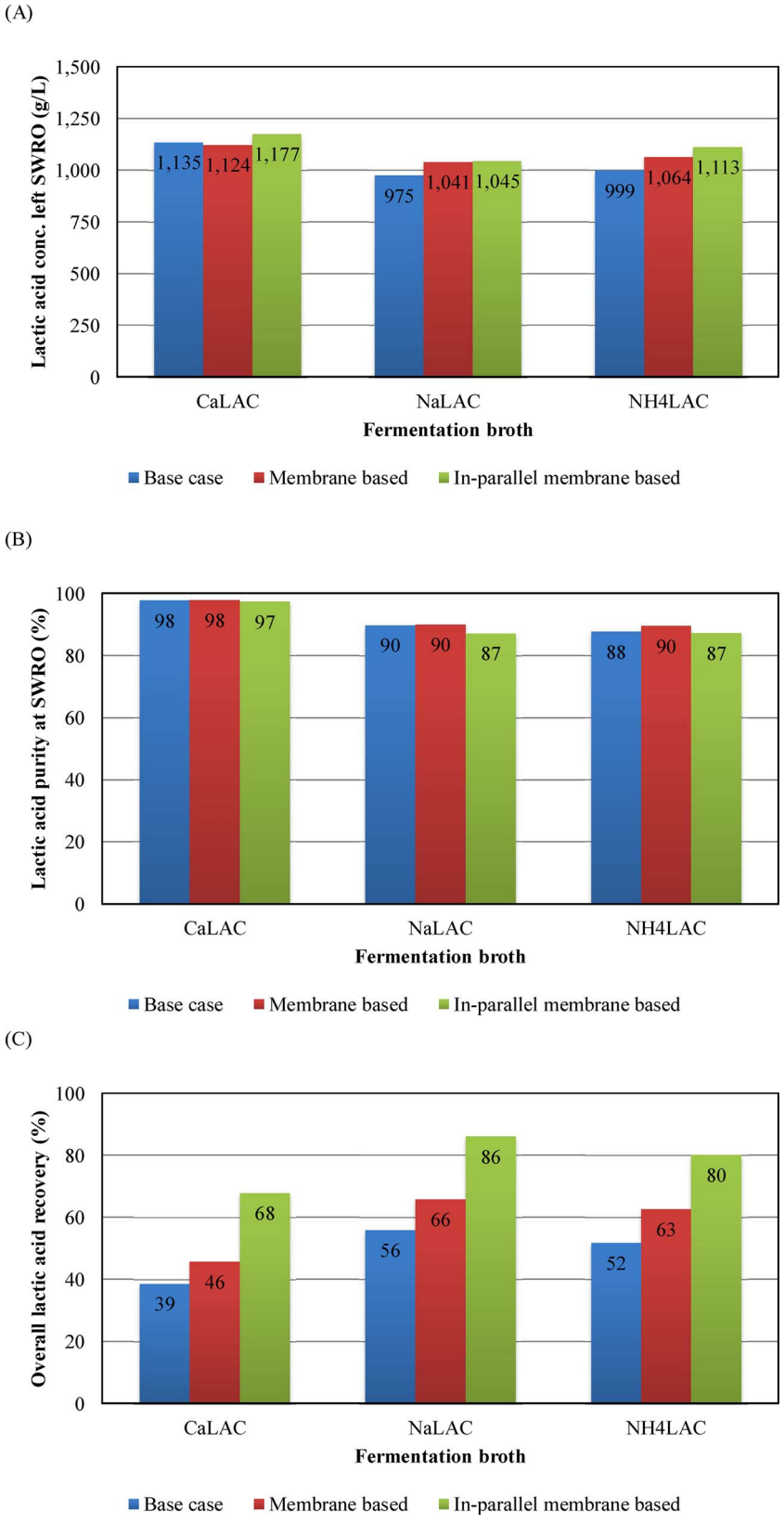

Fig. 2. Comparison of lactic acid recovery performance from fermentation broths by different process schemes. (A) Lactic acid concentration at SWRO unit (g/L); (B) Lactic acid purity at SWRO unit (%); and (C) Overall lactic acid recovery (%).

process units in the recovery process lowered operating costs. The results show that the base process required the highest operating cost per unit kg of lactic acid produced in all feed streams studied (CaLAC broth, NaLAC broth, and NH_4LAC broth). The installation of the centrifuge and UF with the 30 kDa MWCO membrane was responsible for high operating costs. The cost breakdown could further explain this finding due to higher cost spending on consumables and utilities compared to spending in the membrane-based and in-parallel membrane-based

Table 6
Comparison of lactic acid recovery processes reported in previous studies with simulated data obtained in this work.

Downstream Processing Units	Lactic acid product				References
	Final conc. (g/L)	Recovery at final unit (%)	Purity at final unit (%)	Overall recovery (%)	
MF[a], NF[b], and ED[c]	–	–	85.6	–	[6]
Centrifugation, Filtration, Extraction, and Evaporation	400–500	–	98.0	–	[8]
ED	–	70	–	69.5	[13]
Centrifugation, NF, and ED	–	73	–	58.2	[14]
MF, NF, ED, IEX[d], and Distillation	930	–	99.8	38.2	[15]
Evaporation	–	72	55.3	71.5	[16]
Centrifugation, Filtration, Extraction, and Distillation	–	–	91.3	62.2	[24]
Extraction	–	84	–	84.3	[25]
Base case	1135	100	98	39	This work-CaLAC broth
Membrane-based	1124	100	98	46	This work-CaLAC broth
In-parallel membrane-based	1177	100	97	68	This work-CaLAC broth

[a] Microfiltration.
[b] Nanofiltration.
[c] Electrodialysis.
[d] Ion exchanger.

Table 7
Fixed investment costs for proposed downstream processes to recover lactic acid from fermentation broths.

Fixed capital estimate summary	Cost (USD)		
	Base case	Membrane-based	In-parallel membrane-based
1.Total Plant Direct Cost (TPDC)			
a. Equipment purchase cost	2,640,000	733,000	780,000
b. Installation	1,316,000	362,000	384,000
c. Process piping	924,000	256,000	273,000
d. Instrumentation	1,056,000	22,000	312,000
e. Insulation	79,000	73,000	23,000
f. Electrical	264,000	13,000	78,000
g. Buildings	1,188,000	330,000	351,000
h. Yard improvement	396,000	110,000	117,000
i. Auxiliary facilities	1,056,000	293,000	312,000
TPDC	**8,919,000**	**2,472,000**	**2,630,000**
2. Total Plant Indirect Cost (TPIC)			
a. Engineering	2,230,000	618,000	658,000
b. Construction	3,122,000	685,000	921,000
TPIC	**5,352,000**	**1,483,000**	**1,587,000**
3.Total Plant Cost (TPC = TPDC + TPIC)	**14,271,000**	**3,955,000**	**4,209,000**
4.Contractor's Fee & Contingency (CFC)			
a. Contractor's fee	714,000	198,000	210,000
b. Contigency	1,427,000	395,000	421,000
CFC	**2,141,000**	**593,000**	**631,000**
5.Direct Fixed Capital Cost (DFC = TPC + CFC)	**16,411,000**	**4,548,000**	**4,840,000**

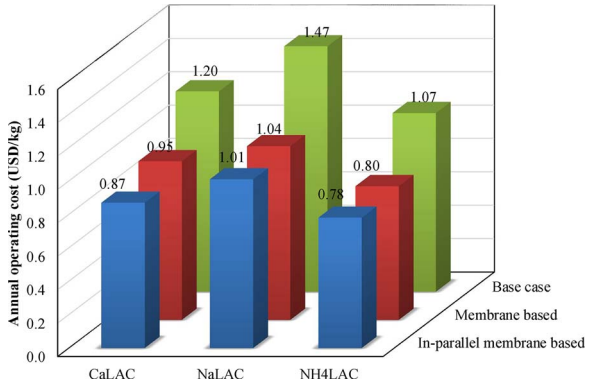

Fig. 3. Comparison of annual operating cost for lactic acid recovery via different downstream processes.

processes (Fig. 4). Further increasing the annual capacity 10-fold, 100-fold and 1000-fold compared to the 100,000 kg basis in the simulation led to similar process performance, due to the same process description and criteria input in the model. However, the results from the economic analysis suggested that more unit operations were required for the larger production capacity with an increasing CAPEX but a decreasing OPEX (Tables S.4–S.6). Compared to the base process, the membrane processes (both membrane based and in-parallel membrane-based processes) required lower CAPEX and OPEX at all scales. In addition, further increasing the production capacity resulted in lower OPEX.

The results in Fig. 3 suggested that using BWRO membrane process integration in the in-parallel membrane-based process led to further operating cost reductions in all feed streams studied. The reductions were 23%, 31%, and 27% compared to those required in the base case process for CaLAC broth, NaLAC broth, and NH_4LAC broth, respectively. Comparing the 3 process schemes proposed in this study, the membrane processes (both the membrane-based and the in-parallel membrane-based processes) demonstrated lower investment costs by approximately 4-fold compared to the base case operation (Table 7). The in-parallel membrane-based process gave the highest lactic acid recovery (Fig. 2(C)), with slightly higher investment costs compared to the membrane-based process (Table 7) with similar operating cost (Table 8); therefore, it was best suited for the recovery and pre-concentration of lactic acid from the fermentation broth among the 3 proposed process schemes in this study.

Table 8 shows the unit cost of lactic acid production per kilogram using conventional lactic acid recovery processes. The conventional recovery process is usually involved acidification, solid removal, neutralization, precipitation, filtration, extraction, adsorption, distillation, and evaporation. The analysis suggested that the number of unit operations and process steps in the downstream process for high-purity lactic acid production usually led to the high recovery costs. High consumption of chemicals was also responsible for the high recovery cost. For instance, a large amount of H_2SO_4 for the acidification of CaLAC broth not only increased the materials/chemicals cost, but also led to an increase in effluent loading, due to the formation of gypsum and wastewater during the operation [12,28]. In some separation units such as distillation, the feed solution with high inorganic contents is prohibited, and thus, the pretreatment unit prior distillation is required. This results in the additional consumption of chemicals and utilities [24]. Energy conservation is mandatory in any operational process. Operations with a phase change such as distillation, evaporation, and crystallization are considered an energy-intensive process (e.g., high steam consumption, high cooling rate). In contrast, the membrane-integrated process was suggested to be an economical route. The

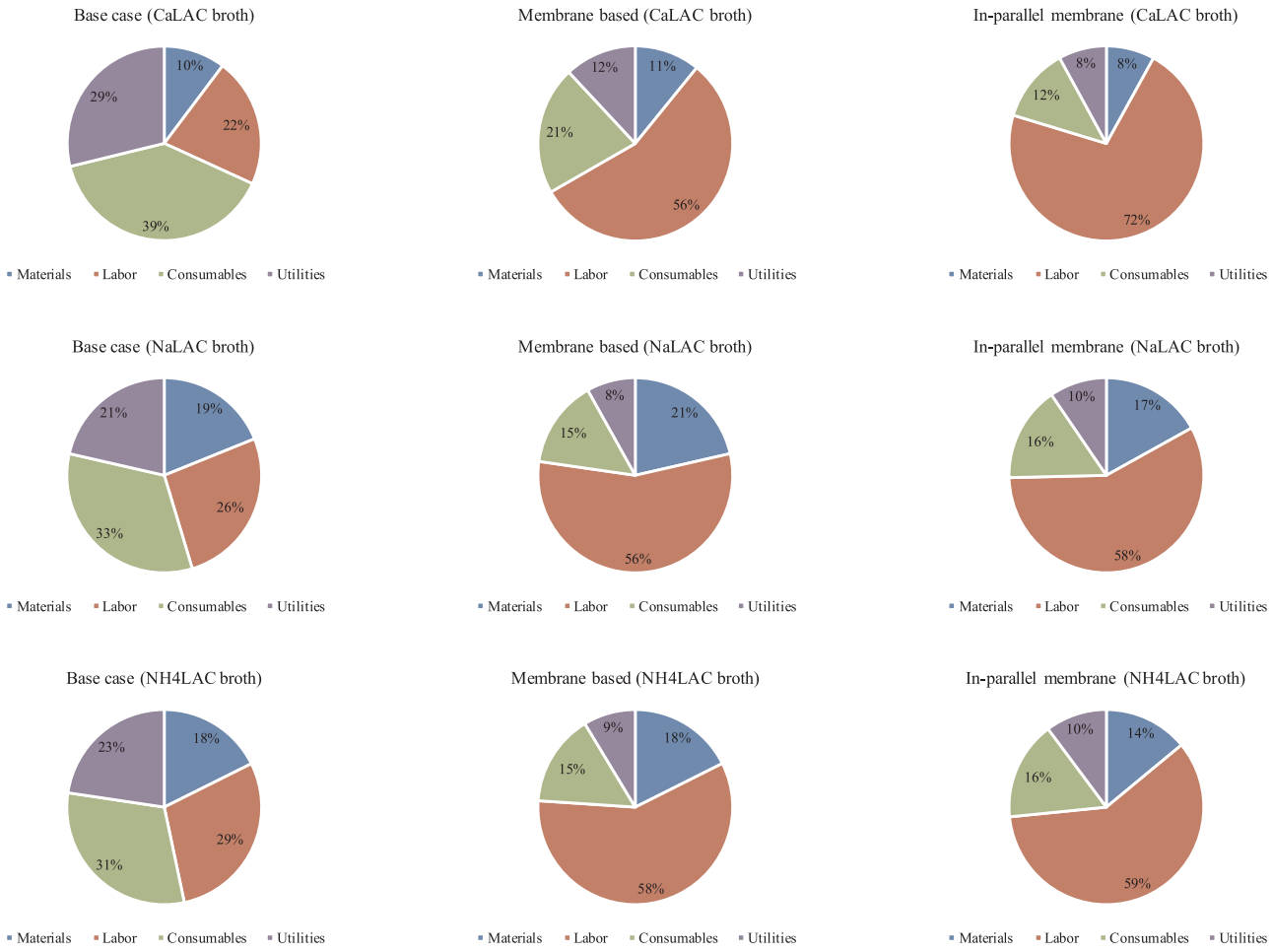

Fig. 4. Operating cost breakdown for lactic acid recovery from fermentation broths via different downstream processes.

Table 8
Economic analysis of conventional lactic acid downstream recovery processes compared to case scenarios proposed in this study.

Downstream processes	Cost (USD/kg lactic acid)	References
1. Reactive extraction, re-extraction, esterification, and reactive distillation	1.59	[27]
2. Addition of lime, precipitation, dissolution in methanol, acidification to separate calcium sulfate, esterification, and hydrolysis by reactive distillation	1.40	
3. Addition of ammonium hydroxide, microfiltration, monopolar electrodialysis, bipolar electrodialysis, esterification, and hydrolysis by reactive distillation	1.74	
4. Reactive extraction	0.92	
5. Base case process	1.07	This work
6. Membrane-based process	0.80	
7. In-parallel membrane-based process	0.78	

membrane separation process relies on the mechanical pressure-driven force that is not involved in phase change. Membrane separation generally occurs at room temperature and is thus considered an energy saving process [12,29]. Currently, dead-end filtration and centrifugation are partially replaced by MF due to economic impact [30]. It was reported that the energy consumption in the RO membrane process was as low as 9–20 kWh/m^3 with the high energy-saving spiral wound module [13,31]. As a result, the proposed processes in this study based on membrane separation could provide a low unit cost of lactic acid compared to those in the previous literatures and the commercial sale price (1.0–1.8 USD/kg) [32].

Therefore, it can be summarized from the simulated data that the proposed membrane-based processes provide new insight in the lactic acid downstream recovery process. The process scenarios not only give a sufficiently high product yield and purity, but are also considered economical and environmentally friendly routes due to cost effectiveness, low chemical consumption, low product contamination, low waste generation, and low energy consumption.

4. Conclusions

Membrane-based integrated processes were proposed for the downstream recovery of lactic acid from fermentation broths. The process economics were evaluated using the technical data previously optimized at the laboratory scale. It was found that the membrane-based processes were suitable for recovering lactic acid from various fermentation broths, i.e., CaLAC, NaLAC, and NH_4LAC. Therefore, we can consider the proposed process schemes as a universal design. The membrane-based processes mainly consisted of MF for cell removal, a series of UF for eliminating proteins, and integrated RO systems to

recover and pre-concentrate lactic acid. The membrane-based processes showed profitable outcomes in terms of sufficiently high product purity and recovery yield, as well as low production cost compared to commercially available products. The simulation data suggested that eliminating the centrifugation and integration of the RO membrane unit led to improved recovery yield. This subsequently lowered the production costs, including both investment and operating costs.

Conflict of interest

The authors declare no conflict of interests.

Compliance with ethical standards

This research does not involve human participants or animals.

Acknowledgments

This work was conducted under the University-Industry Linkage Program with the collaboration of researchers from Chulalongkorn University and PTT Global Chemical Public Company, Limited. Partial financial support from the Grant for International Research Integration: Research Pyramid, Ratchadapiseksomphot Endowment Fund (GCURP_58_01_33_01) and the Thailand Research Fund via the Distinguished Research Professor Grant (DPG5880003) was highly appreciated. The research facility supported by Chulalongkorn Academic Advancement into its 2nd Century Project (CUAASC) is highly acknowledged.

Appendix A. Supplementary data

Supplementary data associated with this article can be found, in the online version, at https://doi.org/10.1016/j.procbio.2018.02.013.

References

[1] Lactic Acid Market by Application, (Biodegradable Polymer, Food, & Beverage, Personal Care & Pharmaceutical) & Polylactic Acid Market by Application (Packaging, Agriculture, Automobile, Electronics, Textile), & by Geography –Global Trends & Forecast to 2020, (2017) (Accessed 22 October 2017), http://www.marketsandmarkets.com/PressReleases/polylacticacid.asp.

[2] S. Thitiprasert, K. Kodama, S. Tanasupawat, P. Prasitchoke, T. Rampai, B. Prasirtsak, V. Tolieng, J. Piluk, S. Assabumrungrat, N. Thongchul, A homofermentative *Bacillus* sp. BC-001 and its performance as a potential L-lactate industrial strain, Bioproc. Biosyst. Eng. 40 (2017) 1787–1799.

[3] K. Hetenyi, A. Nemeth, B. Sevella, Role of pH-regulation in lactic acid fermentation: second steps in a process improvement, Chem. Eng. Process. 50 (2011) 293–299.

[4] S. Nakano, C.U. Ugwu, Y. Tokiwa, Efficient production of D-(−)-lactic acid from broken rice by *Lactobacillus delbrueckii* using $Ca(OH)_2$ as a neutralizing agent, Bioresour. Technol. 104 (2012) 791–794.

[5] J.H. Kim, J.-G. Na, H.J. Shim, Y.K. Chang, Modeling of ammonium lactate recovery and impurity removal from simulated fermentation broth by nanofiltration, J. Membrane. Sci. 396 (2012) 110–118.

[6] J. Sikder, S. Chakraborty, P. Pal, E. Drioli, C. Bhattacharjee, Purification of lactic acid from microfiltrate fermentation broth by cross-flow nanofiltration, Biochem. Eng. J. 69 (2012) 130–137.

[7] S.O. Majekodunmi, A review on centrifugation in the pharmaceutical industry, Am. J. Biomed. Eng. 5 (2015) 67–78.

[8] Y. Hu, T.H. Kwan, W.A. Daoud, C.S.K. Lin, Continuous ultrasonic-mediated solvent extraction of lactic acid from fermentation broths, J. Clean. Prod. 145 (2017) 142–150.

[9] P. Khunnonkwao, P. Boontawan, D. Haltrich, T. Maischberger, A. Boontawan, Purification of L-(+)-lactic acid from pre-treated fermentation broth using vapor permeation-assisted esterification, Process Biochem. 47 (2012) 1948–1956.

[10] H.G. Joglekar, I. Rahman, B. Suresh, B.D. Kulkarni, A. Joshi, Comparative assessment of downstream processing options for lactic acid, Sep. Purif. Technol. 52 (2006) 1–17.

[11] M.I. Gonzalez, S. Alvarez, F.A. Riera, R. Alvarez, Lactic acid recovery from whey ultrafiltrate fermentation broths and artificial solutions by nanofiltration, Desalination 228 (2008) 84–96.

[12] P. Pal, J. Sikder, S. Roy, L. Giorno, Process intensification in lactic acid production: a review of membrane based processes, Chem. Eng. Process 48 (2009) 1549–1559.

[13] X. Wang, Y. Wang, X. Zhang, H. Feng, T. Xu, In-situ combination of fermentation and electrodialysis with bipolar membranes for the production of lactic acid: continuous operation, Bioresour. Technol. 147 (2013) 442–448.

[14] M.-S. Kim, J.-G. Na, M.-K. Lee, H. Ryu, Y.-K. Chang, J.M. Triolo, Y.-M. Yun, D.-H. Kim, More value from food waste: lactic acid and biogas recovery, Water Res. 96 (2016) 208–216.

[15] A.-K. Neu, D. Pleissner, K. Mehlmann, R. Schneider, G.I. Puerta-Quintero, J. Venus, Fermentative utilization of coffee mucilage using *Bacillus coagulans* and investigation of down-stream processing of fermentation broth for optically pure L(+)-lactic acid production, Bioresour. Technol. 211 (2016) 398–405.

[16] A. Komesu, P.F. Martins, B.H. Lunelli, J. Oliveira, R.M. Filho, M.R.W. Maciel, Evaluation of lactic acid purification from fermentation broth by hybrid short path evaporation using factorial experimental design, Sep. Purif. Technol. 136 (2014) 233–240.

[17] S. Tait, W.P. Clarke, J. Keller, D.J. Batstone, Removal of sulfate from high-strength wastewater by crystallation, Water Res. 43 (2009) 762–772.

[18] D.P. Petrides, A. Koulouris, P.T. Lagonikos, The role of process simulation in pharmaceutical process development and product commercialization, Pharm. Eng. 22 (2002) 1–8.

[19] Y. Li, A. Shahbazi, C.T. Kadzere, Separation of cells and proteins from fermentation using ultrafiltration, J. Food Eng. 75 (2006) 574–580.

[20] M.I. Gonzalez, S. Alvarez, F. Riera, R. Alvarez, Economic evaluation of an integrated process for lactic acid production from ultrafiltrated whey, J. Food Eng. 80 (2007) 553–561.

[21] M.I. Gonzalez, S. Alvarez, F.A. Riera, R. Alvarez, Lactic acid recovery from whey ultrafiltrate fermentation broths and artificial solutions by nanofiltration, Desalination 228 (2008) 84–96.

[22] P. Dey, L. Linnanen, P. Pal, Separation of lactic acid from fermentation broth by cross flow nanofiltration: membrane characterization and transport modelling, Desalination 288 (2012) 47–57.

[23] M.K.H. Liew, S. Tanaka, M. Morita, Separation and purification of lactic acid: fundamental studies on the reverse osmosis down-stream process, Desalination 101 (1995) 269–277.

[24] L. Chen, A. Zeng, H. Dong, Q. Li, C. Niu, A novel process for recovery and refining of L-lactic acid from fermentation broth, Bioresour. Technol. 112 (2012) 280–284.

[25] L. Yan, Y.-Q. Sun, Z.-L. Xiu, Sugaring-out extraction coupled with fermentation of lactic acid, Sep. Purif. Technol. 161 (2016) 152–158.

[26] Y. Li, A. Shahbazi, K. Williams, C. Wan, Separate and concentrate lactic acid using combination of nanofiltration and reverse osmosis membranes, Appl. Biochem. Biotechnol. 147 (2008) 1–9.

[27] J.A. Posada, C.A. Cardona, R. Gonzalez, Analysis of the production process of optically pure D-lactic acid from raw glycerol using engineered *Escherichia coli* strains, Appl. Biochem. Biotechnol. 166 (2012) 680–699.

[28] J. Qin, X. Wang, Z. Zheng, C. Ma, H. Tang, P. Xu, Production of L-lactic acid by a thermophilic *Bacillus* mutant using sodium hydroxide as neutralizing agent, Bioresour. Technol. 101 (2010) 7570–7576.

[29] D. White, B. Ditgens, G. Laufenberg, Concentration of metabolites and other organic salts by batch reverse osmosis, J. Food Eng. 53 (2002) 185–192.

[30] Z. Berk, Food Process Engineering and Technology, second ed., Academic Press, 2013.

[31] G. Gesan-Guiziou, Integrated membrane operations in whey processing, in: A. Cassano, E. Drioli (Eds.), Integrated Membrane Operations in the Food Production, Walter de Gruyter, 2014, pp. 147–162.

[32] M.P. Zacharof, R. Lovitt, Complex effluent streams as a potential source of volatile fatty acids, Waste Biomass Valori. 4 (2013) 557–581.

Annals of Microbiology (2018) 68:195–205
https://doi.org/10.1007/s13213-018-1330-6

ORIGINAL ARTICLE

Metabolic responses of *Aspergillus terreus* under low dissolved oxygen and pH levels

Pajareeya Songserm[1] · Aphichart Karnchanatat[2] · Sitanan Thitiprasert[2] · Somboon Tanasupawat[3] · Suttichai Assabumrungrat[4] · Shang-Tian Yang[5] · Nuttha Thongchul[2]

Received: 21 November 2017 / Accepted: 22 February 2018 / Published online: 7 March 2018
© Springer-Verlag GmbH Germany, part of Springer Nature and the University of Milan 2018

Abstract

The metabolic responses of *Aspergillus terreus* NRRL1960 to stress conditions (low dissolved oxygen and pH with limited nitrogen and phosphate) in the two-phase fermentation were investigated in this study. The fermentation kinetics suggested that itaconate production was suppressed under low dissolved oxygen (DO) concentrations. A slight change in pH caused a significant change in itaconate production. The transcriptomic data revealed that under low DO concentration, the glycolytic pathway was uncoupled from the oxidative phosphorylation, resulting in the activation of substrate-level phosphorylation as an alternative route for ATP regeneration. The downregulation of *pdh* genes, the genes encoding ATP synthase and succinate dehydrogenase, confirmed the observation of the uncoupling of the oxidative TCA cycle from glycolysis. It was found that the upregulation of *pyc* resulted in a large pool of oxaloacetate in the cytosol. This induced the conversion of oxaloacetate to malate. The upregulation of the gene encoding fumarate hydratase with the subsequent formation of fumarate was found to be responsible for the regeneration of NADPH and ATP under the condition of a low dissolved oxygen level. The large pool of oxaloacetate drove itaconic acid production also via the oxidative TCA cycle. Nevertheless, the downregulation of ATP synthase genes resulted in the deficiency of the proton-pumping H^+ ATPase and the subsequent stress due to the failure to maintain the physiological pH. This resulted in itaconate production at a low titer. The fermentation kinetics and the transcriptomic data provided in this study can be used for further process optimization and control to improve itaconate production performance.

Keywords *A. terreus* · Central metabolic pathway · Gene expression · Metabolite production · Fermentation

Introduction

Aspergillus sp. has gained much commercial interest as the filamentous fungi in this genus have been reported as the industrial producers of enzymes and metabolites. Besides *Aspergillus niger* and *Aspergillus oryzae*, *Aspergillus terreus* has been used extensively in the commercial production of enzymes (cellulase and xylanase), organic acid (itaconic acid), pharmaceutical product (lovastatin), and several secondary metabolites (geodin, cyclosporin A, questrin, citrinin, and aspulvinone) (Schimmel 1998; Hajjaj et al. 2001; Nazir et al. 2010; Klement and Buchs 2013; Kocabas et al. 2014; Boruta and Bizukojc 2016). Due to its ability to produce several metabolites, many researchers have attempted to identify and to reconstruct the genomic sequences of *A. terreus* for better understanding and for controlling its metabolic network (Birren et al. 2005; Liu et al. 2013). The reconstructed genome-scale metabolic model based on genome annotation and literature mining accurately predicted the physiological

Electronic supplementary material The online version of this article (https://doi.org/10.1007/s13213-018-1330-6) contains supplementary material, which is available to authorized users.

✉ Nuttha Thongchul
Nuttha.T@chula.ac.th

[1] Program in Biotechnology, Faculty of Science, Chulalongkorn University, Bangkok 10330, Thailand

[2] Institute of Biotechnology and Genetic Engineering, Chulalongkorn University, Bangkok 10330, Thailand

[3] Department of Biochemistry and Microbiology, Faculty of Pharmaceutical Sciences, Chulalongkorn University, Bangkok 10330, Thailand

[4] Department of Chemical Engineering, Faculty of Engineering, Chulalongkorn University, Bangkok 10330, Thailand

[5] William G. Lowrie Department of Chemical and Biomolecular Engineering, The Ohio State University, Columbus, OH 43210, USA

responses to the environmental conditions (Liu et al. 2013). The bottleneck reactions in the metabolic pathway could be also elucidated. In bioprocess development, the model that explained the function of the metabolic network is necessary for fermentation process optimization as it reflects the titer, yield, and production rate of the desirable product. A suitable manipulation of *A. terreus* metabolism to reduce the formation of byproducts (e.g., geodin in lovastatin production and cell biomass in itaconate production) is required. Itaconate production by *A. terreus* has long been studied; however, the synthetic pathway has not been clearly elucidated (Liu et al. 2013). The rate-limiting reaction in itaconate production is still unclear and the metabolic evolution proposed to improve the production performance seems insufficient. To overcome the problems addressed previously, a comprehensive understanding of the physiology of *A. terreus* is important.

In this study, the metabolic responses of *A. terreus* and its end product formation were investigated during the cultivation under low dissolved oxygen concentrations and pH. The fermentation kinetics and the transcriptomic data analysis were employed to explain the physiological responses of *A. terreus* to the changes in the environmental conditions, especially under stress conditions (low dissolved oxygen concentration and pH). The results obtained in this study could be deposited in the literature mining as the database for manipulating *A. terreus* cultivation to achieve a high production performance of the desirable end products.

Materials and methods

Microorganisms, inoculum preparation, and medium compositions

A. terreus NRRL1960 was kindly provided by the Agricultural Research Service Culture Collection, US Department of Agriculture, Peoria, IL, USA. For the inoculum preparation, the culture was maintained on Czapek Dox agar and was incubated at 30 °C for 7 days. The spores were harvested with sterile deionized water. The spore concentration was adjusted to 10^6 spores/mL by dilution with sterile deionized water. A total of 10 mL of the spore suspension was used to inoculate the bioreactor.

The medium composition of the one-phase fermentation consisted of (per liter) 180 g glucose, 0.1 g KH_2PO_4, 3 g NH_4NO_3, 1 g $MgSO_4{\cdot}7H_2O$, 5 g $CaCl_2{\cdot}2H_2O$, 1.67 mg $FeCl_3{\cdot}6H_2O$, 8 mg $ZnSO_4{\cdot}7H_2O$, and 15 mg $CuSO_4{\cdot}5H_2O$. The pH of the medium was adjusted to 3.1 with 0.5 M H_2SO_4 (Krull et al. 2017).

In the two-phase fermentation, medium A containing (per liter) 30 g glucose and 5 g yeast extract was used initially for inducing spore germination and initial cell growth. The pH of medium A was adjusted to 3.0. Later, medium A was replaced by medium B to enhance metabolite production with the limited cell growth (Pimtong et al. 2017). The compositions of medium B were (per liter) 100 g glucose, 2.36 g $(NH_4)_2SO_4$, 0.11 g KH_2PO_4, 2.08 g $MgSO_4{\cdot}7H_2O$, 0.13 g $CaCl_2{\cdot}2H_2O$, 0.074 g NaCl, 0.2 mg $CuSO_4{\cdot}5H_2O$, 5.5 mg $FeSO_4{\cdot}7H_2O$, 0.7 mg $MnCl_2{\cdot}4H_2O$, and 1.3 g $ZnSO_4{\cdot}7H_2O$. The pH of medium B was adjusted to 2.0.

Cultivation of *A. terreus* in a 7-L stirred fermentor

The cultivation was performed in the 7-L stirred fermentor (Sartorius Biostat® B) with a filled medium volume of 3 L. Before the cultivation, the fermentor was autoclaved at 121 °C and 15 psig, for 30 min. After sterilization, the fermentor was cooled down before starting the control system. A dissolved oxygen (DO) sensor (Mettler Toledo InPro®6820) was calibrated with sterile pure nitrogen and air. A dissolved CO_2 sensor (Mettler Toledo InPro®50,009(i)) was calibrated with CO_2 gas before the cultivation. The fermentation was initiated by inoculating the fermentor with the spore suspension.

For the typical one-phase fermentation cultivation, after the inoculation, the fermentor was controlled at 30 °C, 350 rpm, and 20% DO, with an initial pH of 3.1. The cultivation was carried out for 132 h (Krull et al. 2017).

For the two-phase fermentation process, the cultivation started with the inoculation of the fermentor that was filled with medium A. The fermentor was operated at 30 °C, 100 rpm, and 0.5 vvm air, for 48 h. During the growth phase, spores were germinated, and the hyphal growth was initiated until a sufficiently high cell concentration was obtained. At the end of the growth phase, medium A was aseptically discharged using the peristaltic pump and the fermentor was filled with the sterile medium B. The culture was incubated at the same temperature but with varied pH and DO levels to induce the production of fermentation metabolites. During the production phase, the pH was automatically controlled by the addition of 5 M KOH. The DO profile and the CO_2 concentration were monitored during the cultivation in the production phase.

Broth samples were collected from the fermentor every 12 h throughout the cultivation for analyses of the remaining glucose and ammonium and for the presence of fermentation metabolites. The cell biomass was collected for dry weight (DW) and transcriptomic analyses. All the experiments were conducted in duplicate for each condition. All the datasets presented for this study are the average values obtained from the duplication.

Complementary DNA library preparation and transcriptomic sequencing and analysis

To understand better the metabolic changes of *A. terreus* NRRL1960 upon the manipulation of the process conditions during the two-phase fermentation, the fermentation sample at

the end of the first phase and those samples during the second phase were collected for RNA extraction, subsequent transcriptome sequencing, and differential expression analysis.

Barcoded RNA libraries were prepared using Lexogen's Quant-Seq 3′ mRNA seq kit from Ion Torrent (Lexogen, Vienna, Austria). This approach generated libraries of the sequences close to the 3′ end of the polyadenylated RNAs, and only one fragment was produced per transcript. The RNA input was quantified by spectrophotometry and by fluorometry. Approximately 300–500 ng of the RNA input was required for library generation. The modified Quant-Seq protocol was performed as suggested for this low input, partially degraded RNA. The External RNA Controls Consortium (ERCC) obtained from Life Technologies (Carlsbad, CA, USA) was spiked into each of the prepared library reactions at the manufacturer's recommended concentration. The library quantification and quality control were performed using the high sensitivity DNA kit and the Agilent 2100 Bioanalyzer (Agilent, Santa Clara, CA, USA).

The DNA templates for sequencing were prepared using the 200 bp v3 OT2 kit and the Ion One Touch 2 platform (Life Technologies). Sequencing was performed on the Ion Proton, with signal processing and base calling performed by the Ion Torrent Suite v5.0.4 (Life Technologies). The raw sequences from each sample were uploaded to Partex Flow. The adapter sequences were trimmed. The bases were then trimmed according to the visual representation and the quality score to a size below 170 bp. The resulting reads were then aligned to *A. terreus* NIH2624 genome references downloaded from http://fungi.ensembl.org/info/website/ftp/index.html using Star 2.4.1d (UniProtKB) (Protein Knowledgebase (UniProt KB) 2017). The transcript quantification was performed using the Partex E/M method available in Partek Flow.

The trimming of the adapters including TGGAATTC TCGGGTG, CACCCGAGAATTCCA, AATCTCGT ATGCCGTCTTCTGCTTGC, AGATCGGAAGAGCT CGTATGCCGTCTTCTGCTTG, AGATC GGAAGAGC GTCGTCTAGGGAAAGAGTGT, and AGATCGGA AGAGCGGTTCAGCAGGAATGCCGAG was performed. The sequence alignment with the *A. terreus* NIH2624 (assembly ASM14961v1) genome was performed using STAR v2.4.2a. Samtools v0.1.19-96b5f2294a was used with the default setting to generate the bam index files. The quantification of gene expression was performed by Htseq v0.6.0 with–f and–s options indicating bam inputs and un-stranded reads, respectively. Cuffdiff v2.1.1 was used to estimate the transcript abundance with the –no-diff and default options to generate the differential analysis files for each of the described comparisons.

Sample analyses

The cell growth and product formation during the fermentation were determined. The product yield was calculated from the ratio of the product formed to the amount of glucose consumed. The volumetric productivity was defined as the total amount of the product formed per unit volume per unit time.

The cell biomass concentration was determined from the cell dry weight. The collected fermentation sample was filtered through Whatman filter paper no.4 to harvest the cell biomass. The cell biomass was rinsed thoroughly with deionized water and dried at 80 °C until a constant dry weight was obtained. The cell concentration (in g/L) was calculated.

High-performance liquid chromatography (HPLC) was used to analyze the remaining glucose and the presence of fermentation metabolites. The fermentation broth was centrifuged at 10000 g for 7 min. The supernatant was collected for the HPLC sample preparation. The sample was diluted and was filtered through a hydrophilic PTFE membrane. The particle-free sample (15 μL) was injected automatically (Shimadzu DGU-20A 5R, Shimadzu SIL-20A HT) into an organic acid column (Biorad, Aminex HPX-87H ion exclusion organic acid column; 300 mm × 7.8 mm) maintained at 40 °C in a column oven (Shimadzu, CTO-20A). A solution of 0.005 M H_2SO_4 was used as the mobile phase at the flowrate of 0.6 mL/min (Shimadzu, LC-20AD). The refractive index detector (Shimadzu RID-20A) was used to detect the remaining glucose while the organic compounds, e.g., glucose, itaconic acid, citric acid, cis-aconitic acid, succinic acid, oxaloacetic acid, L-malic acid, pyruvic acid, fumaric acid, and ethanol, present in the sample were detected by the UV detector at 210 nm (Shimadzu SPD-20A). The standards containing 0–2 g/L of each compound mentioned previously were injected as the references to determine the concentration of each compound in the sample. The chromatogram peak area was selected for comparison basis.

The residual ammoniacal nitrogen was determined by the indophenol blue method (Tzollas et al. 2010). Before the assay, the following reagents were prepared accordingly: (1) phenol-alcohol solution was prepared by dissolving 10 g phenol (reagent grade) into 100 mL ethanol (95% *v*/*v*); (2) 0.5% sodium nitroprusside was prepared by dissolving 1 g sodium nitroprusside into 200 mL water; (3) alkaline solution was prepared by dissolving 100 g trisodium citrate and 5 g sodium hydroxide into 500 mL water; (4) sodium hypochlorite solution was prepared from commercial hypochlorite (Chlorox); and (5) oxidizing solution was prepared on the same day before use from a mixture of 100 mL sodium citrate solution and 25 mL hypochlorite solution. The reaction assay was started by adding a 500 μL sample into the mixture of phenol solution (20 μL), sodium nitroprusside solution (50 μL), and oxidizing solution (125 μL). The reaction was developed for 1 h in darkness. The optical purity of the mixture was measured at the wavelength of 640 nm (Thermo Scientific Multiskan GO), and the ammonia concentration in the sample was calculated from the standard curve.

The residual phosphate was determined by the malachite green method (Baykov et al. 1988). The dye solution was prepared before the assay by adding 60 mL concentrated sulfuric acid into 300 mL water. The solution was allowed to cool down to room temperature before 0.44-g malachite green was supplemented. The orange solution was then prepared on the same day before use by mixing 2.5 mL ammonium molybdate (7.5%) and 0.2 mL Tween 20 (11%) into 10 mL dye solution. For the reaction assay, a 100 μL sample was mixed with a 400 μL orange solution. The absorbance at 630 nm (Thermo Scientific Multiskan GO) was read within 10 min after mixing. The phosphate concentration of the sample was calculated from the standard curve.

Results and discussion

Metabolite production profiles by *A. terreus* NRRL1960 from two cultivation approaches

The fermentation kinetics during the 1-phase fermentation cultivation of *A. terreus* NRRL1960 were observed (Fig. 1). Growth started immediately after inoculation; however, the production of the metabolites was observed after 48 h. This resulted in the low overall volumetric productivity of the metabolites. From the fermentation profiles, it was found that glucose was mainly consumed by *A. terreus* NRRL1960 for cell biomass production (45.1 g/L). Fumaric acid was the major metabolite found in the 1-phase fermentation at the concentration of 41.6 g/L. Succinic acid was found as the second major end product at a concentration lower than 10 g/L. Other intermediates in the TCA cycle, e.g., citric acid and cis-aconitic acid were present in trace amounts while no malic acid and itaconic acid were observed. The evidence of fumarate formation from the 1-phase fermentation by *A. terreus* has been occasionally reported in the previous literature; nevertheless, the finding in this study was confirmed by the HPLC chromatograms of the fermentation samples compared with those of the standards (data not shown) (Jimenez-Quero et al. 2016).

The two-phase fermentation was introduced in the cultivation of *A. terreus* to investigate the production of fermentation metabolites under different environmental conditions. In the two-phase fermentation, spore germination and fungal growth were initiated during the first phase; whereas in the second phase, the growth was limited, allowing the fungi to convert the substrates to other fermentation metabolites (Thitiprasert et al. 2016; Pimtong et al. 2017). By this approach, it can be seen clearly that cell biomass concentration remained relatively constant during the second phase (Fig. 2). Itaconic acid was found to be produced as the major product during the second phase. Fumaric acid and CO_2 production were observed with the trace amount of other metabolites in the TCA cycle (data not shown); however, the concentration was relatively low in comparison to those observed in the typical two-phase cultivation. From the findings in the two-phase fermentation, further experimental observation was conducted under varied environmental conditions for a better understanding of the metabolic response of *A. terreus* NRRL1960 to the process conditions, especially under stress conditions.

Dissolved oxygen and pH regulated metabolite production in the 2-phase fermentation

Table 1 represents the fermentation kinetics data of *A. terreus* NRRL1960 during the second phase in the two-phase fermentation cultivated at low DO levels (10, 15, and 20%). Itaconic acid and fumaric acid were observed in the fermentation broth during the second phase in all of the conditions studied. From the kinetics profiles (data not shown), ethanol was observed

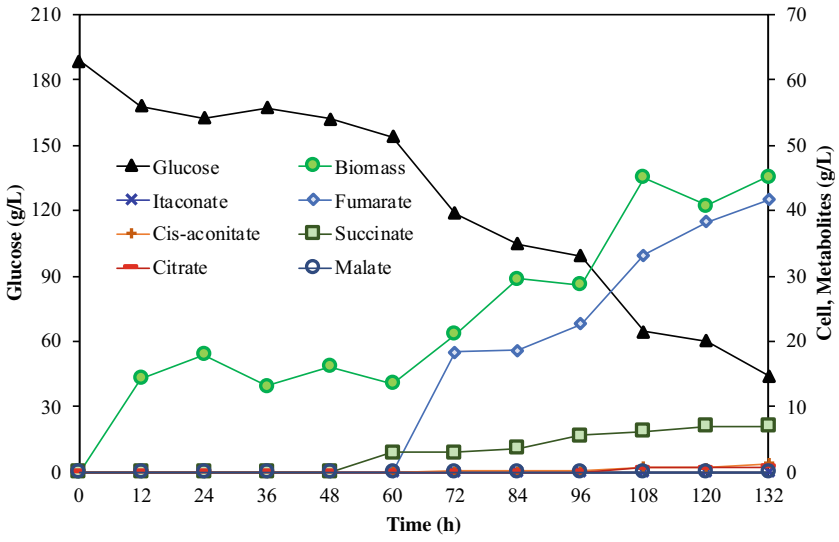

Fig. 1 Metabolite production profiles in 1-phase fermentation by *A. terreus* cultivated at 30 °C, 350 rpm, 20% DO, and initial pH 3.1

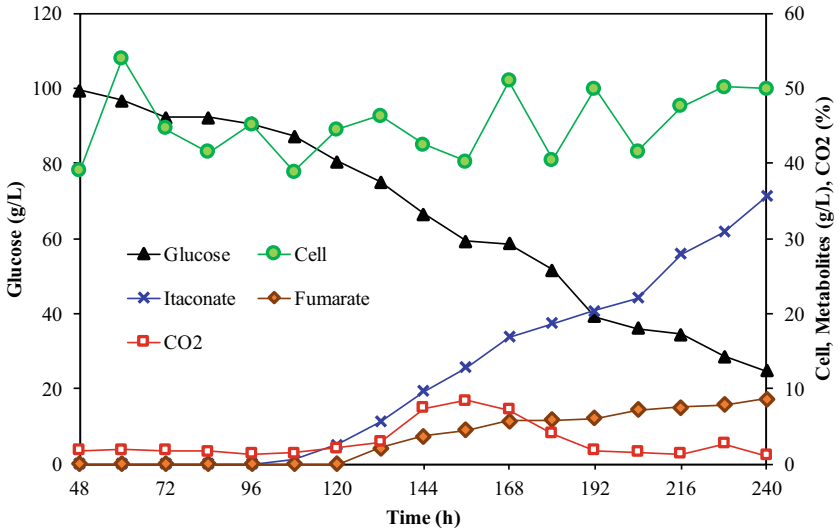

Fig. 2 Metabolite production profiles of *A. terreus* during the production phase in two-phase fermentation. The fermentor was controlled at 30 °C, 100 rpm, 10% DO, and pH 2.0. The C/N weight ratio of the production medium was 100/2.36

later in some operating conditions at the end of the fermentation (Table 1). The formation of ethanol revealed the evidence of oxygen limitation during the cultivation. The final cell concentration and yield fluctuated because of morphological changes occurring during the production phase, which caused difficulties in sampling and quantitative measurement. The results show that increasing the DO level and pH rather lowered the production of the end metabolites (itaconic acid and fumaric acid). Nevertheless, the metabolite production was still limited as observed from the low yield and productivity when compared with the fermentation study operated at the high DO level (Kuenz et al. 2012; Krull et al. 2017).

The phenomenon of low cell biomass production during the second phase in the two-phase fermentation can be explained by the activation of the reductive pyruvate carboxylation together with the oxidation of pyruvate via TCA cycle while the oxidative phosphorylation was uncoupled from the glycolysis. It was reported that the TCA cycle was active during fumaric acid production in case the reductive pyruvate carboxylation was the sole pathway. As a result, ATP generation for cell maintenance and metabolites transportation was limited (Kenealy et al. 1986). With the CO_2 fixation under the aerobic condition, pyruvate carboxylase catalyzed the conversion of pyruvate to oxaloacetic acid and subsequently to fumaric acid. Consequently, citric acid flux in the TCA cycle was somewhat low during the first phase when growth was presumably promoted. However, the glucose metabolism and CO_2 fixation could continue and could lead to the accumulation of citric acid flux in the TCA cycle later when nitrogen became limited which gradually decreased the cell biomass production (Romano et al. 1967).

In the typical 1-phase fermentation cultivation, end product formation followed the growth-associated product-formation kinetics model. Kuenz et al. reported that itaconic acid was produced simultaneously with the growth during the cultivation (Kuenz et al. 2012). It should be noted that itaconic acid fermentation by *A. terreus* is an incomplete oxidation process involving decarboxylation of cis-aconitic acid by cis-aconitate decarboxylase, which interrupts the TCA cycle (Gyamerah 1995a). On the other hand, in the two-phase cultivation, it was found that the metabolite production (both itaconic acid and fumaric acid) followed non-growth-associated product-formation kinetics. This phenomenon could be explained by oxidative phosphorylation being uncoupled from glycolysis under the low DO level with limited ammonium concentration (Fig. 3) (Gyamerah 1995b; Riscaldati et al. 2000; Karaffa et al. 2015). Consequently, the glycolytic flux was enhanced rapidly for ATP regeneration via substrate-level phosphorylation under this condition (Klement and Buchs 2013). With the limited nitrogen and oxygen, pyruvate flux was shifted toward the itaconic acid production route instead of completing the oxidative TCA cycle for biosynthesis.

The evidence of both nitrogen and phosphate limitation confirmed the non-growth-associated product-formation kinetics of end metabolite production during the second phase in the two-phase cultivation (Riscaldati et al. 2000; Papagianni et al. 2005; Boer et al. 2010). Itaconic acid and fumaric acid were found from the fermentation after 96 h when the concentration of ammonium and phosphate became low at 0.29 and 13.0 mg/L, respectively (Fig. 3). This finding was consistent with our previous study indicating that itaconic acid was first observed as the major end product in the fermentation broth when the growth was limited (Songserm et al. 2015). Klement and Buchs also reported that the overproduction of itaconic acid by *A. terreus* required nutrient limitation to uncouple glycolysis from oxidative phosphorylation (Klement and Buchs 2013). Riscaldati et al. reported that itaconic acid production was observed in the fermentation broth when the phosphate concentration in the medium dropped to approximately 10 mg/L, with

Table 1 Effect of dissolved oxygen and pH on the metabolic responses of *A. terreus* NRRL1960 cultivated in medium B at 30 °C and 100 rpm during the second phase in the two-phase fermentation

%DO	pH	Cell[a]		Itaconate				Fumarate		Ethanol	
		Final conc. (g/L)	Yield (g/g)	Final conc. (g/L)	Yield (g/g)	Productivity (g/L h)	Produced at (h)	Final conc. (g/L)	Yield (g/g)	Final conc. (g/L)	Yield (g/g)
10	1.85	64.40±3.31	0.51±0.02	22.37±4.48	0.49±0.04	0.16±0.02	108	6.30±0.14	0.12±0.01	1.95±0.01	0.04±0.01
	2.00	50.00±0.92	0.15±0.02	35.65±0.89	0.52±0.03	0.26±0.02	108	8.70±0.71	0.12±0.01	0±0	0±0
	2.15	46.60±2.09	0.16±0.05	22.39±2.22	0.48±0.03	0.15±0.05	96	9.42±0.70	0.17±0.02	0±0	0±0
	2.30	60.20±3.88	0.42±0.09	15.86±0.94	0.38±0.01	0.13±0.03	108	8.00±0.90	0.13±0.01	0±0	0±0
15	1.85	44.60±0.09	0.31±0.07	23.28±5.81	0.47±0.01	0.19±0.03	132	4.70±0.23	0.08±0.00	1.95±0.00	0.03±0.00
	2.00	54.00±3.56	0.20±0.03	22.85±3.08	0.40±0.05	0.20±0.03	120	5.43±0.37	0.08±0.01	0±0	0±0
	2.15	60.50±3.74	0.25±0.06	8.37±1.21	0.23±0.06	0.06±0.01	132	3.18±0.11	0.07±0.00	0±0	0±0
	2.30	54.70±1.51	0.35±0.04	8.14±3.26	0.25±0.06	0.05±0.00	132	2.22±0.17	0.05±0.00	3.14±0.01	0.07±0.01
20	1.85	43.00±1.17	0.15±0.04	14.73±1.75	0.33±0.04	0.07±0.01	132	5.84±0.25	0.10±0.01	0±0	0±0
	2.00	52.00±2.10	0.22±0.03	12.19±1.42	0.28±0.01	0.08±0.02	120	6.09±0.28	0.09±0.01	0±0	0±0
	2.15	62.40±0.44	0.34±0.05	4.58±2.22	0.19±0.04	0.04±0.00	132	4.34±0.17	0.07±0.00	0±0	0±0
	2.30	54.00±1.83	0.04±0.02	7.99±1.01	0.19±0.01	0.06±0.01	120	4.16±0.31	0.07±0.01	6.44±0.01	0.11±0.01

[a] Total cell biomass production from the beginning to the end of fermentation

the continuously decreasing ammonium concentration from 20 mg/L to less than 1 mg/L, while the cell concentration was slowly increasing from 3 to 10–11 g/L (Riscaldati et al. 2000). Hevekerl et al. claimed that, under the optimized operating conditions, itaconic acid was produced by the 1-day cultivation when the phosphate concentration was decreased (Hevekerl et al. 2014a).

It was reported that in the absence of oxygen, itaconic acid production was immediately stopped in *A. terreus* NRRL1960 (Gyamerah 1995b). The production mechanism involving the protein synthesis was restored slowly only under the aerobic condition (Gyamerah 1995b). To be more specific, itaconic acid production stopped as ATP generation was inhibited (Kuenz et al. 2012; Klement and Buchs 2013). ATP was claimed to be responsible for maintaining a proper physiological pH inside the cells (i.e., near neutral pH), counteracting the acid produced in the fermentation process and the low external pH (Riscaldati et al. 2000; Hevekerl et al. 2014b; Krull et al. 2017). When the extracellular pH was decreased, the permeability of the cell membrane was decreased. The transport of acid metabolites and proton across the membrane only occurred when the sufficient ATP was present (Corte-Real and Leao 1990). In the yeast cultivation, it was stated that the diffusion rate of undissociated acids across the membrane was increased with the decreasing extracellular pH. The same phenomenon was found during the second phase in the two-phase cultivation of *A. terreus* in this study. The different extracellular concentration of itaconic acid was observed from the cultivation with the small change in pH. This can be explained by the different acid dissociation degree at the different cultivation pH which resulted in the different concentration ratio of the undissociated acid and its salt. A detailed explanation on the synthesis of end metabolites in *A. terreus* and the transport across the membrane can be found below.

Itaconic acid was appeared as the major end metabolite produced in the second phase of the two-phase fermentation. It was produced in an undissociated form (H_2IA) in the cytosol. The degree of dissociation shifted from H_2IA to the single-dissociated form (HIA^-) and the double-dissociated form (IA^{2-}) based on the intracellular pH, causing the release of protons and the acidification of the cytosol, which led to stress or growth inhibition of the cells. The dissociated forms (HIA^-) and (IA^{2-}) were not able to pass across the cytoplasmic membrane, while the acid form (H_2IA) could diffuse through the membrane freely via the major facilitator superfamily (Mfs) protein transporters, using the energy from electrochemical gradients across the membrane. The transport of itaconic acid across the cytoplasmic membrane also involved the proton-pumping H^+ ATPase, which required ATP to drive the transport of protons across the membrane (Krull et al. 2017).

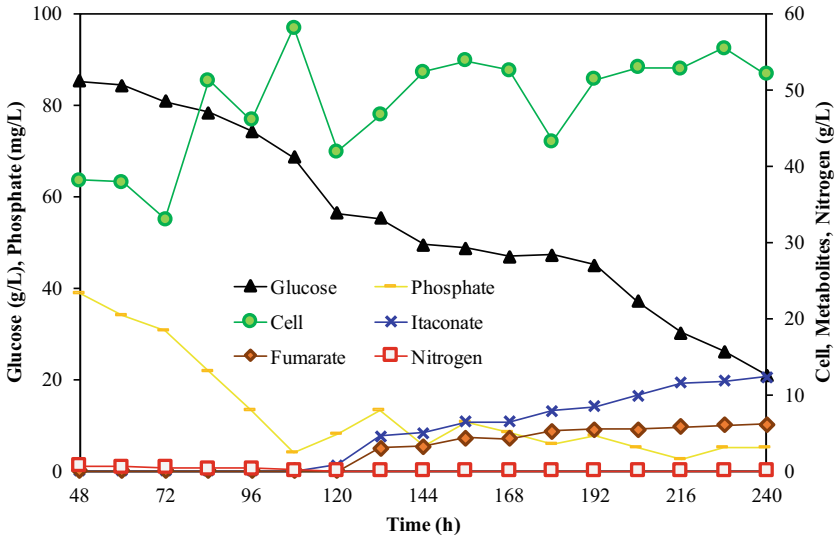

Fig. 3 The fermentation kinetics of *A. terreus* under the limited nitrogen and phosphate during the production phase. The fermentor was controlled at 30 °C, 100 rpm, 20% DO, and pH 2.0. The C/N weight ratio of the production medium was 100/2.36

In case of fumaric acid production at low extracellular pH, it was reported that the undissociated form could passively diffuse back through the cytoplasmic membrane decreasing the intracellular pH. Nonetheless, the transport mechanism of fumaric acid in fungi has not been clearly understood. It is believed that increasing the activity of the dicarboxylic acid transporters could lower the intracellular fumarate concentration in the cytosol and, therefore, could provide the positive effect on the fermentation process performance (Roa Engel et al. 2008, 2011; Xu et al. 2012).

From the previous explanation, it can be summarized that a low pH is necessary in the cultivation of *A. terreus* NRRL1960 for the end metabolite production in order to provide the sufficient amount of proton in exchange with the acid metabolite transport. In addition, ethanol formation and low extracellular concentration of itaconate and fumarate confirmed the evidence of oxygen limitation and insufficient ATP regeneration in the two-phase fermentation system. For further improvement in production performance, the fermentation under high DO level is necessary.

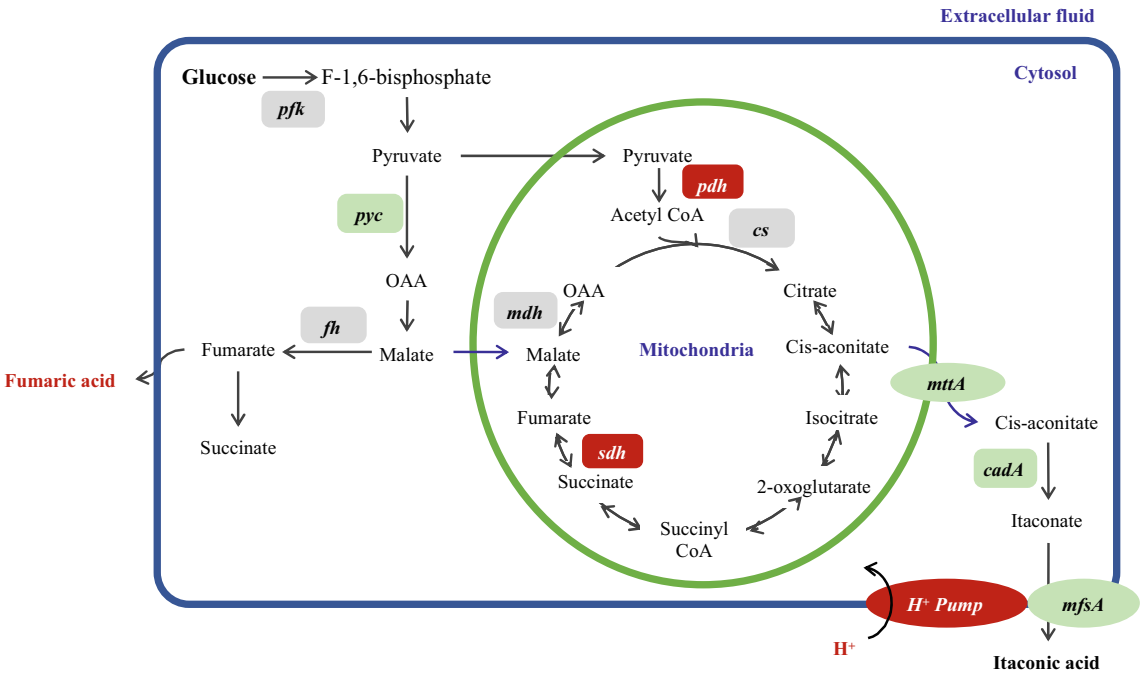

Fig. 4 Metabolic pathway of *A. terreus* and the key genes responsible in glycolysis and TCA cycle. The key genes in the green boxes were overexpressed during the production phase, while the genes in the red boxes were downregulated. The genes in the gray boxes were found to be expressed at certain levels

Gene expression explained metabolic responses of *A. terreus*

To better understand the fermentation kinetics and the metabolic response of *A. terreus* NRRL1960 and, thus, to improve the fermentation performance for desirable end product further, we observed gene expression during the second phase in the two-phase fermentation where the end metabolite production was enhanced. From the selection of one fermentation condition as the representative of the fermentation operation under stress condition (low DO and pH) to conduct transcriptomic analysis, we attempted to correlate the fermentation kinetics results with the regulation of the genes of interest under the specified process conditions. Figure 4 shows the central metabolic pathway of *A. terreus*. Glucose was converted to the key intermediate pyruvate. The key responsible enzyme in this route was phosphofructokinase. Pyruvate was either converted to acetyl CoA by the pyruvate dehydrogenase complex or was carboxylated to oxaloacetate by pyruvate carboxylase. The formation of itaconic acid involved the shuttle of intermediate metabolites between the cytosol and the mitochondria and the formation utilized the different enzymes present in both of the cell compartments. Cis-aconitate was transported into the cytosol via the mitochondrial TCA transporter. Cis-aconitate was then converted to itaconic acid by cis-aconitate decarboxylase. Later, undissociated form of itaconic acid was secreted from the cytosol across the cytoplasmic membrane in exchange for protons via the Mfs transporter (Krull et al. 2017). Fumaric acid synthesis pathway started with the carboxylation of pyruvate by pyruvate carboxylase to oxaloacetate with the presence of ATP and CO_2. Later, oxaloacetate was converted to malic acid by malate dehydrogenase and then to fumaric acid by fumarase or fumarate hydratase (Xu et al. 2012). The transport mechanism of fumaric acid in filamentous fungi has not been studied extensively; however, the transport mechanism in yeast has been studied thoroughly. This was presumably applied for the transport of fumarate in the filamentous fungi (Roa Engel et al. 2008).

Figure 5 describes the transcriptional levels of genes encoding key enzymes involved in glycolysis, TCA cycle, oxidative phosphorylation, and biosynthesis of acid metabolites (itaconic acid and fumaric acid) during the second phase in the two-phase fermentation. The fermentation process was controlled at 30 °C, 100 rpm, 10% DO, and pH 2.0 (see Supplementation Material Online, Table S1). The expression of phosphofructokinase (*pfk*) genes of glycolysis was changed slightly during the production phase (Fig. 5a). The evidence of the downregulation of pyruvate dehydrogenase (*pdhB*, *pdhC*, *pdhA*, and *pdhX*) genes with the upregulation of the pyruvate carboxylase (*pyc*) gene from the heat maps indicated that more pyruvate was carboxylated to oxaloacetate as the fermentation proceeded (Fig. 5a). It was suggested that the limited nitrogen and phosphate and the low DO level were responsible for this metabolic shift (Wynn et al. 2001). The downregulation of the citrate synthase (*cs*) gene was the consequence of the downregulated *pdh* genes, while the expression of the gene encoding aconitase fluctuated (Fig. 5b) (Patel et al. 2014). The upregulation of *pyc* at 144 h resulted in a large pool of oxaloacetate in the cytosol. This induced the conversion of oxaloacetate to malate, to be transported into the mitochondria, while cis-aconitate was transported across the mitochondrial TCA transporter. As a result, the major glucose consumption went to itaconic acid synthesis. This phenomenon was confirmed by the upregulation of the genes encoding mitochondrial TCA transporter (*mttA*), cis-aconitate decarboxylase (*cadA*), and Mfs transporter (*mfsA*) responsible for secreting itaconic acid across the cytoplasmic membrane to the fermentation broth (Fig. 5c) (Hossain et al. 2016). It was also found that the gene encoding fumarate hydratase was slightly upregulated (Fig. 5d). The time course data explaining the upregulation of the genes in itaconic acid cluster was consistent with the fermentation kinetics data describing the production of itaconic acid after 96 h cultivation.

The low production rate of itaconic acid could be explained by the downregulation of four ATP synthase genes (for the ATP synthase subunits d, 4, 5, and 9) (Fig. 5e). As a result, the proton-pumping H^+ ATPase which requires ATP to drive the transport of proton across the membrane in exchange for intracellular H_2IA was shunted (Krull et al. 2017). Together with the upregulated genes of the itaconic acid cluster, this would result in the accumulation of H_2IA and eventually intracellular metabolic stress. In addition to the downregulation of ATP synthase genes, the downregulation of the succinate dehydrogenase gene confirmed that glycolysis was uncoupled from oxidative phosphorylation under the condition of limited nitrogen, phosphate, and dissolved oxygen (Fig. 5d). Succinate dehydrogenase was the only enzyme that participated in both the TCA cycle and the electron transport chain; therefore, the downregulation of this gene resulted in an incomplete TCA cycle (Hartman et al. 2014; Jimenez-Quero et al. 2016). This finding confirmed that glycolysis and oxidative phosphorylation were uncoupled, resulting in limitation of ATP availability and reduction of power regeneration (in the form of NADH and FADH) (Jimenez-Quero et al. 2016). Substrate-level phosphorylation was initiated to allow ATP regeneration, where fumaric acid was the electron acceptor, confirmed by the slight upregulation of the fumarate hydratase gene (Fig. 5d).

Conclusion

The central metabolic pathway of *A. terreus* involves both the biosynthesis and the transport of metabolites across cell compartments. In this study, two-phase fermentation was conducted to study the metabolic responses of *A. terreus* during cultivation under low DO and pH levels. The transcriptomic data analysis was employed to correlate the gene expression level

(a)

gene_id	Gene Name	log2(fold_change)							
		48 vs. 72	48 vs. 96	48 vs. 120	48 vs. 144	48 vs. 168	48 vs. 192	48 vs. 216	48 vs. 240
Glycolysis									
ATEG_07332	6-phosphofructokinase alpha subunit (pfk-alpha)	-0.21	-1.19	-0.26	-0.95	0.00	-0.68	-3.35	-1.85
ATEG_07646	6-phosphofructokinase beta subunit (pfk-beta)	0.88	0.67	1.51	0.03	0.24	-0.89	-1.26	-1.13
ATEG_03737	Pyruvate dehydrogenase (acetyltransferring) (pdhB)	0.55	-2.00	-0.11	-2.39	-0.81	-1.00	-2.98	-1.00
ATEG_04262	Pyruvate dehydrogenase (acetyltransferring) (pdhC)	1.92	-0.78	0.42	-2.17	-2.58	-1.26	-1.76	-0.26
ATEG_06361	Dihydrolipoyllysine-residue acetyltransferase (pdhA)	0.44	-0.54	-1.12	-1.71	-1.89	-3.89	-3.06	-2.30
ATEG_01642	Pyruvate dehydrogenase complex component X (pdhX)	2.09	1.68	1.22	-1.17	0.42	-1.26	-0.76	-1.59
ATEG_05433	Pyruvate carboxylase, cytosol (pyc)	1.89	1.35	2.21	3.10	4.76	3.79	2.94	3.91

(b)

gene_id	Gene Name	log2(fold_change)							
		48 vs. 72	48 vs. 96	48 vs. 120	48 vs. 144	48 vs. 168	48 vs. 192	48 vs. 216	48 vs. 240
Citrate isomer production									
ATEG_07199	Citrate synthase (cs)	-1.30	-1.42	ND	-2.39	ND	ND	ND	-2.81
ATEG_02937	Aconitase	1.74	1.81	2.97	2.51	0.95	0.10	1.72	0.36

(c)

gene_id	Gene Name	log2(fold_change)							
		72 vs. 48	72 vs. 96	72 vs. 120	72 vs. 144	72 vs. 168	72 vs. 192	72 vs. 216	72 vs. 240
Itaconic acid cluster									
ATEG_09970	Mitochondrial TCA transporter (mttA)	ND	4.14	5.02	5.05	5.51	4.93	4.51	4.74
ATEG_09971	Cis-aconitate decarboxylase (cadA)	ND	2.93	4.60	4.03	5.54	4.83	3.73	4.96
ATEG_09972	Major facilitator superfamily transporter (mfsA)	ND	2.31	4.69	5.32	5.10	-0.82	5.72	5.07

(d)

gene_id	Gene Name	log2(fold_change)							
		48 vs. 72	48 vs. 96	48 vs. 120	48 vs. 144	48 vs. 168	48 vs. 192	48 vs. 216	48 vs. 240
Glyoxylate/Dicarboxylate metabolism									
ATEG_01603	Isocitrate dehydrogenase, mitochondrial	1.55	0.98	2.36	0.94	1.88	0.39	0.99	-0.68
ATEG_00467	Isocitrate dehydrogenase (NAD) subunit	-1.32	-1.78	-2.32	-3.91	-4.91	-2.32	-4.08	-2.32
ATEG_07408	Isocitrate dehydrogenase (NAD) subunit	2.41	0.81	3.00	ND	3.39	2.58	ND	1.91
ATEG_03911	2-oxoglutarate dehydrogenase E1 component	1.82	0.81	ND	1.74	1.81	2.00	1.41	2.17
ATEG_05235	Succinate dehydrogenase cytochrome b small subunit	-1.60	-3.00	-3.22	-2.81	-3.81	-5.22	-4.98	-4.22
ATEG_07592	Succinate dehydrogenase [ubiquinone] Fe-S subunit	-1.91	-1.19	-1.00	-0.78	-2.00	-2.68	-2.18	ND
ATEG_07205	Fumarate hydratase class II	0.14	0.34	-1.17	-0.75	0.29	0.22	ND	0.74
ATEG_05653	Malate dehydrogenase	-0.18	0.13	0.58	-1.00	-1.42	-1.19	-2.18	-1.42

(e)

gene_id	Gene Name	log2(fold_change)							
		48 vs. 72	48 vs. 96	48 vs. 120	48 vs. 144	48 vs. 168	48 vs. 192	48 vs. 216	48 vs. 240
ATP Synthase									
ATEG_07080	ATP synthase subunit d	-0.36	-2.29	-2.32	-3.17	-5.91	-3.45	-3.50	-5.91
ATEG_04777	ATP synthase subunit 4	-1.38	-2.45	-2.39	-2.67	-4.32	-4.85	-4.99	-5.95
ATEG_01173	ATP synthase subunit 5	-2.08	ND	-1.58	ND	-1.58	ND	ND	-2.59
ATEG_05268	ATP synthase protein 9	-2.08	-3.65	-3.46	-3.63	-4.46	-6.04	-4.22	-3.72

Fig. 5 Heat maps summarizing the differential expression of the key genes responsible in glycolysis and TCA cycle during the production phase of *A. terreus*. The number in the box indicates the differential gene expression level compared with that at the starting time that the gene was expressed (48 or 72 h). The green box represents the upregulation of the gene. The red box represents the downregulation of the gene. The black box indicates a slight change in gene expression level (log2(fold_change) less than 2). ND represents the fragments per kilobase per million reads (FPKM) at that time was zero (no expression). **a** Glycolytic cluster, **b** citrate isomer, **c** itaconic acid cluster, **d** glyoxylate/dicarboxylate metabolism, and **e** ATP synthase cluster

with the metabolite production kinetics. Under the stress conditions with low DO level and limited nitrogen and phosphate, *A. terreus* produced itaconic acid as the major end product. Fumaric acid was found to the byproduct under these conditions. The production of both itaconic acid and fumaric acid indicated that oxaloacetate simultaneously entered both the reductive carboxylation and the oxidative TCA pathways. The transcriptomic data suggested that a high flux of itaconic acid occurred due to the upregulation of *pyc*. As a result, pyruvate was subsequently converted to oxaloacetate and malate was generated. Malate entered the mitochondria, while cis-aconitate was transported to the cytosol at the *mttA*

transporter resulting in the incomplete oxidative TCA cycle and the uncoupled glycolysis and oxidative phosphorylation. It was observed that the gene encoding fumarate hydratase in the reductive TCA cycle was slightly upregulated. Although the genes in the itaconic acid cluster including *mfsA* were upregulated, the downregulation of ATP synthase caused a strong effect on itaconic acid production as it controlled the transport of protons in exchange for itaconic acid across the cytoplasmic membrane. From the fermentation kinetics and the transcriptomic analysis obtained in this study, it can be suggested that low pH is necessary in the cultivation of *A. terreus* NRRL1960 for the end metabolite production in order to provide the sufficient amount of proton in exchange with the acid metabolite transport. In addition, ethanol formation and low extracellular concentration of itaconate and fumarate confirmed the evidence of oxygen limitation and insufficient ATP regeneration in the two-phase fermentation system. For further improvement in production performance, the fermentation under high DO level is necessary.

Acknowledgements The authors would like to thank Dr. Kaemwich Jantama for his fruitful discussion on transcriptomic analysis. The work in RNA-seq gene expression analysis performed by D. Ashley Hill and her colleagues at ResourcePath, Sterlin, VA, USA are highly appreciated. The authors also thank Timothy Wesselman and Roshni Patel from OnRamp Bioinformatics, Inc. (San Diego, CA, USA) for their outstanding work on analyzing the RNA-seq data and differential gene expression analysis.

Funding Information Partial support from the Grant for International Research Integration: Research Pyramid, Ratchadapiseksomphot Endowment Fund (GCURP_58_01_33_01) and Thailand Research Fund via the Distinguished Research Professor Grant (DPG5880003) are also acknowledged. The research facility support from the Chulalongkorn Academic Advancement into its 2nd Century Project (CUAASC) is highly appreciated. PS is the recipient of the Royal Jubilee Scholarship Program, Thailand Research Fund.

Compliance with ethical standards

Conflict of interest The authors declare that they have no conflict of interest.

Ethical approval This article does not contain any studies with human participants or animals performed by any of the authors.

References

Baykov AA, Evtushenko OA, Avaeva SM (1988) A malachite green procedure for orthophosphate determination and its use in alkaline phosphatase-based enzyme immunoassay. Anal Biochem 171:266–270

Birren BW, Lander ES, Galagan JE, et al (2005) Annotation of the *Aspergillus terreus* NIH264 genome. EMBL/GenBank/DDBJ databases

Boer VM, Crutchfield CA, Bradley PH, Botstein D, Rabinowitz JD (2010) Growth-limiting intracellular metabolites in yeast growing under diverse nutrient limitations. Mol Biol Cell 21:198–211

Boruta T, Bizukojc M (2016) Induction of secondary metabolism of *Aspergillus terreus* ATCC 20542 in the batch bioreactor cultures. Appl Microbiol Biotechnol 100:3009–3022

Corte-Real M, Leao C (1990) Transport of malic acid and other carboxylic acids in the yeast *Hansenula anomala*. Appl Environ Microbiol 56:1109–1113

Gyamerah MH (1995a) Oxygen requirement and energy relations of itaconic acid fermentation by *Aspergillus terreus* NRRL1960. Appl Microbiol Biotechnol 44:20–26

Gyamerah MH (1995b) Factors affecting the growth form of *Aspergillus terreus* NRRL1960 in relation to itaconic acid fermentation. Appl Microbiol Biotechnol 44:356–361

Hajjaj H, Niederberger P, Duboc P (2001) Lovastatin biosynthesis by *Aspergillus terreus* in a chemically defined medium. Appl Environ Microbiol 67:2596–2602

Hartman T, Weinrick B, Vilcheze C, Berney M, Tufariello J, Cook GM, Jacobs WR Jr (2014) Succinate dehydrogenase is the regulator of respiration in *Mycobacterium tuberculosis*. PLoS Pathog 10:1–15

Hevekerl A, Kuenz A, Vorlop KD (2014a) Filamentous fungi in microtiter plates-an easy way to optimize itaconic acid production with *Aspergillus terreus*. Appl Microbiol Biotechnol 98:6983–6989

Hevekerl A, Kuenz A, Vorlop KD (2014b) Influence of the pH on the itaconic acid production with *Aspergillus terreus*. Appl Microbiol Biotechnol 98:10005–10012

Hossain AH, Li A, Brickwedde A, Wilms L, Caspers M, Overkamp K, Punt PJ (2016) Rewiring a secondary metabolite pathway toward itaconic acid production in *Aspergillus niger*. Microb Cell Factories 15:1–15

Jimenez-Quero A, Pollet E, Zhao M, Marchioni E, Averous L, Phalip V (2016) Itaconic and fumaric acid production from biomass hydrolysates by *Aspergillus* strains. J Microbiol Biotechnol 26:1557–1565

Karaffa L, Diaz R, Papp B, Fekete E, Sandor E, Kubicek CP (2015) A deficiency of manganese ions in the presence of high sugar concentrations is the critical parameter for achieving high yields of itaconic acid by *Aspergillus terreus*. Appl Microbiol Biotechnol 99:7937–7944

Kenealy W, Zaady E, Dupreez JC, Stieglitz B, Goldberg I (1986) Biochemical aspects of fumaric acid accumulation by *Rhizopus arrhizus*. Appl Environ Microbiol 52:128–133

Klement T, Buchs J (2013) Itaconic acid–a biotechnological process in change. Bioresour Technol 135:422–431

Kocabas A, Ogel ZB, Bakir U (2014) Xylanase and itaconic acid production by *Aspergillus terreus* NRRL 1960 within a biorefinery concept. Ann Microbiol 64:75–84

Krull S, Hevekerl A, Kuenz A, Prube U (2017) Process development of itaconic acid production by a natural wild type strain of *Aspergillus terreus* to reach industrially relevant final titers. Appl Microbiol Biotechnol 101:4063–4072

Kuenz A, Gallenmuller T, Willke T, Vorlop KD (2012) Microbial production of itaconic acid: developing a stable platform for high product concentrations. Appl Microbiol Biotechnol 96:1209–1216

Liu J, Gao Q, Xu N, Liu L (2013) Genome-scale reconstruction and in silico analysis of *Aspergillus terreus* metabolism. Mol BioSyst 9:1939–1948

Nazir A, Soni R, Saini HS, Kaur A, Chadha BS (2010) Profiling differential expression of cellulases and metabolite footprints in *Aspergillus terreus*. Appl Biochem Biotechnol 162:538–547

Papagianni M, Wayman F, Mattey M (2005) Fate and role of ammonium ions during fermentation of citric acid by *Aspergillus niger*. Appl Environ Microbiol 71:7178–7186

Patel MS, Nemeria NS, Furey W, Jordan F (2014) The pyruvate dehydrogenase complexes: structure-based function and regulation. J Biol Chem 289:16615–16622

Pimtong V, Ounaeb S, Thitiprasert S, Tolieng V, Sooksai S, Boonsombat R, Tanasupawat S, Assabumrungrat S, Thongchul N (2017) Enhanced effectiveness of *Rhizopus oryzae* by

immobilization in a static bed fermentor for L-lactic acid production. Process Biochem 52:44–52

Protein knowledgebase (UniProtKB) of *Aspergillus terreus* NIH2624. Available from www.uniprot.org/uniprot/?query=A+terreus+&sort=score. Accessed March 13, 2017

Riscaldati E, Moresi M, Federici F, Petruccioli M (2000) Effect of pH and stirring rate on itaconate production by *Aspergillus terreus*. J Biotechnol 83:219–230

Roa Engel CA, Straathof AJJ, Zijlmans TW, van Gulik WM, van der Wielen LAM (2008) Fumaric acid production by fermentation. Appl Microbiol Biotechnol 78:379–389

Roa Engel CA, van Gulik WM, Marang L, van der Wielen LAM, Straathof AJJ (2011) Development of a low pH fermentation strategy for fumaric acid production by *Rhizopus oryzae*. Enzym Microb Technol 48:39–47

Romano AH, Bright MM, Scott WE (1967) Mechanism of fumaric acid accumulation in *Rhizopus nigricans*. J Biotechnol 93:600–604

Schimmel TG (1998) Effect of butyrolactone I on the producing fungus, *Aspergillus terreus*. Appl Environ Microbiol 64:3707–3712

Songserm P, Thitiprasert S, Tolieng V, Piluk J, Tanasupawat S, Assabumrungrat S, Yang ST, Karnchanatat A, Thongchul N (2015) Regulating pyruvate carboxylase in the living culture of *Aspergillus terreus* NRRL1960 by L-aspartate for enhanced itaconic acid production. Appl Biochem Biotechnol 177:595–609

Thitiprasert S, Pimtong V, Kodama K, Sooksai S, Tanasupawat S, Assabumrungrat S, Tolieng V, Thongchul N (2016) Correlative effect of dissolved oxygen and key enzyme inhibitors responsible for L-lactate production by immobilized *Rhizopus oryzae* NRRL395 cultivated in a static bed bioreactor. Process Biochem 51:204–212

Tzollas NM, Zachariadis GA, Anthemidis AN, Stratis JA (2010) A new approach to indophenol blue method for determination of ammonium in geothermal waters with high mineral content. Int J Environ Anal Chem 90:115–126

Wynn JP, Hamid AA, Li Y, Ratledge C (2001) Biochemical events leading to the diversion of carbon into storage lipids in the oleaginous fungi *Mucor circinelloides* and *Mortierella alpine*. Microbiology 147:2857–2864

Xu Q, Li S, Huang H, Wen J (2012) Key technologies for the industrial production of fumaric acid by fermentation. Biotechnol Adv 30:1685–1696

Journal of Cleaner Production 185 (2018) 576–587

Contents lists available at ScienceDirect

Journal of Cleaner Production

journal homepage: www.elsevier.com/locate/jclepro

An assessment of the longevity of samarium cobalt trioxide perovskite catalyst during the conversion of greenhouse gases into syngas

Osarieme Uyi Osazuwa [a, b, c], Maksudur R. Khan [a, b], Su Shiung Lam [d], Suttichai Assabumrungrat [e], Chin Kui Cheng [a, b, *]

[a] Centre of Excellence for Advanced Research in Fluid Flow, Universiti Malaysia Pahang, Lebuhraya Tun Razak, 26300 Gambang Kuantan, Pahang, Malaysia
[b] Faculty of Chemical & Natural Resources Engineering, Universiti Malaysia Pahang, Lebuhraya Tun Razak, 26300 Gambang Kuantan, Pahang, Malaysia
[c] Department of Chemical Engineering, University of Benin, PMB 1154, Benin City, Edo State, Nigeria
[d] Eastern Corridor Renewable Energy Group (ECRE), School of Ocean Engineering, University Malaysia Terengganu, 21030 Kuala Terengganu, Malaysia
[e] Center of Excellence in Catalysis and Catalytic Reaction Engineering, Department of Chemical Engineering, Faculty of Engineering, Chulalongkorn University, Bangkok 10330, Thailand

ARTICLE INFO

Article history:
Received 30 October 2017
Received in revised form
25 January 2018
Accepted 6 March 2018
Available online 7 March 2018

Keywords:
Dry (CO_2) reforming
Methane
$SmCoO_3$
Perovskite
Syngas
Longevity

ABSTRACT

Catalytic carbon dioxide (CO_2) reforming of methane (CH_4) has gained interest because it reduces the amount of greenhouse gases in the environment. In addition, the products from the reforming process are utilized as feedstock in the Fischer-Tropsch synthesis. However, rapid catalyst deactivation and sintering due to carbon deposition often accompany the CO_2 reforming of CH_4 reaction. In this study, samarium cobalt trioxides perovskite catalyst was synthesized and employed as catalyst in a 72 h longevity test conducted at 1073 K using CO_2 to reform CH_4 with gas-hourly-space velocity of 30,000 h^{-1}. Feed ratios (0.5–2.0) were varied and excellent catalytic longevity, maximum conversion (above 90%) and yield (above 60%), were obtained at 1.0 feed ratio. Physicochemical properties of the fresh catalyst revealed uniform metallic particles distribution on a single phase perovskite structure, while spent catalyst showed evidence of carbon which was graphitic at 0.5–1.33 feed ratio with C–C and C–H bonds, and formed contaminant of carbon at 2.0 feed ratio with O–C=O bond.

© 2018 Elsevier Ltd. All rights reserved.

1. Introduction

Syngas (H_2 and CO) is a principal feed stock for liquid hydrocarbon production (via Fischer-Tropsch process), and it is generally produced from methane (CH_4) reforming which is a very important reaction in the utilization of the unwanted greenhouse gas (Zahedinezhad et al., 2009). There are several pathways for syngas production viz. steam (H_2O) reforming, (Seo et al., 2009), carbon dioxide (CO_2) reforming of CH_4, (Ayodele et al., 2016; Osazuwa et al., 2017) partial oxidation of CH_4 (Wang et al., 2003) and combination of H_2O and CO_2 (Choudhary and Mondal, 2006). Increase in energy utilization and minimization of the greenhouse effect has placed catalytic CO_2 reforming at a better advantage over other pathways. This is as a result of the consumption CH_4 and CO_2 the two main causes of greenhouse effect. However, coke deposition is a major setback to this process. This has further being stressed by Pompeo et al. (2009) who employed Ni catalyst supported on commercial α-Al_2O_3, modified by addition of CeO_2 and/or ZrO_2, to enhance the stability of the reforming reaction by minimizing the coke deposit. Therefore, the development of a very good and stable catalyst (resistance to deactivation) is of great interest. Noble metal based catalyst have been found to inhibit coke formation (Sutthiumporn and Kawi, 2011), however, their high cost have made nickel (Ni) based catalysts more attractive commercially, even though the latter has a significantly higher affinity for coke (Yentekakis et al., 2015). As a replacement for noble metal and Ni metal supported catalyst, transition metals such as cobalt (Co) can be combined with rare earth metals to develop catalyst which is known as perovskite.

Ideal perovskite oxide (ABO_3); with *A* and *B* as cations and *O* anion (oxygen), possess excellent redox properties which enables high dispersion of nano-scale metal particles in a reducing environment, thereby promoting catalytic performance and inhibiting coke formation on the surface of the catalyst, (Moradi et al., 2012).

* Corresponding author. Faculty of Chemical & Natural Resources Engineering, Universiti Malaysia Pahang, Lebuhraya Tun Razak, 26300 Gambang Kuantan, Pahang, Malaysia.
E-mail address: chinkui@ump.edu.my (C.K. Cheng).

https://doi.org/10.1016/j.jclepro.2018.03.060
0959-6526/© 2018 Elsevier Ltd. All rights reserved.

In addition, the perovskites structure allows for exchange of *A* site with minimum size limit of $r_A = 0.09nm$ and/or *B* site with minimum size limit of $r_B = 0.051nm$ (Zhu et al., 2014), thereby enabling the amalgamation of elements possessing dissimilar oxidation states (Tienthao et al., 2007). The perovskite catalyst can be formulated by employing the Goldschmidt tolerance factor (where $t \leq 1$) represented in eq. (1) (Labhasetwar et al., 2015).

$$t = \frac{(r_A + r_O)}{\{\sqrt{2}(r_B + r_O)\}}, \quad t \leq 1 \tag{1}$$

where t is tolerance factor, and r_A, r_B, r_O are the radii of the ions. Several reporters have used La–Ni based perovskite on CO_2 reforming of CH_4 (Valderrama et al., 2005), $La_{2-x}Sr_xNiO_4$ perovskite oxides (Pichas et al., 2010), iron (Fe) substituted $LaNiO_3$ perovskite oxide (Jahangiri et al., 2013), $LaNiO_3$ nano particles (Zheng et al., 2015).

$La_{1-x}Sr_xNiO_3$ perovskite oxides were prepared by the auto combustion method and used as catalysts precursors in dry reforming of methane by Valderrama et al. (2005). They investigated the reaction using a pulse technique at unity feed ratio. The catalyst samples were characterized using various techniques such as XRD, BET surface area, TPR-TPO and SEM. $LaNiO_3$ exhibited higher activity among all perovskite samples studied while La_2NiO_4 showed no activity. Their study showed the formation of Ni^0, $SrCO_3$ and $La_2O_2CO_3$ phases which hindered the formation of carbon. Dry reforming of CH_4 by CO_2 was studied over $La_{2-x}Sr_xNiO_4$ perovskite-type oxides by Pichas et al. (2010). Upon addition of small amounts of Sr an increase in carbon deposition was observed. However, when Sr was further increased, carbon formation was suppressed. Sol-gel method was employed to synthesize $LaNiO_3$ and $LaNi_{1-x}FeO_3$ ($x = 0.2$, 0.4, 0.6, 0.8 and 1) by Jahangiri et al. (2013). The effects of the promoter (Fe) and reaction temperatures were investigated in the combined reforming of CH_4 and O_2. $LaNiO_3$ exhibited high activity and selectivity with negligible coke formation, while the activity decrease with increasing amount of Fe added to the catalyst sample. Zhu et al. (2015) evaluated the catalytic performance of $La_{0.6}Sr_{0.4}Ni_xCo_{1-x}O_3$ perovskite catalysts in CO_2 reforming of coke oven gas over a fixed bed reactor at reaction temperature of 800 °C. Their observation showed that the partial substitution of Ni by Co enhances the catalytic activity and stability. Catalytic activity and resistance to carbon formation was best exhibited by $La_{0.6}Sr_{0.4}NiO_3$ calcined at 800 °C, due to the formation of $La_2O_2CO_3$ phase which inhibits the carbon deposition, accelerates oxidation of CH_4 and re-energize La_2O_3. Experimental and kinetic investigation of the plasma catalytic dry reforming of methane over perovskite $LaNiO_3$ nanoparticles was reported by Zheng et al. (2015). Compared to various supported La catalyst, $LaNiO_3$ showed better catalytic performance. Results from their study showed that low flowrate of feed gases and high input power were favourable for the conversion of reactants and formation of products but however led to lower energy efficiency. A kinetic model related to argon dilution in plasma-catalytic system and assisted by plasma-catalyst hybrid effect was proposed and employed to enhance the conversion. The model predicted that the reactant conversion rate was an exponential of the discharge energy. The catalytic performance of neodymium-containing mesoporous silica supported nickel catalysts in CH_4 reforming to syngas have been studied by Li et al. (2017). During the investigation, mesoporous silica promoted with neodymium (Nd) was prepared as support using sol-gel method. Ni-based catalyst using Nd-promoted silica (xNdMS; x: molar ratio of Nd/Si = 0.01, 0.02, 0.04, 0.06) were tested for CO_2 reforming of CH_4 and/or oxygen to produce syngas. Ni/0.04 Nd/MS catalyst showed greater activity in a 12 h time on stream however, with time, the catalyst deactivated due to poor stability of Ni/MS catalyst.

Significantly, due to the fact that Co shows less sensitivity towards coke formation and the oxide of Sm is very rich in lattice O_2, the fresh $SmCoO_3$ perovskite catalyst characterization has been carried out and the superior activity of $SmCoO_3$ perovskite catalyst has been tested in CO_2 reforming of CH_4 (Osazuwa et al., 2017) As a continuation of our previous work, the primary objective of the present study is to evaluate the longevity of $SmCoO_3$ perovskite catalyst on the conversion of the major greenhouse gases (CH_4 and CO_2) into syngas which can serve as a cleaner source of energy and feedstock for liquid fuels production via Fisher-Tropsch synthesis. Specifically, the effects of feed ratio on the conversion, yield and spent catalyst (carbon study) were presented.

2. Experimental

2.1. Catalyst synthesis

A sol-gel method adopted from literature was employed to synthesize the $SmCoO_3$ perovskite catalyst (Moradi et al., 2014; Zheng et al., 2015; Zhu et al., 2015). The $Sm(NO_3)_3.6H_2O$ was affixed to the chelating agent in the ratio 1:2 (2 M solution of citric acid) before the resulting solution was mixed with the Co $(NO_3)_2.6H_2O$ at ambient temperature. Continuous stirring of the mixture was carried out for 4 h at 353 K. The resulting gel was then dried at 383 K to obtain a xerogel which was ground into powder in an agate crucible. Prior to calcination, temperature programmed calcination (TPC) was carried out to study the solid-state phase change of the uncalcined catalyst. Subsequently, calcination was carried out at 1123 K with a heating rate of 5 K min^{-1} in a carbolite furnace.

2.2. Catalyst characterization

Temperature programmed oxidation (TPO) was employed to analyse the oxidation of coke on the spent catalyst. The thermogravimetric (TG) and the differential thermogravimetric (DTG) profiles representing the non-isothermal $SmCoO_3$ perovskite catalyst weight loss were obtained using TA instruments, Q500 over temperature ranged 298–1273 K, and employing heating rate of 10 K min^{-1} in a flow of compressed air.

Textural properties of the catalyst, degassed at 573 K and analysed at 77 K were obtained by N_2 multi-layer adsorption-desorption isotherm data, using a thermo scientific acquisition analyser, furnished with degasser station and surfer acquisition software (version 1.2.1). The specific surface area and pore size distribution of the catalyst were computed using the Brunauer–Emmett–Teller (BET) and Barret-Joyner-Halenda (BJH) methods, respectively.

X-ray diffractogram (XRD) analysis of the catalyst was obtained using a RIGAKU miniflex II X-ray diffractometer employing 2θ ranged 3° to 80° with a monochromatized CuK_α radiation wavelength (λ) of 0.154 nm at an increment of 0.02° (2θ), and a counting speed of 1 s.

The morphology and elemental compositions of the catalysts were evaluated using JEOL FESEM-EDX analyser at 30,000 magnifications. High resolution image of the catalyst structure, down to the nano-scale, was obtained with a brightness Schottky-type field emission cathode beam. The elements were obtained from EDX by exciting the inner shell electrons, thereby forming characteristics X-rays with the suitable intensity for analytical data.

Micro-structural morphology of the fresh and spent $SmCoO_3$ perovskite catalyst was obtained using transmission electron microscopy (TEM) at ×20,000 magnification. High energy beam was shone through a very thin sample of the $SmCoO_3$ catalyst material. Due to the interaction between the atoms of the $SmCoO_3$ perovskite

Table 1
Tolerance Factor for $SmCoO_3$ perovskite catalyst: *A*: Rare earth metal (Sm), *B*: Transition earth metal (Co), *C*: Oxygen.

Rare earth metals	Ionic radius (R_A) in nm	Ionic radius (R_B) in nm	Ionic radius (R_C) in nm	Tolerance factor
Samarium	0.124	0.055	0.140	0.96

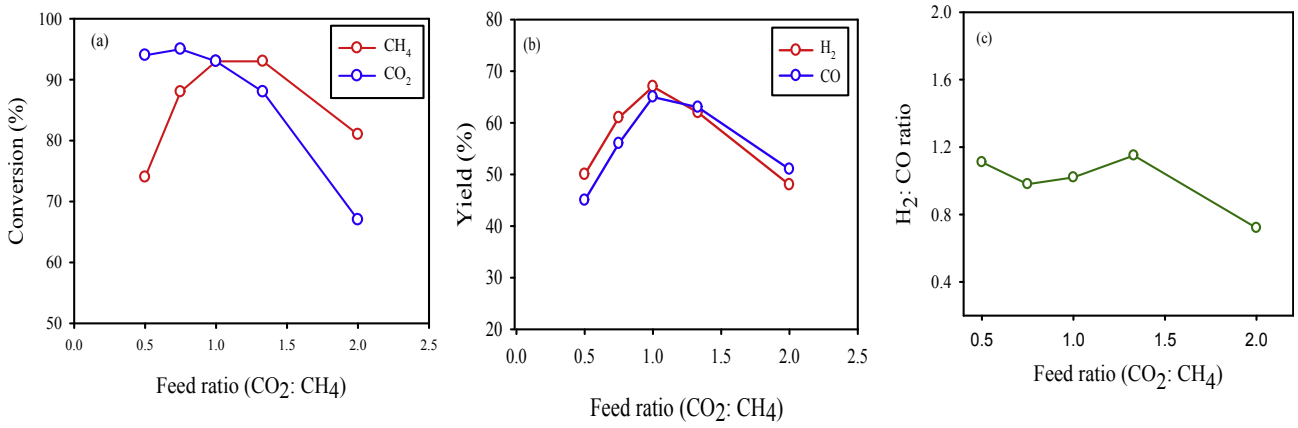

Fig. 1. Effects of Feed ratio (CO_2: CH_4) on catalytic activity (at 1073 K) (a) reactants conversion, (b) product yield (c) H_2: CO ratio.

and the electrons from the microscope, various morphological features of the $SmCoO_3$ perovskite can be visibly observed. In this study, TEM was carried out by a FEI microscope equipment (Tecnai G2 20 Twin) operated at 200 KV. The obtained perovskite samples were dispersed in an ethanol solution, and the suspensions were placed into an ultrasonic bath for 30 min. Each solution was deposited onto a copper grid coated with carbon film, and the alcohol was evaporated. The samples contained in the copper grid were used for the TEM analysis.

Fourier transform infrared spectroscopy (FTIR) was used to identify the surface functional groups of the catalyst using 45° ZnSE IRE equipment (Perkin Elmer Spectrum 100).

X-ray photoelectron spectroscopy (XPS) showing the surface composition, binding energy data and chemical state of the fresh catalyst were acquired using a PHI-5000 Versa Probe spectrometer equipped with a hemispherical electron analyser and non-monochromated Al Kα ($h\nu = 1486.6$ eV) X-ray source. During data acquisition, the background pressure and wide scan spectra were 2.7×10^{-4} Pa, and 117 eV, respectively, with all binding energies referenced to the C 1s hydrocarbon peak at 284.8 eV. Gaussian and Lorentzian lines and atomic sensitivity factors were used to estimate the intensity of the peaks and the atomic percentages.

2.3. Catalytic activity test

Catalytic evaluation of the $SmCoO_3$ perovskite catalyst was conducted in a 10-mm ID stainless steel tubular reactor, with 100 mg of solid catalyst supported on quartz wool. Each experimental runs was carried out for 4 h with previous reduction of the catalyst (for 1 h at 1023 K) by varying the feed ratio from 0.5 to 2.0 at temperature of 1073 K under barometric condition, using a total flow of 50 ml min^{-1} STP, which culminates to WHSV of 30,000 h^{-1}. A gas chromatography instrument (GC-Agilent 6890 N series) furnished with TCD and equipped with two packed columns; Supelco Molecular Sieve 13 × (10 ft × 1/8 in OD × 2 mm ID, 60/80 mesh, stainless steel) and Agilent Hayesep DB (30 ft × 1/8 in OD × 2 mm ID, 100/120 mesh, Stainless Steel) for detecting CO_2, CH_4, H_2 and CO was used to analyse product gas. Helium was employed as a carrier gas with effective column temperature of 393 K and flowrate of 20 ml min^{-1}. Catalytic performance was evaluated using Eq. (2) (Pakhare et al., 2014):

$$X_{CH_4}(\%) = \left[\frac{F_{CH_4}(in) - F_{CH_4}(out)}{F_{CH_4}(in)}\right] \times 100 \quad (2a)$$

$$X_{CO_2}(\%) = \left[\frac{F_{CO_2}(in) - F_{CO_2}(out)}{F_{CO_2}(in)}\right] \times 100 \quad (2b)$$

$$H_2 \text{ yield } (\%) = \frac{F_{H_2}(out)}{2F_{CH_4}(in)} \times 100 \quad (2c)$$

$$CO \text{ yield } (\%) = \frac{F_{CO}(out)}{F_{CH_4}(in) + F_{CO_2}(in)} \times 100 \quad (2d)$$

$$\text{Syngas ratio} \frac{H_2}{CO} = \frac{F_{H_2}(out)}{F_{CO}(out)} \quad (2e)$$

3. Results and discussion

3.1. Goldschmidt tolerance factor estimation

Goldschmidt tolerance factor as in eq. (1) was employed in selecting a rare earth metal of the lanthanide series as the *A* site and cobalt (Co) as the B site. Several rare earth metal; lanthanum, cerium, neodymium, samarium, met the Goldschmidt criterion. However, Samarium (Sm) was selected as the *A* site for this study (cf. eq. (1)). Table 1 list the computation and results for $SmCoO_3$ perovskite, whereby t = 0.96 was obtained. Furthermore, XRD analysis (refers to Section 3.4) confirms the formation of mono crystalline phase of $SmCoO_3$ perovskite structure.

3.2. Effects of feed ratio on the activity of the $SmCoO_3$ perovskite catalyst

The effects of varying the feed ratio (CO_2: CH_4) from 0.5 to 2.0, at

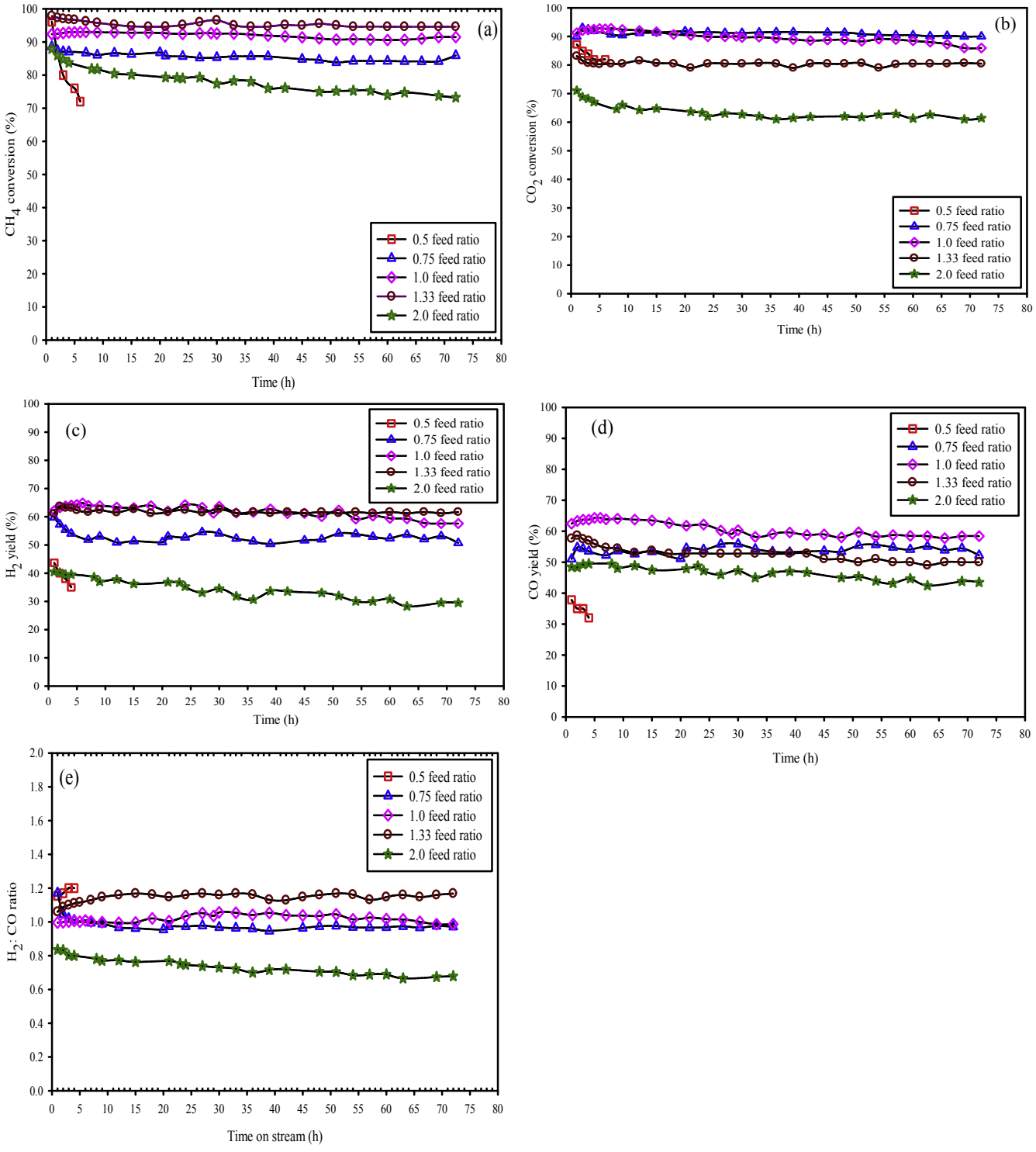

Fig. 2. Longevity test of CO_2 reforming of CH_4 over $SmCoO_3$ perovskite catalyst at 1073 K.

1073 K, on conversion of reactants, product yield and H_2: CO ratio, are shown in Fig. 1a–(c), respectively. Below stoichiometry (feed ratio, CO_2: $CH_4 \leq 1$), conversion of CO_2 and CH_4 increases from 84% to 82% at 0.5 ratio to about 90% and 92% at 1.0 reactant ratio, largely due to increasing CO_2 and hence, increased adsorption of CO_2 at the catalyst interface for surface chemical reaction to take place. At above stoichiometry (feed ratio ≥ 1), conversion of CO_2 and CH_4 drops to about 64% and 79%, respectively, largely due to the decreased CH_4 cracking and insufficient H_2 available to react in the reverse Boudouard reaction (Sazonova et al., 2009).

The effects of feed ratio on product yield, which is reminiscent of the pattern exhibited in Fig. 1a, is represented in Fig. 1b. Below stoichiometry, an increase in H_2 and CO from about 39% to 35% at 0.5 feed ratio to 62% and 61%, respectively, at 1.0 feed ratio was observed. Nevertheless, at above stoichiometry, H_2 and CO yields drops significantly to 34% and 47%, respectively (cf. Fig. 1b).

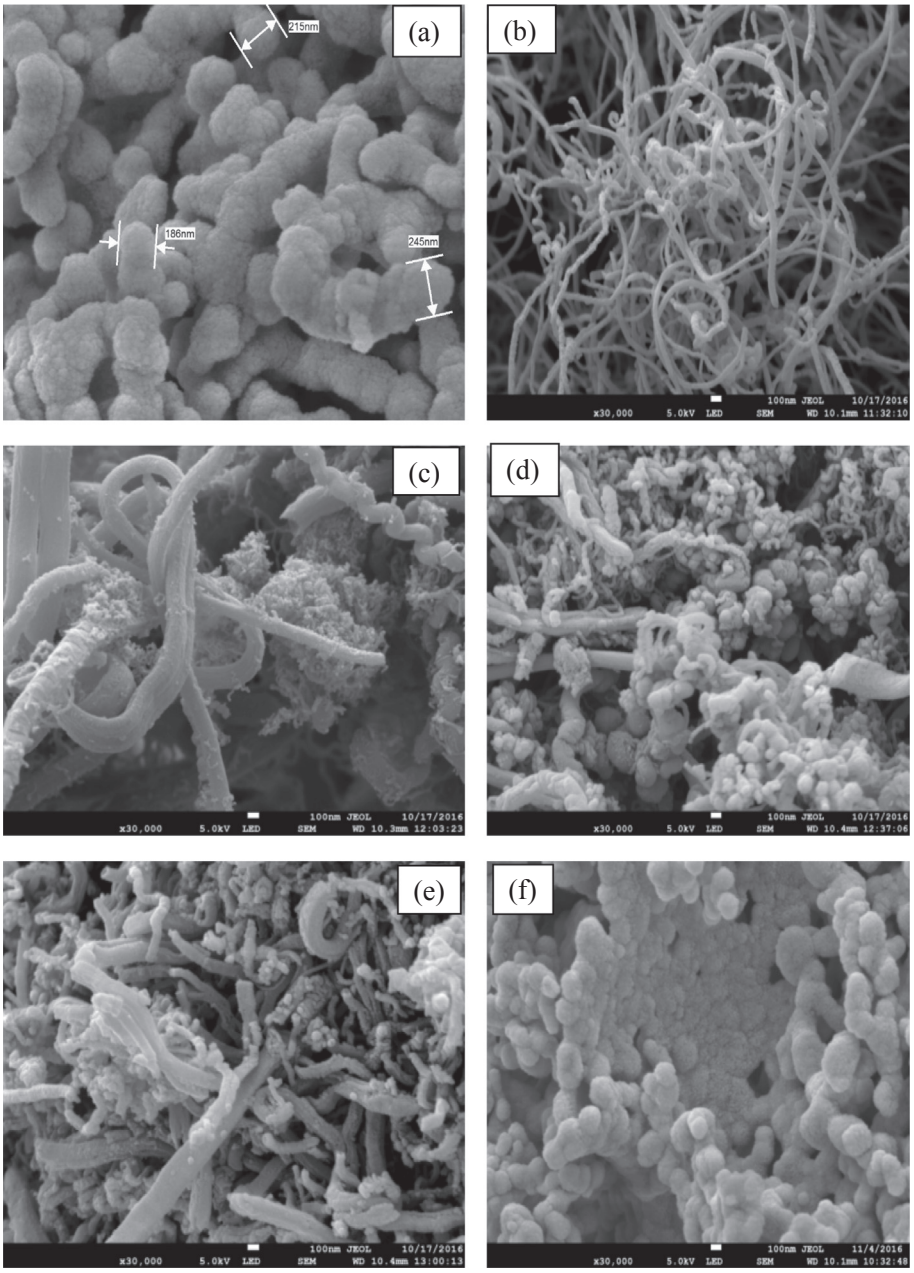

Fig. 3. FESEM images of (a) fresh (b) 0.5 (c) 0.75 (d) 1.0 (e) 1.33 (f) 2.0 spent $SmCoO_3$ perovskite catalyst at ×30,000 magnifications.

Interestingly at 2.0 feed ratio, H_2 yield was lower than CO due to consumption of H_2 to sustain the reverse water gas shift reaction. The same reaction trends were observed in a study on effects of feed ratio on catalytic performance using 5%Ni–3%Mg/Al_2O_3 as catalyst (Alipour et al., 2014).

H_2: CO (syngas) ratio was obtained as a function of feed ratio and the result is represented in Fig. 1c. H_2: CO ratio was slightly above 1.0 at below the stoichiometry, then drops slightly approximately to 1.0 at stoichiometry and then significantly dips to about 0.72 at above stoichiometry. CH_4 cracking could be largely responsible for this trend due to it being the excess reagent at below stoichiometry and the limiting reagent at above stoichiometry.

Similar behaviour was observed when supported iridium catalyst and $LaNiO_3$ were applied in CO_2 reforming of CH_4, respectively, (Wisniewski et al., 2005; Batiot-Dupeyrat et al., 2005).

3.3. Longevity assessment

Since we have proved from our previous works that the $SmCoO_3$ perovskite catalyst possessed excellent activity, subsequently, its longevity was investigated. The longevity was evaluated at 1073 K and at feed ratios (CO_2: CH_4) that ranged 0.5–2.0, over a 72 h time-on-stream (TOS). The results obtained are represented in Fig. 2a–(e).

At feed ratio of 0.5 (below stoichiometry), reaction was unable to proceed beyond 4 h due to excessive carbon deposition owing to the insufficient supply of CO_2 to gasify the accumulated carbon. As a consequence, pressure rapidly built up due to blockage. Another way carbon could have affected the reaction was by encapsulating the active site of catalyst, resulting in the catalyst deactivation (Maneerung et al., 2011).

At feed ratios of 0.75, 1.0 and 1.33, conversions of CO_2 and CH_4 as

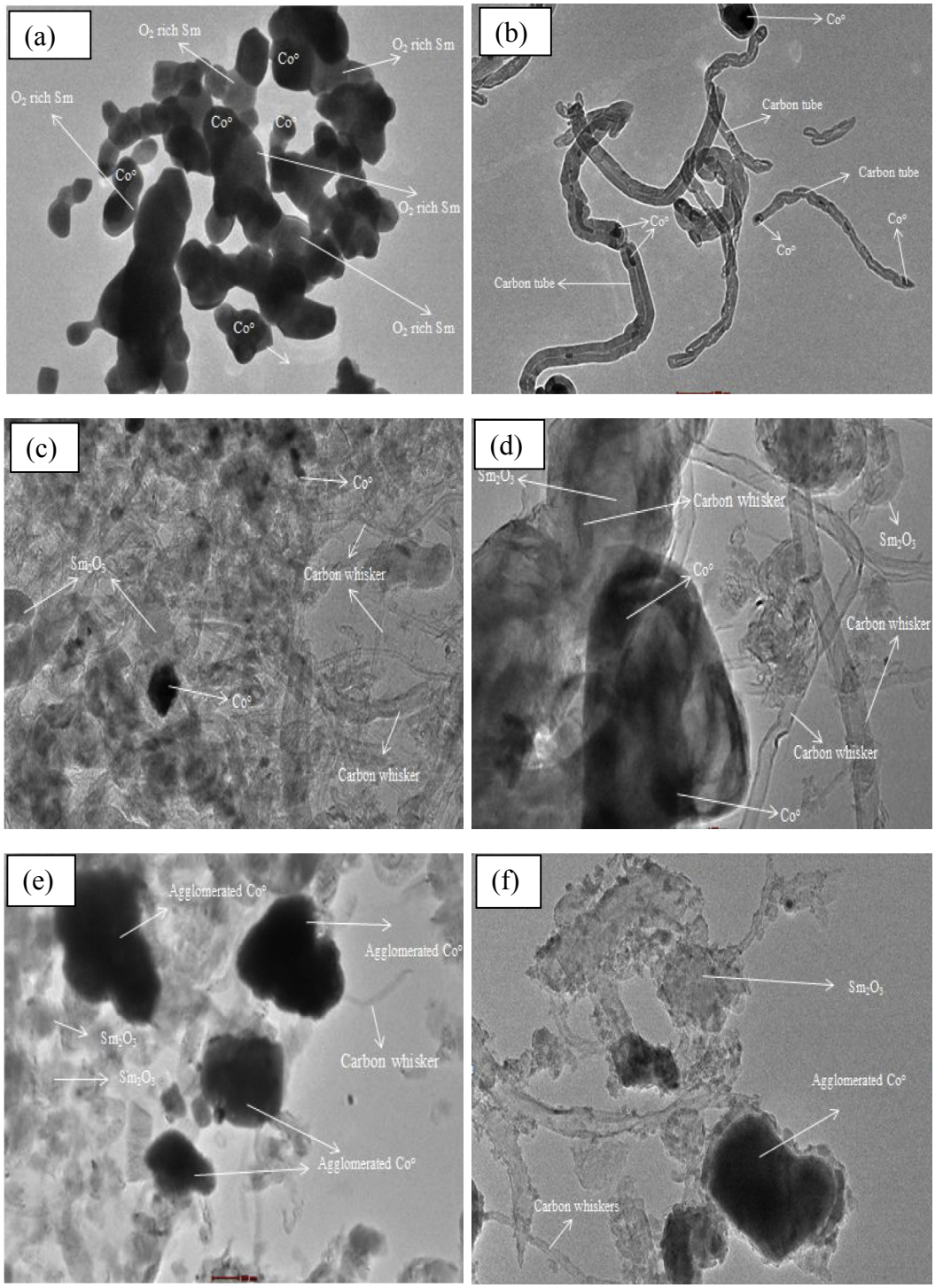

Fig. 4. TEM image of the (a) fresh and spent (at (b) 0.5 (c) 0.75 (d) 1.0 (e) 1.33 (f) 2.0 feed ratios) $SmCoO_3$ perovskite catalyst. (Magnifications ×20,000).

well as the yields of H_2 and CO remained relatively stable over 72 h TOS (cf. Fig. 2a and b). These feed ratios (0.75, 1.0, 1.33) are ideal for the optimal conversion of these greenhouse gases (CO_2 and CH_4) into more useful products, hence, providing cleaner energy source as well as useful feed stock for liquid fuel production. Furthermore, longevity test at 2.0 feed ratio resulted in CO_2 and CH_4 conversion drop of about 14% and 17%, respectively, while a drop in H_2 and CO yield of about 27% and 10%, respectively was observed (cf. Fig. 2c and d).

Interestingly, feed ratio of 1.0 yielded the best conversion; about 90% for CO_2 and 92% for CH_4, and H_2 yield of approximately 62% and CO of 61% (cf. Fig. 2a–d). Moreover, it can be observed that the H_2: CO ratio was stable for all the feed ratios (0.75, 1.0 and 1.33) with the exception of 0.5 and 2.0 feed ratio, which showed evidence of reactor blockage and ratio drop of about 20%, respectively (cf. Fig. 2e).

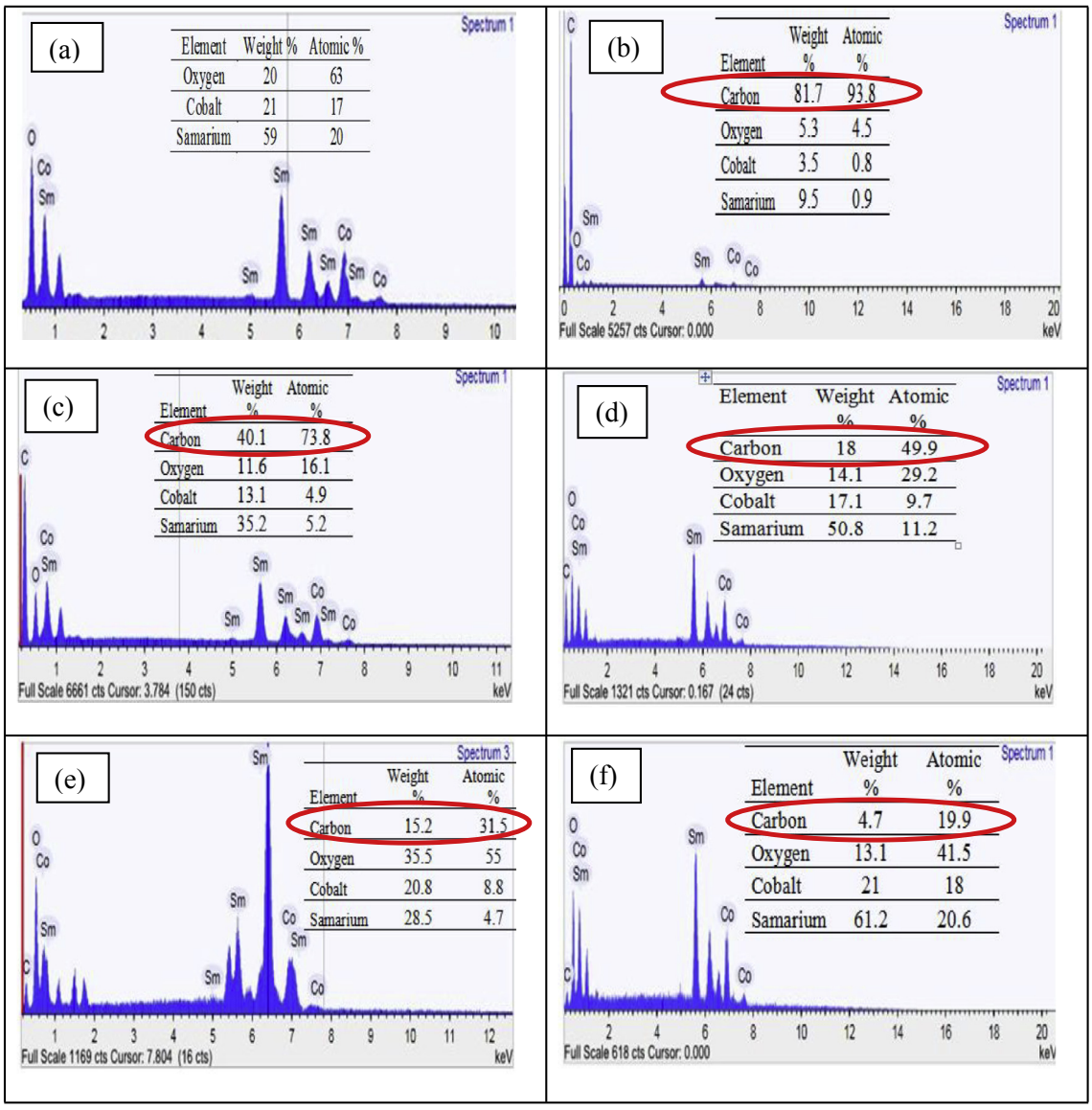

Fig. 5. EDX spectra of the (a) fresh and (b) 0.5 (c) 0.75 (d) 1.0 (e) 1.33 (f) 2.0 feed ratios on spent $SmCoO_3$ perovskite catalyst.

Table 2
Textural properties of fresh and spent $SmCoO_3$ perovskite catalyst.

CO_2:CH_4 ratio	Cumulative pore volume ($cm^3\ g^{-1}$) ± 0.01	Average pore diameter (nm) ± 0.01	BET specific surface area ($m^2\ g^{-1}$) ± 0.01
Fresh	0.86 ×10^{-2}	6.80	6.40
0.50	0.30	5.90	158.80
0.75	0.29	7.20	148.50
1.00	0.28	7.60	138.40
1.33	0.22	7.60	112.00
2.00	0.04	4.20	28.40

3.4. Catalyst characterization

For this section, the spent $SmCoO_3$ perovskite catalysts were collected post reaction for further analysis. Prior to the longevity reaction, the fresh catalyst was characterized and has been reported in our previous work. Several random field emission scanning microscope (FESEM) images of the spent $SmCoO_3$ catalyst particles at 0.5–2.0 feed ratio were captured and representative images were selected to represent the morphology of the spent catalysts as shown in Fig. 3. It can be observed that the as-synthesized fresh catalyst represented in Fig. 3a was comprised of uniform spherical metallic particles that ranged 200–250 nm as against the spent catalysts which showed deposition of carbon whiskers more pronounced at below stoichiometry (0.5 and 0.75) as evident in Fig. 3b and (c) than at higher feed ratios (1.33 and 2.0) as illustrated in Fig. 3e and (f). As CO_2: CH_4 ratios increased, the formation of carbon whiskers reduced, and eventually was undetectable at feed ratio of 2.0. In addition, agglomeration of catalyst

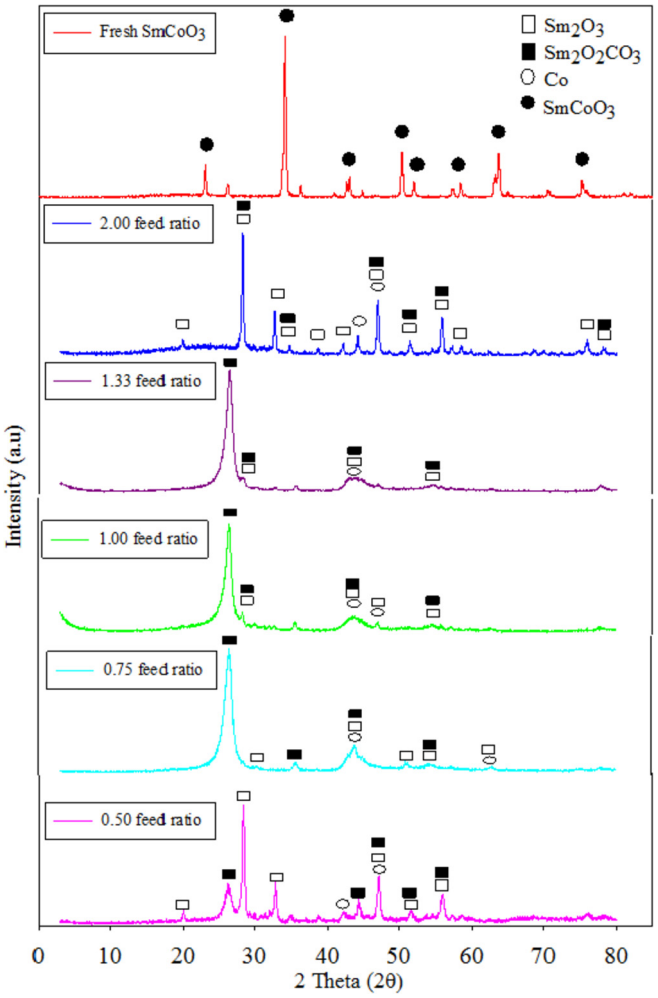

Fig. 6. XRD patterns for fresh and spent $SmCoO_3$ perovskite catalyst for reactants feed ratio of 0.5–2.0.

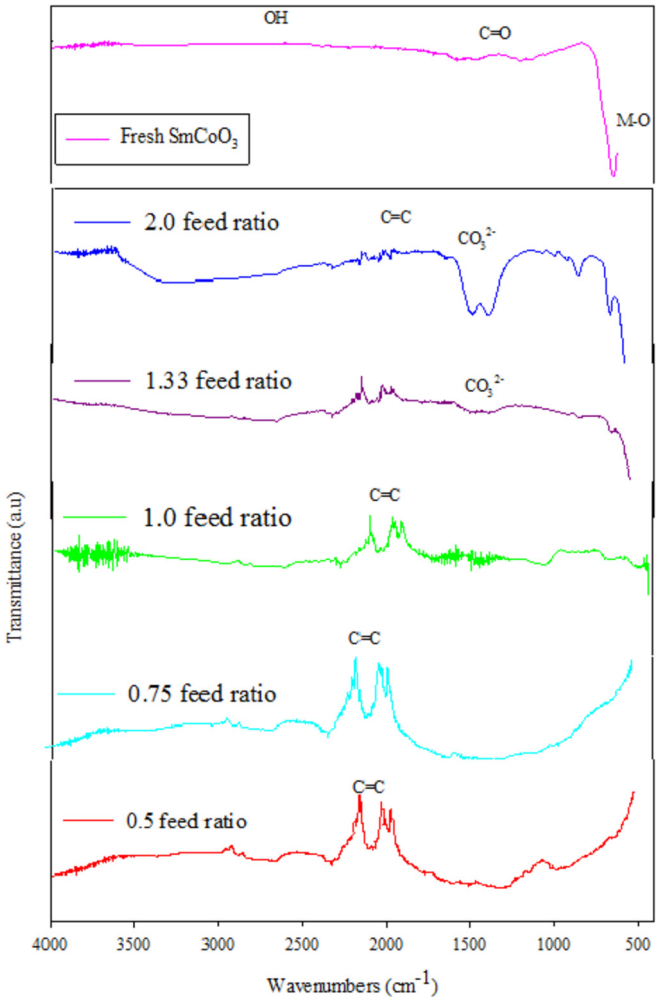

Fig. 7. FTIR spectra of the fresh and spent $SmCoO_3$ perovskite catalyst.

particles not noticed for the fresh catalyst or at lower feed ratio was observed at 2.0 feed ratio (cf. Fig. 3f) with particle size increasing from about 200 nm for fresh catalyst to about 300 nm for spent catalyst at 2.0 feed ratio. Furthermore, at 1.0 feed ratio represented in Fig. 3d a balance of metallic particles and carbon whiskers was noticed which is a good explanation for the excellent stability of the reaction at this feed ratio.

Captured TEM images of fresh and spent $SmCoO_3$ perovskite catalyst for reactants feed ratio from 0.5 to 2.0 showing various degrees of carbon formation are represented in Fig. 4. For the fresh catalyst, well dispersed metallic Co particles embedded in the lattice O_2 rich rare earth metal (Sm) are visible in the image. In the micrograph, the Co^o metals are identified as the darker shaded spherical particles bonded to the lighter shaded lattice O_2 rich Sm. This image (fresh catalyst) was quite different for the spent catalyst (0.5–2.0) as depicted in Fig. 4 (b) – (f). At 0.5 reactants feed ratio (cf. Fig. 4b), the Co^o metals are completely engulfed in the tube-like whiskers of the distinctly visible carbon tubes. Carbon whiskers are also seen at reactant feed ratio of 0.75 (cf. Fig. 4c) and 1.0 (cf. Fig. 4d), although in a more balance scale without engulfment of the metallic Co^o phase by carbon. At reactants feed ratio 1.33 (cf. Fig. 4e) and 2.0 (cf. Fig. 4f), agglomeration of the Co^o metallic phase is noticed. Although, carbon whisker is observed as detected by the EDX at 1.33 and 2.0 feed ratio, it is insignificant as compared to the amount observed at 0.5, 0.75 and 1.0 reactant feed ratios. The shortage of carbon is as a result of limited CH_4 at the 1.33 and 2.0 feed ratios. The metal particles agglomerate/sinter, thereby creating an in-balance in the CO_2 reforming of CH_4 reaction.

Electron dispersive X-ray (EDX) analysis of the fresh $SmCoO_3$ perovksite catalyst previously reported in our paper (Osazuwa et al., 2017) and represented in Fig. 5a shows the elements namely; Sm, Co and O with composition of 20%, 17% and 63%. When compared to the spent catalyst represented in Fig. 5b–(f), the elemental compositions of the spent catalysts shows evidence of carbon, decreasing from 81.1 wt% at below stoichiometry (0.5 feed ratio) to 4.7 wt% at above stoichiometry (2.0 feed ratio). This result shows good consistency with the FESEM analysis (cf. Fig. 3).

The textural properties of the fresh and spent $SmCoO_3$ perovskite catalyst ranged 0.5–2.0 feed ratio are represented in Table 2. From the N_2 physisorption data, BET specific surface area, BJH pore volume and pore diameter were 6.4 $m^2\,g^{-1}$, 8.6 × 10^{-3} $cm^3\,g^{-1}$, and 6.8 nm, respectively, for fresh catalyst. Interestingly, these values are reminiscent of perovskite catalyst previously reported (Goldwasser et al., 2005), (Valderrama et al., 2008). Analysis of the spent catalyst for the various reactants feed ratio (0.5–2.0) was also carried out. In relation to the fresh catalyst, significant increase in specific surface area and pore volume attributed to carbon was observed. The BET specific surface area (158.8 $m^2\,g^{-1}$) and pore volume (0.3 $cm^3\,g^{-1}$) was highest for below stoichiometry (feed ratio of 0.5) reaction, and significantly dropped to 28.4 $m^2\,g^{-1}$ and

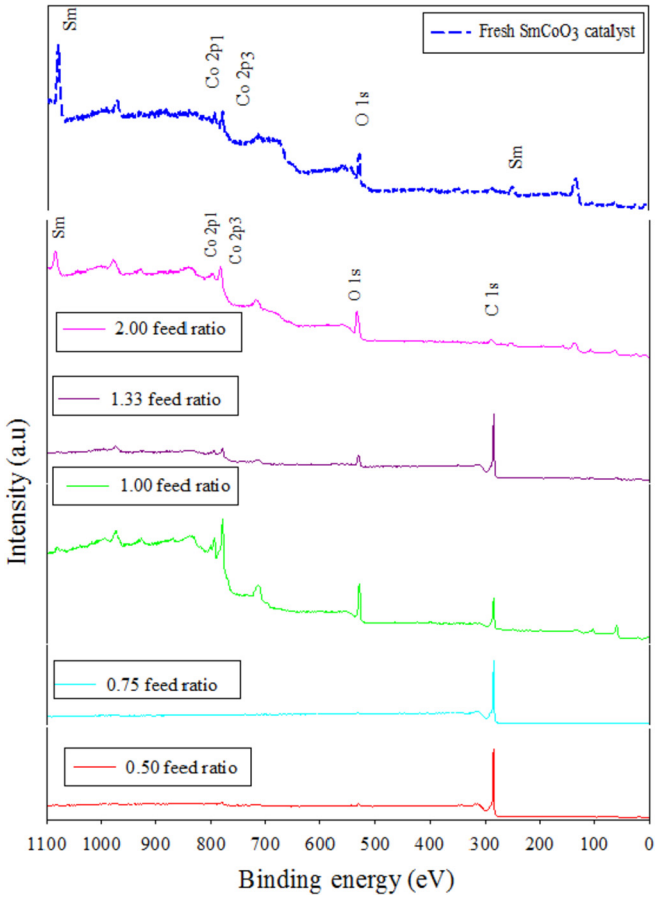

Fig. 8. XPS of the fresh and spent $SmCoO_3$ perovskite catalyst for feed ratio 0.5–2.0 feed ratio.

Table 3
Chemical state and binding energy of spent $SmCoO_3$ perovskite catalyst.

$SmCoO_3$ feed ratio	Chemical state	C 1's binding energy (eV)
0.5	C–C and C–H	284.6
0.75	C–C and C–H	284.6
1.0	C–C and C–H	284.6
1.33	C–C and C–H	284.6
2.0	O–C=O	288.5

$0.04\ cm^3\ g^{-1}$ at above stoichiometry (feed ratio of 2.0). Furthermore, pore size distribution of the fresh catalyst indicates size that ranged between 3 and 10 nm which is typical of perovskite material due to their mesoporous nature (Bakandritsos et al., 2004). As expected, the average pore diameter of the spent $SmCoO_3$ catalyst increased from about 5.9 nm to about 7.6 nm with increasing feed ratio, but dropped at feed ratio of 2.0. This is in agreement with the trend in this study as spent catalyst with lower feed ratios had excess carbon deposition which blocked the catalyst pores; hence, reducing the catalyst pore diameter.

X-ray diffractogram patterns (XRD) of the $SmCoO_3$ perovskite catalysts are presented in Fig. 6. Prior to the reaction, an orthorhombic perovskite structure with the main peak at 2θ value of 33.90° matching JCPDS (00-025-1071) were observed for the fresh catalyst (Osazuwa et al., 2017). In the post longevity test, the samarium oxycarbonate ($Sm_2O_2CO_3$), samarium oxide (Sm_2O_3) and cobalt (Co^o) phases were detected. The $Sm_2O_2CO_3$ phase was formed by the adsorption of CO_2 on Sm_2O_3, thereby increasing CO_2 conversion rate and reducing carbon deposit on the surface of the catalyst (Goldwasser et al., 2003). The most intense peak which was diminishing with feed ratio has been identified as the $Sm_2O_2CO_3$ phase at 28.4° (cf. Fig. 6). Interesting, at feed ratio of 0.5, the Sm_2O_3 phase is more pronounce at 29.3° likely due to limited CO_2 available to adsorb on Sm_2O_3 and form $Sm_2O_2CO_3$. The Sm_2O_3 phase has characteristics of monoclinic structure matching JCPDF 01-086-247 (Ni et al., 2013). Also detected were related to Co, located at about 43.73° and 47.13°, characteristic of Co hexagonal structure matching the JCPDF 01-071-4652 (Gnanamani et al., 2013).

Combined Fourier transform infrared spectroscopy (FTIR) of the fresh and spent $SmCoO_3$ catalyst obtained in the range 400–4000 cm^{-1} are represented in Fig. 7. For the fresh $SmCoO_3$ perovskite catalyst, broad adsorption band at 3375 cm^{-1} representing the hydroxyl group (O–H) stretching mode resulting from the presence of physical and hydrated water is observed (Khoshbin and Haghighi, 2015). The band at 2670 cm^{-1} can be assigned to bonding vibrational mode of adsorbed water (Coates, 2000). Vibration bands at 1506.94 cm^{-1}, 1402.6 cm^{-1}, can be assigned to adsorbed or atmospheric carbon dioxide (Khalil, 2003), while 1124.36 cm^{-1}, and 1060.72 cm^{-1} represents C–O stretching bond (Coates, 2000). Furthermore, the band at 550.9 cm^{-1} is related to stretching metallic oxide (M-O) bond which exist in the internal structure of the catalyst (Kumar et al., 2013). In relation to the fresh $SmCoO_3$ perovskite catalyst, FTIR spectra of the spent catalyst for feed ratio ranged 0.5–2.0 is also depicted in Fig. 7. The peaks observed at about 1980 cm^{-1} and 2100 cm^{-1} are due to stretching C≡C vibration bonds. This bond is evident in all samples (0.5–2.0), but more pronounced at below stoichiometry due to the presence of excess carbon from CH_4 cracking which accumulates and blocks the reactor. However, peaks at about 1513 cm^{-1} belonging to the CO_3^{2-} functional group, which diminished below stoichiometry (0.5 and 0.75), is observed in Fig. 7. The results are in strong agreement with the XRD pattern of the spent catalyst (cf. Fig. 6), which showed existence of a carbonate phase more pronounced at above stoichiometry.

Pre and post reaction XPS analysis of the chemical state and surface elemental composition of the fresh $SmCoO_3$ perovskite catalyst represented in Fig. 8 was carried out. For the fresh catalyst, the spectroscopy shows the surface composition of the catalyst with Sm, Co, and O ratio of 20.6%, 17.8%, and 61.6%, matching the EDX analysis and catalyst formulation employed. In addition, binding energy peaks at 1082 eV corresponding to Sm $3d_5$, 529 eV and 531 eV ascribed to the lattice and dissociative O_2, respectively were noticed (Kuhn and Ozkan, 2008). In addition, peaks at 777 eV and 782 eV attributed to Co $2p_3$ and Co $2p_1$, respectively were also seen (Zhang et al., 2007). For the post reaction XPS analysis of the spent $SmCoO_3$ perovskite catalyst with 0.5–2.0 feed ratio the chemical state for Lorentzian deconvolution peaks for the spent catalysts at 0.5, 0.75, 1.0 and 1.33 feed ratios are approximately 284.6 ± 0.3 eV. These peaks represented in Table 3 can be ascribed to C–C with bond energy of 347 kJ mol^{-1} and C–H with bond energy 413 kJ mol^{-1} present in aliphatic carbon compounds (Moreno-Castilla et al., 2000). Interestingly, a peak shift to about 289 eV related to carboxyl (O–C=O) groups with bond energy 805 kJ mol^{-1} is observed at 2.0 feed ratio (cf. Table 3) (Zhang et al., 2013), (Tao et al., 2014). Higher activation energy is required to overcome the barrier created by the bond energy of the carboxyl group which could account for the lower performance observed at 2.0 feed ratio when compared to 0.5, 0.75, 1.0 and 1.33 feed ratio (cf. Fig. 2). In addition, the most intense C 1s peak (obtained at 284.6 eV) which diminished with increasing feed ratio was observed at 0.5 feed ratio. Several authors have tried to characterize C 1s peak to determine the exact type of carbon formed; (Vu et al., 2011) allotted the peak at 284.6 eV to aliphatic carbon on the

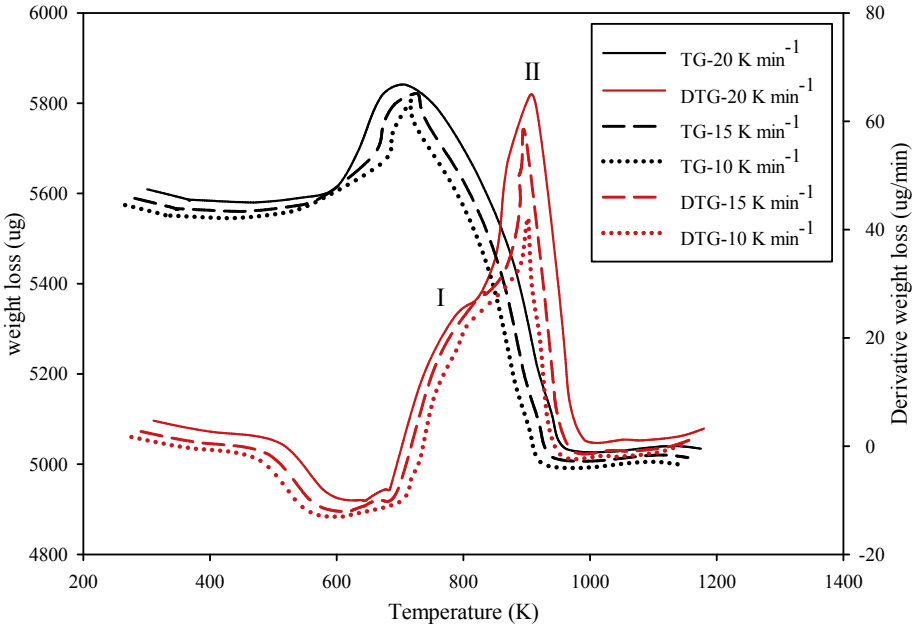

Fig. 9. TPO of the spent $SmCoO_3$ perovskite at 1.0 reactant feed ratio.

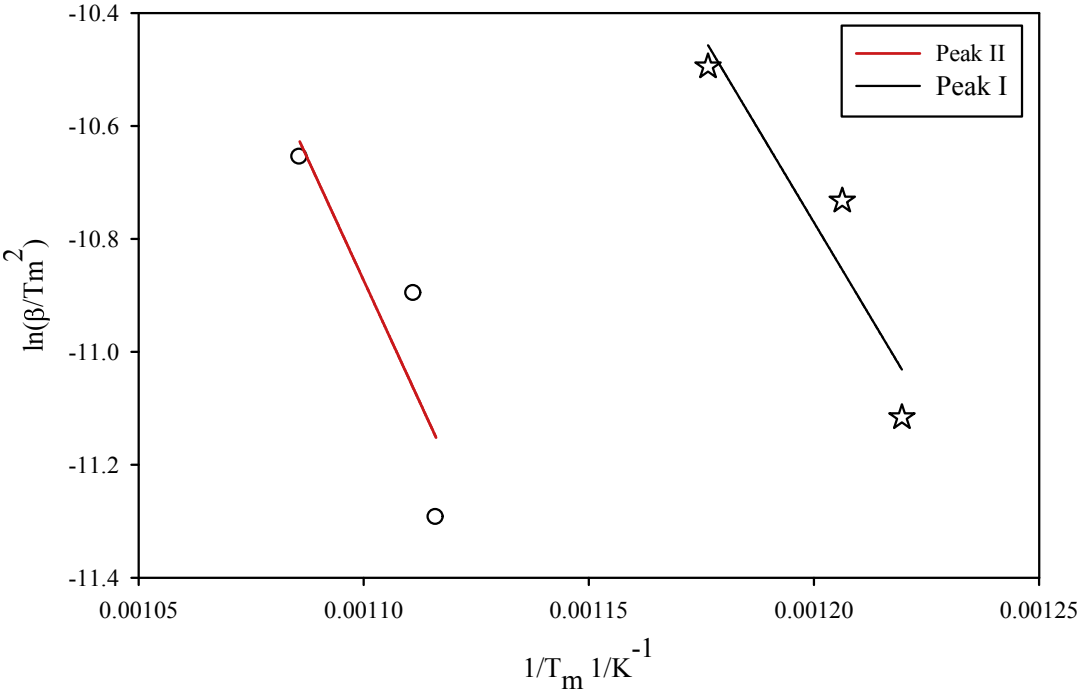

Fig. 10. Linearized Kissinger model to obtain the activation energy of carbon formation.

Table 4
Activation energy for the oxidation of carbon in the spent $SmCoO_3$ perovskite catalyst.

Peak	E (kJ mol^{-1})	R^2
I	110.92	0.93
II	143.89	0.90

catalyst surface and sp hybridized carbon atoms, while (Weckhuysen et al., 1998) considered this peak as graphitic-like carbon. FESEM and TEM images also show carbon in the form of whiskers (cf. Figs. 3 and 4). We therefore postulate a graphitic carbon-type formed on the surface of the catalyst. Furthermore activity drop (catalytic performance decay) observed at 0.5 feed ratio was as a result of excess carbon deposit (from CH_4 decomposition) leading to reactor blockage. This is due to the fact that same carbon type (284.6 eV) was observed for other feed ratios (0.75, 1.0 and 1.33) and the reaction proceeded with excellent stability.

3.5. Temperature programmed oxidation (TPO) and Kissinger modelling of the oxidation of carbon deposited on the spent $SmCoO_3$ perovskite catalyst

Fig. 9 represents the weight loss and derivative weight loss profile of the spent $SmCoO_3$ perovskite catalyst at feed ratio 1.0. Heating rate of 10, 15 and 20 K min^{-1} at temperature range of 298–1273 K were employed in a compressed air flow system to obtain the thermo-gravimetric (TG) and the differential thermo-gravimetric (DTG) profiles. Data obtained were utilized to obtain the activation energy of the oxidation of the deposited carbon on the spent $SmCoO_3$ perovskite catalyst (1.0 feed ratio) using the Kissinger model represented in eq. (3) (Blaine and Kissinger, 2012).

$$\ln\left[\frac{\beta}{T_m^2}\right] = \ln\left[\frac{ZR}{E}\right] - \frac{E}{RT_m} \quad (3)$$

where, β, T_m, Z, R, E are the heating rate, peak temperature, Arrhenius pre-exponential factor, universal gas constant and activation energy, respectively.

The TPO profile shows two peaks; I at about 650–800 K and II at about 900 K. According to existing literature, peaks observed at these temperature are attributed to graphitic forms of carbon (Wang et al., 2012; Son et al., 2014). Furthermore, Son et al. (2014) reported that the graphitic carbon are either retained on the surface of the metallic phase (leading to deactivation) or accumulates in the reactor (leading to reactor blockage). Theses graphitic carbon type are readily converted/removed via the presence of adsorbed CO_2 and lattice O_2, readily available in the metallic oxide phase, hence enhancing the longevity of the catalyst (Sutthiumporn et al., 2012).

Fig. 10 shows the linearized Kissinger plot resulting from the oxidation of carbon during the TGA analysis which was used to obtained kinetic parameters and the coefficient of determination (R^2) tabulated in Table 4. An increase in activation energy from 110.92 kJ mol^{-1} to 143.89 kJ mol^{-1} for peak I to II, respectively, is observed. This implies that activation energy was linearly proportional to time and temperature of oxidation. In addition, the double peak (I and II) confirms two types of carbon were oxidized; the peak I which represents the aliphatic carbon ascribed to C–C bond with lower bond energy (about 347 kJ mol^{-1}) and peak II the C–H bond with a higher bond energy (about 413 kJ mol^{-1}). The higher bond energy at peak II which also translates to higher activation energy (143.89 kJ mol^{-1}) indicating that it was much difficult to oxidized the C–H carbon type than the C–C carbon type with activation energy of 110.92 kJ mol^{-1}.

4. Conclusions

$SmCoO_3$ perovskite catalyst was synthesized using sol-gel citrate method. The as-synthesized catalyst was tested at 1073 K and CO_2: CH_4 ratios of 0.5–2.0. Optimal conversion of unwanted greenhouse gases was attained at feed ratio of unity, with reactant conversions greater than 90.0%, and yields of above 60%. Longevity study was also carried out on the $SmCoO_3$ catalyst with 0.75, 1.0 1.33 feed ratios showing excellent stability over a 72 h TOS. Spent catalyst characterization showed existence of an oxy-carbonate phase (XRD analysis) which was significant in the removal of carbon deposit from the catalyst surface. Strong evidence of carbon (C–C bond) and/or contaminants of carbon (O–C=O) was present as depicted in the FESEM/TEM images, FTIR, TGA and more specifically XPS analysis. This study has generated data (catalyst longevity) for the conversion of unwanted greenhouses gases into cleaner energy sources using the $SmCoO_3$ perovskite catalyst.

Acknowledgement

This work was supported by the Science fund, RDU130501 awarded by the Ministry of Science, Technology and Innovation of Malaysia. We also would like to record our appreciation to Universiti Malaysia Pahang for the PGRS scheme (GRS1503140). OUO is a grateful beneficiary of GRS scholarship conferred by the Institute of Postgraduate Studies of the Universiti Malaysia Pahang. S. Assabumrungrat would like to acknowledge the Thailand Research Fund (DPG5880003).

References

Alipour, Z., Rezaei, M., Meshkani, F., 2014. Effect of alkaline earth promoters (MgO, CaO, and BaO) on the activity and coke formation of Ni catalysts supported on nanocrystalline Al2O3 in dry reforming of methane. J. Ind. Eng. Chem. 20, 2858–2863.
Ayodele, B.V., Hossain, S.S., Lam, S.S., Osazuwa, O.U., Khan, M.R., Cheng, C.K., 2016. Syngas production from CO2 reforming of methane over neodymium sesquioxide supported cobalt catalyst. J. Nat. Gas Sci. Eng. 34, 873–885.
Bakandritsos, A., Steriotis, T., Petridis, D., 2004. High surface area montmorillonite - carbon composites and derived carbons. Chem. Mater 143, 1551–1559.
Batiot-Dupeyrat, C., Gallego, G.A.S., Mondragon, F., Barrault, J., Tatibouët, J.-M., 2005. CO2 reforming of methane over LaNiO3 as precursor material. Catal. Today 107–108, 474–480.
Blaine, R.L., Kissinger, H.E., 2012. Homer kissinger and the kissinger equation. Thermochim. Acta 540, 1–6.
Choudhary, V.R., Mondal, K.C., 2006. CO2 reforming of methane combined with steam reforming or partial oxidation of methane to syngas over NdCoO3 perovskite-type mixed metal-oxide catalyst. Appl. Energy 83, 1024–1032.
Coates, J., 2000. Interpretation of infrared spectra, a practical approach. Encycl. Anal. Chem. 10815–10837.
Gnanamani, M.K., Jacobs, G., Shafer, W.D., Davis, B.H., 2013. Fischer–Tropsch synthesis: activity of metallic phases of cobalt supported on silica. Catal. Today 215, 13–17.
Goldwasser, M., Rivas, M., Pietri, E., Pérez-Zurita, M., Cubeiro, M., Gingembre, L., Leclercq, L., Leclercq, G., 2003. Perovskites as catalysts precursors: CO2 reforming of CH4 on $Ln_{1-x}CaxRu_{0.8}Ni_{0.2}O_3$ (Ln = La, Sm, Nd). Appl. Catal. A Gen. 255, 45–57.
Goldwasser, M.R., Rivas, M.E., Pietri, E., Pérez-Zurita, M.J., Cubeiro, M.L., Grivobal-Constant, A., Leclercq, G., 2005. Perovskites as catalysts precursors: synthesis and characterization. J. Mol. Catal. A Chem. 228, 325–331.
Jahangiri, A., Aghabozorg, H., Pahlavanzadeh, H., 2013. Effects of Fe substitutions by Ni in La–Ni–O perovskite-type oxides in reforming of methane with CO2 and O2. Int. J. Hydrogen Energy 38, 10407–10416.
Khalil, M., 2003. Synthesis, X-ray, infrared spectra and electrical conductivity of La/Ba–CoO_3 systems. Mater. Sci. Eng. A 352, 64–70.
Khoshbin, R., Haghighi, M., 2015. Direct conversion of syngas to dimethyl ether as a green fuel over CuO-ZnO-Al_2O_3/HZSM-5 nanocatalyst: effect of aging time on physicochemical and catalytic properties. J. Renew. Sustain. Energy 7.
Kuhn, J.N., Ozkan, U.S., 2008. Surface properties of Sr- and Co-doped $LaFeO_3$. J. Catal. 253, 200–211.
Kumar, E., Selvarajan, P., Muthuraj, D., 2013. Synthesis and characterization of CeO2 nanocrystals by solvothermal route. Mater. Res. 16, 269–276.
Labhasetwar, N., Saravanan, G., Kumar Megarajan, S., Manwar, N., Khobragade, R., Doggali, P., Grasset, F., 2015. Perovskite-type catalytic materials for environmental applications. Sci. Technol. Adv. Mater. 16, 36002.
Li, B., Su, W., Lin, X., Wang, X., 2017. Catalytic performance and characterization of Neodymium-containing mesoporous silica supported nickel catalysts for methane reforming to syngas. Int. J. Hydrogen Energy 42, 12197–12209.
Maneerung, T., Hidajat, K., Kawi, S., 2011. $LaNiO_3$ perovskite catalyst precursor for rapid decomposition of methane: influence of temperature and presence of H_2 in feed stream. Catal. Today 171, 24–35.
Moradi, G.R., Khosravian, F., Rahmanzadeh, M., 2012. Effects of partial substitution of Ni by Cu in $LaNiO_3$ perovskite catalyst for dry methane reforming. Chin. J. Catal. 33, 797–801.
Moradi, G.R., Rahmanzadeh, M., Khosravian, F., 2014. The effects of partial substitution of Ni by Zn in $LaNiO_3$ perovskite catalyst for methane dry reforming. J. CO_2 Util. 6, 7–11.
Moreno-Castilla, C., López-Ramón, M., Carrasco-Marın, F., 2000. Changes in surface chemistry of activated carbons by wet oxidation. Carbon N. Y. 38, 1995–2001.
Ni, J., Chen, L., Lin, J., Schreyer, M.K., Wang, Z., Kawi, S., 2013. High performance of Mg–La mixed oxides supported Ni catalysts for dry reforming of methane: the effect of crystal structure. Int. J. Hydrogen Energy 38, 13631–13642.
Osazuwa, O.U., Setiabudi, H.D., Rasid, R.A., Cheng, C.K., 2017. Syngas production via methane dry reforming: a novel application of $SmCoO_3$ perovskite catalyst. J. Nat. Gas. Sci. Eng. 37, 435–448.
Pakhare, D., Schwartz, V., Abdelsayed, V., Haynes, D., Shekhawat, D., Poston, J., Spivey, J., 2014. Kinetic and mechanistic study of dry (CO_2) reforming of methane over Rh-substituted $La_2Zr_2O_7$ pyrochlores. J. Catal. 316, 78–92.
Pichas, C., Pomonis, P., Petrakis, D., Ladavos, A., 2010. Kinetic study of the catalytic

dry reforming of CH4 with CO_2 over $La_{2-x}Sr_xNiO_4$ perovskite-type oxides. Appl. Catal. A Gen. 386, 116–123.
Pompeo, F., Gazzoli, D., Nichio, N.N., 2009. Stability improvements of Ni/α-Al_2O_3 catalysts to obtain hydrogen from methane reforming. Int. J. Hydrogen Energy 34, 2260–2268.
Sazonova, N.N., Sadykov, V.A., Bobin, A.S., Pokrovskaya, S.A., Gubanova, E.L., Mirodatos, C., 2009. Dry reforming of methane over fluorite-like mixed oxides promoted by Pt. React. Kinet. Catal. Lett. 98, 35–41.
Seo, J.G., Youn, M.H., Park, S., Chung, J.S., Song, I.K., 2009. Hydrogen production by steam reforming of liquefied natural gas (LNG) over Ni/Al_2O_3–ZrO_2 xerogel catalysts: effect of calcination temperature of Al_2O3–ZrO_2 xerogel supports. Int. J. Hydrogen Energy 34, 3755–3763.
Son, I.H., Lee, S.J., Song, I.Y., Jeon, W.S., Jung, I., Yun, D.J., Jeong, D.-W., Shim, J.-O., Jang, W.-J., Roh, H.-S., 2014. Study on coke formation over Ni/γ-Al_2O_3, Co-Ni/γ-Al_2O_3, and Mg-Co-Ni/γ-Al_2O_3 catalysts for carbon dioxide reforming of methane. Fuel 136, 194–200.
Sutthiumporn, K., Kawi, S., 2011. Promotional effect of alkaline earth over Ni–La_2O_3 catalyst for CO_2 reforming of CH_4: role of surface oxygen species on H_2 production and carbon suppression. Int. J. Hydrogen Energy 36, 14435–14446.
Sutthiumporn, K., Maneerung, T., Kathiraser, Y., Kawi, S., 2012. CO_2 dry-reforming of methane over $La_{0.8}Sr_{0.2}Ni_{0.8}M_{0.2}O_3$ perovskite (M = Bi, Co, Cr, Cu, Fe): roles of lattice oxygen on C–H activation and carbon suppression. Int. J. Hydrogen Energy 37, 11195–11207.
Tao, G., Mingxu, Z., Fanfei, M., 2014. The XPS Analysis of Surface Texture of Different-density-level Cooking Coal of Fenxi County, vol. 2, pp. 59–65.
Tienthao, N., Hassanzahediniaki, M., Alamdari, H., Kaliaguine, S., 2007. Effect of alkali additives over nanocrystalline Co–Cu-based perovskites as catalysts for higher-alcohol synthesis. J. Catal. 245, 348–357.
Valderrama, G., Goldwasser, M.R., Navarro, C.U., de Tatibouët, J.M., Barrault, J., Batiot-Dupeyrat, C., Martínez, F., 2005. Dry reforming of methane over Ni perovskite type oxides. Catal. Today 107–108, 785–791.
Valderrama, G., Kiennemann, A., Goldwasser, M.R., 2008. Dry reforming of CH4 over solid solutions of $LaNi_{1-x}Co_xO_3$. Catal. Today 133–135, 142–148.
Vu, B.K., Song, M.B., Ahn, I.Y., Suh, Y.-W., Suh, D.J., Kim, J.S., Shin, E.W., 2011. Location and structure of coke generated over Pt–Sn/Al_2O_3 in propane dehydrogenation. J. Ind. Eng. Chem. 17, 71–76.
Wang, H., Cong, Y., Yang, W., 2003. Investigation on the partial oxidation of methane to syngas in a tubular $Ba_{0.5}Sr_{0.5}Co_{0.8}Fe_{0.2}O_{3-\delta}$? membrane reactor. Catal. Today 82, 157–166.
Wang, N., Chu, W., Zhang, T., Zhao, X.S., 2012. Synthesis, characterization and catalytic performances of Ce-SBA-15 supported nickel catalysts for methane dry reforming to hydrogen and syngas. Int. J. Hydrogen Energy 37, 19–30.
Weckhuysen, B.M., Rosynek, M.P., Lunsford, J.H., 1998. Characterization of Surface Carbon formed during the Conversion of Methane to Benzene Over Mo/H-ZSM-5 Catalysts, vol. 52, pp. 31–36.
Wisniewski, M., Boréave, A., Gélin, P., 2005. Catalytic CO_2 reforming of methane over $Ir/Ce_{0.9}Gd_{0.1}O_{2-x}$. Catal. Commun. 6, 596–600.
Yentekakis, I.V., Goula, G., Panagiotopoulou, P., Katsoni, A., Diamadopoulos, E., Mantzavinos, D., Delimitis, A., 2015. Dry reforming of methane: catalytic performance and stability of Ir catalysts supported on γ-Al_2O_3, $Zr_{0.92}Y_{0.08}O_{2-\delta}$ (YSZ) or $Ce_{0.9}Gd_{0.1}O_{2-\delta}$ (GDC) supports. Top. Catal. 58, 1228–1241.
Zahedinezhad, M., Rowshanzamir, S., Eikani, M., 2009. Autothermal reforming of methane to synthesis gas: modeling and simulation. Int. J. Hydrogen Energy 34, 1292–1300.
Zhang, J., Wang, H., Dalai, A., 2007. Development of stable bimetallic catalysts for carbon dioxide reforming of methane. J. Catal. 249, 300–310.
Zhang, D., Wang, R., Wang, L., Yang, X., 2013. Coking and deactivation of boron modified Al-MCM-41 for vapor-phase Beckmann rearrangement reaction. J. Mol. Catal. A Chem. 366, 179–185.
Zheng, X.-G., Tan, S.-Y., Dong, L.-C., Li, S.-B., Chen, H.-M., Wei, S.-A., 2015. Experimental and kinetic investigation of the plasma catalytic dry reforming of methane over perovskite $LaNiO_3$ nanoparticles. Fuel Process. Technol. 137, 250–258.
Zhu, J., Li, H., Zhong, L., Xiao, P., Xu, X., Yang, X., Zhao, Z., Li, J., 2014. Perovskite oxides: preparation, Characterizations and applications in heterogeneous catalysis. ACS Catal. 4, 2917–2940.
Zhu, Q., Cheng, H., Zou, X., Lu, X., Xu, Q., Zhou, Z., 2015. Synthesis, characterization, and catalytic performance of $La_{0.6}Sr_{0.4}Ni_xCo_{1-x}O_3$ perovskite catalysts in dry reforming of coke oven gas. Chin. J. Catal. 36, 915–924.

Energy Conversion and Management 171 (2018) 20–30

Contents lists available at ScienceDirect

Energy Conversion and Management

journal homepage: www.elsevier.com/locate/enconman

Conceptual design and life cycle assessment of decentralized power generation by HT-PEMFC system with sorption enhanced water gas shift loop

Unchalee Suwanmanee[a], Dang Saebea[b], Viktor Hacker[c], Suttichai Assabumrungrat[d], Amornchai Arpornwichanop[e], Suthida Authayanun[a,*]

[a] Department of Chemical Engineering, Faculty of Engineering, Srinakharinwirot University, Nakhon Nayok 26120, Thailand
[b] Department of Chemical Engineering, Faculty of Engineering, Burapha University, Chonburi 20131, Thailand
[c] Institute of Chemical Engineering and Environmental Technology, Graz University of Technology, Inffeldgasse 25C, Graz 8010, Austria
[d] Center of Excellence in Catalysis and Catalytic Reaction Engineering, Department of Chemical Engineering, Faculty of Engineering, Chulalongkorn University, Bangkok 10330, Thailand
[e] Computational Process Engineering Research Unit, Department of Chemical Engineering, Faculty of Engineering, Chulalongkorn University, Bangkok 10330, Thailand

ARTICLE INFO

Keywords:
HT-PEMFC
CO_2 capture
Biomass
Sorption-enhanced water gas shift reactor
Life cycle assessment

ABSTRACT

In this work, the decentralized power generation system consisting of a biomass gasifier, high-temperature proton exchange membrane fuel cells (HT-PEMFCs), and a sorption enhanced water gas shift reactor (SE-WGS) is investigated. With very low CO_2 and CO concentrations in the reformate gas, the unconsumed fuel at the anode outlet stream of HT-PEMFC is possibly recirculated to the sorption enhanced water gas shift reactor to improve the performance and overall system efficiency without an increase in the problematic CO poisoning. The effects of CaO/C ratio, fuel utilization, and anode split ratio are analysed. With the anode recirculation, the operation at higher fuel utilization and anode split ratio improves the hydrogen efficiency and the system efficiency. The environmental impacts of the biomass gasification integrated with the SE-WGS and HT-PEMFCs are analysed and compared to the different decentralized HT-PEMFC systems fuelled by biomass using life cycle assessment methodology. The CaO production process is found to be the main cause of global warming impact and damage to human health and ecosystem quality, and no negative effect on resource depletion is observed for all studied power generation systems fuelled by biomass. The implementation of CO_2 capture into the decentralized HT-PEMFC systems to enhance the hydrogen purity and efficiency significantly increases the environmental impact of the systems. Compared to the Thai Mixed Electricity Grid, better global warming impact of power generation from all studied HT-PEMFC systems is observed due to the environmental benefit obtained from the electricity produced from biomass.

1. Introduction

The conversion of renewable resources into hydrogen is considered a promising replacement for the use of fossil fuels because hydrogen is a superior energy carrier that is used as the fuel for highly efficient and emission-free power generation via fuel cells. Currently, 48% of the hydrogen produced worldwide is from natural gas, 30% from petroleum, 18% from coal, and the remaining 4% is generated by water electrolysis [1]. Owing to the increased demand for power and environmental concerns, the development of sustainable feedstocks for hydrogen production is necessary. Thailand is an agroindustry based country with an abundance and variety of agricultural waste and bio-based materials. According to the Alternative Energy Development Plan of Thailand (AEDP 2012–2021), the use of alternative energy resources such as biomass-based fuels is encouraged to replace the need for petroleum and reduce the greenhouse gas emissions [2]. Owing to their environmental friendliness, availability and renewability, biomass and bio-based materials are considered to be attractive raw materials for hydrogen production [3,4].

The gasification process is a well-known process for hydrogen production from lignocellulosic biomass in which the solid biomass is reformed to gaseous products by using air, oxygen or steam as gasifying agents. Lv et al. [5] concluded that steam gasification provides better volume content of hydrogen and carbon dioxide than air gasification.

* Corresponding author.
E-mail address: suthidaa@g.swu.ac.th (S. Authayanun).

https://doi.org/10.1016/j.enconman.2018.05.068
Received 3 February 2018; Received in revised form 30 April 2018; Accepted 19 May 2018
0196-8904/ © 2018 Elsevier Ltd. All rights reserved.

Nomenclature

A	pre-exponential factor for proton conductivity of the PBI membrane
B	activation energy for proton conductivity of the PBI membrane, J mole^{-1} K^{-1}
$C_{dissolve}$	equilibrium concentration, mole cm^{-3}
C_{Pt}	concentration on the catalyst surface, mole cm^{-3}
C_{Pt}^{ref}	reference concentration on the catalyst surface, mole cm^{-3}
D_{ij}^{eff}	binary diffusion coefficient, m^2 s^{-1}
D_{H_2}	diffusion coefficient of hydrogen in phosphoric acid, cm^2 s^{-1}
D_{O_2}	diffusion coefficient of oxygen in phosphoric acid, cm^2 s^{-1}
E_c	activation energy, J mole^{-1} K^{-1}
E_r	reversible cell potential, V
F	Faraday constant, 96,485 C mole^{-1}
G	Gibb free energy, J mole^{-1}
H	enthalpy, kJ
L_c	catalyst loading, mg cm^{-2}
LHV	lower heating value, kJ kg^{-1}
N	molar flux, mole s^{-1} m^{-2}
P	pressure, atm
P_{comp}	power requirement for compressors, W
P_{FC}	fuel cell power output, W
P_{net}	net power output, W
P_{pump}	power requirement for pumps, W
Q_{burn}	heat generation from the anode off-gas in the burner, W
Q_R	total heat recovery from the hydrogen production process, W
Q_T	total heat requirement for the hydrogen production process, W
R	gas constant, 8.314 J mol^{-1} K^{-1}
RH	relative humidity
S	entropy, J K^{-1}
$S_{Pt-anode}$	real platinum surface area
T	cell temperature, K
T_{ref}	reference cell temperature, K
V_{cell}	cell voltage, V
X	mole fraction
a_c	catalyst surface area, m^2 g^{-1}
a_{H_2O}	water activity
h	channel height, m
i	current density, A m^{-2}
i_0	exchange current density, A m^{-2}
i_0^{ref}	reference exchange current density, A m^{-2}
l_m	membrane thickness, m
m	mass flow rate, kg s^{-1}
n	molar flow rate, mole s^{-1}
x	channel length, m

Greek letters

δ	average film thickness, cm
α	transfer coefficient
γ	reaction order
θ_{CO}	CO coverage
σ_m	proton conductivity, S cm^{-1}
η_{ohmic}	ohmic loss, V
η_{act}	activation loss, V
η_{invert}	inverter efficiency
η_H	hydrogen efficiency
η_{sys}	system efficiency

Subscripts and Superscripts

a	anode
burn	burner
c	cathode
m	membrane
i,j	components "i" and "j"
H_2	hydrogen
O_2	oxygen
N_2	nitrogen
H_2O	water
CH_4	methane
CO_2	carbon dioxide
CO	carbon monoxide

Biomass oxygen/steam gasification is an effective technology for hydrogen production with lower energy consumption. However, the hydrogen content in the gaseous products is still too low and the integration of water gas shift reactors for the conversion of CO and water to hydrogen may improve the hydrogen production performance. Furthermore, Srirangan et al. [6] indicated that the moisture content of biomass should be 10–20% and a high amount of energy is necessary for the gasification process of biomass with high moisture content in the absence of a drier unit.

Owing to the high carbon content of biomass, a high amount of CO_2 contents is generated during the reaction of biomass and air in the gasification process. Thus, the high CO_2 dilution is the main problem for this process. In addition, the CO_2 emission during the hydrogen production process is the main cause of global warming. Carbon capture and storage (CCS) technologies have received much attention for their potential to achieve major CO_2 reductions [7]. To enhance the product purity and reduce the environmental problem, there have been many studies of the CO_2 capture concept for the removal of CO_2 from reformate gas [8–10]. CaO is normally applied as CO_2 adsorbent owing to its high CO_2 adsorption performance, low cost, and abundance. Recently, the sorption-enhanced gasification process, which combines the hydrogen production process and the CO_2 separation process using CO_2 adsorbents into a single step, has been investigated by several researchers [11,12]. In addition, since CO can react with water to produce hydrogen and CO_2 through the water gas shift reaction, the integration of a water gas shift reactor and CO_2 capture process into a single stage of a sorption-enhanced water gas shift reactor (SE-WGS) can also enhance the hydrogen yield by removing CO_2 during the reaction. In addition to the capture of CO_2, CaO also reacts with hydrogen sulphide (H_2S) and carbonyl sulphide (COS); thus, the additional sulphur removal components are not required for this system, improving the plant economics and efficiency [13].

To use biomass as a fuel for power generation, the coupling of biomass gasification and solid oxide fuel cell has been increasingly developed for large-scale applications [14]. However, a small-scale, decentralized system is emerging as a viable alternative for power generation using more than one energy source [15]. In addition, small-scale decentralized production processes using locally available renewable resources can reduce the transportation distances and solve the problem of hydrogen storage and infrastructure [16]. The use of local renewable and intermittent energy sources such as wind, solar energy, and biomass is much more feasible for this system [17]. The decentralized generation of electricity from biomass with proton exchange membrane fuel cells for small-scale applications with different levels of hydrogen purification was studied by Toonssen et al. [18]. They revealed that the purity of hydrogen has a significant effect on both the system and hydrogen production efficiencies. The PEMFC system with the lower quality of hydrogen production provides a higher exergy

efficiency owing to the high losses during the purification of the hydrogen gas. In addition, the biomass-fuelled proton exchange membrane fuel cell (PEMFC) system was investigated by Guan et al. [19]. They proposed that the renewable hydrogen-rich gas from manure or forest residues is usable for PEMFCs and can be used in stable fuel cell stack operation. The PEMFC integrated with the biomass gasification system achieves an excellent technical performance with a 20% electrical efficiency and 57% thermal efficiency for 100 kW_e generation.

A high-temperature proton exchange membrane fuel cell (HT-PEMFC) is a promising fuel cell technology that has been developed to solve the main problems of a conventional, low-temperature PEMFC (LT-PEMFC), which are the CO poisoning on Pt catalysts and water management in both the gas diffusion layer and the membrane [20]. Because of the high CO tolerance of the HT-PEMFC compared to the conventional PEMFC, reformate gas can be used as the fuel for HT-PEMFC with simple hydrogen purification processes. Therefore, the HT-PEMFC system is an attractive technology for decentralized power generation. Due to low CO and CO_2 concentration of the product gas from the SEWGS and high CO tolerance of HT-PEMFCs, the implementation of the anode recirculation to SE-WGS loop is novel strategy to efficiently utilize fuel and prevent CO accumulation in the anode at high fuel utilization. Therefore, this should be studied in detail to effectively design the system.

For the consideration of the environmental issues of a power generation system, life cycle assessment (LCA) is an effective tool that can be used to evaluate the environmental impact occurring throughout the entire life cycle of a process [21]. Rillo et al. [22] studied the life cycle assessment of biogas-fed solid oxide fuel cell with a CO_2 recovery system. Environmental assessment of a proton exchange membrane fuel cell with platinum catalyst recovery was investigated by Duclos et al. [23]. Using this method, useful information about the environmental impact can be provided. Further improvement can then be designed to not only enhance the efficiency but also consider the environmental impact of the studied processes.

In this work, the biomass gasification process integrated with an HT-PEMFC system for decentralized power generation is investigated focusing on its system performance and environmental impact. To improve the hydrogen yield and purity in the gas produced from the biomass gasification process and reduce the CO_2 emission, a sorption-enhanced water gas shift reactor is applied to the HT-PEMFC system. In this study, a recirculation of the anode off-gas to the sorption-enhanced water gas shift reactor is proposed to enhance the performance and efficiency of the system. The effects of key operating parameters, i.e., CaO/C ratios, fuel utilization, and anode split ratios on the hydrogen fraction, hydrogen molar flow, the hydrogen efficiency and the system efficiency are investigated. Additionally, life cycle analysis of the biomass gasification process integrated with the sorption-enhanced water gas shift reactor and HT-PEMFC system is studied and compared to the conventional HT-PEMFC system and the HT-PEMFC system based on the sorption-enhanced gasifier. The proposed systems are environmentally analysed in terms of their impact on global warming, human health, ecosystem quality, and energy resources. The environmental data of the developed power generation systems will be beneficial for the design of systems for sustainable electricity generation from renewable energy sources.

2. Process description

In this work, electricity generation from the HT-PEMFC system fuelled by biomass is studied. Due to low CO tolerance of low temperature fuel cells and high CO_2 emission of the biomass gasification process, the combination of water gas shift reaction and CO_2 capture into a single unit, the SE-WGS, is applied. During the water gas shift reaction of the SE-WGS, the CO_2 is simultaneously removed and thus the water gas shift reaction is shifted to the product side. High amount of CO can react with water via this process resulting in higher hydrogen yield and purity and lower CO concentration compared to the conventional water gas shift reactor. Owing to very low CO and CO_2 concentrations of the product gas from the SE-WGS (anode feed stream), the biomass gasification integrated with the SE-WGS and HT-PEMFCs system based anode recirculation is studied in order to enhance the system performance and efficiency. A fraction of the anode off-gas from the HT-PEMFCs is recirculated to the SE-WGS. The remainder is fed to the burner with additional biomass to meet the heat requirement of the gasification process.

Therefore, the biomass gasification integrated with the SE-WGS and HT-PEMFC system is studied and modelled using the Aspen Plus simulator and Matlab. For small-scale decentralized power generation,

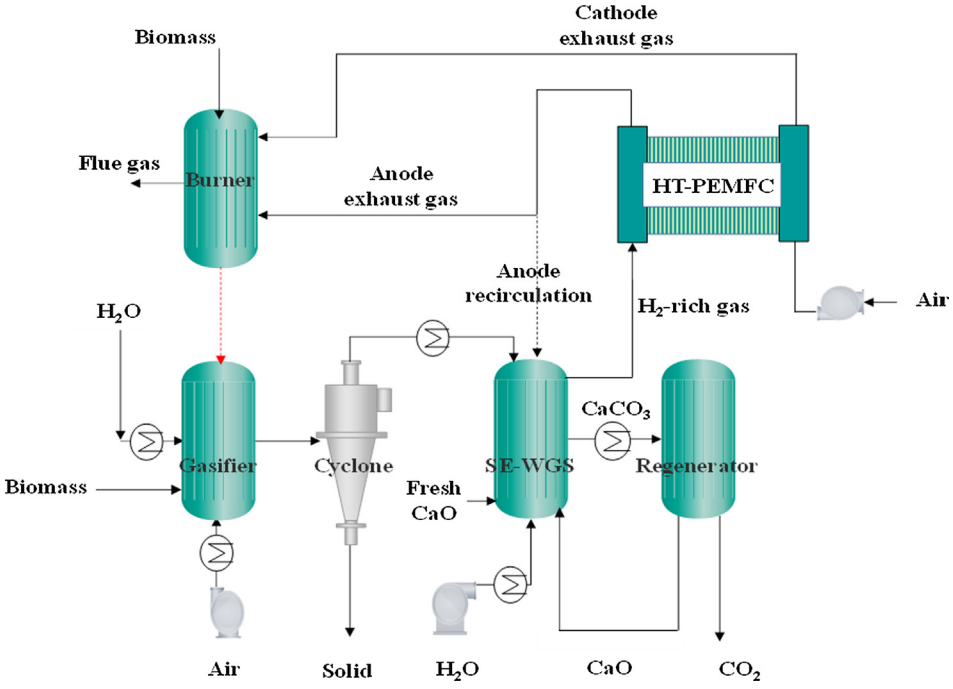

Fig. 1. The biomass gasification process integrated with the SE-WGS and HT-PEMFCs system.

the target power output is 200 kW_e. The design for the gasification process integrated with the SE-WGS and HT-PEMFCs are presented in Fig. 1. Rice husk with a low moisture content (< 10%) is used as the feedstock for the gasification process with air and steam as the gasifying agents. It is specified as the nonconventional component and the results of its proximate and ultimate analysis are shown in Table 1.

The gasification process includes a decomposition reactor and a gasifier. The decomposition reactor is modelled as an RYield reactor used to convert the nonconventional component into the constituent elements of hydrogen, nitrogen, oxygen, sulphur, solid carbon, and ash by specifying the distribution of the product yields based on the ultimate analysis [25]. The RGibbs reactor module is applied for the gasifier by using the approach based on the minimization of the Gibbs free energy. Then, the product gases and solid components from the gasifier are separated by a cyclone unit. In addition, the product gases from the cyclone unit are fed to the sorption enhanced water gas shift reactor modelled as an RGibbs reactor. This unit is applied to simultaneously enhance the hydrogen yield and reduce the CO_2 and CO concentrations in the product gas by using CaO adsorbents. The reactions occurring in this reactor are the water gas shift reaction (Eq. (1)) and CO_2 adsorption (Eq. (2))

$$CO + H_2O \leftrightarrow H_2 + CO_2 \quad (1)$$

$$CaO + CO_2 \leftrightarrow CaCO_3 \quad (2)$$

The regenerator is applied to regenerate the CaO adsorbents by the desorption of CO_2 from CaO. Owing to the endothermicity of the regeneration process, external heat is required and the reaction occurring in the regenerator reactor is shown in Eq. (3). In this work, CaO loss during the process of 20% is assumed [26]. The regenerated CaO is recycled back to the SE-WGS to reduce CO_2 emissions and enhance the hydrogen production performance.

$$CaCO_3 \leftrightarrow CaO + CO_2 \quad (3)$$

Then, the reformate gas is used to generate electricity via HT-PEMFCs. The HT-PEMFC model based on electrochemical equations and a diffusion model and that takes the CO poisoning into account is applied in this work using the Matlab program. The polybenzimidazole (PBI) doped phosphoric acid membrane is used as the electrolyte. The Stefan-Maxwell equation and Fick's law are used to represent the diffusion model of the reactant in the gas diffusion layer and film electrolyte (Table 2) and the parameters for the electrochemical model of the HT-PEMFCs are given in Table 3. In addition, the physical and material property parameters for the HT-PEMFCs used in this study are presented in Table 4.

3. Performance analysis

In this study, the effects of fuel utilization, CaO/C ratio, and anode split ratio on the hydrogen concentration and amount of produced hydrogen, hydrogen efficiency and system efficiency are analysed. The values of the operating parameters for this system are presented in Table 5. The fuel utilization, CaO/C ratio, and anode split ratio are given by:

$$\text{Fuel utilization} = \frac{\text{mole of consumed hydrogen}}{\text{mole of supplied hydrogen}} \quad (4)$$

$$\text{CaO/C ratio} = \frac{\text{molar flow rate of CaO(mol/s)}}{\text{molar flow rate of carbon atom in biomass(mol/s)}} \quad (5)$$

$$\text{Anode split ratio} = \frac{\text{molar flow rate of recycled anode off gas to SE-WGS(mol/s)}}{\text{molar flow rate of total anode off gas(mol/s)}} \quad (6)$$

The efficiency of the hydrogen production process consisting of the biomass gasifier and the sorption enhanced water gas shift reactor can be obtained by the following equation:

$$\%\text{Hydrogen efficiency}(\eta_H) = \frac{m_{H_2} \cdot LHV_{H_2}}{m_{biomass} \cdot LHV_{biomass} + Q_T - Q_R} \cdot 100 \quad (7)$$

where m_{H_2} is the mass flow rate of produced hydrogen, LHV_{H_2} is the lower heating value of hydrogen, $m_{biomass}$ is the mass flow rate of the utilized biomass, and $LHV_{biomass}$ is the lower heating value of the biomass [30]. The total heat requirement (Q_T) is the heat for preheating reactants and gasifying agents, maintaining the gasifier at the reaction temperature, and the regeneration of CaO adsorbent whereas the total heat recovery (Q_R) is calculated from the recovered heat from the outlet stream of the gasifier, the sorption-enhanced water gas shift reactor, and the regenerator.

The power output of the fuel cell (P_{FC}) is calculated from the current density (i) and cell voltage (V_{cell}) as:

$$P_{FC} = i \cdot A \cdot n_{cell} \cdot V_{cell} \quad (8)$$

where A is the active cell area and n_{cell} is the number of cells.The net power output (P_{net}) can be calculated from the fuel cell power output (P_{FC}), the efficiency of the inverter (η_{invert}) for the conversion of DC electricity to AC electricity and the power needed by the auxiliary units such as pumps (P_{pump}), and compressors (P_{comp}) in the system as shown in Eq. (9). The inverter efficiency of 94% is specified in previous work [31].

$$P_{net} = (P_{FC} - P_{pump} - P_{comp}) \cdot \frac{\eta_{invert}}{100} \quad (9)$$

The overall system efficiency is related to the net power output and the total energy input as shown in Eq. (10).

$$\%\text{System efficiency}(\eta_{sys}) = \frac{P_{net}}{m_{biomass} \cdot LHV_{biomass} + Q_T - Q_R - Q_{burn}} \cdot 100 \quad (10)$$

where Q_{burn} is the heat generated from the anode off-gas in the burner, which can be calculated based on the enthalpy balance as shown in Eq. (11). The efficiency of the combustion process is specified as 98% [32].

$$Q_{burn} = \sum_i^C n_{a,out,i} H_{a,out,i} + \sum_i^C n_{c,out,i} H_{c,out,i} - \sum_i^C n_{burn,out,i} H_{burn,out,i} \quad (11)$$

where $n_{a,out}$, $n_{c,out}$ and $n_{burn,out}$ are the molar flow rates of the anode off gas, cathode off-gas and outlet stream of the burner, respectively. $H_{a,out}$, $H_{c,out}$ and $H_{burn,out}$ are the enthalpies of the anode off gas, cathode off-gas and outlet stream of the burner, respectively.

4. Life cycle assessment (LCA)

4.1. Goal and scope definition

The goal of this work is to investigate the environmental performance of electricity generation from the HT-PEMFC systems including the SE-WGS. This system is also compared to other HT-PEMFC systems and the studied systems are divided into four scenarios as follows:

- Scenario 1: The HT-PEMFC system with the biomass gasifier and the

Table 1
Proximate and ultimate analyses of rice husk [24].

Proximate Analysis (%wt)		Ultimate Analysis (%wt, dry basis)	
MS	9.95	C	39.44
VM	55.54	H	3.22
FC	14.99	N	0.08
Ash	19.52	O	37.74
		S	0.01

VM = Volatile matter, MS = Moisture and FC = Fixed carbon.

Table 2
Diffusion models used in simulations of HT-PEMFCs [27,28].

Diffusion models	Equations
Stefan Maxwell models	Anode:
	$\frac{dX_{H_2O}}{dz} = \frac{RT}{P}X_{H_2O}\left(\frac{N_{H_2,g}}{D^{eff}_{H_2,H_2O}}\right)$
	$\frac{dX_{CO_2}}{dz} = \frac{RT}{P}X_{CO_2}\left(\frac{N_{H_2,g}}{D^{eff}_{H_2,CO_2}}\right)\frac{dX_{CO}}{dz} = \frac{RT}{P}X_{CO}\left(\frac{N_{H_2,g}}{D^{eff}_{H_2,CO}}\right)$
	$\frac{dX_{CH_4}}{dz} = \frac{RT}{P}X_{CH_4}\left(\frac{N_{H_2,g}}{D^{eff}_{H_2,CH_4}}\right)$
	$X_{H_2} = 1-X_{CO_2}-X_{H_2O}-X_{CO}-X_{CH_4}$
	Cathode:
	$\frac{dX_{N_2}}{dz} = \frac{RT}{P}X_{N_2}\left(\frac{N_{O_2}}{D^{eff}_{N_2,O_2}} + \frac{N_{H_2O,g}}{D^{eff}_{N_2,H_2O}}\right)$
	$\frac{dX_{H_2O}}{dz} = \frac{RT}{P}\left[X_{H_2O}\left(\frac{N_{O_2}}{D^{eff}_{O_2,H_2O}}\right)-N_{H_2O}\left(\frac{X_{O_2}}{D^{eff}_{O_2,H_2O}} + \frac{X_{N_2}}{D^{eff}_{N_2,H_2O}}\right)\right]$
	$X_{O_2} = 1-X_{N_2}-X_{H_2O}$
Fick's law models	At the anode
	$\frac{N_{H_2}}{S_{Pt-anode}} = \frac{-D_{H_2}(C_{Pt,a}-C_{H_2(dissolve)})}{\delta_{anode}}$
	$C_{H_2(dissolve)} = C^{dissolved}_{H_2}\cdot X_{H_2}\cdot P$
	At the cathode
	$\frac{N_{O_2}}{S_{Pt-cathode}} = \frac{-D_{O_2}(C_{Pt,c}-C_{O_2(dissolve)})}{\delta_{cathode}}$
	$C_{O_2(dissolve)} = C^{dissolved}_{O_2}\cdot X_{O_2}\cdot P$

Table 3
Parameters of electrochemical models of HT-PEMFCs [27,28].

Parameters	Equations
Cell Voltage	$V_{cell} = E_r-\eta_{act,a}-\eta_{act,c}-\eta_{ohmic}$
Reversible cell potential	$E_r = -\left(\frac{\Delta H}{nF}-\frac{T\Delta S}{nF}\right) + \frac{RT}{nF}\ln\left[\frac{(RT)^{1.5}C_{Pt,H_2}C^{0.5}_{Pt,O_2}}{a_{H_2O}}\right]$
Anode activation loss	$\eta_{act,a} = \frac{RT}{\alpha F}\sinh^{-1}\left(\frac{i}{2i_0(1-\theta_{CO})^2}\right)$
	$i_{0,a} = i^{ref}_{0,a}a_{c,a}L_{c,a}\left(\frac{C_{Pt}}{C_{ref,a}}\right)^{\gamma_a}\exp\left[-\frac{E_{c,a}}{RT}\left(1-\frac{T}{T_{ref,a}}\right)\right]$
	$\theta_{CO} = a*\ln\frac{[CO]}{[H_2]} + b*\ln(i)*\ln\frac{[CO]}{[H_2]} + c$
	$a = -0.00012784*T^2 + 0.11717499*T-26.62908873$
	$b = 0.0001416*T^2-0.12813608*T + 28.852463626$
	$c = -0.00034886*T^2 + 0.31596903*T-70.11693333$
Cathode activation loss	$\eta_{act,c} = \frac{RT}{\alpha F}\sinh^{-1}\left(\frac{i}{2i_{0,c}}\right)$
	$i_{0,c} = i^{ref}_{0,c}a_{c,c}L_{c,c}\left(\frac{C_{Pt}}{C_{ref,c}}\right)^{\gamma_c}\exp\left[-\frac{E_{c,c}}{RT}(1-\frac{T}{T_{ref,c}})\right]$
Ohmic loss	$\eta_{ohmic} = \left(\frac{\sigma_m}{l_m}\right)i$
	$\sigma_m = \frac{A}{T}\exp\left(\frac{-B}{R(T)}\right)$

SE-WGS.

- Scenario 2: The HT-PEMFC system with the biomass gasifier and the SE-WGS based anode recirculation.
- Scenario 3: The HT-PEMFC system with the sorption-enhanced gasifier (SE-GS) and the conventional WGS.
- Scenario 4: The HT-PEMFC system with the biomass gasifier and the conventional WGS.

The flow charts for all scenarios are presented in Fig. 2 and all emissions, materials and energy consumption and transport are normalized to the functional unit (FU) of 200 kWh of electricity generation by the HT-PEMFC systems. The rice husk is transported by 15-ton heavy-duty diesel vehicles and the transport of rice husk from the rice field to the power plant involves on average an approximately 90 km round trip [33]. In this work, 10% loss of rice straw during transportation is assumed. In addition, the average distance for the transport of CaO from the cement manufacturing plant to the power plant is 182 km round trip [34].

Table 4
Physical and material property parameters for HT-PEMFCs [29].

Parameters	Value
Faraday constant, F (C mol^{-1})	96,485
Active area, A (m^2)	0.03
Number of cell, n_{cell}	1000
GDL thickness, z (m)	0.0002
Membrane thickness, l_m (m)	4×10^{-5}
Anode film thickness, δ_{anode} (m)	2.5×10^{-9}
Cathode film thickness, $\delta_{cathode}$ (m)	1.48×10^{-9}
Anode reference exchange current density, $i^{ref}_{0,a}$ (A m^{-2})	1440
Cathode reference exchange current density, $i^{ref}_{0,c}$ (A m^{-2})	0.0004
Anode catalyst surface area, $a_{c,a}$ (m^2 g^{-1})	64
Cathode catalyst surface area, $a_{c,c}$ (m^2 g^{-1})	32.25
Anode catalyst loading, $L_{c,a}$ (mg cm^{-2})	0.2
Cathode catalyst loading, $L_{c,c}$ (mg cm^{-2})	0.4
Transfer coefficient at anode, α_a	0.5
Transfer coefficient at cathode, α_c	0.75
Reaction order at anode, γ_a	1
Reaction order at cathode, γ_c	1.375
Anode reference concentration, $c_{ref,a}$ (mole cm^{-3})	0.0002
Cathode reference concentration, $c_{ref,c}$ (mole cm^{-3})	0.0004
Anode activation energy, $E_{c,a}$ (J mole^{-1} K^{-1})	16,900
Cathode activation energy, $E_{c,c}$ (J mole^{-1} K^{-1})	72,400
Anode reference cell temperature, $T_{ref,a}$ (K)	433.15
Cathode reference cell temperature, $T_{ref,c}$ (K)	373.15

Table 5
Operating parameters for HT-PEMFCs integrated with the biomass gasifier and the SE-WGS.

Parameters	Standard condition	Operational range
Gasifier		
Temperature (K)	973	–
Pressure (atm)	1	–
S/F	0.4	–
ER	0.2	–
Sorption enhanced water gas shift reactor		
SE-WGS temperature (K)	773	–
Regenerator temperature (K)	1073	–
Pressure (atm)	1	–
CaO/C ratio	1	0.5–1.25
Anode split ratio	0.5	0–0.5
HT-PEMFCs		
Cell temperature (K)	428	–
Pressure (atm)	1	–
Fuel utilization	0.75	0.65–0.8
Air utilization	0.5	–

4.2. Life cycle inventory (LCI) analysis

The data necessary for the calculation of all of the relevant inputs and outputs are collected based on the production of the 200 kWh of electricity generation of each HT-PEMFC system. In addition, the inventory data for the hydrogen production from the gasifier, hydrogen purification using a water shift reactor and power generation by the HT-PEMFC are estimated from the process simulation performed using the Aspen Plus and Matlab programs. The LCI of CaO is retrieved from the Ecoinvent database 3.0. The heat required for hydrogen production from the gasifier and for hydrogen purification using the conventional WGS and the SE-WGS is supplied by the combustion of rice husk and

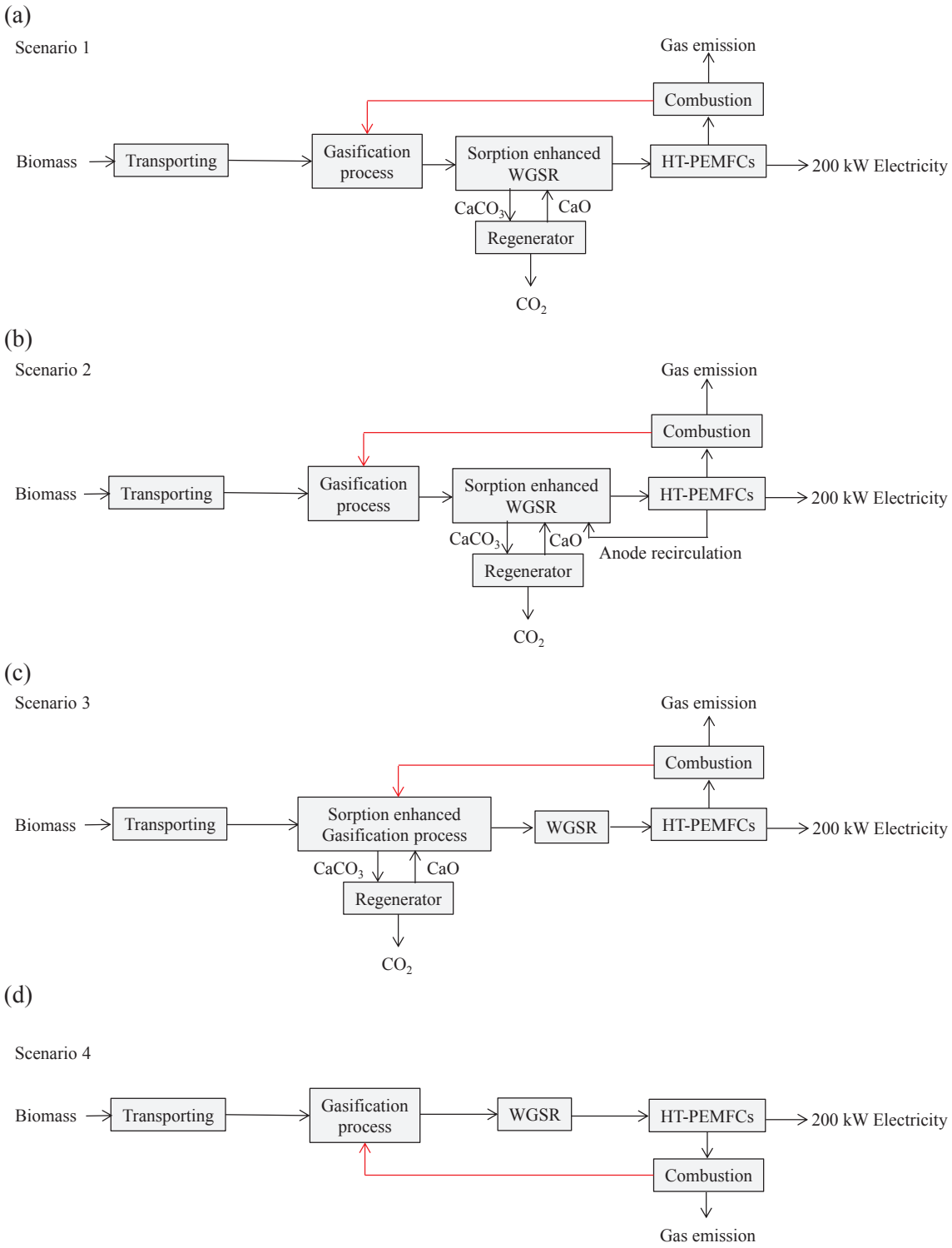

Fig. 2. The system boundaries of electricity generation by different HT-PEMFC systems fuelled by biomass.

anode off-gas in the burner and thus no external heat is consumed for the studied systems. The rice husk is considered as waste and thus, biomass production is not included in this LCA study. Carbon is assumed to be sequestered in a relatively short time frame. Therefore, the net CO_2 emissions are zero for this waste feedstock because of its biogenic origin [35,36]. Furthermore, the electricity used by the pump and compressor is supplied by electricity generation from the HT-PEMFCs.

4.3. Life cycle impact assessment (LCIA)

In this work, the SimaPro 8.2.3 software is applied to carry out the life cycle impact assessment using the LCI data. CML baseline 2000 is used as the life cycle impact assessment method for the calculation of the global warming impact whereas the Eco-indicator 99 is applied to define the "environment damage" in three damage categories (human health, ecosystem quality, and resources). The considered impact category indicators for each damage category are as follows:

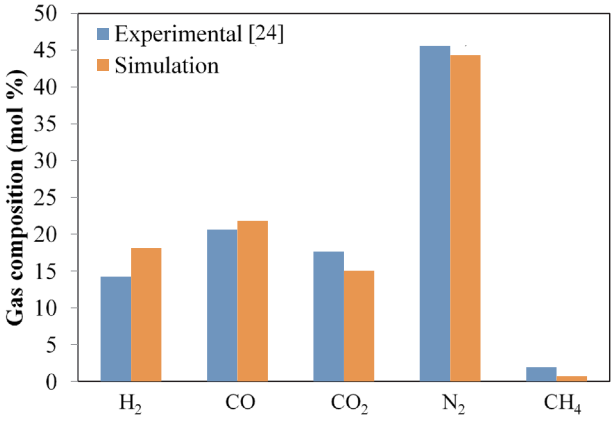

Fig. 3. Validation of the rice husk gasification process.

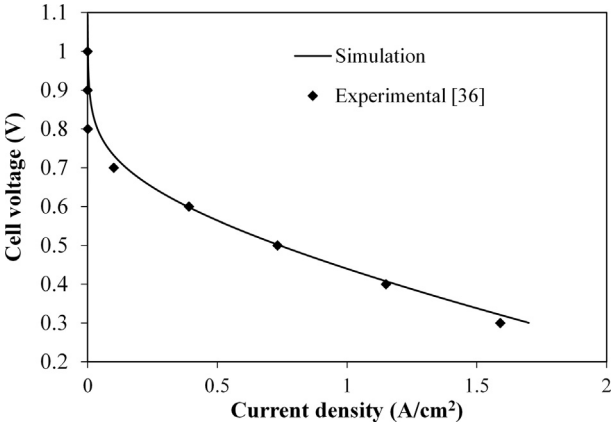

Fig. 4. Validation of the HT-PEMFC at a temperature of 428 K and pure hydrogen operation.

- Human health: climate change, carcinogens, radiation, ozone layer, respiratory organics and respiratory inorganics
- Ecosystem quality: acidification, eutrophication, ecotoxicity and land use
- Resources: fossil fuels and minerals

The normalization and weighting are performed at the damage category level for human health, ecosystem quality, and resources.

5. Results and discussion

5.1. Process simulation

The biomass gasification integrated with the SE-WGS and HT-PEMFCs based anode recirculation for the decentralized power generation is theoretically studied. To confirm the reliability of the model, the simulation results of the rice husk gasification process are compared to the experimental results obtained by Karmakar et al. [24] at the gasifier temperature of 700 °C and equivalence ratio of 0.35 as shown in Fig. 3. Additionally, the validation of the HT-PEMFC at the temperature of 175 °C using the experimental results reported by Li et al. [37] is presented in Fig. 4.

Usually, the hydrogen fraction and hydrogen molar flow rate directly affect the fuel cell performance, as well as the fuel cell efficiency. To reach a high fuel cell power generation efficiency, the suitable conditions of the hydrogen production process for obtaining a high hydrogen fraction and a hydrogen molar flow rate should be determined. Therefore, the effect of the CaO/C ratios, fuel utilization and anode split ratios on the hydrogen fraction and hydrogen molar flow of the product gas from the SE-WGS are shown in Figs. 5 and 6, respectively. From Fig. 5(a), it is found that an increase in the CaO/C ratio can enhance the hydrogen fraction until it reaches the optimal value at the CaO/C ratio of unity. At the CaO/C ratio greater than unity, the CO_2 removal and hydrogen fraction reach a nearly constant value. However, the increase of the anode split ratio has a negative effect on the hydrogen concentration. At a high anode split ratio, most of the anode off-gas is recycled to the SE-WGS and a high amount of N_2 contained in the anode off-gas is also accumulated in the product gas of the SE-WGS. Therefore, the N_2 dilution effect leads to a reduction of the hydrogen fraction at a high anode split ratio.

In addition, the results for the fuel utilization effect on the hydrogen fraction at different anode split ratios are presented in Fig. 5(b) and the simulation results show that fuel utilization has a slight effect on the hydrogen concentration. On the other hand, a high anode split ratio, low fuel utilization and CaO/C ratio of unity are the preferred operating conditions for reaching a high hydrogen molar flow rate as shown in Fig. 6(a) and (b). More CO_2 is captured from the SE-WGS reactive system for a high amount of CaO and thus, the water gas shift reaction is shifted to the product side, leading to greater hydrogen production. Apart from the large nitrogen content in the anode off-gas, a high

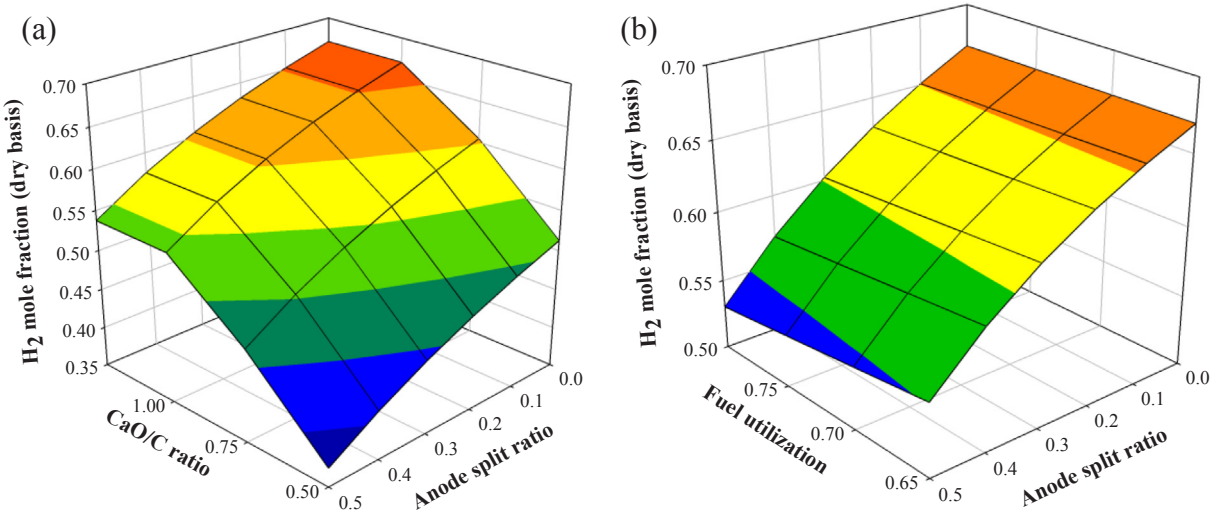

Fig. 5. Hydrogen fraction of rice husk gasifier integrated with the SE-WGS and HT-PEMFCs based anode recirculation at different CaO/C ratios, fuel utilizations and anode split ratios.

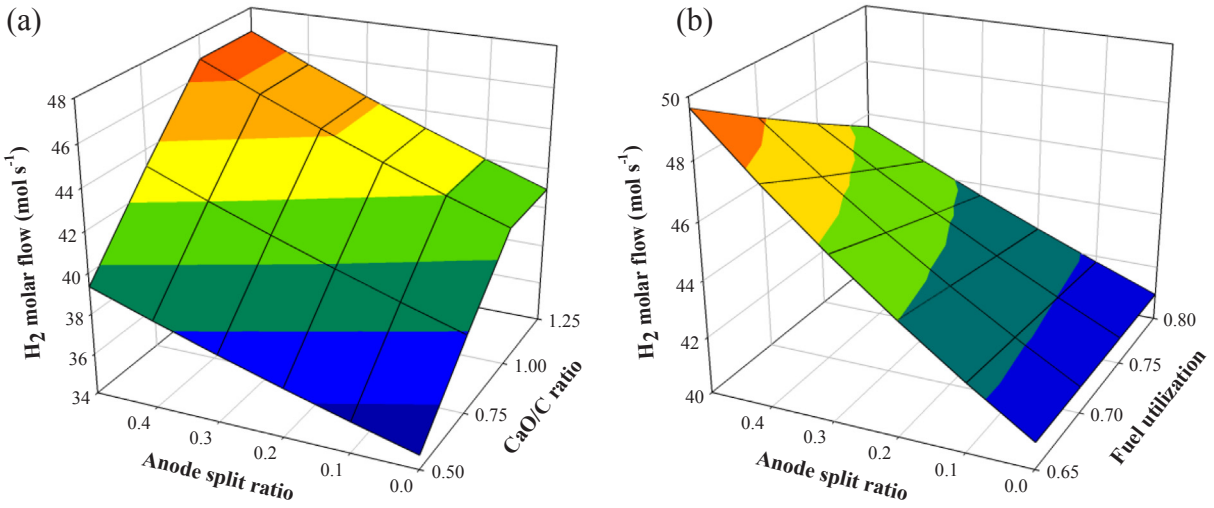

Fig. 6. Hydrogen molar flow of rice husk gasifier integrated with the SE-WGS and HT-PEMFCs based anode recirculation at different CaO/C ratios, fuel utilizations and anode split ratios.

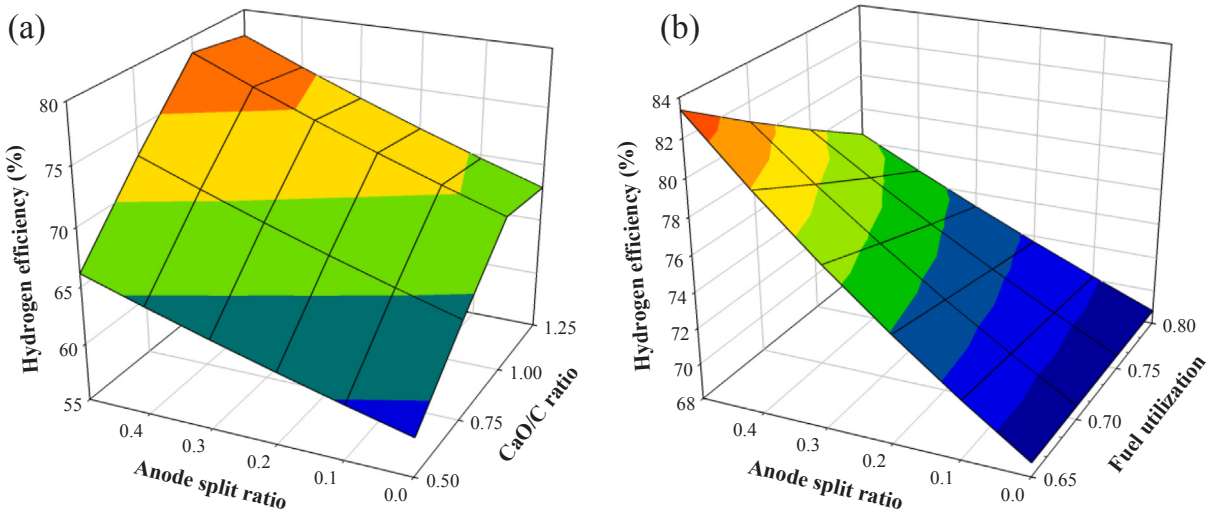

Fig. 7. Hydrogen efficiency of rice husk gasifier integrated with the SE-WGS and HT-PEMFCs based anode recirculation at different CaO/C ratios, fuel utilizations and anode split ratios.

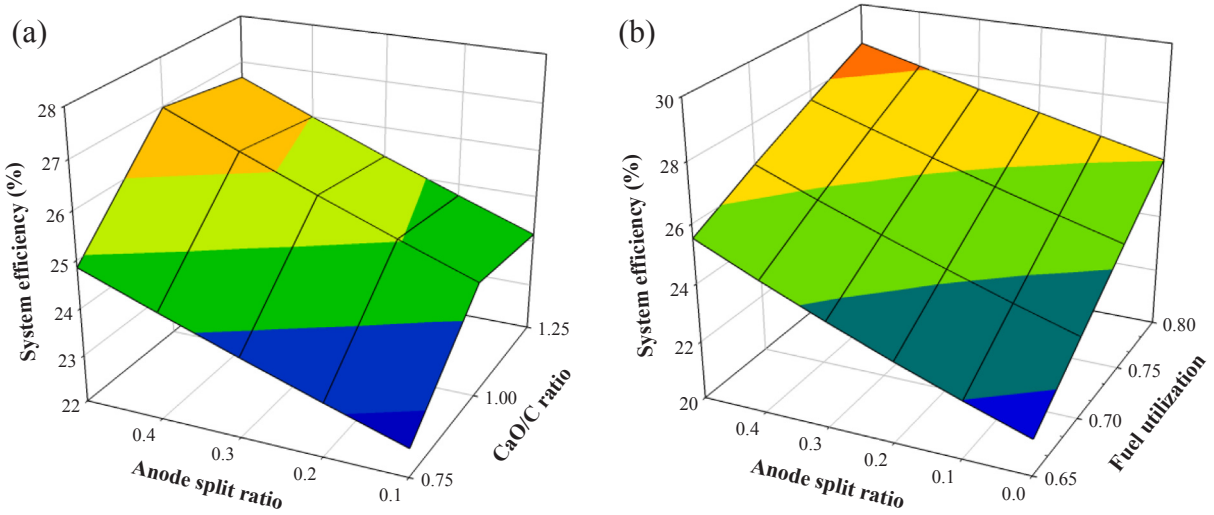

Fig. 8. System efficiency of rice husk gasifier integrated with the SE-WGS and HT-PEMFCs based anode recirculation at different CaO/C ratios, fuel utilizations and anode split ratios.

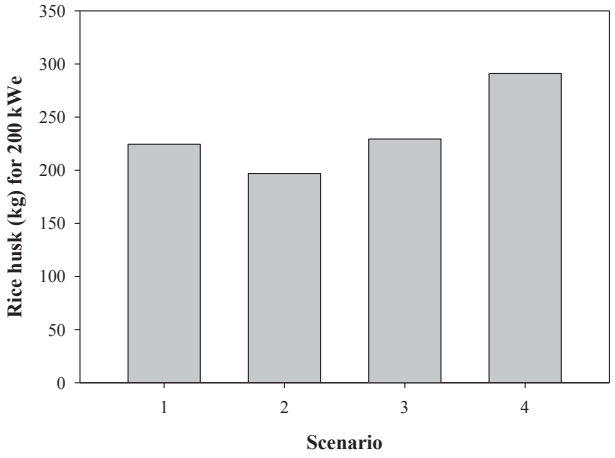

Fig. 9. The overall rice husk consumption of different process scenarios for target power output of 200 kWh.

Table 6
Summary of calculated performance of 200 kW HT-PEMFC systems with the different considered scenarios at the temperature of 700 °C, CaO/C ratio of 1 and ER of 0.2.

Systems	Hydrogen fraction	CO_2 emission (kg)	Hydrogen efficiency (%)
Scenario 1	0.67	2.528	68.77
Scenario 2 (anode split ratio = 0.5)	0.53	1.072	78.63
Scenario 3	0.58	81.176	74.13
Scenario 4	0.44	282.860	57.06

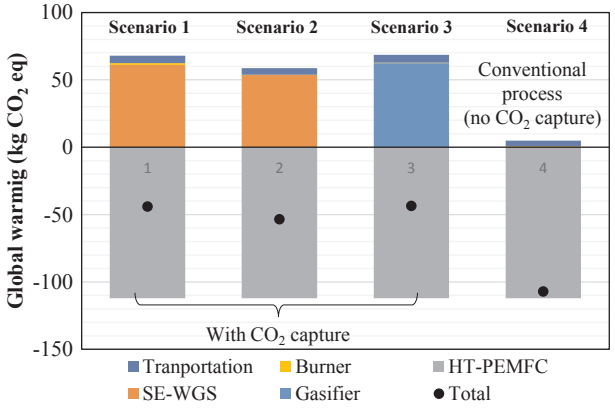

Fig. 10. Global warming impact of the decentralized HT-PEMFC systems.

amount of remaining hydrogen is also returned to the SE-WGS at low fuel utilization and high anode split ratio.

In addition, the effects of the anode split ratio, CaO/C ratio and fuel utilization on the hydrogen efficiency are shown in Fig. 7(a) and (b). It is observed that the maximum hydrogen efficiency can be reached when the SE-WGS is operated at the CaO/C ratio of unity and the anode split ratio of 0.5 (see Fig. 7(a)). Compared to the system without anode recirculation (anode split ratio = 0), the HT-PEMFC system with anode recirculation shows better hydrogen efficiency. This is due to the additional hydrogen production from the SE-WGS and the recycled hydrogen from the anode off-gas. However, it is found that the fuel utilization has a significant effect on the hydrogen efficiency only at high anode split ratios, as shown in Fig. 7(b). In addition, the hydrogen efficiency is constant for the variation of fuel utilization in the case of no anode recirculation. Without the anode recirculation, the hydrogen contained in the anode off-gas is not recycled back to the SE-WGS while the amount of hydrogen produced from the SE-WGS has a direct effect on the hydrogen efficiency.

Furthermore, the results for the overall system efficiency of the biomass gasification integrated with the SE-WGS and HT-PEMFCs based anode recirculation at different CaO/C ratios, fuel utilizations and anode split ratios are shown in Fig. 8(a) and (b). The CaO/C ratio of unity is necessary to achieve maximum system efficiency. Additionally, an increase of the anode split ratio and fuel utilization enhance the overall system efficiency. At high fuel utilization, most of the hydrogen inlet stream is used to generate electricity and thus, the system efficiency increases with this parameter. In addition, it should be noted that no reduction of system efficiency owing to CO poisoning is observed for high anode split ratio and fuel utilization values. Therefore, the fuel inlet stream at the anode from the SE-WGS shows the CO level that is acceptable for HT-PEMFCs despite the application of anode recirculation to the system.

5.2. Life cycle assessment

The energy and material data for each studied system are identified and calculated. All data are used as inputs in the SimaPro software for life cycle assessment calculations. The LCA is performed using the CML 2000 and Eco-indicator 99 methods. The impact category considered for the CML 2000 method is global warming whereas the damage categories for Eco-indicator 99 method are human health, ecosystem quality, and resources. In this work, the consumed electricity of each unit in the decentralized power system is supplied by the power generation from the HT-PEMFCs, whereas the heat required for the hydrogen production process is obtained from the recovered heat in the system and the combustion of biomass. Therefore, the main material input is the biomass (rice husk), and the results for the overall rice husk consumption of each process for the target power output of 200 kWh are presented in Fig. 9. Examination of the simulation results shows that the highest amount of rice husk is consumed for the conventional biomass gasifier integrated with a water gas shift reactor and HT-PEMFCs system (scenario 4), whereas the other systems incorporating CO_2 capture technology utilize lower rice husk amounts. The main reason for this is the increased hydrogen production from CO_2 capture during the reaction and thus, the rice husk requirement is lower at the specified target output.

The performance of the HT-PEMFC systems with various scenarios is shown in Table 6. The results show that the HT-PEMFCs with biomass gasification and SE-WGS system with anode recirculation (scenario 2) show the highest performance in term of hydrogen production and CO_2 emission. Due to the in-situ CO_2 capture in the SE-WGS, the CO_2 emission of the HT-PEMFC systems in scenario 1 and scenario 2 is very low. However, some CO_2 is produced in the water gas shift reactor after the SE-GS (scenario 3) resulting in quite high CO_2 emission for this system. In addition, the highest hydrogen efficiency of the HT-PEMFCs with biomass gasification and the SE-WGS system with anode recirculation (scenario 2) is observed due to the enhancement the hydrogen content from the sorption enhanced water gas shift reaction and the recirculation stream while the hydrogen concentration of this system slightly decreases because of the nitrogen dilution effect. The calculated CO_2 emission in Table 6 is the emission during the process. Therefore, the CO_2 emission of life cycle of the electricity generation is also investigated in the term of the global warming impact. Considering the global warming impact of the decentralized power generation from rice husk in this work, it is found from the examination of the simulation results presented in Fig. 10 that the values for the total global warming impact of all studied systems are negative owing to the power generation from HT-PEMFCs and the net-zero CO_2 emissions of biomass utilization. However, the HT-PEMFCs with biomass gasification and SE-WGS system (scenario 1) and the HT-PEMFCs with the SE-GS and water gas shift system (scenario 3) show the highest total global warming effect. The global warming impact originates mainly from the use of the

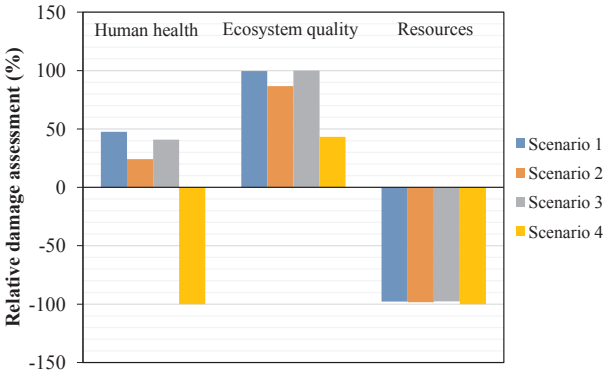

Fig. 11. Relative damage assessment in term of human health, ecosystem quality and resources of the decentralized HT-PEMFC systems.

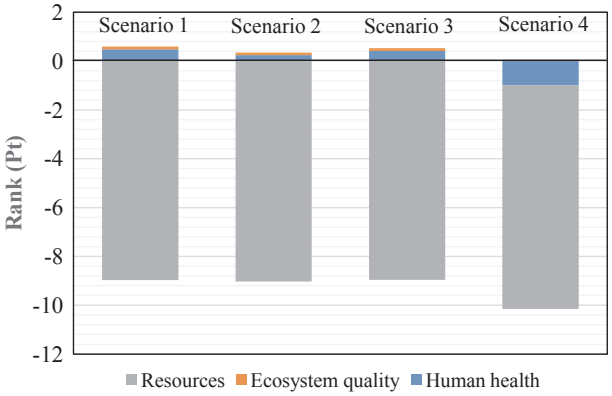

Fig. 12. Overall single score comparison of the decentralized HT-PEMFC systems.

CaO adsorbent in the SE-WGS unit (scenario 1) and in the SE-GS (scenario 3). Although CO_2 capture technology can improve the performance of the system in terms of quality and quantity of hydrogen production [36], the CaO production process is the main cause of greenhouse gas emissions and thus the global warming effect. Since the same CaO/C ratio of unity is applied to the HT-PEMFC systems in scenarios 1, 2 and 3, CaO utilization depends on biomass consumption. Consequently, higher efficiency and lower biomass consumption of the HT-PEMFCs with biomass gasification and the SE-WGS system with anode recirculation (scenario 2) lead to a lower global warming effect compared to the HT-PEMFCs with biomass gasification and the SE-WGS system without the anode recirculation (scenario 1) and the HT-PEMFCs with SE-GS and conventional water gas shift system (scenario 3). In addition, the conventional HT-PEMFC system (scenario 4) shows the lowest global warming impact. Although this system uses the highest amount of rice husk to produce 200 kWh electricity and shows the lowest system efficiency, no CaO is utilized in this system and thus there are no greenhouse gas emissions contributed by CaO production.

Therefore, it can be concluded that the use of CO_2 capture technology can enhance the performance of the decentralized power generation from biomass but this technology leads to an increased global warming impact. However, it should be noted that the biomass is used as the reactant and the heat source in this work. For other fuels such as coal or natural gas, the effect of the greenhouse gas emissions during their production process will be included in the life cycle analysis and the enhancement of the process efficiency by using the CO_2 capture concept may reduce the global warming impact. Furthermore, a comparison of the global warming impact of the HT-PEMFC systems and Thailand's grid electricity generation is performed. It is noted that the inventory data for the electricity used is available from the Thai National Life Cycle Inventory Databases developed by MTEC [38]. It is found that the values of the global warming impact obtained in this study for the electricity produced from all studied HT-PEMFC systems in scenarios 1–4 are lower than the global warming impact of the Thai Mixed Electricity Grid (0.561 kg CO_2 equivalent/kWh electricity) [38]. Owing to the environmental benefit obtained from the electricity production from biomass is used to supplement the Thai Mixed Electricity Grid, the combustion of biomass leads to the avoidance of CO_2 emissions.

In addition, the environmental damage values in three broad categories are calculated and the results of the relative damage assessment based on the highest damage factor among others are shown in Fig. 11. It is found that the conventional HT-PEMFC system without the use of CO_2 capture (scenario 4) has the lowest damage to human health, ecosystem quality and resources. For damage on human health and ecosystem, the systems with the CO_2 capture concept (scenarios 1, 2 and 3) have the relatively high values of these damage category because of the high CO_2 eq emission from the CaO production process whereas the conventional HT-PEMFC system without the CO_2 capture (scenario 4) has the negative value of damage on human health and thus this system has no negative effect on this damage category. In addition, the use of renewable resources as a reactant and energy source for power generation is an advantage of the system studied in this work, and thus the negative value of the relative damage assessment for the damage to resources is observed for all studied systems as shown in Fig. 11.

In addition, the single score comparison of the decentralized rice husk fuelled HT-PEMFC systems is presented in Fig. 12. It is found that there is no negative effect on resource depletion for power generation from all studied scenarios. The relatively small damage to human health and ecosystem is observed when the CO_2 capture technology is applied in scenarios 1, 2 and 3. Furthermore, it is noted that the conventional HT-PEMFC system (scenario 4) is the most attractive process for decentralized power generation from biomass in terms of environmental impact assessment.

6. Conclusions

Biomass gasification systems integrated with the SE-WGS and HT-PEMFCs based anode recirculation are studied in this work for decentralized power generation. The CO_2 capture technology is advantageous for the improvement of hydrogen purity and yield. Therefore, it is possible to recycle the anode off-gas from HT-PEMFCs to SE-WGS with the acceptable dilution and CO poisoning effects. The results show that the HT-PEMFC system with the anode recirculation should be operated at the CaO/C ratio of unity, high fuel utilization and high anode split ratio to achieve maximum efficiency. In addition, the HT-PEMFC system integrated with the SE-WGS can be operated at high anode split ratio and fuel utilization without a significant CO poisoning caused loss. It is concluded that the system performance in terms of the amount of hydrogen produced and the overall system efficiency is enhanced by the anode recirculation. For environmental analysis, it is found that the biomass gasification integrated with the SE-WGS and HT-PEMFCs based anode recirculation (scenario 2) shows the lowest environmental impact compared to the other HT-PEMFC systems with the CO_2 capture (scenarios 1 and 3). However, the use of CaO adsorbent is the main cause of the environmental problem of the decentralized HT-PEMFCs system fuelled by renewable resources.

Acknowledgements

Support from the Srinakharinwirot University (91/2559), the Thailand Research Fund (DPG5880003) and the ASEAN-European Academic University Network (ASEA-UNINET) is gratefully acknowledged.

References

[1] Yang F, Pitchumani R. Fuel and fuel processing. Fuel cell technology. London: Springer; 2006.
[2] DEDE. The Renewable and Alternative Energy Development Plan. Department of Alternative Energy Development and Efficiency - Ministry of Energy, Bangkok, Thailand; 2012.
[3] Lopes DG, da Silva EP, Pinto CS, Neves NP, Camargo JC, Ferreira PFP, et al. Technical and economic analysis of a power supply system based on ethanol reforming and PEMFC. Renew Energy 2012;45:205–12.
[4] Hajjaji N, Houas A, Pons M. Thermodynamic feasibility and life cycle assessment of hydrogen production via reforming of poultry fat. J Clean Prod 2016;134:600–12.
[5] Lv P, Yuan Z, Ma L, Wu C, Chen Y, Zhu J. Hydrogen-rich gas production from biomass air and oxygen/steam gasification in a downdraft gasifier. Renew Energy 2007;32:2173–85.
[6] Srirangan K, Akawi L, Moo-Young M, Chou CP. Towards sustainable production of clean energy carriers from biomass resources. Appl Energy 2012;100:172–86.
[7] Damen K, Troost MV, Faaij A, Turkenburg W. A comparison of electricity and hydrogen production systems with CO_2 capture and storage-Part B: chain analysis of promising CCS options. Prog Energy Combust Sci 2007;33:576–605.
[8] Doranehgard MH, Samadyar H, Mesbah M, Haratipour P, Samiezade S. High-purity hydrogen production with in situ CO_2 capture based on biomass gasification. Fuel 2017;202:29–35.
[9] García-Díez E, García-Labiano F, de Diego LF, Abad A, Gayán P, Adánez J, et al. Optimization of hydrogen production with CO_2 capture by autothermal chemical-looping reforming using different bioethanol purities. Appl Energy 2016;169:491–8.
[10] Wiranarongkorn K, Authayanun S, Assabumrungrat S, Arpornwichanop A. Analysis of thermally coupling steam and tri-reforming processes for the production of hydrogen from bio-oil. Int J Hydrogen Energy 2016;41:18370–9.
[11] Alam S, Kumar JP, Rani YK, Sumana C. Self-sustained process scheme for high purity hydrogen productionusing sorption enhanced steam methane reforming coupled with chemical looping combustion. J Clean Prod 2017;162:687–701.
[12] Han SJ, Song JH, Yoo J, Park S, Kang KH, Song IK. Sorption-enhanced hydrogen production by steamreforming of ethanol over mesoporous Co/CaO-Al_2O_3 xerogel catalysts: effect of Ca/Al molar ratio. Int J Hydrogen Energy 2017;42:5886–98.
[13] Chen S, Xiang W, Wang D, Xue Z. Incorporating IGCC and CaO sorption-enhanced process for power generation with CO_2 capture. Appl Energy 2012;95:285–94.
[14] Din ZU, Zainal ZA. Biomass integrated gasification–SOFC systems: technology and review. Renew Sust Energ Rev 2016;53:1356–76.
[15] Tamalouzt S, Benyahia N, Rekioua T, Rekioua D, Abdessemed R. Performances analysis of WT-DFIG with PV and fuel cell hybrid power sources system associated with hydrogen storage hybrid energy system. Int J Hydrogen Energy 2016;41:21006–21.
[16] Voitic G, Nestl S, Lammer M, Wagner J, Hacker V. Pressurized hydrogen production by fixed-bed chemical looping. Appl Energy 2015;157:399–407.
[17] Bouffard F, Kirschen DS. Centralised and distributed electricity systems. Energy Policy 2008;36:4504–8.
[18] Toonssen R, Woudstra N, Verkooijen AHM. Decentralized generation of electricity from biomass with proton exchange membrane fuel cell. J Power Sources 2009;194:456–66.
[19] Guan T, Chutichai B, Alvfors P, Arpornwichanop A. Biomass-fuelled PEMFC systems: evaluation of two conversion paths relevant for different raw materials. Energy Convers Manage 2015;106:1183–91.
[20] Schuller G, Vazquez FV, Waiblinger W, Auvinen S, Ribeirinha P. Heat and fuel coupled operation of a high temperature polymer electrolyte fuel cell with a heat exchanger methanol steam reformer. J Power Sources 2017;347:47–56.
[21] Matzen M, Demirel Y. Methanol and dimethyl ether from renewable hydrogen and carbon dioxide: alternative fuels production and life-cycle assessment. J Clean Prod 2016;139:1068–77.
[22] Rillo E, Gandiglio M, Lanzini A, Bobba S, Santarelli M, Blengini G. Life Cycle Assessment (LCA) of biogas-fed Solid Oxide Fuel Cell (SOFC) Plant. Energy 2017;126:585–602.
[23] Duclos L, Lupsea M, Mandil G, Svecova L, Thivel PX, Laforest V. Environmental assessment of proton exchange membrane fuel cell platinum catalyst recycling. J Clean Prod 2017;142:2618–28.
[24] Karmakar MK, Mandal J, Haldar S, Chatterjee PK. Investigation of fuel gas generation in a pilot scale fluidized bed autothermal gasifier using rice husk. Fuel 2013;111:584–91.
[25] Nakyai T, Authayanun S, Patcharavorachot Y, Arpornwichanop A, Assabumrungrat S, Saebea D. Exergoeconomics of hydrogen production from biomass air-steam gasification with methane co-feeding. Energy Convers Manage 2017;140:228–39.
[26] Esmaili E, Mostafavi E, Mahinpey E. Economic assessment of integrated coal gasification combined cycle with sorbent CO_2 capture. Appl Energy 2016;169:341–52.
[27] Authayanun S, Mamlouk M, Arpornwichanop A. Maximizing the efficiency of a HT-PEMFC system integrated with glycerol reformer. Int J Hydrogen Energy 2012;37:6808–17.
[28] Mamlouk M, Sousa T, Scott K. A high temperature polymer electrolyte membrane fuel cell model for reformate gas. Int J Electrochemistry 2011;2011:1–18.
[29] Authayanun S, Mamlouk M, Scott K, Arpornwichanop A. Comparison of high-temperature and low-temperature polymer electrolyte membrane fuel cell systems with glycerol reforming process for stationary applications. Appl Energy 2013;109:192–201.
[30] Hosokai S, Matsuoka K, Kuramoto K, Suzuki Y. Modification of Dulong's formula to estimate heating value of gas, liquid and solid fuels. Fuel Process Techno 2016;152:399–405.
[31] Saebea D, Authayanun S, Patcharavorachot Y, Arpornwichanop A. Effect of anode-cathode gas recirculation on the energy recuperation in a solid oxide fuel cell-gas turbine hybrid power system. Energy 2016;94:218–32.
[32] Saebea D, Magistri L, Massardo A, Arpornwichanop A. Cycle analysis of solid oxide fuel cell-gas turbine hybrid systems integrated ethanol steam reformer: energy management. Energy 2017;127:743–55.
[33] Silalertruksa T, Gheewala SH. A comparative LCA of rice straw utilization for fuels and fertilizer in Thailand. Bioresour Techno 2013;150:412–9.
[34] Department of Highway. Distance between provinces in Thailand; 2016. Available at: < http://map-server.doh.go.th > .
[35] IPCC (Intergovernmental Panel on Climate Change). IPCC guidelines for national greenhouse gas inventories. In: Eggleston S, Buendia L, Miwa K, Ngara T, Tanabe K (editors). Agriculture, forestry and other land use, prepared by the national greenhouse gas inventories programme, 4. Institute for Global Environmental Strategies (IGES), Japan; 2006.
[36] Adams PWR, McManus MC. Small-scale biomass gasification CHP utilisation in industry: energy and environmental evaluation. Sustainable Energy Technol Assess 2014;6:129–40.
[37] Li Q, He R, Gao JA, Jensen JO, Bjerrum NJ. The CO poisoning effect in PEMFCs operational at temperatures up to 200°C. J Electrochem Soc 2003;150:A1599–605.
[38] MTEC. Thai National Life Cycle Inventory Database. National Metal and Materials Technology Center, National Science and Technology Development Agency, Pathumthani, Thailand; 2009.

Computers and Chemical Engineering 117 (2018) 159–170

Contents lists available at ScienceDirect

Computers and Chemical Engineering

journal homepage: www.elsevier.com/locate/compchemeng

Comparison of different kraft lignin-based vanillin production processes

Nattanan Wongtanyawat[a], Possawat Lusanandana[a], Nawaporn Khwanjaisakun[a], Pichayapan Kongpanna[a], Janewit Phromprasit[a], Lida Simasatitkul[b], Suksun Amornraksa[c], Suttichai Assabumrungrat[a,*]

[a] Center of Excellence in Catalysis and Catalytic Reaction Engineering, Department of Chemical Engineering, Faculty of Engineering, Chulalongkorn University, Bangkok 10330, Thailand
[b] Department of Industrial Chemistry, King Mongkut's University of Technology North Bangkok, Bangkok 10800, Thailand
[c] The Sirindhorn International Thai-German Graduate School of Engineering (TGGS), King Mongkut's University of Technology North Bangkok, Bangkok 10800, Thailand

ARTICLE INFO

Article history:
Received 12 June 2017
Revised 3 March 2018
Accepted 21 May 2018
Available online 23 May 2018

Keywords:
Vanillin production
Kraft lignin
Process intensification
Process design
Biorefinery

ABSTRACT

This work employed a systematic methodology and process intensification concepts to improve the state-of-the-art vanillin production process from kraft lignin. Particular focus was put on the use of different product separation techniques, including solvent extraction using ethyl acetate, benzene, organic nanofiltration, and adsorption by zeolite. The performance of each proposed process was evaluated in terms of energy consumption, process economics, and environmental impacts. Simulation of the vanillin production processes was performed using the Aspen Plus program while the economic and environmental analyses were conducted using economic analysis tools and LCSoft, respectively. The results revealed that the process using adsorption by zeolite is the best alternative. It offered a slight improvement in energy consumption while its economic result showed 7.37% improvement. It also caused the least environmental impact in all categories.

© 2018 Elsevier Ltd. All rights reserved.

1. Introduction

Vanillin ($C_8H_8O_3$) is a major flavor constituent of vanilla, which is widely used in various industries, such as in the food industry as a flavoring agent, in the cosmetic industry as a fragrance ingredient in perfumes, and in the pharmaceutical industry as a chemical precursor. The current global demand for vanillin is estimated to be around 20,000 tons per year. Natural vanillin can only contribute a very small portion of the market demand, less than 1% of the total vanillin production (Bomgardner, 2014). Consequently, alternative sources and processes for producing vanillin are necessary. At present, vanillin in the world supply is mainly produced from petroleum-based intermediates, especially guaiacol (which is derived from phenol) (Fache et al., 2016). However, vanillin can also be produced from other sources, such as lignin from biomass. Lignocellulosic biomass is a renewable source that can be used as a raw material to produce fuels and value-added chemicals in place of fossil-based carbon sources. It is considered as one of the most prospective raw materials for the future as it is greener and more sustainable (Schorr et al., 2014). Producing vanillin from lignin is thus a sustainable and environmentally friendly choice (Doherty et al., 2011; Peterson et al., 2013).

Lignin is the main constituent present in biomass and is composed of natural aromatic polymers. Around five million metric tons every year are produced as a byproduct and waste (Vishtal and Kraslawski, 2011). In the pulp and paper industry, lignin is produced as black liquor waste from the kraft process, which accounts for over 80 percent of the world chemical pulp production. The lignin from black liquor, also known as kraft lignin, is typically utilized as a low-quality fuel in waste heat boilers for heat and power generation purposes, as well as being used to facilitate the recovery of cooking chemicals (Mikkola et al., 2015). Less than 2% of the kraft lignin is separated from the process as a readily available raw material (Gosselink et al., 2004). Pretreatment of the kraft lignin can be done using various technologies, such as enzymatic processes (Gouveia et al., 2013). Traditionally, lignin is used for the pulp mill, bio-oil (Nguyen et al., 2014), and phenolic compounds (Wahyudiono et al., 2008; Gosselink et al., 2012). Hence, converting lignin into a more valuable product such as furfural (Lamminpää et al., 2015) and vanillin is an attractive option as it can help improve the economic viability of the pulp and pa-

* Corresponding author.
E-mail address: Suttichai.A@chula.ac.th (S. Assabumrungrat).

https://doi.org/10.1016/j.compchemeng.2018.05.020
0098-1354/© 2018 Elsevier Ltd. All rights reserved.

per industry. It would also bring new knowledge in the ecomaterials field, by contributing to decreased greenhouse gas emissions (Wang et al., 2009; Schorr et al., 2014).

The production of vanillin from lignin has been known for more than 50 years. Today, around 15% of the total supply of vanillin comes from lignin, specifically lignosulfonates. A Norwegian company "Borregaard" is the only producer of vanillin from lignin (Borges da Silva et al., 2009). The commercial lignin-to-vanillin production process uses lignin from the sulfite pulping process as the feedstock to produce vanillin through a lignin oxidation reaction. However, the reaction mechanism of the process is complex and not fully understood yet. Recently, alternative lignin-to-vanillin conversion that requires no oxygen has been proposed by Pacek et al. (2013). The new conversion is carried out by means of lignin alkaline hydrolysis. Nevertheless, there are still several limitations for vanillin production from lignin. The first limitation is a low yield of vanillin product due to the difficulty in purification of the vanillin products. Second, lignin depolymerization requires a large amount of energy, acids, and organic solvents in the extraction process. Moreover, the maximum yield of vanillin product can only be attained from softwoods that contain plenty of guaiacyl (G) lignin (Fache et al., 2016).

From an industrial point of view, producing vanillin from kraft lignin is more attractive because more than 90% of the total lignins supplied come from kraft lignin (Pinto et al., 2012). A conventional vanillin production process from kraft lignin is based on acidic oxidation. The downstream separation in such a process typically uses ethyl acetate as a solvent as it shows a high percent recovery of vanillin product from the product stream (Werhan, 2013). However, a large amount of water is required to remove methanol completely from the products prior to the extraction step. To enhance the process viability of the vanillin production from kraft lignin, several process improvement techniques have been studied and proposed (Borges da Silva et al., 2009), including process intensification.

Process intensification is an approach that focuses on development and redesign of an existing process to allow for better exploitation of raw materials, lower energy consumption, and reduced plant size. So, a new process is supposed to be more compact, more energy efficient, and cleaner than its traditional counterpart. For evaluation, sustainability metrics such as energy consumption, materials usage per kilogram of product, and potential environmental impacts are often used as decision-making indicators (Lutze et al., 2012; Babi et al., 2014). An integration of process intensification concepts to achieve sustainable process design was demonstrated by Lutze et al. (2013). There are also several process design examples that use the process intensification concept to improve the performance of processes. For example, Babi et al. (2014) and Mansouri et al. (2013) proposed the superstructure and process intensification for biodiesel production from crude palm oil. Kongpanna et al. (2016) proposed a systematic methodology for the design of optimal superstructure and generation of process alternatives by phenomena-based synthesis using process intensification, with the help of rigorous process simulation and analysis in terms of sustainability, including economics and life cycle assessment (LCA) factors. Process intensification has also been demonstrated with biorefinery involving lignin, such as lignin oxidation in a microreactor (Werhan et al., 2013).

In this work, the process intensification concept was applied to a conventional vanillin production process. Three alternative processes were developed and compared with the original process, to determine the most sustainable process for vanillin production from kraft lignin. To begin with, a base case design was developed and analyzed. Then, areas for plausible process improvements were identified and new improved processes were proposed. To assess and identify a more sustainable production process for vanillin from kraft lignin, several performance indicators of the new processes were evaluated and compared with those of the base case design. These include energy consumption, process economics, and several environmental impact indicators such as global warming potential (GWP), acidification potential (AP), and human toxicity carcinogens (HTC).

2. Systematic methodology

The systematic methodology used in this work is as follows (Kongpanna et al., 2016). First of all, problem definition is defined and necessary process data are gathered. Then, several process technologies are considered and the state-of-the-art technology is identified. In the next step, a base case design is developed and rigorous process simulation is performed. The result obtained from the simulation is then analyzed and the area for process improvement is identified. After that, alternative designs that could improve the process are proposed and assessed. Finally, process performance of the new process is evaluated and compared with those of the base case design, to determine the best vanillin production process. The comparison is done in terms of energy consumptions, economic analysis, and environmental impacts.

2.1. Problem definition

This step is to define the scope of the problem considering from feedstock to end products. It also includes thermodynamic data estimation, process conditions and constraints, target yield, and product specifications. Two main tasks are carried out in this step including data collection and defining of product and process requirements.

In the data collection, essential data such as a list of raw materials, products, and byproducts to be used/produced in the design are gathered. In addition, data on possible production technologies or separation techniques that can be used in the process are also identified and obtained. In the second task, the specifications of products such as production capacity, purity, form, and some specific physical properties are specified. In addition, process constraints as well as process performance requirements in term of economics, environment, and sustainability are specified.

2.2. Assessment of the feasibility of design

After the product and process requirements have been defined and all the necessary data have been gathered, the next step is to look for appropriate process technology for the production of vanillin. Many options for processing operations including feedstock pretreatment, chemical reactions, and separation methods are carefully considered. Understanding of conventional process technologies is also realized in this step. Preliminary synthesis of conceptual processes based on the product and process requirements is then developed by using the following assumptions:

- Our designed capacity of vanillin production is set to 10 kg/h which contributes approximately 0.5% of global vanillin production from the petrochemical route.
- Kraft lignin feed is specified as a pure component.
- The production of nanofiltration, zeolite, and other catalysts are excluded from LCA.
- The catalyst cost is not included in the economic analysis.
- Gate-to-gate boundary is used for LCA analysis.

2.3. Base case design

In general, a conventional or the most reliable process for the production of vanillin obtained from the results of the previous

step is used to create a process flowsheet. This process flowsheet is regarded as a base case design. In practice, the base case design is usually developed based on the most complete and available process data and this is the case for our design. The basic equipment design is also implemented in this step. For instance, specifications of distillation columns including the number of stages, feed location, reflux ratio are considered and defined so that the rigorous simulation of the base case design can be performed accordingly.

2.4. Rigorous process simulation

In this step, a process simulation of the base case design is performed using the Aspen Plus program. The mass and energy balances are also computed for each unit operation. Appropriate unit operation models together with consistent thermodynamic models are selected and employed from the selected simulator. The results obtained from this step are further analyzed in the subsequent steps.

2.5. Process analysis and target setting

The simulation results of the base case design obtained from the previous step are analyzed here. Energy consumption of individual units inside the process is summarized and compared. These data are typically used as an indicator to identify the process deficiencies (regarded as "hot spots" which are considered from high energy consumption in that unit), which will be a target for process improvement. In addition, before proceeding to the next steps, design targets in many aspects such as the purity of the vanillin product are considered and specified.

2.6. Alternative generation

Once the process deficiencies have been identified, the next step is to study and determine alternative processes that can achieve the design targets. There are many possible design targets, e.g., product quality and process efficiency. Sustainability targets such as decrease of energy consumption, waste generation, and environmental impact are also common in many design practices. For simplicity, it is suggested that the alternative processes should be developed only around the section that contains hot spots while the other sections are intact.

2.7. Process evaluation

Several alternative processes are usually created during the alternative generation step. So, we need to identify the best alternative for the vanillin production and this is the main task of this step. Energy consumption and economics of the process are used as common indicators to select the best alternative. In this work, the economic analysis is conducted by using the ECON program (Saengwirun, 2011), which has imported database from plant design and economics for chemical engineers book (Peters, 1991) and expressed by three indicators including capital expenditure (CAPEX) such as Manufacturing Fixed-capital Investment (Direct Cost), Non-manufacturing Fixed-capital Investment (Indirect Cost), and operational expenditure (OPEX) such as raw materials, chemicals and utilities cost, heating, cooling, and electricity. Environmental constraints are also assessed in a comprehensive way, together with technical and economic criteria, using LCA tools. The environmental impacts of a process are commonly represented in terms of carbon footprint (CF), which is the total amount of greenhouse gases produced directly and indirectly by the process from raw materials to products, expressed in equivalent kilograms of carbon dioxide (CO_2). For concerning health issue, LCSoft software is used to calculate important LCA factors (Kalakul et al., 2014).

Table 1
Mass balance for the vanillin production process (outlet from reactor).

Composition	Inlet (kg/hr)	Outlet (kg/hr)
Kraft lignin	122.02	61.01
Sulfuric acid	61.01	35.39
Air	23,864.35	23,608.74
Methanol	6,053.07	5,750.42
Water	1,513.27	1,721.43
Vanillin	–	10.00
Methyl vanillate	–	2.03
Dimethyl Ether	–	139.11
Carbon Dioxide	–	266.24
NO	–	0.85
SO_2	–	18.52

It should be noted that the data used in the assessment include overall mass balance (inlet and outlet of the process) and energy consumption of each unit operation in the process. The result is expressed in terms of CF, which depends on the type of energy sources in each unit operation and also the amount of energy consumed. In addition to the CF, several potential environmental impacts were taken into account, including GWP, AP, ecotoxicological potential (ET), aquatic toxic potential (ATP), HTC, human toxicity noncarcinogenic impact (HTNC), ozone depletion potential (ODP), photochemical oxidation potential (PCOP), human toxicity potential from dermal exposure (HTPE), and human toxicity potential from ingestion and inhalation (HTPI).

3. Results and discussion

3.1. Problem definition

The raw materials used for producing vanillin (kraft lignin, methanol, water, sulfuric acid, and air) are the same for all proposed processes. The main product obtained from every process is vanillin while the byproduct is methyl vanillate. Methanol and water are necessary as they are used to make the acidic feed mixture. Sulfuric acid is used to break down the lignocellulosic structure of kraft lignin. Oxygen used for the oxidation reaction is supplied from the air. Ethyl acetate is used as a solvent for liquid–liquid extraction in the conventional vanillin production process from kraft lignin. Benzene is selected as an alternative solvent for the liquid–liquid extraction. The reaction temperature and pressure of 210 °C and 48 bar are selected, respectively. The purity of the vanillin product was set at 99.5% as a commercial grade. The mass balance for the vanillin production based on 122.02 kg/h of kraft lignin feed to the reactor is shown in Table 1. A block flow diagram of the base case design is represented in Fig. 1.

3.2. Assessment of the feasibility of designs

To assess the feasibility of designs, first of all, reaction kinetics and physical property data of the conventional process from various sources were collected and checked for validity and correctness. Then, essential information needed for planning the process outline was selected. Some physical property data of the main components such as lignin and other chemicals can be found in the Aspen Plus simulation program. Chemical and physical properties data of other components that are not available in the built-in Aspen Plus property database were generated and calculated using the pseudo-component definition in the Aspen Plus program. The lignin, a polymer of aromatic compounds, was reduced into some specific derivatives of lignin after the hydrolysis process. The equilibrium model was selected in this study. From the gathered data, we have considered and chosen a conventional vanillin pro-

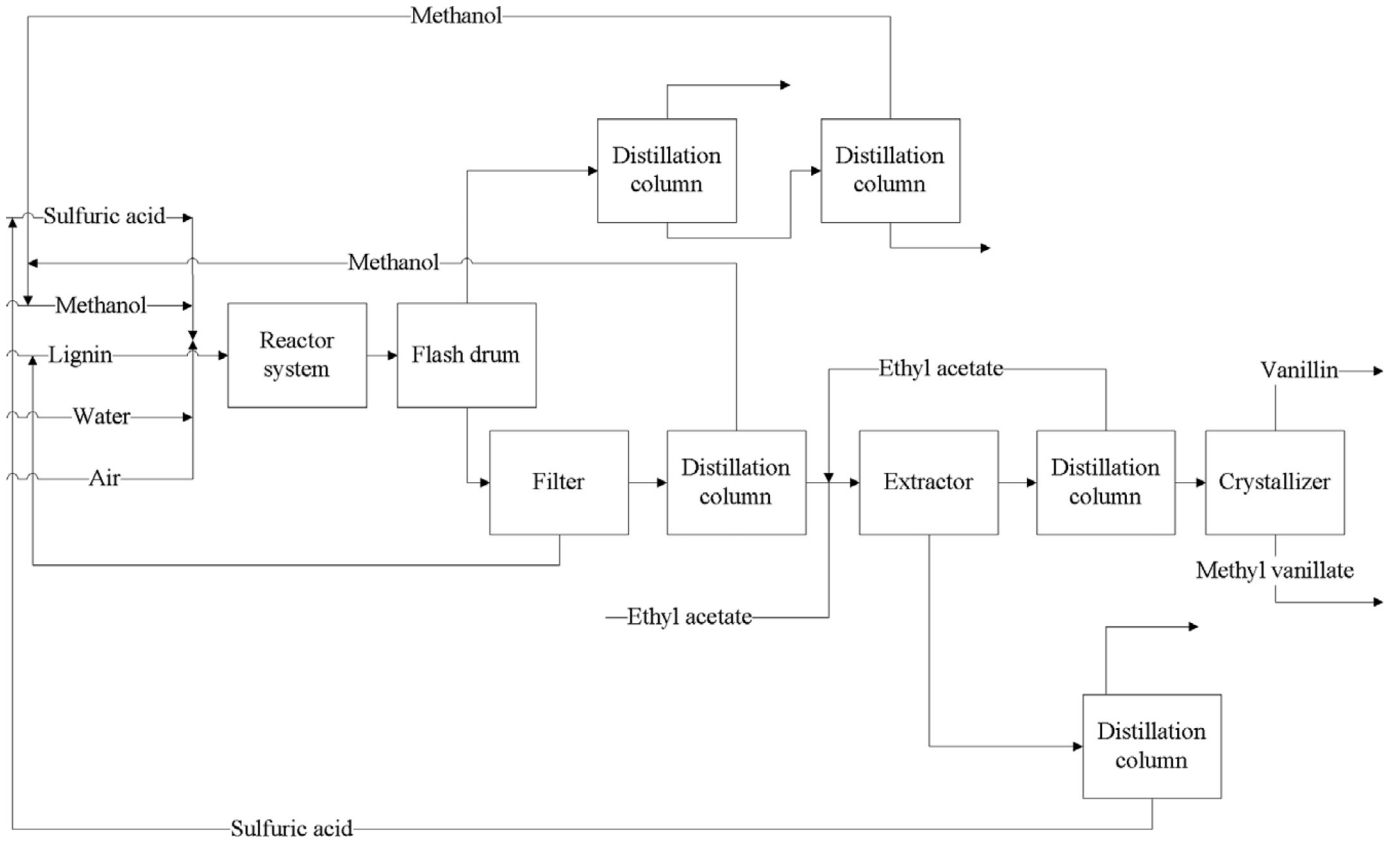

Fig. 1. Block flow diagram of vanillin production process from kraft lignin - Base case (ethyl acetate as solvent).

duction process proposed by Schorr et al. (2014) for use as a base case model in our design.

3.3. Base case design

As seen from Fig. 1, there are four sections involved in the vanillin production process, namely (1) feed preparation, (2) oxidation reaction, (3) phase separation, and (4) product separation. In the feed preparation section, the feed conditions of raw materials consisting of kraft lignin, sulfuric acid, air, water, and methanol are adjusted to appropriate values suitable for the reaction. These conditions are pressure, temperature, and phase of the feeds. Then, the prepared feed is sent to the reaction section where the oxidation reaction between kraft lignin and oxygen takes place. After that, the product output from the reactor comprising mixed products and residual raw materials is passed to the phase-separation section. The phase-separation section consists of a flash drum and two distillation columns. The main task of this section is to separate the gaseous components, which are air, water, and methanol from liquid mixed products. In the last section, product separation, the mixed products are separated from the unconverted lignin by a solid filter. Then, sulfuric acid was removed from the mixed products in an extraction unit, which uses ethyl acetate as a solvent. The vanillin product is finally separated from byproducts using a distillation column and crystallizer.

3.3.1. Conceptual base case

To begin with, kraft lignin together with methanol, water, air, and sulfuric acid are fed into the pretreatment to adjust their pressure and temperature, and to make the kraft lignin suitable to be converted to vanillin in the following reactor. Once the reactions are complete, the mixed products and residual raw materials are sent to a flash drum to separate gaseous components, which are air, methanol, and water from the others. All the liquid substances from the flash drum are then sent to another distillation column to remove the leftover gaseous components. After that, the remaining mixture is sent to an extractor to recover sulfuric acid by using ethyl acetate as a solvent (Werhan, 2013). However, the mixed products obtained from the extractor contain some amount of ethyl acetate. Consequently, another distillation column is required to remove the ethyl acetate completely from the mixed products. Afterward, the mixed products are fed to a crystallizer to separate vanillin from methyl vanillate.

3.4. Rigorous simulations

As presented in Fig. 2, kraft lignin is mixed with sulfuric acid, methanol, and water. Then, the mixed stream passes through a pump (P-101) and a fired heater (E-101) to adjust its pressure and temperature to 210°C and 48 bar, suitable operating conditions for the reaction. At the same time, air is also fed through a compressor (C-101) and a cooler (E-102) to adjust its pressure and temperature. Then, the air is mixed with the pretreated mixed stream and enters the reactor (R-101). An R-Yield reactor is used to perform the oxidation reaction. The product output from the reactor comprising vanillin, methyl vanillate, diethyl ether, and residual raw materials is sent to a flash drum (V-101) for initial product separation. The overhead stream from the flash drum, which contains air, methanol, diethyl ether, and water is passed to a series of distillation columns (V-103, V-104) for methanol recycle. The bottom stream from the flash drum (V-101), which contains unconverted kraft lignin, vanillin, methyl vanillate, sulfuric acid, and other components is passed to a solid filter (F-101) to separate and recycle the unconverted kraft lignin. Afterward, the liquid mixed products are passed to a distillation column (V-102) to separate and recycle the leftover methanol. The bottom product of the column is sent

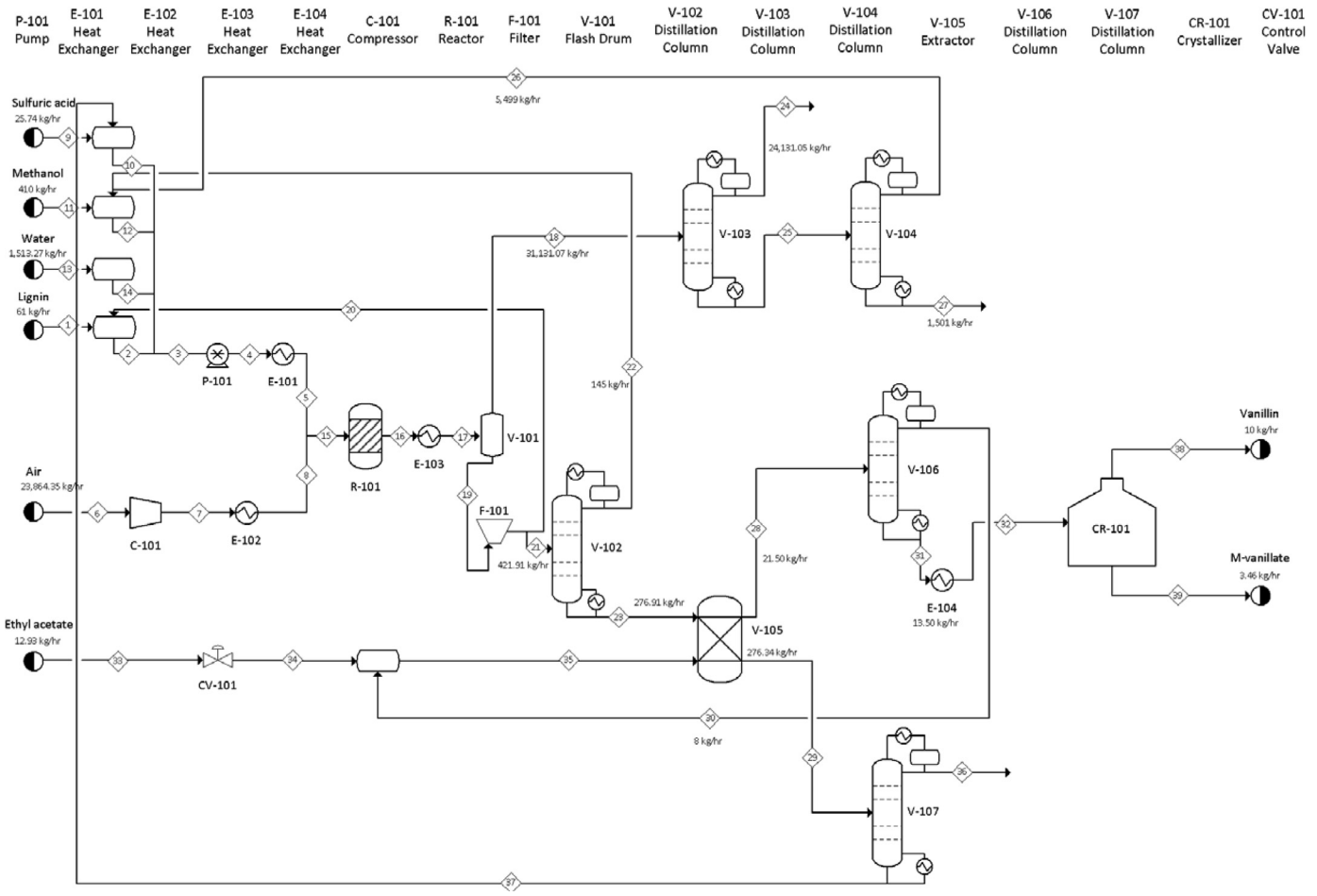

Fig. 2. The production of vanillin from kraft lignin - Base case (ethyl acetate as solvent).

to an extractor (V-105) to recover the sulfuric acid. In the extractor, ethyl acetate is used as a solvent to extract the mixed products from the sulfuric acid and remaining water (Werhan, 2013). The extract stream containing mixed products is fed to a distillation column (V-106) to recover the ethyl acetate solvent, whereas the raffinate stream containing sulfuric acid, some ethyl acetate, and the remaining water is sent to another distillation column (V-107) to separate sulfuric acid and send it back for recycling. The bottom stream of the V-106 column, which consists of vanillin and methyl vanillate is subsequently sent to a crystallizer (CR-101) for final product separation. The crystallizer is operated at 5°C and 1 bar to separate vanillin from methyl vanillate. The purity of vanillin obtained is 99.5%. Using this information, the developed base case design was modeled and simulated by Aspen Plus. The results obtained from the simulation were validated with the results from the conventional process (Schorr et al., 2014) to confirm the validity of the developed model.

3.5. Process analysis and target setting

Energy consumption was selected as a key indicator for identifying process areas for improvement because it has a large impact on both economics and sustainability of the process. Based on the process intensification approach, there are two main sections in a process that are typically focused, namely, the reaction section and downstream separation section. Considering the vanillin synthesis section, it was not suitable to apply the process intensification to this section due to the limitation of available data on vanillin synthesis technology. The downstream separation section, however, had more flexibility to apply the process intensification because information on alternative separation methods were available. Therefore, it is our main target for the process improvement.

From Table 2, it can be seen that the distillation columns (V-103 and V-104) are the units that consume the highest energy in the downstream separation section. However, it is difficult to find a suitable replacement for them because they serve as primary separators in the process and so the reliability issue is very crucial. In this particular case, the other separator unit that is more practical to focus for process improvement would be the extraction column because it can have a direct impact on the subsequent separation train in terms of both energy consumption and environmental impacts. Thus, we have selected the extraction column as the hotspot for process improvement.

3.6. Alternative generation

Three alternative separation processes were proposed and evaluated in this work. The alteration in the alternative processes was emphasized around the extractor (V-105). Hence, the configurations as well as the mass flow rates and energy consumptions in prior sections of the process remained the same in each of the proposed alternative process. In summary, the first alternative process, case 2, was the same process as the base case design, except that the ethyl acetate solvent is replaced by benzene. In case 3, an organic nanofilter was used to remove sulfuric acid and remaining water instead of the solvent extraction technique. In case 4, similar to case 3, zeolite was used as an adsorbent to separate the mixed products from the sulfuric acid and remaining water.

Table 2
Process description of vanillin production process from kraft lignin base case (ethyl acetate as solvent).

Unit	Type of unit	Duty/Work (MJ/hr)	Activity	Energy source	Carbon footprint (kg CO_2 eq.)
C-101	Compressor	19913.77	Electricity usage	Electricity, natural gas, at power plant	51.3809
E-101	Heater	5750.52	Heating	Natural gas, combusted in industrial boiler	1.0230
E-102	Cooler	−15403.27	Cooling	Chilled water, absorption chiller using natural gas	0.7075
E-103	Cooler	−16732.19	Cooling	Chilled water, absorption chiller using natural gas	0.7685
E-104	Cooler	−1.25	Cooling	Chilled water, absorption chiller using natural gas	0.0001
CR-101	Crystallizer	28.41	Heating	Natural gas, combusted in industrial boiler	0.0051
P-101	Pump	109.24	Electricity usage	Electricity, natural gas, at power plant	0.2819
V-101	Flash	9850.11	Heating	Natural gas, combusted in industrial boiler	1.7522
V-102	Condenser	−4274.44	Cooling	Chilled water, absorption chiller using natural gas	0.1963
V-102	Reboiler	4304.44	Heating	Natural gas, combusted in industrial boiler	0.7657
V-103	Condenser	−66645.95	Cooling	Chilled water, absorption chiller using natural gas	3.0610
V-103	Reboiler	55394.92	Heating	Natural gas, combusted in industrial boiler	9.8542
V-104	Condenser	−18160.63	Cooling	Chilled water, absorption chiller using natural gas	0.8341
V-104	Reboiler	18356.38	Heating	Natural gas, combusted in industrial boiler	3.2654
V-106	Condenser	−5.36	Cooling	Chilled water, absorption chiller using natural gas	0.0002
V-106	Reboiler	6.28	Heating	Natural gas, combusted in industrial boiler	0.0011
V-107	Condenser	−1646.95	Cooling	Chilled water, absorption chiller using natural gas	0.0756
V-107	Reboiler	1626.05	Heating	Natural gas, combusted in industrial boiler	4.1955
R-101	Reactor	3104.92	Heating	Residual fuel oil, combusted in industrial boiler	2.0872

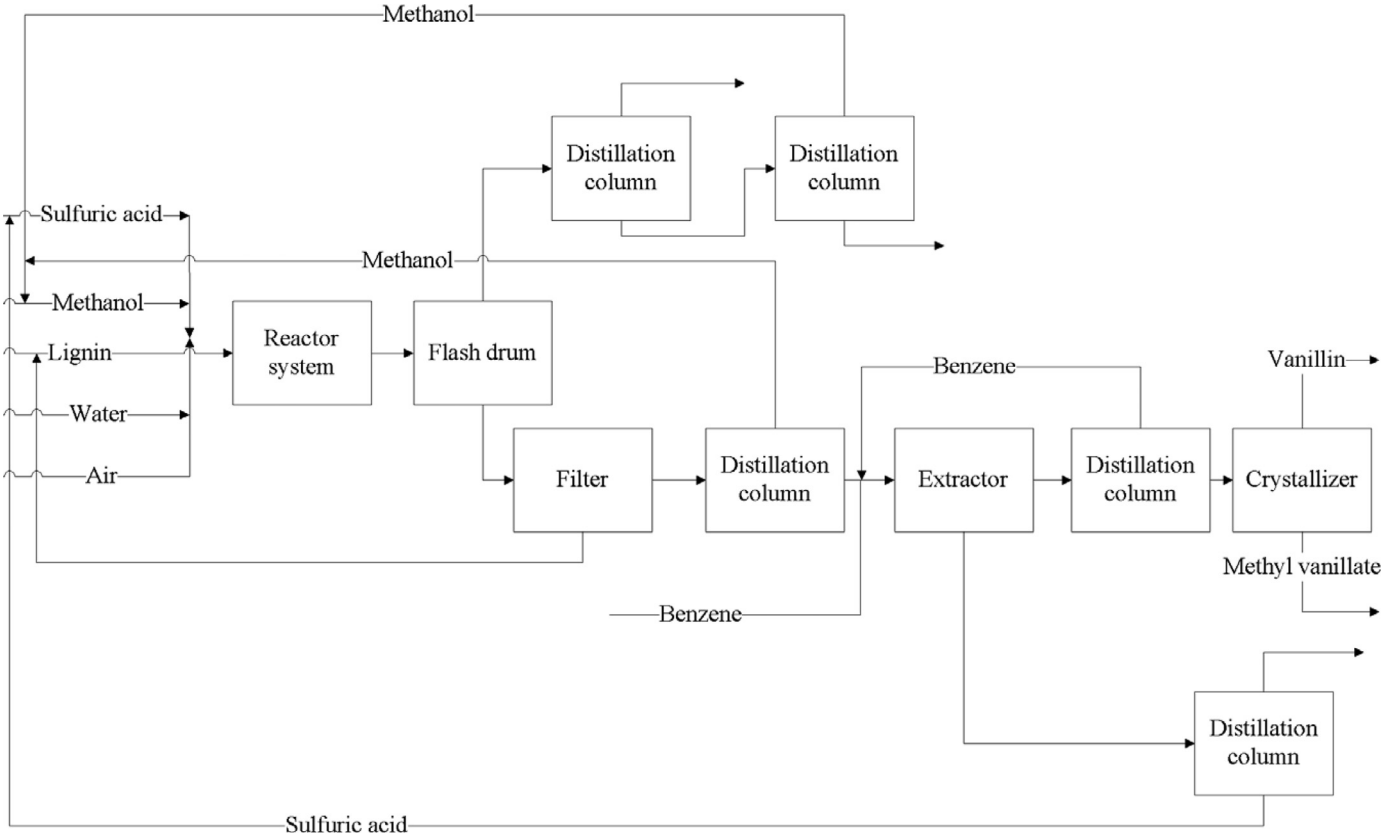

Fig. 3. Block flow diagram of vanillin production process from kraft lignin - Case 2 (benzene as solvent).

3.6.1. Case 2: The production of vanillin from kraft lignin (benzene as solvent)

This alternative process is very similar to the base case design. The block flow diagram is represented in Fig. 3 and the process flowsheet is represented in Fig. 4. The only difference is that benzene is used as a solvent in this case and thus the method for solvent recovery is similar. From Fig. 4, the bottom stream of the distillation column (V-202) is passed through the extractor (V-205) where the mixed products are extracted from the mixture by benzene (Kaygorodov et al., 2010). The extract stream is sent further to a distillation column (V-206) for benzene recovery. The overhead benzene outlet from the distillation column is sent back for recycling whereas the bottom liquid outlet containing mixed products is sent to a cooler (E-204) prior to crystallization.

3.6.2. Case 3: The production of vanillin from kraft lignin (organic nanofilter)

In this case, the mixed products in the bottom stream of the distillation column (V-302) are separated from the sulfuric acid and remaining water by means of filtration using an organic nanofilter (Werhan, 2013) as illustrated by the block flow diagram in Fig. 5 and the process flowsheet in Fig. 6. The bottom stream of the distillation column (V-302) containing vanillin, methyl vanillate, sulfuric acid, and some water is mixed with ethyl acetate to

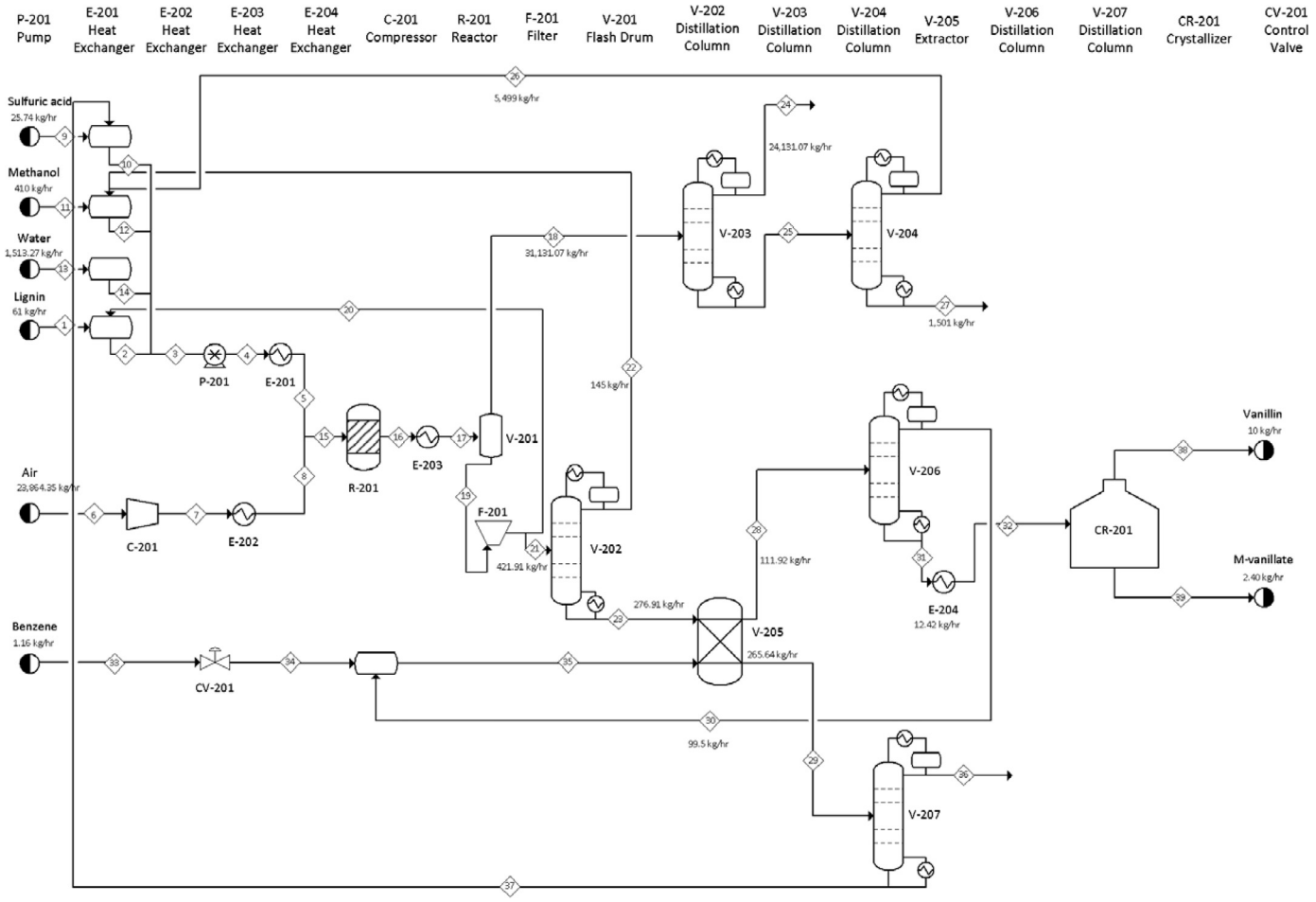

Fig. 4. The production of vanillin from kraft lignin - Case 2 (benzene as solvent).

prepare for filtration. Next, the sulfuric acid, ethyl acetate, and water are split from the mixed products by an organic nanofilter (M-301) and subsequently sent to two distillation columns (V-305 and V-306) for recycle. The bottom stream obtained from the organic nanofilter containing mixed products is sent to a distillation column (V-307) to remove remaining ethyl acetate, before being sent to a crystallizer (CR-301) for final vanillin separation.

3.6.3. Case 4: The production of vanillin from kraft lignin (adsorption by zeolite)

In the last alternative process, the block flow diagram is represented in Fig. 7 and the process flowsheet design is represented in Fig. 8. The mixed products are separated from the sulfuric acid and remaining water by means of adsorption. Zeolite is selected as an adsorbent in this process. In principle, the bottom product of the distillation column (V-402) is passed through a heat exchanger (E-404) to decrease its temperature to 40°C before sending to an adsorber (V-405). In the adsorber, the mixed products are adsorbed by zeolite at 40°C. The sulfuric acid and water that are not adsorbed are separated and recycled. After that, the zeolite is separated from the product solution by centrifugation (F-402) (Ramaswamy et al., 2013). The mixed products then follow the same procedure as the base case design.

3.7. Process evaluation

3.7.1. Energy consumption

The data of energy consumption of each unit in the process can be obtained from Aspen Plus simulations. There are typically three types of energy forms being used in a process, namely hot utilities, cold utilities, and electricity. The break-down energy consumptions for each alternative process are shown in Table 3 (benzene as a solvent), Table 4 (organic nanofilter), and Table 5 (adsorption by zeolite).

A comparison of energy consumptions between the four studied processes is illustrated in Fig. 9. It should be noted that the electricity usages are not presented in the figure because their values are relatively very small compared with the hot and cold utilities. From the result, it was found that case 4 used the lowest energy consumption. This is simply because the energy-intensive distillation column required for solvent extraction is replaced by adsorption, which demands less energy for separation. It was also found that the energy consumption in case 3 was higher than that of the cases 1 and 2 even though the extractor was not used. This is because ethyl acetate usage is required in this process and its usage volume is larger than the cases 1 and 2. As a result, the required energy for separation of ethyl acetate was higher.

3.7.2. Economic analysis

After performing the process simulations, equipment sizing was implemented to generate equipment data. Then, the equipment data were used as input data for an economic analysis tool to estimate the OPEX and CAPEX costs as the main parameters for calculating the profitability of the processes. In this study, the capital investment cost of the process for case 3 (organic nanofilter) and case 4 (zeolite) were obtained from commercial sources (Sterlitech, 2017; Alibaba, 2017). The economic analysis tool used in this study

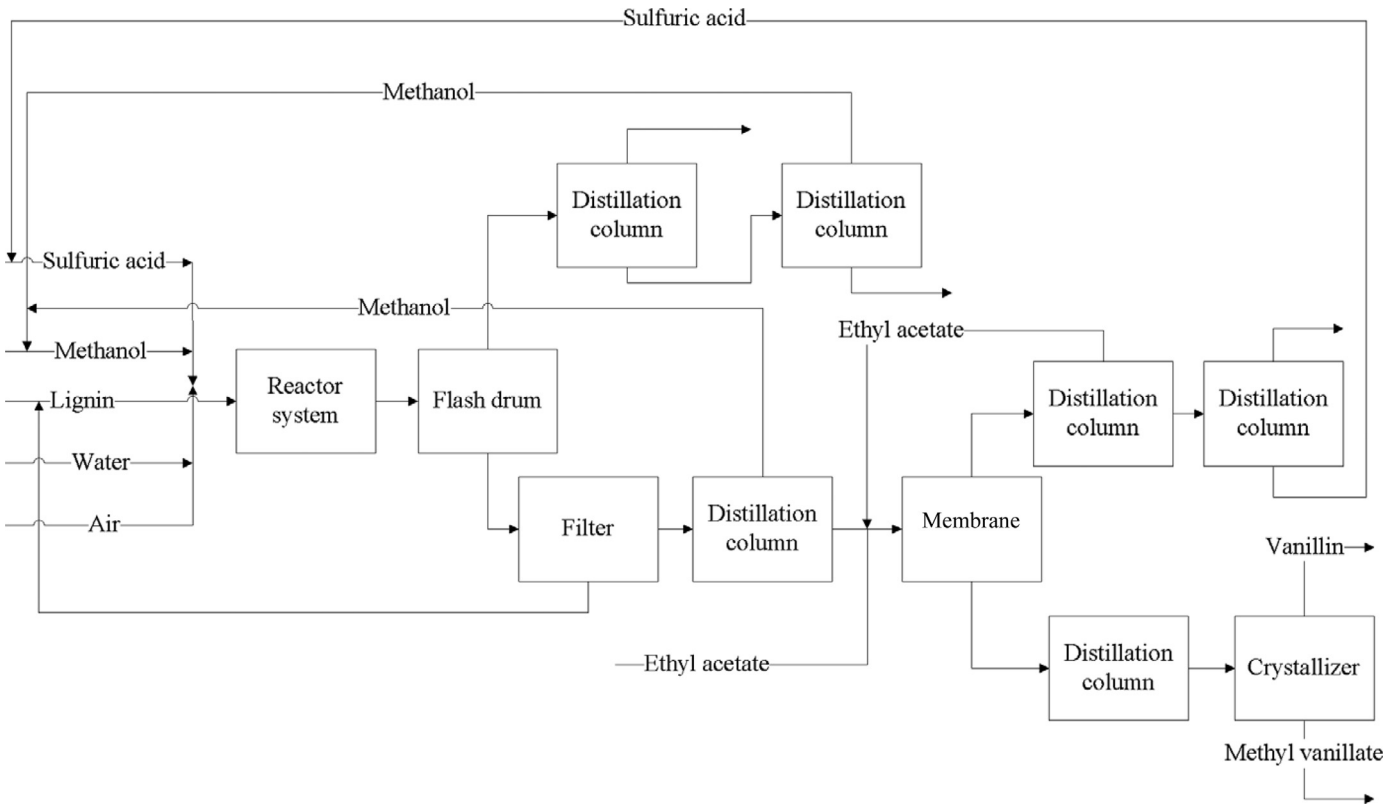

Fig. 5. Block flow diagram of vanillin production process from kraft lignin - Case 3 (organic nanofilter).

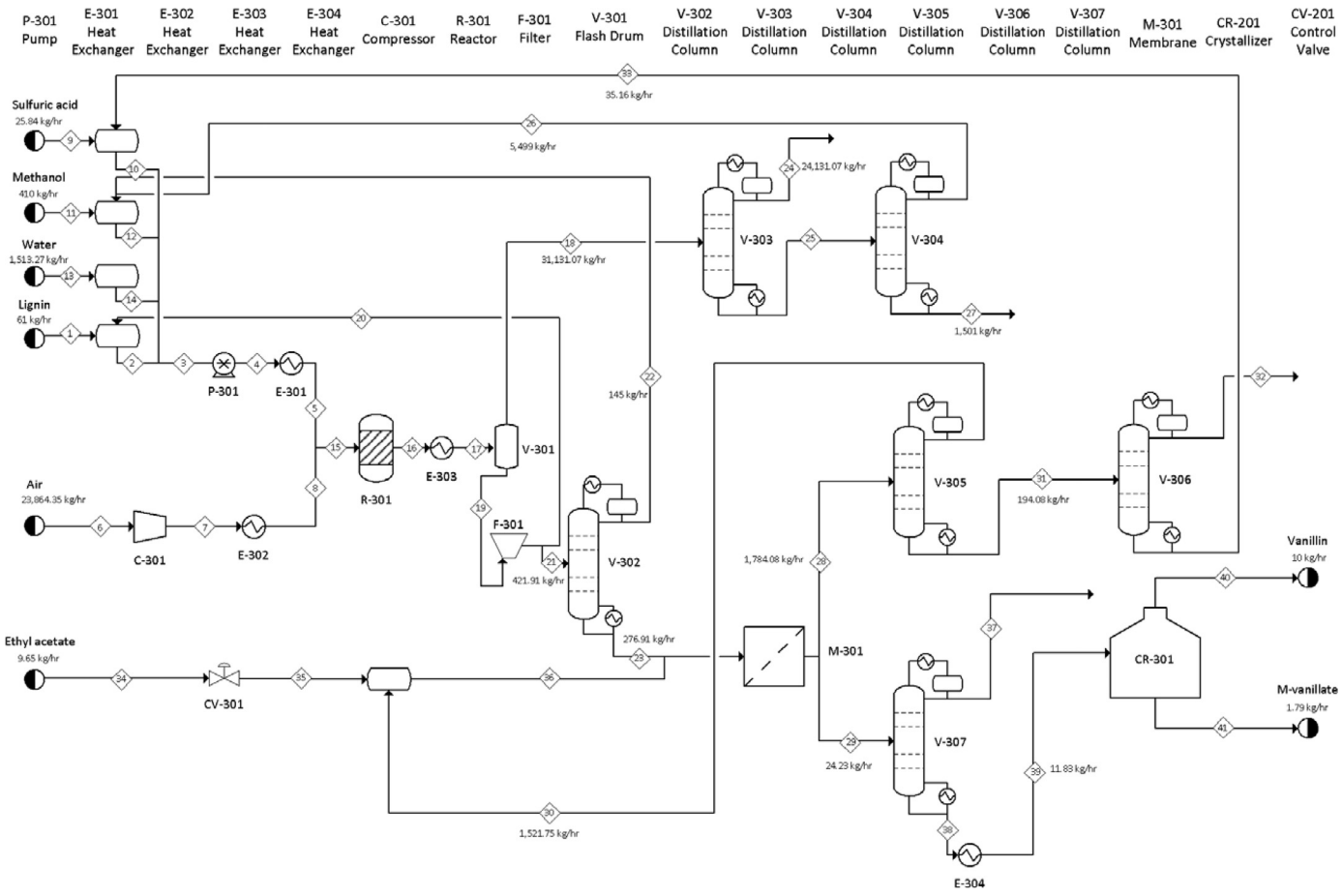

Fig. 6. The production of vanillin from kraft lignin - Case 3 (organic nanofilter).

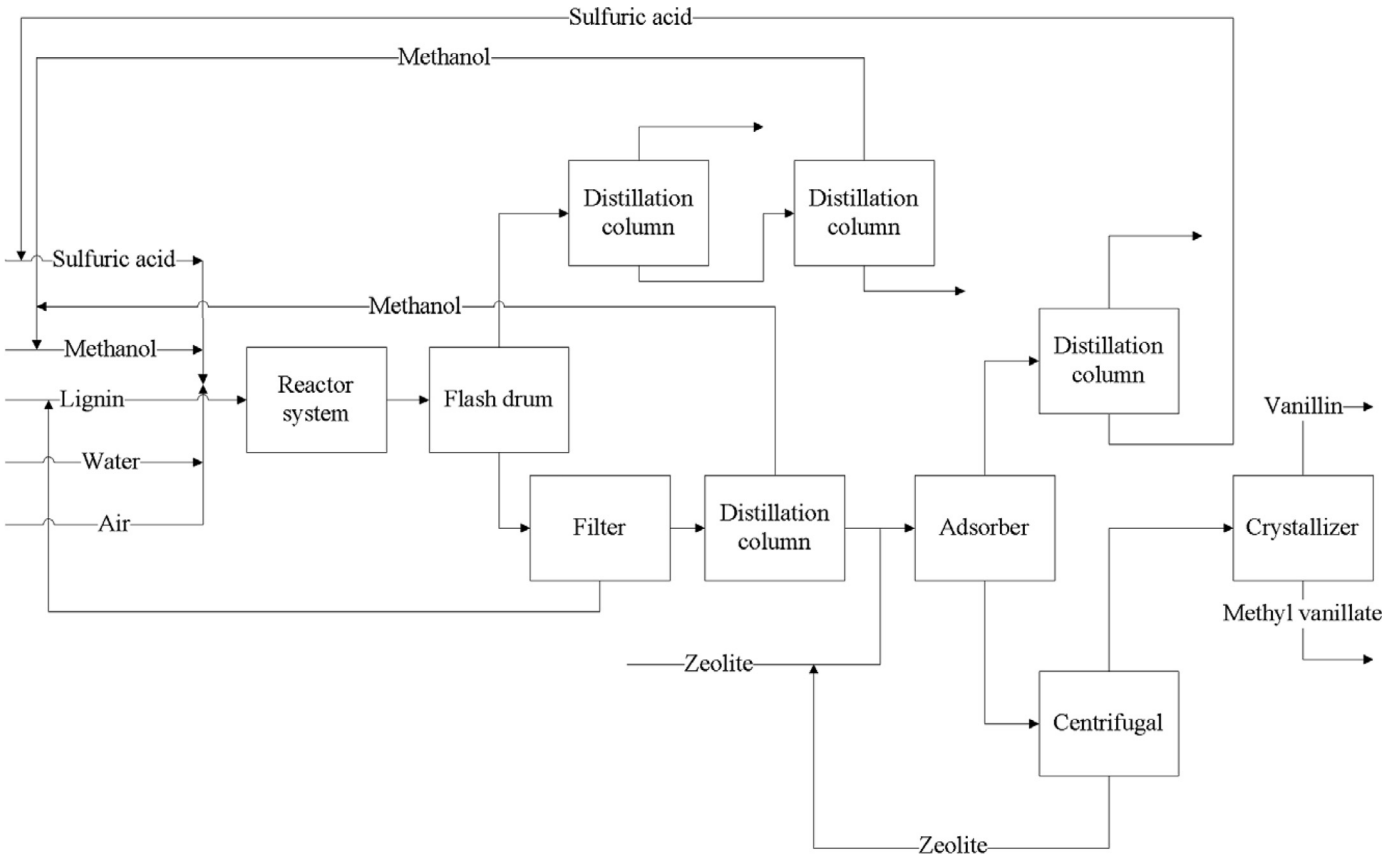

Fig. 7. Block flow diagram of vanillin production process from kraft lignin - Case 4 (adsorption by zeolite).

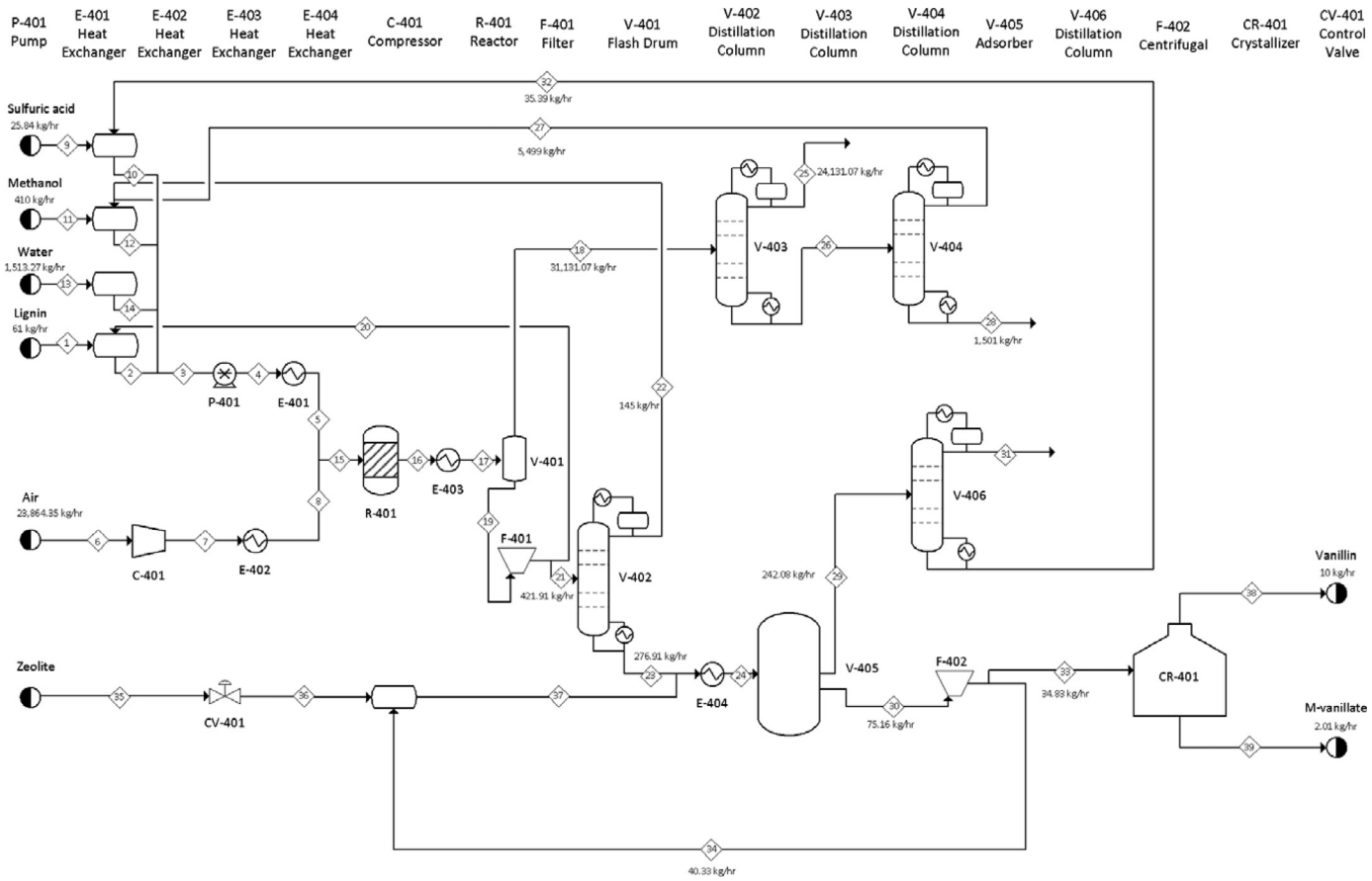

Fig. 8. The production of vanillin from kraft lignin - Case 4 (adsorption by zeolite).

Table 3
Process description of vanillin production process from kraft lignin base case (benzene as solvent).

Unit	Type of unit	Duty/Work (MJ/hr)	Activity	Energy source	Carbon footprint(kg CO_2 eq.)
C-201	Compressor	19913.77	Electricity usage	Electricity, natural gas, at power plant	51.3809
E-203	Cooler	−16732.19	Cooling	Chilled water, absorption chiller using natural gas	0.7685
E-204	Cooler	−3.35	Cooling	Chilled water, absorption chiller using natural gas	0.0002
CR-201	Crystallizer	28.57	Heating	Natural gas, combusted in industrial boiler	0.0051
E-201	Heater	5750.52	Heating	Natural gas, combusted in industrial boiler	1.0230
E-202	Cooler	−15403.27	Cooling	Chilled water, absorption chiller using natural gas	0.7075
P-201	Pump	109.30	Electricity usage	Electricity, natural gas, at power plant	0.2820
V-201	Flash	9850.11	Heating	Natural gas, combusted in industrial boiler	1.7522
V-202	Condenser	−4274.44	Cooling	Chilled water, absorption chiller using natural gas	0.1963
V-202	Reboiler	4304.44	Heating	Natural gas, combusted in industrial boiler	0.7657
V-203	Condenser	−66645.95	Cooling	Chilled water, absorption chiller using natural gas	3.0610
V-203	Reboiler	55394.92	Heating	Natural gas, combusted in industrial boiler	9.8542
V-204	Condenser	−18160.63	Cooling	Chilled water, absorption chiller using natural gas	0.8341
V-204	Reboiler	18356.38	Heating	Natural gas, combusted in industrial boiler	3.2654
V-206	Condenser	−51.97	Cooling	Chilled water, absorption chiller using natural gas	0.0024
V-206	Reboiler	47.76	Heating	Natural gas, combusted in industrial boiler	0.0085
V-207	Condenser	−1672.13	Cooling	Chilled water, absorption chiller using natural gas	0.0768
V-207	Reboiler	1647.83	Heating	Natural gas, combusted in industrial boiler	4.2517
R-201	REACTOR	3104.92	Heating	Residual fuel oil, combusted in industrial boiler	2.0872

Table 4
Process description of vanillin production process from kraft lignin case 3 (organic nanofilter).

Unit	Type of unit	Duty/Work (MJ/hr)	Activity	Energy source	Carbon footprint (kg CO_2 eq.)
C-301	Compressor	19913.77	Electricity usage	Electricity, natural gas, at power plant	51.3809
E-303	Cooler	−16732.19	Cooling	Chilled water, absorption chiller using natural gas	0.7685
E-304	Cooler	−5.23	Cooling	Chilled water, absorption chiller using natural gas	0.0002
CR-301	Crystallizer	28.70	Heating	Natural gas, combusted in industrial boiler	0.0051
E-301	Heater	5741.63	Heating	Natural gas, combusted in industrial boiler	1.0214
E-302	Cooler	−15403.27	Cooling	Chilled water, absorption chiller using natural gas	0.7075
P-301	Pump	109.24	Electricity usage	Electricity, natural gas, at power plant	0.2819
V-301	Flash	9850.11	Heating	Natural gas, combusted in industrial boiler	1.7522
V-302	Condenser	−4274.44	Cooling	Chilled water, absorption chiller using natural gas	0.1963
V-302	Reboiler	4304.44	Heating	Natural gas, combusted in industrial boiler	0.7657
V-303	Condenser	−66645.93	Cooling	Chilled water, absorption chiller using natural gas	3.0610
V-303	Reboiler	55394.79	Heating	Natural gas, combusted in industrial boiler	9.8542
V-304	Condenser	−18160.63	Cooling	Chilled water, absorption chiller using natural gas	0.8341
V-304	Reboiler	18356.38	Heating	Natural gas, combusted in industrial boiler	3.2654
V-305	Condenser	−725.56	Cooling	Chilled water, absorption chiller using natural gas	0.0333
V-305	Reboiler	748.01	Heating	Natural gas, combusted in industrial boiler	0.1331
Unit	Type of unit	Duty/Work (MJ/hr)	Activity	Energy source	Carbon footprint (kg CO_2 eq.)
V-306	Condenser	−1076.67	Cooling	Chilled water, absorption chiller using natural gas	0.0495
V-306	Reboiler	1082.29	Heating	Natural gas, combusted in industrial boiler	0.1925
V-307	Condenser	−94.24	Cooling	Chilled water, absorption chiller using natural gas	0.0043
V-307	Reboiler	99.74	Heating	Natural gas, combusted in industrial boiler	0.0177

Table 5
Process description of vanillin production process from kraft lignin case 4 (adsorption by Zeolite).

Unit	Type of unit	Duty/Work (MJ/hr)	Activity	Energy source	Carbon footprint (kg CO_2 eq.)
C-401	Compressor	19913.77	Electricity usage	Electricity, natural gas, at power plant	51.3809
E-403	Cooler	−16732.19	Cooling	Chilled water, absorption chiller using natural gas	0.7685
E-404	Cooler	−62.58	Cooling	Chilled water, absorption chiller using natural gas	0.0029
CR-401	Crystallizer	25.85	Heating	Natural gas, combusted in industrial boiler	0.0046
E-401	Heater	5750.52	Heating	Natural gas, combusted in industrial boiler	1.0230
E-402	Cooler	−15403.27	Cooling	Chilled water, absorption chiller using natural gas	0.7075
P-401	Pump	109.24	Electricity usage	Electricity, natural gas, at power plant	0.2819
V-401	FLASH	9850.11	Heating	Natural gas, combusted in industrial boiler	1.7522
V-402	Condenser	−4274.44	Cooling	Chilled water, absorption chiller using natural gas	0.1963
V-402	Reboiler	4304.44	Heating	Natural gas, combusted in industrial boiler	0.7657
V-403	Condenser	−66645.95	Cooling	Chilled water, absorption chiller using natural gas	3.0610
V-403	Reboiler	55394.92	Heating	Natural gas, combusted in industrial boiler	9.8542
V-404	Condenser	−18160.63	Cooling	Chilled water, absorption chiller using natural gas	0.8341
V-404	Reboiler	18356.38	Heating	Natural gas, combusted in industrial boiler	3.2654
V-406	Condenser	−1397.74	Cooling	Chilled water, absorption chiller using natural gas	0.0642
V-406	Reboiler	1459.11	Heating	Natural gas, combusted in industrial boiler	0.2596
R-401	Reactor	3104.92	Heating	Residual fuel oil, combusted in industrial boiler	2.0872

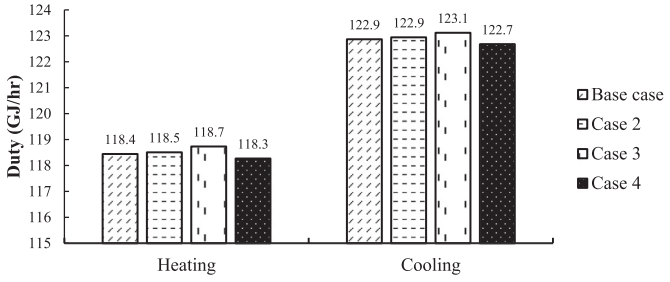

Fig. 9. The energy consumptions of different processes.

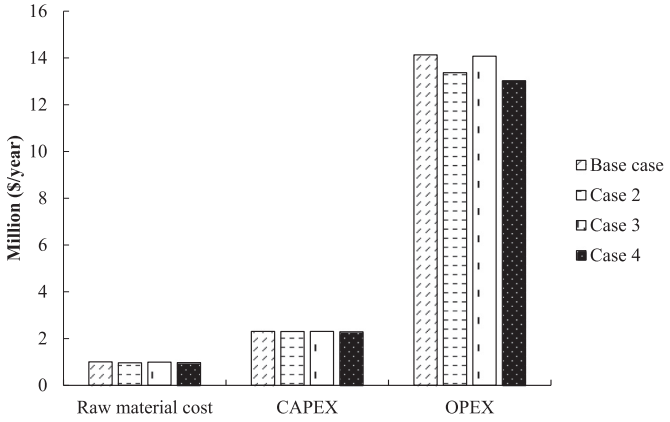

Fig. 10. The costs of different processes.

is ECON software (Peters, 1991; Saengwirun, 2011). The results of economic analysis of the four cases are summarized in Fig. 10.

It was found that the economics of each case are significantly affected by the amount of solvent used in the process. Because case 3 (ethyl acetate as solvent for organic nanofilter) required the highest amount of solvent, its operating cost was the highest compared with the others. For the base case and case 2, they used less solvent than case 3. Hence, their economic results were relatively better. Case 4 (adsorption by zeolite) was clearly found to provide the best economic result. This is because this process did not require a solvent recovery system in the downstream separation process.

3.7.3. Life cycle assessment

LCAs of the base case and alternative processes were performed using the LCSoft program. It is a reliable and proven tool that can be used to identify and quantify environmental impacts of the chemical product and/or the process that makes it (Kalakul et al., 2014; Gargalo et al., 2015). Ten environmental impact indicators were assessed in this work, namely, GWP (CO_2 equivalent), AP (H^+ equivalent), ET (kg 2,4-dichlorophenoxyacetic acid equivalent), HTNC (kg toluene equivalent), HTC (kg of benzene equivalent), ODP (CFC-11 equivalent), HTPI (1/LD 50), HTPE, (1/TWA), ATP (1/LC 50), and PCOP (C_2H_2 equivalent). The assessment results are illustrated in Figs. 11–13. In general, it was found that cases 2 and 3 provided less environmental impacts than the base case. Moreover, case 4 was found to be the most environmentally friendly process as it provided the least environmental impacts.

In summary, case 3 was unexpectedly found to consume higher energy than the other cases. This is due to the need of a large amount of ethyl acetate solvent used in the process. Consequently, the heating and cooling energy required to operate the extractor and solvent recovery system were increased. This reflected on the operating costs of the process, which was the highest among the process candidates. In addition, a large distillation column was required to handle the large volume of solvent and this contributed to a higher equipment cost. In terms of the environmental impacts, case 3 showed the highest impacts on the CF. This is simply because of high chemical usage of the process.

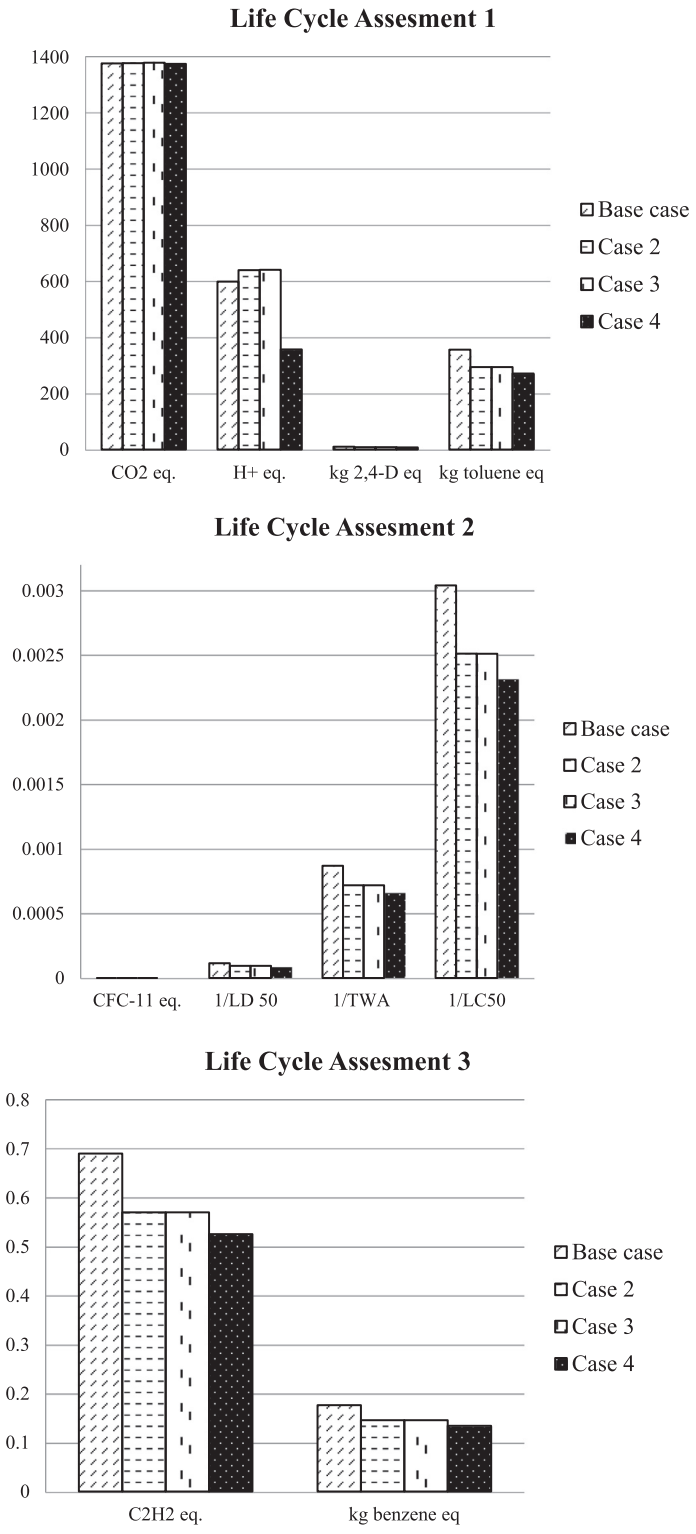

Fig. 11–13. The life cycle assessment 1 (impact indicators of different processes).

The highest energy saving was obtained from case 4, which is only 0.15%. A much better improvement for alternative processes was found in the process economics. Up to 7.37% improvement on process cost reduction could be achieved by the case 4 process.

The reason is that case 4 did not use solvent extraction for separating the mixed products from the sulfuric acid. Therefore, the utility requirements, as well as the operating cost of the process, were decreased. In terms of the environmental impacts, case 4 is also very attractive. Apparently, the process delivered the lowest environmental impacts in all categories. Overall, case 4 demonstrated the best results in all aspects. Hence, it is the best alternative for vanillin production process in this study. Overall, the base case results indicated 6.1 kg lignin usage/kg vanillin, 24.13 GJ/kg vanillin (product), and 137.78 kg CO_2 equivalent/kg vanillin, while the case 4 results were 6.1 kg lignin usage/kg vanillin, 24.10 GJ/kg vanillin (product), and 137.61 CO_2 equivalent/kg vanillin.

4. Conclusion

The process simulations of vanillin production processes from kraft lignin were studied and conducted using the Aspen Plus simulation program. A base case process was designed and used as a reference case for comparison with other alternative processes. Three different alternative processes were proposed based on the process intensification approach. The main difference between these processes was located in the product separation section, especially at the solvent extraction and recovery units. Energy consumption, economic analysis, and life cycle analysis were compared and used to justify the performance of the new processes. The economic and environmental analyses were conducted using economic analysis tools and LCSoft, respectively. The results from the process assessments showed that adsorption by zeolite (case 4) is the best alternative process. It provided 0.15% improvement in energy use, 7.37% on the process cost saving, and significant decreases in environmental impacts.

Acknowledgments

This work was financially supported by the Thailand Research Fund (DPG5880003). Department of Chemical Engineering, Faculty of Engineering, Chulalongkorn University would like to acknowledge The Institutional Research Grant (The Thailand Research Fund), IRG 5780014, and Chulalongkorn University, Contract No. RES_57_411_21_076. The work is a part of the international collaboration project called ProBioRefine led by Prof. Rafiqul Gani from PSE for SPEED. The authors also would like to acknowledge Dr. Pattaraporn Kim-Lohsoontorn for valuable suggestion on Economic analysis.

References

Alibaba. 2017. Zsm-5 zeolite SiO_2/Al_2O_3 Mole Ratio for FCC catalyst. https://www.alibaba.com/product-detail/zsm-5-zeolite-SiO2-Al2O3-Mole_60683260274.html?spm=a2700.7724857.main07.17.7f3e4935ahUaxM&s=p (Accessed 10 December 2017).

Babi, D.K., Lutze, P., Woodley, J.M., Gani, R., 2014. A process synthesis-intensification framework for the development of sustainable membrane-based operations. Chem. Eng. Process. Process Intensif. 86, 173–195.

Bomgardner, M.M., 2014. Following many routes to naturally derived vanillin. Chem. Eng. News 92, 14.

Borges da Silva, E.A., Zabkova, M., Araujo, J., Cateto, C., Barreiro, M., Belgacem, M., Rodrigues, A.E., 2009. An integrated process to produce vanillin and lignin-based polyurethanes from kraft lignin. Chem. Eng. Res. Des. 87, 1276–1292.

Doherty, W.O.S., Mousavioun, P., Fellows, C.M., 2011. Value-adding to cellulosic ethanol: lignin polymers. Ind. Crops Prod. 33, 259–276.

Fache, M., Boutevin, B., Caillol, S., 2016. Vanillin production from lignin and its use as a renewable chemical. ACS Sustain. Chem. Eng. 4, 35–46.

Gargalo, C.L., Chairakwongs, S., Quaglia, A., Sin, G., Gani, R., Chapter 9 – Methods and tools for sustainable chemical process design in: Assessing and Measuring Environmental Impact and Sustainability, (2015) 277–321.

Gosselink, R.J.A., De Jong, E., Guran, B., Abärcheli, A., 2004. Co-ordination net-work for lignin—standardisation, production and applications adapted to market requirements (EUROLIGNIN). Ind. Crops Prod. 20, 121–129.

Gosselink, R.J.A., Teunissen, W., van Dam, J.E.G., De Jong, E., Gellerstedt, G, 2012. Lignin depolymerisation in supercritical carbon dioxide/acetone/water fluid for the production of aromatic chemicals. Bioresour. Technol. 106, 173–177.

Gouveia, S., Fernández-Costas, C., Sanromán, M.A., Moldes, D., 2013. Polymerisation of Kraft lignin from black liquors by laccase from Myceliophthora thermophila: effect of operational conditions and black liquor origin. Bioresour. Technol. 131, 288–294.

Kalakul, S., Malakul, P., Siemanond, K., Gani, R, 2014. Integration of life cycle assessment software with tools for economic and sustainability analyses and process simulation for sustainable process design. J. Clean. Prod. 71, 98–109.

Kongpanna, P., Babi, D.K., Pavarajarn, V., Assabumrungrat, S., Gani, R, 2016. Systematic methods and tools for design of sustainable chemical processes for CO_2 utilization. Comput. Chem. Eng. 87, 125–144.

Kaygorodov, K.L., Chelbina, Y.V., Tarabanko, V.E., Tarabanko, N.V, 2010. Extraction of vanillin by aliphatic alcohols. J. Sib. Federal Univ. Chem. 3, 223–228.

Lamminpää, K., Ahola, J., Tanskanen, J, 2015. Acid-catalysed xylose dehydration into furfural in the presence of Kraft lignin. Bioresour. Technol. 177, 94–101.

Lutze, P, Babi, D.K., Woodley, J.M, Gani, R., 2013. Phenomena based methodology for process synthesis incorporating process intensification. Ind. Eng. Chem. Res. 52, 7127–7144.

Lutze, P., Román-Martinez, A., Woodley, J.M., Gani, R., 2012. A systematic synthesis and design methodology to achieve process intensification in (bio) chemical processes. Comput. Chem. Eng. 36, 189–207.

Mansouri, S., Ismail, M., Babi, D., Simasatitkul, L., Huusom, J., Gani, R., 2013. Systematic sustainable process design and analysis of biodiesel processes. Processes 1, 167–202.

Mikkola, J.P., Sklavounos, E., King, A.W.T., Virtanen, P., 2015. The biorefinery and green chemistry, in *ionic liquids in the biorefinery concept: challenges and perspectives*. RSC Green Chem. 1–37.

Nguyen, T., Maschietti, M., Åmand, L., Vamling, L., Olausson, L., Andersson, S., Theliander, H, 2014. The effect of temperature on the catalytic conversion of kraft lignin using near-critical water. Bioresour. Technol. 170, 196–203.

Pacek, A.W., Ding, P., Garrett, M., Sheldrake, G., Nienow, A.W., 2013. Catalytic conversion of sodium lignosulfonate to vanillin: engineering aspects. Part 1. effects of processing conditions on vanillin yield and selectivity. Ind. Eng. Chem. Res. 52, 8361–8372.

Peters, M.S., Timmerhaus, K.D., 1991. Plant Design and Economics for Chemical Engineers, fourth ed. McGraw-Hill, Singapore.

Peterson, J.R., Romakh, V., Scott, B.M.T., 2013. Method for tiered production of biobased chemicals and biofuels from lignin. U.S. Patent, US20130232852A1.

Pinto, P.C.R., da Silva, E.A.B., Rodrigues, A.E., 2012. Lignin as source of fine chemicals: vanillin and syringaldehyde. In: Biomass Conversion. Springer, New York, pp. 381–420.

Ramaswamy, S., Huang, H.J., Ramarao, B.V. (Eds.), 2013. Separation and Purification Technologies in Biorefineries. John Wiley & Sons, Ltd, United States.

Saengwirun, P., 2011. ECON: A Software for Cost Calculation and Economic Analysis Master of Science Thesis. Thailand: The Petroleum and Petrochemical CollegeChulalongkorn University.

Schorr, D., Diouf, P.N., Stevanovic, T., 2014. Evaluation of industrial lignins for biocomposites production. Ind. Crops Prod. 52, 65–73.

Sterlitech. 2017. Evonik flat sheet membrane, Puramem 280. https://www.sterlitech.com/evonik-flat-sheet-membrane-puramem-280-da-nf-210-x-297-mm-1-pk.html [Accessed 10 December 2017].

Vishtal, A., Kraslawski, A, 2011. Challenge in industrial application of technical-lignins. Bioresources 6, 3547–3568.

Wang, M., Leitch, M., Xu, C., 2009. Synthesis of phenol–formaldehyde resol resins using organosolv pine lignins. Eur. Polym. J. 45, 3380–3388.

Werhan, H., 2013. A Process for the Complete Valorization of Lignin into Aromatic Chemicals Based in Acidic Oxidation Doctorial Thesis. ETH Zurich.

Werhan, H., Assmann, N., von Rohr, P.R, 2013. Lignin oxidation studies in a continuous two-phase flow microreactor. Chem. Eng. Process. 73, 29–37.

Wahyudiono, Sasaki, M., Goto, M., 2008. Recovery of phenolic compounds through the decomposition of lignin in near and supercritical water. Chem. Eng. Process. 47, 1609–1619.

INTERNATIONAL JOURNAL OF HYDROGEN ENERGY XXX (2018) 1–13

Available online at www.sciencedirect.com

ScienceDirect

journal homepage: www.elsevier.com/locate/he

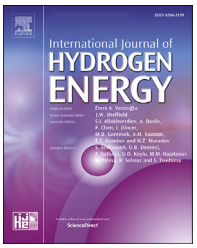

Experimental study of dual fixed bed biochar-catalytic gasification with simultaneous feed of O_2-steam-CO_2 for synthesis gas or hydrogen production

Paripat Kraisornkachit [a], *Supawat Vivanpatarakij* [b,*], *Jon Powell* [c], *Suttichai Assabumrungrat* [a]

[a] *Center of Excellence in Catalysis and Catalytic Reaction Engineering, Department of Chemical Engineering, Faculty of Engineering, Chulalongkorn University, Phyathai Road, Wang Mai, Phatumwan, Bangkok, 10330, Thailand*

[b] *Energy Research Institute, Chulalongkorn University, Phyathai Road, Wang Mai, Phatumwan, Bangkok, 10330, Thailand*

[c] *Energy Engineering Research Group, Faculty of Science and Engineering, University of Nottingham Ningbo China, 199 Tai Kang East Road, Ningbo, 315100, China*

ARTICLE INFO

Article history:
Received 15 February 2018
Received in revised form
27 May 2018
Accepted 10 June 2018
Available online xxx

Keywords:
Biochar gasification
CO_2 reforming
Catalytic gasification
Syngas

ABSTRACT

The catalytic gasification of biochar was investigated in the presence of a Ni/SiO_2 catalyst in a fixed bed reactor with an O_2-steam-CO_2 gas feed. The effects of operating temperature, catalyst nickel loading and composition of O_2-steam-CO_2 feed gas on biochar carbon conversion and gas products were investigated. The results indicate that the highest biochar carbon conversion could be obtained at approximately 800 °C, whilst the 10% Ni/SiO_2 catalyst was shown to produce the greatest syngas yields. The presence of O_2 in the feed gas can result in slightly more CO in the gas product, whilst a higher steam content leads to more H_2 in the gas product. The CO_2 offered a benefit as an adjusting agent for achieving a desired H_2/CO ratio. No evidence of coke deposition on the catalyst was found under any of the tested conditions.

© 2018 Hydrogen Energy Publications LLC. Published by Elsevier Ltd. All rights reserved.

Introduction

The world energy consumption is currently and continually growing. Fossil fuels supply approximately 80% of the current Global energy demands, but due to declining low cost reserves, various renewable energy sources are becoming increasingly important. Biomass resources are renewable energy resources, which like fossil fuels, are carbonaceous feedstocks and compatible with current fossil fuel energy power generation technologies, which in turn provides significant cost benefits and removes a number of implementation barriers [1–4].

Gasification of biomass produces syngas, a fuel gas used in numerous applications such as gas turbine power plants [5–7], Fischer-Tropsch synthesis [8,9], fuel cells [10–12] and other downstream processes [13–15]. Air is commonly used as a gasifying agent in biomass gasification due to its availability

* *Corresponding author.*
E-mail address: supawat.v@chula.ac.th (S. Vivanpatarakij).

https://doi.org/10.1016/j.ijhydene.2018.06.054

0360-3199/© 2018 Hydrogen Energy Publications LLC. Published by Elsevier Ltd. All rights reserved.

Please cite this article in press as: Kraisornkachit P, et al., Experimental study of dual fixed bed biochar-catalytic gasification with simultaneous feed of O_2-steam-CO_2 for synthesis gas or hydrogen production, International Journal of Hydrogen Energy (2018), https://doi.org/10.1016/j.ijhydene.2018.06.054

and low cost; however, the presence of N_2 in the syngas is problematic, as a result of the lower energy density and propensity for NO_x production [16]. These issues can be avoided with the use of O_2 gas as a gasifying agent, leading to a higher heating value, elimination of NO_x production and greater conversion of carbon into CO_2 [17]. However, the use of an O_2 gasifying agent requires the separation of O_2 from N_2, an expensive and energy intensive process. Steam can also be used as an oxidant, the H_2 content in syngas product increases with increasing steam utilization; however, the steam production is associated with large energy demands [3]. Carbon dioxide has been reported for use as a gasifying agent, offering several advantages such as increasing the efficiency of the syngas product, the ability to control the H_2/CO ratio and reducing the CO_2 emission [18–20].

Gasification experiments recently conducted by Gile-Lalaguna et al. [21], involved the use of sewage sludge as a fuel with an air-steam gasifying agent in a fluidized bed gasifier. It was found that the most influential operating parameter was temperature, with increases in temperature not only improving the product gas yield and fuel conversion rate, but also reducing the tar and solids yield. Further, high steam to oxygen ratios favored higher H_2/CO ratios and higher heating values. Many researchers have investigated the use of various catalysts in gasification experiments. A study on gasification by Huang et al. [22] revealed Fe/CaO catalyst to provide a significant improvement in performance when compared to other catalysts. This is attributed to the use of a metal precursor to improve the stability of the support and can enhance the catalytic char-tar gasification.

Miccio et al. [23] studied biomass gasification with different catalyst materials in fluidized bed reactors. Compared to dolomite, olivine and inert quartzite catalysts, Ni-alumina provided the highest H_2 yields, lowest tar production and least catalyst deactivation. The use of novel catalysts possessing Rh, Pt, Pd or Ru supported on CeO_2/SiO_2 have been reported by Tomishige et al. [24]. The results showed that a Ni/CeO_2/SiO_2 catalyst performed similarly to the novel catalysts at high operating temperatures, in addition, biomass with a higher volatile content led to a high tar yield.

The gasifier effluents consist of syngas, unreacted and remaining hydrocarbons, hence the product gas yield can be upgraded using a catalytic reforming process [25–27]. Steam is often used as an oxidant in reforming processes, and a study by Karim and Metwally [28] investigated the kinetics of natural gas steam reforming. They found that the non-catalytic reforming reaction is favored by high temperatures, more than 1500 °C, hence a catalyst must be introduced to avoid this constraint. A study on Ni-based catalytic steam reforming of bio-oil carried out by Azad et al. [29] showed that in the presence of a Ni/Al_2O_3 catalyst the operating temperature can be reduced to 850 °C whilst achieving H_2 yields over 80%. Furthermore, less coke deposition was observed on the Ni/Al_2O_3 catalyst than on the Ni/ZrO_2 catalyst, with optimum Ni loadings being within the range of 5–15%. Recently, investigations into the use of a Ni/CeO_2–SiO_2 catalyst in the CO_2 dry reforming of methane into syngas have been reported by Taufiq-Yap et al. [30]. The results indicate CH_4 and CO_2 conversions as high as 90% can be achieved at temperatures as low as 750 °C, even without CeO_2 in the catalyst. The presence of 9 wt.% CeO_2 in the Ni/CeO_2–SiO_2 catalyst helps to reduce coke deposition and hence improve the catalyst stability. Moreover, increasing steam feed ratios can also reduce coke deposition on catalyst as reported by Vicente et al. [31]. Combined CO_2 and steam reforming of ethanol in the presence of a Ni-based catalyst was investigated by Bednarczuk et al. [32]. They found that using a CO_2/steam feed ratio of 1:1 not only increased the ethanol conversion over Ni/La_2O_3 and Ni/Y_2O_3 but also reduced the carbon deposition on the catalyst via CO formation.

With regards to combined gasification and reforming processes, most research has focused on various types of catalyst and biomass [33–41]. Polypropylene fixed bed catalytic steam gasification in the presence of a Ni catalyst, was investigated by Wu and Williams [33]. Several nickel-based catalysts were used, however, out of those catalysts tested, Ni/Al_2O_3 was shown to provide the highest H_2 production yields. Wu et al. [34] studied the use of a two stage reactor for the gasification of biomass in the presence of a nickel-based catalyst. Several types of biomass were tested including cellulose, hemicellulose and lignin. Lignin, which has a low VOC content and a high fixed carbon content, provided the highest H_2 yields with negligible coke deposition on the catalyst. Gao et al. [35] investigated biomass gasification in porous ceramic reformers (SiO_2, Al_2O_3 and MgO). They found that by increasing the O_2 concentration in the feed gas the CO_2 production increased but the H_2 production decreased. Moreover, increasing the steam concentration in the feed gas not only increased the H_2 production but also reduced the CO_2 content in the gas product. Furthermore, the porous ceramic promoted the formation of water-soluble tar that in turn led to a higher H_2 yield and concentration in the gas product.

In this work, combined fixed bed gasifier and catalytic reformer experiments were studied using an O_2-steam-CO_2 gas feed stream, over a fixed bed of biochar and catalyst for the production of syngas. The influence of the operating temperatures, the O_2-steam-CO_2 feed ratio and percentage of Ni loading on the Ni/SiO_2 catalyst on the process performance were studied. The performance of the process was evaluated in terms of the product gas composition, cold gas efficiency (*CGE*), syngas ratio (H_2/*CO*) and efficiency factor (*EF*) as a CO_2 emission parameter.

Methodology

Materials

Mangrove tree charcoal was used as biochar due to its availability in Thailand. Samples were ground and sieved using a 16–20 mesh size, and then characterized using ultimate and proximate analysis to know the physical and elemental properties.

Catalysts preparation and characterization

Nickel(II) nitrate hexahydrate (Sigma–Aldrich) and commercially available silica sand (SiO_2) (Sigma–Aldrich) were used for preparation of the Ni/SiO_2 catalyst with nickel loadings of

Please cite this article in press as: Kraisornkachit P, et al., Experimental study of dual fixed bed biochar-catalytic gasification with simultaneous feed of O_2-steam-CO_2 for synthesis gas or hydrogen production, International Journal of Hydrogen Energy (2018), https://doi.org/10.1016/j.ijhydene.2018.06.054

5%, 10% and 15% by weight. Nickel(II) nitrate hexahydrate (Sigma–Aldrich) was dissolved in distillated water and then impregnated into the SiO_2 (Sigma–Aldrich) at room temperature and pressure. The catalysts were then dried overnight in an oven at 105 °C and calcined in air at 500 °C for 4 h for the formation of nickel oxide and the removal of the water of crystallization.

Characterization of the fresh catalyst was carried out using X-ray diffraction (XRD) for identification of crystalline materials, BET surface area measurement (BET), scanning electron microscope (SEM) to observe the physical morphology and H_2 temperature-programed reduction (H_2-TPR) to determine a suitable reduction temperature for the catalysts. Finally, thermogravimetric analysis (TGA) was used for analysis of coke deposition on the used catalysts.

Experimental

A schematic diagram of the experimental setup and process is provided in Fig. 1. Ultra-high purity argon was used at a flow rate of 2 ml/s, as a carrier gas for the O_2 (0.06 ml/s) and CO_2 (0.12 ml/s) gases fed into system. Steam was fed as liquid water (0.3 ml/h) into a preheater (180 °C) using a syringe pump, generating steam prior to entering the reactor. Prior to use in the reactions, the catalyst was reduced in a flow of H_2, balanced with argon (50%) for 1.5 h at a suitable temperature determined from H_2-TPR result. All the reaction agents were fed simultaneously into the quartz tube reactor (ID. 8 mm), which contained two separate fixed beds of biochar ($CH_{0.78}O_{0.33}$, weight = 1 g) and catalyst (Ni/SiO_2, weight = 0.05 g) for 3 h and with a gas hourly space velocity (*GHSV*) of 3265 h^{-1}. The reaction effluents were directed to a liquid trap unit and the product gas was sampled to analyze the composition using gas chromatography with a thermal conductivity detector. The experiments were run at various operating temperatures, oxidizing agent feed ratios and Ni loadings (by weight), the results of which are summarized in Table 1.

The main reactions are expected to be as follows:

Boudouard reaction (*BD*):

$$C + CO_2 \leftrightarrow 2CO \qquad \Delta H_r^0 = 172 \ \text{MJ/kmol} \tag{1}$$

Partial oxidation (*PO*):

$$2C + O_2 \leftrightarrow 2CO \qquad \Delta H_r^0 = -221 \ \text{MJ/kmol} \tag{2}$$

Steam reforming (*SR*):

$$C + H_2O \leftrightarrow CO + H_2 \qquad \Delta H_r^0 = 131 \ \text{MJ/kmol} \tag{3}$$

Methane formation (*MF*):

$$C + 2H_2 \leftrightarrow CH_4 \qquad \Delta H_r^0 = -74 \ \text{MJ/kmol} \tag{4}$$

CO_2 reforming (*CR*):

$$CH_4 + CO_2 \leftrightarrow 2CO + 2H_2 \qquad \Delta H_r^0 = 247 \ \text{MJ/kmol} \tag{5}$$

Methane reforming (*MR*):

$$CH_4 + H_2O \leftrightarrow CO + 3H_2 \qquad \Delta H_r^0 = 206 \ \text{MJ/kmol} \tag{6}$$

Table 1 – Operating conditions.

Pressure	Atmosphere
Temperature	400–800 °C
O_2/Biochar ratio (O_2/B; *by mole*)	0–0.5
Steam/Biochar ratio (S/B; *by mole*)	0–2
CO_2/Biochar ratio (CO_2/B; *by mole*)	0–1.5
%Ni loading (by weight)	5–15%

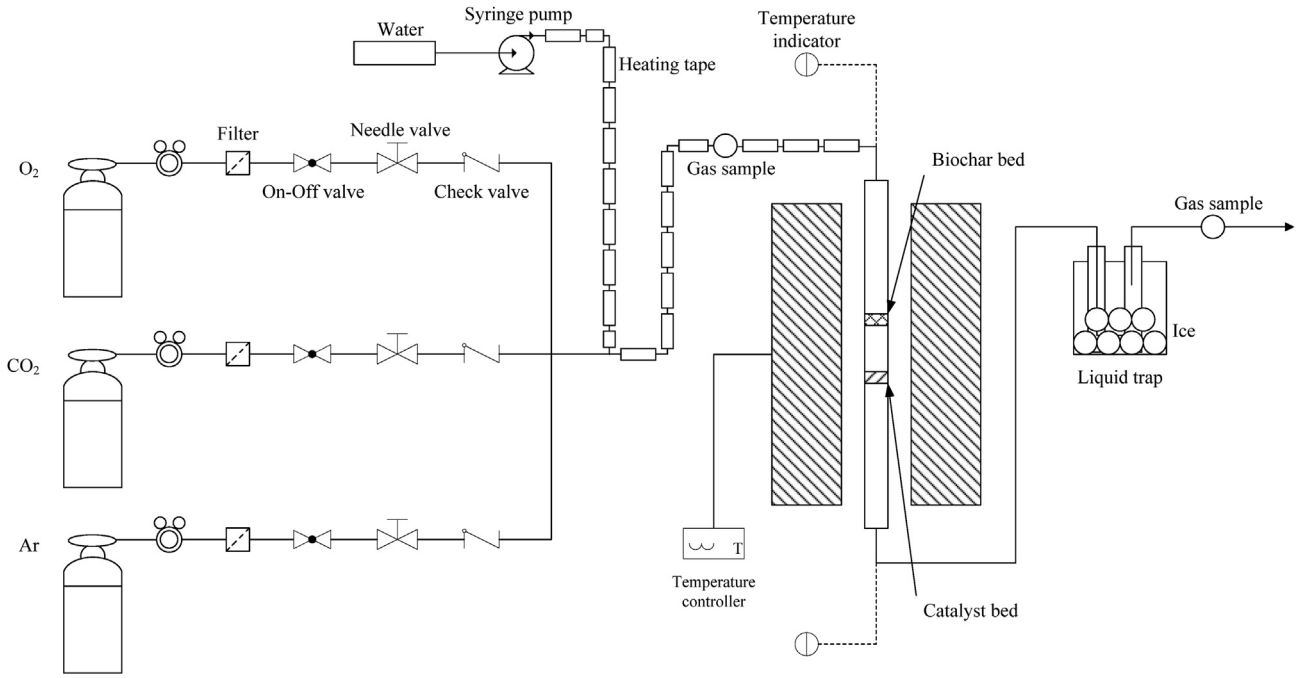

Fig. 1 – Schematic diagram of experimental setup.

Please cite this article in press as: Kraisornkachit P, et al., Experimental study of dual fixed bed biochar-catalytic gasification with simultaneous feed of O_2-steam-CO_2 for synthesis gas or hydrogen production, International Journal of Hydrogen Energy (2018), https://doi.org/10.1016/j.ijhydene.2018.06.054

Water gas shift (WGS):

$$CO + H_2O \leftrightarrow CO_2 + H_2 \qquad \Delta H_r^0 = -41 \text{ MJ/kmol} \tag{7}$$

The gasification process is typically evaluated in terms of the product gas compositions, carbon conversion (Eq. (8)) (as reported by Tomishige et al. [24]), product gas yields (Eq. (9)) (as reported by Moghtaderi [42]), cold gas efficiency (CGE) (Eq. (10)) (as reported in our previous work by Chaiwatanodom et al. [20]) and the efficiency factor (Eq. (14)).

$$Carbon\ conversion\ (\%) = \frac{formation\ of\ (CO + CO_2 + CH_4)}{feeding\ of\ (Carbon + CO_2)} \times 100 \tag{8}$$

$$Yield\ (mol/gram - biomass) = \frac{mole\ of\ product\ gas\ (mole)}{biomass\ feed\ (gram)} \tag{9}$$

Cold gas efficiency (CGE) is used as a means to evaluate a syngas product by comparing the energy provided by the syngas compared to that of the biomass. The equation for calculating the CGE is as follows;

$$CGE\ (-) = \frac{M_{syngas} LHV_{syngas}}{M_{biomass} LHV_{biomass}} \tag{10}$$

where

$$LHV_{biomass}\ (MJ/kg) = \frac{M_{biomass} HHV_{biomass} - 0.5 M_H L_{298}}{M_{biomass}} \tag{11}$$

$$LHV_{syngas}(MJ/kg) = \frac{n_{CO} H^0_{CO,298} + n_{H_2} H^0_{H_2,298} + n_{CH_4} H^0_{CH_4,298}}{M_{syngas}} \tag{12}$$

The high heating value of biochar ($HHV_{biochar}$) (Eq. (13)) was calculated using the correlation proposed by Channiwala and Parikh [43].

$$HHV\ (MJ/kg) = 0.3491 x_C + 1.1783 x_H - 0.1034 x_O \tag{13}$$

The efficiency factor is a parameter used to indicate the net CO_2 produced per unit mass of biomass.

$$Efficiency\ factor\ (mol - CO_2/gram - biomass) = \frac{CO_2\ outlet\ -\ CO_2\ inlet\ (mole - CO_2)}{biomass\ feed\ (gram)} \tag{14}$$

Table 2 – Proximate and ultimate analysis of biochar (mangrove tree charcoal as a representative).

Proximate (wt.%)	
Moisture	5.30
Volatile matters	36.26
Fixed carbon	56.40
Ash	2.05
Ultimate (wt %)	
C	66.46
H	4.37
O (balance)	29.14
Ns	0.03
High heating value (MJ/g)[a]	0.02534

[a] Calculated value based on the correlation proposed by Channiwala and Parikh [43].

Results and discussions

The results of the charcoal and catalyst characterization, as well as the reaction analysis are presented in the following sections.

Biochar characterization

Mangrove charcoal was used as biochar in this study due to the advantage of its low volatile matter content and high fixed carbon content [41]. The proximate and ultimate analyses of

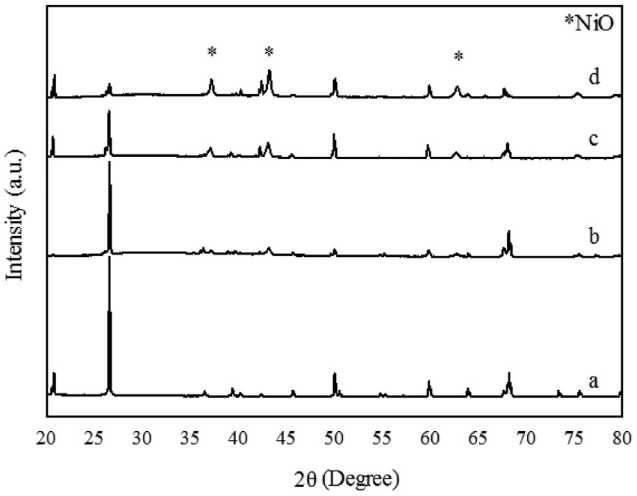

Fig. 2 – XRD patterns of SiO_2 support and Ni/SiO_2 with various %Ni loading: a) SiO_2, b) 5%Ni/SiO_2, c) 10%Ni/SiO_2 and d) 15% Ni/SiO_2.

Table 3 – Surface area of different catalysts.

Catalysts	Surface area (m^2/g)
SiO_2	5.47
5% Ni/SiO_2	3.82
10% Ni/SiO_2	3.28
15% Ni/SiO_2	2.22

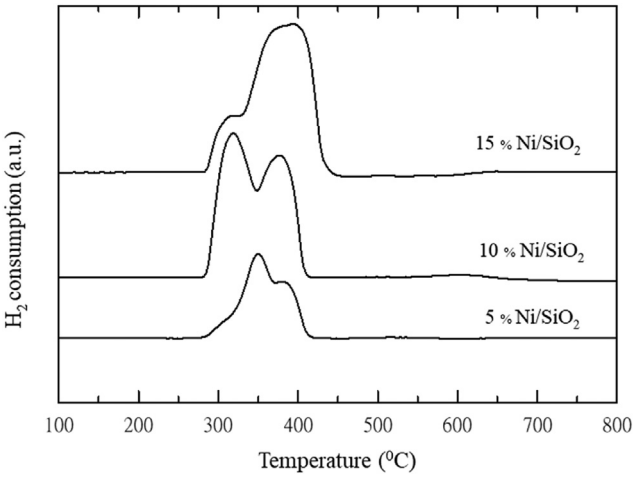

Fig. 3 – H_2-TPR profiles of catalysts.

Please cite this article in press as: Kraisornkachit P, et al., Experimental study of dual fixed bed biochar-catalytic gasification with simultaneous feed of O_2-steam-CO_2 for synthesis gas or hydrogen production, International Journal of Hydrogen Energy (2018), https://doi.org/10.1016/j.ijhydene.2018.06.054

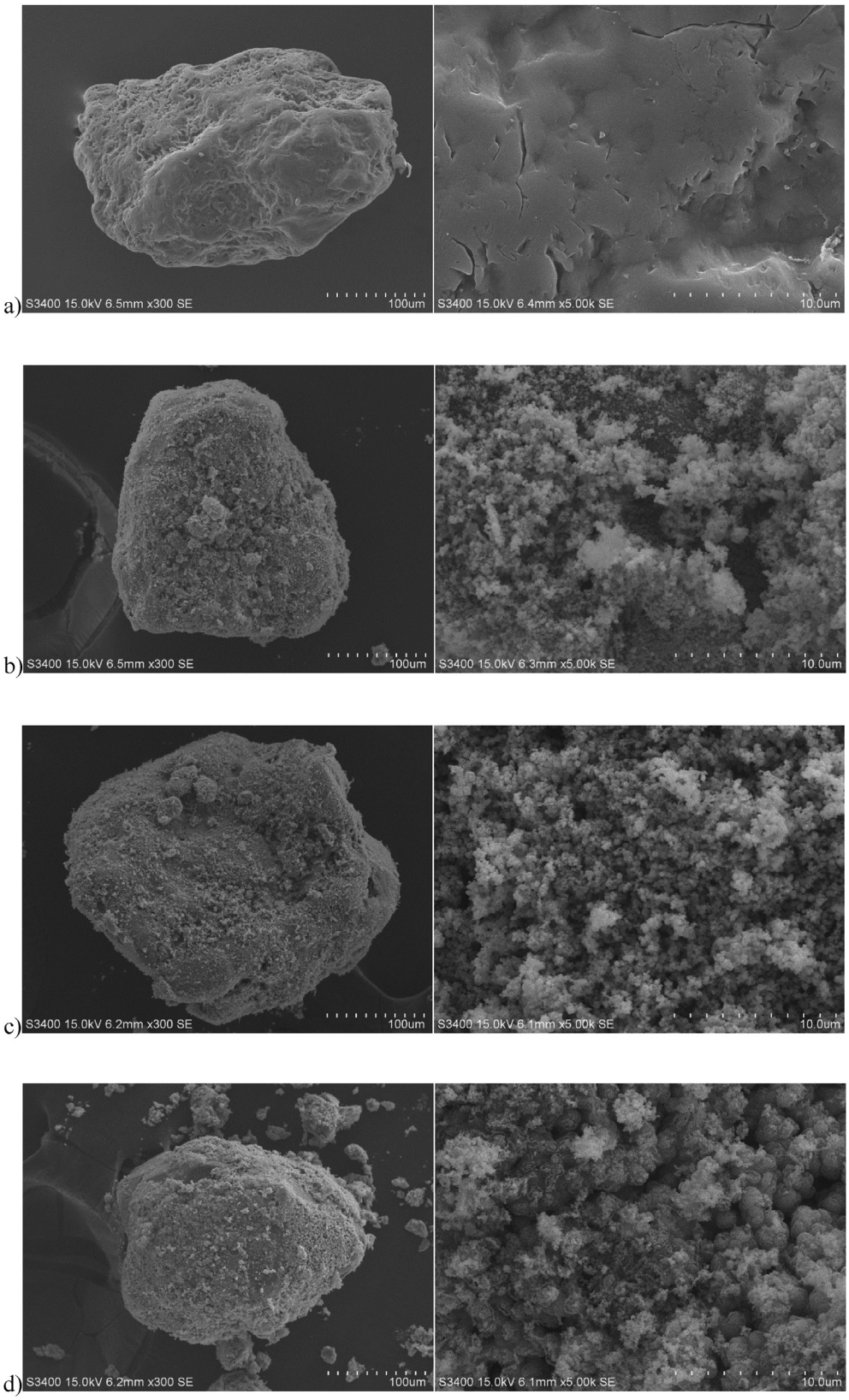

Fig. 4 – SEM images of fresh catalysts: a) SiO_2, b) 5% Ni/SiO_2, c) 10% Ni/SiO_2 and d) 15% Ni/SiO_2.

Please cite this article in press as: Kraisornkachit P, et al., Experimental study of dual fixed bed biochar-catalytic gasification with simultaneous feed of O_2-steam-CO_2 for synthesis gas or hydrogen production, International Journal of Hydrogen Energy (2018), https://doi.org/10.1016/j.ijhydene.2018.06.054

bio-charcoal provide the physical and elemental data of the sample, and the high heating value [46] was also calculated as displayed in Table 2.

Catalysts characterization

The fresh catalysts (Ni/SiO_2) with Ni loadings of 5, 10 and 15% by weight were characterized by XRD. The results are illustrated in Fig. 2. According to Taufiq-Yap et al. [30] and Wang et al. [44], the 2θ angles of 37.2°, 43.3° and 62.9° correspond to nickel oxide, which can be observed on the XRD spectra of all the catalysts tested in this study.

The apparent surface area of catalysts was also investigated using BET surface area measurements, also providing a measure of the number of SiO_2 active sites. Increasing the Ni loading led to a decrease in the apparent surface area of the SiO_2 as shown in Table 3. The SiO_2 support was measured to have the highest apparent surface area (5.47 m^2/g). The value decreases with increasing loading of nickel on support and the lowest surface area (2.2 m^2/g) was obtained for a 15% Ni loading by weight. This apparent trend in surface area with Ni loading is attributed to a decrease in the number of SiO_2 active sites.

The optimal reduction conditions were determined using the H_2-TPR method, the results of which are shown in Fig. 3. Major peaks were observed at 300 and 400 °C, similar to results reported by Taufiq-Yap et al. [30] and Wang et al. [44]. Based on the H_2-TPR results, 400 °C was used as the reducing temperature in the next study.

The physical morphology of fresh catalysts was observed by SEM analysis, images of which are shown in Fig. 4. These results support the analysis of the BET measurements, indicating a decrease in the number of active sites with increasing Ni loading on the catalyst.

Experimental studies

Effect of temperature

To find out suitable operating temperatures, the uncatalyzed reaction of biochar was studied at various temperatures (400, 600 and 800 °C) and the product gas compositions, carbon conversion and gas yields were reported. This test involved reacting 1 g of biochar with feed gas, using gas to biochar carbon mole ratios O_2:S:CO_2:C of 1:2:2:2, without catalyst. Fig. 5a shows the product gas compositions (excluding CO_2 and H_2O) indicating that higher operating temperatures led to more CO but less H_2 in the gas product stream, because of the endothermic boudouard reaction (*BD*) and reverse water gas shift (rWGS) reaction. However, higher operating temperatures lead to an increase in *CGE* and *EF*. The highest *CGE* was observed at 800 °C as a result of the higher product gas yields, as indicated by the *EF* parameter, hence more CO was also

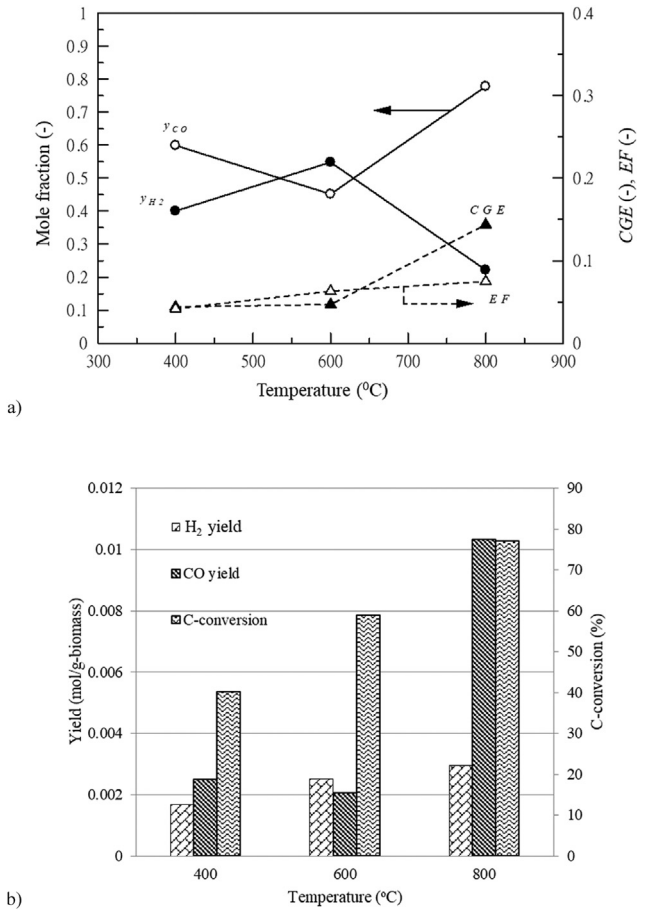

Fig. 5 – Effect of operating temperature on a) product gas composition, CGE and EF b) product gas yield and carbon conversion.

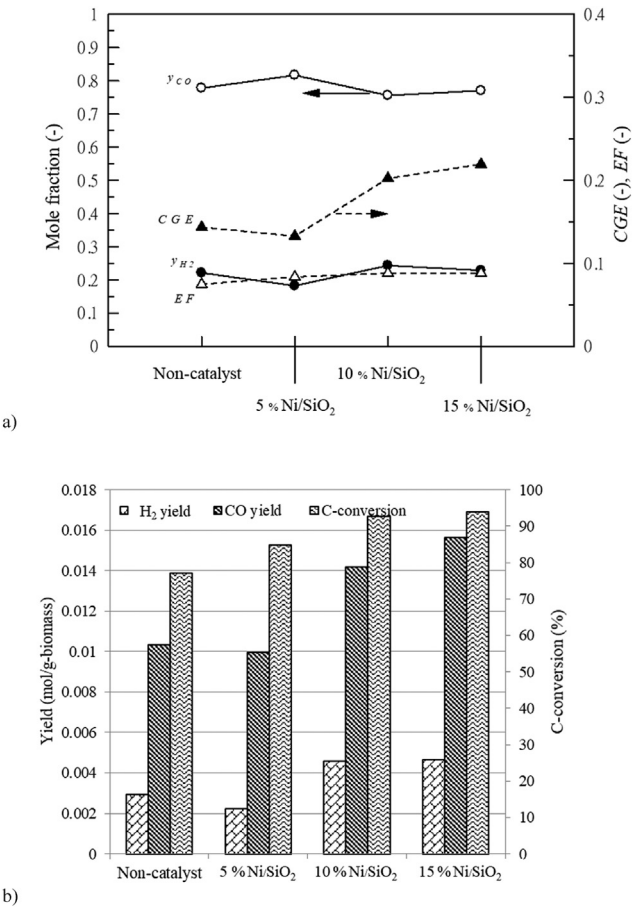

Fig. 6 – Effect of catalysts on a) product gas composition, CGE and EF b) product gas yield and carbon conversion.

Please cite this article in press as: Kraisornkachit P, et al., Experimental study of dual fixed bed biochar-catalytic gasification with simultaneous feed of O_2-steam-CO_2 for synthesis gas or hydrogen production, International Journal of Hydrogen Energy (2018), https://doi.org/10.1016/j.ijhydene.2018.06.054

produced. In addition, the carbon conversion and product gas yield were also investigated, the results of which are shown in Fig. 5b. Increasing temperatures led to higher carbon conversions, reaching a maximum value of 77% at 800 °C, compared to results reported by Kael et al. [45] who achieved a carbon conversion of 100% at temperatures above 800 °C. Despite the difference in the observed carbon conversions, this supports the observed increase in *CGE* and *EF* with increasing temperatures up to 800 °C. Moreover, increasing temperatures also led to a slight increase in H_2 yield and intensely rising CO yields. Based on these results, 800 °C was used as the operating temperature in the next study.

Effect of catalysts

The effect of Ni loading on the performance of the catalyst was investigated, with Ni loadings of 5, 10 and 15% by weight having been tested, the results of which are shown in Fig. 6. The O_2:S:CO_2:C feed mole ratio and temperature were fixed at 1:2:2:2 and 800 °C, respectively for this investigation. With increasing Ni catalyst loading the H_2 and CO compositions in the product gas also increased as shown in Fig. 6a. The increase in H_2 can be explained by the increased conversion of char and tar from biochar in the presence of more catalyst, and this is supported by results reported by Huang et al. [22]. In the view of performance, *CGE* increased with increasing Ni loading because of greater product gas yields. However, for Ni loadings of 10 and 15% by weight there was insignificant change in *CGE*. The results also show an increase in *EF* with increasing Ni loading because of greater CO_2 yields. From Fig. 6b it can be observed that with increasing Ni loading by weight, the syngas product yield as shown by H_2 and CO yields can confirm the reason of increasing *CGE* with Ni% loading by weight. The carbon conversion initially increased with increasing Ni loading but then showed insignificant change with an increase in loading from 10% to 15% by weight. Therefore, from the findings above the 10% by weight of Ni/SiO_2 was chosen as the suitable catalyst.

Effect of O_2/C feed ratio

The effect of O_2 on the process was investigated, with the results shown in Fig. 7. The reactions were carried out using a 10% Ni loading by weight, a temperature of 800 °C and a S:CO_2:C feed mole ratio of 1:1:1. The absence of O_2 led to slightly higher H_2 yields, but lower CO yields than those obtained in the presence of O_2 in the feed stream, as shown in Fig. 7a. The presence of O_2 promoted the partial oxidation (*PO*) and combustion reactions, hence resulting in the formation of CO and CO_2. This is supported by an increase in *EF* with the O_2:C mole ratio increasing from 0 to 1:2. However, the presence of O_2 had no effect on the *CGE* which remained unchanged. Fig. 7b shows that with O_2 present in the feed

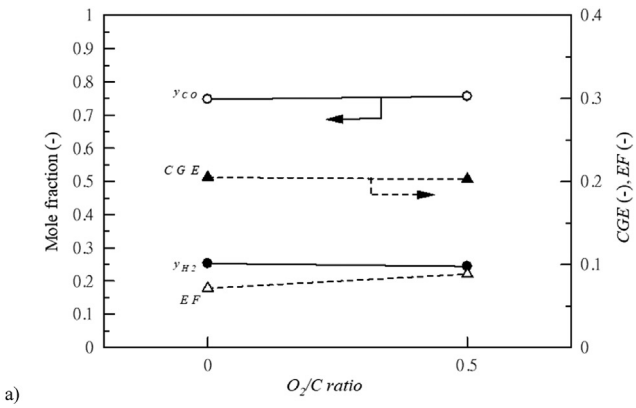

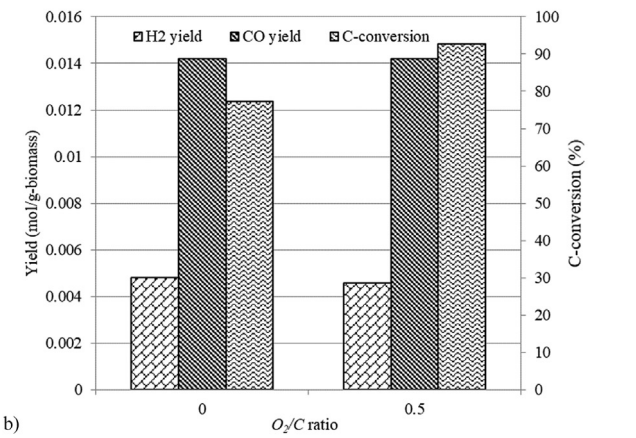

Fig. 7 – Effect of O_2/C ratio on a) product gas composition, CGE and EF b) product gas yield and carbon conversion.

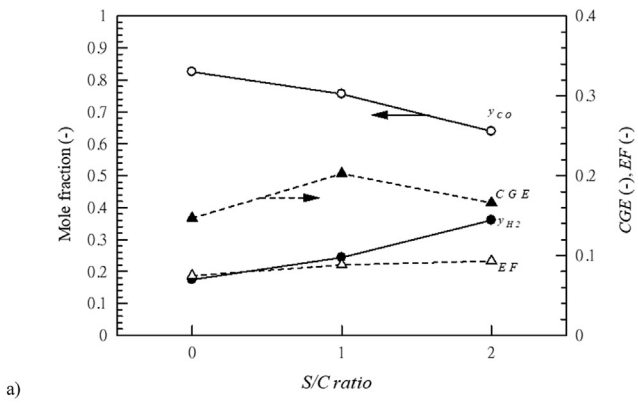

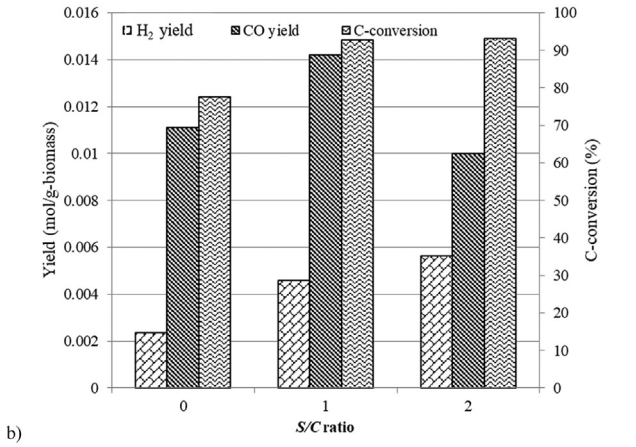

Fig. 8 – Effect of S/C ratio on a) product gas composition, CGE and EF and b) product gas yield and carbon conversion.

Please cite this article in press as: Kraisornkachit P, et al., Experimental study of dual fixed bed biochar-catalytic gasification with simultaneous feed of O_2-steam-CO_2 for synthesis gas or hydrogen production, International Journal of Hydrogen Energy (2018), https://doi.org/10.1016/j.ijhydene.2018.06.054

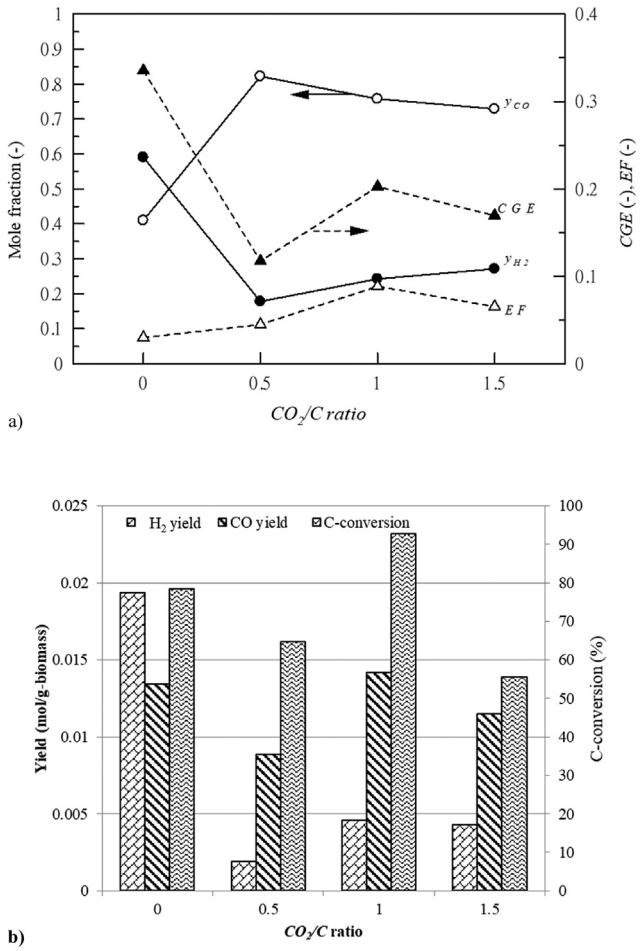

Fig. 9 – Effect of CO_2/C ratio on a) product gas composition, CGE and EF and b) product gas yield and carbon conversion.

stream, the carbon conversion reached a value of 92%. Nevertheless, the syngas yield only changed slightly as shown in Fig. 7a. It should be noted that supplying O_2 as a reaction agent also offers a benefit in terms of energy demands due to the supply of energy from the exothermic partial oxidation (PO) and combustion reactions.

Effect of S/C feed ratio

The effect of the S:C feed ratio was investigated at a temperature of 800 °C, with a 10% Ni loading by weight and 1:2:2 O_2:CO_2:C feed mole ratio. It can be observed that increasing the S:C feed ratio led to an increase in H_2 but a decrease in CO of gas product as illustrated in Fig. 8a. This trend is supported by results reported by Gile-Lalaguna et al. [21] and Wang et al. [47], moreover, increasing the partial pressure of steam in the feed gas can also upgrade the heating value of the syngas product [21]. Increasing concentrations of steam promoted the forward steam reforming (SR) and water gas shift (WGS) reactions, resulting in an increase in the H_2 content [47]. However, the CGE increased with an increase in the S:C mole ratio from of 0–1:1 but decreased for S:C mole ratios greater than 1:1 as a result of excess steam, diluting the CO in the product gas stream. The EF representing the amount of CO_2 produced, increased slightly with an increase in the S/C mole ratio, due to a promotion of the forward water gas shift (WGS) reaction. In Fig. 8b, it is shown that increasing amounts of steam led to an increase in the product gas yield and carbon conversion, but a S:C mole ratio of 2:1 led to lower CO concentrations due to the water gas shift reaction (WGS), supporting the observed decrease in CGE with an increase in S:C mole ratio from 1:1 to 2:1. However, increasing the S:C mole ratio from 1:1 to 2:1 also led to a slight increase in carbon conversion.

Table 4 – Summary of operating conditions.

Parameters	Symbol	y_{H2} (–)	y_{CO} (–)	CGE (–)	EF (–)	Carbon conversion (%)	H_2 yield (mol/g-biomass)	CO yield (mol/g-biomass)	H_2/CO (–)	Operating conditions
Temperature										
400 °C	A	0.4007	0.5993	0.0440	0.0419	40.13	0.0017	0.0025	0.6686	O_2/S/CO_2/C = 0.5/1/1/1
600 °C	B	0.5483	0.4517	0.0469	0.0631	58.90	0.0025	0.0021	1.2140	Non-catalyst
800 °C	C	0.2219	0.7781	0.1436	0.0749	77.03	0.0029	0.0103	0.2851	
% Ni loading										
Non-catalyst	D	0.2219	0.7781	0.1436	0.0749	77.03	0.0029	0.0103	0.2851	O_2/S/CO_2/C = 0.5/1/1/1
5%	E	0.1830	0.8170	0.1330	0.0838	84.76	0.0022	0.0100	0.2240	800 °C
10%	F	0.2439	0.7561	0.2026	0.0883	92.66	0.0046	0.0142	0.3225	
15%	G	0.2294	0.7706	0.2194	0.0884	94.01	0.0047	0.0156	0.2976	
Feed ratio										
O_2/C										S/CO_2/C = 1/1/1
0	H	0.2527	0.7473	0.2048	0.0712	77.20	0.0048	0.0142	0.3381	10% Ni/SiO_2
0.5	F	0.2439	0.7561	0.2026	0.0883	92.66	0.0046	0.0142	0.3225	800 °C
S/C										
0	I	0.1745	0.8255	0.1469	0.0747	77.56	0.0023	0.0111	0.2114	O_2/CO_2/C = 0.5/1/1
1	F	0.2439	0.7561	0.2026	0.0883	92.66	0.0046	0.0142	0.3225	10% Ni/SiO_2
2	J	0.3609	0.6391	0.1660	0.0930	93.11	0.0056	0.0100	0.5648	800 °C
CO_2/C										
0	K	0.5903	0.4097	0.3354	0.0299	78.36	0.0194	0.0134	1.4407	O_2/S/C = 0.5/1/1
0.5	L	0.1778	0.8222	0.1174	0.0448	64.62	0.0019	0.0089	0.2163	10% Ni/SiO_2
1	F	0.2439	0.7561	0.2026	0.0883	92.66	0.0046	0.0142	0.3225	800 °C
1.5	M	0.2711	0.7289	0.1695	0.0652	55.48	0.0043	0.0115	0.3719	

Please cite this article in press as: Kraisornkachit P, et al., Experimental study of dual fixed bed biochar-catalytic gasification with simultaneous feed of O_2-steam-CO_2 for synthesis gas or hydrogen production, International Journal of Hydrogen Energy (2018), https://doi.org/10.1016/j.ijhydene.2018.06.054

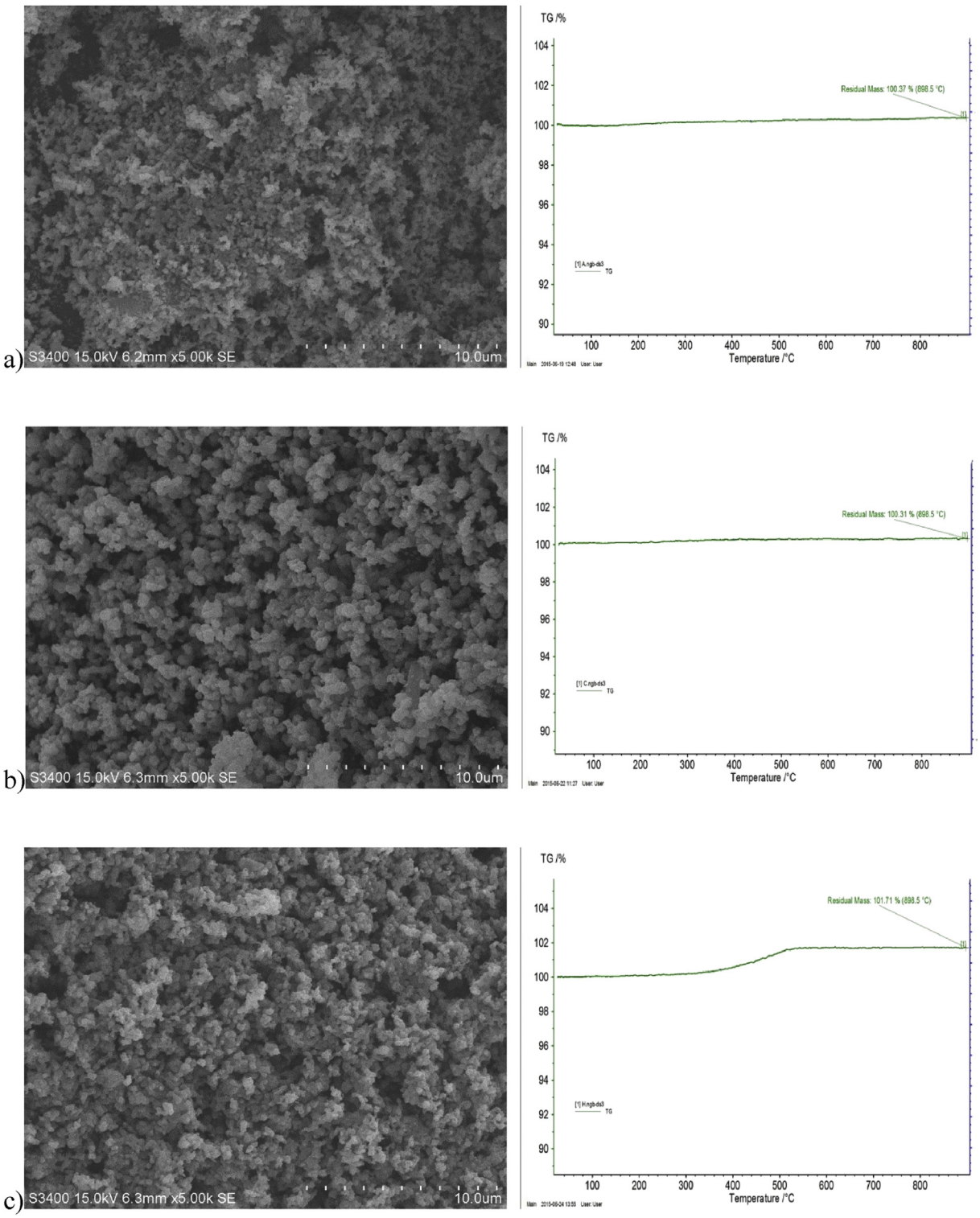

Fig. 10 – SEM images and TGA results of used catalysts on various conditions listed by symbol a) E, b) F, c) G, d) H, e) I, f) J, g) K, h) L and i) M.

Effect of CO_2/C feed ratio

To evaluate the effect of the *CO_2/C ratio*, conditions were maintained at a temperature of 800 °C, a Ni loading of 10% by weight and a S/C feed mole ratio 1:2. The results presented in Fig. 9a, show that the H_2 composition reached a maximum when the CO composition was the lowest, in the absence of CO_2, promoting the forward reaction of the steam reforming (*SR*) and methane reforming (*MR*) reactions. This is supported by the results of Kael et al. [45]. However, an increase in the *CO_2/C* feed mole ratio led to a slight drop in CO and a slight rise in the H_2 concentration due to a promotion of the forward CO_2 reforming (*CR*) reaction. In terms of *CGE*, in the absence of CO_2 the highest

Please cite this article in press as: Kraisornkachit P, et al., Experimental study of dual fixed bed biochar-catalytic gasification with simultaneous feed of O_2-steam-CO_2 for synthesis gas or hydrogen production, International Journal of Hydrogen Energy (2018), https://doi.org/10.1016/j.ijhydene.2018.06.054

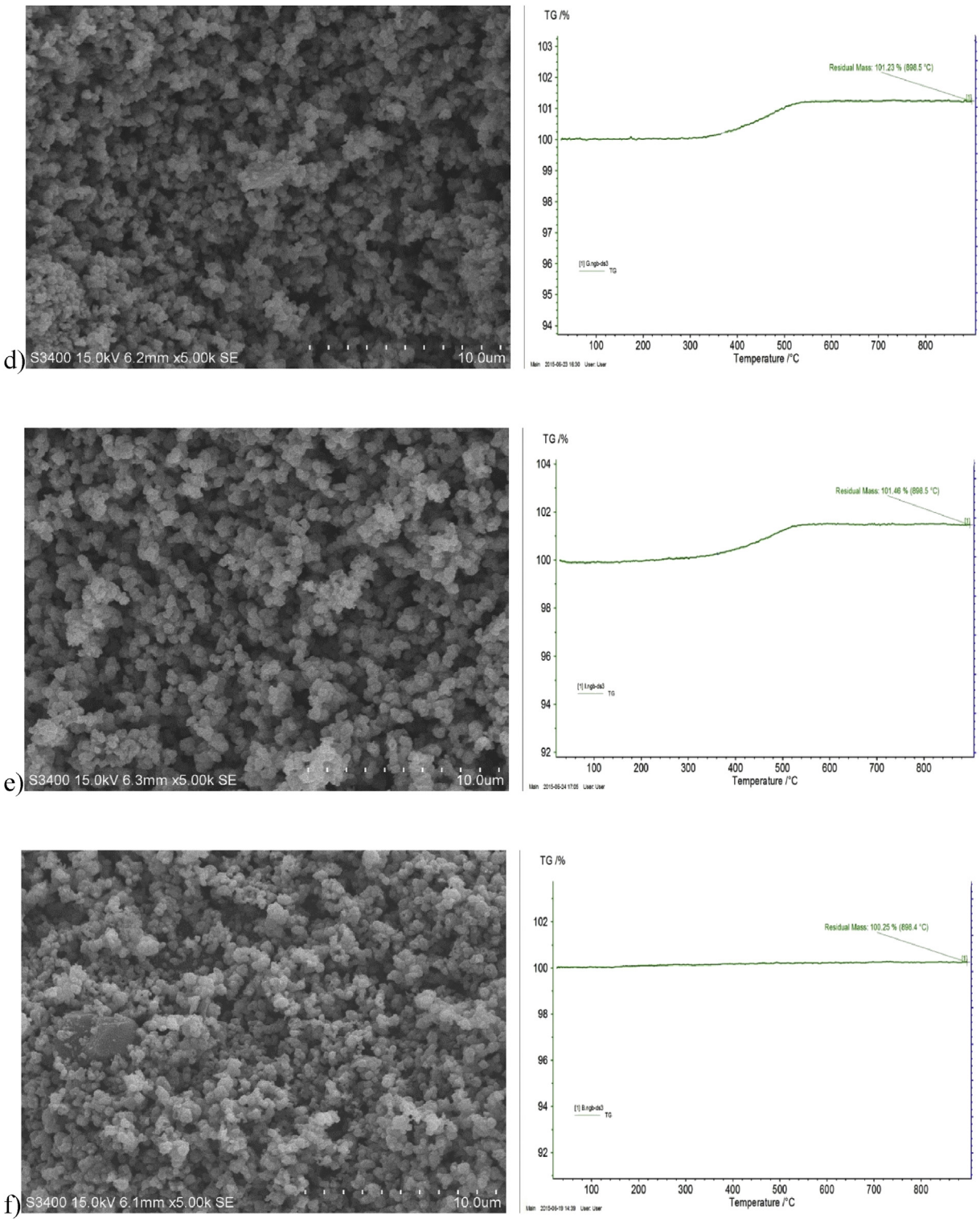

Fig. 10 – *(continued)*.

CGE was obtained as a result of the high syngas yields. The results show the *CGE* to then decline with increasing CO_2/C feed ratios due to the low syngas yields as illustrated in Fig. 9b. The *EF* also slightly increased with increasing CO_2/C feed ratio due to the higher CO_2 concentrations. Changes in the carbon conversion (Fig. 9b) were most significant when increasing the CO_2/C feed mole ratio from 0 to 3:2 except for a mole ratio 1:1, however, the CO_2/C mole ratio of 1:1 offered the highest of carbon conversion indicating the highest syngas yield.

Table 4 summarises the various test conditions and the corresponding C/O and C/H mole ratios, syngas compositions, H_2/CO mole ratios, *CGE* and *EF* values. Subscripts A to M are used for easier identification of each set of conditions. By varying the O_2/C mole ratio from 0 to 0.5 and S/C mole ratio

Please cite this article in press as: Kraisornkachit P, et al., Experimental study of dual fixed bed biochar-catalytic gasification with simultaneous feed of O_2-steam-CO_2 for synthesis gas or hydrogen production, International Journal of Hydrogen Energy (2018), https://doi.org/10.1016/j.ijhydene.2018.06.054

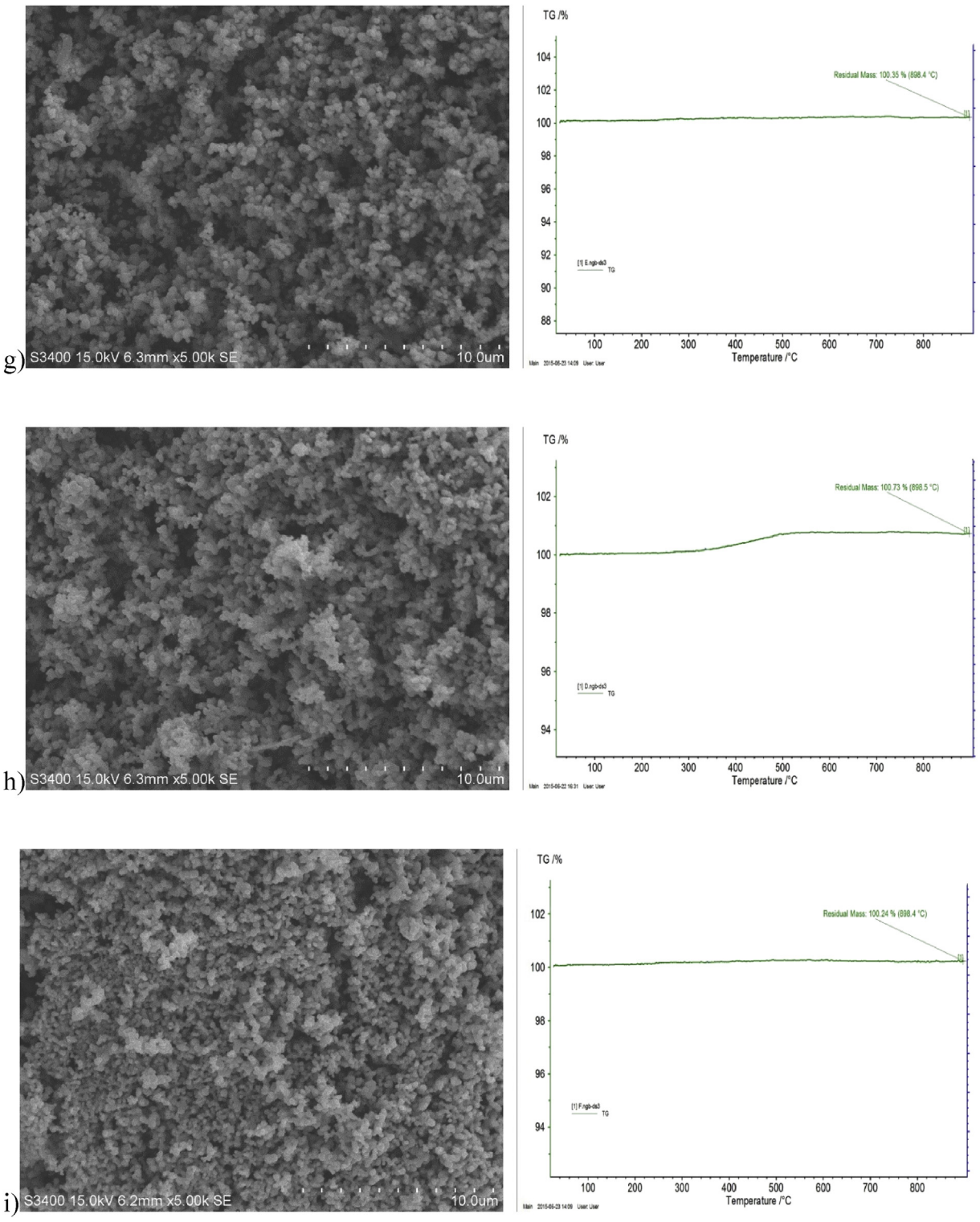

Fig. 10 – *(continued)*.

from 0 to 2, the obtained H_2/CO mole ratio was varied through a small range of 0.2114–0.5648. However, the H_2/CO mole ratio can be varied through a wide range from 0.2163 to 1.4407 by adjusting CO_2/C mole feed ratio. Therefore, using CO_2 as a reaction agent did not only reduce the CO_2 emission but also offered the benefit of a wider available range of H_2/CO ratios available for the syngas product.

Used catalysts characterization

Coke deposition on the catalysts was investigated by the analysis of SEM images. The SEM images are shown in Fig. 10, which indicate no coke deposition took place on the catalysts. The TGA results also show no weight loss of the used catalysts. However, it should be noted that in some cases an

Please cite this article in press as: Kraisornkachit P, et al., Experimental study of dual fixed bed biochar-catalytic gasification with simultaneous feed of O_2-steam-CO_2 for synthesis gas or hydrogen production, International Journal of Hydrogen Energy (2018), https://doi.org/10.1016/j.ijhydene.2018.06.054

increase in weight was observed. This is likely due to the presence of Ni metal in the used catalysts which could be converted to NiO via the TGA tests.

Conclusions

Experiments involving the dual fixed bed catalytic gasification of biochar using a O_2-steam-CO_2 gas feed for syngas production was conducted in this study. It was found that increasing the operating temperature to 800 °C results in a higher syngas yield, carbon conversion, *CGE* and *EF*. The use of a 10% Ni/SiO_2 catalyst improves the performance of a syngas production process as indicated by the increasing *CGE*. Oxygen had an insignificant effect on the gas product, however, increasing the amount of steam in the feed led to a higher H_2 yield. Utilization of carbon dioxide has the added benefit of acting as a H_2/CO mole ratio adjusting agent. Coke deposition was not observed on any of the studied catalysts as indicated by the SEM results.

Acknowledgment

The support from The Thailand Research Fund (DPG5880003) is gratefully acknowledged.

REFERENCES

[1] McKendry P. Energy production from biomass (part 1) overview of biomass. Bioresour Technol 2002;83:37–46.
[2] Vamvuka D, Pitharoulis M, Alevizos G, Repouskou E, Pentari D. Ash effects during combustion of lignite/biomass blends in fluidized bed. Renew Energy 2009;34:2662–71.
[3] Koppatz S, Pfeifer C, Hofbauer H. Comparison of the performance behaviour of silica sand and olivine in a dual fluidised bed reactor system for steam gasification of biomass at pilot plant scale. Chem Eng J 2011;175:468–83.
[4] International Energy Agency (IEA). Key World Energy Statistics. 1st ed. [ebook] p.6. 2017. Available at, https://www.iea.org/publications/freepublications/publication/KeyWorld2017.pdf [Accessed 28 Jun. 2018].
[5] Cau G, Cocco D, Serra F. Energy and cost analysis of small-size integrated coal gasification and syngas storage power plants. Energy Convers Manag 2012;56:121–9.
[6] Giuffrida A, Romano MC, Lozza G. Thermodynamic analysis of air-blown gasification for IGCC applications. Appl Energy 2011;88:3949–58.
[7] Cormos C-C. Assessment of hydrogen and electricity co-production schemes based on gasification process with carbon capture and storage. Int J Hydrogen Energy 2009;34:6065–77.
[8] van Vliet OPR, Faaij APC, Turkenburg WC. Fischer–Tropsch diesel production in a well-to-wheel perspective: a carbon, energy flow and cost analysis. Energy Convers Manag 2009;50:855–76.
[9] Ma W, Jacobs G, Sparks DE, Pendyala VRR, Hopps SG, Thomas GA, et al. Fischer–Tropsch synthesis: effect of ammonia in syngas on the Fischer–Tropsch synthesis performance of a precipitated iron catalyst. J Catal 2015;326:149–60.
[10] Li TS, Xu M, Gao C, Wang B, Liu X, Li B, et al. Investigation into the effects of sulfur on syngas reforming inside a solid oxide fuel cell. J Power Sources 2014;258:1–4.
[11] Khine MSS, Chen L, Zhang S, Lin J, Jiang SP. Syngas production by catalytic partial oxidation of methane over (La0.7A0.3)BO3 (A = Ba, Ca, Mg, Sr, and B = Cr or Fe) perovskite oxides for portable fuel cell applications. Int J Hydrogen Energy 2013;38:13300–8.
[12] Hackett GA, Gerdes K, Song X, Chen Y, Shutthanandan V, Engelhard M, et al. Performance of solid oxide fuel cells operated with coal syngas provided directly from a gasification process. J Power Sources 2012;214:142–52.
[13] Lopez L, Velasco J, Cabrera S, Boutonnet M, Järås S. Effect of syngas conversion and catalyst reduction temperature in the synthesis of ethanol: concentration of water vapor in mesoporous Rh/MCM-41 catalyst. Catal Commun 2015;69:183–7.
[14] Subramani V, Gangwal KS. A review of recent literature to search for an efficient catalytic process for the conversion of syngas to ethanol. Energy Fuels 2008;22:814–39.
[15] Olah GA, Goeppert A, Czaun M, Prakash GK. Bi-reforming of methane from any source with steam and carbon dioxide exclusively to metgas (CO-2H2) for methanol and hydrocarbon synthesis. J Am Chem Soc 2013;135:648–50.
[16] Schuster G, Loffler G, Weigl K, Hofbauer H. Biomass steam gasification - an extensive parametric modeling study. Bioresour Technol 2001;77:71–9.
[17] Cheng G, He P-w, Xiao B, Hu Z-q, Liu S-m, Zhang L-g, et al. Gasification of biomass micron fuel with oxygen-enriched air: thermogravimetric analysis and gasification in a cyclone furnace. Energy 2012;43:329–33.
[18] Heidi CB, Marco JC. CO_2 as a carbon neutral fuel source via enhanced biomass gasification. Environ Sci Technol 2009;43:9030–7.
[19] Mani T, Mahinpey N, Murugan P. Reaction kinetics and mass transfer studies of biomass char gasification with CO_2. Chem Eng Sci 2011;66:36–41.
[20] Chaiwatanodom P, Vivanpatarakij S, Assabumrungrat S. Thermodynamic analysis of biomass gasification with CO_2 recycle for synthesis gas production. Appl Energy 2014;114:10–7.
[21] Gil-Lalaguna N, Sánchez JL, Murillo MB, Rodríguez E, Gea G. Air–steam gasification of sewage sludge in a fluidized bed. Influence of some operating conditions. Chem Eng J 2014;248:373–82.
[22] Huang BS, Chen HY, Chuang K-H, Yang RX, Wey MY. Hydrogen production by biomass gasification in a fluidized-bed reactor promoted by an Fe/CaO catalyst. Int J Hydrogen Energy 2012;37:6511–8.
[23] Miccio F, Piriou B, Ruoppolo G, Chirone R. Biomass gasification in a catalytic fluidized reactor with beds of different materials. Chem Eng J 2009;154:369–74.
[24] Tomishige K, Asadullah M, Kunimori K. Syngas production by biomass gasification using Rh/CeO_2/SiO_2 catalysts and fluidized bed reactor. Catal Today 2004;89:389–403.
[25] Di Carlo A, Borello D, Sisinni M, Savuto E, Venturini P, Bocci E, et al. Reforming of tar contained in a raw fuel gas from biomass gasification using nickel-mayenite catalyst. Int J Hydrogen Energy 2015;40:9088–95.
[26] Wang D, Yuan W, Ji W. Char and char-supported nickel catalysts for secondary syngas cleanup and conditioning. Appl Energy 2011;88:1656–63.
[27] Corella J, Orio A, Toledo J-M. Biomass gasification with air in a fluidized bed exhaustive tar elimination with commercial steam reforming catalysts. Energy Fuels 1999;13:702–9.
[28] Karim GA, Metwally MM. A kinetic investigation of the reforming of natural gas for the production of hydrogen. Int J Hydrogen Energy 1980;5:293–304.

Please cite this article in press as: Kraisornkachit P, et al., Experimental study of dual fixed bed biochar-catalytic gasification with simultaneous feed of O_2-steam-CO_2 for synthesis gas or hydrogen production, International Journal of Hydrogen Energy (2018), https://doi.org/10.1016/j.ijhydene.2018.06.054

[29] Seyedeyn Azad F, Abedi J, Salehi E, Harding T. Production of hydrogen via steam reforming of bio-oil over Ni-based catalysts: effect of support. Chem Eng J 2012;180:145–50.
[30] Taufiq-Yap YH, Sudarno, Rashid U, Zainal Z. CeO2–SiO2 supported nickel catalysts for dry reforming of methane toward syngas production. Appl Catal A – Gen 2013;468:359–69.
[31] Vicente J, Ereña J, Montero C, Azkoiti MJ, Bilbao J, Gayubo AG. Reaction pathway for ethanol steam reforming on a Ni/SiO_2 catalyst including coke formation. Int J Hydrogen Energy 2014;39:18820–34.
[32] Bednarczuk L, Ramírez de la Piscina P, Homs N. H2-production from CO_2-assisted ethanol steam reforming: the regeneration of Ni-based catalysts. Int J Hydrogen Energy 2015;40:5256–63.
[33] Wu C, Williams PT. Hydrogen production by steam gasification of polypropylene with various nickel catalysts. Appl Catal B Environ 2009;87:152–61.
[34] Wu C, Wang Z, Huang J, Williams PT. Pyrolysis/gasification of cellulose, hemicellulose and lignin for hydrogen production in the presence of various nickel-based catalysts. Fuel 2013;106:697–706.
[35] Gao N, Li A, Quan C, Gao F. Hydrogen-rich gas production from biomass steam gasification in an updraft fixed-bed gasifier combined with a porous ceramic reformer. Int J Hydrogen Energy 2008;33:5430–8.
[36] Dou B, Wang K, Jiang B, Song Y, Zhanga C, Chen H, et al. Fluidized-bed gasification combined continuous sorption-enhanced steam reforming system to continuous hydrogen production from waste plastic. Int J Hydrogen Energy 2016;41:3803–10.
[37] Zhang Q, Liu H, Zhang X, Lu G, Wang J, Hu H, et al. Effect of Fe/Ca-based composite conditioners on syngas production during different sludge gasification stages: devolatilization, volatiles homogeneous reforming and heterogeneous catalyzing. Int J Hydrogen Energy 2017;42:29150–8.
[38] Hiblot H, Ziegler-Devin I, Fournet R, Glaude PA. Steam reforming of methane in a synthesis gas from biomass gasification. Int J Hydrogen Energy 2016;41:18329–38.
[39] Leimert JM, Karl J. Nickel membranes for in-situ hydrogen separation in high-temperature fluidized bed gasification processes. Int J Hydrogen Energy 2016;41:9355–66.
[40] Vairakannu P, Kumari G. CO2-Oxy underground coal gasification integrated proton exchange membrane fuel cell operating in a chemical looping mode of reforming. Int J Hydrogen Energy 2016;41:20063–77.
[41] Gujar AC, Baik J, Garceau N, Muradov N, T-Raissi A. Oxygen-blown gasification of pine charcoal in a top-lit downdraft moving-hearth gasifier. Fuel 2014;118:27–32.
[42] Moghtaderi B. Effects of controlling parameters on production of hydrogen by catalytic steam gasification of biomass at low temperatures. Fuel 2007;86:2422–30.
[43] Channiwala SA, Parikh PP. A unified correlation for estimating HHV of solid, liquid and gaseous fuels. Fuel 2002;81:1051–63.
[44] Wang Y, Wu R, Zhao Y. Effect of ZrO_2 promoter on structure and catalytic activity of the Ni/SiO_2 catalyst for CO methanation in hydrogen-rich gases. Catal Today 2010;158:470–4.
[45] Kale GR, Kulkarni BD, Chavan RN. Combined gasification of lignite coal: thermodynamic and application study. J Taiwan Inst Chem Eng 2014;45:163–73.
[46] Lv PM, Xiong ZH, Chang J, Wu CZ, Chen Y, Zhu JX. An experimental study on biomass air-steam gasification in a fluidized bed. Bioresour Technol 2004;95:95–101.
[47] Wang X, Wang N, Zhao J, Wang L. Thermodynamic analysis of propane dry and steam reforming for synthesis gas or hydrogen production. Int J Hydrogen Energy 2010;35:12800–7.

Nomenclature

ΔH_r^0: Heat of reaction at standard condition 298 K (MJ/kmol)
O_2/C: Mole of O_2 as reaction agent per mole of carbon in biochar (–)
S/C: Mole of steam as reaction agent per mole of carbon in biochar (–)
CO_2/C: Mole of CO_2 as reaction agent per mole of carbon in biochar (–)
y_{H2}: Mole fraction of H_2 in product gas (–)
y_{CO}: Mole fraction of CO in product gas (–)
y_{CO2}: Mole fraction of CO_2 in product gas (–)
y_{CH4}: Mole fraction of CH_4 in product gas (–)
M: Mass flow rate (kg/h)
M_H: Mass flow rate of atomic hydrogen in biomass (kg/h)
L_{298}: Latent heat of vaporization of water at standard condition 298 K (MJ/kg)
n_i: Molar flow rate of ith component in syngas product (kmol/h)
$H_{i,298}^0$: Heat of combustion of ith component in syngas product (MJ/kmol)
x_C, x_H, x_O: Mass fraction of carbon, hydrogen and oxygen in biochar (–)
EF: Efficiency factor (–)

Abbreviations

CGE: Cold gas efficiency (–)
BD: Boudouard reaction
PO: Partial oxidation
SR: Steam reforming
MF: Methane formation
CR: CO_2 reforming
MR: Methane reforming
WGS: Water gas shift
rWGS: Reverse water gas shift
LHV: Lower heating value (MJ/kg)
HHV: Higher heating value (MJ/kg)

Please cite this article in press as: Kraisornkachit P, et al., Experimental study of dual fixed bed biochar-catalytic gasification with simultaneous feed of O_2-steam-CO_2 for synthesis gas or hydrogen production, International Journal of Hydrogen Energy (2018), https://doi.org/10.1016/j.ijhydene.2018.06.054

INTERNATIONAL JOURNAL OF HYDROGEN ENERGY XXX (2018) 1–15

Available online at www.sciencedirect.com

ScienceDirect

journal homepage: www.elsevier.com/locate/he

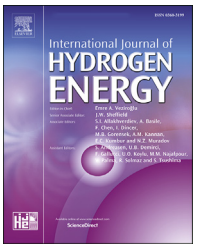

Synthetic CaO-based sorbent for high-temperature CO_2 capture in sorption-enhanced hydrogen production

Piya Pecharaumporn [a], *Suwimol Wongsakulphasatch* [b,*], *Thongchai Glinrun* [c], *Atthaphon Maneedaeng* [d], *Zulkafli Hassan* [e], *Suttichai Assabumrungrat* [a]

[a] *Center of Excellence in Catalysis and Catalytic Reaction Engineering, Department of Chemical Engineering, Faculty of Engineering, Chulalongkorn University, Bangkok, 10330, Thailand*

[b] *Department of Chemical Engineering, Faculty of Engineering, King Mongkut's University of Technology North Bangkok, Bangkok, 10800, Thailand*

[c] *Department of Petrochemical and Environmental Engineering, Faculty of Engineering, Pathumwan Institute of Technology, Bangkok, 10330, Thailand*

[d] *School of Chemical Engineering, Institute of Engineering, Suranaree University of Technology, Nakhon Ratchasima, 30000, Thailand*

[e] *Faculty of Chemical and Natural Resources Engineering, Universiti Malaysia Pahang, Lebuhraya, Tun Razak, 26300, Gambang, Kuantan, Pahang, Malaysia*

ARTICLE INFO

Article history:
Received 22 April 2018
Received in revised form
20 June 2018
Accepted 25 June 2018
Available online xxx

Keywords:
Alumina-containing CaO-based sorbent
High-temperature CO_2 capture
Sorption-enhanced steam methane reforming
H_2 production

ABSTRACT

Calcium precursor and surfactant addition on properties of synthetic alumina-containing CaO-based for CO_2 capture and for sorption-enhanced steam methane reforming process (SE-SMR) were investigated. Results showed that the sorbent derived from calcium D-gluconic acid (CG-AN) offered CO_2 sorption capacity of 0.38 g CO_2/g sorbent, which is greater than 0.17 g CO_2/g sorbent of the sorbent derived from calcium nitrate (CN-AN). Addition of CTAB surfactant during synthesis was found to enhance CO_2 sorption capacity for CG-AN but not for CN-AN sorbents. Stability tests of the modified sorbents for 10 cycles showed that CG-AN-CTAB provided higher CO_2 sorption capacity than CN-AN-CTAB for each corresponding cycle. Incorporation of CG-AN with Ni catalyst (Ni-CG-AN) using wet-mixing technique offered the longest pre-breakthrough period of 60 min for average maximum H_2 purity of 88% at 600 °C and a steam/methane molar ratio of 3.

© 2018 Hydrogen Energy Publications LLC. Published by Elsevier Ltd. All rights reserved.

* *Corresponding author.*
E-mail address: suwimol.w@eng.kmutnb.ac.th (S. Wongsakulphasatch).

https://doi.org/10.1016/j.ijhydene.2018.06.153

0360-3199/© 2018 Hydrogen Energy Publications LLC. Published by Elsevier Ltd. All rights reserved.

Please cite this article in press as: Pecharaumporn P, et al., Synthetic CaO-based sorbent for high-temperature CO_2 capture in sorption-enhanced hydrogen production, International Journal of Hydrogen Energy (2018), https://doi.org/10.1016/j.ijhydene.2018.06.153

Introduction

The demand of hydrogen is expected to continuously increase as hydrogen is considered as an ideal energy carrier [1]. It is also an important feedstock in various chemical and petroleum industries such as the production of ammonia, methanol, or refining of crude oil, etc. [2–4] At present, reforming process has been developed to use in industrial scale such as partial oxidation, dry reforming, or steam reforming, etc. Among these, steam methane reforming process (SMR) has widely been applied to produce hydrogen as this process offers high hydrogen to carbon monoxide ratio and low cost when compared to other technologies [5–8]. However, the process suffers from multi-step operation, high energy requirement, and catalyst deactivation due to severe operating conditions [1,9,10]. To minimize such disadvantages, the concept of process intensification, the combination of reaction and separation process, named "sorption-enhanced steam methane reforming (SESMR)", has been developed and received increased attention [3,11–14]. The SESMR is operated based on Le Chatelier's principle, of which the conversion of reactants to products and the rate of forward reaction can be increased by selectively removing some of the reaction products [15]. As a consequence, by employing this concept, the limitations of conventional SMR process can be diminished; less severe operating conditions can be operated and energy efficiency can be improved as exothermic heat of adsorption could compensate to endothermic heat of reforming reaction. The process allows for the lower capital and operating costs [16,17]. In addition, it is interesting to note that, the ETP BLUE map scenario has indicated that with the use of this integrated technology, energy-related emissions of CO_2 can be reduced up to 50% by 2500 compared to the level reported in 2005 [18].

One of key techniques to improve overall performances of SESMR process is the use of appropriate sorbent and catalyst. A development is the combination of an adsorbent with a catalyst into one-body. The concept of this material is to use the catalyst to speed up the reaction while the sorbent functions to selectively capture CO_2, providing high H_2 purity in a single step as steam reforming, water-gas shift, and carbon dioxide removal can occur simultaneously. Catalyst used for SESMR should resist coke formation by steam reforming, be inactive for side-reactions, maintain the activity at high temperature, and have high mechanical strength as well as good heat transfer properties [19]. Different types of metal oxide, e.g., platinum, nickel, rhodium, gold, etc., have been applied for SESMR process. Among these, nickel oxide has been extensively proved to be suitably used for SESMR due to its good conversion rate of methane and low cost [20–25]. Sorbent applied for SESMR should possess high sorption capacity, fast sorption/desorption kinetics, high thermal and mechanical stability [26]. CaO has been widely used as sorbent for CO_2 capture in SESMR because CaO can capture CO_2 at high temperature, where the reaction of SESMR occurs, with high sorption kinetics and sorption capacity. However, loss-in-capacity problem upon multi-cycle uses due to sintering effect is the drawback of this material [27].

Different performances for SESMR are found to be varied depending upon type and amount of catalyst or sorbent as well as operating condition. For example, Martavaltzi et al. [28] developed a hybrid material by combining sorbent with catalyst for SESMR using Ni-CaO-$Ca_{12}Al_{14}O_{33}$. The results showed that 16% of Ni on the hybrid catalytic sorbent showed 90% H_2 yield at 650 °C and a steam to carbon ratio of 3.4. Kim et al. [1] studied the use of one-body catalytic sorbent, which was composed of CaO, $Ca_{12}Al_{14}O_{33}$ and 7% wt Ni-metallic, for SESMR process operated at 630 °C, atmospheric pressure and a steam to carbon ratio of 3. The results showed that the one-body catalytic sorbent was observed to be very stable and maintained at ca. 94–95% H_2 during sorption enhanced period of around 70 min. Radfarnia and Iliuta [29] developed Al-stabilized CaO-nickel hybrid sorbent-catalyst using wet-mixing method with various nickel loadings, including 12, 18, and 25%wt. The hybrid catalytic sorbent with 25%wt NiO loading offered the best performance for H_2 production, of which average CH_4 conversion and H_2 production efficiency of 99.1% and 96.1%, respectively, can be obtained at 650 °C and a steam to carbon ratio of 4. Xu et al. [30] investigated the performance of bi-functional catalysts Ni/CaO-Al_2O_3 prepared by sol-gel method with different CaO/Al_2O_3 mass ratios on SESMR process. The results showed that the bi-functional catalysts containing CaO/Al_2O_3 mass ratio of 6 or 8 showed H_2 production of 87% for 50 consecutive SESMR runs at 650 °C, 0.1 MPa, and H_2O/CH_4 molar ratio = 2. This result was claimed to be due to high surface area, small Ni particle size, and uniform distribution of Ni, CaO, and $Ca_5Al_{16}O_{14}$. Zhao et al. [31] investigated the performance of Ni/CaO-$CaZrO_3$ bi-functional catalysts on SESMR process. By varying amount of Ni loading and CaO content, the results showed that Ni:CaO:$CaZrO_3$ = 15:60.3:24.7 (%wt) provided the best SESMR performance in terms of activity and stability; 96% H_2 could be obtained for pre-breakthrough period and 73% for post-breakthrough period.

Although the development of one-body hybrid catalytic sorbent has been carried out by several researchers; however, such development is still a challenging task as an appropriate combination of catalyst and sorbent should be considered in order to satisfy the condition where both sorption and reaction conditions of the overall integrated process can be carried out in a single step. In this work, we are interested in improving properties of CaO-based sorbent for high-temperature CO_2 capture and found in sorption-enhanced steam methane reforming process. Properties of CaO-based sorbent have been shown to depend on synthesis method [32], calcium precursor [33], additives [34], synthesis temperature [34], stirring rate [34], etc. Among these, the effect of calcium precursor and the addition of surfactant are subjects of investigation in this study as these two parameters have been found to affect morphologies, crystal structure, and porosities of precipitated calcium carbonate significantly [34–36]. The performances of our synthetic alumina-containing CaO-based sorbents were investigated for high-temperature CO_2 sorption in terms of sorption capacity and sorbent re-usability. Then, one-body catalyst/sorbent materials were synthesized and tested for H_2 production via SESMR process.

Please cite this article in press as: Pecharaumporn P, et al., Synthetic CaO-based sorbent for high-temperature CO_2 capture in sorption-enhanced hydrogen production, International Journal of Hydrogen Energy (2018), https://doi.org/10.1016/j.ijhydene.2018.06.153

Materials and method

Materials

Calcium D-gluconic acid ($C_{12}H_{22}CaO_{14}$ 99%), calcium nitrate tetrahydrate ($Ca(NO_3)_2 \cdot 4H_2O$ 99%), aluminum nitrate nonahydrate precursor ($Al(NO_3)_3 \cdot 9H_2O$) and 2-propanol were used to synthesize CaO-based sorbent. Nickel nitrate hexahydrate ($Ni(NO_3)_2 \cdot 6H_2O$) was used as catalyst precursor. Commercial calcium oxide (CaO) purchased from Riedel-deHaen and commercial alumina (Al_2O_3) purchased from Sigma Aldrich were used as commercial sorbent and support, respectively, for comparison purpose. Cationic surfactant, cetyltrimethylammoniumbromide (CTAB), was used to modify properties of CaO-based sorbent.

Synthesis of alumina-containing CaO-based sorbent

In this work, alumina-containing CaO-based sorbents were synthesized by wet-mixing method with the use of two different precursors: calcium nitrate tetrahydrate and calcium D-gluconic acid. The sorbents synthesized from calcium nitrate tetrahydrate were designated as CN-AN and those synthesized from calcium D-gluconic acid were designated as CG-AN. All sorbents were synthesized with pre-determined controlled composition of $CaO:Ca_{12}Al_{14}O_{33}$ equal to 70:30 %wt.

For CN-AN, 27.6 g of calcium nitrate tetrahydrate and 7.11 g of aluminum nitrate nonahydrate were added into a 190-ml de-ionized water, which were mixed with 32.5 ml of 2-propanol. The solution was continuously stirred at 75 °C for 1 h and then allowed to dry at 120 °C in an oven for 18 h. The obtained powder was collected from the oven and calcined at 500 °C for 3 h in air. Distilled water was later added into the resulting powder and then dried at 120 °C for 2 h and calcined at 900 °C for 1.5 h in air to produce $CaO\text{-}Ca_{12}Al_{14}O_{33}$. The same procedure was conducted for CG-AN with the use of 21.5 g of calcium D-gluconic acid instead of calcium nitrate tetrahydrate and 3 g of aluminum nitrate nonahydrate.

Synthesis of alumina-containing CaO-based sorbent modified by surfactant

Firstly, the desired concentration of CTAB surfactant, being 1, 3, 5, 7 or 10 mM, corresponding to 0.082, 0.246, 0.410, 0.574 or 0.820 g, respectively, was added into 190-mL de-ionized water mixed with 32.5 mL of 2-propanol. The solution was stirred at room temperature until CTAB was totally dissolved. Then, 3 g of aluminum nitrate nonahydrate and 21.5 g of calcium D-gluconic acid were added into the solution. After that, the solution was heated up to 75 °C and continuously stirred for 1 h and then allowed to dry at 120 °C in an oven for 18 h. The powder was collected from the oven and calcined at 500 °C for 3 h in air. Distilled water was added into the resulting powder and then dried at 120 °C for 2 h, followed by calcination at 900 °C for 1.5 h in air. The obtained powder was named as CG-AN-CTAB XX mM. The same method was applied for calcium nitrate precursor CN-AN-CTAB XX mM with the use of 27.6 g of calcium nitrate tetrahydrate and 7.11 g of aluminum nitrate nonahydrate.

Synthesis of one-body catalyst/sorbent material

To synthesize one-body material, Ni was incorporated with alumina-containing CaO-based sorbent by wetness impregnation method. In this work, 12.5%wt of Ni was desired to use as catalyst for SESMR followed Chanburanasiri et al. [22] To prepare the material, 12.5%wt-nickel nitrate hexahydrate ($Ni(NO_3)_2.6H_2O$) was firstly dissolved in 75 ml of de-ionized water. After that, the 2-g synthetic alumina-containing CaO-based sorbent was added into nickel solution. Then, the sample was stirred for 30 min at 100 °C, dried at 100 °C overnight, and calcined at 900 °C for 1.5 h in air. The resulting material was designated as Ni-CG-AN or Ni-CN-AN in case of using alumina-containing CaO-based sorbent without surfactant modification and as Ni-CG-AN-CTAB or Ni-CN-AN-CTAB in case of using alumina-containing CaO-based sorbent with surfactant modification.

To gain an insight into the role of CaO-based alumina sorbent on hydrogen production, the effect of synthesis method of CaO-based sorbent were investigated. Simplified sol-mixing method was selected to compare with wet-mixing. For sol-mixing technique, firstly, calcined calcium D-gluconic acid ($C_{12}H_{22}CaO_{14}$) (at 900 °C, 1.5 h) and aluminum nitrate nonahydrate were added into the 190-ml de-ionized water mixed with 32.5 ml of 2-propanol solution. The mixture solution was continuously stirred at 75 °C for 1 h and then allowed to dry at 120 °C in an oven for 18 h. The powder was collected from the oven and calcined at 500 °C for 3 h in air. Distilled water was added to the resulting powder to form a paste which was then dried at 120 °C for 2 h and calcined at 900 °C for 1.5 h in air. To combine with Ni, 12.5%wt -nickel nitrate hexahydrate ($Ni(NO_3)_2.6H_2O$) was firstly dissolved in 75 ml of de-ionized water. After that, the 2-g synthetic alumina-containing CaO-based sorbent was added into nickel solution. Then, the sample was stirred for 30 min at 100 °C, dried at 100 °C overnight, and calcined at 900 °C for 1.5 h in air. The resulting material was designated as Ni-CG-AN sol-mixing.

Characterization of synthetic materials

Crystallinity of the synthetic materials was characterized by X-ray powder diffraction (XRD), which was determined by D8 Advance of Bruker AXS using Cu Kα radiation ($\lambda = 1.5406$ Å). The pattern was recorded for 2θ ranging from 10 to 80° with an increasing step of 0.04° and a scan speed of 0.5 min^{-1}. Surface texture of the material was measured by N_2 adsorption/desorption technique using Micromeritics Chemisorp 2750. The sample was degassed at 200 °C for 3 h prior to conducting the measurement at −196 °C. The results of N_2 isotherms was used to estimate surface area with the use of BET (Brunauer-Emmett-Teller) method. Total pore volume was estimated from the amount of N_2 adsorbed at relative pressure of 0.99. Pore diameter and pore size distribution of the sample was examined by the BJH (Barrett-Joyner-Hallenda) method [37,38]. Morphology of the samples was detected by scanning electron microscope, SEM (JEOL JSM 6360 LV).

Please cite this article in press as: Pecharaumporn P, et al., Synthetic CaO-based sorbent for high-temperature CO_2 capture in sorption-enhanced hydrogen production, International Journal of Hydrogen Energy (2018), https://doi.org/10.1016/j.ijhydene.2018.06.153

Sorption and SESMR performance tests

In this work, performances of the synthetic alumina-containing CaO-based sorbent on CO_2 sorption and of the one-body catalyst/sorbent on the production of H_2 via SESMR process were conducted using a fixed-bed reactor. Quartz tube with ID = 10 mm, OD = 12 mm, and length = 500 mm was used as the fixed-bed reactor. For CO_2 sorption test, sorbent was packed in the reactor, which was supported by quartz wool. Before conducting CO_2 sorption experiment, the sorbent was pretreated by purging 50-mL/min pure N_2 at 850 °C for 1 h. Then, CO_2 sorption test was carried out by switching the gas to 10 mL/min CO_2 flow (15% v/v, balanced N_2) and reducing the temperature to the desired CO_2 sorption temperature of 600 °C. The sorption duration was carried out until full capacity of the sorbent, which was observed by CO_2 concentration at the outlet equals to that at the inlet. An amount of CO_2 sorption capacity was measured by a mass spectrometer. Multiple cycles of sorption/desorption were repeated in order to test the ability to retain CO_2 sorption capacity. The desorption test was conducted by purging 50 mL/min of pure N_2 at 850 °C for 0.5 h.

CO_2 sorption capacity was calculated from breakthrough curves using the following equation [39]:

$$CO_2 \text{ sorption capacity } \left(g_{CO_2}/g_{sorbent}\right) = \frac{\left[F_{CO_2,in} \times \int_0^t \left(1 - A \cdot \frac{C_{CO_2,out}}{C_{CO_2,in}}\right) dt\right]}{W} \quad (1)$$

where F_{CO_2} is feed flow rate of CO_2 (g min^{-1}), $C_{CO_2,in}$ and $C_{CO_2,out}$ are concentrations of CO_2 at the inlet and outlet of the reactor (%), respectively, t is sorption time (min), W is weight of the sorbent (g), A is calculated from

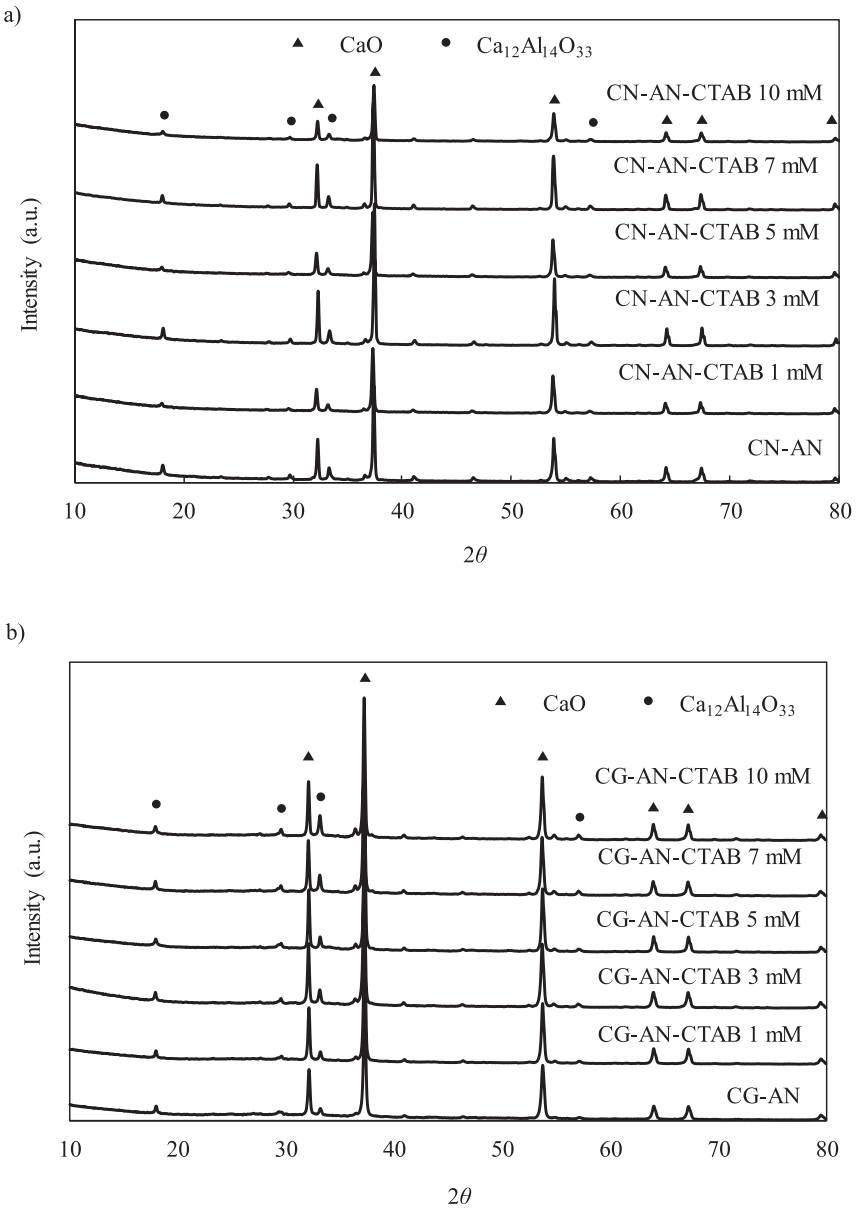

Fig. 1 – XRD patterns of modified sorbents by different concentrations of CTAB; a) CN-AN and b) CG-AN.

Please cite this article in press as: Pecharaumporn P, et al., Synthetic CaO-based sorbent for high-temperature CO_2 capture in sorption-enhanced hydrogen production, International Journal of Hydrogen Energy (2018), https://doi.org/10.1016/j.ijhydene.2018.06.153

$$A = \frac{\upsilon_{N_2}}{\upsilon_{total,in}} \cdot \left(1 + \frac{y_{CO_2}}{\left(1 - y_{CO_2}\right)}\right) \quad (2)$$

where υ_{N_2} is volumetric flow rate of N_2 (ml min^{-1}), $\upsilon_{total,in}$ is total volumetric flow rate of feed stream (ml min^{-1}), y_{CO_2} is volume fraction of CO_2 in the outlet stream.

SESMR was conducted by packing one-body catalyst/sorbent material in the same reactor as carried out with the CO_2 sorption test. Before running the reaction test, the one-body catalyst/sorbent was pretreated at 850 °C for 1 h with N_2 (30 mL/min) and the catalyst sites were reduced in a flow of H_2/N_2 (50% H_2) at 850 °C for 1 h. A 10-mL/min CH_4 was fed into the reactor with the co-flow N_2 of 20 mL/min and steam of 30 mL/min, which would yield the steam-to-methane ratio of 3. In our experiments, the inlet steam was generated by heating liquid water at 150 °C, which was controlled by wrapped thermotape along the injection pipe. The reaction was conducted isothermally at 600 °C under atmospheric pressure. Product compositions were analyzed by gas chromatography (GC-8A, Shimadzu) equipped with a thermal conductivity detector (TCD) using molecular sieve 5A and Parapak-Q packed column. The performances of one-body catalyst/sorbent were examined in terms of CH_4 conversion and product compositions. The conversion of CH_4 is defined as:

$$CH_4 \text{ conversion } (\%) = \frac{\left(F_{CH_{4,in}} - F_{CH_{4,out}}\right)}{F_{CH_{4,in}}} \times 100 \quad (3)$$

where $F_{CH_{4,in}}$ and $F_{CH_{4,out}}$ are molar flow rates of methane at the inlet and the outlet, respectively.

Results and discussions

Effect of calcium precursor and surfactant addition on CaO-based alumina sorbents for CO_2 capture

XRD patterns of modified alumina-containing CaO-based sorbents synthesized by using different precursors and CTAB concentrations are shown in Fig. 1. Typical diffraction peaks assigned to CaO at $2\theta = 28.2, 32.3, 37.4, 53.8, 64.3, 67.6$ and 79.1°

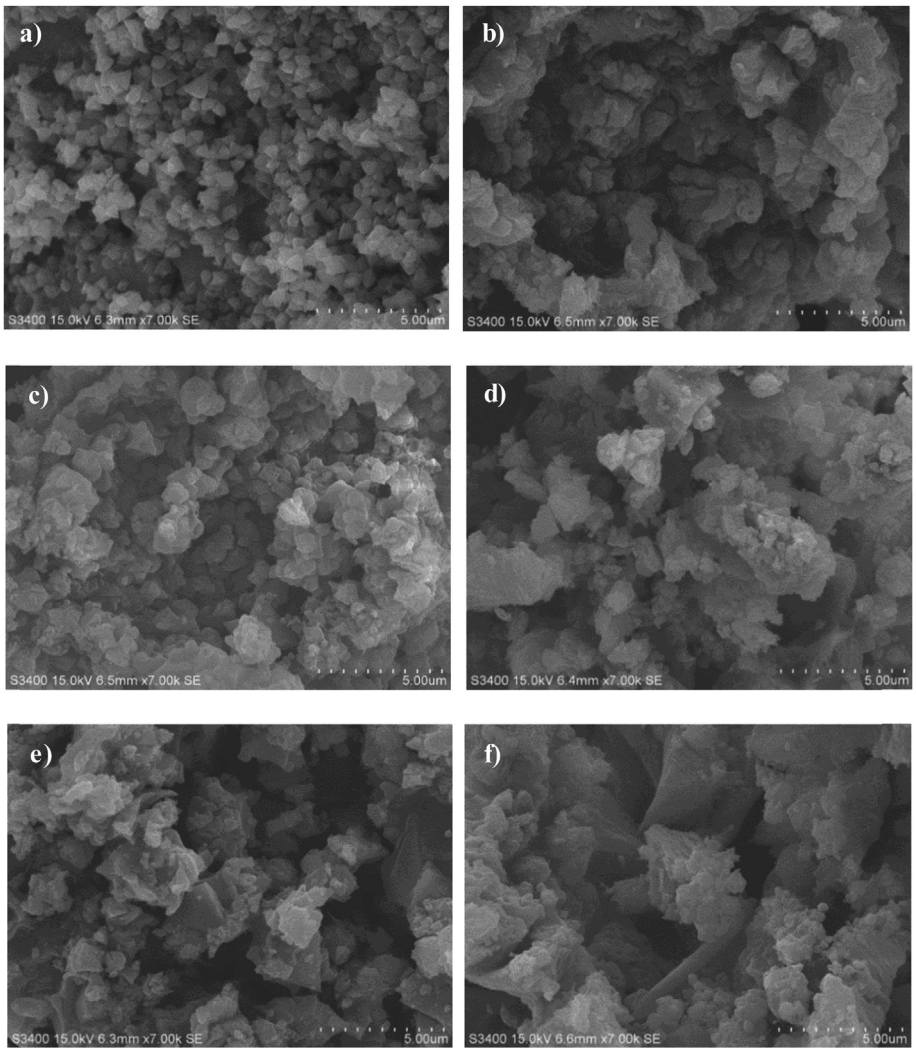

Fig. 2 – SEM images of CN-AN sorbents modified by adding different CTAB concentrations; a) CN-AN without CTAB and b) CN-AN-CTAB 1 mM c) CN-AN-CTAB 3 mM d) CN-AN-CTAB 5 mM e) CN-AN-CTAB 7 mM and f) CN-AN-CTAB 10 mM.

Please cite this article in press as: Pecharaumporn P, et al., Synthetic CaO-based sorbent for high-temperature CO_2 capture in sorption-enhanced hydrogen production, International Journal of Hydrogen Energy (2018), https://doi.org/10.1016/j.ijhydene.2018.06.153

and those of $Ca_{12}Al_{14}O_{33}$ inert support at 2θ of 18, 30, 34 and 57°, are observed for all CN-AN and CG-AN samples investigated here, which is in good agreement with those reported by Cesário et al. [32] and Zhou et al. [33].

Morphologies of CN-AN and CG-AN photographed by SEM are shown in Figs. 2a and 3a, respectively. CN-AN shows uniform distribution of octahedral particles, whereas connected small rounded particles are observed with CG-AN. Particle size of CN-AN is larger than CG-AN; CN-AN has particle size of 0.5 μm in average whereas particle size of CG-AN is 0.3 μm in average. The smaller particle size observed with CG-AN could be attributed to the impurity D-gluconic acid ($C_6H_{12}O_7^{2-}$) is larger than nitrate (NO_3^-); the larger molecular size could obstruct the interaction between calcium and oxygen or calcium and alumina, resulting in weak interaction between such molecules during precipitation and leading to the formation of loosely packing of precipitated particles CaO-$Ca_{12}Al_{14}O_{33}$ (see Fig. 4).

Larger particle size with larger void between particles was observed when CTAB was added into the CN-AN; 1 μm for CN-AN-CTAB 1–5 mM and 3 μm for CN-AN-CTAB 7–10 mM. In contrast, particle size of CG-AN-CTAB sorbents remain unchanged but larger void between particles is observed (see Figs. 2b–f and 3b–f, respectively). The void between particles, which makes the sorbent to be structured with pore, is a result of structure directing by CTAB micelles as shown by the proposed mechanism pictured in Fig. 4. The micelles of CTAB in the solution hindered the interaction between precipitated solids during precipitation; when precipitated solids are washed or heated during calcination, the micelles are removed from the system and left spaces between particles. Increasing CTAB concentration leads to larger void space. This result could be because a number of pore generated by CTAB micelles combined into a single large void space when a number of micelles are increased in the system as shown in Fig. 4b and d [40]. Comparison between CN-AN-CTAB and CG-AN-CTAB for each corresponding CTAB concentration, the results show that CN-AN-CTAB sorbents possess lower BET surface area and pore volume than those of CG-AN-CTAB sorbents, whereas, pore diameter of CN-AN-CTAB sorbents

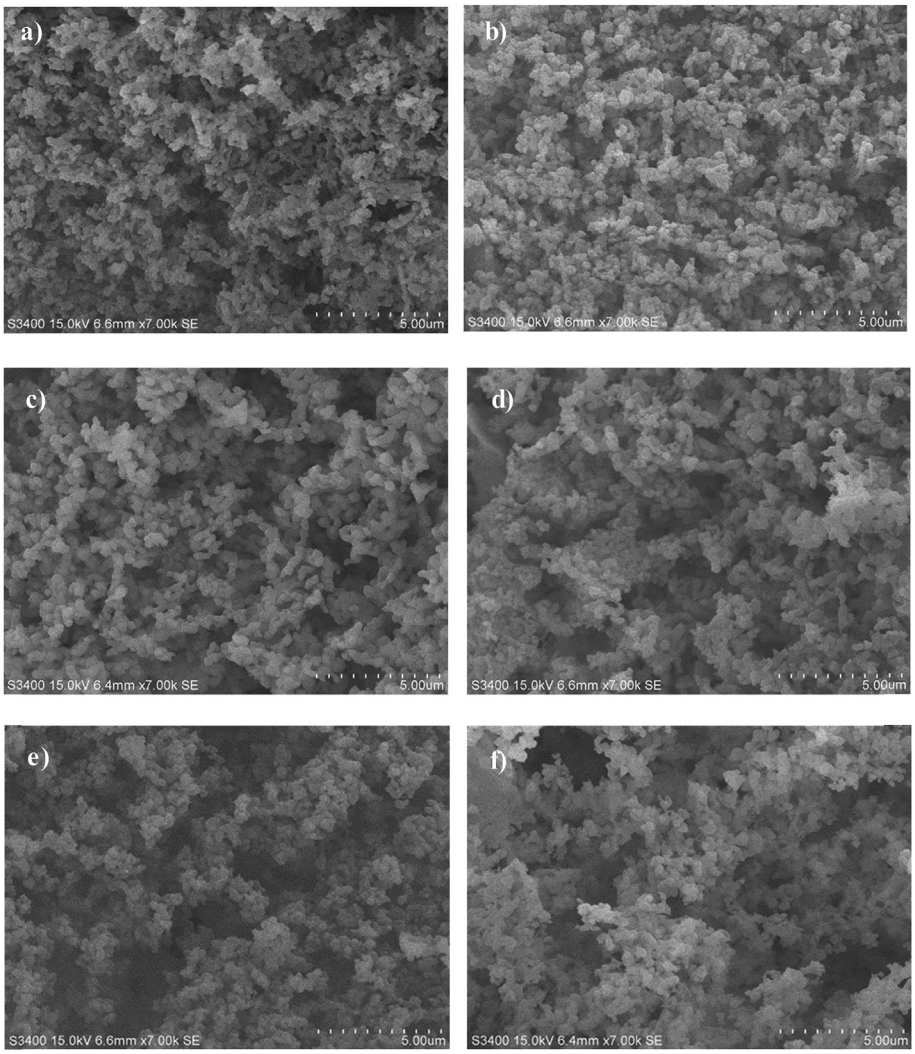

Fig. 3 – SEM images of CG-AN sorbents modified by adding different CTAB concentrations; a) CG-AN without CTAB and b) CG-AN-CTAB 1 mM c) CG-AN-CTAB 3 mM d) CG-AN-CTAB 5 mM e) CG-AN-CTAB 7 mM and f) CG-AN-CTAB 10 mM.

Please cite this article in press as: Pecharaumporn P, et al., Synthetic CaO-based sorbent for high-temperature CO_2 capture in sorption-enhanced hydrogen production, International Journal of Hydrogen Energy (2018), https://doi.org/10.1016/j.ijhydene.2018.06.153

are larger than those of CG-AN-CTAB sorbents. This could probably be due to the effect of molecular structure of calcium precursor; calcium nitrate precursor has smaller molecular size than that of calcium D-gluconic acid, short range interaction would occur for the case of calcium nitrate, leading to dense packing of particles after calcination as evidenced by SEM images depicted in Figs. 2 and 3.

Amount of CO_2 sorption capacity of all CN-AN sorbents are provided in Fig. 5a. The results show that all sorbents provide similar CO_2 sorption capacity of ca. 0.2 g CO_2/g sorbent. This could be due to similar surface texture of all sorbents (Table 1), leading to comparative CO_2 sorption capacity. For the case of CG-AN sorbents (Fig. 5b), higher CO_2 sorption capacity is observed with CG-AN-CTAB when compared to those of CN-

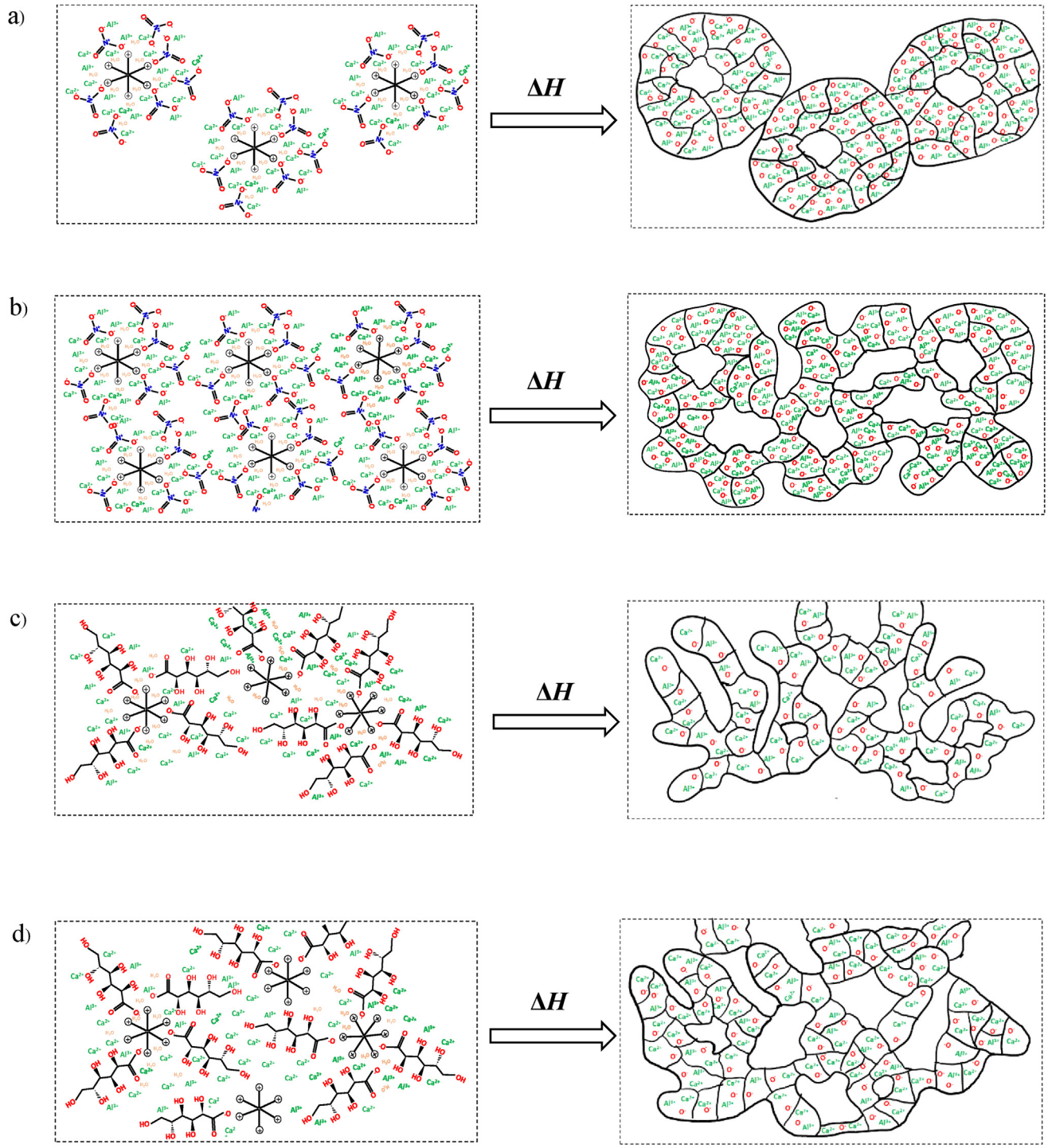

Fig. 4 – Proposed mechanisms of CaO-based sorbent formation for a) CN-AN-CTAB at low CTAB concentration, b) CN-AN-CTAB at high CTAB concentration, c) CG-AN-CTAB at low CTAB concentration, d) CG-AN-CTAB at high CTAB concentration.

Please cite this article in press as: Pecharaumporn P, et al., Synthetic CaO-based sorbent for high-temperature CO_2 capture in sorption-enhanced hydrogen production, International Journal of Hydrogen Energy (2018), https://doi.org/10.1016/j.ijhydene.2018.06.153

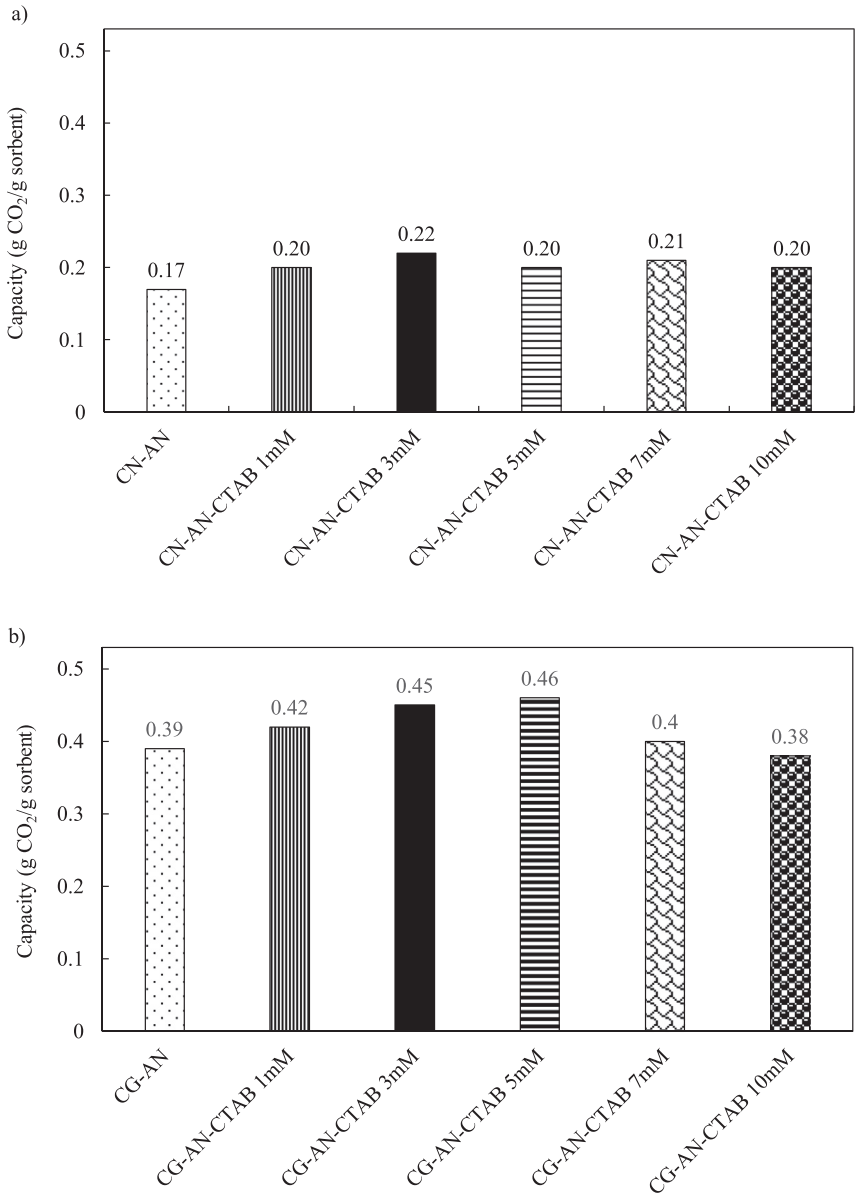

Fig. 5 – CO_2 sorption capacity of a) CN-AN and b) CG-AN sorbents with and without modification by adding CTAB. Sorption condition: atmospheric pressure, sorption temperature = 600 °C, 15%v/v CO_2 (N_2 balanced).

AN-CTAB. This could be attributed to higher surface area and smaller interconnected particle size of the sorbent. When CTAB concentration is increased from 1 mM to 5 mM, CO_2 sorption capacity increases from 0.42 to 0.46 g CO_2/g sorbent and then the sorption capacity declines to 0.38 g CO_2/g sorbent when CTAB concentration is further increased to 10 mM. The increase of sorption capacity at low concentration of CTAB could be attributed to an enhancement of active surface CaO due to void space generated by CTAB micelles and small particle size of the sorbent as discussed previously, whereas the reduction of sorption capacity at higher CTAB concentration could be due to sintering effect. Compared to other solid sorbents, such as Li_4SiO_4 [41], Li_8ZrO_6 [42], Li_2ZrO_3 [42], hydrotalcite [43], or Na_2ZrO_3 [44], etc., as shown in Table 2, our results show that alumina-containing CaO-based sorbents offer good performance on high-temperature CO_2 capture.

Although sorption capacity is an important factor on determining performance of the sorbent; however, for industrial applications, re-usability of the material is another essential property that is needed to be considered. In this study, stability of the synthetic alumina-containing CaO-based sorbents were investigated using CN-AN-CTAB 3 mM and CG-AN-CTAB 3 mM as the previous results showed that these sorbents provide good performance on CO_2 sorption

Please cite this article in press as: Pecharaumporn P, et al., Synthetic CaO-based sorbent for high-temperature CO_2 capture in sorption-enhanced hydrogen production, International Journal of Hydrogen Energy (2018), https://doi.org/10.1016/j.ijhydene.2018.06.153

Table 1 – BET surface area, pore volume, and pore size diameter of modified CN-AN and CG-AN calcium-based sorbents with different CTAB concentrations.

Sample	Surface area (m^2/g)	Pore volume (cm^3/g)	Pore size diameter (nm)
CN-AN	7.3	0.01	8.8
CN-AN-CTAB 1 mM	5.6	0.01	9.4
CN-AN-CTAB 3 mM	6.3	0.01	10.8
CN-AN-CTAB 5 mM	7.5	0.01	15.6
CN-AN-CTAB 7 mM	5.2	0.01	9.7
CN-AN-CTAB 10 mM	6.3	0.01	10.7
CG-AN	11.3	0.01	6.8
CG-AN-CTAB 1 mM	12.4	0.01	4.2
CG-AN-CTAB 3 mM	14.1	0.02	4.6
CG-AN-CTAB 5 mM	12.1	0.02	7.8
CG-AN-CTAB 7 mM	12.0	0.02	7.2
CG-AN-CTAB 10 mM	7.6	0.03	8.5

capacity. The results of CO_2 sorption capacity for 10 cycles run are shown in Fig. 6. The CG-AN-CTAB 3 mM sorbent shows higher sorption capacity than CN-AN-CTAB 3 mM for each corresponding cycle but greater decrease upon multiple repeated cycles is observed. The greater reduction might be due to particles of CG-AN-CTAB 3 mM collapsed and aggregated during heating upon multiple-cycle tests, causing the reduction of CaO active surface. This hypothesis is evidenced by SEM images shown in the inset in Fig. 6 that particles of CN-AN-CTAB are likely unchanged whereas particles of CG-AN-CTAB become larger after 10 cycles test.

One-body hybrid catalytic sorbent for sorption-enhanced steam methane reforming

Effect of calcium precursor and the addition of CTAB surfactant

As seen in the previous section, CN-AN-CTAB 3 mM and CG-AN-CTAB 3 mM are good sorbents for CO_2 capture. In this section, both sorbents were combined with Ni catalyst to use as one-body catalyst/sorbent for SESMR process. Fig. 7 shows

Table 2 – Summary of optimal CO_2 sorption parameters for various sorbents.

Sorbent	Sorption temperature (°C)	P_{CO2} (bar)	Sorption technique	CO_2 sorption capacity ($g_{CO2}/g_{sorbent}$)	Ref.
$CaO\text{-}Ca_{12}Al_{14}O_{33}$	690	0.15	TGA	0.37	[22]
Li_4SiO_4	600	1	TGA	0.37	[35]
Li_8ZrO_6	800	1	TGA	0.35	[36]
K-doped Li_2ZrO_3	550	0.25	TGA	0.22	[37]
Potassium modified hydrotalcite (K-HTC)	400	0.5	CI Microbalance	0.026	[38]
Na_2ZrO_3	800	1	TGA	0.22	[39]
$CaO\text{-}Ca_{12}Al_{14}O_{33}$	600	0.15	Fixed-bed	0.46	This work

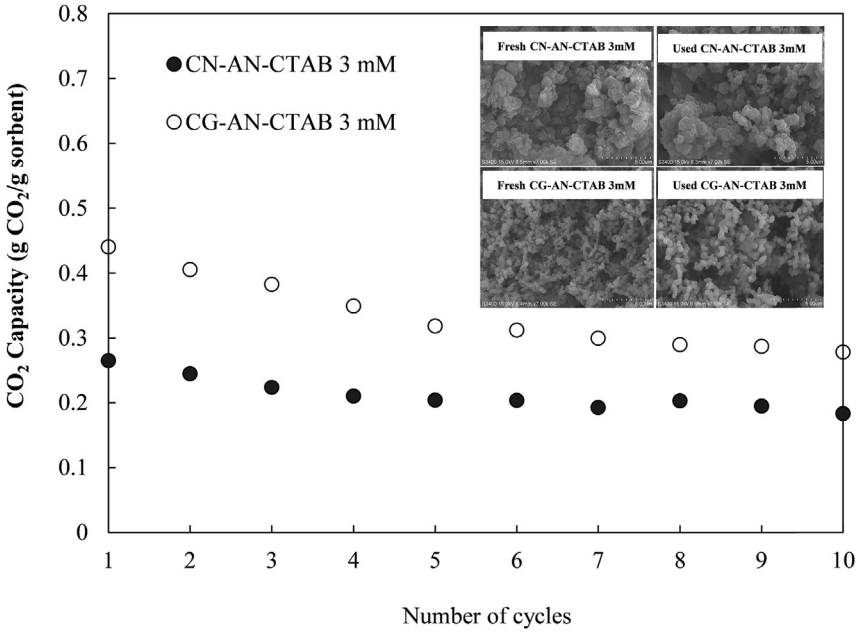

Fig. 6 – Stability test for CG-AN-CTAB 3 mM and CN-AN-CTAB 3 mM modified sorbents. Sorption condition: atmospheric pressure, 600 °C, 15%v/v CO_2 (N_2 balanced). Regeneration condition: atmospheric pressure, 850 °C under pure N_2.

Please cite this article in press as: Pecharaumporn P, et al., Synthetic CaO-based sorbent for high-temperature CO_2 capture in sorption-enhanced hydrogen production, International Journal of Hydrogen Energy (2018), https://doi.org/10.1016/j.ijhydene.2018.06.153

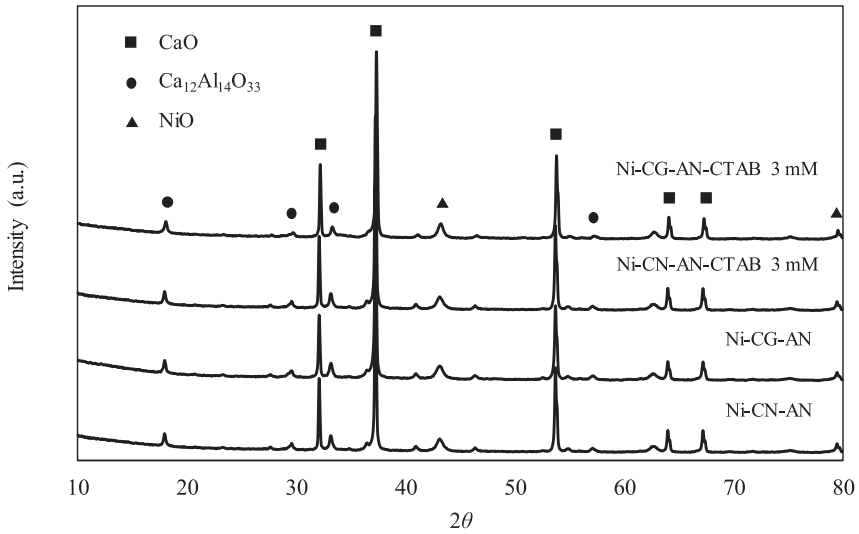

Fig. 7 – XRD patterns of hybrid multi-functional materials: NiO/CaO-$Ca_{12}Al_{14}O_{33}$.

XRD patterns of Ni-CN-AN, Ni-CG-AN, Ni-CN-AN-CTAB 3 mM, and Ni-CG-AN-CTAB 3 mM. The main peaks representing CaO-$Ca_{12}Al_{14}O_{33}$ are observed similar to those found in the case of solely alumina-containing CaO-based sorbent reported previously. The additional peaks representing NiO are observed at 2θ of 43 and 79.1°, and are in consistent with those reported by Moisés et al. [45]. SEM images (Fig. 8) show that Ni-CN-AN has particle size of ca. 0.5 μm and larger particle size of ca. 0.8 μm is observed with Ni-CG-AN. The addition of CTAB leads to an increase of particle size for Ni-CG-AN-CTAB 3 mM to be 1.5 μm, whereas the particle size of Ni-CN-AN-CTAB 3 mM remains nearly the same, ca. 0.5 μm, when compared to the unmodified sorbent Ni-CN-AN.

Fig. 9 shows product compositions (dry basis) obtained from SESMR using our one-body catalyst/sorbent. For the case of using Ni-CN-AN (Fig. 9a), three regions of H_2 production, pre-breakthrough, breakthrough, and post-breakthrough are observed. In the pre-breakthrough period, H_2 purity of ca. 93% could be produced for 30 min, which is higher than the production from SMR at equilibrium ca. 75%. The higher H_2

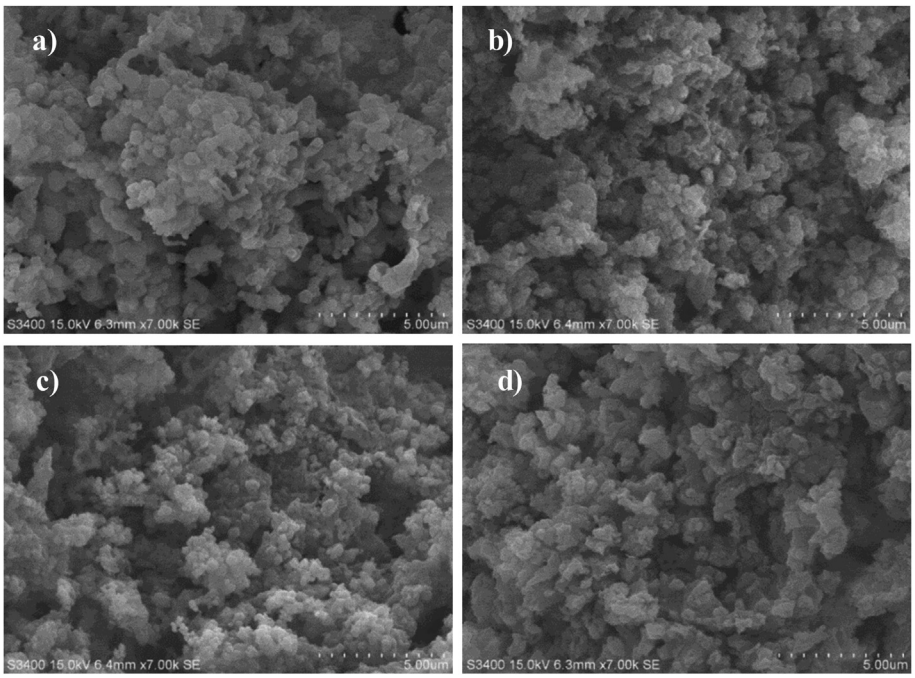

Fig. 8 – SEM images of a) Ni-CN-AN, b) Ni-CG-AN, c) Ni-CN-AN-CTAB 3 mM, d) Ni-CG-AN-CTAB 3 mM.

Please cite this article in press as: Pecharaumporn P, et al., Synthetic CaO-based sorbent for high-temperature CO_2 capture in sorption-enhanced hydrogen production, International Journal of Hydrogen Energy (2018), https://doi.org/10.1016/j.ijhydene.2018.06.153

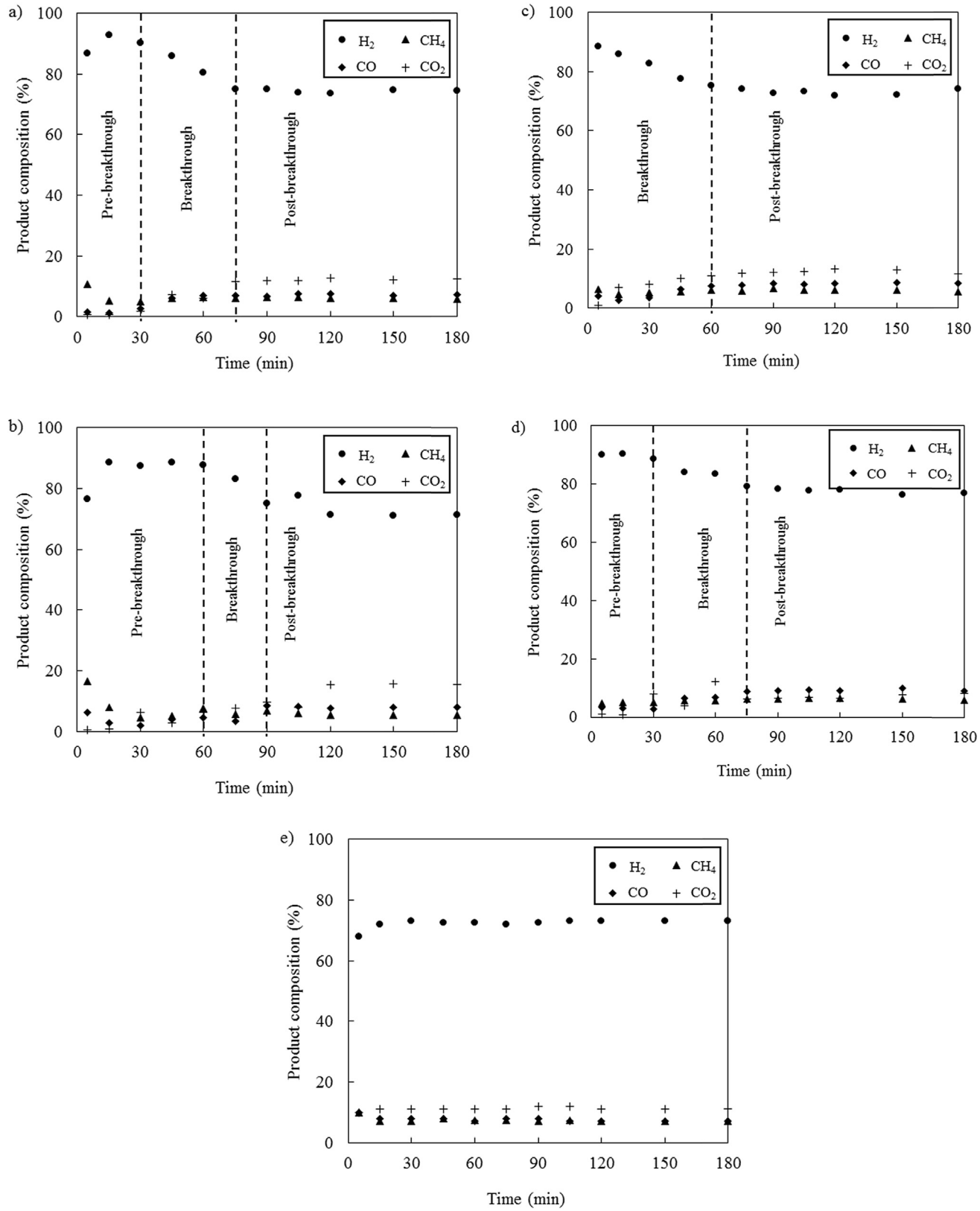

Fig. 9 – Gas product compositions (dry basis) of a) Ni-CN-AN, b) Ni-CG-AN, c) Ni-CN-AN-CTAB 3 mM, d) Ni-CG-AN-CTAB 3 mM, and e) Ni–$Al_2O_{3,commercial}$ from SESMR. Preparation of one-body catalyst/sorbent materials: wet-mixing. Operating conditions: atmospheric pressure, reaction temperature of 600 °C, steam/methane molar ratio of 3, and total flow rate = 60 ml/min.

Please cite this article in press as: Pecharaumporn P, et al., Synthetic CaO-based sorbent for high-temperature CO_2 capture in sorption-enhanced hydrogen production, International Journal of Hydrogen Energy (2018), https://doi.org/10.1016/j.ijhydene.2018.06.153

Table 3 – BET surface area, pore volume, and pore size diameter of modified Ni-CN-AN and Ni-CG-AN.

Sample	Surface area (m^2/g)	Pore volume (cm^3/g)	Pore size diameter (nm)
Ni-CN-AN	12.4	0.02	9.9
Ni-CN-AN-CTAB 3 mM	16.9	0.05	16.8
Ni-CG-AN	13.8	0.04	10.7
Ni-CG-AN-CTAB 3 mM	13.3	0.04	10.5
Ni-CG-AN sol-mixing	16.0	0.03	7.7

production obtained during pre-breakthrough period indicates the enhancement of H_2 production due to the effect of simultaneous CO_2 removal by the alumina-containing CaO-based sorbent. After pre-breakthrough period, H_2 content gradually decreases, while CO, CO_2, and CH_4 contents increase, indicating that the sorbent is gradually saturated and the effect of sorption-enhanced reaction becomes less effective. This period is called breakthrough period. After 75 min, the alumina-containing CaO-based sorbent is saturated with CO_2, the effect of sorption-enhanced reaction is no longer pronounced and the SESMR becomes SMR, which is referred to as post-breakthrough period. In case of Ni-CG-AN (Fig. 9b), longer pre-breakthrough period of 60 min with lesser H_2 production of ca. 88% is observed when compared to Ni-CN-AN. The result of longer pre-breakthrough period could probably be due to higher CO_2 sorption capacity of Ni-CG-AN as a result of void space between particles as well as high surface active exposure (see Table 3). In case of CTAB modified alumina-containing CaO-based sorbent, pre-breakthrough period is not observed for Ni-CN-AN-CTAB 3 mM; H_2 production gradually decreases from 88% and reaches equilibrium (Fig. 9c). The result of no pre-breakthrough period would be due to sintering effect; a number of void space generated by CTAB modified alumina-containing CaO-based sorbents are collapsed at high temperature, leading to the hindrance of either CaO or Ni active surfaces. On the other hand, Ni-CG-AN-CTAB 3 mM offers 30 min of pre-breakthrough period and H_2 produced due to sorption-enhanced reaction is ca. 90%. The observation of pre-breakthrough period could be attributed to the contribution of high CO_2 sorption capacity of CG-AN-CTAB 3 mM sorbent in sorption-enhanced reaction, whereas shorter pre-breakthrough period could be due to particle agglomeration caused from high temperature reaction.

Effect of synthesis method

Two combination techniques, wet-mixing and sol-mixing, were selected to investigate the effect on H_2 production. Fig. 10 shows XRD pattern of one-body catalyst/sorbent materials prepared by wet-mixing and sol-mixing methods. The results show similar compositions and phase formation for both materials as similar XRD patterns representative of CaO, $Ca_{12}Al_{14}O_{33}$, and NiO are observed. SEM images of Ni-CG-AN wet-mixing and Ni-CG-AN sol-mixing shown in the inlet of Fig. 10 reveal Ni-CG-AN sol-mixing possesses larger aggregated particles with larger void space compared to Ni-CG-AN wet-mixing.

Fig. 11 shows product compositions obtained from SESMR using one-body catalyst/sorbent materials prepared by wet-mixing and sol-mixing methods. The results show adsorption period of 30 min with the maximum H_2 purity of 94% is obtained from Ni-CG-AN sol-mixing whereas longer pre-breakthrough time of 60 min with lower maximum H_2 purity of 88% is observed with Ni-CG-AN wet-mixing. The

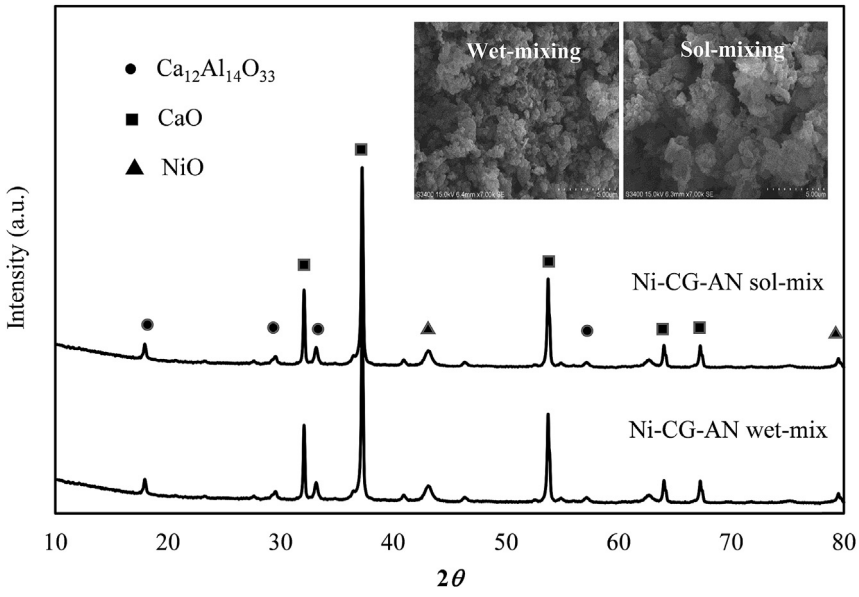

Fig. 10 – XRD pattern of hybrid multi-functional materials: 12.5%Ni-CG-AN-wet mixing and 12.5%Ni-CG-AN sol-mixing.

Please cite this article in press as: Pecharaumporn P, et al., Synthetic CaO-based sorbent for high-temperature CO_2 capture in sorption-enhanced hydrogen production, International Journal of Hydrogen Energy (2018), https://doi.org/10.1016/j.ijhydene.2018.06.153

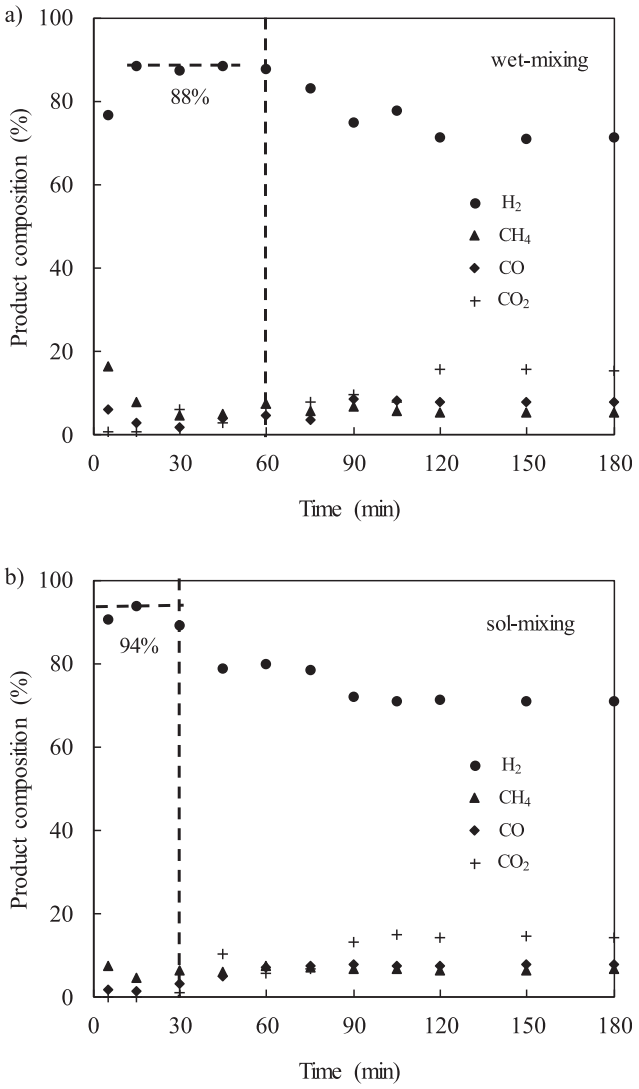

Fig. 11 – Gas product compositions (dry basis) of a) Ni-CG-AN wet-mixing and b) Ni-CG-AN sol-mixing from SESMR. Operating conditions: atmospheric pressure, reaction temperature of 600 °C, steam/methane molar ratio of 3, and total flow rate = 60 ml/min.

improvement of maximum H_2 purity observed with the sorbent prepared by sol-mixing method might be because CaO, which was transform from calcination of calcium D-gluconic acid at 900 °C, reacted with H_2O and became $Ca(OH)_2$. Because of the volume increase from CaO to $Ca(OH)_2$ and the expansion of particle caused by the exothermic hydration of CaO, the aggregates crack and swell and the regular hexagonal crystalloids of $Ca(OH)_2$ are generated, leading to larger active surface of the material [46,47]. This result is inconsistent with surface texture examined by BET as shown in Table 3 that higher surface area is observed with Ni-CG-AN sol-mixing.

Performance comparison of the developed one-body hybrid catalytic sorbent for sorption-enhanced steam methane reforming

Our investigations have shown that synthesis of alumina-containing CaO-based sorbents with the use of different calcium precursors or the addition of structure-directing agent affects properties of the sorbent, which in turn, affects CO_2 sorption capacity and H_2 production. A key finding from our studies is that, for the application to SESMR process, combining sorbent and catalyst into one-body material is not a direct combination of sorption and catalyst performances. As seen, although CG-AN-CTAB 3 mM sorbent offers the highest CO_2 sorption capacity; however, when the sorbent is combined with NiO, sorption-enhanced reaction period has less impact when compared to the unmodified sorbent. This could possibly be due to better distribution of Ni active site on the surface of the sorbent; dense packing of sorbent particles could support Ni better than the loose one, which could result in higher active catalytic sites for steam reforming reaction. However, it is worth to note that performance of hydrogen production depends upon not only properties of multi-functional material but also operating conditions of SESMR process. Table 4 summarizes H_2 production from SESMR process using different sorbent sources, different synthesis methods, and different operating conditions reported in the literature compared with our results. Consistence with other works, high H_2 purity can be obtained with the use of CaO-based sorbent. Our developed materials show that high H_2 purity can be produced at milder operating conditions, i.e., lower temperature and lower steam to methane ratio (S/C).

Table 4 – Comparison of H_2 production using multi-functional materials containing CaO as sorbent.

Catalyst	Source of calcium oxide	Condition		CaO synthesis method	Sorption-enhanced period	Maximum H_2 concentration	Ref.
		T(°C)	S/C[a]				
12.5 wt%Ni/Al_2O_3+CaO	Calcium oxide	600	3	Commercial	10 min	65%	[22]
16%NiO-CaO-$Ca_{12}Al_{14}O_{33}$	Calcium acetate	650	3.4	Sol-mixing	110 min	90%	[27]
18%Ni-CaO-$CaZrO_3$ (CTAB)	Calcium acetate	650	4	Wet-mixing with sonication	18 min	92%	[28]
12.5%Ni-CaO-$Ca_{12}Al_{14}O_{33}$	Calcium D-gluconic acid	600	3	Wet-mixing and hydration	60 min	88%	This work
12.5%Ni-CaO (CTAB)-$Ca_{12}Al_{14}O_{33}$		600	3		45 min	90%	
12.5%Ni-CaO-$Ca_{12}Al_{14}O_{33}$	Calcium nitrate	600	3	Wet-mixing and hydration	30 min	93%	This work
12.5%Ni-CaO (CTAB)-$Ca_{12}Al_{14}O_{33}$		600	3		–	88%	

[a] S/C = steam to methane ratio.

Please cite this article in press as: Pecharaumporn P, et al., Synthetic CaO-based sorbent for high-temperature CO_2 capture in sorption-enhanced hydrogen production, International Journal of Hydrogen Energy (2018), https://doi.org/10.1016/j.ijhydene.2018.06.153

Conclusions

We have investigated the effect of calcium precursor, the addition of structure-directing agent, and synthesis method of CaO-based alumina materials on high-temperature CO_2 capture in sorption-enhanced steam methane reforming. Different calcium precursors provided different polymorphs and also the ability to adsorb CO_2. The sorbents derived from calcium D-gluconic acid (CG) offered higher CO_2 sorption capacity than calcium nitrate (CN) in mixed CO_2/N_2 system (15% v/v CO_2) at 600 °C due to their higher surface area and smaller particle size. Modification properties of alumina-containing CaO-based sorbents by addition of CTAB showed an improvement of CO_2 sorption capacity in case of using calcium D-gluconic acid as calcium precursor. However, modification of alumina-containing CaO-based sorbent by CTAB did not provide favorable role in H_2 production by SESMR as shorter sorption-enhanced reaction period was observed when compared to the unmodified one. An incorporation of the synthetic alumina-containing CaO-based sorbent with Ni to use as one-body catalyst/sorbent for SESMR showed that incorporating 12.5% Ni with CG-AN by wet-mixing method provides the longest pre-breakthrough period of 60 min with 88% H_2 at 600 °C and a steam/methane molar ratio of 3.

Acknowledgements

The authors would like to thank the Ratchadapisek Sompoch Endowment Fund (2016), Chulalongkorn University (CU-59-003-IC) and the Thailand Research Fund (DPG5880003) for funding supports.

REFERENCES

[1] Kim JN, Ko CH, Yi KB. Sorption enhanced hydrogen production using one-body CaO-$Ca_{12}Al_{14}O_{33}$-Ni composite as catalytic absorbent. Int J Hydrogen Energy 2013;38:6072–8.
[2] Harrison DP, Peng ZY. Low-carbon monoxide hydrogen by sorption-enhanced reaction. Int J Chem React Eng 2003;1:1–9.
[3] Rawadieh S, Gomes VG. Steam reforming for hydrogen generation with in situ adsorptive separation. Int J Hydrogen Energy 2009;34:343–55.
[4] Broda M, Manovic V, Imtiaz Q, Kierzkowska AM, Anthony EJ, Müller CR. High-purity hydrogen via the sorption-enhanced steam methane reforming reaction over a synthetic CaO-based sorbent and a Ni catalyst. Environ Sci Technol 2013;47:6007–14.
[5] Koh A, Chen L, Keeleong W, Johnson B, Khimyak T, Lin J. Hydrogen or synthesis gas production via the partial oxidation of methane over supported nickel-cobalt catalysts. Int J Hydrogen Energy 2007;32:725–30.
[6] Ayodele BV, Khan MR, Cheng CK. Production of CO-rich hydrogen gas from methane dry reforming over Co/CeO_2 catalyst. Bull Chem React Eng Catal 2016;11:210–9.
[7] Osazuwa OU, Setiabudi HD, Abdullah S, Cheng CK. Syngas production from methane dry reforming over $SmCoO_3$ perovskite catalyst: kinetics and mechanistic studies. J Hydrogen Energy 2017;42:9707–21.
[8] Liew RK, Chong MY, Osazuwa OU, Nam WL, Phang XY, Su MH, et al. Res Chem Intermed 2018;44:3849–65.
[9] Hufton JR, Mayorga S, Sircar S. Sorption-enhanced reaction process for hydrogen production. AIChE J 1999;45:248–56.
[10] Lee KB, Beaver MG, Caram HS, Sircar S. Production of fuel-cell grade hydrogen by thermal swing sorption enhanced reaction concept. Int J Hydrogen Energy 2008;33:781–90.
[11] Han C, Harrison DP. Simultaneous shift reaction and carbon dioxide separation for the direct production of hydrogen. Chem Eng Sci 1994;49:5875–83.
[12] Balasubramanian B, Ortiz AL, Kaytakoglu S, Harrison DP. Hydrogen from methane in a single-step process. Chem Eng Sci 1999;54:3543–52.
[13] Ding Y, Alpay E. Adsorption-enhanced steam–methane reforming. Chem Eng Sci 2000;55:3929–40.
[14] Park J, Yi KB. Effects of preparation method on cyclic stability and CO_2 absorption capacity of synthetic CaO–MgO absorbent for sorption-enhanced hydrogen production. Int J Hydrogen Energy 2012;37:95–102.
[15] Li Z, Cai N. Modeling of multiple cycles for sorption-enhanced steam methane reforming and sorbent regeneration in fixed bed reactor. Energy Fuels 2007;21:2909–18.
[16] Li Z, Cai N, Huang Y, Han H. Synthesis, Experimental studies, and analysis of a new calcium-based carbon dioxide absorbent. Energy Fuels 2005;19:1447–52.
[17] Xie M, Zhou Z, Qi Y, Cheng Z, Yuan W. Sorption-enhanced steam methane reforming by in situ CO_2 capture on a CaO–$Ca_9Al_{16}O_{18}$ sorbent. Chem Eng J 2012;207–208:142–50.
[18] Felice LD. CO_2 Capture by CaO-based sorbents and sorption enhanced reaction systems, in: 542. In: Suib SL, editor. New and future developments in catalysis: actication of carbon dioxide new and future developments in catalysis, vol. 543; 2013. p. 603–25.
[19] Froment GF. Modeling of catalyst deactivation. Appl Catal A Gen 2001;212:117–28.
[20] Maluf SS, Assaf EM. Ni catalysts with Mo promoter for methane steam reforming. Fuel 2009;88:1547–53.
[21] Zeppieri M, Villa PL, Verdone N, Scarsella M, Filippis P. Kinetic of methane steam reforming reaction over nickel- and rhodium-based catalysts. Appl Catal A Gen 2010;387:147–54.
[22] Chanburanasiri N, Ribeiro MA, Rodrigues AE, Arpornwichanop A, Laosiripojana N, Praserthdam P, et al. Hydrogen production via sorption enhanced steam methane reforming process using Ni/CaO multifunctional catalyst. Ind Eng Chem Res 2011;50:13662–71.
[23] Huang T, Huang W, Huang J, Ji P. Methane reforming reaction with carbon dioxide over SBA-15 supported Ni-Mo bimetallic catalysts. Fuel Process Technol 2011;92:1868–75.
[24] Zhai X, Ding S, Liu Z, Jin Y, Cheng Y. Catalytic performance of Ni catalysts for steam reforming of methane at high space velocity. Int J Hydrogen Energy 2011;36:482–9.
[25] Roh HS, Jun KW, Park SE. Methane-reforming reactions over Ni/Ce-ZrO_2/θ-Al_2O_3 catalysts. Appl Catal A Gen 2003;251:275–83.
[26] Martavaltzi CS, Lemonidou AA. Development of new CaO based sorbent materials for CO_2 removal at high temperature. Microporous Mesoporous Mater 2008;110:119–27.
[27] Lee SY, Park SJ. A review on solid adsorbents for carbon dioxide capture. J Ind Eng Chem 2015;23:1–11.
[28] Martavaltzi CS, Lemonidou AA. Hydrogen production via sorption enhanced reforming of methane: development of a novel hybrid material-reforming catalyst and CO_2 sorbent. Chem Eng Sci 2010;65:4134–40.

Please cite this article in press as: Pecharaumporn P, et al., Synthetic CaO-based sorbent for high-temperature CO_2 capture in sorption-enhanced hydrogen production, International Journal of Hydrogen Energy (2018), https://doi.org/10.1016/j.ijhydene.2018.06.153

[29] Radfarnia HR, Liliuta MC. Development of Al-stabilized CaO-nickel hybrid sorbent-catalyst for sorption-enhanced steam methane reforming. Chem Eng Sci 2014;109:212–9.
[30] Xu P, Zhou Z, Zhao C, Cheng Z. Ni/CaO-Al_2O_3 bifunctional catalysts for sorption-enhanced steam methane reforming. AIChE J 2014;60:3547–56.
[31] Zhao C, Zhou Z, Cheng Z, Fang X. Sol-gel-derived, $CaZrO_3$-stabilized Ni/CaO-$CaZrO_3$ bifunctional catalyst for sorption-enhanced steam methane reforming. Appl Catal B Environ 2016;196:16–26.
[32] Cesário MR, Barros BS, Courson C, Melo DMA, Kiennemann A. Catalytic performances of Ni–CaO–mayenite in CO_2 sorption enhanced steam methane reforming. Fuel Process Technol 2015;131:247–53.
[33] Zhou Z, Qi Y, Xie M, Cheng Z, Yuan W. Synthesis of CaO-based sorbents through incorporation of alumina/aluminate and their CO_2 capture performance. Chem Eng Sci 2012;74:172–80.
[34] Nieto-Sanchez AJ, Olivares-Marin M, Garcia S, Pevida C, Cuerda-Carrea EM. Influence of the operation conditions on CO_2 capture by CaO-derived sorbents prepared from synthetic $CaCO_3$. Chemosphere 2013;93:2148–58.
[35] Szcześ A, Chibowski E, Hołysz L. Influence of ionic surfactants on the properties of freshly precipitated calcium carbonate. Colloids Surf A 2007;297:14–8.
[36] Olivares-Marín M, Cuerda-Correa EM, Nieto-Sánchez A, García S, Pevida C, Román S. Influence of morphology, porosity and crystal structure of $CaCO_3$ precursors on the CO_2 capture performance of CaO-derived sorbents. Chem Eng J 2013;217:71–81.
[37] Lam SS, Liew RK, Cheng CK, Chase HA. Catalytic microwave pyrolysis of waste engine oil using metallic pyrolysis char. Appl Catal, B 2015;176–177:601–17.
[38] Liew RK, Nam WL, Chong MY, Phang XY, Su MH, Yek PNY, et al. Oil palm waste: an abundant and promising feedstock for microwave pyrolysis conversion into good quality biochar with potential multi-applications. Process Saf Environ 2018;115:57–69.
[39] Phromprasit J, Powell J, Assabumrungrat S. Metals (Mg, Sr and Al) modified CaO based sorbent for CO_2 sorption/desorption stability in fixed bed reactor for high temperature application. Chem Eng J 2016;284:1212–23.
[40] Venegas MJ, Fregoso-Israel E, Escamilla R, Pfeiffer H. Kinetic and reaction mechanism of CO_2 sorption on Li_4SiO_4: study of the particle size effect. Ind Eng Chem Res 2007;46:2407–12.
[41] Yin XS, Li SP, Zhang QH, Yu JG. Kinetic and reaction mechanism of CO_2 sorption on Li_4SiO_4: study of the particle size effect. J Am Ceram Soc 2010;93:2837–42.
[42] Xiao Q, Tang X, Liu Y, Zhong Y, Zhu W. Citrate route to prepare K-doped Li2ZrO3 sorbents with excellent CO2 capture properties. Chem Eng J 2011;174:231–5.
[43] Halabi MH, Croon de MHJM, Schaaf van der J, Cobden PD, Schouten JC. High capacity potassium-promoted hydrotalcite for CO_2 capture in H_2 production. Int J Hydrogen Energy 2012;37:4516–25.
[44] Martínez-dlCruz L, Pfeiffer H. Cyclic CO_2 chemisorption-desorption behavior of Na_2ZrO_2: structural, microstructural and kinetic variations produced as a function of temperature. J Solid State Chem 2013;204:298–304.
[45] Moisés RC, Barros B, Zimmermann Y, Courson C, Melo DMA, Kiennemann A. CO_2 sorption enhanced steam reforming of methane using Ni/CaO·$Ca_{12}Al_{14}O_{33}$ catalysts. Adv Chem Lett 2013;1:292–9.
[46] Li Z, Liu Y, Cai N. Effect of CaO hydration and carbonation on the hydrogen production from sorption enhanced water gas shift reaction. Int J Hydrogen Energy 2012;37:11227–36.
[47] Martavaltzi CS, Lemonidou AA. Parametric study of the CaO-$Ca_{12}Al_{14}O_{33}$ synthesis with respect to high CO_2 sorption capacity and stability on multicycle operation. Ind Eng Chem Res 2008;47:9537–43.

Please cite this article in press as: Pecharaumporn P, et al., Synthetic CaO-based sorbent for high-temperature CO_2 capture in sorption-enhanced hydrogen production, International Journal of Hydrogen Energy (2018), https://doi.org/10.1016/j.ijhydene.2018.06.153

ENGINEERING JOURNAL

Article

Two-Dimensional Mathematical Modeling of the Oxidative Coupling of Methane in a Membrane Reactor

Wisitsree Wiyaratn[1,*], Salamah Manundawee[2], Amornchai Arpornwichanop[2], Suttichai Assabumrungrat[2], Anucha Watanapa[3], and Chidporn Worawimut[4]

1 Faculty of Industrial Education and Technology, King Mongkut's University of Technology Thonburi, Bangkok 10140, Thailand
2 Department of Chemical Engineering, Faculty of Engineering, Chulalongkorn University, Bangkok 10330, Thailand
3 Department of Production Technology Education ,Faculty of Industrial Education and Technology, King Mongkut's University of Technology Thonburi, Bangkok 10140, Thailand
4 Learning Innovation and Technology, King Mongkut's University of Technology Thonburi, Bangkok 10140, Thailand
*E-mail: wisitsree.wiy@kmutt.ac.th

Abstract. The oxidative coupling of methane (OCM) in a dense BSCFO membrane reactor (MR) was theoretically studied using a two-dimensional reactor model. The simulation results indicated that increasing the operating temperature results in increased CH_4 conversion and decreased C_2 selectivity. An increase in the methane feed flow rate lowers the CH_4 conversion but increases the C_2 selectivity; however, the effect of the air flow rate on the OCM membrane reactor exhibits an opposite trend. The optimum configuration of the dense BSCFO-MR to provide the best performance was 0.018 m in diameter and 0.2 m. in length at a GHSV of 19452.37 h^{-1} and temperature of 1073 K. Under these optimal conditions, the CH_4 conversion is 43.713 %, the C_2 selectivity is 61.352 % and the C_2 yield is 26.82 %.

Keywords: Oxidative coupling of methane, BSCFO membrane, two-dimensional model, theoretical analysis.

ENGINEERING JOURNAL Volume 20 Issue 1
Received 3 March 2015
Accepted 4 August 2015
Published 29 January 2016
Online at http://www.engj.org/
DOI:10.4186/ej.2016.20.1.17

DOI:10.4186/ej.2016.20.1.17

1. Introduction

Natural gas consists mainly of methane and other potential feedstocks for fuel and chemical synthesis. An oxidative coupling of methane (OCM) is an attractive process that converts methane into higher value-added C_2 hydrocarbon products. The OCM has a long history, beginning with the pioneering work of Keller and Bhasin [1]. Currently, the development and improvement of the OCM to obtain higher methane conversion and higher C_2 hydrocarbons selectivity is receiving much attention from many researchers. The reactor configuration is known to play an important role in producing high yield and high selectivity of ethylene production in the OCM reaction. Various types of reactors, such as fixed bed reactors, fluidized-bed reactors, moving bed chromatographic reactors, and membrane reactors, have been reported [2–14]. Some of this structure poses instability in performance and difficulty in operation which is very crucial for industrial scale reactor even though they are very efficient in point of selectivity and yield [15]. Fixed bed reactor was studied on OCM process which was the easiest to design, scale up, and could be analyzed using mathematical model. Membrane reactor seems to be the most suitable reactor type compared with other reactors. Applications of a membrane reactor combining the separation and reaction into a single unit to control the oxygen concentration along the reactor were found to be promising for enhancing OCM performance and increasing the process economy [16]. Inorganic membranes for OCM process can be divided into 2 classes: porous and dense membranes. On the one hand, porous membranes exhibit high permeability but relatively low selectivity. On the other hand, dense membranes exhibit much better selectivity but lower permeability. Within the category of dense membranes, ionic oxygen conducting membranes (IOCM) offered the unique advantage to provide activated oxygen at its surface while preventing hydrocarbon losses to the trans-membrane side [10]. Especially the composition of reactor product stream such as type and quantity should be considered as an important factor for operating condition [15]. Correspondingly, the design of the membrane reactor using a two-dimensional mathematical model considering both the axial and radial directions was found to be more realistic and provides better prediction accuracy than the one-dimensional one. The need of the two-dimensional model becomes essential when a reactor with a large diameter is operated as the effect of radial dispersion becomes more pronounced. In the reactor design it is important to determine a location where the hot spot is severe so that the operation problem such as catalyst sintering can be avoided and suitable operating condition can be selected.Therefore, in this study, two-dimensional mathematical modeling of OCM to C_2 hydrocarbons in a membrane reactor operating under non-isothermal conditions was investigated using the COMSOL® Multiphysics Program. The model was useful for predicting the OCM performance under a dense $Ba_{0.5}Sr_{0.5}Co_{0.8}Fe_{0.2}O_{3-\delta}$ (BSCFO) [12] membrane and the effect of the operating condition, such as the methane flow rate, air flow rate and temperature, were investigated. Moreover, the performance comparison between Fixed-bed reactors (FBR) and Membrane reactors (MR) was considered. Finally, we focused on determining the optimum dimension of the MR to provide the good performance in the OCM process.

2. Modeling of the OCM Membrane Reactor

2.1. Kinetic Model

Numerous kinetic reaction models have been presented to describe the performance of the OCM process over Na-W-Mn/SiO_2. In this study, the kinetic mechanism and rate expression of the OCM reactions proposed by Danespayeh *et al.* [14] over the Na-W-Mn/SiO_2 catalyst is used. The properties of the catalyst are presented in Table 1.

Table 1. The catalyst property.

Property	Catalyst
	Na-W-Mn/SiO_2
Average pore radius (m)	0.00008
Porosity (-)	0.6
Totousity (-)	1.089
Thermal conductivity (W/m K)	1.35
Permeability (m^2)	4.04669×10^{-10}

2.2. Reactor Model

The transport phenomena were coupled with the reaction kinetics to develop a reactor model. The two-dimensional flow field in a membrane reactor was coupled with the mass and heat transport to simulate the performance of the OCM process as well as the velocity, concentration and temperature profiles. The reactor dimension and condition used in the simulation are summarized in Table 2.

Table 2. Reactor dimension and conditions.

Condition	Dimension
Membrane reactor	
Length (m)	0.2
Tube diameter (m)	0.018
Shell diameter (m)	0.02
Temperature (K)	993-1173
Pressure (kPa)	101.325
Volumetric flow rate in shell (m^3/s)	0.00004-0.00052
Volumetric flow rate in tube (m^3/s)	0.00014-0.0007

2.2.1. Geometry and boundary condition

The membrane reactors considered in this study were double tubular reactors. The tube wall was a dense (BSCFO) membrane. The tube was filled with a bed of catalyst, and the outer shell was an impermeable wall. CH_4 was fed into the reactor from the tube side, whereas a mixture of oxygen and nitrogen resembling air composition were fed into the reactor from the shell side.

All of the reactors were based on the following assumptions:

- Two-dimensional mathematical model
- Steady-state conditions
- Ideal gas behavior was applied for all gas components.
- Diffusivity in the catalyst bed was assumed to follow the Knudsen mechanism.
- Membrane reactor resembled a shell and a tube heat exchanger.

2.2.2. Governing equations

Mass balance: the mass balance for each of the eight (C_i = CH_4, O_2, C_2H_4, C_2H_6, CO, CO_2, H_2, and H_2O) components can be written as follows.

$$\left(\frac{\partial^2 C_i}{\partial r^2} + \frac{1}{2}\frac{\partial C_i}{\partial r}\right) + D_i\frac{\partial^2 C_i}{\partial z^2} - u\frac{\partial C_i}{\partial z} + \rho_B r_i = 0 \quad (1)$$

The rate of production was calculated for each component from the stoichiometry of the reactions.

Energy balance: the energy balance for the reactor can be written as follows.

$$\lambda\left(\frac{\partial^2 T}{\partial r^2} + \frac{1}{2}\frac{\partial T}{\partial r}\right) + \frac{\partial^2 T}{\partial z^2} - u\rho_f C_p\frac{\partial T}{\partial z} + Q = 0 \quad (2)$$

The heat source in Eq. (2), including heat of reaction and heat flux, were computed by

$$Q = \sum_{i=1}^{n}\Delta H_{rxn} r_i + U(T - T_{ex}) \quad (3)$$

Momentum balance: the momentum balance for reactor describes the flow in the porous media. The equation extends Darcy's law combination with the continuity equation:

$$\nabla\left(-\eta(\nabla u + (\nabla u)^T)\right) + \frac{k}{\eta}u = 0 \quad (4)$$

The performance of the reactor was evaluated by the conversion of reactants as well as the selectivity and the yield of the products. The conversion is defined as the fraction of the reactant reacted to the reactant fed. For example, the conversion of methane is

$$\text{CH4 conversion } \% = \frac{F^0_{CH_4} - F_{CH_4}}{F^0_{CH_4}} \times 100 \quad (5)$$

and the C_2 selectivity is defined as the C_2 product formed per reactant consumed.

$$\text{C2 selectivity \%} = \frac{2\times(F_{C2H4}+F_{C2H6})}{(2(F_{C2H4}+F_{C2H6})+F_{CO}+F_{CO2})} \times 100 \quad (6)$$

while yield referred to the specific product formed per reactant fed.

$$\text{C2 yield \%} = \frac{2\times(F_{C2H4}+F_{C2H6})}{F^0_{CH_4}} \times 100 \quad (7)$$

The flux equation of the dense $Ba_{0.5}Sr_{0.5}Co_{0.8}Fe_{0.2}O_{3-\delta}$ membrane [12] is described in Eq (8). The simulations were performed by using the COMSOL® program to determine a suitable model for the OCM process.

The flux equation of $Ba_{0.5}Sr_{0.5}Co_{0.8}Fe_{0.2}O_{3-\delta}$ (BSCFO) membrane can be expressed as

$$J_{O_2} = \frac{\pi L C_i D_a}{2S\ln\left(\frac{r_1}{r_2}\right)} \ln\left(\frac{P_1}{P_2}\right) \quad (8)$$

2.2.3. Numerical solution

The finite element method was proposed to formulate the PDE problem. The developed finite element model of the OCM membrane reactor was solved with quadratic finite element basis functions using a commercial finite element simulation environment, COMSOL. The software runs the finite element analysis together with meshing, which involves a partition of the geometry model into small units of simple shapes, and error control using a variety of numerical solvers. Three application modes were needed. The heat transfer mode was used to model conduction and convection. The mass transfer by convection and diffusion was used to show the concentration and transport of eight species of interest. The Brinkman equation was applied to describe the fluid flow.

2.2.4. Model validation

The validation of the kinetic model for Na-W-Mn/SiO_2 catalyst was carried out first to ensure that the mathematics models could well predict the OCM performances. The models used were two-dimensional plug flow model. Figure 1 shows the comparison of our results with literature reported by Daneshpayeh *et al.* (2009) for Na-W-Mn/SiO_2 catalyst providing conversion of CH_4 at space time in a range of 16.5 – 19 kg m^3/s, temperature at 1048 K. It can be seen that our simulation results agreed well with simulation data from literature.

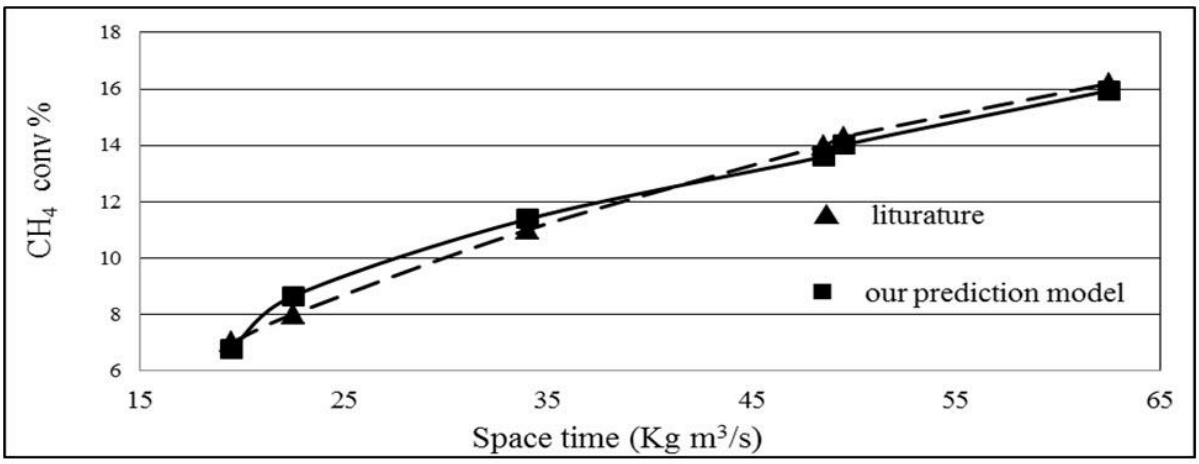

Fig. 1. Comparison between of literature with our prediction model over Na-W-Mn/SiO_2 catalyst.

3. Results and Discussion

3.1. Membrane Reactor

3.1.1. Effect of the methane feed rate

The effect of the methane feed flow rate in a range of 1.38×10^{-4} – 6.88×10^{-4} m^3/s at a temperature of 993 K and an air flow rate of 2.8×10^{-4} m^3/s on CH_4 conversion,% and C_2 selectivity,% are presented in Fig. 1. CH_4 conversion was decreased, whereas C_2 selectivity was increased with the increase of methane feed flow rate. Increasing the methane feed flow rate resulted in a lower contact time, and hence, the CH_4 conversion was decreased. In addition, the methane feed rate also affected the permeation of oxygen into the tube side. Figure 2 shows the O_2 concentration profile at different methane feed flow rate. At a lower methane feed flow rate (Figs. 2a and 2b), the oxygen-permeable membrane passed into the first part of the reactor. The membrane completed conversion at a position of permeation into tube side. However, at a higher methane feed rate (Figs. 2c–2e), the oxygen-permeable membrane passed into tube side in the same position as in the previous case, but it exhibited a lower conversion and was slower than the previous case, which was indicated by the higher oxygen flow rate along length of the reactor. Because of the higher methane feed flow rate, the methane feed rate taking the oxygen flow rate, which was permeated on the tube side, was higher as well. As a result, lower contact between methane and oxygen. This was to make CH_4 conversion less.

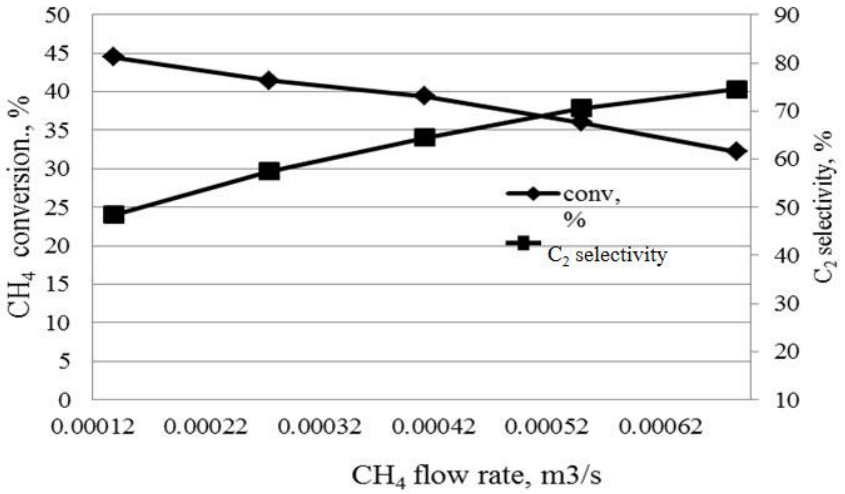

Fig. 2. Effect of the CH_4 feed rate on the CH_4 conversion, % and the C_2 selectivity, % (T =993 K, air flow rate = 2.8×10^{-4} m^3/s).

DOI:10.4186/ej.2016.20.1.17

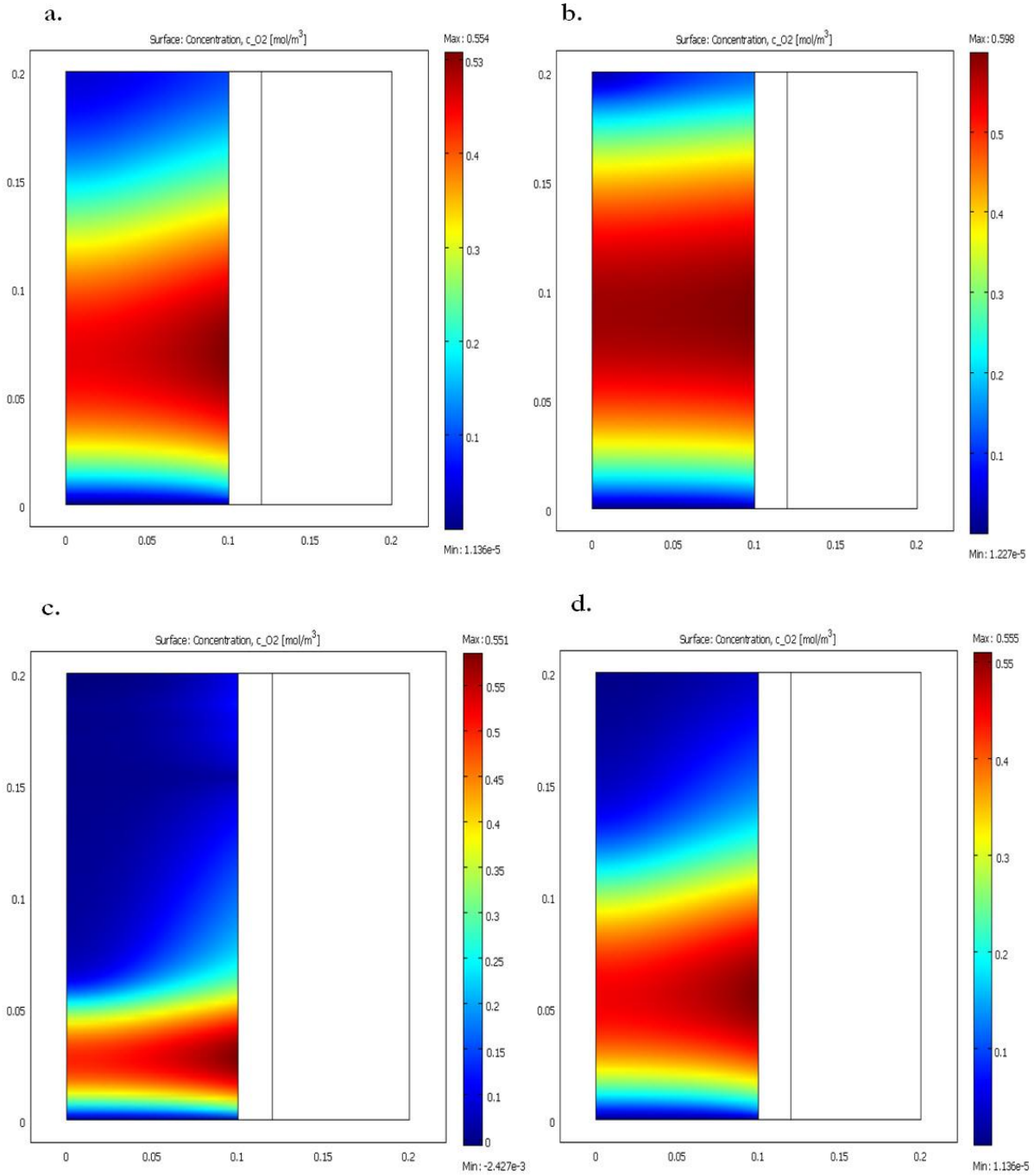

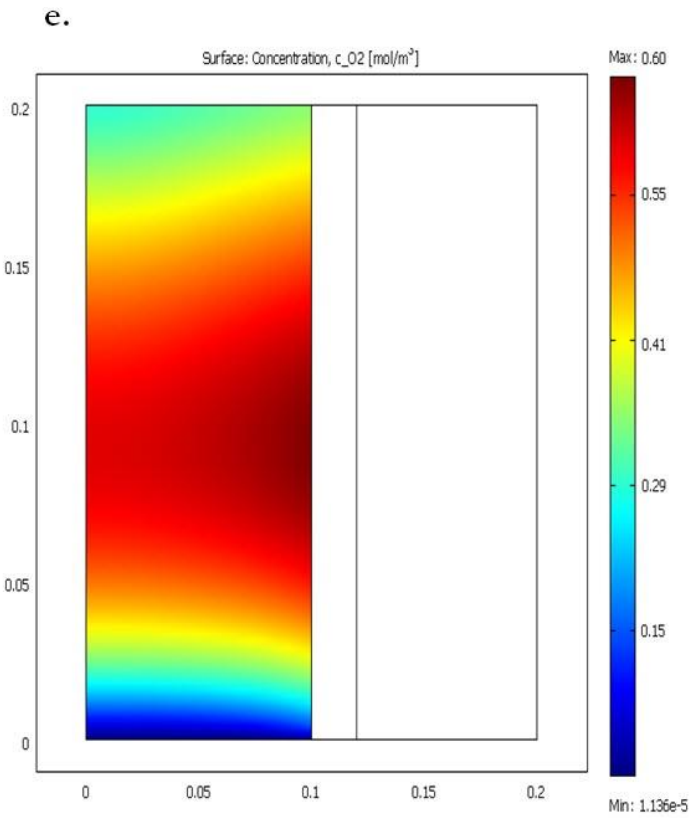

Fig. 3. Effect of the CH_4 feed rate on the O_2 concentration profile at the following CH_4 feed rates: (a) 1.38×10^{-4}, (b) 2.75×10^{-4} (c) 4.13×10^{-4}, (d) 5.5×10^{-4}, and (e) 6.88×10^{-4} m^3/s.

3.1.2. Effect of the air feed rate

The effect of the air feed flow rate in the range of 0.4×10^{-4} – 5.2×10^{-3} m^3/s at a temperature of 993 K and a methane flow rate of 5.5×10^{-4} m^3/s on the CH_4 conversion and the C_2 selectivity are presented in Fig. 3. The CH_4 conversion was increased whereas the C_2 selectivity was decreased with the increase of the air feed flow rate. When increasing the air feed rate, the flux of oxygen permeation increased due to the higher driving force of oxygen across the membrane; as a result, the CH_4 conversion increases. The C_2 selectivity was decreased because a higher amount of oxygen could react with the methyl radical and C_2 product to form carbon oxides.

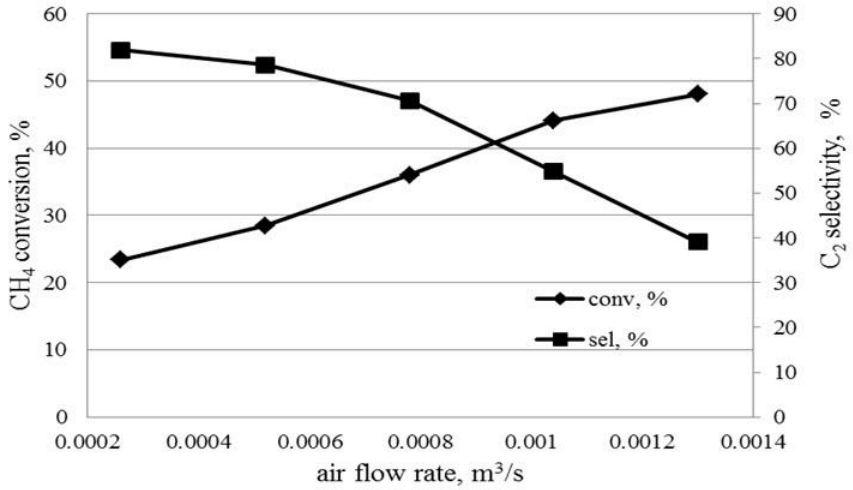

Fig. 4. Effect of the air flow rate on the CH_4 conversion and the C_2 selectivity (T =993 K, CH_4 flow rate = 5.5×10^{-4} m^3/s).

3.1.3. Effect of feed temperature

The effect of temperature in the range of 993 to 1173 K for an air feed rate of 2.8×10^{-4} m^3/s and a methane feed rate of 5.5×10^{-4} m^3/s on the CH_4 conversion and the C_2 selectivity are presented in Fig. 4. The CH_4 conversion was increased, whereas the C_2 selectivity was decreased with the increased temperature. Figures 5a–5e show the temperature profiles at different feed temperatures. The results indicated that the hot spot temperature was always observed due to the accumulation of heat of reaction along the reactor. Figure 5e shows the temperature profiles for both the shell and the tube sides. The temperature increased gradually on the tube side from the inlet to the exit along reactor, especially at the center of the reactor, while the shell side temperature was slightly increased. The trend of the temperature on the tube side was higher than that on the shell side due to the heat released from exothermic reactions. However, at higher temperature (1173 K) the conditions were unfavorable for C_2 yield. Apparently, hot spot formation occurred in the middle of the reactor, which suggests that the MR configuration from packed bed membrane reactor should be changed to a catalytic membrane reactor with a membrane tube coated with catalyst at the inner tube wall to prevent this hot spot problem.

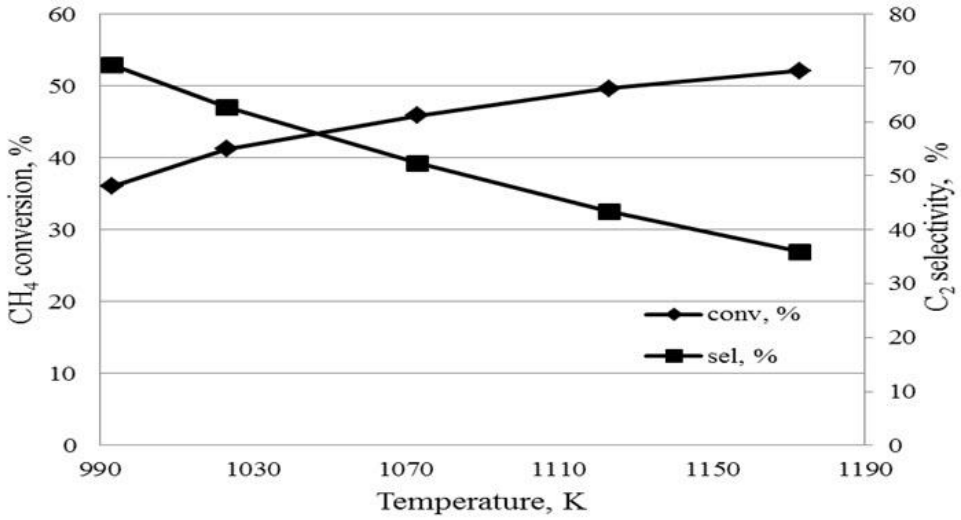

Fig. 5. Effect of temperature on the CH_4 conversion and the C_2 selectivity (air flow rate = 2.8×10^{-4} m^3/s, CH_4 flow rate = $5.5\times10^{-4}m^3/s$).

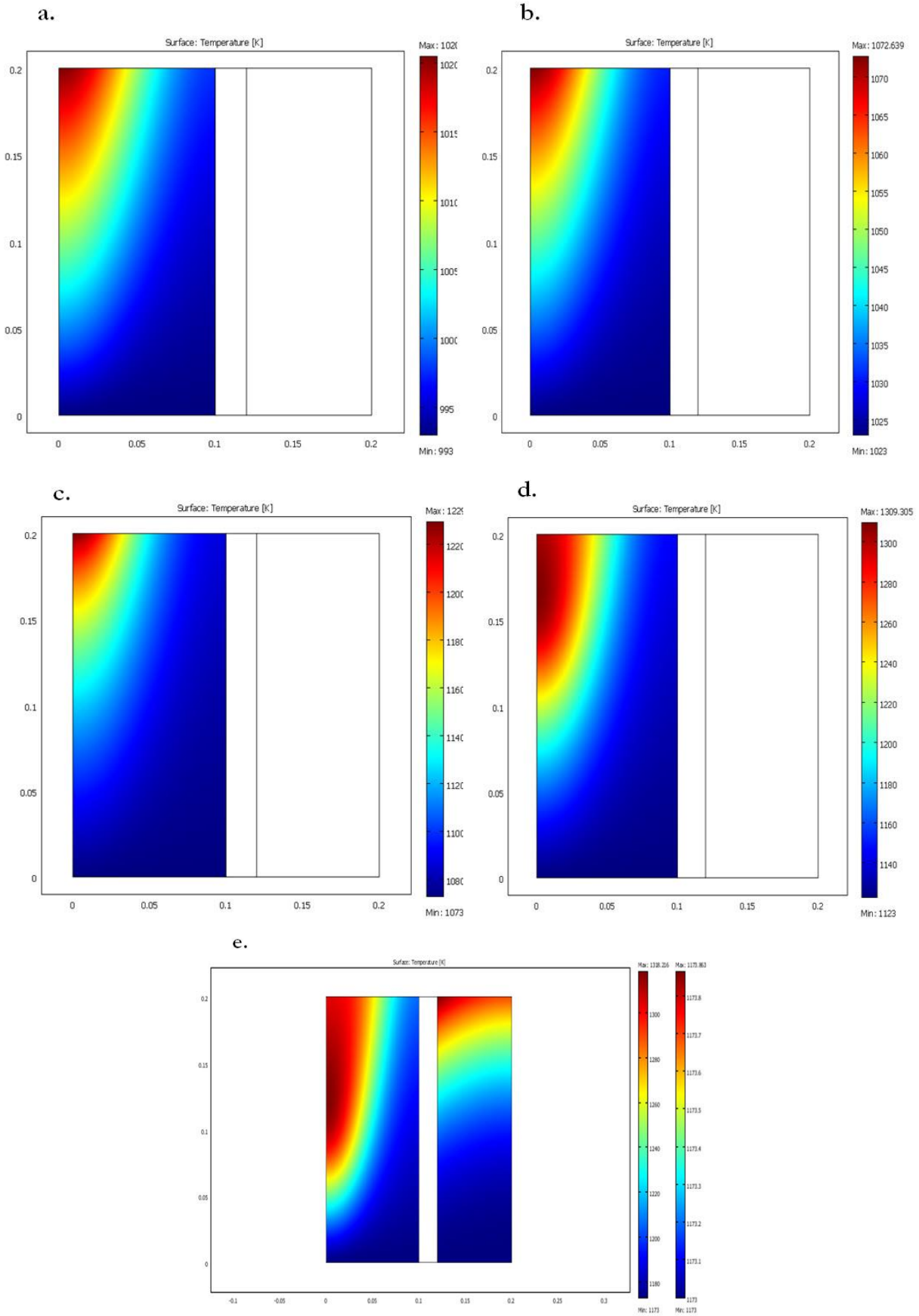

Fig. 6. Temperature profiles at different feed temperatures at T_{inlet}: (a) 993, (b) 1023, (c) 1073, (d) 1123, and (e) 1173 K.

DOI:10.4186/ej.2016.20.1.17

3.2. Comparisons of the Fixed Bed and Membrane Reactors

In this section, the performance comparison between the FBR and the MR is considered based on the same physical dimensions and operating conditions; Na-W-Mn/SiO_2 catalyst loading of 55.983 g, air flow rate of 2.8×10^{-4} m^3/s in FBR (in MR, the flux of oxygen permeated in the tube side is equal to the amount of oxygen that feeds into the FBR), methane flow rate of 8.16×10^{-4} m^3/s and temperature of 1123 K. The maximum yield was found to be 13.5 % for the FBR and 20.11 % for the MR. The main reason for this low performance of the FBR was because the methane and oxygen were fed together into the reactor. Although the CH_4 conversion was high, it was likely to have further oxidation of C_2 products to carbon oxides, which reduces C_2 selectivity. This behavior was different when operating in the membrane reactor. The oxygen concentration in the reactor was controlled and distributed along the length of the membrane; as a result, the formation of C_2 products was promoted over the formation of CO_x. The MR exhibits higher C_2 selectivity than the FBR. Figure 7 shows the different profiles of temperature in FBR and MR. It was obvious that the temperature increase in the FBR was higher than that of the MR. The maximum temperature in the reactor was 1543 K and 1309 K in the FBR and the MR, respectively. Moreover, Fig. 8 shows the temperature effect in the range of 993 to 1173 K on the C_2H_4/C_2H_6 ratio in the C_2 products for an air feed rate of 2.8×10^{-4} m^3/s and a methane feed rate of 5.5×10^{-4} m^3/s. The C_2H_4/C_2H_6 ratio increased with increasing temperature and reached a value of 0.6 in the FBR and 0.8 in the MR at 1173 K. The C_2H_4/C_2H_6 ratio in the MR was much higher than that in the FBR, which was an advantage of the membrane reactor. From the results in this section, the membrane reactor performance was found to be better than that of the fixed bed reactor. Therefore, in the next study, we focus in particular on the membrane reactor.

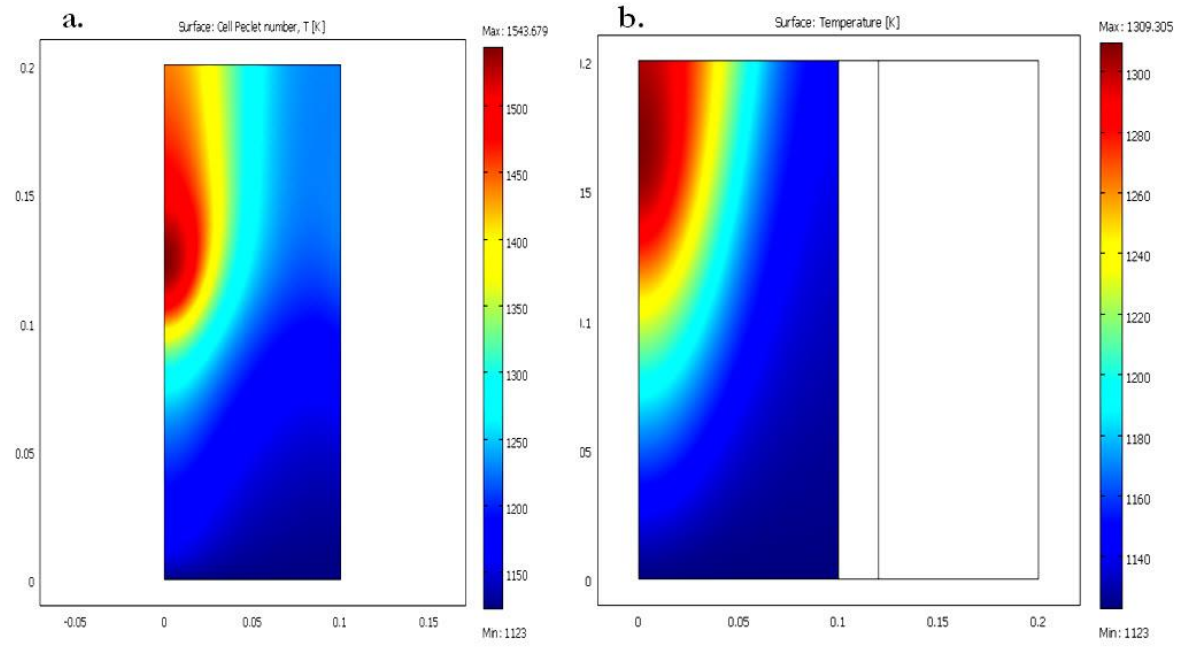

Fig. 7. Temperature profiles for different reactors: (a) FBR and (b) MR. (air flow rate $=1.6\times10^{-4}$ m^3/s, CH_4 flow rate $=5.5\times10^{-4}$ m^3/s)

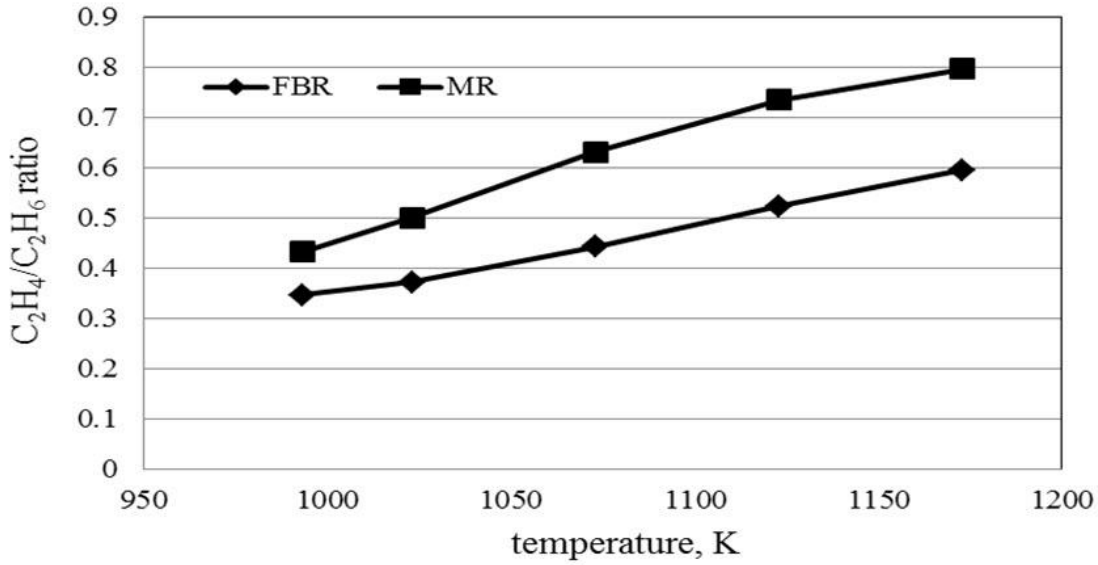

Fig. 8. Comparison of the C_2H_4/C_2H_6 ratio obtained in a FBR and a BSCFO MR over Na-W-Mn/SiO_2 catalyst (air flow rate of 2.8×10^{-4} m^3/s., CH_4 flow rate of 5.5×10^{-4} m^3/s).

3.3. Sizing of the Reactor

In this section, we focus on determining an optimum dimension of MR to provide the best performance in OCM process [16]. The simulations were performed using membrane reactors with different diameters, as summarized in Table 4. The GHSV was kept at the same value for all cases. Table 5 summarizes the different operating conditions used in the simulations of reactors with different sizes.

First, we focus on the characteristics of different diameters of the reactor at a GHSV of 38,904.54 1/h and a temperature of 993 K. Figure 8 shows the membrane area/volume for different diameters of the reactor. The membrane area/volume was observed to decrease, and therefore, oxygen permeation decreased with an increasing reactor diameter. The oxygen permeation had an influence on the reaction rate and the OCM performance. Moreover, the tube diameter affected the variation of the oxygen profile, such as axial and radial dispersion in the tube side, as shown in Fig. 9. For membrane reactors with a small diameter (Figs. 9a–9b), the oxygen permeation was high, especially near the feed inlet, and oxygen was present even at the center of the reactor. For medium diameters (Figs. 9c–9e), the oxygen could permeate through the membrane along the reactor length. The oxygen conversion was found to be lower than that of the small diameter case. In addition, the oxygen concentration in tube side was still high. Furthermore, for larger diameters (Figs. 9f–9g), the oxygen concentration varied significantly along both the axial and radial directions. The concentration of oxygen was not well-distributed throughout in the radius direction, as it was only present near the membrane area (tube wall).

Figure 10 shows the pressure drop over the catalyst bed for the reactors with different diameters. The figure shows that decreasing the reactor diameter causes an increased pressure drop. The difference in size of the membrane reactor obviously influenced the oxygen concentration within the reactor as well as the pressure drop across the catalyst bed.

Figure 11 shows the CH_4 conversion and the C_2 yield for different sizes of the reactor (Table 5) and for different conditions (Table 6). From the simulations, the maximum CH_4 conversion and C_2 yield appeared at the reactor diameter of 0.018 m (model c.), except when the GHSV was 58427.55 1/h at 993 K (Fig. 11a), in which case the maximum CH_4 conversion and C_2 yield occurs at the reactor diameter of 0.027 m (model d.). This result suggests that there is an optimal dimension of the reactor. At a smaller diameter, the membrane area was higher and more oxygen can permeate to the catalyst bed. In this case, the variation of oxygen concentration along the radial direction was not pronounced. These conditions led to higher methane conversion but lower selectivity. However, at too large of a diameter, the lower membrane area resulted in lower oxygen permeation, resulting in the catalyst not being efficiently utilized due to the large variation of oxygen along the radial direction, thus resulting in the lower methane conversion. Therefore, an optimum reactor diameter was observed.

Once we determined the appropriate dimension of the reactor, more simulations were performed under various conditions to determine the best result. The performance of the OCM at different conditions is summarized in Table 7. The best performance was found at a GHSV of 38904.54 1/h and a temperature of 1073 K, offering the highest C_2 yield of 26.82 %.

A comparison of our simulation results with the experimental results is shown in Table 8. For the same membrane type considered in our study, the OCM in a packed bed BSCFO membrane reactor using La-Sr/CaO catalyst reported by [12] and [17] achieved the best C_2 yields of 18 % and 15 %, respectively. For the same catalyst type as considered in our study, the OCM in a packed bed

$Ba_{0.5}Ce_{0.4}Gd_{0.1}Co_{0.8}Fe_{0.2}O_{3-\delta}$ (BCGCFO) membrane reactor using Na-W-Mn/SiO_2 catalyst reported by [18] achieved a C_2 yield of 14.4 %. From all of the results in packed bed membrane reactors that used both the same catalyst and the same membrane as used in our study, our simulation resulted in a higher yield than those reported in the literature. On the contrary, when compared with the result of the catalytic $Ba_{0.5}Ce_{0.4}Gd_{0.1}Co_{0.8}Fe_{0.2}O_{3-\delta}$ (BCGCFO) membrane reactor using Na-W-Mn/SiO_2 catalyst reported by [18], their reported C_2 yield of 34.7 % was better than our results.

Table 3. Comparison between two types of reactor at condition: T= 1123 K, P= 1 atm, air flow rate = 2.8×10^{-4} m^3/s, methane flow rate= 8.16×10^{-4} m^3/s).

Performance	FBR	MR (BSCFO)
CH_4 conversion, %	38.46	37.58
C_2 selectivity, %	35.25	57.23
C_2 yield, %	13.56	21.51

Table 4. Dimension of different sizes of membrane reactor.

Model	**Dimension**		
	r_{tube}(m)	**r_{shell}(m)**	**h(m)**
a.	0.0045	0.010	0.8
b.	0.006	0.013	0.45
c.	0.009	0.018	0.2
d.	0.0135	0.030	0.089
e.	0.018	0.040	0.05
f.	0.0225	0.050	0.032
g.	0.027	0.060	0.022

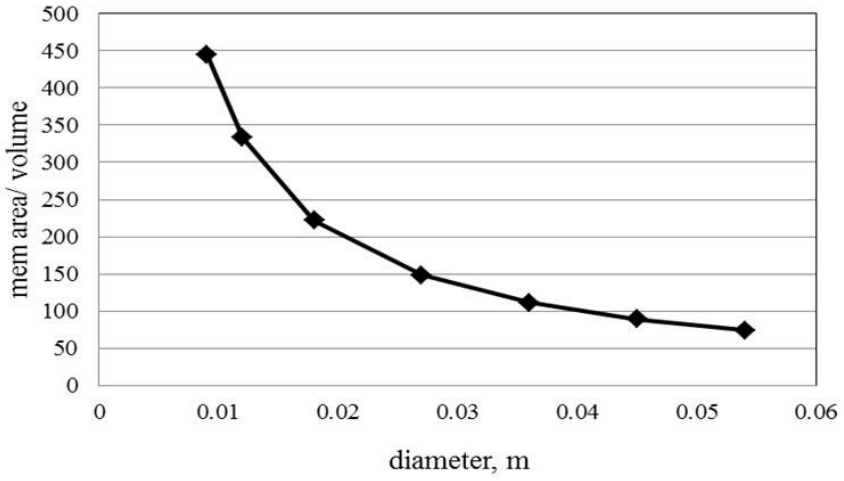

Fig. 9. Membrane/volume for different reactor diameters.

DOI:10.4186/ej.2016.20.1.17

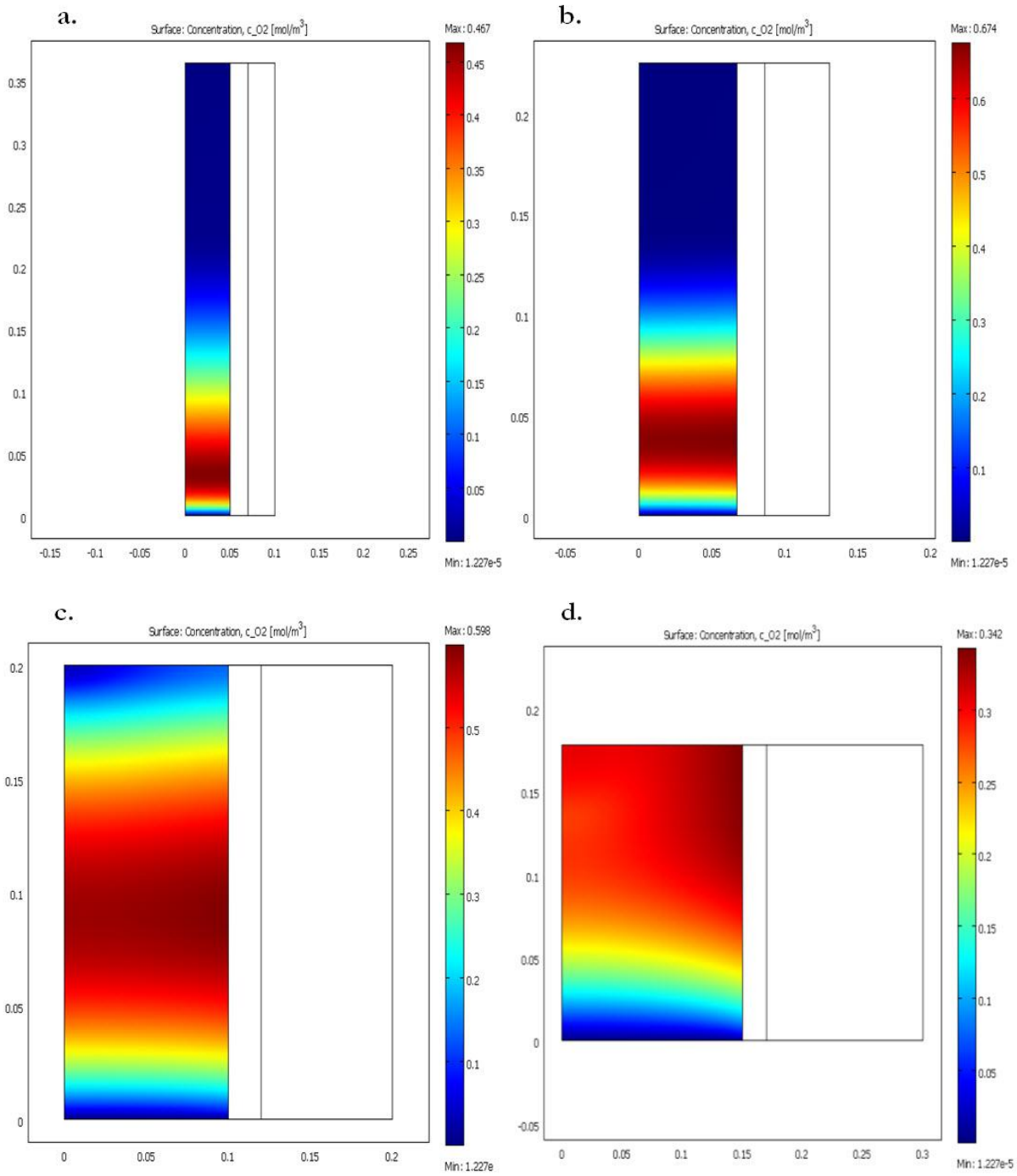

DOI:10.4186/ej.2016.20.1.17

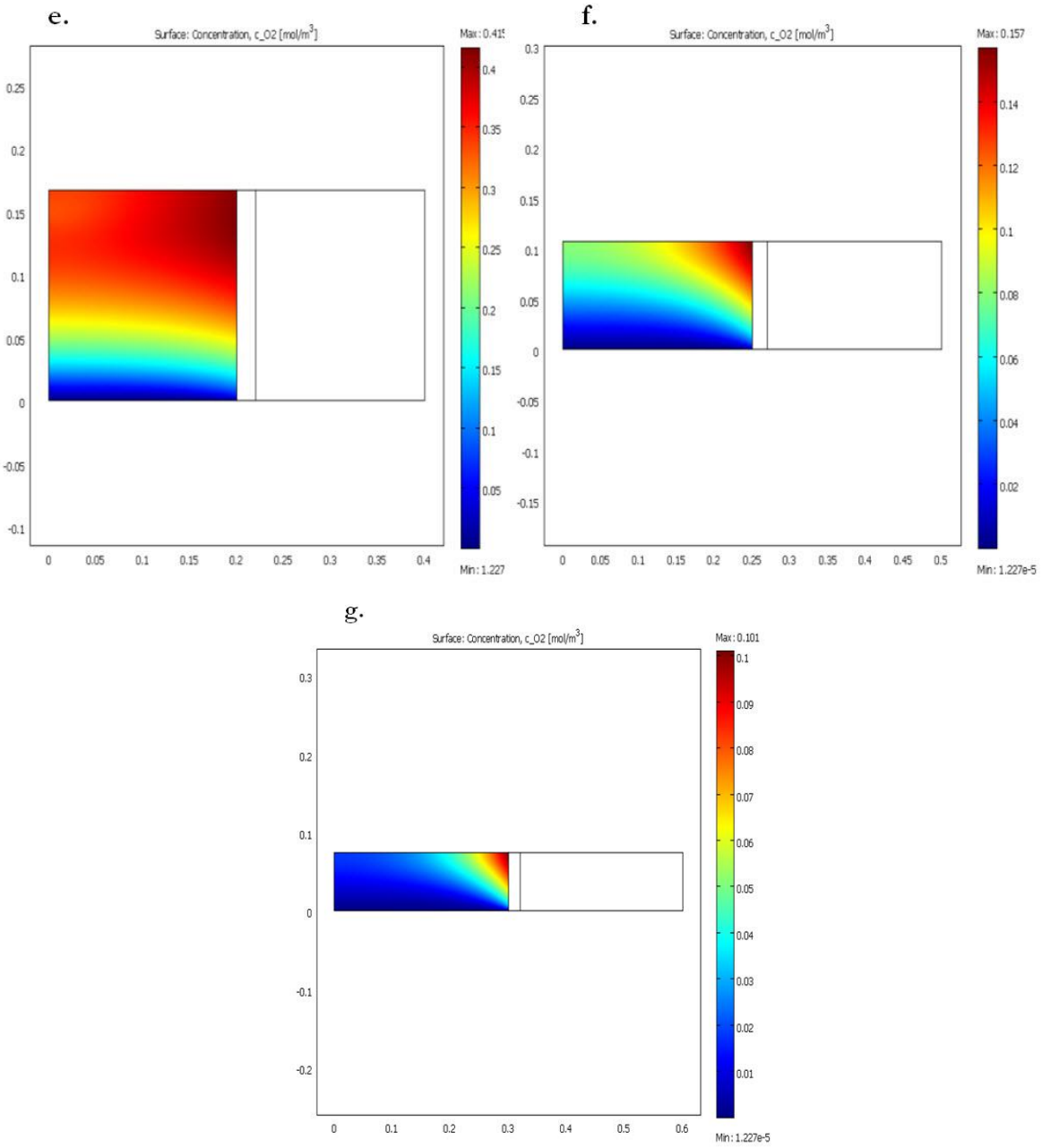

Fig. 10. O_2 concentration profile for different reactor tube diameters.

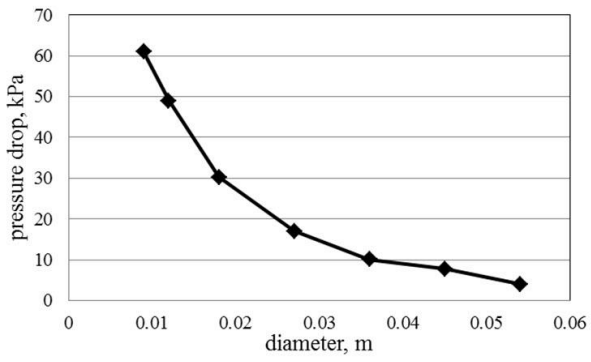

Fig. 11. Pressure drop for different reactor tube diameters (GHSV = 38,904.54 1/h and T = 993 K).

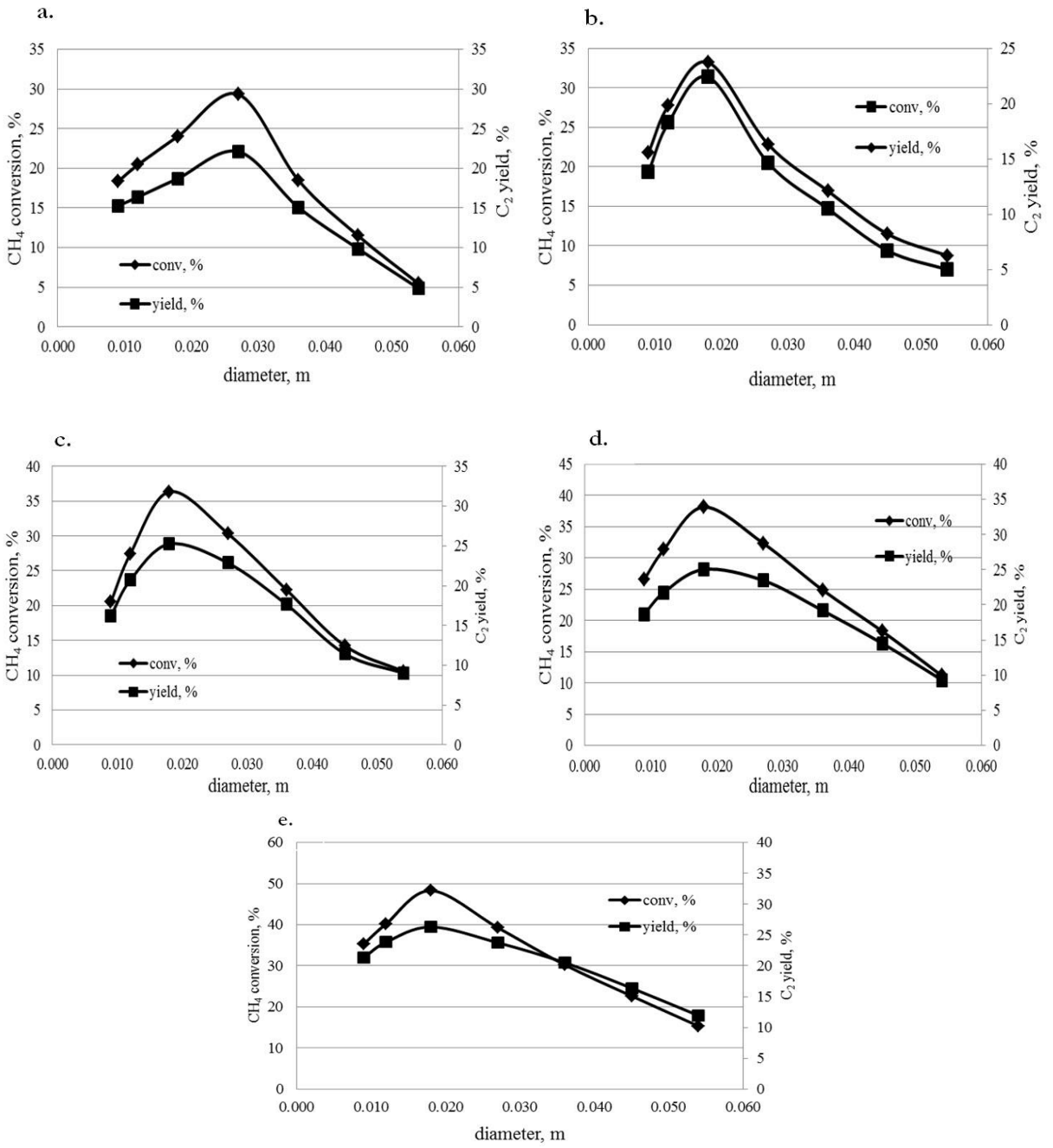

Fig. 12. CH_4 conversion,% and C_2 yield,% for different tube diameters: (a) T= 993 K, GSHV =58427.55 1/h, (b) T= 993 K, GSHV =38904.54 1/h, (c) T= 993 K, GSHV= 19452.27 1/h, (d) T= 1073 K, GSHV =38904.54 1/h, (e) 1173 K, GSHV =38904.54 1/h.

Table 5 Summary OCM performance on optimum reactor at different conditions.

Operating condition		OCM performance		
GHSV (1/h)	T (K)	CH_4 conv, %	C_2 sel, %	C_2 yield, %
58427.55	993	24.051	77.81	18.720
38904.54	993	31.355	75.673	23.272
19452.27	993	36.361	69.412	25.283
38904.54	1073	38.132	65.630	25.026
38904.54	1173	48.285	54.467	26.231
38904.54	1223	52.465	49.653	26.050
38904.54	1273	57.820	43.373	25.087
19452.27	1073	43.713	61.352	26.818
19452.27	1173	50.34	52.973	26.667
19452.27	1223	58.325	41.854	24.241

Table 6. Highest C_2 yield reported for OCM in literature.

Catalyst	Membrane	Type of reactor	Temperature (K)	CH_4 flow rate (m^3/s)	C_2 yield, %	Reported by
Na-W-Mn/SiO_2	BSCFO	PBMR	1073	1.95×10^{-1}	26.82	This work
La-Sr/CaO	BSCFO	PBMR	1123	3.33×10^{-7}	15	Wang *et al.*[12]
La-Sr/CaO	BSCFO	PBMR	1223	1.41×10^{-6}	18	Oliver *et al.*[10]
Na-W-Mn/SiO_2	BCGCFO	PBMR	1123	7.5×10^{-6}	14.4	Bhatia *et al.*[19]
Na-W-Mn/SiO_2	BCGCFO	CMR	1123	7.5×10^{-6}	34.7	Bhatia *et al.*[19]

*$Ba_{0.5}Ce_{0.4}Gd_{0.1}Co_{0.8}Fe_{0.2}O_{3-\delta}$ (BCGCFO)

4. Conclusions

Two-dimensional mathematical modeling of the OCM in a dense BSCFO membrane reactor was investigated in this research. Various operating conditions, such as the methane flow rate, air flow rate and temperature, influence the performance of the OCM reaction. The temperature profiles of a FBR and a dense BSCFO- MR revealed that significant hot spot temperatures were observed for the FBR, unlike the case of the MR. At the optimum dimensions of a dense BSCFO- MR, the values of CH_4 conversion of 43.713 %, C_2 selectivity of 61.352 % and C_2 yield of 26.82 % were obtained.

The performance of the OCM may be improved when changing the reactor configuration, such as a catalytic membrane reactor or fluidized bed reactor. The design of the OCM system utilizing a combination of a reactor and a separation unit with the OCM process to increase the C_2 yield and performance of the OCM process should be considered. Performing a simulation study using a three-dimensional model that accounts for hydrodynamics within the reactor is recommended for future work. This three-dimensional model should represent more realistic phenomena with better prediction accuracy.

Acknowledgements

The authors gratefully acknowledge the Thailand Research Fund and Higher Education Commission and King Mongkut's University of Technology Thonburi for financial support.

References

[1] G. E. Keller and M. M. Bhasin, "Synthesis of ethylene via oxidative coupling of methane: I. Determination of active catalysts," *Journal of Catalysis*, vol. 73, pp. 9–19, 1982.

[2] S. M. Al-Zahrani, "The effects of kinetics, hydrodynamics and feed conditions on methane coupling using fluidized bed reactor," *Catalysis Today*, vol. 64, pp. 217–225, 2001.

[3] W. Kiatkittipong, T. Tagawa, S. Goto, S. Assabumrungrat, K. Silpasup, and P. Praserthdam, "Comparative study of oxidative coupling of methane modeling in various types of reactor," *Chemical Engineering Journal*, vol. 115, pp. 63–71, 2005.
[4] K. Prodip, Z. Yan, and K. R. Ajay, "Multi-objective optimization of simulated countercurrent moving bed chromatographic reactor for oxidative coupling of methane," *Chemical Engineering Science*, vol. 64, pp. 4137–4149, 2009.
[5] O. Louis, H. Stephane, M. Claude, and C. V. V. Andre, "Oxidative coupling of methane using catalyst modified dense perovskite membrane reactors," *Catalysis Today*, vol. 142, pp. 34–41, 2009.
[6] M. R. Quddus, Y. Zhang, and A. K. Ray, "Multi-objective optimization in solid oxide fuel cell for oxidative coupling of methane," *Chemical Engineering Journal*, vol. 165, pp. 639–648, 2010.
[7] M. K. S. Shahri and S. M. Alavi, "Kinetic studies of the oxidative coupling of methane over the $Mn/Na_2WO_4/SiO_2$ catalyst," *Journal of Natural Gas Chemistry*, vol. 18, pp. 25–34, 2009.
[8] Y. Simon, F. Baronne, and P. M. Marquaire, "Kinetic modeling of the oxidative coupling of methane," *Industrial & Engineering Chemistry Research*, vol. 46, pp. 1914–1922, 2007.
[9] C. Y. Thien, A. R. Mohamed, and S. Bhatia, "Process optimization of oxidative coupling of methane for ethylene production using response surface methodology," *Journal of Chemical Technology and Biotechnology*, vol. 82, pp. 81–91, 2007.
[10] L. Olivier, S. P. Haag, C. Mirodatos, and A. C. V. Veen, "Oxidative coupling of methane using catalyst modified dense perovskite membrane reactors," *Catalysis Today*, vol. 142, pp. 34–41, 2009.
[11] Y. K. Kao, L. Lei, and, Y. S. Lin, "Optimum operation of oxidative coupling of methane in porous ceramic membrane reactors," *Catalysis Today*, vol. 82, pp. 255–273, 2003.
[12] H. Wang, C. You, and W. Yung, "Oxygen permeation study in a tubular $Ba_{0.5}Sr_{0.5}Co_{0.8}Fe_{0.2}O_{3-\delta}$ oxygen permeable membrane," *Journal of Membrane Science*, vol. 210, pp. 259–271, 2002.
[13] A. L. Shaula, A. A. Yaremchenko, V. V. Kharton, D. I. Logvinovich, E. N. Naumovich, A. V. Kovalevsky, J. R. Frade, and F. M. B. Marques, "Oxygen permeability of $LaGaO_3$-based ceramic membranes," *Journal of Membrane Science*, vol. 221, pp. 69–77, 2003.
[14] M. Daneshpayeh, K. Abbasali, M. Navid, M. Yadolah, S. Rahmate, and T. Alireza, "Kinetic modeling of oxidative coupling of methane over $Mn/Na_2WO_4/SiO_2$ catalyst," *Fuel Processing Technology*, vol. 90, pp. 403–410, 2009.
[15] R. M. de Brito Alves, C. A. O. Nascimento, and E. C. Biscaia Jr., "Robust integration of RTO and MPC," in *10th International Symposium on Process Systems Engineering, Part A*. Elsevier, British Library, 2009.
[16] H. Wang, C. You, and W. Yung, "Oxidative coupling of methane in Ba0.5Sr0.5Co0.8Fe0.2O3-δ (BSCF) tubular membrane reactors," *Catalysis Today*, vol. 104, pp. 160–167, 2005.
[17] Y. K. Kao, L. Lei, and Y. S. Lin, "A comparative simulation study on oxidative coupling of methane in fixed-bed and membrane reactors," *Industrial & Engineering Chemistry Research*, vol. 36, pp. 3583–3593, 1997.
[18] H. Liu, X. Wang, D. Yung, R. Gao, Z. Wang, and J. Jung, "Scale up and stability test for oxidative coupling of methane over Na2WO4-Mn/SiO2 catalyst in a 200 ml fixed-bed reactor," *Natural Gas Chemistry*, vol. 17, pp. 59–63, 2008.
[19] S. Bhatia, C. Y. Thien, and A. R. Mohamed, "Oxidative coupling of methane (OCM) in a catalytic membrane reactor and comparison of its performance with other catalytic reactors," *Chemical Engineering Journal*, vol. 148, pp. 525–532, 2009.

CHEMICAL ENGINEERING TRANSACTIONS
VOL. 57, 2017
A publication of AIDIC
The Italian Association of Chemical Engineering
Online at www.aidic.it/cet
Guest Editors: Sauro Pierucci, Jiří Jaromír Klemeš, Laura Piazza, Serafim Bakalis
Copyright © 2017, AIDIC Servizi S.r.l.
ISBN 978-88-95608- 48-8; **ISSN** 2283-9216
DOI: 10.3303/CET1757270

Analysis of Unbalanced Pressure PEM Electrolyzer for High Pressure Hydrogen Production

Dang Saebea[a], Yaneeporn Patcharavorachot[b], Viktor Hacker[c], Sutthichai Assabumrungrat[d], Amornchai Arpornwichanop[e] ,Suthida Authayanun[f*]

[a]Department of Chemical Engineering, Faculty of Engineering, Burapha University, Chonburi 20131, Thailand
[b]School of Chemical Engineering, Faculty of Engineering, King Mongkut's Institute of Technology Ladkrabang, Bangkok 10520, Thailand
[c]Institute of Chemical Engineering and Environmental Technology, Graz University of Technology, Inffeldgasse 25C, Graz 8010, Austria
[d]Center of Excellence in Catalysis and Catalytic Reaction Engineering, Department of Chemical Engineering, Faculty of Engineering, Chulalongkorn University, Bangkok 10330, Thailand
[e]Computational Process Engineering Research Unit, Department of Chemical Engineering, Faculty of Engineering, Chulalongkorn University, Bangkok 10330, Thailand
[f]Department of Chemical Engineering, Faculty of Engineering, Srinakharinwirot University, Nakhon Nayok 26120, Thailand
suthidaa@g.swu.ac.th

Proton exchange membrane (PEM) electrolyzer is a promising technology and likely to be an important hydrogen generator. The ability to produce high purity hydrogen and deliver it at relatively high pressure is an important advantage of the PEM electrolyzer technology. In this work, the high pressure PEM electrolyzer without the need for external compression is studied. The simulation of the electrolyzer is performed based on an electrochemical model with consideration of hydrogen permeation. The effect of cathode pressure and membrane thickness on electrolyzer performance is studied. The explosion limit of a hydrogen-oxygen mixture in the anode is also taken into consideration. The electrochemical compression shows advantage in term of delivering hydrogen at high pressure with having less effect on performance and low power requirement. The increase of cathode pressure slightly affects the electrolyzer performance. The high pressure operation at the cathode and the use of thin membranes cause hydrogen crossover from the cathode to anode, especially at high current density operation.

1. Introduction

The hydrogen production from a water electrolysis has several advantages in terms of high purity, simple process, no pollution and availability of sources (Herraiz-Cardona, 2013). Industrial water electrolysis cells have been established for one hundred years (Leroy, 1983). There are four types of electrolyzers available: alkaline, acid, polymer electrolyte membrane and high temperature solid oxide electrolyzers. Proton exchange membrane (PEM) or solid polymer electrolyte (SPE) electrolysis is a promising technology and is likely to be an important hydrogen generator in a hydrogen economy. The ability to produce high purity and high pressure hydrogen is a significant advantage of the PEM electrolyzer technology (Santarelli et al., 2009). In contrast to alkaline electrolyzers, caustic alkaline or acidic fluid electrolyte is not necessary for PEM electrolyzers. The electrolyte for PEM electrolyzers is a polymer membrane. The most commonly used membrane is Nafion with a thickness of less than 0.2 mm (Ursua et al., 2012). In addition, PEM electrolysis has additional advantages over alkaline electrolysis such as lower parasitic energy losses and higher purity hydrogen output. Compared to the alkaline electrolyte, PEM can be operated at higher current densities due to the higher conductivity of the electrolyte (Marangio et al., 2009). The electrodes of PEM electrolyzer typically consist of noble metals, e.g., platinum or iridium. The following reactions take place in a PEM electrolysis cell:

Anode: $H_2O \dashrightarrow \frac{1}{2}O_2 + 2H^+ + 2e^-$ (1)

Please cite this article as: Saebea D., Patcharavorachot Y., Hacker V., Assabumrungrat S., Arpornwichanop A., Authayanun S., 2017, Analysis of unbalanced pressure pem electrolyzer for high pressure hydrogen production, Chemical Engineering Transactions, 57, 1615-1620
DOI: 10.3303/CET1757270

Cathode: $2H^+ + 2e^- \dashrightarrow H_2$ (2)

At the anode, water is oxidized to produce oxygen, electrons and protons. Protons transport across the membrane to the cathode and react with electron to produce hydrogen (Eqs(1) and (2)). PEM electrolyzers are commercially available for low scale production applications. The hydrogen purity is typically above 99.99 vol.% (in some cases up to 99.999 vol.%) without the need of an auxiliary purification equipment (Bhandari et al., 2014). Moreover, low gaseous permeability of the polymeric membranes lowers the risk of flammable mixtures formation. PEM electrolyzers operate at a temperature of around 80 °C and a pressure of up to 15 bar. Typically, PEM electrolyzers have production capacities of 0.06–30 Nm^3H_2/hr. Specific energy demand is typically in the range of 6–8 kWh/Nm^3 H_2 and their efficiencies are in the range of 67–82% (Bhandari et al., 2014).

A solid electrolyte allows for a compact system design with strong/resistant structural properties, which high operational pressures (equal or differential across the electrolyte) are achievable (Medina and Santarelli, 2010). Some commercial models have claimed to reach pressures up to 350 bar (Ayers et al., 2010). System with high pressure operation (Grigoriev et al., 2010) of an electrolyzer (sometimes called electrochemical compression), requires less energy to compress and store hydrogen. High pressure PEM electrolyzers to deliver hydrogen at pressures of 1.4 MPa and 35 MPa were developed by Proton Energy Systems and Mitsubishi, respectively (Barbir, 2005; Witschonke, 2014). In addition, high pressure oxygen production from water electrolysis cell stack has also been developed and it can generate oxygen at pressures over 20 MPa (Roy et al., 2011).

Typically, there are two main technology developments for high pressure electrolysis. The former is to keep the whole electrolyzer stack in a pressure vessel, and the feeding water is pumped to the same pressure of the produced hydrogen (Janssen et al., 2004). The latter is emerging in new applications (Cropley, 2005; Degiorgis et al., 2007), at the present in very small sizes, with an unbalanced pressure across the cell (anode near ambient pressure, whereas the cathode side is maintained at the hydrogen delivery pressure). PEM electrolyzer can produce high purity-hydrogen and deliver it at a relatively high pressure but the high pressure operation at the cathode causes hydrogen crossover from the cathode to anode and thus deteriorates the cell performance. However, the study of unbalance pressure PEM electrolyzer is still limit and the effect of membrane thickness on cell performance at high pressure operation should be considered. In this work, the PEM electrolyzer system to produce high pressure hydrogen with consideration of hydrogen permeation is theoretically investigated. The electrochemical and hydrogen crossover models are coded by Matlab. The effect of cathode pressure and membrane thickness on electrolyzer performance is presented when the explosion limit of a hydrogen-oxygen mixture in the anode is also taken into consideration.

2. PEM electrolyzer model

The electrochemical model of a high pressure PEM electrolyzer is used to investigate its performance and efficiency. The unbalanced pressure between the anode (2 bar) and cathode (10-100 bar) are applied to produce high hydrogen pressure and the effect of a hydrogen permeation is taken into account. In the electrochemical model, the cell voltage can be calculated by adding the open circuit voltage, the maximum voltage, by various losses (i.e., activation, concentration and ohmic losses) as shown in Eq(3).

$$V = E + \eta_{ac} + \eta_d + \eta_{ohm} \tag{3}$$

The open circuit voltage can be calculated by the fraction of proton back-permeation to total proton permeation (k) and Gibb's free energy (G) as shown in Eqs(4)-(8). The hydrogen permeation is shown in Eq(7) (Kim et al., 2013).

$$E = -(1-k)\frac{\Delta G}{2F} \tag{4}$$

$$\Delta G = \Delta G^\circ + RT_m \ln \frac{p_{H,c} p_{O,a}^{1/2}}{p_{W,a}} \tag{5}$$

$$k = \frac{\gamma_a \dot{n}_{H,per}}{\dot{n}_H + \gamma_a \dot{n}_{H,per}} \tag{6}$$

$$\dot{n}_{H,per} = \frac{D_H}{H_H} \frac{p_{H,c} - p_{H,a}}{h_m} \tag{7}$$

$$\dot{n}_H = \frac{i}{2F} - \gamma_a \dot{n}_{H,per} \tag{8}$$

The activation loss and ohmic loss are shown as follows:

$$\eta_{ac} = \frac{RT_a}{\alpha_a F}\text{arcsinh}\frac{i}{2i_{0,a}} + \frac{RT_c}{\alpha_c F}\text{arcsinh}\frac{i}{2i_{0,c}} \tag{9}$$

$$\eta_{ohm} = ir_e + h_{mem}\frac{i}{\sigma_{mem}} \tag{10}$$

$$\sigma_{mem} = (0.005139\gamma_{mem} - 0.00326)\exp\left[1268\left(\frac{1}{303} - \frac{1}{T_m}\right)\right] \tag{11}$$

In addition, the concentration loss can be calculated from Fick's law as shown in Table 1.

Table 1: *Concentration loss model*

Parameters	Equations
Concentration loss	$\eta_d = \frac{RT_a}{4F}\ln\frac{C_{a,O}}{C_{0,O,a}} + \frac{RT_c}{2F}\ln\frac{C_{c,H}}{C_{0,H,c}}$
O_2 concentration at catalyst surface	$C_{0,O,a} = C_{O_2,ch} + \frac{\delta_{e,an}}{D_{eff,an}}\dot{n}_{O_2}$
	$C_{O_2,ch} = \frac{\dot{n}_{O_2}}{\dot{n}_{O_2} + \dot{n}_{H_2O,an}} \cdot \frac{P_{an}}{RT_{an}}$
H_2 concentration at catalyst surface	$C_{0,H,c} = C_{H_2,ch} + \frac{\delta_{e,cat}}{D_{eff,cat}}\dot{n}_{H_2}$
	$C_{H_2,ch} = \frac{\dot{n}_{H_2}}{\dot{n}_{H_2} + \dot{n}_{H_2O,cat}} \cdot \frac{P_{cat}}{RT_{cat}}$

It is noted that details of the model describing the voltage losses used in this study can be found in Marangio et al. (2009). The simulation model of high pressure PEM electrolyzer is solved by Matlab.

3. Results and discussion

The performance of high temperature PEM electrolyzer is studied under the cathode pressure varying from 10 to 100 bar. The effect of cathode pressure on the voltage and current density relationship is shown in Figure 1.

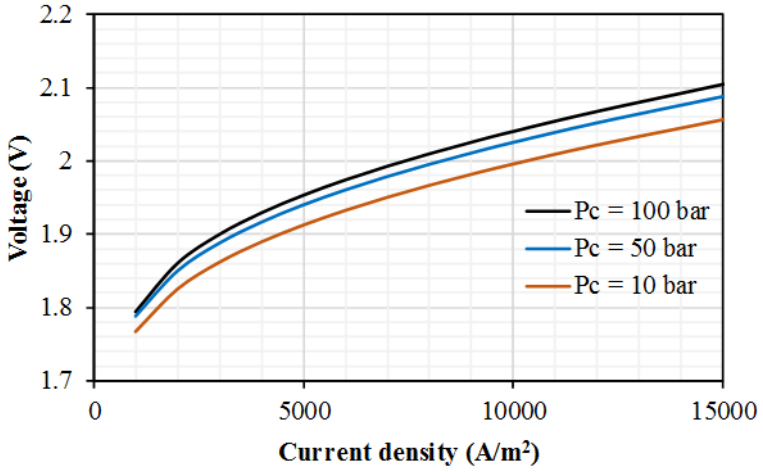

Figure 1: Voltage and current density relationship of high pressure PEM electrolyzer at different cathode pressures

It is observed that the voltage slightly increases with increasing cathode pressure. This results in a higher power demand when hydrogen is produced at high pressure. In addition, the hydrogen concentration at the anode and hydrogen permeated flux caused by the hydrogen crossover phenomena is shown in Figure 2. It is found that an increase in cathode pressure results in the increase of both the hydrogen concentration and hydrogen concentration flux at the anode. This is because a high pressure difference between the cathode and anode promotes the hydrogen permeation from the high pressure to low pressure side (the anode pressure is specified at 2 bar). The hydrogen permeated flux increases with the increasing current density because the high amount of hydrogen is produced at high current densities and this results in high concentration gradient between the cathode and the anode. Although high hydrogen is permeated to the anode at high current density, more oxygen is also produced at high current density. Therefore, high hydrogen concentration at the anode is observed at low current density up to 6000 A/m^2 and the operation at high current density has slightly effect on hydrogen permeation as shown in Figure 2. However, the hydrogen fraction in the anode mixture stream consisting of oxygen and hydrogen is below the explosion limit at all of the studied operational cathode pressures.

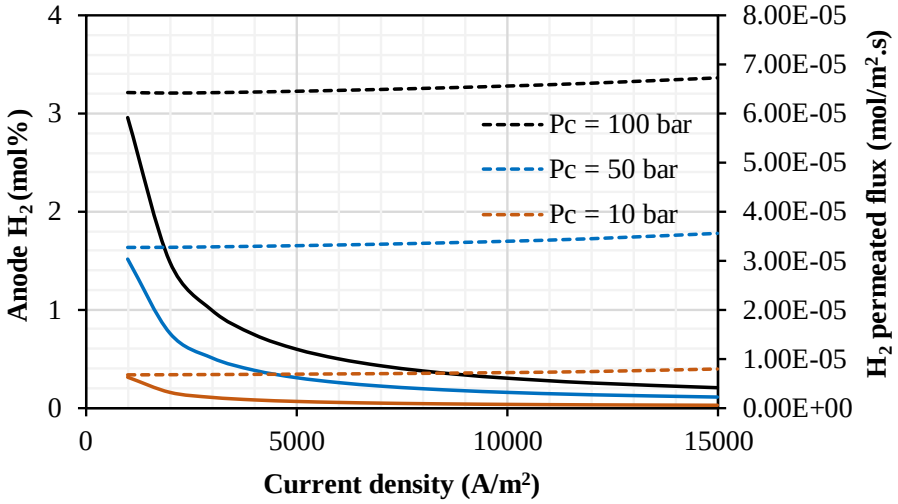

Figure 2: Effect of current density and pressure on anode hydrogen concentration (solid line) and hydrogen permeated flux (dash line) in the high pressure PEM electrolyzer.

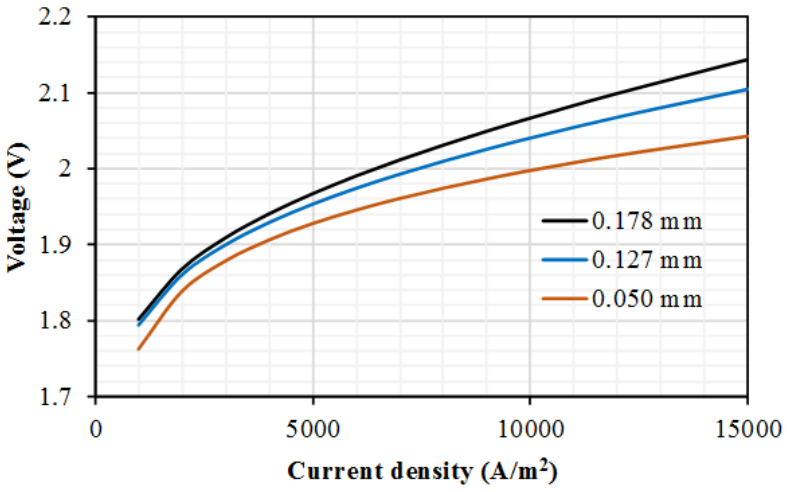

Figure 3: Voltage and current density relationship of the high pressure PEM electrolyzer at different membrane thickness.

Furthermore, the effect of membrane thickness of 50, 127 and 178 μm for Nafion 112, Nafion 115 and Nafion 117, respectively, on the performance of high pressure PEM electrolyzer is investigated and the simulation results are shown in Figure 3. From the results, it is found that thinner membranes provide higher performance at high pressure operation. The use of thick membrane result in the increase of ohmic loss and thus the high

voltage operation is observed. However, the membrane thickness also affects the hydrogen permeation from the cathode to anode. The effect of membrane thickness on hydrogen fraction on anode stream and hydrogen permeated flux at high cathode pressure (100 bar) is shown in Figure 4. The opposite trend is observed when the results are compared with effect of membrane thickness on electrolyzer performance in Figure 3. It is found that the use of thick membrane has the positive effect on the reduction of hydrogen crossover. Hydrogen easily permeates from the cathode to anode when thin membrane is applied. In addition, the hydrogen fraction in the anode stream is over the explosion limit at membrane thickness of 50 μm with low-current density operation but the hydrogen is below the explosion limit (5.7% at 100 bar) at all studied current density when the membrane thickness of 127 and 178 μm is used.

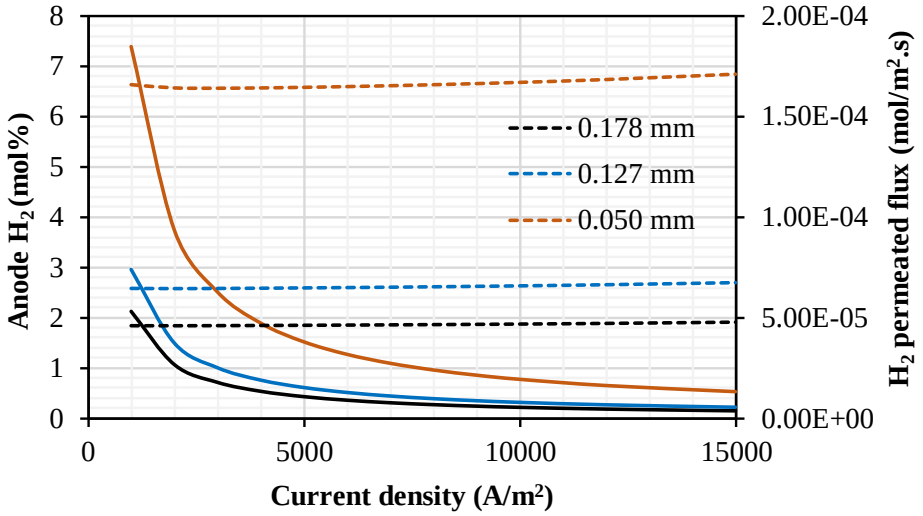

Figure 4: Effect of current density and membrane thickness on anode hydrogen concentration (solid line) and hydrogen permeated flux (dash line) in the high pressure PEM electrolyzer.

4. Conclusions

The simulation of a high pressure PEM electrolyzer without the need for external compression based on electrochemical model is studied for clean hydrogen production. High pressure operation of the PEM electrolyzer brings the advantage of delivering hydrogen at a high pressure with the acceptable hydrogen permeation. The concentration of hydrogen at the anode increases with increasing pressure at the cathode and reducing membrane thickness and current density. Compared to thinner membrane, the use of thick membrane provides lower performance. However, the high hydrogen permeation is promoted with the use of thin membrane and high cathode pressure operation.

Acknowledgments

Support from Srinakharinwirot University, Thailand research fund (DPG5880003) and the Ernst Mach-Grants-ASEA-UNINET is gratefully acknowledged.

Reference

Ayers K.E., Anderson E.B., Capuano C., Carter B., Dalton L., Hanlon G., et al., 2010, Research advances towards low cost, high efficiency PEM electrolysis. ECS Trans., 33, 3-15.

Barbir F., 2005, PEM electrolysis for production of hydrogen from renewable energy sources Sol. Energy, 78, 661-669.

Bhandari R., Trudewind C.A., Zapp P., 2014, Life cycle assessment of hydrogen production via electrolysis – a review. J. Clean. Product., 85, 151-163.

Cropley C., Low-cost, high pressure hydrogen generator, Fy2005 progress report, DOE hydrogen program (2005).

Degiorgis L., Santarelli M., Cali M., 2007, Hydrogen from renewable energy: a pilot plant for thermal production and mobility. J. Power Sources, 171, 237-246.

Grigoriev S.A., Kalinnikov A.A., Millet P., Porembsky V.I., Fateev V.N., 2010, Mathematical modeling of high pressure PEM water electrolysis. J. Appl. Electrochem.,40, 921-932.

Herraiz-Cardona I., González-Buch C., Ortega E., García-Antón J., Pérez-Herranz V., 2013, Energy Efficiency Improvement of Alkaline Water Electrolysis by using 3D Ni Cathodes Fabricated via a Double-Template Electrochemical Process. Chemical Engineering Transactions, 32, 451-456.

Hertel T., Over H., Bludau H., Gierer M., Ertl G., 1994a, The invention of a new solid surface, Surf. Sci. 301, 10-25.

Janssen H., Bringmann J.C., Emonts B., Schroeder V., 2004, Safety related studies on hydrogen production in high pressure electrolysers. Int. J. Hydrogen Energy, 29, 759-770.

Kim H., Park M., Lee K.S., 2013, One-dimensional dynamic modeling of a high-pressure water electrolysis system for hydrogen production. Int. J. Hydrogen Energy, 38, 2596–2609.

Leroy R.L., 1983, Industrial water electrolysis-present and future, Int. J. Hydrogen Energy, 8, 401–417.

Marangio F., Santarelli M., Cali M., 2009, Theoretical model and experimental analysis of a high pressure PEM water electrolyser for hydrogen production. Int. J. Hydrogen Energy, 34, 1143-1158.

Medina P., Santarelli M., 2010, Analysis of water transport in a high pressure PEM electrolyzer. Int. J. Hydrogen Energy, 35, 5173-5186.

Roy R.J., Graf J.C., Gallus T.D., Rios D.L., Smith S.R., Diderich G.S., 2011, Development testing of a high differential pressure (HDP) water electrolysis cell Stack for the high pressure oxygen generating assembly (HPOGA), SAE Int. J. Aerosp., 4, 19-28.

Santarelli M., Medina P., Cali M.,2009, Fitting regression model and experimental validation for a high pressure PEM electrolyzer. Int. J. Hydrogen Energy, 34, 2519–2530.

Ursua A., Gandia L.M., Sanchis P., 2012, Hydrogen production from water electrolysis: current status and future trends. Proc. of the IEEE, 100, 410-426.

Witschonke R., 2004, Mitsubishi generates 350 bar hydrogen without compressor Fuel Cells Bull., 2004, 8-9.

CHEMICAL ENGINEERING TRANSACTIONS
VOL. 57, 2017
A publication of AIDIC
The Italian Association of Chemical Engineering
Online at www.aidic.it/cet
Guest Editors: Sauro Pierucci, Jiří Jaromír Klemeš, Laura Piazza, Serafim Bakalis
Copyright © 2017, AIDIC Servizi S.r.l.
ISBN 978-88-95608- 48-8; **ISSN** 2283-9216
DOI: 10.3303/CET1757272

Performance Analysis of Solid-oxide Electrolysis Cells for Syngas Production by H_2O/CO_2 Co-electrolysis

Dang Saebea[*a], Suthida Authayanun[b], Yaneeporn Patcharavorachot[c], Soipatta Soisuwan[a], Suttichai Assabumrungrat[d], Amornchai Arpornwichanop[e]

[a]Department of Chemical Engineering, Faculty of Engineering, Burapha University, Chonburi 20131, Thailand
[b]Department of Chemical Engineering, Faculty of Engineering, Srinakharinwirot University, Nakorn Nayok 26120, Thailand
[c]School of Chemical Engineering, Faculty of Engineering, King Mongkut's Institute of Technology Ladkrabang, Bangkok 10520, Thailand
[d]Center of Excellence on Catalysis and Catalytic Reaction Engineering, Department of Cehmical Engineering, Chulalongkorn Univeristy, Bangkok 10330, Thailand
[e]Computational Process Engineering Research Unit, Department of Chemical Engineering, Faculty of Engineering, Chulalongkorn University, Bangkok 10330, Thailand
dangs@eng.buu.ac.th

High-temperature solid oxide electrolysis cells (SOECs) are promising technologies to store excess renewable energy generation. In this work, the mathematical model of SOEC, which can describe the behaviour of a cathode-supported SOEC operating for H_2O and CO_2 co-electrolysis, is developed from mass balance, dusty gas model, and electrochemical model. The validated SOEC model is used to analyse the influence of the reversible water-gas shift reaction taking place on the cathode on the performance of the SOEC for syngas production. The simulation results show that the reverse water-gas shift reaction is highly pronounced at the cathode surface due to high CO_2 component and can contribute to CO production. The rate of water-gas shift reaction increases along the depth of the cathode to the three-phase boundary. At the three-phase boundary, an increase in operating temperatures results in the enhancement of the rate of water-gas shift reaction. Additionally, regarding the SOEC performance, the electrical energy consumed for co-electrolysis in SOEC decreases with increasing temperature because the activation overpotentials and ohmic overpotentials are lower.

1. Introduction

The global energy consumption has increased continuously whereas fossil fuel as main energy has depleted. Presently, renewable energy sources, such as solar and wind, have received considerable attention due to their abundance and sustainability (Saebea et al., 2016). However, these types of energy are restricted in time and space, intermittence, and site specific. Hydrogen production technologies have been developed rapidly (Saebea et al., 2014). The use of electricity from solar cells or wind turbines to produce hydrogen via electrolyzers is a promising way to convert their unstable energies to a stable chemical energy (Ebbesen et al., 2012). Among various types of the electrolysis cells, solid oxide electrolysis cells (SOECs) have received considerable attention because of theirs high efficiency and high feed impurity tolerance (Ferrero et al., 2013). Additionally, the SOECs are able to reduce an amount of CO_2 by electrolysis of CO_2 to CO. In general, the CO_2 electrolysis consumes high electrical power (Kazempoor & Braun, 2015). However, the power consumption of CO_2 electrolysis can be reduced by simultaneously electrolyzing H_2O and CO_2 because more CO can be generated via the reverse water-gas shift (RWGS) reaction (Menon et al., 2014). Because the RWGS reaction is reversible, the reaction direction depends on its operating conditions. As the electrochemical reactions, kinetic reactions, mass transfers, and charge transfers of H_2O/CO_2 co-electrolysis in SOEC are quite complicated. The understanding of primary operating parameters on physical phenomenon in SOEC is required to provide its optimal conditions.

Please cite this article as: Saebea D., Authayanun S., Patcharavorachot Y., Soisuwan S., Assabumrungrat S., Arpornwichanop A., 2017, Performance analysis of solid-oxide electrolysis cells for syngas production by h2o/co2 co-electrolysis, Chemical Engineering Transactions, 57, 1627-1632 DOI: 10.3303/CET1757272

The aim of this study is to analyse the influence of the RWGS reaction taking place on the cathode and the SOEC performance for the syngas production. The SOEC model is based on mass balances, the electrochemical model, and the dusty gas model to explain the multiple reactions and multi-component mass transport in SOEC. Additionally, the influence of operating temperatures on the cell performance is investigated.

2. Modelling of SOEC

A planar solid oxide electrolysis cell (SOEC) is considered in this study, as shown in Figure 1. The production of H_2 and CO in SOEC needs the electricity input in order to proceed the electrolysis reaction. H_2O and CO_2 are converted to H_2 and CO at the cathode/electrolyte interface via co-electrolysis (Eqs (1) and (2)). Oxygen ions produced at the cathode diffuse through the electrolyte to the anode and the oxygen occurs from the oxidation reaction at the anode, shown in Eq(3). Moreover, the WGS reaction occurs at the cathode porous material of SOEC and can be expressed in Eq(4). The WGS reaction as the equilibrium reaction over nickel catalyst can shift forward and backward reactions depending on the operating condition. This reaction has an important influence on the CO production and can reduce the power input in the SOEC (Ni, 2012).

Reduction reaction (cathode):

$$H_2O+2e^- \longrightarrow H_2+O^{2-} \quad (1)$$

$$CO_2+2e^- \longrightarrow CO+O^{2-} \quad (2)$$

Oxidation reaction (Anode):

$$2O^{2-} \longrightarrow O_2+4e^- \quad (3)$$

Water-gas shift reaction:

$$CO+H_2O \longleftrightarrow H_2+CO_2 \quad (4)$$

The gaseous species in air and fuel channels transport in the electrode to the three-phase boundary. The RWGS reaction takes place in the porous cathode. The transports of gas molecules in the electrode are considered as the one-dimensional diffusion along the electrode thickness from the reaction-diffusion equation, which is given by:

$$\frac{\varepsilon}{RT}\frac{\partial(y_i P)}{\partial t} = -\nabla N_i + R_i \quad (5)$$

where y_i is the molar fraction of component i, ε is the electrode porosity, P is the total pressure, R_i is the reaction rate of component i, and N_i is the molar flux of component i.
The molar flux of multi-component H_2-H_2O-CO-CO_2 systems is represented by the dusty gas model, which can express the relationship between molar fluxes, molar concentrations, pressure gradient, and concentration gradients as:

$$\frac{N_i}{D_{i,k}^{eff}} + \sum_{j=1, j\neq i}^{n} \frac{y_j N_i - y_i N_j}{D_{ij}^{eff}} = -\frac{P}{RT}\frac{dy_i}{dx} \quad (6)$$

where $D_{i,k}^{eff}$ is the Knudsen diffusivity of component i and D_{ij}^{eff} is the binary diffusivity of component between i and j.

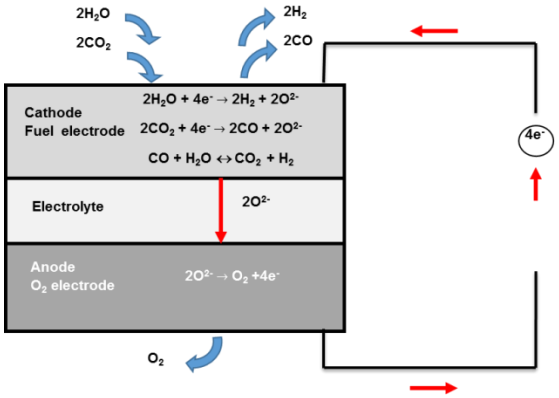

Figure 1: Schematic side view of a planar solid oxide electrolysis cell.

The net current density is the sum of current density for the H_2O electrolysis and CO_2 electrolysis. The partition ratio of the current density of H_2O and CO_2 at the electrode/electrolyte interface is calculated from the normalization factor (γ), which is given by

$$i = I_{H_2} + I_{CO} = \gamma i_{H_2} + (1\text{-}\gamma) i_{CO} \tag{7}$$

where

$$\gamma = \frac{y_{H_2O}^{TPB}}{y_{H_2O}^{TPB} + y_{CO_2}^{TPB}} \tag{8}$$

The difference of thermodynamic potential among the electrode reactions is the reversible potential that can be calculated by the Nernst equation as:

$$E_{H_2}^{rev} = E_{H_2}^{0} + \frac{RT}{2F} \ln \left[\frac{P_{H_2}^{TPB} \left(P_{O_2}^{TPB} \right)^{\frac{1}{2}}}{P_{H_2O}^{TPB}} \right] \tag{9}$$

$$E_{CO}^{rev} = E_{CO}^{0} + \frac{RT}{2F} \ln \left[\frac{P_{CO}^{TPB} \left(P_{O_2}^{TPB} \right)^{\frac{1}{2}}}{P_{CO_2}^{TPB}} \right] \tag{10}$$

where E^0 the open-circuit potential at standard pressure and P_i^{TPB} is the partial pressure of component *i*.
The cell performance can be evaluated from the cell operating voltage (Eqs (11) and (12)). The actual cell voltage, V_{cell}, is more than the reversible voltage. This is due to the overpotential and internal resistance losses, i.e., the ohmic overpotential (η_{ohm}) and the activation overpotentials (η_{act}).

$$V_{cell} = E_{H_2}^{rev} + \left| \eta_{ohm}(i_{H_2}) \right| + \left| \eta_{act}(i_{H_2}) \right| \tag{11}$$

$$V_{cell} = E_{CO}^{rev} + \left| \eta_{ohm}(i_{CO}) \right| + \left| \eta_{act}(i_{CO}) \right| \tag{12}$$

The ohmic overpotential can be expressed as:

$$\eta_{ohm} = iR_T \tag{13}$$

where R_T is the internal resistance of cell related to the thickness and the conductivity as:

$$R_T = \frac{d_e}{\sigma_e} \tag{14}$$

The activation overpotentials can be described by the non-linear Butler–Volmer equation, which relates to the current density by considering the charge transfer at the three-phase boundary as a rate-limiting step and the activation overpotentials. The activation overpotentials for the electrochemical reduction of H_2O and CO_2 are given by

$$i_{H_2} = i_{H_2}^{0} \left[\exp\left(\frac{(1+\beta_a) F \eta_{act,c}}{RT} \right) - \exp\left(-\frac{\beta_c F \eta_{act,c}}{RT} \right) \right] \tag{15}$$

$$i_{CO} = i_{CO}^{0} \left[\exp\left(\frac{\beta_a F \eta_{act,c}}{RT} \right) - \exp\left(-\frac{(1+\beta_c) F \eta_{act,c}}{RT} \right) \right] \tag{16}$$

The Butler–Volmer equation for the anodic activation overpotential can be shown in Eq(17).

$$i_i = i_{O_2}^{0} \left[\exp\left(\frac{\beta_a F \eta_{act,a}}{RT} \right) - \exp\left(-\frac{\beta_c F \eta_{act,a}}{RT} \right) \right] \tag{17}$$

where β is the charge transfer coefficient (usually taken to be 0.5), i_i^0 is the exchange current density. The kinetic and cell parameters can be found in the literatures (Suwanwarangkul, 2003; Janardhanan et al., 2007; Narasimhaiah & Janardhanan, 2013).

3. Results and discussion

The SOEC for H_2O/CO_2 co-electrolysis is simulated based on the mathematical equations shown in the previous section. The SOEC model including the mass balances and electrochemical model, which are the nonlinear and differential equations, is solved by using MATLAB. To validate the SOFC model, the I-V characteristic curves of the SOEC from the model prediction is compared with the experimental data performed at DTU Energy conversion (Ebbesen et al., 2012). Table 1 shows cell parameters used for model validation. Figure 2 presents the comparison between the simulated and experimental results. It can be seen that the results of model prediction shows good agreement with the experiment data.

Table 1: Cell parameters for the model validation

Parameters	Value	Parameters	Value
Porosity , ε (-)	0.35	Cathode thickness , d_c (μm)	500
Tortuosity, ξ (-)	5.0	Anode thickness , d_a (μm)	50
Average pore radius , r_p (μm)	3.56x 10^{11}	Electrolyte thickness , d_e (μm)	50

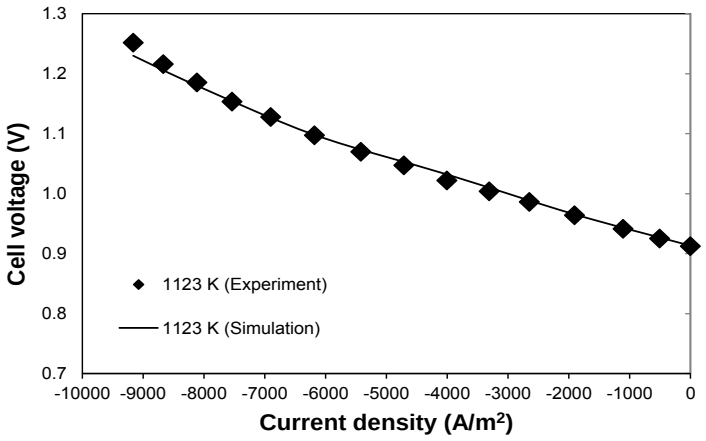

Figure 2: Comparison between the experimental and model-predicted I-V curves of SOEC at 1123 K and 1 bar.

The validated model was used to study the behavior and performance of SOEC. To study the influence of the operating parameters on the SOEC performance for H_2O/CO_2 co-electrolysis, the inlet gas compositions are fixed at 40% H_2O, 40% CO_2, 10% H_2, and 10% CO and air is introduced at the anode side. To investigate the influence of the RWGS reaction on the cathode for the syngas production from the co-electrolysis in the SOEC, the WGS reaction rate and the gas composition along the cathode thickness at various temperatures are considered in Figure 3a and 3b, respectively. From Figure 3a, it can indicate that the WGS reaction rates are negative value at the cathode surface because of high CO_2 and H_2O composition. The RWGS reaction has an impact on the cell performance at a range of the cathode thickness between 0-200 μm. Thus, the mole fraction of CO is higher than that of H_2, as shown in Figure 3b. The WGS reaction rates increase from the cathode surface to the three-phase boundary along the cathode thickness. This is caused by an increase in the amount of CO, resulting in a high driving force of the WGSR in the forward direction. When considering the effect of temperature, the WGS reaction rate decreases with increasing temperature at the cathode thickness range of 0-200 μm whereas the increase in temperature enhances the WGS reaction rate at the thicker cathode greater than 200 μm.

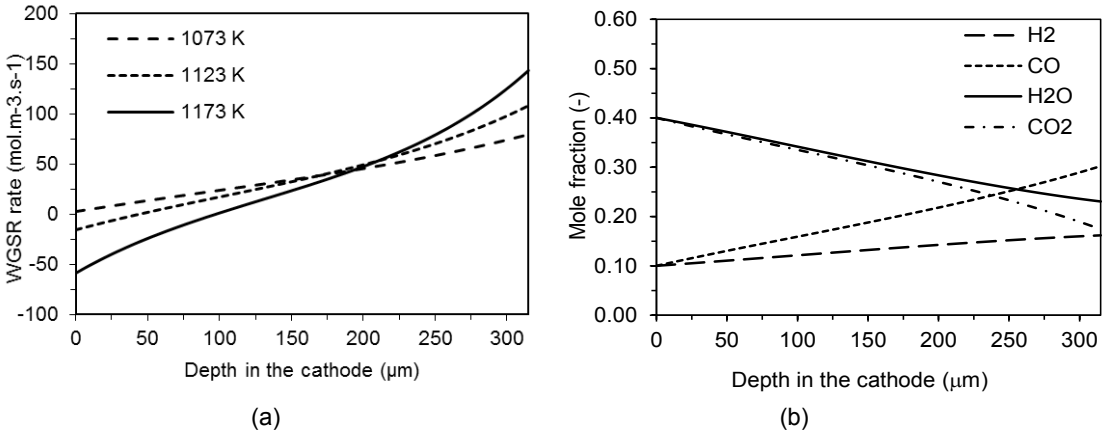

Figure 3: Effect of temperature on (a) WGSR rate and (b) gas composition at 1073 K as a function of the depth in the cathode.

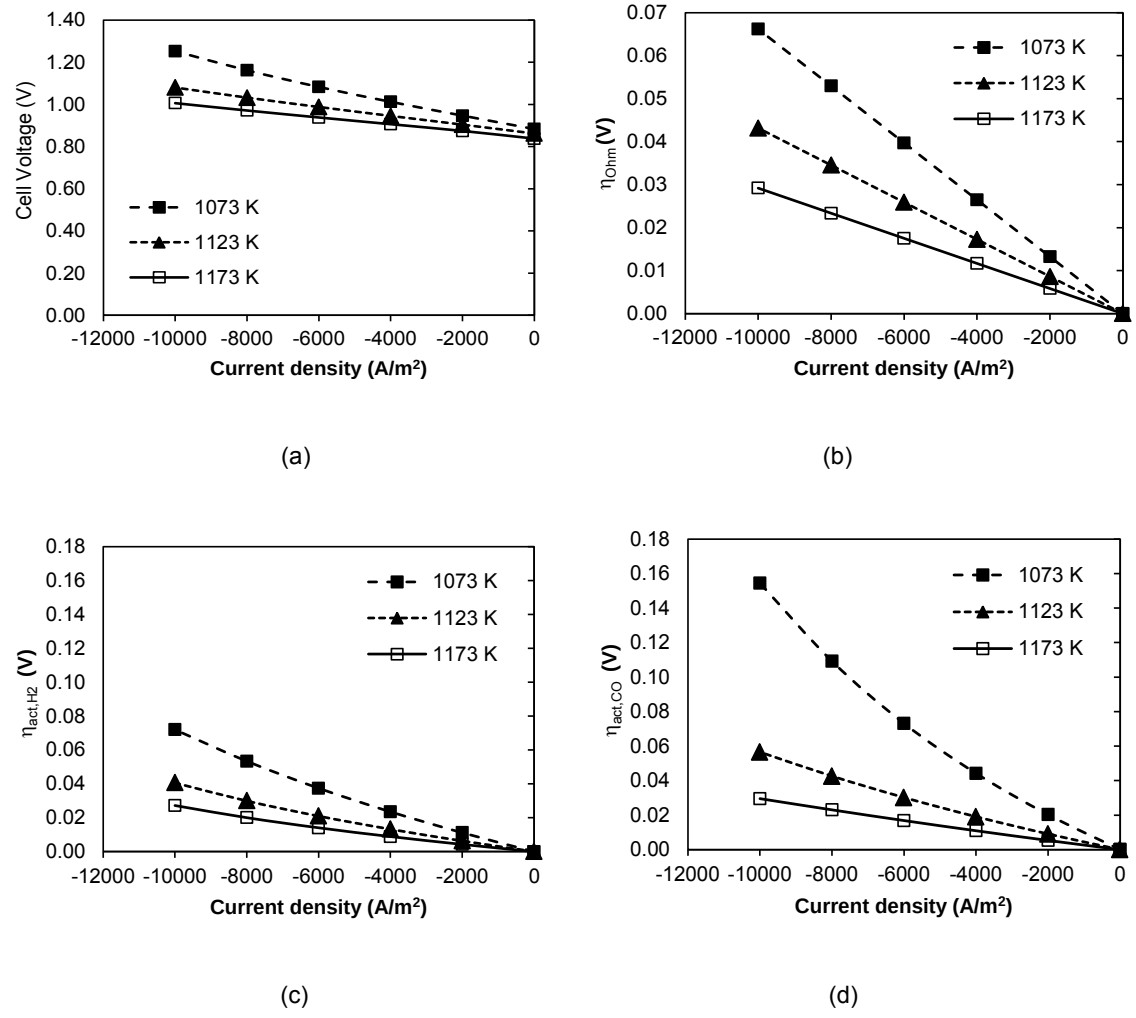

Figure 4: Effect of temperature on (a) cell voltage; (b) ohmic overpotential; (c) activation overpotentials for H_2O electrolysis; and (d) activation overpotentials for CO_2 electrolysis as a function of current density.

The operating temperature is a key factor affecting the SOEC performance. The effect of operating temperature on the cell voltage as a function of current density for H_2O/CO_2 co-electrolysis is illustrated in

Figure 4a. It is found that the cell voltage decreases with an increase in the operating temperature, resulting in reduction of the power supply for co-electrolysis in the SOEC. The increase in the operating temperature can increase thermal energy demand. On the contrary, the electrical energy demand subsides and it causes to decrease the reversible voltage.
The effect of the operating temperature on the ohmic overpotentials as a function of the current density is illustrated in Figure 4b. The ohmic overpotentials is lower at higher cell temperature. This is mainly due to the high conductivity of YSZ electrolyte at high operating temperatures, resulting in a decrease in the cell resistance. Moreover, an increase in the operating temperature has an effect on a decrease in the internal voltage losses. Figure 4c and 4d show the activation overpotentials of H_2O and CO_2 electrolysis as a function of the current density, respectively. It can be seen that the activation overpotentials decrease when the cell temperature increases. This results from the higher rate of the electrode reaction with a higher temperature, leading to the increase in the exchange current density. When comparing the H_2O and CO_2 electrolysis, the activation overpotentials occurring in the CO_2 electrolysis is higher than that in H_2O electrolysis about 53.4%, 28.2%, and 7.9% for 1073, 1123 K, and 1173 K, respectively (at the current density of 10,000 A/m^2). Thus, the increase in operating temperature has high effect on diminishing the activation overpotentials of CO_2 electrolysis.

4. Conclusions

In this study, the electrochemical model of a solid oxide electrolysis cell (SOEC) for H_2O and CO_2 co-electrolysis is presented and the model prediction is verified by comparing with the experiment data from the literature. The validated model is used to study the effect of a water gas shift (WGS) reaction in the cathode during the H_2O and CO_2 co-electrolysis on the SOEC performance. It is found that the WGS reaction rate depends on the gas composition and operating temperature. An increase in the operating temperature decreases the WGS reaction rate at the cathode surface, owing to high CO_2 compositions. On the other hand, the CO component is higher at thicker cathode, resulting in an increase in the WGS reaction rate with increasing temperature. Moreover, the power supply required for the co-electrolysis in the SOEC can be reduced by the increase of the operating temperature. The activation and ohmic overpotentials decrease when the cell operates at a higher temperature.

Acknowledgements

The authors would like to express their gratitude for financial support from Burapha University (No.152/2559) and the Thailand Research Fund (No. DPG5880003).

References

Ebbesen S.D., Knibbe R., Mogensen M., 2012, Co-Electrolysis of Steam and Carbon Dioxide in Solid Oxide Cells, Journal of the Electrochemical Society, 159, F482-F489.

Ferrero D., Lanzini A., Santarelli M., Leone P., 2013, A comparative assessment on hydrogen production from low- and high-temperature electrolysis, International Journal of Hydrogen Energy, 38, 3523-3536.

Janardhanan V.M., Deutschmann O., 2007, Numerical study of mass and heat transport in solid-oxide fuel cells running on humidified methane, Chemical Engineering Science, 62 (18), 5473-5486.

Kazempoor P., Braun R.J., 2015, Hydrogen and synthetic fuel production using high temperature solid oxide electrolysis cells (SOECs), International Journal of Hydrogen energy, 40, 3599-3612.

Menon V., Janardhanan, V.M., Deutschmann, O., 2014, A mathematical model to analyze solid oxide electrolyzercells (SOECs) for hydrogen production, Chemical Engineering Science, 110, 83–93.

Narasimhaiah G., Janardhanan V.M., 2013, Modeling CO_2 electrolysis in solid oxide electrolysis cell, Journal of Solid State Electrochemistry, 17, 2361-2370.

Ni M., 2012, 2D thermal modeling of a solid oxide electrolyzer cell (SOEC) for syngas production by H_2O/CO_2 co-electrolysis, International Journal of hydrogen energy, 37, 6389-6399.

Saebea D., Authayanun S., Patcharavorachot Y., Arpornwichanop A., Enhancement of hydrogen production for steam reforming of biogas in fluidized bed membrane reactor, Chemical Engineering Transactions, 39, 1177-1182.

Saebea D., Authayanun S., Patcharavorachot Y., Arpornwichanop A., Performance evaluation of low-temperature solid oxide fuel cells with SDC-based electrolyte, Chemical Engineering Transactions, 52, 223-228.

Suwanwarangkul R., Croiset E., 2003, Performance comparison of Fick's, dusty-gas and Stefan-Maxwell models to predict the concentration overpotentials of a SOFC anode, Journal of Power Sources, 9-18.

1st galley

Original Paper
Special articles: JCREN
特集：JCREN

Purification and Upgrading from Biogas to Biomethane

Chidporn WORAWIMUT※1†, Supawat VIVANPATARAKIJ※2, Anucha WATANAPA※3, Wisitsree WIYARATN※4, and Suttichai ASSABUMRUNGRAT※5

(Received November 6, 2017)

Biomethane could be upgraded from biogas to increase its heating value, avoid corrosion and eliminate toxicity. The simplest and most common technique for upgrading biogas is absorption process. In this study, two processes between water scrubbing and chemical scrubbing with diethanolamine (DEA) solution integrated with regeneration and recirculation are compared through Aspen Plus simulations. The aim of this study is to find the suitable operational condition in absorption process in order to increase the efficiency of the process in recovery methane and to decrease the energy consumption in the system. Our model was developed by including one additional absorber unit. Results show that the systems, both water scrubbing and chemical scrubbing, can achieve high purity of biomethane of >96 %v/v. In comparison between models for water scrubbing, our proposed system offers higher methane recovery of 4.68% of and 7,863.07 kW of energy of biomethane. In chemical scrubbing process, our system was able to decrease the pressure of absorber from 55.2 to 10 bar. Consequently, the recovery methane and energy of biomethane were increased while the energy consumption of system was decreased.

Key Words
You need to add 2 - 3 key words.

1. Introduction

Bioenergy is one of the promising choices. It is a very attractive renewable energy source [1) 2)]. Biogas is produced by the process of anaerobic digestion [3)]. Biogas has properties close to natural gas which can be used as fuel. However, biogas contains some impurities such as hydrogen sulphide (H_2S), water (H_2O) and carbon dioxide (CO_2). Trace components are targeted to while upgrading biogas to biomethane in order to adjust the calorific value and to meet requirements for some gas appliances [4) ~ 6)].

There are various biogas purification and upgrading technologies such as absorption (water scrubbing and chemical scrubbing), adsorption (pressure swing adsorption), cryogenic separation, and membrane technology [7)]. One of the simplest and most common technique is absorption process [8) 9)].

In this work we focused on the comparison of two processes between water scrubbing and chemical scrubbing using diethanolamine (DEA) with regeneration of absorbent for purification and upgrading of biogas from swine manure. The absorption processes are modeled in Aspen Plus by considering the quality of biomethane requirement, recovery methane, energy of biomethane, and energy consumption. The systems included with one additional absorber unit were also proposed in order to improve the recovery methane and the energy consumption of the system.

※1 Department of Learning Innovation and Technology, Faculty of Industrial Education and Technology, King Mongkut's University of Technology Thonburi, Thailand
※2 Energy Research Institute, Chulalongkorn University Thailand
※3 Department of Production Technology Education, Faculty of Industrial Education and Technology, King Mongkut's University of Technology Thonburi Thailand
※4 Faculty of Industrial Education and Technology, King Mongkut's University of technology Thonburi Thailand
※5 Center of Excellence in Catalysis and Catalytic Reaction Engineering, Department of Chemical Engineering, Faculty of Engineering, Chulalongkorn University Thailand
† Corresponding author: chidporn.wor@mail.kmutt.ac.th

2. Procedures

Water scrubbing and chemical scrubbing models developed in Aspen Plus software were validated with the results reported by Cozma *et al.* [8] and Niu *et al.* [9] respectively.

In order to determine a suitable absorbent flow rate required to obtain the desired biomethane according to standard of biomethane quality of E.ON [10] and to calculate the energy consumption needed for the whole process, the process simulations were carried out. The flow diagram for water scrubbing and chemical scrubbing using diethanolamine (DEA) with regeneration and recirculation of absorbent is applied as shown in Fig. 1 to describe physical absorption using NRTL (non-random-two liquid/with ideal gas and Henry's Law) as the property estimation method. The Radfrac module without a condenser and a reboiler in Aspen was selected to model the absorber and the desorber. To model the absorber and desorber units the equilibrium-stage gas-liquid system was selected. Biogas production from swine farm wastes was used in this work. The compositions of biogas are 68% CH_4, 24% CO_2, 3000 ppm H_2S, 2% N_2, 0.1% O_2 and 5.6% H_2O [11]. Biogas is fed from the bottom of absorber 1 while absorbent enters from the top of the column. Both biogas and absorbent are at 30 °C. The number of stages of absorbers 1, 2, and desorber are 7, 5, and 10 respectively. The pressure is reduced from 10 to 1 bar in order to minimize methane loss in the flash column where CO_2-enriched absorbent leaving the absorber 1 is transferred. Water released from this flash column along with the gas containing CO_2, CH_4, H_2S, N_2, and O_2 is fed to absorber 2. The raw biogas is mixed with the gas from the absorber 2. Rich solvent after leaving from the flash column and absorber 2 are sent to a mixer and then fed to the desorption column. Gas such as carbon dioxide and hydrogen sulfide are released from absorbent at a pressure of 3 bar and a temperature of 30 °C. The treated absorbent is recirculated (LIQREG) back to the top of the absorber. Absorbent stream is assumed to recycle continuously in a closed loop.

3. Results and Discussion

The information of pressurized water scrubbing in Cozma *et al.* [8] and chemical absorption with DEA in Niu *et al.* [9] were used for validating the absorption models. The results of the gas outlet compositions as shown in Table 1 were found to be in good agreement with those from the studies of Cozma *et al.* and Niu *et al.* at their reported conditions , indicating that our models can well represent the physical absorption and chemical absorption.

Both water scrubbing and chemical scrubbing were further simulated in order to find the absorbent flow rate needed for obtaining a 96% v/v biomethane according to standard of biomethane quality of E.ON. The biogas compositions used in the simulations were 68% CH_4, 24% CO_2, 3000 ppm H_2S, 2% N_2, 0.1% O_2 and 5.6% H_2O [11]. Moreover, the corresponding values of biomethane purity,

Table 1 Simulation results in comparison of pressurized water scrubbing and DEA scrubbing in validation

Parameters	Water scrubbing		DEA scrubbing	
	Cozma *et al.* [8]	Our simulation	Niu *et al.* [9]	Our simulation
Product gas (mole fraction)				
CH_4	0.967	0.956	0.837	0.842
CO_2	0.009	0.006	0.001	0.003
H_2S (ppm)	0.006	0.000	<4	0.000
N_2	0.011	0.023	-	-
O_2	0.010	0.013	-	-
H_2O	0.002	0.002	0.001	0.001
DEA	-	-	0.000	0.000

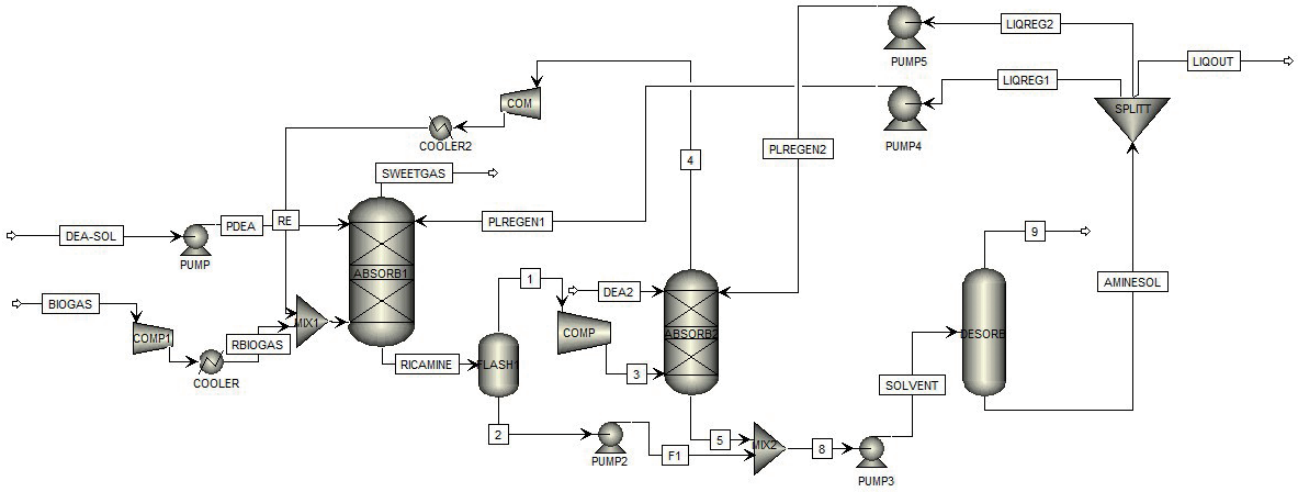

Fig. 1 DEA absorption process flowsheet

1st galley

recovery methane, energy of biomethane, and energy consumption in the system were determined.

Table 2 shows the simulation results of the pressurized water scrubbing system by comparing between the system of Cozma *et al.* and our system shown in Fig 1. The operational conditions, such as biogas compositions, biogas flow rate, total water flow rate, and pressure of absorber and desorber, were set the same. However, the model of Cozma *et al.* could not achieve 96% v/v biomethane, the purity according to the quality standard of E.ON. Furthermore, the results of our system showed 4.68% higher in the recovery methane and energy of biomethane was 7,863.07 kW higher than Cozma *et al.* model. However, the energy consumption of our system was 1,714.41 kW higher than Cozma *et al.* model. In our proposed system, the numbers of absorber were 2 which offered the increased absorption capacity but demanded higher energy consumption.

Table 2 also shows the simulation results of the DEA scrubbing system by comparing between the system of Niu *et al.* and our system shown in Fig 1. Mass concentration of DEA solution was set at 30 wt%. Model of Niu *et al.* used DEA solution flow rate and water flow rate equal to 2,500 and 65.885 kmol/hr respectively and the pressure of absorber as 55.16 bar which was quite high in order to obtain 96% v/v biomethane which resulted in higher overall energy consumption. However, the system of Niu *et al.* used the quantity of absorbent less than our system while the pressure of absorber was higher than our system which was only 10 bar. In consideration of recovery methane, energy of biomethane, and energy consumption our model was better than Niu *et al.* model by increase of 12.9%, 21,695.85 kW, and 4,232.23 kW respectively. The solubility increased with increasing pressure which resulted in higher power consumption.

4. Conclusion

In this work the comparison between the previous and our proposed systems for water scrubbing and chemical scrubbing using diethanolamine (DEA) with regeneration of absorbent for purification and upgrading of biogas coming from swine manure were investigated. In the process of water scrubbing and chemical scrubbing in our system could obtain the quality of biomethane requirement according to standard of E.ON. Furthermore, the efficiency of the process in recovery methane and energy of biomethane was higher. In consideration of chemical scrubbing process our system was able to decrease the pressure of absorber from 55.16 to 10 bar. The decreased pressure of absorber increased the flow rate of the absorbent. Consequently, the recovery methane and energy of biomethane were increased while the energy consumption of system was decreased.

Acknowledgment

The authors gratefully acknowledge the financial support provided by the Thailand Research Fund (Grant

Table 2 Design results of biogas purification and upgrading process to biomethane for pressurized water scrubbing and DEA scrubbing

Parameters	Water scrubbing		DEA scrubbing	
	Cozma *et al.* [8]	Our simulation	Niu *et al.* [9]	Our simulation
Biogas flow rate (kmol/hr)	1,000	1,000	1,000	1,000
Total water flow rate (kmol/hr)	16,000 [a]	16,000 [b]	65.885	-
Total DEA solution flow rate (kmol/hr)	-	-	2,500	16,000 [c]
Absorbent to biogas ratio	16	16	2.5	16
$P_{absorber}$ (bar)	10	10	55.16	10
$P_{desorber}$ (bar)	3	3	1.827	3
Product gas (%)				
CH_4	93.514	96.005	96.076	96.026
CO_2	0.124	0.320	0.341	0.310
H_2S	0.000	0.000	0.000	0.000
N_2	5.313	3.098	3.320	3.114
O_2	0.892	0.154	0.163	0.155
H_2O	0.156	0.424	0.100	0.395
Recovery methane (%)	85.28	89.96	76.57	89.47
Energy of biomethane (kW)	143,532.68	151,395.75	128,873.25	150,569.10
Energy consumption (kW)	9,595.52	11,309.93	15,563.27	11,331.04

a Fresh water flow rate: 500 kmol/hr, recirculated water flow rate: 15,500 kmol/hr.

b Fresh water flow rate to absorber 1: 375 kmol/hr, recirculated water flow rate to absorber 1: 11,625 kmol/hr, fresh water flow rate to absorber 2: 125 kmol/hr, recirculated water flow rate to absorber 2: 3,875 kmol/hr.

c Fresh DEA solution flow rate to absorber 1: 375 kmol/hr, recirculated DEA solution flow rate to absorber 1: 11,625 kmol/hr, fresh DEA flow rate to absorber 2: 125 kmol/hr, recirculated DEA flow rate to absorber 2: 3,875 kmol/hr

number DPG5880003) and King Mongkut's University of Technology Thonburi through the "KMUTT 55th Anniversary Commemorative Fund".

References

1) Khan, M.; Yasmin, T.; Shakoor, A., *Renewable Sustainable Energy Rev.*, **51**, 785-797 (2015)
2) Energy plus, http://energy.go.th/2015/wp-content/uploads/2016/02/ep_56_oct_dec.pdf (Last access: 2016.1.15)
3) Aggarangsi, P.; Tippayawong, N.; Moran, J. C.; Rerkkriangkrai, P., *Energy for Sustainable Development*, **17**, 371-377 (2013)
4) Pipatmanomai, S.; Kaewluan, S.; Vitidsant, T., *Applied Energy*, **86**, 669-674 (2009)
5) Budzianowski, W., *Renewable Sustainable Energy Rev.*, **54**, 1148-1171 (2016)
6) Yang, L.; Ge, X.; Wan, C.; Yu, F.; Li, Y., *Renewable Sustainable Energy Rev.*, **40**, 1133-1152 (2014)
7) Sun, Q.; Li, H.; Yan, J.; Liu, L.; Yu, Z.; Yu, X., *Renewable Sustainable Energy Rev.*, **51**, 521-532 (2015)
8) Cozma, P.; Wukovits, W.; Mamaliga, I.; Friedl, A.; Gavrilescu, M., *Clean Technol. Environ. Policy*, **17**, 373-391 (2015)
9) Niu, M.; Rangaiah, G., *Int. J. Greenhouse Gas Control*, **29**, 221-230 (2014)
10) E.ON, Future quality aspects of biogas injected to Natural Gas Grid, http://www.elforsk.se/PageFiles/2163/Bilaga%205_H%C3%A5kan%20Eriksson%20Eon.pdf (Last access: 2016.1.15)
11) Chuichulcherm, S.; Kasichan, N.; Srinophakun, P.; Saisriyoot, M.; Thanapimmetha, A., *J. Cleaner Prod.*, **142**, 1267-1273 (2017)

คำขอรับสิทธิบัตร/อนุสิทธิบัตร

☑ การประดิษฐ์
☐ การออกแบบผลิตภัณฑ์
☐ อนุสิทธิบัตร

ข้าพเจ้าผู้ลงลายมือชื่อในคำขอรับสิทธิบัตร/อนุสิทธิบัตรนี้ ขอรับสิทธิบัตร/อนุสิทธิบัตร ตามพระราชบัญญัติสิทธิบัตร พ.ศ. 2522 แก้ไขเพิ่มเติมโดยพระราชบัญญัติสิทธิบัตร (ฉบับที่ 2) พ.ศ 2535 และพระราชบัญญัติสิทธิบัตร (ฉบับที่ 3) พ.ศ 2542

สำหรับเจ้าหน้าที่

วันรับคำขอ 15 พ.ย. 2559	เลขที่คำขอ 1601006845
วันยื่นคำขอ 15 พ.ย. 2559	

สัญลักษณ์จำแนกการประดิษฐ์ระหว่างประเทศ

ใช้กับแบบผลิตภัณฑ์

ประเภทผลิตภัณฑ์

วันประกาศโฆษณา	เลขที่ประกาศโฆษณา
วันออกสิทธิบัตร/อนุสิทธิบัตร	เลขที่สิทธิบัตร/อนุสิทธิบัตร

ลายมือชื่อเจ้าหน้าที่

1.ชื่อที่แสดงถึงการประดิษฐ์/การออกแบบผลิตภัณฑ์
เครื่องปฏิกรณ์แบบเยื่อแผ่นประเภทโมโนลิทควบคู่ความร้อนสำหรับผลิตไฮโดรเจน

2.คำขอรับสิทธิบัตรการออกแบบผลิตภัณฑ์นี้เป็นส่วนหนึ่งของคำขอรับสิทธิบัตรการออกแบบผลิตภัณฑ์อย่างอื่นด้วยหรือไม่
ในจำนวน คำขอ ที่ยื่นในคราวเดียวกัน

ยกเว้นค่าธรรมเนียม
ตามกฎกระทรวง พ.ศ. ๒๕๔๗ ว่าด้วยอัตราค่าธรรมเนียมและการยกเว้นค่าธรรมเนียม สำหรับสิทธิบัตร อนุสิทธิบัตร และประกาศคณะกรรมการสิทธิบัตร

3.ผู้ขอรับสิทธิบัตร/อนุสิทธิบัตร และที่อยู่ (เลขที่ ถนน ประเทศ)
ดูที่หน้า 3

3.1 สัญชาติ
3.2 โทรศัพท์
3.3 โทรสาร
3.4 อีเมล์

4.สิทธิในการขอรับสิทธิบัตร/อนุสิทธิบัตร
☐ ผู้ประดิษฐ์/ผู้ออกแบบ ☑ ผู้รับโอน ☐ ผู้ขอรับสิทธิโดยเหตุอื่น

5.ตัวแทน(ถ้ามี)/ที่อยู่ (เลขที่ ถนน จังหวัด รหัสไปรษณีย์)
ดูที่หน้า 3

5.1 ตัวแทนเลขที่
5.2 โทรศัพท์
5.3 โทรสาร
5.4 อีเมล์

6.ผู้ประดิษฐ์/ผู้ออกแบบผลิตภัณฑ์ และที่อยู่ (เลขที่ ถนน ประเทศ)
ดูที่หน้า 3

7. คำขอรับสิทธิบัตร/อนุสิทธิบัตรนี้แยกจากหรือเกี่ยวข้องกับคำขอเดิม
ผู้ขอรับสิทธิบัตร/อนุสิทธิบัตร ขอให้ถือว่าได้ยื่นคำขอรับสิทธิบัตร/อนุสิทธิบัตรนี้ ในวันเดียวกับคำขอรับสิทธิบัตร
เลขที่ วันยื่น เพราะคำขอรับสิทธิบัตร/อนุสิทธิบัตรนี้แยกจากหรือเกี่ยวข้องกับคำขอเดิมเพราะ
☐ คำขอเดิมมีการประดิษฐ์หลายอย่าง ☐ ถูกคัดค้านเนื่องจากผู้ขอไม่มีสิทธิ ☐ ขอเปลี่ยนแปลงประเภทของสิทธิ

หมายเหตุ ในกรณีที่ไม่อาจระบุรายละเอียดได้ครบถ้วน ให้จัดทำเป็นเอกสารแนบท้ายแบบพิมพ์นี้โดยระบุหมายเลขกำกับข้อและหัวข้อที่แสดงรายละเอียดเพิ่มเติมดังกล่าวด้วย

8.การยื่นคำขอนอกราชอาณาจักร

วันยื่นคำขอ	เลขที่คำขอ	ประเทศ	สัญลักษณ์จำแนกการประดิษฐ์ระหว่างประเทศ	สถานะคำขอ
8.1				
8.2				
8.3				

8.4 ☐ ผู้ขอรับสิทธิบัตร/อนุสิทธิบัตรขอสิทธิให้ถือว่าได้ยื่นคำขอนี้ในวันที่ได้ยื่นคำขอรับสิทธิบัตร/อนุสิทธิบัตรในต่างประเทศเป็นครั้งแรกโดย
☐ ได้ยื่นเอกสารหลักฐานพร้อมคำขอนี้ ☐ ขอยื่นเอกสารหลักฐานหลังจากวันยื่นคำขอนี้

9.การแสดงการประดิษฐ์ หรือการออกแบบผลิตภัณฑ์ ผู้ขอรับสิทธิบัตร/อนุสิทธิบัตรได้แสดงการประดิษฐ์ที่หน่วยงานของรัฐเป็นผู้จัด
วันแสดง วันเปิดงานแสดง ผู้จัด

10.การประดิษฐ์เกี่ยวกับจุลชีพ

10.1 เลขทะเบียนฝากเก็บ	10.2 วันที่ฝากเก็บ	10.3 สถาบันฝากเก็บ/ประเทศ

11.ผู้ขอรับสิทธิบัตร/อนุสิทธิบัตร ขอยื่นเอกสารภาษาต่างประเทศก่อนในวันยื่นคำขอนี้ และจะจัดยื่นคำขอรับสิทธิบัตร/อนุสิทธิบัตรนี้ที่จัดทำเป็นภาษาไทยภายใน 90 วัน นับจากวันยื่นคำขอนี้ โดยขอยื่นเป็นภาษา
☐ อังกฤษ ☐ ฝรั่งเศส ☐ เยอรมัน ☐ ญี่ปุ่น ☐ อื่นๆ

12.ผู้ขอรับสิทธิบัตร/อนุสิทธิบัตร ขอให้อธิบดีประกาศโฆษณาคำขอรับสิทธิบัตร หรือรับจดทะเบียน และประกาศโฆษณาอนุสิทธิบัตรนี้ หลังจากวันที่ เดือน พ.ศ
☐ ผู้ขอรับสิทธิบัตร/อนุสิทธิบัตรขอให้ใช้รูปเขียนหมายเลข ในการประกาศโฆษณา

13.คำขอรับสิทธิบัตร/อนุสิทธิบัตรนี้ประกอบด้วย
ก. แบบพิมพ์คำขอ 3 หน้า
ข. รายละเอียดการประดิษฐ์ หรือคำพรรณนาแบบผลิตภัณฑ์ 6 หน้า
ค. ข้อถือสิทธิ 2 หน้า
ง. รูปเขียน 4 รูป 2 หน้า
จ. ภาพแสดงแบบผลิตภัณฑ์
☐ รูปเขียน รูป หน้า
☐ ภาพถ่าย รูป หน้า
ฉ. บทสรุปการประดิษฐ์ 1 หน้า

14.เอกสารประกอบคำขอ
☐ เอกสารแสดงสิทธิในการขอรับสิทธิบัตร/อนุสิทธิบัตร
☐ หนังสือรับรองการแสดงการประดิษฐ์/การออกแบบผลิตภัณฑ์
☐ หนังสือมอบอำนาจ
☐ เอกสารรายละเอียดเกี่ยวกับจุลชีพ
☐ เอกสารการขอนับวันยื่นคำขอในต่างประเทศเป็นวันยื่นคำขอในประเทศไทย
☐ เอกสารขอเปลี่ยนแปลงประเภทของสิทธิ
☐ เอกสารอื่น ๆ

15. ข้าพเจ้าขอรับรองว่า
☑ การประดิษฐ์นี้ไม่เคยยื่นขอรับสิทธิบัตร/ อนุสิทธิบัตรมาก่อน
☐ การประดิษฐ์นี้ได้พัฒนาปรับปรุงมาจาก.....

16.ลายมือชื่อ (☐ ผู้ขอรับสิทธิบัตร / อนุสิทธิบัตร; ☑ ตัวแทน)
นายบัญชา วงศ์ณัฐภัทร

หมายเหตุ บุคคลใดยื่นขอรับสิทธิบัตรการประดิษฐ์หรือการออกแบบผลิตภัณฑ์ หรืออนุสิทธิบัตร โดยการแสดงข้อความอันเป็นเท็จแก่พนักงานเจ้าหน้าที่ เพื่อให้ได้ไปซึ่งสิทธิบัตรหรืออนุสิทธิบัตร ต้องระวางโทษจำคุกไม่เกินหกเดือน หรือปรับไม่เกินห้าพันบาท หรือทั้งจำทั้งปรับ

3.ผู้ขอรับสิทธิบัตร/อนุสิทธิบัตร และที่อยู่ (เลขที่ ถนน ประเทศ)

จุฬาลงกรณ์มหาวิทยาลัย
อยู่ที่ 254 ถนนพญาไท แขวงวังใหม่ เขตปทุมวัน กรุงเทพฯ 10330
3.1 สัญชาติ ไทย 3.2 โทรศัพท์ 0-2218-4180 3.3 โทรสาร 0-2218-4181

สำนักงานกองทุนสนับสนุนการวิจัย
อยู่ที่ ชั้น 14 อาคาร เอส เอ็ม ทาวเวอร์ 979/17-21 ถนนพหลโยธิน แขวงสามเสนใน เขตพญาไท กรุงเทพฯ 10400
3.1 สัญชาติ ไทย 3.2 โทรศัพท์ 0-2278-8200 3.3 โทรสาร 0-2298-0476

5. ตัวแทน(ถ้ามี)/ที่อยู่ (เลขที่ ถนน จังหวัด รหัสไปรษณีย์)
นายมงคล แก้วมหา
อยู่ที่ สถาบันทรัพย์สินทางปัญญาแห่งจุฬาลงกรณ์มหาวิทยาลัย 254 อาคารวิจัยจุฬาลงกรณ์มหาวิทยาลัย ชั้น 14 ถนนพญาไท แขวงวังใหม่ เขตปทุมวัน กรุงเทพฯ 10330
5.1 ตัวแทนเลขที่ 1453 5.2 โทรศัพท์ 0-2218-4180 5.3 โทรสาร 0-2218-4181

และ/หรือ

นายบัญชา วงศ์ณัฐภัทร
อยู่ที่ สถาบันทรัพย์สินทางปัญญาแห่งจุฬาลงกรณ์มหาวิทยาลัย 254 อาคารวิจัยจุฬาลงกรณ์มหาวิทยาลัย ชั้น 14 ถนนพญาไท แขวงวังใหม่ เขตปทุมวัน กรุงเทพฯ 10330
5.1 ตัวแทนเลขที่ 2392 5.2 โทรศัพท์ 0-2218-4180 5.3 โทรสาร 0-2218-4181 5.4 อีเมล์ Bancha.V@chula.ac.th

6.ผู้ประดิษฐ์/ผู้ออกแบบผลิตภัณฑ์ และที่อยู่ (เลขที่ ถนน ประเทศ)

ศาสตราจารย์ ดร.สุทธิชัย อัสสะบำรุงรัตน์
อยู่ที่ คณะวิศวกรรมศาสตร์ จุฬาลงกรณ์มหาวิทยาลัย ถนนพญาไท แขวงวังใหม่ เขตปทุมวัน กรุงเทพฯ 10330

ผู้ช่วยศาสตราจารย์ ดร.สมพงษ์ พุทธิวิสุทธิศักดิ์
อยู่ที่ คณะวิศวกรรมศาสตร์ จุฬาลงกรณ์มหาวิทยาลัย ถนนพญาไท แขวงวังใหม่ เขตปทุมวัน กรุงเทพฯ 10330

นายธารา จิวานุรักษ์
อยู่ที่ คณะวิศวกรรมศาสตร์ จุฬาลงกรณ์มหาวิทยาลัย ถนนพญาไท แขวงวังใหม่ เขตปทุมวัน กรุงเทพฯ 10330

รายละเอียดการประดิษฐ์

ชื่อที่แสดงถึงการประดิษฐ์

เครื่องปฏิกรณ์แบบเยื่อแผ่นประเภทโมโนลิทควบคู่ความร้อนสำหรับผลิตไฮโดรเจน

สาขาวิทยาการที่เกี่ยวข้องกับการประดิษฐ์

สาขาวิชาการด้านวิศวกรรมเคมีในส่วนที่เกี่ยวข้องกับเครื่องปฏิกรณ์แบบเยื่อแผ่นสำหรับทำปฏิกิริยาเพื่อการผลิตไฮโดรเจน และสาขาวิชาการวิศวกรรมเครื่องกลในส่วนเกี่ยวข้องกับการออกแบบเชิงกลศาสตร์ของเครื่องปฏิกรณ์แบบเยื่อแผ่นประเภทโมโนลิทควบคู่ความร้อน

ภูมิหลังของศิลปะหรือวิทยาการที่เกี่ยวข้อง

ไฮโดรเจนเป็นแหล่งพลังงานทางเลือกรูปแบบหนึ่งสำหรับทดแทนการใช้เชื้อเพลิงที่เป็นสาเหตุของการเกิดปัญหาสิ่งแวดล้อมและสภาวะโลกร้อนในปัจจุบัน เช่น ฟอสซิล แก๊สธรรมชาติ และถ่านหิน เป็นต้น นอกจากนี้ความต้องการด้านพลังงานที่เพิ่มขึ้นตามการเติบโตของชุมชนเมืองและความสนใจด้านสิ่งแวดล้อม ทำให้ความต้องการสำหรับการใช้ไฮโดรเจนเป็นแหล่งพลังงานเพิ่มขึ้นอย่างมาก เครื่องปฏิกรณ์สำหรับผลิตไฮโดรเจนจึงถูกศึกษาและพัฒนาเพื่อตอบสนองต่อความต้องการด้านพลังงานและการใช้พลังงานไฮโดรเจนที่หลากหลายขึ้นเพื่อลดปัญหาด้านสิ่งแวดล้อม

สำหรับด้านอุตสาหกรรม ปฏิกิริยาสำหรับผลิตไฮโดรเจนส่วนใหญ่ ได้แก่ ปฏิกิริยาปฏิรูปด้วยไอน้ำ (Steam reforming reaction) ปฏิกิริยาดรายรีฟอร์มมิง (Dry reforming reaction) ปฏิกิริยาการแตกตัว (Cracking reaction) ปฏิกิริยาดีไฮโดรจีเนชัน (Dehydrogenation reaction) เป็นต้น โดยใช้เครื่องปฏิกรณ์แบบเบดนิ่ง (Fixed bed reactor) ซึ่งพบปัญหาจุดเย็น (Cold spot) ภายในเครื่องปฏิกรณ์และส่งผลต่อประสิทธิภาพในการผลิตไฮโดรเจน ทำให้กระบวนการผลิตต้องการเครื่องปฏิกรณ์ขนาดใหญ่ที่บรรจุตัวเร่งปฏิกิริยาปริมาณมากไว้ภายใน นอกจากนี้กระบวนการผลิตไฮโดรเจนต้องการพลังงานความร้อนจากภายนอกเนื่องจากปฏิกิริยาสำหรับผลิตไฮโดรเจน ส่วนมากเป็นปฏิกิริยาดูดความร้อน (Endothermic reaction) และผลิตภัณฑ์ที่ได้มีการเจือปนของแก๊สอื่น จึงไม่เหมาะสมกับการนำไปใช้งานหรือการจัดเก็บโดยตรง ดังนั้นกระบวนการผลิตไฮโดรเจนจำเป็นต้องมีเครื่องปฏิกรณ์อื่นๆเพื่อเพิ่มความบริสุทธิ์ของไฮโดรเจน เช่น เครื่องปฏิกรณ์วอเตอร์ แก๊ส ชิฟต์ (Water gas shift reactor) เครื่องปฏิกรณ์เลือกเกิดปฏิกิริยาออกซิเดชันกับแก๊สคาร์บอนมอนอกไซด์ (CO Preferential Oxidation Reaction) เครื่องปฏิกรณ์แบบเยื่อแผ่น (Membrane reactor) เป็นต้น เนื่องด้วยสาเหตุข้างต้นทำให้กระบวนการผลิตไฮโดรเจนมักมีขนาดใหญ่และถูกจำกัดการใช้งานให้อยู่ภายโรงงานหรืออุตสาหกรรมขนาดใหญ่

การแก้ปัญหาเครื่องปฏิกรณ์สำหรับการผลิตไฮโดรเจนแบบดั้งเดิมนั้น ได้มีการนำเสนอเครื่องปฏิกรณ์แบบช่องจุลภาค (Micro channel reactor) ซึ่งถูกพัฒนาให้ที่มีขนาดเล็ก น้ำหนักเบา และมีประสิทธิภาพสูง เพื่อใช้สำหรับการผลิตไฮโดรเจน และทำให้เครื่องปฏิกรณ์ชนิดนี้สามารถนำมาใช้งาน

ได้หลากหลายมากขึ้น โดยเครื่องปฏิกรณ์ประเภทโมโนลิท (Monolithic reactor) เป็นเครื่องปฏิกรณ์แบบช่องจุลภาคประเภทหนึ่ง ที่มีการใช้งานเชิงพาณิชย์อย่างกว้างขวาง เช่น เครื่องฟอกไอเสียรถยนต์ และโครงสร้างของเครื่องปฏิกรณ์ประเภทต่างๆ รวมถึงเครื่องปฏิกรณ์สำหรับการผลิตไฮโดรเจน เครื่องปฏิกรณ์ประเภทโมโนลิทมีลักษณะเป็นโครงสร้างรวมของช่องจุลภาคจำนวนมาก และสามารถควบรวมกระบวนการหลายกระบวนการสำหรับการเกิดปฏิกิริยาไว้ภายในเครื่องปฏิกรณ์เครื่องเดียว เพื่อลดจำนวนเครื่องปฏิกรณ์และขนาดของกระบวนการผลิตลง สำหรับการผลิตไฮโดรเจน การพัฒนาเครื่องปฏิกรณ์ประเภทโมโนลิทสามารถแบ่งออกเป็น สอง ประเภทคือ เครื่องปฏิกรณ์อุณหภาพประเภทโมโนลิท ซึ่งควบรวมการเกิดปฏิกิริยาสำหรับผลิตไฮโดรเจน กับปฏิกิริยคายความร้อน (Exothermic reaction) เช่น การออกซิเดชันบางส่วน (Partial oxidation) และ การเผาไหม้ (Combustion) เป็นต้น เพื่อเป็นแหล่งพลังงานภายในเครื่องปฏิกรณ์ และ เครื่องปฏิกรณ์แบบเยื่อแผ่นประเภทโมโนลิท ซึ่งควบรวมการเกิดปฏิกิริยาสำหรับผลิตไฮโดรเจน กับกระบวนการแยกไฮโดรเจนด้วยเยื่อเลือกผ่าน (Membrane separation) เพื่อเพิ่มความบริสุทธิ์ของผลิตภัณฑ์

งานวิจัยด้านเครื่องปฏิกรณ์อุณหภาพประเภทโมโนลิท หรือเครื่องปฏิกรณ์ชนิดรวมปฏิกิริยาคายความร้อนส่วนมากเป็นการพัฒนาวิธีการป้อนสารที่แยกช่องระหว่างปฏิกิริยาเผาไหม้และปฏิกิริยาปฏิรูปไฮโดรคาร์บอน ตัวอย่างเช่น สิทธิบัตรของสหรัฐอเมริกา 5,980,838 (Hippel และคณะ) ออกแบบลักษณะของหัวจ่ายแก๊สสองสายสำหรับเครื่องปฏิกรณ์อุณหภาพประเภทโมโนลิทโดยมีระบบหล่อเย็นด้วยน้ำในบริเวณหัวจ่าย และศึกษาในส่วนของเครื่องปฏิกรณ์ซึ่งมีการจัดเรียงช่องระหว่างปฏิกิริยาดูดและคายความร้อนในแบบขนาน ซึ่งถูกกล่าวถึงในสิทธิบัตรของสหรัฐอเมริกา 09/893,777 (Hippel และคณะ) นอกจากนี้ในสิทธิบัตรของสหรัฐอเมริกา 11/482,464 (Leveson) ใช้หลักการตัดบางส่วนของโครงสร้างโมโนลิทเพื่อใช้เป็นช่องสำหรับการป้อนแก๊สสองสายแยกกัน สำหรับการรวมกระบวนการแยกไฮโดรเจนด้วยเยื่อเลือกผ่านกับเครื่องปฏิกรณ์ประเภทโมโนลิท Kim และคณะ (2009) ศึกษาการเคลือบพาลาเดียมด้วยวิธีการเคลือบแบบไม่ใช้ไฟฟ้า เยื่อเลือกผ่านพาลาเดียมที่ได้มีความหนา 8 ไมโครเมตรและสามารถแยกไฮโดรเจนได้อย่างมีประสิทธิภาพ นอกจากนี้การแยกแก๊สโมเลกุลเล็กโดยใช้โครงสร้างรูพรุนของโมโนลิทและการจำกัดช่องทางออกถูกกล่าวถึงในสิทธิบัตรของสหรัฐอเมริกา 7,572,311 (Zuberi) วิธีการจำกัดช่องทางออกถูกนำมาประยุกต์ใช้สำหรับการผลิตไฮโดรเจน ซึ่งถูกกล่าวในสิทธิบัตรของสหรัฐอเมริกา 7,575,729 (Numata และ Iguchi) และ สิทธิบัตรของสหรัฐอเมริกา 11/636,936 (Jiang)

สำหรับเครื่องปฏิกรณ์แบบเยื่อแผ่นประเภทโมโนลิทควบคู่ความร้อนซึ่งรวมปฏิกิริยาคายความร้อนและกระบวนการแยกไฮโดรเจนด้วยเยื่อเลือกผ่าน การรวมทั้งสองกระบวนการค่อนข้างซับซ้อน ดังเช่นการรวมปฏิกิริยาเผาไหม้และปฏิกิริยาปฏิรูปไฮโดรคาร์บอนซึ่งถูกป้อนและเกิดปฏิกิริยาร่วมกันภายในในช่องเดียวกัน ไฮโดรเจนที่ผลิตได้บางส่วนแพร่ผ่านเยื่อเลือกผ่านไปสู่ช่องผลิตภัณฑ์ แต่กระบวนการนี้มีข้อเสียหลายด้าน เช่น ไม่สามารถใช้อากาศในการเผาไหม้ได้โดยตรง เนื่องจากมีปริมาณแก๊สไนโตรเจนมากเกินไป ซึ่งส่งผลต่อความสามารถในการแยกไฮโดรเจนได้ต่ำลง

นอกจากนี้อุณหภูมิภายในเครื่องปฏิกรณ์สูงมากทำให้ส่งผลเสียต่อประสิทธิภาพของปฏิกิริยาปฏิรูปไฮโดรคาร์บอนและยากต่อการควบคุมสภาวะที่เหมาะสมของเครื่องปฏิกรณ์ เครื่องปฏิกรณ์แบบเยื่อแผ่นประเภทโมโนลิทควบคู่ความร้อนที่แยกกระบวนการทั้งสองถูกพัฒนาในลักษณะที่ซับซ้อนมากขึ้น โดยการแบ่งโมโนลิทเป็นสองส่วนสำหรับเป็นแหล่งพลังงานและกระบวนการแยก ในส่วนของการเกิดปฏิกิริยาถูกออกแบบให้มีการเคลื่อนที่ผ่านแหล่งพลังงานและกระบวนการแยกสลับกันไป เครื่องปฏิกรณ์ประเภทนี้ถูกกล่าวในสิทธิบัตรของสหรัฐอเมริกา 8815183 (Sutherland และ Woodfin) แต่อย่างไรก็ตามเครื่องปฏิกรณ์ประเภทนี้มีความซับซ้อนเกินไปไม่เหมาะสมต่อการนำมาใช้งาน

จากที่กล่าวมาข้างต้นจึงเป็นที่มาของการประดิษฐ์ของเครื่องปฏิกรณ์แบบเยื่อแผ่นประเภทโมโนลิทควบคู่ความร้อนสำหรับผลิตไฮโดรเจนที่แยกส่วนการเกิดปฏิกิริยาคายความร้อน การเกิดปฏิกิริยาสำหรับผลิตไฮโดรเจน และกระบวนการแยกไฮโดรเจนด้วยเยื่อเลือกผ่าน ด้วยผนังของโครงสร้างโมโนลิท การประดิษฐ์เครื่องปฏิกรณ์นี้สามารถใช้โครงสร้างของโมโนลิทเชิงพาณิชย์ที่มีอยู่ในปัจจุบัน และกล่าวถึงการจัดเรียงของกระบวนการทั้งสามกระบวนการภายในเครื่องปฏิกรณ์เพื่อให้มีประสิทธิภาพการผลิตไฮโดรเจนสูงสุด โดยเครื่องปฏิกรณ์เพียงเครื่องเดียวสามารถผลิตไฮโดรเจนที่มีความบริสุทธิ์สูงและมีขนาดเล็กมากเมื่อเทียบกับกระบวนการผลิตไฮโดรเจนแบบดั้งเดิม การประดิษฐ์เครื่องปฏิกรณ์ดังกล่าวยังไม่ถูกระบุในสิทธิบัตรไทยและสิทธิบัตรนานาชาติ

ลักษณะและความมุ่งหมายของการประดิษฐ์

การประดิษฐ์นี้เกี่ยวข้องกับเครื่องปฏิกรณ์แบบเยื่อแผ่นประเภทโมโนลิทควบคู่ความร้อนสำหรับผลิตไฮโดรเจน โดยกระบวนการผลิตไฮโดรเจน ซึ่งประกอบด้วยสามส่วนคือ กระบวนการเกิดปฏิกิริยาคายความร้อนเพื่อเป็นแหล่งพลังงาน กระบวนการเกิดปฏิกิริยาสำหรับผลิตไฮโดรเจน และ กระบวนการแยกไฮโดรเจนเพื่อเพิ่มความบริสุทธิ์ของไฮโดรเจน การรวมกระบวนการผลิตไฮโดรเจนทั้งหมดไว้ในเครื่องปฏิกรณ์เครื่องเดียว ทำให้กระบวนการผลิตมีขนาดเล็กลงจากแบบดั้งเดิม และเครื่องปฏิกรณ์มีประสิทธิภาพเพิ่มขึ้น เนื่องจากมีการกระจายพลังงานความร้อนที่ดีขึ้นและมีการเปลี่ยนสมดุลของปฏิกิริยาสำหรับผลิตไฮโดรเจน ไปในทิศทางที่เกิดเป็นไฮโดรเจนมากขึ้น ซึ่งช่วยลดค่าใช้จ่ายในการผลิตไฮโดรเจน

ความมุ่งหมายของการประดิษฐ์นี้คือ การประดิษฐ์เครื่องปฏิกรณ์แบบเยื่อแผ่นประเภทโมโนลิทควบคู่ความร้อน ที่สามารถผลิตไฮโดรเจนบริสุทธิ์สูงซึ่งเหมาะสมสำหรับการใช้งานกับเซลล์เชื้อเพลิงโดยตรง และมีขนาดเล็กสามารถใช้งานได้หลากหลายได้ทั้งในระบบเคลื่อนที่และไม่เคลื่อนที่ เช่น ภายในรถยนต์ โรงงานขนาดเล็ก สถานที่เติมเชื้อเพลิงไฮโดรเจน เป็นต้น

คำอธิบายรูปเขียนโดยย่อ

รูปที่ 1 แสดงเครื่องปฏิกรณ์แบบเยื่อแผ่นประเภทโมโนลิทควบคู่ความร้อนสำหรับผลิตไฮโดรเจน

รูปที่ 2 ลักษณะของช่องสำหรับการเกิดปฏิกิริยาสำหรับผลิตไฮโดรเจน (R) ปฏิกิริยาคายความร้อน (C) และการแยกไฮโดรเจนผ่านเยื่อเลือกผ่าน (M) ภายในเครื่องปฏิกรณ์แบบเยื่อแผ่นประเภทโมโนลิทควบคู่ความร้อน

รูปที่ 3 การเรียงแบบสลับช่องตามระนาบ ของกระบวนการเกิดปฏิกิริยาสำหรับผลิตไฮโดรเจน (R, R1, R2) ปฏิกิริยาคายความร้อน (C, C1, C2) และการแยกไฮโดรเจนผ่านเยื่อเลือกผ่าน (M, M1, M2) ภายในเครื่องปฏิกรณ์แบบเยื่อแผ่นประเภทโมโนลิทควบคู่ความร้อน

รูปที่ 4 การจัดเรียงแบบสลับช่องโดยสมบูรณ์ ของกระบวนการเกิดปฏิกิริยาสำหรับผลิตไฮโดรเจน (R, R1, R2) ปฏิกิริยาคายความร้อน (C, C1, C2) และการแยกไฮโดรเจนผ่านเยื่อเลือกผ่าน (M, M1, M2) ภายในเครื่องปฏิกรณ์แบบเยื่อแผ่นประเภทโมโนลิทควบคู่ความร้อน

การเปิดเผยการประดิษฐ์โดยสมบูรณ์

รูปที่ 1 แสดงเครื่องปฏิกรณ์แบบเยื่อแผ่นประเภทโมโนลิทควบคู่ความร้อนสำหรับการผลิตไฮโดรเจน ซึ่งมีลักษณะเป็นโครงสร้างโมโนลิท ซึ่งส่วนมากผลิตจากคอร์เดียไรท์ (Cordierite, $2MgO_2Al_2O_35SiO_2$) โดยวัสดุนี้มีการขยายตัวทางความร้อนต่ำทำให้เหมาะสมกับการใช้งานที่อุณหภูมิสูง นอกจากนี้โครงสร้างโมโนลิทยังสามารถผลิตจากวัสดุอื่น เช่น อะลูมินา (Alumina) ทองแดง เป็นต้น ภายในโครงสร้างโมโนลิท (1) ประกอบด้วยช่องเหลี่ยมหรือกลมจำนวนหนึ่งแสดงในพื้นที่หน้าตัด (2)

รูปที่ 2 แสดงประเภทของช่องที่จัดเรียงอยู่ภายในเครื่องปฏิกรณ์แบบเยื่อแผ่นประเภทโมโนลิทควบคู่ความร้อน ซึ่งประกอบด้วย

ช่อง R เป็นช่องสำหรับทำปฏิกิริยาสำหรับผลิตไฮโดรเจนจากเชื้อเพลิง ภายในช่อง R ตัวเร่งปฏิกิริยาสำหรับปฏิกิริยาผลิตไฮโดรเจน (3) เช่น โลหะผสมของนิกเกิลหรือนิกเกิลออกไซด์ และเยื่อเลือกผ่านสำหรับแยกไฮโดรเจน (4) เช่น โลหะผสมของพาลาเดียมหรือพาลาเดียมซิลเวอร์ เคลือบอยู่บนผนังของโครงสร้างโมโนลิท โดยการเคลือบควรเคลือบตัวเร่งปฏิกิริยาซ้อนทับชั้นของเยื่อเลือกผ่านที่เคลือบอยู่บนผนังของโครงสร้างโมโนลิท เพื่อป้องกันการเกิดความเสียหายของเยื่อเลือกผ่านขณะทำปฏิกิริยา

ช่อง C เป็นช่องสำหรับเป็นแหล่งพลังงานของเครื่องปฏิกรณ์แบบเยื่อแผ่นประเภทโมโนลิทควบคู่ความร้อน ซึ่งได้จากปฏิกิริยาคายความร้อน เช่น การเผาไหม้เชื้อเพลิง หรือ การออกซิเดชันบางส่วน โดยอาจทำปฏิกิริยาร่วมกับตัวเร่งปฏิกิริยา ตัวเร่งปฏิกิริยา (5) เช่น โลหะแพลทินัม ถูกใช้สำหรับการเผาไหม้ พลังงานที่ได้จากปฏิกิริยาคายความร้อนเกิดขึ้นบนผนังของโครงสร้างและสามารถถ่ายเทไปสู่ช่อง R โดยตรงด้วยการนำความร้อน ทำให้ภายในเครื่องปฏิกรณ์แบบเยื่อแผ่นประเภทโมโนลิทควบคู่ความร้อนมีการกระจายความร้อนที่ดีและช่วยลดการเกิดจุดร้อนและจุดเย็น (Hot and cold spots) ภายในโครงสร้าง

ช่อง M เป็นช่องทางผ่านของผลิตภัณฑ์ซึ่งเป็นไฮโดรเจนบริสุทธิ์สูง ที่ได้จากการแพร่ผ่านเยื่อเลือกผ่านของช่อง R และผนังโครงสร้างของโมโนลิทซึ่งมีรูพรุน การแพร่ของไฮโดรเจนถูกควบคุมด้วยความต่างของความดันระหว่างช่อง R และช่อง M ทำให้ไม่จำเป็นต้องใช้แก๊สกวาด (Sweep gas) จำพวกแก๊สเฉื่อยเช่น แก๊สไนโตรเจน ดังที่ใช้ในเครื่องปฏิกรณ์แบบเยื่อแผ่นทั่วไป ดังนั้นภายในช่อง M จะมีพื้นที่ว่างยังไม่เกิดการแยกไฮโดรเจนในบริเวณขาเข้าของช่อง M ดังนั้นบริเวณนี้จึงถูกพัฒนาเป็นส่วนยึดจับ (6) ของหัวจ่าย เพื่อเพิ่มความแข็งแรงในการยึดจับ ป้องกันการสะสมของไฮโดรเจนในบริเวณขาเข้าและป้องกันการรั่วของแก๊สซึ่งอาจก่อให้เกิดอันตรายได้

โดยการจัดเรียงของช่อง R, C และ M ภายในเครื่องปฏิกรณ์แบบเยื่อแผ่นประเภทโมโนลิทควบคู่ความร้อน แบ่งออกเป็น 2 แบบ คือ การจัดเรียงแบบสลับช่องตามระนาบ หรือ การจัดเรียงแบบสลับช่องโดยสมบูรณ์

รูปที่ 3 แสดงการจัดเรียงแบบสลับช่องตามระนาบ ของช่อง R, C และ M ภายในเครื่องปฏิกรณ์แบบเยื่อแผ่นประเภทโมโนลิทควบคู่ความร้อน โดยการเรียงแบบสลับช่องตามระนาบ (7) ช่องชนิดเดียวกันจะถูกเรียงในระนาบเดียวกัน โดยแต่ละระนาบจะเปลี่ยนชนิดของช่องสลับกันไป ทำให้สูญเสียพื้นที่บางส่วนสำหรับการถ่ายเทความร้อนและการแยกไฮโดรเจน ซึ่งส่งผลต่อประสิทธิภาพในการผลิตไฮโดรเจน การจัดเรียงแบบสลับช่องตามระนาบนี้ อาจจัดรวมกันเป็นกลุ่มของช่อง R, C และ M (8) หรือในกรณีที่รวมกระบวนการมากกว่า สาม กระบวนการขึ้นไป (9) คือมีช่องทำปฏิกิริยาสำหรับผลิตไฮโดรเจนจากเชื้อเพลิง R1 และ R2 ช่องสำหรับเป็นแหล่งพลังงาน C1 และ C2 และช่องทางผ่านของผลิตภัณฑ์ M1 และ M2

รูปที่ 4 แสดงการจัดเรียงแบบสลับช่องโดยสมบูรณ์ ของช่อง R, C และ M ภายในเครื่องปฏิกรณ์แบบเยื่อแผ่นประเภทโมโนลิทควบคู่ความร้อน โดยการจัดเรียงแบบสลับช่องโดยสมบูรณ์ (10) ช่องแต่ละชนิดถูกจัดเรียงสลับกันไปคล้ายตารางหมากรุก ทำให้พื้นที่ทั้งหมดถูกใช้สำหรับการถ่ายเทความร้อนและการแยกไฮโดรเจน ซึ่งส่งผลทำให้มีประสิทธิภาพในการผลิตไฮโดรเจนสูงขึ้นอย่างชัดเจน การจัดเรียงแบบสลับช่องโดยสมบูรณ์นี้ อาจจัดรวมกันเป็นกลุ่มของช่อง R, C และ M (11) หรือในกรณีที่รวมกระบวนการมากกว่า สาม กระบวนการขึ้นไป (12) คือมีช่องทำปฏิกิริยาสำหรับผลิตไฮโดรเจนจากเชื้อเพลิง R1 และ R2 ช่องสำหรับเป็นแหล่งพลังงาน C1 และ C2 และช่องทางผ่านของผลิตภัณฑ์ M1 และ M2

สำหรับการใช้งานเครื่องปฏิกรณ์แบบเยื่อแผ่นประเภทโมโนลิทควบคู่ความร้อน เชื้อเพลิงเช่น ก๊าซธรรมชาติ แก๊สชีวภาพ เมทานอล เอทานอล น้ำมันดีเซล แอมโมเนีย ถ่านหิน เป็นต้น สามารถนำมาใช้เป็นสารตั้งต้นในกระบวนการผลิตไฮโดรเจน สารที่เหลือจากการทำปฏิกิริยาซึ่งประกอบด้วยแก๊สสังเคราะห์ (Synthesis gas, Syngas) สามารถนำมาใช้เป็นเชื้อเพลิงร่วมสำหรับปฏิกิริยาคายความร้อนเพื่อเพิ่มประสิทธิภาพในการผลิต

นอกจากนี้การเพิ่มความดันในการทำปฏิกิริยาสำหรับผลิตไฮโดรเจน ในช่อง R ส่งผลให้มีความต่างของความดันระหว่างช่อง R และช่อง M มากขึ้น ทำให้สามารถแยกไฮโดรเจนได้ปริมาณมากขึ้นและช่วยเลื่อนสมดุลของปฏิกิริยาไปข้างหน้าทำให้สามารถผลิตไฮโดรเจนได้เพิ่มขึ้น แต่อย่างไรก็ตามการเพิ่มความดันถูกจำกัดด้วยความแข็งแรงของโครงสร้างโมโนลิท

อัตราการไหลของเชื้อเพลิงสำหรับปฏิกิริยาสำหรับผลิตไฮโดรเจน และปฏิกิริยาคายความร้อนควรถูกควบคุมให้อยู่ในปริมาณที่เหมาะสม เนื่องจากปริมาณเชื้อเพลิงทั้งสองส่วนส่งผลต่ออุณหภูมิในการเกิดปฏิกิริยาภายในเครื่องปฏิกรณ์ โดยถ้าอุณหภูมิสำหรับการทำปฏิกิริยาต่ำเกินไปทำให้ผลิตไฮโดรเจนได้น้อยเนื่องจากสารตั้งต้นไม่สามารถทำปฏิกิริยาได้สมบูรณ์ แต่ถ้าอุณหภูมิสำหรับการทำปฏิกิริยาสูงเกินไปทำให้เกิดปฏิกิริยาย้อนกลับของปฏิกิริยาวอเตอร์ แก๊ส ชิฟต์ (Reverse water gas shift reaction) ทำให้ผลิตไฮโดรเจนได้ลดลง

วิธีการในการประดิษฐ์ที่ดีที่สุด

เหมือนกับที่ได้กล่าวมาแล้วในหัวข้อการเปิดเผยการประดิษฐ์โดยสมบูรณ์

ข้อถือสิทธิ

1. เครื่องปฏิกรณ์แบบเยื่อแผ่นประเภทโมโนลิทควบคู่ความร้อนสำหรับผลิตไฮโดรเจน มีโครงสร้างภายในเป็นโครงสร้างโมโนลิท (1) ซึ่งประกอบด้วยช่องเหลี่ยมหรือกลมจำนวนหนึ่งแสดงในพื้นที่หน้าตัด (2) โดยแบ่งช่องออกเป็น สาม ประเภท จัดเรียงอยู่ภายในเครื่องปฏิกรณ์แบบเยื่อแผ่นประเภทโมโนลิทควบคู่ความร้อน ประกอบด้วย

ช่อง R เป็นช่องสำหรับทำปฏิกิริยาสำหรับผลิตไฮโดรเจนจากเชื้อเพลิง ภายในช่อง R ตัวเร่งปฏิกิริยา (3) และเยื่อเลือกผ่านสำหรับแยกไฮโดรเจน (4) เคลือบอยู่บนผนังของโครงสร้างโมโนลิท โดยตัวเร่งปฏิกิริยาเคลือบ หรือ บรรจุอยู่บนชั้นของเยื่อเลือกผ่าน

ช่อง C เป็นช่องสำหรับเป็นแหล่งพลังงานของเครื่องปฏิกรณ์แบบเยื่อแผ่นประเภทโมโนลิทควบคู่ความร้อน ซึ่งได้จากปฏิกิริยาคายความร้อนโดยทำปฏิกิริยาร่วมกับตัวเร่งปฏิกิริยา (5) พลังงานที่ได้นี้เกิดขึ้นบนผนังของโครงสร้างและสามารถถ่ายเทไปสู่ช่อง R โดยตรงด้วยการนำความร้อน

ช่อง M เป็นช่องทางผ่านของผลิตภัณฑ์ซึ่งเป็นแก๊สไฮโดรเจนบริสุทธิ์สูง ที่ได้จากการแพร่ผ่านเยื่อเลือกผ่านของช่อง R และผนังโครงสร้างของโมโนลิทซึ่งมีรูพรุน ภายในช่อง M มีพื้นที่ว่างบริเวณขาเข้าของช่อง M (6) เนื่องจากเป็นช่วงที่ยังไม่เกิดการแยกไฮโดรเจน

2. เครื่องปฏิกรณ์แบบเยื่อแผ่นประเภทโมโนลิทควบคู่ความร้อนสำหรับผลิตไฮโดรเจน ตามข้อถือสิทธิที่ 1 ที่ซึ่ง พื้นที่ว่างบริเวณขาเข้าของช่อง M (6) เป็นส่วนการยึดจับ เพื่อยึดจับหรือเพิ่มความแข็งแรงในการยึดจับระหว่างหัวจ่ายกับเครื่องปฏิกรณ์แบบเยื่อแผ่นประเภทโมโนลิทควบคู่ความร้อนหรือเครื่องปฏิกรณ์แบบเยื่อแผ่น

3. เครื่องปฏิกรณ์แบบเยื่อแผ่นประเภทโมโนลิทควบคู่ความร้อนสำหรับผลิตไฮโดรเจน ตามข้อถือสิทธิที่ 1 หรือ 2 ข้อใดข้อหนึ่ง ที่ซึ่งพื้นที่ว่างบริเวณขาเข้าของช่อง M (6) เป็นส่วนป้องกันการสะสมของไฮโดรเจนในบริเวณขาเข้าหรือป้องกันการรั่วของแก๊ส ภายในเครื่องปฏิกรณ์แบบเยื่อแผ่นประเภทโมโนลิทควบคู่ความร้อนหรือเครื่องปฏิกรณ์แบบเยื่อแผ่น

4. เครื่องปฏิกรณ์แบบเยื่อแผ่นประเภทโมโนลิทควบคู่ความร้อนสำหรับผลิตไฮโดรเจน ตามข้อถือสิทธิที่ 1 ที่ซึ่ง การจัดเรียงของช่อง R, C และ M ภายในเครื่องปฏิกรณ์แบบเยื่อแผ่นประเภทโมโนลิทควบคู่ความร้อน เลือกได้จาก การจัดเรียงแบบสลับช่องตามระนาบ (7, 8, 9) หรือ การจัดเรียงแบบสลับช่องโดยสมบูรณ์ (10, 11, 12)

5. เครื่องปฏิกรณ์แบบเยื่อแผ่นประเภทโมโนลิทควบคู่ความร้อนสำหรับผลิตไฮโดรเจน ตามข้อถือสิทธิที่ 4 ที่ซึ่ง การจัดเรียงแบบสลับช่องตามระนาบ เลือกได้จาก การรวมกระบวนการ (7) หรือกลุ่มของกระบวนการต่างๆสำหรับทำปฏิกิริยาใดๆ ตั้งแต่สามกระบวนการขึ้นไป (8,9)

6. เครื่องปฏิกรณ์แบบเยื่อแผ่นประเภทโมโนลิทควบคู่ความร้อนสำหรับผลิตไฮโดรเจน ตามข้อถือสิทธิที่ 4 ที่ซึ่ง การจัดเรียงแบบสลับช่องโดยสมบูรณ์ เลือกได้จาก การรวมกระบวนการ (10) หรือกลุ่มของกระบวนการต่างๆสำหรับทำปฏิกิริยาใดๆ ตั้งแต่สามกระบวนการขึ้นไป (11,12)

บทสรุปการประดิษฐ์

การประดิษฐ์นี้เกี่ยวข้องกับเครื่องปฏิกรณ์แบบเยื่อแผ่นประเภทโมโนลิทควบคู่ความร้อน ซึ่งใช้โครงสร้างโมโนลิทเชิงพาณิชย์ในการรวมกระบวนการสำหรับผลิตไฮโดรเจนไว้ภายในโครงสร้างโมโนลิท ซึ่งประกอบด้วย ปฏิกิริยาคายความร้อนเพื่อเป็นแหล่งพลังงาน ปฏิกิริยาสำหรับผลิตไฮโดรเจนจากเชื้อเพลิง และการแยกไฮโดรเจนผ่านเยื่อเลือกผ่าน กระบวนการผลิตไฮโดรเจนถูกจัดเรียงภายในโครงสร้างโมโนลิท ซึ่งแบ่งออกเป็น การจัดเรียงแบบสลับช่องตามระนาบ หรือ การจัดเรียงแบบสลับช่องโดยสมบูรณ์ โดยการจัดเรียงมีอิทธิพลต่อประสิทธิภาพในการผลิตไฮโดรเจน นอกจากนี้ยังมีการใช้ประโยชน์จากพื้นที่ว่างบริเวณขาเข้าของช่อง M ซึ่งถูกพัฒนาเป็นส่วนยึดจับของหัวจ่ายเพื่อเพิ่มความแข็งแรงในการยึดจับ การรวมกระบวนการผลิตไฮโดรเจนไว้ด้วยกัน ส่งผลให้ผลิตไฮโดรเจนได้มีประสิทธิภาพเพิ่มขึ้น ไฮโดรเจนที่ผลิตได้มีความบริสุทธิ์สูง ค่าใช้จ่ายในการผลิตไฮโดรเจนลดลง และเครื่องปฏิกรณ์นี้มีขนาดเล็กซึ่งสามารถใช้งานได้หลากหลายทั้งในระบบเคลื่อนที่และไม่เคลื่อนที่ เช่น ภายในรถยนต์ โรงงานขนาดเล็ก สถานที่เติมเชื้อเพลิงไฮโดรเจน เป็นต้น

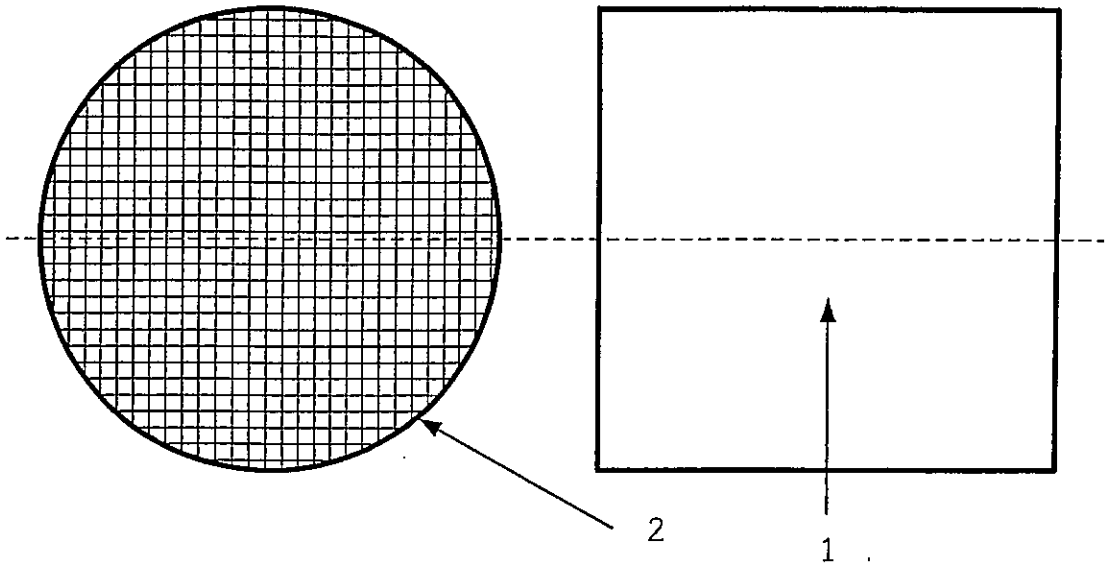
2
1

รูปที่ 1

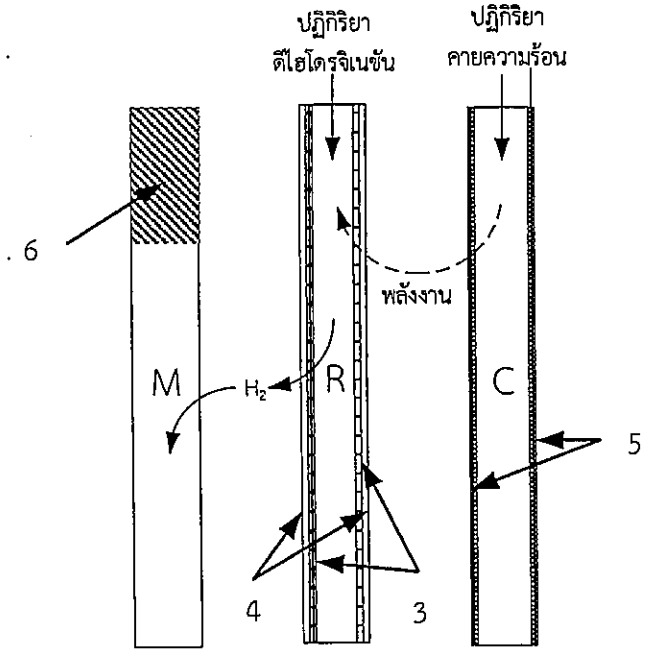
ปฏิกิริยา
ดีไฮโดรจิเนชัน
ปฏิกิริยา
คายความร้อน
6
พลังงาน
M
H_2
R
C
5
4
3

รูปที่ 2

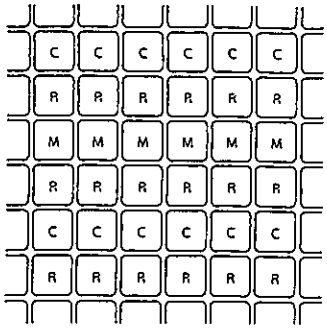

7

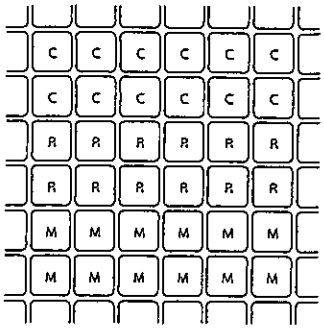

8

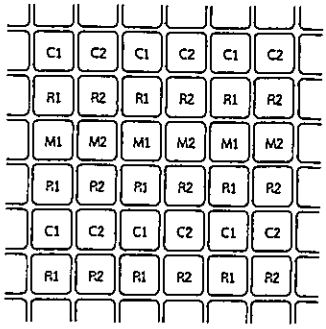

9

รูปที่ 3

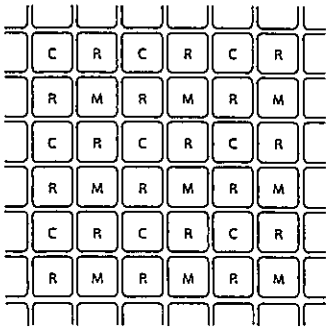

10

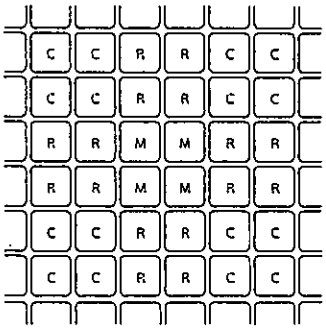

11

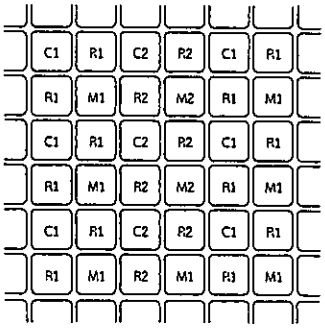

12

รูปที่ 4